SECOND EDITION

Fluid Film Lubrication

ANDRAS Z. SZERI

CAMBRIDGE

This page intentionally left blank

Fluid Film Lubrication

Second Edition

Fluid film bearings are machine elements that should be studied within the broader context of tribology. The three subfields of tribology – friction, lubrication, and wear – are strongly interrelated. The last decade has witnessed significant advances in the area of fluid film lubrication and its applications, and this second edition offers a look at some of these advances. This edition adds to the fundamentals of fluid film lubrication a discourse on surface effects and the inclusion of treatment of flow with significant inertia within the section on turbulence. Basic ideas of the multigrid method are conveyed along with multilevel multi-integration in the treatment of elastohydrodynamic lubrication. The chapter on lubrication with non-Newtonian fluids discusses the impact of the so-named qualitative EHL. This chapter also contains a thorough discussion of blood as a lubricant, with a view of the application of lubrication theory to LVADs. New chapters have been included on ultra-thin films, both liquid and gaseous, and lubrication of articulating joints and their replacement. Some of the most recent literature is discussed.

Andras Z. Szeri is the Robert Lyle Spencer Professor of Mechanical Engineering at the University of Delaware. He is a member of ASME and AAM and is on the editorial board of *Microsystem Technologies* and *Applied Mechanics and Engineering*.

Fluid Film Lubrication

Second Edition

ANDRAS Z. SZERI
University of Delaware

CAMBRIDGE
UNIVERSITY PRESS

CAMBRIDGE UNIVERSITY PRESS
Cambridge, New York, Melbourne, Madrid, Cape Town, Singapore,
São Paulo, Delhi, Dubai, Tokyo, Mexico City

Cambridge University Press
32 Avenue of the Americas, New York, NY 10013-2473, USA

www.cambridge.org
Information on this title: www.cambridge.org/9780521898232

First published 1998
First paperback edition 2005
Second edition first published 2011

Printed in the United States of America

A catalog record for this publication is available from the British Library.

Library of Congress Cataloging in Publication data

Szeri, A. Z.
Fluid film lubrication / Andras Z. Szeri. – 2nd ed.
p. cm.
Includes bibliographical references and index.
ISBN 978-0-521-89823-2 (hardback)
1. Fluid-film bearings. I. Title.
TJ1073.5.S97 2011
621.8′22–dc22 2010046243

ISBN 978-0-521-89823-2 Hardback

To my wife Mary for her continued encouragement

Contents

Preface to the Second Edition

For the successful operation of mechanical devices, from spinning computer disks to automobiles to large electric generators of nuclear power stations, it is essential that the components that are destined to move relative to one another do so with low friction and rate of wear. This is made possible through appropriate design and utilization of fluid film bearings. Traditionally, fluid film lubrication was a purely mechanical subject, but with the emergence of bioengineering, the technology also finds application in lubricating artificial joints, contact lenses, and mechanical heart pumps, to name a few. In this second edition, I have tried to give a flavor of some of these advances. The contents of the first edition remain valid by and large, as they deal with the fundamentals that have changed little. Thus, this edition represents addition, rather than revision, of material. Chapter 2 is rewritten, however, to align it with a more complete discussion of constitutive theory. Chapter 3, the chapter covering thick-film lubrication, features a section on surface texturing; another section treats surface roughness in a more thorough manner. The chapter on turbulence includes the handling of flow with significant inertia. In the treatment of elastohydrodynamic lubrication, covered in Chapter 8, I tried to convey basic ideas of the multigrid method and touched on multilevel multi integration. The chapter on lubrication with non-Newtonian fluids discusses the "qualitative" EHL, and contains a discourse on lubrication with piezoviscous fluids, relative to the Reynolds equation. This chapter also comprises a thorough discussion of blood as lubricant, with a view to the application of lubrication theory to artificial organs. Chapters 12 and 13 are new. In the first of these, I concentrate on ultra-thin films, both liquid and gaseous. The chapter discusses and classifies recent research results and, particularly for gas films but also for liquid films, outlines design principles. The chapter closes with the listing of 92 up-to-date references. The last chapter, Biotribology, is devoted to lubrication of the hip joint. Its two principal sections discuss lubrication of natural joints and artificial joints. The first of these presents the various theories of natural joint lubrication including microelastohydrodynamic lubrication, biphasic models, and boundary lubrication. The second section lists the various existing constructs of total hip replacement and their relative performance. This last chapter surveys 60 references in all.

Compared to the first edition, the second edition contains more than 70 new pictorial representations of recent research results. I trust that the reader will find these additions worthwhile.

Preface to the First Edition

Fluid film bearings are machine elements which should be studied within the broader context of tribology, "the science and technology of interactive surfaces in relative motion and of the practices related thereto."* The three subfields of tribology – friction, lubrication, and wear – are strongly interrelated. Fluid film bearings provide but one aspect of lubrication. If a bearing is not well designed, or is operated under other than the design conditions, other modes of lubrication, such as boundary lubrication, might result, and frictional hearting and wear would also have to be considered.

Chapter 1 defines fluid film bearings within the context of the general field of tribology, and is intended as an introduction; numerous references are included, however, should a more detailed background be required. Chapters 2, 3, and 4 outline classical lubrication theory, which is based on isothermal, laminar operation between rigid bearing surfaces. These chapters can be used for an advanced undergraduate or first-year graduate course. They should, however, be augmented with selections from Chapter 8, to introduce the students to the all-important rolling bearings, and from Chapter 9, to make the student realize that no bearing operation is truly isothermal. Otherwise, the book will be useful to the industrial practitioner and the researcher alike. Sections in small print may be omitted on first reading – they are intended for further amplification of topics. In writing this book, my intent was to put essential information into a rational framework for easier understanding. So the objective was to teach, rather than to compile all available information into a handbook. I have also included thought-provoking topics; for example, lubrication with emulsions, the treatment of which has not yet reached maturity. I expect significant advances in this area as it impacts on the environment.

The various chapters were read by Dr. M. L. Adams, Case Western Reserve University; Dr. M. Fillon, University of Poitiers, France; Dr. S. Jahanmir, National Institute for Standards and Technology; Dr. F. E. Kennedy, Dartmouth College; Mr. O. Pinkus, Sigma Inc.; Dr. K. R. Rajagopal, Texas A & M University; Dr. A. J. Szeri, University of California at Berkeley; and Dr. J. A. Tichy, Rensselaer Polytechnic Institute. However, in spite of the considerable assistance I received from various colleagues, any mistakes are mine alone.

The typing was expertly done by my daughter Maria Szeri-Leon and son-in-law Jorge Leon. I am grateful to them for their diligence and perseverance; not even their wedding interrupted the smooth flow of the project. I would also like to thank Ms. Florence Padgett, Editor at Cambridge University Press, for suggesting the project and for having confidence in me. My thanks are also due to Ms. Ellen Tirpak, Senior Project Manager at TechBooks, for providing expert editing of the manuscript.

*British Lubrication Engineering Working Group, 1966.

CHAPTER 1

Introduction

The term *tribology*, meaning the *science* and *technology of friction, lubrication*, and *wear*, is of recent origin (Lubrication Engineering Working Group, 1966), but its practical aspects reach back to prehistoric times. The importance of tribology has greatly increased during its long history, and modern civilization is surprisingly dependent on sound tribological practices.

The field of tribology affects the performance and life of all mechanical systems and provides for reliability, accuracy, and precision of many. Tribology is frequently the pacing item in the design of new mechanical systems. Energy loss through friction in tribo-elements is a major factor in limits on energy efficiency. Strategic materials are used in many tribo-elements to obtain the required performance.

Experts estimate that in 1978 over 4.22×10^6 Tjoule (or four quadrillion Btu) of energy were lost in the United States due to simple friction and wear – enough energy to supply New York City for an entire year (Dake, Russell, and Debrodt, 1986). This translates to a $20 billion loss, based on oil prices of about $30 per barrel. Most frictional loss occurs in the chemical and the primary metal industries. The metalworking industry's share of tribological losses amount to 2.95×10^4 Tjoule in friction and 8.13×10^3 Tjoule in wear; it has been estimated that more than a quarter of this loss could be prevented by using surface modification technologies to reduce friction and wear in metal working machines. The unsurpassed leader in loss due to wear is mining, followed by agriculture.

1.1 Historical Background

There is little evidence of tribological practices in the early Stone Age. Nevertheless, we may speculate that the first fires made by humans were created by using the heat of friction. In later times hand- or mouth-held bearings were developed for the spindles of drills, which were used to bore holes and start fires. These bearings were often made of wood, antlers, or bone; their recorded use covers some four millennia. Among the earliest-made bearings were door sockets, first constructed of wood or stone and later lined with copper, and potter's wheels, such as the one unearthed in Jericho, dated 2000 BC. The wheel contained traces of bitumen, which might have been used as a lubricant.

Lubricants were probably used on the bearings of chariots, which first appeared ca. 3500 BC (McNeill, 1963). One of the earliest recorded uses of a lubricant, probably water, was for transportation of the statue of Ti ca. 2400 BC. Considerable development in tribology occurred in Greece and Rome beginning in the fourth century BC, during and after the time of Aristotle. Evidence of advanced lubrication practices during Roman times is provided by two pleasure boats that sank in Lake Nemi, Italy, ca. AD 50; they contain what might be considered prototypes of three kinds of modern rolling-element bearings. The Middle Ages saw a further improvement in the application of tribological principles, as evidenced by the development of machinery such as the water mill. An excellent account

of the history of tribology up to the time of Columbus is given by Dowson (1973). See also Dowson's *History of Tribology* (Dowson, 1979).

The basic laws of friction were first deduced correctly by da Vinci (1519), who was interested in the music made by the friction of the heavenly spheres. They were rediscovered in 1699 by Amontons, whose observations were verified by Coulomb in 1785. Coulomb was able to distinguish between static friction and kinetic friction but thought incorrectly that friction was due only to the interlocking of surface asperities. It is now known that friction is caused by a variety of surface interactions. These surface interactions are so complex, however, that the friction coefficient in dry sliding still cannot be predicted.

The scientific study of lubrication began with Rayleigh, who, together with Stokes, discussed the feasibility of a theoretical treatment of film lubrication. Reynolds (1886) went even further; he detailed the theory of lubrication and discussed the importance of boundary conditions. Notable subsequent work was done by Sommerfeld and Michell, among others. However, for many years the difficulty of obtaining two-dimensional solutions to Reynolds' pressure equations impeded the application of lubrication theory to bearing design. This impediment was finally removed with the arrival of the digital computer (Raimondi and Boyd, 1958).

In contrast to friction, the scientific study of wear is more recent. As sliding wear, a term often used to define progressive removal of material due to relative motion at the surface, is caused by the same type of interaction as friction, the quantitative prediction of wear rate is fraught with the same difficulties. The situation is even more gloomy, as under normal conditions the value of the coefficient of friction between different metal pairs changes by one order of magnitude at most, while corresponding wear rates can change by several orders. Although there have been attempts to predict wear rate, Archard's formula (Archard, 1953) being perhaps the most noteworthy in this direction, for the foreseeable future at least, the designer will have to rely on experimentation and handbook data (see Peterson and Winer, 1980).

1.2 Tribological Surfaces

Even early attempts to develop a theory of friction recognized the fact that all practically prepared surfaces are rough on the microscopic scale. The aspect ratio and the absolute height of the hills, or *asperities*, and valleys one observes under the microscope vary greatly, depending on material properties and on the method of surface preparation. Roughness height may range from 0.05 μm or less on polished surfaces to 10 μm on medium-machined surfaces, to even greater values on castings. Figure 1.1 shows a size comparison of the various surface phenomena of interest in tribology.

When two solid surfaces are brought into close proximity, actual contact will be made only by the asperities of the two surfaces, specifically along areas over which the atoms of one asperity surface are within the repulsive fields of the other.[1] The *real area of contact* A_r, which is the totality of the individual asperity contact areas, is only a fraction of the *apparent*

[1]The equilibrium spacing of atoms is on the order of 0.2–0.5 nm (2–5 Angstrom); at distances less than the equilibrium spacing, the repulsive forces dominate, while at greater distances the forces of attraction are influential. The equilibrium spacing changes with temperature; macroscopically we recognize this change as thermal expansion.

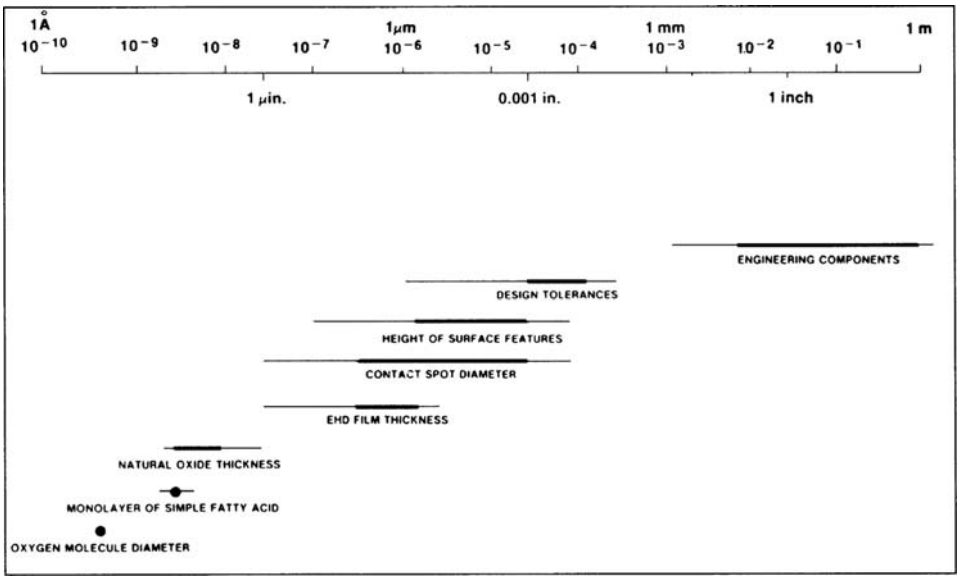

Figure 1.1. Comparative size of surface-related phenomena. (Reprinted with permission from Williamson, J. B. P. The shape of surfaces. In Booser, E. R. *CRC Handbook of Lubrication*. Copyright CRC Press, Boca Raton, Florida, © 1984.)

area of contact, perhaps as small as 1/100,000 at light loads. The areas of individual asperity contacts are typically 1 to 5 μm across and 10 to 50 μm apart.

The topography of engineering surfaces indicates features of four different length scales: (1) *error of form* is a gross deviation from shape of the machine element, (2) *waviness* is of a smaller scale and may result from heat treatment or from vibration of the workpiece or the tool during machining, (3) *roughness* represents closely spaced irregularities and includes features that are intrinsic to the process that created the surface, and (4) surface features on the *atomic scale* are important for the recording industry and in precision machining.

One of the methods used for describing surface roughness consists of drawing a fine stylus across it. The stylus is usually a conical diamond with a radius of curvature at its tip of the order of 2 μm. The movement of the stylus is amplified, and both vertical and horizontal movements are recorded electronically for subsequent statistical analysis. The instrument designed to accomplish this is the *profilometer*. Clearly, such an instrument is limited in resolution by the diameter and the radius of curvature of the tip of the stylus. A profilometer trace[2] of an engineering surface is shown in Figure 1.2.

Two modern instruments, the scanning *electron microscope* and the *transmission electron microscope* (Sherrington and Smith, 1988), have resolution higher than profilometers and are employed extensively in surface studies. *Optical interferometers*, which can record surface profiles without distortion or damage, have recently come into use thanks to advances

[2]That the vertical amplification is typically 10–1000 times greater than the horizontal one has led to the popular misconception that engineering surfaces support steep gradients. Machined surfaces have aspect ratios normally found in the topography of the Earth, the slopes rarely exceeding 5–10°; Figure 1.2 is a distortion of this.

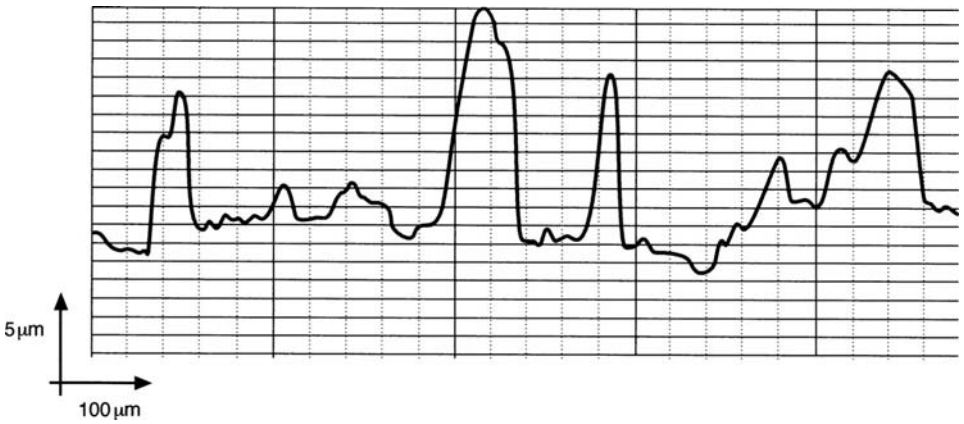

Figure 1.2. Profilometer trace of a rolled metal specimen. The vertical magnification is 20 times the horizontal magnification.

in microprocessors. Vertical resolution of the order of 1 nm has been achieved by optical interferometers, although the maximum measurable height is somewhat limited by the depth of focus of these instruments (Bhushan, Wyant, and Meiling, 1988). The *atomic force microscope* measures the forces between a probe tip and the surface and has been used for topographical measurement of surfaces on the nanometers scale. Its modification, known as the *friction force microscope* (Ruan and Bhushan, 1994) is used for friction studies on the atomic scale. Details of these recent additions to the arsenal of the surface scientist can be found in the excellent review article by Bhushan, Israelachvili, and Landman (1995).

To discuss surface roughness quantitatively, let $\xi(x)$ represent the height of the surface above an arbitrary datum at the position x, and let $\bar{\xi}$ be its mean value as depicted in Figure 1.3. Furthermore, denote by $|\eta(x)|$ the vertical distance between the actual surface at x and the mean. Surface roughness is often characterized in terms of the *arithmetic average*, R_a, of the absolute value of surface deviations from the mean

$$R_a = \frac{1}{L}\int_{-L/2}^{L/2} |\eta(x)|dx, \tag{1.1}$$

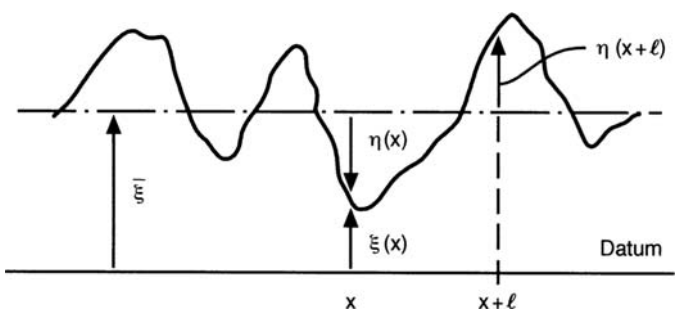

Figure 1.3. Schematics of a surface showing mean surface height, $\bar{\xi}$, and surface deviation from mean height, $\eta(x)$.

or in terms of its *standard deviation* [i.e., root mean square (rms)], R_q, defined by

$$R_q^2 = \frac{1}{L}\int_{-L/2}^{L/2} \eta^2(x)\,dx. \tag{1.2}$$

where L is the sample length.

The rms value, Eq. (1.2), is some 10–20% greater than the R_a value for many common surfaces; for surfaces with Gaussian distribution $R_q = 1.25R_a$. Typical values of R_a for metals prepared by various machining methods are: turned, 1–6 μm; course ground, 0.5–3 μm; fine ground, 0.1–0.5 μm; polished, 0.06–0.1 μm; and super finished, 0.01–0.06 μm.

Another quantity used in characterizing surfaces is the *autocorrelation function,* $R(\ell)$, it has the definition (see Figure 1.3)

$$R(\ell) = \frac{1}{L}\int_{-L/2}^{L/2} \eta(x)\eta(x+\ell)\,dx. \tag{1.3}$$

$R(\ell)$ attains its maximum value at $\ell = 0$, equal to ${R_q}^2$, then vanishes rapidly as ℓ is increased. Its normalized value, $r(\ell) = R(\ell)/R_q^2$, is called the *autocorrelation coefficient*. Peklenik (1968) analyzed surfaces that were produced by different machining techniques and proposed a surface classification based on the shape of the correlation function and the magnitude of the correlation length $\lambda_{0.5}$, defined by $R(\lambda_{0.5}) = 0.5$.

The Fourier cosine transform, $P(\omega)$, of the autocorrelation function

$$P(\omega) = \frac{2}{\pi}\int_0^\infty R(\ell)\cos(\omega\ell)\,d\ell, \tag{1.4}$$

is a quantity particularly suitable to the study of machined surfaces (see Figure 1.5), since it clearly depicts and separates strong surface periodicities that may result from the machining process (i.e., waviness).

There are other numerical characteristics of surfaces in use; to define these we make recourse to probability theory. To this end consider the random *variable* ξ, representing the height of the surface at some position x relative to an arbitrary datum, and examine the event $\xi < y$, signifying that the random variable ξ has a value less than the number y. The probability of this event occurring, designated by $P(\xi < y)$, is a function of y. Define the *integral distribution function* by $F(y) = P(\xi < y)$, then $F(-\infty) = 0$, $F(+\infty) = 1$ and $0 \le F(y) \le 1$. The random variable ξ is considered known if its integral distribution, $F(y)$, is given.

For any two numbers y_2 and y_1, where $y_2 > y_1$, the probability of the event $\xi < y_2$ is given by the sum of the probabilities that $\xi < y_1$ and $y_1 \le \xi < y_2$ or

$$\begin{aligned} P(\xi < y_2) &= P(\xi < y_1 \quad \text{or} \quad y_1 \le \xi < y_2) \\ &= P(\xi < y_1) + P(y_1 \le \xi < y_2). \end{aligned} \tag{1.5}$$

From Eq. (1.5) we find that

$$\begin{aligned} P(y_1 \le \xi < y_2) &= P(\xi < y_2) - P(\xi < y_1) \\ &= F(y_2) - F(y_1), \end{aligned} \tag{1.6}$$

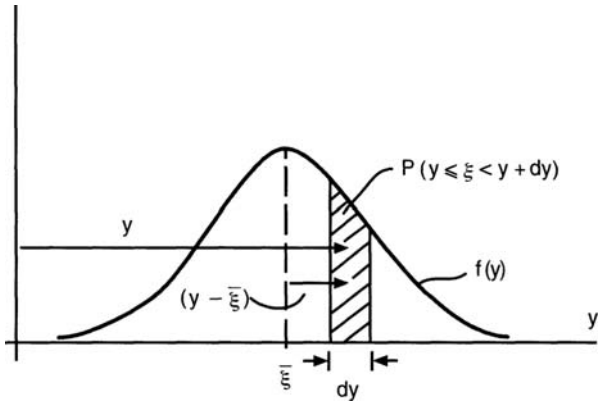

Figure 1.4. Illustration of the probabilistic terminology used.

In the case of a continuous random quantity the distribution function is differentiable. Define the *probability density function* or *probability distribution* by

$$f(y) = \lim_{\Delta y \to 0} \frac{F(y + \Delta y) - F(y)}{\Delta y}. \tag{1.7}$$

From here we can show that the probability that the random variable ξ has a value between y and $y + dy$ is

$$P(y \leq \xi < y + dy) = F(y + dy) - F(y) = f(y)\, dy,$$

and that the probability that ξ is located between the numbers a and b is

$$P(a \leq \xi < b) = \int_a^b f(y)\, dy.$$

Instead of the probability density function $f(y)$ itself, its various moments are often employed. The first *initial moment*, given by

$$\bar{\xi} = \int_{-\infty}^{\infty} y f(y)\, dy, \tag{1.8}$$

is the *mean value* of the random variable ξ (Figure 1.4). It is equivalent to R_a of Eq. (1.1).

The fluctuation about the mean can now be defined by $\eta = \xi - \bar{\xi}$; this is the (random) quantity appearing in Eqs. (1.1) and (1.2).

The first *central moment*, i.e., the moment about the mean, of the probability density function is zero. Its second central moment

$$\sigma^2 = \int_{-\infty}^{\infty} (y - \bar{\xi})^2 f(y)\, dy \tag{1.9}$$

is nonnegative, and it is called the *variance* of the random variable ξ. The square root of the variance is termed the *standard deviation* and is equivalent to the rms. of the deviation from the mean, $\sigma = R_q$.

Many variables that express the results of physical, biological, or medical experiments are, at least to first approximation, distributed according to

$$f(y) = \frac{1}{\sigma\sqrt{2\pi}} \exp[-(y - \bar{\xi})^2 / 2\sigma^2], \tag{1.10}$$

the so-called *normal* or *Gaussian* distribution. For this reason, the normal distribution has played an important role in the development of statistical theory, and one frequently

encounters Eq. (1.10) in applications. We note from Eq. (1.10) that if the random variable ξ is normally distributed, it is characterized completely by its mean value $\bar{\xi}$ and its standard deviation σ. The simplicity in representation this affords is the reason why there is often great compulsion to declare a distribution Gaussian even though it may deviate from Eq. (1.10).

Other statistical quantities in use for surface characterization are the third and fourth (nondimensional) central moments, the *skewness, Sk*, and the *kurtosis* or "hump," *K*, respectively

$$Sk = \frac{1}{\sigma^3}\int_{-\infty}^{\infty}(y-\bar{\xi})^3 f(y)\,dy, \quad K = \frac{1}{\sigma^4}\int_{-\infty}^{\infty}(y-\bar{\xi})^4 f(y)\,dy. \tag{1.11}$$

Both *Sk* and *K* are dimensionless numbers; $Sk = 0$ indicates perfect symmetry, while *K* is small for a flat, broad distribution. For normal distribution $Sk = 0$ and $K = 3$.

There are many ways to statistically characterize surface roughness. Which of the characterizations is best is application dictated.

It has been shown recently (Sayles and Thomas, 1978) that the value of the various averages defined here changes with the sampling length *L*, i.e., surface roughness is a nonstationary random function of position. It is then more amenable to treatment by fractal methods (Majumdar and Bhushan, 1990; Wang and Komvopoulos, 1994).

Figure 1.5 shows statistical characteristics of some machined surfaces:

Manufacturing processes	R_a (μm)	σ (μm)	*Sk*	*K*	Peak to valley height (μm)	Figure
Shaping, fine	8.0	11.0	0	2.8	47.0	1.5 (a)
Milling	2.3	2.7	+0.22	2.4	13.0	1.5 (b)
Surface grinding	1.0	1.3	+0.17	3.1	15.0	1.5 (c)
Superfinish	0.18	0.25	+0.32	5.9	1.6	1.5 (d)

The asperity-height distribution of many engineering surfaces is approximately Gaussian. Several surface-finishing processes, such as bead-blasting, which are the cumulative result of a large number of random happenings, will encourage a Gaussian distribution.[3] Other processes, including wear, will destroy it. Figure 1.6 follows such a process. A mild steel pad lubricated with SAE-20 oil was worn against a finely ground hard steel flat (N.B., when plotted on probability paper, the Gaussian distribution appears as a straight line).

1.3 Friction

If two solid bodies, in direct or indirect surface contact, are made to slide relative to one another there is always a resistance to the motion called friction. Friction is beneficial in many instances, and we may even try to increase it. However, in other cases friction is energy consuming, and we endeavor to decrease it, although it may never be eliminated entirely.

[3] Let the *n* random variables $\xi_1, \ldots, \xi_n$ be independent. Then the *central limit theorem* asserts, under very general conditions, that in the limit as $n \to \infty$ the standardized sum $(\xi - \bar{\xi})/\sigma$ approaches Gaussian distribution (Cramer, 1955). Here $\bar{\xi} = \bar{\xi}_1 + \cdots + \bar{\xi}_n$, $\sigma^2 = \sigma_1^2 + \cdots + \sigma_n^2$ and $\xi = \xi_1 + \cdots + \xi_n$.

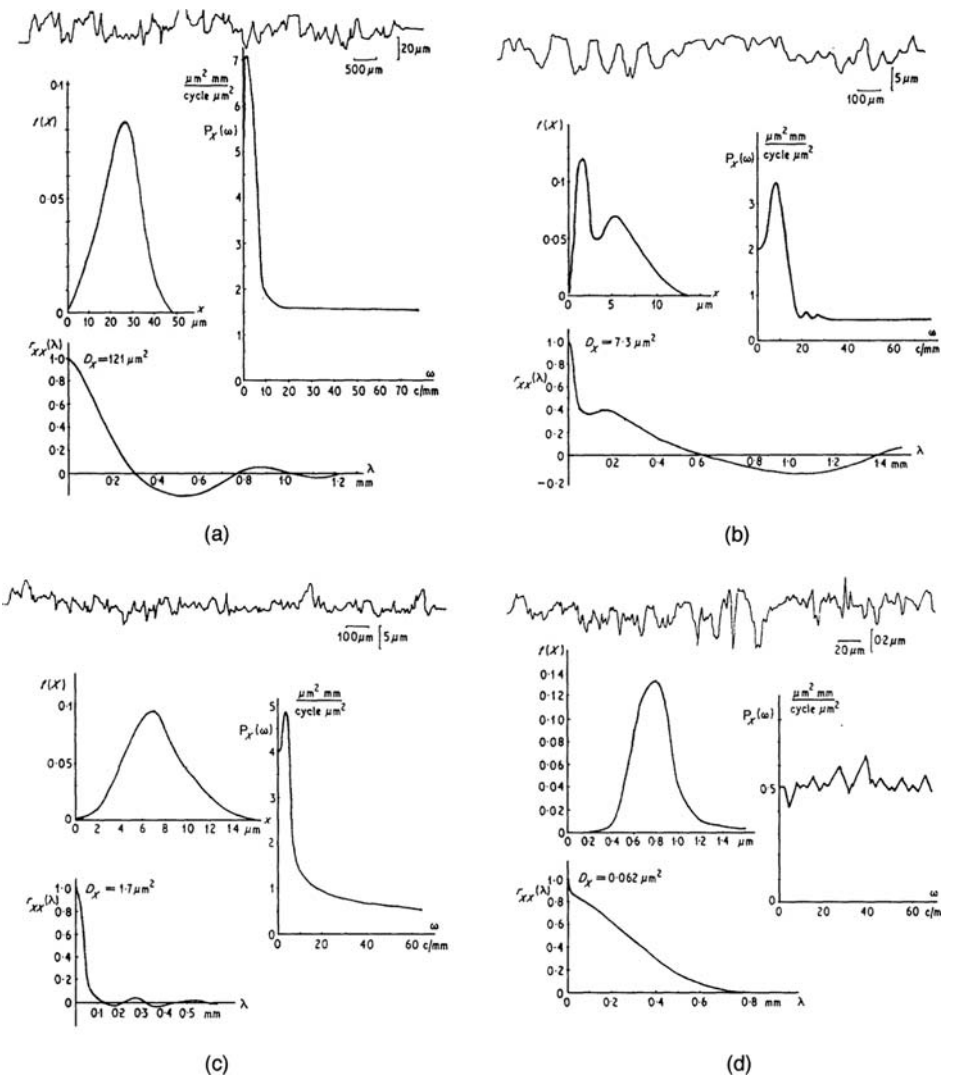

Figure 1.5. Examples of engineering surfaces (a) fine shaped; (b) milled; (c) surface ground (d) superfinished: their distributions, autocorrelation functions, power spectra. (Reprinted by permission of the Council of the Institution of Mechanical Engineers from Peklenik, J. New developments in surface characterization and measurements by means of random process analysis, *Proc. Inst. Mech. Engrs.* **182**, Pt. 3K, 108–126, 1968.)

Friction is present in all machinery, and it converts part of the useful kinetic energy to heat, thus decreasing the overall efficiency of the machine. About 30% of the power in an automobile (Hershey, 1966) and about 1.5% in a modern turbojet engine is wasted through friction. The two journal bearings of a large generator dissipate perhaps 0.75 MW or more. In 1951, G. Vogelpohl estimated that one-third to one-half of the world's energy production is consumed by friction (Fuller, 1956). Not all friction is undesirable, however, and in numerous instances we promote it, e.g., in brakes.

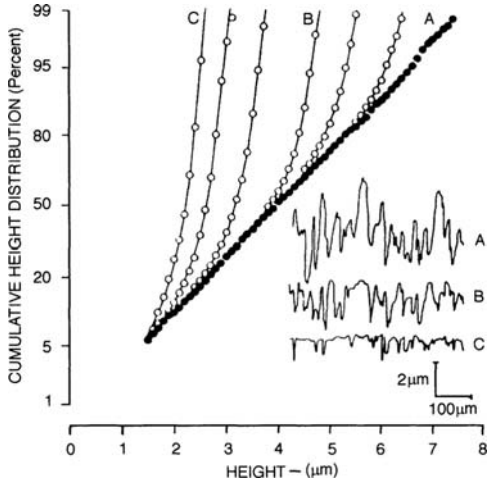

Figure 1.6. The effect of wear. The initial height distribution (A) and six non-Gaussian distributions (open circles) of a bead blasted surface represent, from right to left, progressive states. Height distributions of this form are typical of those created by stratified secondary preparation processes. (Reprinted with permission from Williamson, J. B. P. The shape of surfaces. In Booser, E. R. *CRC Handbook of Lubrication*. Copyright CRC Press, Boca Raton, Florida, © 1984.)

Laws of Friction

The two basic laws of friction:

1. Friction force F is proportional to the normal force W between surfaces,
2. Friction force is independent of the (apparent) area of contact,

were first deduced by da Vinci (1519) and discussed by Amontons (1699). Coulomb (1785) verified these laws experimentally.[4] Coulomb's observation that "kinetic friction is nearly independent of the sliding speed" is at times referred to as the third law of friction. The laws of friction have remained intact for more than 400 years, and even modern experimental research supports them in numerous cases.

This is not true, however, for the origin of friction as discussed by Coulomb. At first Coulomb inclined toward the view that friction is produced by molecular adhesion between the interacting surfaces, which is somewhat in line with present-day theories. Later Coulomb rejected this in favor of the view that friction is produced by interlocking surface asperities. According to this theory, the frictional force is the force required to lift the load over the asperities. Considering that sliding down the asperities releases as much energy as was spent on climbing up, Coulomb's friction is nondissipative, as was first pointed out by Leslie in 1804.

[4]To derive Amontons' laws, we need the assumption that the real area of contact is proportional to the normal load $A_r = qW$, where q is a constant. If now we denote the friction force per unit area by τ, we have for the friction force $F = \tau A_r$, and Amontons' laws follow at once. In the adhesion theory of friction of Bowden and Tabor (1986), the constant q is made equal to the yield pressure p_0.

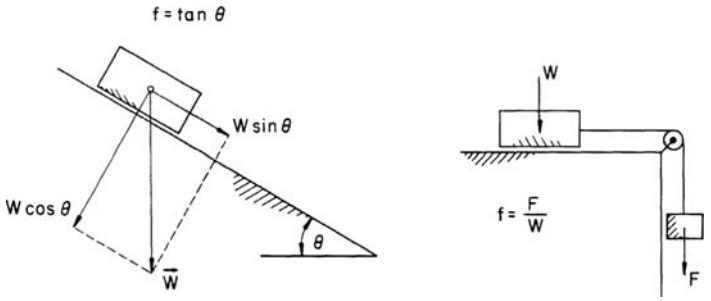

Figure 1.7. Elementary methods of measuring friction.

Most current theories recognize that frictional force in metals arises from three sources: (1) the force necessary to shear *adhesive junctions*, formed at the real area of contact between the asperities; (2) the deformation force, due to the *ploughing* of the asperities of the harder metal through the asperities of the softer one; and (3) *asperity deformation*, which is responsible for the static coefficient of friction – Suh (1986) lists the force required for this as the third source of frictional force. Though these three forces, and the three effects causing them, are not independent, it is customary to treat friction as a result of adhesion interactions, plowing interactions, and asperity deformations. In elastomers, elastic and viscoelastic effects dominate, while in ceramics the type of bonding (ionic in MgO and Al_2O_3 and covalent in TiC, diamond, and SiC) limits plastic flow and the high plastic strains associated with junction growth, at room temperature.

The idea of formation of adhesive junctions (cold welding) over the area of real contact seems frivolous at first, until one considers ultraclean metallic surfaces. When such surfaces are brought together in high vacuum ($P < 10^{-8}$ Pa), the atoms of the real area of contact approach one another across the interface. When they are within 2 nm (20 Angstrom), long distance, weak van der Waals forces are first experienced. As the interfacial distance is decreased to 0.2–0.1 nm, a full metallic bond will form and the pieces weld together. The experiments of Buckley (1977) have been concerned with the force required to overcome this so-called *cold welding*. The adhesive forces are sometimes greater than the forces necessary to press the metals together. However, the metallic bond is completely broken if extended to 0.5 nm, thus a surface film of this thickness signifies that only weak van der Waals forces are acting. As a result, one should expect considerable reduction in adhesive strength. These ideas recently have been confirmed by molecular dynamics simulations (Landman, Luedtke, and Ringer, 1992).

Two elementary methods of measuring static friction, both considered by Leonardo da Vinci, are illustrated in Figure 1.7. Though these methods are quick and convenient, they have had limited success due to the response of the systems being too slow for variations in the coefficient of friction to be detected. Once the body has started moving it will accelerate under constant force, for in general $f_{\text{static}} > f_{\text{kinetic}}$. Even such a variation in friction can hardly be detected by these simple methods. More sophisticated devices for measuring friction are described by Bowden and Tabor (1986), who identify cleanliness of the surface as the single most important factor in achieving repeatable friction results. Surface contaminants, even when present in a layer only one molecule thick, are capable of drastically modifying the friction coefficient because of the reduction in adhesive interactions. Table 1.1 lists f_{static} and f_{dynamic} for various surface pairs under both dry and greasy (lubricated) conditions.

Table 1.1. *Coefficients of static and dynamic friction*[a,b]

	Static		Dynamic	
Materials	Dry	Greasy[c]	Dry	Greasy[c]
Hard steel on hard steel	0.78(1)	0.11(1,a)	0.42(2)	0.03(5,h)
		0.23(1,b)		0.08(5,c)
		0.15(1,c)		0.08(5,i)
		0.11(1,d)		0.06(5,j)
		0.01(17,p)		0.08(5,d)
		0.01(18,h)		0.11(5,k)
				0.10(5,l)
				0.11(5,m)
				0.12(5,a)
Mild steel on mild steel	0.74(19)		0.57(3)	0.09(3,a)
				0.19(3,u)
Hard steel on graphite	0.21(1)	0.09(1,a)		
Hard steel on Babbitt	0.70(11)	0.23(1,b)	0.33(6)	0.16(1,b)
(ASTM 1)		0.15(1,c)		0.06(1,c)
		0.08(1,d)		0.11(1,d)
		0.09(1,e)		
Hard steel on Babbitt	0.42(11)	0.17(1,b)	0.35(11)	0.14(1,b)
(ASTM 8)				
		0.11(1,c)		0.07(1,c)
		0.09(1,d)		0.07(1,d)
		0.08(1,e)		0.08(11,h)
Hard steel on Babbitt		0.25(1,b)		0.13(1,b)
(ASTM 10)				
		0.12(1,c)		0.06(1,c)
		0.10(1,d)		0.06(1,d)
		0.11(1,e)		
Mild steel on cadmium silver				0.10(2,f)
Mild steel on phosphor bronze			0.34(3)	0.17(2,f)
Mild steel on copper lead				0.15(2,f)
Mild steel on cast iron		1.83(15,c)	0.23(6)	0.13(2,f)
Mild steel on lead	0.95(11)	0.5(1,f)	0.95(11)	0.30(11,f)
Nickel on mild steel			0.64(3)	0.18(3,x)
Aluminum on mild steel	0.61(8)		0.47(3)	
Magnesium on mild steel			0.42(3)	
Magnesium on magnesium	0.6(22)	0.08(22,y)		
Teflon on Teflon	0.04(22)			0.04(22,f)
Teflon on steel	0.04(22)			0.04(22,f)
Tungsten carbide on tungsten carbide	0.2(22)	0.12(22,a)		
Tungsten carbide on steel	0.5(22)	0.08(22,a)		
Tungsten carbide on copper	0.35(23)			
Tungsten carbide on iron	0.8(23)			
Bonded carbide on copper	0.35(23)			
Bonded carbide on iron	0.8(23)			
Cadmium on mild steel			0.46(3)	

(*continued*)

Table 1.1 *(continued)*

	Static		Dynamic	
Materials	Dry	Greasy[c]	Dry	Greasy[c]
Copper on mild steel			0.36(3)	0.18(17,a)
Nickel on nickel	1.10(16)		0.53(3)	0.12(3,w)
Brass on mild steel	0.51(8)		0.44(6)	
Brass on cast iron			0.30(6)	
Zinc on cast iron	0.85(8)		0.21(7)	
Magnesium on cast iron			0.25(7)	
Copper on cast iron	1.05(16)		0.29(7)	
Tin on cast iron			0.32(7)	
Lead on cast iron			0.43(7)	
Aluminium on aluminium	1.05(16)		1.4(3)	
Glass on glass	0.94(8)	0.01(10,p)	0.40(3)	0.09(3,a)
		0.01(10,q)		0.12(3,v)
Carbon on glass			0.18(3)	
Granite on mild steel			0.39(3)	
Glass on nickel	0.78(8)		0.56(3)	
Copper on glass	0.68(8)		0.53(3)	
Cast iron on cast iron	1.10(16)		0.15(9)	0.07(9,d)
				0.06(9,n)
Bronze on cast iron			0.22(9)	0.08(9,n)
Oak on oak (parallel to grain)	0.62(9)		0.48(9)	0.16(9,r)
Oak on oak (perpendicular)	0.54(9)		0.32(9)	0.07(9,s)
Leather on oak (parallel)	0.61(9)		0.52(9)	
Cast iron on oak			0.49(9)	0.08(9,n)
Leather on cast iron			0.56(9)	0.36(9,t)
				0.13(9,n)
Laminated plastic on steel			0.35(12)	0.05(12,t)
Fluted rubber bearing on steel				0.05(13,t)

[a] From Baumeister, T. *Handbook of Mechanical Engineers*, 7th ed. Copyright McGraw Hill Book Co., ©1967. With permission.

[b] Key to lubricants used: a, oleic acid; b, Atlantic spindle oil (light mineral); c, castor oil; d, lard oil; e, Atlantic spindle oil plus 2% oleic acid; f, medium mineral oil; g, medium mineral oil plus 1/2% oleic acid; h, stearic acid; i, grease (zinc oxide base); j, graphite; k, turbine oil plus 1% graphite; l, tubine oil plus 1% stearic acid; m, turbine oil (medium mineral); n, olive oil; p, palmitic acid; q, ricinoleic acid; r, dry soap; s, lard; t, water; u, rape oil; v, 3-in-1 oil; w, octyl alcohol; x, triolein; y, 1% lauric acid in paraffin oil.

[c] Note that "Greasy" is not sufficient to describe surface condifions. The friction coefficient depends on other factors such as speed, load, enviroment, etc. Thus Table 1.1 is, necessarily, an oversimplification.

Asperity Contact

For the sake of this illustration, assume that the two surfaces in contact have hemispherical-shaped asperities of radii r_1 and r_2, respectively. As the normal load is slowly increased, contact is first made by the most prominent asperities. According to Hertz (Johnson, 1992), the deformation of these asperities is initially elastic and the region

of contact is a circle with radius

$$a = \left(\frac{3WR}{2E'}\right)^{1/3}. \tag{1.12}$$

Here W is the load, E' is the effective contact modulus[5], R is the effective radius

$$\frac{1}{E'} = \frac{1}{2}\left(\frac{1-\nu_1^2}{E_1} + \frac{1-\nu_2^2}{E_2}\right), \quad \frac{1}{R} = \frac{1}{r_1} + \frac{1}{r_2}, \tag{1.13}$$

and E_1, ν_1 and E_2, ν_2 are Young's modulus and Poisson's ratio for the two solids, respectively.

At this elastic stage the real area of contact is proportional to $W^{2/3}$ and, using Eq. (1.12), the mean pressure over the contact circle is given by

$$\bar{p} = \frac{2}{3\pi}\left(\frac{3WE'^2}{2R^2}\right)^{1/3}. \tag{1.14}$$

As the load is increased the mean pressure $\bar{p}$ will also increase, until the elastic limit (of the softer of the two materials) is reached. This will first occur at the point Z, located at $z/a = 0.48$ (when $\nu = 0.3$) below the center of the contact circle, as indicated in Figure 1.8; here the shear stress first achieves its yield value k (Johnson, 1992). The yield value[6] of the shear stress is equal to $0.5\sigma_{yp}$, where σ_{yp} is the *yield stress in uniaxial tension*. At the instant of reaching the yield value of shear, the mean contact pressure attains the value $\bar{p} \approx 1.1\sigma_{yp}$.

Though the elastic limit is attained at $Z = 0.48$ as the mean contact pressure reaches $\bar{p} = 1.1\sigma_{yp}$, plastic flow is not yet possible due to the constraining influence of the surrounding material in which deformation is still mainly elastic. Consequently, if the load is removed at this stage, only a slight amount of residual deformation is noticeable.

As the normal load is further increased, the zone of plastic deformation propagates outward from the point where it first occurred, until it eventually reaches the surface; the value of the mean pressure is now $\bar{p} = p_0 \approx 3\sigma_{yp}$. The mean pressure at this point is essentially the *indentation hardness* value, H, of the material. This is why, for ductile metals, $H \approx 3\sigma_{yp}$. For hard tool steel E = 200 GPa, $\sigma_{yp} \approx 1.96$ GPa; an asperity of radius $r = 1$ μm will deform plastically when the load is less than 10^{-5} N.

Addition of a tangential force to the normal load introduces several effects. The location of the maximum shear stress moves closer to the surface. Friction also increases the maximum value reached by von Mises yield parameter

$$J_2 = \tfrac{1}{6}\{(\sigma_x - \sigma_y)^2 + (\sigma_y - \sigma_z)^2 + (\sigma_z - \sigma_x)^2\} + \tau_{xy}^2 + \tau_{yz}^2 + \tau_{zx}^2$$

so that yielding will occur at lower loads. This is shown in Figure 1.9, where the von Mises yield parameter is plotted against f for $\nu = 0.3$.

For single asperity contact, Eq. (1.12), the contact area is proportional to the 2/3 power of the load and not to its first power, as apparently is required by Amontons' laws (see footnote 4). The asperities of real surfaces, however, are not of uniform height, as indicated

[5]Note that Johnson (1992) uses $E^* = E'/2$ instead of our E'. The latter, our notation, is generally employed in discussions on elastohydrodynamic lubrication (EHL).

[6]According to the Tresca yield criterion, a ductile material will yield under a slowly applied complex state of stress when the maximum shear stress equals that which exists at yielding in a static tensile test of the metal, i.e., at $\tau_{\max} = \sigma_{yp}/2$. Plastic flow in metals occurs along crystal planes so that a critical shear stress criterion is preferable to other yield criteria.

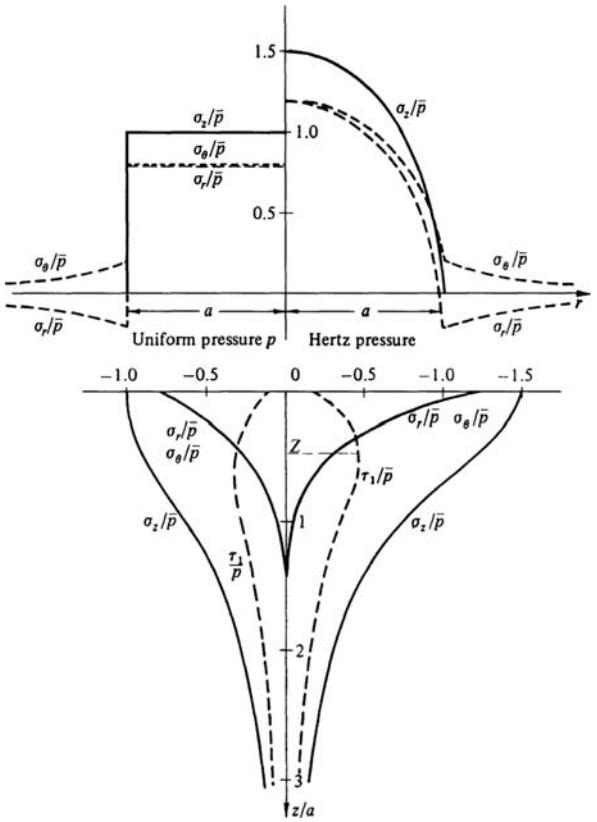

Figure 1.8. Stress distribution at the surface and along the axis of symmetry caused by (left) uniform pressure and (right) Hertz pressure acting on a circular area of radius a. (Reprinted with permission from Johnson, K. L. *Contact Mechanics*. Copyright Cambridge University Press, © 1992.)

by the profilometer trace in Figure 1.2, and do not all engage immediately as load is first applied. Upon increasing the load, the number of asperities that take active part in carrying the load will also increase. If, as in the probabilistic contact model of Greenwood and Williamson (Greenwood, 1992), the number of asperity contacts is allowed to increase with increasing load in such a manner that the average size of each asperity contact can remain constant, the real area of contact becomes proportional to the load itself rather than to its 2/3 power. Thus, even though the deformation is elastic, the Greenwood and Williamson model supports Amontons' law.

To illustrate this, we follow Greenwood (1992) and consider a rough surface with asperity height distribution $f(y)$, located at distance d from a perfectly smooth surface, as in Figure 1.10. If there are a total of N asperities (per unit area), the number of asperity contacts with the plane is

$$\begin{aligned} n &= N \times P(d \le \xi) = N \times [1 - P(\xi < d)] \\ &= N \times \left[\int_{-\infty}^{\infty} f(\hat{y})\, d\hat{y} - \int_{-\infty}^{d} f(\hat{y})\, d\hat{y} \right] \\ &= N \times \int_{d}^{\infty} f(\hat{y})\, d\hat{y}. \end{aligned} \tag{1.15a}$$

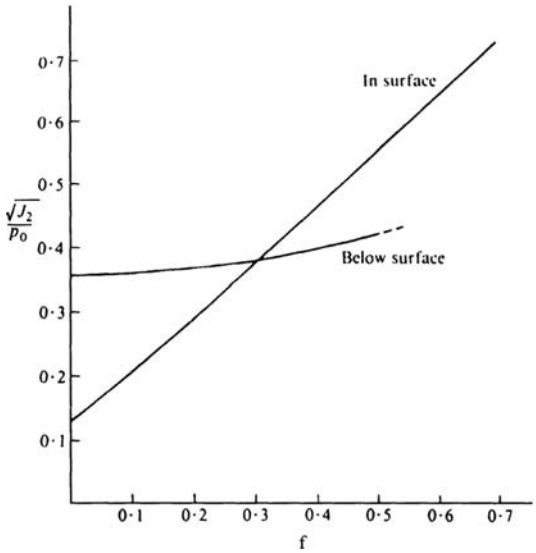

Figure 1.9. Variation of the maximum von Mises yield parameter, in and below the surface. With friction in excess of 0.5, there is no longer a clear maximum. (Reprinted by permission of the Council of the Institution of Mechanical Engineers from Hamilton, G. M. Explicit equations for the stress beneath a sliding spherical contact. *Proc. I. Mech. E.*, 197, 53–59, 1983.)

For a single asperity, we can obtain both the area of contact $\pi a^2 = \pi r\delta$, and the load $w = (2/3)E'\sqrt{r\delta^3}$, in terms of the asperity compression $\delta = (z - d)$ and the radius of curvature r. Then the total area of contact, A_r, and the total load, W, are given, respectively, by (Johnson, 1992)

$$A_r = N\pi r \int_y^\infty (\hat{y} - d) f(\hat{y})\, d\hat{y} \tag{1.15b}$$

and

$$W = \frac{2}{3} N E' r^{1/2} \int_d^\infty (\hat{y} - d)^{2/3} f(\hat{y})\, d\hat{y}. \tag{1.15c}$$

These equations can be evaluated once the probability distribution is known. Greenwood and Williamson (Greenwood, 1992) chose an exponential distribution, $f(y) = \exp(-\lambda/y)$, and found

$$n = \frac{N}{\lambda} e^{-\lambda d}, \tag{1.16a}$$

$$A_r = \frac{N\pi r}{\lambda^2} e^{-\lambda d}, \tag{1.16b}$$

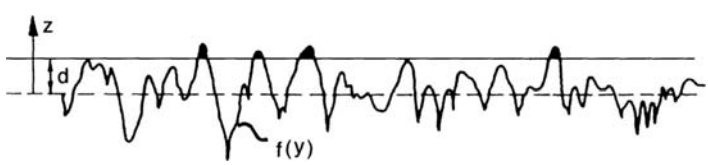

Figure 1.10. Loading a rough surface, of asperity height distribution $f(y)$, against a smooth plane a distance d apart.

and

$$W = \frac{1}{2} N E' \left(\frac{\pi r}{\lambda^5}\right)^{1/2} e^{-\lambda d}, \tag{1.16c}$$

so that

$$A_r = \sqrt{\frac{2\lambda \pi r}{E'}} W \tag{1.16d}$$

and the area of contact is directly proportional to load, as required by Amontons' laws.

Though the above derivation was for fully elastic deformation, we can glimpse at the onset of plastic flow (Greenwood, 1992). The fraction of asperity contacts at which plastic deformation occurs is proportional to δ_y/σ, where σ is the standard deviation of asperity height, Eq. (1.9), and δ_y is the asperity compression at first yield, i.e., when $\bar{p} \approx H/3$. Greenwood and Williamson (1966) defined the so-called *plasticity index* ψ to be inversely proportional to $\sqrt{\sigma/\delta_y}$, so that

$$\psi = \frac{E'}{2H} \sqrt{\frac{\sigma}{r}}. \tag{1.17}$$

$\Psi \approx 1$ corresponds to 1% of the total contact area at yielded contacts. Asperity contact will become plastic when the plasticity index exceeds unity (note that Ψ is independent of the average pressure $\bar{p}$). For metal surfaces produced by normal engineering methods, $0.1 < \Psi < 100$.

Adhesion Theory of Friction

In metals it has been found that the pressure, p_0, that the asperities can support when subjected to localized plastic deformation is approximately constant. In the plastic range, then, if we double the load, the area of contact must also double in order to maintain a constant yield pressure. Let $A_1, A_2, A_3, \ldots$ represent a series of areas of contact, supporting loads W_1, W_2, $W_3, \ldots$ If W is the total load and A_{ro} is the total area of real contact under normal load, we have

$$\begin{aligned} &= W_1 + W_2 + W_3 + \cdots \\ &= p_0 A_1 + p_0 A_2 + p_0 A_3 + \cdots \\ &= p_0 (A_1 + A_2 + A_3 + \cdots) \\ &= p_0 A_{ro}. \end{aligned} \tag{1.18}$$

From this it follows that the area of real contact A_{ro} is dependent neither on the size nor on the shape of the area of apparent contact. It is determined only by the yield pressure p_0 and the load (Bowden and Tabor, 1956).

Note that the real area of contact is proportional to the load when the deformation is plastic, as is required by Amontons' law. However, fully plastic deformation of the asperities seems feasible when the surfaces are used only a limited number of times. It is not realistic to expect the same surface, say the surface of a cylinder, to deform plastically during every one of the millions of times the other surface, the piston in this case, makes a pass. One is inclined to think that after a short run-in period almost all the plastic (irreversible)

deformations that were to take place have done so, and that after run-in the load carrying deformation will be mainly elastic. On the second and successive passes the material is subjected to the combined action of contact stresses and residual stresses from previous passes; the effect of the latter is such as to make yielding less likely.[7] The trouble with this line of thought is that, at least according to the Hertz analysis for an isolated, single asperity, Eq. (1.12), the area of contact in elastic deformation is proportional to the 2/3 power of the load, which would negate Amontons' law. If, as in the probabilistic contact model of Greenwood and Williamson (Greenwood, 1992), the number of asperity contacts is allowed to increase with increasing load in such a manner that the average size of each asperity contact can remain constant, the real area of contact becomes proportional to the load itself rather than to its 2/3 power, Eq. (1.16d). Thus, even though the deformation is elastic, the Greenwood and Williamson model supports Amontons' law.

As the surfaces make contact only at the tips of their asperities, the pressures are extremely high. Over the regions of intimate contact strong adhesion takes place, and the specimens become, in effect, a continuous body (cold welding). As the surfaces are made to slide over one another, the just welded junctions are sheared. Let s represent the shear strength of the material and A_{ro} the area of real contact. We may then write $A_{ro} \times s$ for the shear force. For the *coefficient of friction* we have

$$f = \frac{F}{W} = \frac{A_{ro}s}{A_{ro}p_0} = \frac{s}{p_0} = \frac{\text{junction shear strength}}{\text{yield pressure}}. \tag{1.19}$$

This conclusion will be considerably altered in practice. For most materials, s is of order $0.2 \times p_0$, so that according to this model $f = 0.2$. This is far too small. For identical metals in normal atmosphere $f = O(1)$ and for clean metals in vacuum f can reach 10 or larger. This compelled Bowden and Tabor to modify Eq. (1.19) and the argument leading up to it.

The asperities are already loaded to their elastic limit by the normal load as the interfacial tangential force is applied. To support the combined normal and tangential forces, the plasticity condition at the junction would now be exceeded, which cannot be, unless there were an appropriate increase of the real area of contact, from A_{ro} to some A_r. This mechanism, referred to as junction growth, has a profound effect on the value of the coefficient of friction.

Junction Growth

In the previous section the real area of contact A_{ro} was determined solely by the normal load and the yield pressure, $A_{ro} = W/p_0$. When a tangential load is also applied, it is more appropriate to calculate the real area of contact on the basis of the combined tangential and normal loading.

When subjecting a slab of solid material to the combination of (a) simple shear τ and (b) normal loading p, the Tresca yield criterion, viz., $k \equiv \tau_{\max} = \sigma_{yp}/2$, takes the form (Figure 1.11)

$$4\tau^2 + p^2 = \sigma_{yp}^2. \tag{1.20}$$

[7] This is known as the *shakedown principle* (Johnson, 1992).

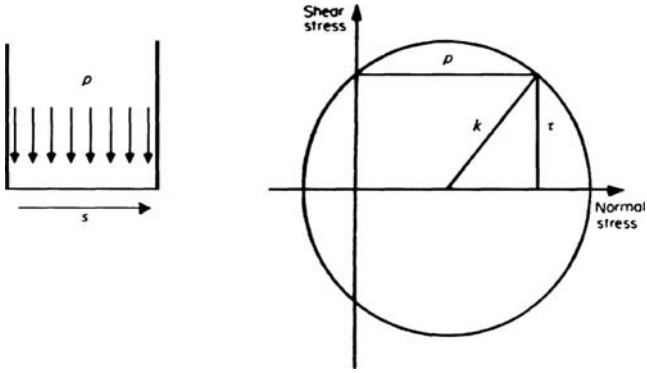

Figure 1.11. Simple loading of an asperity and the corresponding Mohr's circle. (Reprinted with permission from Arnell, R. D., Davies, P. B., Halling, J. and Whomes, T. L. *Tribology Principles and Design Applications.* Copyright Springer Verlag, © 1991.)

Substituting $p = W/A_r$ and $\tau = F/A_r$ into Eq. (1.20), we find that

$$\frac{A_r}{A_{ro}} = \sqrt{1 + \left(\frac{2F}{W}\right)^2}. \tag{1.21}$$

Here, A_r is the area of real contact under the combined normal and tangential loads and $A_{ro} = W/\sigma_{yp}$. Equation (1.21) verifies our earlier assertion on junction growth. The coefficient of friction is now given by

$$f = \frac{1/2}{\sqrt{\left(\frac{k}{\tau}\right)^2 - 1}}. \tag{1.22}$$

There is nothing in this model, Eq. (1.21), to limit junction growth, which continues indefinitely if (1) the surfaces are perfectly clean and (2) the metals are very ductile (Tabor, 1981).

When present, contaminants will limit junction growth. To illustrate this mechanism, let τ_i represent the interfacial yield stress, which is less than or equal to the shear yield stress of the asperity material in bulk, k. We now write $F = A_r\ \tau_i$ for the tangential force and obtain from the Tresca yield criterion, Eq. (1.20), an improved formula for the coefficient of friction

$$f = \frac{1/2}{\sqrt{\left(\frac{k}{\tau_i}\right)^2 - 1}}. \tag{1.23}$$

The variation of f with τ_i is illustrated in Figure 1.12.

In analogy with combined loading and shear, p and τ acting on an actual adhesive junction are assumed by Childs (1992) to obey

$$p^2 + \alpha\tau^2 = \beta k^2, \tag{1.24}$$

where α and β are constants. In place of Eqs. (1.22) and (1.23), Childs obtains

$$\frac{A_r}{A_{ro}} = \sqrt{1 + \alpha\left(\frac{F}{W}\right)^2}, \qquad f = \frac{\pi}{k}\left[\beta - \alpha\left(\frac{\tau}{k}\right)^2\right]^{-1/2} \tag{1.25}$$

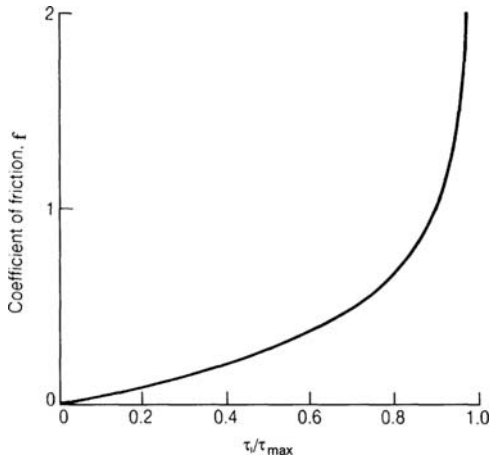

Figure 1.12. Junction growth: variation of the coefficient of friction with the interfacial yield stress τ_i.

Equation (1.25) suggests that junction growth is not the only possible mechanism for reducing friction. If τ/k is of order unity and $\beta > \alpha + 1$, then $f < 1$ results from the second part of Eq. (1.25). It is also indicated that a small amount of weakening at the interface, caused by a thin contaminant film of shear strength τ, can produce a significant reduction in the coefficient of friction. This is the principle underlying boundary lubrication, and lubrication by soft metal films.

Ploughing

For a hard conical asperity riding on a softer metal, we can illustrate the magnitude of the ploughing term by considering a conical asperity of semi-angle θ, shown in Figure 1.13.

The pressure needed to make the softer material flow ahead of the advancing hard asperity can be taken to be the hardness, H, of the softer material. The normal and tangential forces supported by the asperity may then be calculated, respectively, as

$$\begin{aligned} W &= \left(\frac{\pi r^2}{2}\right) H = \frac{1}{2} H \pi r h^2 \tan^2 \theta, \\ F_p &= rhH = Hh^2 \tan\theta. \end{aligned} \tag{1.26}$$

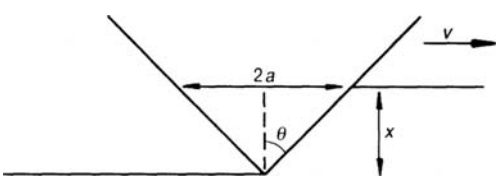

Figure 1.13. A conical asperity of semi-angle θ indents a softer metal: a model for ploughing.

Under these idealized conditions, the coefficient of friction due to ploughing is

$$f_p = \frac{F_p}{W} = \frac{2\cot\theta}{\pi}. \tag{1.27}$$

Under normal circumstances the slope of the asperities rarely exceeds 5–10°, fixing the range of θ at 85–80°; this yields the ploughing component of the coefficient of friction lying between 0.07 and 0.14. As the ploughing component is small, it may be considered additive to the adhesion component. A more thorough plasticity theory is called for to nonlinearly combine the two contributions to friction (Suh, 1986).

Friction of Metals

The coefficient of friction is given as the sum of three terms, f_a, f_p, and f_d the adhesion component, the ploughing component, and the deformation component, respectively. According to Suh (1986), the adhesion component for metals varies from about 0 to 0.4, depending on the presence of a contaminant layer covering the asperities. The ploughing component is smaller than the adhesion component, usually not exceeding 0.1, except for identical metals sliding against one another, having wear particles trapped between the surfaces. The friction component due to asperity deformation, f_d, can be as large as 0.4 to 0.75 in special cases, and is believed to be responsible for the static coefficient of friction (Suh, 1986).

Suh (1986) defines six stages of surface interaction that characterize time-dependent friction behavior of metals (Figure 1.14). The relative importance of f_a, f_p, and f_d changes from stage to stage. Stage I is characterized by ploughing of the surface by asperities; the coefficient of friction is largely independent of material combinations. In Stage II the value of friction is beginning to rise. The slope is steeper if wear particles generated by asperity deformation and fracture become trapped. The swift increase in the number of wear particles gives the friction curve a steep slope during Stage III; another contributor here is adhesion due to the rapid increase of clean surfaces. Friction remains constant during Stage IV as adhesion and asperity deformation are constant now, as is the number of trapped wear particles. Stage V occurs when a very hard stationary slider is slid against a soft specimen. The asperities of the slider are gradually removed, creating a mirror finish

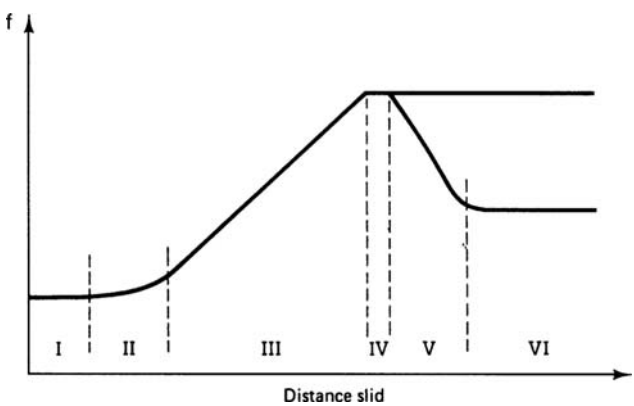

Figure 1.14. Six stages in the frictional force versus distance slid relationship. (Reprinted with permission from Suh, N. P. *Tribophysics.* Copyright Prentice-Hall, © 1986.)

of the hard surface. A decrease in friction will result in this case, due to the decrease in asperity deformation and plowing. In Stage VI the hard surface is mirror smooth and the value of the friction levels off. Stages V and VI do not occur if it is the hard slider that moves and the soft specimen that is stationary (Suh, 1986).

Friction of Polymers

The interfacial bonding of polymers is of van der Waals type, the same as in the bulk of the material. The tendency for shear to occur is in the bulk material (Briscoe and Tabor, 1978). Two notable exceptions are Teflon (PTFE) and Ultra High Molecular Weight Polyethylene (UHMWPE). When a polymer is sliding on metal or another polymer, the deformation is mostly elastic, with virtually no plastic flow. For a given surface roughness the value of the plasticity index for polymers is an order less than for metals.

Most polymers exhibit lower coefficient of friction at high normal load (Archard, 1953). At low sliding velocity the coefficient of friction is generally low, it increases with sliding speed to a maximum, then decreases again (Ettles, 1981).

Another important factor to take into account is that many polymers are viscoelastic. Viscoelastic materials are both solid-like and fluid-like in their response to stress; the work of deformation is neither completely stored, as in elastic solids, nor completely dissipated, as in viscous fluids. These materials show a marked increase of flow stress with strain rate. The coefficient of friction of polymers, sliding against one another or against a metal, varies so widely that tabulation of friction coefficients would be meaningless. For viscoelastic materials Amontons' laws are not applicable.

Voyutski (1963) found that in most cases interfacial bonding is strongly strengthened by diffusion of polymer chains across the interface. Polymers generally soften early or have low melting points and poor heat conductivity. At high relative speed, the surface layers often melt. However, friction still has both an adhesive component and a deformation component.

Friction of Ceramics

The bonding within ceramics is largely covalent and very strong, but the force of adhesion across the interface between contacting ceramics is of the van der Waals type and is partly ionic. Friction is generally lower for ceramics than for metals owing to the weaker interfacial bonds. These interfacial bonds will, at least in the absence of high temperatures, be weaker than the bulk (Hutchings, 1992). Therefore, when surfaces are pulled or slid apart, the break tends to occur along the original interface. If the ceramic is brittle, surface cracks may develop at the rear of the moving junction, increasing the rate of energy dissipation. The reader may wish to consult Jahanmir (1994) for further details on the tribological properties of ceramics.

Thermal Effects of Friction

Almost all of frictional energy is dissipated in the form of heat. Continuous rubbing of surfaces can build up not only significant temperatures but also large temperature gradients in the contacting bodies. The nonuniform thermal expansion that accompanies this can lead to loss of dimensional tolerance in the case of machine components.

It is relatively easy to set up energy conservation equations once the geometry and thermal characteristics of the bodies are known and to calculate the average temperature

field for given energy input. But heat does not enter the system in any easily definable manner. Furthermore, it is generated instantaneously at the random asperity contacts of the two surfaces. The instantaneous and random asperity temperatures, the so-called *flash temperatures* that result from asperity interaction, are significantly higher than the *nominal temperature* given by our steady-state energy conservation equations. A solution for flash temperatures can be found in a book by Carslaw and Jaeger (1959), but this solution is far too detailed to be reproduced here. For some recent work and bibliography, the reader is referred to Tian and Kennedy (1993) and Tian and Kennedy (1994). The first of these papers deals with the nominal surface temperature rise, while the second discusses local flash temperature rise; the total frictional temperature rise is considered to be given by the sum of these.

1.4 Wear

Wear is the progressive loss of substance of a body, due to relative motion at its surface. Many different types of wear have been identified. Godfrey (1980), e.g., recognized a dozen different types of wear, though at times it is not easy to differentiate between them. In this introduction to wear we follow Rabinowicz (1965) and list four main types: sliding wear, abrasive wear, corrosion, and surface fatigue. Only sliding wear and abrasive wear will be discussed in some detail.

Research into wear follows two lines, wear modeling and the study of damaged surfaces. Wear modeling, with the objective of engineering prediction of wear rates, is the older of the two aspects of wear research. The study of damaged surfaces owes its existence to significant recent advances in experimental methods and microscopy equipment.

Sliding Wear

In contrast to that of friction, the scientific study of sliding wear is recent. As friction and sliding wear are caused by the same type of surface interaction, the quantitative prediction of wear rates is fraught with the same difficulties as that of friction. However, the situation is even more bleak, as under normal conditions the value of the coefficient of friction between different metal pairs changes by one order of magnitude at most, while corresponding wear rates can change by several orders. There have been numerous attempts made in the past to predict wear rate, Archard's formula (Archard, 1953) being one of the most noteworthy in this direction.

To arrive at Archard's wear rate equation, consider the asperities of opposing surfaces as they make contact with one another while supporting the yield pressure p_0 of the softer material. Asperity contacts are assumed to occur uniformly over circular contact areas of radius a. The elemental load carried by each asperity is then $\delta W = \pi a^2 p_0$, and the total load supported by n asperities is the sum

$$W = \pi p_0 \sum_n a^2. \tag{1.28}$$

Now picture the asperities as having hemispherical tips of volume $(2/3)\pi a^3$. On separating from its main body an asperity tip will contribute $\delta V = (2/3)\pi a^3$ to the wear volume.[8]

[8]That the asperities are spherical and that the asperity is completely removed is a gross simplification of actual conditions.

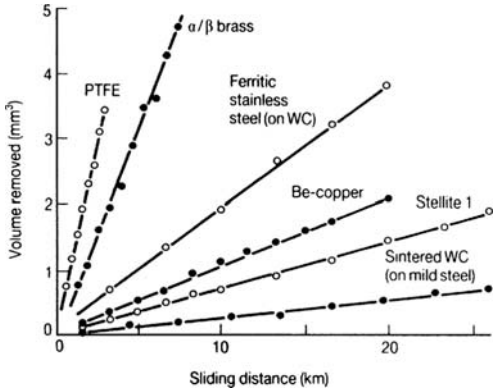

Figure 1.15. Variation of wear rate, for various materials. (Reprinted with permission from Archard, J. F. and Hirst, W. The wear of metals under unlubricated conditions. *Proc. Roy. Soc.*, **A 236**, 397–410, 1956.)

However, not every asperity will break off on contact. If the probability of a particular asperity breaking off on first contact is κ, then the wear volume per sheared distance per asperity is

$$\delta Q = \kappa \left(\frac{\delta V}{2a} \right) = \frac{\kappa \pi}{3} a^2. \tag{1.29}$$

Summing Eq. (1.29) for n asperities, substituting for $\Sigma_n \, a^2$ from Eq. (1.28), and recognizing that the yield pressure equals the hardness value H, we have the wear volume per distance slid, i.e., the *wear rate*, as

$$Q = K \frac{W}{H}, \tag{1.30a}$$

where the wear coefficient $K = \kappa/3$ is a pure number. It is found that $K < 1$ always, and that the value of K can vary by several orders of magnitude when conditions change,[9] even for the same material pair. Equation (1.30) is *Archard's wear rate formula*.

When written in the form[10]

$$V \propto \frac{W}{H} L, \tag{1.30b}$$

where $V = QL$ is the volume of material worn, Archard's wear rate formula has the following interpretation, called *Archard's laws* for sliding wear:[11]

(1) The wear volume is proportional to the distance slid,
(2) The wear volume is proportional to the total load,
(3) The wear volume is inversely proportional to the hardness of the softer material.

We find confirmation of the first of these relationships in the original paper of Archard and Hirst (1956). The relevant figure is reproduced in Figure 1.15.

[9] For lubricated sliding wear, Archard's wear rate formula is supplied with another coefficient $\alpha < 1$, which characterizes the ratio of the area of metal to metal contact to the apparent area.

[10] This was developed for metals assuming plastic deformation. It may or may not apply to other materials.

[11] It should be obvious that, on using Archard's equation in the form of Eq. (1.30), we can substitute wear rate in place of wear volume.

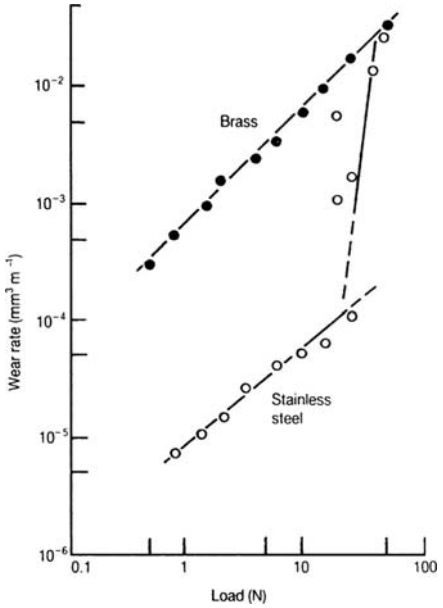

Figure 1.16. There is transition from mild to severe wear in stainless steel, while brass obeys Archard's law in the whole load range. (Reprinted with permission from Archard, J. F. and Hirst, W. The wear of metals under unlubricated conditions. *Proc. Roy. Soc.*, **A 236**, 397–410, 1956.)

The second relationship, viz., that the wear volume (or, the wear rate), is proportional to the applied load, holds for metals in certain load ranges. Often at low load the wear rate is small (*mild wear*), and increases linearly with load, up to a *critical load*. On reaching the critical load, the mechanism that produces mild wear becomes unstable and transition to *severe wear* takes place, the wear coefficient often changing by several orders of magnitude. This situation is well illustrated in Figure 1.16, which shows transition from mild to severe wear in stainless steel. Brass, on the other hand, undergoes no transition and obeys Archard's first law throughout the load range of Figure 1.16.

It is now generally recognized that the wear of a soft material against a hard one can be characterized as *mild* or *severe*. In severe wear there is metallic contact of newly exposed surfaces and severe surface damage. Severe wear takes place under conditions where a protective oxide film is unable to form during the time available between interasperity contacts. Mild wear, on the other hand, is manifested when, at light load and speed, there is sufficient time between asperity interactions for oxide formation even at the prevailing "low" reaction rate. Mild wear will also be encountered at high temperatures, caused either by high rate of frictional heating (Figure 1.17), or by external heating, when the reaction rate is sufficiently high to promote formation of a protective oxide film in the time available.

There are, hence, two transitions. The T_1 transition is from mild to severe wear, and occurs as the load (or the speed) is increased. The rate of exposure of virgin metal surface during severe wear is opposed by the increasing rate of contamination of the surfaces by reaction with the ambient atmosphere. As the temperature increases above some critical T_2, 250–350°C in Lancaster's experiments for a carbon steel pin sliding against tool steel, a second transition takes place, this time from severe to mild wear. Here T_2 is a nominal

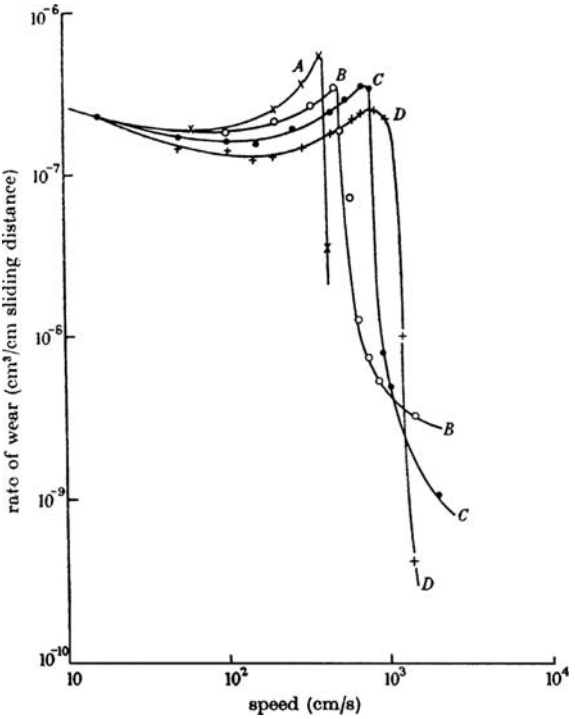

Figure 1.17. Variation of the rate of wear for pins with frictional heating. Apparent contact area increasing from A to D. (Reprinted with permission from Lancaster, J. K. The formation of surface films at the transition between mild and severe metallic wear. *Proc. Roy. Soc.*, **A 273**, 466–483, 1963.)

surface temperature, the flash temperature, that characterizes individual asperity interactions and has no effect on the transition. Figure 1.18 shows the variation in the wear rate with varying load for a carbon steel pin sliding against tool steel.

Qualitatively, transition remains the same irrespective of whether heating occurs by external means or as a consequence of friction (Lancaster, 1963). The variation of wear rate with sliding speed at different temperatures is illustrated in Figure 1.19. At low speed, mild wear results from the 'large' times available for oxidation; at high speeds, mild wear is the consequence of increased rates of oxidation. The magnitudes of critical loads and speeds will also depend on temperature. Changing the surrounding atmosphere to pure oxygen will also vary the critical conditions (speed and load) for transition.

Classification of sliding wear into mild wear and severe wear infers linking the wear mechanism to elastic contacts and plastic contacts, respectively (Kragelskii and Marchenko, 1982). Resulting from mild wear, the surface roughness is of the order of $R_a \approx 0.5\ \mu$m and the wear debris particle dimension is in the range $d_p = 0.01 - 1\ \mu$m. Mild wear dominates both at low speed and high temperature, where oxidation can keep balance with the rate of exposure of fresh surfaces, allowing the formation of an oxide layer. This last condition facilitates a lower coefficient of friction. On the other hand, severe wear will create a rough surface, with the arithmetic average of roughness R_a reaching 25 μm. The wear debris is now made up of particles of dimension $d_p \approx 200\ \mu$m, and surface oxidation can no

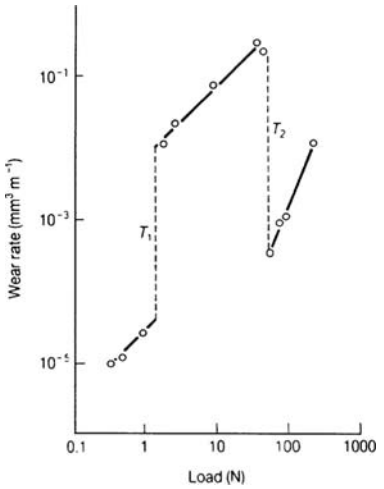

Figure 1.18. Variation of wear rate with load, for carbon steel pin riding on tool steel. (Reprinted with permission from Welsh, N. C. The dry wear of steels. *Phil. Trans. Roy. Soc.*, **A 257**, 31–70, 1965.)

longer keep up with the exposure of fresh surfaces; therefore, the coefficient of friction is usually large. Further increasing the load increases frictional work, leading to increased temperature and, thus, to increased rate of oxidation. Formation of oxide film that can be attained between successive asperity interactions grows exponentially with load as the load is increased, other things being equal, while the time between collisions decreases linearly (Amell et al. 1991) and a second transition from severe wear to mild wear may occur.

In an effort to develop a simple design guide, Lim and Ashby (1978) graphed the various wear regimes for given pairs of materials, thereby producing *wear maps*. The vertical axis of the graphs is normalized pressure and the horizontal axis is normalized sliding velocity. A wear map for soft carbon steel sliding on the same, in air at room temperature, is shown in Figure 1.20.

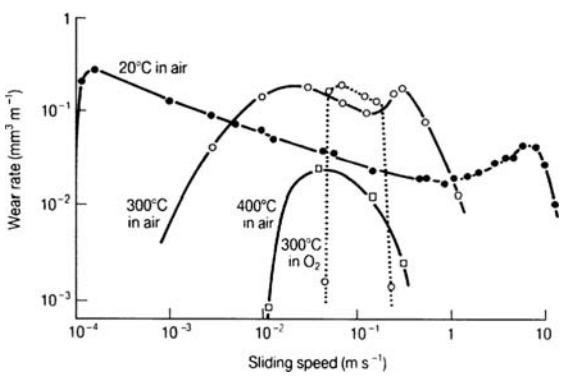

Figure 1.19. The variation of wear rate with sliding speed at different ambient temperatures for brass sliding against steel, – in air; . . . . . , in oxygen. (Reprinted with permission from Lancaster, J. K. The formation of surface films at the transition between mild and severe metallic wear. *Proc. Roy. Soc.*, **A 273**, 466–483, 1963.)

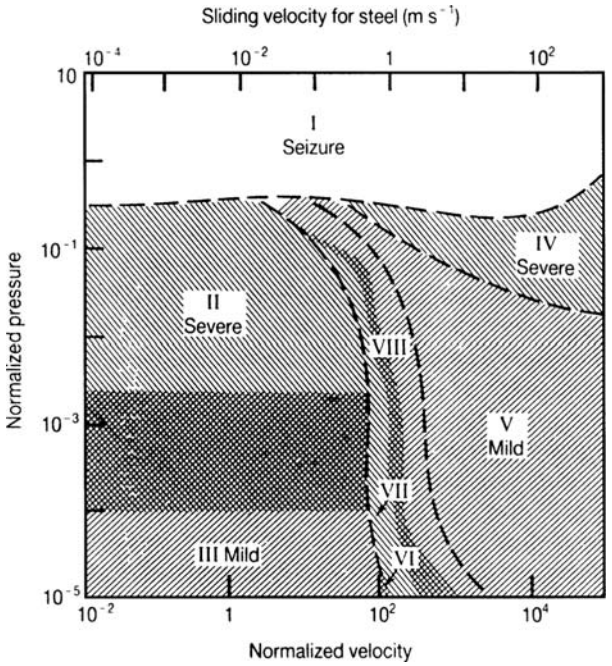

Figure 1.20. Wear map for soft carbon steels at room temperature in air. (Printed with permission from Lim, S. C. and Ashby, M. F. Wear mechanism maps. *Acta Metall.*, **35**, 1–24, 1987.)

Region I in Figure 1.20 is characterized by high contact pressure and gross seizure of the surfaces. Region II represents severe wear at high loads and low speed, while Region III has mild wear at low load and speed. Thermal effects, which were hitherto unimportant, become significant in Regions IV and V, both of which have increased reaction rate with the ambient atmosphere. Regions VI, VII, and VIII represent narrow transition regimes. For more detailed discussion of the significance and characteristics of the various regions of the wear map of Figure 1.20, the reader is referred to Lim and Ashby (1987).

In the model described above, the idea that wear particle size is related to contact patch size has been advanced. Rabinowicz (1965) suggested that energy considerations govern wear particle size. He noted that the strain energy associated with plastic contact of elastic bodies is $H^2/2E$ per unit volume of the material. The surface energy of the wear particle is $2\pi a^2\gamma$, where γ is the surface energy per unit of surface area. Rabinowicz then required that the stored elastic energy in the particle volume exceed the surface energy

$$\frac{2}{3}\pi a^3 \frac{H^2}{2E} > 2\pi a^2 \gamma$$

or

$$a > \frac{6E\gamma}{H^2}.$$

Furthermore if $E/H = k$, a constant, then

$$a > \frac{k\gamma}{H}.$$

Table 1.2. *Wear coefficient $K \times 10^6$ for sliding wear, Eq. (1.30)*

	Metal-on-Metal				Metal-on-Nonmetal
Lubrication	Identical	Soluble	Intermediate	Insoluble	Nonmetal-on-Nonmetal
None	1500	500	100	15	3
Poor	300	100	20	3	1.5
Good	30	10	2	0.3	1
Excellent	1	0.3	0.1	0.03	0.5

(Reprinted with permission from Rabinowicz, E. Wear coefficients, in Booser, E. R., *CRC Handbook of Lubrication*. Copyright CRC Press, Boca Raton, Florida, ©1984.)

Rabinowicz provided evidence to support his arguments, one implication of which is that there exists a minimum size of particles that can be generated through deformation.

Instead of attempting to find and tabulate the wear coefficient for pairs of metals (and conditions), we follow Rabinowicz and divide sliding systems into a limited number of categories, then give appropriate wear coefficient data for each category. The categories are: identical, soluble, intermediate, insoluble, nonmetal-on-nonmetal, and metal-on-nonmetal. For metals, the two principal factors that determine the wear coefficient are (1) the degree of lubrication and (2) the metallurgical compatibility, as indicated by the mutual solubility. Wear coefficients for adhesive wear for the five categories are given in Table 1.2, while Figure 1.21, after Rabinowicz, illustrates compatibility for metal pairs. The corresponding compatibility relationship is listed in Table 1.3.

Table 1.3. *Compatibility relationship for metals*

Symbol	Metallurgical solubility	Metallurgical compatibility	Sliding compatibility	Anticipated wear
◯	100%	Identical	Very poor	Very high
⊙	>1%	Soluble	Poor	High
◯	0.1–1%	Intermed. soluble	Intermediate	Intermediate
◒	<0.1%	Interm. insoluble	Intermed. or good	Intermed. or low
●	Two liquid phases	Insoluble	Very good	Very low

(Reprinted with permission from Rabinowicz, E. Wear coefficients, in Booser, E. R., *CRC Handbook of Lubrication*. Copyright CRC Press, Boca Raton, Florida, ©1984.)

Abrasive Wear

It is usual to distinguish between two-body abrasion, in which the asperities of the harder surface abrade the softer surface, and three-body abrasion, in which hard particles trapped between two surfaces abrade one or possibly both surfaces.

The mechanics of two-body abrasion closely resembles that of ploughing, as discussed earlier, except that in ploughing material is pushed aside while in abrasive wear some cutting is also involved. Referring to Figure 1.13, we find the normal load supported as in Eq. (1.26). The volume of material displaced by the cone while creating a groove of length ℓ is $\ell h^2 \tan\theta$. If a fraction, ε, of the displaced material becomes wear debris, then the wear

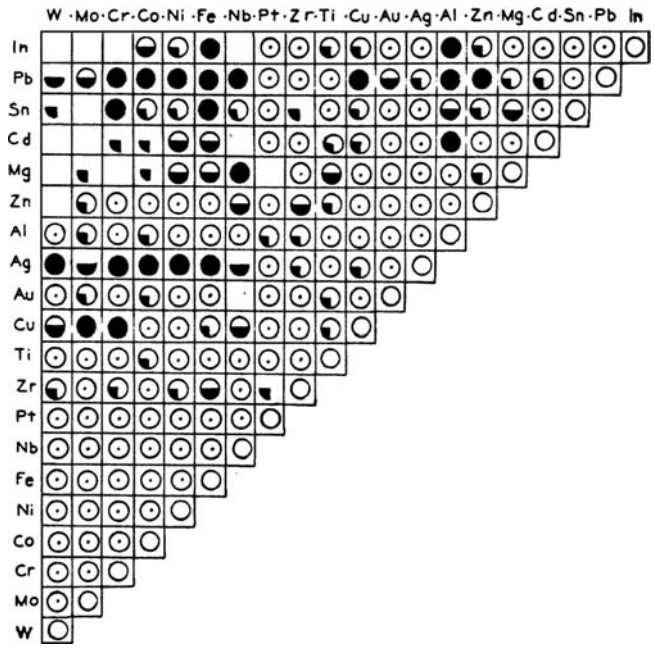

Figure 1.21. Compatibility diagram for metal pairs. The significance of the symbols is shown in Table 1.3. (Reprinted with permission from Rabinowicz, E. Wear coefficients. In Booser, E. R., *CRC Handbook of Lubrication*. Copyright CRC Press, Boca Raton, Florida, © 1984.)

volume produced in unit ploughing distance is

$$q = \varepsilon h^2 \tan \theta.$$

Substituting now for h^2 from Eq. (1.26), we obtain

$$q = \frac{2\varepsilon W}{\pi H \tan\theta}.$$

Summing for all asperities engaged in abrading the surface, we find that the total wear volume removed per unit sliding distance is

$$Q = \frac{\hat{k} W}{H}. \tag{1.31}$$

In Eq. (1.31) W is the applied normal load and $\hat{K}$ is a coefficient (Hutchings, 1992). We note that formally Eq. (1.31) is identical to Archard's rate equation for adhesive wear, Eq. (1.30).

We conclude this section with the observation that there has been considerable interest in recent years in methods of predicting wear rates. Investigations have concentrated on two problem areas, *running in*, which is a time-dependent phenomenon, and *steady state*, which is homogeneous in time.

1.5 Effect of Lubrication

Lubrication is used to reduce/prevent wear and lower friction. The behavior of sliding surfaces is strongly modified with the introduction of a lubricant between them. If we plot, for example, for a journal bearing, the coefficient of friction against $\mu N/P$, where

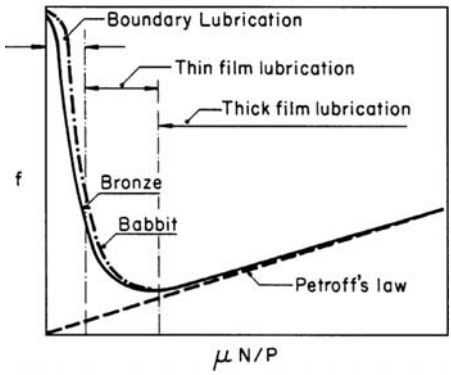

Figure 1.22. Lubrication regimes.

μ is the lubricant viscosity, N is the shaft speed, and $P = W/LD$ is the specific load, we find that at large values of $\mu N/P$, the friction coefficient, is low and is proportional to $\mu N/P$. This is the regime of *thick-film* lubrication. Upon decreasing $\mu N/P$, the friction passes through a minimum value, as indicated schematically in Figure 1.22, and we enter into the regime of *mixed lubrication*. For even smaller values of $\mu N/P$, the coefficient of friction increases rapidly, marking the complete breakdown of the lubricant film in this so-called *boundary lubrication* regime. Table 1.4 compares average values of the coefficient of friction in the various lubrication regimes.

Thick-film Lubrication

When the minimum film thickness exceeds, say, 2.5 μm, Petroff's law[12] is approximately obeyed by a lightly loaded journal bearing. The coefficient of friction is small and depends on no other material property of the lubricant than its bulk viscosity. This type of lubrication is called thick-film lubrication. In many respects this is the simplest and most desirable kind of lubrication to have.

Mixed Lubrication

The low $\mu N/P$ branch of the curve in Figure 1.22 represents varying degrees of thin-film lubrication, a name given by Hersey (1966) to the lubrication regime in which the coefficient of friction depends on surface roughness and on a lubricant property that Hersey terms "oiliness." The transition from thick-film lubrication to mixed lubrication takes place around the minimum point of the f-$\mu N/P$ curve. As the value of $\mu N/P$ is made smaller, the film becomes thinner and some of the opposing asperities touch. The friction coefficient now depends on the surface roughness, the material properties of the solids, and the material properties of the lubricant. For increasing smoothness the minimum point of the f-$\mu N/P$ curve shifts to the left.

[12]Petroff postulates a uniform shear stress $\tau_w = \mu U/P$ acting on the journal. The coefficient of friction $f = F/W$ is then given by $f = 2\pi^2 \mu RN/PC$. In conventional oil-lubricated bearings $C/R \sim 1/500$, and we write $f = \text{const} \times \mu N/P$. In older literature, the symbol Z (for the German *Zähigheit*) is used for viscosity and Petroff's law is written as $f \alpha\ ZN/P$.

Table 1.4. *Average values of the coefficient of friction*

Lubrication type	Friction coefficient	Degree of wear
Unlubricated	0.5–2.0	Heavy
Boundary and thin film	0.05–0.15	Slight
Thick film	0.001	None

Boundary Lubrication

In boundary lubrication, the film is so thin that its properties are no longer the same as those of the bulk. If the speed is reduced or the load is increased, the lubricant film becomes thinner than the height of some of the asperities. If these asperities are covered by a suitable molecular layer of lubricant, they will not weld together. This will be the case if the lubricant contains small amounts of surface-active materials. Typical active materials are long-chain fatty acids, alcohols, and esters. For this type of lubrication the friction coefficient is typically 0.1. Mixed lubrication can simply be viewed as a mixture of hydrodynamic lubrication and boundary lubrication. Mixed lubrication is a term often applied to conditions to the left of the minimum point of the f-$\mu N/P$ curve.

This concept of boundary lubrication must be revised when applied to mineral oils. It has been found that mineral oils under contact pressures of the order of 0.5–3 GPa increase their viscosity 100- or even 1000-fold. The oil, which is trapped between the elastically deformed solid surfaces, behaves as a virtual solid, preventing contact of the asperities. For this type of lubrication to occur the surfaces must be smooth and well aligned.

Solid Lubrication

Some metals show strong mechanical anisotropy, being strong in compression but weak in shear along certain directions. These metals may acquire low-friction sliding surfaces under loading. For special materials such as molybdenum disulfide (MoS_2) and graphite, the crystal structure is in the form of tightly bonded layers lying on one another, as shown in Figure 1.23.

In both graphite and molybdenum disulfide the bond between the interlayer atoms is due to covalent forces and is very strong. The lamella-to-lamella forces, on the other hand, are van der Waals type weak forces.[13] When rubbed against a metal these solids will transfer material onto a metallic substrate. The transfer film will be oriented so that the weak bond is on its outer face. Thus, in sliding contact only this weak bond need be broken where asperities on the harder body contact the film-covered substrate. For MoS_2 the transfer process is more or less independent of ambient conditions surrounding the bodies. For graphite, however, moisture (or other contaminants such as simple hydrocarbons) must be available to weaken the interlayer bond strength of the solid. This effect is of importance in high-altitude rockets. In the reduced moisture levels at high altitude, brush wear in the electric generators becomes extreme and large amounts of carbon dust are formed.

[13]Note that the distance between the lamellae is 0.34 nm for carbon and 0.349 nm in the molybdenum disulfide, putting them safely out of range of short distance, i.e., strong forces. The interlayer atomic distance in graphite, on the other hand, is only 0.142 nm.

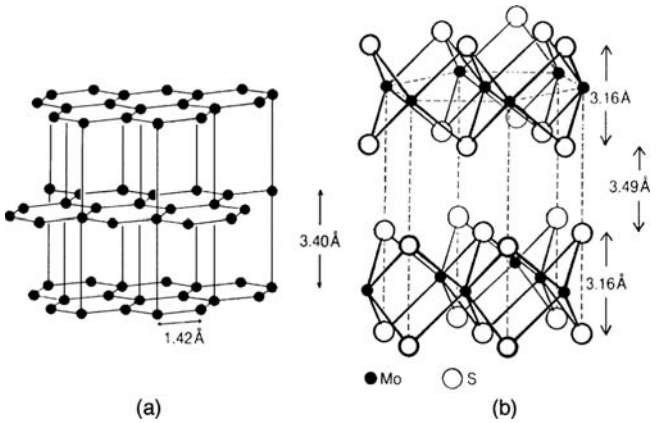

Figure 1.23. The structures of (a) graphite and (b) molybdenum disulfide. (Reprinted with permission from Hutchings, I. M. *Tribology: Friction and Wear of Engineering Materials*. Copyright CRC Press, Boca Raton, Florida, © 1992.)

Very small amounts of organic compounds or moisture will inhibit this wear (Bisson and Anderson, 1964). Not all lamellar solids exhibit small friction; some are more isotropic.

1.6 Fluid Film Bearings

Bearings are machine elements whose function is to promote smooth relative motion at low friction between solid surfaces. The surfaces might be in direct contact, but if they are not, the lubricant film separating them can be liquid, gaseous, or solid.

Considering the global geometry of the surfaces, a bearing may be *conformal* or *counterformal*. The conformal condition is depicted in part (a) of Figure 1.24. In conformal bearings, a prototype of which is the journal bearing, the apparent area of contact is large. The maximum film pressure is of the same order of magnitude as the *specific bearing load*, defined by $P = W/A$, where W is the external load and A is the projected (normal to the load) bearing area.[14] The film pressures are relatively small in conformal bearings and the lubricant film is thick. In consequence, the bulk deformation of the bearing surfaces is relatively unimportant or at least less important than the deformation of the asperities, say, during the running-in period.

The counterformal condition, illustrated in part (b) of Figure 1.24, is typically found in gear lubrication and in rolling-contact bearings. There the contact stresses are extremely high and the film is thin. The lubricant oil exhibits properties in this high-pressure contact zone that might be significantly different from its properties in bulk; it behaves as a virtual solid. The elastic deformation of the solid surfaces forms an essential component of the analysis of these bearings. One of the first investigator to study the elastic deformation of contacts was Hertz, and the counterformal condition is often referred to as the *Hertzian* condition.

When there is a continuous fluid film separating the solid surfaces we speak of fluid film bearings. There are two principal ways of creating and maintaining a load-carrying film between solid surfaces in relative motion. We call a bearing *self-acting*, and say

[14]For journal bearings, irrespective of the arc length, the specific bearing load is defined as P/LD, where L is the length and D is the diameter of the bearing.

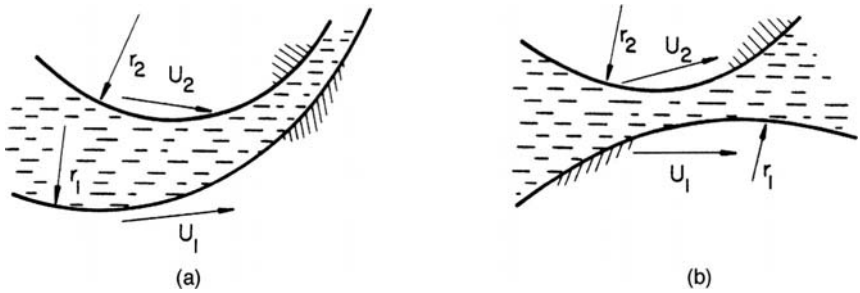

Figure 1.24. (a) Conformal and (b) counterformal geometry.

that it operates in the *hydrodynamic mode* of lubrication, when the film is generated and maintained by the viscous drag of the surfaces themselves, as they are sliding relative to one another. The bearing is *externally pressurized*, and it operates in the *hydrostatic mode*, when the film is created and maintained by an external pump that forces the lubricant between the solid surfaces. The term fluid is used here to designate either a liquid or a gaseous substance, but there are some fundamental differences between liquid-lubricated bearings and gas-lubricated bearings because of the compressibility of gases. For this reason this book will discuss both liquid-lubricated bearings and gas-lubricated bearings, although in separate chapters. However, for the purpose of this introduction it is sufficient to illustrate the method of operation of liquid film bearings only. Liquid-lubricated bearings are compared on the basis of film thickness and coefficient of friction in Table 1.5.

Table 1.5. *Comparison of liquid film bearings*

Lubrication mode	Film thickness (μm)	Friction coefficient
Hydrostatic	50–5	10^{-6}–10^{-3}
Hydrodynamic	10–1	10^{-3}–10^{-2}
Elastohydrodynamics	1–0.1	10^{-3}–10^{-2}

Hydrostatic Bearings

Hydrostatic lubrication is, in principle, the simplest mode of liquid film lubrication. The load-carrying film is both created and maintained by external means, the essential property of this lubrication mode being that the load-carrying surface is floated, irrespective of whether there is relative motion.

Part (a) of Figure 1.25 illustrates the geometry of a hydrostatic bearing at the commencement of its operation. The lubricant is supplied to the recess at the supply pressure p_S either directly by a pump or via a manifold and flow restrictor. The load-carrying runner will be supported by and will rest on the land as long as the supply pressure is below the value W/A_R, where A_R is the recess area. The runner will lift-off as soon as the supply pressure reaches W/A_R. At this stage lubricant flow out of the recess and over the land will commence, and the solid surfaces will be separated by a continuous lubricant film, as shown in part (b) of Figure 1.25. The recess pressure is now given by $p_R = p_S - \Delta p$, where Δp represents line losses, including those encountered in the flow control devices. Varying the supply pressure once lift-off has occurred will simply vary the film thickness h but will leave the recess pressure unchanged.

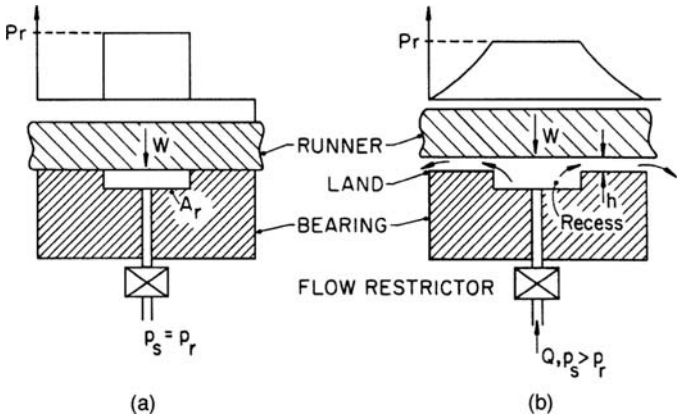

Figure 1.25. Hydrostatic bearing schematics (a) before and (b) after lift-off.

Generally speaking, hydrostatic systems use several evenly spaced pads, as shown in Figure 1.26, so that asymmetric load distributions may be managed. Under normal conditions, depicted by position I in Figure 1.26, the external load W is distributed equally between the two hydrostatic pads A and B with uniform and equal film thickness. Tilting the runner to position II will have the effect of decreasing the film thickness h_A over pad A and increasing the film thickness h_B over B.

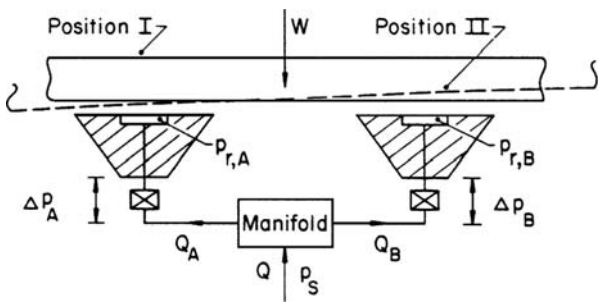

Figure 1.26. Operation with flow restrictors.

Because of the increased resistance to flow over pad A, the rate of lubricant flow Q_A will decrease. This will cause the recess pressure $p_{R,A}$ to increase, as there is now less pressure drop across the flow restrictor in line A. On the other hand, the increase in film thickness over pad B will lead to a decrease in the recess pressure $p_{R,B}$.

Operation with flow restrictors may be summarized as follows:

$$ps = p_{R,A} + \Delta p_A = p_{R,B} + \Delta p_B = \text{const.}$$

$$\text{Pad } A \begin{cases} Q_A^{II} < Q_A^I \\ \Delta p_A^{II} < \Delta p_A^I \\ p_{R,A}^{II} > p_{R,A}^I \end{cases} \qquad \text{Pad } B \begin{cases} Q_B^{II} > Q_B^I \\ \Delta p_B^{II} > \Delta p_B^I \\ p_{R,B}^{II} < p_{R,B}^I \end{cases} .$$

The net effect of the action of the two pads will be a restoring moment on the runner.

An externally pressurized bearing equipped with *flow restrictors* is called a *compensated* bearing. Flow restrictor design influences bearing stiffness, required supply pressure, required pumping power, and lubricant flow.

Among the advantages of hydrostatic bearings are:

(1) Low friction (vanishing with relative speed)
(2) Unaffected by discontinuous motion of the runner
(3) Exact positioning of the runner, as film thickness can be controlled accurately
(4) Capable of supporting heavy loads
(5) Only moderate temperature rise across pad because of large film thickness
(6) Continuous outflow of lubricant prevents ingress of dirt

Among the disadvantages of externally pressurized systems we list:

(1) Requirement for auxiliary external equipment
(2) Risk of lubrication failure because of failure of auxiliary equipment
(3) High power consumption by pumps
(4) Necessity of constant supervision
(5) High initial cost

Despite their many disadvantages, externally pressurized bearings are widely used. Machine tools using this type of bearing can grind parts round within 0.05 μm, with a 0.025 μm surface finish. The lubricant can be either gaseous or liquid. Gaseous lubricant is often used in lightly loaded applications (high-speed drills, gyroscopes, torque meters), whereas liquid systems are normally used for heavier loads. Examples of the latter are the bearings of the 200-inch optical telescope at Mount Palomar, which weighs 500 tons, and the 140-foot radio telescope at Green Bank, with a support weight of 2000 tons in addition to wind loads. Oil lifts, working in the hydrostatic mode, are often built into the hydrodynamic bearings of large rotating apparatus to aid starting and stopping.

Hydrodynamic Bearings

To understand the operation of bearings in the hydrodynamic mode, consider fluid flow between two solid surfaces. Both surfaces extend to infinity in the direction perpendicular to the plane of Figure 1.27 and are slightly inclined toward one another. A typical value for the slope of the solid surfaces in industrial bearings is 0.001 radian. The top surface in Figure 1.27 is sliding in its own plane, with a velocity, U, relative to the lower surface, dragging the lubricant with it into the convergent (in the direction of relative motion) gap. No external pressure gradient is imposed on the flow.

If the fluid pressure were uniform everywhere in the film, with the flow induced solely by the motion of the slider, the flow rate from left to right would be given by $Q = Uh/2$. But the film thickness h varies along the gap, whereas the principle of mass conservation requires Q to be constant.

The apparent inconsistency is removed if we allow for the existence of a pressure flow of varying strength and direction, such that it aids shear flow where $hU/2$ is small (i.e., where the gap is narrow) and hinders it where it is large. In this way we arrive at a uniform flow rate so that mass conservation is satisfied. The type of pressure curve that would induce the desired pressure flow is shown in Figure 1.27, it is readily measured in hydrodynamic bearings.

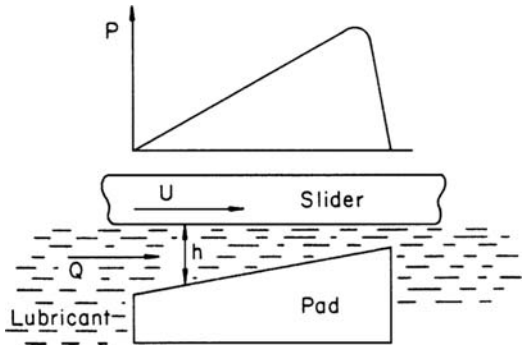

Figure 1.27. Schematics of a plane slider.

The plane slider of Figure 1.27 is the prototype of the hydrodynamic *thrust bearing*. One of the more frequent functions of hydrodynamic bearings is to support rotating shafts; thrust bearings are employed in these cases if the load vector is parallel to the axis of rotation.

If the motion that the bearing must accommodate is rotational and the load vector is perpendicular to the axis of rotation, the hydrodynamic bearings employed are *journal bearings*.

When the lubricant is incompressible, the film temperature is nearly uniform, and the load vector is fixed in space, as shown in Figure 1.28, the operating conditions of a journal bearing of aspect ratio L/D can be uniquely characterized with reference to a single dimensionless parameter. This parameter, the *Sommerfeld number*, is defined as

$$S = \frac{\mu N}{P}\left(\frac{R}{C}\right)^2,$$

where C represents the radial clearance, i.e., the difference between the bearing and journal radii $C = R_B - R_J$, $P = W/LD$ is the specific bearing load, N is the rotational speed, and μ is the dynamic viscosity of the lubricant. Following accepted practice, we put $R_B = R$ in the definition of the Sommerfeld number.

The journal will be concentric with the bearing under the condition $P \to 0$ or $N \to \infty$, i.e., when $S \to \infty$. On decreasing the speed or increasing the load – in general, on decreasing the value of the parameter S – the journal will occupy an eccentric position of eccentricity e, its center sinking below the center of the bearing. As $S \to 0$ the solid surfaces approach one another and the lubricant film eventually fails, resulting in high temperatures and considerable wear due to rubbing. The movement of the journal center is generally not

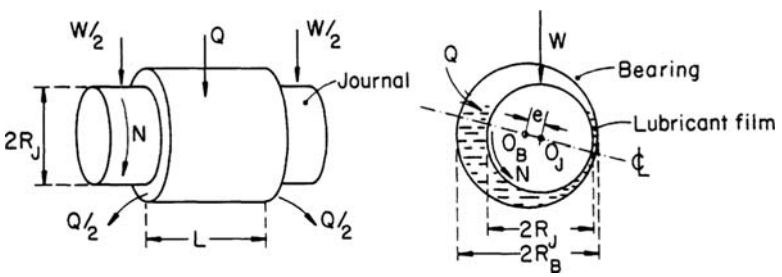

Figure 1.28. Schematics and nomenclature of a journal bearing.

along a straight line. But its locus, well represented by a semicircle of diameter C, can be predicted in many cases to the required accuracy.

The oil required for hydrodynamic lubrication can be fed from an oil reservoir under gravity, it may be supplied from a sump by rings, disks, or wicks. The bearing might even be made of a porous metal impregnated with oil, which "bleeds" oil to the bearing surface as the journal rotates. Most porous metal bearings, however, operate in the mixed or even in the boundary lubrication regime.

Hydrodynamic bearings vary enormously both in their size and in the load they support. At the low end of the specific-load scale we find bearings used by the jeweler, and at the high end we find the journal bearings of a large turbine generator set, which might be 0.8 m in diameter and carry a specific load of 3 MPa, or the journal bearings of a rolling mill, for which a specific load of 30 MPa is not uncommon. Gas bearings, on the other hand, operate at low specific load (0.03 MPa) but often at high speeds. The high-speed, air turbine-driven dental drill is capable of 500,000 rev/min.

Elastohydrodynamic Lubrication

The term elastohydrodynamic lubrication (EHL) is reserved for hydrodynamic lubrication applied to lubricant films between elastically deforming solids. The principles of EHL are readily applicable to such diverse objects as gears, rolling-element bearings, and human and animal joints. In general, bearings that are lubricated in the EHL mode are of low geometric conformity, and, in the absence of a lubricant film and of elastic deformation, the opposing surfaces would contact in a point (ball bearings) or along a line (gears or roller bearings).

If the solid surfaces that are lubricated in the EHL mode have large elastic modulus, the contact pressures will be large, perhaps of the order of 1 GPa. The film thickness will be correspondingly small, of the order of 1 μm. Under such conditions the material properties of the lubricant will be distinctly different from its properties in bulk. This change in lubricant properties, when coupled with the effects of elastic deformation of the solid surfaces, yields film thicknesses one or two orders of magnitude larger than those estimated from constant viscosity theory applied to nondeforming surfaces.

EHL theory may be viewed as a combination of hydrodynamic lubrication, allowance for the pressure dependence of viscosity, and elastic deformation of the bounding surfaces. The subject of elastohydrodynamic lubrication is outlined in Chapter 8.

1.7 Bearing Selection

While promoting smooth relative motion of the contact surfaces, bearings will necessarily constrain such motions to occur (1) about a point, (2) about a line, (3) along a line, or (4) in a plane.

Our main concern here is with motions that are constrained to proceed about a line and in a plane. When continuous, both of these types of motion include rotation, the former situation calling for journal bearings and the latter for thrust bearings.

There are four methods of supporting the contact load in the cases above: (1) letting the surfaces rub against one another, (2) separating the surfaces by a fluid film, (3) rolling one surface over another, and (4) separating the surfaces by electromagnetic forces.

A fifth method, that of introducing a flexible member between the surfaces, is not suitable for continuous motion and is mentioned here only for the sake of completeness. Of the four

methods of dealing with contact forces, our interest is with dry rubbing bearings, fluid film bearings, and rolling-element bearings. These may be journal bearings or thrust bearings, according to the constraining influence they are required to supply.

Rubbing Bearings

The friction and wear of rubbing surfaces has been discussed in earlier sections of this chapter. It is sufficient to only consider frictional heating here. The rate of heat generated is given by FU, where F is the frictional force and U is the relative velocity of the surfaces. If A is the projected bearing area, then the risk of overheating is some function of

$$\frac{FU}{A} = fPU, \tag{1.32}$$

where $P = W/A$ is the specific bearing load. Overheating may result in seizure of the surfaces and should be avoided. The performance of dry rubbing bearings is also limited by an upper value of P, above which fatigue or extrusion of the bearing material may occur, and by a wear rate [which again is proportional to the product PU, Eq. (1.31)], as excessive wear leads to slackness of the machine elements. To avoid excessive wear, rubbing bearings are, in general, lubricated by a thin film of solid lubricant.

Dry rubbing and boundary-lubricated bearings are best suited to low speeds and intermittent duty. They provide high stiffness once loaded heavily, but they are the least-stiff bearings under light load. Safe maximum PU values have been determined experimentally, but these must be used with caution.

Rolling-Element Bearings

Bearings based on rolling-sliding are called rolling-element bearings. In a typical application this type of bearing usually provides for more precise shaft positioning than hydrodynamic bearings (but where extreme precision in positioning is required, externally pressurized bearings are called for). These bearings perform well when subjected to repeated starts-stops under full load. They are best suited to low-speed high-load situations. Rolling-element bearings have little inherent damping capacity, leading to excessive plastic deformation of raceways and premature fatigue under repeated shock loads.

With well-designed rolling-element bearings, wear is microscopic through most of the life of the bearing. The ultimate limit of bearing performance is often surface fatigue of the elements or the raceway. Rolling contact fatigue is characterized by the fairly rapid formation of large wear fragments, signaling the end of bearing life. Up until such time, there is no detectable wear in well-lubricated rolling-contact bearings. Therefore, it is inappropriate to discuss wear rate in these bearings, and the term *bearing life* is preferable. Bearing life is a function of the load and the total number of revolutions. Empirically, it has been found that the bearing life, L, is inversely proportional to the third power of the load W.

Fluid Film Bearings

Wear is not a consideration in fluid film bearings, since in a well-designed fluid film bearing the surfaces are always separated by a continuous fluid film. One of the

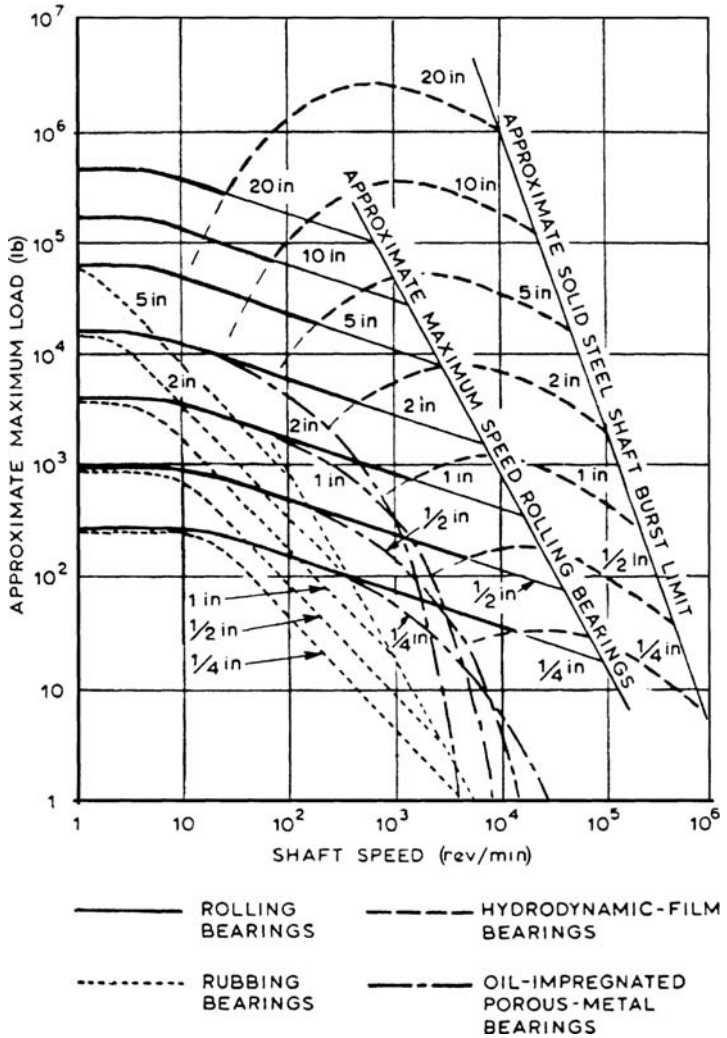

Figure 1.29. Load-speed characteristics of journal bearings. (From the Tribology Subseries Item No. 65,007, *General Guide to the Choice of Journal Bearing Type*, by permission of Engineering Sciences Data Unit Ltd., London.)

exceptions to this rule is the heavily loaded self-acting (hydrodynamic) bearing during starting-stopping.

If the bearing is externally pressurized, the load capacity is virtually independent of surface speeds, although at high speeds a decrease of load capacity might be expected because of thermal and/or inertial effects.

If the bearing is of the self-acting type, the load capacity increases with surface speed initially. However, when the rate of heat generation becomes high enough to influence lubricant viscosity, the load capacity drops off. If the bearing is self-contained, an additional constraint is presented by the minimum film thickness limit at low speeds and by the heat removal (maximum Babbitt temperature) limit at high speeds. Hydrodynamic bearings are

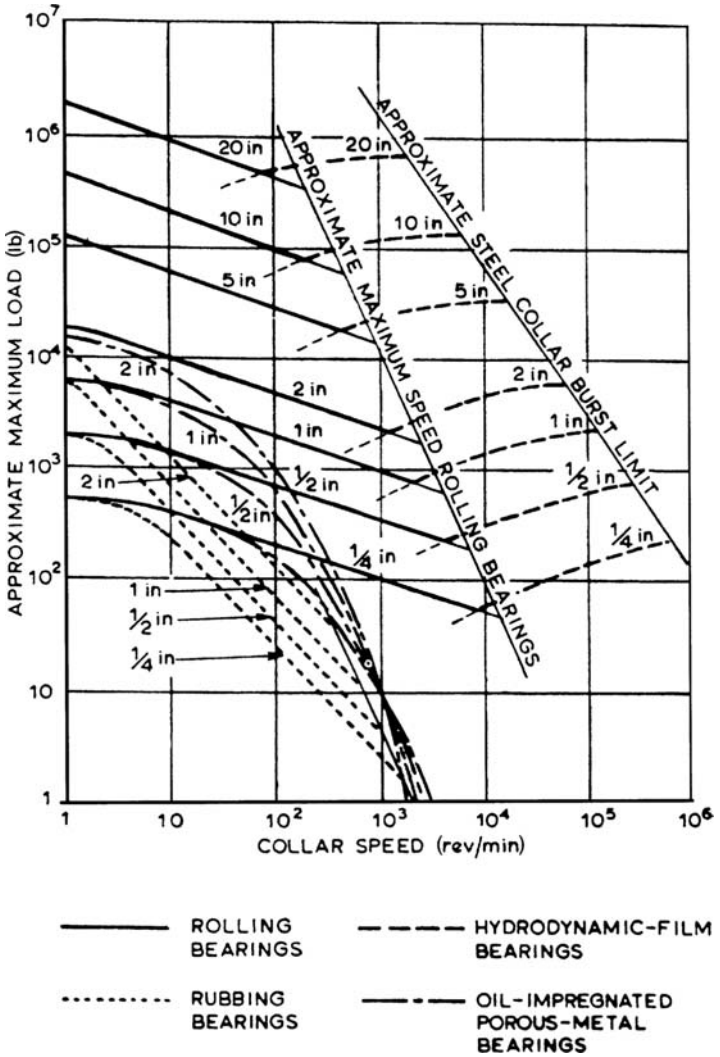

Figure 1.30. Load-speed characteristics of thrust bearings. (From the Tribology Subseries Item No. 65,007, *General Guide to the Choice of Thrust Bearing Type*, by permission of Engineering Sciences Data Unit Ltd., London.)

best suited by their load-speed character to applications where the load increases with speed, whereas hydrostatic bearings are most useful in situations where the load is independent of speed.

The performance of steadily loaded journal bearings and of thrust bearings is shown in Figures 1.29 and 1.30, respectively. These figures are reproduced from a paper by Neale (1967) and show only general trends. The reader interested in bearing selection is referred to the *Tribology Handbook* by Neale (1973) and to an exhaustive article in *Machine Design* (1978). Considerations other than load and speed may often have overriding importance in bearing selection. Tables 1.6 and 1.7 may be used to advantage in bearing selection.

Table 1.6. *Advantages and limitations of journal bearings*

Condition	General comments	Journal bearing type						
		Rubbing bearings	Oil-impregnated porous metal bearings	Rolling-element bearings	Hydrodynamic fluid film bearings	Hydrostatic fluid film bearings	Self-acting gas bearings	Externally pressurized gas bearings
High temperature	Attention to differential expansions and their effect on fits and clearances is necessary	Normally satisfactory depending on material	Attention to oxidation resistance of lubricant is necessary	Up to 100°C no limitations; from 100 to 250°C stabilized bearings and special lubrication procedures are probably required	Attention to oxidation resistance of lubricant is necessary		Excellent	Excellent
Low temperature	Attention to differential expansions and starting torques is necessary		Lubricant may impose limitations; consideration of starting torque is necessary	Below −30°C special lubricants are required; consideration of starting torque is necessary	Lubricant may impose limitations; consideration of starting torque is necessary	Lubricant may impose limitations	Excellent; thorough drying of gas is necessary	
External vibration	Attention to the possibility of fretting damage is necessary (except for hydrostatic bearings)	Normally satisfactory except when peak of impact load exceeds load-carrying capacity		May impose limitation; consult manufacturer	Satisfactory	Excellent	Normally satisfactory	Excellent

(*continued*)

Table 1.6 *(continued)*

Condition	General comments	Journal bearing type						
		Rubbing bearings	Oil-impregnated porous metal bearings	Rolling-element bearings	Hydrodynamic fluid film bearings	Hydrostatic fluid film bearings	Self-acting gas bearings	Externally pressurized gas bearings
Space requirements		Small radial extent		Bearings of many different proportions; small axial extent	Small radial extent but total space requirement depends on the lubrication feed system		Small radial extent	Small radial extent, but total space requirement depends on the gas feed system
Dirt or dust		Normally satisfactory; sealing is advantageous	Sealing is important		Satisfactory; filtration of lubricant is important		Sealing important	Satisfactory
Vacuum		Excellent	Lubricant may impose limitations				Not normally applicable	Not applicable when vacuum has to be maintained
Wetness and humidity	Attention to possibility of metallic corrosion is necessary	Normally satisfactory depending on material	Normally satisfactory; sealing advantageous	Normally satisfactory, but special attention to sealing may be necessary	Satisfactory		Satisfactory	
Radiation		Satisfactory	Lubricant may impose limitations				Excellent	
Low starting torque		Not normally recommended	Satisfactory	Good	Satisfactory	Excellent	Satisfactory	Excellent

Low running torque								
Accuracy of radial location		Poor	Good			Excellent	Good	Excellent
Life		Finite but predictable			Theoretically infinite but affected by infinite filtration and number of stops and starts	Theoretically infinite	Theoretically infinite but affected by number of stops and starts	Theoretically infinite
Combination of axial and load-carrying capacity		A thrust face must be provided to carry the axial loads		Most types capable of dual duty	A thrust face must be provided to carry the axial loads			
Silent running		Good for steady loading	Excellent	Usually satisfactory; consult manufacturer	Excellent	Excellent except for possible pump noise	Excellent	Excellent except for possible compressor noise
Simplicity of lubrication		Excellent		Excellent with self-contained grease or oil lubrication	Self-contained assemblies can be used with certain limits of load, speed, and diameter; beyond this, oil circulation is necessary	Auxiliary high pressure is necessary	Excellent	Pressurized supply of dry clean gas is necessary

(*continued*)

Table 1.6 *(continued)*

Condition	General comments	Journal bearing type						
		Rubbing bearings	Oil-impregnated porous metal bearings	Rolling-element bearings	Hydrodynamic fluid film bearings	Hydrostatic fluid film bearings	Self-acting gas bearings	Externally pressurized gas bearings
Availability of standard parts		Good to excellent depending on type	Excellent		Good		Not available	
Prevention of contamination product and surroundings		Improved performance can be obtained by allowing a process liquid to lubricate and cool the bearing, but wear debris may impose limitations	Normally satisfactory, but attention to sealing is necessary, except where a process liquid can be used as a lubricant				Excellent	
Frequent stop-starts		Excellent	Good	Excellent	Good	Excellent	Poor	Excellent
Frequent change of rotating direction			Generally good		Generally good			
Running costs			Very low		Depends on Complexity of lubrication system	Cost of lubricant supply has to be considered	Nil	Cost of gas supply has to be considered

(From ESDU< 1965, by permission of Engineering Sciences Data Unit Ltd., London.)

Table 1.7 *Advantages and limitations of thrust bearings*

Condition	General comments	Thrust bearing type						
		Rubbing bearings	Oil-impregnated porous metal bearings	Rolling-element bearings	Hydrodynamic fluid film bearings	Hydrostatic fluid film bearings	Self-acting gas bearings	Externally pressurized gas bearings
High temperature	Attention to differential expansions and their effect upon axial clearance is necessary	Normally satisfactory depending on material	Attention to oxidation resistance of lubricant is necessary	Up to 100°C no limitations; from 100 to 250°C stabilized bearings and special lubrication procedures are probably required	Attention to oxidation resistance of lubrication is necessary		Excellent	
Low temperature	Attention to differential expansions and starting torques is necessary		Lubricant may impose limitations; consideration of starting torque is necessary	Below − 30°C special lubricants are required; consideration of starting torque is necessary	Lubricant may impose limitations; consideration of starting torque is necessary	Lubricant may impose limitations	Excellent; thorough drying of gas is necessary	
External vibration	Attention to the possibility of fretting damage is necessary (except for hydrostatic bearings	Normally satisfactory except when peak of impact load exceeds load-carrying capacity		May impose limitations; consult manufacturer	Satisfactory	Excellent	Normally satisfactory	Excellent

(*continued*)

Table 1.7 *(continued)*

Condition	General comments	Thrust bearing type						
		Rubbing bearings	Oil-impregnated porous metal bearings	Rolling-element bearings	Hydrodynamic fluid film bearings	Hydrostatic fluid film bearings	Self-acting gas bearings	Externally pressurized gas bearings
Space requirements		Small radial extent		Bearings of many different proportions are available	Small radial extent but total space requirement depends on the lubrication feed system		Small radial extent	Small radial total space requirement depends on gas feed system
Dirt or dust		Normally satisfactory; sealing advantageous		Sealing is important	Satisfactory; filtration of lubricant is important		Sealing important	Satisfactory
Vacuum		Excellent	Lubricant may impose limitations				Not normally applicable	Not applicable when vacuum has to be maintained
Wetness and humidity	Attention to possibility of metallic corrosion is necessary	Normally satisfactory depending on material	Normally satisfactory; sealing advantageous	Normally satisfactory, but special attention to sealing is perhaps necessary	Satisfactory			
Radiation		Satisfactory	Lubricant may impose limitations				Excellent	

Low starting torque		Not normally recom-mended	Satisfactory	Good	Satisfactory	Excellent	Satisfactory	Excellent
Low running torque					Satisfactory		Excellent	
Accuracy of radial location		Good				Excellent	Good	Excellent
Life		Finite but can be estimated			Theoretically infinite but affected by filtration and number of stops and starts	Theoretically infinite	Theoretically infinite but affected by number of stops and starts	Theoretically infinite
Combination of axial and load-carrying capacity		A journal bearing surface must be provided to carry the radial loads		Some types capable of dual duty	A journal bearing surface must be provided to carry the radial loads			
Silent running		Good for steady loading	Excellent	Usually satisfactory; consult manufacturer	Excellent	Excellent, except for possible pump noise	Excellent	Excellent, except for possible compressor noise

(*continued*)

Table 1.7 *(continued)*

Condition	General comments	Thrust bearing type						
		Rubbing bearings	Oil-impregnated porous metal bearings	Rolling-element bearings	Hydrodynamic fluid film bearings	Hydrostatic fluid film bearings	Self-acting gas bearings	Externally pressurized gas bearings
Simplicity of lubrication		Excellent		Excellent with self-contained grease lubrication; with large sizes or high speeds, oil lubrication might be necessary	Self-contained assemblies can be used with certain limits of load, speed, and diameter; beyond this, oil circulation is necessary	Auxiliary high pressure is necessary	Excellent	Pressurized supply of dry, clean gas is necessary
Availability of standard parts		Good to excellent depending on type	Excellent		Good	Poor		
Prevention of contamination of product and surroundings		Performance can be improved by allowing a process liquid to lubricate and cool the bearing, but wear debris may impose limitations	Normally satisfactory, but attention to sealing is necessary, except where a process liquid can be used as a lubricant				Excellent	

Tolerance to manufacturing and assembly inaccuracies				Good	Satisfactory	Poor	Satisfactory	Poor	Satisfactory
Type of motion	Frequent start-stops			Excellent		Good	Excellent		Excellent
	Unidirectional			Suitable					
	Bidirectional			Suitable		Some types are suitable	Suitable	Some types are suitable	Suitable
	Oscillatory					Unsuitable		Unsuitable	
Running costs				Very low		Depends on complexity of lubrication system	Cost of lubricant supply has to be considered	Nil	Cost of gas supply has to be considered

(From ESDU, 1967, by permission of Engineering Sciences Data Unit Ltd., London.)

1.8 Nomenclature

A	projected bearing area
A_r	area of contact
C	journal bearing radial clearance
D	diameter
E	elastic modulus
F	friction force
H	hardness
L	bearing length
N	shaft revolution
O_B, O_J	bearing, journal center
P	specific bearing load
Q	lubricant flow rate, wear rate
R	radius
R_B, R_J	bearing, journal radius
S	Sommerfeld number
U	velocity
V	wear volume
W	external load
Ψ	plasticity number
e	journal eccentricity
k	shear strength
f	coefficient of friction (F/W)
p	pressure
p_0	yield pressure
p_R, p_S	supply, recess pressure
Δp	pressure drop
μ	viscosity
a	radius
h	asperity height, film thickness
ℓ	asperity spacing
$\bar{p}$	average pressure,
κ_N	probability
σ	standard deviation
σ_Y	limiting tensile stress
τ	tangential stress
τ_c	shear strength
τ_j	junction failure stress
τ_m	maximum shear stress

1.9 References

Amontons, G. 1699. De la Resistance Causee dans les Machines. *Roy. Soc.* (Paris), 206.

Archard, J. F. 1953. Contact and rubbing of flat surfaces. *J. Appl. Phys.*, **24**, 981–988.

Archard, J. F. and Hirst, W. 1956. The wear of metals under unlubricated conditions. *Proc. Roy. Soc.*, **A 236**, 397–410.

Archard, J. F. 1957. *Proc. Roy. Soc.*, **A 243**, 190.

Arnell, R. D., Davies, P. B., Halling, J. and Whomes, T. L. 1991. *Tribology Principles and Design Applications*. Springer Verlag, New York.

Bhushan, B., Israelachvili, J. N. and Landman, U. 1995. Nanotribology: friction, wear and lubrication at the atomic scale. *Nature*, **374**, 607–616.

Bhushan, B., Wyant, J. C. and Meiling, J. 1988. New three-dimensional non-contact digital optical profiler. *Wear*, **122**, 301–312.

Bisson, E. E. and Anderson, W. J. 1964. *Advanced Bearing Technology*. NASA Spec. Publ. SP-38.

Booser, E. R. 1984. *Handbook of Lubrication. Volume II*. CRC Press, Boca Raton, Florida.

Bowden, F. P. and Tabor, D. 1986. *The Friction and Lubrication of Solids*, Vol. 1 (paperback ed.). Oxford Univ. Press, Oxford.

Bowden, F. P. and Tabor, D. 1964. *The Friction and Lubrication of Solids*, Vol. 2. Oxford Univ. Press, Oxford.

Bowden, F. P. and Rowe, G. W. 1956. The adhesion of clean metals. *Proc. Roy. Soc.*, **A 233**, 429–442.

Briscoe, B. J. and Tabor, D. 1978. The friction and wear of polymers: The role of mechanical properties. Polymer J., **10**, 74–96.

Buckley, D. H. 1977. The metal-to-metal interface and its effect on adhesion and friction. *J. Coll.* Interface Sci., **58**, 36–53.

Childs, T. C. C. 1992. Deformation and flow of metals in sliding friction. In *Fundamentals of Friction in Macroscopic and Microscopic Processes*. NATO ASI Series, Kluwer, Dordrecht.

Coulomb, C. A. 1785. Theorie des Machines Simples. *Mem. Math. Phys. Acad. Sci.*, **10**, 161.

Cramer, H. 1955. *The Elements of Probability Theory*. Wiley, New York.

da Vinci, L. 1519. *The Notebooks of Leonardo da Vinci*, E. Macurdy (ed.). Reynal & Hitchcock, New York, 1938.

Dake, L. S., Russel, J. A. and Debrodt, D. C. 1986. A review of DOE ECUT Tribology Surveys. *ASME Journal of Tribology*, **108**, 497–501.

Dowson, D. 1973. Tribology before Columbus. *Mech. Eng.*, **95**, 12–20.

Dowson, D. 1979. *History of Tribology*. Lomgman, London and New York.

Ettles, C. M. 1987. Polymer and elastomer friction in the thermal control regime. *ASLE Trans.*, **30**, 149–159.

General guide to the choice of journal bearing type. 1965. *Tribology Subseries Item No. 65007.* Engineering Sciences Data Unit Ltd., 251–259, Regent Street, London.

General guide to the choice of thrust bearing type. 1967. *Tribology Subseries Item No. 65033.* Engineering Sciences Data Unit Ltd., 251–259, Regent Street, London.

Fuller, D. D. 1956. *Theory and Practice of Lubrication for Engineers*. Wiley, New York.

Godfrey, D. 1980. *Wear Control Handbook*. ASME New York.

Greenwood, J. A. and Williamson, J. B. 1966. Contact of nominally flat surfaces. *Proc. Roy. Soc.*, **A 295**, 300–319.

Greenwood, J. A. 1992. Contact of rough surfaces. In *Fundamentals of Friction: Macroscopic and Microscopic Processes*. (I. L. Singer and H. M. Pollock, eds.), pp. 37–56. Kluwer, Dordrecht.

Hamilton, G. M. 1983. Explicit equations for the stress beneath a sliding spherical contact. *Proc. I. Mech. E.*, **197**, 53–59.

Hutchings, I. M. 1992. *Tribology: Friction and Wear of Engineering Materials*. CRC Press, Boca Raton.

Hersey, M. D. 1966. *Theory and Research in Lubrication*. Wiley, New York.

Jahanmir, S. 1994. *Friction and Wear of Ceramics*. Marcel Dekker, New York.

Johnson, K. L. 1992. *Contact Mechanics* (paperback ed.). Cambridge University Press.

Kragelskii, I. V. and Marchenko, E. A. 1982. Wear of machine components. *ASME Journal of Tribology*, **104**, 1–7.

Lancaster, J. K. 1963. The formation of surface films at the transition between mild and severe metallic wear. *Proc. Roy. Soc.*, **A 273**, 466–483.

Landman, U., Luedtke, W. D. and Ringer, E. M. 1992. Molecular dynamics simulations of adhesive contact formation and friction. In *Fundamentals of Friction in Macroscopic and Microscopic Processes*. NATO ASI Series, Kluwer, Dordrecht.

Lim, S. C. and Ashby, M. F. 1987. Wear mechanism maps. *Acta Metall.*, **35**, 1–24.

Lubrication Engineering Working Group, Dept. of Ed. and Sci. 1966. *Lubrication* (*Tribology*). H.M.S.O., London.

McNeill, W. 1963. *The Rise of the West, A History of the Human Community*. University of Chicago Press.

Majumdar, A. and Bhushan, B. 1990. Role of fractal geometry in roughness characterization and contact mechanics of surfaces. *ASME Journal of Tribology*, **112**, 205–216.

Merchant, M. E. 1940. The mechanism of static friction. *J. Appl. Phys.*, **11**, 230.

Neale, M. M. 1967. Selection of bearings and lubricants. *Proc. Inst. Mech. Eng.* **182**, pt. **3A**, 547–556.

Neale, M. J. 1978. *Tribology Handbook*. Butterworth, London.

Mechanical Drives. 1978. *Mach. Design*, **50**, no. 15, 137–236.

Peterson, M. B. and Winer, W. O. 1980. *Wear Control Handbook*. ASME Press.

Peklenik, J. 1968. New developments in surface characterization and measurements by means of random process analysis. *Proc. Inst. Mech. Engrs.*, **182**, Pt. 3K, 108–126.

Rabinowicz, E. 1965. *Friction and Wear of Materials*. Wiley, New York.

Raimondi, A. A. and Boyd, J. 1958. A solution of the finite journal bearing and its application to analysis and design. *ASLE Trans.*, **1**, 159–209.

Reynolds, O. 1886. On the theory of lubrication and its application to Mr. Tower's experiments. *Philos. Trans. Roy. Soc.*, **177**, 157–234.

Ruan, J.-A. and Bhushan B., 1994. Atomic scale friction measurements using friction force microscopy. *ASME Journal of Lubrication Technology*, **116**, 378–388.

Sayle, R. S. and Thomas, T. R. 1979. Measurements of the statistical microgeometry of engineering surfaces. *ASME Journal of Lubrication Technology*, **101**, 409–418.

Sherrington, I. and Smith, E. H. 1988. Modern measurement techniques in surface metrology, *Wear*. **125**, 271–288.

Suh, N. P. 1986. *Tribophysics*. Prentice-Hall, Englewood Cliffs.

Tabor, D. 1939. Junction growth in metallic friction, the role of combined stresses and surface contamination. *Proc. Roy. Soc.*, **A 251**, 378.

Tabor, D. 1981. Friction – The present state of our understanding. *ASME Journal of Lubrication Technology*, **103**, 169–179.

Tian, X. and Kennedy, F. E. 1993. Contact surface temperature models of finite bodies in dry and boundary lubricated sliding systems. *ASME Journal of Tribology*, **115**, 411–418.

Tian, X. and Kennedy, F. E. 1994. Maximum and average flash temperatures in sliding contacts. *ASME Journal of Tribology*, **116**, 187–174.

Voyutski, S. S. 1963. *Autoadhesion and Adhesion of Polymers*. Wiley, New York.

Wang, S. and Komvopoulos, K. 1994. A fractal theory of the interfacial temperature distribution in the slow sliding regime: Parts I & II. *ASME Journal of Tribology*, **116**, 812–832.

Welsh, N. C. 1965. The dry wear of steels. *Phil. Trans. Roy. Soc.*, **A 257**, 31–70.

Basic Equations

2.1 Fluid Mechanics

The equations employed to describe the flow of lubricants in bearings result from simplifications of the governing equations of fluid mechanics. It is appropriate, therefore, to devote a chapter to summarizing pertinent results from that subject. This summary will not be limited to concepts necessary to appreciate the classical theory of lubrication. A more than elementary discussion of fluid behavior is called for here, as various nonlinear effects will be studied in later chapters.

Our discussion begins with the mathematical description of motion, followed by the definition of stress. We will then derive Cauchy's equations of motion by substituting the rate of change of linear momentum of a fluid body and the forces acting on it into Newton's second law. This will yield three equations, one in each of the three coordinate directions. For an incompressible fluid these three equations will contain twelve unknowns: three velocity components (u, v, w) and nine stress components $\left(T_{xx}, T_{xy}, \ldots, T_{zz}\right)$. For compressible fluids there is an additional unknown, the density; for incompressible fluids the density is known a priori. To render the problem well posed, i.e., to have the number of equations agree with the number of unknowns so that a unique solution might exist, we will need to find additional equations. A fourth equation is easy to come by, by way of the principle of conservation of mass. The situation further improves on recognizing that only six of the nine stress components are independent, due to symmetry of the stress tensor. However, on specifying incompressibility of the fluid, a tenth unknown, the fluid pressure makes its debut. In contrast, for a compressible fluid both the pressure and the density are variables, but as they are connected through the equation of state, we count them as representing a single unknown. In summary, for both compressible and incompressible fluid we end up having four equations and ten unknowns. Six additional equations are required.

Up to this point our discussion applies equally well not only to fluids but also to all continuous media, irrespective of material properties. However, if we wish to obtain the six additional equations that are still needed to close the problem, we can no longer retain this generality. Accounting for the material behavior of the particular fluid under consideration is, in fact, the ruse that will yield the missing equations. Material behavior of a class of materials is postulated in a *constitutive theory*, the mathematical statement of which is the set of *constitutive equations* for the class.

The simplest constitutive theory for fluids postulates that the normal stress components are equal while the shear stress components vanish identically; this defines what is called an *inviscid* or *ideal fluid*. When the corresponding constitutive equations are substituted into Cauchy's equations of motion, *Euler's equations* result. These equations have relative simplicity. However, inviscid fluids do not abound in nature and Euler's equations do not hold near solid surfaces. In engineering practice Euler's equations are featured mostly in the external flow problems of aerodynamics.

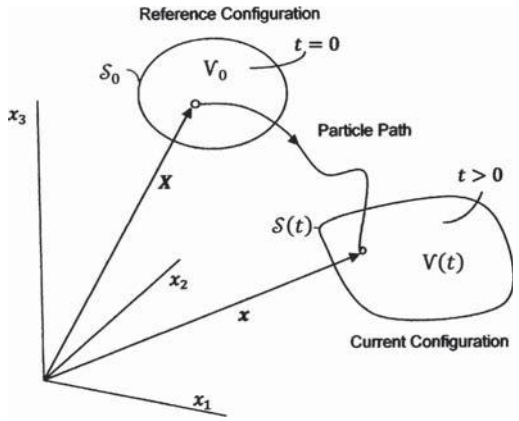

Figure 2.1. Motion of a fluid body.

A somewhat more complicated constitutive theory states that the stress is linearly dependent on the rate of deformation (a more complete definition will be given later). This is the constitutive theory of a *Newtonian fluid*. When the corresponding constitutive equations are substituted into Cauchy's equations of motion, the *Navier–Stokes equations* result. Newtonian theory is extremely useful as its predictions agree well with experimental data on a large class of common fluids such as water or air.

Not all fluids are *linearly viscous* (a term often used to describe Newtonian behavior); in particular, polymers and some other man-made fluids are not. Some naturally occurring fluids, such as crude oil, also belong to the class of *non-Newtonian fluids*. In some of these the current state of stress at a point is a nonlinear function of the current state of deformation of the neighborhood of that point. In others, the state of stress is determined by the whole *history* of this deformation. There are materials, which are both solid-like and fluid-like in their response to stress, in the sense that the work of deformation is neither completely stored as in solids, nor completely dissipated as in fluids. These substances, displaying both elasticity and viscosity, are called *viscoelastic* materials.

Kinematics

Picture a body of fluid as it is moving through physical space and concentrate on an inner part of this body of volume $\mathcal{V}(t)$, enclosed by the surface $\mathcal{S}(t)$.[1] Think of this fluid as consisting entirely of infinitesimal *particles* or *material points* (the terms *particle* and *material point* will be used interchangeably). Each such material point occupies one, and only one, *spatial point* at any given time. To specify the location of spatial points we employ an orthogonal Cartesian coordinate system (x_1, x_2, x_3).

For the purpose of future identification we assign permanent names to each of the infinity of fluid particles within $\mathcal{V}(t)$. This is best achieved by momentarily freezing the flow, initializing our clock, and assigning as permanent particle names the coordinates of the spatial point that the material point happens to occupy in this frozen configuration (Figure 2.1). We call this frozen configuration the *reference configuration* of the fluid. The

[1] Generally, we shall use script capital letters to designate volumes and surfaces that move with the fluid and script lowercase letters for volumes and surfaces that are fixed in space.

coordinates of a particle in the reference configuration are called its *reference coordinates*, or *Lagrangian coordinates*, or *material coordinates*, and are designated by capital letters (X_1, X_2, X_3). They are assigned to, and will be retained by, fluid particles as their permanent name. Particle position in the reference configuration, i.e., particle name, is thus identified by the position vector $\boldsymbol{X} = (X_1, X_2, X_3)$.

When it is not essential to discriminate among the various components of a vector, say, the position vector $\boldsymbol{x} = (x_1, x_2, x_3)$, i.e., when all coordinate directions have equal importance in a mathematical statement, we shall write x_i to represent the components. Should it become necessary to state the number of the components explicitly, we shall write x_i, $i = 1, 2, 3$. Here i, the index, ranges over 1, 2, 3 and the symbolism is called index notation. We shall use the notation x_1, x_2, or x_3, however, when wishing to draw attention to a particular component.

Upon unfreezing the fluid body, motion resumes. The particle that occupied the spatial position $\boldsymbol{X} = (X_1, X_2, X_3)$ at $t = 0$, now, at time $t > 0$, occupies another position $\boldsymbol{x} = (x_1, x_2, x_3)$. The continuous sequence of configurations that results from increasing the parameter t is called a motion.

Motion is defined, therefore, by the mapping

$$x_i = \chi_i(\boldsymbol{X}, t), \quad t \geq 0, \quad i = 1, 2, 3 \tag{2.1}$$

where it is understood that Eq. (2.1) is the index notation representation of the vector equation, $\boldsymbol{x} = \boldsymbol{\chi}(\boldsymbol{X}, t), t \geq 0$.

Equation (2.1) signifies that the particle that occupied position $\boldsymbol{X}$ in the reference configuration is located in point $\boldsymbol{x}$ at current time t. The coordinates x_i are called *Eulerian* or *spatial coordinates*. If $\boldsymbol{X}$ is fixed while t varies, Eq. (2.1) describes the *path* of particle $\boldsymbol{X}$. If, on the other hand, t is kept constant, Eq. (2.1) is the mapping of the reference configuration onto the configuration at time t.

We shall insist on Eq. (2.1) being invertible, so that no two particles occupy the same spatial point simultaneously, and no particle can be found at two different locations at the same time. In other words, we shall study only motions that can be characterized by *deformation functions* that possess single-valued inverse (this by no means constrains us in our investigations). The Jacobian of our motion is, thus, bounded

$$0 < J = \left| \frac{\partial \boldsymbol{x}}{\partial \boldsymbol{X}} \right| < \infty$$

We further assume that a sufficient number of derivatives of χ_i and its inverse χ_i^{-1} exist and are continuous. For such motions we may invert Eq. (2.1) and write

$$X_i = \chi_i^{-1}(\boldsymbol{x}, t). \tag{2.2}$$

Equation (2.2), or its vector representation $\boldsymbol{X} = \boldsymbol{\chi}^{-1}(\boldsymbol{x}, t)$, informs that the spatial point $\boldsymbol{x}$ at time t is being occupied by the particle that was located in position $\boldsymbol{X}$ in the reference configuration.

There are two viewpoints in fluid mechanics: (1) the *Lagrangian view* fixes attention on a given material point, i.e., holds $\boldsymbol{X}$ constant and describes the changes this material point experiences while moving through space (varying $\boldsymbol{x}$), and (2) the *Eulerian view* fixes attention on a spatial point, i.e., holds $\boldsymbol{x}$ constant and investigates how conditions change at that particular spatial point as various particles (varying $\boldsymbol{X}$) stream through it. Accordingly, variables associated with material points are given the qualifier *material* or *Lagrangian*,

while variables associated with spatial points are named *spatial* or *Eulerian*. The two types of variables are, of course, related to one another in unique fashion through the motion, Eq. (2.1), of the fluid: for example, the velocity at a fixed point $\boldsymbol{x}$ in space will vary with time, provided that the velocity of the string of particles. . . , $\boldsymbol{X}_k$, $\boldsymbol{X}_{k+1}$, . . . streaming through it varies from particle to particle at the instant when located at $\boldsymbol{x}$.

Velocity

Velocity is defined as the time rate of change of particle position. In Lagrangian representation we write

$$V_i(\boldsymbol{X}, t) = \frac{\partial x_i(\boldsymbol{X}, t)}{\partial t}. \tag{2.3}$$

Here, the V_i are the components of the velocity of a given particle (note that particle identity $\boldsymbol{X}$ is held constant during differentiation) as it travels along its path. By means of the motion of the fluid, Eq. (2.2), we can transform the Lagrangian variables V_i into the Eulerian variables v_i, where the v_i represent the velocity at the spatial point $\boldsymbol{x}$:

$$\boldsymbol{V}(\boldsymbol{X}, t) = \boldsymbol{V}\left[\boldsymbol{\chi}^{-1}(\boldsymbol{x}, t), t\right] = \boldsymbol{v}(\boldsymbol{x}, t). \tag{2.4}$$

Acceleration

Acceleration is the time rate of change of velocity. It is the sum of its two components: (1) the *local acceleration* and (2) the *convective acceleration*. Local acceleration can be observed at a fixed point $\boldsymbol{x}$ of space, when the velocity $\boldsymbol{V}$ of the fluid particles that pass through that point varies from particle to particle. It is, therefore, the time derivative of the velocity $\boldsymbol{v}(\boldsymbol{x}, t)$ with $\boldsymbol{x}$ held constant. Convective acceleration, on the other hand, is the rate of change of particle velocity as is experienced by a particle while propelled along its path by the prevailing velocity field. It is, therefore, the product of the velocity of the particle and the spatial rate of change of this velocity.

The fact that there are two types of accelerations is acknowledged mathematically by the statement that the velocity is both explicit and implicit function of time, so that

$$a_i = \frac{dv_i}{dt} = \left(\frac{\partial v_i}{\partial t} + \frac{\partial v_i}{\partial x_1}\frac{dx_1}{dt} + \frac{\partial v_i}{\partial x_2}\frac{dx_2}{dt} + \frac{\partial v_i}{\partial x_3}\frac{dx_3}{dt}\right). \tag{2.5}$$

Here, $\boldsymbol{a} = (a_1, a_2, a_3)$ is the acceleration vector. The first term on the right-hand side of Eq. (2.5) is the i^{th} component of local acceleration, the sum of the last three terms represents the i^{th} component of the convective acceleration.

On recognizing that

$$\frac{dx_1}{dt} = v_1, \quad \frac{dx_2}{dt} = v_2, \quad \frac{dx_3}{dt} = v_3, \tag{2.6}$$

Eq. (2.5) can be written as

$$\frac{dv_i}{dt} = \left(\frac{\partial v_i}{\partial t} + v_1\frac{\partial v_i}{\partial x_1} + v_2\frac{\partial v_i}{\partial x_2} + v_3\frac{\partial v_i}{\partial x_3}\right) = \frac{\partial v_i}{\partial t} + \sum\nolimits_{j=1}^{3} v_j\frac{\partial v_i}{\partial x_j}$$

To simplify notation, we dispense with the summation sign and adopt the *summation convention*: whenever an index appears exactly twice within the same term, summation

is implied with respect to that index over its range. The abbreviated form of Eq. (2.5) is then

$$\frac{dv_i}{dt} = \frac{\partial v_i}{\partial t} + v_j \frac{\partial v_i}{\partial x_j}, \tag{2.7}$$

where the index j is repeated in the last term. Equation (2.7) can be cast in a vectorial form as

$$\boldsymbol{a} = \frac{d\boldsymbol{v}}{dt} = \frac{\partial \boldsymbol{v}}{\partial t} + \boldsymbol{v} \cdot \text{grad}\, \boldsymbol{v}. \tag{2.8}$$

Equation (2.8) is a special case of the formula

$$\frac{d\psi}{dt} = \frac{\partial \psi}{\partial t} + \boldsymbol{v} \cdot \text{grad}\, \psi \tag{2.9}$$

that expresses the time rate of change of the arbitrary quantity ψ, apparent to an observer situated on the moving particle, instantaneously at position $\boldsymbol{x}$. Equation (2.9) defines the *material derivative* of $\psi(\boldsymbol{x}, t)$ relative to the Eulerian frame.

The Transport Theorem

The equations of mechanics, prominently among them Newton's second law, are written for bodies of fixed mass, i.e., for *material volumes* composed of the same material points (particles). Material volumes are often referred to as *systems* in fluid mechanics. The volume $\mathcal{V}(t)$ and closed surface $\mathcal{S}(t)$ of a system change continually (cf., Figure 2.1) as the system is propelled along its path by the motion, however, there is no mass transfer across $\mathcal{S}(t)$ by definition.

Although systems are indispensable concepts in theoretical analyses, there is only limited practical interest, e.g., in the fortunes suffered by a specific body of fluid as it proceeds, say, from reservoir – through hydraulic turbine – to ocean, except in diffusion studies. Of practical concern is what transpires within a certain designated, fixed, spatial volume, the so-called *control volume* (the volume enclosing the turbine, in this instance) as the fluid streams through it, unobstructed in its motion by the *control surface*. Therefore, statements that apply to control volumes would be more useful in applications. In other words, one needs to translate to control-volume-language the laws of mechanics that have been established for systems. This task is accomplished by the *Reynolds transport theorem:*

$$\frac{d}{dt} \int_{\mathcal{V}} \psi \, d\upsilon = \int_{\mathcal{V}} \left(\frac{d\psi}{dt} + \psi \, \text{div}\, \boldsymbol{v} \right) d\upsilon. \tag{2.10}$$

The quantity $\psi(\boldsymbol{x}, t)$ is a scalar or vector function of position. The integral on the left-hand side represents the total amount of ψ contained in the system $\mathcal{V} = \mathcal{V}(t)$; it is a well-defined function of time, but the limits of this integral are time dependent. Notwithstanding, its time rate of change can be easily computed as indicated in Eq. (2.10).

Two results from mathematics are needed here to prove the Reynolds transport theorem, the formula that relates the volume element of the fixed reference configuration $\mathcal{V}_0 = \mathcal{V}(0)$ to the volume element in the moving, current configuration $\mathcal{V}(t)$

$$d\upsilon = J \, d\upsilon_0 \tag{2.11}$$

and Euler's formula for the time rate of change of the Jacobian (Serrin, 1959)

$$\frac{dJ}{dt} = J \operatorname{div} \boldsymbol{v}. \tag{2.12}$$

Let ψ represent a fluid property per unit volume, then, as the volume in the reference state remains unchanged in time, the rate of change of ψ contained in the system of volume $\mathcal{V}(t)$ can be written as

$$\begin{aligned}\frac{d}{dt}\int_{\mathcal{V}} \psi(\boldsymbol{x}) d\upsilon = \frac{d}{dt}\int_{\mathcal{V}_0} \psi(\boldsymbol{X}) J \, d\upsilon_0 &= \int_{\mathcal{V}_0} \left(\frac{d\psi(\boldsymbol{X})}{dt} J + \psi(\boldsymbol{X}) \frac{dJ}{dt} \right) d\upsilon_0 \\ &= \int_{\mathcal{V}_0} \left(\frac{d\psi(\boldsymbol{X})}{dt} + \psi(\boldsymbol{X}) \operatorname{div} \boldsymbol{v} \right) J \, d\upsilon_0. \end{aligned} \tag{2.13}$$

Applying Eq. (2.11) again leads to Eq. (2.10).

An alternative form of the transport theorem follows from the manipulation

$$\frac{d\psi}{dt} + \psi \operatorname{div} \boldsymbol{v} = \frac{\partial \psi}{\partial t} + \boldsymbol{v} \cdot \operatorname{grad} \psi + \psi \operatorname{div} \boldsymbol{v} = \frac{\partial \psi}{\partial t} + \operatorname{div} (\psi \boldsymbol{v})$$

where we appealed to Eq. (2.9). Now, on employing the divergence theorem to the volume integral of $\operatorname{div}(\psi \boldsymbol{v})$ we arrive at

$$\frac{d}{dt}\int_{\mathcal{V}} \psi(\boldsymbol{x}) \, d\upsilon = \frac{\partial}{\partial t}\int_{\upsilon} \psi \, d\upsilon + \oint_{\mathcal{S}} \psi \, \boldsymbol{v} \cdot \boldsymbol{n} d\mathcal{S}. \tag{2.14}$$

Here, $\boldsymbol{v} \cdot \boldsymbol{n}$ is the component of the velocity along the outward normal $\boldsymbol{n}$; the first integral on the right-hand side represents the total rate of change of ψ within the fixed volume υ instantaneously coinciding with the material volume $\mathcal{V}$ while the second integral is the net through flow of ψ across its closed surface $\mathcal{S}$. This is our second representation of the transport theorem.

Equation of Continuity

An immediate use for the transport theorem (2.10) is found as follows. By definition there is no mass transfer in or out of a system, hence the *principle of conservation of mass* requires that the total mass of fluid $\mathcal{M}$ in a material volume stay constant during the motion of the system. By replacing ψ with the density ρ (a fluid property per unit volume when the property is the mass $\mathcal{M}$) in Eq. (2.10) we find

$$\frac{d}{dt}\mathcal{M} = \frac{d}{dt}\int_{\mathcal{V}} \rho \, d\upsilon = \int_{\mathcal{V}} \left(\frac{d\rho}{dt} + \rho \operatorname{div} \boldsymbol{v} \right) d\upsilon = 0. \tag{2.15}$$

As the limit of the integral is arbitrary, the integrand itself is required to vanish, leading to the equation of conservation of mass, often called the *equation of continuity*.

For a *compressible fluid*

$$\frac{d\rho}{dt} + \rho \operatorname{div} \boldsymbol{v} = 0 \tag{2.16a}$$

or, by taking into account Eq. (2.9),

$$\frac{\partial \rho}{\partial t} + \operatorname{div} (\rho \boldsymbol{v}) = 0. \tag{2.16b}$$

For an *incompressible fluid* $\rho = \text{const} > 0$, thus Eq. (2.16b) takes the form

$$\operatorname{div} \boldsymbol{v} = 0. \tag{2.16c}$$

If the fluid property in question is an *intensive property*, i.e., expressed as property per unit mass $F = \psi/\rho$, we have, on applying Eq. (2.16) to Eq. (2.10),

$$\frac{d}{dt}\int_{\mathcal{V}} \rho\, F\, d\mathcal{v} = \int_{\mathcal{V}} \rho \frac{dF}{dt}\, d\mathcal{v}. \tag{2.17}$$

Stress

Consider a fluid body in its present configuration and an interior part, b, of this body that has volume $\mathcal{V}$ enclosed by surface $\mathcal{S}$. The various forces that may act on the interior part b are of two types: (1) *body forces*, which are long-range forces that act through the mass centers of the fluid, and (2) *surface forces*, which are short-range forces that act across surfaces or interfaces. The former are characterized by the *body force per unit mass* $\boldsymbol{f}(\boldsymbol{x})$ and the latter are characterized by application of *Cauchy's stress principle*, which states that *on any imaginary closed surface there is a distribution of stress vectors* $\boldsymbol{t}$*, such that the resultant and moment of* $\boldsymbol{t}$ *are equivalent to the resultant and moment of the actual forces that are exerted by the material outside the surface on the material inside* (Serrin, 1959).

Forces acting on fluid bodies are defined by means of integrals:

$$\textit{Body force:} \qquad \boldsymbol{F}_B = \int_{\mathcal{V}} \boldsymbol{f}\, \rho\, d\mathcal{v} \tag{2.18}$$

$$\textit{Surface force:} \qquad \boldsymbol{F}_S = \oint_{\mathcal{S}} \boldsymbol{t}\, d\mathcal{s}. \tag{2.19}$$

The stress vector, in general, is not perpendicular to the surface on which it acts. Furthermore, both its direction and its magnitude depend on the orientation of the surface. To show this, we write Newton's second law for a fluid particle having the form of a small tetrahedron,[2] cut out by the three coordinate planes through the point P, and by the inclined surface element $\Delta\mathcal{s}_n$; the latter has orientation $\boldsymbol{n}$, as indicated in Figure 2.2. Let $\boldsymbol{t}_n$ be the *surface traction* acting on $\Delta\mathcal{s}_n$ and let $\boldsymbol{t}_{(-i)}$ represent the surface traction acting on $\Delta\mathcal{s}_i$, the projection of $\Delta\mathcal{s}_n$ onto the $x_i = \text{const}$ coordinate plane. How the stress vector $\boldsymbol{t}_n$ is related to the stress vectors $\boldsymbol{t}_{(-1)}$, $\boldsymbol{t}_{(-2)}$, $\boldsymbol{t}_{(-3)}$ acting on the 'negative' side of the coordinate surfaces can be deduced from the principle of conservation of linear momentum.

Newton's second law, the principle of *conservation of linear momentum*, states that *the rate of change of linear momentum of a material volume equals the resultant force on the volume*

$$\frac{d}{dt}\int_{\mathcal{V}} \rho\, \boldsymbol{v}\, d\mathcal{v} = \int_{\mathcal{V}} \rho\, \boldsymbol{f}\, d\mathcal{v} + \oint_{\mathcal{S}} \boldsymbol{t}\, d\mathcal{s}. \tag{2.20}$$

[2]Simple shapes often make for simple analysis; however, the shape of the fluid body is not central to the argument.

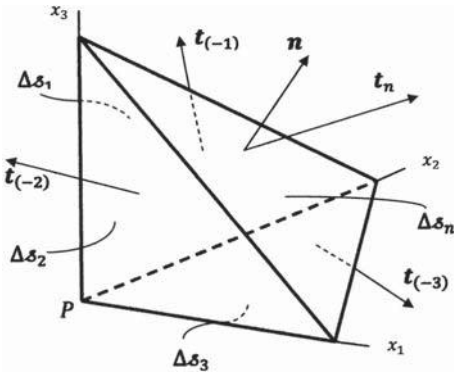

Figure 2.2. Equilibrium of tress vectors on an elementary particle of volume.

When this principle is written for our fixed fluid volume in Figure 2.2 and Eq. (2.17) is applied to the integral on the left-hand side, we obtain

$$\int_{\Delta\mathcal{V}} \rho \left(\frac{d\boldsymbol{v}}{dt} - \boldsymbol{f} \right) d\mathcal{v} = \oint_{\Delta\mathcal{S}} \boldsymbol{t}\, d\mathcal{s}. \tag{2.21}$$

An estimate of the integrals in Eq. (2.21) may be made using the mean value theorem for integrals

$$\rho^* \left(\frac{d\boldsymbol{v}^*}{dt} - \boldsymbol{f}^* \right) \Delta\mathcal{v} = \boldsymbol{t}_n^* \Delta\mathcal{s}_n + \boldsymbol{t}_{(-k)}^* \Delta\mathcal{s}_k. \tag{2.22}$$

Here, ρ^*, $\boldsymbol{v}^*$ and $\boldsymbol{f}^*$ represent the value of ρ, $\boldsymbol{v}$ and $\boldsymbol{f}$, respectively, somewhere within $\Delta\mathcal{v}$ and $\boldsymbol{t}_n^*$ and $\boldsymbol{t}_{(-k)}^*$ are the values of $\boldsymbol{t}_n$ and $\boldsymbol{t}_{(-k)}$ somewhere on $\Delta\mathcal{s}_n$ and $\Delta\mathcal{s}_k$, the starred quantities chosen so as to abide by Eq. (2.22).

Let the characteristic dimension of the tetrahedron $l \to 0$ so that P approaches the surface from the interior and observe that

$$\lim_{l\to 0} \frac{\Delta\mathcal{v}}{\Delta\mathcal{s}_n} = 0; \quad \Delta\mathcal{s}_k = n_k \Delta\mathcal{s}_n; \quad \boldsymbol{t}_{(-k)} = -\boldsymbol{t}_{(k)}.$$

It then follows from Eq. (2.22) that the stress vector acting on the arbitrary surface at a point is a linear combination of the stress vectors on the coordinate surfaces through the point. The coefficients in this relationship are the direction cosines characterizing the orientation of the surface (Stokes, 1845)

$$\boldsymbol{t}_n = n_k \boldsymbol{t}_{(k)} \tag{2.23}$$

The components of the surface traction $\boldsymbol{t}_{(k)}$ acting on the kth coordinate plane will be designated by the capital letter T with appropriate indices. We adopt the scheme of Figure 2.3, by which the first index specifies the orientation of the plane on which the surface traction acts while the second index specifies the direction of the component itself.

Writing $\boldsymbol{t}$ for $\boldsymbol{t}_n$ and designating the components of $\boldsymbol{t}$ and $\boldsymbol{t}_{(k)}$ by

$$\boldsymbol{t} = (t_1,\ t_2,\ t_3), \text{ and } \boldsymbol{t}_{(k)} = (T_{k1},\ T_{k2},\ T_{k3})$$

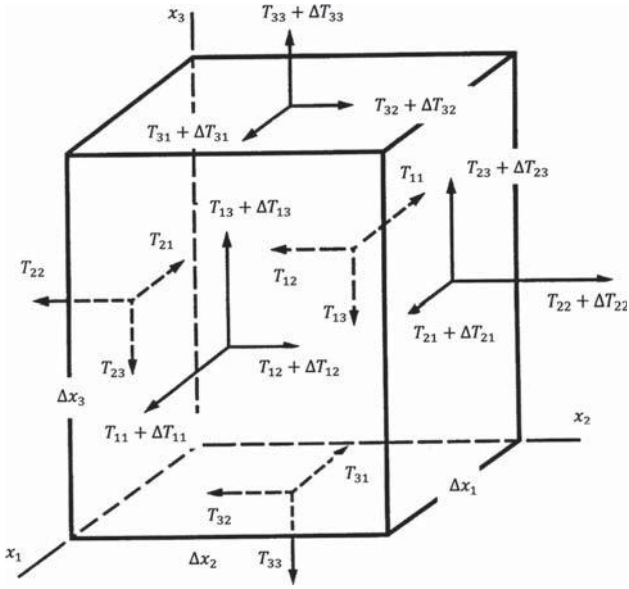

Figure 2.3. Convention for designating stress components.

we can write

$$[t_1, \quad t_2, \quad t_3] = [n_1, n_2, n_3] \begin{bmatrix} T_{11} & T_{21} & T_{31} \\ T_{12} & T_{22} & T_{32} \\ T_{13} & T_{23} & T_{33} \end{bmatrix}; \quad t_i = n_j T_{ij}$$

or, in concise form,

$$\boldsymbol{t} = \boldsymbol{n} \cdot \boldsymbol{T} \tag{2.24}$$

where the entity $\boldsymbol{T} = \left(T_{ij}\right), i, j = 1, 2, 3$ is the *stress tensor*.

We conclude here that the stress vector $\boldsymbol{t}$ acting on an arbitrary surface through a point can be computed from Eq. (2.24) once the nine components of the stress tensor $\boldsymbol{T} = \left(T_{ij}\right), i = j = 1, 2, 3$ as well as the orientation of the surface $\boldsymbol{n} = (n_1, n_2, n_3)$ have been determined.

The actual situation is somewhat less demanding, however. Under widely acceptable conditions (i.e., when there are no surface or body couples), the stress tensor is *symmetric* and hence has only six independent components. To show this, consider the stresses that contribute to a torque, say M_3 about the x_3-axis in Figure 2.3

$$M_3 = (T_{12} - T_{21})\, \Delta x_1 \Delta x_2 \Delta x_3.$$

The *principle of conservation of angular momentum*[3] (Newton's second law, applied to a rotating system) requires that the *torque is balanced by the product of the moment of*

[3]In continuum mechanics, for non-polar media symmetry of the stress tensor is assumed (Boltzmann postulate), then conservation of angular momentum follows (Serrin, 1959).

inertia and the angular acceleration. Denoting the angular velocity about x_3 by ω_3, in the present context this means that

$$(T_{12} - T_{21})\,\Delta x_1 \Delta x_2 \Delta x_3 = \frac{1}{12}\rho \Delta x_1 \Delta x_2 \Delta x_3 \left(\Delta x_1^2 + \Delta x_2^2\right) \frac{d\omega_3}{dt}.$$

After division by the volume element $\Delta \upsilon = \Delta x_1 \Delta x_2 \Delta x_3$ and shrinking the parallelepiped to the point P, the right-hand side vanishes, demonstrating that $T_{12} = T_{21}$. But if the stress tensor is symmetric $\boldsymbol{T} = \boldsymbol{T}^T$, only six of the nine stress components will occur in the equations of motion.

Cauchy's Equations of Motion

Equation (2.20) can now be written in the form

$$\int_{\upsilon} \rho \frac{d\boldsymbol{v}}{dt} d\upsilon = \int_{\upsilon} \rho \boldsymbol{f}\, d\upsilon + \oint_{\mathcal{S}} \boldsymbol{n} \cdot \boldsymbol{T} d\mathcal{S}. \tag{2.25}$$

Using the divergence theorem on the second term on the right-hand side, we obtain

$$\oint_{\mathcal{S}} \boldsymbol{n} \cdot \boldsymbol{T} d\mathcal{S} = \int_{\upsilon} \operatorname{div} \boldsymbol{T} d\upsilon$$

and Eq. (2.25) assumes the form

$$\int_{\upsilon} \left(\rho \frac{d\boldsymbol{v}}{dt} - \rho \boldsymbol{f} - \operatorname{div} \boldsymbol{T} \right) d\upsilon = 0. \tag{2.26}$$

As the integration limits are arbitrary the integrand itself is required to vanish, leading to *Cauchy's equation of motion*,

$$\rho \frac{d\boldsymbol{v}}{dt} = \rho \boldsymbol{f} + \operatorname{div} \boldsymbol{T}. \tag{2.27a}$$

In component form the equation reads

$$\begin{aligned}
\rho \left(\frac{\partial u}{\partial t} + u \frac{\partial u}{\partial x} + v \frac{\partial u}{\partial y} + w \frac{\partial u}{\partial z} \right) &= \frac{\partial T_{xx}}{\partial x} + \frac{\partial T_{xy}}{\partial y} + \frac{\partial T_{xz}}{\partial z} + \rho f_x \\
\rho \left(\frac{\partial v}{\partial t} + u \frac{\partial v}{\partial x} + v \frac{\partial v}{\partial y} + w \frac{\partial v}{\partial z} \right) &= \frac{\partial T_{xy}}{\partial x} + \frac{\partial T_{yy}}{\partial y} + \frac{\partial T_{yz}}{\partial z} + \rho f_y \\
\rho \left(\frac{\partial w}{\partial t} + u \frac{\partial w}{\partial x} + v \frac{\partial w}{\partial y} + w \frac{\partial w}{\partial z} \right) &= \frac{\partial T_{xz}}{\partial x} + \frac{\partial T_{yz}}{\partial y} + \frac{\partial T_{zz}}{\partial z} + \rho f_z.
\end{aligned} \tag{2.27b}$$

Constitutive Equations

Most problems in engineering fluid mechanics fall into one of two categories: (1) a moving boundary or a pressure gradient induces flow, or (2) a moving fluid exerts force on its boundaries. In the first case, the fluid yields to stress by deforming while in the second case stress is the consequence of deformation. We know from experience, however, that not all fluids are alike: some, such as water or air, flow readily, while others, such as honey

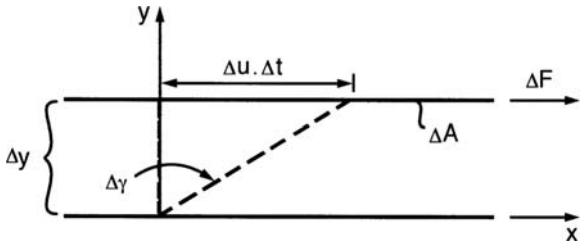

Figure 2.4. Definition of viscosity.

and asphalt, show reluctance to flow. We are thus led to the necessity of knowing, within the context of responding to stress, the behavior of particular fluids.

Perhaps one of the simplest experiments we can perform in studying the force-motion behavior of fluids involves two parallel plates, both submerged in the fluid under investigation. The plates are separated by a short distance Δy, as indicated in Figure 2.4. The idea here is to mark with dye the fluid particles along a generic line at right angles to the plates and then to observe the motion of this line of color (a *material line* as $\boldsymbol{X}$ is held constant during the experiment) as the upper plate is moved with small velocity Δu relative to the lower plate.

A short time Δt into the experiment the dye line will still be straight but will be inclined to its original direction at the small angle $\Delta\gamma$. For small values of Δu and Δt the angular deformation $\Delta\gamma$ is given by

$$\Delta\gamma \approx \tan\,\Delta\gamma = \frac{\Delta u\,\Delta t}{\Delta y}. \tag{2.28}$$

It was first recorded by Newton that in common fluids the surface traction τ, defined by $\tau = \Delta F/\Delta A$, where ΔF is the force required to move the top plate of area ΔA, is proportional to the time rate of change of the angular deformation:

$$\tau \propto \frac{\Delta\gamma}{\Delta t} \propto \frac{\Delta u}{\Delta y}.$$

At the limit $\Delta y \to 0$, as the plates are moved closer to one another, we can write the differential form of the above relationship as

$$\tau = \mu\frac{du}{dy}. \tag{2.29}$$

The factor of proportionality μ is called the *molecular viscosity*, or simply the *viscosity* of the fluid, and Eq. (2.29) is referred to as *Newton's law of viscosity*. When μ is constant or is dependent on temperature at most, as for water, air and common petroleum–oil lubricants at low pressures, the fluid is said to be a *Newtonian fluid*. *Non-Newtonian fluids*, and there are a host of them, are said to be *shear thinning* if μ decreases when the fluid is sheared at increasing rate and *shear thickening* in the opposite case.

Equation (2.29) is restrictive in that it applies only to a single dimension. We will generalize it to three-dimensional flows by replacing:

(1) y, by the triplet (x_1, x_2, x_3);
(2) du/dy, by the nine spatial derivatives of velocity $\partial v_j/\partial x_i$; and
(3) τ, by the nine components of the viscous stress[4] tensor τ.

[4]That part of the stress $\boldsymbol{T}$ that is due to viscous action (definition follows).

The spatial derivatives of velocity can conveniently be organized into a two-dimensional array; they form the components of the *velocity gradient tensor* $\boldsymbol{L}$

$$\boldsymbol{L} = \begin{bmatrix} \dfrac{\partial u}{\partial x} & \dfrac{\partial v}{\partial x} & \dfrac{\partial w}{\partial x} \\ \dfrac{\partial u}{\partial y} & \dfrac{\partial v}{\partial y} & \dfrac{\partial w}{\partial y} \\ \dfrac{\partial u}{\partial z} & \dfrac{\partial v}{\partial z} & \dfrac{\partial w}{\partial z} \end{bmatrix},$$

$$L_{ij} = \frac{\partial v_j}{\partial x_i}. \tag{2.30}$$

Based on the above, our extension of Newton's law of viscosity to three dimensions might take the form

$$\boldsymbol{\tau} = \boldsymbol{f}(\boldsymbol{L}) \tag{2.31}$$

where $\boldsymbol{f}(\boldsymbol{L})$ is a yet unspecified tensor-valued function of the velocity gradient tensor, except that this equation might imply more than we would like.

The reason for our objecting to Eq. (2.31) is simply that $\boldsymbol{L}$ carries superfluous information: it contains particulars of both rate of rigid body rotation and rate of deformation. As advanced by Stokes,

> *"the difference between the pressure (i.e., stress, in modern parlance) on a plane in a given direction passing through any point P of a fluid in motion and the pressure which would exist in all direction about P if the fluid in its neighborhood were in a state of relative equilibrium depends only on the relative motion of the fluid immediately about P; and that the relative motion due to any motion of rotation may be eliminated without affecting the differences of the pressures above mentioned"* (Stokes, 1845).

To illustrate the principle that stress cannot depend on rigid body motion, consider two observers, O and O^*, one stationary and the other rotating, while both are simultaneously monitoring the behavior of the same fluid particle. If stress depended on rigid body rotation then O^*, whose *frame of reference* is fixed to the rotating particle and, therefore, finds the particle to be at rest, would conclude that the particle was free of stress. On the other hand, O, whose frame of reference is stationary, would see the particle rotate and report a nonzero state of stress. We expect, however, that the state of stress is independent of observer motion. The only way out of this dilemma is to postulate that stress *may not depend on rotation.* Rotation is not *frame indifferent*; its value depends on the motion or position of the observer. In contrast, deformation of a fluid element, as we will show later, is independent of the motion of the observer and is thus a candidate argument for $\boldsymbol{f}$ in Eq. (2.31). Frame indifferent quantities are also called *objective* quantities and are the only ones that should enter into a constitutive equation.

General Motion of a Fluid Particle

In order to develop a facility to judge the frame indifference of a motion-associated quantity, and hence to construct constitutive theorems, we need to investigate the general

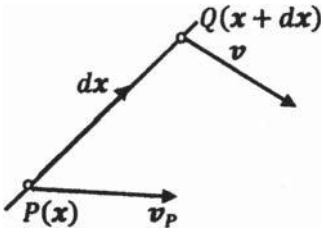

Figure 2.5. Relative motion of material points: velocity at Q relative to that at P.

motion of the fluid. To this end consider the *relative motion* of arbitrary particles P and Q, the latter being located in some neighborhood of the former (Figure 2.5).

We estimate the motion of Q relative to P by expanding the velocity about point P in Taylor series,

$$\boldsymbol{v} = \boldsymbol{v}_p + d\boldsymbol{x} \cdot \operatorname{grad} \boldsymbol{v} + O(d\boldsymbol{x}^2). \tag{2.32}$$

At this stage it is expedient to split the *velocity gradient* tensor $\boldsymbol{L} = \operatorname{grad} \boldsymbol{v}$ into its symmetric and skew symmetric parts (Cartesian decomposition),

$$\operatorname{grad} \boldsymbol{v} = \tfrac{1}{2}(\boldsymbol{L} + \boldsymbol{L}^T) + \tfrac{1}{2}(\boldsymbol{L} - \boldsymbol{L}^T).$$

$$\stackrel{\text{def}}{=} \boldsymbol{D} + \boldsymbol{\Omega}. \tag{2.33}$$

The symmetric tensor $\boldsymbol{D} = \boldsymbol{D}^T$ is called the *stretching* tensor while the skew symmetric tensor $\boldsymbol{\Omega} = -\boldsymbol{\Omega}^T$ is called the *spin* tensor. Relative to orthogonal Cartesian coordinates and arranged in two-dimensional arrays, the stretching tensor and the spin tensor have the components, respectively,

$$\boldsymbol{D} = \frac{1}{2}\begin{bmatrix} 2\dfrac{\partial u}{\partial x} & \left(\dfrac{\partial u}{\partial y} + \dfrac{\partial v}{\partial x}\right) & \left(\dfrac{\partial u}{\partial z} + \dfrac{\partial w}{\partial x}\right) \\ \left(\dfrac{\partial u}{\partial y} + \dfrac{\partial v}{\partial x}\right) & 2\dfrac{\partial v}{\partial y} & \left(\dfrac{\partial w}{\partial y} + \dfrac{\partial v}{\partial z}\right) \\ \left(\dfrac{\partial u}{\partial z} + \dfrac{\partial w}{\partial x}\right) & \left(\dfrac{\partial w}{\partial y} + \dfrac{\partial v}{\partial z}\right) & 2\dfrac{\partial w}{\partial z} \end{bmatrix} \tag{2.34a}$$

and

$$\boldsymbol{\Omega} = \begin{bmatrix} 0 & \omega_z & -\omega_y \\ -\omega_z & 0 & \omega_x \\ \omega_y & -\omega_x & 0 \end{bmatrix} = \frac{1}{2}\begin{bmatrix} 0 & \left(\dfrac{\partial v}{\partial x} - \dfrac{\partial u}{\partial y}\right) & \left(\dfrac{\partial w}{\partial x} - \dfrac{\partial u}{\partial z}\right) \\ \left(\dfrac{\partial u}{\partial y} - \dfrac{\partial v}{\partial x}\right) & 0 & \left(\dfrac{\partial w}{\partial y} - \dfrac{\partial v}{\partial z}\right) \\ \left(\dfrac{\partial u}{\partial z} - \dfrac{\partial w}{\partial x}\right) & \left(\dfrac{\partial v}{\partial z} - \dfrac{\partial w}{\partial y}\right) & 0 \end{bmatrix}. \tag{2.34b}$$

The vorticity vector $\boldsymbol{\omega}$ is defined in Eq. (2.37).

Substituting the decomposition equation (2.33) into Eq. (2.32) and neglecting higher order terms results in

$$\boldsymbol{v} = \boldsymbol{v}_P + d\boldsymbol{x} \cdot \boldsymbol{D} + d\boldsymbol{x} \cdot \boldsymbol{\Omega}. \tag{2.35}$$

The second term on the right-hand side can be written as

$$d\boldsymbol{x} \cdot \boldsymbol{D} = \text{grad}\left(\tfrac{1}{2}\,\mathcal{D}\right) \tag{2.36}$$

where the imaginary surface, $\mathcal{D} = d\boldsymbol{x} \cdot \boldsymbol{D} \cdot d\boldsymbol{x} = \text{const.}$, is a closed surface, the so-called *rate of strain quadric*, constructed about the point P. The right-hand side of Eq. (2.36) represents a velocity field normal to the surface at each point. There are three mutually perpendicular directions (the principal axes) in this velocity field, which suffer instantaneous stretching but not instantaneous rotation. The rates of extension per unit length of fluid elements along these directions are the eigenvalues of $\boldsymbol{D}$ (Truesdell and Rajagopal, 2000).

By defining the *vorticity vector* $\boldsymbol{\omega} = \text{curl}\,\boldsymbol{v}$ it also follows that

$$d\boldsymbol{x} \cdot \boldsymbol{\Omega} = \tfrac{1}{2}\boldsymbol{\omega} \times d\boldsymbol{x} \tag{2.37}$$

where $\boldsymbol{\omega}$ represents the rigid body rotation of the principal directions of $\boldsymbol{D}$.

Taking into account Eqs. (2.36) and (2.37), the velocity at Q relative to P can now be written as

$$\boldsymbol{v} = \boldsymbol{v}_P + \text{grad}\,\left(\tfrac{1}{2}\,\mathcal{D}\right) + \tfrac{1}{2}\boldsymbol{\omega} \times d\boldsymbol{x}. \tag{2.38}$$

Equation (2.38) proves that *an arbitrary instantaneous motion is, at each point, the superposition of a uniform velocity of translation, a dilatation along three mutually perpendicular axes, and a rigid body rotation of these axes* (Serrin, 1959). The order of this superposition is arbitrary.

Objectivity

We will now show that the stretching tensor is objective but the spin tensor is not. A quantity is said to be objective (frame indifferent) if it is invariant under all changes of frame. A frame $[O, \boldsymbol{x}, t]$ consists of an orthogonal Cartesian coordinate system (origin O) and a clock. Consider two frames $[O, \boldsymbol{x}, t]$ and $[O^*, \boldsymbol{x}^*, t^*]$, related to each other through

$$\begin{aligned} \boldsymbol{x}^* &= \boldsymbol{c}\,(t) + \boldsymbol{Q}\,(t) \cdot \boldsymbol{x} \\ t^* &= t - a. \end{aligned} \tag{2.39}$$

Here, $\boldsymbol{Q}\,(t)$ is a time dependent orthogonal matrix $\boldsymbol{Q} \cdot \boldsymbol{Q}^{\boldsymbol{T}} = \boldsymbol{I}$ that specifies the instantaneous orientation of $(O, \boldsymbol{x})$ relative to $(O^*, \boldsymbol{x}^*)$, $\boldsymbol{c}\,(t)$ is the instantaneous distance between O and O^*, and a is a constant.This is the most general change of frame that preserves distance, time interval, and the sense of time (Truesdell and Noll, 1992).

Under the change of frame indicated above, objective vectors $\boldsymbol{\sigma}$ and tensors $\boldsymbol{\Phi}$ transform, respectively, as

$$\begin{aligned} \boldsymbol{\sigma}^* &= \boldsymbol{Q}\,(t) \cdot \boldsymbol{\sigma} \\ \boldsymbol{\Phi}^* &= \boldsymbol{Q}\,(t) \cdot \boldsymbol{\Phi} \cdot \boldsymbol{Q}^T\,(t)\,. \end{aligned} \tag{2.40}$$

To demonstrate the transformation laws, let the vector $\boldsymbol{\sigma} = \boldsymbol{x}_1 - \boldsymbol{x}_2$ represent the position of some $\boldsymbol{x}_2$ relative to some $\boldsymbol{x}_1$. In the starred frame the corresponding quantity is the vector $\boldsymbol{\sigma}^* = \boldsymbol{x}_1^* - \boldsymbol{x}_2^*$. Substituting from Eq. (2.39) into this last formula leads to

$$\boldsymbol{\sigma}^* = \boldsymbol{Q} \cdot (\boldsymbol{x}_1 - \boldsymbol{x}_1) = \boldsymbol{Q} \cdot \boldsymbol{\sigma}.$$

To demonstrate Eq. (2.40) for the objective tensor $\boldsymbol{\Phi}$, construct the objective vector $\boldsymbol{\gamma} = \boldsymbol{\Phi} \cdot \boldsymbol{\sigma}$. In the starred frame this vector is represented by $\boldsymbol{\gamma}^* = \boldsymbol{\Phi}^* \cdot \boldsymbol{\sigma}^*$ so that

$$\boldsymbol{\gamma}^* = \boldsymbol{Q} \cdot \boldsymbol{\gamma} = \boldsymbol{Q} \cdot \boldsymbol{\Phi} \cdot \boldsymbol{\sigma}$$

$$\boldsymbol{\gamma}^* = \boldsymbol{\Phi}^* \cdot \boldsymbol{\sigma}^* = \boldsymbol{\Phi}^* \cdot \boldsymbol{Q} \cdot \boldsymbol{\sigma}.$$

Equating now the right-hand sides and observing that $\boldsymbol{Q}^{-1} = \boldsymbol{Q}^T$ leads to the second part of Eq. (2.40). It can be shown with the aid of Eq. (2.39) and the definitions for $\boldsymbol{D}$ and $\boldsymbol{\Omega}$, that $\boldsymbol{D}^* = \boldsymbol{Q} \cdot \boldsymbol{D} \cdot \boldsymbol{Q}^T$ and $\boldsymbol{\Omega}^* = \boldsymbol{Q} \cdot \boldsymbol{\Omega} \cdot \boldsymbol{Q}^T + \boldsymbol{Q} \cdot d\boldsymbol{Q}/dt$. Comparison with Eq. (2.40) will then show that $\boldsymbol{D}$ is objective but $\boldsymbol{\Omega}$ is not (the selection $\boldsymbol{Q} = \boldsymbol{I}, d\boldsymbol{Q}/dt = -\boldsymbol{\Omega}$ results in $\boldsymbol{\Omega}^* = \boldsymbol{0}$ even though $\boldsymbol{\Omega} \neq \boldsymbol{0}$). Thus, if the stress depended on the spin tensor, the starred observer $[O^*, \boldsymbol{x}^*, t^*]$ would not observe stress while her counterpart $[O, \boldsymbol{x}, t]$ would.

With the help of Figure 2.6 we now illustrate rotation, stretching, and angular deformation of a fluid particle, as prescribed by the velocity gradient tensor $\boldsymbol{L}$.

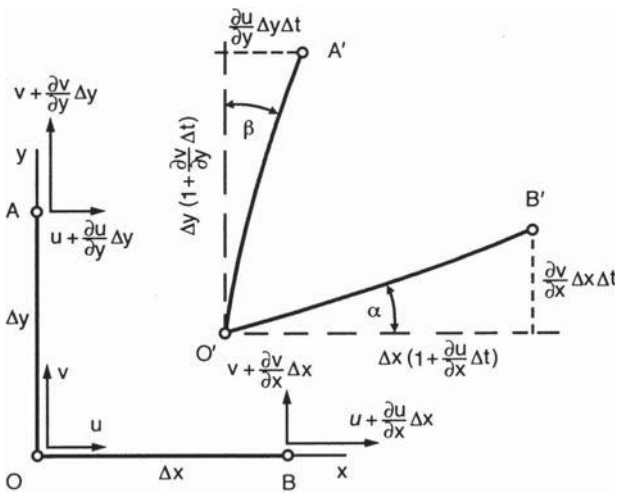

Figure 2.6. Deformation of a fluid particle.

Figure 2.6 depicts a fluid particle located on the positively directed (x, y) face of a rectangular parallelepiped and observed from the $+z$ (outward normal) direction, at two time instances; at time t the particle is rectangular in shape, but deforms by time $t + \Delta t$. During the time interval Δt the particle undergoes average rotation $(\alpha - \beta)/2$ in the positive (counterclockwise) sense. The time rate of change of this rotation (angular velocity) is

$$\omega_z = \frac{1}{2}\left(\frac{d\alpha}{dt} - \frac{d\beta}{dt}\right) \tag{2.41a}$$

where

$$\frac{d\alpha}{dt} = \lim_{\Delta t \to 0} \frac{1}{\Delta t}\left(\tan^{-1} \frac{\frac{\partial v}{\partial x}\Delta x\,\Delta t}{\Delta x + \frac{\partial u}{\partial x}\Delta x\,\Delta t}\right) = \frac{\partial v}{\partial x} \tag{2.41b}$$

$$\frac{d\beta}{dt} = \lim_{\Delta t \to 0} \frac{1}{\Delta t} \left(\tan^{-1} \frac{\frac{\partial u}{\partial y} \Delta y \Delta t}{\Delta y + \frac{\partial v}{\partial y} \Delta y \Delta t} \right) = \frac{\partial u}{\partial y}. \tag{2.41c}$$

Substituting into Eq. (2.41a) yields

$$\omega_z = \frac{1}{2} \left(\frac{\partial v}{\partial x} - \frac{\partial u}{\partial y} \right). \tag{2.42a}$$

On the negatively directed (x, y) face of the parallelepiped the average rate of rotation appears to be $-\omega_z$ as viewed from the $-z$ (outward normal) direction. (That the same rigid body rotation can be evaluated as either ω_z or $-\omega_z$ depending on the position of the observer, confirms our earlier assertion that rotation is not objective.)

Similarly, motion in the positively oriented coordinate faces (y, z) and (x, z), as observed from the $+x$ and $+y$ coordinate directions, respectively, gives

$$\omega_x = \frac{1}{2} \left(\frac{\partial w}{\partial y} - \frac{\partial v}{\partial z} \right), \quad \omega_y = \frac{1}{2} \left(\frac{\partial u}{\partial z} - \frac{\partial w}{\partial x} \right). \tag{2.42b}$$

The spin tensor $\boldsymbol{\Omega}$ is constructed from the rotations $\omega_x, \omega_y, \omega_z$ as shown in Eq. (2.34).

To illustrate that the elements of the stretching tensor $\boldsymbol{D}$ contain information on the rate of deformation, consider again the fluid particle depicted in Figure 2.6. At time t the two material lines $\overline{OA}$ and $\overline{OB}$, which form the sides of the particle, are perpendicular to each other. At the later time $t + \Delta t$ they the two material lines are shown inclined at angle $(\pi/2 - \gamma_z)$, where $\gamma_z = (\alpha + \beta)$ is the angular deformation. The time rate of γ_z is

$$\frac{d\gamma_z}{dt} = \left(\frac{d\alpha}{dx} + \frac{d\beta}{dy} \right).$$

Substituting into this equation from Eq. (2.41) yields the rate of the angular deformation, or shearing in the (x, y) plane, as

$$\frac{d\gamma_z}{dt} = \left(\frac{\partial v}{\partial x} + \frac{\partial u}{\partial y} \right). \tag{2.43a}$$

In similar fashion, in the (x, z) and the (y, z) planes, respectively, we have

$$\frac{d\gamma_y}{dt} = \left(\frac{\partial w}{\partial x} + \frac{\partial u}{\partial z} \right), \qquad \frac{d\gamma_x}{dt} = \left(\frac{\partial v}{\partial z} + \frac{\partial w}{\partial y} \right). \tag{2.43b}$$

Note that on the opposing, negatively directed coordinate surfaces we calculate identical shearings (demonstrating that deformation is objective). We equate the shearings to twice the off-diagonal elements of the stretching tensor $\boldsymbol{D}$:

$$\frac{d\gamma_z}{dt} = 2D_{12}, \ \frac{d\gamma_y}{dt} = 2D_{13}, \ \frac{d\gamma_x}{dt} = 2D_{23}.$$

Also, because of the frame indifference of shearings referred earlier, we are allowed to put

$$D_{21} = D_{12}, \ D_{31} = D_{13}, \ D_{32} = D_{23}.$$

To calculate the diagonal elements of the matrix $\boldsymbol{D}$, define the *stretching* of an infinitesimal fluid line, originally of length ℓ stretched to length $\ell + \Delta\ell$ in time Δt, as

$$d = \frac{1}{\ell} \lim_{\Delta t \to 0} \frac{\Delta \ell}{\Delta t}.$$

If the line element is in the x-coordinate direction, along the horizontal side of the rectangle in Figure 2.6, we have $\ell_x = \Delta x$ and $\Delta \ell_x = (\partial u/\partial x)\,\Delta x \Delta t$, so that

$$d_x = \frac{1}{\ell_x} \lim_{\Delta t \to 0} \frac{\Delta \ell_x}{\Delta t} = \frac{\partial u}{\partial x}$$

and, similarly, in other coordinate directions

$$d_y = \frac{\partial v}{\partial y}, \quad d_z = \frac{\partial w}{\partial z}.$$

Putting $D_{11} = d_x$, $D_{22} = d_y$, and $D_{33} = d_z$, the stretching tensor acquires the form shown in Eq. (2.34).

The Navier–Stokes Equations

The last sentence of the quote from Stokes (1845) appearing after Eq. (2.31) states that the stress at point P cannot depend on the rigid body rotation of its neighborhood, characterized by $\boldsymbol{\Omega}$, but it does depend on its deformation as described by $\boldsymbol{D}$. The significant difference between $\boldsymbol{\Omega}$ and $\boldsymbol{D}$ that Stokes alludes to is that the latter of these quantities is independent of the position or motion of the observer while rotation can appear positive, negative, or zero, depending on the position or motion of the observer. In other words $\boldsymbol{D}$ is *objective* while $\boldsymbol{\Omega}$ is not. Stokes' statement voices the common observation that stress can depend only on objective quantities.

In addition to insisting that stress depend only on objective quantities, it appears to be reasonable to postulate that stress itself is objective,[5] thus under the change of frame (2.39), stress transforms according to

$$\boldsymbol{T}^* = \boldsymbol{Q}(t) \cdot \boldsymbol{T} \cdot \boldsymbol{Q}(t)^T. \tag{2.44}$$

This statement, which also applies to the viscous stress, $\boldsymbol{\tau}^* = \boldsymbol{Q} \cdot \boldsymbol{\tau} \cdot \boldsymbol{Q}^T$, has immediate consequence. Following Stokes (1845), we let stress depend on the rate of deformation, then in the unstarred and starred frames, respectively,

$$\boldsymbol{\tau} = \boldsymbol{f}(\boldsymbol{D}), \text{ and } \boldsymbol{\tau}^* = \boldsymbol{f}(\boldsymbol{D}^*).$$

From the second equation $\boldsymbol{\tau}^* = \boldsymbol{Q}\boldsymbol{\tau}\boldsymbol{Q}^T = \boldsymbol{f}(\boldsymbol{Q}\boldsymbol{D}\boldsymbol{Q}^T)$ and, substituting for $\boldsymbol{\tau}$, from the first, it follows that $\boldsymbol{f}$ has the special property,

$$\boldsymbol{Q}\boldsymbol{f}(\boldsymbol{D})\boldsymbol{Q}^T = \boldsymbol{f}(\boldsymbol{Q}\boldsymbol{D}\boldsymbol{Q}^T). \tag{2.45}$$

A function that satisfies condition (2.45) is called an *isotropic function*, and the material it represents an *isotropic material.* Isotropy signifies that, regardless its orientation, a given deformation produces the same intrinsic response; in other words, there is no preferred direction either in the fluid or in space. The Stokes fluid and its subclass the Newtonian fluid are specializations of $\boldsymbol{f}(\boldsymbol{D})$ in Eq. (2.45).

The definition of *Stokes fluid* is (Serrin, 1959)

[1] $\boldsymbol{T}$ is a continuous function of the deformation tensor $\boldsymbol{D}$.
[2] $\boldsymbol{T}$ does not depend explicitly on position $\boldsymbol{x}$ (spatial homogeneity).

[5] In continuum mechanics this requirement is embodied in the Principle of Material Frame-Indifference (Truesdell and Noll, 1992).

[3] There is no preferred direction in space or fluid (isotropy).
[4] When $\boldsymbol{D} = \boldsymbol{0}$, $\boldsymbol{T}$ reduces to $-p\boldsymbol{I}$ (hydrostatic stress).

The class of fluids is further narrowed to that of Newtonian fluids when

[5] $\boldsymbol{T}$ is linear in $\boldsymbol{D}$.

Let $\boldsymbol{\tau} = \boldsymbol{T} - p\boldsymbol{I}$ define the *viscous stress tensor,* which vanishes when $\boldsymbol{D} = \boldsymbol{0}$, and, to comply with [1], [2], and [4], put

$$\boldsymbol{\tau} = \boldsymbol{f}(\boldsymbol{D}). \tag{2.46}$$

This constitutive relationship will now be re-written relative to the principal coordinate system (indicated by an over bar) of the stretching tensor $\boldsymbol{D}$,

$$\bar{\boldsymbol{\tau}} = \boldsymbol{f}(\bar{\boldsymbol{D}}); \bar{D}_{kl} = \begin{pmatrix} d_{(1)} & 0 & 0 \\ 0 & d_{(2)} & 0 \\ 0 & 0 & d_{(3)} \end{pmatrix}. \tag{2.47}$$

Either of the two specific rotations $\boldsymbol{Q}^{(1)} = \text{diag}(-1, -1, 1)$ and $\boldsymbol{Q}^{(2)} = \text{diag}(1, -1, -1)$ in Eq. (2.45) will transform that equation to

$$\boldsymbol{Q}^{(\alpha)} \bar{\boldsymbol{\tau}} \boldsymbol{Q}^{(\alpha)T} = \boldsymbol{f}(\boldsymbol{Q}^{(\boldsymbol{\alpha})} \bar{\boldsymbol{D}} \boldsymbol{Q}^{(\boldsymbol{\alpha})T}) = \boldsymbol{f}(\bar{\boldsymbol{D}}) = \bar{\boldsymbol{\tau}}, \alpha = 1,\ 2. \tag{2.48}$$

With $\alpha = 1$, Eq. (2.48) yields

$$\begin{pmatrix} \bar{\tau}_{11} & \bar{\tau}_{12} & -\bar{\tau}_{13} \\ \bar{\tau}_{21} & \bar{\tau}_{22} & -\bar{\tau}_{23} \\ -\bar{\tau}_{31} & -\bar{\tau}_{32} & \bar{\tau}_{33} \end{pmatrix} = \begin{pmatrix} \bar{\tau}_{11} & \bar{\tau}_{12} & \bar{\tau}_{13} \\ \bar{\tau}_{21} & \bar{\tau}_{22} & \bar{\tau}_{23} \\ \bar{\tau}_{31} & \bar{\tau}_{32} & \bar{\tau}_{33} \end{pmatrix}.$$

This shows that when $\boldsymbol{\tau}$ is expressed relative to the principal coordinate system of $\boldsymbol{D}$, the components $\bar{\tau}_{13}$, $\bar{\tau}_{31}$, $\bar{\tau}_{23}$, and $\bar{\tau}_{32}$ vanish. By changing to $\alpha = 2$ in Eq. (2.48), two other off-diagonal stress components $\bar{\tau}_{12}$ and $\bar{\tau}_{21}$ also vanish, proving that two tensors related by an isotropic function possess the same principal directions,

$$\begin{pmatrix} \tau_{(1)} & 0 & 0 \\ 0 & \tau_{(2)} & 0 \\ 0 & 0 & \tau_{(3)} \end{pmatrix} = \boldsymbol{f} \begin{pmatrix} d_{(1)} & 0 & 0 \\ 0 & d_{(2)} & 0 \\ 0 & 0 & d_{(3)} \end{pmatrix}.$$

It is hence permissible to write

$$\tau_{(i)} = f_i \left(d_{(1)},\ d_{(2)},\ d_{(3)}\right) \tag{2.49}$$

where the $\tau_{(i)}$ are the eigenvalues of the viscous stress tensor $\boldsymbol{\tau}$.

It can be shown that Eq. (2.49) has the equivalent polynomial representation[6] (Serrin, 1959)

$$\boldsymbol{T} = \alpha_0(\Theta, II_{\boldsymbol{D}}, III_{\boldsymbol{D}})\boldsymbol{1} + \alpha_1(\Theta, II_{\boldsymbol{D}}, III_{\boldsymbol{D}})\boldsymbol{D} + \alpha_2(\Theta, II_{\boldsymbol{D}}, III_{\boldsymbol{D}})\boldsymbol{D}^2 \tag{2.50}$$

[6]For this, more general, non-linear, case (Stokes fluid) the reader is referred to the excellent article by Serrin (1959), also the first edition of this book. Constitutive equation (2.50) has been occasionally employed in the study of aspects of non-linear material behavior. It should be borne in mind, however, that no fluid is known presently that would obey (2.50) with $\alpha_2 \neq 0$.

where the invariants of $\boldsymbol{D}$ are defined as

$$\Theta = tr\boldsymbol{D}, \quad II_{\boldsymbol{D}} = \tfrac{1}{2}\left[(tr\boldsymbol{D})^2 - tr\boldsymbol{D}^2\right], \; III_{\boldsymbol{D}} = \det \boldsymbol{D}.$$

However, if Eq. (2.49) is constrained to be linear as per specification [5], we have

$$\begin{aligned}
\tau_{(1)} &= a_{11}d_{(1)} + a_{12}d_{(2)} + a_{13}d_{(3)} \\
\tau_{(2)} &= a_{21}d_{(1)} + a_{22}d_{(2)} + a_{23}d_{(3)} \\
\tau_{(3)} &= a_{31}d_{(1)} + a_{32}d_{(2)} + a_{33}d_{(3)}.
\end{aligned} \tag{2.51}$$

Permutation of $d_{(1)}, d_{(2)}, d_{(3)}$, say into $d_{(3)}, d_{(1)}, d_{(2)}$, can be achieved by orthogonal transformation that will permute the $\tau_{(i)}$ in the same order, leaving the a_{ij} unchanged

$$\begin{aligned}
\tau_{(3)} &= a_{12}d_{(1)} + a_{13}d_{(2)} + a_{11}d_{(3)} \\
\tau_{(1)} &= a_{22}d_{(1)} + a_{23}d_{(2)} + a_{21}d_{(3)} \\
\tau_{(2)} &= a_{32}d_{(1)} + a_{33}d_{(2)} + a_{31}d_{(3)}.
\end{aligned}$$

Equating appropriate right-hand sides from above, and continuing this process, will result in

$$\begin{aligned}
a_{11} &= a_{22} = a_{33} \\
a_{12} &= a_{21} = a_{23} = a_{32} = a_{31} = a_{13}.
\end{aligned}$$

We now designate the common value of the first row by $\lambda + 2\mu$ and the second row by 2μ, where μ is the Newtonian viscosity[7] (the physical meaning of λ will be investigated later). It therefore follows that

$$\begin{aligned}
\tau_{(i)} &= \lambda\left(d_{(1)} + d_{(2)} + d_{(3)}\right) + 2\mu d_{(i)} \\
&= \lambda\Theta + 2\mu d_{(i)}.
\end{aligned}$$

Transforming to a general coordinate system yields the constitutive equation for a *compressible Newtonian fluid*,

$$\boldsymbol{T} = (-p + \lambda\Theta)\,\boldsymbol{I} + 2\mu\boldsymbol{D} \tag{2.52}$$

where p is the thermodynamic pressure while μ and λ are scalar functions of the thermodynamic state.

For an *incompressible Newtonian fluid* $\Theta = 0$ and (2.51) yields

$$\boldsymbol{T} = -p\boldsymbol{I} + 2\mu\boldsymbol{D}. \tag{2.53}$$

In this case, the case for incompressible fluid, p is a fundamental dynamic variable.

The *Navier–Stokes equation for a compressible Newtonian fluid* results from substituting the constitutive equation (2.52) into Cauchy's equations of motion (2.27a)

$$\rho\frac{d\boldsymbol{v}}{dt} = \text{grad}\,(-p + \lambda\Theta) + \text{div}\,(2\mu\boldsymbol{D}) + \rho\boldsymbol{f}. \tag{2.54a}$$

For the imcompressible fluid $\Theta \equiv 0$ and we have

$$\rho\frac{d\boldsymbol{v}}{dt} = -\text{grad}\,p + \text{div}\,(2\mu\boldsymbol{D}) + \rho\boldsymbol{f}. \tag{2.54b}$$

[7] That the constant μ is indeed the Newtonian viscosity can be seen by applying (2.53) to unidirectional, simple shear flow and obtaining $T_{12} = \mu\,(du/dy)$.

Relative to orthogonal Cartesian coordinates the component equations for a compressible fluid are

$$\rho\left(\frac{\partial u}{\partial t}+u\frac{\partial u}{\partial x}+v\frac{\partial u}{\partial y}+w\frac{\partial u}{\partial z}\right)$$
$$=\frac{\partial}{\partial x}\left[-p+\lambda\left(\frac{\partial u}{\partial x}+\frac{\partial v}{\partial y}+\frac{\partial w}{\partial z}\right)+2\mu\frac{\partial u}{\partial x}\right]+\frac{\partial}{\partial y}\left[\mu\left(\frac{\partial u}{\partial y}+\frac{\partial v}{\partial x}\right)\right]$$
$$+\frac{\partial}{\partial z}\left[\mu\left(\frac{\partial u}{\partial z}+\frac{\partial w}{\partial x}\right)\right]+\rho f_x$$

$$\rho\left(\frac{\partial v}{\partial t}+u\frac{\partial v}{\partial x}+v\frac{\partial v}{\partial y}+w\frac{\partial v}{\partial z}\right)$$
$$=\frac{\partial}{\partial y}\left[-p+\lambda\left(\frac{\partial u}{\partial x}+\frac{\partial v}{\partial y}+\frac{\partial w}{\partial z}\right)+2\mu\frac{\partial v}{\partial y}\right]+\frac{\partial}{\partial x}\left[\mu\left(\frac{\partial u}{\partial y}+\frac{\partial v}{\partial x}\right)\right]$$
$$+\frac{\partial}{\partial z}\left[\mu\left(\frac{\partial v}{\partial z}+\frac{\partial w}{\partial y}\right)\right]+\rho f_y$$

$$\rho\left(\frac{\partial w}{\partial t}+u\frac{\partial w}{\partial x}+v\frac{\partial w}{\partial y}+w\frac{\partial w}{\partial z}\right)$$
$$=\frac{\partial}{\partial z}\left[-p+\lambda\left(\frac{\partial u}{\partial x}+\frac{\partial v}{\partial y}+\frac{\partial w}{\partial z}\right)+2\mu\frac{\partial w}{\partial z}\right]+\frac{\partial}{\partial x}\left[\mu\left(\frac{\partial u}{\partial z}+\frac{\partial w}{\partial x}\right)\right]$$
$$+\frac{\partial}{\partial y}\left[\mu\left(\frac{\partial v}{\partial z}+\frac{\partial w}{\partial y}\right)\right]+\rho f_z. \tag{2.55}$$

The Navier–Stokes equations for an incompressible fluid can be obtained either from Eq. (2.54) or from Eq. (2.55) by substituting $\Theta = 0$, although the meaning of p is distinctly different in incompressible fluid from that of in compressible fluid.

It is customary to define the *mechanical* (*average*) *pressure* $\bar{p}$ as the negative of the mean normal stress,

$$-\bar{p}\overset{\text{def}}{=}\frac{1}{3}T_{ii}=-p+\left(\lambda+\frac{2}{3}\mu\right)\Theta \tag{2.56}$$
$$\bar{p}-p=-\left(\lambda+\frac{2}{3}\mu\right)\operatorname{div}\boldsymbol{v}=\left(\lambda+\frac{2}{3}\mu\right)\frac{1}{\rho}\frac{d\rho}{dt}.$$

For an incompressible fluid $\operatorname{div}\boldsymbol{v}=0$ and p equals the mechanical pressure. For compressible fluids the *coefficient of bulk viscosity* $(\lambda+\frac{2}{3}\mu)$ is a measurable quantity, but for expedience it is often assumed to be zero. This, so-called *Stokes assumption*, appears to be reasonable for monatomic gases, but does not hold for polyatomic gases or for liquids (Serrin, 1959; Vincenti and Kruger, 1965). But in any case, it suggests the order of magnitude estimate $(\lambda/\mu)=O(1)$, which we will find useful when constructing the thin film approximation of the equations of motion.

The Navier–Stokes problem consists of the equation of continuity (2.16), the three equations of motion (2.55), the *equation of state* in case of compressible fluids, and the boundary and initial conditions. For an ideal gas the equation of state is

$$p=\rho\mathcal{R}\theta \tag{2.57}$$

where $\mathcal{R}$ is the gas constant and θ is the absolute temperature.

The *boundary conditions* on velocity are *no-slip* for incompressible fluids, but also for compressible fluids at low Knudsen number.[8] The condition $Kn < 0.001$ characterizes continuum flow, for Kn larger than this rarefaction effects must be taken into account. However, for $0.001 < Kn < 0.1$ the Navier–Stokes equation is still useful but only with *slip-flow* boundary condition. For higher values of the Knudsen number, the Navier–Stokes equation loses its validity and various forms of the Boltzmann equation must be employed (see Chapter 12). The pressure might be imposed on the fluid externally, in which case it will be defined on part of the boundary. Otherwise, there are no boundary conditions on pressure; pressure is induced by the flow so as to obey the constraint of mass conservation.

2.2 The Thin-Film Approximation

To find solutions of the full Navier–Stokes and continuity equations is far from elementary, and in applications one looks for ways to simplify these equations. Various, well-researched simplifications are available to the analyst. When the equations have been properly normalized, the condition $\mathrm{Re} \to \infty$ determines (inviscid) *Euler flow*. The condition $\mathrm{Re} \to 0$ defines (inertialess) *Stokes flow.* When density change is taken into account in the body force term alone, we are defining *Boussinesq flow*. The *boundary layer approximation* applies in the vicinity of solid boundaries and at high Reynolds number. This last mentioned simplification was arrived at only after careful order of magnitude analysis of the various terms of the equations, not unlike the Reynolds lubrication approximation, which preceded it by two decades.

Simplification of the Navier–Stokes equations is made particularly easy in lubrication by the geometry of typical lubricant films. Under normal conditions, the in-plane dimensions of the film are significantly greater than its thickness. Let L_{xz} designate the *length scale* of the lubricant film in the (x, z) plane and L_y its length scale across its thickness in the y direction (Figure 2.7), then for typical lubricant films $\varepsilon = (L_y/L_{xz})$ is $O(10^{-3})$.

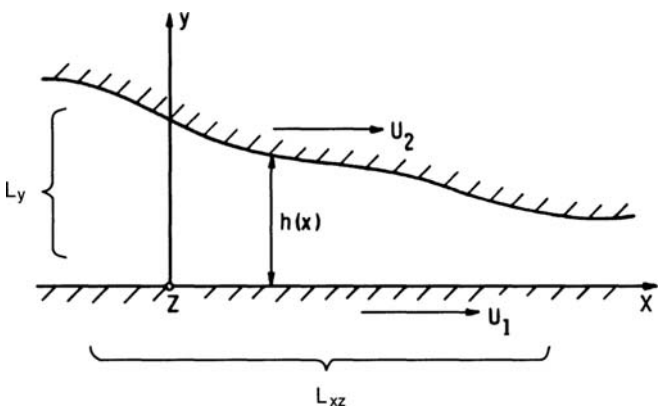

Figure 2.7. Bearing surfaces coordinate axes and length scales.

Reynolds developed the thin film approximation in his efforts to explain the experimental results of Beauchamp Tower. While studying Tower's report on railroad bearings, Reynolds

[8]The Knudsen number is the ratio of the mean free path to the characteristic dimension of the flow $Kn = \lambda/h$. In current computer magnetic drives $h \sim 10\,\mathrm{nm}$ while for air $\lambda \sim 60\,\mathrm{nm}$.

identified "*crucial proof... that the surfaces were completely and continuously separated by a film of oil; this film being maintained by the motion of the journal, although the pressure in the oil at the crown of the bearing was shown by actual measurement to be as much as 625 lbs. per sq. inch above the pressure in the oil bath*" (Reynolds, 1886). It further occurred to Reynolds as possible that "*the film of oil might be sufficiently thick for the unknown boundary actions to disappear, in which case the results would be deducible from the equations of hydrodynamics*."

Having two greatly differing length scales is what makes the analysis of fluid film bearings relatively simple. This property of the film will be utilized for estimating the order of magnitude of the various terms of the governing equations. The equations will then be simplified by deleting terms that are judged to be too small to cause significant effect (from here on forward the body force $\boldsymbol{f}$ will be neglected on account of the film having small body weight relative to the magnitude of viscous and pressure forces).

To perform this "thin-film" simplification, normalize the variables participating in the governing equations. The definition

$$(\bar{x},\ \bar{y},\ \bar{z}) = \frac{1}{L_{xz}}\left(x,\ \frac{1}{\varepsilon}y,\ z\right) \tag{2.58a}$$

renders the range of the *nondimensional coordinates* $(\bar{x}, \bar{y}, \bar{z})$ to be $\epsilon[0, 1]Z$. The velocity is normalized in like manner. For this, designate the characteristic value of the velocity in the (x, z) plane of the film by U^*. Obviously, the *velocity scale* in the direction across the film will not equal U^*; in fact, intuition says that it will be considerably smaller than U^* as the flow is judged to be approximately parallel to the (x, z) plane. An estimate for V^*, the velocity scale across the film, can be secured from the equation of continuity (written here for incompressible fluids)

$$\frac{\partial \bar{u}}{\partial \bar{x}} + \left(\frac{V^*}{\varepsilon U^*}\right)\frac{\partial \bar{v}}{\partial \bar{y}} + \frac{\partial \bar{w}}{\partial \bar{z}} = 0.$$

The three terms in this equation will be of the same order of magnitude if we choose

$$(\bar{u},\ \bar{v},\ \bar{w}) = \tfrac{1}{U^*}\left(u,\ \tfrac{1}{\varepsilon}v,\ w\right). \tag{2.58b}$$

In addition, we define normalized pressure,[9] time, viscosity, density, and λ by

$$\bar{p} = \mathrm{R}_\varepsilon \frac{p}{\rho^* U^{*2}};\quad \bar{t} = \frac{U^* t}{L_{xz}};\quad \bar{\mu} = \frac{\mu}{\mu^*};\quad \bar{\rho} = \frac{\rho}{\rho^*};\quad \bar{\lambda} = \frac{\lambda}{\lambda^*}. \tag{2.58c}$$

The *Reynolds number Re* and the *reduced Reynolds number* R_ε are defined, respectively, by

$$\mathrm{Re} = \frac{\rho^* L_y U^*}{\mu^*};\quad \mathrm{R}_\varepsilon = \varepsilon\,\mathrm{Re}. \tag{2.58d}$$

The normalized (nondimensional) form of the continuity and Navier–Stokes equations is

$$\frac{\partial \bar{\rho}}{\partial \bar{t}} + \bar{\rho}\left(\frac{\partial \bar{u}}{\partial \bar{x}} + \frac{\partial \bar{v}}{\partial \bar{y}} + \frac{\partial \bar{w}}{\partial \bar{z}}\right) = 0 \tag{2.59}$$

[9] Had we put $P = p/\rho^* U^{*2}$ the pressure would disappear on taking the limit $\mathrm{R}_\varepsilon \to 0$, leaving four scalar equations to be satisfied by three unknown velocity components.

$$\mathrm{R}_\varepsilon \bar{\rho}\left(\frac{\partial \bar{u}}{\partial \bar{t}}+\bar{u}\frac{\partial \bar{u}}{\partial \bar{x}}+\bar{v}\frac{\partial \bar{u}}{\partial \bar{y}}+\bar{w}\frac{\partial \bar{u}}{\partial \bar{z}}\right)=-\frac{\partial \bar{p}}{\partial \bar{x}}+\frac{\partial}{\partial \bar{y}}\left(\bar{\mu}\frac{\partial \bar{u}}{\partial \bar{y}}\right) \tag{2.60a}$$

$$+\varepsilon^2\left\{\left(\frac{\lambda_0}{\mu_0}\right)\frac{\partial}{\partial \bar{x}}\left[\bar{\lambda}\left(\frac{\partial \bar{u}}{\partial \bar{x}}+\frac{\partial \bar{v}}{\partial \bar{y}}+\frac{\partial \bar{w}}{\partial \bar{z}}\right)\right]+\frac{\partial}{\partial \bar{x}}\left(2\bar{\mu}\frac{\partial \bar{u}}{\partial \bar{x}}\right)\right.$$

$$\left.+\frac{\partial}{\partial \bar{y}}\left(\bar{\mu}\frac{\partial \bar{v}}{\partial \bar{x}}\right)+\frac{\partial}{\partial \bar{z}}\left[\bar{\mu}\left(\frac{\partial \bar{u}}{\partial \bar{z}}+\frac{\partial \bar{w}}{\partial \bar{x}}\right)\right]\right\}$$

$$\varepsilon^2\left\{\mathrm{R}_\varepsilon \bar{\rho}\left(\frac{\partial \bar{v}}{\partial \bar{t}}+\bar{u}\frac{\partial \bar{v}}{\partial \bar{x}}+\bar{v}\frac{\partial \bar{v}}{\partial \bar{y}}+\bar{w}\frac{\partial \bar{v}}{\partial \bar{z}}\right)-\left(\frac{\lambda_0}{\mu_0}\right)\frac{\partial}{\partial \bar{y}}\left[\bar{\lambda}\left(\frac{\partial \bar{u}}{\partial \bar{x}}+\frac{\partial \bar{v}}{\partial \bar{y}}+\frac{\partial \bar{w}}{\partial \bar{z}}\right)\right]\right. \tag{2.60b}$$

$$-\frac{\partial}{\partial \bar{y}}\left(2\bar{\mu}\frac{\partial \bar{v}}{\partial \bar{y}}\right)-\frac{\partial}{\partial \bar{x}}\left(\bar{\mu}\frac{\partial \bar{u}}{\partial \bar{y}}\right)-\frac{\partial}{\partial \bar{z}}\left(\bar{\mu}\frac{\partial \bar{w}}{\partial \bar{y}}\right)$$

$$\left.-\varepsilon^2\left[\frac{\partial}{\partial \bar{x}}\left(\bar{\mu}\frac{\partial \bar{v}}{\partial \bar{x}}\right)+\frac{\partial}{\partial \bar{z}}\left(\bar{\mu}\frac{\partial \bar{v}}{\partial \bar{z}}\right)\right]\right\}=-\frac{\partial \bar{p}}{\partial \bar{y}}$$

$$\mathrm{R}_\varepsilon \bar{\rho}\left(\frac{\partial \bar{w}}{\partial \bar{t}}+\bar{u}\frac{\partial \bar{w}}{\partial \bar{x}}+\frac{\partial \bar{w}}{\partial \bar{y}}+W\frac{\partial \bar{w}}{\partial \bar{z}}\right)=-\frac{\partial \bar{p}}{\partial \bar{z}}+\frac{\partial}{\partial \bar{y}}\left(\bar{\mu}\frac{\partial \bar{w}}{\partial \bar{y}}\right) \tag{2.60c}$$

$$+\varepsilon^2\left\{\left(\frac{\lambda_0}{\mu_0}\right)\frac{\partial}{\partial \bar{z}}\left[\bar{\lambda}\left(\frac{\partial \bar{u}}{\partial \bar{x}}+\frac{\partial \bar{v}}{\partial \bar{y}}+\frac{\partial \bar{w}}{\partial \bar{z}}\right)\right]+\frac{\partial}{\partial \bar{z}}\left(2\bar{\mu}\frac{\partial \bar{w}}{\partial \bar{z}}\right)\right.$$

$$\left.+\frac{\partial}{\partial \bar{y}}\left(\bar{\mu}\frac{\partial \bar{v}}{\partial \bar{z}}\right)+\frac{\partial}{\partial \bar{x}}\left[\bar{\mu}\left(\frac{\partial \bar{u}}{\partial \bar{z}}+\frac{\partial \bar{w}}{\partial \bar{x}}\right)\right]\right\}.$$

The thin film approximation follows from letting $\varepsilon^2 \to 0$

$$\frac{\partial \bar{\rho}}{\partial \bar{t}}+\bar{\rho}\left(\frac{\partial \bar{u}}{\partial \bar{x}}+\frac{\partial \bar{v}}{\partial \bar{y}}+\frac{\partial \bar{w}}{\partial \bar{z}}\right)=0 \tag{2.61}$$

$$\mathrm{R}_\varepsilon \bar{\rho}\left(\frac{\partial \bar{u}}{\partial \bar{t}}+\bar{u}\frac{\partial \bar{u}}{\partial \bar{x}}+\bar{v}\frac{\partial \bar{u}}{\partial \bar{y}}+\bar{w}\frac{\partial \bar{u}}{\partial z}\right)=-\frac{\partial \bar{p}}{\partial \bar{x}}+\frac{\partial}{\partial \bar{y}}\left(\bar{\mu}\frac{\partial \bar{u}}{\partial \bar{y}}\right) \tag{2.62a}$$

$$0=-\frac{\partial \bar{p}}{\partial \bar{y}} \tag{2.62b}$$

$$\mathrm{R}_\varepsilon \bar{\rho}\left(\frac{\partial \bar{w}}{\partial \bar{t}}+\bar{u}\frac{\partial \bar{w}}{\partial \bar{x}}+\bar{v}\frac{\partial \bar{w}}{\partial \bar{y}}+\bar{w}\frac{\partial \bar{w}}{\partial z}\right)=-\frac{\partial \bar{p}}{\partial \bar{z}}+\frac{\partial}{\partial \bar{y}}\left(\bar{\mu}\frac{\partial \bar{w}}{\partial \bar{y}}\right). \tag{2.62c}$$

Equation (2.62b) shows that to present order of approximation the pressure does not vary across the film and $p = p(x, z, t)$ alone.

As Eqs. (2.62) were arrived at on the basis of the thin-film (or, more properly said, small-slope) assumption, for results generated by them to be acceptable the value of ε must be kept suitably small. The designer, however, will not be satisfied just by being told to keep the aspect ratio small, she will want to know how small is sufficiently small. We shall

return to this topic at the end of the present chapter where we investigate the region of validity of the equations in $(\varepsilon, \mathrm{R}_\varepsilon)$ space.

The Reynolds Equation

Equations (2.61) and (2.62) form the basis of the *lubrication theory of Osborne Reynolds*. But to arrive at that theory, additional assumptions are yet to be made. In this section we will make these assumptions and develop the (classical) *Reynolds theory of lubrication*.

The principal simplifying assumptions of the theory derive from the observation that the lubricant flow, at least in a first approximation, is isoviscous and laminar and that it takes place in an "almost parallel" thin film of negligible curvature. The mathematical statement of this is the *Reynolds equation* in lubricant pressure; it was formulated by Osborne Reynolds just over a century ago.

Reynolds based his theory of lubrication on the following assumptions (Reynolds, 1886):

(1) The continuum description is valid.
(2) The Navier–Stokes equations hold.
(3) Compressibility is ignored.
(4) The viscosity is constant.
(5) The film is thin, therefore:
    (a) Lubricant flow is free of eddies (i.e., it is laminar).
    (b) Lubricant inertia is negligible.

In contrast to assumptions (1), (2), and (5), which are central to the theory, neglecting compressibility is not indispensable to the development of lubrication theory and assumption (3) was made by Reynolds simply because Tower's experiments were performed with an incompressible lubricant and Reynolds intentions were to explain the results of these experiments. As will be shown in Chapter 9, inclusion of lubricant compressibility requires but small modifications in the formulation.

In thrust bearings the lubricant film is bounded by plane surfaces. In journal bearings the bounding surfaces are no longer plane, nevertheless, in relation to its thickness the film curves only very gently. In fact, the ratio of film thickness to radius of curvature in most practical bearings is at most of order ε. Therefore, assumption (5) is also a statement on film curvature; as a consequence, it is permissible to describe fluid film lubrication relative to an orthogonal Cartesian coordinate system. We arbitrarily fix the y axis of this Cartesian system in the direction of the minimum film dimension; its (x, z) plane thus coincides with the "plane" of the lubricant film.

In journal bearings we select the bearing surface to be the $y = 0$ "plane". Although, in reality, all vectors normal to this surface intersect in the center of the bearing, in the approximate world of lubrication theory we consider these normal vectors to be parallel to each other; i.e., we focus on such short distances along these vectors that the fact that they intersect at what seems to us a very great distance, remains unnoticed. This is the essence of neglecting film curvature.

When assumptions (1)–(5) are applied to the equations of motion and continuity we obtain, now in terms of the primitive variables,

$$\frac{\partial p}{\partial x} = \mu \frac{\partial^2 u}{\partial y^2} \tag{2.63}$$

$$\frac{\partial p}{\partial z} = \mu \frac{\partial^2 w}{\partial y^2} \tag{2.64}$$

$$\frac{\partial u}{\partial x} + \frac{\partial v}{\partial y} + \frac{\partial w}{\partial z} = 0. \tag{2.65}$$

Naturally, these equations follow from Eqs. (2.62) on assuming that $\mathrm{R}_\varepsilon < 1$, or, equivalently, that $\varepsilon \mathrm{Re} < 1$. Now in most bearing applications the Reynolds number can be large, in fact the flow can still be laminar in journal bearings right up to $\mathrm{Re} \sim 1000$. Thus our limit on the reduced Reynolds number could be interpreted as a limit on the magnitude of the aspect ratio ε; in fact it must not exceed 1/1000. A more detailed discussion of this topic can be found in Chapter 5 of this book.

The equations of motion may now be integrated twice with respect to y, since by assumption (5) or Eq. (2.62b) neither $\partial p/\partial x$ nor $\partial p/\partial z$ varies across the film

$$u = \frac{1}{2\mu} \frac{\partial p}{\partial x} y^2 + Ay + B$$

$$w = \frac{1}{2\mu} \frac{\partial p}{\partial z} y^2 + Cy + D.$$

A, B, C, and D are either constants or, at most, functions of x and z. Their value must be chosen so that u and w satisfy prescribed boundary conditions in y.

The boundary conditions for u and w are

$$\begin{aligned} u &= U_1, \quad w = 0 \quad \text{at} \quad y = 0 \\ u &= U_2, \quad w = 0 \quad \text{at} \quad y = h \end{aligned} \tag{2.66}$$

where U_1 and U_2 represent the velocity of the bearing surfaces as indicated in Figure 2.7.

Substituting the velocity into the boundary conditions (2.66) evaluates the integration constants and yields the velocity distribution

$$\begin{aligned} u &= \frac{1}{2\mu} \frac{\partial p}{\partial x} (y^2 - yh) + \left(1 - \frac{y}{h}\right) U_1 + \frac{y}{h} U_2 \\ w &= \frac{1}{2\mu} \frac{\partial p}{\partial z} (y^2 - yh). \end{aligned} \tag{2.67}$$

The pressure gradient in Eq. (2.67) is, as yet, unknown. But since the pressure p is an induced pressure, the sole function of which is to guarantee compliance with the principle of conservation of mass, it can be evaluated from the condition that both u and w satisfy the equation of continuity. This seems to be a reasonable scheme, but it has one serious flaw. If u and w are substituted into Eq. (2.65) the resulting single equation will contain two unknowns[10] v and p, and, unless v is specified, we have insufficient information to determine p. This difficulty will be alleviated by integrating, in effect averaging, the equation of continuity across the film, as the averaged equation will contain the velocity component v only in the values it assumes on the boundaries at $y = 0$ and $y = h(x, t)$. As

[10]The problem originates with the approximation itself; the set of reduced equations, Eqs. (2.63) to (2.65), contain four unknowns u, v, w and p, but only three equations. Of course, one could employ the fourth equation $\partial p/\partial y = 0$ to eliminate the pressure by differentiation with respect to y and end up with three equations in three unknowns. Thus, in reality, the Reynolds thin-film approximation leaves us with a well defined system.

the approach velocity of the surfaces is presumed known during this analysis, integration across the film eliminates one of the two remaining unknowns.

Integrating the equation of continuity (2.65) across the film results in

$$v|_0^{h(x,t)} = -\int_0^{h(x,t)} \frac{\partial u}{\partial x} dy - \int_0^{h(x,t)} \frac{\partial w}{\partial z} dy. \tag{2.68}$$

Interchanging integration and differentiation in Eq. (2.68) and substituting u and v from Eq. (2.67) we obtain[11]

$$\begin{aligned} v|_0^{h(x,t)} = &-\frac{\partial}{\partial x}\left[\frac{1}{2\mu}\frac{\partial p}{\partial x}\int_0^{h(x,t)} (y^2 - yh)dy\right] - \frac{\partial}{\partial z}\left[\frac{1}{2\mu}\frac{\partial p}{\partial z}\int_0^{h(x,t)} (y^2 - yh)dy\right] \\ &- \frac{\partial}{\partial x}\int_0^{h(x,t)} \left[\left(1 - \frac{y}{h}\right)U_1 + \frac{y}{h}U_2\right]dy + U_2\frac{\partial h}{\partial x}. \end{aligned} \tag{2.69a}$$

Evaluating the integrals and taking into account that

$$v|_0^{h(x,t)} = -(V_1 - V_2) = \frac{dh}{dt} \tag{2.69b}$$

where $V_1 - V_2$ is the velocity of approach of the surfaces, we obtain the *Reynolds equation* for lubricant pressure

$$\frac{\partial}{\partial x}\left(\frac{h^3}{\mu}\frac{\partial p}{\partial x}\right) + \frac{\partial}{\partial z}\left(\frac{h^3}{\mu}\frac{\partial p}{\partial z}\right) = 6(U_1 - U_2)\frac{\partial h}{\partial x} + 6h\frac{\partial (U_1 + U_2)}{\partial x} + 12(V_2 - V_1). \tag{2.70}$$

It is emphasized that $\boldsymbol{V}_1 = (U_1, V_1)$ and $\boldsymbol{V}_2 = (U_2, V_2)$ are the velocities of "corresponding" points, each fixed to one of the bearing surfaces.[12] The velocities $\boldsymbol{V}_1$ and $\boldsymbol{V}_2$ result from rigid body motion, which may include both rotation and translation, of the bearing surfaces. It will be to our advantage in later work to separate rigid body translation from rigid body rotation. Thus, we decompose the velocity of surface 2, surface 1 being the reference surface, according to the scheme

$$\begin{aligned} U_2 &= U_{2,r} + U_{2,t} \\ V_2 &= V_{2,r} + V_{2,t} \end{aligned} \tag{2.71}$$

so that $(U_{2,r}, V_{2,r})$ and $(U_{2,t}, V_{2,t})$ are caused by rotation and translation, respectively.

For the plane slider in Figure 2.8, and for *thrust bearings* in general, the rotational components of the velocity are identically zero. The translational components are usually prescribed relative to the (x, y, z) coordinate system of the runner (now surface 1); thus

$$\begin{aligned} U_2 &= U_{2,t}, \qquad U_{2,r} \equiv 0 \\ V_2 &= V_{2,t}, \qquad V_{2,r} \equiv 0. \end{aligned} \tag{2.72}$$

[11] Here we employ Leibnitz's rule for differentiating under the integral sign

$$\frac{d}{dx}\int_A^B f(x,t)\,dt = \int_A^B \frac{\partial f(x,t)}{\partial x}dt + f(x,B)\frac{dB}{dx} - f(x,A)\frac{dA}{dx}.$$

[12] We call two points, one fixed to the bearing surface and the other to the runner surface, corresponding points at the instant when they are located on the same normal to the reference surface. For journal bearings the pad surface is the reference surface. For the plane slider, on the other hand, it is expedient to designate the runner surface as the reference surface.

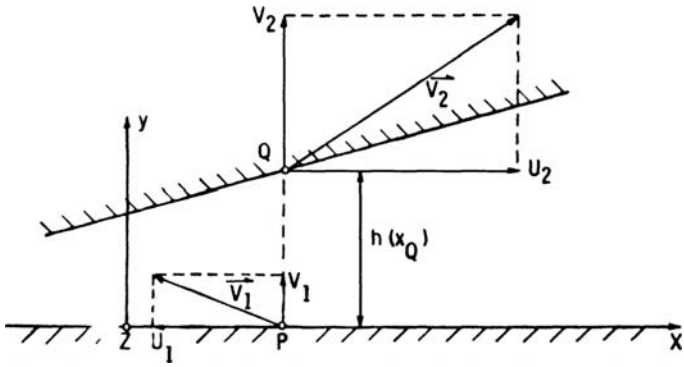

Figure 2.8. Velocities for rigid body translation of bearing surfaces.

Interpreting the film thickness as the normal distance between a point fixed on the bearing (point Q in Figure 2.8) and the runner surface (x, z plane), we find that the film thickness changes if and only if the bearing is given a translational velocity $V_{2,t} - V_1 = V_2 - V_1$ in the y direction, relative to the runner. Such change of film thickness is uniform in x and so is its time rate. Thus

$$U_1 - U_2 = U_1 - U_{2,t}$$
$$V_2 - V_1 = V_{2,t} - V_1 = \frac{\partial h}{\partial t}.$$

We find, furthermore, that both U_1 and U_2 are constant when the surfaces are rigid and thus for thrust bearings the Reynolds equation (2.70) reduces to

$$\frac{\partial}{\partial x}\left(\frac{h^3}{\mu}\frac{\partial p}{\partial x}\right) + \frac{\partial}{\partial z}\left(\frac{h^3}{\mu}\frac{\partial p}{\partial z}\right) = 6(U_1 - U_2)\frac{\partial h}{\partial x} + 12(V_2 - V_1). \tag{2.73}$$

Pressure generation in thrust bearings thus depends on the translational velocity of the bearing surfaces relative to one another but not on the absolute value of the velocity. We are therefore permitted to recast Eq. (2.73) into a form that contains only relative velocities. We will do this in order to bring out the essentials of the analysis. The result is the *Reynolds equation for thrust bearings*; that is, for bearings where only translation of the surfaces is involved,

$$\frac{\partial}{\partial x}\left(\frac{h^3}{\mu}\frac{\partial p}{\partial x}\right) + \frac{\partial}{\partial z}\left(\frac{h^3}{\mu}\frac{\partial p}{\partial z}\right) = 6U_0\frac{\partial h}{\partial x} + 12V_0. \tag{2.74}$$

Here,

$$U_0 = U_1 - U_2, \quad V_0 = V_2 - V_1$$

are the relative velocities in the directions parallel and perpendicular, respectively, to the reference (runner) surface.

To generate positive (load carrying) pressures in the film, it is necessary that the right-hand side of Eq. (2.74) be negative; that is,

$$U_0\frac{\partial h}{\partial x} < 0, \quad \frac{\partial h}{\partial t} < 0. \tag{2.75}$$

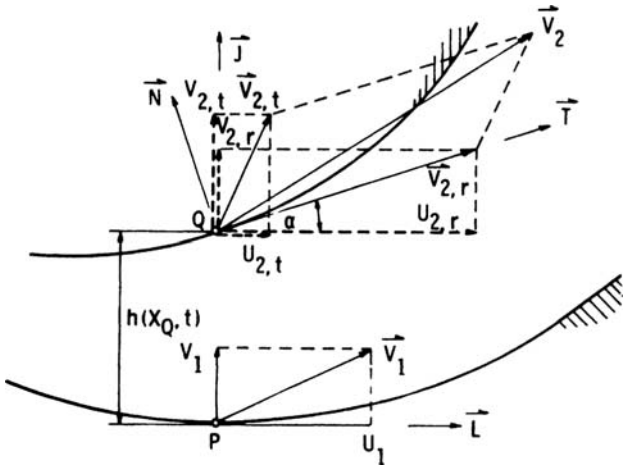

Figure 2.9. Velocities for translation and rotation of bearing surfaces.

The first of these conditions specifies a film that is convergent in space (in the direction of relative motion), and the second specifies a film that is convergent in time.

In *journal bearings* one encounters both rotation and translation of the bearing surfaces. The velocity $\boldsymbol{V}_2$ of an arbitrary point Q, fixed to the runner surface as in Figure 2.9, is given by the sum of its velocity in rigid body translation $\boldsymbol{V}_{2,t}$ and the velocity $\boldsymbol{V}_{2,r}$ that is caused by rigid body rotation of the journal. From Figure 2.9 we have

$$U_{2,r} = |\boldsymbol{V}_{2,r}| \cos \alpha = |\boldsymbol{V}_{2,r}| \left[1 - \frac{1}{2} \left(\frac{\partial h}{\partial x} \right)^2 + \cdots \right] \approx |\boldsymbol{V}_{2,r}| \tag{2.76a}$$

as $(\partial h/\partial x) \ll 1$ by assumption.

We may also write

$$V_{2,r} = |\boldsymbol{V}_{2,r}| \sin \alpha = U_{2,r} \tan \alpha \approx |\boldsymbol{V}_{2,r}| \frac{\partial h}{\partial x}. \tag{2.76b}$$

On the other hand, $U_{2,r}$ is easily replaced by U_2. In journal bearings

$$\frac{U_{2,t}}{U_{2,r}} = O(10^{-3})$$

and the following approximation is acceptable in most cases:

$$U_2 = U_{2,r} + U_{2,t} = U_{2,r} \left(1 + \frac{U_{2,t}}{U_{2,r}} \right) \approx U_{2,r}. \tag{2.76c}$$

Equation (2.76b) then takes the form

$$\begin{aligned} V_{2,r} &\approx U_2 \frac{\partial h}{\partial x} \\ V_2 &\approx V_{2,t} + U_2 \frac{\partial h}{\partial x}. \end{aligned} \tag{2.77}$$

The first and the last terms on the right-hand side of Eq. (2.70) are combined as follows:

$$\begin{aligned} 6(U_1 - U_2)\frac{\partial h}{\partial x} + 12\frac{dh}{dt} &= 6(U_1 - U_2)\frac{\partial h}{\partial x} + 12\left(V_{2,t} + U_2\frac{\partial h}{\partial x} - V_1\right) \\ &= 6(U_1 + U_2)\frac{\partial h}{\partial x} + 12\left(V_{2,t} - V_1\right) \\ &= 6(U_1 + U_2)\frac{\partial h}{\partial x} + 12\frac{\partial h}{\partial t}. \end{aligned} \tag{2.78}$$

As an alternative to Eq. (2.78) we might have started with the interpretation that the film thickness $h = h(x, t)$ is the normal distance between a point, Q, of the journal and the surface of the bearing. The film thickness, according to this interpretation, might be changing for one or both of the following reasons: (1) rigid body translation of the journal center relative to the bearing along a bearing radius (local change), and (2) rotation of the journal (convective change). The latter motion forces Q and h to move within a clearance gap of varying width, with velocity $U_{2,r}$. Therefore, recognizing that h is dependent on t both explicitly and implicitly through the motion, we obtain (see Eq. (2.5))

$$\frac{dh}{dt} = \frac{\partial h}{\partial t} + \frac{dx}{dt}\frac{\partial h}{\partial x} = \frac{\partial h}{\partial t} + U_{2,r}\frac{\partial h}{\partial x}$$

and recover Eq. (2.78) approximately. (For thrust bearings the second term on the right-hand side vanishes.)

Taking now Eq. (2.78) into account, Eq. (2.70) reduces to

$$\frac{\partial}{\partial x}\left(\frac{h^3}{\mu}\frac{\partial p}{\partial x}\right) + \frac{\partial}{\partial z}\left(\frac{h^3}{\mu}\frac{\partial p}{\partial z}\right) = 6\frac{\partial}{\partial x}\left[h(U_1 + U_2)\right] + 12(V_{2,t} - V_1). \tag{2.79}$$

Pressure generation in journal bearings has been shown thus to depend on (1) the sum of the tangential velocities $U_0 = U_1 + U_2$ and (2) the difference of the normal velocities $V_0 = V_{2,t} - V_1$. Equation (2.79) may then be recast into a form that contains U_0 and V_0 rather than the absolute value of the individual velocity components.

$$\frac{\partial}{\partial x}\left(\frac{h^3}{\mu}\frac{\partial p}{\partial x}\right) + \frac{\partial}{\partial z}\left(\frac{h^3}{\mu}\frac{\partial p}{\partial z}\right) = 6U_0\frac{\partial h}{\partial x} + 6h\frac{\partial U_0}{\partial x} + 12V_0. \tag{2.80}$$

Equations (2.74) and (2.80) are formally identical, but for the term $6h\,(\partial U_0/\partial x)$, which must be retained in Eq. (2.80) to account for journal motion under dynamic loading. However, it should be borne in mind that the interpretation put on the velocity U_0 is distinctly different in the two cases. If the bearing surface is stationary, and this will be assumed unless explicitly stated otherwise, then $U_0 = U_2$ for journal bearings and $U_0 = U_1$ for thrust bearings.

Practical Upper Bound for ε

We aim now to provide preliminary estimate for the largest value of ε at which predictions from Eqs. (2.62) can be expected to hold. For infinite extent of the flow domain

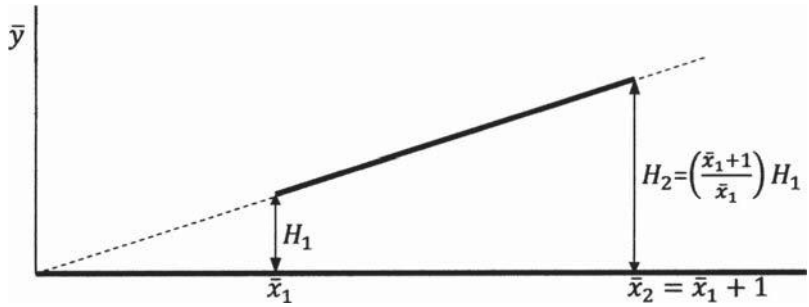

Figure 2.10. Geometry of the plane slider.

in the z – direction, steady state, and isothermal operations, Eqs. (2.61) and (2.62) provide the quasi one-dimensional system (Szeri and Snyder, 2006)

$$\mathrm{R}_\varepsilon\left(\bar{u}\frac{\partial\bar{u}}{\partial\bar{x}}+\bar{v}\frac{\partial\bar{u}}{\partial\bar{y}}\right)=-\frac{\partial\bar{p}}{\partial\bar{x}}+\frac{\partial^2\bar{u}}{\partial\bar{y}^2},\ \frac{\partial\bar{u}}{\partial\bar{x}}+\frac{\partial\bar{v}}{\partial\bar{y}}=0. \tag{2.81}$$

The results we shall quote here relate to flow between inclined, flat planes, i.e., the 'plane slider' (Figure 2.10). We put $\bar{x}=x/L_{xz}$, $\bar{y}=y/L_y$, $H_1=H(\bar{x}_1)$ and $H_2=H(\bar{x}_2)$ for the nondimensional coordinates and film thickness at outlet and inlet, respectively, with length scales $L_y=(h_1+h_2)/2$ and $L_{xz}=B=x_2-x_1$, where x_1 defines the position of the outlet and $x_2>x_1$ the inlet.

Introduction of the stream function $\Psi\,(\bar{x},\bar{y})$ into (2.81) leads to

$$\mathrm{R}_\varepsilon\left(H\frac{\partial\Psi}{\partial\eta}\frac{\partial^3\Psi}{\partial\eta^2\partial\xi}-2\frac{dH}{d\bar{x}}\frac{\partial\Psi}{\partial\eta}\frac{\partial^2\Psi}{\partial\eta^2}-H\frac{\partial\Psi}{\partial\xi}\frac{\partial^3\Psi}{\partial\eta^3}\right)-\frac{\partial^4\Psi}{\partial\eta^4}=0,\quad 0\le\xi,\ \eta\le 1. \tag{2.82}$$

Here, we also affected the change of variables

$$\xi=\bar{x}-\bar{x}_1$$
$$\eta=\bar{y}/H\,(\bar{x}),\quad H=h\,(x)\,/L_y$$

The no-slip boundary conditions on the solid boundaries are

$$\Psi=0,\quad \frac{\partial\Psi}{\partial\eta}=-H,\quad \text{at}\,\eta=0$$

$$\Psi=Q^*,\quad \frac{\partial\Psi}{\partial\eta}=0,\quad \text{at}\,\eta=1, \tag{2.83}$$

where Q^* is the dimensionless flow rate, an additional unknown. To ensure that the problem remains mathematically well posed we must also increase the number of independent equations. This we do by constraining the average pressure at outlet to equal its value at inlet:

$$\int_0^1\int_0^1 H(\xi)\frac{\partial P}{\partial\xi}d\xi d\eta=0. \tag{2.84}$$

We approximate $\Psi(\xi,\ \eta)$ by piecewise polynomial functions (deBoor, 1978) and apply Galerkin's method to evaluate the coefficients in the approximation. The resulting system of nonlinear algebraic equations can be written in the form

$$G(\omega) = 0, \quad \omega = (u,\ \sigma)\,, \tag{2.85}$$

where u is the vector of state variables and σ is the vector of parameters. The computational scheme for solving Eq. (2.85), i.e., parametric continuation followed by the Gauss–Newton method, can be found in Dai et al. (1992).

The principal conclusion from Eq. (2.62) is the invariance of the pressure across the film. To investigate the upper bound of ε for this conclusion to hold, we look at flow between inclined planes of various aspect ratios. As long as Eqs. (2.62) hold, the pressure on the upper plate, $P(h)$, and the pressure on the lower plate, $P(0)$, are approximately equal, becoming identical at the limit $\varepsilon \to 0$. This may be investigated quantitatively by computing a pressure difference coefficient

$$d_p = 100\,|P\,(h) - P(0)|_{\max}\,/\,P(h)_{\max}. \tag{2.86}$$

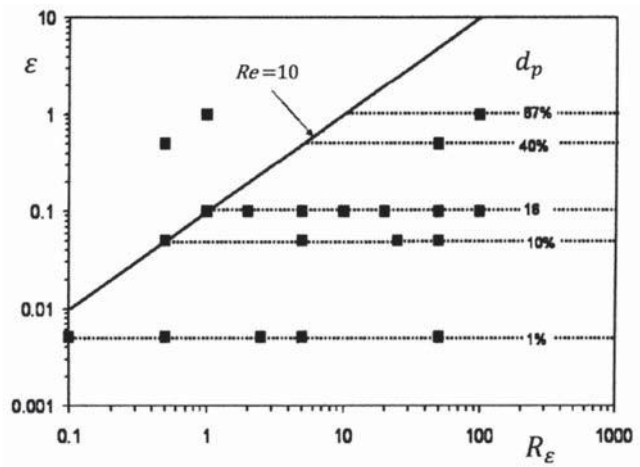

Figure 2.11. Pressure difference coefficient d_p for various values of the aspect ratio and reduced Reynolds number (With kind permission from Springer Science & Business Media: *Meccanica*, Convective inertia effects in wall-bounded thin film flows, 41, 2006, 473–482, Szeri, A. Z and Snyder, V., Figure 2).

In Figure 2.11 we indicate the value of d_p, calculated from the full Navier–Stokes problem employing FIDAP, as a function of the parameters ε and R_ε. We restrict attention here arbitrarily to $\mathrm{Re} > 10$, accepting this as a lower bound on the Reynolds number for applications. For "small" values of the aspect ratio, Figure 2.11 appears to support the assertion of Eq. (2.62): for $\varepsilon \leq 0.05$, $d_p \leq 1\%$, and even for the wider range $\varepsilon \leq 0.1$, $d_p < 16\%$, though the increase in d_p for $\varepsilon > 0.1$ is quite rapid. Thus, for $\varepsilon \leq 0.1$, we have the approximate relationship $d_p \approx f(\mathrm{R}_\varepsilon)$. This conclusion seems to hold well for $\mathrm{R}_\varepsilon \leq 100$.

Figure 2.12 plots the ratio of actual pressure over its zero Reynolds number value against R_ε, as calculated by FIDAP from the full Navier–Stokes problem at various values of $\varepsilon \leq 0.1$. Data for different ε values collapse onto a single curve, confirming again that

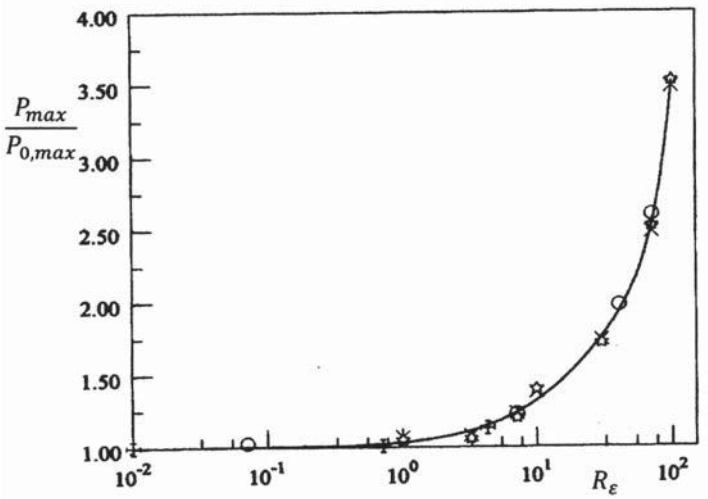

Figure 2.12. Variation of $P_{\max}/P_{0,\max}$ with R_ε Re, FIDAP (+, $\varepsilon = 0.005$; o, $\varepsilon = 0.05$; $_*$, $\varepsilon = 0.08$; $\times$, $\varepsilon = 0.1$; (With kind permission from Springer Science & Business Media: *Meccanica*, Convective inertia effects in wall-bounded thin film flows, 41, 2006, 473–482, Szeri, A. Z. and Snyder, V., Figure 3).

under the stated conditions the aspect ratio is not a strong parameter of the flow, that is $P_{\max}/P_{0,\max} \approx g\,(\mathrm{R}_\varepsilon)$.

Figure 2.13 compares lubricant force from two sources, FIDAP solution of the full Navier–Stokes problem and the stream function–Galerkin formulation of Eq. (2.82). Two

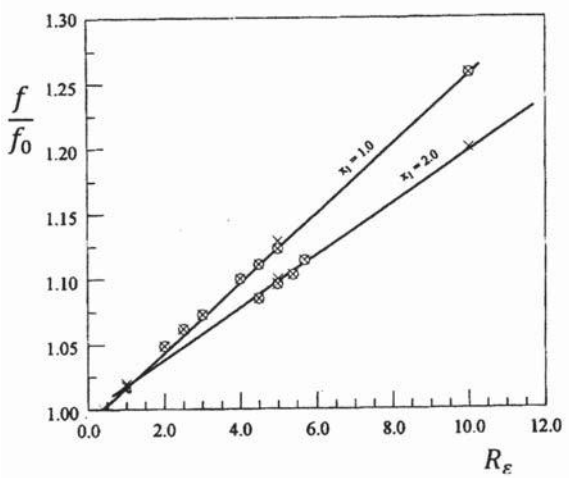

Figure 2.13. Normalized force, $\varepsilon \leq 0.1$; o, approximation; x, Navier–Stokes (With kind permission from Springer Science & Business Media: *Meccanica*, Convective inertia effects in wall-bounded thin film flows, 41, 2006, 473–482, Szeri, A. Z. and Snyder, V., Figure 5).

channel geometries, $h_2/h_1 = 2$ and $h_2/h_1 = 3/2$, are depicted in this figure, the force is normalized with its zero Reynolds number value.

This simplified analysis suggests that under conditions similar to those assumed here, the thin film approximation (2.62) will yield acceptable results when the local value of the aspect ratio, i.e., film slope, is less than 1 in 10. If the aspect ratio is greater than this, the approximation no longer holds and the pressure must be calculated from the full Navier–Stokes equations.

2.3 Nomenclature

$\mathcal{D}$	rate of strain quadric
$\boldsymbol{D}$	stretching tensor
$\boldsymbol{F}_B, \boldsymbol{F}_S$	body, surface force
J	Jacobian
$\boldsymbol{L}$	velocity gradient tensor
$L_y, L_{x,z}$	characteristic lengths
$\mathcal{M}$	mass
$\boldsymbol{M}$	torque
$\mathcal{R}$	gas constant
Re, R_ε	Reynolds numbers
$\mathcal{S}, \mathcal{s}$	surface
$\boldsymbol{T}$	stress tensor
$\boldsymbol{V}, \boldsymbol{v}$	velocity
$\mathcal{V}, \mathcal{v}$	volume
X_i, x_i	Cartesian coordinates
$\boldsymbol{\Omega}$	spin tensor
$\boldsymbol{a}$	acceleration
$d_{(i)}$	principal values of $\boldsymbol{D}$
$\boldsymbol{e}_i$	Cartesian base vectors
$\boldsymbol{f}$	body force, constitutive function
h	film thickness
$\boldsymbol{n}$	unit normal vector
p	pressure
t	time
$\boldsymbol{t}$	stress vector
λ	dilatational viscosity
μ	viscosity
ρ	density
ε	aspect ratio
$\boldsymbol{\tau}$	viscous stress tensor
$\tau_{(i)}$	principal values of τ
$\boldsymbol{\chi}$	deformation function
ψ	material property per unit volume
$\boldsymbol{\omega}$	vorticity vector
$(\cdot)^*$	characteristic quantity
$(\cdot)_r$, $(\cdot)_t$	radial, tangential
$\overline{(\cdot)}$	normalized

2.4 References

Dai, R. X., Dong, Q. M. and Szeri, A. Z. 1992. Flow between eccentric rotating cylinders: bifurcation and stability. *Int. J. Engrg. Sci.*, **30**, 1323–1340.

de Boor, C. 1978. *A Practical Guide to Splines.* Springer-Verlag, Berlin.

Reynolds, O. 1886. On the theory of lubrication and its application to Mr. Tower's experiments. *Philos. Trans. Roy. Soc.*, **177**, 159–209.

Serrin, J. 1959. *Mathematical Principles in Classical Fluid Mechanics*. In *Encyclopedia of Physics* (S. Flugge and C. Truesdell, eds.), Vol. VIII, Springer-Verlag, Berlin.

Stokes, G.G. 1845. On the theories of the internal friction of fluids in motion, and of the equilibrium and motion of elastic solids. *Trans. Camb. Phil. Soc.* **8**, 287–305.

Szeri, A. Z. and Snyder, V. 2006. Convective inertia effects in wall-bounded thin film flows. *Meccanica*, **41**, 473–482.

Truesdell and, C. and Rajagopal, K. R. 2000. *An Introduction to the Mechanics of Fluids.* Birkhauser, Boston, Basel, Berlin.

Truesdell, C, and Noll, B. 1992. *The Non-Linear Field Theories of Mechanics*. Springer-Verlag. Berlin, Heidelberg, New York.

Vincenti, W. G. and Kruger, C. H. 1965. *Introduction to Physical Gas Dynamics*, John Wiley & Sons, New York.

Thick-Film Lubrication

Fluid film lubrication naturally divides into two categories. *Thin-film* lubrication is usually met with in counter-formal contacts, principally in rolling bearings and in gears. The thickness of the film in these contacts is of order of 1 μm or less, and the conditions are such that the pressure dependence of viscosity and the elastic deformation of the bounding surfaces must both be taken into account.

Thick-film lubrication is encountered in externally pressurized bearings, also called *hydrostatic bearings*, and in self-acting bearings, called *hydrodynamic bearings*. Of the latter, there are two kinds: journal bearings and thrust bearings. The film thickness in these conformal-contact bearings is at least an order of magnitude larger than in counter-formal bearings. In consequence, the prevailing pressures are orders of magnitude smaller, so that neither the pressure dependence of viscosity nor the elastic deformation of the surfaces plays important roles. If, in addition, the lubricant is linearly viscous and the reduced Reynolds number is small, the classical Reynolds theory, as derived in the previous chapter, will apply.

This chapter discusses isothermal processes only. It should be realized, however, that bearings never operate under truly isothermal conditions, and under near isothermal conditions only in exceptional cases. Viscous dissipation and consequent heating of the lubricant are always present, and the change in viscosity must be accounted for when analyzing thick-film lubrication problems. In restricted cases, where design and operating conditions are such as to suggest "uniform" temperature rise of the lubricant, the "effective viscosity" approach of Chapter 9 might be employed. In other, again very limited, cases, where heat conduction into the bearing surfaces can be neglected, the "adiabatic theory" might be useful. But in the great majority of practical cases, particularly under turbulent flow conditions, full thermohydrodynamic theory, including thermal/elastic deformations of the bearing surfaces, must be employed.

3.1 Externally Pressurized Bearings

Hydrostatic bearings of non-uniform film thickness are discussed by Heller and Shapiro (1968) and by Szeri and Phillips (1974). The effect of fluid inertia is considered by Szeri and Adams (1978), and the coupled effects of nonuniform viscosity and fluid inertia can be found in Gourley (1977).

Here we derive the theory of externally pressurized bearings under the assumptions of (1) steady loading, (2) constant sliding velocity, and (3) uniform film thickness.

The applicable form of the Reynolds equation is obtained from Eq. (2.80) by substitution of $\mu = \text{const.}$, $h = \text{const}$, and $U_0 = V_0 = 0$:

$$\frac{\partial^2 p}{\partial x^2} + \frac{\partial^2 p}{\partial z^2} = 0, \quad \text{or} \quad \nabla^2 p = 0, \tag{3.1}$$

where ∇^2 is the two-dimensional Laplace operator.

The boundary conditions on pressure are

$$\begin{aligned} p &= p_r \quad \text{on} \quad \Gamma_i \\ p &= p_a \quad \text{on} \quad \Gamma_o. \end{aligned} \tag{3.2}$$

Here Γ_i, stands for the recess boundary, Γ_o represents the pad external boundary, p_r is the recess pressure, and p_a is the ambient pressure. (Without loss of generality we put $p_a = 0$ for the incompressible lubricant.)

Equation (3.1), together with the boundary conditions in Eq. (3.2), represents a Dirichlet problem of applied mathematics. The solution of this problem is straightforward when obtained numerically, but it is somewhat difficult to obtain analytically (Szeri, 1975). There are two pad geometries, however, for which solutions of Eq. (3.1) exist in closed form, the circular step and the annular geometries.

Pad Characteristics

Irrespective of the geometry or size of a hydrostatic pad, its performance characteristics can be written in the form

$$W = a_f A p_r, \tag{3.3a}$$

$$Q = q_f \frac{h^3}{\mu} p_r, \tag{3.3b}$$

$$H_p = q_f \frac{h^3}{\mu} p_r p_s, \tag{3.3c}$$

$$H_f = h_f \frac{\mu U_M^2 A}{h}, \tag{3.3d}$$

where W is the external load, Q is the flow rate of the lubricant, H_p is the required pumping power, H_f is the frictional loss, A is the pad area (including the area of the recess), and U_M is the maximum sliding velocity of the runner relative to the pad.

The quantities a_f, q_f, and h_f are commonly referred to as the *area factor*, the *flow factor*, and the *friction factor*, respectively. These factors are dimensionless – that is, they are independent of the size of the bearing pad but dependent on its geometry. They may be evaluated for the particular geometry by the designer or, for the more common geometries such as rectangular and sector, can be extracted from the literature (Rippel, 1963; Szeri, 1975).

Exactly how a_f, q_f, and h_f are obtained will be illustrated for the circular step geometry of radii R_1 and $R_2 > R_1$. Equation (3.1) is first written in polar coordinates for simplicity, and then made nondimensional through the substitutions:

$$p = p_r \bar{p}, \quad r = R_2 \bar{r}, \tag{3.4}$$

where R_2 is the pad outer radius.

Substitution results in the following differential equation and boundary conditions:

$$\begin{aligned} &\frac{d}{d\bar{r}}\left(\bar{r}\frac{d\bar{p}}{d\bar{r}}\right) = 0, \\ &\bar{p} = 1 \quad \text{at} \quad \bar{r} = \frac{R_1}{R_2}, \\ &\bar{p} = 0 \quad \text{at} \quad \bar{r} = 1, \end{aligned} \tag{3.5}$$

in place of Eqs. (3.1) and (3.2).

The solution of system Eq. (3.5) is

$$\bar{p} = \frac{\ln \bar{r}}{\ln (R_1/R_2)}. \tag{3.6}$$

We are now in the position to evaluate the bearing load capacity W as follows:

$$\begin{aligned} W &= \pi R_1^2 p_r + 2\pi \int_{R_1}^{R_2} rp\, dr \\ &= \pi R_1^2 p_r \left[1 + \frac{2(R_2/R_1)^2}{\ln (R_1/R_2)} \int_{R_1/R_2}^{1} \bar{r} \ln \bar{r}\, d\bar{r}\right] \\ &= \frac{1 - (R_1/R_2)^2}{2\ln(R_2/R_1)} A p_r. \end{aligned} \tag{3.7}$$

Consistent with the thin-film assumption of lubrication theory, the radial component of the velocity is given by

$$u_r = \frac{1}{2\mu}\frac{dp}{dr} y\,(y - h), \tag{3.8}$$

so that the flow rate out of the bearing can be calculated from the formula

$$Q = \int_0^h 2\pi r u_r\, dy = \frac{\pi}{6\ln (R_2/R_1)} \frac{h^3 pr}{\mu}. \tag{3.9}$$

The pumping power H_p required to pressurize the lubricant to the supply pressure p_s is the product of supply pressure and flow rate:

$$H_p = p_s Q,$$

or, when substituting from Eq. (3.9),

$$H_p = \frac{\pi}{6\ln (R_2/R_1)} \frac{h^3 p_s p_r}{\mu}. \tag{3.10}$$

In hydrostatic bearings the depth of the recess is much greater than the thickness of the film, and thus viscous dissipation due to shearing motion of the bearing surfaces occurs

mainly over the land. There, because of symmetry, the tangential velocity distribution across the gap is approximately linear, and the uniform shear stress is $\tau = \mu r\omega/h$.[1] The power loss from shearing motion can be calculated from

$$H_f = \int_A r\omega\tau \, dA = \frac{1-(R_1/R_2)^4}{2}\frac{\mu U_M^2 A}{h}. \tag{3.11}$$

Here U_M is the maximum tangential velocity of the runner over the land of the stationary bearing pad.

Equations (3.7)–(3.11) show that, for circular step bearings, the dimensionless performance factors are

$$a_f = \frac{1-(R_1/R_2)^2}{2\ln(R_2/R_1)}, \tag{3.12a}$$

$$q_f = \frac{\pi}{6\ln(R_2/R_1)}, \tag{3.12b}$$

$$h_f = \frac{1-(R_1/R_2)^4}{2}. \tag{3.12c}$$

The total power loss in the bearing (excluding line losses and power loss encountered in flow restrictors) is given by

$$H_T = H_p + H_f = qf\frac{h^3}{\mu}p_r p_s + h_f\frac{\mu U_M^2 A}{h}. \tag{3.13}$$

The dependence of H_T on the film thickness and the viscosity is shown in Figure 3.1 for a certain hydrostatic bearing.

Optimization

The curves of Figure 3.1 suggest the existence of optimum values h_{opt}, μ_{opt} of the film thickness and the viscosity, respectively. If they exist, these optimum values are given by the conditions

$$\frac{\partial H_T}{\partial h} = 0, \tag{3.14a}$$

$$\frac{\partial H_T}{\partial \mu} = 0. \tag{3.14b}$$

[1] In the classical theory of hydrostatic bearings, the relative velocity, U_0, has no effect on the flow in the direction orthogonal to U_0. Coupling between orthogonal directions is achieved by the nonlinear terms of the equation of motion, and these are neglected in the present analysis.

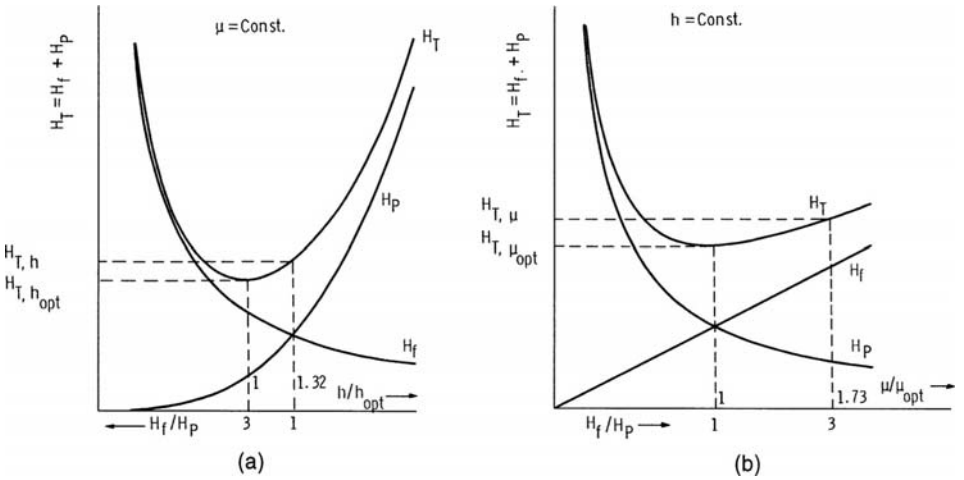

Figure 3.1. Total power loss for hydrostatic bearing as function of (a) the dimensionless film thickness and (b) the dimensionless viscosity.

Substitution of H_T from Eq. (3.13) into Eqs. (3.14a) and (3.14b) yields the optimum film thickness at constant viscosity and the optimum viscosity at constant film thickness, respectively.[2]

$$h_{\text{opt}} = \left(\frac{h_f \mu^2 U_M^2 A}{3 q_f p_r p_s} \right)^{1/4}, \tag{3.15a}$$

$$\mu_{\text{opt}} = \left(\frac{q_f h^4 p_r p_s}{h_f U_M^2 A} \right)^{1/2}. \tag{3.15b}$$

When substituting h_{opt} into Eqs. (3.3c) and (3.3d), we find that

$$\frac{H_f}{H_p} = 3 \tag{3.16a}$$

and Eq. (3.13) yields

$$H_{T,h_{\text{opt}}} = \frac{4}{3^{3/4}} \left(q_f h_f^3 p_r p_s \mu^2 U_M^6 A^3 \right)^{1/4}. \tag{3.16b}$$

If, on the other hand, one employs the optimum value of the viscosity in Eqs. (3.3c) and (3.3d), one is led to the conditions

$$\frac{H_f}{H_p} = 1, \tag{3.17a}$$

$$H_{T,\mu_{\text{opt}}} = 2\sqrt{q_f h_f A p_r p_s}\, h U_M. \tag{3.17b}$$

[2]Note that the set of simultaneous equations (3.14) has only the trivial solution $\mu = 0 = h$, and thus we are compelled to optimize the functions $H_T^{(h)} \equiv H_T(h, \mu)|_{\mu=\text{const.}}$ and $H_T^{(\mu)} \equiv H_T(h, \mu)|_{h=\text{const.}}$ separately.

Condition (3.16a) states that for a given value of the viscosity, the total power loss has a minimum when the film thickness is chosen such that the frictional power loss equals three times the pumping power loss. Condition (3.17a) asserts that the total power loss is a minimum if, for a given constant film thickness, the viscosity is selected so as to yield equal values of the frictional power loss and the pumping power loss.

Obviously conditions (3.16a) and (3.17a) cannot be satisfied simultaneously (see footnote 2). We then wish to know the maximum variation of H_T when the ratio H_f/H_p is in the interval $1 \leq H_f/H_p \leq 3$. Calculating the total power loss at constant viscosity, and under the requirement $H_p = H_f$, we obtain

$$H_{T,h} = 2\left(q_f h_f^3 p_r p_s \mu^2 U_M^6 A^3\right)^{1/4}. \tag{3.18}$$

We may also calculate the total power loss at constant film thickness for the condition $H_f = 3H_p$, obtaining

$$H_{T,\mu} = \frac{4}{\sqrt{3}}\sqrt{q_f h_f A p_r p_s}\, h U_M. \tag{3.19}$$

Comparison of Eqs. (3.16b) and (3.18) and of Eqs. (3.17b) and (3.19) shows that

$$\left.\begin{aligned} 1 \leq \frac{H_{T,h}}{H_{T,h_{\text{opt}}}} &\leq 1.1398 \\ 1.1547 \geq \frac{H_{T,\mu}}{H_{T,\mu_{\text{opt}}}} &\geq 1 \end{aligned}\right\} \quad \text{for } 3 \geq \frac{H_f}{H_p} \geq 1. \tag{3.20}$$

We have just demonstrated that a plane hydrostatic bearing, irrespective of its geometry, will operate at less than 16% above minimum total power as long as the ratio H_f/H_p is held between the values 1 and 3 (Figure 3.1). It would therefore seem to matter little what value of H_f/H_p we design for within this range. This conclusion is misleading, however, and we do well to design for $H_f/H_p = 1$, for reasons indicated below.

Assuming that all the generated heat is spent on increasing the temperature of the lubricant, the lubricant temperature rise ΔT is given by

$$c\rho Q \Delta T = H_T,$$

so that

$$\Delta T = \frac{1}{\rho c}\left(\frac{h_f}{q_f}\frac{\mu^2 U_M^2 A}{h^4 p_r} + p_s\right). \tag{3.21}$$

Let us assume for simplicity that $p_r = kp_s$, $k = \text{const}$, then ΔT may easily be optimized with respect to p_s. From the condition

$$\frac{\partial \Delta T}{\partial p_s} = 0$$

we derive the optimum value (in terms of temperature rise) of the supply pressure

$$p_{s,\text{opt}} = \sqrt{\frac{h_f}{q_f}\frac{A}{k}}\,\mu\frac{U_M}{h^2}. \tag{3.22}$$

With $p_s = p_{s,\text{opt}}$ Eqs. (3.3c) and (3.3d) yield Eq. (3.17a) once more, and Eq. (3.21) reduces to

$$\Delta T_{p_s,\text{opt}} = \frac{2}{\rho c} p_s. \tag{3.23}$$

As one might expect, from the fact that Eq. (3.17a) was recovered on optimizing ΔT with respect to p_s, substitution of μ_{opt} from Eq. (3.15b) into Eq. (3.21) yields the result already given by Eq. (3.23).

Operation with Flow Restrictors

To successfully support asymmetric loads, multipad bearings with built-in pressure regulators must be used (see Section 1.6). Regulation of pad pressure is accomplished by use of a flow restrictor between the pressure source and the pad. The most common forms of the control devices (see Chapter 1) used in externally pressurized bearings are (1) viscous restrictors (capillary), (2) turbulent restrictors (orifice), and (3) constant flow devices (valve, pump).

The oil film stiffness of the bearing depends on the control mechanism. When calculating bearing stiffness, the supply system and the type of bearing have to be considered as forming a system. The analysis of such a lubrication system will be shown here for a plane bearing with capillary restrictor (Opitz, 1968).

The resistance to flow over the land is $R_B = \mu / q_f h^3$ from Eq. (3.3c), whereas the resistance of the capillary $R_C = 128\mu\ell^2/\pi d^4$ is given by the Hagen-Poiseuille law. Here ℓ is the length of the capillary and d is its diameter.

From Eq. (3.3a) the arbitrary load W at h is

$$\begin{aligned} W &= a_f A p_r \\ &= a_f A p_s \frac{R_B}{R_C + R_B}, \end{aligned} \tag{3.24}$$

and for the reference load W_0 at h_0 we have

$$W_0 = a_f A p_s \frac{R_{B_o}}{R_C + R_{B_o}}. \tag{3.25}$$

The ratio of loads W/W_0 can now be calculated:

$$\frac{W}{W_0} = \frac{1 + \xi}{1 + \xi X^3}, \tag{3.26}$$

where

$$\xi = \frac{R_{B_o}}{R_C} \quad \text{and} \quad X = \frac{h}{h_0}.$$

The numerical value of ξ is thus equal to the ratio of the resistance over the land and the capillary resistance for the static load W_0. The ratio of supply pressure to recess pressure is given, under the same condition, by $p_s/p_r = \xi + 1$.

We find the dimensionless bearing stiffness by differentiating Eq. (3.26) with respect to h:

$$\lambda \equiv -\frac{\partial (W/W_0)}{\partial (h/h_0)} = -\frac{3\xi (1 + \xi) X^2}{\left(1 + \xi X^3\right)^2}. \tag{3.27}$$

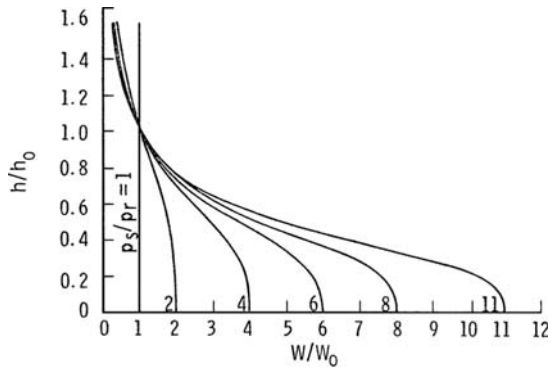

Figure 3.2. Operation with capillary restrictors: film thickness versus load for constant ratios of the supply pressure to the recess pressure.

The ratio X is plotted against W/W_0 in Figure 3.2. Figure 3.3 shows the variation of $\lambda/(1+\xi)$ with X. Inherent control by shallow parallel or tapered recesses is a more recent development (Rowe and O'Donoghue, 1971).

The feature of shallow recess control is that inlet pressure remains constant while pad coefficients vary. No external control devices are required, and therefore inherently controlled bearings are very compact and simple.

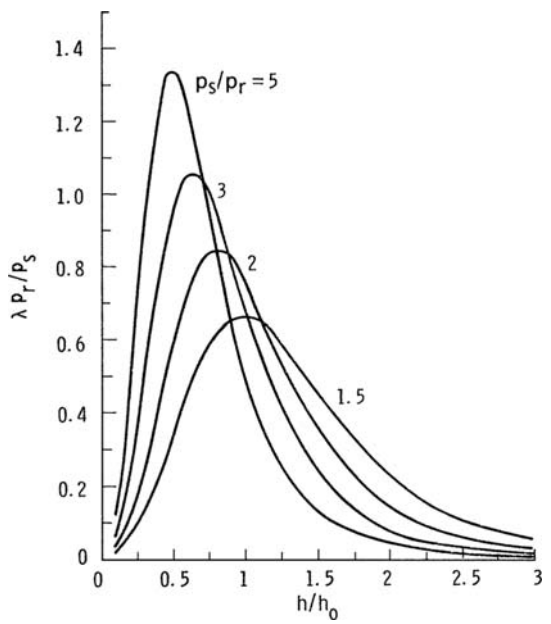

Figure 3.3. Operation with capillary restrictor: dimensionless bearing stiffness versus film thickness.

3.2 Journal Bearings

Support of rotating shafts is one of the most common applications of hydrodynamic bearings. The load in such applications is either perpendicular to the axis of rotation or coincident with it. In the former case we speak of a radial load, and the shaft is supported by a journal bearing. Thrust bearings are employed when the load is axial. Although the previously derived Reynolds equation of lubrication is applicable to bearings of either type, these two basic types of hydrodynamic bearings will be discussed under separate headings in this section.

In their simplest form, a journal and its bearing consist of two eccentric, rigid, cylinders. The outer cylinder (bearing) is usually held stationary while the inner cylinder (journal) is made to rotate at an angular velocity ω. In addition to this rigid body rotation the journal may also acquire a velocity of translation. The components of the translational velocity are $\dot{e}$ and $e(\dot{\psi} + \dot{\phi})$ measured along the line of centers $\overline{O_B O_J}$ and perpendicular to it, respectively, as depicted in Figure 3.4.

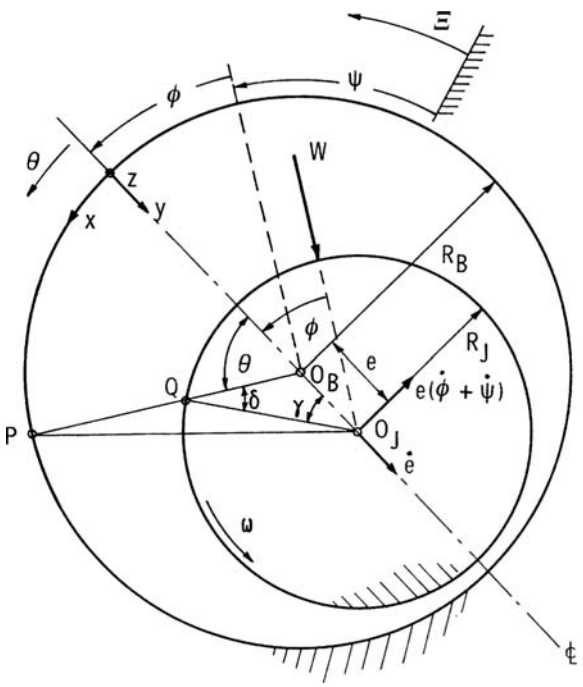

Figure 3.4. Journal bearing geometry and nomenclature.

Because the journal is eccentric with the bearing, the clearance gap between the cylidrical surfaces is not uniform around the circumference of the bearing. When the width of this gap is measured along a bearing radius, it is referred to as the film thickness and is customarily given the symbol h.

We will now establish the dependence of h on the angular coordinate θ. Let P be an arbitrary point of the bearing surface. The angular position of P relative to the line of centers $\overline{O_B O_J}$ is characterized by θ, as illustrated in Figure 3.4.

From the triangle $O_J Q O_B$ we may write

$$\frac{\overline{QO_B}}{\sin\gamma} = \frac{R_J}{\sin\theta} = \frac{e}{\sin\delta},$$

and as

$$\begin{aligned}\gamma &= \theta - \delta \\ &= \theta - \arcsin\left(\frac{e}{R_J}\sin\theta\right),\end{aligned}$$

the distance $\overline{QO_B}$ is given by

$$\begin{aligned}\overline{QO_B} &= \frac{R_J}{\sin\theta}\sin\left[\theta - \arcsin\left(\frac{e}{R_J}\sin\theta\right)\right] \\ &= \sqrt{R_J^2 - e^2\sin^2\theta} - e\cos\theta. \end{aligned} \tag{3.28}$$

The film thickness, h, at the arbitrary position P of angular coordinate θ is given by

$$\begin{aligned}h &= R_B - \overline{QO_B} \\ &= C + R_J + e\cos\theta - R_J\sqrt{1 - \left(\frac{e}{R_J}\right)^2\sin^2\theta}.\end{aligned}$$

Here we put $R_B = R_J + C$, where C is the radial clearance.

The expression under the square root sign may be expanded in a binomial series as $e/R_J \ll 1$:

$$\sqrt{1 - \left(\frac{e}{R_J}\right)^2\sin^2\theta} = 1 - \frac{1}{2}\left(\frac{e}{R_J}\sin\theta\right)^2 - \frac{1}{8}\left(\frac{e}{R_J}\sin\theta\right)^4 - \cdots.$$

Therefore, to order (e/R_J) the approximate expression for film thickness is

$$\begin{aligned}h &= C + e\cos\theta \\ &= C(1 + \varepsilon\cos\theta).\end{aligned} \tag{3.29}$$

Here $\varepsilon = e/C$, $0 \le \varepsilon \le 1$ is the bearing eccentricity ratio. Typically, in liquid-lubricated journal bearings $C/R_J \approx 0.002$, and we find Eq. (3.29) to be of sufficient accuracy in most practical cases (Dai, Dong, and Szeri, 1992).

Having established the dependence of the film thickness on the angular coordinate, we are in a position to evaluate the right-hand side of Eq. (2.80). The angular coordinate θ is related to a fixed direction, Ξ in Figure 3.5, through the attitude angle ϕ and the instantaneous load direction ψ. This permits us to rewrite Eq. (3.29) as

$$h = C + e\cos\left[\Xi - (\phi + \psi)\right]. \tag{3.30}$$

Having this new expression for film thickness greatly facilitates calculation of the squeeze film term in Eq. (2.80)

$$\begin{aligned}V_0 &= \frac{\partial h}{\partial t} \\ &= \frac{de}{dt}\cos\left[\Xi - (\psi + \phi)\right] + e\frac{d(\psi + \phi)}{dt}\sin\left[\Xi - (\psi + \phi)\right] \\ &= \dot{e}\cos\theta + e(\dot{\phi} + \omega_W)\sin\theta.\end{aligned} \tag{3.31}$$

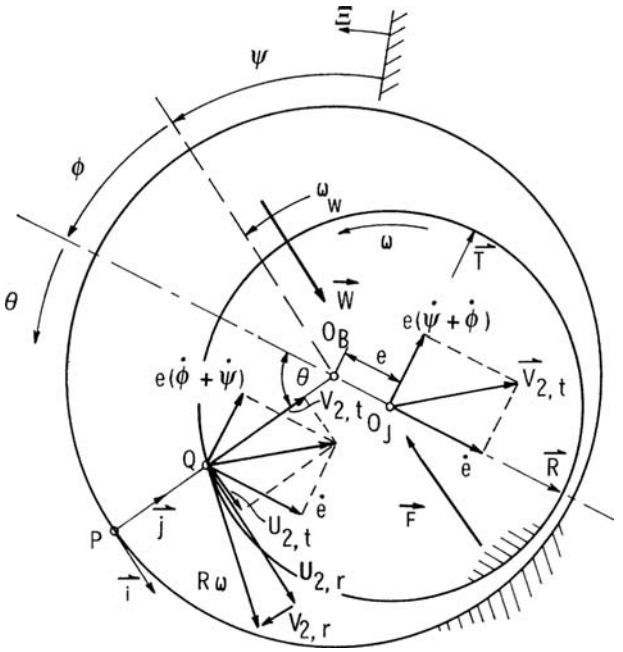

Figure 3.5. Journal velocities and journal bearing nomenclature.

Here $\omega_W = d\psi/dt$ is the frequency of rotation of the applied load, a dot above a quantity signifies its time rate of change, and we assume that the bearing is stationary.

Let ($\boldsymbol{R}$, $\boldsymbol{T}$) represent a Cartesian coordinate system centered at O_J with unit vectors $\boldsymbol{R}$ and $\boldsymbol{T}$ parallel and perpendicular, respectively, to the line of centers, as illustrated in Figure 3.5. The matrix of transformation from the ($\boldsymbol{R}$, $\boldsymbol{T}$) coordinate system to the (x, y) coordinate system, which is centered at P and has unit vectors $\boldsymbol{i}$ and $\boldsymbol{j}$, is given by

$$(M) = \begin{pmatrix} \sin\theta & -\cos\theta \\ \cos\theta & \sin\theta \end{pmatrix}.$$

Thus we have

$$\begin{pmatrix} U_{2,t} \\ V_{2,t} \end{pmatrix} = (M) \begin{pmatrix} \dot{e} \\ e(\dot{\phi} + \dot{\psi}) \end{pmatrix},$$

and the first two terms on the right-hand side of Eq. (2.80) simplify as follows (Szeri, 1980):

$$\begin{aligned} 6U_0 \frac{\partial h}{\partial x} + 6h \frac{\partial U_0}{\partial x} &= 6 \frac{\partial}{\partial x} \left[h U_{2,r} \left(1 + \frac{U_{2,t}}{U_{2,r}} \right) \right] \\ &= 6 \frac{\partial}{\partial x} \left\{ hR\omega \left[1 + \frac{C}{R} \left(\frac{\dot{\varepsilon}}{\omega} \sin\theta - \varepsilon \frac{\dot{\phi} + \dot{\psi}}{\omega} \cos\theta \right) \right] \right\} \\ &\approx 6R\omega \frac{\partial h}{\partial x}. \end{aligned} \tag{3.32}$$

Approximation (3.32) is good to order C/R, provided that $\dot{\varepsilon}$, $\dot{\phi}$ and $\dot{\psi}$ are all of order ω or smaller.

The sum of Eqs. (3.31) and (3.32) yields the right-hand side of Eq. (2.80) for a stationary bearing

$$\frac{\partial}{\partial x}\left(\frac{h^3}{\mu}\frac{\partial p}{\partial x}\right)+\frac{\partial}{\partial z}\left(\frac{h^3}{\mu}\frac{\partial p}{\partial z}\right)=6R\omega\frac{\partial h}{\partial x}+12\left[\dot{e}\cos\theta+e\left(\dot{\phi}+\omega_W\right)\sin\theta\right]. \tag{3.33}$$

In general both $\dot{e}$ and $\dot{\phi}$ are different from zero, for even when subject to an external load that is constant[3] in both magnitude and direction, the journal center orbits around its *static equilibrium position*. For a well-designed bearing the amplitudes of such orbits are exceedingly small, so that motion of the journal center will not need to be considered when calculating steady-state performance. However, when investigating stability of the orbiting motion of the journal, or when calculating journal response to dynamic loading, $\dot{\varepsilon}$, $\dot{\phi}$, and ω_W must be taken into account. We will consider only steady-state performance of journal bearings in this chapter, so unless otherwise stated $\dot{\varepsilon}=\dot{\phi}=\omega_W=0$.

It will be to our advantage to bring Eq. (3.33) into a nondimensional form. This may be achieved by the following transformation:

$$\begin{aligned} &x=R\theta, \qquad z=\frac{L}{2}\bar{z}\\ &h=CH=C(1+\varepsilon\cos\theta), \qquad p=\mu N\left(\frac{R}{C}\right)^2\bar{p}. \end{aligned} \tag{3.34}$$

Here θ, $\bar{z}$, H, and $\bar{p}$ are the dimensionless circumferential coordinate, the dimensionless axial coordinate, the dimensionless film thickness, and the dimensionless pressure, respectively. We also make the assumption $\mu=$ const., a condition that is rarely, if at all, attained in practice.

The nondimensional pressure equation is

$$\frac{\partial}{\partial\theta}\left(H^3\frac{\partial\bar{p}}{\partial\theta}\right)+\left(\frac{D}{L}\right)^2\frac{\partial}{\partial\bar{z}}\left(H^3\frac{\partial\bar{p}}{\partial\bar{z}}\right)=12\pi\frac{\partial H}{\partial\theta}. \tag{3.35}$$

Equation (3.35) is usually solved on the computer, using finite difference (Raimondi and Boyd, 1958) or finite-element (Reddi, 1970) methods. Approximate analytical solutions of the full equation are also possible, although these tend to be somewhat complicated (Szeri and Powers, 1967; Safar and Szeri, 1972).

There are two approximations to Eq. (3.35) that have closed-form analytical solutions. Before investigating these, we interpret Eq. (3.35) as a condition for flow continuity. The terms

$$\frac{\partial}{\partial\theta}\left(H^3\frac{\partial\bar{p}}{\partial\theta}\right), \qquad \left(\frac{D}{L}\right)^2\frac{\partial}{\partial\bar{z}}\left(H^3\frac{\partial\bar{p}}{\partial\bar{z}}\right), \qquad 12\pi\frac{\partial H}{\partial\theta}$$

represent the dimensionless rates of change at a point, each in its own direction, of the circumferential pressure flow, the axial pressure flow, and the shear flow, respectively. In a finite bearing these three quantities are all of the same order of magnitude.

[3]Even minute changes that might occur in a nominally constant load, e.g., when the mass center of the shaft does not coincide with its geometric center due to shaft deflection or to manufacturing inaccuracies, will perturb the equilibrium position. So will fluctuations in temperature or shaft speed.

If the bearing is "infinitely" long, there is no pressure relief in the axial direction and we have $\partial \bar{p}/\partial \bar{z} = 0$. Axial flow is therefore absent, and changes in shear flow must be balanced by changes in circumferential pressure flow alone. This condition will also apply in first approximation to finite bearings, leading to the so-called *long-bearing* theory (Reynolds, 1886), if the aspect ratio $L/D > 2$. When this condition is satisfied[4] we are permitted to approximate Eq. (3.35) by

$$\frac{d}{d\theta}\left(H^3 \frac{d\bar{p}}{d\theta}\right) = 12\pi \frac{dH}{d\theta}. \tag{3.36}$$

If, on the other hand, a finite bearing is made progressively shorter while operating at the same speed and the same eccentricity ratio, it will generate lower and lower pressures because of the progressively greater pressure relief in the axial direction. This leads to decreased circumferential pressure flow, while the axial pressure flow will have increased. In such cases we may write Eq. (3.35) in the approximate form

$$\frac{\partial}{\partial \bar{z}}\left(H^3 \frac{\partial \bar{p}}{\partial \bar{z}}\right) = 12\pi \left(\frac{L}{D}\right)^2 \frac{\partial H}{\partial \theta}. \tag{3.37}$$

The ratio L/D at which axial pressure flow first dominates circumferential pressure flow, depends on the eccentricity ratio, $L/D = 0.25$, being a safe figure under normal operating conditions. The theory that is based on Eq. (3.37) is termed the *short-bearing theory* (DuBois and Ocvirk, 1955).

Before the availability of digital computers, the short-bearing and long-bearing approximations represented the sole practical methods for obtaining solutions to bearing problems. They yield good results when applied judiciously and to the appropriate bearing geometry, but great care should be exercised in interpreting results obtained by these approximations – the long-bearing solution should be particularly suspect. These approximations still remain useful in theoretical work or when a large number of solutions of the same bearing configuration are required. Such a situation may arise, for instance, when computing nonlinear journal orbits. During such computations the oil film forces must be evaluated at each time step, leading to a considerable volume of computations.

Short-Bearing Theory

The applicable form of the Reynolds equation is given by Eq. (3.37) and the pressure boundary conditions are

$$\bar{p} = \bar{p}_a \quad \text{at} \quad \bar{z} = \pm 1. \tag{3.38}$$

Notice that it is not possible to prescribe boundary conditions at constant θ. Thus we have no way of specifying arbitrary bearing arc when using the short-bearing approximation. This represents the principal limitation of short-bearing theory.

The solution of Eq. (3.37) that satisfies the conditions specified in Eq. (3.38) is

$$\bar{p} = 6\pi \left(\frac{L}{D}\right)^2 \frac{1}{H^3} \frac{\partial H}{\partial \theta}\left(\bar{z}^2 - 1\right) + \bar{p}_a, \tag{3.39}$$

where $\bar{p}_a$ is the dimensionless ambient pressure.

[4] If the condition on the aspect ratio is not satisfied, the long-bearing theory can lead to serious errors and must be applied judiciously.

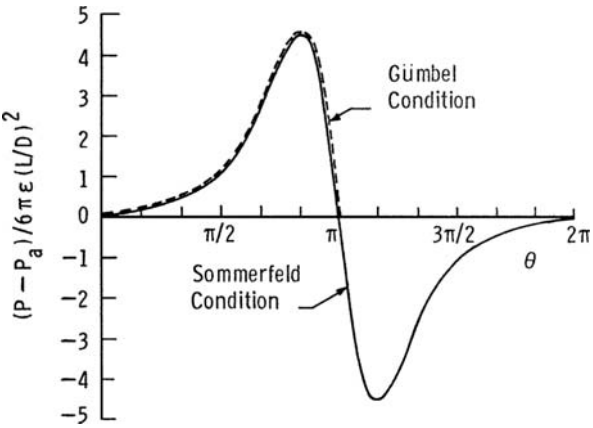

Figure 3.6. Circumferential pressure distribution according to short bearing theory, Eq. (3.39).

It is seen from Eq. (3.39) that the gauge pressure $\bar{p} - \bar{p}_a$ is a 2π periodic function of θ. It is antisymmetric with respect to the position of minimum film thickness $\theta = \pi$.

According to theory, therefore, below-ambient pressures of the same order of magnitude as above-ambient pressures are generated, as shown in Figure 3.6.

The center of the rotating journal will remain in a fixed position (its static equilibrium position) as long as the external load $\boldsymbol{W}$ is exactly balanced by the resultant pressure force $\boldsymbol{F}$. Relative to the ($\boldsymbol{R}$, $\boldsymbol{T}$) coordinate system of Figure 3.5 we have

$$\begin{aligned} &\boldsymbol{W} = W\cos\phi\,\boldsymbol{R} - W\sin\phi\,\boldsymbol{T}, \quad W = (\boldsymbol{W}\cdot\boldsymbol{W})^{1/2} \\ &\boldsymbol{F} = F_R\boldsymbol{R} + F_T\boldsymbol{T}, \quad F = (\boldsymbol{F}\cdot\boldsymbol{F})^{1/2} = \left(F_R^2 + F_T^2\right)^{1/2} \end{aligned} \tag{3.40a}$$

where $\boldsymbol{R}$ and $\boldsymbol{T}$ are unit vectors directed along the line of centers and perpendicular to it, respectively.

For static equilibrium of the journal

$$\boldsymbol{W} + \boldsymbol{F} = 0$$

or

$$\begin{aligned} W\cos\phi + F_R &= 0, \\ -W\sin\phi + F_T &= 0. \end{aligned} \tag{3.40b}$$

The components $F_R < 0$ and $F_T > 0$ of the pressure force are given by

$$F_R = \int_{-L/2}^{L/2}\int_0^{R\theta_2} p\cos\theta\,dx\,dz, \tag{3.40c}$$

$$F_T = \int_{-L/2}^{L/2}\int_0^{R\theta_2} p\sin\theta\,dx\,dz. \tag{3.40d}$$

Here θ_2 represents the angular position of the trailing edge of the lubricant film, which might or might not be located at $\theta = 360^\circ$.

For the time being we assume that the lubricant cannot withstand tension of any magnitude and that the film ruptures at $\theta_2 = \pi$, where, according to theory, film pressure exactly equals ambient (now zero) pressure. The integrations in Eq. (3.40) are then to be performed over the active bearing arc $0 < \theta < \pi$. If f_R and f_T are the nondimensional radial and tangential force components, respectively, then

$$f_R \equiv \frac{F_R/LD}{\mu N(R/C)^2} = -2\pi \left(\frac{L}{D}\right)^2 \int_0^\pi \cos\theta \frac{\partial H/\partial\theta}{H^3}\, d\theta \tag{3.41a}$$

and

$$f_T \equiv \frac{F_T/LD}{\mu N(R/C)^2} = -2\pi \left(\frac{L}{D}\right)^2 \int_0^\pi \sin\theta \frac{\partial H/\partial\theta}{H^3}\, d\theta. \tag{3.41b}$$

To evaluate the integrals in Eq. (3.41), we make the following substitution due to Sommerfeld (1904):

$$H = 1 + \varepsilon\cos\theta = \frac{1-\varepsilon^2}{1-\varepsilon\cos\psi}, \tag{3.42a}$$

so that

$$\sin\theta = \frac{\sqrt{1-\varepsilon^2}\sin\psi}{1-\varepsilon\cos\psi}, \quad \cos = \frac{\cos\psi - \varepsilon}{1-\varepsilon\cos\psi}, \tag{3.42b}$$

and

$$d\theta = \frac{\sqrt{1-\varepsilon^2}}{1-\varepsilon\cos\psi} d\psi. \tag{3.42c}$$

The integrals in Eq. (3.41) can now be evaluated:

$$\int_0^\pi \cos\theta \frac{\partial H/\partial\theta}{H^3} d\theta = -\frac{\varepsilon}{(1-\varepsilon^2)^2} \int_0^\pi \sin\psi\,(\cos\psi - \varepsilon)\, d\psi = \frac{2\varepsilon^2}{(1-\varepsilon^2)^2} \tag{3.43}$$

and

$$\int_0^\pi \sin\theta \frac{\partial H/\partial\theta}{H^3} d\theta = \frac{-\varepsilon}{(1-\varepsilon^2)^{3/2}} \int_0^\pi \sin^2\psi d\psi = -\frac{\pi\varepsilon}{2(1-\varepsilon^2)^{3/2}}. \tag{3.44}$$

Integrals of the type

$$A_k^{i,j} = \int_{\beta_1}^{\beta_2} \frac{\sin^i\beta\cos^j\beta}{(1+\varepsilon\cos\beta)^k},$$

useful in journal bearing analysis, have been listed by Gross (1962), Cameron (1966), and others.

Substitution of Eqs. (3.43) and (3.44) into Eq. (3.41) results in the dimensionless force components:

$$f_R = -\left(\frac{L}{D}\right)^2 \frac{4\pi\varepsilon^2}{(1-\varepsilon^2)^2},$$
$$f_T = \left(\frac{L}{D}\right)^2 \frac{\pi^2\varepsilon}{(1-\varepsilon^2)^{3/2}}. \tag{3.45}$$

The bearing Sommerfeld number defined by

$$S \equiv \frac{\mu N}{P}\left(\frac{R}{C}\right)^2 = \left(f_R^2 + f_T^2\right)^{-1/2} \tag{3.46}$$

is a dimensionless number, which is used to characterize bearing performance.[5]

For the short bearing with boundary condition $\bar{p} = 0$ at $\theta_2 = \pi$ we have

$$S\left(\frac{L}{D}\right)^2 = \frac{\left(1-\varepsilon^2\right)^2}{\pi\varepsilon\sqrt{\pi^2(1-\varepsilon^2)+16\varepsilon^2}}. \tag{3.47}$$

The attitude angle, which is measured from the load line to the line of centers in the direction of journal rotation, is given by

$$\phi = \arctan\left|\frac{f_T}{f_R}\right|$$
$$= \arctan\left(\frac{\pi}{4}\frac{\sqrt{1-\varepsilon^2}}{\varepsilon}\right). \tag{3.48}$$

The journal locus as given by Eq. (3.48) is almost semicircular in shape and is often referred to as the *equilibrium semicircle*[6] (Figure 3.7).

In short-bearing theory the circumferential pressure gradient is neglected. Implicit in this is the assumption that the distribution of the circumferential velocity across the film is linear, so that the shear stress is $\tau_{xy} = \mu U_2/h$.

The friction force is given by

$$F_\mu = L\int_0^{2\pi R} \tau_{xy}\, dx$$
$$= \frac{2\pi^2\mu LDN}{\sqrt{1-\varepsilon^2}}\frac{R}{C}$$

[5] In general, characterization of isothermal bearings requires two independent parameters, the most practical choice being the Sommerfeld number, S, and the ratio, α/β. The latter specifies the position of the load line relative to the leading edge of the bearing arc (Figure 3.9). With the present boundary conditions, $\beta = \pi$ and $\alpha = \pi - \phi$ so that $\alpha/\beta = 1 - \phi/\pi$, and thus α/β is no longer independent of S. This leaves the Sommerfeld number as the sole parameter.

[6] For a semicircle of radius 0.5 centered at ($\varepsilon = 0.5$, $\phi = 0$), we have $\tan\phi = \sqrt{1-\varepsilon^2}/\varepsilon$.

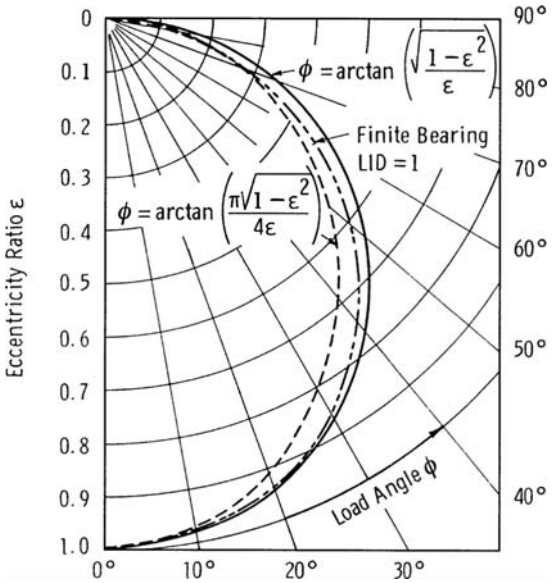

Figure 3.7. Journal loci: (---) short-bearing theory, Eq. (3.48); (–––) finite bearing; (––) semicircle.

and the dimensionless friction variable by

$$c_\mu \equiv \frac{R}{C}\frac{F_\mu}{W} = \frac{2\pi^2 S}{\sqrt{1-\varepsilon^2}}. \tag{3.49}$$

The total side flow (both sides included) is calculated from the formula

$$Q_s = 2\int_0^{\pi R}\int_0^{h(x)} w\,dy\,dx \tag{3.50}$$

or in dimensionless form, after performing the indicated integration across the film with respect to y, by

$$q_s \equiv \frac{Q_s}{NRLC} = -\frac{1}{12}\left(\frac{D}{L}\right)^2 \int_0^{\pi} H^3 \frac{\partial \bar{p}}{\partial \bar{z}}\bigg|_{\bar{z}=\pm 1} d\theta. \tag{3.51}$$

Substituting for $\partial\bar{p}/\partial\bar{z}$, we have

$$q_s = 2\pi\varepsilon. \tag{3.52}$$

The predictions of short-bearing theory and accurate two-dimensional numerical solutions at $L/D = 1/4$ are compared in Table 3.1.

Although the length/diameter ratio of numerous industrial bearings might be small enough for their performance to be calculated on the basis of short-bearing theory, the latter theory cannot be used unless the bearing is of 180° (noncavitating film) or 360° (cavitating

Table 3.1. *Performance prediction for a full journal bearing (L/D = 1/4)*

Parameter	Short-bearing approximation, $\theta_2 = \pi$/exact solution[a]		
ε	0.1	0.6	0.9
S	15.84/16.20	1.00/1.07	0.053/0.074
ϕ	82.71/82.31	46.32/46.72	20.83/21.85
c_μ	314.2/322.1	24.67/26.73	2.40/3.50
q_s	0.628/0.621	3.77/3.72	5.65/5.59

[a]Computer solution of finite bearing obtained with the Swift-Stieber boundary condition $\bar{p} = \partial\bar{p}/\partial\theta = 0$ at $\theta = \theta_2$.

film) arc. To remove this constraint of the short-bearing theory, and also to increase the range of applicable L/D ratios, O'Donoghue, et al. (1970) proposed solution for pressure, see Eq. (3.39), in the form

$$\bar{p}\,(\theta, \bar{z}) = \bar{p}_c(\theta)(1 - \bar{z}^2). \tag{3.53}$$

Here $\bar{p}_c(\theta)$ is the center line pressure. Substitution of Eq. (3.53) into Eq. (3.35) yields the differential equation

$$\frac{d}{d\theta}\left(H^3\frac{d\bar{p}_c}{d\theta}\right) - 2\left(\frac{D^2}{L}\right)H^3\bar{p}_c = 12\pi\frac{\partial H}{\partial\theta}. \tag{3.54}$$

Performance calculations based on Eq. (3.54) are displayed in Table 3.2. The boundary condition used here is the Swift-Stieber condition, $p = \partial p/\partial\theta = 0$ at $\theta = \theta_2$.

Boundary Conditions

When in pure form, liquids can withstand tensile stresses that are certainly of the order of tens or even hundreds of atmospheres (Temperly, 1975). If contaminated they will

Table 3.2. *Performance prediction for a full journal bearing (L/D = 1/2)*

	Short-bearing[a] Eq. (3.37)	Modified short bearing[b] Eq. (3.54)	Finite bearing[b] Eq. (3.35)
$\varepsilon = 0.1$			
S	3.96	4.496	4.310
c_μ	78.56	88.703	85.6
$\varepsilon = 0.6$			
S	0.250	0.331	0.319
c_μ	6.169	8.399	8.10
$\varepsilon = 0.9$			
S	0.0133	0.0359	0.0313
c_μ	0.602	1.790	1.60

[a]Trailing edge boundary at $\theta = \pi$.
[b]Trailing edge boundary at $\bar{p} = \partial\bar{p}/\partial\theta = 0$.

cavitate, however, when the pressure drops below the saturation pressure of the dissolved gases (gaseous cavitation). Vapor cavitation (boiling) of the liquid occurs when the pressure falls to the vapor pressure.

Under normal operating conditions a lubricant film of converging-diverging geometry is expected to cavitate within the diverging part of the clearance, where, on the assumption of a continuous lubricant film, theory predicts negative pressures. This much is clear. Still, the subjects of considerable discussion, however, are (1) the exact position of the film-cavity interface and (2) the boundary conditions that apply at that interface.

A typical pressure curve for the lubricant film of a journal bearing shows the pressure increasing from its value at inlet, which is located at say, $\theta = 0$, with the angular coordinate θ, until it reaches a maximum somewhere still within the convergent part of the clearance space. Thereafter, the pressure decreases sharply to a small negative value (the subcavity pressure) just to rise again to the level of the cavity pressure p_{cav}. Dyer and Reason (1976) showed that if the journal eccentricity is smaller than some critical value, $\varepsilon_{\text{crit}}$, where $\varepsilon_{\text{crit}}$ is inversely proportional to the bearing clearance, then a tensile stress greater than the oil vapor pressure may be developed in the film. They actually measured a tensile stress of 740 kPa in the oil film of a steadily loaded journal bearing. The cavity pressure is essentially constant and equals the saturation pressure of the lubricant. The saturation pressure, on the other hand, is equal to or is just below the ambient atmospheric pressure, as the lubricant is exposed to the ambient atmosphere for long periods of time under normal operating conditions.

The solid curve in Figure 3.6 represents the lubricant pressure as obtained under the so-called *Sommerfeld boundary condition,* which assumes the clearance space to be full of lubricant and allows for subambient pressures. This condition yields results that are physically unreasonable (e.g., shaft displacement is always at right angles to the applied load), except in special circumstances. For instance, by locating an oil groove at the position of minimum film pressure, Floberg (1961) demonstrated that a continuous, full Sommerfeld pressure curve can be maintained experimentally. The journal locus is represented by a straight line under such conditions, with a load angle of $\phi = \pi/2$. Raimondi and Boyd (1958) refer to the Sommerfeld condition as a *type I boundary condition* and find it useful for calculating bearings that operate under high ambient pressures.

The half-Sommerfeld or *Gümbel boundary condition*, although obtaining the pressure on the assumption of a continuous lubricant film, neglects the subambient pressure loop completely when calculating bearing performance. The short-bearing performance in Eqs. (3.45)–(3.52) was obtained under this condition. Although the Gümbel condition yields a pressure curve that is at variance with experimental data, it does give closed-form solution for bearing performance and is, therefore, still employed in theoretical work. A pressure profile obtained with the Gümbel condition is shown by the dashed curve in Figure 3.6.

H. W. Swift, on the basis of a stability argument, and W. Stieber, from considerations of flow continuity at the film-cavity interface, arrived at identical conditions, namely that

$$\frac{\partial p}{\partial \theta} = 0 \qquad p = p_{\text{cav}} \tag{3.55}$$

at the cavitation boundary. The cavity pressure differs little from, and is usually taken to be equal to, atmospheric pressure. The *Swift-Stieber boundary condition*, as it is referred to in the literature, has been shown by Cameron and Wood to lead to both minimum potential energy and maximum load capacity of the bearing, and by Christopherson to

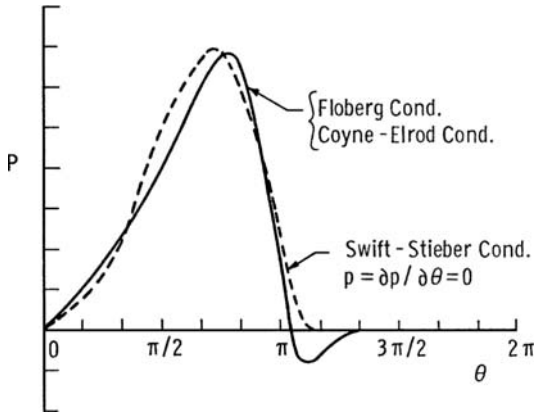

Figure 3.8. Circumferential pressure distribution according to various trailing edge boundary conditions.

yield minimum bearing friction (Cameron, 1966). The Swift-Stieber condition is unable to predict the subcavity pressures that occur just upstream from the cavitation boundary. It is nevertheless the most widely used boundary condition in numerical work. It leads to fairly good agreement with experimental data, particularly at large eccentricities, and is easy to incorporate into most numerical schemes. A typical pressure distribution obtained with the Swift-Stieber condition is shown by the dashed curve in Figure 3.8.

For a long bearing, the pressure gradient $d\bar{p}/d\theta$ can be obtained from Eq. (3.36) by integration

$$\frac{d\bar{p}}{d\theta} = \frac{12\pi}{H^2} + \frac{A'}{H^3}. \tag{3.56}$$

Here A' is an integration constant. When this expression for $d\bar{p}/d\theta$ together with $U_1 = 0$ is substituted into Eq. (2.59a), we obtain

$$\begin{aligned} \bar{u} &= \frac{u}{R\omega} \\ &= \left(3 + \frac{A''}{H}\right)\left(\bar{y}^2 - \bar{y}\right) + \bar{y}, \end{aligned} \tag{3.57}$$

where $\bar{u}$ is the dimensionless circumferential velocity and $\bar{y} = y/h$ is the dimensionless coordinate across the film.

The constant A'' in Eq. (3.57) can be evaluated from continuity considerations, which demand that at the cavity-film interface where $H = H_{\text{cav}}$ we have

$$\int_0^l \bar{u} d\bar{y} = \frac{H_\infty}{H_{\text{cav}}} \equiv \hat{\alpha}. \tag{3.58}$$

Equation (3.58) assumes that the cavity-fluid interface is a straight line beneath which all the fluid flows to form a uniform layer of thickness $h_\infty = CH_\infty$. Back substitution into Eq. (3.56) yields

$$\frac{d\bar{p}}{d\theta} = \frac{12\pi}{H^2}(1 - 2\hat{\alpha}), \tag{3.59}$$

The pressure gradient at film separation would thus be completely specified by Eq. (3.59) had the film separated from the stationary surface at right angles. For this case, Coyne and

Elrod (1970a, 1970b) determined the value of $\hat{\alpha}$ in terms of the group $\mu U/\sigma$, the surface tension parameter of Taylor (1964). Here σ is the surface tension of the lubricant.

The second boundary condition of Coyne and Elrod at the film-cavity interface is

$$p = -\frac{\sigma}{r} + \Delta p, \tag{3.60}$$

where r is the radius of curvature of the interface. The precise value of the transition pressure correction Δp, which is dependent on $\mu U/\sigma$, is of minor importance, particularly at small values of the surface tension parameter. Pressure profiles based on the Coyne-Elrod conditions show a subcavity pressure loop as indicated in Figure 3.8.

Smith (1975) sought to apply the Coyne-Elrod condition to bearings of finite width and found good agreement for all values of the parameter $\mu U/\sigma$ at high eccentricities. At moderate eccentricities the condition led to a contradiction, which precluded its applicability.

In contradiction to Coyne and Elrod, Floberg (1964) observed that in the cavitated region oil flow takes place in narrow strips, the quantity of lubricant adhering to the runner and passing under the cavities being negligible. Because of the low viscosity of the air or gases that occupy the cavities between the strips and because of the geometry of the strips, the pressure is essentially constant within the cavitated region and is equal to the saturation pressure of the dissolved gases. Under normal loading, subcavity pressures are negligible, and the lowest lubricant film pressure is equal to the cavitation pressure. At the end of the pressure buildup the oil flow leaving the continuous-film domain is

$$Q_{\text{cav}}^{-} = \frac{Uh}{2} - \frac{h^3}{12\mu}\frac{\partial p}{\partial x}, \tag{3.61}$$

while the flow entering the cavitation region is

$$Q_{\text{cav}}^{+} = \tilde{\omega}\frac{Uh}{2}. \tag{3.62}$$

The symbol $\tilde{\omega}$ stands for the fractional width of the oil in the cavitation region.

From the equality $Q_{\text{cav}}^{-} = Q_{\text{cav}}^{+}$, we obtain

$$(1 - \tilde{\omega})\frac{Uh}{2} - \frac{h^3}{12\mu}\frac{\partial p}{\partial x} = 0. \tag{3.63}$$

By assumption $p \geq p_{\text{cav}}$ and $0 < \tilde{\omega} < 1$, thus Eq. (3.63) is satisfied only if

$$\frac{\partial p}{\partial x} = 0, \tag{3.64a}$$

$$\tilde{\omega} = 1. \tag{3.64b}$$

The second of these conditions means that oil will fill the whole width at the film-cavity interface.

If the average pressure in the film is low, then the subcavity pressure will have an influence on the position of the film-cavity interface and, according to Floberg (1965), should be taken into account. There is now a finite number of lubricant strips in the cavitated region. The assumption that no oil enters or leaves the gas-filled regions between the strips leads to the condition

$$\frac{\partial \bar{p}}{\partial \theta} - \frac{\partial \bar{p}}{\partial \bar{z}}\frac{\partial \theta}{\partial z} = \frac{12\pi}{H^2}. \tag{3.65}$$

Condition (3.65) is applicable at both upstream and downstream film-cavity interfaces.

Both the Coyne-Elrod, Eqs. (3.59) and (3.60), and the Floberg, Eq. (3.65), conditions yield subcavity pressures upstream of the lubricant strip, in agreement with experiments. They are, however, difficult to implement in numerical schemes.

Savage (1977) considered the leading edge of the cavity and wrote an interface force balance in the form

$$p(c) + \frac{\sigma}{r} = 0, \tag{3.66}$$

where $p(c)$ is the fluid pressure at the cavitation boundary, σ is the surface tension of the lubricant, and r is the radius of curvature of the cavity-fluid interface. The interface $x = c$ is constantly subject to small disturbances. Let ξ be such a small disturbance, caused by fluctuation of fluid pressure, so that a point on the cavitation boundary originally at (c, y) is displaced to a new position $(c + \xi, y)$.

In its new, perturbed, position the force on the interface is given by the residue of Eq. (3.66) when the latter is written for that new position. Since $|\xi| < c$ we are permitted to write

$$\begin{aligned} F(c+\xi) &= p(c+\xi) + \frac{\sigma}{r(c+\xi)} \\ &= F(c) + F'(c)\xi + O(\xi^2) \\ &= \frac{d}{dx}\left(p + \frac{\sigma}{r}\right)\xi + O(\xi^2). \end{aligned} \tag{3.67}$$

The interface will return to its original position $x = c$ under the action of $F(c + \varepsilon)$, provided that F and ξ have opposite algebraic signs. Thus the criterion for the existence of a straight cavity-fluid interface is

$$\frac{d}{dx}\left(p + \frac{\sigma}{r}\right) < 0. \tag{3.68}$$

In writing Eq. (3.68) we neglected terms of order ξ^2.

Both the Sommerfeld condition and the Gümbel condition are easy to apply in analytical work but give results that are at variance with experimental data. The Swift-Stieber condition, although unable to reproduce the subcavity pressure loop, leads to acceptable results for bearing performance and is easy to implement in most numerical methods. The separation and Floberg conditions are difficult to implement in any numerical scheme and will not be considered further. The interested reader is referred to *Cavitation and Related Phenomena in Lubrication*, edited by Dowson et al. (1975). See also Dowson and Taylor (1979).

Long-Bearing Theory[7]

The pressure differential equation under the condition of vanishing axial flow, valid for long bearings, is given by Eq. (3.36)

$$\frac{d}{d\theta}\left(H^3\frac{d\bar{p}}{d\theta}\right) = 12\pi\frac{dH}{d\theta}. \tag{3.36}$$

Integration twice with respect to θ yields

$$\bar{p}(\theta) = 12\pi\int_0^\theta \frac{H(\theta') - A}{H^3(\theta')}d\theta' + B. \tag{3.69}$$

[7] Caution is advised when employing the long-bearing theory; if the condition $(L/D) > 2$ is not satisfied, the results of the theory will be misleading.

The pressure distribution in Eq. (3.69) will be subjected to some of the simpler boundary conditions discussed previously.

Sommerfeld Condition

To determine the integration constants A and B in Eq. (3.69), we specify the Sommerfeld boundary conditions for the full (360°arc) bearing

$$\begin{aligned} \bar{p}\,(0) &= \bar{p}_i \\ \bar{p}\,(2\pi) &= \bar{p}\,(0)\,. \end{aligned} \tag{3.70}$$

Substituting $\bar{p}(\theta)$ from Eq. (3.69) into Eq. (3.70) we have

$$A = \frac{\int_0^{2\pi} (d\theta/H^2(\theta))}{\int_0^{2\pi} (d\theta/H^3(\theta))}, \quad B = \bar{p}_i\,.$$

Using the Sommerfeld substitution, Eq. (3.42), we find that

$$\int \frac{d\theta}{H^3(\theta)} = \frac{1}{(1-\varepsilon^2)^{5/2}} \left(\psi - 2\varepsilon \sin\psi + \frac{\varepsilon^2 \psi}{2} + \frac{\varepsilon^2}{4} \sin 2\psi \right) \tag{3.71}$$

and

$$\int \frac{d\theta}{H^2(\theta)} = \frac{1}{(1-\varepsilon^2)^{3/2}} (\psi - \varepsilon \sin\psi)\,. \tag{3.72}$$

Since the limits $\theta = 0, 2\pi$ correspond to the limits $\psi = 0, 2\pi$, we have for the Sommerfeld boundary condition

$$A = \frac{2(1-\varepsilon^2)}{2+\varepsilon^2}, \tag{3.73}$$

and the dimensionless pressure distribution is given by

$$\bar{p}\,(\theta) = \frac{12\pi\varepsilon \sin\psi}{(2+\varepsilon^2)(1-\varepsilon^2)^{3/2}} (2 - \varepsilon^2 - \varepsilon\cos\psi) + \bar{p}_i\,. \tag{3.74}$$

From Eq. (3.42) we have

$$\cos\psi = \frac{\varepsilon + \cos\theta}{1 + \varepsilon\cos\theta}, \tag{3.75a}$$

$$\sin\psi = \frac{\sqrt{1-\varepsilon^2}\sin\theta}{1+\varepsilon\cos\theta}. \tag{3.75b}$$

Substituting Eq. (3.75) into Eq. (3.74), we obtain the pressure distribution in terms of the original variable θ:

$$\bar{p}\,(\theta) = \frac{12\pi\varepsilon \sin\theta(2+\varepsilon\cos\theta)}{\left(2+\varepsilon^2\right)(1+\varepsilon\cos\theta)^2} + \bar{p}_i\,. \tag{3.76}$$

The function $\bar{p}(\theta)$ as given by Eq. (3.76) is 2π periodic in θ and is antisymmetric with respect to $\theta = \pi$. Thus the theory predicts negative values of the gauge pressure $\bar{p}(\theta) - \bar{p}_i$ of the same magnitude as its positive values.

The components of the oil film force are obtained when the pressure of Eq. (3.76) is substituted into Eq. (3.41). In dimensionless form we have

$$f_R = \frac{1}{2}\int_0^{\theta_2} \bar{p}\cos\theta\, d\theta, \tag{3.77a}$$

$$f_T = \frac{1}{2}\int_0^{\theta_2} \bar{p}\sin\theta\, d\theta. \tag{3.77b}$$

To evaluate Eq. (3.77) we need the following integrals:

$$\begin{aligned}\int_0^{\theta_2} \bar{p}\cos\theta\, d\theta &= (\bar{p}\sin\theta)_0^{\theta_2} - \int_0^{\theta_2} \sin\theta \frac{d\bar{p}}{d\theta} d\theta \\ &= -\int_0^{\theta_2} \sin\theta \frac{d\bar{p}}{d\theta} d\theta \\ &= -12\pi \int_0^{\theta_2} \sin\theta \left[\frac{H(\theta) - A}{H^3(\theta)}\right] d\theta \\ &= \frac{12\pi}{1-\varepsilon^2}\left[\cos\psi + \frac{A}{1-\varepsilon^2}\left(\frac{\varepsilon}{4}\cos 2\psi - \cos\psi\right)\right]_0^{\psi_2},\end{aligned} \tag{3.78}$$

$$\begin{aligned}\int_0^{\theta_2} \bar{p}\sin\theta\, d\theta &= (-\bar{p}\cos\theta)_0^{\theta_2} - \int_0^{\theta_2} \cos\theta \frac{d\bar{p}}{d\theta} d\theta \\ &= 12\pi \int_0^{\theta_2} \cos\theta \left[\frac{H(\theta) - A}{H^3(\theta)}\right] d\theta \\ &= \frac{12\pi}{(1-\varepsilon^2)^{3/2}}\left\{\sin\psi - \varepsilon\psi - \frac{A}{1-\varepsilon^2}\left[(1+\varepsilon^2)\sin\psi \right.\right. \\ &\quad \left.\left. -\varepsilon\left(\frac{3\psi}{2} + \frac{\sin 2\psi}{4}\right)\right]\right\}_0^{\psi_2}.\end{aligned} \tag{3.79}$$

For the Sommerfeld condition we have

$$\theta_2 = \psi_2 = 2\pi \qquad A = \frac{2(1-\varepsilon^2)}{2+\varepsilon^2}$$

and find that

$$f_R = 0, \tag{3.80a}$$

$$f_T = \frac{12\pi^2\varepsilon}{(2+\varepsilon^2)(1-\varepsilon^2)^{1/2}} = \frac{1}{S}. \tag{3.80b}$$

These equations show that under Sommerfeld condition the displacement of the journal is always at right angles to the applied load; that is, $\phi = \pi/2$. This most unsatisfactory result demonstrates the incorrectness of the Sommerfeld condition when applied to cavitating films.

Gümbel Condition

The Gümbel condition is $\theta_2 = \psi_2 = \pi$ and Eqs. (3.77)–(3.79) give

$$f_R = -\frac{12\pi\varepsilon^2}{(2+\varepsilon^2)(1-\varepsilon^2)}, \tag{3.81a}$$

$$f_T = \frac{6\pi^2\varepsilon}{(2+\varepsilon^2)(1-\varepsilon^2)^{1/2}}. \tag{3.81b}$$

The journal locus is calculated from

$$\tan\phi = \left|\frac{f_T}{f_R}\right|. \tag{3.82a}$$

When substituting for the force components from Eq. (3.81), we obtain

$$\phi = \arctan\frac{\pi}{2}\frac{\sqrt{1-\varepsilon^2}}{\varepsilon}. \tag{3.82b}$$

The bearing Sommerfeld number is calculated from Eq. (3.81) and has the value

$$S = \frac{(2+\varepsilon^2)(1-\varepsilon^2)}{6\pi\varepsilon\sqrt{4\varepsilon^2+\pi^2(1-\varepsilon^2)}}. \tag{3.83}$$

Swift-Stieber Conditions

For the long bearing, these conditions are represented by

$$\bar{p}\,(\theta_{\text{cav}}) = 0, \tag{3.84a}$$

$$\left.\frac{d\,\bar{p}}{d\theta}\right|_{\theta_{\text{cav}}} = 0, \tag{3.84b}$$

where θ_{cav} is the unknown angular position of the cavitation boundary. In general $\theta_{\text{cav}} = \theta_{\text{cav}}(\bar{z})$ when θ_{cav} is calculated from Eq. (3.84), but for the long bearing $\theta_{\text{cav}} = \text{const}$. Substituting $\bar{p}(\theta)$ from Eq. (3.69) into Eq. (3.84b), we obtain

$$A = H\,(\theta_{\text{cav}})\,. \tag{3.85}$$

Back substitution into Eq. (3.69) yields the pressure distribution

$$\bar{p}\,(\theta) = 12\pi\int_0^{\theta}\frac{H\,(\theta) - H\,(\theta_{\text{cav}})}{H^3\,(\theta)}d\theta. \tag{3.86}$$

The value of θ_{cav} is as yet unknown but can be determined from the remaining boundary condition, Eq. (3.84a); thus substitution of $\bar{p}(\theta)$ yields the condition

$$\int_0^{\theta_{\text{cav}}}\frac{H\,(\theta) - H\,(\theta_{\text{cav}})}{H^3\,(\theta)}\,d\theta = 0. \tag{3.87}$$

When written in terms of the Sommerfeld angle ψ of Eq. (3.42a), Eq. (3.87) is equivalent to

$$\varepsilon\,(\sin\psi_{\text{cav}}\cos\psi_{\text{cav}} - \psi_{\text{cav}}) + 2\,(\sin\psi_{\text{cav}} - \psi_{\text{cav}}\cos\psi_{\text{cav}}) = 0. \tag{3.88}$$

Table 3.3. *Position of cavitation boundary in long bearings, as calculated from the Swift-Stieber condition*

ε	ψ_{cav} (rad)	θ_{cav} (rad)
0.1	4.44510	4.34974
0.2	4.39769	4.21195
0.3	4.35099	4.08021
0.4	4.30484	3.95451
0.5	4.25905	3.83438
0.6	4.21346	3.71892
0.7	4.16785	3.60645
0.8	4.12203	3.49369
0.9	4.07574	3.37195

Here ψ_{cav} corresponds to θ_{cav}, and we made use of

$$H(\theta_{\text{cav}}) = \frac{1-\varepsilon^2}{1-\varepsilon\cos\psi_{\text{cav}}}. \tag{3.89}$$

The values of ψ_{cav} and θ_{cav} are displayed in Table 3.3 (Szeri and Powers, 1967). The entries of Table 3.3 represent accurate solutions of Eq. (3.88).

The dimensionless force components are obtained from Eqs. (3.77), (3.86), and (3.89):

$$f_R = \frac{3\pi\varepsilon(1-\cos\psi_{\text{cav}})^2}{(1-\varepsilon^2)(1-\varepsilon\cos\psi_{\text{cav}})}, \tag{3.90a}$$

$$f_T = -\frac{6\pi(\psi_{\text{cav}}\cos\psi_{\text{cav}} - \sin\psi_{\text{cav}})}{(1-\varepsilon^2)^{1/2}(1-\varepsilon\cos\psi_{\text{cav}})}. \tag{3.90b}$$

When deriving Eq. (3.90), we made use of Eq. (3.87).

The bearing Sommerfeld number is obtained by substituting for f_R and f_T in Eq. (3.46):

$$\frac{1}{S} = \frac{3\pi}{(1-\varepsilon^2)^{1/2}(1-\varepsilon\cos\psi_{\text{cav}})}\left[\frac{\varepsilon^2(1-\cos\psi_{\text{cav}})^4}{1-\varepsilon^2} + 4(\psi_{\text{cav}}\cos\psi_{\text{cav}} - \sin\psi_{\text{cav}})^2\right]^{1/2}. \tag{3.91}$$

The journal-center locus is given by

$$\tan\phi = \frac{2(\sin\psi_{\text{cav}} - \psi_{\text{cav}}\cos\psi_{\text{cav}})}{(1-\cos\psi_{\text{cav}})^2}\frac{\sqrt{1-\varepsilon^2}}{\varepsilon}. \tag{3.92}$$

To calculate the frictional losses we observe that at $U_1 = 0$, $U_2 = U = R\omega$, Eq. (2.59a) gives

$$\begin{aligned}\tau &= \mu\frac{\partial u}{\partial y}\\ &= \frac{1}{2}\frac{\partial p}{\partial x}(2y-h) + \frac{\mu}{h}U.\end{aligned} \tag{3.93}$$

Table 3.4. *Long-bearing solutions*

	Gümble condition		Swift-Stieber condition	
ε	S, Eq. (3.83)	ϕ, Eq. (3.82)	S, Eq. (3.91)	ϕ, Eq. (3.92)
0.1	0.33704	86.339	0.24144	69.032
0.2	0.16736	82.596	0.12373	66.900
0.3	0.11004	78.679	0.08376	64.464
0.4	0.08053	74.472	0.06289	61.638
0.5	0.06177	69.819	0.04931	58.296
0.6	0.04795	64.477	0.03895	54.234
0.7	0.03639	58.035	0.02993	49.098
0.8	0.02549	49.675	0.02110	42.181
0.9	0.01392	37.263	0.01151	31.666

The shear stress on the journal is

$$\tau_0 = \frac{h}{2}\frac{\partial p}{\partial x} + R\omega\frac{\mu}{h}. \tag{3.94}$$

The total shear force on the journal is obtained by integrating τ_0 over the journal surface

$$\begin{aligned} F_\mu &= \int_{-L/2}^{L/2}\int_0^{\pi D}\left(\frac{h}{2}\frac{\partial p}{\partial x} + \frac{R\omega\mu}{h}\right)dx\,dz \\ &= \pi\mu DLN\frac{R}{C}\int_{-1}^{1}\int_0^{2x}\left(\frac{H}{4\pi}\frac{\partial\,\bar{p}}{\partial\theta} + \frac{1}{H}\right)d\theta\,d\bar{z}. \end{aligned} \tag{3.95}$$

Integrating the first term by parts, we find that

$$F_\mu = \pi\mu DLN\frac{R}{C}\left(\frac{\varepsilon f_T}{2\pi} + \frac{2\pi}{\sqrt{1-\varepsilon^2}}\right). \tag{3.96}$$

The friction variable, c_μ, is obtained from Eq. (3.96) and the definition of the attitude angle ϕ:

$$\begin{aligned} C_\mu &\equiv \frac{R}{C}\frac{F_\mu}{W} \\ &= \frac{\varepsilon\sin\phi}{2} + \frac{2\pi^2 S}{\sqrt{1-\varepsilon^2}}. \end{aligned} \tag{3.97}$$

Of course, it would have been better to employ Eq. (3.94) only in the range $0 \le \theta \le \theta_{\text{cav}}$ and estimate the drag in the cavitated region from flow continuity considerations.

Table 3.4 contains long-bearing Sommerfeld numbers calculated by the Gümbel condition from Eq. (3.83) and by the Swift-Stieber condition from Eq. (3.91). The entries in Table 3.4 do not fully agree with the results usually quoted in the literature (Raimondi and Boyd, 1958; Cameron, 1966; Pinkus and Sternlicht, 1961), possibly because previous calculations relied on inaccurate values of θ_{cav}.

Finite Journal Bearings

The length/diameter ratio of industrial bearings is customarily in the range $0.25 < L/D < 1.5$; neither the short-bearing nor the long-bearing approximations apply to these bearings. Furthermore, the angular extent of large industrial bearings is rarely 360°; common ranges are $30^\circ < \beta < 60^\circ$ in pivoted-pad bearings and $120^\circ < \beta < 160^\circ$ in the "viscosity pump" bearings of large rotating machinery. If the pad is centrally loaded (Figure 3.9), the ratio $\alpha/\beta = 1/2$, where the angle α is measured from the pad leading edge to the load line. For offset loading, $\alpha/\beta \neq 1/2$.

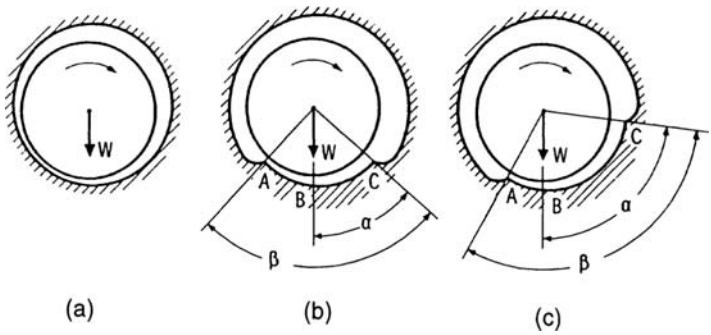

Figure 3.9. Fixed type journal bearings. (a) Full bearing, $\beta = 360^\circ$; (b) partial bearing, centrally loaded, $\alpha = \beta/2$; and (c) partial bearing, eccentrically loaded (offset), $\alpha \neq \beta/2$. (Reprinted with permission from Raimondi, A. A. and Szeri, A. Z. Journal and thrust bearings. In Booser E. R., *CRC Handbook of Lubrication.* Copyright CRC Press, Boca Raton, Florida, © 1984.)

Over a finite bearing pad of diameter D, axial length L, and arc β, the lubricant pressure satisfies the equation

$$\frac{\partial}{\partial\theta}\left(H^3\frac{\partial\bar{p}}{\partial\theta}\right) + \left(\frac{D}{L}\right)^2\frac{\partial}{\partial\bar{z}}\left(H^3\frac{\partial\bar{p}}{\partial\bar{z}}\right) = 12\pi\frac{\partial H}{\partial\theta}. \tag{3.35}$$

Solutions of Eq. (3.35) are usually sought subject to the Swift-Stieber boundary conditions

$$\bar{p} = 0 \quad \text{at} \quad \bar{z} = \pm 1, \tag{3.98a}$$

$$\bar{p} = 0 \quad \text{at} \quad \theta = \theta_1, \theta_1 + \beta, \tag{3.98b}$$

$$\bar{p} = \frac{\partial\bar{p}}{\partial\theta} \quad \text{at} \quad \theta = \theta_{\text{cav}}(\bar{z}). \tag{3.98c}$$

As the dimensionless film thickness is given by

$$\begin{aligned} H &= 1 + \varepsilon\cos\theta \\ &= 1 + \varepsilon\cos\left(\theta_1 + \frac{x}{R}\right), \end{aligned} \tag{3.99}$$

where θ_1 is the angular coordinate of the pad leading edge $x = 0$, the pressure differential equation and its boundary conditions contain four dimensionless parameters in all:

$$\{L/D, \beta, \varepsilon, \theta_1\}. \tag{3.100}$$

Two of these parameters, L/D and β, describe bearing geometry and remain fixed for a particular bearing. The other two parameters, ε and θ_1, specify the position of the rotating shaft within the bearing and are therefore dependent on loading conditions and lubricant viscosity.

Loading conditions and lubricant viscosity of an isothermal bearing can be characterized with the aid of two parameters, the Sommerfeld number S, which is the inverse of the dimensionless lubricant force Eq. (3.46), and the ratio α/β, where α is the angular position of the pad trailing edge relative to the load line (Figure 3.9). Specifying the couple (ε, θ_1) in Eqs. (3.35) and (3.98) and solving these yields a pair of values $(S, \alpha/\beta)$ from the formulas

$$S = \left(f_R^2 + f_T^2\right)^{-1/2}, \tag{3.46}$$

$$\frac{\alpha}{\beta} = \frac{1}{\beta}\left[\pi - (\theta_1 + \phi)\right]. \tag{3.101}$$

The dimensionless force components f_R and f_T are given by

$$f_R = \frac{1}{2}\int_0^1 \int_{\theta_1}^{\theta_1+\beta} \bar{p}\cos\theta \, d\theta \, d\bar{z}, \tag{3.102a}$$

$$f_T = \frac{1}{2}\int_0^1 \int_{\theta_1}^{\theta_1+\beta} \bar{p}\sin\theta \, d\theta \, d\bar{z}, \tag{3.102b}$$

and

$$\phi = \arctan\left|\frac{f_T}{f_R}\right|. \tag{3.102c}$$

Thus, corresponding to each ordered pair (ε, θ_1) there exists another ordered pair $(S, \alpha/\beta)$; the mapping of the (ε, θ_1) plane into the $(S, \alpha/\beta)$ plane is defined by the pressure differential equation (3.35) and its boundary conditions (3.98), Eq. (3.46), and Eq. (3.101). This mapping is one-to-one and invertible. In a physical experiment, one specifies the load vector, the speed of rotation, and the lubricant viscosity – that is, the couple $(S, \alpha/\beta)$ – and permits the journal to select its own equilibrium position (ε, θ_1).

We thus have two equivalent parametric representations of journal bearing operations. The parameters in Eq. (3.100) are the natural set of parameters to use in numerical work, while the set

$$\{L/D, \beta, S, \alpha/\beta\} \tag{3.103}$$

is the obvious one to employ in a physical experiment.

The designer employs this latter set of parameters (3.103), and the task of the numerical analyst is to find the (ε, θ_1) couple that corresponds to the designer's $(S, \alpha/\beta)$ couple. This necessarily leads to solution of a nonlinear problem, which can be written in the symbolic form

$$S - \Omega_1(\varepsilon, \theta_1) = 0, \tag{3.104a}$$

$$\frac{\alpha}{\beta} - \Omega_2(\varepsilon, \theta_1) = 0. \tag{3.104b}$$

Here the functions Ω_1 and Ω_2 represent integrals of the pressure differential equation and the integrals involved in Eqs. (3.46) and (3.101).

The set of nonlinear equations (3.104) is conveniently solved by Newton's method. The nth iterated solution can be obtained from

$$\begin{bmatrix} \dfrac{\partial \Omega_1}{\partial \varepsilon} & \dfrac{\partial \Omega_1}{\partial \theta_1} \\ \dfrac{\partial \Omega_2}{\partial \varepsilon} & \dfrac{\partial \Omega_2}{\partial \theta_1} \end{bmatrix} \begin{bmatrix} \varepsilon^{(n)} - \varepsilon^{(n-1)} \\ \theta_1^{(n)} - \theta_1^{(n-1)} \end{bmatrix} = \begin{bmatrix} \Omega_1 - S \\ \Omega_2 - \dfrac{\alpha}{\beta} \end{bmatrix}, \quad n = 1, 2, 3, \ldots . \tag{3.105}$$

An extensive set of solutions of centrally loaded, isothermal bearings was published by Raimondi and Boyd (1958). Solutions for eccentrically loaded partial arc bearings were compiled by Pinkus and Sternlicht (1961).

The performance curves in Figures 3.10, taken from Raimondi and Szeri (1984), are for a centrally loaded fixed-pad partial bearing of $L/D = 1$, $\beta = 160^\circ$ and various values of the Reynolds number. (Some of the curves in the figures are for turbulent flow conditions. Lubrication in the turbulent regime is discussed in Chapter 7, where we will again make reference to Figure 3.10.)

Figure 3.11 illustrates the effect of shifting the load position (i.e., varying the value of α/β, where α is measured from the pad leading edge to the load vector, and β is the pad angle) on the position of the journal center.

It can be seen from Figure 3.11 that if $\alpha/\beta > 0.665$ for $L/D = 1$ and $\beta = 120^\circ$ the journal can be expected to rub the cap of the bearing.

Pivoted-pad bearings, in which the pad is free to rotate so that it may choose its own orientation relative to the load line, are often used in practice. For these, the value of α is dictated by the pivot position, as the resultant torque on the pad must vanish. Pivoted pad journal bearings are discussed in Chapter 4, within the context of lubricant film dynamic properties.

Cavitation Algorithm

In this section we discuss an algorithm, due originally to Elrod and Adams (Elrod and Adams, 1974; Elrod, 1981) and modified subsequently by Vijayaraghavan and Keith (1989), that is designed to automatically handle cavitation in liquid-lubricated bearings.

We begin the analysis with the time dependent form of the Reynolds equation valid for compressible flow, Eq. (11.6)

$$\frac{\partial (\rho h)}{\partial t} + \frac{\partial}{\partial x}\left(\frac{\rho h U}{2} - \frac{\rho h^3}{12\mu}\frac{\partial p}{\partial x}\right) - \frac{\partial}{\partial z}\left(\frac{\rho h^3}{12\mu}\frac{\partial p}{\partial z}\right) = 0. \tag{3.106}$$

The pressure-density relationship that is required by Eq. (3.106) is given through the definition of the *bulk modulus* β

$$p = p_c + \beta \ln\left(\frac{\rho}{\rho_c}\right), \tag{3.107}$$

where p_c and ρ_c are the pressure and density, respectively, in the cavitated region.[8]

[8]The cavitation pressure is approximately constant and the lubricant flow in the cavitation zone is due to shear.

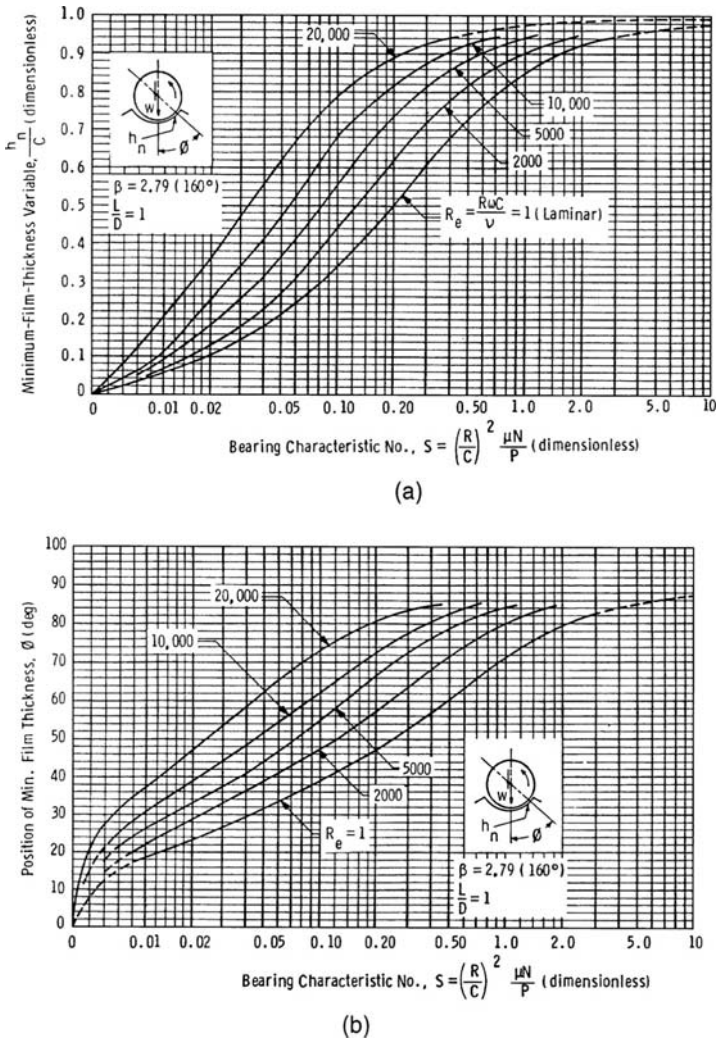

Figure 3.10. Performance curves for a centrally loaded, fixed partial journal bearing: (a) minimum film thickness, (b) attitude angle, (c) friction variable, and (d) inlet flow variable. (Reprinted with permission from Raimondi, A. A. and Szeri, A. Z. Journal and thrust bearings. In Booser, E. R., *CRC Handbook of Lubrication.* Copyright CRC Press, Boca Raton, Florida. © 1984.)

In the region of cavitation the principle of mass conservation leads to the equation

$$\frac{\partial(\rho h)}{\partial t} + \frac{\partial}{\partial x}\left(\frac{\rho h U}{2}\right) = 0. \tag{3.108}$$

In an effort to combine Eqs. (3.106) and (3.108) into a single equation, Elrod and Adams introduced a switching function, g, defined by

$$g = \begin{cases} 1, & \text{in full film region} \\ 0, & \text{in cavitated region.} \end{cases} \tag{3.109}$$

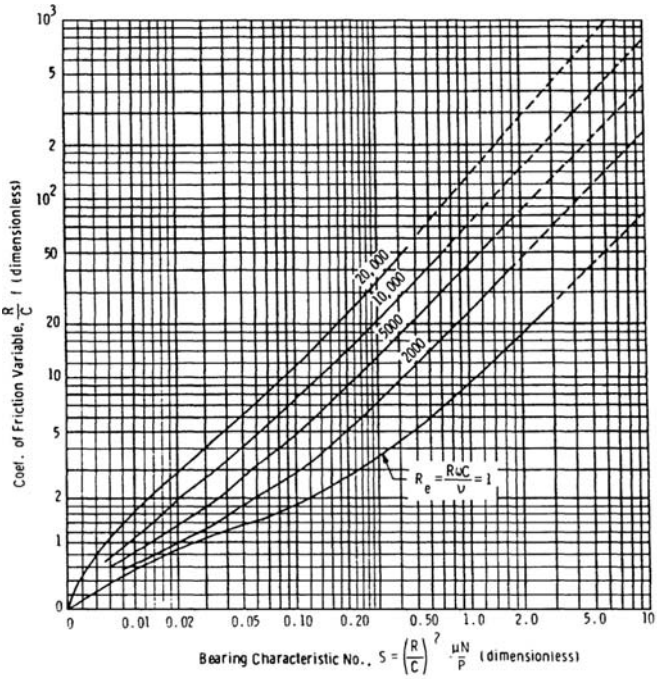

Figure 3.10 (*cont.*)

Introducing g from Eq. (3.109), using $p = p_c + g\beta \ln \phi$ from Eq. (3.107) and employing the notation $\rho = \rho_c \phi$, we obtain from Eq. (3.108)

$$\frac{\partial(\phi h)}{\partial t} + \frac{\partial}{\partial x}\left(\frac{Uh\phi}{2} - \frac{\beta h^3}{12\mu} g \frac{\partial \phi}{\partial x}\right) - \frac{\partial}{\partial z}\left(\frac{\beta h^3}{12\mu} g \frac{\partial \phi}{\partial z}\right) = 0. \tag{3.110}$$

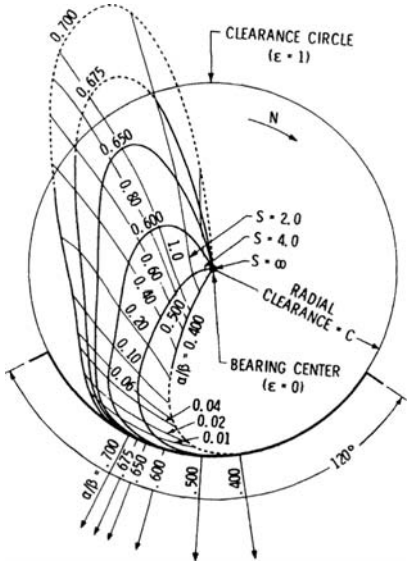

Figure 3.11 Locus of journal center for offset loads, $L/D = 1$, $\beta = 120^\circ$. (Reprinted with permission from Raimondi, A. A. Theoretical study of the effect of offset loads on the performance of a 120° partial journal bearing. *ASLE Trans.*, 2, 147–157, 1959.)

The variable ϕ has dual meaning: it may be interpreted as the ratio of densities in the full film region and as the volume fraction of the lubricant in the cavitated region (Vijayaraghavan and Keith, 1990a).

In the full film region where $g = 1$, Eq. (3.110) is an elliptic partial differential equation. In the cavitated region $g = 0$ and Eq. (3.110) yields

$$\frac{\partial \Phi}{\partial t} + \frac{U}{2}\frac{\partial \Phi}{\partial x} = 0 \tag{3.111}$$

in terms of the new variable $\Phi = \phi h$. Differentiating Eq. (3.111) twice, first with respect to t then with respect to x, we obtain

$$\frac{\partial^2 \Phi}{\partial t^2} + \frac{U}{2}\frac{\partial^2 \Phi}{\partial t\, \partial x} = 0,$$

$$\frac{\partial^2 \Phi}{\partial t\, \partial x} + \frac{U}{2}\frac{\partial^2 \Phi}{\partial x^2} = 0. \tag{3.112}$$

Eliminating the mixed derivatives in Eqs. (3.112), we have

$$\frac{\partial^2 \Phi}{\partial t^2} - \left(\frac{U}{2}\right)^2 \frac{\partial^2 \Phi}{\partial x^2} = 0. \tag{3.113}$$

As this is a hyperbolic equation, we have a change of type of the PDE at the cavitation boundary; the numerical methods designed for solving Eq. (3.105) with $g = 1$ for full film and Eq. (3.113) for cavitating film, must take this change into consideration (Vijayaraghavan and Keith, 1991).

In the cavitated region Vijayaraghavan and Keith (1990a) recommend the use of second-order upwind-differencing, while central-differencing suffices in the full film region. They

also follow Jameson (1975) by adding high-order artificial viscosity terms (Anderson et al., 1984) to the shear flow term in the cavitated region

$$\frac{\partial}{\partial x}(\phi h) \equiv \frac{\partial \Phi}{\partial x} \approx \frac{\partial}{\partial x}\left[\Phi - (1-g)\left(\frac{\partial^2 \Phi}{\partial x^2}\frac{\Delta x^2}{2} - \frac{\partial^3 \Phi}{\partial x^3}\frac{\Delta x^3}{8}\right)\right], \tag{3.114}$$

where Δx is the mesh spacing. With the addition of the artificial viscosity terms, the whole equation can now be centrally differenced with the consequences that (1) in the full film region, central differencing remains in effect on substituting $g = 1$, and (2) in the cavitated region, the central-differencing automatically switches to second-order upwind-differencing on account of the switch function being zero there.

For numerical work Eq. (3.110) is nondimensionalized

$$\frac{\partial(\phi H)}{\partial \bar{t}} + \frac{1}{4\pi}\frac{\partial}{\partial \bar{x}}(\phi H) = \frac{\bar{\beta}}{48\pi^2}\frac{\partial}{\partial \bar{x}}\left(H^3 g \frac{\partial \phi}{\partial \bar{x}}\right) + \frac{\bar{\beta}}{48\,(L/D)^2}\frac{\partial}{\partial \bar{z}}\left(H^3 g \frac{\partial \phi}{\partial \bar{z}}\right). \tag{3.115}$$

Here we used

$$\bar{x} = x/2\pi R, \quad \bar{z} = z/L, \quad H = h/C, \quad \bar{\beta} = \frac{\beta}{\mu\omega}\left(\frac{C}{R}\right)^2, \quad \bar{\Phi} = \phi H \quad \bar{t} = \omega t.$$

The finite differencing of Eq. (3.115) is explained in more detail in Vijayaraghavan and Keith, 1990b). Its final results are[9]

$$\left(\frac{\partial \bar{\Phi}}{\partial \bar{x}}\right)_i \approx \frac{1}{2\Delta \bar{x}}[g_{i+1/2}\bar{\Phi}_{i+1} + (2 - g_{i+1/2} - g_{i-1/2})\bar{\Phi}_i - (2 - g_{i-1/2})\bar{\Phi}_{i-1}] + \frac{1}{2\Delta x}[(1 - g_{i+1/2})\bar{\Phi}_i - (2 - g_{i+1/2} - g_{i-1/2})\bar{\Phi}_{i-1} + (1 - g_{i-1/2})\bar{\Phi}_{i-2}] \tag{3.116a}$$

for the shear flow term and

$$\left[\frac{\partial}{\partial \bar{x}}\left(-H^3 g \frac{\partial \phi}{\partial \bar{x}}\right)\right]_i = \left[\frac{\partial}{\partial \bar{x}}\left(-H^3 \frac{\partial g\,(\phi - 1)}{\partial \bar{x}}\right)\right]_i \approx -\frac{1}{\Delta \bar{x}^2}\left[H^3_{i+1/2} g_{i+1}(\phi_{i+1} - 1) - \left(H^3_{i+1/2} + H^3_{i-1/2}\right) g_i (\phi_i - 1) + H^3_{i-1/2} g_{i-1}(\phi_{i-1} - 1)\right] \tag{3.116b}$$

for the pressure term in $\bar{x}$. To obtain the $\bar{z}$ equation, replace i by j and $\bar{x}$ by $\bar{z}$ in Eq. (3.116b).

As relaxation methods require large computing times to convergence, Woods and Brewe (1989) incorporated a multigrid technique into the Elrod algorithm. Vijayaraghavan and Keith (1990b), on the other hand, advocate Newton iteration, coupled with an approximate factorization technique. The algorithm has been successfully applied to finite grooved bearings and flared misaligned bearings (Vijayaraghavan and Keith, 1990c). In context of coating flows see Gurfinkel and Patera (1997).

[9]Note that the shear flow term has been split to preserve tridiagonality of the coefficient matrix.

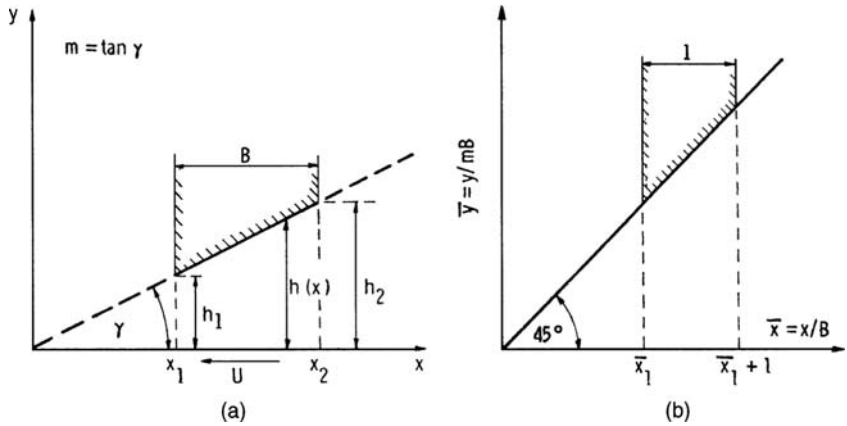

Figure 3.12. (a) The plane slider and (b) its nondimensional representation.

3.3 Thrust Bearings

Thrust bearings in their simplest form consist of two inclined plane surfaces that slide relative to one another. The geometry of the bearing surface is commonly rectangular or sector shaped, but other geometries are possible.

Plane Slider

The schematics of the fixed plane slider, the prototype of thrust bearings, is shown in Figure 3.12(a). Let B represent the dimension of the slider in the direction of relative motion; then the gradient m of the surfaces is calculated from

$$m = \frac{h_2 - h_1}{B}. \tag{3.117}$$

Here h_1 and h_2 represent the minimum value and the maximum value, respectively, of the film thickness.

The applicable form of the Reynolds equation is given in Eq. (2.74). To render this equation dimensionless, we make the following transformation:

$$x = B\bar{x} \qquad y = mB\bar{y} \qquad z = \frac{L}{2}\bar{z} \qquad p = \frac{6\mu U}{Bm^2}\bar{p}. \tag{3.118}$$

On the nondimensional $\bar{x}$, $\bar{y}$ plane of Figure 3.12, part (b), the $\bar{x}$ axis represents the runner surface of all plane sliders. The bearing surface projects onto the 45° line through the origin. In this representation the dimensionless parameter $\bar{x}_1 = x_1/B$ serves to locate the bearing pad, which is now of unit length when measured along the $\bar{x}$ direction, relative to the origin of the $(\bar{x}, \bar{y})$ coordinate system. To specify bearing axial length and thereby to complete the geometric description of the lubricant film, we need one more parameter, say, the aspect ratio B/L.

On this basis, when substituting Eq. (3.118) into the Reynolds equation and its boundary conditions, we would expect the appearance of the two dimensionless parameters $\bar{x}_1$ and B/L. This is indeed the case, for we find that

$$\frac{\partial}{\partial \bar{x}}\left(\bar{x}^3 \frac{\partial \bar{p}}{\partial \bar{x}}\right) + 4\left(\frac{B}{L}\right)^2 \frac{\partial}{\partial \bar{z}}\left(\bar{x}^3 \frac{\partial \bar{p}}{\partial \bar{z}}\right) = -1, \tag{3.119}$$

$$\bar{p}\,(\bar{x}, \pm 1) = 0, \tag{3.120a}$$

$$\bar{p}\,(\bar{x}_1, \bar{z}) = \bar{p}\,(\bar{x}_1 + 1, \bar{z}) = 0. \tag{3.120b}$$

The boundary conditions in Eq. (3.120) specify zero pressure on the pad boundaries, as we have $\bar{x}_1 = x_1/B$ and $\bar{x}_1 + 1 = (x_1 + B)/B = x_2/B$.

The distribution of the dimensionless pressure is identical in all bearings that have identical values of B/L and $\bar{x}_1$. The runner velocity U, the lubricant viscosity μ, and the slope m enter into the calculations only as constant multipliers when computing actual pressures.

The lubricant film force is given by

$$F = \int_{-L/2}^{L/2} \int_{x_1}^{x_2} p\,(x, z)\, dx\, dz$$

or in nondimensional form by[10]

$$f \equiv \frac{F h_1^2}{\mu U L B^2} = 6\bar{x}_1^2 \int_0^1 \int_{x_1}^{\bar{x}_1+1} \bar{p}\,(\bar{x}, \bar{z})\; d\bar{x}\, d\bar{z}. \tag{3.121}$$

The x coordinate of the center of pressure may be found from

$$F x_p = \int_{-L/2}^{L/2} \int_{x_1}^{x_2} x p\,(x, z)\, dx\, dz. \tag{3.122}$$

Writing $x_p = x_1 + B\delta$, in terms of dimensionless variables, Eq. (3.122) reduces to

$$\delta = -\bar{x}_1 + \frac{6\bar{x}_1^2}{f} \int_0^1 \int_{\bar{x}_1}^{\bar{x}_1+1} \bar{x}\, \bar{p}\,(\bar{x}, \bar{z})\, d\bar{x}\, d\bar{z}. \tag{3.123}$$

Here δ is the nondimensional distance between the center of pressure and the leading edge of the pad.

Because of the simplicity of the boundary condition Eq. (3.120), Eq. (3.119) has a straightforward analytical solution. Equation (3.119) is first made homogeneous by assuming the pressure to be of the form

$$\bar{p}\,(\bar{x}, \bar{z}) = \bar{p}_\infty\,(\bar{x}) - \bar{p}^*\,(\bar{x}, \bar{z})\,. \tag{3.124}$$

[10] In place of the dimensionless force as defined in Eq. (3.121), some authors, notably Raimondi and Boyd (1955), employ the *Kingsbury number* K_f. These two quantities are related through $K_f = \bar{x}_1^2/f$.

Here $\bar{p}_\infty(\bar{x})$ is the long-bearing solution and $\bar{p}^*$ represents the correction resulting from the finiteness of the bearing. The function $\bar{p}_\infty(\bar{x})$ satisfies

$$\frac{d}{d\bar{x}}\left(\bar{x}^3\frac{d\bar{p}_\infty}{d\bar{x}}\right) = -1, \tag{3.125a}$$

$$\bar{p}_\infty(\bar{x}_1) = \bar{p}_\infty(\bar{x}_1 + 1) = 0, \tag{3.125b}$$

$$\bar{p}_\infty = \frac{(\bar{x} - \bar{x}_1)(\bar{x}_1 + 1 - \bar{x})}{(2\bar{x}_1 + 1)\bar{x}^2}. \tag{3.125c}$$

The boundary-value problem for $\bar{p}^*(\bar{x}, \bar{z})$ is

$$\frac{\partial}{\partial\bar{x}}\left(\bar{x}^3\frac{\partial\bar{p}^*}{\partial\bar{x}}\right) + 4\left(\frac{B}{L}\right)^2\frac{\partial}{\partial\bar{z}}\left(\bar{x}^3\frac{\partial\bar{p}^*}{\partial\bar{z}}\right) = 0, \tag{3.126a}$$

$$\bar{p}^*(\bar{x}_1, \bar{z}) = \bar{p}^*(\bar{x}_1 + 1, \bar{z}) = 0, \tag{3.126b}$$

$$\bar{p}^*(\bar{x}, \pm 1) = \bar{p}_\infty(\bar{x}), \tag{3.126c}$$

and if the form $\bar{p}^* = \phi(\bar{x})\psi(\bar{z})$ is assumed, the functions ϕ and ψ satisfy

$$\frac{d}{d\bar{x}}\left(\bar{x}^3\frac{d\phi}{d\bar{x}}\right) + 4\left(\frac{B}{L}\right)^2\lambda^2\bar{x}^3\phi = 0, \tag{3.127a}$$

$$\phi(\bar{x}_1) = \phi(\bar{x}_1 + 1) = 0, \tag{3.127b}$$

$$\frac{d^2\psi}{d\bar{z}^2} - \lambda^2\psi = 0. \tag{3.128}$$

The function ψ, normalized at the ends of its interval, is

$$\psi = \frac{\cosh\lambda\bar{z}}{\cosh\lambda}. \tag{3.129}$$

The Sturm-Liouville problem, Eq. (3.127), was solved by Hays (1958) in terms of Bessel functions but at the cost of some computational stability problems. Instead we interpret Eqs. (1.27a) and (1.27b) as the Euler condition for the isoperimetric problem of the minimization of

$$\int_{\bar{x}_1}^{\bar{x}_1+1}\bar{x}^3\left(\frac{d\phi}{d\bar{x}}\right)^2 d\bar{x},$$

subject to the conditions

$$\int_{\bar{x}_1}^{\bar{x}_1+1}\bar{x}^3\phi^2(\bar{x})\,d\bar{x} = \text{const.}$$

and

$$\phi(\bar{x}_1) = \phi(\bar{x}_1 + 1) = 0.$$

Introducing λ as the Lagrange multiplier and changing the dependent variable to

$$v(\bar{x}) = \bar{x}^{3/2}\phi(\bar{x}),$$

the problem becomes that of minimizing (Szeri and Powers, 1970):

$$I = \int_{\bar{x}_1}^{\bar{x}_{1+1}} \left[(v')^2 + \frac{3}{4\bar{x}^2} v^2 - 4 \left(\frac{B}{L} \right)^2 \lambda^2 v^2 \right] d\bar{x}. \tag{3.130}$$

Adapting the Rayleigh-Ritz method (Hildebrand, 1965), we assume that $v(\bar{x})$ can be represented by a series of functions that satisfy the boundary conditions. If sines are chosen, $v(\bar{x})$ has the form

$$v_n(\bar{x}) = \sum_m x_{mn} \sin m\pi (\bar{x} - \bar{x}_1), \tag{3.131}$$

under the restriction that

$$\sum_m x_{mn}^2 = 1.$$

By the usual arguments of variational calculus, the problem in Eq. (3.130) is transformed into the matrix problem

$$AX = X\Lambda^2. \tag{3.132}$$

Here $X = [x_m]$, $\Lambda^2 = \text{diag}\{\lambda_1^2, \lambda_2^2, \ldots\}$, and $A = [a_{mn}]$, which is the Rayleigh-Ritz matrix whose elements are (δ_{mn} is the Kronecker delta)

$$a_{mn} = \frac{1}{4} \left(\frac{L}{B} \right)^2 (mn\pi^2 \delta_{mn} + q_{mn}).$$

The symbol q_{mn} stands for the definite integral

$$\frac{3}{2} \int_{\bar{x}_1}^{\bar{x}_1+1} \frac{\sin n\pi (\bar{x} - \bar{x}_1) \sin m\pi (\bar{x} - \bar{x}_2)}{\bar{x}^2} d\bar{x}.$$

Assuming that the problem can be solved, the expression for $\bar{p}^*(\bar{x}, \bar{z})$ is

$$\bar{p}^*(\bar{x}, \bar{z}) = \bar{x}^{-3/2} \sum_n a_n v_n(\bar{x}) \frac{\cosh \lambda_n \bar{z}}{\cosh \lambda_n}. \tag{3.133}$$

Here the coefficients a_n are chosen by orthogonality of the eigenfunctions to make $\bar{p}^*$ satisfy the boundary condition Eq. (3.126c)

$$a_n = 2 \int_{\bar{x}_1}^{\bar{x}_1+1} \bar{x}^{3/2} \bar{p}_\infty(\bar{x}) v_n(\bar{x}) d\bar{x}. \tag{3.134}$$

Often the lubricant pressure is of no interest. If that is the case, we can dispense with computing $\bar{p}$ from Eq. (3.124) and evaluate the load capacity, oil flow, and center of pressure (pivot position) directly (Szeri and Powers, 1970). The procedure will be demonstrated for the load capacity alone.

The nondimensional oil film force is written as

$$f = f_\infty - f^*, \tag{3.135}$$

where f_∞, the long-bearing force, is generated by $\bar{p}_\infty(\bar{x})$ and has the representation

$$f_\infty = 6\bar{x}_1^2 \left[\ln \left(1 + \frac{1}{\bar{x}_1} \right) - \frac{2}{2\bar{x}_1 + 1} \right]. \tag{3.136}$$

It follows that f^* is the force correction resulting from the finiteness of the bearing. Substitution of Eq. (3.134) into Eq. (3.133) yields

$$f^* = \int_0^1 \int_{\bar{x}_1}^{\bar{x}_1+1} \bar{p}^*(\bar{x}, \bar{z})\, d\bar{x}\, d\bar{z}$$
$$= 12\bar{x}_1^2 \sum_k \left(\sum_n b_n x_{nk} \right) \lambda_k^{-1} \tanh \lambda_k \left(\sum_m x_{mk} c_m \right). \tag{3.137a}$$

Our expression for f^* may be written in the compact form, using matrix notation

$$f^* = 12\bar{x}_1^2 b^T X \Lambda^{-1} \tanh \Lambda\, X^T c. \tag{3.137b}$$

Here

$$c_m = \int_{\bar{x}_1}^{\bar{x}_1+1} \frac{\sin m\pi(\bar{x} - \bar{x}_1)}{\bar{x}^{3/2}}\, d\bar{x},$$
$$b_m = \int_{\bar{x}_1}^{\bar{x}_1+1} \bar{x}^{3/2} \bar{p}_\infty(\bar{x}) \sin m\pi(\bar{x} - \bar{x}_1)\, d\bar{x},$$

and b and c are column vectors, having elements $b_1, b_2, b_3, \ldots$ and $c_1, c_2, c_3, \ldots$, respectively.

It is permissible to write, Eq. (3.137b)

$$X\Lambda^{-1} \tanh \Lambda X^T = X\Lambda^{-1} X^T (X \tanh \Lambda X^T) = A^{-1/2} \tanh A^{1/2}, \tag{3.138a}$$

as the following equalities hold

$$X\Lambda^n X^T = (X\Lambda X^T)^n = A^{n/2} \tag{3.138b}$$

for any rational number n, and

$$X \tanh \Lambda X^T = X \sinh \Lambda X^T X\, (\cosh \Lambda)^{-1} X^T.$$

In order to transform this last expression, we note that

$$X(\cosh \Lambda)^{-1} X^T = [(X^T)^{-1} \cosh \Lambda (X)^{-1}]^{-1}$$
$$= (X \cosh \Lambda\, X^T)^{-1}$$
$$= (\cosh X\Lambda\, X^T)^{-1}.$$

Here we took into account the orthogonality of the eigenvectors of the Sturm-Liouville problem and utilized the series expansion for cosh Λ.

Our final expression for the dimensionless force Eq. (3.135) is

$$f = 6\bar{x}_1^2 \left[\ln\left(1 + \frac{1}{\bar{x}_1}\right) - \frac{2}{2\bar{x}_1 + 1} - 2b^T A^{-1/2} \tanh A^{1/2} c \right]. \tag{3.139}$$

The term $A^{-1/2} \tanh A^{1/2}$ can be calculated without recourse to the eigenvalue problem in Eq. (3.132) by making use of Padé approximations of the form

$$\frac{\tanh \lambda^{1/2}}{\lambda^{1/2}} \approx \frac{\sum_n e_n \lambda^n}{\sum_m d_m \lambda^m}. \tag{3.140}$$

Since hydrodynamic action requires convergence of the film shape in the direction of relative motion, fixed pad sliders cannot carry load when the direction of rotation is

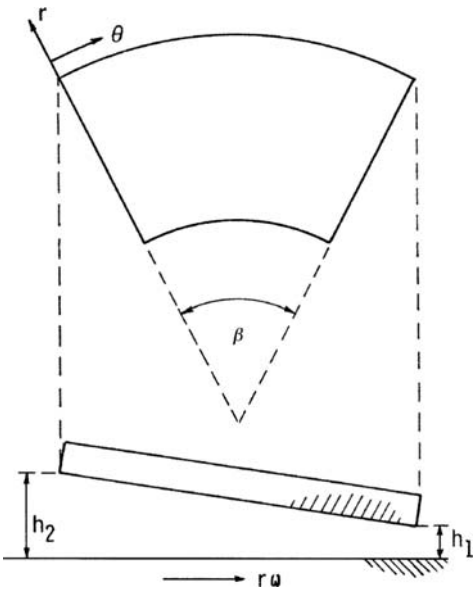

Figure 3.13. Sector thrust pad geometry.

reversed. If the bearing is to be operated in either the forward or the reverse direction, a combination of two pads with their surfaces sloping in opposite directions is required. Operation of such a configuration is possible only if the diverging lubricant film cavitates. If the ambient pressure is too high for the film to cavitate, then pivoted pad bearings are often used. Normally a flat pad will carry load efficiently only if the pivot is offset – that is, located between the center of the pad and the trailing edge – so that $0.5 < \delta < 1$. But with the pivot so placed, the pad can carry load effectively in only one direction. Szeri and Powers (1970) tabulate oil film force, oil flow, and pivot location for the parameter range $1/8 < \bar{x}_1 < 10$ and $1/8 < L/B < 16$.

When the pads are loaded, they deform, and the film shape is no longer given by $h = mx$. Crowning might also be machined into the pad deliberately. Curved pads were first investigated by Raimondi (1960).

Sector Thrust Bearing

The film shape for the sector thrust pad of Figure 3.13 is given by

$$h = h_2 - (h_2 - h_1)\frac{\theta}{\beta}, \tag{3.141}$$

where h_2 and h_1 are the maximum and minimum film thicknesses, respectively, and β is the angular span of the sector.

The Reynolds equation (2.74) in cylindrical polar coordinates, with V_0 set equal to zero, is

$$\frac{\partial}{\partial r}\left(rh^3\frac{\partial p}{\partial r}\right) + \frac{1}{r}\frac{\partial}{\partial \theta}\left(h^3\frac{\partial p}{\partial \theta}\right) = 6\mu\omega r\frac{\partial h}{\partial \theta}. \tag{3.142}$$

Introducing the new variable (Tao, 1959)

$$\phi = \frac{\beta}{h_2 - h_1} h$$

and the notation

$$K = \frac{6\mu\omega}{(h_2 - h_1)^2}\beta^2$$

into Eq. (3.142), the Reynolds equation reduces to

$$r\frac{\partial}{\partial r}\left(r\frac{\partial p}{\partial r}\right) + \frac{1}{\phi^3}\frac{\partial}{\partial \phi}\left(\phi^3\frac{\partial p}{\partial \phi}\right) = -Kr^2\phi^{-3}. \tag{3.143}$$

The solution of Eq. (3.143) is sought in the form

$$p(r, \phi) = p_1(r, \phi) + p_2(r, \phi),$$

where $p_1(r, \phi)$ satisfies the homogeneous equation and $p_2(r, \phi)$ is a particular solution of Eq. (3.143). The homogeneous equation is reduced to two ordinary differential equations:

$$r^2\zeta'' + r\zeta' - \lambda^2\zeta = 0, \tag{3.144a}$$

$$\xi'' + 3\phi^{-1}\xi' + \lambda^2\xi = 0, \tag{3.144b}$$

by introduction of

$$p_1(r, \phi) = \zeta(r)\,\xi(\phi).$$

Equation (3.144a) is of the Sturm-Liouville type when specifying zero boundary conditions for pressure and has solutions in terms of Bessel functions. Equation (3.144b), on the other hand, is amenable to direct integration. Details of the solution are given by Tao (1959).

Numerical solutions of the sector thrust bearing are given by Pinkus (1958) and Pinkus and Sternlicht (1961). The plot in Figure 3.14 showing the nondimensional load variable plotted against the radial slope parameter for various values of the tangential slope parameter, is taken from Raimondi and Szeri (1984). These solutions were obtained via Galerkin's method, employing global interpolating functions. Pivoted-pad thrust bearings employ supporting pivots, as shown in Figure 3.15, at the center of film pressure. While the performance of pivoted-pad bearings is theoretically identical to that of a fixed-pad bearing having the same slope, the pivoted type has the advantages of (1) self-aligning capability, (2) automatically adjusting pad inclination to optimally match the needs of varying speed and load, and (3) operation in either direction of rotation. Theoretically, the pivoted-pad can be optimized for all speeds and loads by judicious pivot positioning, whereas the fixed-pad bearing can be designed for optimum performance only for one operating condition. Although pivoted-pad bearings involve somewhat greater complexity, standard designs are readily available for medium to large size machines. Pivoted-pad thrust bearings are further discussed in Chapters 4 and 9, within the context of dynamic properties and thermal effects.

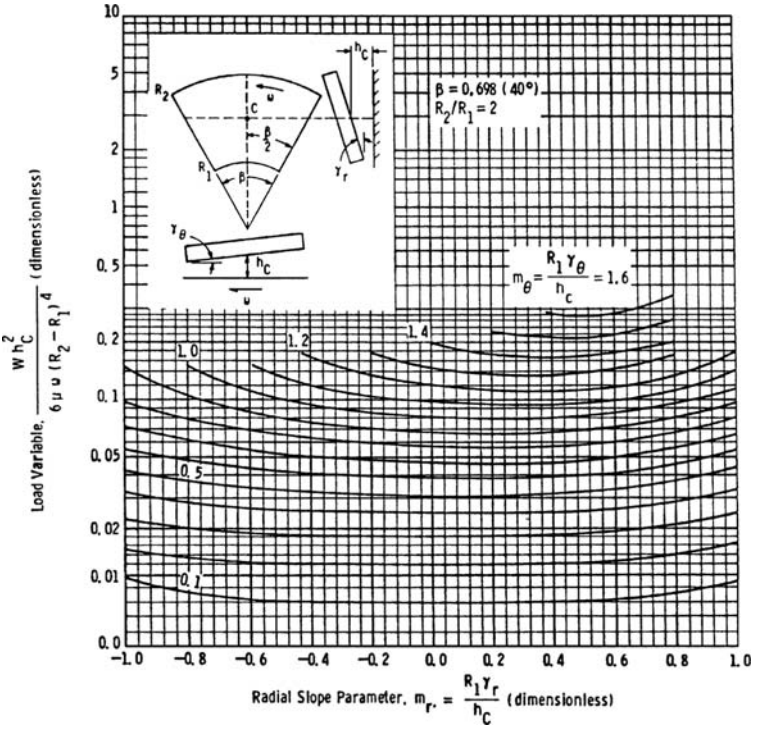

Figure 3.14. Load capacity chart for thrust pad sector. (Reprinted with permission from Raimondi, A. A. and Szeri, A. Z. Journal and thrust bearings. In Booser E. R., *CRC Handbook of Lubrication*. Copyright CRC Press, Boca Raton, Florida. © 1984.)

3.4 Effects of Surface Topography

Surface Roughness

All previous developments are based on the assumption of perfectly smooth bearing surfaces. In reality, however, engineering surfaces are covered with asperities. These asperities appear small relative to thick films, but might exert strong influence when the film is thin. To appreciate this, consider a $D = 50$ mm journal bearing operating at $\varepsilon = 0.8$, with minimum film thickness $h_{min} = 10\,\mu$m. Even for ground surfaces of this bearing, asperity heights might reach $\delta \approx 1.25\,\mu$m with lateral spacing ten-times this value. For simplicity, let us replace the real surface between two adjacent asperities by an 'equivalent' plane slider, and define across-the-film characteristic length by $\ell_y \approx [h_{min} + (h_{min} - \delta)]/2$ while setting $\ell_{xz} \approx 10\delta$. Then for 'local' aspect ratio, we have $\ell_y/\ell_{xz} \approx 0.75$, casting doubts on the applicability of the Reynolds equations under such conditions. In cases when the lubrication approximation still holds even though the surfaces are rough, we are said to be dealing with *Reynolds roughness*. When there is significant pressure variation across the film due to surface roughness, to the extent that the lubrication approximation is no longer valid, Stokes equation instead of Reynolds equation must be employed; in this latter case we are dealing with *Stokes roughness* (Elrod, 1973). If, in addition, the Reynolds number is finite, all solutions must be based on the Navier-Stokes equation. Just where the

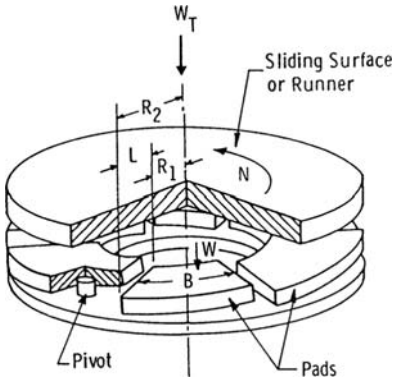

Figure 3.15. Pivoted-pad thrust bearing geometry. (Reprinted with permission from Raimondi, A. A. and Szeri, A. Z. Journal and thrust bearings. In Booser, E. R., *CRC Handbook of Lubrication*. Copyright CRC Press, Boca Raton, Florida. © 1984.)

demarcation between roughness regimes lies, is not currently known. Compounding the difficulties is the fact that the asperity height distribution for most machined surfaces is random, and statistical methods must be applied when attempting to model lubrication between rough surfaces.[11]

Statistical Methods

Tzeng and Saibel (1967) were among the first to apply statistical methods to lubrication of rough surfaces. They investigated the inclined plane slider having one-dimensional roughness transverse to the direction of relative motion. This analysis was, almost immediately, extended by Christensen and Tonder (Christensen and Tonder, 1969; Tonder and Christensen, 1971), and there have been many other attempts since. The method employed by these investigators is based on statistical averaging of the Reynolds Equation. As remarked by Tripp (1983), the Reynolds equation has the property, unusual among equations of mathematical physics, that the boundary conditions are incorporated into the equation – it is this feature of the Reynolds equation that offers hope for ensemble averaging the equation itself.

Christensen and Tonder (1969) make two fundamental assumptions in their analysis: (1) the magnitude of the pressure ripples due to surface roughness is small and the variance of the pressure gradient in the roughness direction is negligible, and (2) the flow in the direction transverse to roughness direction has negligible variance.

The first step in the analysis is to average the Reynolds equation. Applying the expectation operator, E, to each of the terms of Eq. (2.74), we write

$$\frac{\partial}{\partial x} E\left(h^3 \frac{\partial p}{\partial x}\right) + \frac{\partial}{\partial z} E\left(h^3 \frac{\partial p}{\partial z}\right) = 6\mu U \frac{\partial E(h)}{\partial x}. \tag{3.145}$$

The film thickness, h, is separated into two parts $h = \bar{h} + \eta$, where $\bar{h}$ denotes the nominal, smooth, part of the film geometry while η is the variation due to surface roughness. For

[11] There have been attempts to represent surface roughness by Fourier series. These efforts, however, should be considered as investigating waviness rather than roughness.

reasons not explained, other than a reference to assumption (1), Christensen and Tonder assert that the expected value of the product of two stochastic variables equals the product of the expected values, and write

$$\frac{\partial}{\partial x} E\left(h^3 \frac{\partial p}{\partial x}\right) = \frac{\partial}{\partial x}\left[\frac{\partial \bar{p}}{\partial x} E(h^3)\right], \tag{3.146}$$

where $\bar{p} = E(p)$.

The flow in the z direction, assumed of having zero variance by assumption (2) above, can be written as

$$h^3 \frac{\partial p}{\partial z} = q_z.$$

On averaging, we have

$$\frac{\partial \bar{p}}{\partial z} = q_z E\left(\frac{1}{h^3}\right), \qquad q_z = \frac{1}{E(h^{-3})} \frac{\partial \bar{p}}{\partial z}. \tag{3.147}$$

By combining Eqs. (3.146) and (3.147), we obtain the ensemble averaged Reynolds equation

$$\frac{\partial}{\partial x}\left[\frac{\partial \bar{p}}{\partial x} E(h^3)\right] + \frac{\partial}{\partial z}\left[\frac{\partial \bar{p}}{\partial z} \frac{1}{E(h^{-3})}\right] = 6\mu U \frac{\partial}{\partial x} E(h), \tag{3.148a}$$

valid for a bearing with longitudinal, one-dimensional roughness (Christensen and Tonder, 1969). For transverse, one-dimensional roughness, Tonder and Christensen (1972) find

$$\frac{\partial}{\partial x}\left[\frac{\partial \bar{p}}{\partial x} \frac{1}{E(h^{-3})}\right] + \frac{\partial}{\partial z}\left[\frac{\partial \bar{p}}{\partial z} E(h^3)\right] = 6\mu U \frac{\partial}{\partial x}\left[\frac{E(h^{-2})}{E(h^{-3})}\right]. \tag{3.148b}$$

They have also attempted to extend these result to three-dimensional roughness, but only with limited success.

Patir and Cheng (1978) published an analysis of three-dimensional surface roughness, resulting in flow factors that are to be included in the Reynolds equation. Their idea was to (1) characterize the surface by its autocorrelation function (see Peklenik, 1968), (2) computer-generate sets of rough surfaces that have the specified autocorrelation, (3) solve Reynolds equation for microbearings constructed with the computer-generated surfaces, (4) calculate flow factors for use with a Reynolds equation that employs the nominal film thickness and accounts for the surface roughness of the microbearings, and (5) average a large number of flow factors to obtain statistical representation.

For given Gaussian surface roughness distribution we can calculate the autocorrelation in a straightforward manner. If η_{ij} denotes the asperity amplitude at the nodal position $x_i = i\,\Delta \boldsymbol{x}$, $z_j = j\,\Delta z$, the discrete autocorrelation function is defined by the $n \times m$ matrix

$$R_{pq} = R(p\Delta x, q\,\Delta z) = E(\eta_{ij}\eta_{i+p,j+q}) \qquad \begin{matrix} p = 0, 1, 2, \ldots, n-1 \\ q = 0, 1, 2, \ldots, m-1 \end{matrix} \tag{3.149}$$

Our goal is to invert Eq. (3.149), i.e., to generate an $N \times M$ matrix of roughness amplitudes having Gaussian height distribution that possesses a specified autocorrelation (Patir, 1978). To this end, using random number generator, we construct an $(N + n) \times (M + m)$

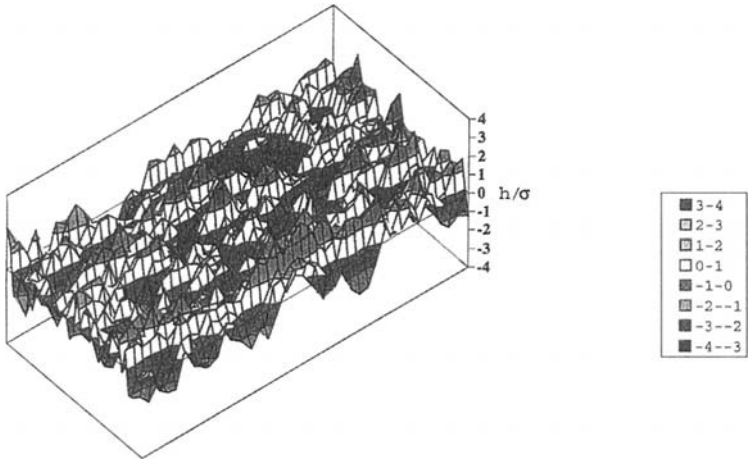

Figure 3.16. Computer-generated surface with isotropic roughness and specified autocorrelation function.

matrix $(\kappa_{i,j})$ whose elements are independent, identically distributed, Gaussian random numbers. The roughness heights are then obtained as the sum

$$\eta_{ij} = \sum_{k=1}^{n} \sum_{\ell=1}^{m} a_{kl} \kappa_{i+k,j+l}, \qquad \begin{matrix} i = 1, 2, \ldots, N \\ j = 1, 2, \ldots, M \end{matrix} \tag{3.150}$$

where the a_{kl} are the coefficients yet to be determined, so as to give the desired correletion matrix.

To find the coefficients a_{kl}, substitute Eq. (3.150) into Eq. (3.149), taking into account that the κ_{ij} are uncorrelated and have unit variance, i.e.,

$$E(\kappa_{ij}\kappa_{kl}) = \begin{cases} 1 & \text{if } i = k,\ j = l \\ 0 & \text{otherwise} \end{cases} \tag{3.151}$$

and obtain

$$R_{pq} = \sum_{k=1}^{n-p} \sum_{l=1}^{m-q} a_{kl} a_{k+p,l+q} \qquad \begin{matrix} p = 0, 1, \ldots, n-1 \\ q = 0, 1, \ldots, m-1. \end{matrix} \tag{3.152}$$

This represents nm simultaneous, deterministic equations from which to calculate the set of nm coefficients a_{kl}. Once these coefficients are known, substitution into Eq. (3.150) yields the required asperity height distribution (Patir, 1978). Hu and Tonder (1992) further improved on Patir's scheme for generating rough surfaces of specified statistical properties by using Fast Fourier Transform (FFT) methods to commute between spectral space and physical space.

It is now possible, either with the help of Eq. (3.150) or by utilizing Hu and Tonder's scheme, to generate surfaces with specified autocorrelation. Figure 3.16 shows such a computer-generated surface.

It is also possible to construct microbearings with, and to fit-finite-difference mesh to, the computer generated surfaces. Solution of Reynolds equation will then proceed in two phases. To calculate the pressure flow factors ϕ_x and ϕ_z, the microbearing is subjected to

mean pressure gradients $(p_1 - p_2)/(x_2 - x_1)$ and $(p_1 - p_2)/(z_2 - z_1)$, respectively, where $(x_2 - x_1)(z_2 - z_1)$ is the dimension of the microbearing. The pressure flow factor ϕ_x, for example, is calculated from

$$\phi_x = E\left(h\frac{\partial p}{\partial x}\right) \Big/ \left[\bar{h}^3 \frac{(p_2 - p_1)}{(x_2 - x_1)}\right].$$

To calculate the shear flow factor ϕ_s, sliding is specified and the mean pressure gradient eliminated (Patir and Cheng, 1979).

In the next step, the flow factors are averaged, having been calculated for a large number of microbearings. The Reynolds equation now takes the form

$$\frac{\partial}{\partial x}\left(\phi_x \frac{h^3}{12\mu}\frac{\partial \bar{p}}{\partial x}\right) + \frac{\partial}{\partial z}\left(\phi_z \frac{h^3}{12\mu}\frac{\partial \bar{p}}{\partial z}\right) = \frac{U_1 + U_2}{2}\frac{\partial \bar{h}}{\partial x} + \frac{U_1 - U_2}{2}\sigma\frac{\partial \phi_s}{\partial x} + \frac{\partial \bar{h}}{\partial t}. \quad (3.153)$$

Part (a) of Figure 3.17 plots the pressure flow factor ϕ_x, and part (b) plots the shear flow factor ϕ_s versus h/σ, where σ is the composite rms roughness [see Eq. (1.2)]. Contact of opposing asperities is first made when $h/\sigma \approx 3$; for values less than this the lubrication approximation no longer holds (Stokes roughness regime) and the flow factors become increasingly inaccurate. In any case, the flow factors are very sensitive to the numerical scheme employed (Peeken et al. 1997).

The theory has been extended to EHL (Ai and Zheng, 1989; Chang and Webster, 1991). Others to discuss lubrication between rough surfaces were Elrod (1973, 1979), who used a two variable expansion procedure, Tripp (1983), Mitsuya and Fukui (1986), Bhushan and Tonder (1989), and Ai and Cheng (1994, 1996). The last two of these papers treats the prescribed surface profile as a deterministic function and employs the multigrid method (Lubrecht, ten Napel, and Bosma, 1986) for solving the Reynolds equation.

When the asperities touch, the lubrication approximation ceases to be valid (Sun and Chen, 1977) and one has to solve Stokes equations. To date, there has been little work done on Stokes roughness.

Homogenization

We begin by writing the steady-state Reynolds equation in form

$$\nabla \cdot \left(h_\eta^3 \nabla p_\eta\right) - \Lambda \frac{\partial h_\eta}{\partial x_1} = 0, \quad \nabla = \left(\frac{\partial}{\partial x_1}, \frac{\partial}{\partial x_2}\right), \quad (3.154)$$

where $\Lambda = 6\mu U$ and the index η refers the adjoining quantity to the prevailing surface roughness, characterized by the length scale η.

Our fundamental assumption is that surface roughness results from $n_r \times n_r$ repetitions of a basic roughness pattern over a representative cell of dimension $\eta \times \eta$, $\eta = 1/n_r$. In consequence, the perturbation of the normalized film thickness $h(x_1, x_2)$ caused by surface roughness alone can be represented by the periodic function $h_1(\xi_1, \xi_2)$. Here $(\xi_1, \xi_2) = [(x_1/\eta), (x_2/\eta)]$ are local variables running over the unit cell $\Xi = [0, 1] \times [0, 1]$.

Denoting the global film thickness by $h_0(x_1, x_2)$, the total, perturbed, film thickness is given by

$$h_\varepsilon(\boldsymbol{x}) = h_0(\boldsymbol{x}) + h_1(\boldsymbol{\xi}). \quad (3.155)$$

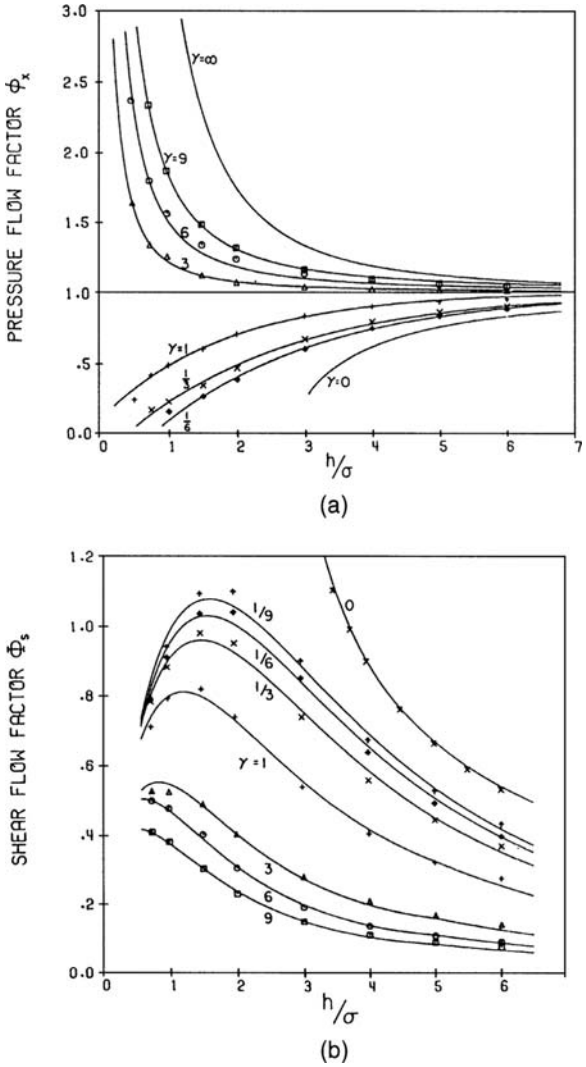

Figure 3.17. Flow factors for rough surfaces: (a) pressure flow factor, (b) shear flow factor; $\gamma = \lambda_{0.5x}/\lambda_{0.5z}$ (Eq. 1.3). (Reprinted with permission from Patir, N. and Cheng, H. S. An average flow model for determining effects of three-dimensional roughness on partial hydrodynamic lubrication. *ASME Journal of Lubrication Technology*, 100, 12–17, 1978; Patir, N. and Cheng, H. S. Application of average flow model to lubrication between rough sliding surfaces. *ASME Journal of Lubrication Technology*, 101, 220–230, 1979.)

Moreover, by assumption, the corresponding pressure can be represented by the asymptotic expansion

$$p_\eta(\boldsymbol{x}) = p_0(\boldsymbol{x}) + \eta p_1(\boldsymbol{x}, \boldsymbol{\xi}) + \eta^2 p_2(\boldsymbol{x}, \boldsymbol{\xi}) + \cdots . \tag{3.156}$$

Using the chain rule of differentiation, we have

$$\nabla(\cdot) = \nabla(\cdot) + \frac{1}{\eta}\nabla_\xi(\cdot); \qquad \nabla_\xi = \left(\frac{\partial}{\partial_{\xi 1}}, \frac{\partial}{\partial \xi_2}\right), \tag{3.157}$$

and when (3.156) and (3.157) are substituted into Eq. (3.154), we obtain

$$\begin{aligned}
&\frac{1}{\eta}\left\{\nabla_\xi \cdot \left[h_\eta^3(\nabla p_0 + \nabla_\xi p_1)\right] - \Lambda \frac{\partial h_\eta}{\partial \xi_1}\right\} \\
&\quad + \left\{\nabla \cdot \left[h_\eta^3(\nabla p_0 + \nabla_\xi p_1)\right] + \nabla_\xi \cdot \left(h_\eta^3 \nabla p_1\right) - \Lambda \frac{\partial h_\eta}{\partial x_1}\right\} \\
&\quad + \eta\left\{\nabla \cdot \left(h_\eta^3 \nabla p_1\right)\right\} + \cdots = 0.
\end{aligned} \tag{3.158}$$

Equating now the coefficients of the various powers of η to zero, we obtain a pair of coupled differential equations in the two unknowns p_0 and p_1

$$\nabla_\xi \cdot \left[h_\eta^3(\nabla p_0 + \nabla_\xi p_1)\right] = \Lambda \frac{\partial h_\eta}{\partial \xi_1}, \tag{3.159}$$

$$\nabla \cdot \left[h_\eta^3(\nabla p_0 + \nabla_\xi p_1)\right] = \Lambda \frac{\partial h_\eta}{\partial x_1} - \nabla_\xi \cdot \left(h_\eta^3 \nabla p_1\right). \tag{3.160}$$

These equations can be easily uncoupled however, owing to the linearity of Eq. (3.154), by observing that

$$p_1 = \omega_1 \frac{\partial p_0}{\partial x_1} + \omega_2 \frac{\partial p_0}{\partial x_2} + \omega_3 + C(x_1, x_2), \tag{3.161}$$

solves Eq. (3.159), provided that the auxiliary variables $\omega_1, \omega_2, \omega_3$ satisfy, respectively, the constraints

$$\nabla_\xi \cdot \left(h_\eta^3 \nabla_\xi \omega_1\right) = -\frac{\partial h_\eta^3}{\partial \xi_1}, \tag{3.162a}$$

$$\nabla_\xi \cdot \left(h_\eta^3 \nabla_\xi \omega_2\right) = -\frac{\partial h_\eta^3}{\partial \xi_2}, \tag{3.162b}$$

$$\nabla_\xi \cdot \left(h_\eta^3 \nabla_\xi \omega_3\right) = \Lambda \frac{\partial h_\eta}{\partial \xi_1}. \tag{3.162c}$$

Substituting p_1 from (3.161) into Eq. (3.160), we obtain

$$\begin{aligned}
&\frac{\partial}{\partial x_1}\left\{h_\eta^3\left[\left(1 + \frac{\partial \omega_1}{\partial \xi_1}\right)\frac{\partial p_0}{\partial x_1} + \frac{\partial \omega_2}{\partial \xi_1}\frac{\partial p_0}{\partial x_2}\right]\right\} \\
&\quad + \frac{\partial}{\partial x_2}\left\{h_\eta^3\left[\frac{\partial \omega_1}{\partial \xi_2}\frac{\partial p_0}{\partial x_1} + \left(1 + \frac{\partial \omega_2}{\partial \xi_2}\right)\frac{\partial p_0}{\partial x_2}\right]\right\} \\
&\quad = \Lambda \frac{\partial h_\varepsilon}{\partial \xi_1} - \nabla \cdot \left(h_\eta^3 \nabla_\xi \omega_3\right) - \nabla_\xi \cdot \left(h_\eta^3 \nabla p_1\right).
\end{aligned} \tag{3.163}$$

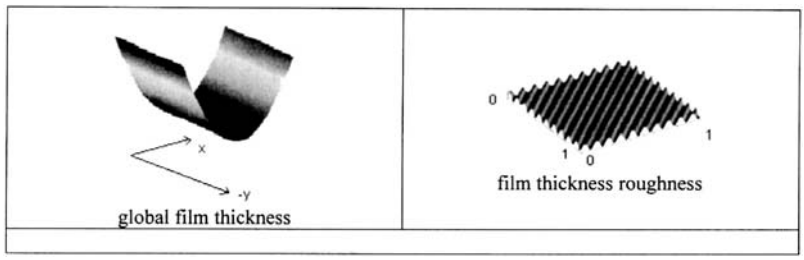

Figure 3.18. Journal bearing film geometry, isotropic case (Reprinted with permission from Kane, M. and Bou-Said, B. Comparison of homogenization and direct techniques for the treatment of roughness in incompressible lubrication. *ASME Journal of Tribology*, **126**, 733–737, 2004).

To eliminate dependence on local variables we integrate Eq. (3.163) over the unit square Ξ while paying attention to the periodicity of the functions involved. Using matrix notation

$$A(\boldsymbol{x}) = \begin{bmatrix} \int_\Xi h_\eta^3 \left(1 + \dfrac{\partial \omega_1}{\partial \xi_1}\right) d\xi & \int_\Xi h_\eta^3 \dfrac{\partial \omega_2}{\partial \xi_1} d\xi \\ \int_\Xi h_\eta^3 \dfrac{\partial \omega_1}{\partial \xi_2} d\xi & \int_\Xi h_\eta^3 \left(1 + \dfrac{\partial \omega_2}{\partial \xi_2}\right) d\xi \end{bmatrix},$$

$$B(\boldsymbol{x}) = \begin{bmatrix} \int_\Xi \left(h_\eta^3 \dfrac{\partial \omega_3}{\partial \xi_1} - \Lambda h_\eta\right) d\xi \\ \int_\Xi h_\eta^3 \dfrac{\partial \omega_3}{\partial \xi_2} d\xi \end{bmatrix}, \tag{3.164}$$

we write the integrated form of Eq. (3.163), the homogenized Reynolds equation, in the form

$$\nabla \cdot [A(\boldsymbol{x}) \nabla P_0 + B(\boldsymbol{x})] = 0, \qquad P_0 = 0 \quad \text{on} \quad \partial\Omega, \tag{3.165}$$

where we consider ∇P_0 a column vector.

The advantage of the homogenization scheme is purely computational. If in the solution of the local problem (3.162) a mesh of size $n_1 \times n_2$ were required to accurately portray the roughness pattern over the unit cell Ξ, the number of mesh points necessitated by the complete deterministic solution would be of the order of $r^2 (n_1 \times n_2)$. Kane and Bou-Said (2004) compared results of homogenization with those of deterministic computations in a highly loaded contact of a journal bearing for the roughness pattern

$$h_1 = \alpha sin \left(2\pi \frac{\delta_1 \xi_1 + \delta_2 \xi_2}{\delta_1 + \delta_2}\right).$$

Here α is the roughness amplitude and the pattern is transverse for $\delta_1 = 1$, $\delta_0 = 0$ and longitudinal when $\delta_1 = 0$, $\delta_0 = 1$. Figure 3.18 displays the corresponding global film thickness h_0 as well as its perturbation over the representative unit cell Ξ.

Figure 3.19 compares deterministic solutions with results of homogenization for $\alpha = 0.3 h_{\min}$. The latter technique seems to be insensitive to the number of representative cells while the deterministic solution necessitates increasing the number of discretization points as n_r is increased.

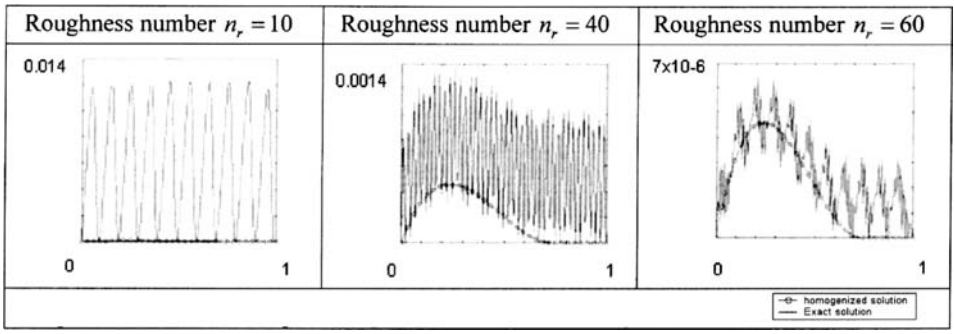

Figure 3.19. Variation of pressure profile with roughness number (Reprinted with permission from Kane, M. and Bou-Said, B. Comparison of homogenization and direct techniques for the treatment of roughness in incompressible lubrication. *ASME Journal of Tribology*, **126**, 733–737, 2004).

Application of homogenization to gas bearing is more involved than the case discussed here, as the Reynolds equation characterizing compressible lubricant is nonlinear. Difficulties arise when trying to decouple the global from the local problems. The full nonlinear case, for which the coefficients $A_{11}, \ldots, A_{22}$ and B_1, B_2 are dependent on P_0 was discussed by Buscaglia and Jai (2000) and by Jai and Bou-Said (2002). Almqvist and Dasht (2006) linearized the gas-bearing problem by assuming constant bulk modulus $\beta = \rho\,(\partial p/\partial\rho)$; in this case the analysis of the compressible and incompressible cases is formally identical.

Surface Texturing

Classical lubrication theory does not allow for the generation and maintenance of a load carrying film between parallel surfaces. Yet already in 1891 Beauchamp Tower reported on successfully operating a parallel thrust bearing, consisting of a plane collar rotating against a fixed annulus (Cameron, 1966). This, of course, does not repudiate classical theory but simply points to the fact that if any of its assumptions are violated, the theory, and its predictions, no longer holds. In Tower's bearing the correct mechanism that allowed lubricant film to develop is, in all probability, related to thermal distortion of the bearing surfaces, thus violating the "rigid surface" assumption. Violating the "smooth surface," assumption by the introduction of microroughness into the inlet section can, again, lend load capacity to parallel surfaces in relative motion (Tonder, 2001; Li and Chen, 2007).

It has been known for some time that texturing of the surface can produce beneficial effects in seals and in parallel thrust bearings (Hamilton et al., 1966; Anno et al., 1968, 1969). Various techniques are available for bringing about the texturing of surfaces, but laser surfaces texturing (LST) is probably the most advanced method devised so far (Etsion, 2005). Lasers are convenient to use, are environmentally friendly, and able to produce identical dimples at high surface density. Each of such dimples can then serve as a miniature hydrodynamic bearing. Other intended uses of the dimples might be as micro-reservoirs for lubricant or as microtraps for wear debris; here, however, we are interested in LST-created dimples as microbearings.

Etsion and co-workers were among the first to theoretically analyze the effects of LST on parallel thrust bearings (Etsion and Burstein, 1996). In one of their more recent papers

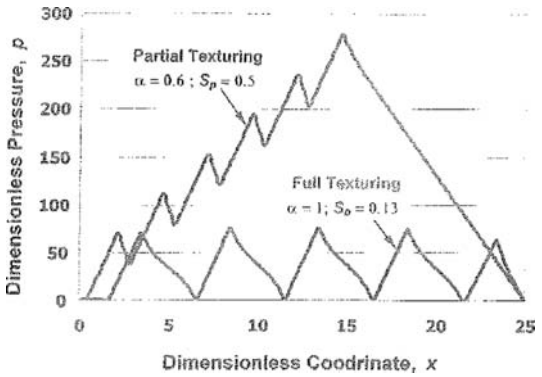

Figure 3.20. Typical pressure distribution for partial and full texturing of parallel thrust bearing (Reprinted with permission from Brizmer, V., Kligerman, Y. and Etsion, I. A laser surface textured parallel thrust bearing. *Tribol. Trans.*, **46** (3), 397–403, 2003, Taylor & Francis Group).

(Brizmer et al., 2003), they consider texturing with spherical segment shaped microdimples. They rely on the Reynolds equation and the Swift-Stieber cavitation boundary condition to represent flow over the dimples. When setting the pressure inside the cavitation zone to zero, the pressure distribution becomes asymmetric, yielding positive load bearing capacity. In the case of a fully structured surface, that is when the surface is completely covered by dimples, they find that the dimples do not interact but operate as independent microbearings. The result in this fully textured case is a saw tooth like, periodic, pressure distribution yielding a modest load capacity. But if the surface is only partially textured, the texturing starting at and extending in the downstream direction from the inlet, the dimples interact and produce a step-like pressure distribution over the textured portion of the pad, reaching a maximum value at the start of the untextured section and falling to zero in the groove (Figure 3.20).

In compressible flow where the cavitation effect is absent, the pressure profile is made nonsymmetric by compressibility effects; this then enables generation of a load bearing capacity (Etsion et al., 1999; Kligerman and Etsion, 2001). In a follow up paper Etsion et al. (2004) provide experimental support for their theoretical conclusions. It is notable, however, that this analysis, as it is based on the Reynolds equation, does not allow for contributions from fluid inertia.

Arghir et al. (2003) are unwilling to accept Etsion's rationale for the generation of load capacity of textured parallel bearings. Instead, they work with the full Navier–Stokes equations for steady flow and find that the zero inertia assumption (Stokes equation) is unqualified to model flow over macro-roughness in the normally anticipated Reynolds number range. Their conclusion is that the "net pressure gain is a pure inertia effect." On increasing the Reynolds number, the pressure computed from the Navier–Stokes equation displays increasing asymmetry, as depicted in Figure 3.21, thus leading to positive load carrying capacity over the dimple.

In clear contrast to this "convective inertia mechanism," and in support of the "cavitation mechanism" formulated by Etsion, Dobrica and Fillon (2009) find that for sliders, in general, "inertia has negative effects, reducing load capacity." There are, thus, contradictory explanations as to the actual origin of the excess pressure. Of course, if the surfaces converge in the direction of relative motion thus generating considerable pressure even in the absence

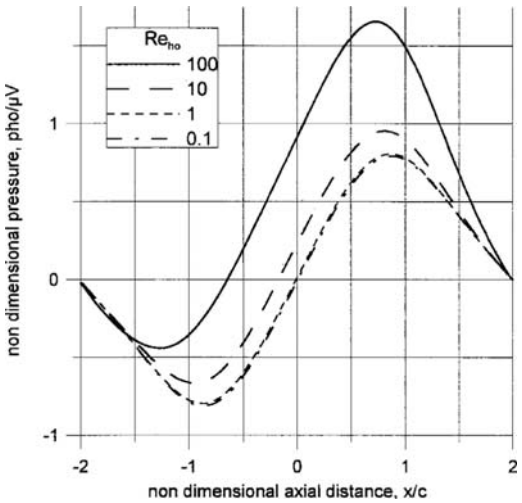

Figure 3.21. Pressure distributions on the flat moving wall facing textured surface (Reprinted with permission from Arghir, M., Roucou, N., Helene, M. and Frene, J. Theoretical analysis of the incompressible laminar flow in a macro-roughness cell. *ASME Journal of Tribology*, **125**, 309–318, 2003).

of texturing, cavitation appears less likely to occur and one would have to fall back on convective inertia effects as the primary justification of the extra pressure effect, if, indeed, it existed at all.

To investigate the influence of both the positioning and the size of two-dimensional, cylindrical, dimples in a convergent geometry, Cupillard et al. (2008) positioned a pattern of 10 dimples alternatively in the inlet zone where of $dp/dx > 0$ (configuration 1), in the vicinity of the maximum pressure where $p \approx p_{\max}$ (configuration 2) and in the outlet zone where $dp/dx < 0$ (configuration 3) of a journal bearing. Dimples were characterized by their width w and their depth d and, depending on size, spanned an angle $24 \leq \Delta\theta^\circ \leq 71$ (Figure 3.22). In this work lubricant flow was governed by the steady-state Navier–Stokes equations and the Rayleigh–Plesset multiphase cavitation algorithm (Plesset, 1949). Computing with "deep" dimples, i.e., $d/h_{\min} > 1$, Cupillard and his coauthors found that each of the three configurations distorted the smooth-surface pressure

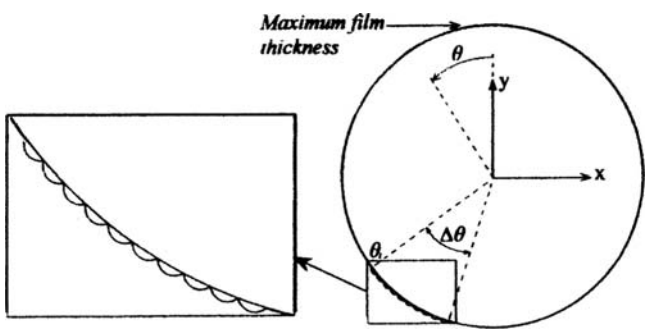

Figure 3.22. Dimple configuration (Reproduced with permission from Cupillard, S., Glavatskih, S. and Cervantes, M. J. Computational fluid dynamics analysis of a journal bearing with surface texturing. *Proc IMechE Journal of Engineering Tribology*, **222**, 97–107, 2008, Professional Engineering Publishing).

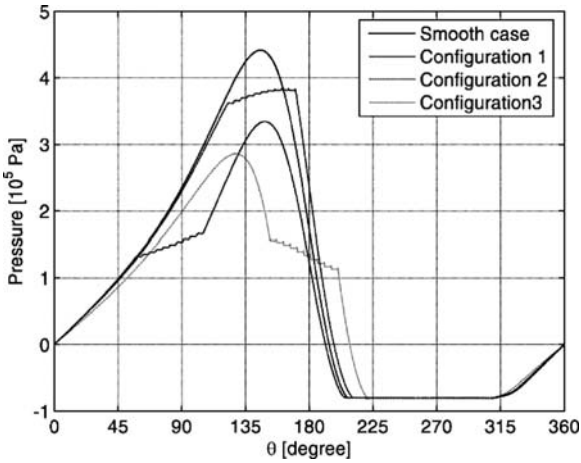

Figure 3.23. Pressure distribution in journal bearing with partially textured surface (Reproduced with permission from Cupillard, S., Glavatskih, S. and Cervantes, M. J. Computational fluid dynamics analysis of a journal bearing with surface texturing. *Proc IMechE Journal of Engineering Tribology*, **222**, 97–107, 2008, Professional Engineering Publishing).

profile to some degree, and that the distortion was always unfavorable as portrayed in the pressure plots of Figure 3.23. But they also found that in all configurations the dimples had the effect of reducing friction torque on the bearing, possibly by virtually eliminating frictional losses over the area occupied by the dimples. The magnitude of this reduction of friction, however, varied from configuration to configuration.

On computing the change in the coefficient of friction due to simultaneous changes in both load and friction force, Cupillard et al. discovered that it was positive for configurations 1 and 3 but decreased for dimple configuration 2 as shown in Table 3.5. This finding is in agreement with that of Brajdic-Mitidieri et al. (2005) on reduction of the friction coefficient in pocketed pad bearings. An increase in the friction coefficient was observed, however, at both low and high eccentricity ratios, but possibly due to eccentricity ratio dependent change in the position of the pressure maximum relative to the fixed dimple configuration.

It has been known for some time (Tonder, 2001) that roughening of the inlet section provides a lift to the parallel plate thrust bearing. In a follow up, Cupillard et al. investigated the effect of locating a set of shallow dimples at $\theta_i = 0^\circ$, $\Delta\theta = 48^\circ$. While keeping the eccentricity ratio constant at $\varepsilon = 0.61$, the friction coefficient increased for both

Table 3.5. *Changes in load, friction force and coefficient of friction* ($d/h_{min} = 30.1$, $w = 0.004\,m$, $\varepsilon = 0.61$)

Configuration (θ_i)	Load (%)	Friction (%)	Coefficient of friction
1 (57°)	–23.1	–9.2	+18.2
2 (122°)	–2.8	–10.7	–8.1
3 (152°)	–25.5	–16.2	+12.5

Table 3.6. *Changes in load, friction force and coefficient of friction* ($d = 45\,nm$, $w = 0.004\,m$)

Eccentricity ratio	Load (%)	Friction (%)	Coefficient of friction
0.05	+41.4	−0.8	−29.9
0.1	+14.5	−0.5	−13.1
0.15	+6.3	−0.3	−6.2
0.2	+3.1	+0.3	−2.7
0.3	−1.7	−0.2	+1.6

$d/h_{\min} = 0.34$ and $d/h_{\min} = 1.0$. It did decrease, however, on changing to $\varepsilon \leq 0.2$. The data obtained at various eccentricity ratios and $d = 45$ nm is displayed in Table 3.6.

Their main conclusion here is that to improve bearing performance at high eccentricities, deep dimples could be placed in the region of maximum pressure, bearing in mind, though, that improper positioning of the dimples may lead to pressure deterioration instead of pressure enhancement. At low eccentricities reduction of friction coefficient can be achieved by locating shallow dimples just downstream of the position of maximum film thickness. This latter action seems to originate from an additional pressure build-up rather than from a reduction of the frictional force.

3.5 Nomenclature

A	area of hydrostatic pad
B	slider width (in direction of motion)
C	radial clearance
D	bearing diameter
$\boldsymbol{F},\ F_R,\ F_T$	oil film force, radial and tangential components
$\boldsymbol{F}_\mu$	friction force
H	dimensionless film thickness
$H_p,\ H_f, H_T$	pumping power, shear power, total power
K_f	Kingsbury number
L	bearing length
N	shaft speed
O_B, O_J	center of bearing, journal
P	lubricant force per projected bearing area
Q	flow rate
Q_s	slider leakage
$R = R_B, R_J$	radius of bearing, journal
R_1, R_2	hydrostatic pad inner and outer radii
R_B, R_C	resistance resulting from bearing, capillary
S	Sommerfeld number
U, V	surface velocity components
U_0	effective surface velocity
U_M	maximum surface velocity
$\boldsymbol{V}, U, V$	surface velocity
V_0	squeeze velocity

$\boldsymbol{W}$	external load
a_f	area factor
c_μ	coefficient of friction
d	diameter of capillary restrictor
$\boldsymbol{f},\ f_R,\ f_T$	dimensionless lubricant force, radial and tangential components
$h,\ h_1,\ h_2$	film thickness, minimum and maximum values
h_1	perturbation on film thickness
h_f	friction factor
ℓ	length of capillary restrictor
m	slope of bearing surfaces
n	geometric constant
n_r	roughness number
$p,\ p_c$	pressure, center line pressure
$p_r,\ p_a,\ p_s$	recess, ambient, supply pressures
p_i	inlet pressures
p_1	perturbation on pressure
q_s	dimensionless side leakage
q_f	flow factor
t	time
$u_i(u,\ v,\ w)$	lubricant velocity components
$\boldsymbol{v}(u, v, w)$	lubricant velocity (components)
$x_i(x,\ y,\ z)$	orthogonal Cartesian coordinates
x_p	pivot position
$\Gamma_i,\ \Gamma_O$	recess boundary, pad outside boundary
$\psi,\ \alpha$	angular coordinates
α	position of load relative to pad leading edge
α	roughness amplitude
β	pad angle
δ	dimensionless pivot position, asperity height
ε	eccentricity ratio
η	wavelength of roughness pattern
θ	angular coordinate measured from line of centers
$\theta_1,\ \theta_2$	angular coordinates of pad leading edge, trailing edge
λ	dimensionless bearing stiffness
μ	lubricant viscosity
ξ	resistance ratio
ρ	lubricant density
σ	surface tension, rms roughness
τ	shear stress
τ_0	wall stress
ϕ	attitude angle
ω	shaft angular velocity
ω_w	angular frequency of applied load
$(\overline{\ })$	dimensionless quantity
$(\ )_{cav}$	evaluated at fluid–cavity interface
$(\ )_\varepsilon$	pertaining to roughness ε

3.6 References

Ai, X. and Cheng, H. S. 1994. A transient EHL analysis for line contacts with measured surface roughness using multigrid technique. *ASME J. Tribol.*, **116**, 549–58.

Ai, X. and Cheng, H. S. 1996. The effect of surface structure on EHL point contacts. *ASME J. Tribol.*, **118**, 569–66.

Ai, X. and Zheng, L. 1989. A general model for microelastohydrodynamic lubrication and its full numerical solution. *ASME J. Tribol.*, **111**, 569–76.

Almqvist, A. and Dasht, J. 2006. The homogenization process of the Reynolds equation describing compressible liquid flow. *Tribol. Int.,* **39**, 994–1002.

Anno, J., Walowit, J. A. and Allen, C. M. 1968. Microasperity lubrication. *ASME J. Lubr. Techol.*, **90**, 351–355.

Anno, J., Walowit, J. A. and Allen, C. M. 1969. Load support and leakage from microasperity-lubricated face seals. *ASME J. Lubr. Techol.*, **91**, 726–731.

Arghir, M., Roucou, N., Helene, M. and Frene, J. 2003. Theoretical analysis of the incompressible laminar flow in a macro-roughness cell. *ASME J. Tribol.*, **125**, 309–318.

Bhushan, B. and Tonder, K. 1989. Roughness induced shear and squeeze film effects in magnetic recording – Part i: Analysis. *ASME J. Tribol.*, **111**, 220–27.

Brajdic-Mitidieri, P., Gosman, A. D., Ioannides, E. and Spikes, H. A. 2005. CFD analysis of low friction pocketed pad bearing. *J. Tribol.*, **127**, 803–812.

Brizmer, V., Kligerman, Y. and Etsion, I. 2003. A laser surface textured parallel thrust bearing. *Tribol. Trans.*, **46** (3), 397–403.

Buscaglia, G. C. and Jai, M. 2000. A new numerical scheme for non uniform homogenized problems: application to the non linear Reynolds compressible equation. *Math. Probl. Eng.*, **7**, 355–378.

Cameron, A. 1966. *The Principles of Lubrication*. Wiley, New York.

Chang, L. and Webster, M. N. 1991. A study of elastohydrodynamic lubrication of rough surfaces. *ASME J. Tribol.*, **103**, 110–15.

Christensen, H. and Tonder, K. 1969. Tribology of rough surfaces: stochastic models of hydrodynamic lubrication. *Sintef Report*, Trondheim, Norway. No. 10/69-18.

Coyne, J. C. and Elrod, H. G. 1970a. Conditions for the rupture of a lubricating film, Part 1, Theoretical model. *Trans. ASME Ser. F.* **92**. 451–457.

Coyne, J. C. and Elrod, H. G. 1970b. Conditions for the rupture of a lubricating film, Part II, New boundary conditions for Reynolds' equation, *ASME Pap. 70-Lub-3.*

Cupillard, S., Glavatskih, S. and Cervantes, M. J. 2008. Computational fluid dynamics analysis of a journal bearing with surface texturing. *Proc IMechE J.*, **222**, 97–107.

Dai, R. X., Dong, Q., and Szeri, A. Z. 1992. Approximations in lubrication theory, *ASME J. Tribol.*, **114**, 14–25.

Dobrica, M. B. and Fillon, M. 2009. About the validity of Reynolds equation and inertia effects in textured sliders of infinite width. *Proc. IMechE J.,* **223**, 69–78.

Dowson, D. and Taylor, C. M. 1979. Cavitation in bearings. *Ann. Rev. Fluid. Mech.,* **11**, 35–66..

Dowson, D., Godet, M. and Taylor, C. M.(eds.).1975. *Cavitation and Related Phenomena in Lubrication*, Institute of Mechanical Engineers, London.

DuBois, G. B. and Ocvirk, F. W. 1955. Analytical derivation and experimental evaluation of short-bearing approximation for full journal bearings. *Natl. Advis. Comm. Aeronaut. Rep. 1157.*

Dyer, D. and Reason, B. R. 1976. A study of tensile stresses in a journal-bearing oil film. *J. Mech. Eng. Sci.*, **18**, 46–52.

Elrod, H. G. 1973. Thin film lubrication theory for Newtonian fluids with surfaces possessing striated roughness or grooving. *ASME J. Lubr. Technol.*, **95**, 484–89.

Elrod, H. G. 1979. A general theory for laminar lubrication with Reynolds roughness. *ASME J. Lubr. Technol.*, **101**, 8–14.

Elrod, H. G. 1981. A cavitation algorithm. *J. Lub. Tech.*, **103**, 350–54.

Elrod, H. G. and Adams, M. L. 1974. A computer program for cavitation and starvation problems. *Leeds-Lyon Conference on Cavitation*, Leeds University, England.

Etsion, I. 2005. State of the art in laser surface texturing. *ASME J. Tribol.*, **127**, 248–253.

Etsion, I. and Burstein, L. 1996. A model for mechanical face seals with regular microsurface structure. *Tribol. Trans.*, **39** (3), 677–683.

Etsion, I., Halperin, G., Brizmer, V. and Kligerman, Y. 2004. Experimental investigation of laser surface textured parallel thrust bearings. *Tribol. Lettr.*, **17** (2), 295–300.

Etsion, I., Kligerman, Y. and Halperin, G. 1999.Analytical and experimental investigation of laser textured mechanical face seal. *Tribol. Trans.*, **42** (3), 511–516.

Finlayson, B. 1972. *The Method of Weighted Residuals*. Academic Press, New York.

Floberg, L. 1961. On hydrodynamic lubrication with special reference to cavitation in bearings. *Chalmers Tek. Hoegsk. Handl.*, Dissertation.

Floberg, L. 1964. Cavitation in lubricating oil films. In *Cavitation in Real Liquids*, R. Davies (ed.), American Elsevier, New York. Floberg, L. 1965. On hydrodynamic lubrication with special reference to sub-cavity pressures and number of streamers in cavitation regions. *Acta Polytech. Scand. Mech. Eng. Ser.*, 19, 3–35.

Gourley, W. E. 1977. *Laminar flow between closely spaced rotating disks with variable viscosity*. M.Sc. Thesis, Univ. of Pittsburgh.

Gross, W. A. 1962. *Gas Film Lubrication*. Wiley, New York.

Hamilton, D. B., Walowit, J. A. and Allen, C. M. 1966. A theory of lubrication by micro irregularities. *ASME J. Basic Eng.*, **88**, 177–185.

Hays, D. F. 1958. Plane sliders of finite width. *Trans. ASLE,* **1**, 233–240.

Heller, S. and Shapiro, W. 1968. A numerical solution for the incompressible hybrid journal bearing with cavitation. *Trans. ASME*, ser. *F*, **90**, 508–515.

Hildebrand, F. B. 1965. *Methods of Applied Mathematics*. Prentice-Hall Inc., Englewood Cliffs, NJ.

Hu, Y. Z. and Tonder, K. 1992. Simulation of 3-D Random surface by 2-D digital filter and Fourier analysis. *Int. J. Mach. Tools Manufact.*, **32**, 38–93.

Jai, M. and Bou-Said, B. 2002. A comparison of homogenization and averaging techniques for the treatment of roughness in slip-flow-modified Reynolds equation. *ASME J. Tribol.*, **124**, 327–335.

Jameson, A. 1975. Transonic potential flow calculations in conservative form. *Proceedings of 2nd Computational Conference*, Hartford, pp. 148–161.

Kane, M. and Bou-Said, B. 2004. Comparison of homogenization and direct techniques for the treatment of roughness in incompressible lubrication. *ASME J. Tribol.*, **126**, 733–737.

Kligerman, Y. and Etsion, I. 2001. Analysis of hydrodynamic effects in surface textured circumferential gas seals. *STLE Paper* no. 01-AM-10.

Li, J. and Chen, H. 2007. Evaluation on applicability of Reynolds equation for squared transverse roughness compared to CFD. *J. Tribol*, **129**, 963967.

Lubrecht, A. A., ten Napel, W. E. and Bosma, R. 1986. Multigrid, an alternative method for calculating film thickness and pressure profile in elastohydrodynamic line contacts. *ASME J. Tribol.*, **110**, 551–56.

Lund, J. W. 1964. Spring and damping coefficients for the tilting-pad journal bearing. *ASLE Trans.*, **7**, 342–52.

Lund, L. and Tonder, K. 1997. Numerical simulation of the effects of three-dimensional roughness on hydrodynamic lubrication: correlation coefficients. *ASME J. Tribol.*, **119**, 315–22.

Mitsuya, Y. and Fukui, S. 1986. Stokes roughness effects on hydrodynamic lubrication. *ASME J. Tribol.*, **108**, 151–8.

O'Donoghue, J. P., Koch, P. R. and Hooke, C. J. 1970. Approximate short bearing analysis and experimental results obtained using plastic bearing liners. *Proc. Inst. Mech. Eng.,* **184**, pt. 3L, 190–196.

Opitz, H. 1968. Pressure Pad Bearings. In *Lubrication and Wear: Fundamentals and Application to Design. Proc. Inst. Mech. Eng.*, 182, pt. 3A.

Patir, N. 1978. A numerical procedure for random generation of rough surfaces. *WEAR*, **47**, 263–77.

Patir, N. and Cheng, H. S. 1978. An average flow model for determining effects of three-dimensional roughness on partial hydrodynamic lubrication. *ASME J. Lubr. Technol.*, **100**, 12–7.

Patir, N. and Cheng, H. S. 1979. Application of average flow model to lubrication between rough sliding surfaces. *ASME J. Lubr. Technol.*, **101**, 220–30.

Peeken, H. J., Knoll, G., Rienäcker, A., Lang, J. and Schönen, R. 1997. On the numerical determination of flow factors. *ASME J. Tribol.*, **119**, 259–64.

Peklenik, J. 1968. New developments in surface characterization and measurements by means of random process analysis. *Proc. Inst. Mech. Eng., London,* **182** (3K), 108–26.

Pinkus, O. 1958. Solutions of the tapered-land sector thrust bearing. *Trans. ASME,* **80**, 1510–1516.

Pinkus, O. and Sternlicht, B. 1961. *Theory of Hydrodynamic Lubrication*., McGraw-Hill, New York.

Plesset, M. S. 1949. The dynamics of cavitation bubbles. *J. Appl. Mech.*, **16**, 277–282.

Raimondi, A. A. 1959. Theoretical study of the effect of offset loads on the performance of a partial journal bearing. *Trans. ASLE,* **2**, 147–57.

Raimondi, A. A. 1960. The influence of longitudinal and transverse profile on the load capacity of pivoted pad bearings. *Trans. ASLE,* **3**, 265–76.

Raimondi, A. A. and Boyd, J. 1955. Applying bearing theory to the analysis and design of pad-type bearings. *Trans. ASME,* **77**, 287–309.

Raimondi, A. A. and Boyd, J. 1958. A Solution for the finite journal bearing and Its application to analysis and design, *Trans. ASLE,* **1**, 159–209.

Raimondi, A. A., and Szeri, A. Z. 1984. Journal and thrust Bearings. In *Handbook of Lubrication*, E. R. Booser, ed., Vol II, CRC Press, Boca Raton, FL.

Reddi, M. M. 1970. Finite element solution of the incompressible lubrication problem. *Trans. ASME, Ser. F*, **91**, 524–533.

Reynolds, O. 1886. On the theory of lubrication and its application to Mr. Beauchamp Tower's experiments. *Philos. Trans. Roy. Soc.,* **177**, pt. 1.

Rippel, H. C. 1963. *Cast Bronze Hydrostatic Bearing Manual*, Cast Bronze Bearing Institute, Cleveland.

Rowe, W. B. and O'Donoghue, J. P. 1971. A review of hydrostatic bearing design. In *Externally Pressurized Bearings*, pp. 157–187, Instit. Mech. Engrs. London.

Safar, Z. S. and Szeri, A. Z. 1972. A variational solution for the 120-degree partial journal bearing. *J. Mech. Eng. Sci.,* **14**, 221–223.

Savage, M. D. 1977. Cavitation in lubrication. *J. Fluid Mech.,* **80**, 743–767.

Smith, E. 1975. *A Study of Film Rupture in Hydrodynamic Lubrication*. Ph.D. Thesis, Univ. of Leeds.

Sommerfeld, A. 1904. Zürhydrodynamische theorie der Schmiermittelreibung, *Z. Math. Phys.*, **50**, 97–155.

Sun, D. C. and Chen, K.K. 1977. First effects of Stokes roughness of hydrodynamic lubrication. *ASME J. Lubr. Technol.*, **99**, 2–9.

Szeri, A. Z. 1975. Hydrostatic bearing pads: a matrix iterative solution. *Trans. ASLE,* **19**, 72–78.

Szeri, A. Z. 1980. *Tribology: Friction, Lubrication, and Wear*. Hemisphere Publishing Corporation. New York.

Szeri, A. Z. and Adams, M. L. 1978. Laminar flow between closely spaced rotating disks. *J. Fluid Mech.*, **86**, 1–14.

Szeri, A. Z. and Philips, C. 1974. An iterative solution for the plane hybrid bearing. *Trans. ASLE,* **18**, 116–122.

Szeri, A. Z. and Powers, D. 1967. Full journal bearings in laminar and turbulent regimes. *J. Mech. Eng. Sci.*, **9**, 167–176.

Szeri, A. Z. and Powers, D. 1970. Pivoted plane pad bearings: a variational solution. *Trans. ASME, Ser. F.*, **92**, 466–472.

Tao, L. N. 1959. The hydrodynamic lubrication of sector thrust bearings. *6th Midwest. Conf. Fluid Mech.*, Austin, Tex., 406–416.

Taylor, G. I. 1964. Cavitation in hydrodynamic lubrication. In *Cavitation in Real Liquids*, R. Davies (ed.), American Elsevier, New York.

Temperley, H. N. V. 1975. The tensile strength of liquids, in Cavitation and Related Phenomena in Lubrication. 11–13, Institution of Mechanical Engineers, London.

Tonder, K. 2001. Inlet roughness tribodevices: dynamic coefficients and leakage. *Tribol. Int.*, **34** (12), 847–852.

Tonder, K. and Christensen, H. 1972. Waviness and roughness in hydrodynamic lubrication. *Proc. Instn. Mech. Engrs.*, **186**, 807–12.

Tripp, J. H. 1983. Surface roughness effects in hydrodynamic lubrication: the flow factor method. *ASME J. Lubr. Technol.*, **105**, 458–465.

Tzeng, S.T. and Saibel, E. 1967. Surface roughness effect on slider lubrication. *ASLE Trans.*, **10**, 334–38.

Vijayaraghavan, D. and Keith, T. G. 1990a. An efficient, robust, and time accurate numerical scheme applied to a cavitation algorithm. *ASME J. Tribol.*, **112**, 44–51.

Vijayaraghavan, D. and Keith, T. G. 1990b. Grid transformation and adaption techniques applied in the analysis of cavitated journal bearings. *ASME J. Tribol.*, **112**, 52–59.

Vijayaraghavan, D. and Keith, T. G. 1990c. Analysis of a finite grooved misaligned journal bearing considering cavitation and starvation effects. *ASME J. Tribol.*, **112**, 60–67.

Vijayaraghavan, D. Keith, T. G. and Brew, D. E. 1991. Extension of transonic flow computational concepts in the analysis of cavitated bearings. *ASME J. Tribol.*, **113**, 539–46.

Woods, C. M. and Brewe, D. E. 1988. The solution of the Elrod algorithm for a dynamically loaded journal bearing using multigrid techniques. *ASME / STLE Tribology Conference*, Baltimore, Paper JAT 8–10.

Dynamic Properties of Lubricant Films

The behavior of rotors is strongly influenced by the characteristics of their supports. The forces generated on a journal by the lubricant film of its bearings are nonlinear functions of the position and velocity of the journal center.[1] Thus, to calculate the critical speeds and vibration amplitudes of rotors and to examine their stability against self-excited vibrations, knowledge of the response of the bearing lubricant film to journal displacements and velocities is essential.

In Figure 4.1 we schematize a rotor, of weight $2W$, and its support. Under steady load, the journal center is displaced from the bearing center to the steady operating position, O_{J_S}.

Rotor response to small excitation will be as shown in Figure 4.2. When the supporting bearings are rigid, shaft vibration amplitude varies with shaft speed, as indicated by the solid curve. This type of response would be expected when the rotor is running on rolling-contact bearings. Rigidly supported rotors cannot be operated at a *critical speed*[2] and can become "hung" on the critical when attempting to drive through.

We add spring and considerable damping to the system, in addition to the shaft spring and damping already present, when replacing the rigid supports with hydrodynamic bearings. This additional stiffness and damping will, as indicated in Figure 4.2, lower the critical speed below that calculated for rigid supports, and reduce the amplitude of vibration of the rotor.

The above example shows excitation occurring at running speed. In practice, however, excitation may occur at speeds other than running speed and might be caused by magnetic pulls, aerodynamic forces on turbine or compressor blades (Alford, 1965), gear impacts etc. Lubricant films themselves might originate destructive self-excited vibrations, which include *oil whip* at somewhat less than one-half running speed (Hagg, 1946). The self-excited vibration occurring at exactly one-half (or other exact submultiple) of the running speed is known as *subharmonic resonance* (Den Hartog, 1956).

In Figure 4.3 we reduce the rotor-bearing configuration of Figure 4.1 to a simple dynamical system consisting of a mass, springs, and dashpots. In this schematic, half the rotor mass, $M = W/g$, is concentrated at O_{J_S}, the steady running position of the journal. If excitation, F, at some frequency, Ω, is applied to this system, the mass center will respond by orbiting about O_{J_S}, its instantaneous orbital position denoted by O_J. It is implied here that the dynamic displacement $(O_{J_S} - O_J)$ is small relative to bearing clearance. For "large" dynamic displacements and velocities the behavior of lubricant films is strongly nonlinear, rendering the representation in Figure 4.3 very approximate.

[1] A more thorough examination of the problem reveals that the force on an orbiting journal is dependent on acceleration as well as on position and velocity (see e.g., Szeri, Raimondi, and Giron, 1983). For simplicity, however, we do not include acceleration, i.e., fluid inertia, effects here, and leave their analysis to Chapter 5.

[2] By critical speed we understand any rotor resonance that is excited by rotor unbalance. There can be, thus, several critical speeds.

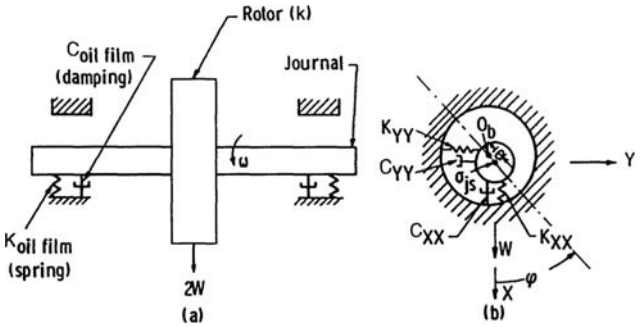

Figure 4.1. Dynamical elements of rotor-shaft configuration. (Reprinted with permission from Raimondi, A. A. and Szeri, A. Z. Journal and thrust bearings. In Booser, E. R., *CRC Handbook of Lubrication*. Copyright CRC Press, Boca Raton, Florida. © 1984.)

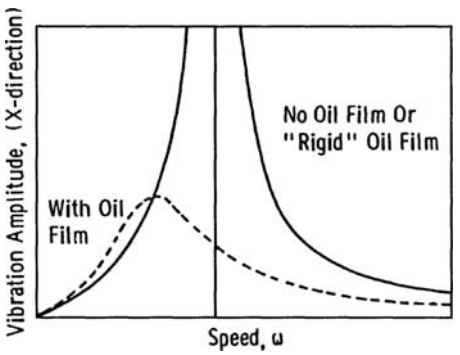

Figure 4.2. Effect of oil film on shaft response. (Reprinted with permission from Raimondi, A. A. and Szeri, A. Z. Journal and thrust bearings. In Booser, E. R., *CRC Handbook of Lubrication*. Copyright CRC Press, Boca Raton, Florida. © 1984.)

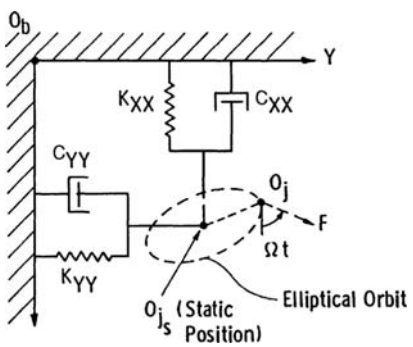

Figure 4.3. Representation of oil film as a simple dynamical system of springs and dampers (cross-film springs K_{xy}, K_{yx} and dampers C_{xy}, C_{yx} are not shown). (Reprinted with permission from Raimondi, A. A. and Szeri, A. Z. Journal and thrust bearings. In Booser, E. R., *CRC Handbook of Lubrication.* Copyright CRC Press, Boca Raton, Florida. © 1984.)

For small dynamic displacements and velocities of the journal the oil film forces may be linearized about their static equilibrium value, but even in this linear approximation the lubricant film cannot be simulated by a simple elastic-dissipative system. Cross-coupling stiffness and damping are needed to describe the relationship between the incremental oil-film forces and the journal displacements and velocities that cause them:

$$\begin{pmatrix} dF_x \\ dF_y \end{pmatrix} = -\begin{pmatrix} K_{xx} & K_{xy} \\ K_{yx} & K_{yy} \end{pmatrix}\begin{pmatrix} x \\ y \end{pmatrix} - \begin{pmatrix} C_{xx} & C_{xy} \\ C_{yx} & C_{yy} \end{pmatrix}\begin{pmatrix} \dot{x} \\ \dot{y} \end{pmatrix}. \tag{4.1}$$

In this chapter, we will show how to evaluate the *linearized force coefficients* $K_{xx}, \ldots, C_{yy}$. These coefficients define the rotor support for critical speed calculations.

For example, if a vibrating system, consisting of a rigid rotor of mass $2M$ running on hydrodynamic bearings, is excited by a force F at frequency Ω, its response is described by the equations of motion

$$\begin{aligned} M\ddot{x} + C_{xx}\dot{x} + C_{xy}\dot{y} + K_{xx}x + K_{xy}y &= F\cos\Omega t, \\ M\ddot{y} + C_{yy}\dot{y} + C_{yx}\dot{x} + K_{yy}y + K_{yx}x &= F\sin\Omega t. \end{aligned} \tag{4.2}$$

By making the right-hand sides of these equations vanish, existence of any self-excited vibrations can also be investigated (Den Hartog, 1956). When the bearing constitutes an element in a complex dynamical system, it is usually incorporated in the system's equations of motion through its spring and damping coefficients. All eight oil film coefficients are required in order to make accurate dynamical analyses of rotor-shaft configurations.

4.1 Fixed Pad

Linearized Force Coefficients

Let O_B represent the center of the bearing in Figure 4.4. The static equilibrium position of the rotating shaft is O_{J_S}, the eccentricity is ε_0, and the attitude angle is ϕ_0. The components of the lubricant force, resolved along the fixed directions ($\boldsymbol{R}$, $\boldsymbol{T}$), are $(F_R)_0$ and $(F_T)_0$.[3]

If there is a small unbalanced force on the journal, the journal will orbit about its static equilibrium position (e_0, ϕ_0). At a particular instant it will occupy position O_J, a generic point on the orbit. In O_J the eccentricity is $e = e_0 + \Delta e$, the attitude angle is $\phi = \phi_0 + \Delta\phi$, and the journal possesses instantaneous velocities $\dot{e}$ and $e\dot{\phi}$. The instantaneous lubricant force now has components F_r and F_t, relative to the instantaneous radial and tangential coordinates r and t, respectively.

The instantaneous force will now be referred to the fixed (R, T) coordinate system,

$$\begin{pmatrix} F_R \\ F_T \end{pmatrix} = \begin{pmatrix} \cos\Delta\phi & -\sin\Delta\phi \\ \sin\Delta\phi & \cos\Delta\phi \end{pmatrix}\begin{pmatrix} F_r \\ F_t \end{pmatrix}. \tag{4.3}$$

For small departures from equilibrium we have the approximations

$$\cos\Delta\phi \approx 1, \qquad \sin\Delta\phi \approx \Delta\phi$$

[3]Note that here $F_R > 0$ when pointing away from the origin of the (e, ϕ) coordinate system. This is contrary to the scheme adopted by some authors (Pinkus and Sternlicht, 1961; Lund, 1964), but follows accepted mathematical notation (see, e.g., Trumpler, 1966).

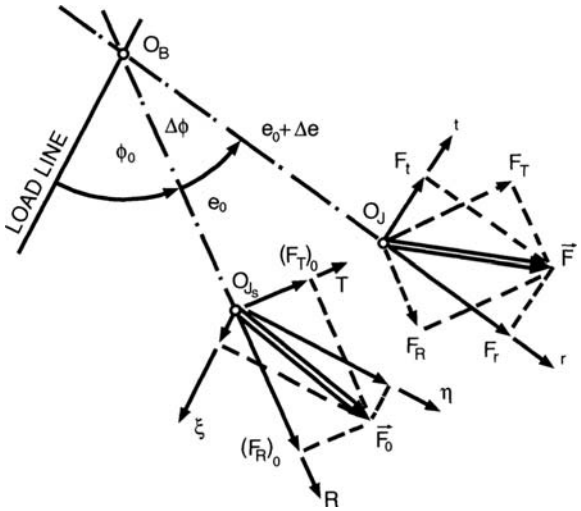

Figure 4.4. Force decomposition in journal bearings (for illustration only; not to scale).

and Eq. (4.3) can be written as

$$\begin{aligned} F_R &= F_r - \Delta\phi F_t, \\ F_T &= \Delta\phi F_r + F_t. \end{aligned} \tag{4.4}$$

We are interested in evaluating the increase in the force components[4] over their equilibrium values, due to departure from the equilibrium

$$\begin{aligned} \Delta F_R &= F_R - (F_R)_0, \\ \Delta F_T &= F_T - (F_T)_0. \end{aligned} \tag{4.5}$$

The force excess can be evaluated from Eq. (4.4) according to

$$\begin{aligned} \Delta F_R &= F_r - (F_R)_0 - \Delta\phi F_t, \\ \Delta F_T &= \Delta\phi F_r + F_t - (F_T)_0\,. \end{aligned} \tag{4.6}$$

The scalar functions F_r and F_t are now expanded in Taylor series about the equilibrium position. For F_r we have, neglecting higher-order terms,

$$F_r = (F_R)_0 + \left(\frac{\partial F_R}{\partial e}\right)_0 de + \left(\frac{\partial F_R}{\partial \phi}\right)_0 d\phi + \left(\frac{\partial F_R}{\partial \dot{e}}\right)_0 d\dot{e} + \left(\frac{\partial F_R}{\partial \dot{\phi}}\right)_0 d\dot{\phi}, \tag{4.7}$$

where all derivatives are evaluated in the equilibrium position, as indicated by the zero subscript. The expansion is similar for F_t.

Substituting the Taylor expansions for F_r and F_t into Eq. (4.6) and, again, neglecting higher-order terms, we obtain (from here on we drop the zero subscript, remembering that

[4]The force increment is resolved relative to the fixed (R, T) axes in Eq. (4.5).

all derivatives are evaluated at equilibrium)

$$\begin{pmatrix} dF_R \\ dF_T \end{pmatrix} = \begin{pmatrix} \dfrac{\partial F_R}{\partial \varepsilon} & \dfrac{\partial F_R}{\partial \phi} - F_T \\ \dfrac{\partial F_T}{\partial \varepsilon} & \dfrac{\partial F_T}{\partial \phi} + F_R \end{pmatrix} \begin{pmatrix} d\varepsilon \\ d\phi \end{pmatrix} + \begin{pmatrix} \dfrac{\partial F_R}{\partial \dot{\varepsilon}} & \dfrac{\partial F_R}{\partial \dot{\phi}} \\ \dfrac{\partial F_T}{\partial \dot{\varepsilon}} & \dfrac{\partial F_T}{\partial \dot{\phi}} \end{pmatrix} \begin{pmatrix} d\dot{\varepsilon} \\ d\dot{\phi} \end{pmatrix}. \tag{4.8}$$

To calculate the force derivatives required in Eq. (4.8), we have to go to the Reynolds equation (3.33), which we nondimensionalize according to Eq. (3.34). However, under dynamic loading conditions it is appropriate to employ another nondimensional pressure $\hat{p}$ that is related to $\bar{p}$ of Eq. (3.34) through[5]

$$\hat{p} = \frac{\bar{p}}{\left(1 - 2\dot{\phi}/\omega\right)}.$$

Note that at static equilibrium ($\varepsilon = \varepsilon_0$, $\phi = \phi_0$, $\dot{\phi} = \dot{\varepsilon} = 0$) the pressure defined under dynamic loading, $\hat{p}$, reduces to the pressure defined under static loading, $\bar{p}$.

In terms of the *dynamic pressure* $\hat{p}$, as it will be referred to here, the nondimensional Reynolds equation has the form.

$$\frac{\partial}{\partial\theta}\left(H^3\frac{\partial\hat{p}}{\partial\theta}\right) + \left(\frac{D}{L}\right)^2 \frac{\partial}{\partial\bar{z}}\left(H^3\frac{\partial\hat{p}}{\partial\bar{z}}\right) = -12\pi\varepsilon\sin\theta + 24\pi\frac{\dot{\varepsilon}/\omega}{\left(1 - 2\dfrac{\dot{\phi}}{\omega}\right)}\cos\theta. \tag{4.9}$$

As noted from Eq. (4.9), the dynamic pressure $\hat{p}$ is a function of the variables ε, ϕ, $\dot{\varepsilon}/\omega$ and $\dot{\phi}/\omega$. Its dependence on the attitude angle ϕ enters through the definition of the film thickness

$$\begin{aligned} H &= 1 + \varepsilon\cos\theta \\ &= 1 + \varepsilon\cos[\Xi - (\phi + \psi)], \end{aligned}$$

where $\Xi = 0$ is a fixed position (Figure 3.5).

We solve Eq. (4.9) subject to the Swift-Stieber boundary condition to obtain the force coefficients. The nondimensional force components are

$$\bar{F}_R = \frac{F_R/LD}{\mu N(R/C)^2} = \left(1 - 2\frac{\dot{\phi}}{\omega}\right)\left[\frac{1}{2}\int_0^1\int_0^{\theta_2}\hat{p}\cos\theta\, d\theta\, d\bar{z}\right], \tag{4.10a}$$

$$\bar{F}_T = \frac{F_T/LD}{\mu N(R/C)^2} = \left(1 - 2\frac{\dot{\phi}}{\omega}\right)\left[\frac{1}{2}\int_0^1\int_0^{\theta_2}\hat{p}\sin\theta\, d\theta\, d\bar{z}\right]. \tag{4.10b}$$

Employing the notation

$$f_R = \frac{1}{2}\int_0^1\int_0^{\theta_1}\hat{p}\cos\theta\, d\theta\, d\bar{z},$$

$$f_T = \frac{1}{2}\int_0^1\int_0^{\theta_1}\hat{p}\sin\theta\, d\theta\, d\bar{z},$$

[5] Although Eq. (3.33) is linear in ω, $\dot{e}$, and $\dot{\phi}$, superposition of three separate solutions is not permitted, owing to the nonlinear condition $p \geq 0$, and to the fact that the $p = 0$ contour is, in general, dependent on all three parameters ω, $\dot{e}$, and, $\dot{\phi}$. However, at least two of the variables, ω and $\dot{\phi}$, enter the equation in the form $(\omega - 2\dot{\phi})$. It is this property of Eq. (3.34) that is being exploited here.

we can write Eq. (4.10) in the symbolic form

$$\bar{F}_R = \left(1 - 2\frac{\dot{\phi}}{\omega}\right) f_R \left[\varepsilon, \phi, \frac{\dot{\varepsilon}/\omega}{(1 - 2\dot{\phi}/\omega)}\right], \tag{4.11a}$$

$$\bar{F}_T = \left(1 - 2\frac{\dot{\phi}}{\omega}\right) f_T \left[\varepsilon, \phi, \frac{\dot{\varepsilon}/\omega}{(1 - 2\dot{\phi}/\omega)}\right]. \tag{4.11b}$$

The partial derivatives of the force components may now be evaluated:

$$\begin{aligned}
\frac{\partial \bar{F}_R}{\partial \varepsilon} &= (1 - 2\dot{\phi}/\omega)\frac{\partial f_R}{\partial \varepsilon}, \\
\frac{\partial \bar{F}_R}{\partial \phi} &= (1 - 2\dot{\phi}/\omega)\frac{\partial f_R}{\partial \phi}, \\
\frac{\partial \bar{F}_R}{\partial(\dot{\varepsilon}/\omega)} &= (1 - 2\dot{\phi}/\omega)\frac{\partial f_R}{\partial\left(\dfrac{\dot{\varepsilon}/\omega}{1 - 2\dot{\phi}/\omega}\right)}\frac{1}{(1 - 2\dot{\phi}/\omega)}, \\
\frac{\partial \bar{F}_R}{\partial(\dot{\phi}/\omega)} &= -2f_R + (1 - 2\dot{\phi}/\omega)\frac{\partial f_R}{\partial\left(\dfrac{\dot{\varepsilon}\omega}{1 - 2\dot{\phi}/\omega}\right)}\frac{(2\dot{\varepsilon}/\omega)}{(1 - 2\dot{\phi}/\omega)^2}.
\end{aligned} \tag{4.12}$$

When Eq. (4.12) is evaluated at the equilibrium point $\varepsilon = \varepsilon_0$, $\phi = \phi_0$, $\dot{\varepsilon} = 0$, $\dot{\phi} = 0$, we obtain[6] (Szeri, 1966)

$$\begin{pmatrix} d\bar{F}_R \\ d\bar{F}_T \end{pmatrix} = \begin{pmatrix} \dfrac{\partial f_R}{\partial \varepsilon} & \dfrac{\partial f_R}{\varepsilon \partial \phi} - \dfrac{f_T}{\varepsilon} \\ \dfrac{\partial f_T}{\partial \varepsilon} & \dfrac{\partial f_T}{\varepsilon \partial \phi} + \dfrac{f_R}{\varepsilon} \end{pmatrix} \begin{pmatrix} d\varepsilon \\ \varepsilon d\phi \end{pmatrix} + \begin{pmatrix} \dfrac{\partial f_R}{\partial \dot{\varepsilon}/\omega} & -\dfrac{2f_R}{\varepsilon} \\ \dfrac{\partial f_T}{\partial \dot{\varepsilon}/\omega} & -\dfrac{2f_T}{\varepsilon} \end{pmatrix} \begin{pmatrix} d(\dot{\varepsilon}/\omega) \\ \varepsilon d(\dot{\phi}/\omega) \end{pmatrix}. \tag{4.13}$$

The first matrix on the right describes the oil film response to shaft displacement and is called the (nondimensional) stiffness matrix, $\bar{\boldsymbol{k}}$. The second matrix describes response to velocities $\dot{\varepsilon}/\omega$ and $\varepsilon d(\dot{\phi}/\omega)$ and is called the (nondimensional) damping matrix, $\bar{\boldsymbol{c}}$:

$$\bar{\boldsymbol{k}} = \begin{pmatrix} \dfrac{\partial f_R}{\partial \varepsilon} & \dfrac{\partial f_R}{\varepsilon \partial \phi} - \dfrac{f_T}{\varepsilon} \\ \dfrac{\partial f_T}{\partial \varepsilon} & \dfrac{\partial f_T}{\varepsilon \partial \phi} + \dfrac{f_R}{\varepsilon} \end{pmatrix}, \tag{4.14a}$$

$$\bar{\boldsymbol{c}} = \begin{pmatrix} \dfrac{\partial f_R}{\partial \dot{\varepsilon}/\omega} & -\dfrac{2f_R}{\varepsilon} \\ \dfrac{\partial f_T}{\partial \dot{\varepsilon}/\omega} & -\dfrac{2f_T}{\varepsilon} \end{pmatrix} \tag{4.14b}$$

(note that we dropped the zero suffix for convenience, remembering that all forces and force derivatives are to be evaluated under conditions of static equilibrium).

[6] We note that the rate of change of f_R with respect to its argument $(\dot{\varepsilon}/\omega)/(1 - 2\dot{\phi}/\omega)$ can be evaluated at arbitrary value of $\dot{\phi}$, say zero, varying $\dot{\varepsilon}/\omega$ only.

The nondimensional matrices $\bar{\boldsymbol{k}}$ and $\bar{\boldsymbol{c}}$ are related to their dimensional counterparts $\boldsymbol{k}$ and $\boldsymbol{c}$, respectively, through

$$\bar{\boldsymbol{k}} = \frac{C}{LD\mu N\left(\frac{R}{C}\right)^2}\boldsymbol{k}, \qquad \bar{\boldsymbol{c}} = \frac{C\omega}{LD\mu N\left(\frac{R}{C}\right)^2}\boldsymbol{c}. \tag{4.14c}$$

The elements $\boldsymbol{k}$ and $\boldsymbol{c}$ have dimensions force/length and force/velocity, respectively. The nondimensionalization

$$\bar{\bar{\boldsymbol{k}}} = \frac{C}{W}\boldsymbol{k} \quad \text{and} \quad \bar{\bar{\boldsymbol{c}}} = \frac{C\omega}{W}\boldsymbol{c}, \tag{4.14d}$$

where W is the external load on the journal, is sometimes also employed in the literature. Then $\bar{\bar{\boldsymbol{k}}} = S\bar{\boldsymbol{k}}$ and $\bar{\bar{\boldsymbol{c}}} = S\bar{\boldsymbol{c}}$, where S is the Sommerfeld number.

Analytical Solutions

Long Bearings

Under dynamic conditions the pressure is given by

$$\begin{aligned}\hat{p} = 12\pi &\left[\int_0^\theta \frac{d\theta}{H^2} - \frac{\int_0^{\theta_2}\frac{d\theta}{H^2}}{\int_0^{\theta_2}\frac{d\theta}{H^3}}\int_0^\theta \frac{d\theta}{H^3}\right] \\ &+ 24\pi\left[\int_0^\theta \frac{\sin\theta}{H^2}d\theta - \frac{\int_0^{\theta_2}\frac{\sin\theta}{H^2}d\theta}{\int_0^{\theta_2}\frac{d\theta}{H^3}}\int_0^\theta \frac{d\theta}{H^3}\right]\frac{\dot{\varepsilon}/\omega}{\left(1-2\dot{\phi}/\omega\right)}.\end{aligned} \tag{4.15}$$

Here $\theta = \theta_2$ is the position of the film-cavity interface. The integrals can be evaluated using the Sommerfeld substitution (3.42), in which the boundaries $\theta = 0$ and π, and $\theta = 0$ and 2π translate to $\psi = 0$ and π and $\psi = 0$ and 2π, respectively.

For the *Sommerfeld boundary condition* $\bar{p}(0) = \bar{p}(2\pi)$, Eq. (4.15) integrates to

$$\hat{p} = 12\pi\left\{\frac{\varepsilon\sin\theta(2+\varepsilon\cos\theta)}{(2+\varepsilon^2)(1+\varepsilon\cos\theta)^2} + \frac{1}{\varepsilon}\left[\frac{1}{(1+\varepsilon\cos\theta)^2} - \frac{1}{(1+\varepsilon)^2}\right]\frac{\dot{\varepsilon}/\omega}{\left(1-2\dot{\phi}/\omega\right)}\right\}. \tag{4.16}$$

[Under Gümbel boundary conditions, $p(0) = p(\pi)$, $p \geq 0$, there is an additional term on the right-hand side of Eq. (4.16) as shown by Trumpler (1966).]

The force components are calculated from Eq. (4.16) according to Eq. (3.78)

$$\begin{aligned} f_R &= -\frac{12\pi^2}{(1-\varepsilon^2)^{3/2}}\frac{\dot{\varepsilon}/\omega}{(1-2\dot{\phi}/\omega)}, \\ f_T &= \frac{12\pi^2\varepsilon}{(2+\varepsilon^2)(1-\varepsilon^2)^{1/2}}. \end{aligned} \tag{4.17}$$

Table 4.1. *Analytical stiffness and damping coefficients*

	Long bearing		Short bearing
	Sommerfeld BC.	Gümbel BC.	Gümbel BC.
$\bar{k}_{RR}$	0	$\dfrac{-24\pi\varepsilon(2+\varepsilon^4)}{(2+\varepsilon^2)^2(1-\varepsilon^2)^2}$	$-\dfrac{8\pi\varepsilon(1+\varepsilon^2)}{(1-\varepsilon^2)^3}\left(\dfrac{L}{D}\right)^2$
$\bar{k}_{RT}$	$\dfrac{-12\pi^2}{(2+\varepsilon^2)^2(1-\varepsilon^2)^{1/2}}$	$\dfrac{-6\pi^2}{(2+\varepsilon^2)^2(1-\varepsilon^2)^{1/2}}$	$\dfrac{-\pi^2}{(1-\varepsilon^2)^{3/2}}\left(\dfrac{L}{D}\right)^2$
$\bar{k}_{TR}$	$\dfrac{12\pi^2(2-\varepsilon^2+2\varepsilon^4)}{(2+\varepsilon^2)^2(1-\varepsilon^2)^{3/2}}$	$\dfrac{6\pi^2(2-\varepsilon^2+2\varepsilon^4)}{(2+\varepsilon^2)(1-\varepsilon^2)^{3/2}}$	$\dfrac{\pi^2(1+2\varepsilon^2)}{(1-\varepsilon^2)^{5/2}}\left(\dfrac{L}{D}\right)^2$
$\bar{k}_{TT}$	0	$\dfrac{-12\pi\varepsilon}{(2+\varepsilon^2)^2(1-\varepsilon^2)}$	$\dfrac{-4\pi\varepsilon}{(1-\varepsilon^2)^2}\left(\dfrac{L}{D}\right)^2$
$\bar{c}_{RR}$	$\dfrac{-12\pi^2}{(1-\varepsilon^2)^{3/2}}$	$\dfrac{-12\pi}{(1-\varepsilon^2)^{3/2}}\left[\dfrac{\pi}{2}-\dfrac{8}{\pi(2+\varepsilon^2)}\right]$	$-\dfrac{2\pi^2(1+2\varepsilon^2)}{(1-\varepsilon^2)^{5/2}}\left(\dfrac{L}{D}\right)^2$
$\bar{c}_{RT}$	0	$\dfrac{24\pi\varepsilon}{(2+\varepsilon^2)(1-\varepsilon^2)}$	$\dfrac{8\pi\varepsilon}{(1-\varepsilon^2)^2}\left(\dfrac{L}{D}\right)^2$
$\bar{c}_{TR}$	0	$\dfrac{24\pi\varepsilon}{(2+\varepsilon^2)(1-\varepsilon^2)}$	$\dfrac{8\pi\varepsilon}{(1-\varepsilon^2)^2}\left(\dfrac{L}{D}\right)^2$
$\bar{c}_{TT}$	$\dfrac{-24\pi^2}{(2+\varepsilon^2)(1-\varepsilon^2)^{1/2}}$	$\dfrac{-12\pi^2}{(2+\varepsilon^2)(1-\varepsilon^2)^{1/2}}$	$-\dfrac{2\pi^2}{(1-\varepsilon^2)^{3/2}}\left(\dfrac{L}{D}\right)^2$
S	$\dfrac{(2+\varepsilon^2)\sqrt{1-\varepsilon^2}}{12\pi^2\varepsilon}$	$\dfrac{(2+\varepsilon^2)(1-\varepsilon^2)}{6\pi\varepsilon\sqrt{4\varepsilon^2+\pi^2(1-\varepsilon^2)}}$	$\dfrac{(1-\varepsilon^2)^2(D/L)^2}{\pi\varepsilon\sqrt{\pi^2(1-\varepsilon^2)+16\varepsilon^2}}$

There is no dependence on θ in full journal bearings so that $\partial f_R/\partial\theta = \partial f_T/\partial\theta = 0$, and on substituting Eq. (4.17) into Eq. (4.14) we obtain the $\bar{\boldsymbol{k}}$ and $\bar{\boldsymbol{c}}$ matrices, as shown in Table 4.1.

For the *Gümbel boundary conditions*, $\bar{p}(0) = \bar{p}(\pi)$, the force components are[7]

$$f_R = -\frac{12\pi\varepsilon^2}{(2+\varepsilon^2)(1-\varepsilon^2)} - \frac{12\pi}{(1-\varepsilon^2)^{3/2}}\left[\frac{\pi}{2}-\frac{8}{\pi(2+\varepsilon^2)}\right]\frac{\dot{\varepsilon}/\omega}{(1-2\dot{\phi}/\omega)}, \tag{4.18a}$$

$$f_T = -\frac{6\pi^2\varepsilon}{(2+\varepsilon^2)(1-\varepsilon^2)^{1/2}} + \frac{24\pi\varepsilon}{(2+\varepsilon^2)(1-\varepsilon^2)}\frac{\dot{\varepsilon}/\omega}{(1-2\dot{\phi}/\omega)}. \tag{4.18b}$$

[7]Note that if the pressure is evaluated under the Sommerfeld boundary conditions $p(0) = p(2\pi) = 0$, and then integrated from $\theta = 0$ to $\theta = \pi$ (i.e., $p \geq 0$), the dynamic part of f_R in Eq. (4.18a) will be different (Vance, 1988). Our analysis agrees with that of Hori (1959) and Trumpler (1966).

Short Bearings

Under the Gümbel condition, $p \geq 0$, the pressure distribution is

$$\left(\frac{D}{L}\right)^2 \bar{p} = 6\pi \frac{(1-\bar{z}^2)}{(1-\varepsilon\cos\theta)^3}\left[\varepsilon\sin\theta - 2\frac{\dot{\varepsilon}/\omega}{(1-2\dot{\phi}/\omega)}\cos\theta\right] \tag{4.19}$$

and the force components are

$$\begin{aligned}\left(\frac{D}{L}\right)^2 f_R &= -\frac{4\pi\varepsilon^2}{(1-\varepsilon^2)^2} - \frac{2\pi^2(1+2\varepsilon^2)}{(1-\varepsilon^2)^{5/2}}\frac{\dot{\varepsilon}/\omega}{(1-2\dot{\phi}/\omega)},\\ \left(\frac{D}{L}\right)^2 f_T &= \frac{\pi^2\varepsilon}{(1-\varepsilon^2)^{3/2}} + \frac{8\pi\varepsilon}{(1-\varepsilon^2)^2}\frac{\dot{\varepsilon}/\omega}{(1-2\dot{\phi}/\omega)}.\end{aligned} \tag{4.20}$$

The linearized spring and damping coefficients derived from Eq. (4.20) are shown in Table 4.1, they are obtained by substituting Eq. (4.20) into Eq. (4.14).

Coordinate Transformations

In place of a single, fixed bearing pad, multiple pivoted-pads are often employed. The characteristics of pivoted-pad bearings are evaluated by combining the characteristics of single pads in suitable manner. With this in view, it is expedient to transform the characteristics of the single pad, i.e., the $\bar{\boldsymbol{k}}$ and $\bar{\boldsymbol{c}}$ matrices of Eq. (4.14), to a coordinate system (ξ, η) that is fixed relative to the pivot and is located in the static equilibrium position O_{J_S}. The ξ axis passes through the pivot, and the (ξ, η) axes are related to the (R, T) axes by rotation through ϕ_0.

It is easily seen from Figure 4.4 that under the coordinate transformation

$$\begin{pmatrix} d\bar{\xi} \\ d\bar{\eta} \end{pmatrix} = \boldsymbol{Q}\begin{pmatrix} d\varepsilon \\ \varepsilon d\phi \end{pmatrix}, \qquad \boldsymbol{Q} = \begin{pmatrix} \cos\phi_0 & -\sin\phi_0 \\ \sin\phi_0 & \cos\phi_0 \end{pmatrix}, \tag{4.21}$$

where the angle ϕ_0 is measured from $\bar{\xi}$ to ε counterclockwise and $\bar{\xi} = \varepsilon/C$, $\bar{\eta} = \eta/C$, the force components $(d\bar{F}_R,\ d\bar{F}_T)$ are transformed according to

$$\begin{pmatrix} d\bar{F}_\xi \\ d\bar{F}_\eta \end{pmatrix} = \boldsymbol{Q}\begin{pmatrix} d\bar{F}_R \\ d\bar{F}_T \end{pmatrix}. \tag{4.22}$$

Substituting from Eqs. (4.21) and (4.14) into Eq. (4.22), we find that

$$\begin{pmatrix} d\bar{F}_\xi \\ d\bar{F}_\eta \end{pmatrix} = \boldsymbol{Q}\bar{\boldsymbol{k}}\boldsymbol{Q}^T\begin{pmatrix} \bar{\xi} \\ \bar{\eta} \end{pmatrix} + \boldsymbol{Q}\boldsymbol{c}\bar{\boldsymbol{Q}}^T\begin{pmatrix} \dot{\bar{\xi}} \\ \dot{\bar{\eta}} \end{pmatrix}. \tag{4.23}$$

Employing the notation[8]

$$\bar{\boldsymbol{K}} = -\boldsymbol{Q}\bar{\boldsymbol{k}}\boldsymbol{Q}^T, \quad \bar{\boldsymbol{C}} = -\boldsymbol{Q}\bar{\boldsymbol{c}}\boldsymbol{Q}^T \tag{4.24}$$

and by substitution into Eq. (4.23),

$$\begin{pmatrix} d\bar{F}_\xi \\ d\bar{F}_\eta \end{pmatrix} = -\bar{\boldsymbol{K}}\begin{pmatrix} \bar{\xi} \\ \bar{\eta} \end{pmatrix} - \bar{\boldsymbol{C}}\begin{pmatrix} \dot{\bar{\xi}} \\ \dot{\bar{\eta}} \end{pmatrix}. \tag{4.25}$$

[8]The transformation in Eq. (4.24) identifies $\bar{\boldsymbol{k}}$ and $\bar{\boldsymbol{c}}$ as second-order Cartesian tensors.

The component of the stiffness and damping matrices in Eq. (4.24) are given by (Lund, 1964; Szeri, 1966)

$$\begin{aligned}
\bar{K}_{\xi\xi} &= -\frac{\partial f_R}{\partial \varepsilon}\cos^2\phi - \frac{\partial f_T}{\varepsilon\partial\phi}\sin^2\phi + \left(\frac{\partial f_T}{\partial\varepsilon} + \frac{\partial f_R}{\varepsilon\partial\phi}\right)\frac{\sin 2\phi}{2} - \frac{f_\eta}{\varepsilon}\sin\phi,\\
\bar{K}_{\xi\eta} &= -\frac{\partial f_R}{\varepsilon\partial\phi}\cos^2\phi + \frac{\partial f_T}{\partial\varepsilon}\sin^2\phi + \left(\frac{\partial f_T}{\varepsilon\partial\phi} - \frac{\partial f_R}{\partial\varepsilon}\right)\frac{\sin 2\phi}{2} + \frac{f_\eta}{\varepsilon}\cos\phi,\\
\bar{K}_{\eta\xi} &= -\frac{\partial f_T}{\partial\varepsilon}\cos^2\phi + \frac{\partial f_R}{\varepsilon\partial\phi}\sin^2\phi + \left(\frac{\partial f_T}{\varepsilon\partial\phi} - \frac{\partial f_R}{\partial\varepsilon}\right)\frac{\sin 2\phi}{2} + \frac{f_\xi}{\varepsilon}\cos\phi,\\
\bar{K}_{\eta\eta} &= -\frac{\partial f_T}{\varepsilon\partial\phi}\cos^2\phi - \frac{\partial f_R}{\partial\varepsilon}\sin^2\phi - \left(\frac{\partial f_R}{\varepsilon\partial\phi} + \frac{\partial f_T}{\partial\varepsilon}\right)\frac{\sin 2\phi}{2} - \frac{f_\xi}{\varepsilon}\cos\phi,
\end{aligned} \tag{4.26a}$$

$$\begin{aligned}
\bar{C}_{\xi\xi} &= -\frac{\partial f_R}{\partial\dot{\varepsilon}/\omega}\cos^2\phi + \frac{\partial f_T}{\partial\dot{\varepsilon}/\omega}\frac{\sin 2\phi}{2} - \frac{2f_\xi}{\varepsilon}\sin\phi,\\
\bar{C}_{\xi\eta} &= -\frac{\partial f_T}{\partial\dot{\varepsilon}/\omega}\sin^2\phi - \frac{\partial f_R}{\partial\dot{\varepsilon}/\omega}\frac{\sin 2\phi}{2} + \frac{2f_\xi}{\varepsilon}\cos\phi,\\
\bar{C}_{\eta\xi} &= -\frac{\partial f_T}{\partial\dot{\varepsilon}/\omega}\cos^2\phi - \frac{\partial f_R}{\partial\dot{\varepsilon}/\omega}\frac{\sin 2\phi}{2} - \frac{2f_\eta}{\varepsilon}\sin\phi,\\
\bar{C}_{\eta\eta} &= -\frac{\partial f_R}{\partial\dot{\varepsilon}/\omega}\sin^2\phi - \frac{\partial f_T}{\partial\dot{\varepsilon}/\omega}\frac{\sin 2\phi}{2} + \frac{2f_\eta}{\varepsilon}\cos\phi.
\end{aligned} \tag{4.26b}$$

Here we employed the notation

$$\begin{pmatrix} f_\xi \\ f_\eta \end{pmatrix} = \boldsymbol{Q}\begin{pmatrix} f_R \\ f_T \end{pmatrix}. \tag{4.26c}$$

and dropped the zero subscript on ϕ_0 to conform with accepted notation.

For a vertical load, $f_\eta = 0$ and $f_\xi = 1/S$; the Sommerfeld number S is defined in Eq. (3.46).

4.2 Stability of a Flexible Rotor

Consider a weightless elastic shaft supporting a disk of mass M at its midpoint. The shaft, in its turn, is supported by identical, single pad journal bearings at its end points. In Figure 4.5, the geometric center of a bearing pad is designated by O_B. Under the load $W = Mg$, the center of the rotating journal occupies its static equilibrium position O_{J_S}, while the mass center moves to O_M, due to the deflection of the shaft. We define an orthogonal Cartesian coordinate system (x, y) with origin in O_{J_S}, as shown in Figure 4.3, so O_M has coordinates (x_2, y_2).

If the rotor-bearing system is undisturbed, the rotor will remain in its static equilibrium position. If disturbed and the disturbances are small, the rotor will leave its equilibrium position and proceed along a closed orbit around it. This is what occurs in well designed, stable, rotor-bearing systems. Under other, unstable, conditions the rotor is unable to find a *limit cycle* and its path spirals outward until metal to metal contact between rotor and bearing occurs. There is great practical importance attached, therefore, to knowing the

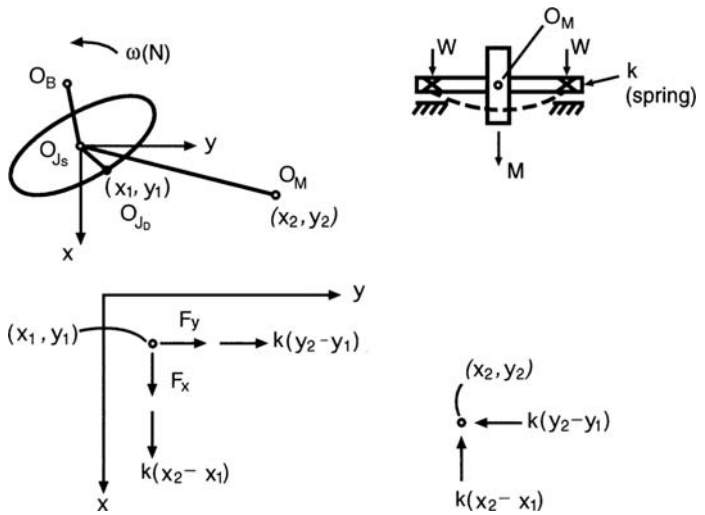

Figure 4.5. Schematic of flexible rotor supported on two identical journal bearings. $[O_{j_s}(0, 0); O_{J_D}(x_1, y_1); O_M(x_2, y_2)]$.

criteria that demarcates stable from unstable operation. To find this criteria we begin with the equations of motion:

rotor:

$$\begin{aligned} -k(x_2 - x_1) &= M\ddot{x}_2 \\ -k(y_2 - y_1) &= M\ddot{y}_2 \end{aligned} \tag{4.27}$$

bearing:

$$\begin{aligned} 2dF_x + k(x_2 - x_1) &= 0 \\ 2dF_y + k(y_2 - y_1) &= 0 \end{aligned} \tag{4.28}$$

Here k is the shaft stiffness and dF_x, dF_y are the components of the lubricant force that is exerted on the shaft in excess of the equilibrium force $F_x = \boldsymbol{W}$, $F_y = 0$. The force increments (dF_x, dF_y) are given by Eq. (4.1).

To solve Eqs. (4.27) and (4.28), we assume that both O_J and O_M undergo harmonic motion of the type

$$\begin{pmatrix} x_1 \\ y_1 \end{pmatrix} = \begin{bmatrix} X_1 \\ Y_1 \end{bmatrix} e^{\nu t}, \quad \begin{pmatrix} x_2 \\ y_2 \end{pmatrix} = \begin{bmatrix} X_2 \\ Y_2 \end{bmatrix} e^{\nu t}. \tag{4.29}$$

The eigenvalue ν in Eq. (4.29) is, in general, complex,

$$\nu = \mathcal{R}(\nu) + i\mathcal{J}(\nu),$$

and we have

$$e^{\nu t} = e^{R(\nu)t}\left[\cos \mathcal{J}(\nu)\, t + i \sin \mathcal{J}(\nu)\, t\right].$$

The real part of ν is called the *damping exponent.* If $\mathcal{R}(\nu) < 0$, the motion is *stable*, and it is unstable if $\mathcal{R}(\nu) > 0$. The *neutral state* of stability (*threshold of stability*) is characterized by $\mathcal{R}(\nu) = 0$. The imaginary part of ν is the *damped natural frequency* (the orbiting frequency).

Substituting Eq. (4.29) into Eqs. (4.27) and (4.28) and taking into account Eq. (4.1), we obtain

$$\begin{bmatrix} \dfrac{kM\nu^2}{M\nu^2+k} + 2K_{xx} + 2\nu C_{xx} & 2K_{xy} + 2\nu C_{xy} \\ 2K_{yx} + 2\nu C_{yx} & \dfrac{kM\nu^2}{M\nu^2+k} + 2K_{yy} + 2\nu C_{yy} \end{bmatrix} \begin{bmatrix} X_1 \\ Y_1 \end{bmatrix} = \begin{bmatrix} 0 \\ 0 \end{bmatrix}. \tag{4.30}$$

We nondimensionalize Eq. (4.30) according to

$$\begin{aligned} &\{K_{ij}, \omega C_{ij}, k\} = \frac{LD\mu N\,(R/C)^2}{C}\{\bar{K}_{ij}, \bar{C}_{ij}, \bar{k}\}, \\ &\{X_1, Y_1\} = C\left\{\bar{X}_1, \bar{Y}_1\right\}, \qquad \nu = \omega\bar{\nu}, \quad \omega = \omega_N\bar{\omega}. \end{aligned} \tag{4.31}$$

Here $\omega_N = \sqrt{k/M}$ is the natural frequency of the rotor and the overbar signifies, as before, nondimensional quantities.

Employing the rotation

$$\alpha = \frac{\bar{k}\,\bar{\nu}\bar{\omega}^2}{\bar{\nu}^2\bar{\omega}^2 + 1} \qquad (\text{a real number}), \tag{4.32}$$

we obtain the nondimensional form of Eq. (4.30)

$$\begin{bmatrix} \alpha + 2\bar{K}_{xx} + 2\bar{\nu}\bar{C}_{xx} & 2\bar{K}_{xy} + 2\bar{\nu}\bar{C}_{xy} \\ 2\bar{K}_{yx} + 2\bar{\nu}\bar{C}_{yx} & \alpha + 2\bar{K}_{yy} + 2\bar{\nu}\bar{C}_{yy} \end{bmatrix} \begin{bmatrix} \bar{X}_1 \\ \bar{Y}_1 \end{bmatrix} = \begin{bmatrix} 0 \\ 0 \end{bmatrix}. \tag{4.33}$$

Equation (4.33) possesses a nontrivial solution if and only if the system determinant vanishes. By expanding the determinant and equating it to zero, we would obtain a fourth order polynomial in $\bar{\nu}$. Solving this so-called *frequency (characteristic) equation* would yield $\bar{\nu}$.

Instead of solving directly for $\bar{\nu}$, however, we will seek conditions for marginal stability, a state that is characterized by the vanishing of the real part of $\bar{\nu}$. To this end, we separate the determinant in Eq. (4.33) into its real and imaginary parts, which are then individually equated to zero.

The real part of the determinant of Eq. (4.33) is

$$\begin{vmatrix} \alpha + 2\bar{K}_{xx} & 2\bar{K}_{xy} \\ 2\bar{K}_{yx} & \alpha + 2\bar{K}_{yy} \end{vmatrix} + \bar{\nu}^2 \begin{vmatrix} 2\bar{C}_{xx} & 2\bar{C}_{yx} \\ 2\bar{C}_{xy} & 2\bar{C}_{yy} \end{vmatrix} = 0 \tag{4.34}$$

and its imaginary part is

$$\begin{vmatrix} 2\bar{C}_{xx} & 2\bar{K}_{xy} \\ 2\bar{C}_{yx} & \alpha + 2\bar{K}_{yy} \end{vmatrix} \bar{\nu} + \begin{vmatrix} \alpha + 2\bar{K}_{xx} & 2\bar{C}_{xy} \\ 2\bar{K}_{yx} & 2\bar{C}_{yy} \end{vmatrix} \bar{\nu} = 0. \tag{4.35}$$

Since $\bar{\nu} \neq 0$, we can divide Eq. (4.35) by $\bar{\nu}$, and on expanding the determinants obtain

$$\alpha = \frac{2(\bar{K}_{xy}\bar{C}_{yx} + \bar{K}_{yx}\bar{C}_{xy} - \bar{k}_{yy}\bar{C}_{xx} - \bar{K}_{xx}\bar{C}_{yy})}{(\bar{C}_{xx} + \bar{C}_{yy})}. \tag{4.36}$$

Using the definition of α, we find the instability threshold value of the relative frequency as

$$\bar{\omega}_c^2 = \frac{\alpha}{\bar{\nu}^2(\bar{k} - \alpha).} \tag{4.37}$$

in terms of α, $\bar{k}$, and the yet undetermined whirl ratio $\bar{\nu}$.

If $\bar{\omega} > \bar{\omega}_c$, the system is unstable. At $\bar{\omega}_c = 1$, instability sets in at the system natural frequency, $\omega_N = \sqrt{k/M}$.

To render Eq. (4.37) useful, we need to determine the whirl ratio $\bar{\nu} = \nu/\omega$; this can be accomplished by expanding Eq. (4.34)

$$\bar{\nu}^2 = \frac{\alpha^2 + 2(\bar{K}_{xx} + \bar{K}_{yy})\alpha + 4(\bar{K}_{xx}\bar{K}_{yy} - \bar{K}_{xy}\bar{K}_{yx})}{4(\bar{C}_{xx}\bar{C}_{yy} - \bar{C}_{yx}\bar{C}_{xy})}. \tag{4.38}$$

In the state of neutral stability $\bar{\nu}$ is purely imaginary:

$$\bar{\nu} = i\mathcal{J}(\bar{\nu}) \tag{4.39}$$

and

$$\frac{\nu_{\text{whirl}}}{\omega} = \sqrt{-\bar{\nu}^2}, \tag{4.40}$$

where $\bar{\nu}^2$ is given by Eq. (4.38).

Note that both $\bar{\omega}_c$ and $\bar{\nu}$ are functions of the (dimensionless) shaft stiffness, $\bar{k}$, and the elements of the (dimensionless) bearing stiffness and damping matrices, $\bar{\boldsymbol{K}}$ and $\bar{\boldsymbol{C}}$; the latter two being evaluated at, and depending on, the static equilibrium position of the journal (ε_0, ϕ_0). Thus, for a given system, a stability chart can be prepared as a sole function of the static position of the journal, or, alternatively, as a sole function of the Sommerfeld number.

The stability characteristics of a flexible rotor carried on full journal bearings that are supported on a rigid foundation can be estimated from Figure 4.6 (Raimondi and Szeri, 1984).

In Figure 4.6 we plotted the stability parameter

$$\bar{M} = \frac{C}{W} M\omega^2 \tag{4.41}$$

against the short-bearing Sommerfeld number.

4.3 Pivoted-Pad Journal Bearings

Tilting-pad journal bearings consist of a number of individually pivoted pads or shoes (Figure 4.7). Pivoting makes relatively high loading possible where shaft deflection or misalignment is a factor. The most important features of tilting-pad journal bearings are (1) small cross-coupling coefficients resulting in inherent stability, (2) availability of preloading to achieve relatively high stiffness (important with vertical rotors), and (3) operation with clearances smaller than considered desirable for fixed-pad journal bearings.

Normal practice is to construct all pads alike and space them uniformly around the circumference. When the number of pads is large, there is little difference in bearing performance between two alternatives: load line passing through a pivot or between pivots. When the number of pads is small, however, the load-between-pads orientation is preferred;

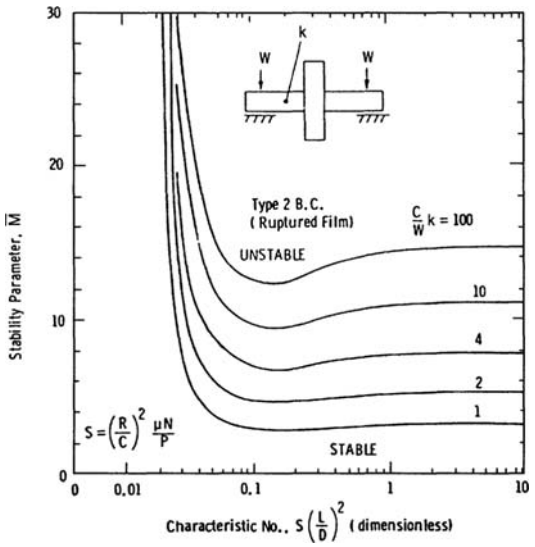

Figure 4.6. Stability of single mass rotor on full journal bearings, mounted on a rigid support. (Reprinted with permission from Raimondi, A. A. and Szeri, A. Z. Journal and thrust bearings. In Booser, E. R., *CRC Handbook of Lubrication.* Copyright CRC Press, Boca Raton, Florida. © 1984.)

in this case the load capacity is greater, the temperature rise is lower as the load is distributed more uniformly, and the lateral stiffness and damping are greater.

Load capacity is not unduly sensitive to pivot location when using oil lubricants. In these cases, the pivot is usually positioned at pad center to preserve independence from direction of journal rotation. When using low-viscosity fluids (water, liquid metals, and particularly gases), however, load capacity is sensitive to pivot location, and the pivot must be offset toward the trailing edge (Boyd and Raimondi, 1962).

Figure 4.8 illustrates a pad of angular extent β, which is machined to radius $R + C$ (position 1). In the absence of tilting, the film thickness is uniform (equal to C) and no hydrodynamic force can be developed. However, if the pad is now moved to position 2, by

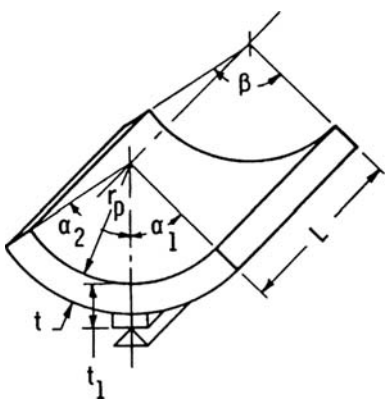

Figure 4.7. Pivoted-pad schematics. (Reprinted with permission from Ralmondi, A. A. and Szeri, A. Z. Journal and thrust bearings. In Booser, E. R., *CRC Handbook of Lubrication.* Copyright CRC Press, Boca Raton, Florida. © 1984.)

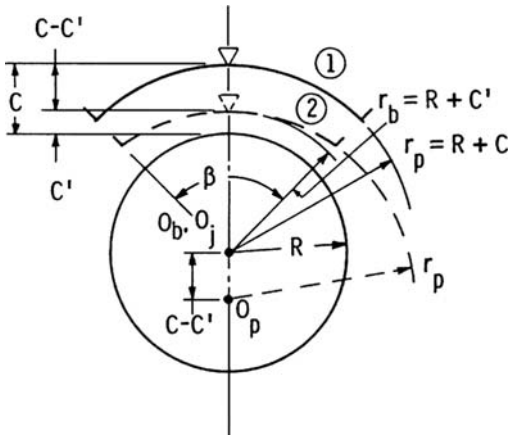

Figure 4.8. Preloading of pad. (Reprinted with permission from Raimondi, A. A. and Szeri, A. Z. Journal and thrust bearings. In Booser, E. R., *CRC Handbook of Lubrication.* Copyright CRC Press, Boca Raton, Florida. © 1984.)

displacing the pivot radially inward a distance $(C - C')$, there results a nonuniform film thickness and, consequently, a hydrodynamic force that preloads the journal. Bearings of vertical machines operate almost concentric with their journal. To overcome the low radial stiffness and consequent *spragging*, vertical machines are often equipped with preloaded guide bearings.

Preload is characterized by the *preload coefficient* $m = (C - C')/C$, where $0 \leq m \leq 1$. Each pad is preloaded usually the same amount in vertical machines, while in horizontal machines often the top pads only are preloaded to prevent spragging.

A pivoted pad will track the orbiting journal by rocking about its pivot. The influence of pad inertia on the dynamic coefficients of the pad is negligible except when approaching pad resonance. At pad resonance, the journal and pad motions are 90° out of phase. The onset of pad resonance can be determined from the value of the *critical mass parameter* and requires calculation of the polar moment of inertia, I_p, of the pad.

Referring to Figure 4.7, we have

$$I_p = 2r_p^2 M_p \left\{ 1 + f_1 - \left[\frac{(\sin\alpha_1 + \sin\alpha_2)}{\beta} f_2 \right] \right\}, \tag{4.42}$$

where

$$f_1 = \left[\left(\frac{t_1}{r_p}\right) + \frac{1}{2}\left(\frac{t_1}{r_p}\right)^2 + \frac{1}{2}\left(\frac{t}{r_p}\right) + \frac{1}{4}\left(\frac{t}{r_p}\right)^2 \right],$$

$$f_2 = \left[1 + \left(\frac{t_1}{r_p}\right) \right] \left[1 + \left(\frac{t}{r_p}\right) + \frac{1}{2}\left(\frac{t}{r_p}\right)^2 \right] \Bigg/ \left[t + \frac{1}{2}\left(\frac{t}{r_p}\right) \right],$$

and M_p is the pad mass. Design data, such as shown in Figures 4.10 to 4.14, are often calculated on the (admittedly unrealistic) assumption that the pivot point is located on the pad surface; for this case $t_1/r_p = t/r_p = 0$ in Eq. (4.42).

The first researchers to compute the linearized spring and damping coefficients of a full journal bearing were Lund and Sternlicht (1962). Corresponding calculations for a partial

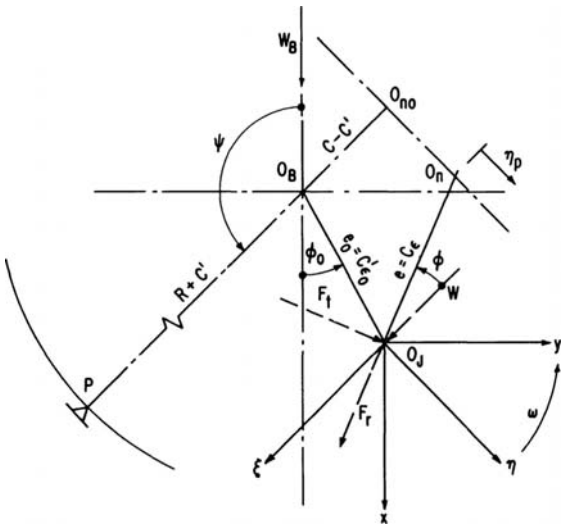

Figure 4.9. Coordinate systems for the pivoted-pad. (Reprinted with permission from Lund, J. W. Spring and damping coefficients for the tilting-pad journal bearing. *ASLE Trans.*, 7, 342, 1964.)

bearing were made by Szeri (1966). Analysis of tilting pad bearings is more complicated. Lund (1964) presented a pad assembly method in which he assumed harmonic motion for both journal and pad. Shapiro and Colsher (1977) and later Allaire, Parsell, and Barrett (1981) published a pad perturbation method that calculates a complete coefficient matrix for the tilting pad bearing. In this latter scheme, the coefficient matrix is independent of pad motion; frequency dependence and inertial dependence enter the analysis of the rotor-bearing system only when a specific pad motion is assumed. In the sequel, we give details of both the pad assembly method of Lund (1964), and the pad perturbation method of Shapiro and Colsher (Allaire, Parsell, and Barrett, 1981).

Pad Assembly Method

Coefficient for Single Tilting Pad

In Figure 4.9, the symbol O_B marks the position of the bearing center and O_J the instantaneous position of the shaft center. The center of curvature of the pad is at O_{no} in the absence of load and at O_n when fully loaded and tilted. The bearing load vector, W_B, is in the vertical, and the pivot point, P, is located at an angle, ψ, relative to the load line. With respect to O_B, the eccentricity of the journal center, O_J, is $e_0 = c\varepsilon_0$ at the attitude angle ϕ_0. The eccentricity of the journal is $e = c\varepsilon$ relative to the instantaneous pad center, and the attitude angle, ϕ, is measured from the load line for the pad, which, by necessity, connects O_J and P. Representing the radius of the journal by R, the radius of the pad is $\overline{O_n P} = R + C$, while the pivot circle, centered at O_B, has radius $\overline{O_B P} = R + C'$. From geometric consideration, we have

$$\begin{aligned} \varepsilon \cos\phi &= 1 - \frac{C'}{C} - \varepsilon_0 \cos(\psi - \phi_0) \\ &= m - \varepsilon_0 \cos(\psi - \phi_0)\,, \end{aligned} \tag{4.43}$$

where m is the preload coefficient defined earlier.

If the position of the journal, O_J, relative to the bearing, O_B, is known, i.e., if the couple (ε_0, ϕ_0) is specified, Eq. (4.43) and the requirement that the load on the pad, W, passes through the pivot, P, are sufficient to determine the couple (ε, ϕ) for each pad. The components of the required lubricant force are obtained from the force equilibrium in Eq. (3.40b). Knowing (ε, ϕ) enables calculation of individual pad performance, which can then be summed (vectorially) to yield performance characteristics for the bearing.

Unfortunately (ε_0, ϕ_0) is not known a priori, and the best the designer can do is assume ε_0, and use the condition that $\boldsymbol{W}_B$ is purely vertical to calculate the corresponding ε_0. This procedure is, at least, tedious. If, however, the pivots are arranged symmetrically with respect to the load line, the pads are centrally pivoted and are identical, we have $\phi_0 \equiv 0$, and the journal moves along the load vector $\boldsymbol{W}_B$.

In the following discussion of the pad assembly method, we assume that all conditions for $\phi_0 \equiv 0$ are met.

Referring to Figure 4.9, we note that under dynamic load the pad center oscillates about O_n. Denoting the amplitude of this oscillation of the pad center by η_p and representing the pad moment of inertia by I_p, Eq. (4.42), we can write the equation of motion of the pad as

$$I_p \frac{\ddot{\eta}_p}{R_p} = -R_p d F_\eta. \tag{4.44}$$

Setting $M_p = I_p/{R_p}^2$, Eq. (4.44) becomes

$$M_p \ddot{\eta}_p = K_{\eta\xi}\xi + C_{\eta\xi}\dot{\xi} + K_{\eta\eta}(\eta_p - \eta) + C_{\eta\eta}(\dot{\eta}_p - \dot{\eta}). \tag{4.45}$$

We can relate pad motion, η_p, to the motion of the journal, η, by assuming that both journal and pad execute synchronous motion according to

$$(\xi, \eta) = (\hat{\xi}, \hat{\eta})e^{i\omega t}, \qquad \eta_p = \hat{\eta}_p e^{i\omega t}. \tag{4.46}$$

Equation (4.46) is for the common case of unbalance excitation, when, necessarily, excitation occurs at the shaft running speed, ω.

Unlike fixed arc bearings, the spring and damping coefficients of pivoted-pad bearings are dependent upon the frequency, Ω, of the excitation force. For excitation at frequency $\Omega \neq \omega$, we should use

$$(\hat{\xi}, \hat{\eta})e^{i\Omega t}, \qquad \hat{\eta}_p e^{i\Omega t}.$$

in Eq. (4.46). Bearing characteristics for non-synchronous excitation $\Omega/\omega \neq 1$ are presented by Raimondi and Szeri (1984). Here, for simplicity, we only treat synchronous excitation $\Omega/\omega = 1$ and use Eq. (4.46).

Substituting Eq. (4.46) into Eq. (4.45) yields

$$\hat{\eta} - \hat{\eta}_P = -[(K_{\eta\xi} + i\omega C_{\eta\xi})\xi + M_p\omega^2\eta](p - iq), \tag{4.47}$$

where

$$(p, q) \equiv (K_{\eta\eta} - M_p\omega^2, \omega C_{\eta\eta})/\left[\left(K_{\eta\eta}^2 - M_p\omega^2\right)^2 + (\omega C_{\eta\eta})^2\right].$$

Equation (4.47) can now be used to eliminate η_p from

$$\begin{pmatrix} dF_\xi \\ dF_\eta \end{pmatrix} = -\boldsymbol{K}\begin{pmatrix} \xi \\ \eta - \eta_p \end{pmatrix} - \boldsymbol{C}\begin{pmatrix} \dot{\xi} \\ \dot{\eta} - \dot{\eta}_p \end{pmatrix}, \tag{4.48}$$

which is the dimensional counterpart of Eq. (4.25), written for a pivoting pad. Thus, replacing $(\eta - \eta_p)$ in Eq. (4.48) from Eq. (4.47), we have

$$\begin{aligned} dF_\xi &= -\big(K'_{\xi\xi} + i\omega C'_{\xi\xi}\big)\hat{\xi} - \big(K'_{\xi\eta} + i\omega C'_{\xi\eta}\big)\hat{\eta}, \\ dF_\eta &= -\big(K'_{\eta\xi} + i\omega C'_{\eta\xi}\big)\hat{\xi} - \big(K'_{\eta\eta} + i\omega C'_{\eta\eta}\big)\hat{\eta}. \end{aligned} \tag{4.49a}$$

where $K'_{\xi\xi}$, $C'_{\xi\xi}$, etc. are the spring and damping coefficients for the tilting pad given by (Lund, 1964):

$$\begin{aligned} K'_{\xi\xi} &= K_{\xi\xi} - (pK_{\xi\eta} + q\omega C_{\xi\eta})K_{\eta\xi} - (qK_{\xi\eta} - p\omega C_{\xi\eta})\omega C_{\eta\xi}, \\ \omega C'_{\xi\xi} &= \omega C_{\xi\xi} - (pK_{\xi\eta} + q\omega C_{\xi\eta})\omega C_{\eta\xi} + (qK_{\xi\eta} - p\omega C_{\xi\eta})K_{\eta\xi}, \\ K'_{\xi\eta} &= -M_p\omega^2(pK_{\xi\eta} + q\omega C_{\xi\eta}), \\ \omega C'_{\xi\eta} &= M_p\omega^2(qK_{\xi\eta} - p\omega C_{\xi\eta}), \\ K'_{\eta\xi} &= -M_p\omega^2(pK_{\eta\xi} + q\omega C_{\eta\xi}), \\ \omega C'_{\eta\xi} &= M_p\omega^2(qK_{\eta\xi} - p\omega C_{\eta\xi}), \\ K'_{\eta\eta} &= -M_p\omega^2(qK_{\eta\eta} + q\omega C_{\eta\eta}) = -M_p\omega^2(1 + pM_p\omega^2), \\ \omega C'_{\eta\eta} &= M_p\omega^2(qK_{\eta\eta} - p\omega C_{\eta\eta}) = (M_p\omega^2)^2 q. \end{aligned} \tag{4.49b}$$

If the pad has no inertia, then $M_p = 0$ and only $K'_{\xi\xi}$ and $C'_{\xi\xi}$ are nonzero. This is on account of the pad freely tilting about the pivot.

The transformation from fixed-pad data to dynamic-pad data may be looked upon as allowing the pad to pitch so that the load will pass through the pivot.

Bearing Coefficients

In the previous section we obtained the spring and damping coefficients for the nth tilting pad relative to its own (local) coordinate system (ξ, η). It will be to our advantage during assembly if the coefficients for each of the pads are referred to a global coordinate system, (x, y) in Figure 4.9, of the bearing. The coordinate transformation from a local coordinate system (ξ, η) to the global system (x, y) is

$$\begin{pmatrix} x \\ y \end{pmatrix} = \boldsymbol{Q}\begin{pmatrix} \xi \\ \eta \end{pmatrix}, \quad \boldsymbol{Q} = \begin{pmatrix} \cos(\pi - \psi_n) & \sin(\pi - \psi_n) \\ -\sin(\pi - \psi_n) & \cos(\pi - \psi_n) \end{pmatrix}, \tag{4.50a}$$

where ψ_n is the pivot angle of the nth pad (Figure 4.9), measured counterclockwise from the load line.

Under the coordinate transformation Eq. (4.50a), the components of the incremental force dF transform according to the formula

$$\begin{pmatrix} dF_x \\ dF_y \end{pmatrix} = \boldsymbol{Q}\begin{pmatrix} dF_\xi \\ dF_\eta \end{pmatrix}. \tag{4.50b}$$

Combining Eqs. (4.49a), (4.50a), and (4.50b), we obtain

$$\begin{pmatrix} dF_x \\ dF_y \end{pmatrix} = -\boldsymbol{Q}\boldsymbol{K}'\boldsymbol{Q}^T\begin{pmatrix} x \\ y \end{pmatrix} - \boldsymbol{Q}\boldsymbol{C}'\boldsymbol{Q}^T\begin{pmatrix} \dot{x} \\ \dot{y} \end{pmatrix}. \tag{4.51}$$

Writing

$$K^{(n)} = \boldsymbol{Q}\boldsymbol{K}'\boldsymbol{Q}^T, \qquad \boldsymbol{C}^{(n)} = \boldsymbol{Q}\boldsymbol{C}'\boldsymbol{Q}^T \tag{4.52}$$

for the stiffness and damping matrix of the nth pad, referred to the (x, y) global coordinate system, we have

$$\begin{pmatrix} dF_x^{(n)} \\ dF_y^{(n)} \end{pmatrix} = -\boldsymbol{K}^{(n)} \begin{pmatrix} x \\ y \end{pmatrix} - \boldsymbol{C}^{(n)} \begin{pmatrix} \dot{x} \\ \dot{y} \end{pmatrix}. \tag{4.53a}$$

The matrices in Eq. (4.53a) have components calculated by substituting Eq. (4.49) into Eq. (4.52):

$$\begin{aligned}
K_{xx}^{(n)} &= K'_{\xi\xi} \cos^2 \psi_n + K'_{\eta\eta} \sin^2 \psi_n - (K'_{\xi\eta} + K'_{\eta\xi}) \cos \psi_n \sin \psi_n, \\
\omega C_{xx}^{(n)} &= \omega C'_{\xi\xi} \cos^2 \psi_n + \omega C'_{\eta\eta} \sin^2 \psi_n - (\omega C'_{\xi\eta} + \omega C'_{\eta\xi}) \cos \psi_n \sin \psi_n, \\
K_{xy}^{(n)} &= K'_{\xi\eta} \cos^2 \psi_n - K'_{\eta\xi} \sin^2 \psi_n + (K'_{\xi\xi} - K'_{\eta\eta}) \cos \psi_n \sin \psi_n, \\
\omega C_{xy}^{(n)} &= \omega C'_{\xi\eta} \cos^2 \psi_n - \omega C'_{\eta\xi} \sin^2 \psi_n + (\omega C'_{\xi\xi} - \omega C'_{\eta\eta}) \cos \psi_n \sin \psi_n, \\
K_{yx}^{(n)} &= K'_{\eta\xi} \cos^2 \psi_n - K'_{\xi\eta} \sin^2 \psi_n + (K'_{\xi\xi} - K'_{\eta\eta}) \cos \psi_n \sin \psi_n, \\
\omega C_{yx}^{(n)} &= \omega C'_{\eta\xi} \cos^2 \psi_n - \omega C'_{\xi\eta} \sin^2 \psi_n + (\omega C'_{\xi\xi} - \omega C'_{\eta\eta}) \cos \psi_n \sin \psi_n, \\
K_{yy}^{(n)} &= K'_{\eta\eta} \cos^2 \psi_n + K'_{\xi\xi} \sin^2 \psi_n + (K'_{\xi\eta} + K'_{\eta\xi}) \cos \psi_n \sin \psi_n, \\
\omega C_{yy}^{(n)} &= \omega C'_{\eta\eta} \cos^2 \psi_n + \omega C'_{\xi\xi} \sin^2 \psi_n + (\omega C'_{\xi\eta} + \omega C'_{\eta\xi}) \cos \psi_n \sin \psi_n,
\end{aligned} \tag{4.53b}$$

A summation over N pads that make up the bearing yields the bearing spring and damping coefficients:

$$\{\mathcal{K}, \mathcal{C}\} = \sum_{n=1}^{N_{\text{pad}}} \left\{ \boldsymbol{K}^{(n)}, \boldsymbol{C}^{(n)} \right\}. \tag{4.54}$$

If the pads are assumed to have no inertia – and this assumption is good for conditions far from pad resonance – we may write

$$\boldsymbol{K}^{(n)} = K'_{\xi\xi} \boldsymbol{Y}_{(n)}, \qquad \boldsymbol{C}^{(n)} = C'_{\xi\xi} \boldsymbol{Y}_{(n)}, \tag{4.55}$$

where

$$\boldsymbol{Y}_{(n)} = \begin{pmatrix} \cos^2 \psi_n & \dfrac{1}{2} \sin^2 \psi_n \\ \dfrac{1}{2} \sin^2 \psi_n & \sin^2 \psi_n \end{pmatrix}$$

for the nth pad.

At zero preload, symmetry about the x axis, and load-between-pads arrangement, Eq. (4.43) gives

$$\varepsilon_0 = \frac{\varepsilon \cos \phi}{-\cos \left[\dfrac{(N-1)\pi}{N} \right]}$$

where we put $\phi = (N-1)\pi/N$ for the lowermost pad. The maximum value of ε_0 is obtained with $\varepsilon = 1$ and $\phi = 0$

$$\max(\varepsilon_0) = \frac{1}{-\cos \left[\dfrac{(N-1)\pi}{N} \right]}.$$

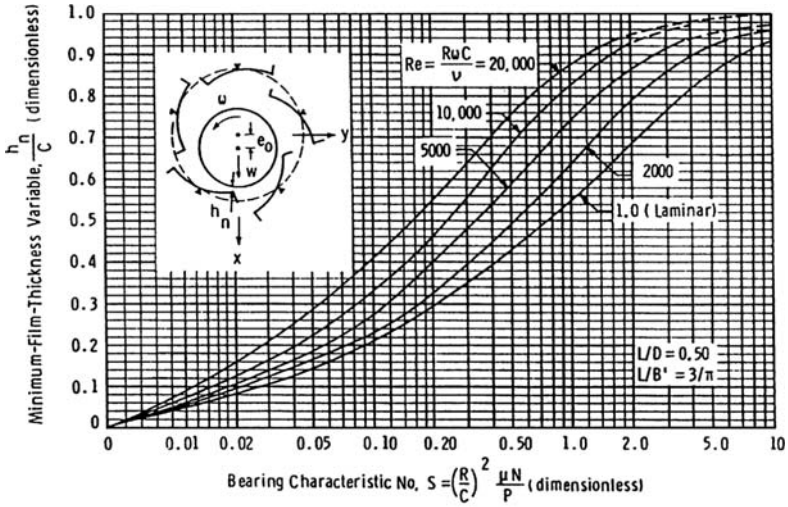

Figure 4.10. Minimum film thickness variable versus (a) bearing characteristic number and (b) normalized bearing eccentricity ratio: five 60° tilting pads, central loading, no preload, inertialess pad, $L/D = 0.5$. (Reprinted with permission from Raimondi, A. A. and Szeri, A. Z. Journal and thrust bearings. In Booser, E. R., *CRC Handbook of Lubrication*. Copyright CRC Press, Boca Raton, Florida. © 1984.)

The normalized bearing eccentricity $0 \leq \varepsilon'_0 \leq 1$ is defined as

$$\varepsilon'_0 = \frac{\varepsilon_0}{\max(\varepsilon_0)}.$$

For the five-padbearing of Figures 4.10 to 4.13, $\max(\varepsilon_0) = 1.2361$.

Figures 4.10 to 4.13 plot performance characteristics for a five-pad pivoted-pad bearing of $L/D = 0.5$. The pads are identical and are arranged symmetrically with respect to the load

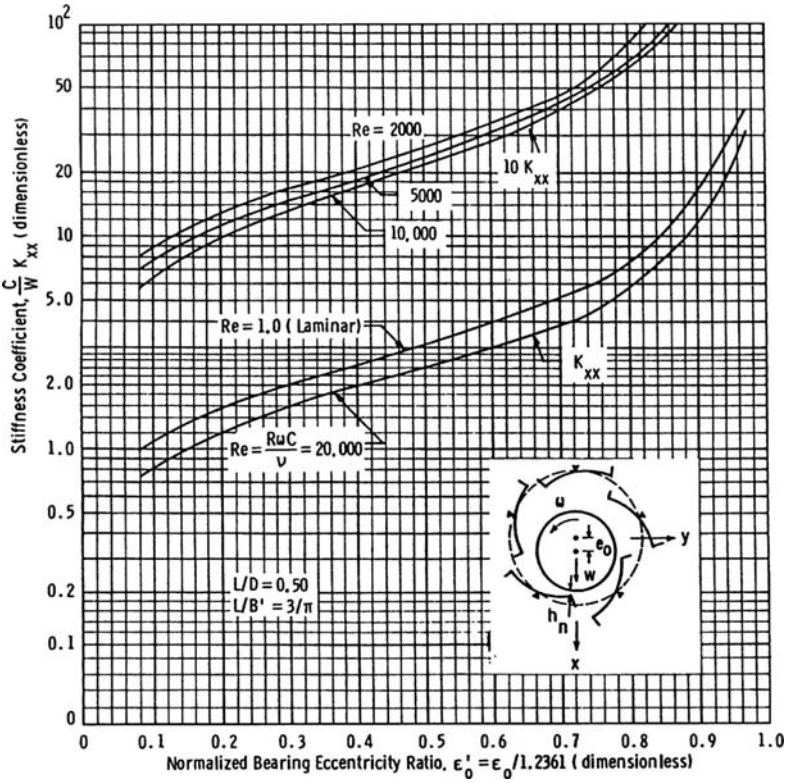

Figure 4.11. Bearing vertical stiffness: five 60° tilting pads, central loading, no pre-load, inertialess pad, $L/D = 0.5$. (Reprinted with permission from Raimondi, A. A. and Szeri, A. Z. Journal and thrust bearings. In Booser, E. R., *CRC Handbook of Lubrication*. Copyright CRC Press, Boca Raton, Florida. © 1984.)

line, hence the journal moves along the vertical, $\phi_0 = 0$. Figure 4.10 shows the variation of the minimum film thickness parameter $H_{\min}$ against (a) bearing characteristic number, and (b) against normalized bearing eccentricity ratio.

Figures 4.11 and 4.12 plot vertical and horizontal bearing stiffness, respectively, and Figure 4.13 contains information on bearing damping.

If the nth pad and the $(N - n + 1)$th pad are identical and are symmetrically placed relative to the load line, then

$$\psi_{(N-n+1)} = (2\pi - \psi_n),$$
$$\frac{1}{2}\sin\psi_{(N-n+1)} = -\frac{1}{2}\sin\psi_n,$$

hence, for symmetry about the load line, the cross-coupling terms in Eq. (4.53) vanish.

To investigate the motion of a pad, we write Eq. (4.47) in the form

$$\eta_p = \frac{(K_{\eta\xi} + i\omega C_{\eta\xi})\xi + (K_{\eta\eta} + i\omega C_{\eta\eta})\eta}{K_{\eta\eta} - M_p\omega^2 + i\omega C_{\eta\eta}}. \tag{4.56}$$

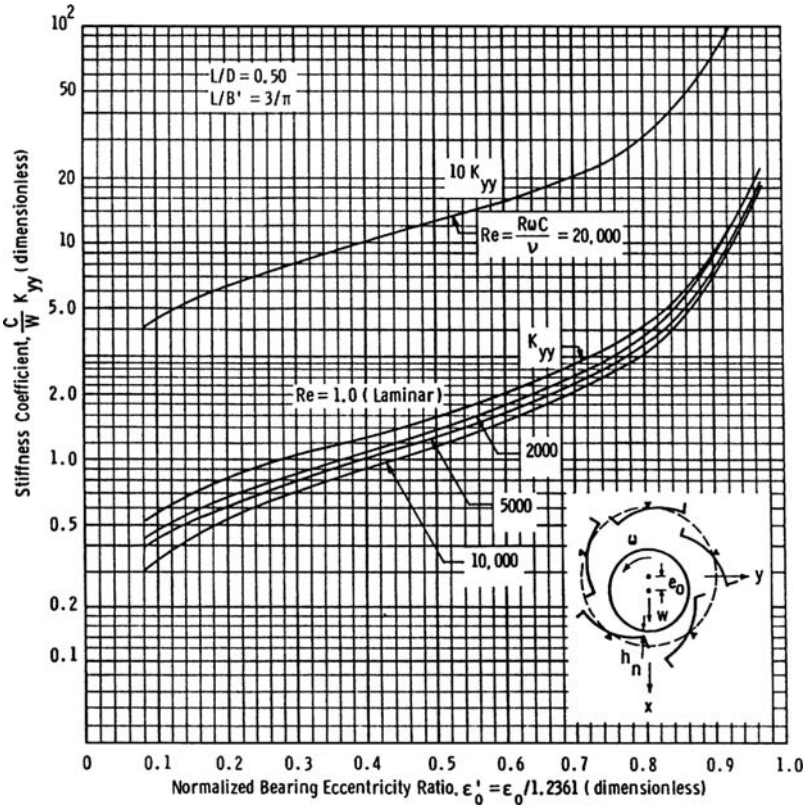

Figure 4.12. Bearing horizontal stiffness: five 60° tilting pads, central loading, no preload, inertialess pad, $L/D = 0.5$. (Reprinted with permission from Raimondi, A. A. and Szeri, A. Z. Journal and thrust bearings. In Booser, E. R., *CRC Handbook of Lubrication*. Copyright CRC Press, Boca Raton, Florida. © 1984.)

Let $\eta_p = \eta_0$ for zero pad inertia, $M_p = 0$

$$\eta_0 = \eta + \frac{K_{\eta\xi} + i\omega C_{\eta\xi}}{K_{\eta\eta} + i\omega C_{\eta\eta}}\xi. \tag{4.57}$$

The ratio η_p/η_0 is a complex quantity that can be written as

$$\left(\frac{\eta_p}{\eta_0}\right) = \left|\frac{\eta_p}{\eta_0}\right| \exp\{i[\arg(\eta_0) - \arg(\eta_p)]\},$$

where

$$\arg(\eta_0) - \arg(\eta_p) = \tan^{-1}\left\{\frac{\omega C_{\eta\eta} M_p \omega^2}{K_{\eta\eta}(K_{\eta\eta} - M_p\omega^2) + (\omega C_{\eta\eta})^2}\right\}. \tag{4.58}$$

The phase angle $[\arg(\eta_0) - \arg(\eta_p)]$ reaches $\pi/2$ when the denominator in Eq. (4.58) vanishes. At this juncture, the pad is said to possess critical mass, M_{CRIT}

$$\omega^2 M_{\text{CRIT}} = \frac{K_{\eta\eta}^2 + (\omega C_{\eta\eta})^2}{K_{\eta\eta}}. \tag{4.59a}$$

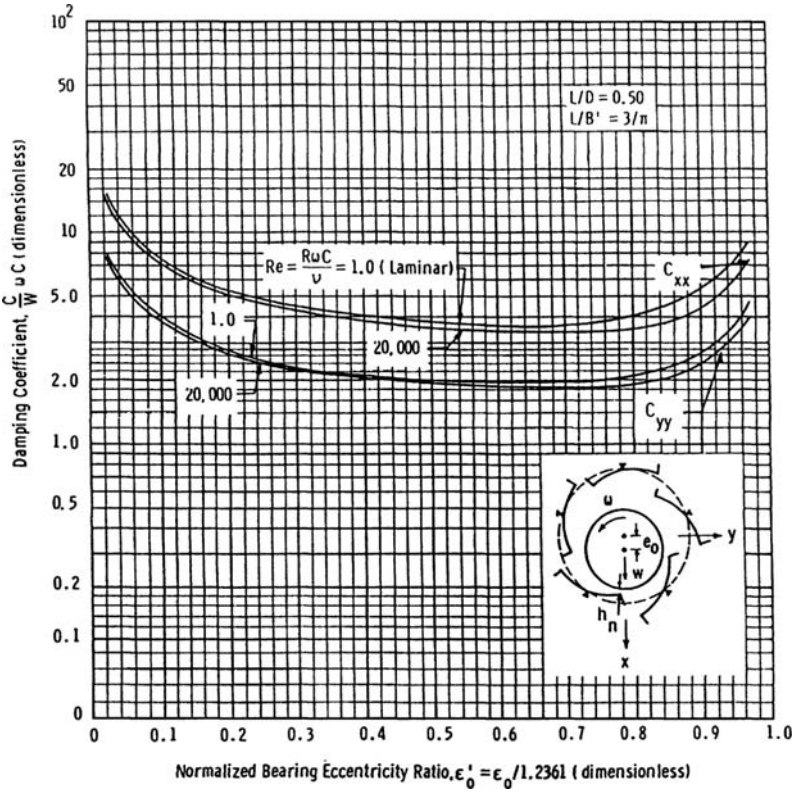

Figure 4.13. Bearing damping: five 60° tilting pads, central loading preload, inertialess pad, $L/D = 0.5$. (Reprinted with permission from Raimondi, A. A. Szeri, A. Z. Journal and thrust bearings. In Booser, E. R., *CRC Handbook of Lubrication*. Copyright CRC Press, Boca Raton, Florida. © 1984.)

If the pad mass satisfies Eq. (4.59a), the conditions for pad resonance are satisfied. In dimensionless form, Eq. (4.59a) is often expressed as

$$\frac{CW_B M_{\text{CRIT}}}{\left[\mu DL\left(\frac{R}{C}\right)^2\right]^2} = \frac{1}{4\pi S^2}\frac{\left(\frac{CK_{\eta\eta}}{W_B}\right)^2 + \left(\frac{C\omega C_{\eta\eta}}{W_B}\right)^2}{\left(\frac{CK_{\eta\eta}}{W_B}\right)}, \tag{4.59b}$$

where W_B is the total load on the bearing and S is the bearing Sommerfeld number. The critical pad mass for the five-pad bearing is plotted in Figure 4.14.

The computational algorithm of tilting-pad bearings is as follows (Nicholas et al., 1979):

1. The fixed-pad stiffness and damping coefficients $\bar{\boldsymbol{K}}$ and $\bar{\boldsymbol{C}}$ are obtained by displacement and velocity perturbation about the equilibrium positions, Eq. (4.26).
2. The pad dynamic coefficients $\bar{\boldsymbol{K}}'$ and $\bar{\boldsymbol{C}}'$ are calculated using Eq. (4.49). These coefficients, along with the fixed-pad Sommerfeld number, S, are labeled with the dimensionless pivot film thickness, H_p, and stored.

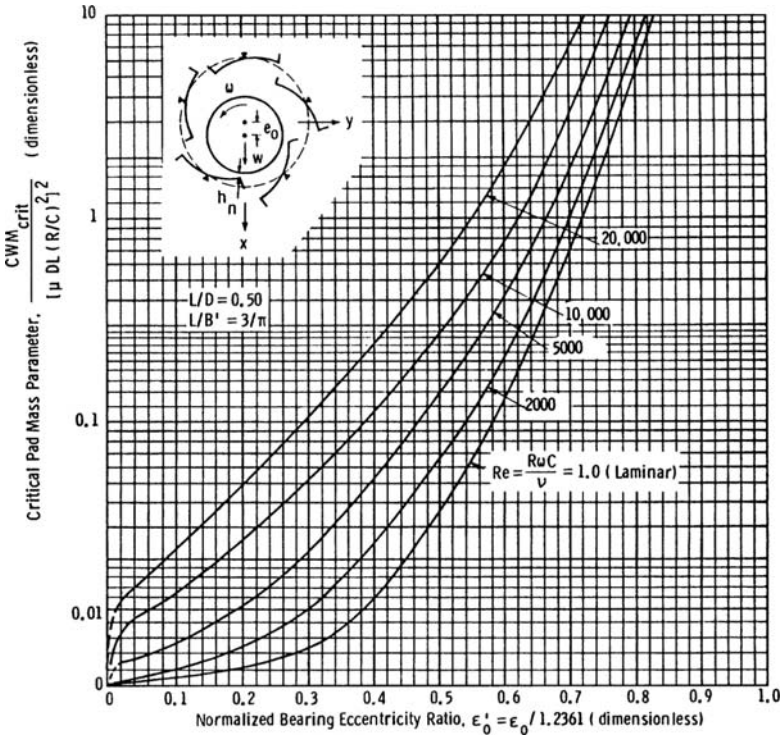

Figure 4.14. Pad critical mass: five 60° tilting pads, central loading, no preload, inertialess pad, $L/D = 0.5$. (Reprinted with permission from Raimondi, A. A. and Szeri, A. Z. Journal and thrust bearings. In Booser, E. R., *CRC Handbook of Lubrication*. Copyright CRC Press, Boca Raton, Florida. © 1984.)

3. A bearing eccentricity ratio ε_0 (as the shaft moves along the vertical, for centrally pivoted, symmetrically arranged pads, $\phi_0 \equiv 0$) is selected, and the pivot film thickness for the nth pad, H_{pn}, $n = 1, 2, 3, \ldots, N$, is calculated.
4. $\bar{\boldsymbol{K}}'$, $\bar{\boldsymbol{C}}'$ at given H_{pi} are obtained by interpolation and transferred to the global (x, y) coordinate system, Eq. (4.52), to find $\bar{\boldsymbol{K}}^{(n)}$, $\bar{\boldsymbol{C}}^{(n)}$, $n = 1, 2, 3, \ldots, N$.
5. Use of Eq. (4.54) leads to the bearing dynamic coefficients $\mathcal{K}, \mathcal{C}$
6. The dimensionless load on each pad is given by

$$\bar{F}_x^{(n)} = -\frac{\cos\psi_n}{S_n}, \qquad \bar{F}_y^{(n)} = -\frac{\sin\psi_n}{S_n}, \tag{4.60}$$

and for the complete bearing

$$F_x = \sum_{n=1}^{N} F_x^{(n)} = \frac{1}{S}, \qquad F_y = 0 \tag{4.61}$$

Pad Perturbetion Method

Compared to fixed-pad bearings, analysis of tilting-pad bearings is complicated by the fact that in addition to the degrees of freedom of the shaft, one has also to consider the degrees of freedom associated with the pivoting of the pads. This was not done in the previous section; Lund's method does not provide the dynamical coefficients associated with the degrees of freedom of the pads. Instead, Lund assumes synchronous pad motion right from the start, Eq. (4.46), thereby reducing pad data before interpolation and assembly.

The pad perturbation method, on the other hand, calculates and stores the stiffness and damping coefficients associated with all degrees of freedom of a single pad over the whole range of eccentricities (pivot film thicknesses). The performance characteristics of the tilting pad bearing are then calculated in the following steps:

(1) Fix the position of the journal ($\phi_0 = 0$ for symmetric arrangement of identical, centrally pivoted pads).
(2) From geometry, calculate the pivot film thickness for each pad and interpolate from previously stored pad data, to obtain pad characteristics at operating conditions.
(3) Obtain bearing characteristics by proper summation of individual pad characteristics.

Excitation frequency and pad inertia enter the analysis of the rotor-bearing system only when specific pad motion is assumed. Shapiro and Colsher (1977) describe this reduction of the results of the pad assembly method to "standard" 4×4 stiffness and damping matrices.

The rotor of the rotor-bearing system is assumed rigid and the bearings comprise N pads, each pad assuming its own orientation $\delta_i, i = 1, \ldots, N$. The equations of motion for rotor (2 degrees of freedom) and pads (1 degree of freedom each) are (Allaire et al., 1981)

Rotor:

$$M\ddot{x} + K_{xx}x + K_{xy}y + C_{xx}\dot{x} + C_{xy}\dot{y} + \sum_{i=1}^{N}(K_{x\delta i}\delta_i + C_{x\delta i}\dot{\delta}_i) = 0 \tag{4.62a}$$

$$M\ddot{y} + K_{yx}x + K_{yy}y + C_{yx}\dot{x} + C_{yy}\dot{y} + \sum_{i=1}^{N}(K_{y\delta_i}\delta_i + C_{y\delta i}\dot{\delta}_i) = 0 \tag{4.62b}$$

ith pad, $i = 1, \ldots, N$

$$I_p\ddot{\delta}_i + K_{\delta\delta_i}\delta_i + C_{\delta\delta_i}\dot{\delta}_i + K_{\delta x_i}x_i + K_{\delta y_i}y_i + C_{\delta x_i}\dot{x}_i + C_{\delta y_i}\dot{y}_i = 0 \tag{4.62c}$$

The coefficients in Eq. (4.62) have the form

$$K_{xx} = -\frac{\Delta F_x}{\Delta x}, C_{yy} = -\frac{\Delta F_y}{\Delta \dot{y}}, K_{x\delta_i} = -\frac{\Delta F_x}{\Delta \delta_i}, C_{y\dot{\delta}_i} = -\frac{\Delta F_y}{\Delta \dot{\delta}_i},$$
$$K_{\delta\delta_i} = -\frac{\Delta M_\delta}{\Delta \delta_i}, C_{\delta\delta_i} = -\frac{\Delta M_\delta}{\Delta \dot{\delta}_i}, K_{\delta x_i} = -\frac{\Delta M_\delta}{\Delta x_i}, C_{\delta y_i} = -\frac{\Delta M_\delta}{\Delta \dot{y}_i}.$$

The first set is obtained by perturbing the equilibrium state of the rotor while constraining the pads. The second set is obtained by constraining the rotor in its equilibrium state and perturbing the pitch angle of the ith pad. The equations of motion, Eqs. (4.62), contain a total of $8 + 10N$ coefficients.

The full stiffness matrix of a five-pad bearing, for example, is (Shapiro and Colsher, 1977; Allaire et al., 1981)

$$
\begin{array}{c|ccccccc}
 & \Delta x & \Delta y & \Delta\delta_1 & \Delta\delta_2 & \Delta\delta_3 & \Delta\delta_4 & \Delta\delta_5 \\
\hline
-\Delta F_x & K_{xx} & K_{xy} & K_{x\delta_1} & K_{x\delta_2} & K_{x\delta_3} & K_{x\delta_4} & K_{x\delta_5} \\
-\Delta F_y & K_{yx} & K_{yy} & K_{y\delta_1} & K_{y\delta_2} & K_{y\delta_3} & K_{y\delta_4} & K_{y\delta_5} \\
-\Delta M_1 & K_{\delta_1 x} & K_{\delta_1 y} & K_{\delta\delta_1} & 0 & 0 & 0 & 0 \\
-\Delta M_2 & K_{\delta_2 x} & K_{\delta_2 y} & 0 & K_{\delta\delta_2} & 0 & 0 & 0 \\
-\Delta M_3 & K_{\delta_3 x} & K_{\delta_3 y} & 0 & 0 & K_{\delta\delta_3} & 0 & 0 \\
-\Delta M_4 & K_{\delta_4 x} & K_{\delta_4 y} & 0 & 0 & 0 & K_{\delta\delta_4} & 0 \\
-\Delta M_5 & K_{\delta_5 x} & K_{\delta_5 y} & 0 & 0 & 0 & 0 & K_{\delta\delta_5}
\end{array}
\tag{4.63}
$$

Similarly for the damping matrix. Note that these matrices are $(N + 2) \times (N + 2)$, where N is the number of pads. Further details of the pad perturbation method of calculating tilting-pad bearing performance can be found in Shapiro and Colsher (1977) and Allaire et al. (1981). For an application of the pad perturbation method, see Section 4.4 on pivoted-pad thrust bearings.

Thermal effects on the stability characteristics of bearings can be considerable. Their importance can be gauged from Table 4.2, which is taken from Suganami and Szeri (1979).

The domain of stable bearing operations changes considerably due to the viscosity nonuniformity that is caused by uneven viscous dissipation in the film. Figure 4.15 illustrates the size, i.e., the Peclet number, effect on stability boundaries.

Table 4.2. *Stiffness and damping coefficients and threshold speed of stability for single mass rigid rotor*

Regime	Model	K_{xx}	K_{xy}	K_{yx}	K_{yy}	C_{xx}	C_{xy}	C_{yx}	C_{yy}	$\bar{M}$
Laminar	Isothermal (ISO)	0.944	−0.076	4.31	5.83	0.598	1.25	1.25	9.25	1.79
	Adiabatic (ADI)	0.832	0.0038	3.85	5.89	0.492	0.940	0.934	7.95	3.08
	Thermohydrodynamic (THD), $D = 20$ cm	1.02	0.0415	4.69	6.14	0.565	1.13	1.12	8.74	2.31
Turbulent	Isothermal (ISO)	0.878	−0.0192	3.94	5.90	0.534	1.04	1.04	8.16	2.77
	Thermohydrodynamic (THD), $D = 60$ cm	0.792	0.052	3.6	5.94	0.455	0.768	0.769	7.01	14.5

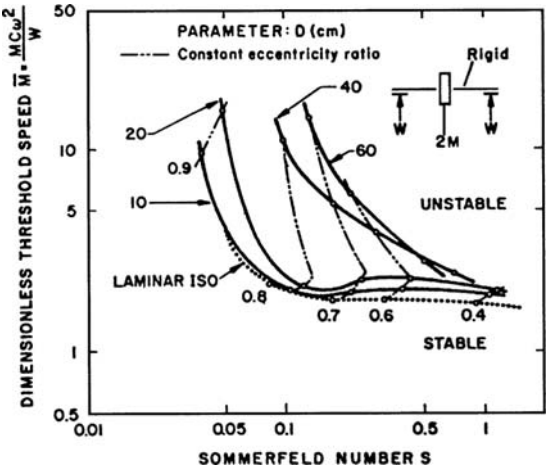

Figure 4.15. Stability of single mass rigid rotor ($N = 3600$ rpm, $C/R = 0.002$, $t = 50°$C). (Reprinted with permission from Suganami, T. and Szeri, A. Z. A parametric study of journal bearing performance: the 80 degree partial are bearing. *ASME Journal of Lubrication Technology*, **101**, 486–491, 1979.)

The effects of inertia and turbulence on dynamic bearing characteristics and on the stability of rotor-bearing system have recently been discussed by Capone, Russo, and Russo (1991).

4.4 Pivoted-Pad Thrust Bearing

The bearing is constructed from N identical, equally spaced, sector–shaped pivoted pads. The pad angle is β, the pad radii are R_1, and $R_2 > R_1$, and the pad thickness is d. The pivot point is located at a distance $(d - \ell)$ from the pad working surface (see Figure 4.16). Because of this assumed uniformity of geometry, it is sufficient for us to consider performance of a single pad. Bearing performance will be obtained by suitable multiplication of single-pad performance.

The pad, pivoted in one point about which it is free to rotate (Figure 3.15), has three rotational degrees of freedom. During the motion of the runner about its equilibrium position, the pad will pivot in a manner that is determined by the dynamics of the whole system, viz., the runner, the oil film, and the pad.

We follow the work of Allaire, Parsell, and Barrett (1981), and evaluate 4×4 spring and damping matrices for each pad. The four degrees of freedom are the rectilinear motion of the runner and the rotational modes of the pad. The motion of the runner and the motion of the pad are connected by means of Euler's rotational equations.

The inertial coordinate system (X, Y, Z) has its origin on the runner surface when the latter is in its undisturbed static equilibrium position, and its Z axis is normal to the runner surface. When occupying its unperturbed static position, the pad is inclined to the runner at angles ψ_X, ψ_Y.

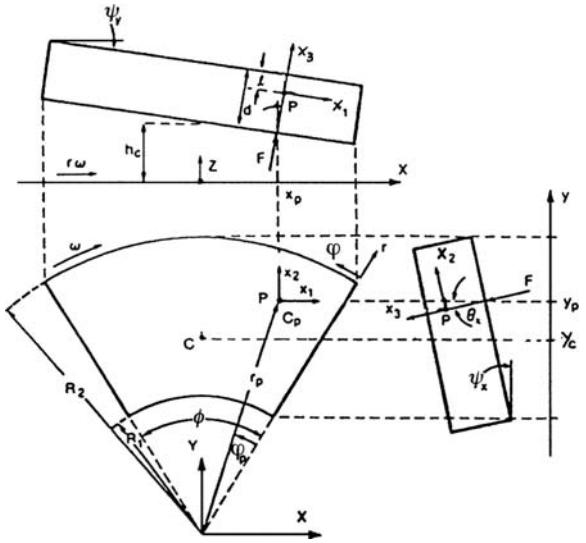

Figure 4.16. Pad schematics. (Reprinted with permission from Jeng, M. C. and Szeri, A. Z. A thermohydrodynamic solution of pivoted thrust pads: Part 3 – linearized force coefficients. *ASME Journal of Tribology*, **108**, 214–218, 1986.)

Let (x_1, x_2, x_3) be an inertial orthogonal Cartesian coordinate system, whose origin is located in the pivot point, at a distance $(d - \ell)$ from pad surface. The (x_1, x_2) plane is parallel to the pad surface in the unperturbed position and x_3 is normal to it.

We denote by $(\xi_1, \xi_2, \xi_3,)$ the body axes, with origin in the pivot point, that rotate with the pad. When the pad is occupying its static equilibrium position the ξ_i coordinate system coincides with the x_i system. The instantaneous (small) rotation of the ξ_i coordinate axes relative to the x_i coordinate axes during motion of the pad is measured by the rotation vector $\alpha = (\alpha_1, \alpha_2, \alpha_3)$.

Let F_0 and F represent the lubricant force in static equilibrium and during a small departure of the runner from the condition of static equilibrium, respectively. Then for small excursion of the runner $Z(t)$ about $Z = 0$, $\dot{Z} = 0$ we may write

$$dF = F - F_0 = \left[\frac{\partial F}{\partial Z}\right]_{Z=\dot{Z}=0} Z + \left[\frac{\partial F}{\partial \dot{Z}}\right]_{Z=\dot{Z}=0} \dot{Z}. \tag{4.64a}$$

The linearized force coefficients Eq. (4.64a) are the system stiffness

$$K = \left[\frac{\partial F}{\partial Z}\right]_{Z=\dot{Z}=0} \tag{4.64b}$$

and the system damping

$$C = \left[\frac{\partial F}{\partial \dot{Z}}\right]_{Z=\dot{Z}=0} \tag{4.64c}$$

Had we fixed the bearing in any particular position, the linearized force coefficients K and C would be easy to calculate

$$\begin{aligned} -\frac{\partial F}{\partial Z} &= \lim_{\Delta h_c \to 0} \frac{F(h_c + \Delta h_c, 0) - F(h_c, 0)}{\Delta h_c}, \qquad \Delta h_c = -Z, \\ -\frac{\partial F}{\partial \dot{Z}} &= \lim_{\Delta \dot{h}_c \to 0} \frac{F(h_c, \Delta \dot{h}_c) - F(h_c, 0)}{\Delta \dot{h}_c}, \qquad \Delta \dot{h}_c = -\dot{Z}, \end{aligned} \tag{4.65}$$

where h_c is the film thickness in the geometric center of the pad. If, however, the pad is free to pivot, the excursion $Z(t)$ of the runner introduces six unknowns to the problem: $\alpha_n(t)$ and $\dot{\alpha}_n(t)$, $n = 1, 2, 3$. Or, to state this differently, tilt of the pad not only causes a righting moment on the pad but introduces forces on the runner as well. The pad has three degrees of freedom, and thus the spring and damping matrices of the system are each 4×4, the four degrees of freedom being the Z motion of the runner and the rotational modes of the pad.

For a pivoting pad, we are thus forced to employ the more complicated Taylor expansion (see Shapiro and Colsher, 1977)

$$dF = \frac{\partial F}{\partial Z} Z + \frac{\partial F}{\partial \dot{Z}} \dot{Z} + \sum \left[\frac{\partial F}{\partial \alpha_n} \alpha_n + \frac{\partial F}{\partial \dot{\alpha}_n} \dot{\alpha}_n \right] \tag{4.66}$$

valid for Z, $\dot{Z}$, α_n and $\dot{\alpha}_n$ small.

In Eq. (4.66), we treat the instantaneous force F as a function of eight kinematic variables[9]

$$F = F(Z, \dot{Z}, \alpha_n, \dot{\alpha}_n), \qquad F_0 = F(0, 0, 0, 0), \qquad n = 1, 2, 3 \tag{4.67}$$

and, accordingly, the partial derivatives are evaluated keeping all but one variable constant, e.g.,

$$\begin{aligned} \frac{\partial F}{\partial Z} &= \lim_{Z \to 0} \frac{F(Z, 0, 0, 0) - F_0}{Z}, \\ \frac{\partial F}{\partial \alpha_2} &= \lim_{\alpha_2 \to 0} \frac{F(0, 0, \alpha_2, 0) - F_0}{\alpha_2}. \end{aligned} \tag{4.68}$$

Employing the notation

$$\begin{aligned} \frac{\partial F}{\partial Z} &= K_{Z,Z}, \qquad \frac{\partial F}{\partial \dot{Z}} = C_{Z,Z}, \\ \frac{\partial F}{\partial \alpha_j} &= K_{Z,j}, \qquad \frac{\partial F}{\partial \dot{\alpha}_j} = C_{Z,j}, \qquad j = 1, 2, 3, \end{aligned} \tag{4.69}$$

Equation (4.66) assumes the form

$$dF = K_{Z,Z} Z + C_{Z,\dot{Z}} \dot{Z} + \sum_{n=1}^{3} [K_{Z,n} \alpha_n + C_{Z,n} \dot{\alpha}_n]. \tag{4.70}$$

The stiffness and damping coefficients in Eq. (4.70) are obtained via the pad perturbation method (Shapiro and Colsher, 1977).

[9] We omit h_c, θ_x, and θ_y, which specify the equilibrium position of the pad, from the argument of F.

Equation (4.70) contains six unknowns, α_n, $\dot{\alpha}_n$, $n = 1, 2, 3$ assuming that Z, $\dot{Z}$ are prescribed. Of course, the α_n, $\dot{\alpha}_n$ are determined by the motion of the runner, i.e., they are dependent on Z, $\dot{Z}$ through the equations of motion for the pad. These equations (Euler's rotational equations) admit solutions with an exponential time factor and, therefore, can be reduced to a linear algebraic system in the amplitudes.

To make use of the above mentioned property of the Euler rotational equations or, ostensibly at this moment, to reduce the number of unknowns in Eq. (4.70), assume that the runner executes small harmonic motion with angular frequency Ω and amplitude ψ (Jeng and Szeri, 1986)

$$Z = \psi \exp(i\Omega t), \tag{4.71a}$$

$$\dot{Z} = i\Omega\psi \exp(i\Omega t). \tag{4.71b}$$

The motion of the pad, as induced by the motion of the runner, will also be harmonic, and we write[10]

$$\alpha_n = A_n \exp(i\Omega t), \tag{4.72a}$$

$$\dot{\alpha}_n = i\Omega A_n \exp(i\Omega t). \tag{4.72b}$$

With the aid of Eqs. (4.71) and (4.72), Eq. (4.70) takes the form

$$dF \exp(-i\Omega t) = [K_{Z,Z} + i\Omega C_{Z,Z}]\psi + \sum_{n=1}^{3} [K_{Z,n} + i\Omega C_{Z,n}]A_n. \tag{4.73}$$

In this form, the equation for dF contains only three unknowns, A_n, $n = 1, 2, 3$. These unknowns are related to the amplitude of the runner motion, ψ, through Euler's rotational equations (Goldstein, 1950)

$$\begin{aligned} I_{11}\ddot{\alpha}_1 - I_{12}\ddot{\alpha}_2 - I_{13}\ddot{\alpha}_3 &= \tau_1, \\ -I_{21}\ddot{\alpha}_1 + I_{22}\ddot{\alpha}_2 - I_{23}\ddot{\alpha}_3 &= \tau_2, \\ -I_{31}\ddot{\alpha}_1 - I_{32}\ddot{\alpha}_2 + I_{33}\ddot{\alpha}_3 &= \tau_3, \end{aligned} \tag{4.74}$$

where I_{11}, $I_{22}, \ldots, I_{33}$ are elements of the inertia matrix. These equations are written relative to the $\{x_1, x_2, x_3\}$ coordinate system, located in the pivot point P. Prior to writing Eq. (4.74), we made the assumption that both $\boldsymbol{\alpha}$ and $\dot{\boldsymbol{\alpha}}$ are small, so that products like $\dot{\alpha}_n\dot{\alpha}_m$; $n, m = 1, 2, 3$, are neglected.

In Eq. (4.74), $\boldsymbol{\tau} = (\tau_1, \tau_2, \tau_3)$ is the torque on the pad resulting from the applied forces and moments relative to $\{x_1, x_2, x_3\}$, $\boldsymbol{\alpha} = (\alpha_1, \alpha_2, \alpha_3)$ is the rotation vector about the same axes, and $\alpha_n = A_n \exp(i\Omega t)$.

The torque components τ_1, τ_2, and τ_3 are dependent on the motion of both runner and pad. For small departures from equilibrium, we are permitted to terminate the Taylor expansion at first order and write

$$\tau_k = \frac{\partial \tau_k}{\partial Z} Z + \frac{\partial \tau_k}{\partial \dot{Z}} \dot{Z} + \sum_{n=1}^{3} \left[\frac{\partial \tau_k}{\partial \alpha_n} \alpha_n + \frac{\partial \tau_k}{\partial \dot{\alpha}_n} \dot{\alpha}_n \right], \quad k = 1, 2, 3. \tag{4.75}$$

[10] It would make no difference in the final outcome had we permitted a phase shift of pad motion relative to runner motion.

The definitions

$$\begin{aligned} \frac{\partial \tau_k}{\partial Z} &= K_{k,Z} \qquad \frac{\partial \tau_k}{\partial \dot{Z}} = C_{k,Z}, \\ \frac{\partial \tau_k}{\partial \alpha_n} &= K_{kn,} \qquad \frac{\partial \tau_k}{\partial \dot{\alpha}_n} = C_{kn}, \end{aligned} \tag{4.76}$$

and Eqs. (4.71) and (4.72) enable us to write Eq. (4.75) in the form

$$\tau_k \exp(-i\Omega t) = [K_{k,Z} + i\Omega C_{k,Z}]\psi + \sum_{n=1}^{3} [K_{kn} + i\Omega C_{kn}]A_n, \quad k = 1, 2, 3. \tag{4.77}$$

Although we do not constrain the pad from motion about x_3, the coefficients K_{k3} and C_{k3}, $k = 1, 2, 3$, will be neglected on account of being small (Mote, Shajer, and Telle, 1983). The torque component τ_3 is also found to be small and is neglected in the analysis.

Substituting Eq. (4.77) into Eq. (4.74), taking into account Eqs. (4.72), we obtain the following linear algebraic system

$$(\boldsymbol{M} + \boldsymbol{N})\,\boldsymbol{A} = \boldsymbol{R}\psi. \tag{4.78}$$

Here $\boldsymbol{R}$ is a column vector of elements

$$R_k = K_{k,Z} + i\Omega C_{k,Z}, \tag{4.79}$$

and the matrices $\boldsymbol{M}$ and $\boldsymbol{N}$ have the definition

$$-M_{km} = (K_{km} + i\Omega C_{km} + \Omega^2 I_{km}), \tag{4.80}$$

$$\boldsymbol{N} = \text{diag}(2\Omega^2 I_{11}, 2\Omega^2 I_{22}, 2\Omega^2 I_{33}). \tag{4.81}$$

The linear system, Eq. (4.78), yields

$$\begin{aligned} \boldsymbol{A} &= (\boldsymbol{M} + \boldsymbol{N})^{-1}\,\boldsymbol{R}\psi \\ &= \boldsymbol{a}\psi, \end{aligned} \tag{4.82}$$

where

$$\boldsymbol{a} = (\boldsymbol{M} + \boldsymbol{N})^{-1}\,\boldsymbol{R}.$$

Note that $\boldsymbol{a} = \mathcal{R}(\boldsymbol{a}) + i\mathcal{J}(\boldsymbol{a})$ is a complex vector, it includes both the amplitude and the phase angle of the pad motion about P.

The force response, dF, of Eq. (4.70) to the excitation Eqs. (4.71) and (4.72) is harmonic, and when Eq. (4.82) is substituted into Eq. (4.73), we obtain

$$dF \exp(-i\Omega t) = (\mathcal{K} + \mathcal{C}i\Omega)\,\psi. \tag{4.83}$$

From Eq. (4.83), the system stiffness and system damping are identified, respectively, as

$$\mathcal{K} = K_{Z,Z} + \sum_{n=1}^{3} \{K_{Z,n}\mathcal{R}(a_n) - \Omega C_{Z,n}\mathcal{J}(a_n)\} \tag{4.84}$$

and

$$\mathcal{C} = C_{Z,Z} + \sum_{n=1}^{3} \{C_{Z,n}\mathcal{R}(a_n) - K_{Z,n}\mathcal{J}(a_n)/\Omega\}. \tag{4.85}$$

The nondimensional inertia tensor

$$\bar{\boldsymbol{I}} = \frac{\omega h_c}{\mu_*(\Delta R)^4}\boldsymbol{I} \tag{4.86}$$

can be evaluated in closed form. It has components

$$\bar{I}_{11} = \bar{M}_p\left\{\frac{1}{4}\left(1+\frac{\sin\beta}{\beta}\right)+\frac{\bar{d}^2}{3\left(\bar{R}_2^2+\bar{R}_1^2\right)}[\bar{\ell}^3+(1-\bar{\ell})^3]+\frac{\bar{Y}_p(\bar{Y}_p-2\bar{Y}_c)}{\left(\bar{R}_2^2+\bar{R}_1^2\right)}\right\}, \tag{4.87a}$$

$$\bar{I}_{22} = \bar{M}_p\left\{\frac{1}{4}\left(1-\frac{\sin\beta}{\beta}\right)+\frac{\bar{d}^2}{3\left(\bar{R}_2^2+\bar{R}_1^2\right)}[\bar{\ell}^3+(1-\bar{\ell})^3]+\frac{\bar{X}_p^2}{\left(\bar{R}_2^2+\bar{R}_1^2\right)}\right\}, \tag{4.87b}$$

$$\bar{I}_{33} = \bar{M}_p\left\{\frac{1}{2}+\frac{[\bar{r}_p+\bar{R}_1]^2-2\bar{Y}_p\bar{Y}_c}{\left(\bar{R}_2^2+\bar{R}_1^2\right)}\right\}, \tag{4.87c}$$

$$\bar{I}_{12} = \bar{M}_p\left\{\frac{\bar{X}_p(\bar{Y}_p-\bar{Y}_c)}{\left(\bar{R}_2^2+\bar{R}_1^2\right)}\right\}, \tag{4.87d}$$

$$\bar{I}_{13} = -\bar{M}_p\left\{\frac{\bar{X}_p\bar{Z}_c}{\left(\bar{R}_2^2+\bar{R}_1^2\right)}\right\}, \tag{4.87e}$$

$$\bar{I}_{23} = \bar{M}_p\left\{\frac{2\left(\bar{R}_2^3-\bar{R}_1^3\right)\bar{d}[\bar{\ell}^2-(1-\bar{\ell})^2]}{3\left(\bar{R}_2^4-\bar{R}_1^4\right)}\frac{\sin\beta/2}{\beta}-\frac{\bar{Y}_p\bar{Z}_c}{\left(\bar{R}_2^2+\bar{R}_1^2\right)}\right\}, \tag{4.87f}$$

where

$$M_p = \frac{\left(R_2^2-R_1^2\right)\beta t}{2}\rho_p = \frac{\mu_*(\Delta R)^4}{\omega h_c\left(R_2^2+R_1^2\right)}\bar{M}_p \tag{4.88}$$

is the pad mass, ρ_p is the pad density, and d is the pad thickness.

In Eq. (4.87) we made use of the abbreviations

$$\bar{R}_1 = \frac{R_1}{\Delta R},\quad \bar{d} = \frac{d}{\Delta R},\quad \bar{\ell} = \frac{\ell}{d},\quad \bar{R}_2 = \frac{R_2}{\Delta R},\quad \bar{r} = \frac{r-R_1}{\Delta R},\quad \Delta R = R_2 - R_1. \tag{4.89}$$

The distance $(d-\ell)$ measures the separation between the center of pressure (r_p, φ_p) and the pivot location, P; if the pad is supported on its surface, then $d-\ell=0$. The coordinates (X_p, Y_p, Z_p) and (X_c, Y_c, Z_c) are the coordinates of the pivot point, P, and the geometric center, C, of the pad, respectively, relative to the $\{X, Y, Z\}$coordinate system (Figure 4.16). In normalized form,

$$\begin{aligned}
\bar{X}_p &= [\bar{r}_p+\bar{R}_1]\sin\left[\beta\left(\frac{1}{2}-\bar{\varphi}_p\right)\right]\\
\bar{Y}_p &= [\bar{r}_p+\bar{R}_1]\cos\left[\beta\left(\frac{1}{2}-\bar{\varphi}_p\right)\right]\\
\bar{Z}_p &= 0,
\end{aligned} \tag{4.90}$$

$$\begin{aligned}\bar{X}_c &= 0,\\ \bar{Y}_c &= \frac{4}{3\beta}\left(\frac{\bar{R}_2^3-\bar{R}_1^3}{\bar{R}_2^2-\bar{R}_1^2}\right)\sin\frac{\beta}{2}\\ \bar{Z}_c &= \frac{1}{2}\bar{d}\,(2\ell-1)\,.\end{aligned} \tag{4.91}$$

Here $\bar{r}_p$ is the nondimensional radial coordinate of the center of pressure.

The foregoing equations may be nondimensionalized by specifying a force coefficient, c_F, and a torque coefficient, c_τ, through the formulas

$$\begin{aligned}c_F &= \frac{\mu_*\omega\,(\Delta R)^4}{h_c^2},\\ c_\tau &= \frac{\mu_*\omega\,(\Delta R)^4}{h_c},\end{aligned} \tag{4.92}$$

so that we may write

$$F = c_F\bar{F}, \qquad \boldsymbol{\tau} = c_\tau\bar{\boldsymbol{\tau}} \tag{4.93}$$

which serve as definition for the nondimensional quantities $\bar{F}$ and $\bar{\boldsymbol{\tau}}$.

Defining, furthermore, nondimensional spring and damping coefficients through

$$K_{Z,j} = c_F\bar{K}_{Z,j}; \qquad C_{Z,j} = \frac{c_F}{\omega}\bar{C}_{Z,j}, \tag{4.94a}$$

$$K_{Z,Z} = \frac{c_F}{h_c}\bar{K}_{Z,Z}; \qquad C_{Z,Z} = \frac{c_F}{h_c\omega}\bar{C}_{Z,Z}, \tag{4.94b}$$

$$K_{k,Z} = \frac{c_\tau}{h_c}\bar{K}_{k,Z}; \qquad C_{k,Z} = \frac{c_\tau}{\omega h_c}\bar{C}_{k,Z}, \tag{4.94c}$$

$$K_{mn} = c_\tau\bar{K}_{mn}; \qquad C_{mn} = \frac{c_\tau}{\omega}\bar{C}_{mn}, \tag{4.94d}$$

and setting

$$\bar{t} = \omega t, \qquad \bar{\psi} = \psi/h_c, \qquad \hat{\Omega} = \frac{\Omega}{\omega},$$

the dimensionless system stiffness and system damping, the counterpart of Eq. (4.84), is given by

$$\bar{\mathcal{K}} = \bar{K}_{Z,Z} + \sum_{n=1}^{3}\{\bar{K}_{Z,n}\mathcal{R}(a_n) - \bar{\Omega}\bar{C}_{Z,n}\mathcal{J}(a_n)\}, \tag{4.95a}$$

$$\bar{\mathcal{C}} = \bar{C}_{Z,Z} + \sum_{n=1}^{3}\left\{\bar{C}_{Z,n}\mathcal{R}(a_n) + \bar{K}_{Z,n}\mathcal{J}(a_n)/\bar{\Omega}\right\}, \tag{4.95b}$$

so that

$$\mathcal{K} = \frac{c_F}{h_c}\bar{\mathcal{K}}, \qquad \mathcal{C} = \frac{c_F}{h_c\omega}\bar{\mathcal{C}}. \tag{4.96}$$

The quantities $\mathcal{K}$ and $\mathcal{C}$ have physical dimensions of stiffness (= force/length) and damping (= force/velocity), respectively.

Table 4.3. *Linearized stiffness and damping coefficients*

	$\bar{\mathcal{K}}$		$\bar{\mathcal{C}}$	
$\bar{\Omega}$	$\bar{\mu} = 1.0$	$\bar{\mu} = \bar{\mu}(T)$	$\bar{\mu} = 1.0$	$\bar{\mu} = \bar{\mu}(T)$
0.1	0.4523	0.1717	0.3108	0.1407
0.5	0.4907	0.1746	0.3120	0.1393
1.0	0.4921	0.1747	0.3121	0.1392
5.0	0.4926	0.1747	0.3121	0.1392
10.0	0.4926	0.1747	0.3121	0.1392

$R_2/R_1 = 2.545$, $\beta = 24^\circ$, $\bar{\varepsilon} = 0$, $m_x = 0.0$, $m_y = 1.0$, Re $= 500$. (Reprinted with permission from Jeng, M. C. and Szeri, A. Z. A thermohydrodynamic solution of pivoted thrust pads: Part 3 − linearized force coefficients. *ASME Journal of Tribology*, **108**, 214–218, 1986.)

Table 4.3 illustrates the effect of $\bar{\Omega}$, the ratio of excitational to rotational frequencies. At least for the geometry depicted, dependence of both the system stiffness $\bar{\mathcal{K}}$ and the system damping $\bar{\mathcal{C}}$ on $\bar{\Omega}$ appears to be insignificant. A stronger effect, that due to the temperature dependence of viscosity, is also depicted in this table; both the stiffness, $\bar{\mathcal{K}}$, and the damping, $\bar{\mathcal{C}}$, are affected by the temperature dependence of viscosity.

Table 4.4 tabulates $\bar{\mathcal{K}}$ and $\bar{\mathcal{C}}$ values for various magnitudes of the nondimensional pad mass, $\bar{M}_p$. The dependence of system stiffness and damping on $\bar{M}_p$ seems to be of little significance.

Figure 4.17 illustrates the dependence of $\bar{\mathcal{K}}$ and $\bar{\mathcal{C}}$ on the crowning of the pad. The pad deformation parameter, $\bar{\varepsilon}$, is defined by Jeng, Zhou, and Szeri (1986) as the ratio of the maximum deflection in the $y - z$ plane (Figure 4.16) to the pad center film thickness, h_c. This figure depicts calculations at $\bar{\Omega} = 1.0$ and $\bar{\Omega} = 0.1$, performed in an iterative manner so that the position of the pivot point remained fixed. This meant that the pad tilt parameter had to be adjusted from solution to solution and also from iteration to iteration between the pressure

Table 4.4. *Linearized stiffness and damping coefficients*

$\bar{M}_p$	$\bar{\mathcal{K}}$	$\bar{\mathcal{C}}$
479.82	0.4921	0.3121
47.982	0.4870	0.3119
4.7982	0.4453	0.3112
0.47982	0.4629	0.3219
0.047982	0.4925	0.3120

$R_2/R_1 = 2.545$, $\beta = 24^\circ$, $\bar{\varepsilon} = 0$, $\bar{\Omega} = 1.0$, $m_x = 0.0$, $m_y = 1.0$, Re $= 500$. (Reprinted with permission from Jeng, M. C. and Szeri, A. Z. A thermohydrodynamic solution of pivoted thrust pads: Part 3 − linearized force coefficients. *ASME Journal of Tribology*, **108**, 214–218, 1986.)

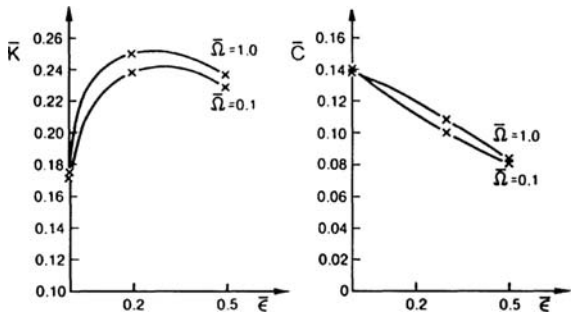

Figure 4.17. Variations of system stiffness $\bar{\mathcal{K}}$ and system damping $\bar{\mathcal{C}}$ with pad deformation parameter $\bar{\varepsilon}$; $R_2/R_1 = 2.545$, $b = 24^\circ$, $m_x = 0.0$, $m_y = 1.0$, Re $= 500$. (Reprinted with permission from Jeng, M. C. and Szeri, A. Z. A thermohydrodynamic solution of pivoted thrust pads: Part 3 – linearized force coefficients. *ASME Journal of Tribology*, **108**, 214–218, 1986.)

and the energy equations (Jeng, Zhou, and Szeri, 1986). Dependence of system stiffness and system damping on pad deformation seems to be strong. The solutions in Figure 4.17 were obtained from thermohydrodynamic bearing performance, i.e., the viscosity in this solution is dependent on temperature and thus has a three-dimensional distribution.

4.5 Nomenclature

C	pad clearance
$\mathcal{C}$	system damping
C'	pivot circle clearance
$C_{xx}, C_{xy}, C_{yx}, C_{yy}$	bearing damping coefficients
$C_{\xi\xi}, C_{\xi\eta}, C_{\eta\xi}, C_{\eta\eta}$	fixed-pad damping coefficients
$C'_{\xi\xi}, C'_{\xi\eta}, C'_{\eta\xi}, C'_{\eta\eta}$	tilting-pad damping coefficients
D	journal diameter
e	journal center eccentricity with respect to pad center
e_0	journal center eccentricity with respect to bearing center
F_r, F_t	radial and tangential components of pressure-force
F_ξ, F_η	force components in ξ and η-directions
f_r, f_t	radial and tangential components of dimensionless pad force
f_ξ, f_η	compoents in ξ and η-directions of dimensionless pad fore
I	transverse mass moment of inertia of shoe around pivot
$\mathcal{K}$	system damping
$K_{xx}, K_{xy}, K_{yx}, K_{yy}$	bearing spring coefficients
$K_{\xi\xi}, K_{\xi\eta}, K_{\eta\xi}, K_{\eta\eta}$	fixed-pad spring coefficients
$K'_{\xi\xi}, K'_{\xi\eta}, K'_{\eta\xi}, K'_{\eta\eta}$	tilting-pad spring coefficients
L	bearing length, inches
M_{CRIT}	critical pad mass
R	journal radius
R_P	radius of pivot circle
S_B	bearing Sommerfeld number
S	pad Sommerfeld number
W	load

x, y	coordinates of journal center with respect to the bearing
ε	eccentricity ratio with respect to the pad center
ε_0	eccentricity ratio with respect to the bearing center
η_p	amplitude for pad center motion
δ_i	*deflection, ith pad*
ξ, η	coordinates of journal center with respect to the pad
ϕ	attitude angle with respect to the pad load line
ϕ_0	attitude angle with respect to the bearing load line
n	angle from vertical (negative x-axis) to pad pivot point
ω	angular speed of shaft

Thrust Bearings

$\mathbf{A}(A_i)$	amplitude of angular perturbation
$C_{Z,Z}$; C_{Z_n}	damping
$C_{k,m}$; $C_{n,Z}$	damping
$\mathcal{C}$	system damping
C	pad geometric center
C_p	center of pressure
f	lubricant force
$\mathbf{I}$	inertia tensor
$K_{Z,Z}$; $K_{Z,n}$	stiffness
$K_{k,n}$; $K_{n,Z}$	stiffness
$\mathcal{K}$	system stiffness
M_p	pad mass
R_1, R_2	inner, outer pad radius
Re	global Reynolds number ($= R_2\omega h_c/v_*$)
(X, Y, Z)	inertial coordinates
r, φ	pad angular coordinates
Ω	frequency of runner motion
c_F, c_τ	force, torque coefficients
d	pad thickness
ℓ	depth of pivot point
m_x	radial tilt parameter ($= R_1\theta_x/h_c$)
m_y	azimuthal tilt parameter ($= R_1\theta_y/h_c$)
h_c	film thickness at C
θ_x, θ_y	pad tilt angles
t	time
$\boldsymbol{\alpha}(\alpha_i)$	angular motion of pad
β	pad angle
$\bar{\rho}$	lubricant density
ω	runner angular velocity
ν, μ	viscosity
$\boldsymbol{\tau}, (\tau_i)$	torque
$(\dot{})$	time derivative
$(-)$	nondimensional quantity
$\mathcal{R}, \mathcal{J}$	real, imaginary part
$(\,)_*$	reference quantity

4.6 References

Alford, J. S. 1965. Protecting turbomachinery from self-excited rotor whirl. *ASME J. Eng. Power*, **87**, 333.

Allaire, P. E., Parsell, J. K. and Barrett, L. E. 1981. A pad perturbation method for the dynamic coefficients of tilting-pad journal bearings. *Wear*, **72**, 29–44.

Boyd, J. and Raimondi, A. A. 1962. Clearance considerations in pivoted pad journal bearings. *ASLE Trans.*, **5**, 418.

Capone, G., Russo, M. and Russo, R. 1991. Inertia and turbulence effects on dynamic characteristics and stability of rotor-bearings systems. *ASME Journal of Tribology*, **113**, 58–64.

Den Hartog, J. P. 1956. *Mechanical Vibrations*, 4th ed. McGraw-Hill, New York.

Goldstein, H. 1950. *Classical Mechanics*. Addison-Wesley.

Hagg, A. C. 1946. Influence of oil-film journal bearings on the stability of rotating machines. *ASME Trans. J. Appl. Mech.* **68**, A211.

Hori, Y. 1959. A theory of oil whip. *ASME J. Appl. Mech.*, **26**, 189–198.

Jeng, M. C. and Szeri, A. Z. 1986. A thermohydrodynamic solution of pivoted thrust pads: Part 3 – linearized force coefficients. *ASME Journal of Tribology*, **108**, 214–218.

Jeng, M. C., Zhou, G. R. and Szeri, A. Z. 1986. A thermohydrodynamic solution of pivoted thrust pads: Part 2 – static loading. *ASME Journal of Tribology*, **108**, 208–213.

Lund, J. W. 1964. Spring and damping coefficients for the tilting-pad journal bearing. *ASLE Trans.*, **7**, 342.

Lund, J. W. and Sternlicht, B. 1962. Rotor bearing dynamics with emphasis on attenuation. *ASME J. Basic Engr.*, **84**, 491–502.

Mote, C. D., Shajer, G. S. and Telle, L. I. 1983. Hydrodynamic sector bearings as circular saw guides. *ASME Journal of Lubrication Technology*, **105**, 67–76.

Nicholas, J. C., Gunter, E. J. and Allaire, P. E. 1979. Stiffness and damping properties for the five-pad tilting pad bearing. *ASLE Trans.*, **22**, 113–224.

Pinkus, O. and Sternlicht, B. 1961. *Theory of Hydrodynamic Lubrication*. McGraw-Hill, New York.

Raimondi, A. A. and Szeri, A. Z. 1984. Journal and thrust bearings. *CRC Handbook of Lubrication*, E. R. Booser (ed.), pp. 413–462.

Shapiro, W. and Colsher, R. 1977. Dynamic characteristics of fluid-film bearings. *Proc. 6th Turbomachinery Symp.*, Texas A&M University, 39–54.

Suganami, T. and Szeri, A. Z. 1979. A parametric study of journal bearing performance: the 80 degree partial arc bearing. *ASME Journal of Lubrication Technology*, **101**, 486–491.

Szeri, A. Z. 1966. Linearized force coefficients of a 110° partial journal bearing. *Proc. Inst. Mech. Engr.*, **181**, Pt. 3B, Paper No. 8.

Szeri, A. Z., Raimondi, A. A. and Giron, A. Linear force coefficients for squeeze-film damper. *ASME Journal of Lubrication Technology*, **105**, 326–334.

Trumpler, R. P. 1966. *Design of Film Bearings*. MacMillan, New York.

Vance, J. M. 1988. *Rotordynamics of Turbomachinery*. Wiley, New York.

Effects of Fluid Inertia

The essence of lubrication theory is the recognition that the problem possesses two length scales (see Figure 2.7). Let the length scale in the "plane" of the film be denoted by L_{xz}, and let L_y be the length scale across the film; for conventional bearing geometries $(L_y/L_{xz}) = O(10^{-3})$. We utilize these length scales to normalize the equations of motion. To this end, define nondimensional coordinates, denoted by overbar, as follows

$$\{\bar{x}, \bar{y}, \bar{z}\} = \frac{1}{L_{xz}} \left\{ x, \left(\frac{L_{xz}}{L_y}\right) y, z \right\}. \tag{2.58a}$$

Furthermore, let U_* represent the characteristic velocity in the plane of the film. The equation of continuity then requires $U_*(L_y/L_{xz})$ to be the velocity scale across the film, and we arrive at the following definition for normalized velocity:

$$\{\bar{u}, \bar{v}, \bar{w}\} = \frac{1}{U_*} \left\{ u, \left(\frac{L_{xz}}{L_y}\right) v, w \right\}, \tag{2.58b}$$

where the overbar again denotes normalized, i.e., $O(1)$, nondimensional quantity. The nondimensional pressure and time are chosen to be

$$\bar{p} = \frac{p}{\rho U_*^2} \left(\frac{L_y}{L_{xz}}\right) \mathrm{Re}, \qquad \bar{t} = \Omega t. \tag{2.58c}$$

Here Ω is the characteristic frequency of the flow, and the Reynolds number has the definition $\mathrm{Re} = L_y U_*/\nu$. The assumption $\Omega \approx U^*/L_{xz}$ yields the second of (2.58c).

Substituting into the Navier-Stokes equations and neglecting terms of order $(L_y/L_{xz})^2$, but retaining we obtain

$$\Omega^* \frac{\partial \bar{u}}{\partial \bar{t}} + \mathrm{R}_\varepsilon \bar{\mathbf{v}} \cdot \nabla \bar{u} = -\frac{\partial \bar{p}}{\partial \bar{x}} + \frac{\partial^2 \bar{u}}{\partial \bar{y}^2}, \tag{2.62a}$$

$$\Omega^* \frac{\partial \bar{w}}{\partial \bar{t}} + \mathrm{R}_\varepsilon \bar{\mathbf{v}} \cdot \nabla \bar{w} = -\frac{\partial \bar{p}}{\partial \bar{z}} + \frac{\partial^2 \bar{w}}{\partial \bar{y}^2}. \tag{2.62b}$$

Here $\Omega^* = L_y^2 \Omega/\nu$ and $\mathrm{R}_\varepsilon = (L_y/L_{xz})\,\mathrm{Re}$ are the *reduced frequency* and the *reduced Reynolds number*, respectively, and $p = p(x, z)$ alone.

The continuity equation is, of course, form invariant under the transformation Eqs. (2.58)

$$\frac{\partial \bar{u}}{\partial \bar{t}} + \frac{\partial \bar{v}}{\partial \bar{y}} + \frac{\partial \bar{w}}{\partial \bar{z}} = 0. \tag{2.16c}$$

According to Eqs. (2.58a) and (2.58b), lubricant inertia effects assume importance when $\Omega^* > 1$ and/or $\mathrm{R}_\varepsilon > 1$. The three limiting cases that are instructive to consider here are: (1) *temporal inertia* limit, characterized by $\mathrm{R}_\varepsilon/\Omega^* \to 0$, $\Omega^* > 1$; (2) the *convective inertia*

limit, characterized by $\Omega^*/\mathrm{R}_\varepsilon \to 0$, $\mathrm{R}_\varepsilon > 1$; and (3) the *total inertia* limit, characterized by $\mathrm{R}_\varepsilon/\Omega^* \to O(1)$, $\mathrm{R}_\varepsilon > 1$.

5.1 Temporal Inertia Limit, $\mathrm{R}_\varepsilon \to 0$, $\Omega^* \geq 1$

When one of the bearing surfaces undergoes rapid, small-amplitude oscillation, the condition $\Omega^* \gg \mathrm{R}_\varepsilon$ is approximately satisfied. In this case, we retain the temporal inertia terms in Eqs. (2.53) and (2.54) but drop the terms representing convective inertia (Schlichting, 1968). Expressed in primitive variables, the equations of motion have now the reduced form

$$\begin{aligned} \rho\frac{\partial u}{\partial t} &= -\frac{\partial p}{\partial x} + \mu\frac{\partial^2 u}{\partial y^2}, \\ \rho\frac{\partial w}{\partial t} &= -\frac{\partial p}{\partial z} + \mu\frac{\partial^2 w}{\partial y^2}. \end{aligned} \tag{5.1}$$

We note that these equations are linear.

To accelerate a solid body through a fluid, a force must applied to accelerate the mass of the body itself. Additional force must also be applied to accelerate the mass of fluid that is being set in motion by the body. The added mass coefficient, C_M, is defined as the factor that multiplies the mass of the displaced fluid to give the mass of the accelerated fluid. Studies of added mass can be traced back to Stokes (Rosenhead, 1963). More recently, Chen et al. (1976) expressed Eq. (5.1) in terms of the stream function and found an exact solution to the resulting linear fourth-order partial differential equation in terms of Bessel functions. They were able to show that for a rod vibrating in a "large" cylinder filled with viscous fluid, both the *added mass coefficient,* C_M, and the *damping coefficient,* C_v, have their maximum at small Ω^* and decrease with $\Omega^* \uparrow$. This was also demonstrated by the analysis of Brennen (1976), who obtained a large Reynolds number limit for the added mass coefficient. Brennen found that for the ratio of C_M obtained at $\Omega^* \to 0$ to its value obtained at $\Omega^* \to \infty$ is ≈ 1.2. Tichy and Modest (1978) solved Eq. (5.1) for an arbitrary two-dimensional surface executing normal oscillation and found the classical lubrication solution for pressure to be in error, due to neglect of inertia forces. This analysis was extended later by Modest and Tichy (1979) to combined oscillation and sliding. Mulcahy (1980) was able to show that for $\Omega^* < 25$ the added mass coefficient, C_M, is independent of the reduced frequency and that in the range $0 < \Omega^* < 25$ the ratio C_M/C_v is linear in the reduced frequency according to the formula $C_M/C_v \approx \Omega^*/10$. For Ω^* . 25 Mulcahy found that $C_M = C_M(\Omega^*)$ and that it is a decreasing function for $\Omega^* \uparrow$, as indicated by earlier investigators.

5.2 Convective Inertia Limit, $\Omega^* \to 0$, $\mathrm{R}_\varepsilon \geq 1$

In journal or thrust bearings in near steady state at high Reynolds number we have $\mathrm{R}_\varepsilon \gg \Omega^*$. This condition approximates to the limit $\Omega^*/\mathrm{R}_\varepsilon \to 0$, and we neglect temporal inertia in favor of convective inertia. When written in terms of primitive variables, this limit

results in the equations

$$\rho\left(u\frac{\partial u}{\partial x}+v\frac{\partial u}{\partial y}+w\frac{\partial u}{\partial z}\right)=-\frac{\partial p}{\partial x}+\mu\frac{\partial^2 u}{\partial y^2},$$
$$\rho\left(u\frac{\partial w}{\partial x}+v\frac{\partial w}{\partial y}+w\frac{\partial w}{\partial z}\right)=-\frac{\partial p}{\partial z}+\mu\frac{\partial^2 w}{\partial y^2}. \tag{5.2}$$

Sestieri and Piva (1982) applied Eq. (5.2) to a plane slider in a numerical analysis. They showed significant inertia effects, up to 40% in load, for $R_\varepsilon = 8$. Care must be taken, however, when interpreting the results of Sestieri and Piva. As was pointed out by Constantinescu and Galetuse (1982), a reduced Reynolds number of $R_\varepsilon = 8$ for the slider geometry of Sestieri and Piva translates to Re = 25,000 in a conventional journal bearing.

Szeri and Snyder (2006) recently investigated the plane slider and asserted that Eq. (5.2) is a valid first extension of the classical Reynolds equation to higher Reynolds number flows (c.f., the last section of Chapter 2), provided that the thin film approximation is not violated. By keeping the runner plane and perturbing the film thickness to $h + \Delta h$, $\Delta h(x) = \delta\cos(n\pi x)$, they further concluded that the sign of the load capacity change due to inertial effects is dictated by local film geometry approaching the outlet

$$sgn(f_{Re} - f_0) = -sgn\frac{dh}{dx}\Big|_{x_{out}}$$

Here x is increasing in the flow direction, i.e., $(x_{out} - x_{in})U > 0$ and the index of f is indicative of the value of the flow Reynolds number.

For long cylinders at $R_\varepsilon = 30$ San Andres and Szeri (1985) obtain, from numerical solutions of the exact equations, a 47% change in pressure due to inertia when $C/R = 1.0$. But as $(C/R) \downarrow$, the results from the exact equations decrease monotonically to the results of classical lubrication theory. Above Re = 2,000 the flow becomes turbulent, but even there inertial effects can be neglected according to Constantinescu and Galetuse (1982).

The method of averaged inertia was employed for the steady problem by Osterle, Chou, and Saibel (1957) for a long bearing, and by Constantinescu (Constantinescu, 1970; Constantinescu and Galetuse, 1982). The more recent of these papers finds that in conventional journal bearings convective inertia effects can be neglected in the range $0 < R_\varepsilon < 10$. Although at the upper end of the range inertia effects do appear, they are still small in comparison with other nonlinear effects such as thermal distortion. Burton and Hsu (1974) find that at small downward vertical load the journal center might rise above the bearing center, as was shown experimentally by Black and Walton (1974). Others to use the method of averaged inertia were Launder and Leschziner (1978).

Journal Bearings

In one of the early publications on flow between eccentric rotating cylinders, Wannier (1950) discussed the problem without restricting the geometry; he used a complex variable technique to solve the biharmonic equation, satisfied by the stream function in Stokes flow. Wannier showed that the Reynolds equation of classical lubrication theory (Reynolds, 1886) constitutes the zero-order approximation to the Navier-Stokes equations

when the stream function is expanded in powers of the film thickness. Wood (1957), using a modified bipolar coordinate system that reduces to polar coordinates when the eccentricity vanishes, analyzed the boundary layers that develop on the two cylinders at large Reynolds numbers. The small parameter of the perturbation analysis is the eccentricity ratio, and the solution is expressed in combinations of Bessel functions.

The effect of fluid inertia is estimated from a perturbation of the Stokes flow in Kamal's (1966) analysis. Kamal's inertial correction is incorrect, however, as was pointed out first by Ashino (1975) and later by Ballal and Rivlin (1976); even their solution of the Stokes problem shows disagreement with recent results. Another small perturbation analysis with the eccentricity ratio as the parameter was published by Kulinski and Ostratch (1967). Yamada (1968) neglected curvature effects and solved the boundary layer equations for the case of a rotating outer cylinder. Assuming a perturbation series in the clearance ratio, Yamada showed that the results of the unperturbed flow agree with those of lubrication theory. The importance of the inertial correction is found in the pressure distribution: the largest negative pressure is greater in magnitude than the largest positive pressure. This conclusion also received support from Sood and Elrod (1974).

DiPrima and Stuart (1972a) obtained inertial corrections to the linearized problem at small clearance ratios and at small values of the modified Reynolds number. Their zero-order approximation is identical to lubrication theory. Results presented by DiPrima et al. are in good agreement with those of Yamada. The perturbation analysis of Ballal and Rivlin (1976) is one of the most complete analyses performed to date on the flow between eccentric rotating cylinders, but the solution is incorrect except for Stokes flow (San Andres and Szeri, 1985), as the boundary conditions are not satisfied for $\mathrm{Re} > 0$. San Andres and Szeri (1985) worked out an accurate numerical solution of the exact equations and applied it to the wide-gap problem with arbitrary rotation of the cylinders. The analysis was recently extended to account for heat transfer in a fluid with temperature dependent viscosity by Dai, Dong, and Szeri (1991) and Kim and Szeri (1996) and to Rivlin-Ericksen fluids of third grade by Christie, Rajagopal, and Szeri (1987).

The questions we shall investigate here are:

(1) What is *the effect of neglecting convective lubricant inertia*?
(2) What is the *effect of neglecting curvature* of the lubricant film?

To answer these questions we shall examine three models for flow in a long journal bearing. The first model *retains both inertia and curvature* of the film and is based on the full Navier-Stokes equations. The second model *retains film curvature but neglects inertia* and results from application of the lubrication approximation in the natural coordinates that provide exact representation of the curved boundaries. The third model, classical lubrication theory, *neglects both inertia and film curvature* and results from application of the lubrication approximation in Cartesian coordinates.

Navier-Stokes Model

We employ a bipolar coordinate system for the representation of the flow field between infinite, rotating eccentric cylinders. The bipolar coordinate system $\{\hat{\alpha},\ \hat{\beta}\}$ is related to the Cartesian coordinate system $\{X, Y\}$ through

$$\hat{\alpha} + i\hat{\beta} = -2\coth^{-1}\frac{(X + iY)}{a}, \tag{5.3}$$

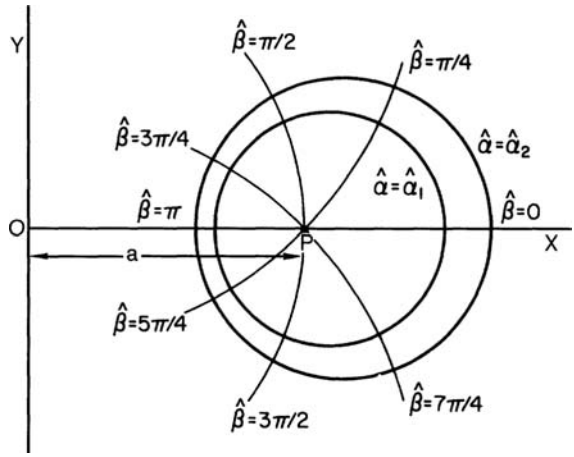

Figure 5.1. Geometry and coordinate systems for eccentric cylinders.

where a is the separation between the pole and the origin of the $\{X, Y\}$ system (Figure 5.1). In the bipolar coordinate system, the cylinders of radii r_1 and r_2, $r_1 < r_2$, have the simple representation $\hat{\alpha} = \hat{\alpha}_1$ and $\hat{\alpha} = \alpha_2$, $\hat{\alpha}_1 < \alpha_2 < 0$, respectively. The scale factor, H, of the bipolar coordinate system (Ritchie, 1968) is

$$H = \frac{a}{(\cosh\hat{\alpha} - \cos\hat{\beta})}.$$

The equations of motion and continuity defining the two-dimensional flow field are first written relative to the bipolar coordinate system (Ritchie, 1968) and then nondimensionalized as follows:

$$\begin{aligned}
&\alpha = \Delta\,(\hat{\alpha} - \hat{\alpha}_1)\,, \qquad \beta = \frac{\hat{\beta}}{2\pi}, \qquad \Delta = \frac{1}{\hat{\alpha}_2 - \hat{\alpha}_1}, \\
&\{U, V\} = \frac{r_1\omega}{\sinh|\hat{\alpha}_1|}\,\{u, v\}\,, \qquad p = \frac{\rho r_1^2\omega^2}{\sinh^2|\hat{\alpha}_1|}\,p \\
&H = ah, \quad \mathrm{Re} = \frac{r_1\omega C}{\nu}, \quad C = r_2 - r_1, \quad \eta = \frac{r_1}{r_2}.
\end{aligned} \tag{5.4a}$$

Here P represents the pressure and $\{U, V\}$ are the physical components of velocity relative to the bipolar coordinate system, while p and $\{u, v\}$ are their dimensionless counterparts. Dynamic conditions in the flow are represented by the Reynolds number, Re, calculated on the mean gap width. In terms of bipolar coordinates the eccentricity ratio is given by

$$\varepsilon = \frac{\sinh(\hat{\alpha}_1 - \hat{\alpha}_2)}{\sinh\hat{\alpha}_1 - \sinh\hat{\alpha}_2}. \tag{5.4b}$$

We intend to solve the steady-state problem. It is well documented, however, that for equal interpolation of velocity and pressure the mixed formulation of the steady-state Navier-Stokes equation yields a singular system. To circumvent this (*Babushka-Brezzi stability criteria*), Hughes, Franca, and Balestra (1986) employed an ingenious weighting procedure that resulted in a stable system. Though this system contains extra terms in the equation of mass conservation, in the limit its solutions are those of the Stokes problem.

In 1991 de Sampiao obtained results similar to those of Hughes et al., by manipulating the steady-state equation for mass conservation and the time-discretized form of the momentum equations. Zienkiewicz and Woo (1991) generalized the procedure by considering the artificial compressibility formulation for the equation of mass conservation (Fletcher, 1991), instead of its steady-state form. We follow Zienkiewicz and Woo (1991) closely and apply their scheme to a Galerkin B-spline formulation of our nonzero Reynolds number flow.

Thus, although we are interested in the steady-state problem, we still write the equations of motion and the equation of mass conservation in their unsteady (nondimensional) form:

$$\begin{aligned} \frac{\partial u}{\partial t} &= f^{(1)}(u, v, p), \\ \frac{\partial v}{\partial t} &= f^{(2)}(u, v, p), \\ \frac{1}{c^2}\frac{\partial p}{\partial t} &+ \operatorname{div} \boldsymbol{v} = 0. \end{aligned} \tag{5.5}$$

Here we employed the notation

$$\begin{aligned} f^{(1)}(u, v, p) = &-\frac{\Delta}{h} u \frac{\partial u}{\partial \alpha} - \frac{1}{2\pi h} v \frac{\partial u}{\partial \beta} + uv \sin\hat{\beta} - v^2 \sinh\hat{\alpha} \\ &- \frac{\Delta}{h}\frac{\partial p}{\partial \alpha} + \frac{(1-\eta)}{\eta \mathrm{Re}}\left[\frac{1}{h^2}\left(\Delta^2 \frac{\partial^2 u}{\partial \alpha^2} + \frac{1}{(2\pi)^2}\frac{\partial^2 u}{\partial \beta^2}\right)\right. \\ &\left. - \frac{2\Delta \sin\hat{\beta}}{h}\frac{\partial v}{\partial \alpha} + \frac{\sinh\hat{\alpha}}{\pi h}\frac{\partial v}{\partial \beta} - \frac{\cosh\hat{\alpha} + \cos\hat{\beta}}{h} u\right], \end{aligned} \tag{5.6a}$$

$$\begin{aligned} f^{(2)}(u, v, p) = &-\frac{\Delta}{h} u \frac{\partial v}{\partial \alpha} - \frac{1}{2\pi h} v \frac{\partial v}{\partial \beta} + uv \sinh\hat{\alpha} - u^2 \sin\hat{\beta} \\ &- \frac{1}{2\pi h}\frac{\partial p}{\partial \beta} + \frac{(1-\eta)}{\eta \mathrm{Re}}\left[\frac{1}{h^2}\left(\Delta^2 \frac{\partial^2 v}{\partial \alpha^2} + \frac{1}{(2\pi)^2}\frac{\partial^2 v}{\partial \beta^2}\right)\right. \\ &\left. + \frac{2\Delta \sin\hat{\beta}}{h}\frac{\partial u}{\partial \alpha} + \frac{\sinh\hat{\alpha}}{\pi h}\frac{\partial u}{\partial \beta} - \frac{\cosh\hat{\alpha} + \cos\hat{\beta}}{h} v\right]. \end{aligned} \tag{5.6b}$$

The divergence of the velocity field $\boldsymbol{v} = (u, v)$ has the (nondimensional) form

$$\operatorname{div} \boldsymbol{v} = \frac{1}{h}\left(\Delta \frac{\partial u}{\partial \alpha} + \frac{1}{2\pi}\frac{\partial v}{\partial \beta}\right) - u \sinh\hat{\alpha} + v \sin\hat{\beta}. \tag{5.7}$$

We could seek a steady-state solution to our problem by finding the time-asymptotic solution to Eq. (5.5), subject to no-slip conditions at the wall

$$\begin{aligned} &u = 0, v = \sinh|\hat{\alpha}_1| \quad \text{at} \quad \alpha = 0, \\ &u = v = 0 \qquad\qquad\quad \text{at} \quad \alpha = 1. \end{aligned} \tag{5.8a}$$

In addition to the boundary conditions, we must also ensure periodicity of the solution and its derivatives in β:

$$\frac{\partial^{(n)}\varphi}{\partial\beta^n}(\alpha, 0) = \frac{\partial^{(n)}\varphi}{\partial\beta^n}(\alpha, 1) \qquad \begin{matrix} n = 0, 1, 2, \ldots \\ \varphi = u, v, p. \end{matrix} \tag{5.8b}$$

Equations (5.5) and (5.6) define the pressure only within an arbitrary constant. We set this constant to zero by enforcing the condition $p(0, 0) = 0$. There can be no other conditions specified on the pressure.

The condition $p(0, 0) = 0$ together with Eq. (5.8) and appropriate initial values could be used to obtain $\{u(\alpha, \beta, t), v(\alpha, \beta, t), \rho(\alpha, \beta, t)\}$ from Eq. (5.5). To this end, we would discretize the continuity equation according to

$$\frac{p^{(n+1)} - p^{(n)}}{c^2\delta t} = -\text{div}\, \boldsymbol{v}^{(n+1/2)} \tag{5.9}$$

The velocity components at the $n + 1/2$ time level can be obtained from the equations of motion (5.5):

$$\boldsymbol{v}^{(n+1/2)} = \boldsymbol{v}^{(n)} + \frac{\delta t}{2}\left(f^{(1)}, f^{(2)}\right)\Big|_n \tag{5.10}$$

so that now

$$\frac{p^{(n+1)} - p^{(n)}}{c^2\delta t} = -\text{div}\, \boldsymbol{v}^{(n)} - \frac{\delta t}{2}\,\text{div}\left(f^{(1)}, f^{(2)}\right)\Big|_n. \tag{5.11}$$

Steady state is characterized by $\partial u/\partial t = 0,\ \partial v/\partial t = 0$ in Eq. (5.5) and by $p^{(n+1)} = p^{(n)}$ in Eq. (5.11). In consequence, to arrive directly at steady state we solve the following system of equations:

$$f^{(1)}(u, v, p) = 0, \tag{5.12a}$$

$$f^{(2)}(u, v, p) = 0, \tag{5.12b}$$

$$\text{div}\, \boldsymbol{v} + \frac{\delta t}{2}\text{div}\left(f^{(1)}, f^{(2)}\right) = 0, \tag{5.12c}$$

subject to boundary conditions (5.8a) and periodicity condition (5.8b)

We intend to approximate the set of unknowns $\{u(\alpha, \beta), v(\alpha, \beta), p(\alpha, \beta)\}$ by piecewise polynomial functions. Thus, we partition the interval [0, 1] for x, where x represents α or β, in turn, as

$$\pi : 0 = x_1 < x_2 < \cdots < x_\ell < x_{\ell+1} = 1.$$

Let $p_1(x), \ldots, p\ell(x)$ be any sequence of ℓ polynomials, each of order k (i.e., of degree $<k$), and denote the collection of all piecewise polynomial functions $h(x)$ by $P_{k,\pi}$:

$$P_{k,\pi}\left\{h(x) : h(x) = p_i(x) \quad \text{if} \quad x \in [x_i, x_{i+1}],\ 1 \le i \le \ell\right\}.$$

$P_{k,\pi}$ is a linear space, and since there are ℓ subintervals, the dimension of $P_{k,\pi}$ is $k\ell$.

Consider now subspaces $S_{k,\pi,\nu}$ of $P_{k,\pi}$ generated by imposing smoothness constraints on elements of $P_{k,\pi}$ at the interior breakpoints x_i, $2 \leq i \leq \ell$. Let $\nu = \{\nu_i\}_{i=2}^{\ell}$ be a nonnegative integer sequence, with $\nu_i \leq k$, all i, where ν_i denotes the smoothness index of the piecewise polynomial subspace $S_{k,\pi,\nu}$ at the breakpoint x_i, so that $h^{(j)}(x_i^+) = h^{(j)}(x_i^-)$, $0 \leq j \leq \nu - 1$. Then the dimension N of the subspace $S_{k,\pi,\nu}$ is given by

$$\dim S_{k,\pi,\nu} = k + \sum_{i=2}^{\ell} (k - \nu_i).$$

We now construct a basis for $S_{k,\pi,\nu}$ such that each element of the basis has local support and each element is nonnegative. To generate such a basis, we employ the recurrence relation (deBoor, 1978)

$$A_{i,k}(x) = \frac{x - t_i}{t_{i+k-1} - t_i} A_{i,k-1}(x) + \frac{t_{i+k} - x}{t_{i+k} - t_{i+k+1}} A_{i+1,k-1}(x)$$

$$A_{j,1} = \begin{cases} 1 & \text{for} \quad x \in [t_j, t_{j+1}], \\ 0 & \text{otherwise.} \end{cases}$$

Here $t = \{t_i\}_{i=1}^{N+K}$ is any nondecreasing sequence such that

(1) $t_i \leq t_2 \leq \cdots \leq t_k \leq x_\ell$ and $x_{\ell+1} \leq t_{N+1} \leq \cdots \leq t_{N+k}$;
(2) the number x_i, $2 \leq i \leq \ell$, occurs exactly $d_i = k - \nu_i$ times in t.

The sequence of $A_1, A_2, \ldots, A_N$ of B-splines of order k for the knot sequence t is a basis for $S_{k,\pi,\nu}$. The choice of t translates the desired amount of smoothness at breakpoints, and the Curry-Schoenberg theorem (deBoor, 1978) permits construction of a B-spline basis for any particular piecewise polynomial space $S_{k,\pi,\nu}$.

The B-splines thus defined provide a partition of unity:

$$\left.\begin{array}{l} A_i(x) \geq 0, \; 1 \leq i \leq N, \\ \displaystyle\sum_{i=1}^{N} A_i(x) = 1 \end{array}\right\} x \in [x_1, x_{\ell+1}].$$

Other relevant properties of B-splines are

$$\left.\begin{array}{ll} A_1(x_1) = A_N(x_{\ell+1}) = 1 & A_j(x_1) = 0 \, (j > 1), \\ A_j(x_{\ell+1}) = 0 (j < N), & A_j(x) = 0 (x \notin [t_j, t_{j+k}]) \end{array}\right\}$$

$$\left.\begin{array}{ll} A_1'(x_1) = -A_2'(x_1) \neq 0, & A_j'(x_1) = 0 \, (j > 2), \\ A_N'(x_{\ell+1}) = -A_{N-1}'(x_{\ell+1}) \neq 0, & A_j'(x_{\ell+1}) = 0 \, (j < N - 1) \end{array}\right\}.$$

In the present calculations we employ quartic B-spline basis, i.e., $k = 5$, and write $\{A_i(\alpha)$: $1 \leq i \leq N_\beta\}$ for the set of normalized B-splines relative to $k_\alpha, \pi_\alpha, \nu_\alpha$.

In similar manner, we define the normalized B-splines $\{B_j(\beta)$: $1 \leq j \leq N_\beta)$ on $0 \leq \beta \leq 1$. However, the requirement that the solution be periodic in β, Eq. (5.8b), suggest that we construct another basis $\{b_j(\beta)$: $1 \leq j \leq N\beta - 3\}$ from the B_j that is periodic in β, and use the periodic $\{b_j\}$ in place of the nonperiodic $\{B_j\}$. Let $c = 2B_2''(0)/B_3''(0)$ and define matrices Φ and Ψ as

$$\Phi = \begin{bmatrix} I_3 & 0 & \Psi \\ 0 & I_{N_{\beta-6}} & 0 \end{bmatrix}, \qquad \Psi = \begin{bmatrix} c & 2 & 1 \\ -c & -1 & 0 \\ 1 & 0 & 0 \end{bmatrix},$$

where I_3 and I_{N_y-6} are unit matrices, then the new base vectors, $\{b_i\}_{i=1}^{N_y-3}$, are given by

$$b = \Phi B = (b_1,\ b_2, \ldots,\ b_{N_{y-3}})^T, \qquad B = (B_1, \ldots,\ B_{Ny})^T.$$

It can be verified that the sequence $\{b_i\}$ is a basis for a subspace of $S_{k,\pi,v}$ defined as

$$\Omega_{k,\pi,v} = \left\{\omega(z) \in S_{k,\pi,v} : \omega^{(n)}(0) = \omega^{(n)}(1), \qquad n = 0, 1, 2\right\}.$$

The expansions

$$\begin{aligned} u(\alpha, \beta) &= \sum_{i=2}^{N_\alpha - 1} \sum_{j=1}^{N_\beta - 3} u_{ij} A_i(\alpha) b_j(\beta), \\ v(\alpha, \beta) &= \sinh|\hat{\alpha}_1| A_1(\alpha) + \sum_{i=2}^{N_a - 1} \sum_{j=1}^{N_\beta - 3} v_{ij} A_i(\alpha) b_j(\beta), \\ p(\alpha, \beta) &= \sum_{i=1}^{N_\alpha} \sum_{j=1}^{N_\beta - 3} p_{ij} A_i(\alpha) b_j(\beta), \end{aligned} \tag{5.13}$$

where the $A_i(\alpha)$, $i = 1, \ldots\ N_\alpha$ are normalized splines in α and the $b_j, j = 1, \ldots, N_\beta - 3$ are periodic splines in β, satisfy the boundary and periodicity conditions (5.8). The u_{ij}, v_{ij}, p_{ij} are unknown coefficients, to be determined later.

Part (a) of Figure 5.2 displays normalized B-splines $A_i(\alpha)$, $i = 1, \ldots, N_\alpha$, for $N_\alpha = 10$, $k_\alpha = 5$, $v_\alpha = 4$, and part (b) displays periodic B-splines $b_j, j = 1, \ldots, N_\beta - 3$, for $N_\beta = 10$, $k_\beta = 5$ and $v_\beta = 4$. These splines possess three continuous derivatives at internal breakpoints.

Substituting expansions (5.13) into the equations of motion and continuity (5.12), multiplying through by $F_{rs}(\alpha, \beta)$, and integrating over the domain, in accordance with Galerkin's method, we obtain

$$\left\langle f^{(1)}(\alpha, \beta),\ F_{rs}(\alpha, \beta)\right\rangle = 0, \tag{5.14a}$$

$$\left\langle f^{(2)}(\alpha, \beta),\ F_{rs}(\alpha, \beta)\right\rangle = 0, \tag{5.14b}$$

$$\langle \operatorname{div} \boldsymbol{v}(\alpha, \beta),\ F_{rs}(\alpha, \beta)\rangle + \frac{\delta t}{2}\left\langle \operatorname{div}\left[f^{(1)}(\alpha, \beta),\ f^{(2)}(\alpha, \beta)\right],\ F_{rs}(\alpha, \beta)\right\rangle = 0. \tag{5.14c}$$

Here we used the symbol $F_{rs}(\alpha, \beta) \equiv A_r(\alpha) b_s(\beta)$ and the symbol $\langle \cdot, \cdot \rangle$ to represent the inner product of two functions calculated over the domain $0 \le \alpha, \beta \le 1$.

Our task can now be defined as solving the discretized system of equations (5.14) subject to the single condition $p(0, 0) = 0$, which takes the form

$$p_{1,1} = 0.$$

This formulation, which closely follows that of Zienkiewicz and Woo (1991), leads to a nonsingular algebraic system for the steady-state Navier-Stokes problem.

The system of nonlinear algebraic equations that result from the Galerkin discretization, Eq. (5.14), can be put into concise form:

$$\tilde{G}(\mu) = 0, \qquad \mu = (u, \lambda), \tag{5.15}$$

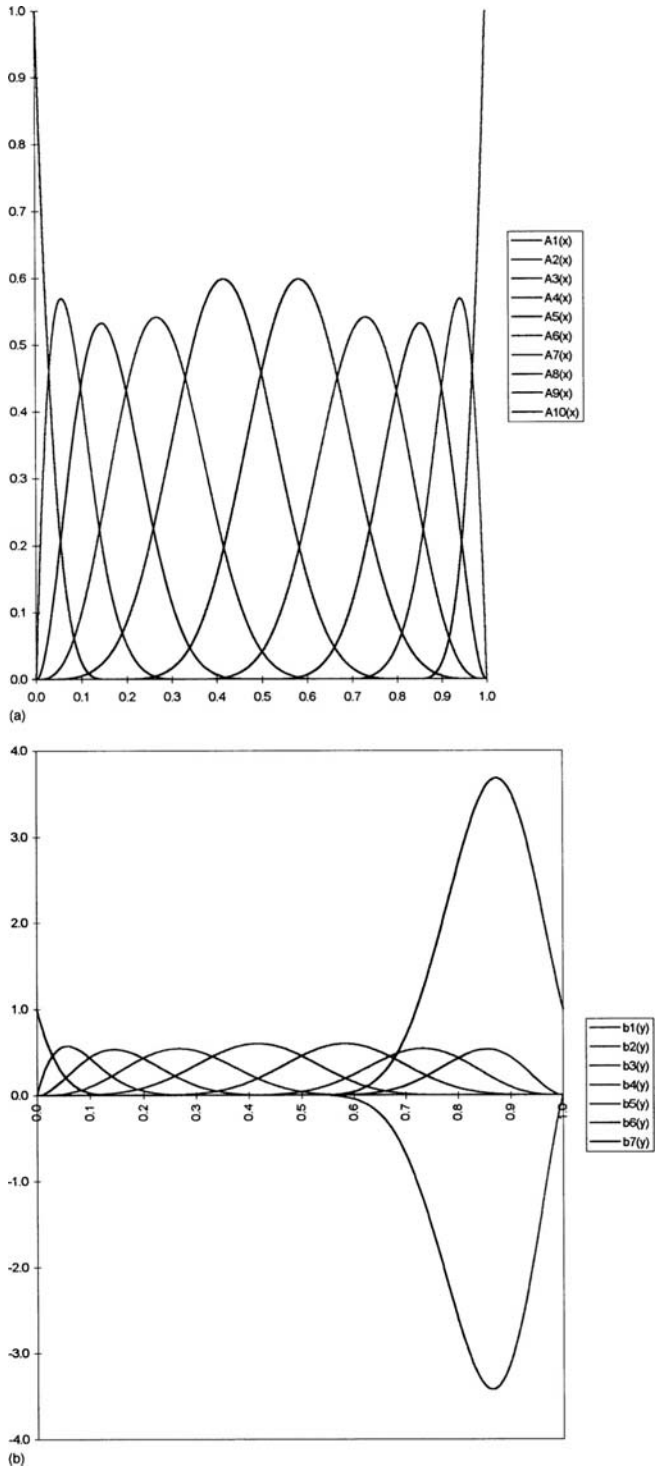

Figure 5.2. *B*-splines: (a) normalized splines $A_i(\alpha)$, (b) periodic splines $b_i(\beta)$. ($N_\alpha = N_\beta = 10$, $k_\alpha = k_\beta = 5$)

where u is the vector of state variables $\{u_{ij}, v_{ij}, p_{i,j}\}$ and λ is the vector of parameters Δ, η, ε, and Re.

The set of nonlinear equations (5.15) is difficult to solve for parameter values outside a narrow range, and we employ parametric continuation in conjunction with Gauss-Newton iteration (Ortega and Rheinboldt, 1970). Parametric continuation is a scheme that allows for systematic determination of starting points for the iteration; using this technique one can trace out the solution in parameter space. The simplest continuation scheme would be to employ the solution obtained at, say, Re = 1 where the solution is easy to come by, as starting point for the iteration at, say, Re = 10, where the solution is more difficult to obtain.[1] There are, of course, efficient schemes to accomplish this. Details can be found, e.g., in Keller (1977) and Seydel (1988); the solution scheme detailed in Chapter 6 was taken from Szeri and Al-Sharif (1995).

Lubrication Approximation in Bipolar Coordinates

While in the previous section our aim was to solve the exact Navier-Stokes problem, in the present section the objective is to find approximate solutions for thin films but without neglecting film curvature. To discover the correct approximation, we make use of the geometry of the thin film by recognizing the existence of two different scale lengths that are three orders of magnitude apart. The length scales we adopt are $L_\beta = r_1$ along the principal dimension of the film and $L_\alpha = r_1\,(\alpha_2 - \alpha_1)$ across it. The continuity equation is normalized according to

$$\alpha = \Delta\,(\hat{\alpha} - \hat{\alpha}_1)\,, \quad \beta = \hat{\beta}/2\pi, \quad V = r_1\omega v, \qquad \Delta = \frac{1}{(\hat{\alpha}_2 - \hat{\alpha}_1)} \tag{5.16}$$

as the azimuthal velocity is of order $r_1\omega$. Then, to have the terms of the continuity equation balance, we must scale the â component of the velocity as

$$U = \frac{1}{2\pi\,\Delta} r_1\omega u. \tag{5.17}$$

The normalized pressure $\bar{p}(\alpha, \beta)$ is defined through

$$\begin{aligned} \bar{p} &= 2\pi\,\frac{p}{\rho U_*^2}\left(\frac{L_\alpha}{L_\beta}\right) r_e, \\ U_* &= r_1\omega, \quad r_e = \frac{U_* L_\alpha}{\nu}, \qquad L_\alpha = r_1\,(\hat{\alpha}_2 - \hat{\alpha}_1)\,, \qquad L_\beta = r_1. \end{aligned} \tag{5.18}$$

We are now ready to write the normalized equations of motion, neglecting terms of the order $(\hat{\alpha}_2 - \hat{\alpha}_1)^2$ or smaller. This order of approximation is consistent with lubrication approximation, as

$$\frac{r_2 - r_1}{r_1} = \frac{2\cosh\dfrac{\hat{\alpha}_2 + \hat{\alpha}_1}{2}\sinh\dfrac{\hat{\alpha}^2 - \hat{\alpha}_1}{2}}{\sinh\hat{\alpha}_1} \approx \frac{(\alpha_2 - \hat{\alpha}_1)}{\tanh\hat{\alpha}_1} \tag{5.19}$$

and $\tanh(\hat{\alpha}_1 = O\,(1)$ for conventional bearing geometries.

[1] Parametric continuation is a particularly useful technique for mapping out solutions in case of solution multiplicity (Keller, 1977).

The normalized equations of motion thus take the form

$$\frac{\partial \bar{p}}{\partial \alpha} = 0$$
$$-\frac{1}{(2\pi)^2 h}\frac{\partial \bar{p}}{\partial \beta} = \frac{1}{h^2 \sinh \hat{\alpha}_1}\frac{\partial^2 v}{\partial \alpha^2} + r_e^*\left[\frac{1}{h}\left(u\frac{\partial v}{\partial \alpha} + v\frac{\partial v}{\partial \beta}\right)\right]. \tag{5.20}$$

Note that $r_e^* \equiv \frac{1}{2\pi\Delta} r_e$ is the reduced Reynolds number of the problem, analogous to R_ε of Eq. (2.58). The condition $R_\varepsilon \to 0$ of classical lubrication theory is equivalent, thus, to $r_e^* \to 0$ and, upon applying this limit, Eq. (5.20) reduces to

$$-\sinh \hat{\alpha}_1 \frac{h}{(2\pi)^2}\frac{\partial \bar{p}}{\partial \beta} = \frac{\partial^2 v}{\partial \alpha^2}, \quad \frac{\partial \bar{p}}{\partial \alpha} = 0, \tag{5.21}$$

with boundary conditions

$$u = 0, v = 1 \quad \text{at} \quad \alpha = 0, \tag{5.22a}$$
$$u = v = 0 \quad \text{at} \quad \alpha = 1, \tag{5.22b}$$

To solve Eq. (5.21), we integrate twice with respect to α and obtain

$$v = \frac{1}{C}\int_0^\alpha \int_0^\phi h(\eta, \beta)\frac{d\bar{p}(\beta)}{d\beta}\, d\eta\, d\phi + \alpha f(\beta) + F(\beta), \quad C \equiv \frac{-(2\pi)^2}{\sinh \hat{\alpha}_1}. \tag{5.23a}$$

Here $f(\beta)$ and $F(\beta)$ are arbitrary functions of β and serve to make Eq. (5.23) satisfy the boundary conditions (5.22).

The complete solution of Eq. (5.21) that satisfies the boundary conditions (5.22) is

$$v = \frac{1}{C}\frac{d\bar{p}(\beta)}{d\beta}\left[\int_0^\alpha \int_0^{\bar{\alpha}} h(\eta, \beta) d\eta\, d\bar{\alpha} - \alpha \int_0^1 \int_0^{\bar{\alpha}} h(\eta, \beta) d\eta d\bar{\alpha}\right] + (1 - \alpha). \tag{5.23b}$$

Substitution into the integrated (across the film) continuity equation yields

$$\frac{\partial}{\partial \beta}\left\{\frac{\partial \bar{p}}{\partial \beta}\int_0^1 h(\alpha, \beta)\left[\int_0^\alpha I(\bar{\alpha}, \beta)\, d\bar{\alpha} - \alpha \int_0^1 I(\bar{\alpha}, \beta)\, d\bar{\alpha} - C(1 - \alpha)\right] d\alpha\right\} = 0,$$
$$I(\alpha, \beta) \equiv \int_0^\alpha h(\phi, \beta)\, d\phi. \tag{5.24}$$

The innermost integral of Eq. (5.24) was obtained analytically while the other integrals necessary to solve for $\bar{p}$ were performed via Gaussian quadrature (Dai, Dong, and Szeri, 1992). The boundary conditions are $\bar{p}(0) = \bar{p}(1) = 0$.

To investigate the limit of the sequence of results obtained with sequentially smaller values of C/r_1, we compare at $\mathrm{Re} = 0$ solutions from the Navier-Stokes equations with those of the bipolar lubrication theory as $(\hat{\alpha}_2 - \hat{\alpha}_1) \to 0$. Table 5.1 displays results for Sommerfeld boundary conditions, while Table 5.2 was obtained for Gümbel conditions. These tables contain the Sommerfeld number (inverse of nondimensional force) and the nondimensional spring coefficients (4.14a). The data indicate that on decreasing the clearance ratio both the Navier-Stokes theory and the bipolar lubrication theory converge to a common limit, this limit being the classical lubrication theory of Reynolds.

The exact, zero Reynolds number solution of Ballal and Rivlin (1976) valid for arbitrary clearance ratio, can be employed to study film curvature effects. When this solution is

Table 5.1. *Convergence of solutions with* $(C/R) \to 0$

Theory	(C/R)	S	k_{RR}	k_{RT}	k_{TR}	k_{TT}
Navier-Strokes	0.002	0.16880	0.0	59.2402	−59.2492	0.0
	0.001	0.16883	0.0	59.2300	−59.2385	0.0
	0.0005	0.16885	0.0	59.2249	−59.2330	0.0
Reynolds	0.0	0.16886	0.0	59.2198	−59.2288	0.0
Bipolar lubrication	0.0005	0.16891	0.0	59.2037	−59.1951	0.0
	0.001	0.16898	0.0	59.1786	−59.1703	0.0
	0.002	0.16912	0.0	59.1285	−59.1208	0.0

$\varepsilon = 0.1$, Re = 0.0 Sommerfeld condition. (From Dai, R. X., Dong, Q. M. and Szeri, A. Z. Approximations in hydrodynamic lubrication. *ASME Journal of Tribology*, **114**, 14–25, 1992.)

expanded in powers of the clearance ratio, the first two terms correspond to the Myllerup and Hamrock (1994) solution, which employs regular perturbation:

$$\bar{p} = \frac{12\pi\varepsilon \sin\theta(2+\varepsilon\cos\theta)}{(2+\varepsilon^2)(1+\varepsilon\cos\theta)^2} + \left(\frac{C}{R}\right)\frac{4\pi\varepsilon\sin\theta(1+5\varepsilon^2+2\varepsilon(2+\varepsilon^2)\cos\theta)}{(2+\varepsilon^2)(1+\varepsilon\cos\theta)^3} + O\left(\frac{C}{R}\right)^2.$$

The first term is seen to be identical to the solution of the Reynolds equation under full film boundary conditions [cf. Eq. (3.76)], while the second term is the first order curvature correction

An alternative way of interpreting the results of Tables 5.1 and 5.2 is by calculating the nondimensional group $P/\mu N$, where P is the average pressure defined as $P = W/LD$. The results are shown in Table 5.3 at various values of (C/R). It may be concluded here that

$$P_{BP} < P_{RE} < P_{NS},$$

Table 5.2. *Convergence of solutions with* $(C/R) \to 0$

Theory	(C/R)	S	k_{RR}	k_{RT}	k_{TR}	k_{TT}
Navier-Stokes	0.002	0.33692	3.8022	29.6201	−29.6246	1.8943
	0.001	0.33698	3.8026	29.6150	−29.6192	1.8944
	0.0005	0.33701	3.8029	29.6125	−29.6165	1.8945
Reynolds	0.0	0.33704	3.8085	29.6099	−29.6144	1.8945
Bipolar lubrication	0.0005	0.33706	3.8080	29.6075	−29.6118	1.8943
	0.001	0.33732	3.8042	29.5851	−29.5892	1.8924
	0.002	0.33760	3.7999	29.5604	−29.5642	1.8903

$\varepsilon = 0.1$, Re = 0.0 Gümbel condition. (From Dai, R. X., Dong, Q. M. and Szeri, A. Z. Approximations in hydrodynamic lubrication. *ASME Journal of Tribology*, **114**, 14–25, 1992.)

Table 5.3. *Effect of film curvature on $P/\mu N$*

		$(P/\mu N) \times 10^{-5}$		
Boundary condition	(C/R)	Navier-Stokes	Reynolds	Bipolar lubrication
Sommerfeld	0.002	7.4202	7.4175	7.4052
	0.001	29.6754	29.6701	29.6454
	0.0005	118.6908	118.6802	118.6732
Gümbel	0.002	14.8104	14.8052	14.7824
	0.001	59.2311	59.2207	59.1786
	0.0005	236.8966	236.8826	236.8125

$\varepsilon = 0.1$, Re $= 0.0$. (From Dai, R. X., Dong, Q. M. and Szeri, A. Z. Approximations in hydrodynamic lubrication. *ASME Journal of Tribology*, **114**, 14–25, 1992.)

where P_{BP}, P_{RE}, and P_{NS} represent the specific pressure according to the bipolar lubrication theory, the lubrication theory of Reynolds, and the Navier-Stokes theory, respectively. Thus, neglect of the higher order terms in Eq. (2.55) underestimates the specific bearing pressure at all values of the clearance ratio (C/R), i.e., P_{BP}, $P_{RE} < P_{NS}$. Neglect of the curvature of the lubricant film, on the other hand, leads to an overestimate of the specific pressure, i.e., $P_{BP} < P_{RE}$. The net effect is shown in that the specific pressure of lubrication theory, P_{RE}, is bracketed by the specific pressures P_{BP} and P_{NS}. This convergence of both the bipolar lubrication theory and the Navier-Stokes theory to the classical lubrication theory shows that the latter constitutes the proper limit as $(C/R) \to 0$.

The Sommerfeld number, S, and the stiffness matrix, $\boldsymbol{k}$, can now be calculated for $0 < \text{Re} < \text{Re}_{CR}$. Table 5.4 contains the results of these computations at $\varepsilon = 0.1$, 0.5, and 0.7. The data of Table 5.4 clearly demonstrate that the Sommerfeld number remains virtually constant for all $\text{Re} < \text{Re}_{CR}$. The largest change is encountered with Gümbel boundary conditions at $\varepsilon = 0.1$, amounting to -6.5% change in S when increasing the Reynolds number from zero to $\text{Re} = 900$, i.e., $\text{R}_\varepsilon = 1.8$. The critical Reynolds number here is $\text{Re}_{CR} = 932$. Looking at the data of Table 5.4, it does become obvious, however, that significant changes are encountered in the diagonal components of the stiffness matrix k_{RR}, k_{TT}, which increase apparently linearly with the Reynolds number. Changes in bearing stiffness, of course, alter the stability characteristics of the bearing for actual running conditions, as contrasted to the inertialess world of classical lubrication theory.

These calculations suggest a generalization of the conclusion offered by DiPrima and Stuart (1972b): "first order correction for inertia does not affect the vertical force or torque, but does introduce a horizontal force." Our extension is: *Correction for inertia does not affect the resultant force or torque nor the off-diagonal components of the stiffness matrix. It does, however, induce changes in the diagonal components, the changes being linear in the Reynolds number*. In fact, the conclusions of DiPrima and Stuart hold not only in the qualitative but also in the quantitative sense. The small perturbation theory calculates the radial force component, $\bar{F}_R$, for Sommerfeld boundary condition at $(C/R = 0.002)$, from (DiPrima and Stuart, 1972b)

$$\bar{F}_R = \frac{2\pi^2}{35\varepsilon(2+\varepsilon^2)}\left[-(7+8\varepsilon^2) + \frac{\sqrt{1-\varepsilon^2}}{2+\varepsilon}(14+44\varepsilon^2+5\varepsilon^4)\right]\text{R}_\varepsilon. \tag{5.25}$$

Table 5.4. *Effect of lubricant inertia* ($C/R = 0.002$)

ε	Boundary condition	Re	S	k_{RR}	k_{RT}	k_{TR}	k_{TT}
0.1	Sommerfeld	0.0	0.16880	7.3×10^{-6}	59.2402	−59.2492	7.6×10^{-6}
		50.0	0.16880	0.1836	59.2499	−59.2588	0.1944
		100.0	0.16879	0.3673	59.2525	−59.2603	0.3889
		500.0	0.16865	1.8374	59.2708	−59.2786	1.9447
		900.0	0.16836	3.3091	59.2923	−59.3151	3.5016
	Gümbel	0.0	0.33692	3.8122	29.6201	−29.6246	1.8943
		50.0	0.33565	3.9047	29.7259	−29.7068	1.9963
		100.0	0.33440	3.9977	29.8318	−29.7891	2.0946
		500.0	0.32451	4.7619	30.6823	−30.4498	2.9076
		900.0	0.31480	5.5616	31.5366	−31.1138	3.7663
0.5	Sommerfeld	0.0	0.03288	5.2×10^{-6}	60.8262	−67.7159	3.2×10^{-6}
		50.0	0.03288	0.1323	60.8262	−67.6976	0.0811
		100.0	0.03288	0.2750	60.8282	−67.6160	0.1491
		500.0	0.03288	1.3347	60.8296	−67.6094	0.7453
		900.0	0.03287	2.4734	60.8326	−67.5939	1.3415
	Gümbel	0.0	0.06174	27.2012	30.4131	−33.8579	11.1500
		50.0	0.06172	27.1428	30.4081	−33.7024	11.1937
		100.0	0.06169	27.1031	30.4077	−33.5617	11.2470
		500.0	0.06150	26.6237	30.4031	−32.4737	11.5515
		900.0	0.06129	26.0506	30.3997	−31.5835	11.8643
0.7	Sommerfeld	0.0	0.02143	1.1×10^{-7}	66.6671	−104.60	-2.8×10^{-8}
		50.0	0.02143	0.3630	66.6671	−104.60	−0.0173
		100.0	0.02143	0.7259	66.6671	−104.60	−0.0346
		500.0	0.02143	3.6294	66.6669	−104.60	−0.1730
		1100.0	0.02143	7.9823	66.6666	−104.61	−0.3798
	Gümbel	0.0	0.03636	73.4232	33.3335	−52.3011	−20.7935
		50.0	0.03632	73.6046	33.3782	−52.4787	−20.8022
		100.0	0.03628	73.7861	33.4228	−52.6563	−20.8110
		500.0	0.03597	75.2469	33.7795	−54.0772	−20.8839
		1100.0	0.03551	77.4519	34.3127	−56.2057	−21.0019

(From Dai, R. X., Dong, Q. M. and Szeri, A. Z. Approximations in hydrodynamic lubrication. *ASME Journal of Tribology*, **114**, 14–25, 1992.)

In Table 5.5, we compare our numerical results for $\bar{F}_R$ with that of Eq. (5.25) and show excellent agreement for $\mathrm{Re} < \mathrm{Re}_{CR}$ and for all $\varepsilon \leq 0.7$ for conventional journal bearing geometry. This conclusion still holds for larger values of (C/R), as indicated in Table 5.6.

The results obtained here demonstrate convincingly that lubricant inertia has negligible effect on load carrying capacity in noncavitating film, for isothermal laminar flow of the lubricant. The stability characteristics of the bearing are, however, affected by lubricant inertia. These conclusions apply to practical bearing operations directly, and assert that bearing load can be calculated from classical, i.e., noninertial, theory. To investigate stability, however, one must take lubricant inertia into account, even during laminar flow of the lubricant.

Table 5.5. *Comparison of numerical solution with small perturbation solution*

		$\bar{F}_R$	$\bar{F}_R$
ε	Re	Numerical solution	DiPrima and Stuart
0.1	10.0	0.0039	0.0038
	100.0	0.0389	0.0382
	500.0	0.1945	0.1910
	900.0	0.3502	0.3438
0.3	50.0	0.0446	0.0446
	100.0	0.0892	0.0892
	500.0	0.4461	0.4461
	900.0	0.8029	0.8030
0.5	50.0	0.0406	0.0372
	100.0	0.0746	0.0745
	500.0	0.3727	0.3724
	900.0	0.6708	0.6702
0.7	50.0	−0.0121	−0.0122
	100.0	−0.0242	−0.0244
	500.0	−0.1211	−0.1220
	1100.0	−0.2660	−0.2683
	1145.0	−0.2760	−0.2793

$C/R = 0.002$, Sommerfeld condition. (From Dai, R. X., Dong, Q. M. and Szeri, A. Z. Approximations in hydrodynamic lubrication. *ASME Journal of Tribology*, **114**, 14–25, 1992.)

Solutions are obtained here under Sommerfeld and Gümbel boundary conditions, neither of which is particularly useful in practice. There is some evidence (You and Lu, 1987) that in journal bearings lubricant inertia has a tendency of stretching the film in the direction of rotation. This result of You and Lu was obtained by extrapolation from the small perturbation analysis of Reinhardt and Lund (1975). Ota et al. (1995) confirm the conclusions of You and Lu on fluid inertia caused film stretching.

Hydrostatic Bearings

For simplicity and because most of the published results on the effect of fluid inertia in hydrostatic lubrication are related to this bearing type, we consider here only the circular step bearing.

When both surfaces of a circular step bearing are stationary and parallel and when fluid inertia is neglected, theory requires a logarithmic pressure drop to maintain viscous dissipation. Experiments performed at low flow rates verify this theoretical result (Coombs and Dowson, 1965).

If the throughflow Reynolds number, defined by

$$R_Q = \frac{Q}{2\pi \nu h},$$

Table 5.6. *Effect of fluid inertia on solution*

Boundary conditions	Re	S	k_{RR}	k_{RT}	k_{TR}	k_{TT}	$(\bar{F}_R)_{\text{Numerical}}$	$(\bar{F}_R)_{\text{DiPrima}}$
Sommerfeld	0.0	0.03118	0.00	64.14	−74.73	0.00	0	0
	50.00	0.03089	13.17	64.26	−74.05	7.90	3.9483	3.7236
	100.0	0.03005	25.18	64.67	−72.13	15.74	7.8722	7.4472
	150.0	0.02880	35.23	65.39	−69.18	23.40	11.6990	11.1708
Gümbel	0.0	0.05883	28.32	32.07	−37.36	11.28	–	–
	50.0	0.05555	20.55	32.33	−24.60	15.85	–	–
	100.0	0.05088	11.71	32.92	−13.26	21.48	–	–
	150.0	0.04568	3.56	33.87	−4.35	27.75	–	–

$C/R = 0.02$, $\varepsilon = 0.5$, $\text{Re}_{CR} = 128.64$. (From Dai, R. X., Dong, Q. M. and Szeri, A. Z. Approximations in hydrodynamic lubrication. *ASME Journal of Tribology*, **114**, 14–25, 1992.)

where Q is the volumetric rate of throughflow, is increased, convective inertia gains importance. Its effect is to increase the pressure in the radial direction rapidly at small radii and moderately at large radii. Convective inertia effects far outweigh viscous dissipation at small values of the dimensionless radius, defined by

$$\rho = \frac{r}{h\sqrt{R_Q}},$$

whereas at large ρ the creeping flow solution remains essentially correct (Figure 5.3).[2]

Livesey (1960) argued that departure from parallel flow must be slight even at large flow rates and retained $u\partial u/\partial r$, where u is the creeping solution, as the significant inertia term. Livesey's analysis yields

$$\frac{\partial \bar{P}}{\partial \rho} = -\frac{12}{\rho} + \frac{2K}{\rho^3}. \tag{5.26}$$

In this equation

$$\bar{P}(\rho) = \frac{h}{\mu v R_Q} \int_0^h p(r, z)\, dz \tag{5.27}$$

is a dimensionless average pressure. The pressure gradient of creeping flow can be obtained from Eq. (3.6); in our present notion it is $d\bar{P}/d\rho = -12/\rho$. The value of K was given by Livesey as 0.6, subsequent authors gave $K = 0.72$ (Moller, 1963) and $K = 0.77143$ (Jackson and Symmons, 1965).

There is further distortion of the creeping flow profile due to centrifugal inertia, if the runner surface is made to rotate (Figure 5.4). Osterle and Hughes (1958) demonstrated that this distortion can be large enough to diminish the load capacity of a hydrostatic bearing. Their solution was based on the assumption of negligible convective inertia and

[2]This statement is in complete agreement with the conclusion that inertia becomes important for $\text{R}_\varepsilon \geq 1$. In the present example the characteristic velocity is $U_* = Q/2\pi r$ and the characteristic dimension $L_y = h$. Then $\text{Re} = (h/r)R_Q$ and $\text{R}_\varepsilon = 1/\rho^2$; thus, inertia effects will be insignificant when $\rho > 1$.

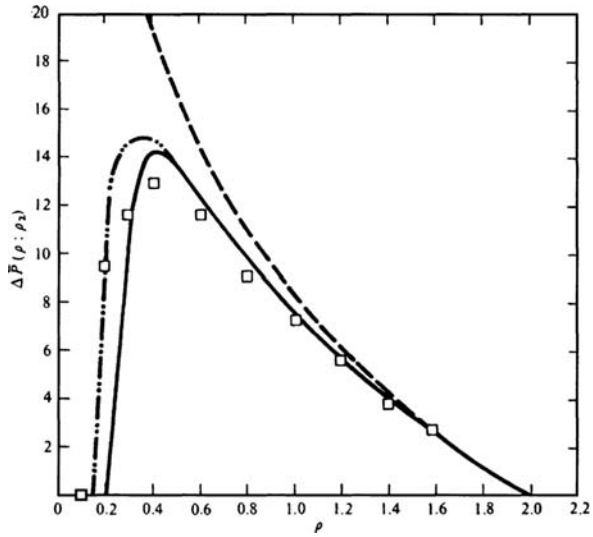

Figure 5.3. Flow between stationary parallel disks. Effect of convective inertia on pressure. (□) Experimental values of Jackson and Symmons (1965). Theoretical curves: (– – – –) creeping flow, Eq. (3.26); (— .. —) Jackson and Symmons (1965); (—) Szeri and Adams. (Reprinted with the permission of Cambridge University Press from Szeri, A. Z. and Adams, M. L. Laminar throughflow between closely spaced rotating disks. *J. Fluid Mech*., **86**, 1–14, 1978.)

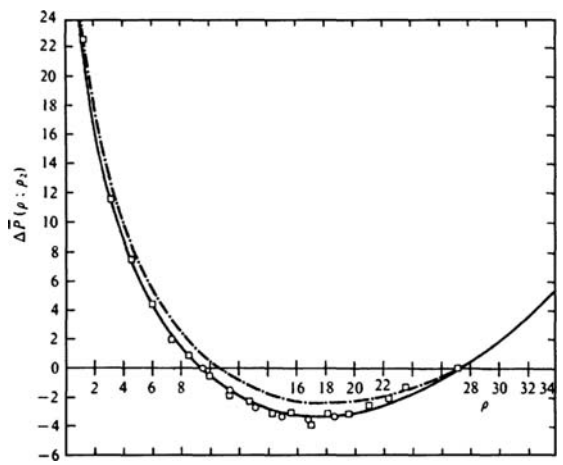

Figure 5.4. Flow between rotating parallel disks, $E = 2.9$. Effect of rotational inertia on pressure. Experimental values: (□) Coombs and Dowson (1965), (◯) Nirmal (Szeri and Adams, 1978). Theoretical curves: (—..—) Osterle and Hughes (1958), (—) Szeri and Adams. (Reprinted with the permission of Cambridge University Press from Szeri, A. Z. and Adams, M. L. Laminar flow between closely spaced rotating disks. *J. Fluid Mech*., **86**, 1–14, 1978.)

on a rotational inertia that was calculated from a linear circumferential velocity. The radial pressure gradient for this case was found to be

$$\frac{d\bar{P}}{d\rho} = -\frac{12}{\rho} + \frac{3\rho}{10E^2}. \tag{5.28}$$

Here $E = \nu/h^2\omega$ is the Ekman number and ω is the runner angular velocity. [The condition $R_\varepsilon \geq 1$ now assumes the form $\rho/E^2 \geq O(1)$.]

In a more thorough analysis of the problem, we consider two parallel disks of radius r^2 located at a distance h apart. The lower disk is stationary, and the upper disk rotates at the angular velocity ω. We write the equations of motion relative to cylindrical polar coordinates, assuming rotational symmetry, as

$$u_r\frac{\partial u_r}{\partial r} - \frac{u_\theta^2}{r} + u_z\frac{\partial u_r}{\partial z} = \nu\left(\nabla^2 u_r - \frac{u_r}{r^2}\right) - \frac{1}{\rho}\frac{\partial p}{\partial r}, \tag{5.29a}$$

$$\frac{u_r}{r}\frac{\partial}{\partial r}(ru_\theta) + u_z\frac{\partial u_\theta}{\partial z} = \nu\left(\nabla^2 u_\theta - \frac{u_\theta}{r^2}\right), \tag{5.29b}$$

$$u_r\frac{\partial u_z}{\partial r} + u_z\frac{\partial u_z}{\partial z} = \nu\nabla^2 u_z - \frac{1}{p}\frac{\partial p}{\partial z}, \qquad 0 < r_1 < r < r_2 \qquad 0 < z < h. \tag{5.29c}$$

Eliminating the pressure between the first and third equations by cross differentiation and writing the resulting equations in terms of the stream function Ψ, defined through

$$u_r = \frac{1}{r}\frac{\partial\Psi}{\partial z} \qquad u_z = -\frac{1}{r}\frac{\partial\Psi}{\partial r}, \tag{5.30}$$

we obtain the following system of equations (Szeri and Adams, 1978):

$$\frac{\partial\Psi}{\partial z}\frac{\partial\left(D^2\Psi\right)}{\partial r} - \frac{\partial\Psi}{\partial r}\frac{\partial\left(D^2\Psi\right)}{\partial z} - \frac{1}{r}\frac{\partial u_\theta^2}{\partial r} = \nu\left(r^3D^2 + 4\frac{\partial}{\partial r}\right)D^2\Psi, \tag{5.31a}$$

$$\frac{\partial\Psi}{\partial z}\frac{\partial(ru_\theta)}{\partial r} - \frac{\partial\Psi}{\partial r}\frac{\partial(ru_\theta)}{\partial z} = \nu r^3 D^2(ru_\theta). \tag{5.31b}$$

The operator D^2 in Eqs. (5.31) has the definition

$$D^2 = \frac{1}{r^2}\left(\nabla^2 - \frac{2}{r}\frac{\partial}{\partial r}\right).$$

Equations (5.31) are supplemented with the boundary conditions

$$\begin{aligned} &\frac{\partial\Psi}{\partial r} = \frac{\partial\Psi}{\partial z} = u_\theta = 0 \quad \text{at} \quad z = 0,\\ &\frac{\partial\Psi}{\partial r} = \frac{\partial\Psi}{\partial z} = 0, \qquad u_\theta = r\omega \quad \text{at} \quad z = h,\\ &\Psi(r,h) - \Psi(r,0) = \frac{Q}{2\pi}. \end{aligned} \tag{5.32}$$

The last condition of Eqs. (5.32) expresses global conservation of mass. In addition, we need boundary conditions on both Ψ and u_θ at $r = r_1$ (recess radius) and $r = r_2$.

It can be shown (Szeri, Schneider, Labbe, and Kaufman, 1983) that a minimum of four dimensionless parameters are required to characterize the problem as given by Eqs. (5.31) and (5.32). But if the spacing of the disks is narrow – that is, if $h/r_2 \ll 1$ – then the radial variation of the shear stress is negligible, and we have the approximation

$$D^2 \approx \frac{1}{r^2}\frac{\partial^2}{\partial z^2} \qquad \frac{h}{r_2} \ll 1. \tag{5.33}$$

Under the thin-film approximation, the problem can be characterized by a single dimensionless variable. To show this, we substitute

$$\begin{aligned} &z = \zeta h, \qquad r = h\sqrt{R_Q \rho} \\ &\Psi = h\nu R_Q \bar{\Psi}, \qquad u_\theta = h\omega\sqrt{R_Q}\rho\bar{\Omega} \end{aligned} \tag{5.34}$$

into Eqs. (5.31) and obtain

$$\frac{d\bar{\Psi}}{\partial\zeta}\frac{\partial}{\partial\rho}\left(\frac{1}{\rho^2}\frac{\partial^2\bar{\Psi}}{\partial\zeta^2}\right) - \frac{\partial\bar{\Psi}}{\partial\rho}\frac{\partial}{\partial\zeta}\left(\frac{1}{\rho^2}\frac{\partial^2\bar{\Psi}}{\partial\zeta^2}\right) - \frac{1}{E^2}\frac{\partial\left(\rho\bar{\Omega}^2\right)}{\partial\zeta} = \frac{1}{\rho}\frac{\partial^4\bar{\Psi}}{\partial\zeta^4}, \tag{5.35a}$$

$$\frac{d\bar{\Psi}}{\partial\zeta}\frac{\partial(\rho^2\bar{\Omega})}{\partial\rho} - \frac{\partial\bar{\Psi}}{\partial\rho}\frac{\partial(\rho^2\bar{\Omega})}{\partial\zeta} = \rho\frac{\partial^2\left(\rho^2\bar{\Omega}\right)}{\partial\zeta^2}. \tag{5.35b}$$

With the aid of Eq. (5.34), we also transform the boundary conditions into dimensionless form

$$\begin{aligned} &\frac{\partial\bar{\Psi}}{\partial\rho} = \frac{\partial\bar{\Psi}}{\partial\zeta} = \bar{\Omega} = 0 \quad \text{at} \quad \zeta = 0, \\ &\frac{\partial\bar{\Psi}}{\partial\rho} = \frac{\partial\bar{\Psi}}{\partial\zeta} = 0, \qquad \bar{\Omega} = 1 \quad \text{at} \quad \zeta = 1, \\ &\bar{\Psi}(\rho, 1) - \bar{\Psi}(\rho, 0) = 1. \end{aligned} \tag{5.36}$$

Equations (5.35a) and (5.35b) are now parabolic, and thus boundary conditions can no longer be prescribed at r_2. Furthermore, since the film is thin, the precise form of the upstream boundary (now initial) condition becomes unimportant; thus, in Eqs. (5.35) and (5.36) we have a one-parameter family of flows.

The parabolic system of Eqs. (5.35) and (5.36) has been solved, after reduction to ordinary differential equations by the Galerkin method, with a predictor-corrector equation solver. The solutions show strong interaction between circumferential and radial flows, leading to consistently lower torque on the stationary disk. The radial derivative of the dimensionless average pressure is given by (Szeri and Adams, 1978)

$$\begin{aligned} \frac{d\bar{P}}{d\rho} = &-\frac{12}{\rho} + \frac{6}{5\rho^3} + \frac{\rho}{3E^2} + \sum_n \left[\frac{96}{\pi^2\rho^2}X_n\left(f_n' - \frac{1}{\rho}f_n\right) - Z_n f_n\right. \\ &\left. + \frac{\rho}{E^2}\left(\frac{1}{2}g_n^2 - \frac{2(-1)^n}{\pi n}g_n\right)\right] + \sum_{n,m} Y_{n,m}\left(\frac{\pi}{\rho^3}f_n f_m - \frac{2\pi}{\rho^2}f_n' f_m\right). \end{aligned} \tag{5.37}$$

Here $f_n(\rho)$ and $g_n(\rho)$ are the coefficients in the Galerkin expansions for $\bar{\Psi}$ and $\bar{\Omega}$, respectively, and X_n, $Y_{n,m}$, and z_n are constants. The reader may wish to compare Eq. (5.37) to Eq. (5.28), obtained by simpler means.

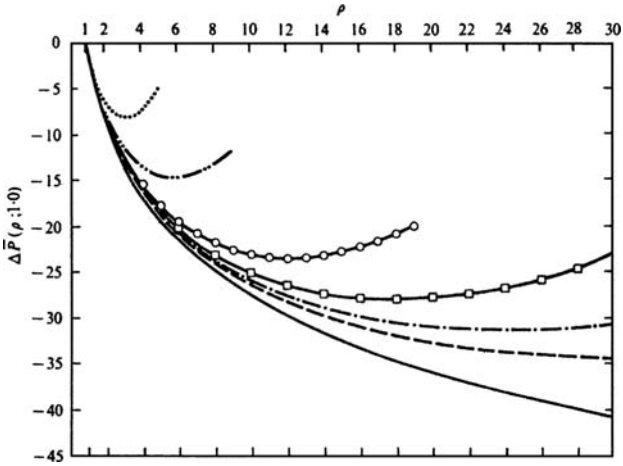

Figure 5.5. Dimensionless pressure profiles in fluid between rotating parallel disks for various values of the Ekman number. . . . , $E = 0.5$; –..–, $E = 0.9$; –o–, $E = 2.0$; —, $E = 2.9$; –.–, $E = 3.9$; - - -, $E = 4.9$; ——, $E = 100.0$ (∼creeping flow). (Reprinted with the permission of Cambridge University Press from Szeri, A. Z. and Adams, M. L. Laminar through flow between closely spaced rotating disks. *J. Fluid Mech.*, **86**, 1–14, 1978.)

At any radial position r,

$$p(r) = p(r_1) + \frac{\mu \nu R_Q}{h^2} \Delta \bar{P}(\rho; \rho_1), \tag{5.38}$$

where $\Delta \bar{P}(\rho; \rho_1) \equiv \bar{P}(\rho) - \bar{P}(\rho)$ and is calculated from Eq. (5.37). It can be shown that the initial conditions are washed out completely within a short distance, so that

$$\Delta \bar{P}(\rho_c; \rho_b) = \Delta \bar{P}(\rho_c; \rho_a) - \Delta \bar{P}(\rho_b; \rho_a) \quad \rho_a < \rho_b < \rho_c \tag{5.39}$$

is independent of the initial conditions on $\bar{\Psi}$ and $\bar{\Omega}$ and is valid for all thin films without backflow, at points sufficiently far removed from the inlet.

In Figure 5.5, pressure profiles are plotted for various values of the Ekman number, i.e., for various rates of rotation at given viscosity, against the nondimensional radius. Let us say our recess boundary is located at $\rho_1 = 2$. In the absence of rotation, the profile labeled 'creeping flow' applies, and we see that no matter where the pad outer edge ρ_2, $\rho_2 > \rho_1$, might be located, the pressure decreases monotonically from the recess all the way to the pad outer edge. Now, since at the pad outer edge the pressure is ambient by supposition, the pressure will be above ambient everywhere within the clearance gap, yielding a force capable of supporting an external load. Conditions change drastically, however, when rotation is added, i.e., when the Ekman number is made finite. For finite values of the Ekman number, the pressure is no longer a monotonic decreasing function of ρ; for any nonzero rotation it is possible to select a pad outer radius such that a region of subambient pressure will exist within the clearance gap. If the region of subambient pressure is sufficiently large and the film does not cavitate, a negative pressure force might be developed that will tend to draw the runner towards the bearing. Of course the film is expected to cavitate when the pressure falls below ambient; in any case, and the hydrostatic bearing will loose its load carrying capacity. Subambient pressures and the resulting cavitation can be avoided by choosing

$\rho_1 < \rho_2 < \rho_{\min}(E)$, where $\rho_{\min}$ is the location where $\Delta \bar{P}$ reaches its minimum for a given Ekman number.

The calculations above were performed for constant lubricant viscosity. It is possible to include the lubricant energy equation in Eq. (5.29) and also to account for the temperature dependence of lubricant viscosity (Gourley, 1977).

5.3 Total Inertia Limit, $\Omega^*/\mathrm{R}_\varepsilon \to 1$, $\mathrm{Re} \geq 1$

The conditions of this limit are by far the most demanding mathematically, as the equations are now time dependent as well as nonlinear:

$$\begin{aligned}
\rho\left(\frac{\partial u}{\partial t} + u\frac{\partial u}{\partial x} + \upsilon\frac{\partial u}{\partial y} + w\frac{\partial u}{\partial z}\right) &= -\frac{\partial p}{\partial x} + \mu\frac{\partial^2 u}{\partial y^2}, \\
\rho\left(\frac{\partial w}{\partial t} + u\frac{\partial w}{\partial x} + \upsilon\frac{\partial w}{\partial y} + w\frac{\partial w}{\partial z}\right) &= -\frac{\partial p}{\partial z} + \mu\frac{\partial^2 w}{\partial y^2}.
\end{aligned} \tag{5.40}$$

Equation (5.40) was solved by Reinhardt and Lund (1975) for journal bearings to first order in a perturbation series in R_ε, the zero-order solution representing the classical Reynolds theory. At small values of the Reynolds number regular perturbation in R_ε will work, as was shown by Kuzma (1967), Tichy and Winer (1970), and Jones and Wilson (1974), but care must be exercised as the perturbation series is divergent (Grim, 1976). There are also numerical solutions available (Hamza, 1985).

Another approach is via the "method of averaged inertia" (Szeri, Raimondi, and Giron-Duarte, 1983), which was first employed in this country by Osterle, Chou, and Saibel (1975), but in connection with limit (3). For more recent work, see San Andres and Vance (1987).

The Method of Small Perturbations

Journal Bearings

We follow Reinhardt and Lund (1974) and apply small perturbation analysis to Eq. (5.40). We also put here $L_{xz} = R$ and $L_y = C$, where R is the radius and C the radial clearance, and employ Eqs. (2.58a) to (2.58c), to nondimensionalize Eq. (5.40). Our small parameter is the reduced Reynolds number $\mathrm{R}_\varepsilon \equiv (L_y/L_{xz})\mathrm{Re} = C^2\omega/\nu$, and we write

$$\begin{Bmatrix} \bar{u} \\ \bar{v} \\ \bar{w} \\ \bar{p} \end{Bmatrix} = \begin{Bmatrix} \bar{u}^{(0)} \\ \bar{v}^{(0)} \\ \bar{w}^{(0)} \\ \bar{p}^{(0)} \end{Bmatrix} + \mathrm{R}_\varepsilon \begin{Bmatrix} \bar{u}^{(1)} \\ \bar{v}^{(1)} \\ \bar{w}^{(1)} \\ \bar{p}^{(1)} \end{Bmatrix} + O\left(\mathrm{R}_\varepsilon^2\right). \tag{5.41}$$

Substituting these expansions into Eq. (5.40) and collecting like terms, we obtain *To zero order*:

$$\begin{aligned}
\frac{\partial \bar{p}^{(0)}}{\partial \bar{x}} &= \frac{\partial^2 \bar{u}^{(0)}}{\partial \bar{y}^2} \\
\frac{\partial \bar{p}^{(0)}}{\partial \bar{z}} &= \frac{\partial^2 \bar{w}^{(0)}}{\partial \bar{y}^2} \\
\frac{\partial \bar{u}^{(0)}}{\partial \bar{x}} + \frac{\partial \bar{v}^{(0)}}{\partial \bar{y}} + \frac{\partial \bar{w}^{(0)}}{\partial \bar{z}} &= 0.
\end{aligned} \tag{5.42}$$

Following the procedure of Section 2.2, Eqs. (5.42) can be combined to yield a single equation in pressure,

$$\frac{\partial}{\partial \bar{x}}\left\{\bar{h}^3\frac{\partial \bar{p}^{(0)}}{\partial \bar{x}}\right\}+\frac{\partial}{\partial \bar{z}}\left\{\bar{h}^3\frac{\partial \bar{p}^{(0)}}{\partial \bar{z}}\right\}=6\frac{\partial \bar{h}}{\partial \bar{x}}+12\frac{\partial \bar{h}}{\partial \bar{t}}, \tag{5.43}$$

which we recognize as the Reynolds equation (2.80).

To first order:

$$\begin{aligned}
\frac{\partial^2 \bar{u}^{(1)}}{\partial \bar{y}^2}&=\frac{\partial \bar{p}^{(1)}}{\partial \bar{x}}+\bar{u}^{(0)}\frac{\partial \bar{u}^{(0)}}{\partial \bar{x}}+\bar{v}^{(0)}\frac{\partial \bar{u}^{(0)}}{\partial \bar{y}}+\bar{w}^{(0)}\frac{\partial \bar{u}^{(0)}}{\partial \bar{z}}+\frac{\partial \bar{u}^{(0)}}{\partial \bar{t}}\\
\frac{\partial^2 \bar{w}^{(1)}}{\partial \bar{y}^2}&=\frac{\partial \bar{p}^{(1)}}{\partial \bar{z}}+\bar{u}^{(0)}\frac{\partial \bar{w}^{(0)}}{\partial \bar{x}}+\bar{v}^{(0)}\frac{\partial \bar{w}^{(0)}}{\partial \bar{y}}+\bar{w}^{(0)}\frac{\partial \bar{w}^{(0)}}{\partial \bar{z}}+\frac{\partial \bar{w}^{(0)}}{\partial \bar{t}}\\
\frac{\partial \bar{u}^{(1)}}{\partial \bar{x}}&+\frac{\partial \bar{v}^{(1)}}{\partial \bar{y}}+\frac{\partial \bar{w}^{(1)}}{\partial \bar{z}}=0.
\end{aligned} \tag{5.44}$$

It is, again, possible to eliminate the velocities and obtain a single equation in pressure:

$$\begin{aligned}
&\frac{\partial}{\partial \bar{x}}\left\{\bar{h}^3\frac{\partial \bar{p}^{(1)}}{\partial \bar{x}}\right\}+\frac{\partial}{\partial \bar{z}}\left\{\bar{h}^3\frac{\partial \bar{p}^{(1)}}{\partial \bar{z}}\right\}=\frac{\partial}{\partial \bar{x}}\left\{-\frac{3\bar{h}^7}{560}\frac{\partial}{\partial \bar{x}}\left[\left(\frac{\partial \bar{p}^{(0)}}{\partial \bar{x}}\right)^2+\left(\frac{\partial \bar{p}^{(0)}}{\partial \bar{z}}\right)^2\right]\right.\\
&\quad-\frac{3\bar{h}^6}{140}\frac{\partial \bar{h}}{\partial \bar{x}}\left(\frac{\partial \bar{p}^{(0)}}{\partial \bar{x}}\right)^2+\frac{\bar{h}^5}{20}\frac{\partial^2 p^{(0)}}{\partial \bar{x}^2}+\frac{13\bar{h}^4}{140}\frac{\partial \bar{h}}{\partial \bar{x}}\frac{\partial \bar{p}^{(0)}}{\partial \bar{x}}-\frac{\bar{h}^2}{10}\frac{\partial \bar{h}}{\partial \bar{x}}\\
&\quad\left.-\frac{3\bar{h}^6}{140}\frac{\partial \bar{h}}{\partial \bar{z}}\frac{\partial \bar{p}^{(0)}}{\partial \bar{x}}\frac{\partial \bar{p}^{(0)}}{\partial \bar{z}}+\frac{13\bar{h}^4}{70}\frac{\partial \bar{p}^{(0)}}{\partial \bar{x}}\frac{\partial \bar{h}}{\partial \bar{t}}+\frac{\bar{h}^5}{10}\frac{\partial^2 \bar{p}^{(0)}}{\partial \bar{x}\partial \bar{t}}\right\}\\
&\quad+\frac{\partial}{\partial \bar{z}}\left\{-\frac{3\bar{h}^7}{560}\frac{\partial}{\partial \bar{z}}\left[\left(\frac{\partial \bar{p}^{(0)}}{\partial \bar{x}}\right)^2+\left(\frac{\partial \bar{p}^{(0)}}{\partial \bar{z}}\right)^2\right]\right.\\
&\quad-\frac{3\bar{h}^6}{140}\frac{\partial \bar{h}}{\partial \bar{x}}\frac{\partial \bar{p}^{(0)}}{\partial \bar{x}}\frac{\partial \bar{p}^{(0)}}{\partial \bar{z}}+\frac{\bar{h}^5}{20}\frac{\partial^2 \bar{p}^{(0)}}{\partial \bar{x}\partial \bar{z}}+\frac{13\bar{h}^4}{140}\frac{\partial \bar{h}}{\partial \bar{x}}\frac{\partial \bar{p}^{(0)}}{\partial \bar{z}}\\
&\quad\left.-\frac{3\bar{h}^6}{140}\frac{\partial \bar{h}}{\partial \bar{z}}\left(\frac{\partial \bar{p}^{(0)}}{\partial \bar{z}}\right)^2+\frac{13\bar{h}^4}{70}\frac{\partial \bar{p}^{(0)}}{\partial \bar{z}}\frac{\partial \bar{h}}{\partial \bar{t}}+\frac{\bar{h}^5}{10}\frac{\partial^2 \bar{p}^{(0)}}{\partial \bar{z}\partial \bar{t}}\right\}.
\end{aligned} \tag{5.45}$$

Thus, the zero-order pressure equation of the perturbation scheme is the classical Reynolds equation (5.43), while Eq. (5.45) gives the first-order pressure correction.

It is obvious from Eq. (5.43) that

$$\bar{p}^{(0)}=\bar{p}^{(0)}(\bar{x},\bar{z};\bar{h},\dot{\bar{h}}), \tag{5.46a}$$

and, because the derivative $\partial \bar{p}^{(0)}/\partial \bar{t}$ occurs in Eq. (5.45),

$$\bar{p}^{(1)}=\bar{p}^{(1)}(\bar{x},\bar{z};\bar{h},\dot{\bar{h}},\ddot{\bar{h}}). \tag{5.46b}$$

Let ψ be the angular coordinate measured from the load line that coincides with the vertical axis, as shown in Figure 5.6. Then $\psi=\theta+\phi$, where ϕ is the attitude angle, and

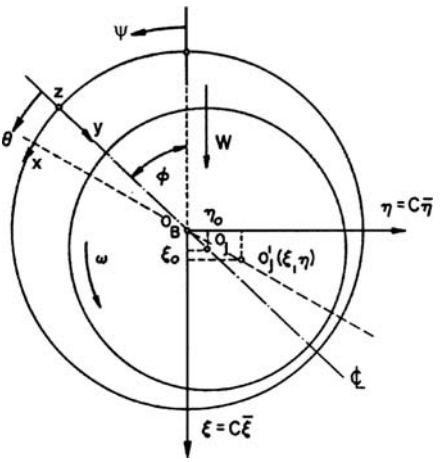

Figure 5.6. Journal bearing geometry for analysis of fluid inertia effects.

we have

$$\begin{aligned} \bar{h} &= \frac{h}{C} \\ &= 1 + \varepsilon \cos(\psi - \phi) \\ &= 1 + \bar{\xi} \cos\psi + \bar{\eta} \sin\psi. \end{aligned} \tag{5.47}$$

Here $\bar{\xi}$ and $\bar{\eta}$ are nondimensional Cartesian coordinates (Figure 5.6).

If we superimpose dynamic motions of small amplitudes, $\Delta\bar{\xi}$, and, $\Delta\bar{\eta}$, about the equilibrium position $(\bar{\xi}_0,\ \bar{\eta}_0)$. the film thickness will vary according to

$$\Delta\bar{h} = \Delta\bar{\xi} \cos\psi + \Delta\bar{\eta} \sin\psi. \tag{5.48}$$

From Eqs. (5.41) and (5.48), we have the first-order Taylor expansion about the equilibrium position $(\bar{\xi}_0,\ \bar{\eta}_0)$

$$\begin{aligned} \bar{p} = \bar{p}_0^{(0)} &+ \bar{p}_{\bar{\xi}}^{(0)} \Delta\bar{\xi} + \bar{p}_{\bar{\eta}}^{(0)} \Delta\bar{\eta} + \bar{p}_{\dot{\bar{\xi}}}^{(0)} \Delta\dot{\bar{\xi}} + \bar{p}_{\dot{\bar{\eta}}}^{(0)} \Delta\dot{\bar{\eta}} \\ &+ R_\varepsilon \left[\bar{p}_0^{(1)} + \bar{p}_{\bar{\xi}}^{(1)} \Delta\bar{\xi} + \bar{p}_{\bar{\eta}}^{(1)} \Delta\bar{\eta} + \bar{p}_{\dot{\bar{\xi}}}^{(1)} \Delta\dot{\bar{\xi}} + \bar{p}_{\dot{\bar{\eta}}}^{(1)} \Delta\dot{\bar{\eta}} + \bar{p}_{\ddot{\bar{\xi}}}^{(1)} \Delta\ddot{\bar{\xi}} + \bar{p}_{\ddot{\bar{\eta}}}^{(1)} \Delta\ddot{\bar{\eta}} \right] \end{aligned} \tag{5.49}$$

Equation (5.49) can now be substituted into Eqs. (5.43) and (5.48). Collecting again like terms, we end up with a set of 12 linear partial differential equations for the determination of

$$\left\{ \bar{p}_0^{(0)}, \bar{p}_{\bar{\xi}}^{(0)}, \ldots, \bar{p}_{\ddot{\bar{\eta}}}^{(1)} \right\}. \tag{5.50}$$

In formulating these equations, we take into account that

$$\bar{h} = \bar{h}_0 + \Delta\bar{h},$$

where

$$\bar{h}_0 = 1 + \bar{\xi}_0 \cos\psi + \bar{\eta}_0 \sin\psi$$

and

$$(\bar{h})^n = (\bar{h}_0)^n + n\,(h_0)^{n-1}\,\Delta\bar{h} + O[(\Delta\bar{h})^2].$$

The vertical and horizontal components of the force perturbations corresponding to the various pressure perturbations, Eq. (5.49), are obtained from

$$\begin{Bmatrix} f^{(\alpha)}_{\bar{\xi},\bar{\omega}} \\ f^{(\alpha)}_{\bar{\eta},\bar{\omega}} \end{Bmatrix} = \frac{\pi}{2}\left(\frac{D}{L}\right)\int_{-(L/D)}^{(L/D)}\int_{\bar{x}_1}^{\bar{x}_2} \bar{p}^{(\alpha)}_{\bar{\omega}} \begin{Bmatrix} \cos\psi \\ \sin\psi \end{Bmatrix} d\psi\, d\bar{z} \qquad \begin{matrix} \alpha = 0, 1 \\ \bar{\omega} = \bar{\xi}, \dot{\bar{\xi}}, \ldots, \ddot{\bar{\eta}}. \end{matrix} \tag{5.51}$$

We arrange the force components obtained in Eq. (5.51) in matrix form:

$$\boldsymbol{K}^{(\alpha)} = -\begin{bmatrix} f^{(\alpha)}_{\bar{\xi},\bar{\xi}} & f^{(\alpha)}_{\bar{\xi},\bar{\eta}} \\ f^{(\alpha)}_{\bar{\eta},\bar{\xi}} & f^{(\alpha)}_{\bar{\eta},\bar{\eta}} \end{bmatrix}, \tag{5.52a}$$

$$\boldsymbol{C}^{(\alpha)} = -\begin{bmatrix} f^{(\alpha)}_{\bar{\xi},\dot{\bar{\xi}}} & f^{(\alpha)}_{\bar{\xi},\dot{\bar{\eta}}} \\ f^{(\alpha)}_{\bar{\eta},\dot{\bar{\xi}}} & f^{(\alpha)}_{\bar{\eta},\dot{\bar{\eta}}} \end{bmatrix}, \tag{5.52b}$$

$$\boldsymbol{D} = -\begin{bmatrix} f^{(1)}_{\bar{\xi},\ddot{\bar{\xi}}} & f^{1}_{\bar{\xi},\ddot{\bar{\eta}}} \\ f^{1}_{\bar{\eta},\ddot{\bar{\xi}}} & f^{(1)}_{\bar{\eta},\ddot{\bar{\eta}}} \end{bmatrix}. \tag{5.52c}$$

Let $\Delta \boldsymbol{f} = \boldsymbol{f} - \boldsymbol{f}_0$ signify the perturbation of the nondimensional oil-film force due to the small motion $(\Delta\bar{\xi},\ \Delta\bar{\eta})$ about the point of static equilibrium $(\bar{\xi}_0,\ \bar{\eta}_0)$; then, using the notation of Eq. (5.52), we can write

$$\Delta \boldsymbol{f} = -\left(\boldsymbol{K}^{(0)} + \mathrm{R}_\varepsilon \boldsymbol{K}^{(1)}\right)\Delta\bar{\boldsymbol{\xi}} - \left(\boldsymbol{C}^{(0)} + \mathrm{R}_\varepsilon \boldsymbol{C}^{(1)}\right)\Delta\dot{\bar{\boldsymbol{\xi}}} - \mathrm{R}_\varepsilon \boldsymbol{D}\Delta\ddot{\bar{\boldsymbol{\xi}}}. \tag{5.53}$$

Here $\Delta\bar{\xi} = (\Delta\bar{\xi},\ \Delta\bar{\eta})$ is the (nondimensional) displacement vector. The diagonal elements of $\boldsymbol{D}$, the inertia coefficient matrix, are plotted against ε in Figure 5.7.

It is obvious from Eq. (5.53) that the incremental force on the journal away from static equilibrium depends on acceleration as well as displacement and velocity of the journal, as was asserted earlier in Chapter 4.

Squeeze Flow Between Parallel Plates

Two distinct problems have been considered by researchers: one in which the upper plate moves impulsively from rest with prescribed velocity toward the fixed lower plate (Kuzma, 1967; Tichy and Winer, 1970; Jones and Wilson, 1974; and Hamza and MacDonald, 1981), and another in which the upper plate moves under the action of a prescribed body force of constant magnitude (Weinbaum et al., 1985; and Yang and Leal, 1993).

We shall employ cylindrical polar coordinates (r, θ, z) and suppose that the fixed disk is at $z = 0$ and the moving disk is located at $z = h(t)$. Assuming the problem has axial symmetry, we may state it in terms of a Stokes stream function $\Psi(r, z)$

$$u_r = \frac{1}{r}\frac{\partial \Psi}{\partial z}, \qquad u_z = -\frac{1}{r}\frac{\partial \Psi}{\partial r}. \tag{5.54}$$

Let h_0 and R, the initial separation and the radius of the disks, be chosen as characteristic length in z and r, respectively. Also, let W_* be the characteristic velocity in z, the precise

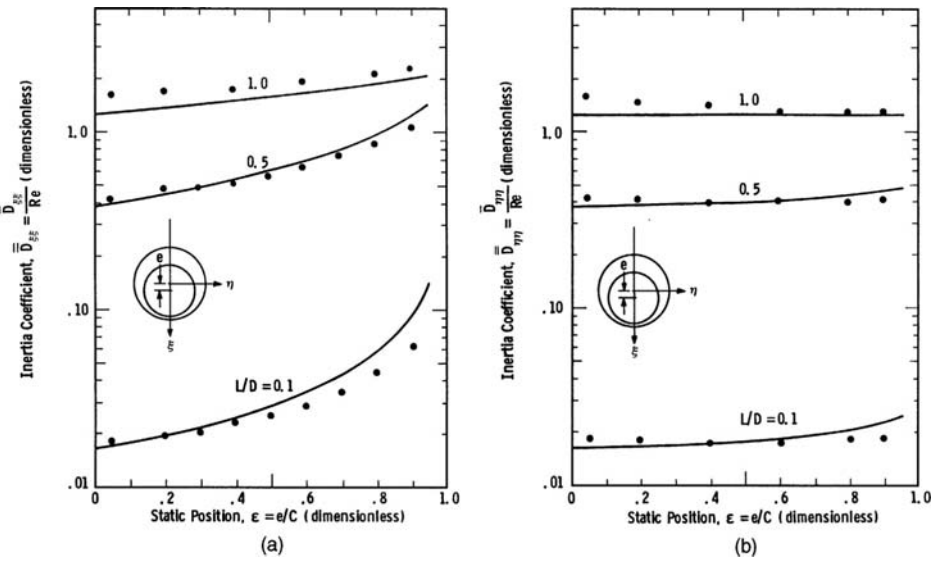

Figure 5.7. Inertial coefficients for journal bearing; (a) $D_{\xi\xi}$, (b) $D_{\eta\eta}$: —, Szeri et al., (1983); • Reinhardt and Lund, (1974). (Reprinted with permission from Szeri, A. Z., Raimondi, A. A. and Giron-Duarte, A. Linear force coefficients for squeeze-film dampers. *ASME Journal of Lubrication Technology*, **105**, 326–334, 1983.)

form of which is to be defined later. Then, the equation of continuity dictates that the characteristic velocity in r is

$$U_* = W_* \left(\frac{r_0}{h_0} \right).$$

We nondimensionalize the stream function and the coordinates according to

$$\Psi = R^2 W_* \bar{\Psi}, \qquad r = R\bar{r}, \qquad z = h_0 \bar{z}.$$

The problem has two spatial dimensions r and z. We can eliminate dependence on r by making use of the von Karman (1921) similarity transformation

$$\bar{\Psi} = \bar{r}^2 \bar{G}(\bar{z}, \bar{t}), \qquad \bar{u}_r = \bar{r} \frac{\partial \bar{G}(\bar{z}, \bar{t})}{\partial \bar{z}}, \qquad \bar{u}_\theta = -2\bar{G}(\bar{z}, \bar{t}). \tag{5.55}$$

On substituting assumption (5.55) into the r component of the Navier-Stokes equations, we obtain (dropping the over bar)

$$\mathrm{Re}[G_{zt} + (G_z)^2 - 2GG_{zz}] - G_{zzz} = -\frac{1}{r} \frac{\partial p}{\partial r}. \tag{5.56}$$

The z component of the equation simply serves to evaluate the rate of change of pressure across the film and need not be considered here.

To arrive at Eq. (5.56), we used

$$T_* = \frac{h_0}{W_*}, \qquad P_* = \frac{\mu W_*}{h_0} \left(\frac{R}{h_0} \right)^2, \qquad \mathrm{Re} = \frac{h_0 W_*}{\nu}$$

for characteristic time, characteristic pressure, and squeeze Reynolds number, respectively, and dropped the bar that signifies nondimensionality.

The left side of Eq. (5.56) is at most a function of z and t, while the right side is at most a function of r and t, which prompts us to put

$$\frac{1}{r}\frac{\partial p}{\partial r} = A(t). \tag{5.57}$$

Here $A(t)$ is an instantaneous constant.

Constant Approach Velocity

This is characterized by the boundary conditions[3]

$$G = G_z = 0 \quad \text{at} \quad z = 0, \tag{5.58a}$$

$$G = 1/2, G_z = 0 \quad \text{at} \quad z = 1 - t, \tag{5.58b}$$

and the initial condition[4] (Jones and Wilson, 1974)

$$G = \frac{1}{2}z \quad \text{at} \quad t = 0^+. \tag{5.59}$$

The characteristic velocity in the z-direction is chosen in this case to be the constant velocity of approach, $W_* = W$. To eliminate the pressure term, we differentiate Eq. (5.56) with respect to z. However, as the boundary condition (5.58a) is not easy to apply, we transform to a moving coordinate system (y, T) as follows:

$$G(z,t) \to F(y,T), \qquad 0 \le y = -z/T \le 1, \qquad 0 \le T = t - 1 \le 1.$$

The boundaries are now fixed at $y = 0$ (stationary plate) and $y = 1$ (moving plate), and Eq. (5.59) takes the form

$$-yTF_{yyy} - 2TF_{yy} + T^2F_{yyT} + 2TFF_{yyy} = \mathrm{Re}^{-1}F_{yyyy}. \tag{5.60}$$

The transformed boundary conditions are given by

$$F = F_y = 0, \quad \text{on } y = 0 \quad \text{(fixed disk)} \tag{5.61a}$$

$$F = 1/2, \quad F_y = 0, \quad \text{on } y = 1 \quad \text{(moving disk)} \tag{5.61b}$$

and the initial condition by

$$F = y/2, \quad \text{at} \quad T = -1. \tag{5.62}$$

Following Jones and Wilson (1974), we seek solution for small Reynolds number and assume that

$$F = \sum_{n=0} \varepsilon^n f_n(y), \qquad \varepsilon = T\mathrm{Re}. \tag{5.63}$$

Note that $|\varepsilon| = W_* h(t)/\nu$ is the instantaneous Reynolds number.

[3]Note that the instantaneous film thickness is given by $H(t) = \frac{h(t)}{h_0} = 1 - \frac{W}{h_0}t = 1 - \bar{t}$.

[4]To arrive at this initial condition, Jones and Wilson argue that vorticity is unchanged across $t = 0$ by the velocity impulse, and as the only vorticity component is rG_{zz}, we have $G_{zz} = 0$. This integrates to our initial condition.

On substituting Eq. (5.63) into Eq. (5.60), we obtain

$$f_0'''' + \varepsilon[f_1'' - y f_0''' - 2f_0'' + 2f_0 f_0'''] + \varepsilon^2[f_2'''' + f_2'' - y f_1''' - 2f_1'' + 2(f_0''' f_1 + f_0 f_1'''')] + \cdots = 0 \tag{5.64}$$

The leading-order term supplies the lubrication approximation

$$f_0 = \frac{3}{2}y^2 - y^3, \tag{5.65a}$$

and for the first-order correction we obtain

$$f_1 = \frac{1}{70}y^7 - \frac{1}{20}y^6 + \frac{3}{20}y^5 - \frac{1}{4}y^4 + \frac{5}{28}y^3 - \frac{3}{70}y^2. \tag{5.65b}$$

Though these functions satisfy the boundary conditions, they do not satisfy the initial condition and, therefore, cannot be valid for short times.

From Eq. (5.59), the first three terms of the series (5.63) yield[5]

$$\frac{1}{r}\frac{\partial p}{\partial r} = 6T^3\left\{1 - \frac{5}{28}(T\mathrm{Re}) - \frac{277}{323{,}400}(T\mathrm{Re})^2 + \cdots\right\}. \tag{5.66a}$$

To study conditions at short times, Jones and Wilson scale the time variable with the Reynolds number and find that the leading inner solution term of Eq. (5.60) is

$$F_{yyT} = \mathrm{Re} F_{yyyy}.$$

Solution of this diffusion-type equation, found by separation of variables, leads to

$$\frac{1}{r}\frac{\partial p}{\partial r} = 6T^3\{1 + 4\exp[\lambda^2(T+1)/\mathrm{Re}] + \cdots\}, \tag{5.66b}$$

where $\lambda = 3\pi - 4/3\pi$ is an eigenvalue. From Eq. (5.66b), we can estimate the elapse of time after start for the initial condition to loose influence on the pressure gradient.

For large Reynolds number, the flow is of the boundary layer type and matching of inner and outer solutions is employed. Further details of the analysis are available in the paper by Jones and Wilson (1974).

Constant Applied Force

Following Yang and Leal (1993), for $\mathrm{Re} \ll 1$ we choose the characteristic velocity as

$$W_* = \frac{4}{\pi}\frac{f h_0^3}{\mu R^4}, \qquad f = mg,$$

then the characteristic time is

$$T_* = \frac{\pi}{4}\frac{\mu R^4}{f h_0^2}.$$

This choice of velocity and time scales is suggested by the equation of motion for the body encompassing the upper plate. For $\mathrm{Re} \ll 1$, we may neglect inertia of both fluid and body, and the equation of motion of the body reduces to a balance of viscous forces

[5]Note that the right-hand side of Eq. (5.66a) is to be divided by Re to obtain agreement with Eq. (13.2) of Jones and Wilson, as they scale the pressure with ρW^2 and the radial coordinate with d.

and the weight, f, of the body. The pressure term $A(t)$, Eq. (5.60), is then calculated form considering the equation of motion for the body containing the upper plate. We find in this manner that

$$A(t) = 1 + \mathrm{Re}\beta \frac{d^2H}{dt^2}, \qquad \beta = \frac{4h_0 m}{\pi \rho R^4}, \qquad \mathrm{Re} = \frac{4\rho f h_0^4}{\pi \mu^2 R^4} \ll 1. \tag{5.67}$$

Equation (5.60) now takes the form

$$\frac{\partial^2 G}{\partial z \partial t} + \left(\frac{\partial G}{\partial z}\right)^2 - 2G\frac{\partial^2 G}{\partial z^2} - \frac{1}{\mathrm{Re}}\frac{\partial^3 G}{\partial z^3} = \frac{1}{\mathrm{Re}} + \beta \frac{d^2H}{dt^2} \tag{5.68a}$$

with boundary conditions

$$\begin{aligned} &G = -\frac{1}{2}\frac{dH}{dt}, \qquad \frac{\partial G}{\partial z} = 0 \quad \text{at} \quad z = H, \\ &G = \frac{\partial G}{\partial z} = 0 \quad \text{at} \quad z = 0, \\ &G = 0, \quad H = 1 \quad \text{at} \quad t = 0. \end{aligned} \tag{5.68b}$$

We seek solution of Eq. (5.68) in the form of a regular perturbation expansion:

$$G(z,t) = G^{(0)}(z,t) + \mathrm{Re}G^{(1)}(z,t) + \cdots, \tag{5.69a}$$

$$H(t) = H^{(0)}(t) + \mathrm{Re}H^{(1)}(t) + \cdots. \tag{5.69b}$$

The zero-order solution contains one unknown integration constant, c_0,

$$G^{(0)} = \frac{1}{4}\left(H^{(0)}z^2 - \frac{2}{3}z^3\right), \qquad H^{(0)} = \left(\frac{3}{t + c_0}\right)^{1/2}. \tag{5.70}$$

The solution in Eq. (5.70) completely satisfies the boundary conditions but not the initial condition, confirming our earlier conclusion that regular perturbation in Re cannot solve Eq. (5.68) for short times. The reason is that the problem possesses two very different time scales, the classical signature of a singular perturbation problem. The "outer" time scale, $T_* = h_0/W_*$, and the expansions (5.69) characterize long-term behavior. Short-time behavior, on the other hand, is characterized by the "inner" time scale, $T_\nu = h_0^2/\nu$. The ratio of the time scales is $T_\nu/T_* = \mathrm{Re}$, which we have assumed to be asymptotically small.

Equation (5.69) will suffice as the outer solution. To obtain the inner solution, we have to rescale the problem. The inner and outer (time) variables, $\bar{t}$ and t respectively, are related by $\bar{t} = t/\mathrm{Re}$. Rescaling Eq. (5.68) accordingly, we obtain the equation valid for short times

$$\frac{\partial^2 \tilde{G}}{\partial z \partial \tilde{t}} - \frac{\partial^3 \tilde{G}}{\partial z^3} - 1 = \mathrm{Re}\left[2\tilde{G}\frac{\partial^2 \tilde{G}}{\partial z^2} - \left(\frac{\partial \tilde{G}}{\partial z}\right)^2\right] + \frac{\beta}{\mathrm{Re}}\frac{d^2\tilde{H}}{d\tilde{t}^2}. \tag{5.71}$$

Here the tilde denotes the variables in the inner (short time) region.

To obtain the "inner" solution, i.e., to solve Eq. (5.71), we assume that

$$\tilde{G}(z,\tilde{t}) = \tilde{G}^{(0)}(z,\tilde{t}) + \mathrm{Re}\tilde{G}^{(1)}(z,\tilde{t}) + \cdots, \tag{5.72a}$$

$$\tilde{H}(\tilde{t}) = \tilde{H}^{(0)} + \mathrm{Re}\tilde{H}^{(1)}(\tilde{t}) + \cdots, \qquad \tilde{H}^{(0)} = 1. \tag{5.72b}$$

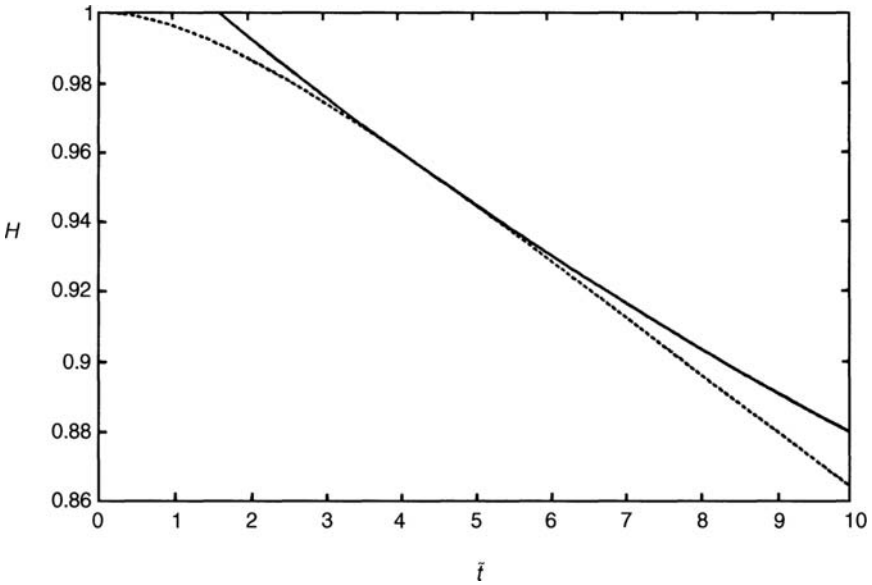

Figure 5.8. Composite uniform approximation to the film thickness as function of the small time variable $\bar{t}$ at $\mathrm{Re} = 0.1$; – –, $\beta = 10$; - - - -, $\beta = 0$. (Reprinted with permission from Yang, S.-M. and Leal, G. Thin fluid film squeezed with inertia between two parallel plane surfaces. *ASME Journal of Tribology*, **115**, 632–639, 1993.)

The governing equation and boundary and initial conditions for the leading-order terms $\tilde{G}^{(0)}$ and $\tilde{H}^{(1)}$ are

$$\frac{\partial^2 \tilde{G}^{(0)}}{\partial z \partial \tilde{t}} - \frac{\partial^3 \tilde{G}^{(0)}}{\partial z^3} = 1 + \beta \frac{d^2 \tilde{H}^{(1)}}{d\tilde{t}^2}, \tag{5.73a}$$

$$\tilde{G}^{(0)} = \frac{\partial \tilde{G}^{(0)}}{\partial z} = 0 \qquad \text{at} \quad z = 0, \tag{5.73b}$$

$$\frac{\partial \tilde{G}^{(0)}}{\partial z} = 0, \qquad \tilde{G}^{(0)} = -\frac{1}{2} \frac{d\tilde{H}^{(1)}}{d\tilde{t}} \quad \text{at} \quad z = 1, \tag{5.73c}$$

$$\tilde{G}^{(0)} = 0, \quad \tilde{H}^{(1)} = 0 \quad \text{at} \quad \tilde{t} = 0, \tag{5.73d}$$

The system (5.73) is amenable to solution via separation of variables (Yang and Leal, 1953). Yang and Leal evaluate the first two terms in both inner and outer expansions, and from these construct H in the overlap region by matching. This is depicted in Figure 5.8.

The Method of Averaged Inertia

This method was employed for the steady state lubrication problem by Osterle, Chou, and Saibel (1957) and by Constantinescu (Constantinescu 1970; Constantinescu and Galetuse, 1982). Here we follow Szeri, Raimondi, and Giron (1983) and write Eq. (5.2) in

the form

$$\frac{\partial u}{\partial t}+u\frac{\partial u}{\partial x}+v\frac{\partial u}{\partial y}+w\frac{\partial u}{\partial z}=-\frac{1}{\rho}\frac{\partial p}{\partial x}+\frac{1}{\rho}\frac{\partial T_{xy}}{\partial y},$$
$$\frac{\partial w}{\partial t}+u\frac{\partial w}{\partial x}+v\frac{\partial w}{\partial y}+w\frac{\partial w}{\partial z}=-\frac{1}{\rho}\frac{\partial p}{\partial z}+\frac{1}{\rho}\frac{\partial T_{zy}}{\partial y}. \tag{5.74}$$

As we are interested in average (across the film) quantities here, we integrate Eq. (5.74) across the film and on using the averaged continuity equation

$$\frac{\partial}{\partial x}\int_0^{h(x,t)} u\,dy+\frac{\partial}{\partial z}\int_0^{h(x,t)} w\,dy+\left(v-u\frac{\partial h}{\partial x}\right)\Bigg|_{h(x,t)}=0 \tag{5.75}$$

obtain

$$\frac{\partial}{\partial t}\int_0^h u\,dy+\frac{\partial}{\partial x}\int_0^h u^2\,dy+\frac{\partial}{\partial z}\int_0^h uw\,dy$$
$$-\left\{u\left(\frac{\partial}{\partial x}\int_0^h u\,dy+\frac{\partial}{\partial z}\int_0^h w\,dy\right)\right\}\Bigg|_h=-\frac{h}{\rho}\frac{\partial p}{\partial x}+\frac{1}{\rho}T_{xy}|_0^h+u|_h\frac{\partial h}{\partial t}, \tag{5.76a}$$

$$\frac{\partial}{\partial t}\int_0^h w\,dy+\frac{\partial}{\partial x}\int_0^h u\,wdy+\frac{\partial}{\partial z}\int_0^h w^2\,dy=-\frac{h}{\rho}\frac{\partial p}{\partial z}+\frac{1}{\rho}T_{zy}\Bigg|_0^h. \tag{5.76b}$$

Partial differentiation of Eq. (5.76a) with respect to x and of Eq. (5.76b) with respect to z and addition of the resulting equations yields

$$\frac{\partial}{\partial x}\left(\frac{h}{\rho}\frac{\partial p}{\partial x}\right)+\frac{\partial}{\partial z}\left(\frac{h}{\rho}\frac{\partial p}{\partial z}\right)$$
$$=\frac{\partial}{\partial x}\left(\frac{T_{xy}|_0^h}{\rho}\right)+\frac{\partial}{\partial z}\left(\frac{T_{zy}|_0^h}{\rho}\right)+U_P\frac{\partial^2 h}{\partial x\,\partial t}-\frac{\partial^2}{\partial x\,\partial t}\int_0^h u\,dy$$
$$-\frac{\partial^2}{\partial x^2}\int_0^h u^2dy-2\frac{\partial^2}{\partial x\,\partial z}\int_0^h uw\,dy-\frac{\partial^2}{\partial z\,\partial t}\int_0^h w\,dy$$
$$-\frac{\partial^2}{\partial z^2}\int_0^h w^2dy+U_P\left(\frac{\partial^2}{\partial x^2}\int_0^h u\,dy+\frac{\partial^2}{\partial x\,\partial z}\int_0^h w\,dy\right) \tag{5.77}$$

Here U_P is shaft surface velocity in rigid body translation.

We make our first significant assumption here: that the shape of the velocity profile is not strongly influenced by inertia, so the viscous terms are approximated by (Constantinescu, 1970)

$$T_{xy}|_0^h=-\frac{12\mu}{h}\left(U-\frac{1}{2}U_P\right);\qquad T_{zy}|_0^h=-\frac{12\mu}{h}W. \tag{5.78}$$

Here

$$U=\frac{1}{h}\int_0^h u\,dy;\qquad W=\frac{1}{h}\int_0^h \omega\,dy \tag{5.79}$$

are the components of the average velocity vector.

Our second significant assumption

$$\int_0^h u^2 dy = hU^2; \qquad \int_0^h u\omega\, dy = hUW; \qquad \int_0^h \omega^2 dy = hW^2 \tag{5.80}$$

equates the average of a product to the product of the averages and is not possible to defend.[6] Nevertheless, it has been used by several researchers, beginning with Constantinescu (1970).

Assumptions (5.78) and (5.80) permit us to write (5.79) in the form

$$\begin{aligned}
&\frac{\partial}{\partial x}\left(\frac{h^3}{\mu}\frac{\partial p}{\partial x}\right) + \frac{\partial}{\partial z}\left(\frac{h^3}{\mu}\frac{\partial p}{\partial z}\right) \\
&\quad = 12\left\{v|_h - \frac{1}{2}U_P\frac{\partial h}{\partial x}\right\} + \frac{h^2}{\nu}\left\{U_P\frac{\partial^2 h}{\partial x\,\partial t} - \frac{\partial^2(hU)}{\partial x\,\partial t} - \frac{\partial^2\left(hU^2\right)}{\partial x^2}\right. \\
&\qquad \left. - 2\frac{\partial^2(hUW)}{\partial x\,\partial z} - \frac{\partial^2(hW)}{\partial z\,\partial t} - \frac{\partial^2(hW^2)}{\partial z^2} + U_P\frac{\partial^2(hU)}{\partial x^2} + U_P\frac{\partial^2(hW)}{\partial x\,\partial z}\right\}.
\end{aligned} \tag{5.81}$$

We will apply Eq. (5.81) to a squeeze film damper (Szeri et al., 1983). A schematic of the damper is shown in Figure 5.9.

To nondimensionalize Eq. (5.81), we apply the transformation

$$\begin{aligned}
&h = CH, \quad t = \bar{t}/\omega, \quad x = R\bar{x}, \quad z = \frac{1}{2}\bar{z}, \quad \bar{U} = U/\delta\omega, \\
&\bar{W} = W/\delta\omega, \quad \mathrm{Re} = \frac{\delta\omega C}{\nu}, \quad p = 12\mu\omega\left(\frac{R}{C}\right)^2\bar{p}.
\end{aligned} \tag{5.82}$$

Here Ω is the characteristic frequency, δ is the characteristic orbit radius, and $\delta\omega$ is the characteristic velocity of the system.

The dimensionless form of Eq. (5.81) is

$$\begin{aligned}
&\frac{\partial}{\partial x}\left(H^3\frac{\partial\bar{p}}{\partial\bar{x}}\right) + \left(\frac{D}{L}\right)^2\frac{\partial}{\partial\bar{z}}\left(H^3\frac{\partial\bar{p}}{\partial\bar{z}}\right) = \frac{\partial H}{\partial t} - \frac{1}{2}\left(\frac{\delta}{R}\right)U_P\frac{\partial H}{\partial\bar{x}} + \frac{\mathrm{Re}}{12}\left(\frac{C}{R}\right)H^2 \\
&\quad \times\left\{U_P\frac{\partial^2 H}{\partial\bar{x}\,\partial\bar{t}} - \frac{\partial^2 H\bar{U}}{\partial\bar{x}\,\partial\bar{t}} - \left(\frac{D}{L}\right)^2\frac{\partial^2 H\bar{W}}{\partial\bar{z}\,\partial\bar{t}} - \left(\frac{\delta}{R}\right)\left[\frac{\partial^2 H\bar{U}^2}{\partial\bar{x}^2} + 2\left(\frac{D}{L}\right)\right.\right. \\
&\quad \left.\left. \times\ \frac{\partial^2 H\bar{U}\bar{W}}{\partial\bar{z}\,\partial\bar{x}} + \left(\frac{D}{L}\right)^2\frac{\partial^2 H\bar{W}^2}{\partial\bar{z}^2} - U_P\frac{\partial^2 H\bar{U}}{\partial\bar{x}^2} - \left(\frac{D}{L}\right)\bar{U}_P\frac{\partial^2 H\bar{W}}{\partial\bar{x}\partial\bar{z}}\right]\right\}
\end{aligned} \tag{5.83}$$

Considering that $\delta = O(C)$ and therefore $(\delta/R) = O(10^{-3})$, it seems possible to simplify Eq. (5.83) by deleting all terms which are multiplied by (δ/R). We will not do this, however, as our intention is to introduce the short-bearing approximation at this stage via the equation of continuity Eq. (5.75).

Introducing the short bearing approximation $\bar{U} \cong \frac{1}{2}\bar{U}_p$ into Eq. (5.75), we have

$$\frac{\partial H\bar{W}}{\partial\bar{z}} \approx \left(\frac{L}{D}\right)\left(\frac{R}{\delta}\right)\left\{\frac{1}{2}\left(\frac{\delta}{R}\right)\bar{U}_P\frac{\partial H}{\partial\bar{x}} - \frac{\partial H}{\partial t}\right\} \approx -\left(\frac{L}{D}\right)\left(\frac{R}{\delta}\right)\frac{\partial H}{\partial\bar{t}}. \tag{5.84}$$

[6] Hashimoto (1994) appears to have overcome the necessity of having to assume Eq. (5.80). This, however, is purely illusory, as he makes the equally indefensible assumption that $\partial T_{xy}/\partial y = \text{const.}$ across the film, true only for zero inertia.

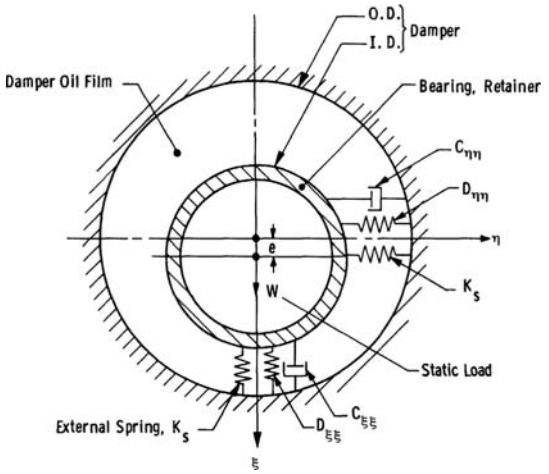

Figure 5.9. Basic elements (cross-coupling not shown) of squeeze-film damper. (Reprinted with permission from Szeri, A. Z., Raimondi, A. A. and Giron-Duarte, A. Linear force coefficients for squeeze-film dampers. *ASME Journal of Lubrication Technology*, **105**, 326–334, 1983).

This leads to the following approximation of Eq. (5.83) when we neglect terms multiplied by (δ/R):

$$\frac{\partial}{\partial x}\left(H^3\frac{\partial \bar{p}}{\partial \bar{x}}\right)+\left(\frac{D}{L}\right)^2\frac{\partial}{\partial \bar{z}}\left(H^3\frac{\partial \bar{p}}{\partial \bar{z}}\right)=\frac{\partial H}{\partial \bar{t}}+\frac{H^2}{12}\mathrm{R}_\varepsilon\left\{\frac{\partial^2 H}{\partial \bar{t}^2}+\frac{2}{H}\left(\frac{\partial H}{\partial t}\right)^2\right\} \tag{5.85}$$

Here $\mathrm{R}_\varepsilon = \mathrm{Re}(C/\delta)$ is the reduced Reynolds number.

Further details can be found in Szeri, Raimondi, and Giron (1983). Here we show the diagonal terms of the inertia coefficient matrix $\boldsymbol{D}$, i.e., the added mass tensor, in Figure 5.7. This figure also contains results from small perturbation analysis (Reinhardt and Lund, 1974). The analysis of Szeri, Raimondi, and Giron (1983), when cavitation is accounted for, yields results as shown in Figure 5.10.

Zhang, Ellis, and Roberts (1993) attempted to verify recent "averaged inertia" analyses, as applied to squeeze, film dampers. They found that in the cases they considered, the pressure field can be expressed as

$$p = 12\left(\frac{z^2}{2}-\frac{L^2}{8}\right)+12\left\{\mu\left(\frac{1}{h^3}\frac{\partial h}{\partial t}\right)+\rho\left(\frac{k_1}{h}\frac{\partial^2 h}{\partial t^2}\right)-\rho\left[\frac{k_2}{h^2}\left(\frac{\partial h}{\partial t}\right)^2\right]\right\}. \tag{5.86}$$

The values of the numerical constants k_1 and k_2 in Eq. (5.86) for the various analyses are shown in Table 5.7. In the San Andres and Vance (1986) analysis, the k_1, k_2 values depend on the flow regime considered. At low Re, the analysis yields values identical to those of Tichy and Bou-Said (1991); at large Re the k_1, k_2 values agree with those of

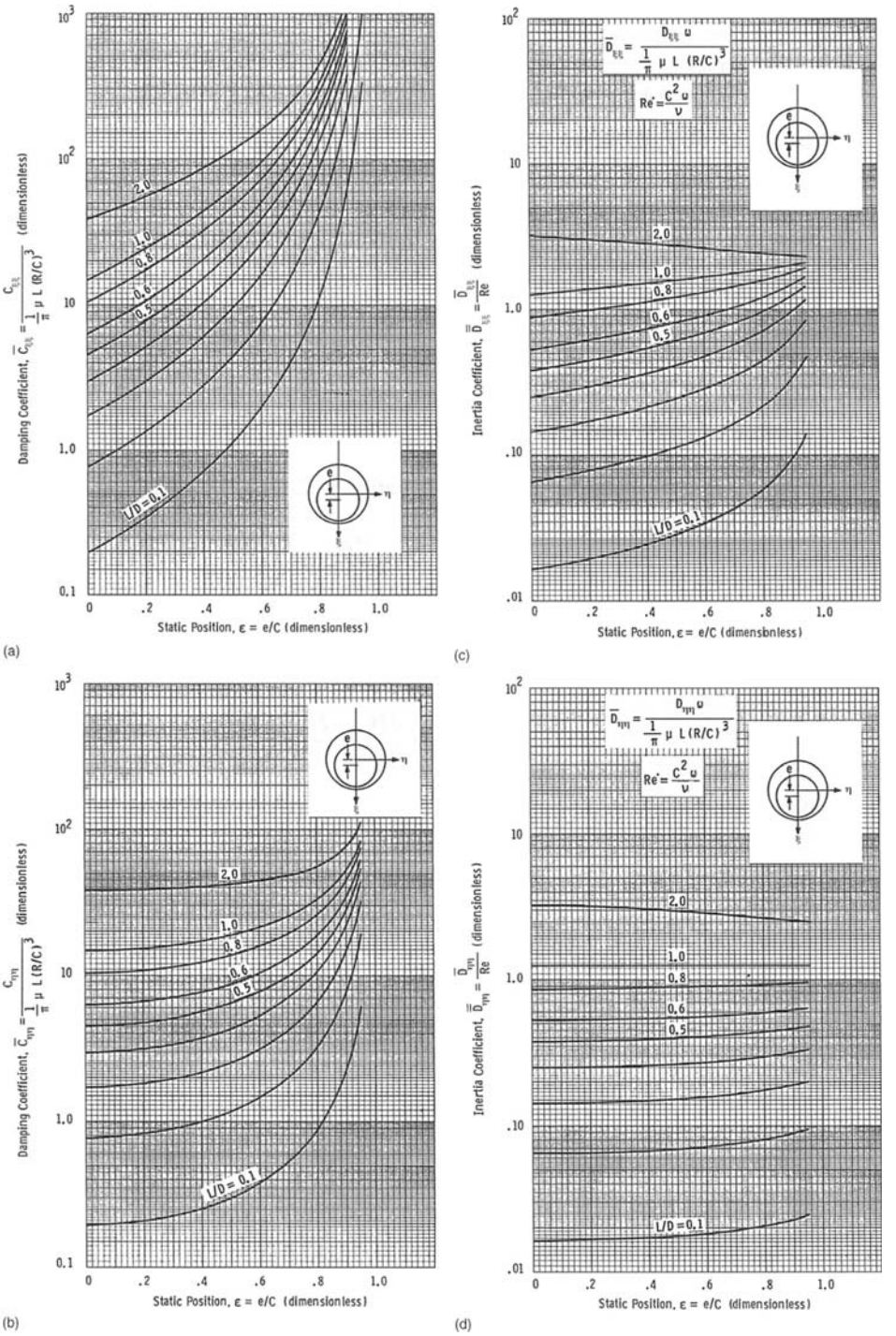

Figure 5.10. Inertia coefficients in presence of cavitation. (Reprinted with permission from Szeri, A. Z., Raimondi, A. A. and Giron-Duarte, A. Linear force coefficients for squeeze-film dampers. *ASME Journal of Lubrication Technology*, **105**, 326–334, 1983).

Table 5.7. *Numerical constants for inertia terms*

	Tichy and Bou-Said (1991) El-Shafei and Crandall (1991)	Szeri et al. (1983)	Trichy and Modest (1980) El-Shafei and Crandall (1991)
k_1	1/12	1/12	1/10
k_2	1/5	1/6	17/70

Szeri et al. (1985). At moderate Re values, San Andres and Vance propose k_1, k_2 between bounds identified in Table 5.7.

5.4 Nomenclature

A_i, B_i, b_i	B-splines
C	radial clearance
$\boldsymbol{C}, \boldsymbol{K}, \boldsymbol{D}$	linearized force coefficient matrices
E	Ekman number
F_R, F_T	radial, tangential force component
H	film thickness, dimensionless
L_y, L_{yz}	characteristic lengths
$L_\alpha,\ L_\beta$	characteristic lengths
$\bar{P}$	average pressure, dimensionless
Q	flow rate
Re, R_Q, r_e	Reynolds numbers
R	radius
U, V, W	velocity components
W	load
S	Sommerfeld number
$\phi,\ \psi$	angular coordinates
ψ	stream function
Ω	characteristic frequency, angular velocity
c	velocity of sound
h	film thickness
p	pressure
t	time
u, v, w	velocity components (Cartesian)
$u_r,\ u_\theta,\ u_z$	velocity components (polar)
$(x,\ y),\ (\xi,\ \eta)$	Cartesian coordinates
$(r,\ \theta,\ z)$	polar coordinates
$(\hat{a},\ \hat{\beta})$	bipolar coordinates
ε	eccentricity ratio
$\rho,\ \zeta$	dimensionless coordinates
$\rho,\ \mu,\ \nu$	density, viscosity, kinematic viscosity
ω	angular velocity
$(\ )_*$	characteristic quantity
$(^-)$	dimensionless quantity

5.5 References

Ashino, I. 1975. Slow motion between eccentric rotating cylinders. *Bulletin, Japan Soc. Mech. Engrs.*, **18**, 280–285.

Ballal, B. and Rivlin, R. S. 1976. Flow of a Newtonian fluid between eccentric rotating cylinders. *Arch. Rational Mech. Anal.*, **62**, 237–274.

Black, H. F. and Walton, M. H. 1974. Theoretical and experimental investigations of a short 360° journal bearing in the transition superlaminar regime. *J. Mech. Eng. Sci.*, **16**, 286–297.

Brennen, C. 1976. On the flow in an annulus surrounding a whirling cylinder. *J. Fluid Mech.*, **75**, 173–191.

Burton, R. A. and Hsu, Y. C. 1974. The incompressible turbulent-thin-film short bearing with inertial effects. *ASME Trans., Ser. F*, **96**, 158–163.

Chen, S. S., Wambsganss, M. W. and Jendrzejczyk, J. 1976. Added mass and damping of a vibrating rod in confined viscous fluids. *ASME J. Appl. Mech.*, **43**, 325–329.

Christie, I., Rajagopal, K. R. and Szeri, A. Z. 1987. Flow of a non-Newtonian fluid between eccentric rotating cylinders. *Intl. J. Eng. Sci.*, **25**, 1029–1047.

Constantinescu, V. N. 1970. On the influence of inertia forces in turbulent and laminar self-acting films. *ASME Journal of Lubrication Technology*, **92**, 473–481.

Constantinescu, V. N. and Galetuse, S. 1982. Operating characteristics of journal bearing in turbulent inertial flow. *ASME Journal of Lubrication Technology*, **104**, 173–179.

Coombs, J. A. and Dowson, D. 1965. An experimental investigation of the effects of lubricant inertia in hydrostatic thrust bearings. *Proc. Inst. Mech. Eng.*, **179**, pt. 3, 96–108.

Dai, R. X., Dong, Q. M. and Szeri, A. Z. 1991. Flow of variable viscosity fluid between eccentric rotating cylinders. *Intl. J. Non-Linear Mech.*, **27**, 367–389.

Dai, R. X., Dong, Q. M. and Szeri, A. Z. 1992. Approximations in hydrodynamic lubrication. *ASME Journal of Tribology*, **114**, 14–25.

de Sampaio, P. A. B. 1991. Galerkin formulation for the incompressible Navier-Stokes equations using equal order interpolation for velocity and pressure. *Internat. J. Numer. Methods Engrg.*, **31**, 1134–1149.

DeBoor, C. 1978. *A Practical Guide to Splines*. Springer-Verlag, New York.

DiPrima, R. C. and Stuart, J. T. 1972a. Non-local effects in the stability of flow between eccentric rotating cylinders. *J. Fluid Mech.*, **54**, 393–415.

DiPrima, R. C. and Stuart, J. T. 1972b. Flow between eccentric rotating cylinders. *ASME Journal of Lubrication Technology*, **94**, 266–274.

El-Shafei, A. and Crandall, S. H. 1991. Fluid inertia forces in squeeze, film dampers in rotating machinery and vehicle dynamics. *ASME DE*, **35**, 219–228.

Fletcher, C. A. J. 1991. *Computational Techniques for Fluid Dynamics*. Springer-Verlag, New York.

Gourley, W. E. 1977. *Laminar flow between closely spaced rotating disks with variable viscosity*. M. Sc. Thesis, University of Pittsburgh.

Grim, R. J. 1976. Squeezing flows of Newtonian films. *App. Sci. Res.*, **32**, 149–166.

Hamza, E. A. 1985. A fluid film squeezed between two rotating parallel plane surfaces. *ASME Journal of Tribology*, **107**, 110–115.

Hashimoto, H. 1994. Viscoelastic squeeze film characteristics with inertia effects between two parallel circular plates under sinusoidal motion. *ASME Journal of Tribology*, **116**, 161–166.

Hughes, T. J. R., Franca, L. P. and Balestra, M. 1986. A new finite element formulation for computation fluid dynamics. *Comput. Methods Appl. Math. Engrg.*, **59**, 85–99.

Jackson, J. D. and Symmons, G. R. 1965. An investigation of laminar radial flow between two parallel disks. *Appl. Sci. Res. Sect. A*, **15**, 59–75.

Jones, A. F. and Wilson, S. D. R. 1974. On the failure of lubrication theory in squeezing flow. *ASME Journal of Lubrication Technology*, **97**, 101–104.

Kamal, M. M. 1966. Separation in the flow between eccentric rotating cylinders. *ASME J. of Basic Engineering*, **88**, 717–724.

Keller, H. B. 1977. Numerical solutions of bifurcation and non-linear eigenvalue problems. In *Applications of Bifurcation Theory*, P. Rabinowitz (ed.). Academic Press, New York.

Kim, E. and Szeri, A. Z. 1997. On the combined effects of lubricant inertia and viscous dissipation in long bearings. *ASME Journal of Tribology*, **119**, 76–84.

Kulinski, E. and Ostratch, S. 1967. Journal bearing velocity profiles for small eccentricity and moderate modified Reynolds number. *ASME J. Appl. Mech.*, **89**, 16–22.

Kuzma, D. 1967. Fluid inertia effects in squeeze films. *App. Sci. Res.*, **18**, 15–20.

Launder, B. E. and Leschziner, M. 1978. Flow in finite-width, thrust bearings including inertial effects, I and II. *ASME Trans., Ser. F*, **100**, 330–345.

Livesey, J. L. 1960. Inertia effects in viscous flows. *Int. J. Mech. Sci.*, **1**, 81–88.

Modest, M. F. and Tichy, J. A. 1978. Squeeze film flow in arbitrarily shaped journal bearings subject to oscillations. *ASME Journal of Lubrication Technology*, **100**, 323–329.

Mulcahy, T. M. 1980. Fluid forces on rods vibrating in finite length annular regions. *ASME J. Appl. Mech.*, **47**, 234–240.

Myllerup, C. M. and Hamrock, B. J. 1994. Perturbation approach to hydrodynamic lubrication theory. *ASME Journal of Tribology*, **116**, 110–118.

Ortega, J. M. and Rheinboldt, W. C. 1970. *Iterative Solution of Non-Linear Equations in Several Variables*. Academic Press, New York.

Osterle, J. F. and Hughes, W. F. 1958. Inertia induced cavitation in hydrostatic thrust bearings. *Wear*, **4**, 228–233.

Osterle, J. F., Chou, Y. T. and Saibel, E. 1975. The effect of lubricant inertia in journal bearing lubrication. *ASME Trans.*, **79**, Ser. F, 494–496.

Ota, T., Yoshikawa, H., Hamasuna, M., Motohashi, T. and Oi, S. 1995. Inertia effects on film rapture in hydrodynamic lubrication. *ASME Journal of Tribology*, **117**, 685–660.

Reinhardt, E. and Lund, J. W. 1975. The influence of fluid inertia on the dynamic properties of journal bearings. *ASME Trans., Ser. F*, **97**, 159–167.

Reynolds, O. 1986. On the theory of lubrication and its application to Mr. Beachamp Tower's experiments. *Phil. Trans. Roy. Soc.*, **177**, 157–234.

Ritchie, G. S. 1968. On the stability of viscous flow between eccentric rotating cylinders. *J. Fluid Mech.*, **32**, 131–144.

Rosenhead, L. 1963. *Laminar Boundary Layers*. Oxford University Press.

San Andres, A. and Szeri, A. Z. 1985. Flow between eccentric rotating cylinders. *ASME J. Appl. Mech.*, **51**, 869–878.

San Andres, A. and Vance, J. 1987. Force coefficients for open-ended squeeze-film dampers, executing small amplitude motions about an off-center equilibrium position. *ASLE Trans.*, **30**, 384–393.

Schlichting, H. 1968. *Boundary Layer Theory*, 6th ed. Pergamon, London.

Sestieri, A. and Piva, R. 1982. The influence of fluid inertia in unsteady lubrication films. *ASME Journal of Lubrication Technology*, **104**, 180–186.

Seydel, R. 1988. *From Equilibrium To Chaos*. Elsevier, New York.

Sood, D. R. and Elrod, H. G. 1974. Numerical solution of the incompressible Navier-Stokes equations in doubly-connected regions. *AIAA J.*, **12**, 636–641.

Szeri, A. Z. and Adams, M. L. 1978. Laminar through flow between closely spaced rotating disks. *J. Fluid Mech.*, **86**, 1–14.

Szeri, A. Z. and Al-Sharif, A. 1995. Flow between finite, steadily rotating eccentric cylinders. *Theoret. Comput. Fluid Dynamics*, **7**, 1–28.

Szeri, A. Z., Raimondi, A. A. and Giron-Duarte, A. 1983. Linear force coefficients for squeeze-film dampers. *ASME Journal of Lubrication Technology*, **105**, 326–334.

Szeri, A. Z., Schneider, S. J., Labbe, F. and Kaufman, H. N. 1983. Flow between rotating disks. Part 1: basic flow. *J. Fluid Mech.*, **134**, 103–131.

Szeri, A. Z. and Snyder, V. 2006. Convective inertia effects in wall-bounded thin film flows. *Meccanica*, **41**, 473–482.

Tichy, J. and Bou-Said, B. 1991. Hydrodynamic lubrication and bearing behavior with impulsive loads. *STLE Tribology Transactions*, **34**, 505–512.

Tichy, J. and Modest, M. 1978. Squeeze film flow between arbitrary two-dimensional surfaces subject to normal oscillations. *ASME Journal of Lubrication Technology*, **100**, 316–322.

Tichy, J. and Winer, W. 1970. Inertial considerations in parallel circular squeeze-film bearings. *ASME Journal of Lubrication Technology*, 588–592.

Von Karman, T. 1921. Über laminare und turbuleute Reibung. *ZAMM*, **1**, 233–252.

Wannier, G. 1950. A contribution to the hydrodynamics of lubrication. *Quart. Appl. Math.*, **8**, 1–32.

Weinbaum, S., Lawrence, C. J. and Kuang, Y. 1985. The inertial drainage of a thin fluid layer between parallel plates with a constant normal force. Part 1. Analytical solutions: inviscid and small but finite-Reynolds-number limits. *J. Fluid Mechanics*, **121**, 315–343.

Wood, W. 1957. The asymptotic expansions at large Reynolds numbers for steady motion between non-coaxial rotating cylinders. *J. Fluid Mech.*, **3**, 159–175.

Yamada, Y. 1968. On the flow between eccentric cylinders when the outer cylinder rotates. *Japan Soc. Mech. Engrs.*, **45**, 455–462.

Yang, S.-M. and Leal, G. 1993. Thin fluid film squeezed with inertia between two parallel plane surfaces. *ASME Journal of Tribology*, **115**, 632–639.

You, H. L. and Lu, S. S. 1987. Inertia effects in hydrodynamic lubrication with film rupture. *ASME Journal of Tribology*, **109**, 86–90.

Zhang, J., Ellis, J. and Roberts, J. B. 1993. Observations on the nonlinear fluid forces in short cylindrical squeeze, film dampers. *ASME Journal of Tribology*, **115**, 692–698.

Zienkiewicz, O. C. and Woo, J. 1991. Incompressibility without tears: how to avoid restrictions of mixed formulation. *Internat. J. Numer. Methods Engrg.*, **32**, 1189–1203.

Flow Stability and Transition

Classical lubrication theory is unable to predict the performance of large bearings accurately, particularly under conditions of heavy load and/or high rotational speed. The reason for this failure of the theory can be traced to two assumptions, (1) laminar flow and (2) constant, uniform viscosity. A third assumption, that of negligible fluid inertia, yields erroneous results only in special cases and, for the most part, can be left intact. The object of this and the next chapters is to investigate the shortcomings of classical theory due to the assumption of laminar flow. The effects of nonuniform viscosity will be discussed in Chapter 9, while Chapter 5 dealt with fluid inertia effects.

It will be shown in Chapter 7, Eq. (7.59), that under isothermal conditions the pressure generated in an infinitely long "turbulent" lubricant film of thickaness h has the same magnitude as the pressure that can be obtained in an otherwise identical "laminar" film of thickness

$$\frac{12}{12 + k_x\,(\mathrm{Re})}h.$$

The turbulence function $k_x(\mathrm{Re}) \geq 0$, thus a change from laminar to turbulent flow at fixed film geometry results in an increase in load capacity (Figure 3.10). The rate of heat generation in the lubricant film also changes on passing from the laminar to the turbulent regime. It is thus essential to know at the design stage in which flow regime will the bearing operate.

> The actual conditions are far more complicated than alluded to in the previous paragraph. As suggested by Figure 9.7, the law governing energy dissipation changes abruptly on changing from the laminar mode of flow, in turbulent flow the rate of energy dissipation can be significantly higher. This higher rate of heat generations may lead to higher lubricant temperature, and, in consequence, to lower lubricant viscosity. Lower viscosity, in its turn, results in a loss of load capacity. There are thus two competing influences in effect; the apparent decrease in film thickness, which increases load capacity, and the decrease in lubricant viscosity, which tends to decrease it. The result of the ensuing competition under particular circumstances can only be predicted by detailed calculations (see Chapter 9).

There are two basic modes of flow in nature: laminar and turbulent. Under certain conditions, the laminar mode of flow is stable while under others, turbulence prevails. The rate of degradation of kinetic energy and the mechanism of diffusion are quite different in these two flow regimes, hence the ability to predict the appropriate flow regime in particular cases is of great technical importance. The process of moving from one flow regime to another is known as transition. In some cases, transition from the basic laminar flow is directly to turbulent flow, e.g., in a cylindrical pipe. In other cases, a sequence of secondary laminar flows separate the basic flow from turbulence, each member of the sequence being distinct from the others and each being stable in its own domain of parameter space. In Couette flow between concentric cylinders, Coles (1965) observed 74 such transitions, each appearing at a certain well-defined and repeatable speed.

Flow transition is preceded by flow instability. Instability of basic laminar flow occurs when a parameter, λ, defined by the ratio of destabilizing force to stabilizing force, reaches a critical value (Rosenhead, 1963). In isothermal flow, instability arises in one of two basic forms:

(1) *Centrifugal instability* occurs in flows with curved streamlines when the (destabilizing) centrifugal force exceeds in magnitude the (stabilizing) viscous force. The relevant parameter is the Taylor number:

$$\lambda \equiv T_a \sim \frac{\text{measure of centrifugal force}}{\text{measure of viscous force}}.$$

The instability is often characterized by a steady secondary laminar flow (Taylor-Görtler vortices).

(2) *Parallel flow instability* is characterized by propagating waves (Tollmien-Schlichting waves). The inertia force is destabilizing and the viscous force is stabilizing in this case, and the parameter is the Reynolds number:

$$\lambda \equiv \text{Re} \sim \frac{\text{measure of inertia force}}{\text{measure of viscous force}}.$$

Instability of this kind occurs in pipe flow and in the boundary layer.

In the following sections, we shall give more precise definition of the concept of stability, then discuss ways how the critical value of the parameter, λ_{CR}, that separates stable from unstable flows, may be calculated.

6.1 Stability

Let $\{\boldsymbol{U}(\boldsymbol{x}, t),\ p(\boldsymbol{x}, t)\}$ and $\{\boldsymbol{u}(\boldsymbol{x}, t),\ p(\boldsymbol{x}, t)\}$ represent the basic laminar flow and a perturbation of this flow, respectively. Furthermore, let

$$\{\hat{\boldsymbol{U}}(\boldsymbol{x}, t),\ \hat{P}(\boldsymbol{x}, t)\} = \{\boldsymbol{U}(\boldsymbol{x}, t) + \boldsymbol{u}(\boldsymbol{x}, t),\ P(\boldsymbol{x}, t) + p(\boldsymbol{x}, t)\} \tag{6.1}$$

represent the perturbed flow.

If, with passage of time, the perturbed flow approaches the basic flow, we say that the basic flow is asymptotically stable. Otherwise, the basic flow is unstable. If the basic flow remains stable irrespective of the initial magnitude of the perturbation, the basic flow is said to be globally stable. If the flow is globally stable and is such that some norm of the perturbation never increases in time, not even instantaneously, the basic flow is said to be globally and monotonically stable.

In some cases, the basic flow is stable only if the initial value of the perturbation is suitably small. We then term the basic flow conditionally stable.

Stability Criteria

To give precise mathematical meaning to the stability criteria of the previous paragraph, define the average kinetic energy per unit mass, $\mathcal{E}(t)$, of the perturbation $\boldsymbol{u}(\boldsymbol{x}, t)$

$$\mathcal{E}(t) = \frac{1}{2V} \int_V |\boldsymbol{u}|^2 dv. \tag{6.2}$$

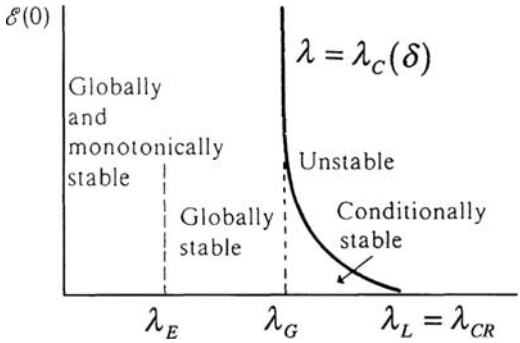

Figure 6.1. Stability limits for the basic flow.

We shall call the basic flow $\{\boldsymbol{U}(\boldsymbol{x}, t),\ P(\boldsymbol{x}, t)\}$ *globally stable* if

$$\lim_{t\to\infty} \frac{\mathcal{E}(t)}{\mathcal{E}(0)} \to 0, \tag{6.3}$$

irrespective of the magnitude of $\mathcal{E}(0)$, the initial value of the kinetic energy of perturbation. The limiting value of the parameter λ for global stability is designated by the symbol λ_G. When $\lambda > \lambda_G$, a perturbation can always be found that destabilizes the basic flow.

We shall call the basic flow *globally and monotonically stable if*, in addition to Eq. (6.3), we also have

$$\lim_{t\to\infty} \frac{d\mathcal{E}(t)}{dt} < 0 \quad \text{for all } t > 0. \tag{6.4}$$

The greatest lower bound for global and monotonic stability, designated by λ_E and called the energy stability limit, represents a *sufficient condition for stability*: no matter how strong the perturbation may be, if $\lambda < \lambda_E$ the perturbation will die out monotonically. λ_E is called the energy stability limit because it is calculated by the energy method. If the basic flow is globally stable but not monotonically stable, a perturbation can always be found, the kinetic energy of which will initially increase with time before decaying to zero.

The flow is *conditionally stable* if

$$\lim_{t\to\infty} \frac{\mathcal{E}(t)}{\mathcal{E}(0)} \to 0, \quad \text{whenever } \mathcal{E}(0) < \delta. \tag{6.5}$$

δ is called the attracting radius of the stable flow. For global or unconditional stability $\delta \to \infty$. The linear limit of the parameter $\lambda = \lambda_L$ is defined by $\delta \to 0$. If $\lambda > \lambda_L$, the flow will be unstable, no matter how weak the perturbation may be. Therefore, the linear limit λ_L, so called because it is calculated from linear equations, represents a *sufficient condition for instability*.

It can be shown (Joseph, 1976) that $\lambda_L \geq \lambda_E$. In cases when these two stability limits coincide (e.g., in Bénard convection) an infinitesimal perturbation is just as dangerous as any finite perturbation. In other cases, the basic flow might be stable to infinitesimal disturbances but is unstable to finite disturbances. Pipe flow, by keeping out finite disturbances, can be kept laminar past Re = 100,000, yet, under ordinary circumstances, laminar flow is guaranteed only up to Re = 2,000 (Hinze, 1987). Figure 6.1, after Joseph (1976), is a schematic displaying the various stability regimes and defining criteria.

Stability Analysis

To derive the equations that govern stability of the basic flow, consider a closed container of volume, $\mathcal{V}(t)$, and surface, $\mathcal{S}(t)$, completely filled with a viscous fluid. The fluid is brought into motion by external forces or by the motion of the boundary. The velocity and pressure of this motion, denoted by $\{\boldsymbol{U}, P\}$ is governed by the Navier-Stokes (2.54) and continuity (2.16) equations and appropriate boundary and initial conditions. In nondimensional form, we have

$$\frac{\partial \boldsymbol{U}}{\partial t} + \boldsymbol{U} \cdot \nabla \boldsymbol{U} - \frac{1}{\mathrm{Re}} \nabla^2 \boldsymbol{U} + \nabla P - \boldsymbol{f} = 0, \tag{6.6a}$$

$$\operatorname{div} \boldsymbol{U} = 0, \tag{6.6b}$$

$$\begin{aligned} &\text{B.C.: } U(\boldsymbol{x}, t) = U_s(\boldsymbol{x}, t), && \boldsymbol{x} \in \mathcal{S}(t), \quad t \geq 0, \\ &\text{I.C.: } U(\boldsymbol{x}, 0) = U_0(\boldsymbol{x}), \qquad \operatorname{div} U_0 = 0, && \boldsymbol{x} \in \mathcal{V}(0). \end{aligned} \tag{6.6c}$$

Consider another motion of the fluid, defined by $\{\hat{\boldsymbol{U}}, \hat{P}\} = \{\boldsymbol{U} + \boldsymbol{u}, P + p\}$, that is obtained by perturbing the initial condition $\boldsymbol{U}_0$ to $\hat{\boldsymbol{U}}_0 = \boldsymbol{U}_0 + \boldsymbol{u}_0$. The perturbed flow $\hat{\boldsymbol{U}}$ satisfies the same boundary conditions as the basic flow $\boldsymbol{U}$; it is also governed by the Navier-Stokes and continuity equations

$$\frac{\partial \hat{\boldsymbol{U}}}{\partial t} + \hat{\boldsymbol{U}} \cdot \nabla \hat{\boldsymbol{U}} - \frac{1}{\mathrm{Re}} \nabla^2 \hat{\boldsymbol{U}} + \nabla \hat{P} - \boldsymbol{f} = 0, \tag{6.7a}$$

$$\operatorname{div} \hat{\boldsymbol{U}} = 0. \tag{6.7b}$$

The evolution equation of the perturbation $\boldsymbol{u}$ is obtained by subtracting Eq. (6.6) from Eq. (6.7)

$$\frac{\partial \boldsymbol{u}}{\partial t} + \boldsymbol{U} \cdot \nabla \boldsymbol{u} + \boldsymbol{u} \cdot \nabla \boldsymbol{U} + \boldsymbol{u} \cdot \nabla \boldsymbol{u} - \frac{1}{\mathrm{Re}} \nabla^2 \boldsymbol{u} + \nabla p = 0, \tag{6.8a}$$

$$\operatorname{div} \boldsymbol{u} = 0, \qquad \boldsymbol{u}|_{\mathcal{S}} = 0, \tag{6.8b}$$

$$\boldsymbol{u}|_{t=0} = \boldsymbol{u}_0(\boldsymbol{x}), \quad \operatorname{div} \boldsymbol{u}_0 = 0. \tag{6.8c}$$

We are assured by the uniqueness property of the Navier-Stokes problem (Joseph, 1972) that the null solution $\boldsymbol{u}(\boldsymbol{x}, t), \equiv 0$ is the only possible solution to Eq. (6.8) for zero initial perturbation $\boldsymbol{u}_0 \equiv 0$. But what if $\boldsymbol{u}_0 \not\equiv 0$? Will the perturbation vanish (stability) or will it increase (instability) in time?

The problem specified by Eq. (6.8) is a nonlinear initial boundary value problem. Though it does not lend itself to easy solution, it has been solved numerically in various cases, in particular for flow between concentric cylinders by Marcus (1984a,b). Such solutions trace the evolution in time of the initial perturbation $\boldsymbol{u}_0$.

We may also use Eq. (6.8) to calculate the energy limit of stability $\lambda_E \equiv \mathrm{Re}_E$, to do this we first transform it into the evolution equation for the kinetic energy $\mathcal{E}(t)$ of the perturbation.

Energy Stability

To obtain the evolution equation for $\mathcal{E}(t)$, first form the scalar product of Eq. (6.8a) with the velocity and integrate the result over the volume $V(t)$. Application of the Reynolds Transport Theorem[1] and the boundary condition $\boldsymbol{u}|_{\mathcal{S}} = 0$ leads to (Joseph, 1 1976)

$$\frac{d\mathcal{E}}{dt} = \mathcal{J} - \frac{1}{\mathrm{Re}}\mathcal{D} = -\mathcal{D}\left(\frac{1}{\mathrm{Re}} - \frac{\mathcal{J}}{\mathcal{D}}\right). \tag{6.9a}$$

Here

$$\mathcal{J} = -\int_{\mathcal{V}} \boldsymbol{u}\cdot\nabla\boldsymbol{U}\cdot\boldsymbol{u}\,d\mathcal{V} \tag{6.9b}$$

is the production of kinetic energy of perturbation, and

$$\mathcal{D} = \int_{\mathcal{V}} |\nabla\boldsymbol{u}|^2 d\mathcal{V} \tag{6.9c}$$

is its dissipation. Designating the maximum value[2] of the ratio $\mathcal{J}/\mathcal{D}$ in Eq. (6.9) by $1/\mathrm{Re}_E$

$$\frac{1}{\mathrm{Re}_E} = \max\left(\frac{\mathcal{J}}{\mathcal{D}}\right), \tag{6.10}$$

Eq. (6.9a) can be written in the form

$$\begin{aligned}\frac{d\mathcal{E}}{dt} &= -\mathcal{D}\left(\frac{1}{\mathrm{Re}} - \frac{1}{\mathrm{Re}_E} + \frac{1}{\mathrm{Re}_E} - \frac{\mathcal{J}}{\mathcal{D}}\right)\\ &\le -\mathcal{D}\left(\frac{1}{\mathrm{Re}} - \frac{1}{\mathrm{Re}_E}\right),\end{aligned} \tag{6.11}$$

as

$$\frac{1}{\mathrm{Re}_E} - \frac{\mathcal{J}}{\mathcal{D}} \ge 0.$$

Equation (6.11) shows that the flow is monotonically stable, Eq. (6.4), i.e., $d\mathcal{E}/dt \le 0$, if $\mathrm{Re} < \mathrm{Re}_E$.

The energy stability limit Re_E can be calculated from Eq. (6.10) for given basic flow $\boldsymbol{U}$ by the following scheme: (1) for every admissible perturbation[3] $\boldsymbol{u}$, calculate $\mathcal{J}$ from Eq. (6.9b) and $\mathcal{D}$ from Eq. (6.9c); (2) the particular perturbation that gives the largest value for the ratio $\mathcal{J}/\mathcal{D}$ is the critical perturbation, and this $\mathcal{J}/\mathcal{D}$ ratio is the inverse of the energy stability limit.

Rather than arbitrarily choosing perturbations in search of the critical one, as was done by Orr (1907), we find it more effective to pose Eq. (6.10) as a problem in the calculus of variations and to calculate Re_E from a linear eigenvalue problem (Joseph, 1976). The

[1] The Reynolds Transport Theorem (Serrin, 1959a; White, 1991) is concerned with finding the time rate of change of the total property associated with a material volume $\mathcal{V}(t)$, Eq. (2.10).

[2] That the maximum exists in bounded regions follows from the Poincaré inequality (Joseph, 1976). The derivation is not valid when the region is unbounded, though a justification is available for infinite regions whenever the disturbances can be assumed spatially periodic at each time instant (Serrin, 1959b).

[3] A perturbation is admissible if it is divergence free and satisfies no-slip boundary conditions, Eq. (6.8c).

energy stability limit for concentric, rotating cylinders (unloaded journal bearings) was first calculated by Serrin (1959b), but in this case, unlike that of Bénard convection, the linear limit and the energy limit are widely separated. Thus Re_E does not have practical significance for us in cylinder flows.

Linear Stability

There is another way we can make use of Eq. (6.8) for steady U. By assuming the perturbation $\boldsymbol{u}(x, t)$ to be infinitesimal, we may neglect the quadratic term $\boldsymbol{u} \cdot \nabla \boldsymbol{u}$ and obtain

$$\frac{\partial \boldsymbol{u}}{\partial t} + U \cdot \nabla \boldsymbol{u} + \boldsymbol{u} \cdot \nabla U - \frac{1}{\mathrm{Re}} \nabla^2 \boldsymbol{u} + \nabla p = 0. \tag{6.12}$$

As this equation is linear (the basic flow $\boldsymbol{U}$ is known), one can exploit superposition, i.e., solve Eq. (6.12) for each (Fourier) component of the perturbation (Chandrasekhar, 1961).

Equation (6.12) loses validity once the initially infinitesimal perturbation has grown too large, but for short times it will trace the evolution of the originally infinitesimal $\boldsymbol{u}(\boldsymbol{x}, t)$. As it contains time only through the first derivative, we look for solutions with an exponential time factor

$$\boldsymbol{u}(\boldsymbol{x}, t) = \boldsymbol{v}(\boldsymbol{x}) e^{-ict}, \qquad p(\boldsymbol{x}, t) = \pi(\boldsymbol{x}) e^{-ict}. \tag{6.13}$$

By substituting Eq. (6.13) into Eq. (6.12), we find that solutions of the type Eq. (6.13) exist, provided there are numbers, c, for which the problem

$$-ic\boldsymbol{v} + \boldsymbol{U} \cdot \nabla \boldsymbol{v} + \boldsymbol{v} \cdot \nabla \boldsymbol{U} - \frac{1}{\mathrm{Re}} \nabla^2 \boldsymbol{v} + \nabla \pi = 0 \tag{6.14}$$

has nontrivial solutions. The particular numbers, c, for which Eq. (6.14) is amenable to solution, are the eigenvalues, and the corresponding solutions, $\boldsymbol{v}(\boldsymbol{x})$, are the eigenfunctions.

Each of the infinity of eigenvalues is, in general, complex $c = c_r + ic_i$, and we write

$$e^{-ict} = e^{c_i t} (\cos c_r t - i \sin c_r t). \tag{6.15}$$

We call c_i the amplification factor. If $c_i < 0$ for all c, the disturbance will decay in time and the flow is stable.[4] If, on the other hand, $c_i > 0$ for at least one c, the disturbance will grow in time and the flow is unstable.[5] Neutral stability is characterized by $c_i = 0$ for the leading eigenvalue, while all other eigenvalues have negative imaginary parts; the lowest value of the Reynolds number at which this occurs is the linear limit of stability, indicated here by $R_{CR} \equiv (\mathrm{Re})_L$ and referred to simply as the critical Reynolds number.

The term $(\cos c_r t - \boldsymbol{i} \sin c_r t)$ in Eq. (6.15) represents a motion that is periodic in time, with period c_r. There are two ways in which neutral stability, $c_i = 0$, might be achieved. For certain basic flows, $c_r \neq 0$ at neutral stability, thus neutral stability is characterized by a time-periodic secondary (laminar) flow. If $c_r = 0$ when $c_i = 0$, the secondary (laminar) flow

[4] This is conditional stability, under the condition that initially the perturbation is infinitesimal. The flow might or might not be stable yet to finite disturbances.

[5] This is a sufficient condition for instability; if the flow is unstable to infinitesimal disturbance, it will certainly be unstable to finite disturbances.

appearing in the neutral stability state is steady, and we say that the basic flow exchanges its stability with (or transfers it to) the bifurcating flow (Chandrasekhar, 1960; Joseph, 1976). Which of these cases occurs in practice depends, of course, on the basic flow field $\{\boldsymbol{U}, P\}$.

Taylor (1923) was the first to employ linear stability analysis in the study of flow between concentric cylinders, though the method had been applied half a century earlier to other flows (Kelvin, 1871). Flow between eccentric cylinders was investigated by DiPrima and Stuart (1972, 1975) among others. Cylinder flows will be discussed in detail in later sections.

Bifurcation Analysis

We saw in the previous section that the conditions for neutral stability signal the appearance of a new solution, $\boldsymbol{v}(\boldsymbol{x})e^{-ict}$. This *bifurcating solution* might be steady or it might be unsteady, depending on whether $c_i = c_r = 0$ or $c_i = 0$, $c_r \neq 0$, respectively, at criticality.

For Re slightly larger than Re_{CR}, the bifurcating solution will grow exponentially, Eq. (6.13), the growth being dictated by the amplification factor, c_i. In some cases, this exponential growth remains unchecked, and we conclude that the bifurcating solution is unstable. In other cases, however, the perturbation will interact with the basic flow, modifying the rate of energy transfer, Eq. (6.9b), from basic flow to perturbation, so as to arrive at an equilibrium state. The equilibrated bifurcating flow is stable in the neighborhood of the critical point $\mathrm{Re} = \mathrm{Re}_{CR}$. Bifurcation analysis is concerned with stable bifurcating solutions (Iooss and Joseph, 1982).

Bifurcating solutions emanate from the basic flow at so-called *singular points* where the Jacobian matrix $(\partial \boldsymbol{v}/\partial \boldsymbol{x})$ becomes singular (Seydel, 1988) – in fact, we locate such solutions by finding points on the solution curve where the Jacobian determinant vanishes. The Lyapunov conditional stability theorem (Joseph, 1976) tells us that the first bifurcation point found when increasing Re is identical to the linear limit of stability, Re_{CR}. In this sense, bifurcation analysis, which locates the first critical point of the basic flow, and linear stability analysis, which calculates the linear stability limit, are equivalent.

Where bifurcation analysis has the advantage over linear stability analysis is that while the latter is valid only within an infinitesimal neighborhood of the critical point, bifurcation analysis permits the tracing of solution branches far away from critical points, as it employs the full Navier-Stokes and continuity equations. At the bifurcating point, we can switch to the new branch and continue the solution well into the supercritical, i.e., $\mathrm{Re} > \mathrm{Re}_{CR}$, range.

Bifurcating solutions that exist for values of $\mathrm{Re} < \mathrm{Re}_{CR}$ are called *subcritical*; those which exist for values of $\mathrm{Re} > \mathrm{Re}_{CR}$ are termed *supercritical* (Figure 6.2). It can be shown that subcritical bifurcating solutions are unstable and supercritical bifurcating solutions are stable (Iooss and Joseph, 1982).

We will illustrate two methods of calculating R_{CR} in the sequel. Bifurcation analysis will be employed to calculate the critical Reynolds number for eccentric rotating cylinders, while linear stability analysis will be used to study flow between rotating disks. Rotating disks are important in the computer industry. Rotating disk flows can also serve as approximation to flows in annular thrust bearings. Eccentric cylinder flows, on the other hand, are closely related to flow in journal bearings.

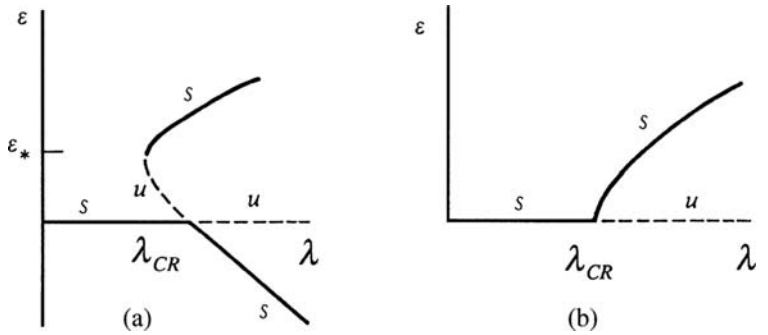

Figure 6.2. Simple bifurcating solutions: (a) subcritical, (b) supercritical bifurcation. The solid lines represent stable solutions, *s*, the dotted lines represent unstable solutions, *u*.

6.2 Flow between Concentric Cylinders

Centrifugal instability was first studied by Couette and by Lord Rayleigh. On the basis of energy considerations, Rayleigh derived a criterion of stability for inviscid fluids, viz., that if the square of the circulation increases outward, the flow is stable. An explanation of Rayleigh's criterion in terms of the centrifugal force field and pressure gradient was later given by von Karman (Lin, 1967).

To illustrate the argument constructed by von Karman, we consider a fluid ring located at $r = r_1$ and concentric with the axis of rotation. In steady state, the centrifugal force, $\rho \boldsymbol{v}_1^2/r_1$, on the element of the ring must be balanced by pressure forces; this serves us in estimating the steady-state pressure field. Consider now displacing the ring to $r = r_2$. The angular momentum (rv) will be conserved during this displacement in accordance with Kelvin's theorem,[6] so in its new surrounding the centrifugal force acting on the ring is given by

$$\rho \frac{v^2}{r} = \rho \frac{(r_1 v_1)^2}{r_2} \frac{1}{r_2} = \rho \frac{(r_1 v_1)^2}{r_2^3}.$$

Because at $r = r_2$ the prevailing pressure force equals $\rho v_2^2/r_2$, the fluid ring will continue in its motion outward, provided that

$$\rho \frac{(r_1 v_1)^2}{r_2^3} > \rho \frac{v_2^2}{r_2}.$$

This simplifies to the Rayleigh stability criterion: In the absence of viscosity a necessary and sufficient condition for a distribution of angular velocity to be stable is that

$$\frac{d}{dr}(r^2\omega)^2 > 0 \tag{6.16}$$

everywhere in the interval.

When applied to flow between concentric cylinders, Rayleigh's criterion means that the flow is potentially unstable if the inner cylinder is rotating and the outer cylinder is

[6] Kelvin's circulation theorem states that in an inviscid fluid the angular momentum per unit mass of a fluid element (rv) remains constant [note that $\Gamma = 2\pi rv$ is the circulation round the circle $r = \text{const.}$ (Milne-Thomson, 1968)].

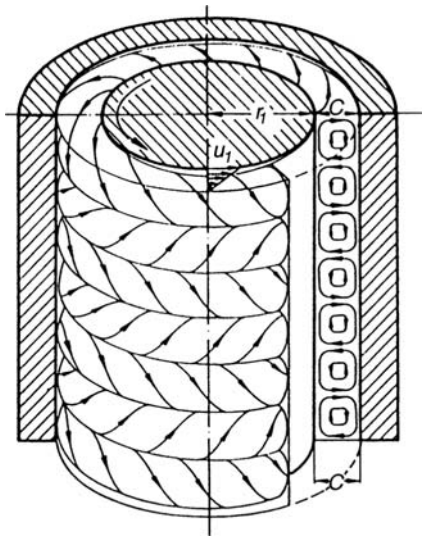

Figure 6.3. Taylor vortices between concentric cylinders, with the inner cylinder rotating and the outer cylinder stationary. (Reprinted with permission from Schlichting, H. *Boundary Layer Theory* 6th ed. Pergamon, London. Copyright 1968.)

stationary, but it is not susceptible to instability of the centrifugal type if the inner cylinder is at rest and the outer cylinder is rotating.[7] However, the flow in the latter case does become unstable at higher rotation (Coles, 1965), the shear flow instability occurring at Re $\sim$ 2,000.

When the inner cylinder of radius r_1 is rotated at the angular speed ω and the outer cylinder of radius r_2, $r_2 = r_1 + C$, $C > 0$ is kept stationary, the circumferential velocity (the only nonzero velocity component for long cylinders) is given by

$$v(r) = \frac{r_1^2 \omega}{r_2^2 - r_1^2}\left[\frac{r_2^2}{r} - r\right]. \tag{6.17}$$

On increasing the rate of rotation, this flow becomes unstable. Taylor (1923) showed that, when instability occurs, the disturbance assumes the form of cellular, toroidal vortices that are equally spaced along the axis of the cylinder (Figure 6.3). The appearance of this so-called *Taylor vortex flow* has a strong influence on the magnitude of the torque required to rotate the inner cylinder. The stability parameter of the problem is the Taylor number, which is proportional to the ratio of the centrifugal force to the viscous force. The definition we use is that of Drazin and Reid (1984) for the "average" Taylor number:

$$T = \frac{2(1-\eta)}{(1+\eta)}\mathrm{Re}^2, \quad \mathrm{Re} = \frac{r_1 \omega C}{v}, \quad \eta = \frac{r_1}{r_2} < 1,$$

where Re is the Reynolds number.

By assuming that the neutral (marginal) state of stability is stationary and that the radial clearance C is small[8] when compared to the radius r_1, Taylor was able to calculate the first

[7] Synge (Lin, 1967) showed Rayleigh's criterion to be sufficient for viscous fluids.

[8] The formula $T^{1/2} = (C/r_1)^{1/2}$ Re, valid for $\eta \to 1$, follows from the approximation $(1-\eta)/(1+\eta) \approx C/2r_1$.

critical value of T. The currently accepted minimum value of the critical Taylor number, T_{CR} is (Drazin and Reid, 1984)

$$T_{CR} = 1694.95, \qquad \mathrm{Re}_{CR} = 41.2\left(\frac{r_1}{C}\right)^{1/2}. \tag{6.18}$$

This is within 1% of the value calculated by Taylor in 1923.

As the Taylor number is increased above its critical value, the axisymmetric Taylor vortices become unstable to nonaxisymmetric disturbances. Pairs of vortex cells that are symmetrical, $T = T_{CR}$, now become distorted (Mobbs and Younes, 1974). The boundaries between adjacent vortex cells assume a wavy form, with the waves traveling azimuthally at the average velocity of the basic Couette flow (Coles, 1965). The number of azimuthal waves increases on further increasing the Taylor number, until turbulence eventually makes its appearance. Concentric cylinder flows are discussed in detail by Koshmieder (1993). More recent numerical work on concentric cylinder flows was reported by Deng (2006), and by Deng and Braun (2007). They applied the three dimensional Navier-Stokes based code CFD-ACE+ to simulate the flow of the fluid. The multiplicity of stable and unstable solutions and the transition among these solutions were investigated and it was concluded that pressure played a significant role in the formation and merging of the Taylor cells in the axial direction and the waves in the circumferential direction.

Nonuniqueness of the flow was first demonstrated by Coles (1965), who documented as many as 26 distinct time-dependent states at a given Reynolds number. Coles found the different states by approaching the final Reynolds number along different paths in parameter space. Earlier, Landau and Lifshitz (1959) suggested that transition to turbulence may occur as an infinite sequence of supercritical bifurcations, each contributing a new degree of freedom to the motion. Although attractive, this conjecture had to be abandoned in light of theoretical (Ruelle and Takens, 1971; Newhouse, Ruelle, and Takens, 1978) and experimental (Gollub and Swinney, 1975; Gollub and Benson, 1980) research, which indicates that chaotic behavior occurs after a small number of transitions.

The value of the critical Taylor number depends on the clearance ratio C/r_1 (Coles, 1965) but not on the aspect ratio L/C (Cole, 1976), where L is the length of the cylinders. Only the Taylor number for the appearance for waviness is strongly dependent on L/C. Cole observed formation of a single counterrotating vortex pair in an open-ended annulus of length $L = 5C$. Schwartz et al. (1964) found that a superimposed axial flow has a stabilizing influence. The sole effect of slow axial flow is to translate the Taylor cells axially, but with higher axial flow the cell pattern assumes a spiral form. DiPrima (1960) also showed that superimposed axial flow has a stabilizing influence.

Couette flow is not a solution of the finite length problem. The presence of endplates, located a distance L apart, will force all three velocity components to vary with position. A corkscrew motion with axial structure, known as Ekman pumping, emerges even at small values of the Reynolds number. The experimental observations of Benjamin and Mullin (1981, 1982), performed in an apparatus having a relatively small aspect ratio, $\Gamma = L/C$, indicate at higher Reynolds numbers the existence of a number of distinct steady flows that are supported by identical boundary conditions. More importantly, these experiments reveal "an essentially continuous process: namely as Re is gradually raised through a narrow quasi-critical range, arrays of axisymmetric, counter-rotating cells spread from the end and finally link-up and become ordered prominently at the center of the Taylor apparatus" (Benjamin and Mullin, 1982).

Benjamin and Mullin (1982) experimented with a Taylor apparatus of $\eta = 0.6$ and $\Gamma = 12.6$ and found that the "primary" cellular flow, reached by gradual increases in Re,

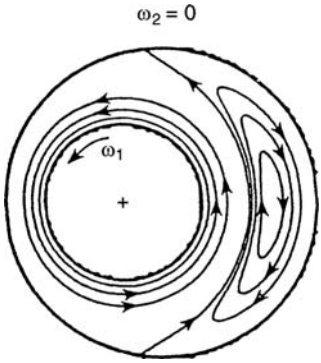

Figure 6.4. Subcritical Couette flow with recirculation. (Reprinted with permission from San Andres, A. and Szeri, A. Z. Flow between eccentric rotating cylinders. *ASME J. Appl. Mech.*, **51**, 869–878, 1984.)

was comprised of 12 cells. This primary flow was stable for a range of Reynolds number values below the threshold for the onset of traveling waves. Benjamin and Mullin also found flows other than the primary flow: "normal" flows, exhibiting both inward flow at the stationary endplates and an even number of cells, and "anomalous" flows comprising an odd number of cells and/or exhibiting anomalous rotation. They observed a total of 20 different flows, and, by applying degree theory, Benjamin (1978) predicted that the problem has at least 39 solutions, 19 of which are unstable.[9]

Theoretical analyses of infinite cylinder flows at slightly supercritical Reynolds numbers show a continuum of periodic solutions of wavelength λ, which are possibly stable when λ is located within some interval $(\lambda_c^-, \lambda_c^+)$ centered around the critical value, λ_c, for strict bifurcation of the Couette flow. Estimates for this λ interval were first made by Chandrasekhar (1961) and Kogelman and DiPrima (1976), and were subsequently improved by Nakaya (1975). The experiments of Burkhalter and Koschmieder (1977a) are not in contradiction with this theory, once the part of the flow that seems to be "directly, influenced" by the endplates is neglected, and the observed wavelengths fall within the narrowest of the three $(\lambda_c^-, \lambda_c^+)$ intervals. It has been suggested (Benjamin and Mullin, 1982) that this "continuum" of cellular flows of the infinite geometry is the result of taking the limit $\Gamma \to \infty$, thereby increasing the multiplicity of steady flows, each of which represents the primary flow of its particular Γ interval.[10]

6.3 Flow between Eccentric Cylinders

For $R < R_{CR}$ and $\varepsilon < 0.3$, the flow is a Couette flow. On increasing the eccentricity ratio above $\varepsilon \approx 0.3$, a recirculation cell makes its appearance (Kamal, 1966), this flow being stable up to $\mathrm{Re} < \mathrm{Re}_{CR}$. Such a recirculating flow pattern is shown in Figure 6.4 for Stokes flow at $\eta = 0.5$ and $\varepsilon = 0.5$.

On further increasing the Reynolds number past its critical value, $\mathrm{Re} = \mathrm{Re}_{CR}$, the two-dimensional basic laminar flow loses its stability to a new flow with three-dimensional structure, similar to the case of concentric cylinders (Dai, Dong, and Szeri, 1992). Wilcock (1950) and Smith and Fuller (1956) were the first to recognize that flow transition also takes

[9]The Leray-Schauder degree theory is concerned with the topology of certain Banach-space mappings. In its application to fluid mechanics, the theory ascertains that, at any value of the parameter, the number of stable solution branches exceeds the number of unstable branches by one.

[10]Dai and Szeri (1990) were able to follow a branch comprised of 28 normal cells, and another branch of 30 anomalous cells, to $\Gamma = 200$. Note, that $\Gamma = 500$ for a short bearing of $L/D = 0.1$ and $r_1/C = 500$.

place between eccentric cylinders. Analytically, the problem was first treated by DiPrima (1963). DiPrima's local theory shows the flow to be least stable at the position of maximum film thickness, along a vector extending from the center of the inner cylinder to the center of the outer cylinder. The critical Taylor number, T_{CR}, calculated at this position first decreases as the eccentricity ratio, $\varepsilon = e/C$ (where e is the eccentricity of the cylinders), increases from zero and remains below its concentric value in the range $0 < \varepsilon < 0.6$. For $\varepsilon > 0.6$, T_{CR} increases rapidly with increasing ε. This finding is, however, not in agreement with experimental results. Experimental data (e.g., Vohr, 1968) indicate that the eccentricity has a stabilizing effect over its whole range. Vohr also finds the maximum intensity of vortex motion not at the point of maximum film thickness, as predicted by local theory, but at the 50° position downstream from it.

DiPrima's local theory is based on the parallel flow assumption, i.e., on neglecting the effect of the azimuthal variation of the tangential velocity, and is no longer thought to represent the physics of the problem. In a second attempt to explain the dependence of T_{CR} on ε, DiPrima and Stuart (1972) examined the whole flow field (nonlocal theory), considering the tangential velocity to be a function of both r and θ. The most dramatic result of the newer theory is that it no longer places maximum vortex intensity at the position of maximum instability but rather at 90° downstream of it. This theory also shows $T_{CR}(\varepsilon)$ to be a monotonically increasing function, described by

$$T_{CR} = 1695\left(1 + 1.162\frac{C}{r_1}\right)(1 + 2.624\varepsilon^2). \tag{6.19}$$

Agreement with experiment is acceptable, however, only in the range $0 < \varepsilon < 0.3$. In a more recent nonlinear theory, DiPrima and Stuart (1975) found that the position of maximum vortex activity is at $\Theta_{\max} \to 90°$ only if the supercritical Taylor number vanished and $\Theta_{\max} \to 0°$ as $T_{SC} \to \infty$. [The supercritical Taylor number is defined as $T_{SC} = (T - T_{CR})/\varepsilon$.] Although they found agreement in one specific case with Vohr's observation of $\Theta_{\max} = 50°$ for maximum vortex activity, they raised the question of the applicability of their small perturbation solution under Vohr's experimental conditions.

Castle and Mobbs (1968) found two kinds of instabilities of flow between eccentric cylinders. The type of cellular flow that occurs at low speeds does not extend all the way to the stationary (outer) cylinder, while the second type of instability occurs at higher rotational speeds and exhibits vortices that straddle the clearance gap completely. According to Mobbs and Younes (1974), it is the latter group of vortices that are usually detected by experiments, as their existence is revealed by torque measurements on the stationary cylinder. The first, lower mode of instability lies close to that predicted by the local theories of Ritchie (1968) and DiPrima (1963). According to DiPrima and Stuart (1972), "it seems possible, therefore, that this incipient mode may be a manifestation of local instabilities." But they also admit the possibility that the slower mode represents another instability that cannot be accounted for by the nonlocal theory. The slower incipient mode was also detected by Versteegen and Jankowski (1969) and by and Frêne and Godet (1974). Koschmieder (1976), on the other hand, was unable to find instability of the first kind in his apparatus, nor could he detect maximal vortex action downstream from the position of maximum gap width. Nevertheless, he found $T_{CR}(\varepsilon)$ to be a monotonic increasing function, somewhat as predicted by nonlocal theories. It seems that the nonlocal theory correlates better with instability of the second type, while instability of the first type is predicted by local theories (Figure 6.4).

Li (1977) investigated the onset of instability in nonisothermal flows between rotating cylinders and found that a positive radial temperature gradient, as might exist in journal

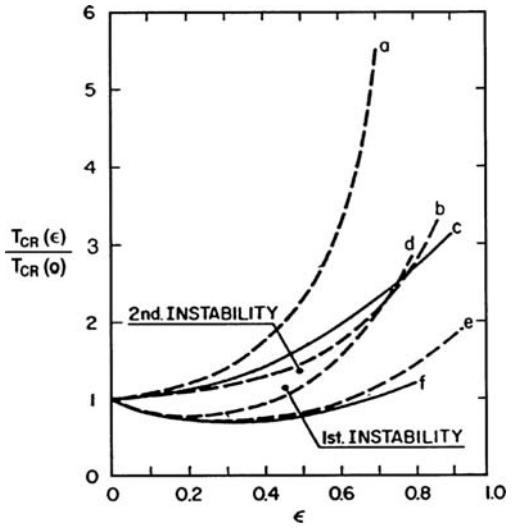

Figure 6.5. Effect of eccentricity ratio on critical speed for instability. (–) theory, (– –) experiment, (a) Castle and Mobbs (1968), (b) Vohr (1968), (c) DiPrima and Stuart (1972), (d) Castle and Mobbs (1968), (e) Frêne and Godet (1974), and (f) DiPrima (1963).

bearings, is strongly destabilizing, particularly at high Prandtl numbers. Li also suggested that under certain conditions the neutral (marginal) stability is oscillatory. Li's conclusion that a positive temperature gradient is destabilizing seems to be verified by the experiments of Gardner and Ulschmid (1980).[11]

Though there have been numerous calculations of concentric cylinder flows [Weinstein, 1977a,b; Frank and Meyer-Spasche, 1981; Marcus, 1984a,b; Cliff et al., 1985, 1986; Meyer-Spasche and Keller 1978 and 1980], the numerical treatment of eccentric cylinder flows has been hindered in the past by two circumstances: (1) the partial differential equations that model the basic flow contain the Reynolds number and the eccentricity ratio as parameters and numerical solutions are difficult to obtain at large values of these parameters and (2) classical stability analysis leads to an eigenvalue problem for partial, rather than for ordinary, differential equations, increasing numerical complexity considerably. Nevertheless a linear stability analysis has been published recently by Oikawa, Karasndani, and Funakoshni (1989a,b), who use Chebyshev-Fourier expansion and the pseudo-spectral method (Gottlieb and Orszag, 1977).

In the next section, we investigate the effect of cylinder eccentricity on Couette-Taylor transition between infinite rotating cylinders, using bifurcation analysis. To do this, we employ Galerkin's method with B-spline basis functions to the system of equations that govern the motion of the fluid and locate critical points by detecting the vanishing of the Jacobian determinant during parametric continuation. The first bifurcation from Couette flow provides us with the linear stability limit (Joseph, 1976). At the bifurcation point, we switch to the new branch by locating its tangent in parameter space and continue the

[11] According to their data (Figure 9.9), turbulence must have set in at value $\mathrm{Re} = 1{,}100$ of the global Reynolds number, $\mathrm{Re} = R\omega C/\nu$. The value of the local Reynolds number $\mathrm{Re}_h = R\omega h/\nu$ is even smaller at transition to turbulence; it is in the range $360 < \mathrm{Re}_h < 560$.

solution into the supercritical range; this allows investigation of the bifurcating flow and calculation of the torque which the bifurcating flow exerts on the cylinders.

Critical Reynolds Number

We employ a bipolar coordinate system for the representation of the flow field between infinite, rotating eccentric cylinders. The bipolar coordinate system $\{\hat{\alpha},\ \hat{\beta},\ \hat{\gamma}\}$ is related to the Cartesian coordinate system $\{X, Y, Z\}$ through

$$\hat{\alpha} + i\hat{\beta} = -2\coth^{-1}\frac{(X+iY)}{a}, \quad \hat{\gamma} = Z, \tag{6.20}$$

where a is the separation between the pole and the origin of the $\{X, Y, Z\}$ system (Figure 5.1). In the bipolar coordinate system, the cylinders of radii r_1 and r_2, $r_1 < r_2$, have the simple representation $\hat{\alpha} = \hat{\alpha}_1$ and $\hat{\alpha} = \hat{\alpha}_2$, $\hat{\alpha}_1 < \alpha_2 < 0$, respectively. The scale factor of the bipolar coordinate system is given by (Ritchie, 1968)

$$H = \frac{a}{\left(\cosh\hat{\alpha} - \cos\hat{\beta}\right)}.$$

The nondimensional equations of motion and mass conservation are

$$\begin{aligned}
&\frac{\Delta}{h}u\frac{\partial u}{\partial\alpha} + \frac{1}{2\pi h}v\frac{\partial u}{\partial\beta} + w\frac{\partial u}{\partial\gamma} - uv\sin\hat{\beta} + v^2\sinh\hat{\alpha} \\
&\quad = -\frac{\Delta}{h}\frac{\partial p}{\partial\alpha} + \frac{(1-\eta)}{\eta\mathrm{Re}}\left[\frac{1}{h^2}\left(\Delta^2\frac{\partial^2 u}{\partial\alpha^2} + \frac{1}{(2\pi)^2}\frac{\partial^2 u}{\partial\beta^2}\right) + \vartheta^2\frac{\partial^2 u}{\partial\gamma^2}\right. \\
&\qquad \left. - \frac{2\Delta\sin\hat{\beta}}{h}\frac{\partial v}{\partial\alpha} + \frac{\sinh\hat{\alpha}}{\pi h}\frac{\partial v}{\partial\beta} - \frac{\cosh\hat{\alpha}+\cos\hat{\beta}}{h}u\right],
\end{aligned} \tag{6.21a}$$

$$\begin{aligned}
&\frac{\Delta}{h}u\frac{\partial v}{\partial\alpha} + \frac{1}{2\pi h}v\frac{\partial v}{\partial\beta} + w\frac{\partial v}{\partial\gamma} - uv\sinh\hat{\alpha} + u^2\sin\hat{\beta} \\
&\quad = -\frac{1}{2\pi h}\frac{\partial p}{\partial\beta} + \frac{(1-\eta)}{\eta\mathrm{Re}}\left[\frac{1}{h^2}\left(\Delta^2\frac{\partial^2 v}{\partial\alpha^2} + \frac{1}{(2\pi)^2}\frac{\partial^2 v}{\partial\beta^2}\right) + \vartheta^2\frac{\partial^2 v}{\partial\gamma^2}\right. \\
&\qquad \left. + \frac{2\Delta\sin\hat{\beta}}{h}\frac{\partial u}{\partial\alpha} - \frac{\sinh\hat{\alpha}}{\pi h}\frac{\partial u}{\partial\beta} - \frac{\cosh\hat{\alpha}+\cos\hat{\beta}}{h}v\right],
\end{aligned} \tag{6.21b}$$

$$\begin{aligned}
&\frac{\Delta}{h}u\frac{\partial w}{\partial\alpha} + \frac{1}{2\pi h}v\frac{\partial w}{\partial\beta} + w\frac{\partial w}{\partial\gamma} \\
&\quad = -\vartheta^2\frac{\partial p}{\partial\gamma} + \frac{(1-\eta)}{\eta\mathrm{Re}}\left[\frac{1}{h^2}\left(\Delta^2\frac{\partial^2 w}{\partial\alpha^2} + \frac{1}{(2\pi)^2}\frac{\partial^2 w}{\partial\beta^2}\right) + \vartheta^2\frac{\partial^2 w}{\partial\gamma^2}\right].
\end{aligned} \tag{6.21c}$$

The divergence of the velocity field $\boldsymbol{v} = (u, v, w)$ has the (nondimensional) form

$$\mathrm{div}\,\boldsymbol{v} = \frac{1}{h}\left(\Delta\frac{\partial u}{\partial\alpha} + \frac{1}{2\pi}\frac{\partial v}{\partial\beta} + h\frac{\partial w}{\partial\gamma}\right) - u\sinh\hat{\alpha} + v\sin\hat{\beta}. \tag{6.22}$$

Equations (6.21) and (6.22) are nondimensional. They were nondimensionalized according to

$$\alpha = \Delta(\hat{\alpha} - \hat{\alpha}_1), \quad \beta = \frac{\hat{\beta}}{2\pi}, \quad \gamma = \frac{\hat{\gamma}}{r_1}, \quad \Delta = \frac{1}{\hat{\alpha}_2 - \hat{\alpha}_1},$$
$$\{U, V, W\} = \frac{r_1\omega}{\sinh|\hat{\alpha}_1|}\left\{u, v, \frac{1}{\vartheta}w\right\}, \quad \vartheta = \frac{a}{r_1}, \quad C = r_2 - r_1, \tag{6.23}$$
$$p = \frac{P}{\rho r_1^2\omega^2}\sinh^2|\hat{\alpha}_1|, \quad h = \frac{H}{a}, \quad \mathrm{Re} = \frac{r_1\omega C}{\nu}.$$

Here P represents the pressure and $\{U, V, W\}$ represents the physical components of velocity relative to the bipolar coordinate system. Dynamic conditions in the flow are represented by the Reynolds number, Re, calculated on the mean gap width.

We anticipate that although at small values of the Reynolds number fluid motion proceeds in $z = \text{const.}$ planes, at some higher rotation this basic laminar flow will give up its stability to a more complex laminar flow that possesses periodic structure in γ for cylinders of infinite length. Accordingly, we Fourier analyze the flow field as follows (Meyer-Spasche and Keller, 1980):

$$\{u, v, p\} = \sum_{j=0}^{N_z}\{u_j, v_j, p_j\}\cos j\kappa\gamma$$
$$w = \sum_{j=1}^{N_z} w_j \sin j\kappa\gamma \tag{6.24}$$

and investigate the individual Fourier components, obtained by substituting Eqs. (6.24) into the equations of motion and continuity (Dai, Dong, and Szeri, 1992).

Let λ represent the length of a cell in the Z direction (not yet fixed). We shall restrict attention to

$$Z \in \left[-\frac{\lambda}{2}, \frac{\lambda}{2}\right],$$

thus the solution domain of Eqs. (6.20) is defined by

$$0 \le \alpha \le 1, \quad 0 \le \beta \le 1, \quad -\frac{\pi}{\kappa} \le \gamma \le \frac{\pi}{\kappa}, \tag{6.25}$$

where $\kappa = 2\pi r_1/\lambda$ is the nondimensional wave number. The wavelength λ, and thus the wave number κ, is a parameter of the problem, and we obtain the critical Reynolds number, Re_{CR}, from computing $d\,\mathrm{Re}(\kappa)/d\kappa = 0$.

The boundary conditions accompanying Eqs. (6.21) are no slip on the walls

$$u(0, \beta, \gamma) = w(0, \beta, \gamma) = 0, \; v(0, \beta, \gamma) = \sinh|\hat{\alpha}_1|,$$
$$u(1, \beta, \gamma) = v(1, \beta, \gamma) = w(1, \beta, \gamma) = 0. \tag{6.26a}$$

We also require periodicity of the solution and its derivatives in β

$$\phi^{(n)}(\alpha, 0, \gamma) = \phi^{(n)}(\alpha, 1, \gamma), \quad \phi = u, v, w, p \quad n = 0, 1, 2, \ldots \tag{6.26b}$$

Equations (6.21) define pressure only within an arbitrary constant. We set this constant to zero by requiring that $p(0, 0, 0) = 0$.

At this stage, Dai et al., (1992) eliminated the pressure, p_j, $j \geq 1$, from the component equations so as to keep the discretized system nonsingular.[12]

The expansions

$$
\begin{aligned}
u_k(\alpha, \beta) &= \sum_{i=2}^{N_\alpha - 1} \sum_{j=1}^{N_\beta - 3} u_{ijk} A_i(\alpha) b_j(\beta), \quad 0 \leq k \leq N_\gamma, \\
v_0(\alpha, \beta) &= \sinh |\hat{\alpha}_1| A_1(\alpha) + \sum_{i=2}^{N_\alpha - 1} \sum_{j=1}^{N_\beta - 3} v_{ij0} A_i(\alpha) b_j(\beta), \\
v_k(\alpha, \beta) &= \sum_{i=2}^{N_\alpha - 1} \sum_{j=1}^{N_\beta - 3} v_{ijk} A_i(\alpha) b_j(\beta), \quad 1 \leq k \leq N_\gamma, \\
w_k(\alpha, \beta) &= \sum_{i=2}^{N_\alpha - 1} \sum_{j=1}^{N_\beta - 3} w_{ijk} A_i(\alpha) b_j(\beta), \quad 1 \leq k \leq N_\gamma, \\
p_0(\alpha, \beta) &= \sum_{i=1}^{N_\alpha} \sum_{j=1}^{N_\beta - 3} p_{ij} A_i(\alpha) b_j(\beta),
\end{aligned}
\tag{6.27}
$$

where the $A_i(\alpha)$, $i = 1, \ldots N_\alpha$ are normalized splines in α and the b_j, $j = 1, \ldots, N_\beta - 3$, are periodic splines in β, satisfy the boundary conditions (6.26a) and the periodicity condition (6.26b).

Next, we substitute Eqs. (6.27) into the component equations, obtained by Fourier decomposition of the equations of motion and continuity, and apply Galerkin's method (Dai et al., 1992). The discretized system of equations are then solved subject to the single condition $p(0, 0, 0) = 0$, which takes the form $p_{1,1} = 0$.

The system of algebraic equations that result from Galerkin's method can be written in the form

$$F(u, \sigma) = 0. \tag{6.28}$$

Here $F : U \oplus \Sigma \subset R^n \to R^m$, dim $U = m$, dim $\Sigma = n - m$. $u \in U$ is the vector of state variables and $\sigma \in \Sigma$ is the vector of parameters η, ν, Re, ε.

In the computational scheme, we fix three of the parameters, say η, ϑ, and ε, and vary the Reynolds number, Re; thus, $n - m = 1$ and the regular manifold of Eq. (6.28) is a path.

The objective here is to solve the nonlinear algebraic system Eq. (6.28) for various values of σ, now signifying a single parameter, the Reynolds number, $\sigma \equiv$ Re. The solution $u^* = u(\sigma^*)$ is guaranteed by the implicit function theorem in the neighborhood of the points (u, σ), where $F_u(u, \sigma)$, the Fréchet derivative of $F(u, \sigma)$, is non-singular. The computational scheme for obtaining $u^* = u(\sigma^*)$ is then straightforward: (1) first locate a point (u^0, σ^0) in $(n + 1)$ space that lies within the neighborhood of attraction[13] of (u^*, σ^*), then (2)

[12] The pressure may be retained, at significant savings on algebra, if the scheme of Eq. (5.12) due to Zienkiewicz and Woo (1991) is employed. An extension to the full Navier–Stokes problem can be found in Szeri and Al-Sharif (1996).

[13] Attraction in terms of the numerical scheme, not in the sense of fluid dynamics.

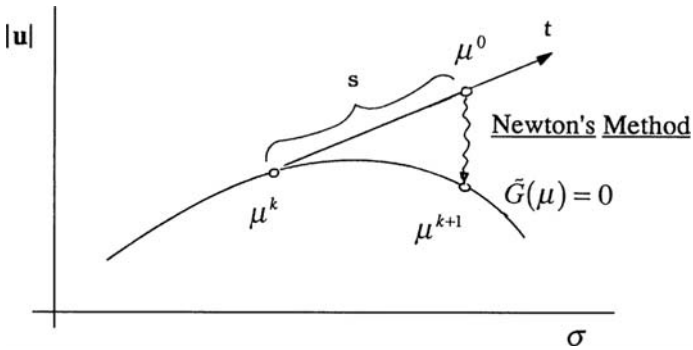

Figure 6.6. Schematics of the iterative solution of Eq. (6.29).

employ a suitable iterative scheme that guarantees convergence $(u^0, \sigma^0) \to (u^*, \sigma^*)$. Phase (1), i.e., the *predictor*, is simplest when (u^0, σ^0) is obtained by stepping along the tangent to the manifold from a known point (Figure 6.6). The step size, s, is constrained by the requirement that (u^0, σ^0) lie in the neighborhood of attraction of (u^*, σ^*).

For convenience of notation, we rewrite Eq. (6.28) in the form

$$\tilde{G}(\mu) = 0, \quad \mu = (\mu, \sigma). \tag{6.29}$$

Local Iteration

We employ the Gauss-Newton method (Ortega and Rheinboldt, 1970)

$$D\tilde{G}(\mu^k)(\mu^k - \mu^{k+1}) = \tilde{G}(\mu^k) \quad k = 0, 1, 2, \ldots \tag{6.30}$$

to solve Eq. (6.29) by iteration, starting from a suitable initial point μ^0. Here

$$D\tilde{G}(x^k) = (D_u\tilde{G}(\mu^k), D_\sigma\tilde{G}(\mu^k)) \in R^{m\times n}$$

is the augmented Jacobian of $\tilde{G}(\mu)$ evaluated at $\mu = \mu^k$. (Note that the Jacobian is calculated analytically.)

To solve Eq. (6.30) for μ^{k+1}, perform the Q-R factorization

$$D\tilde{G}(\mu^k)^T = Q\begin{pmatrix}\Re\\0\end{pmatrix}, \tag{6.31}$$

where $Q \in R^{n\times n}$ is orthogonal and $\Re \in R^{m\times m}$ is upper triangular, and observe that

$$\left(\Re^T, 0\right) Q^T Q \begin{pmatrix}\Re^{-T}\\0\end{pmatrix} = I$$

and

$$D\tilde{G}(x^k) = (\Re^T, 0)Q^T.$$

This implies that Eq. (6.30) has the solution

$$\mu^{k+1} = \mu^k - Q\begin{pmatrix}\Re^{-T}\\0\end{pmatrix}\tilde{G}(\mu^k) \quad k = 0, 1, 2, \ldots, \tag{6.32}$$

where $\Re^{-T}$ is the inverse of $\Re$ transpose.

Local iteration of the solution proceeds thus along the following steps:

(1) Select[14] a starting point, $\mu = \mu^0$,
(2) For $k = 0, 1, 2, \ldots$ until convergence
  (a) Solve the triangular system: $\Re^T \varpi = \tilde{G}(\mu^k)$,
  (b) Compute the next iterate: $\mu^{k+1} = \mu^k - Q\begin{pmatrix}\varpi \\ 0\end{pmatrix}$

Continuation of the solution

The Q-R decomposition

$$D\tilde{G}(\mu^k)^T = Q\begin{pmatrix}\Re \\ 0\end{pmatrix}$$

indicates that the last column of Q is tangential to the solution manifold, so that the tangent vector at μ^k is given by

$$t = Qe_n,$$

where $e_n = (0, 0, \ldots, 1)^T$.

The simplest way to find a starting point, μ^0, for the Gauss-Newton iteration is by computing

$$\mu^0 = \mu + st,$$

where s is a variable step and μ is a known point (Figure 6.5).

The iteration scheme depicted by Eq. (6.30) breaks down at critical points, μ_c, where the Jacobian $D_u\tilde{G}(\mu_c)$ is singular. If, as in the present example,

$$\text{rank}[D_u\tilde{G}(\mu_c)] = n - 1 \tag{6.33}$$

and $D_\sigma \tilde{G}(\mu_c) \in \text{range}[D_u\tilde{G}(\mu_c)]$, the point μ_c is a simple bifurcation point where exactly two branches with two distinct tangents intersect. [There is also a condition on the second derivatives. For technical details the reader is referred to Iooss and Joseph (1976) and to Keller (1977).]

Although a simple bifurcation point is characterized by the singularity of the augmented Jacobian $D\tilde{G}$, computationally we are looking for the change of sign of

$$\det\left[D\tilde{G}(\mu^k)^T, t\right]$$

for continuously varying tangent vector, t. This is achieved by examining the test function

$$\tau = \text{sgn}(r_{11} \times r_{22} \times \cdots \times r_{mm}),$$

where the r_{ii}, $1 \le i \le m$, are the diagonal elements of $\Re$.

In order to continue along the new branch at bifurcation, $\mu = \mu_c$, we need the tangent, q, to the bifurcating branch. Aided by the fact that the bifurcating branches emanate

[14] To obtain the solution at low Reynolds numbers, often $\mu^0 = 0$ will suffice, i.e., all variables may be set equal to zero prior to starting the iteration. At high Reynolds numbers this scheme, in general, will not work. Thus, when seeking solution at high Reynolds numbers, μ^0 must be a point (i.e., solution) that was obtained from low Reynolds number solutions by some type of extrapolation.

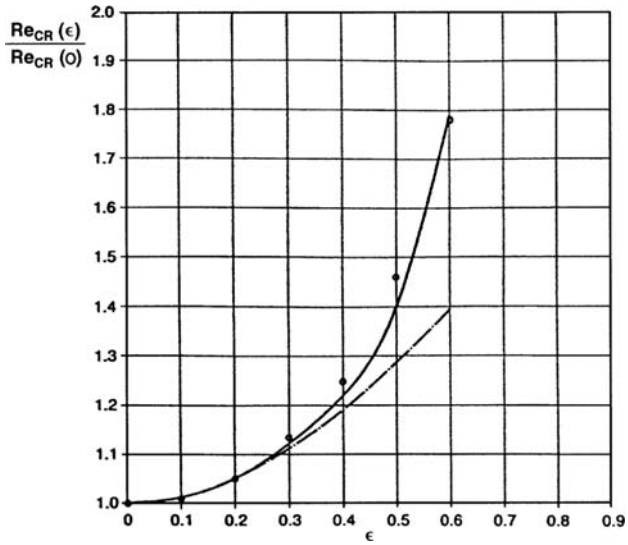

Figure 6.7. Variation of critical Reynolds number with eccentricity ratio, $\eta = 0.912$: $- \cdot - \cdot -$, DiPrima and Stuart (1972); •, Vohr (1968), experimental; —, Dai, Dong, and Szeri (1992). (Reprinted from *International Journal of Engineering Science*, Vol. 30, Dai, R. X., Dong, Q. M. and Szeri, A. Z. Flow between eccentric rotating cylinders: bifurcation and stability, pp. 1323–1340, Copyright (1990), with kind permission from Elsevier Science Ltd, The Boulevard, Langford Lane, Kidlington 0X5 1GB, UK.)

symmetrically at the bifurcation point, $\mu = \mu_c$, we are able to find a good approximation to the tangent of the bifurcating branch by simply calculating

$$q = Qe_m, \quad e_m = (0, \ldots, 0, 1, 0)^T.$$

Since $|r_{mm}| = \min(r_{ii}) \approx 0$, $1 \le i \le m$, the corresponding row vector in $D\tilde{G}$ is closest to being a linear combination of the other rows of $D\tilde{G}$ and

$$q \in \text{null}[D\tilde{G}(\mu_c), t].$$

Evaluation and decomposition of the Jacobian consumes most of the computational effort. With a system of 1,452 equations and $R < R_{CR}$, Dai et al., (1992) required 120 sec of CPU time on the Cray Y-MP/832 for one Newtonian iteration, and three iterations to converge to an error $<10^{-6}$. For supercritical conditions, 300 sec per iteration was required, but convergence was achieved, again, in three steps. For continuation in Re, fixed ε, 20 solutions were necessary to reach the critical point, starting from a low Reynolds number solution that was obtained with $\mu^0 = 0$.

Figure 6.7 illustrates the variation of the normalized critical Reynolds number with eccentricity ratio, at $\eta = 0.912$. The bifurcation calculations were performed with $N_x = N_y = 16$ and $N_z = 3$. The figure also contains data from small perturbation solutions by DiPrima and Stuart (1972), with correction from DiPrima and Stuart (1975). The experimental data was obtained from torque measurements at $\eta = 0.91$ by Vohr (1968). The bifurcation results are in good agreement with the experimental data of Vohr; they also agree with DiPrima and Stuart as $\varepsilon \to 0$, where the DiPrima and Stuart small perturbation analysis is valid, but diverge from the latter as ε increases.

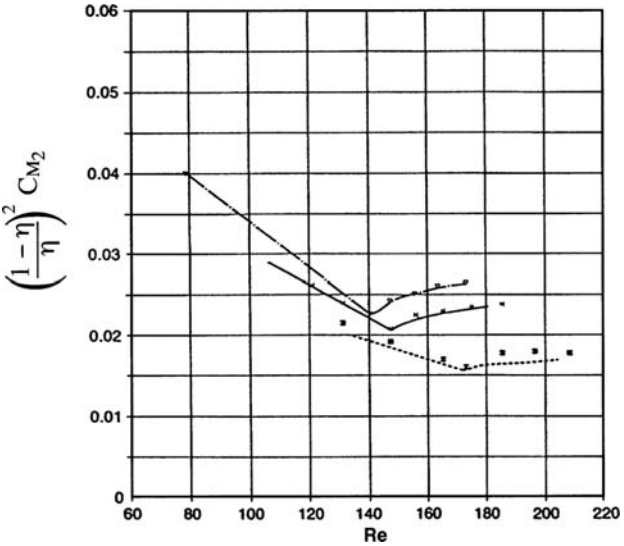

Figure 6.8. Comparison of numerical (Dai et al., 1990) and experimental (Castle and Mobbs, 1968) torque data at $\eta = 0.912$ ($- \cdot - \cdot -$, $\varepsilon = 0.0$; - - - $\varepsilon = 0.2$; — $\varepsilon = 0.4$;). (Reprinted from *International Journal of Engineering Science*, Vol. 30, Dai, R. X., Dong, Q. M. and Szeri, A. Z. Flow between eccentric rotating cylinders: bifurcation and stability, pp. 1323–1340, Copyright (1990), with kind permission from Elsevier Science Ltd, The Boulevard, Langford Lane, Kidlington 0X5 1GB, UK.)

Let M_1 and M_2 represent the torque on the inner and the outer cylinder, respectively, and define the torque coefficient C_{M_i} (Schlichting, 1960) through

$$C_{M_i} = \frac{2M_i}{\pi\rho\omega^2 L r_1^4}, \quad i = 1, 2. \tag{6.34}$$

Figure 6.8 compares torque results calculated on the outer cylinder at $\eta = 0.912$ with experimental data by Castle and Mobbs (1968) by plotting

$$C_{M_2}\frac{(1-\eta)^2}{\eta^2},$$

indicating supercritical bifurcation at Re_{CR}. There is good agreement especially at small ε.

Torque Measurements

Torque measurements for the concentric case have been made by Taylor (1923), Wendt (1933), Donelly (1958), and Vohr (1968) and were reviewed by Bilgen and Boulos (1973). It is a simple matter to show that if the friction force, F_μ, depends on ρ, μ, ω, r_1, C, and L, where C is the radial clearance and L is the length of the cylinders, the dependence must be of the form

$$\frac{F_\mu}{\rho\omega^2 r_1^3 L} = f\left(\frac{C}{r_1}, \frac{\rho\omega r_1 C}{\mu}\right) \tag{6.35}$$

on dimensional grounds.

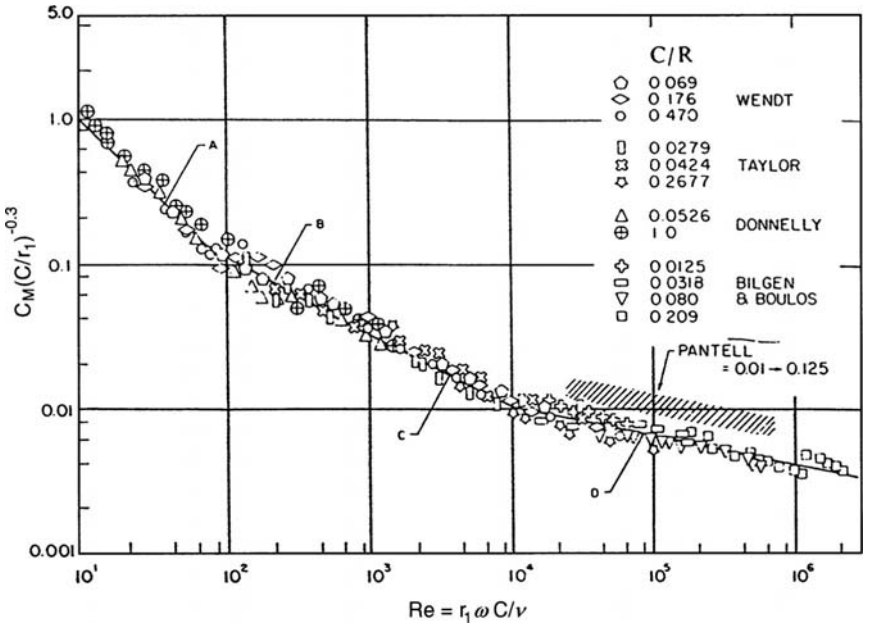

Figure 6.9. Variation of modified torque coefficient with Couette Reynolds number: (A) Eq. (6.37a); (B) Eq. (6.37b); (C) Eq. (6.37d); (D) Eq. (6.37e). (Reprinted with permission from Bilgen, E. and Boulos, R. Functional dependence of torque coefficient of coaxial cylinders on gap width and Reynolds numbers. *ASME Trans., Ser. G*, **95**, 122–126, 1973.)

Defining the torque coefficient C_M as in Eq. (6.34), Eq. (6.35) can be written in the approximate form (Bilgen and Boulos, 1973)

$$C_M = \lambda \left(\frac{C}{r_1}\right)^{\alpha} \mathrm{Re}^{\beta}, \tag{6.36}$$

where the Reynolds number is defined by $\mathrm{Re} = \rho r_1 \omega C/\mu$.

By analyzing available experimental data, Bilgen and Boulos achieved the best fit to Eq. (6.36) with $\alpha \approx 0.3$. The value of the exponent β is dependent not only on the Reynolds number in the laminar or the turbulent regimes but on both the Reynolds number and the clearance ratio C/r_1 in the vortex flow regime.

Laminar regime: $\mathrm{Re} \leq 64$

$$C_M = 10 \left(\frac{C}{r_1}\right)^{0.3} \mathrm{Re}^{-1.0} \tag{6.37a}$$

Transition regime: $64 < \mathrm{Re} \leq 500$

$$C_M = 2 \left(\frac{C}{r_1}\right)^{0.3} \mathrm{Re}^{-0.6} \qquad \text{if } \frac{C}{r_1} \geq 0.07 \tag{6.37b}$$

$$C_M = 2 \left(2 + \frac{C}{r_1}\right) \left\{1 + 1.45 \left[1 - \left(\frac{T_c}{T_a}\right)\right]\right\} \mathrm{Re}^{-1.0} \qquad \text{if } \frac{C}{r_1} < 0.07 \tag{6.37c}$$

Turbulent regime: $\mathrm{Re} > 500$

$$C_M = 1.03 \left(\frac{C}{r_1}\right)^{0.3} \mathrm{Re}^{-0.5} \qquad 500 < \mathrm{Re} \leq 10^4 \tag{6.37d}$$

$$C_M = 0.065 \left(\frac{C}{r_1}\right)^{0.3} \mathrm{Re}^{-0.20} \qquad \mathrm{Re} > 10^4 \tag{6.37e}$$

The maximum mean deviation of the experimental data from these equations is ± 5.8, ± 10.4, and $\pm 8.35\%$ in the laminar, transition, and turbulent regimes, respectively (Bilgen and Boulos, 1973), as shown in Figure 6.9.

6.4 Rotating Disk Flows

Thorough stability analysis of thrust bearing flows has not yet been accomplished. Among the flows that have been analyzed, flow between parallel rotating disks is the flow closest to thrust bearing flows. Disk flows also warrant consideration due to their relevance to magnetic disk storage systems, and to flow over certain hydrostatic pads.

The first systematic study of rotating disk flows was made by von Karman (1923), who assumed that the axial velocity is independent of the radial coordinate. This assumption led to a similarity transformation that was shown by Batchelor (1951) to be applicable even when the fluid is bounded by two infinite rotating disks. Based on the examination of the governing equations, Batchelor predicted that at high Reynolds numbers a thin boundary layer will develop on each disk, with the main body of the fluid rotating at a constant rate intermediate between disk velocities. This prediction was challenged by Stewartson (1953), who reasoned that at high Reynolds number the flow outside the boundary layers would be purely axial, thus inaugurating one of the longstanding controversies of fluid mechanics.

The similarity transformation, available when the disks are infinite, reduces the number of spatial dimensions of the problem to one. Although it is questionable whether the reduced model approximates to the physical problem, the equations resulting from the similarity transformation have been subject to intense analytical and numerical probing. An excellent review of the work on infinite disk flows can be found in Zandbergen and Dijkstra (1987).

Flow between finite, parallel disks was first investigated both experimentally and numerically by Szeri and Adams (1978) and by Szeri, Schneider, Labbe, and Kaufman (1983). Dijkstra and van Heijst (1983) found the finite disk solution to be unique for all values of the parameters considered: of the Batchelor type for weak and of the Stewartson type for strong counterrotation. Brady and Durlofsky (1987) investigated the relationship of the axisymmetric flow between large but finite coaxial rotating disks to the Karman similarity solution. They combined asymptotics with numerical analysis and showed that the finite disk solution and the similarity solution coincide over a decreasing portion of the flow domain as the Reynolds number is increased. Although this conclusion might seem counterintuitive and perhaps defies old wisdom, it does reinforce the assertion that finite disk and infinite disk flows are qualitatively different (Szeri, Giron, Schneider, and Kaufman, 1983). Despite the availability of solutions for finite disks, the computation of disk flow is far from elementary. Much of recent work on finite disk flows finds relevance in magnetic disk storage systems (Tzeng and Fromm, 1990; Tzeng and Humphrey, 1991; Humphrey,

Schuler, and Iglesias, 1992; Radel and Szeri, 1997). In these applications nonuniformities in flow can affect disk rotational stability, with attendant drastic effects on read-write performance; the current read-write head to disk separation is on the order of 100 nm or less.

Turning now to stability of rotating disk flows, we find that most investigations are of flows bounded by a single rotating disk. Gregory, Stuart, and Walker (1955) examined stability at infinite Reynolds number and found good agreement with experimental data on the direction of wave propagation but overestimated the number of vortices that appear at criticality. Brown (1961) extended their analysis by considering stability at finite Reynolds number. The basic flow equations contain curvature and Coriolis terms in the work of Kobayashi, Kohama, and Takamadate (1980). Szeri and Giron (1984) retain the axial velocity in addition to the terms considered by Kobayashi et al. Their result shows favorable agreement with experimental data.

Experimentally, Faller (1963) found two types of instabilities. The waves of each of these form a series of horizontal roll vortices, whose spacing is related to the thickness of the boundary layer. Others who studied these instabilities include Faller and Kaylor (1966), Tatro and Mollo-Christensen (1967), Caldwell and Van Atta (1970), and Weidman and Redekopp (1976). The Ekman velocity profile exhibits numerous inflection points, each of which might give rise to instabilities. Faller and Kaylor found that the location of the type I vortices, which are stationary or nearly so, coincides with the first inflection point of the radial velocity. The analysis of Gregory, Stuart, and Walker (1955) of inviscid instabilities of the flow on a single, infinite, rotating disk confirms this.

Linear Stability Analysis

The flow field is bounded by two parallel disks of finite radii, located at $Z = 0$ and $Z = s$, with respect to the inertial cylindrical coordinate system (R, Θ, Z). The lower disk rotates with angular velocity Ω relative to the upper disk. Experimental evidence shows that the instabilities that may occur take the form of spirals, with their radius vector decreasing in the direction of rotation of the disks. Based on this evidence, and on the assertion that this type of instability should be a general feature of all rotating boundary layers (Greenspan, 1968), it is logical to select, as reference, an orthogonal, curvilinear coordinate system (x^1, x^2, x^3) that is related to the local geometry of the spiral vortices (Figure 6.10). The direction of the x^2 axis is chosen to coincide with axis of the spiral vortices (inclined locally at the yet unknown angle ε to the R direction). The x^1 axis intersects the x^2 axis perpendicularly, so that the x^1 axis is in the direction of propagation of the spiral vortices.

The origin of the (x^1, x^2, x^3) coordinate system is located on the lower disk at $R = r$, some Θ, via the transformation (Gregory, Stuart and Walker, 1955)

$$T: \begin{cases} x^1 = r\left[\ln\left(\dfrac{R}{r}\right)\cos\varepsilon - (\Theta + \Omega t)\sin\varepsilon\right] \\ x^2 = r\left[\ln\left(\dfrac{R}{r}\right)\sin\varepsilon + (\Theta + \Omega t)\cos\varepsilon\right] \\ x^3 = Z \end{cases}. \tag{6.38}$$

The scale factors of the $\{x_i\}$ coordinate system are

$$h_1 = h_2 = (R/r) = h, \quad h_3 = 1.$$

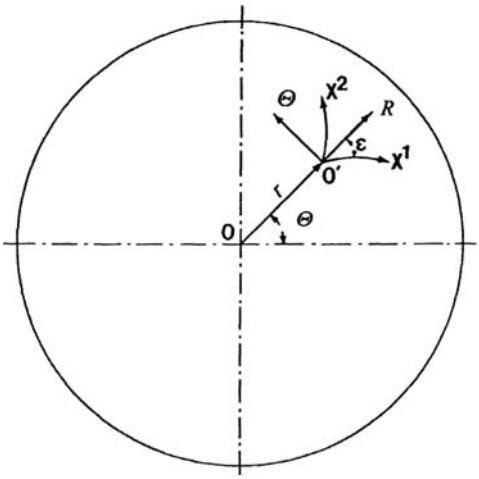

Figure 6.10. Coordinate systems employed in the linear stability analysis of disk flows.

We next calculate the physical components $\{V_1, V_2, V_3\}$ of the basic flow velocity relative to $\{x^i\}$, which are given by

$$\begin{cases} V_1 = \cos\varepsilon(U_R) - \sin\varepsilon(r\Omega - V_\Theta) \\ V_2 = \sin\varepsilon(U_R) + \cos\varepsilon(r\Omega - V_\Theta) \\ V_3 = W_z \end{cases} \tag{6.39}$$

where $\{U_R, V\Theta, W_Z\}$ is the flow velocity in the cylindrical polar coordinate system $\{R, \Theta, Z\}$.

In accordance with the linear theory of stability, the basic flow is perturbed by an infinitesimal wave. We look for instability to perturbation which propagates in the x^1 direction, the direction of least stability, with speed $(\beta/\alpha)_r$, the real part of (β/α), relative to $\{x^i\}$ and a wavelength of $2\pi/\alpha$. Let $\{\boldsymbol{u}; p\}$ represent the perturbation, then

$$\{\boldsymbol{u}(\boldsymbol{x}); p(\boldsymbol{x})\} = \{\boldsymbol{v}(x^3); \pi(x^3)\} e^{i(\alpha x^1 - \beta t)}. \tag{6.40}$$

The linearized equations that govern the evolution of the perturbation {see Eq. (6.14)} are given by Greenspan (1968)

$$\begin{aligned} &-i\lambda\boldsymbol{v} + \boldsymbol{V}\cdot\operatorname{grad}\boldsymbol{v} + \boldsymbol{v}\cdot\operatorname{grad}\boldsymbol{V} + 2\boldsymbol{\Omega}\times\boldsymbol{v} = -\operatorname{grad}\frac{\pi}{p} + \nu\nabla^2\boldsymbol{v} \\ &\operatorname{div}\boldsymbol{v} = 0. \end{aligned} \tag{6.41}$$

Using the notation

$$\vartheta = \frac{s}{r}, \quad \delta = \frac{s}{hr}, \quad m_i = \frac{s}{h^2}\frac{\partial h}{\partial x^i}, \quad \Gamma_{ij} = \frac{s^2}{h^3}\frac{\partial^2 h}{\partial x^i \partial x^j}, \quad i, j = 1, 2,$$

Eq. (6.41) is nondimensionalized in accordance with

$$\begin{aligned} &\{x^i\} = r\{x, y, \vartheta z\}, \quad \{V_1, V_2, V_3\} = V_0\{U, V, \vartheta W\} \\ &\mathrm{Re} = \frac{V_0 s}{\nu}, \quad \sigma = \frac{\alpha s}{h}, \quad c = \frac{\beta h}{\alpha V_0}, \end{aligned} \tag{6.42}$$

where $V_0 = r\Omega$ is the local surface velocity. Upon decomposing Eq. (6.41) along $\{x^i\}$ and substituting in Eq. (6.42), the following set of equations results:

$$-i\sigma cu - (m_1 v + i\sigma v - m_2 u)\, V + \vartheta \left(\frac{du}{dz} - i\sigma w\right) W$$
$$- \left(m_1 V + \delta \frac{\partial V}{\partial x} - m_2 V - \delta \frac{\partial U}{\partial y}\right) v + \left(\frac{\partial U}{\partial z} - \delta\vartheta \frac{\partial W}{\partial x}\right) w + 2\vartheta v \tag{6.43a}$$
$$= -\frac{1}{V_0}\delta \frac{\partial \bar{\pi}}{\partial x} - \frac{1}{\mathrm{Re}}\left[-\frac{d^2 u}{dz^2} + i\sigma \frac{dw}{dz} - (2m_1 m_2 - \Gamma_{12} + i\sigma m_2)\, v + \left(2m_2^2 - \Gamma_{22}\right) u\right],$$

$$-i\sigma cv + \vartheta \frac{dv}{dz} W + (m_1 v + i\sigma v - m_2 u)\, U + \frac{\partial V}{\partial z} w + \left(m_1 V + \delta \frac{\partial V}{\partial x} - m_2 U\right) u - 2\vartheta u$$
$$= -\delta \frac{\partial V}{\partial y} v - \frac{1}{\mathrm{Re}}\left[-\frac{d^2 v}{dz^2} + (i\sigma m_2 - 2m_1 m_2 + \Gamma_{12})\, u + \left(2m_1^2 - \Gamma_{11} + \sigma^2\right) v\right], \tag{6.43b}$$

$$-i\sigma cw - \left(\frac{du}{dz} - i\sigma w\right) U - \frac{\partial v}{\partial z} V - \left(\frac{\partial U}{\partial z} - \delta\vartheta \frac{\partial W}{\partial x}\right) u + \left(\delta\vartheta \frac{\partial W}{\partial y} - \frac{\partial V}{\partial z}\right) v$$
$$= -\frac{1}{V_0}\frac{\partial \bar{\pi}}{\partial z} - \frac{1}{\mathrm{Re}}\left[i\sigma \frac{du}{dz} + i\sigma m_1 w + \sigma^2 w + m_1 \left(\frac{du}{dz} - i\sigma w\right) + m_1 \frac{dv}{dz}\right], \tag{6.43c}$$

$$(m_1 + i\sigma)u + m_2 v + \frac{dw}{dz} = 0. \tag{6.44}$$

Cross differentiation eliminates the pressure, and substitution from the equation of continuity (6.44) eliminates the velocity component u. We further simplify these equations by utilizing the approximations

$$\begin{aligned} &\delta \approx \vartheta, \quad m_1 \approx \delta \cos\varepsilon, \quad m_2 \approx \delta \sin\varepsilon \\ &\Gamma_{11} \approx \delta^2 \cos^2\varepsilon, \quad \Gamma_{12} \approx \delta^2 \sin\varepsilon \cos\varepsilon, \qquad \Gamma_{22} \approx \delta^2 \sin^2\varepsilon. \end{aligned} \tag{6.45}$$

The algebra is tedious, and we refer the reader here to Giron (1982) and Szeri, Giron, Schneider, and Kaufman (1983).

We seek solutions in the weak form

$$\begin{aligned} v(z) &= \sum_{i=2}^{N-1} v_i B_i(z), \\ w(z) &= \sum_{j=3}^{N-2} w_j B_j(z). \end{aligned} \tag{6.46}$$

Here the $B_i(z)$, $1 \le i \le N$ are B-splines defined over a partition in $z \in [0, 1]$. The expansions in Eqs. (6.46) satisfy the boundary conditions

$$v = w = \frac{dw}{dz} = 0 \quad (z = 0, 1). \tag{6.47}$$

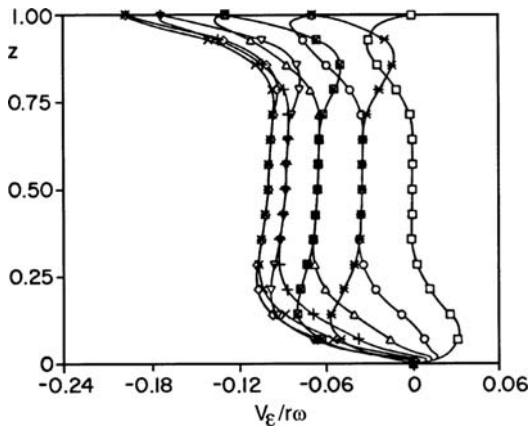

Figure 6.11. Basic flow velocity, resolved along direction ε : $\square$, $\varepsilon = 0°$; $\bigcirc$, 20°; Δ, 40°; $+$, 60°; $\times$, 80°; $\diamond$, 100°; ∇, 120°; $\boxtimes$, 140°; $*$, 160°. (Reprinted with the permission of Cambridge University Press, from Szeri, A. Z., Giron, A., Schneider, S. J. and Kaufman, H. N. Flow between rotating disks. Part 2. Stability. *J. Fluid Mech.*, **134**, 133–154, 1983.)

The condition $d_w/d_z = 0$ at $z = 0$, 1 is a derived boundary conditions; it is obtained from the equation of continuity (6.44).

Expansions (6.46), together with spline expansions for the (numerically or experimentally) known basic flow, are now substituted into the reduced equations of motion in an application of Galerkin's method. Multiplication through by the elements of the test functions $\{B_i(z)\}_{i=1}^N$ and integration over the domain $0 \le z \le 1$ lead to the complex algebraic eigenvalue problem

$$|\boldsymbol{X} - c\boldsymbol{Y}| = 0, \tag{6.48}$$

where, in general, $c = c_r + ic_i$.

The flow is marginally or neutrally stable if there is one eigenvalue with $c_i = 0$ and $c_i > 0$ for all other eigenvalues. It is unstable if at least one eigenvalue exists with $c_i < 0$. The marginal state is steady if $c_r = 0$.

We now illustrate some results for parallel, infinite, disk flows at a fixed value, say $E^{-1} = 100$, of the Ekman number. To identify the most dangerous direction for wave propagation, the basic flow velocity is resolved along various directions as characterized by the angle ε (Figure 6.11). The neutral stability curve of each of the resolved velocity profiles is then calculated from the eigenvalue problem (6.48), by identifying (σ, Re) couples that yield the neutrality condition $c_i = 0$ (Figure 6.12). For each of the orientations, ε, the lowest achievable Reynolds number yielding $c_i = 0$ is now identified and plotted against ε in Figure 6.13. This last Figure shows that the perturbation that propagates at $\varepsilon \approx 17°$ to the radius is the most dangerous one, giving the critical Reynolds of $\mathrm{Re}_{CR} = 5000$. Therefore, a basic flow characterized by $E^{-1} = 100$ is unstable to infinitesimal disturbances whenever $r \ge 50s$.

The scheme described here will yield results even if the basic flow is available only experimentally (Szeri, Giron, Schneider, and Kaufman, 1983).

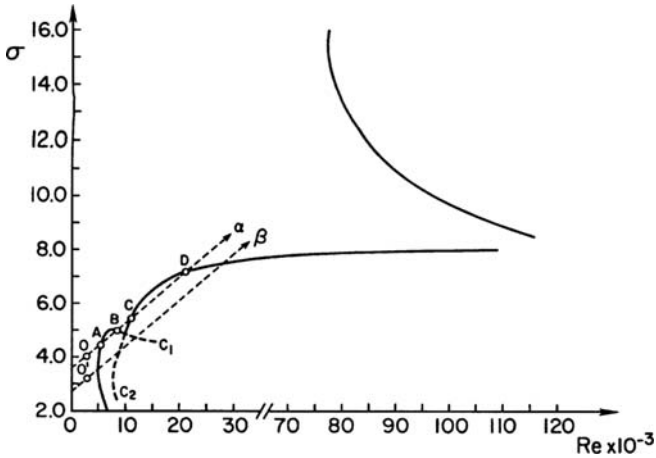

Figure 6.12. Stability diagram at $E^{-1} = 100$, $\varepsilon = 17^{\circ}$. (Reprinted with the permission of Cambridge University Press from Szeri, A. Z., Giron, A., Schneider, S. J. and Kaufman, H. N. Flow between rotating disks. Part 2. Stability. *J. Fluid Mech.*, **134**, 133–154, 1983.)

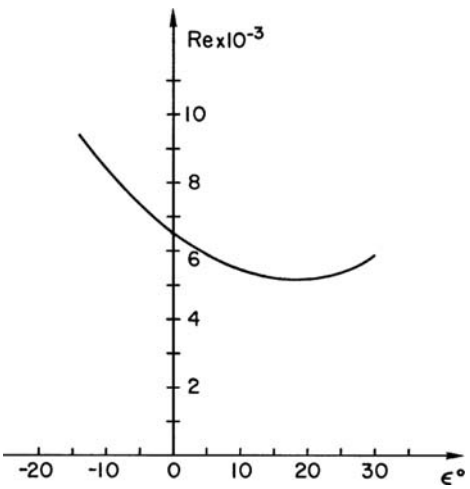

Figure 6.13. Variation of the Reynolds number for neutral stability with orientation ε. (Reprinted with the permission of Cambridge University Press from Szeri, A. Z., Giron, A., Schneider, S. J. and Kaufman, H. N. Flow between rotating disks. Part 2. Stability. *J. Fluid Mech*., **134**, 133–154, 1983.)

6.5 Nomenclature

A_i	B-spline
C	radial clearance
C_M	coefficient of torque
$\mathcal{D}$	rate of energy dissipation
$\mathcal{E}$	kinetic energy of perturbation
H	scale factor

$\mathcal{J}$	rate of energy production
P	pressure
Re	Reynolds number
$\boldsymbol{V}$	basic flow velocity
b_i	periodic spline
c	eigenvalue
p	pressure
r_1, r_2	inner, outer radii
$\boldsymbol{v}$	perturbation
α, β, γ	bipolar coordinates
R, Θ, Z	cylindrical polar coordinates
$\{x^i\}$	curvilinear coordinates
ε	coordinate orientation
U_R, V_Θ, W_Z	basic flow velocity
V_i	basic flow velocity
$(.)_r$, $(.)_i$	real, imaginary part
$(.)_0$	initial value

6.6 References

Batchelor, G. K. 1951. Note on a class of solutions of the Navier-Stokes equations representing rotationally symmetric flow. *Q. J. Mech. Appl. Maths.*, **4**, 29.

Benjamin, T. B. 1978. Bifurcation phenomena in steady flows of a viscous liquid. *Proc. Roy. Soc. London*, **A 359**, 1–43.

Benjamin, T. B. and Mullin, T. 1981. Anomalous modes in the Taylor experiment. *Proc. Roy. Soc. London* **A 377**, 221–249.

Benjamin, T. B. and Mullin, T. 1982. Notes on the multiplicity of flows in the Taylor experiment. *J. Fluid Mech.*, **121**, 219–230.

Bilgen, E. and Boulos, R. 1973. Functional dependence of torque coefficient of coaxial cylinders on gap width and Reynolds numbers. *ASME Trans., Ser. G*, **95**, 122–126.

Brady, J. F. and Durlofsky, L. 1987. On rotating disk flow. *J. Fluid Mech.*, **175**, 363–394.

Brown, W. B. 1961. A stability criterion for three-dimensional boundary layers. In *Boundary Layer and Flow Control* (G. V. Lachman, ed.). Vol. 2, pp. 913–923. Pergamon Press.

Burkhalter, J. E. and Koschmieder, E. L. 1974. Steady supercritical Taylor vortices after sudden starts. *Phys. Fluids*, **17**, 1929–1935.

Caldwell, D. R. and Van Atta, C. W. 1970. Characteristics of Ekman boundary layer instabilities. *J. Fluid Mech.*, **44**, 79–95.

Castle, P. and Mobbs, F. S. 1968. Hydrodynamic stability of flow between eccentric rotating cylinders: visual observations and torque measurements. *Proc. Inst. Mech. Eng.*, **182**, 41–52.

Chandrasekhar, S. 1961. *Hydrodynamic and Hydromagnetic Stability*. Oxford University Press, Oxford.

Cliff, K. A. and Mullin, T. 1985. A numerical and experimental study of anomalous modes in the Taylor experiment *J. Fluid Mech.*, **153**, 243–258.

Cliff, K. A. and Spence, A. 1986. Numerical calculations of bifurcations in the finite Taylor problem. In *Numerical Methods for Fluid Dynamics* (K. W. Morton and M. J. Baines, eds.), pp. 155–176. Clarendon Press, Oxford.

Cole, J. A. 1976. Taylor-vortex instability and annulus length effects. *J. Fluid Mech.*, **75**, 1–15.

Coles, D. 1965. Transition in circular Couette flow. *J. Fluid Mech.*, **21**, 385–425.

Dai, R. X. and Szeri, A. Z. 1990. A numerical study of finite Taylor flows. *Internat. J. Nonlinear Mech.*, **25**, 45–60.

Dai, R. X., Dong, Q. M. and Szeri, A. Z. 1992. Flow between eccentric rotating cylinders: bifurcation and stability. *Internat. J. Engrg. Sci.*, **30**, 1323–1340.

Deng, D. 2007. A numerical and experimental investigation of Taylor flow instabilities in narrow gaps and their relationship to turbulent flow in bearings. *Ph.D. Dissertation, University of Akron*.

Deng, D. and Barun, M. J. 2007. Taylor vortices induced instability (transition flow) versus 'turbulence' in concentric cylinders separated by microscale clearances. *Tribology International*, **50**(4), 573–584.

Dijkstra, D. and van Heijst, G. J. F. 1983. The flow between two finite rotating disks enclosed by a cylinder. *J. Fluid Mech.*, **128**, 123–254.

DiPrima, R. C. 1960. The stability of a viscous fluid between rotating cylinders with axial flow. *J. Fluid Mech.*, **9**, 621–631.

DiPrima, R. C. 1963. A note on the stability of flow in loaded journal bearings. *ASLE Trans.*, **6**, 249–253.

DiPrima, R. C. and Stuart, J. T. 1972. Non-local effects in the stability of flow between eccentric rotating cylinders. *J. Fluid Mech.*, **54**, 393–415.

DiPrima, R. C. and Stuart, J. T. 1975. The nonlinear calculation of Taylor vortex flow between eccentric rotating cylinders. *J. Fluid Mech.*, **67**, 85–111.

Donelly, R. J. 1958. Experiments on the stability of viscous flow between rotating cylinders. *Proc. Roy. Soc. London*, **A 266**, 312–325.

Drazin, P. G. and Reid, W. H. 1984. *Hydrodynamic Stability*. Cambridge University Press, Cambridge.

Faller, A. J. 1963. An experimental study of the instability of the laminar Ekman boundary layer. *J. Fluid Mech.*, **15**, 560–576.

Faller, A. J. and Kaylor, R. E. 1966. Investigations of stability and transition in rotating boundary layers. In *Dynamics of Fluids and Plasmas* (S. I. Pai, ed.), pp. 239–255. Academic.

Frank, G. and Meyer-Spasche, R. 1981. Computation of transitions in Taylor vortex flow. *Z. Agnew. Math. Phys.*, **32**, 710–720.

Frêne, J. and Godet, M. 1974. Flow transition criteria in a journal bearing. *ASME Journal of Lubrication Technology*, **96**, 135–140.

Gardner, W. W. and Ulschmid, J. G. 1974. Turbulence effects in two journal bearing applications. *ASME Trans., Ser. F*, **96**, 15–21.

Giron, A. 1982. *Stability of Rotating Disk Flows.* Ph.D. Dissertation, University of Pittsburgh.

Gollub, J. P. and Benson, S. V. 1980. Many roads to turbulent convection. *J. Fluid Mech.*, **100**, 449–470.

Gollub, J. P. and Swinney, H. L. 1975. Onset of turbulence in rotating fluids. *Phys. Rev. Let.*, **35**, 927–930.

Gottlieb, D. and Orszag, S. A. 1977. *Numerical Analysis of Spectral Methods: Theory and Applications*. SIAM, Philadelphia.

Greenspan, H. P. 1968. *The Theory of Rotating Fluids.* Cambridge University Press.

Gregory, N., Stewart, J. T. and Walker, W. S. 1955. On the stability of three-dimensional boundary layers with application to the flow due to a rotating disk. *Philos. Trans. Roy. Soc. London, Ser. A*, **248**, 155–199.

Hinze, J. O. 1974. *Turbulence*, 2d ed. McGraw-Hill, New York.

Humphrey, J. A. C., Schuler, C. A. and Iglesias, I. 1992. Analysis of viscous dissipation in disk storage systems and similar flow configurations. *Phys. Fluids A 4*, **7**, 1415–1427.

Iooss, G. and Joseph, D. D. 1980. *Elementary Stability and Bifurcation Theory.* Springer-Verlag, New York.

Joseph, D. D. 1976. *Stability of Fluid Motions*. Springer-Verlag, New York.

Kamal, M. M. 1966. Separation in the flow between eccentric rotating cylinders. *ASME J. Basic Engineering*, **88**, 717–724.

Karman, T. von. 1921. Über laminare und turbulente Reibung. *Z. Angew. Math. Mech.*, **1**, 233–252.

Keller, H. B. 1977. Numerical solutions of bifurcation and nonlinear eigenvalue problems. In *Applications of Bifurcation Theory* (P. Rabinowitz, ed.). Academic Press, New York.

Kelvin, Lord. 1871. Hydrokinetic solutions and observations. *Phil. Mag.*, **42**, 362–377.

Kobayashi, R., Kohama, Y. and Takamadate, C. 1980. Spiral vortices in boundary layer transition regime on a rotating disk. *Acta. Mech.*, **35**, 71–82.

Kogelman, S. and DiPrima, R. C. 1970. Stability of spatially periodic supercritical flows in hydrodynamics. *Phys. Fluids*, **13**, 1–11.

Koschmieder, E. L. 1976. Taylor vortices between eccentric cylinders. *Phys. Fluids*, **19**, 1–4.

Koschmieder, E. L. 1993. *Bénard cells and Taylor Vortices.* Cambridge University Press, Cambridge.

Landau, L. D. and Lifshitz, E. M. 1959. *Fluid Mechanics.* Pergamon Press, Oxford.

Li, C. H. 1977. The effect of thermal diffusion on flow stability between two rotating cylinders. *ASME Trans., Ser. F*, **99**, 318–322.

Lin, C. C. 1967. *The Theory of Hydrodynamic Stability.* Cambridge University Press, Cambridge.

Marcus, P. S. 1984a. Simulation of Taylor-Couette flow, I – numerical methods and comparison with experiment. *J. Fluid Mech.*, **146**, 45–64.

Marcus, P. S. 1984b. Simulation of Taylor-Couette flow, II – numerical results for wavy vortex flow with one traveling wave. *J. Fluid Mech.*, **146**, 65–113.

Meyer-Spasche, R. and Keller, H. B. 1978. *Numerical study of Taylor-vortex flows between rotating cylinders*. California Institute of Technology.

Meyer-Spasche, R. and Keller, H. B. 1980. Computations of the axisymmetric flow between rotating cylinders. *J. Comput. Phys.*, **35**, 100–109.

Milne-Thomson, L. M. 1968. *Theoretical Hydrodynamics*. Macmillan, New York.

Mobbs, F. R. and Younes, M. A. 1974. The Taylor vortex regime in the flow between eccentric rotating cylinders. *ASME Trans., Ser. F*, **96**, 127–134.

Nakaya, C. 1974. Domain of stable periodic vortex flows in a viscous fluid between concentric circular cylinders. *J. Phys. Soc. Japan*, **26**, 1146–1173.

Newhouse, S., Ruelle, D. and Takens, F. 1978. Occurrence of strange attractors near quasiperiodic flows on T^m, $m \geq 3$. *Common. Math. Phys.*, **64**, 35–40.

Oikawa, M., Karasndani, T. and Funakoshni, M. 1989a. Stability of flow between eccentric rotating cylinders. *J. Phys. Soc. Japan*, **58**, 2355–2364.

Oikawa, M., Karasndani, T. and Funakoshni, M. 1989b. Stability of flow between eccentric rotating cylinders with wide gap. *J. Phys. Soc. Japan*, **58**, 2209–2210.

Orr, W. M. F. 1907. The stability or instability of the steady motions of a perfect liquid and of a viscous liquid. *Proc. Roy. Irish Acad.*, **27A**, 9–138.

Ortega, J. M. and Rheinboldt, W. C. 1970. *Iterative Solution of Nonlinear Equations in Several Variables.* Academic Press, New York.

Radel, V. and Szeri, A. Z. 1997. Symmetry braking bifurcation in finite disk flow. *Phys. Fluids*, **9**(6), 1–7.

Ritchie, G. S. 1968. On the stability of viscous flow between eccentric rotating cylinders. *J. Fluid Mech.*, **32**, 131–144.

Rosenhead, L. 1963. *Laminar Boundary Layers.* Oxford University Press.

Ruelle, D. and Takens, F. 1971. On the nature of turbulence. *Commun. Math. Phys.*, **20**, 167–192.

San Andres, A. and Szeri, A. Z. 1984. Flow between eccentric rotating cylinders. *ASME J. Appl. Mech.*, **51**, 869–878.

Schlichting, H. 1968. *Boundary Layer Theory*, 6th ed. Pergamon, London.

Schwartz, K. W., Springer, B. E. and Donelly, R. J. 1964. Modes of instability in spiral flow between rotating cylinders. *J. Fluid Mech.*, **20**, 281–289.

Serrin, J. 1959a. Mathematical Principles of Classical Fluid Mechanics. In *Handbuch der Physik, VIII/I*, (S. Flügge and C. Truesdell, eds.). Springer Verlag, Heidelberg.

Serrin, J. 1959b. On the stability of viscous motion. *Arch. Rational Mech. Anal.*, **3**, 1.

Seydel, R. 1988. *From Equilibrium to Chaos.* Elsevier, New York.

Smith, M. I. and Fuller, D. D. 1956. Journal bearing operations at superlaminar speeds. *ASME Trans., Ser. F*, **78**, 469–474.

Stewartson, K. 1953. On the flow between rotating co-axial disks. *Proc. Camb. Phil. Soc.*, **3**, 333–341.

Szeri, A. Z. and Adams, M. L. 1978. Laminar throughflow between closely spaced rotating disks. *J. Fluid Mech.*, **86**, 1–14.

Szeri, A. Z. and Al-Sharif, A. 1995. Flow between finite, steadily rotating eccentric cylinders. *Theoret. Comput. Fluid Dyn.*, **7**, 1–28.

Szeri, A. Z. and Giron, A. 1984. Stability of flow above a rotating disk. *Int. J. Num. Methods.* **4**, 989–996.

Szeri, A. Z., Schneider, S. J., Labbe, F. and Kaufman, H. N. 1983. Flow between rotating disks. Part 1. Basic flow. *J. Fluid Mech.*, **134**, 103–132.

Szeri, A. Z., Giron, A., Schneider, S. J. and Kaufman, H. N. 1983. Flow between rotating disks. Part 2. Stability. *J. Fluid Mech.*, **134**, 133–154.

Tatro, P. R. and Mollo-Christensen, E. L. 1967. Experiments on Ekman layer stability. *J. Fluid Mech.*, **77**, 531–543.

Taylor, G. I. 1923. Stability of a viscous liquid contained between two rotating cylinders. *Philos. Trans. Roy., Soc.*, **A 223**, 289–343.

Tzeng, H. M. and Fromm, J. E. 1990. Air flow study in a cylindrical enclosure containing multiple co-rotating disks. *ISROMAC-3*, Hawaii.

Tzeng, H.-M. and Humphrey, J. A. C. 1991. Co-rotating disk flow in an axisymmetric enclosure with and without a bluff body. *Int. J. Heat and Fluid Flow*, **12**, 3, 194–201.

Versteegen, P. L. and Jankowski, D. F. 1969. Experiments in the stability of viscous flow between eccentric rotating cylinders. *Phys. Fluids*, **12**, 1138–1143.

Vohr, J. H. 1968. An experimental study of Taylor vortices and turbulence in flow between eccentric, rotating cylinders. *ASME Trans.*, **90**, 285–296.

Weidman, P. D. and Redekopp, L. G. 1975. On the motion of a rotating fluid in the presence of an infinite rotating disk. In *Proc. 12th Biennal Fluid Dyn. Symp.*, Bialowicza, Poland.

Weinstein, M. 1977a. Wavy vortices in the flow between long eccentric cylinders, I – linear theory. *Proc. Roy. Soc. London*, **A 354**, 441–457.

Weinstein, M. 1977b. Wavy vortices in the flow between long eccentric cylinders, II – nonlinear theory. *Proc. Roy. Soc. London*, **A 354**, 459–489.

Wendt, F. 1933. Turbulente strömungen zwischen zwei rotierenden konaxialen Zylindern. *Ing. Arch.*, **4**, 577–595.

White, F. M. 1991. *Fluid Mechanics*. McGraw-Hill, New York.

Wilcox, D. E. 1950. Turbulence in high speed journal bearings. *ASME Trans., Ser. F*, **72**, 825–834.

Zandbergen, P. J. and Dijkstra, D. 1987. Von Karman swirling flows. *Annual Rev. Fluid Mech.*, **19**, 465–492.

Zienkiewicz, O. C. and Woo, J. 1991. Incompressibility without tears: how to avoid restrictions of mixed formulation. *Internal. J. Numer. Methods Eng.*, **32**, 1189–1203.

Turbulence

Instability of laminar flow leads to flow transition and, on further increase of the Reynolds number, to eventual turbulence. The object of this chapter is to investigate bearing performance under turbulent conditions.

In journal bearings, turbulence makes its first appearance at Re $\approx$ 2000 (DiPrima, 1963).[1] Opinions on the minimum value of the Reynolds number for turbulence in thrust bearings are somewhat divided, but here again the value Re $\approx$ 2000 seems acceptable (Frêne, 1977). Once turbulence has set in, the importance of the precise mechanism of the instability and of the transition that resulted in turbulence diminishes. Nevertheless, some authorities maintain that if turbulence was obtained by spectral evolution, then the cellular flow pattern will persist into turbulence and affect the velocity profile-shear stress relationship (Burton and Carper, 1967). Existing theories of turbulence do not account for such occurrences; nevertheless, they show substantial agreement with experimental data from near-isothermal bearing experiments.

7.1 Equations of Turbulent Motion

Turbulence is an irregular fluid motion in which the various flow properties, such as velocity and pressure, show random variation with time and with position. Because of this randomness the instantaneous value of a flow property has little practical significance, it is the average value of that property that is of engineering interest.

To make our ideas precise, we represent a dependent variable by the sum of its average (denoted by an uppercase letter and an overbar) and its fluctuating component (denoted by a lowercase letter and a prime), so that

$$p = \bar{P} + p' \qquad v_i = \bar{V}_i + v_i' \qquad i = 1, 2, 3. \tag{7.1}$$

The average value, say $\bar{U} \equiv \bar{V}_1$ of the velocity component $u \equiv v_1$, is interpreted as a time average and is calculated according to

$$\bar{U}(T) = \frac{1}{T}\int_0^T u\,(t+\tau)\,d\tau \quad T_1 \le T \le T_2. \tag{7.2a}$$

Here T_1 is the time scale of turbulence (time scale of largest eddies in the flow) and T_2 is the time scale of "slow" variations of the flow that, because of their relative slowness, do not appropriately belong to turbulence.

In turbulence theory (Monin and Yaglom, 1973), $\bar{U}$ represents the stochastic average of u; that is, the average of a large number of ostensibly identical experiments. If $u(t)$ is

[1] This value seems to hold for isothermal bearing operations only. Strong thermal effects may lower the critical value of the Reynolds number considerably (Li, 1977; Gardner and Ulschmid, 1974).

a stationary random function of time, i.e., its mean value is constant and its correlation function depends only on the difference $\tau = (t_2 - t_1)$, then it can be proved that

$$\bar{U} = \lim_{T\to\infty} \frac{1}{T} \int_0^T u(t)\, dt,$$

provided that

$$\lim_{T\to\infty} \frac{1}{T} \int_0^T B(\tau)\, d\tau = 0.$$

This last condition on the integral of the correlation function $B(\tau) = \overline{u'(t)u'(t+\tau)}$ is easily satisfied in turbulence, since the velocities at distant (in either time or space) points are uncorrelated, leading to $B(\tau) \to 0$ as $\tau \to \infty$.

If the turbulence is homogeneous, say in the x direction, then we have correspondence between the stochastic average and the space average taken along x, according to

$$U = \lim_{X\to\infty} \frac{1}{X} \int_0^X u(x)\, dx. \tag{7.2b}$$

Although actual turbulent flows are in general, neither stationary nor homogeneous, averaging is defined according to the approximate formulas of Eq. (7.2).

When Eq. (7.1) is substituted into the Navier-Stokes equation, we obtain

$$\rho \left[\frac{\partial(\bar{V}_i + v_i')}{\partial t} + (\bar{V}_k + v_k') \frac{\partial(\bar{V}_i + v_i')}{\partial x_k} \right] = -\frac{\partial(\bar{P} + p')}{\partial x_i} + \frac{\partial}{\partial x_j}[2\mu(\bar{D}_{ij} + d_{ij}')]. \tag{7.3}$$

Here $\bar{D}_{ij} = \frac{1}{2}(\partial \bar{V}_i/\partial x_j + \partial \bar{V}_j/\partial x_i)$ and $d_{ij}' = \frac{1}{2}(\partial v_i'/\partial x_j + \partial v_j'/\partial x_i)$ are the stretching tensors for the mean motion and the fluctuation, respectively.

Our aim is to derive equations of motion for mean values. To this end, we average Eq. (7.3) according to the rules

$$\overline{f+g} = \bar{f} + \bar{g}, \tag{7.4a}$$

$$\overline{af} = a\bar{f} \quad a = \text{const.}, \tag{7.4b}$$

$$\overline{\lim_{n\to\infty} f_n} = \lim_{n\to\infty} \bar{f}_n, \tag{7.4c}$$

$$\overline{\bar{f}g} = \overline{fg} \tag{7.4d}$$

first established by Reynolds. Averaging leads to

$$\rho \left[\frac{\partial \bar{V}_i}{\partial t} + \bar{V}_k \frac{\partial \bar{V}_i}{\partial x_k} \right] = \frac{\partial \bar{P}}{\partial x_i} + \frac{\partial}{\partial x_j}(2\mu \bar{D}_{ij}) - \rho \overline{v_j' \frac{\partial v_i'}{\partial x_j}}. \tag{7.5}$$

The averaged equation of motion, Eq. (7.5), can be put into a more convenient form with the aid of the continuity equation for the fluctuation, which is derived below.

Substitution into the equation of continuity [Eq. (2.16c)] in terms of mean and fluctuating components gives

$$\frac{\partial \bar{V}_i}{\partial x_i} + \frac{\partial v_i'}{\partial x_i} = 0. \tag{7.6}$$

Taking the average value of this equation in accordance with Eqs. (7.4) leads to the equation of continuity for the mean flow. By subtracting the mean flow continuity equation from

Eq. (7.6), we obtain the continuity equation for the fluctuation. That is, for the mean motion and the fluctuation we have, respectively,

$$\frac{\partial \bar{V}_i}{\partial x_i} = 0, \tag{7.7a}$$

$$\frac{\partial v_i'}{\partial x_i} = 0. \tag{7.7b}$$

Equation (7.7b) is now used to put the last term of Eq. (7.5) into the desired form:

$$\overline{v_j' \frac{\partial v_i'}{\partial x_j}} = \frac{\partial}{\partial x_j}\overline{(v_i' v_j')},$$

so that Eq. (7.5) now reads

$$\rho\left[\frac{\partial \bar{V}_i}{\partial t} + \bar{V}_k \frac{\partial \bar{V}_i}{\partial x_k}\right] = \frac{\partial}{\partial x_j}(-\bar{P}\delta_{ij} + 2\mu \bar{D}_{ij} - \rho\overline{v_i' v_j'}). \tag{7.8}$$

The term in parentheses on the right-hand side is the average stress tensor in turbulent flow,

$$\bar{T}_{ij} = -\bar{P}\delta_{ij} + 2\mu \bar{D}_{ij} - \rho\overline{v_i' v_j'}. \tag{7.9}$$

The stress tensor $\bar{T}_{ij}$ is, thus, the sum of contributions from the mean flow $-\bar{P}\delta_{ij} + 2\mu \bar{D}_{ij}$ and contributions from the turbulence fluctuation,

$$\tau_{ij} = \rho\overline{v_i' v_j'}. \tag{7.10}$$

The latter is called the apparent (or Reynolds) stress tensor.[2] Its components are unknown variables in Eq. (7.8). For physical origin of τ_{ij} see Schlichting (1968).

The system consisting of the equations of motion [Eqs. (2.41b)], the equation of continuity [Eq. (2.44b)], and the appropriate boundary and initial conditions defines a mathematically well-posed problem for laminar flow, which, at least in theory, can be solved to obtain the four unknowns v_1, v_2, v_3 and p. The number of equations in the system available to characterize the mean flow remains the same as the flow becomes turbulent, the system now consisting of the mean flow equations of motion, Eq. (7.8), and of continuity, Eq. (7.7a), and the boundary and initial conditions; yet the number of unknowns has increased to 10. (The Reynolds stress tensor is symmetric and has, therefore, only six independent components.)

In turbulent flow, we thus have only four equations from which to determine 10 unknowns. As there does not seem to be any possibility of deriving additional equations on purely theoretical grounds, we are forced into (1) making assumptions concerning the character of the flow and (2) considering experimental data, when wishing to close the turbulence problem. This predicament gives rise to the so-called phenomenological or semi-empirical models of turbulence.

[2] In laminar flow $\bar{P} = p$ and $\bar{V}_i = v_i$ so that $-\rho\overline{v_i' v_j'} \equiv 0$, and we recover from Eq. (7.9) $T_{ij} = -\rho\delta_{ij} + 2\mu D_{ij}$, the constitutive equation for a Newtonian fluid.

It is, of course, possible to derive transport equations for components of the Reynolds stress tensor (Hinze, 1975). These transport equations have the form

$$\frac{D}{Dt}\overline{(v_i'v_j')} = -\left(\overline{v_j'v_k'}\frac{\partial \bar{V}_i}{\partial x_k} + \overline{v_i'v_k'}\frac{\partial \bar{V}_j}{\partial x_k}\right) - 2\nu\overline{\frac{\partial v_i'}{\partial x_k}\frac{\partial v_j'}{\partial x_k}} + \overline{\frac{p'}{\rho}\left(\frac{\partial v_j'}{\partial x_j} + \frac{\partial v_j'}{\partial x_i}\right)}$$
$$-\frac{\partial}{\partial x_k}\left(\overline{v_i'v_j'v_k'} - \nu\overline{\frac{\partial v_i'v_j'}{\partial x_k}} + \overline{\frac{p'}{\rho}(\delta_{jk}v_j' + \delta_{ik}v_j')}\right). \tag{7.11}$$

Inclusion of the six additional equations in our system of governing equations is of no help with the closure problem as we have acquired 10 additional unknowns in the process: the 10 independent components of the third-order correlation tensor $T_{ijk} = \overline{v_i'v_j'v_k'}$. The closure problem is not peculiar to turbulence, it is common to all nonlinear stochastic processes.

A number of models of turbulence have been proposed, each one designed to supply additional equations. They range from the simple, such as the constant eddy viscosity hypothesis of Boussinesq, to the sophisticated, exemplified by the 28-equation model of Kolovandin (Ng and Spalding, 1972).

Before we discuss the various mathematical models of turbulence and examine how they may be applied to the turbulent flow of a lubricant in the clearance space of a bearing, we reduce the equations of motion by taking into account the simplifying features of the lubricant film geometry.

Let L_{xz}, L_y represent the characteristic dimensions of the film as in Figure 2.7, and let U^* be the characteristic velocity in the "plane" of the film. Normalized variables are defined as follows (c.f., Eq. (2.58)):

$$(X,\ Y,\ Z) = \frac{1}{L_{xz}}\left(x,\ \frac{1}{\varepsilon}y,\ z\right), \qquad T = \left(\frac{U^*}{L_{xz}}\right)t$$
$$(U,\ V,\ W) = \frac{1}{U^*}\left(\overline{U},\ \frac{1}{\varepsilon}\overline{V},\ \overline{W}\right), \qquad (u,\ v,\ w) = \frac{1}{v^*}(u',\ v',\ w'), \tag{7.12}$$
$$P = \frac{\mathrm{R}_\varepsilon}{\rho U^{*2}}\overline{P}, \qquad \mathrm{R}_\varepsilon = \varepsilon\mathrm{Re}, \qquad \mathrm{Re} = \frac{\rho L_y U^*}{\mu}, \qquad \varepsilon = \frac{L_y}{L_{xz}}.$$

Here we assumed that the various fluctuating components of the velocity are all of the same order of magnitude, $\approx O(v^*)$.

Substituting Eq. (7.12) into Eq. (7.8), rearranging and setting $\kappa = (u^*/U^*)^2$ yields

$$\mathrm{R}_\varepsilon\left[\frac{dU}{dT} + \kappa\left(\frac{\partial\overline{uu}}{\partial X} + \frac{\partial\overline{uw}}{\partial Z}\right)\right] + \kappa\mathrm{Re}\frac{\partial\overline{uv}}{\partial Y} = -\frac{\partial P}{\partial X} + \frac{\partial^2 U}{\partial Y^2} + \varepsilon^2\left(\frac{\partial^2 U}{\partial X^2} + \frac{\partial^2 U}{\partial Z^2}\right) \tag{7.13a}$$

$$\varepsilon^2\left[\mathrm{R}_\varepsilon\frac{dV}{dT} - \frac{\partial^2 V}{\partial Y^2} - \varepsilon^2\left(\frac{\partial^2 V}{\partial X^2} + \frac{\partial^2 V}{\partial Z^2}\right)\right] = -\frac{\partial P}{\partial Y} - \kappa\mathrm{R}_\varepsilon\left[\frac{\partial\overline{uv}}{\partial Y} + \varepsilon\left(\frac{\partial\overline{vu}}{\partial X} + \frac{\partial\overline{vw}}{\partial Z}\right)\right] \tag{7.13b}$$

$$\mathrm{R}_\varepsilon\left[\frac{dW}{dT} + \kappa\left(\frac{\partial\overline{wu}}{\partial x} + \frac{\partial\overline{ww}}{\partial z}\right)\right] + \kappa\mathrm{Re}\frac{\partial\overline{vw}}{\partial Y} = -\frac{\partial P}{\partial Z} + \frac{\partial^2 W}{\partial Y^2} + \varepsilon^2\left(\frac{\partial^2 W}{\partial X^2} + \frac{\partial^2 W}{\partial Z^2}\right) \tag{7.13c}$$

Here

$$\frac{d}{dT} = \frac{\partial}{\partial T} + U\frac{\partial}{\partial X} + V\frac{\partial}{\partial Y} + W\frac{\partial}{\partial Z}$$

symbolizes (dimensionless) material derivative based on mean velocity.

In the spirit of the thin-film analysis of Chapter 2, we now delete terms in (7.17) that are multiplied by powers of ε

$$\mathrm{R}_\varepsilon\left[\frac{dU}{dT} + \kappa\left(\frac{\partial\overline{uu}}{\partial X} + \frac{\partial\overline{uw}}{\partial Z}\right)\right] + \kappa\mathrm{Re}\frac{\partial\overline{uv}}{\partial Y} = -\frac{\partial P}{\partial X} + \frac{\partial^2 U}{\partial Y^2} \tag{7.14a}$$

$$\kappa\mathrm{R}_\varepsilon\frac{\partial\overline{uv}}{\partial Y} = -\frac{\partial P}{\partial Y} \tag{7.14b}$$

$$\mathrm{R}_\varepsilon\left[\frac{dW}{dT} + \kappa\left(\frac{\partial\overline{wu}}{\partial X} + \frac{\partial\overline{ww}}{\partial Z}\right)\right] + \kappa\mathrm{Re}\frac{\partial\overline{vw}}{\partial Y} = -\frac{\partial P}{\partial Z} + \frac{\partial^2 W}{\partial Y^2} \tag{7.14c}$$

(1) Assuming now that $\kappa \approx 0(1)$, a condition that has been shown to exist in wake flow (Hinze, 1979) but, in effect, has been applied to wall bounded thin-film flows by the early researchers of the subject, leads us to

$$\mathrm{R}_\varepsilon\left(\frac{dU}{dT} + \frac{\partial\overline{uu}}{\partial X} + \frac{\partial\overline{uw}}{\partial Z}\right) = -\frac{\partial P}{\partial X} + \frac{\partial^2 U}{\partial Y^2} - \mathrm{Re}\frac{\partial\overline{uv}}{\partial Y} \tag{7.15a}$$

$$\mathrm{R}_\varepsilon\frac{\partial\overline{uv}}{\partial Y} = -\frac{\partial P}{\partial Y} \tag{7.15b}$$

$$\mathrm{R}_\varepsilon\left(\frac{dW}{dT} + \frac{\partial\overline{wu}}{\partial X} + \frac{\partial\overline{ww}}{\partial Z}\right) = -\frac{\partial P}{\partial Z} + \frac{\partial^2 W}{\partial Y^2} - \mathrm{Re}\frac{\partial\overline{vw}}{\partial Y} \tag{7.15c}$$

These equations can be combined into a single, Reynolds-type equation in pressure only if the Reynolds number is constrained, $\mathrm{Re} < \varepsilon^{-1}$, in which case we are lead to

$$\frac{\partial\bar{P}}{\partial X} = \frac{\partial}{\partial y}\left(\mu\frac{\partial\bar{U}}{\partial y} - \rho\overline{u'v'}\right), \tag{7.16a}$$

$$\frac{\partial\bar{P}}{\partial Y} = 0, \tag{7.16b}$$

$$\frac{\partial\bar{P}}{\partial Z} = \frac{\partial}{\partial y}\left(\mu\frac{\partial\bar{W}}{\partial y} - \rho\overline{v'w'}\right). \tag{7.16c}$$

(2) When the cross section presented to the flow changes more rapidly, thus violating the small slope assumption locally, the flow is definitely under strong influence from the bounding walls. In such cases, it seems prudent to assume that $\kappa \approx 0(\varepsilon)$, a condition that has been shown to exist in channel flow (Hinze, 1979). Under these conditions the

turbulent film equations that apply are

$$\frac{\partial \bar{P}}{\partial X} = \frac{\partial}{\partial y}\left(\mu \frac{\partial \bar{U}}{\partial Y} - \rho \overline{u'v'}\right) + \rho \frac{d\bar{U}}{dt}, \tag{7.17a}$$

$$\frac{\partial \bar{P}}{\partial Y} = 0, \tag{7.17b}$$

$$\frac{\partial \bar{P}}{\partial Z} = \frac{\partial}{\partial y}\left(\mu \frac{\partial \bar{W}}{\partial Y} - \rho \overline{w'v'}\right) + \rho \frac{d\bar{W}}{dt}. \tag{7.17c}$$

According to this second analysis, mean-flow inertia is of the same order of magnitude as the surviving Reynolds stresses and both quantities should be taken into account.

In neither of the above two cases is the physics of turbulence well represented by a Reynolds-type equation. Nevertheless, we follow accepted practice in this chapter and consider (7.16) to be valid between smooth walls.

To calculate bearing performance under turbulent conditions, several researchers, (Constantinescu, 1962; Ng and Pan, 1965; Elrod and Ng, 1967) employ Eqs. (7.16), resorting to the more acceptable model of Eqs. (7.17) only when specifically investigating lubricant inertia effects (Constantinescu and Galetuse, 1979; Landau and Leschziner, 1978).

The earliest turbulent lubrication models employed equation Eqs. (7.16) and the ideas of (1) mixing length (Constantinescu, 1959), (2) eddy viscosity (Ng and Pan, 1965; Elrod and Ng, 1967), and (3) empirical drag laws (Hirs, 1973; Black and Walton, 1974). Closure is obtained in these models by relating the Reynolds stress to the mean flow characteristics. Such representations, when used in conjunction with Eqs. (7.16), can lead to relationships between the mean velocity and the mean pressure gradient. To obtain the governing equation for pressure, the mean velocity, now in terms of the mean pressure, is substituted into the equation of continuity in a development that parallels the laminar flow case. Several of the available models yield a formally identical turbulent Reynolds equation of the form

$$\frac{\partial}{\partial x}\left(\frac{h^3}{\mu k_x}\frac{\partial \bar{P}}{\partial x}\right) + \frac{\partial}{\partial z}\left(\frac{h^3}{\mu k_z}\frac{\partial \bar{P}}{\partial z}\right) = \frac{1}{2}U_0 \frac{\partial h}{\partial x}. \tag{7.18}$$

Here $k_x = k_x(R_h)$ and $k_z = k_z(R_h)$, where $R_h = U_* h/\nu$ is the local Reynolds number, thus in these formulations turbulence is accounted for by weighting the film thickness with some function of R_h. Since $k_x, k_z \geq 12$, the equality holding for laminar flow, the apparent film thickness, $h/{k_x}^{1/3}$, $h/{k_z}^{1/3}$, employed in performance calculations is smaller than the geometric film thickness, h, therefore, turbulent conditions yield higher pressures, for the same film geometry, than do laminar conditions. Most turbulence models are in agreement with this conclusion, it is in the actual form of the turbulence functions $k_x(x, z; \mathrm{Re})$, $k_z(x, z; \mathrm{Re})$ where they differ (see Figure 7.4). But the difference in performance predictions between the various models is often insignificant, except perhaps at extreme conditions such as high eccentricity in a journal bearing.

7.2 Turbulence Models

Perhaps the first attempt to provide a mathematical model of turbulence was made by Boussinesq in 1877, when he proposed a relation between the Reynolds stresses and the

mean velocity gradient in the form

$$\tau_{ij} = -\rho\overline{v_i' v_j'} = \rho\varepsilon_m \left(\frac{\partial \bar{V}_i}{\partial x_j} + \frac{\partial \bar{V}_j}{\partial x_i} \right), \tag{7.19}$$

so that the mean stress in the fluid is given by

$$\bar{T}_{ij} = -\bar{P}\delta_{ij} + \mu \left(1 + \frac{\varepsilon_m}{\nu}\right) \left(\frac{\partial \bar{V}_i}{\partial x_j} + \frac{\partial \bar{V}_j}{\partial x_j} \right). \tag{7.20}$$

Equation (7.20) is analogous to the constitutive equation of Stokes for laminar flow, except that, unlike the molecular viscosity μ, the eddy viscosity ε_m is not a material constant.

The eddy viscosity, ε_m, depends on the structure of turbulence itself. Therefore, to complete the model of Boussinesq, ε_m has to be related to measurable quantities of the turbulent flow. Workers in the field of turbulence who use Boussinesq's model, Eq. (7.20), accomplish this in various ways.

Prandtl (1963) reasoned that the eddy viscosity is given by

$$\varepsilon_m = \ell^2 \left| \frac{\partial \bar{U}}{\partial y} \right| \tag{7.21}$$

when dealing with a two-dimensional mean flow along the solid wall, which is located at $y = 0$. In Prandtl's theory, the mixing length, ℓ, is analogous to the mean free path of the kinetic theory of gases. (It is shown in the kinetic theory of gases that if v_m is the rms. molecular velocity and ℓ is the mean free path between collisions, then $\mu \sim \rho v_m \ell$, where μ is the molecular viscosity.) To illustrate the analogy, without actually considering details, we follow Prandtl and consider a two-dimensional mean flow that is parallel to the $y = 0$ plane (a solid wall) so that

$$\bar{U} = \bar{U}(y) \qquad \bar{V} = \bar{W} = 0.$$

Although turbulence is three dimensional, we focus attention on only one Reynolds stress component $-\rho\overline{u'v'}$ and write, in accordance with Eq. (7.19), the approximation

$$\tau_{xy} \approx -\rho\overline{u'v'} = \rho\varepsilon_m \frac{d\bar{U}}{dy}. \tag{7.22}$$

Here we neglected the viscous stress, so Eq. (7.22) is not valid in regions where viscous effects are of the same order of magnitude as turbulence effects.

To have dimensional homogeneity in Eq. (7.22), the eddy viscosity, ε_m, must have the physical dimensions of (length^2)/(time). This requirement is satisfied when, in analogy to the kinetic theory, we choose ε_m to be represented by the product of a characteristic length and a characteristic velocity. The length parameter is selected in such a way that it permits the local friction velocity

$$v_* = \sqrt{|\tau_{xy}|/\rho}$$

to be used as the velocity parameter. Thus we have, by definition,

$$\varepsilon_m = \ell \times v_* \qquad \text{and} \qquad |\tau_{xy}| = \rho v_*^2.$$

Substitution for ε_m into Eq. (7.22) yields

$$|\tau_{xy}| = \rho v_*^2 = \rho\varepsilon_m \frac{d\bar{U}}{dy} = \rho(\ell \times v_*) \frac{d\bar{U}}{dy}.$$

By comparison of the second and last terms we arrive at Eq. (7.21), so that

$$\tau_{xy} = -\rho\overline{u'v'} = \rho\ell^2 \left|\frac{d\bar{U}}{dy}\right| \frac{d\bar{U}}{dy}. \tag{7.23}$$

[Note that the absolute sign in Eqs. (7.21) and (7.23) was introduced to ensure that $\varepsilon_m \geq 0$ whatever the sign of $d\bar{U}/dy$.]

In a simple application of the theory, where there is only one characteristic dimension associated with the problem (e.g., the distance from the wall in channel flow or the width of the turbulent mixing zone in jets and wakes), we may assume proportionality between this characteristic dimension and the mixing length ℓ.

The velocity profile that may be obtained from Eq. (7.23) by integration is not valid at the wall. There, in the so-called viscous sublayer, we have $\mu|d\bar{U}/dy| \gg \rho|\overline{u'v'}|$, and the velocity profile is determined as

$$\tau_w = \mu \frac{d\bar{U}}{dy}, \tag{7.24}$$

where τ_w is the wall stress.

In an application to boundary-layer flows, Prandtl integrated Eq. (7.23) within the constant stress layer; that is, in the layer outside the viscous sublayer that is still close enough to the wall so that the condition $\tau_{xy} = \tau_w$ is approximately satisfied. Within this layer, as the only length parameter is the distance from the wall, Prandtl assumed that

$$\ell = \kappa y, \tag{7.25}$$

where κ is a dimensionless constant that must be deduced from experiment.

When Eq. (7.25) and $\tau_{xy} \approx \tau_w$ are substituted into Eq. (7.23) and the latter is integrated, we obtain

$$\bar{U} = \frac{v_*}{\kappa} \ln\, y + C. \tag{7.26}$$

The integration constant C can be determined in either of two ways.

First, by fixing attention on the layer $y = y_0$ ($y_0 = h/2$ in channel flow and $y_0 = \delta$ in the boundary layer, where δ is the boundary-layer thickness), where the velocity, $\bar{U}$, is equal to its maximum value U_0, we have from Eq. (7.26)

$$U_0 = \frac{v_*}{\kappa} \ln\, y_0 + C. \tag{7.27}$$

The integration constant C can now be eliminated between the last two equations, and we obtain a particular form of the velocity defect law,

$$U_0^+ - \bar{U}^+ = \frac{1}{\kappa} \ln \frac{y_0}{y}, \tag{7.28}$$

that is valid within the constant stress layer. Here we used the notation $U_0^+ = U_0/v_*$ and $\bar{U}^+ = \bar{U}/v_*$. Experimental verification of the velocity defect law is given in Figure 7.1.

Alternatively, the constant C in Eq. (7.26) may be determined from the condition that the turbulent velocity distribution of Eq. (7.23) must join onto the velocity of the viscous sublayer of Eq. (7.26) somewhere in the vicinity of the wall. Thus, the condition on the velocity distribution in Eq. (7.26) is $\bar{U} = 0$ at $y = y_L$. The thickness of the viscous sublayer

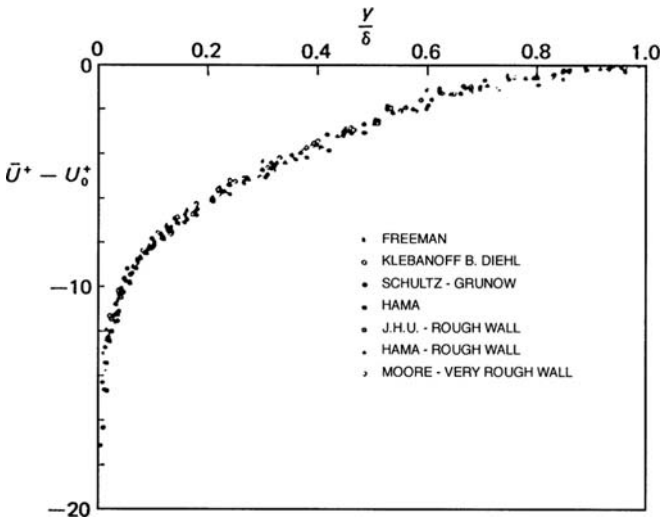

Figure 7.1. Experimental verification of the velocity defect law, Eq. (5.34). (Reprinted with permission from Clauser, F. H. The turbulent boundary layer. *Adv. Appl. Mech.*, **4**, 1–51, 1965.)

y_L is determined by conditions at the (smooth) wall, characterized by $v_* = \sqrt{\tau_w/\rho}$ and by the kinematic viscosity ν. Then, by dimensional reasoning, we must have

$$y_L = \beta \frac{\nu}{v_*}, \quad y_L^+ = \beta. \tag{7.29}$$

Substituting into Eq. (7.26), we find

$$\bar{U}^+ = \frac{1}{\kappa}(\ln\ y^+ - \ln \beta). \tag{7.30}$$

This is Prandtl's universal logarithmic distribution. Here $y^+ = y v_*/\nu$ is the dimensionless distance from the wall, and the constant β depends on the nature of the wall surface.

In Eqs. (7.28) and (7.30), we found two universal velocity distribution laws. When these are written in the more general form,

$$U_0^+ - \bar{U}^+ = f(\hat{y}) \qquad \hat{y} = \frac{y}{y_0} \tag{7.31}$$

and

$$\bar{U}^+ = F(y^+) \qquad y^+ = \frac{y v_*}{\nu}, \tag{7.32}$$

they are known as the velocity defect law and the law of the wall, respectively.[3] Experimental verification of the law of the wall is shown in Figure 7.2.

The law of the wall, Eq. (7.32), is valid in the wall region, which comprises the viscous sublayer adjacent to the wall, the constant stress layer farther out in the fully turbulent region, and the buffer zone separating the two. The logarithmic velocity distribution of

[3]The velocity defect law, Eq. (7.31), and the law of the wall, Eq. (7.32), can be arrived at on purely dimensional grounds. Then, the requirement that there must be a region of overlap where both equations are valid leads to the logarithmic laws, Eqs. (7.28) and (7.30), without use of the mixing length theory. For details of this more appealing approach see Townsend (1977) and Hinze (1975).

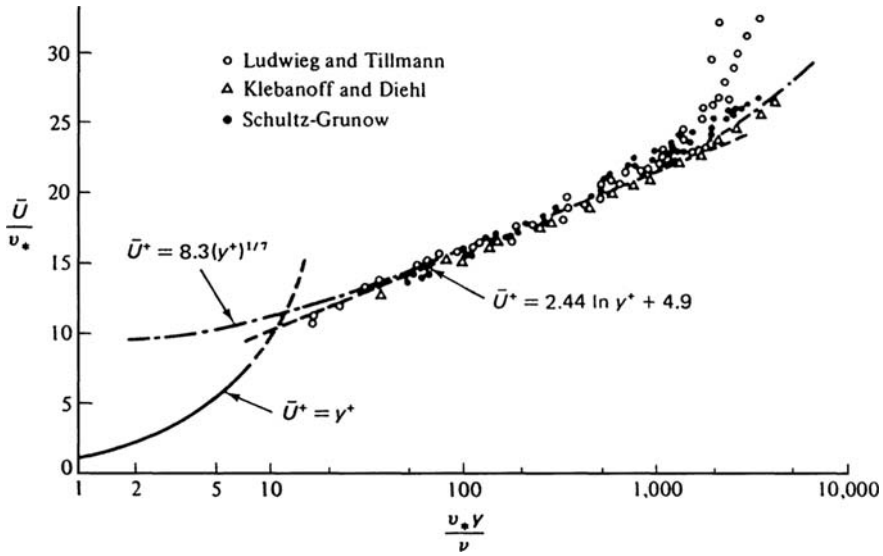

Figure 7.2. Experimental verification of the law of the wall, Eq. (5.32). (Reprinted with permission from Hinze, J. O. *Turbulence*, 2nd ed. McGraw-Hill, New York. Copyright 1975.)

Prandtl, Eq. (7.30), which is Prandtl's simplified version of the law of the wall, does not account for the buffer zone but joins the velocity profile of the constant stress layer abruptly to the velocity profile of the viscous sublayer.

Much effort has been directed toward making Boussinesq's hypothesis, Eq. (7.19), applicable in the whole wall layer by providing a universal eddy viscosity profile there. It was shown by Reichardt and later by Elrod (Hinze, 1975) that such an eddy viscosity distribution must satisfy two requirements:

$$\begin{aligned} \lim_{y^+ \to 0} \frac{\varepsilon_m}{\nu} &= \text{const.} \times (y^+)^3, \\ \lim_{y^+ \to \infty} \frac{\varepsilon_m}{\nu} &= \text{const.} \times (y^+). \end{aligned} \tag{7.33}$$

The second condition is necessary to have agreement with Eq. (7.26), and the first follows from the equation of continuity when there is streamwise variation of the mean values.

One of the more successful eddy viscosity profiles was devised by Reichardt (Monin and Yaglom, 1973). His eddy viscosity

$$\frac{\varepsilon_m}{\nu} = k \left(y^+ - \delta_l^+ \tanh \frac{y^+}{\delta_\ell^+} \right), \tag{7.34}$$

where k and δ_ℓ^+ are constants, δ_ℓ^+ being related to the thickness of the viscous sublayer, satisfies the two conditions of Eq. (7.33) and is in good agreement with experimental data.

In the Kolmogoroff-Prandtl energy model, it is assumed that the eddy viscosity can be represented as the product of two characteristic quantities of turbulence

$$\varepsilon_m = A \left(\frac{\overline{q^2}}{2} \right)^{1/2} \Lambda, \tag{7.35}$$

where A is a numerical constant, $\overline{q^2}/2 = \overline{v_i' v_i'}/2$ is the kinetic energy of the turbulent fluctuation per unit mass, and Λ is an integral length scale.

The length scale Λ in Eq. (7.35) may be made proportional to the characteristic dimension of the problem, as suggested by Prandtl. In the analysis of flow near a wall, Wolfshtein (1969) employed the modified van Driest formula (Hinze, 1975)

$$\Lambda = y\left(1 - e^{-\Lambda_\eta \mathrm{Re}_q}\right), \tag{7.36}$$

where A_η is a constant and $\mathrm{Re}_q = y\sqrt{\overline{q^2}}/2\nu$ is a local Reynolds number. Ng and Spalding (1972), in contrast, recommended that Λ be calculated from a transport equation.

The turbulent kinetic energy for use in Eq. (7.36) is given by a transport equation, which is obtained from Eq. (7.11) by contraction:

$$\frac{D}{Dt}\left(\frac{\overline{q^2}}{2}\right) = -\frac{\partial}{\partial x_i}\overline{v_i'\left(\frac{p'}{\rho} + \frac{q^2}{2}\right)} - \overline{v_i' v_j'}\frac{\partial \bar{V}_j}{\partial x_i} + 2\nu\frac{\partial}{\partial x_i}\overline{v_j' d_{ij}'} - \varepsilon. \tag{7.37}$$

The terms on the right-hand side of Eq. (7.37) represent (1) the convective diffusion by turbulence of the total turbulence energy, (2) the rate of production of turbulence, (3) the work by the viscous shear stresses of the turbulent motion, and (4) the rate of viscous dissipation of turbulent energy

$$\begin{aligned} \varepsilon &= 2\nu\overline{d_{ij}' d_{ij}'} \\ &= \nu\overline{\left(\frac{\partial v_i'}{\partial x_j} + \frac{\partial v_j'}{\partial x_i}\right)\frac{\partial v_i'}{\partial x_j}}. \end{aligned} \tag{7.38}$$

In internal flows subject to a strong favorable pressure gradient, Jones and Launder (1972) put $\varepsilon \sim (\overline{q^2})^{3/2}/\Lambda$ in Eq. (7.35), so that their eddy viscosity is given by

$$\varepsilon_m = C\frac{(\overline{q^2})^2}{4\varepsilon} \tag{7.39}$$

and ε is calculated from a transport equation (Hinze, 1975).

7.3 Constantinescu's Model

The approach in Constantinescu's turbulent lubrication model (Constantinescu, 1959) is based on the Prandtl mixing length hypothesis, Eq. (7.21). Following Prandtl's ideas, the mixing length is made to vanish at the walls and to vary linearly with the distance from the nearest wall:

$$\left.\begin{aligned} \ell &= ky \qquad 0 \le y \le \frac{h}{2} \\ \ell &= ky' \qquad 0 \le y' \le \frac{h}{2} \end{aligned}\right\}, \tag{7.40}$$

where $y' = h - y$. Substituting for ℓ from Eq. (7.40) and for $-\overline{\rho u'v'}$ from Eq. (7.23) into Eq. (7.15a), the equation of turbulent motion in a long bearing ($\partial \bar{P}/\partial z = 0,\ \bar{W} = 0$) is obtained. For $0 \le y \le h/2$ this equation has the nondimensional form

$$\frac{\partial}{\partial \hat{y}}\left(k^2 \hat{y}^2 R_h \left|\frac{\partial U}{\partial \hat{y}}\right| \frac{\partial U}{\partial \hat{y}} + \frac{\partial U}{\partial \hat{y}}\right) - \frac{h^2}{\mu U_*}\frac{\partial \bar{P}}{\partial x} = 0, \tag{7.41}$$

where $R_h = U_* h/\nu$ is the local Reynolds number and

$$\hat{y} = \frac{y}{h} \qquad U = \frac{\bar{U}}{U_*}.$$

$U_* = U_2$ is the velocity of the runner in the x direction relative to the stationary bearing surface ($U_1 = 0$).

Equation (7.41) may now be integrated,

$$A\hat{y}^2 \frac{\partial U}{\partial \hat{\hat{y}}}\left|\frac{\partial U}{\partial \hat{y}}\right| + \frac{\partial U}{\partial \hat{y}} + B\hat{y} - C = 0, \tag{7.42}$$

where we use the notation

$$A = k^2 R_h, \qquad B = -\frac{h^2}{\mu U_*}\frac{\partial \bar{P}}{\partial x}.$$

The integration constant, C, in Eq. (7.42) corresponds to the dimensionless wall stress [as $\hat{y} \to 0$, Eq. (7.42) reduces to $C = (\partial U/\partial \hat{y})|_{\hat{y}=0} = h\tau_w/\mu U_*$]. It may therefore take on positive, zero, or negative value. In addition, in the lubricant film we encounter (1) pressure flow in the direction of motion ($B > 0$), (2) pure shear flow ($B = 0$), and (3) pressure flow opposing shear flow ($B < 0$). The velocity gradient, $\partial U/\partial \hat{y}$, might take on positive or negative values. Thus, since all possible flow situations must be accounted for, Eq. (7.42) represents a total of $3 \times 3 \times 2 = 18$ distinct cases.

We can show, however, that not all 18 cases yield real and therefore physically possible velocity profiles. As an example, consider the following combination of the parameters:

$$C > 0; \quad B = -B' < 0; \quad \frac{\partial U}{\partial \hat{y}} < 0. \tag{7.43}$$

Equation (7.42) now assumes the form

$$A\hat{y}^2\left(\frac{\partial U}{\partial \hat{y}}\right)^2 - \frac{\partial U}{\partial \hat{y}} + B'\hat{y} + C = 0. \tag{7.44}$$

Solving formally for $\partial U/\partial \hat{y}$, we have

$$\frac{\partial U}{\partial \hat{y}} = \frac{1 \pm \sqrt{1 - 4A\hat{y}^2(B'\hat{y} + C)}}{2A\hat{y}^2}. \tag{7.45}$$

Equation (7.45) must satisfy two conditions simultaneously: (1) that $1 \ge 4A\ \hat{y}^2(B'\hat{y} + C)$, so that the solution is real, and (2) that $\partial U/\partial \hat{y} < 0$, so that the last condition in Eq. (7.43) is satisfied. This, of course, is not possible, leading to the conclusion that

Eq. (7.43) does not represent a possible flow in the bearing clearance. Physically acceptable solutions of Eq. (7.42) are obtained only in the following 10 cases:

	1	2	3	4	5	6	7	8	9	10
B	−	−	−	−	0	0	+	+	+	+
C	−	−	0	+	+	−	−	0	+	+
$\partial U/\partial \hat{y}$	−	+	+	+	+	−	−	−	−	+

Instead of integrating Eq. (7.42) rigorously in these 10 cases, Constantinescu chose to follow Prandtl and divided the flow regime $0 \le \hat{y} \le 1/2$ into two layers.

In the viscous sublayer $0 \le \hat{y} \le \hat{y}_L$ the effect of the Reynolds stress is negligible, and here we have

$$\frac{\partial U}{\partial \hat{y}} + B\hat{y} - C = 0, \tag{7.46}$$

whereas in the turbulent core the effect of molecular viscosity is small, and we take

$$A\hat{y}^2 \frac{\partial U}{\partial \hat{y}} \left| \frac{\partial U}{\partial \hat{y}} \right| + B\hat{y} - C = 0. \tag{7.47}$$

Equations (7.46) and (7.47) are to be solved simultaneously, with similar equations for the other half of the channel. These calculations will now be illustrated in one case, at the position of maximum film pressure. There the following conditions and approximate differential equations apply:

Sliding surface ($\hat{y}' = 0$), *case* 6

$B = 0$; $\quad C = -C' < 0$; $\quad \partial U/\partial \hat{y}' < 0$

$$\frac{\partial U}{\partial \hat{y}'} = -C' \qquad \text{viscous sublayer} \tag{7.48a}$$

$$A\hat{y}'^2 \left(\frac{\partial U}{\partial \hat{y}'} \right)^2 + C' = 0 \quad \text{turbulent core} \tag{7.48b}$$

Stationary surface ($\hat{y} = 0$), *case* 5

$B = 0$; $\quad C > 0$; $\quad \partial U/\partial \hat{y} > 0$

$$\frac{\partial U}{\partial \hat{y}} = C \quad \text{viscous sublayer} \tag{7.48c}$$

$$A\hat{y}^2 \left(\frac{\partial U}{\partial \hat{y}} \right)^2 - C = 0 \quad \text{turbulent core.} \tag{7.48d}$$

Integrating Eqs. (7.48a) to (7.48d), we obtain the following four-segment velocity profile:

$$U = \begin{cases} -C'\hat{y}' + K' & 0 \le \hat{y}' \le \hat{y}'_L \\ C'_2 - \sqrt{\dfrac{C'}{A}} \ln \hat{y}' & \hat{y}'_L \le \hat{y}' \le 0.5 \\ C_2 + \sqrt{\dfrac{C}{A}} \ln \hat{y} & \hat{y}_L \le \hat{y} \le 0.5 \\ C\hat{y} + K & 0 \le \hat{y} \le \hat{y}_L. \end{cases} \tag{7.49}$$

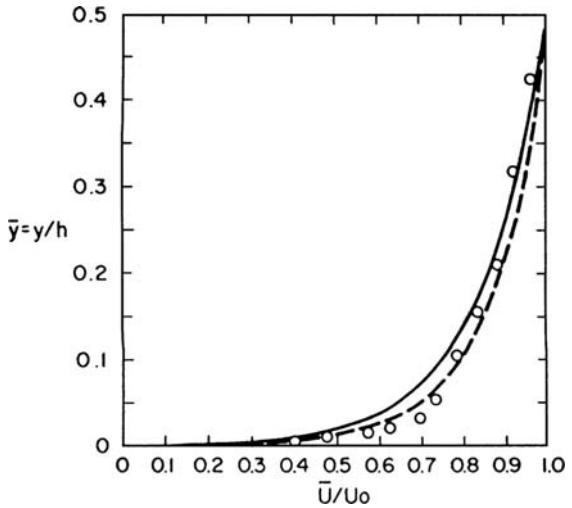

Figure 7.3. Velocity profile of plane Couette flow at Re = 40,000. Curves are theoretical predictions: (—) Constantinescu (1959), Eq. (7.50); (- - -) Elrod and Ng (1967). (○) experimental values of Robertson (1959).

The integration constants C, C', C_2, C_2', K, and K', the boundary-layer thickness $\hat{y}_L$ and $\hat{y}_L'$ can be evaluated by imposing the following conditions:

(1) No slip at the solid walls
(2) Continuity of both the velocity and the velocity gradient at the edge of viscous sublayers
(3) Continuity of both the velocity and the velocity gradient in the center of the channel.

Imposing these conditions on Eq. (7.49), we find that $\hat{y}_L = \hat{y}_L' = (CA)^{-1/2}$; that is, $y_L^+ = 1/k$ and

$$U = \begin{cases} 1 - C\hat{y}' & 0 \le \hat{y}' \le (CA)^{-1/2} \\ 1 - \sqrt{\dfrac{C}{A}}\left[1 + \ln\left(\hat{y}'\sqrt{CA}\right)\right] & (CA)^{-1/2} \le \hat{y}' \le 0.5 \\ \sqrt{\dfrac{C}{A}}\left[1 + \ln\left(\hat{y}\sqrt{CA}\right)\right] & (CA)^{-1/2} \le \hat{y} \le 0.5 \\ C\hat{y} & 0 \le \hat{y} \le (CA)^{-1/2} \end{cases} \tag{7.50}$$

Here the constant, C, is given by the transcendental equation

$$1 - \sqrt{\frac{C}{A}}\left(2 + \ln\frac{CA}{4}\right) = 0. \tag{7.51}$$

Equation (7.51) has the solution $C = 37.8097$ at $A = 6400$, or Re = 40,000 and $k = 0.4$. When this value of C is substituted into Eq. (7.50), the velocity distribution in pure Couette flow at Re = 40,000 is obtained according to Constantinescu's model (Figure 7.3). The shear stress is uniform across the channel and has the value $\tau/\rho U_*^2 = 37.8097/R_h$.

If the flow was laminar throughout the channel, the velocity distribution would be represented by the single equation

$$U = \frac{1}{2} B_x(\hat{y} - \hat{y}^2) + \hat{y} \tag{7.52}$$

and the average velocity U_m by

$$\begin{aligned} U_m &= \int_0^1 U d\hat{y} = U_{mp} + U_{ms} \\ &= \frac{1}{12} B_x + \frac{1}{2}. \end{aligned} \tag{7.53}$$

Here $U_{mp} = B_x/12$ is the average velocity of pressure flow and $U_{ms} = 1/2$ is the average velocity of shear flow. Thus, from Eq. (7.53) we find for laminar flow that

$$B_x = 12 U_{mp}. \tag{7.54}$$

That is, in the laminar regime the average velocity of pressure-induced flow varies linearly with the pressure parameter B_x.

For turbulent flow $\bar{U}_{ms} = 0.5$ again, and when values of U_{mp} are plotted against B_x for different values of the Reynolds number, the resulting plots can be described by the approximate relationship:

$$B_x \equiv -\frac{h^2}{\mu U_*} \frac{\partial \bar{P}}{\partial x} = k_x(R_h) U_{mp}. \tag{7.55}$$

An analysis, similar to the one above, yields the following relationship between axial pressure drop and average velocity of pressure flow in the same direction [the axial flow is decoupled from the circumferential flow in Constantinescu's analysis; for the Reynolds stress in Eq. (7.15c), he takes $-\rho\overline{v'w'} = \rho \ell^2 |\partial \bar{W}/\partial y| \partial \bar{W}/\partial y$]:

$$B_z \equiv -\frac{h^2}{\mu U_*} \frac{\partial \bar{P}}{\partial z} = k_z(R_h) W_{mp}, \tag{7.56}$$

where W_{mp} is the dimensionless average velocity of the axial pressure flow induced by B_z.

Via curve fitting, Constantinescu's analysis yields

$$k_x = 12 + 0.53(k^2 R_h)^{0.725}, \tag{7.57a}$$

$$k_z = 12 + 0.296(k^2 R_h)^{0.65}. \tag{7.57b}$$

Notice that for $\mathrm{Re} \to 0$, Eqs. (7.55) and (7.56) reduce to Eq. (7.54), i.e., laminar flow is included in Constantinescu's model. The variation of k_x and k_z with Re_h is shown in Figure 7.4.

Substituting $U_m = U_{mp} + U_{ms}$ and $W_m = W_{mp}$ into the once-integrated continuity equation,

$$\frac{\partial}{\partial x}(\bar{U}_m h) + \frac{\partial}{\partial z}(\bar{W}_m h) + \frac{1}{U_0} \frac{dh}{dt} = 0, \tag{7.58}$$

we obtain the differential equation that models the distribution of pressure in a turbulent lubricant film:

$$\frac{\partial}{\partial x}\left(\frac{h^3}{\mu k_x} \frac{\partial \bar{P}}{\partial x}\right) + \frac{\partial}{\partial z}\left(\frac{h^3}{\mu k_z} \frac{\partial \bar{P}}{\partial z}\right) = \frac{U_0}{2} \frac{\partial h}{\partial x} + V_0. \tag{7.59}$$

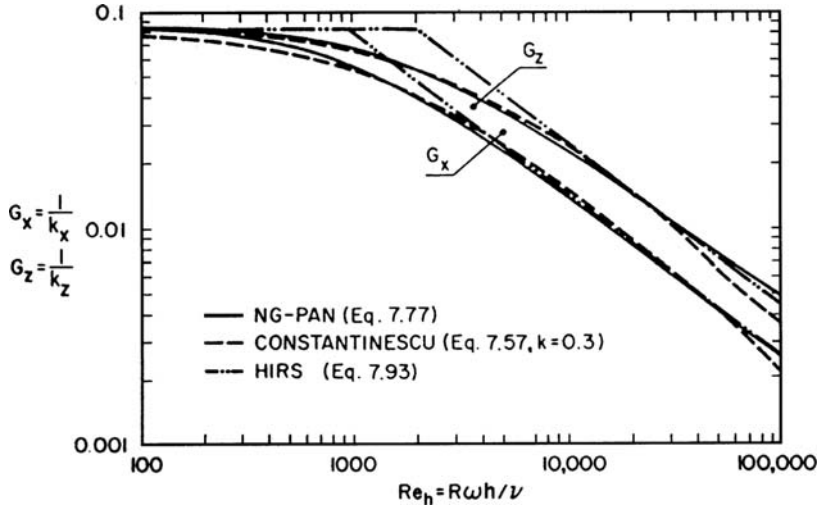

Figure 7.4. Variation of the turbulence functions G_x and G_z with Reynolds number. Comparison of various theories.

Here $-V_0 = V_1 - V_2$ is the squeeze velocity and $U_0 = U_2$, or U_1, depending on whether Eq. (7.59) is being used for a slider bearing or a journal bearing (see Section 2.2).

Arwas and Sternlicht (1963) found that in order to correlate theory with experiment, the empirical constant k in Eq. (7.40) must be a function of the Reynolds number and the eccentricity ratio. In later publications, Constantinescu himself recommended $k = 0.125\ \mathrm{Re}_h^{0.07}$.

Constantinescu's turbulent lubrication theory may be criticized on the following grounds:

(1) The change from viscous sublayer to turbulent core is abrupt (discontinuity in shear stress), no account is taken of the buffer zone.
(2) The predicted thickness of the viscous sublayer does not agree with experimental findings. (For pure shear flow, we obtained $y_L^+ = 1/k \approx 2.5$, whereas measurements give twice this value.)
(3) The linearization $B_x = k_x(\mathrm{Re})U_{mp}$ is inaccurate at large B (i.e., the theory is not applicable for externally pressurized bearings or for self-acting bearings at large eccentricity ratios).
(4) Turbulent Couette flow has $U_{mp} = 0$; thus, its representation is not possible by Eq. (7.55).
(5) Orthogonal flows are decoupled.

This criticism is, of course, not intended to detract from Constantinescu's seminal work in turbulent lubrication.

7.4 Ng-Pan-Elrod Model

In an effort to construct a turbulent lubrication model that is consistent with channel flow data, Ng (1964) investigated the applicability of Reichardt's eddy diffusivity

formulation, Eq. (7.34). For two-dimensional flow the Boussinesq hypothesis, Eq. (7.20), is

$$\frac{d\bar{U}^+}{dy^+} = \frac{1}{1+\varepsilon_m/\nu}, \tag{7.60}$$

where the velocity has been made nondimensional with the shear velocity at the wall $v_* = (|\tau_w|/\rho)^{1/2}$. By integrating Eq. (7.60) with ε_m/ν as given by Reichardt's formula, and fitting the resulting velocity profile to experimental data in the $0 < y^+ < 1000$ range, Ng optimized Reichardt's constants and found the values

$$k = 0.4 \quad \delta_\ell^+ = 10.7. \tag{7.61}$$

For $y^+ > 1000$, theoretical prediction and experimental data are at variance. Nevertheless, in his first paper Ng assumed that Eq. (7.34) applies not only in the constant-stress region but over the whole width of the channel. To take into account the presence of two boundaries, the flow is divided into two regions. In the upper layer, given by $y_1 < y < h$, the eddy viscosity is calculated with the upper wall shear stress τ_h. In the lower layer, defined by $0 < y < y_1$, the eddy viscosity is evaluated with the lower wall shear τ_0. It is required then that ε_m/ν be a unique function of $y^+ = yv_*/\nu$, where $v_* = (|\tau_h|/\rho)^{1/2}$ or $v_* = (|\tau_0|/\rho)^{1/2}$, depending on location, with the consequence that the nondimensional coordinate $\hat{y}_1 = y_1/h$ of the interface between upper and lower layers is given by

$$\hat{y}_1 = \frac{\sqrt{\tau_h}}{\sqrt{\tau_h}+\sqrt{\tau_0}}. \tag{7.62}$$

In a further development, the linearized theory of Ng and Pan (1965), Reichardt's eddy viscosity distribution is still assumed to hold over the whole channel width. Following a suggestion of Elrod's, however, ε_m/ν is now calculated with the local total shear, placing the boundary between upper and lower layers in the center plane of the channel. Thus, ε_m/ν remains isotropic and its derivative has a discontinuity at the channel center. Substituting

$$\tau_{xy} = \mu\frac{\partial\bar{U}}{\partial y} - \rho\overline{u'v'} = \mu\left(1+\frac{\varepsilon_m}{\nu}\right)\frac{\partial\bar{U}}{\partial y} \tag{7.63a}$$

and

$$\tau_{zy} = \mu\frac{\partial\bar{W}}{\partial y} - \rho\overline{v'w'} = \mu\left(1+\frac{\varepsilon_m}{\nu}\right)\frac{\partial\bar{W}}{\partial y} \tag{7.63b}$$

into Eq. (7.15), and integrating twice formally with respect to y, we obtain the velocity distribution

$$\bar{U} = \frac{1}{\mu}\left[\tau_{xy}\left(\frac{h}{2}\right)\int_0^y \frac{dy'}{1+\varepsilon_m/\nu} + \frac{\partial\bar{P}}{\partial x}\int_0^y \frac{y'-h/2}{1+\varepsilon_m/\nu}dy'\right], \tag{7.64a}$$

$$\bar{W} = \frac{1}{\mu}\left[\tau_{xy}\left(\frac{h}{2}\right)\int_0^y \frac{dy'}{1+\varepsilon_m/\nu} + \frac{\partial\bar{P}}{\partial z}\int_0^y \frac{y'-h/2}{1+\varepsilon_m/\nu}dy'\right]. \tag{7.64b}$$

Here $\tau_{xy}(h/2)$ and $\tau_{zy}(h/2)$ are integration constants to be determined from the boundary conditions.

Substituting Eqs. (7.64a) and (7.64b) into the continuity equation (7.7a) and integrating with respect to y would yield a differential equation in lubricant pressure, Eq. (7.81).

(A detailed derivation of this equation is given in Chapter 9 in a discussion on thermohydrodynamic theory.) Such an equation would be nonlinear, for to calculate $\bar{U}$ and $\bar{W}$ in Eqs. (7.64) one must already know the total shear $|\tau| = (\tau_{xy}^2 + \tau_{zy}^2)^{1/2}$. Thus, Eqs. (7.64) presuppose knowledge of the velocity field.

To avoid an iterative procedure, Ng and Pan made the assumption that the flow is a small perturbation of turbulent Couette flow

$$\begin{aligned} \tau_{xy} &= \tau_c + \delta\tau_x \qquad \frac{\delta\tau_x}{\tau_c} \ll 1, \\ \tau_{zy} &= \delta\tau_z \qquad\qquad \frac{\delta\tau_z}{\tau_c} \ll 1, \end{aligned} \tag{7.65}$$

so that

$$|\tau| = \tau_c + \delta\tau_x + O\left(\delta\tau_x^2\right). \tag{7.66}$$

Here τ_c is the turbulent Couette stress and $\delta\tau_x$ and $\delta\tau_z$ are the perturbations of τ_c in the x and z directions, respectively.

But if τ is only a small perturbation of τ_c, the eddy viscosity that yields the shear stress τ is a small perturbation of the Couette flow eddy viscosity, and we may write

$$\frac{\varepsilon_m}{\nu}(\bar{y}; |\tau|) = \frac{\varepsilon_m}{\nu}(\bar{y}; \tau_c) + \left.\frac{\partial(\varepsilon_m/\nu)}{\partial|\tau|}\right|_{|\tau|=\tau_c} \delta\tau_x + O\left(\delta\tau_x^2\right), \tag{7.67}$$

where $\bar{y} = y/h$ is the dimensionless normal coordinate. Using the notation

$$\begin{aligned} f_c(\bar{y}) &= 1 + \frac{\varepsilon_m}{\nu}(\bar{y}; \tau_c) \\ &= 1 + \kappa\left[\bar{y}h_c^+ - \delta_\ell^+ \tanh\left(\frac{\bar{y}h_c^+}{\delta_\ell^+}\right)\right], \end{aligned} \tag{7.68}$$

where

$$h_c^+(x, z) = \frac{h}{\nu}\sqrt{\frac{|\tau_c|}{\rho}}$$

and

$$\begin{aligned} g_c(\bar{y}) &= \tau_c \left.\frac{\partial(\varepsilon_m/\nu)}{\partial|\tau|}\right|_{|\tau|=\tau_c} \\ &= \frac{1}{2}\kappa\bar{y}h_c^+ \tanh^2\left(\frac{\bar{y}h_c^+}{\delta_\ell^+}\right), \end{aligned} \tag{7.69}$$

Eq. (7.67) can be put in the abbreviated form

$$\frac{\varepsilon_m}{\nu}(\bar{y}; |\tau|) = f_c(\bar{y}) - 1 + g_c(\bar{y})\frac{\delta\tau_x}{\tau_c} + O\left(\delta\tau_x^2\right). \tag{7.70}$$

When

$$\left(1 + \frac{\varepsilon_m}{\nu}\right)^{-1} = \frac{1}{f_c(\bar{y})}\left(1 - \frac{g_c(\bar{y})}{f_c(\bar{y})}\frac{\delta\tau_x}{\tau_c}\right) + O\left(\delta\tau_x^2\right).$$

is substituted into Eqs. (7.64a) and (7.64b) and terms of order $(\delta\tau_x^2)$ are neglected, we obtain

$$U = \frac{\bar{U}}{U_*} = \frac{h\tau_c}{\mu U_*}\int_0^{\bar{y}} \frac{d\eta}{f_c(\eta)} + \left(\tau_{xy}\left(\frac{1}{2}\right) - \tau_c\right)\frac{h}{\mu U_*}\int_0^{\bar{y}} \frac{1}{f_c(\eta)} \times \left(1 - \frac{g_c(\eta)}{f_c(\eta)}\right)d\eta + B_x\int_0^{\bar{y}} \frac{\frac{1}{2} - \eta}{f_c(\eta)}\left(1 - \frac{g_c(\eta)}{f_c(\eta)}\right)d\eta, \tag{7.71a}$$

$$W = \frac{\bar{W}}{U_*} = \frac{h\tau_{zy}(1/2)}{\mu U_*}\int_0^{\bar{y}} \frac{d\eta}{f_c(\eta)} + B_z\int_0^{\bar{y}} \frac{\frac{1}{2} - \eta}{f_c(\eta)}d\eta. \tag{7.71b}$$

Observing that in pure shear flow $B_x = 0$ and $\tau_{xy}(1/2) - \tau_c = 0$, we have

$$\frac{h\tau_c}{\mu}\int_0^1 \frac{d\eta}{f_c(\eta)} = U_*. \tag{7.72}$$

Both $f_c(\bar{y})$ and $g_c(\bar{y})$ are symmetrical with respect to $\bar{y} = 1/2$. Thus, satisfaction of the remaining boundary conditions,

$$\bar{U} = U_0 \quad \text{at} \quad y = h, \quad \bar{W} = 0 \quad \text{at} \quad y = h, \tag{7.73}$$

leads to

$$\tau_{xy}\left(\frac{1}{2}\right) = \tau_c, \quad \tau_{zy}\left(\frac{1}{2}\right) = 0.$$

Equations (7.71a) and (7.71b) can be simplified to

$$U = \frac{1}{2} + \frac{(h_c^+)^2}{R_h}\int_{1/2}^{\bar{y}} \frac{d\eta}{f_c(\eta)} + B_x\int_0^{\bar{y}} \frac{\frac{1}{2} - \eta}{f_c(\eta)}\left(1 - \frac{g_c(\eta)}{f_c(\eta)}\right)d\eta, \tag{7.74a}$$

$$W = B_z\int_0^{\bar{y}} \frac{\frac{1}{2} - \eta}{f_c(\eta)}\,d\eta. \tag{7.74b}$$

Substituting for $\bar{U}$ and $\bar{W}$ in the continuity equation (7.7a) yields the linearized turbulent lubrication equation. This is formally identical to Constantinescu's equation (7.59), but here the coefficients k_x and k_z are defined by

$$\frac{1}{k_x} \equiv G_x = \int_0^1 d\bar{y}\int_0^{\bar{y}} \frac{\frac{1}{2} - \eta}{f_n(\eta)}\left(1 - \frac{g_c(\eta)}{f_c(\eta)}\right)d\eta, \tag{7.75a}$$

$$\frac{1}{k_x} \equiv G_z = \int_0^1 d\bar{y}\int_0^{\bar{y}} \frac{\frac{1}{2} - \eta}{f_c(\eta)}d\eta. \tag{7.75b}$$

Both k_x and k_z depend on h_c^+ through Eqs. (7.68), (7.69), and (7.75). The local value of h_c^+, on the other hand, is dependent on the local film thickness through Eq. (7.72), which has the dimensionless form

$$R_h = (h_c^+)^2\int_0^1 \frac{d\eta}{f_c(\eta)}, \tag{7.76}$$

The coefficients k_x and k_z depend, therefore, on the local Reynolds number. A good representation of this dependence was obtained by least-squares fitting of polynomials to Eqs. (7.75a) and (7.75b), with the results (Figure 7.4)

$$\frac{1}{k_x} = \begin{cases} \dfrac{1}{12} & R_h < 100 \\ \displaystyle\sum_n a_n (\log R_h)^{n-1} & 100 \le R_h < 10{,}000 \\ 0.014 - 0.0114\,(\log R_h - 4.0) & R_h > 10{,}000 \end{cases} \tag{7.77a}$$

$$\frac{1}{k_z} = \begin{cases} \dfrac{1}{12} & R_h < 100 \\ \displaystyle\sum_n b_n (\log R_h)^{n-1} & 100 \le R_h < 10,000 \\ 0.023 - 0.0182\,(\log R_h - 4.0) & R_h > 10{,}000 \end{cases} \tag{7.77b}$$

$$a_1 = -0.4489 \quad a_2 = 0.6703 \quad a_3 = -0.2904 \quad a_4 = 0.0502 \quad a_5 = -0.00306$$
$$b_1 = -0.3340 \quad b_2 = 0.4772 \quad b_3 = -0.1822 \quad b_4 = 0.02628 \quad b_5 = -0.001242.$$

To render the theory of Ng and Pan applicable even at large pressure gradients, Elrod and Ng substituted $\bar{U}$ and $\bar{W}$ from Eqs. (7.71a) and (7.71b) directly into the boundary condition Eqs. (7.73) and subsequently into the continuity equation (7.7a). They also removed the most objectionable component of the Ng and Pan model, namely, that Reichardt's eddy viscosity distribution is valid over the whole channel.

In the nonlinear model of Elrod and Ng (1967), Reichardt's formula is retained only in the constant stress region. In the core region the eddy, viscosity is assumed to be given by a constant value ε_c. This value is obtained from a generalized form of Clauser's formula (1965),

$$\varepsilon_c = \frac{1}{56} \int_0^{y_0} |U_0 - \bar{U}| dy, \tag{7.78}$$

where U_0 is the maximum value of $\bar{U}$ at the given $x = \text{const}$, position.

To introduce the *Elrod-Ng analysis* (Elrod and Ng, 1967), set $\varepsilon = \min(\varepsilon_m, \varepsilon_c)$ where ε_c is defined by (7.78) while ε_m is obtained from a modification of Reinhardt's formula (7.34), which now contains local stress rather than wall stress. Substituting into (7.16) and applying the boundary conditions $\bar{U}(1) = U^*$ and $\bar{W}(1) = 0$ yields the velocity distribution

$$U = B_x \left[\frac{J(1)}{I(1)} I(Y) - J(Y) \right] + \frac{I(Y)}{I(1)}, \tag{7.79}$$

$$W = B_z \left[\frac{J(1)}{I(1)} I(Y) - J(Y) \right]. \tag{7.80}$$

The following notation is employed here:

$$I(\eta) = \int_0^\eta \frac{dY'}{1 + \frac{\varepsilon}{\bar{V}}}, \quad J(\eta) = \int_0^\eta \frac{dY'}{1 + \frac{\varepsilon}{\bar{V}}}.$$

Substitution of (7.79) into the mean flow continuity equation and integration across the film yields

$$\frac{\partial}{\partial x}\left\{\frac{h^3}{\mu}\frac{\partial \bar{P}}{\partial x}\left[\frac{J(1)}{I(1)}\bar{I}-\bar{J}\right]\right\}+\frac{\partial}{\partial z}\left\{\frac{h^3}{\mu}\frac{\partial \bar{P}}{\partial z}\left[\frac{J(1)}{I(1)}\bar{I}-\bar{J}\right]\right\}=\frac{\partial}{\partial x}\left[\frac{hU_0\bar{I}}{I(1)}\right] \tag{7.81a}$$

or

$$\frac{\partial}{\partial x}\left\{\frac{h^3}{\mu}\frac{\partial \bar{P}}{\partial x}\left[\frac{J(1)}{I(1)}\bar{I}-\bar{J}+\frac{\left(\frac{1}{2}-\frac{\bar{I}}{I(1)}\right)}{\frac{h^3\partial\bar{P}}{\mu\nu\partial x}}\frac{hU_0}{\nu}\right]\right\}+\frac{\partial}{\partial z}\left\{\frac{h^3}{\mu}\frac{\partial \bar{P}}{\partial z}\left[\frac{J(1)}{I(1)}\bar{I}-\bar{J}\right]\right\}=\frac{U_0}{2}\frac{\partial h}{\partial x}. \tag{7.81b}$$

Here $\bar{I}$ and $\bar{J}$ represent averaged values of I and J, respectively.

Consistent with the notation of Ng and Pan (1965), we now define the nonlinear turbulence coefficients

$$G_x = J(1)\frac{\bar{I}}{I(1)}-\bar{J}+\frac{\left(\frac{1}{2}-\frac{\bar{I}}{I(1)}\right)}{B_x},$$

$$G_z = J(1)\frac{\bar{I}}{I(1)}-\bar{J},$$

and obtain the modified Reynolds equation

$$\frac{\partial}{\partial x}\left(\frac{h^3}{\mu}G_x\frac{\partial \bar{P}}{\partial x}\right)+\frac{\partial}{\partial z}\left(\frac{h^3}{\mu}G_z\frac{\partial \bar{P}}{\partial z}\right)=\frac{U_0}{2}\frac{\partial h}{\partial x}. \tag{7.82}$$

When $B_x \to 0$, $\bar{I}/I(1) \to 1/2$, thus G_x has finite value in Couette flow. The coefficients G_x and G_z depend only on the local Reynolds number hU_0/ν and the pressure gradient $(h^3/\mu\nu)(\partial\bar{P}/\partial x,\ \partial\bar{P}/\partial z)$.

There have been various studies published more recently that, in some way, are linked to the Ng-Pan-Elrod model. An example is the work of Frene and co-workers (Lucas et al., 1994) who employ the Van Driest formula and Prandtl's mixing length model in place of Reichardt's eddy viscosity but retain Clauser's formula for core eddy viscosity. For smooth surfaces, Lucas et al. obtain results that are very close to those of the Elrod-Ng model; they also offer an extension to rough walls.

7.5 Bulk Flow Model of Hirs

The bulk flow theory of turbulent lubrication by Hirs (1973) does not attempt to analyze turbulence in all its details. Instead it relies on an easily measured global characteristic of the flow, namely the relationship between average velocity and wall stress. In a hydrodynamic bearing, we encounter two basic flow types, pressure flow and shear flow. But more general flows, which result from the combined action of a pressure gradient and the sliding of one of the surfaces, are also encountered. All these flow types have to be considered by the theory [see the discussion following Eq. (7.45)].

Analyzing the then-available experimental data for pressure flow in a pipe, Blasius discovered a simple relationship between the wall stress and the Reynolds number that is calculated on the average velocity. This drag law, said to be valid for $\mathrm{Re} \le 10^5$, also applies

to pressure flow between parallel plates separated by a distance h. In the latter case, it has the form

$$\frac{\tau_0}{\frac{1}{2}\rho U_a^2} n_0 (\mathrm{Re})^{m_0}, \tag{7.83}$$

where $\mathrm{Re} = U_a h/\nu$ is the Reynolds number based on the average velocity (Schlichting, 1968),

$$U_a = \frac{1}{h}\int_0^h \bar{U}\, dy.$$

While analyzing their own and also Couette's experimental results, Davies and White (1928) found a relationship between wall stress and average velocity of shear flow between two parallel surfaces. The drag law for Couette flow may be put into a form that is identical to the one obtained earlier by Blasius for pressure flow. Thus, following Hirs (1973), for shear flow between parallel plates a distance h apart we write

$$\frac{\tau_1}{\frac{1}{2}\rho U_a^2} = n_1 (\mathrm{Re})^{m_1}. \tag{7.84}$$

In these equations, U_a represents the average value of the mean flow velocity relative to the surface on which the wall stress τ_1 is being evaluated. Thus, in Eq. (7.84) $U_a = U_*/2$, where U_* is the velocity of the sliding surface when the equation is applied to the stationary surface, and $U_a = -U_*/2$ when applied to the sliding surface.[4]

For the particular case of Reynolds number equality between Eqs. (7.83) and (7.84), we have the following value for the ratio of Poiseuille wall stress to Couette wall stress

$$\frac{\tau_0}{\tau_1} = \frac{n_0}{n_1} (\mathrm{Re})^{m_0 - m_1}$$

An exhaustive survey of available experimental data (Hirs, 1974) shows that $m_0 = m_1 = -0.25$ and $a = n_0/n_1 = 1.2$. Motivated by this relative insensitivity of the wall stress to the type of flow, Hirs assumed wall stress to be additive in the sense that if τ_1 is due to the relative velocity U_* of the surfaces and τ_0 is due to the pressure gradient $d\bar{P}/dx$, then the wall stress τ that is caused by the combined action of U_* and $d\bar{P}/dx$ can be calculated from $\tau = \tau_0 + a\tau_1$ on the stationary surface and $\tau = \tau_0 - a\tau_1$ on the sliding surfaces. Furthermore, the Couette shear τ_1 is approximately equal to $(n_1/n_0)\tau_0$.

A Couette flow of wall stress τ_1 is then equivalent, at least as far as Eq. (7.83) is concerned, to a pressure flow that is maintained by the fictitious pressure gradient

$$\frac{dP_1}{dx} = -\frac{2}{h} a\tau_1. \tag{7.85}$$

To arrive at this relationship, consider force equilibrium on a control volume of length Δx and height h under the action of pressure forces ph and $-(p + \Delta p)h$ and shear force $2a\tau_1$.

Utilizing the ideas above, Eqs. (7.83) and (7.84) may now be written for generalized channel flows. [Here and in what follows, we assume the bearing to be held stationary and put $U_1 = 0$. A slight generalization of ideas is required if the bearing surface is given a

[4] The functions on the right-hand sides of Eqs. (7.83) and (7.84) must be odd functions. Alternatively, we may write Eqs. (7.83) and (7.84) in the more appropriate form: $2\tau_{0,1}/\rho U_a^2 = n_{0,1}(|\mathrm{Re}|)^{m0,1}\ \mathrm{sgn}(U_a)$.

velocity different from zero. For details see Hirs (1973).]

Stationary surface

$$\frac{-h\,(d/d\,x)\,(\bar{P}+P_1)}{\rho U_a^2} = n_0\left(\frac{U_a h}{\nu}\right)^{m_0} \tag{7.86a}$$

Sliding surface

$$\frac{-h\,(d/d\,x)\,(\bar{P}-P_1)}{\rho\,(U_a-U_*)^2} = n_0\left(\frac{(U_a-U_*)\,h}{\nu}\right)^{m_0}. \tag{7.86b}$$

On eliminating the fictitious pressure gradient $d\,P_1/dx$ between Eqs. (7.86a) and (7.86b), we obtain the actual pressure gradient in terms of the average velocity U_a and the relative velocity of sliding U:

$$\frac{d\,\bar{P}}{d\,x} = -\frac{n_0}{2}\left\{\frac{\rho U_a^2}{h}\left(\frac{U_a h}{\nu}\right)^{m_0} + \frac{\rho\,(U_a-U_*)^2}{h}\left[\frac{U_a-U_*)h}{\nu}\right]^{m_0}\right\}. \tag{7.87}$$

It is worth noting that the magnitude of the weighing factor $a = n_0/n_1$ never enters Eq. (7.87) and thus has no effect on the pressure gradient.

Equation (7.87) is valid for unidirectional flow; that is, for flow in the direction of the representative pressure gradient. However, this direction need not coincide with the direction of relative velocity U [x direction in Eq. (7.87)], in which case there will be two component equations, one in the x direction and the other in the z direction.

The orthogonal components of Eq. (7.86a) are

$$\frac{-h(\partial/\partial x)(\bar{P}+P_1)}{\rho U_a S_a} = n_0\left(\frac{S_a h}{\nu}\right)^{m_0}, \tag{7.88a}$$

$$\frac{-h(\partial/\partial z)(\bar{P}+P_1)}{\rho W_a S_a} = n_0\left(\frac{S_a h}{\nu}\right)^{m_0}, \tag{7.88b}$$

where $S_a = (U_a^2 + W_a^2)^{1/2}$ is the magnitude of the average velocity vector $\boldsymbol{S}_a = U_a\boldsymbol{i} + W_a\boldsymbol{k}$.

Raising all terms of Eqs. (7.88a) and (7.88b) to the second power and adding the results leads to the equation

$$\frac{-h(d/d\,s)(\bar{P}+P_1)}{\rho S_a^2} = n_0\left(\frac{S_a h}{\nu}\right)^{m_0}. \tag{7.89}$$

Equation (7.89) is identical, except for a slight difference in notation, to Eq. (7.86a), suggesting that our procedure for taking component equations (7.88a) and (7.88b) is correct.

When the orthogonal component equations are written for Eq. (7.86b) also, we have

$$\frac{-h(\partial/\partial x)(\bar{P}-P_1)}{\rho\,(U_a-U_*)\,S_b} = n_0\left(\frac{S_b h}{\nu}\right)^{m_0}, \tag{7.90a}$$

$$\frac{-h(\partial/\partial z)(\bar{P}-P_1)}{\rho W_a S_b} = n_0\left(\frac{S_b h}{\nu}\right)^{m_0}, \tag{7.90b}$$

where $S_b = [(U_a - U_*)^2 + W_a^2]^{1/2}$. If P_1 is eliminated between Eqs. (7.88a) and (7.90a) and between Eqs. (7.88b) and (7.90b), we obtain the pressure gradient in terms of the components of the average velocities, the velocity of the sliding surface, the film thickness, and the viscosity and density of the fluid.

The dimensionless pressure flow coefficients G_x and G_z can be obtained from

$$G_x = \frac{\frac{1}{2} - U_a/U_*}{(h^2/\mu U_*)(\partial \bar{P}/\partial x)} \qquad G_z = \frac{-W_a/U_*}{(h^2/\mu U_*)(\partial \bar{P}/\partial z)} \tag{7.91}$$

by substitution. If Couette flow dominates so that the following conditions apply,

$$G_x \frac{h^3}{\mu \nu} \frac{\partial \bar{P}}{\partial x} \ll \frac{1}{2} R_h \qquad G_z \frac{h^3}{\mu \nu} \frac{\partial \bar{P}}{\partial z} \ll \frac{1}{2} R_h,$$

then Eq. (7.91) reduces to

$$G_x = \frac{1}{2 + m_0} G_z, \qquad G_z = \frac{2^{1+m_0}}{n_0} R_h^{-(1+m_0)}. \tag{7.92}$$

Hirs (1974) uses $n_0 = 0.066$ and $m_0 = -0.25$ for smooth surfaces and $\mathrm{Re} \leq 10^5$. With these values, Eq. (7.92) gives the approximate formulas:

$$k_x \equiv \frac{1}{G_x} = 0.0687\ R_h^{0.75}, \tag{7.93a}$$

$$k_z \equiv \frac{1}{G_z} = 0.0392\ R_h^{0.75}. \tag{7.93b}$$

At high Reynolds numbers the predictions of Ng, Pan, and Elrod and those of Hirs are almost identical and it is only in and near the transition regime that any significant discrepancy occurs. Neither of these theories agrees completely in this region with the calculation of Ho and Vohr but Elrod and Ng come closest.

Ho and Vohr (1974) used the Kolmogorov-Prandtl energy model of turbulence; they calculated the kinetic energy from its transport equation (7.37) and the length scale Λ from the van Driest formula (7.36). Figure 7.5 shows comparisons between the models of Ho and Vohr, Elrod-Ng (nonlinear) and Ng-Pan (linear) for two cases. In Figure 7.5(a) the pressure gradient is parallel to the surface velocity while in Figure 7.5(b) it is orthogonal – the definition used here is $GRADP = R_h\ (B_x, B_z)$, where $R_h = Uh/\nu$ is the local Reynolds number. Figure 7.5(a) displays a distinctive peak in G_x in the transition regime.

Other than a slight quantitative discrepancy here, both theories agree remarkably well. However, Launder and Spalding caution against interpreting this as proof of the correctness of the Ng-Pan-Elrod model. According to these authors, consistently accurate prediction of internal flows under severe favorable pressure gradient can be achieved only if one calculates the length scale from a transport equation, rather than from an algebraic formula.

Of the theories discussed here, the Ng-Pan-Elrod theory and the bulk flow theory of Hirs are to be preferred over Constantinescu's model. There is, however, little to choose between the Ng-Pan-Elrod theory and the bulk flow theory. The latter may be extended to flow between rough or grooved surfaces as experimental data become available. Extension

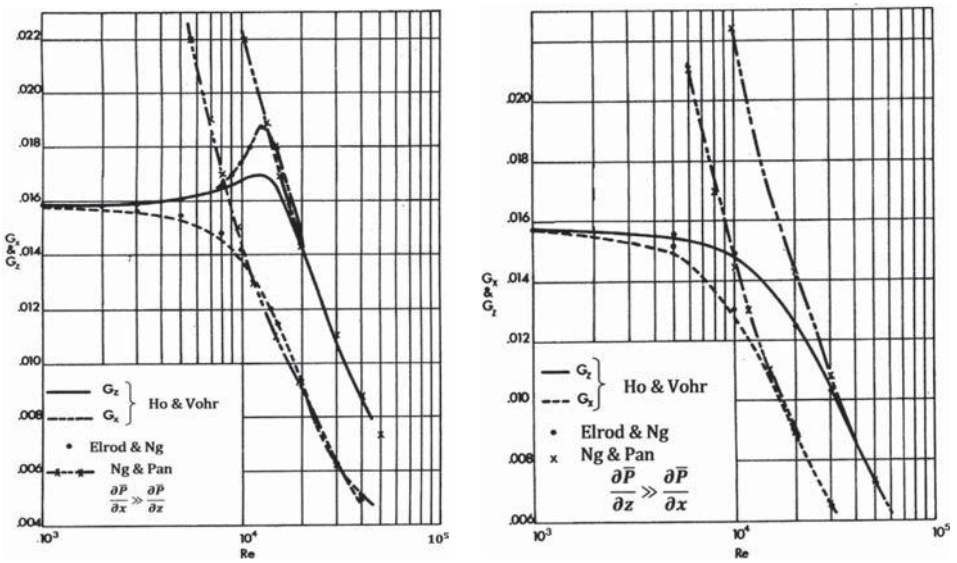

Figure 7.5. Values of G_x and G_z for $GRADP = -5 \times 10^5$ (Reprinted with permission from Ho, M. K. and Vohr, J. H. Application of Energy Model of Turbulence to Calculation of Lubricant Flows, *Trans. ASME,* ser. F, **96**, 95–102, 1974).

of the Ho-Vohr model to include fluid inertia is also possible. The effect of turbulence on journal bearing performance can be gauged from Figure 3.10. Thermal effects and turbulence are discussed in Chapter 9.

Turbulent lubricant flow between *rough surfaces* has been discussed by several researchers. Hashimoto and Wada (1989) use ideas from the Hirs model and combine resistance laws for rough surfaces for Poiseuille and Couette flows. The same ideas are applied by several other authors. In contrast, Lucas et al. (1994) apply Prandtl's mixing length theory, calculating the mixing length from the Van Driest formula based on local stress; for the completely rough regime the Van Driest formula does not apply, and an appeal is made to the Rotta and Granville mixing length expression. In contrast, Brunetiere and Tournerie (2009) replace $(y^+\sqrt{\bar{\tau}})$ with $(y^+\bar{\tau})$ in Reinhardt's modified eddy viscosity formula (7.79) and add an extra term, which vanishes at the wall and tends to zero in the logarithmic region

$$\frac{\varepsilon_m}{\nu} = \kappa \left\{ y^+\bar{\tau} - \delta_\ell^+ \tanh\left(\frac{y^+\bar{\tau}}{\delta_\ell^+}\right) + \delta_k^+ y^+\bar{\tau}\left[1 - \tanh\left(\frac{y^+\bar{\tau}}{\delta_k^+}\right)\right]\right\}. \tag{7.94}$$

The empirical constant δ_k^+ relates to the quality of the surface roughness. Some of the prediction of Brunetiere and Tournerie for velocity distribution between rough walls is shown in Figure 7.6. The agreement appears to be good, but one should remember that the theoretical reasoning for the adopted corrections might not stand up to scrutiny.

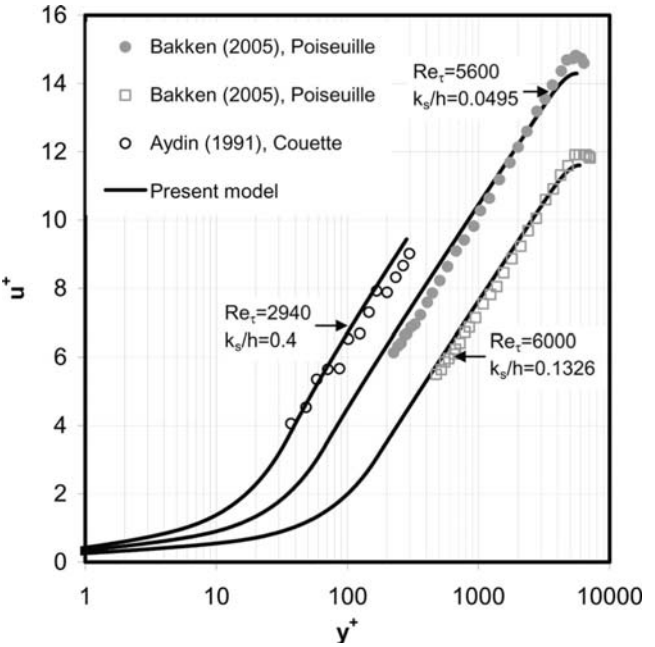

Figure 7.6. Velocity profile for Couette and Poiseuille flows between rough walls (Reprinted with permission from Brunetiere, N. and Tournerie, B. Study of hydrostatic mechanical face seals in turbulent rough flow. *ASME Journal of Tribology,* **131**, 1–10, 2009).

7.6 Turbulence with Inertia Retained

Turbulent flow with inertia effects is computed by one of two ways. Applying canned software such as FLUENT it is now relatively simple to solve the thin-film turbulent flow equations (Villasmil et al., 2005; Billy et al., 2006; Wang and Priestman, 2007). The perturbation method of Pan (1973) is an extension of the Ng-Pan linearized turbulent theory and was offered for all Reynolds numbers. An entirely new approach was taken by Constantinescu (Constantinescu, 1970; Constantinescu and Galetuse, 1974) who applied the method of averaged inertia. It appears that the first of these methods, CFD solution of the thin-film equations, is not warranted in many instances, and the significantly simpler method of averaged inertia will serve the engineering designer.

Method of Averaged Inertia

A number of investigators have employed the method of averaged inertia for the study of turbulent flows in situations where sudden changes of the cross-section occur (Constantinescu and Galetuse, 1974; Frene et al., 2006; Brunetiere et al., 2008). Here we follow the analysis of Constantinescu (Constantinescu, 1970; Constantinescu and Galetuse, 1974; Frene et al., 2006). The essence of this method consists of replacing fluid inertia forces by their cross-section averaged value. To achieve this, Eqs. (7.17) are rearranged, taking into account the equation of continuity of the mean flow (7.7a), and integrated across the

film with boundary conditions $\bar{U}(0) = U_0,\ \bar{W}(0) = 0$ and $\bar{U}(h) = \bar{W}(h) = 0$

$$\begin{aligned}
&\rho\frac{\partial}{\partial x}\int_0^h \bar{U}^2 dy + \rho\bar{U}\bar{V}|_0^h + \rho\frac{\partial}{\partial z}\int_0^h \bar{U}\bar{W}dy = -h\frac{\partial \bar{P}}{\partial x} - \tau_{xy}|_0^h,\\
&\rho\frac{\partial}{\partial x}\int_0^h \bar{U}\bar{W}dy + \rho\bar{W}\bar{V}|_0^h + \rho\frac{\partial}{\partial z}\int_0^h \bar{W}^2 dy = -h\frac{\partial \bar{P}}{\partial z} - \tau_{zy}|_0^h,\\
&\frac{\partial}{\partial x}\int_0^h \bar{U}dy + \bar{V}|_0^h + \frac{\partial}{\partial z}\int_0^h \bar{W}dy = 0.
\end{aligned} \tag{7.95}$$

The integrals occurring in (7.95) are approximated by the polynomials

$$\begin{aligned}
&\int_0^h \bar{U}^2 dy = \alpha U_m^2 h + \beta U_0^2 h - \gamma U_m U_0 h,\\
&\int_0^h \bar{U}\bar{W}dy = \alpha U_m W_m h - \frac{\gamma}{2}U_m U_0 h,\\
&\int_0^h \bar{W}^2 dy = \alpha W_m^2 h,
\end{aligned} \tag{7.96}$$

where $U_m = \frac{1}{h}\int_0^h \bar{U}dy$ and $W_m = \frac{1}{h}\int_0^h \bar{W}dy$ are the components of the mean flow and U_0 represents the relative sliding velocity of the boundaries.

For inertialess laminar flow the integrals occurring in (7.96) are easy to evaluate and are given by substituting $\alpha = 6/5$, $\beta = 2/15$, $\gamma = 1/5$.

For turbulent flow Constantinescu takes

$$\alpha \cong 1 \quad \beta = \frac{0.885}{\mathrm{Re}^{0.367}} \quad \gamma \cong 0.$$

The crucial assumption is made at this point, that on introduction of inertia forces the velocity profiles retain their previous, inertialess, shape and change only in magnitude. It is permissible then to write

$$\tau_{xy}|_0^h = -\frac{k_x\mu}{h}\left(U_m - \frac{1}{2}U_0\right), \quad \tau_{zy}|_0^h = -\frac{k_z\mu}{h}W_m. \tag{7.97}$$

The first of (7.97) can be somewhat improved when corrected to

$$\tau_{xy}|_0^h = -\frac{k_x\mu}{h}\left(U_m - \frac{1}{2}U_0\right) + \delta\rho U_m^2\frac{\partial h}{\partial x}, \tag{7.98}$$

where $\delta = 2/15$ for laminar and $\delta = 1.95/\mathrm{Re}^{0.43}$ for turbulent flow.

We thus have three unknowns U_m, W_m, and $\bar{P}$ and a system of three equations (7.95) which can be solved iteratively, starting perhaps, from the inertialess case. This procedure has been used by several authors (Launder and Leschziner, 1975; King and Taylor, 1975).

Table 7.1. *Bearing performance comparison*

	Laminar (Re = 1)	Turbulent (Re = 7,634)
Minimum film thickness (μm)	18.2	40.0
Attitude angle (deg.)	30	45
Viscous dissipation (W)	1520	4398

To illustrate the effect of turbulence, we calculate some of the performance characteristics of a $\beta = 160^\circ$ fixed pad bearing, under the following conditions:

$$W = 10{,}000\,\text{N}$$
$$N = 12{,}000\ \text{rpm}$$
$$D = 0.1\,\text{m}$$
$$L = 0.1\,\text{m}$$
$$C = 0.0001\,\text{m}$$
$$\mu = 8.2 \times 10^{-4}\,\text{Pa}\cdot\text{s}$$
$$\nu = 8.23 \times 10^{-7}\,\text{m}^2/\text{s}.$$

The specific pressure, Sommerfeld and Reynolds numbers are given by

$$P = \frac{W}{LD} = 10^6\text{Pa}, \quad S = \frac{\mu N}{P}\left(\frac{R}{C}\right)^2 = 0.041, \quad \text{Re} = \frac{R\omega C}{\nu} = 7{,}634$$

(i) Entering Figure 3.10 with the parameter values $S = 0.041$ and Re $= 1$, we obtain the column labeled "Laminar" in Table 7.1.

(ii) The actual parameter values $S = 0.041$ and Re $= 7{,}634$, on the other hand, yield the column labeled "Turbulent" in Table 7.1.

The real difference between turbulent and laminar predictions is not that we require a 6 hp motor whereas laminar theory only asks for a 2 hp motor, but that most of the 4 hp difference between the two estimates is used up in raising the temperature of the lubricant; laminar theory is incapable of predicting this increased dissipation. For large bearings, such as employed in the power generation industry, as much as 600–800 hp is dissipated per bearing – if this is not taken into account at the design stage, bearing failure through overheating and seizure will result.

It was mentioned, when discussing laminar theory, that isothermal operation of bearings is a rarity and not the rule. This statement is even more true in the case of large bearings operating in the turbulent regime. In such cases there can be no excuse for designing on the assumption of isothermal operation, unless there is compelling evidence to support that assumption. Thermal effects in turbulent bearings are discussed in Chapter 9.

7.7 Nomenclature

A	modified local Reynolds number
B_x, B_z	components of dimensionless pressure gradient
C	radial clearance

D	bearing diameter
D_{ij}	stretching tensor
F_μ	friction force
G_x, G_z	turbulence functions
L	bearing axial length
N	shaft rotational speed
$\bar{P}$	mean turbulent pressure
P_1	fictitious pressure
R	journal radius
Re	global Reynolds number
R_h	local Reynolds number
S	Sommerfeld number
S_A	average velocity
U_{mp}	component of mean pressure flow
U_{ms}	component of mean shear flow
a	shear–stress ratio
c_μ	friction coefficient
d'_{ij}	fluctuating component of stretching tensor
f_c, g_c	turbulent functions
h	film thickness
h_c^+	reduced film thickness
k	mixing length constant
k_x, k_z	turbulence coefficients
ℓ	mixing length
m_0, m_1	exponents for pressure flow, shear flow
n_0, n_1	coefficients for pressure flow, shear flow
p	lubricant pressure
$q^2/2$	turbulent kinetic energy per unit mass
t	time
$u_i(u, v, w)$	velocity components
v^*	shear velocity
$x_i(x, y, z)$	ortogonal Cartesian coordinates
y_L	thickness of viscous sublayer
δ_{ij}	Kronecker delta
δ_ℓ^+	constant
ε	eccentricity ratio
ε	turbulent dissipation
ε_m, ε_c	eddy diffusivity, core eddy diffusivity
λ	coefficient
μ	dynamic viscosity
ν	kinematic viscosity
ρ	density
T_{ij}	stress tensor
τ_{ij}	apparent stress
τ_c	Couette stress
τ_w	wall stress
τ_0, τ_h	wall stress at $y = 0$, $y = h$

τ_0, τ_1	wall stress resulting from Poiseuille flow, Couette flow
$()_1$	evaluated at surface 1 (reference surface)
$()_2$	evaluated at surface 2
$()_m$	average value
$(-)$	mean turbulent quantities
$()'$	fluctuating turbulent quantities

7.8 References

Arwas, E. B. and Sternlicht B. 1963. Analysis of plane cylindrical journal bearings in turbulent regime. *ASME Pap. 63-LUB-11.*

Aydin, E. and Leutheusser, H. 1991. Plane-Couette flow between smooth and rough walls. *Exp. Fluids*, **11**, 302–312.

Bakken, O., Krogstad, P., Ashrafian, A. and Anderson, H. 2005. Reynolds number effects in the outer layer of the turbulent flow in a channel with rough walls. *Phys. Fluids*, **17**, 065101.

Billy, F., Arghir, M., and Pineau, G. 2006. Navier-Stokes analysis of a regular two dimensional roughness pattern under turbulent flow regime. *J. Lubrication*, **128**, 122–130.

Black, H. F. and Walton, M. H. 1974. Theoretical and experimental investigations of a short 360° journal bearing in the transition superlaminar regime. *J. Mech. Eng. Sci.*, **16**, 287–297.

Brunetiere, N. and Tournerie, B. 2009. Study of hydrostatic mechanical face seals. *ASME Journal of Tribology*, **131**, 1–10.

Brunetiere, N. Galenne, E., Tournerie, B. and Pierre-Danos, I. 2008. Modeling of non-laminar phenomena in high reliability hydrostatic seals operating in extreme conditions. *Tribol. Int.*, **41**, 211–220.

Burton, R. A. and Carper, H. J. 1967. An experimental study of annular flows with applications in turbulent film lubrication. *ASME Trans.*, **89**, 381–391.

Clauser, F. H. 1965. The turbulent boundary layer. *Adv. Appl. Mech.*, **4**, 1–51.

Constantinescu, V. N. 1959. On turbulent lubrication. *Proc. Inst. Mech. Eng.*, **173**, 881–889.

Constantinescu, V. N. 1962. Analysis of bearings operating in turbulent regime. *ASME Trans.*, **82**, 139–151.

Constantinescu, V. N. 1970. On the influence of inertia forces in turbulent and laminar self-acting films. *ASME Trans.*, **92**, 473–481.

Constantinescu, V. N. and Galetuse, S. 1974. On the possibilities of improving the accuracy of the evaluation of inertia forces in laminar and turbulent films. *J. Lub. Tech.*, **96**, 69–79.

Davies, S. T. and White, C. M. 1928. An experimental study of the flow of water in pipes of rectangular cross section. *Proc. Roy. Soc., London*, **A 92**, 119.

DiPrima, R. C. 1963. A note on the stability of flow in loaded journal bearings. *ASLE Trans.*, **6**, 249–253.

Elrod, H. G. and Ng, C. W. 1967. A theory for turbulent films and its application to bearings. *ASME Trans.*, **89**, 347–362.

Frene, J. 1977. Tapered land thrust bearing operating in both laminar and turbulent regimes. *ASLE Paper. 77-AM-8-4.*

Frene, J., Arghir, M., Constantinescu, V. 2006. Combined thin film and Navier-Stokes analysis in high Reynolds number lubrication. *Tribol. Int.*, **39**, 734–747.

Gardner, W. W. and Ulschmid, J. G. 1974. Turbulence effects in two journal bearing applications. *ASME Trans.*, **96**, 15–21.

Hashimoto, H. and Wada, S. 1989. Theoretical approach to turbulent lubrication problems including surface roughness effects. *ASME Journal of Tribology*, **111**, 17–22.

Hinze, J. O. 1975. *Turbulence*, 2d ed. McGraw-Hill, New York.

Hirs, G. G. 1973. Bulk flow theory for turbulence in lubricant films. *ASME Trans., Ser. F*, **95**, 137–146.

Hirs, G. G. 1974. A systematic study of turbulent film flow. *ASME Trans., Ser. F*, **96**, 118–126.

Ho, M. K. and Vohr J. H. 1974. Application of energy model of turbulence to calculation of lubricant flows. *ASME Trans., Ser. F*, **96**, 95–102.

Jones, W. P. and Launder B. E. 1972. The prediction of laminarization with a two equation model of turbulence. *Int. J. Heat Mass Transfer*, **15**, 301–313.

Kettleborough, C. F. 1965. Turbulent and inertia flow in slider bearings. *ASLE Trans.*, **8**, 287–295.

King, K. F. and Taylor, C. M. 1975. Laminar and turbulent lubrication of the finite width plane inclined slider bearing including a consideration of mean convective inertia effects. *Proc. Leeds-Lyon Symp. on Superlaminar Flow in Bearings.* I. Mech. Engrs. Publication, London.

Launder, B. E. and Spalding, D. B. 1972. *Lectures in Mathematical Models of Turbulence.* Academic Press, London.

Launder, B. E. and Leschziner, M. 1978. Flow in finite-width thrust bearing including inertial effects, I and II. *ASME Trans., Ser. F*, **100**, 330–345.

Li, C. H. 1977. The effect of thermal diffusion on flow stability between two rotating cylinders. *ASME Trans.*, **99**, 318–322.

Lucas, V., Danaila, S., Bonneau, O. and Frene, J. 1994. Roughness influence on turbulent flow through annual seals. *ASME Journal of Tribology*, **116**, 321–329.

Monin, A. S. and Yaglom, A. M. 1973. *Statistical Fluid Mechanics.* Volume **1**. MIT Press, Mass.

Ng, C. W. 1964. Fluid dynamic foundation of turbulent lubrication theory. *ASLE Trans.*, **7**, 311–321.

Ng, C. W. and Pan, C. H. T. 1965. A linearized turbulent lubrication theory. *ASME Trans.*, **87**, 675–688.

Ng, K. H. and Spalding, D. B. 1972. Turbulence model for boundary layer near walls. *Phys. Fluids*, **15**, 20–30.

Pan, C. H. T. 1973. Calculation of pressure, shear, and flow in lubricating films for high speed bearings. ASME Paper No. 73-LubS-21.

Prandtl, L. 1963. *The Mechanics of Viscous Fluids*. Division G, in Aerodynamic Theory (W. F. Durand, ed.). Vol. 3. Dover, New York.

Raimondi, A. A. and Szeri, A. Z. 1984. Journal and thrust bearings. In *Handbook of lubrication*, II (E. R. Booser, ed.). CRC Press, Boca Raton.

Robertson, J. M. 1959. On turbulent plane Couette flow. *Proc. 6th Midwestern Conf. Fluid Mech.* Austin, Texas, pp. 169–182.

Schlichting, H. 1968. *Boundary Layer Theory*, 6th ed. Pergamon, London.

Townsend, A. A. 1977. *The Structure of Turbulent Shear Flow.* 2d ed. Cambridge University Press, Cambridge.

Wang, J. and Priestman, G. H. Flow simulation in a complex fluidics using three turbulence models and unstructured grids. *Int. J. Num. Methds. Heat and Fluid Flow*, **19**, 484–500.

Willasmil, L. A., Childs, D. and Chen, H. C. 2005. Understanding friction factor behavior in liquid annular seals with deliberately roughened surfaces. *ASME Journal of Tribology*, **127**, 213–222.

Wolfshtein, M. 1969. The velocity and temperature distribution in one dimensional flow with turbulence augmentation and pressure gradient. *Int. J. Heat Mass Transfer*, **12**, 301–308.

Elastohydrodynamic Lubrication

Elastohydrodynamic lubrication (EHL) is the name given to hydrodynamic lubrication when it is applied to solid surfaces of low geometric conformity that are capable of, and are subject to, elastic deformation. In bearings relying on EHL principles, the pressure and film thickness are of order 1 GP and 1 μm, respectively – under such conditions, conventional lubricants exhibit material behavior distinctly different from their bulk properties at normal pressure. In fact, without taking into account the viscosity-pressure characteristics of the liquid lubricant and the elastic deformation of the bounding solids, hydrodynamic theory is incapable of explaining the existence of continuous lubricant films in highly loaded gears and rolling-contact bearings. This is illustrated in the next section, by applying isoviscous lubrication theory to a rigid cylinder rolling on a plane.

When two convex, elastic bodies come into contact under zero load, they touch along a line (e.g., a cylinder and a plane or two parallel cylinders) or in a point (e.g., two spheres or two crossed cylinders). On increasing the normal contact load from zero, the bodies deform in the neighborhood of their initial contact and yield small, though finite, areas of contact; this deformation ensures that the surface stresses remain finite. For a *nominal line contact* the shape of the finite contact zone is an infinite strip, for a *nominal point contact* it is an ellipse. Nominal line contacts possess only one spatial dimension and are, therefore, easier to characterize than the two-dimensional nominal point contacts.

8.1 Rigid Cylinder Rolling on a Plane

The geometry of the cylinder-plane combination is shown in Figure 8.1. Let h_0 be the minimum separation between the infinitely long cylinder of radius R and the plane; then, at any angular position θ the film thickness is given by

$$h = -\frac{R}{n}\,(1 + n\cos\theta)\,, \tag{8.1}$$

where $n = -R/(h_0 + R)$ is constant for given geometry. We note that Eq. (8.1) is of the same form as Eq. (3.29), which was derived for journal bearings, if only one puts $C = -R/n$ and $\varepsilon = n$. In consequence, many of the previously derived journal bearing formulas remain applicable.

For the (infinite) cylinder-plane geometry, the Reynolds equation (3.33) reduces to

$$\frac{d}{dx}\left(\frac{h^3}{\mu}\frac{dp}{dx}\right) = 6U_0\frac{dh}{dx}, \tag{8.2}$$

and its first integral is given by

$$\frac{dp}{dx} = 6\mu U_0\frac{h - h_2}{h^3}. \tag{8.3}$$

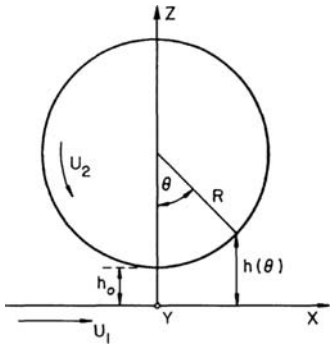

Figure 8.1. Cylinder-plane geometry and nomenclature.

We now introduce the transformation

$$\bar{p} = \frac{ph_0}{\mu U_0}, \quad \bar{h} = \frac{hm}{R}, \quad \theta = \sin^{-1}\left(\frac{x}{R}\right)$$

to obtain a nondimensional representation of the pressure gradient in Eq. (8.3),

$$\frac{d\bar{p}}{d\theta} = \frac{6h_0 n^2}{R}\left(\cos\theta \frac{\bar{h}(\theta) - \bar{h}(\theta_2)}{\bar{h}^3(\theta)}\right). \tag{8.4}$$

Implicit in this equation is the condition

$$\frac{d\bar{p}}{d\theta} = 0 \quad \text{at} \quad \theta = \theta_2,$$

where θ_2 represents the as yet unknown position of the trailing edge liquid-cavity interface.

The pressure distribution can be found formally from Eq. (8.4) by a second integration,

$$\bar{p} = \frac{6h_0 n^2}{R}\int_{\theta_1}^{\theta} \cos\theta \frac{\bar{h}(\theta) - \bar{h}(\theta_2)}{\bar{h}^3(\theta)}\, d\theta + B. \tag{8.5}$$

We subject this pressure distribution to the second of the Swift-Stieber boundary conditions, viz., $\bar{p}(\theta_2) = 0$, and find that θ_2 is determined by the condition

$$\int_{\theta_1}^{\theta_2} \cos\theta \frac{\bar{h}(\theta) - \bar{h}(\theta_2)}{\bar{h}^3(\theta)}\, d\theta = 0 \tag{8.6a}$$

or, when written in terms of the Sommerfeld angle ψ of Eq. (3.42), by the condition

$$\left[(\cos\psi_2 + n) - \sin\psi - \frac{1}{2}\sin\psi\cos\psi - \left(\frac{1}{2} + n\cos\psi_2\right)\psi\right]_{\psi_1}^{\psi_2} = 0, \tag{8.6b}$$

where, for a given ψ_1, Eq. (8.6b) serves to determine ψ_2.

For simplicity, we assume that the continuous film commences at $x = -\infty$ and, therefore, put $\theta_1 = -\pi/2$. The corresponding $\psi_1 = \arccos(n)$ was found from Eq. (3.42a). Equation (8.6b) is now in the form $\psi_2 = \psi_2[-n/(n+1)]$, where $-n/(n+1) = R/h_0$. Table 8.1 lists ψ_2 for typical values of R/h_0. Once ψ_2 is known, $\bar{h}(\theta_2)$ can be calculated and substituted into Eq. (8.5) to obtain the pressure distribution. Having found the pressure distribution,

Table 8.1. *Rigid cylinder on a plane*

R/h_0	ψ_2(rad)	θ_2(deg)	$\bar{w}'$
10	0.8520	11.3105	1.3985×10
10^2	0.8833	3.8200	2.2140×10^2
10^3	0.8868	1.2166	2.4103×10^3
10^4	0.8872	0.3850	2.4423×10^4
10^5	0.8887	0.1220	2.4444×10^5
10^6	0.8871	0.0385	2.4473×10^6

we can evaluate the component of the lubricant force that acts normal to the plane. If w' represents this force per unit axial width, we have

$$w' = \int_{x_1}^{x_2} p\, dx = R \int_{\theta_1}^{\theta_2} p \cos\theta\, d\theta. \tag{8.7}$$

Substituting the dimensionless quantities defined above, integrating by parts as in Eqs. (3.78) and taking into account Eq. (8.4), Eq. (8.7) yields

$$\bar{w}' = -6n^2 \left[\int_{\theta_1}^{\theta_2} \frac{\sin\theta \cos\theta}{(1 + n\cos\theta)^2}\, d\theta + \bar{h}(\theta_2) \int_{\theta_1}^{\theta_2} \frac{\sin\theta\cos\theta}{(1+n\cos\theta)^3} d\theta \right], \tag{8.8}$$

where we set $\bar{w}' = w'/\mu U_0$.

The integrals in Eq. (8.8) are easily evaluated when using either the Sommerfeld substitution, Eq. (3.42), or partial fractions. In terms of the Sommerfeld angle ψ, the result is

$$\bar{w}' = 6 \left[\frac{1 - n\cos\psi}{1 - n^2} + \ln \frac{1 - n^2}{1 - n\cos\psi} + \frac{n^2}{2(1-n^2)^2} \frac{2n\cos\psi - \cos^2\psi}{1 - n\cos\psi_2} \right]_{\psi_1}^{\psi_2}. \tag{8.9}$$

Table 8.1 contains $\bar{w}'$ as calculated from Eq. (8.9) at selected values of R/h_0. From the values in Table 8.1, we find that the approximate relationship

$$\frac{h_0}{R} = 2.44 \frac{\mu U_0}{w'} \tag{8.10}$$

holds over a wide range of R/h_0 and may serve as a means to calculate the minimum film thickness ratio for given mechanical input.

We now follow Dowson and Higginson (1977) and estimate the film thickness for a gear tooth contact. Typical values for the lubricant viscosity, surface speeds, and loads are

$$\mu = 0.075\,\text{Pa} \cdot \text{s}, \qquad U_1 = U_2 = 5.0\,\text{m/s},$$
$$U_0 = U_1 + U_2 = 10.0\,\text{m/s} \qquad w' = 26.5\,\text{kN/cm}.$$

Substituting these values into Eq. (8.10), we find the dimensionless minimum film thickness to be

$$\frac{h_0}{R} = 0.69 \times 10^{-6}.$$

If $R = 2.5$ cm, assuming that is the neighborhood of contact the gear geometry is satisfactorily represented by an "equivalent cylinder" of radius R rolling on a plane, we obtain

$$h_0 = 0.0172\,\mu\text{m}. \tag{8.11}$$

This value is small in comparison with even the best surface finishes encountered in gear manufacturing. It is almost two orders of magnitude smaller than the mean film thickness between two steel disks of $R = 3.81$ cm under a load of 1.96 kN/cm, as measured by Crook (1958). Typical rms surface finish for ball bearings is 0.1 μm for the ball and 0.25 μm for the raceway; for helical gears, ground and shaved, it is in the range 0.2–0.4 μm. Thus, our conclusion must be that classical hydrodynamic theory cannot explain the existence of a continuous lubricant film in highly loaded contacts. We must, therefore, look for appropriate extension of Reynolds' theory to explain continuous-film lubrication of counter-formal contacts.

8.2 Elastohydrodynamic Theory

The above analysis of the cylinder-plane geometry was first performed by H. M. Martin in 1916. Although Martin's negative conclusion on the existence of a continuous hydrodynamic film in highly stressed EHL contacts was completely in opposition to experimental evidence, it, nevertheless, discouraged theoretical research on lubricated counter-formal contacts for two decades.

The assumptions that limited Martin's analysis were (1) constant lubricant viscosity and (2) rigid bounding surfaces. The first significant extension to classical hydrodynamic theory came in 1936 when W. Peppler allowed the contacts to deform elastically; but Peppler also put forth an erroneous proposition, viz., that the pressure cannot exceed the Hertzian pressure of unlubricated contacts. The second extension, removal of the uniform, constant viscosity constraint, came in 1945 when Gatcombe allowed the lubricant viscosity to change with pressure. A good representation of the pressure dependence of viscosity of mineral oils is given by the formula

$$\mu = \mu_0 \exp(\alpha p), \tag{8.12}$$

where μ_0 and α are material constants of the lubricant.[1]

Substituting for μ in Eq. (8.3) and integrating the resulting equation, we obtain

$$\frac{d\bar{q}}{d\theta} = \frac{6h_0 n^2}{R}\left(\frac{\bar{h} - \bar{h}_2}{\bar{h}_3}\cos\theta\right). \tag{8.13}$$

The (dimensionless) *reduced pressure*, defined by

$$\bar{q} = \frac{h_0}{\mu_0 U_0 \alpha}\left(1 - e^{-\alpha p}\right), \quad q = \frac{\mu_0 U_0}{h_0}\bar{q}, \tag{8.14}$$

[1]The pressure-viscosity coefficient α of the Barus (1889) formula (8.12) is in the range $1.5 - 2.5 \times 10^{-8}$. The lower end of the range is for "paraffinic" oils while the upper end for "naphtenic" oils (Jones et al., 1975). However, this formula does not give good results at higher pressures, and application of the Barus equation to pressures in excess of 0.5 MPa may lead to serious errors.

is thus shown to satisfy the same equation as the isoviscous pressure, Eq. (8.4). Any pressure distribution found for the constant viscosity case may, therefore, be readily used for pressure-dependent viscosity through the formula

$$\begin{aligned} p &= -\frac{1}{\alpha}\ln\left(1-\bar{q}\frac{\mu_0 U_0 \alpha}{h_0}\right) \\ &= -\frac{1}{\alpha}\ln(1-\alpha q)\,. \end{aligned} \tag{8.15}$$

Equation (8.15) yields infinitely large pressure at the position where $q = 1/\alpha$, as was first remarked by Blok (1950). The solid surfaces, of course, cannot sustain limitless pressures. They will deform elastically and our simple analysis breaks down; nevertheless, it points to the necessity of having to consider both the pressure dependence of the viscosity and the deformation of the surfaces when considering continuous film lubrication of highly loaded contacts. Figure 8.2 dramatizes the development of EHL theory. The individual contributions of elastic deformation of surfaces and of pressure dependence of lubricant viscosity are relatively modest. However, they combine nonlinearly to yield a much increased load capacity and a new film shape.

The first satisfactory solution to account for the effects of both elastic deformation and pressure dependence of viscosity was reported by A. N. Grubin in 1949. His work, and that

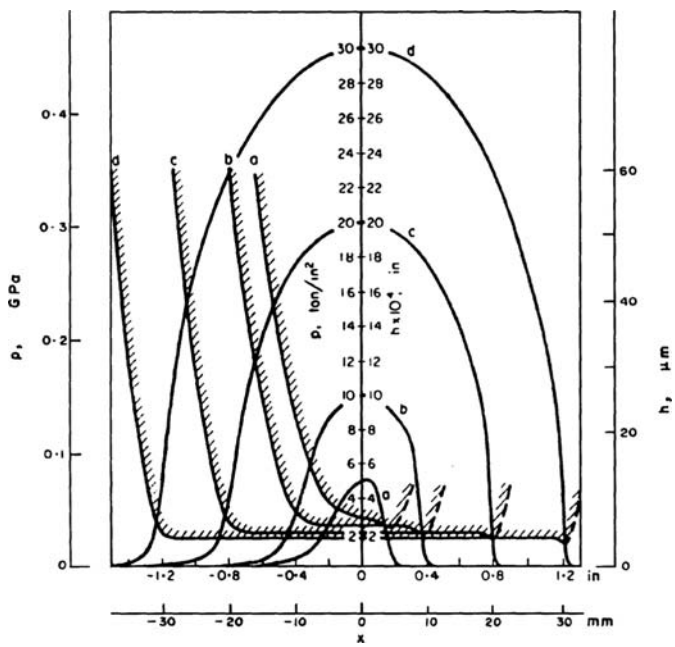

Figure 8.2. Pressure distribution and film shapes for same center line film thickness: (a) constant viscosity, rigid cylinders; (b) pressure-dependent viscosity, rigid cylinders; (c) constant viscosity, elastic cylinders; (d) pressure-dependent viscosity, elastic cylinders. (Reprinted by permission of the Council of the Institution of Mechanical Engineers from Dowson, D. and Higginson, G. R. A numerical solution to the elastohydrodynamic problem. *J. Mech. Eng. Sci.*, **1**, 6–15, 1959.)

of A. I. Petrushevich in 1951, established most of the essential properties of EHL solutions in concentrated contacts:

(1) The film is of almost uniform thickness over most of the contact zone. It displays, however, a typical and sudden decrease just upstream of the trailing edge.
(2) The pressure distribution curve follows the Hertzian ellipse over most of the contact zone.
(3) A sharp second pressure maximum exists (Figure 8.4), particularly at high speeds and light loads.

The first of these properties easily follows from Eq. (8.3), once it is acknowledged that $\mu = \mu(p)$. If μ is very large, and it might be several orders of magnitude larger than under atmospheric conditions, $(h - h_2)$ cannot deviate much from zero so as to constrain dp/dx from becoming excessive; this makes for an almost constant film thickness in the high-pressure zone. At the trailing edge, on the other hand, the pressure must rapidly drop to zero as here the Swift-Stieber conditions apply. To sustain the required large negative pressure gradient there, the film thickness must decrease sharply just upstream of the trailing edge.

The second and third properties of EHL contacts follow from the observation that at large load and small speed the film thickness is orders of magnitude smaller than the elastic deformation, thus the pressure distribution will be close to the Herzian distribution for dry contacts. At low load and high speed, on the other hand, the elastic deformation of the surfaces remains insignificant when compared to the film thickness, thus the pressure distribution will approach that of the rigid cylinder.

The physical parameters that are required to characterize the EHL problem can be conveniently combined into independent nondimensional parameters (groups); as the number of the resulting dimensionless groups is smaller than the number of physical parameters, this nondimensionalization of the problem facilitates presentation of the results. Assuming pure rolling and considering only nominal line contacts, Dowson and Higginson (1977) combined the physical variables of the isothermal EHL problem into four[2] convenient dimensionless parameters:

film thickness parameter $H = h_0/R$
load parameter $W = w/E'RL$
speed parameter $U = \mu_0\tilde{u}/E'R$
materials parameter $G = \alpha E'$

and through numerical solution of the appropriate equations, obtained the following relationship for the minimum film-thickness variable:

$$H = 1.6\frac{G^{0.6}U^{0.7}}{W^{0.13}}. \tag{8.16}$$

Here R is the effective radius at contact and L is its axial length, E' is the effective contact modulus, $\tilde{u} = U_0/2$ is the effective speed, and w is the load.

[2]This set of nondimensional parameters must be augmented with the *ellipticity parameter*, $k = b/a$, when discussing nominal point contact. Here a and b are the semi-axes of the contact ellipse, expressible in terms of the principal curvatures of the contacting bodies. (The full definition of parameters for nominal point contact will be given later.)

In practice the nondimensional parameters vary greatly, as $10^{-13} \leq U \leq 10^{-8}$, $3 \times 10^{-5} \leq W \leq 3 \times 10^{-4}$, and $2.5 \times 10^3 \leq G \leq 7.5 \times 10^3$.

Writing the Dowson-Higginson formula for minimum film thickness, Eq. (8.16), in the dimensional form, we obtain

$$h = 1.6 \frac{\alpha^{0.6} (\mu_0 \tilde{u})^{0.7} E'^{0.03} R^{0.43}}{w^{0.13}}. \tag{8.17}$$

Equation (8.17) indicates that the film thickness is virtually independent of the elastic modulus of the material and is only a weak function of the external load.

For complete solution of the isothermal EHL problem, we have to satisfy simultaneously the following equations:

(1) The Reynolds equation,
(2) The viscosity-pressure relationship,
(3) The equations of elasticity.

It was discovered early on that the conventional iterative scheme represented by

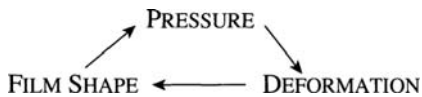

does not always converge. This is particularly true when there is large elastic deformation of the surfaces. To correct for this, Dowson and Higginson (1959) proposed the so-called *inverse hydrodynamic solution*. The essence of the inverse solution is calculation of the film shape that would produce a specified pressure distribution. This same pressure distribution is also employed to calculate surface deformations for plane strain. The remainder of the computation consists of systematic alteration of the pressure distribution to bring the film shape and surface deformation into agreement.

The inverse hydrodynamic method is essentially a one-dimensional method, but here it works well. As a starting point, we perform the indicated differentiation in Eq. (8.2) and obtain

$$h^3 \frac{d}{dx}\left(\frac{1}{\mu}\frac{dp}{dx}\right) - \frac{dh}{dx}\left(6U_0 - \frac{3h^2}{\mu}\frac{dp}{dx}\right) = 0.$$

The second term of this equation will vanish when

$$\frac{dh}{dx} = 0$$

or when

$$\frac{dp}{dx} = \frac{2\mu U_0}{h^2}$$

(the first condition defines the point of inflection $d^2p/dx^2 = 0$ in an isoviscous lubricant).

Inspection of Figure 8.4 (below) will convince the reader that the first condition is satisfied at the point of minimum film thickness near the trailing edge, while the second condition is satisfied at a position $x = a$ within the inlet zone where the film thickness has the value

$$h_a = \sqrt{\frac{2\mu_a U_0}{(dp/dx)_a}}.$$

Substituting h_a into Eq. (8.3) yields

$$h_2 = \frac{2}{3}h_a. \tag{a}$$

The once-integrated Reynolds Eq. (8.3) may also be rearranged to yield

$$K\bar{h}^3 - \bar{h} + 1 = 0, \tag{b}$$

where

$$K = \frac{h_2^2}{6\mu U_0}\frac{dp}{dx}, \quad \bar{h} = \frac{h}{h_2}.$$

Thus, knowing μ and U_0, the complete film shape can be found for an arbitrary dp/dx distribution from Eqs. (a) and (b). Details of the inverse hydrodynamic method are discussed by Dowson and Higginson (1959, 1977).

Figures 8.3 and 8.4 show pressure distributions and film shapes for two different material combinations, steel and mineral oil ($G = 5000$) and bronze and mineral oil ($G = 2500$).

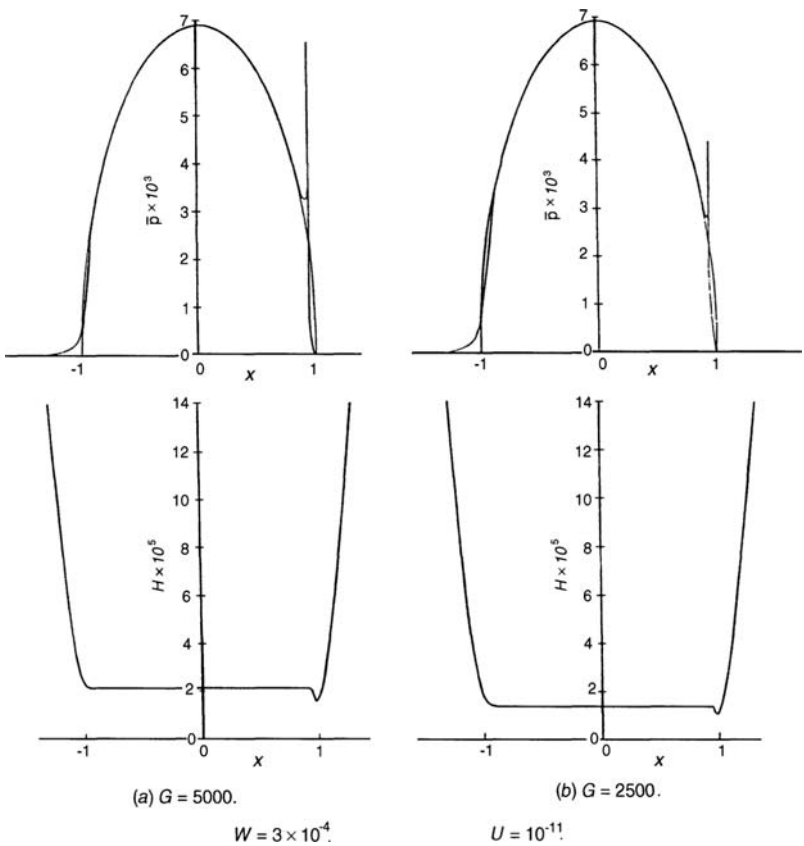

Figure 8.3. Pressure and film thickness in EHL contact for (a) steel and mineral oil and (b) bronze and mineral oil under high load, $\bar{p} = p/E'$, $H = h/R$. (Reprinted by permission of the Council of the Institution of Mechanical Engineers from Dowson, D. and Higginson, G. R. Effect of material properties on the lubrication of elastic rollers. *J. Mech. Eng. Sci.*, **2**, 188–194, 1960.)

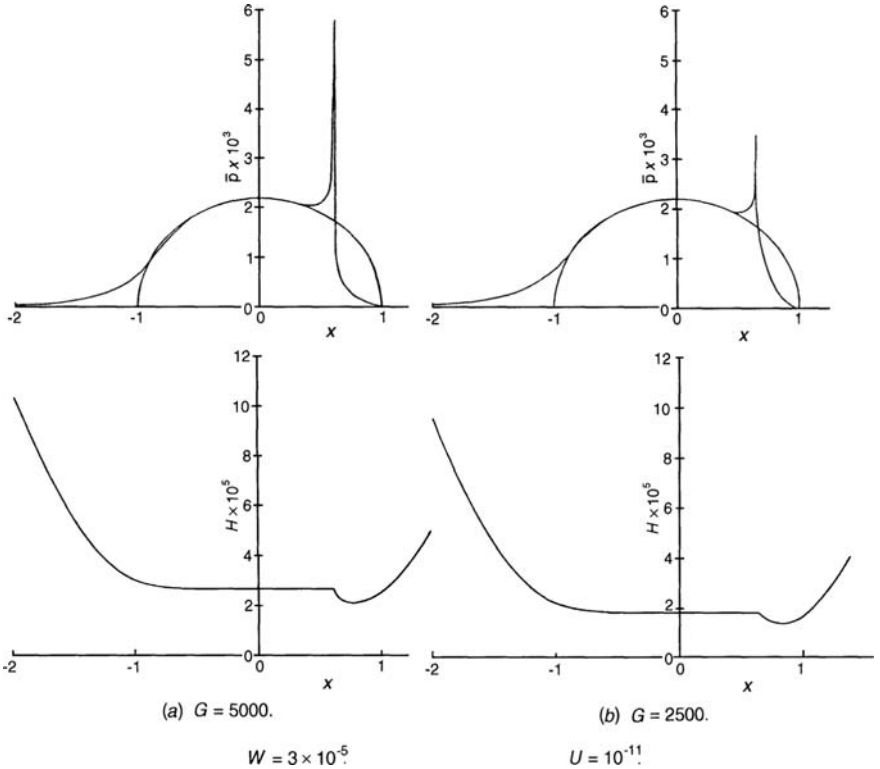

Figure 8.4. Pressure and film thickness in EHL contact for (a) steel and mineral oil and (b) bronze and mineral oil under low load, $\bar{p} = p/E'$, $H = h/R$. (Reprinted by permission of the Council of the Institution of Mechanical Engineers from Dowson, D. and Higginson, G. R. Effect of material properties on the lubrication of elastic rollers. *J. Mech. Eng. Sci.*, **2**, 188–194, 1960.)

These solutions were calculated by Dowson and Higginson (1960) using the inverse hydrodynamic method. The necking down of the film near the outlet, which might be as high as 25%, and the sharp second pressure maximum are easily noticeable in Figures 8.3 and 8.4. We note that the departure from the Hertzian pressure distribution is more pronounced at the lower load, consistent with our earlier reasoning.

The speed effect is well demonstrated by the curves of Figure 8.5, which were obtained for a liquid lubricant whose density was also allowed to change with pressure. The most significant effect of lubricant compressibility (not shown) is a slight lowering of the pressure peak and its displacement into the upstream direction from its constant density position.

A slight reduction of the pressure peak occurs also on introduction of thermal effects into the analysis, but only at higher speeds and moderate-to-high slip between rollers. At lower speeds, the pressure peak becomes more severe. The film thickness in the contact zone is not greatly influenced by temperature effects (Cheng and Sternlicht, 1965).

For pure rolling, Cheng (1965) and Cheng and Sternlicht (1965) reported no significant thermal effects on either the pressure level or the film thickness but found that the temperature has a major influence on the friction force. Kim and Sadeghi (1992), on the other hand, found that thermal effects can reduce film thickness by as much as 15%. Calculated

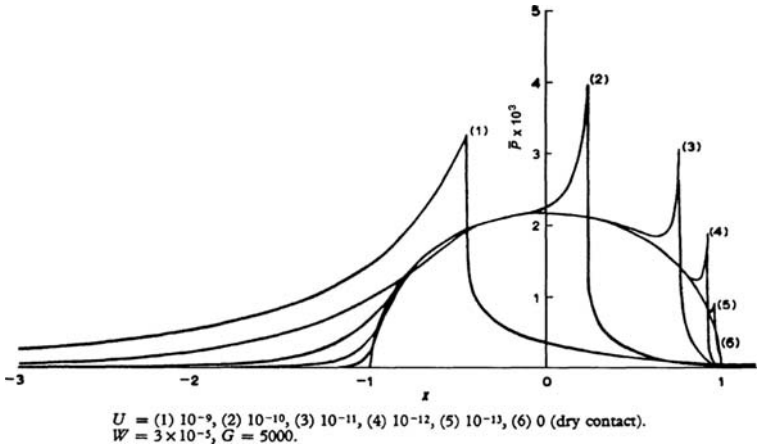

Figure 8.5. Effect of surface velocity on pressure distribution in EHL contact, $\bar{p} - p/E'$. (Reprinted by permission of the Council of the Institution of Mechanical Engineers from Dowson, D., Higginson, G. R. and Whitaker, A. V. Elastohydrodynamic lubrication: A survey of isothermal solutions. *J. Mech. Eng. Sci.*, **4**, 121–126, 1962.)

and measured film thicknesses in EHL contacts are compared in Figure 8.6 (Dowson et al., 1959; Cheng and Sternlicht, 1965; Sibley and Orcutt, 1961; Crook, 1958; Archard et al., 1961).

We alluded previously to the fact that thin films and high contact pressures are not always found in, nor are essential to, elastohydrodynamic lubrication. The lubrication of natural and artificial biological joints (Tanner, 1966; Dowson, 1967), the viscous hydroplaning of automobile tires (Browne, Whicker, and Rohde, 1975), and the lubrication of compliant slider and journal bearings belong to this problem area.

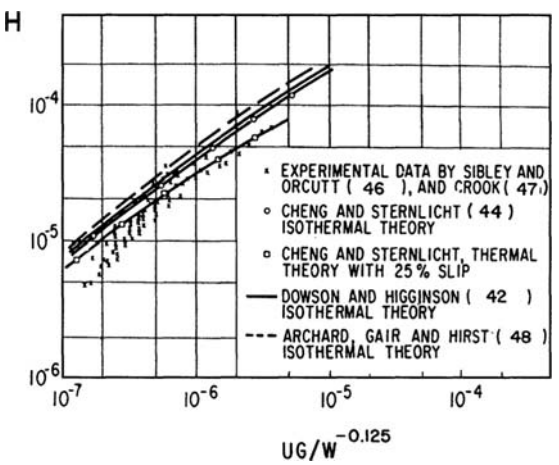

Figure 8.6. Comparison of predicted and measured film thickness variable in EHL contacts. (Reprinted with permission from Cheng, H. S. and Sternlicht, B. A numerical solution for the pressure, temperature and film thickness between two infinitely long lubricated rolling and sliding cylinders, under heavy loads. *ASME Trans., Ser. D*, **87**, 695–707, 1965.)

Elastic deformation of surfaces can also cause significant effects in conformal bearings. Carl (1964) found that elastic distortion of journal bearings leads to increased film thickness and reduced peak pressure at low loads. Benjamin and Castelli (1971) were the first to treat finite compliant bearings analytically and found severe change in the journal locus, as compared to rigid bearings. Oh and Huebner (1973) applied the finite-element method to a finite bearing. Oh and Rohde (1977) extended finite-element analysis to compressible finite journal bearings. In another paper, Rohde and Oh (1975) presented the first complete thermoelastohydrodynamic analysis of a finite slider. An excellent review of pre-1978 work was given by Rohde (1978). For more recent work, see Mittwollen and Glienicke (1990), Bouchoule et al. (1996), and Monmousseau et al. (1996), as referenced in Chapter 9.

8.3 Contact Mechanics

Consider two convex bodies, $\bar{B}_1$ and $\bar{B}_2$, which make contact in a single point, O, under vanishing load. We intend to find out what happens at the contact as the load is increased. To facilitate this discussion, we replace our very general bodies $\bar{B}_1$, $\bar{B}_2$ by the ellipsoids, B_1, B_2, that are illustrated in Figure 8.7. The ellipsoid B_1 has the same principal curvatures, r_{1x} and r_{1y}, as the body $\bar{B}_1$ at O, while the ellipsoid B_2 possesses the same principal curvatures, r_{2x} and r_{1y}, as $\bar{B}_2$ at O. The principal curvatures, r_{1x} and r_{2x}, lie in the

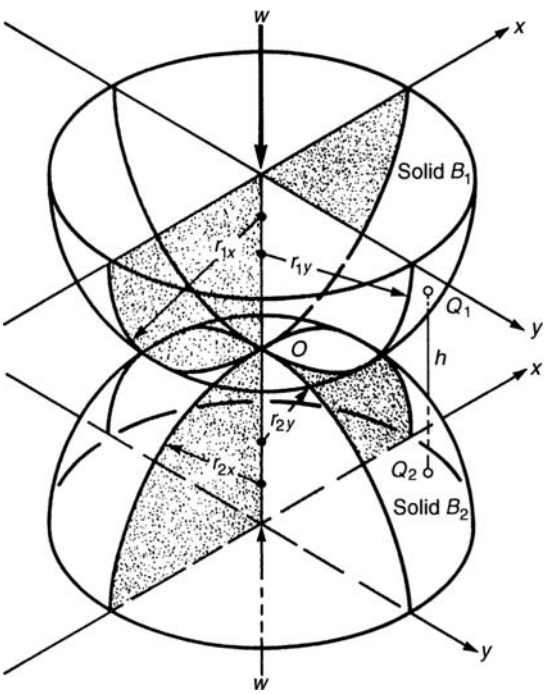

Figure 8.7. Geometry of counterformal contact between two convex bodies. (Hamrock, B. J. and Dowson, D. 1981. *Ball Bearing Lubrication*. Copyright John Wiley & Sons. © 1981. Reprinted by permission of John Wiley & Sons, Inc.)

same[3] plane $x = 0$ and r_{1y}, r_{2y} lie in the plane $y = 0$. The surfaces of the ellipsoids near the point of contact can be represented by the equations

$$\begin{aligned} z_1 &= A_1 x^2 + A_2 xy + A_3 y^2, \\ z_2 &= B_1 x^2 + B_2 xy + B_3 y^2. \end{aligned} \tag{8.18}$$

The distance, h, between two points, such as Q_1 and Q_2 in Figure 8.7, is then

$$h = z_1 + z_2 = (A_1 + B_1)\, x^2 + (A_2 + B_2)\, xy + (A_3 + B_3)\, y^2. \tag{8.19}$$

We can always choose directions for x and y such as to make the coefficient of the product xy in Eq. (8.19) vanish. This way we obtain

$$h = z_1 + z_2 = Ax^2 + By^2 = \frac{1}{2R_x} x^2 + \frac{1}{2R_y} y^2. \tag{8.20}$$

Here R_x, R_y are the principal relative radii of curvature, defined by

$$\frac{1}{R_x} = \left(\frac{1}{r_{1x}} + \frac{1}{r_{2x}} \right), \quad \frac{1}{R_y} = \left(\frac{1}{r_{1y}} + \frac{1}{r_{2y}} \right).$$

The contours of constant gap h between the undeformed surfaces are the ellipses

$$\frac{x^2}{(\sqrt{2hR_x})^2} + \frac{y^2}{(\sqrt{2hR_y})^2} = 1, \tag{8.21}$$

the ratio of whose axes are given by $(R_y/R_x)^{1/2}$.

If now we press the bodies together, they deform in the neighborhood of the point of their first contact, O, and touch over a finite area. The contact area also has the shape of an ellipse, the ratio of whose semi-axes, b/a, depends on $(R_y/R_x)^{1/2}$ alone. But $\kappa = b/a$ equals $(R_y/R_x)^{1/2}$ only in the limit $R_y/R_x \to 1$ (Johnson, 1992).[4] The ratio of the semiaxes,

$$\kappa = \frac{b}{a},$$

is called the ellipticity parameter.[5]

Two additional indicators of contact geometry that will be used in the sequel are

Curvature sum:

$$S_c = \frac{1}{\mathcal{R}} = \frac{1}{R_x} + \frac{1}{R_y} \tag{8.22}$$

Curvature difference:

$$D_c = \frac{1}{S_c} \left[\left(\frac{1}{r_{1x}} - \frac{1}{r_{1y}} \right) + \left(\frac{1}{r_{2x}} - \frac{1}{r_{2y}} \right) \right].$$

[3] For the general case when the principal radii of curvature are not aligned, see Timoshenko and Goodier (1951).

[4] The contact ellipse is somewhat skinnier than the ellipse $h = \text{const.}$, Eq. (8.21).

[5] We select x as the direction of relative motion, so $2b$ is the axis of the contact ellipse normal to the direction of fluid entrainment.

It was shown by Hertz (1881) that the pressure distribution over the elliptical contact is given by (Johnson, 1992)

$$p = p_H \left[1 - \left(\frac{x}{a}\right)^2 - \left(\frac{y}{b}\right)^2 \right] \tag{8.23a}$$

and

$$p_H = \frac{3w}{2\pi ab}. \tag{8.23b}$$

Here a and b are the lengths of the semi-axes of the contact ellipse, w is the load, and p_H is the maximum value of p.

As mentioned earlier, the values of a and b depend only on geometry; they must be determined before the pressure can be evaluated from Eqs. (8.23). It was Harris (1991) who showed how to calculate a and b. Knowing the curvatures $1/R_x$, $1/R_y$, we can determine the curvature difference, D_c, in Eq. (8.22). D_c, on the other hand, can be expressed purely in terms of the ellipticity parameter, κ as

$$D_c = \frac{(\kappa^2 + 1)\mathcal{E} - 2\mathcal{F}}{(\kappa^2 - 1)\mathcal{E}}, \tag{8.24}$$

where $\mathcal{E}$ and $\mathcal{F}$ are complete elliptic integrals of the second and first kind, respectively:

$$\mathcal{E} = \int_0^{\pi/2} \left[1 - \left(1 - \frac{1}{\kappa^2}\right) \sin^2 \phi \right]^{1/2} d\phi, \tag{8.25a}$$

$$\mathcal{F} = \int_0^{\pi/2} \left[1 - \left(1 - \frac{1}{\kappa^2}\right) \sin^2 \phi \right]^{-1/2} d\phi. \tag{8.25b}$$

Equation (8.24) is, thus, of the form

$$D_c = f(\kappa). \tag{8.26a}$$

Equation (8.26a) enables us to find the value of the curvature difference, D_c, for given value of the ellipticity parameter κ. But this is not what we need. We would like to calculate κ for given value of D_c, i.e., we require the inverse of Eq. (8.26a)

$$\kappa = f^{-1}(D_c). \tag{8.26b}$$

Once in posession of this inverse relationship, Eq. (8.26b), we can, for given D_c, calculate the ellipticity parameter κ, and with κ in hand determine the contact ellipse semi-axes a, b, and the deflection δ according to (Harris, 1991)

$$a = \left[\frac{6\kappa^2 \mathcal{E} w \mathcal{R}}{\pi E'} \right]^{1/3}, \tag{8.27a}$$

$$b = \left[\frac{6\mathcal{E} w \mathcal{R}}{\pi \kappa E'} \right]^{1/3}, \tag{8.27b}$$

$$\delta = \mathcal{F} \left[\frac{9}{2\mathcal{E}\mathcal{R}} \left(\frac{w}{\pi \kappa E'} \right)^2 \right]^{1/3}, \tag{8.27c}$$

and the stress distribution from Eqs. (8.23). Here

$$\frac{1}{E'} = \frac{1}{2}\left[\frac{1-\nu_1^2}{E_1} + \frac{1-\nu_2^2}{E^2}\right]$$

as before, Eq. (1.13).

Unfortunately, $f(\kappa)$ is a transcendental function, thus its inverse in Eq. (8.26b) must be obtained numerically (Hamrock and Anderson, 1973). Here we shall adopt, instead, the approximation

$$\kappa \approx \bar{\kappa} = 1.0339\left(\frac{R_y}{R_x}\right)^{0.636} \tag{8.28a}$$

obtained by Brewe and Hamrock (1977) by curve fitting. In place of Eq. (8.28a), some authorities prefer

$$\bar{\kappa} = \alpha_r^{2/\pi}, \quad \alpha_r = \left(\frac{R_y}{R_x}\right). \tag{8.28b}$$

Brewe and Hamrock (1977) also supply us with an excellent approximation to the elliptic integrals in Eqs. (8.25):

$$\mathcal{E} \approx \bar{\mathcal{E}} = 1.0003 + \frac{0.5968}{\alpha_r}, \tag{8.29a}$$

$$\mathcal{F} \approx \bar{\mathcal{F}} = 1.5277 + 0.6023\,\ln\alpha_r. \tag{8.29b}$$

Later Hamrock and Brewe (1983) recommended the simpler forms

$$\bar{\mathcal{E}} = 1 + \left(\frac{\pi}{2} - 1\right)\Big/\alpha_r,$$

$$\bar{\mathcal{F}} = \frac{\pi}{2} + \left(\frac{\pi}{2} - 1\right)\ln\alpha_r.$$

Using Eqs. (8.28) and (8.29) in Eqs. (8.27), we obtain the approximate values $\bar{a}$, $\bar{b}$, and $\bar{\delta}$. This approximation can be used with confidence for $0.01 \le \alpha_r \le 100$.

By taking $\kappa \to \infty$, we get a *nominal line contact* that, on increasing the load, w, from zero, develops into an infinite-strip contact area of width $2b$. Then

$$p = p_H\left[1 - \left(\frac{y}{b}\right)^2\right]^{1/2} \tag{8.30a}$$

and

$$p_H = \frac{2w'}{\pi b} \tag{8.30b}$$

where w' is the load per unit length of the strip. The half-width of the contact area can be calculated from

$$b = \left(\frac{8w'R_x}{\pi E'}\right)^{1/2}. \tag{8.30c}$$

Table 8.2. *Parameters employed in EHL design formulas*

	Type of contact	
Parameter	Point	Line
Film Thickness, H	h/R_x	h/R_x
Load, W	w/R_x^2E'	w/R_xLE'
Speed, U	$\mu_0 V/E'R_x$	$\mu_0\tilde{u}/E'R_x$
Materials, G	$\alpha E'$	$\alpha E'$
Ellipticity, κ	b/a	

8.4 Nondimensional Groups

If we wish to design for continuous lubricant film in a counter-formal contact, we must be able to predict the minimum film thickness. If the predicted film thickness is large in comparison with the rms surface finish, and if sufficient amount of lubricant is made available, the chances are that on application a continuous EHL film will result. If the conditions for continuous film are not satisfied, partial EHL or boundary lubrication will be obtained.

Having identified the minimum film thickness as the primary parameter in EHL design, we will employ the formulas that are currently in use to calculate it.

It was indicated earlier, Eq. (8.16), that dimensional analysis of the EHL problem yields

$$\phi\,(H, U, W, G, \kappa) = 0. \tag{8.31}$$

Here we extended Eq. (8.16a) by including the ellipticity parameter κ so as to make Eq. (8.31) applicable also to point contacts. For the two types of contacts, viz., nominal line and nominal point, the parameters in Eq. (8.31) have somewhat different definition, as shown in Table 8.2. Here

$$\frac{1}{R_x} = \frac{1}{r_{1x}} + \frac{1}{r_{2x}}, \qquad \frac{1}{E'} = \frac{1}{2}\left[\frac{1-\nu_1^2}{E_1} + \frac{1-\nu_2^2}{E_1}\right],$$

$$\tilde{u} = (u_1 + u_2)/2, \qquad V = (u^2 + v^2)^{1/2}.$$

According to Eq. (8.31), the film thickness variable, H, depends on four independent nondimensional groups U, W, G, and κ. This is a great improvement over a primitive variable representation and, as usual, dimensional analysis facilitates the presentation of results. However, tabulation of H as a function of four nondimensional groups is still a formidable task. Fortunately, it has been noticed by a number of researchers that, with little sacrifice to accuracy of representation, the number of nondimensional groups involved in determining the film thickness can be reduced by one, when employing a new set of nondimensional groups. Elements of this new set are constructed by combining the elements

of the set in Eq. (8.31); for nominal point contact they are:

$$\left.\begin{aligned} g_H &= \left(\frac{W}{U}\right)^2 H \\ g_V &= \left(\frac{GW^3}{U^2}\right)^2 \\ g_E &= W^{8/3}U^2 \\ \kappa &= 1.0339\left(\frac{R_y}{R_x}\right)^{0.636} \end{aligned}\right\} \quad \text{nominal point contact.} \tag{8.32}$$

Besides reducing the number of parameters of the problem and thereby facilitating presentation of results, a further advantage in using Eqs. (8.32) is that the new parameters are easily identified with the main characteristics of EHL. Thus, g_H represents film thickness, g_V represents deviation from isoviscosity, g_E represents significance of elastic deformation, and κ represents the geometry of the contact.

We now have the relationship

$$g_H = \Psi(g_V, g_E, \kappa). \tag{8.33}$$

Our task now is to find the function $\Psi(g_V, g_E, \kappa)$ over practical ranges of its arguments. This task could be accomplished in one of two ways: (1) analytically, by simultaneous solution of all the relevant equations of the system or (2) numerically, by solving the EHL problem for a large number of inputs (g_V, g_E, κ) and then curve fitting to the supersurface $g_H = \Psi(g_V, g_E, \kappa)$ in four-dimensional parameter space.

Lubrication Regimes

Analytical solution of Eq. (8.33) is clearly out of the question, and we proceed by the numerical method (the details of these calculations are presented in the next section). But before doing that, let us first examine asymptotic cases $g_V = g_E = 0$; $g_E = 0$, $g_V \neq 0$; and $g_V = 0$, $g_E \neq 0$, leaving the case $g_V \neq 0$, $g_E \neq 0$, for last.

(1) $g_V = 0$, $g_E = 0$: *Rigid-Isoviscous Regime*

In this lubrication regime the pressure is low enough that it leaves the viscosity unaltered and is unable to cause significant elastic deformation of the surfaces. This is the condition encountered in hydrodynamic journal and thrust bearings (see Chapter 3), and, to a lesser extent, in lightly loaded counter-formal contacts. It is the regime of classical hydrodynamic lubrication.

(2) $g_V \neq 0$, $g_E = 0$: *Rigid-Piezoviscous Regime*

We encounter this lubrication regime in applications that exhibit pressures high enough to effectively change the lubricant's viscosity from its inlet value, yet not so high as to initiate significant elastic deformation in the bearing material.[6]

[6]We should recognize that, by judiciously changing the pressure-viscosity coefficient, α, and the effective Young's modulus, E', we could relocate our process from the $g_V \neq 0$, $g_E = 0$ regime to the $g_V = 0$, $g_E \neq 0$ regime.

(3) $g_E \neq 0, g_V = 0$: *Elastic-Isoviscous Regime*

Though this regime is characterized by significant elastic deformation, the pressure is not high enough to affect the viscosity of the particular lubricant employed. An example for lubrication in the elastic-isoviscous regime is human and animal joints lubricated by sinovial fluid (Dowson and Wright, 1981). Operation in this regime is often termed *soft EHL*. Automobile tires and elastomeric machine elements also operate in this regime.

(4) $g_E \neq 0, g_V \neq 0$: *Elastic-Piezoviscous Regime*

This is the regime of full EHL, also called *hard EHL*. The elastic deformation of the surfaces can be orders of magnitude larger than the thickness of the film and the lubricant viscosity can be orders of magnitude higher than its bulk value.

We note here that the parameters g_V and g_E differ in nominal point contacts from that in nominal line contacts. Definition (8.31) is valid for nominal point contacts.

In nominal line contacts, we drop the ellipticity parameter from the list of nondimensional variables and define

$$\left.\begin{aligned} g_H &= \left(\frac{W}{U}\right) H \\ g_V &= \frac{W^{3/2} G}{U^{1/2}} \\ g_E &= \frac{W}{U^{1/2}} \end{aligned}\right\} \quad \text{nominal line contact.} \tag{8.34}$$

The various lubrication regimes are depicted in Figures 8.8 to 8.11.

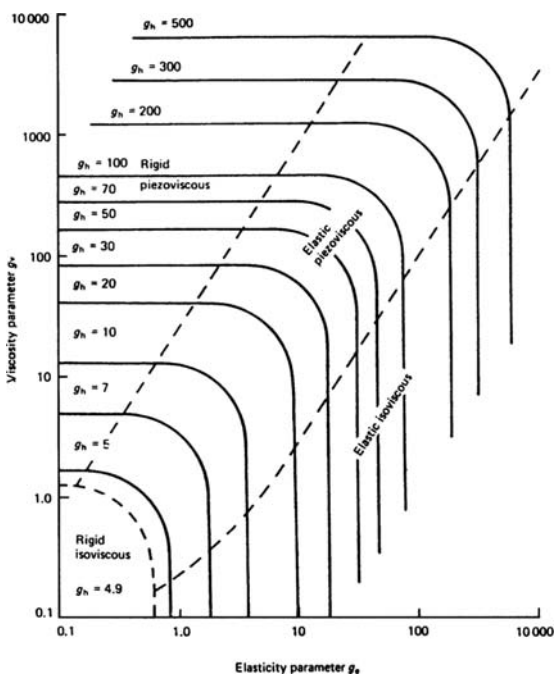

Figure 8.8. Map of lubrication regimes for nominal line. (Reprinted with permission from Arnell, R. D., Davies, P. B., Halling, J. and Whomes, T. L. *Tribology Principles and Design Applications*. Copyright Springer Verlag, © 1991.)

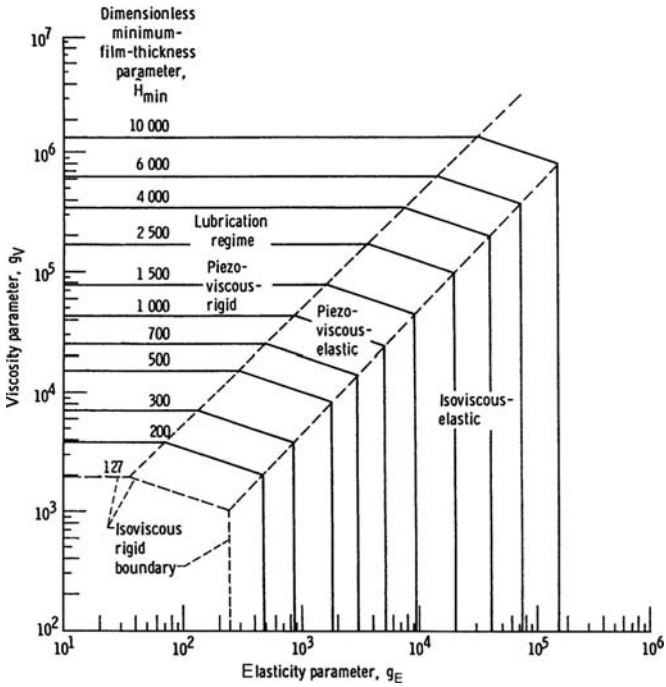

Figure 8.9. Map of lubrication regimes for nominal point contact, $\kappa = 3$. (Hamrock, B. J. and Dowson, D. 1981. *Ball Bearing Lubrication*. Copyright John Wiley & Sons, © 1981. Reprinted by permission of John Wiley & Sons, Inc.)

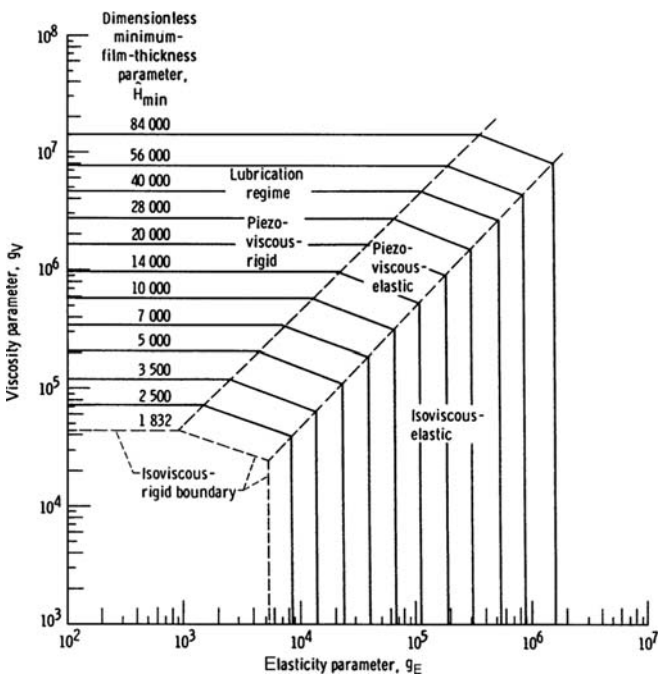

Figure 8.10. Map of lubrication regimes for nominal point contact, $\kappa = 3$. (Hamrock, B. J. and Dowson, D. 1981. *Ball Bearing Lubrication*. Copyright John Wiley & Sons, © 1981. Reprinted by permission of John Wiley & Sons, Inc.)

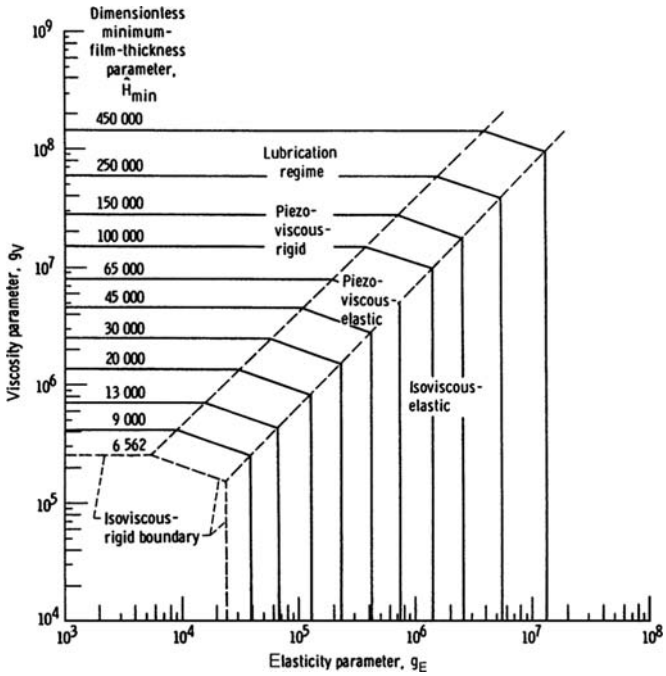

Figure 8.11. Map of lubrication regimes for nominal point contact, $\kappa = 6$. (Hamrock, B. J. and Dowson, D. 1981. *Ball Bearing Lubrication*. Copyright John Wiley & Sons, © 1981. Reprinted by permission of John Wiley & Sons, Inc.)

In the following, we list the formulas applicable in the various regimes:

Film-Thickness Design Formulas

Nominal Line Contact (Arnell, Davis, Halling, and Whomes, 1991)

(1) *Rigid-Isoviscous Regime:*

$$g_{H_{\min}} = 2.45. \tag{8.35a}$$

(2) *Rigid-Piezoviscous Regime:*

$$g_{H_{\min}} = 1.05 g_V^{2/3}. \tag{8.35b}$$

(3) *Elastic-Isoviscous Regime:*

$$g_{H_{\min}} = 2.45 g_E^{0.8}. \tag{8.35c}$$

(4) *Full EHL Regime:*

$$g_{H_{\min}} = 1.654 g_V^{0.54} g_E^{0.06}. \tag{8.35d}$$

Nominal Point Contact (Hamrock, 1990)

(1) *Rigid-Isoviscous regime:*

$$g_{H_{\min}} = 128\alpha_r\lambda_b^2\left[0.131\tan^{-1}\left(\frac{\alpha_r}{2}\right) + 1.683\right]^2, \tag{8.36a}$$

where

$$\lambda_b = \left(1 + \frac{2}{3\alpha_r}\right)^{-1}.$$

(2) *Rigid-Piezoviscous regime:*

$$g_{H_{\min}} = 141 g_V^{0.375}[1 - e^{-0.0387\alpha_r}]. \tag{8.36b}$$

(3) *Elastic-Isoviscous regime:*

$$g_{H_{\min}} = 8.70 g_E^{0.67}[1 - 0.85e^{-0.31\kappa}]. \tag{8.36c}$$

(4) *Full EHL regime:*

$$g_{H_{\min}} = 3.42 g_V^{0.49} g_E^{0.17}[1 - e^{-0.68\kappa}]. \tag{8.36d}$$

Comparison of Figures 8.9, 8.10, and 8.11 shows the strong effect the value of elliptic eccentricity κ has on regime boundaries.

A valuable aid for design of line contacts has been published by ESDU (1985): Film Thickness in Lubricated Hertzian Contacts (EHL): Part I, Item No. 85027, London. See also Harris (1991) and Hamrock (1991).

In the next section we give details of a numerical scheme that makes calculation of Eq. (8.31) possible, leading to the formulas (8.35) and (8.36).

8.5 Analysis of the Line Contact Problem

The full EHL problem does not yield to analytical solutions and numerical methods must be employed. Prior to discussing the relevant numerical methods, we will list the set of equations and boundary conditions that must be satisfied simultaneously by any solution of the problem. This set contains equations of fluid dynamics, equations of elasticity, and state equations for the fluid that characterize its viscosity-pressure and density-pressure behavior. We will not list energy conservation equations, however, and deal here only with isothermal processes. The analysis of nominal line contacts is made simpler by the fact that it employs only ordinary differential equations; it does, however, retain most of the features of the EHL problem. For further study, the interested reader should consult the various articles that have appeared in the ASME Journal of Tribology, as well as the book by Hamrock and Dowson (1981).

Elastic Deformation

Figure 8.12 depicts a semi-infinite elastic body, located in $z > 0$ and loaded along its y-axis. The components of strain resulting from the uniform line loading w'

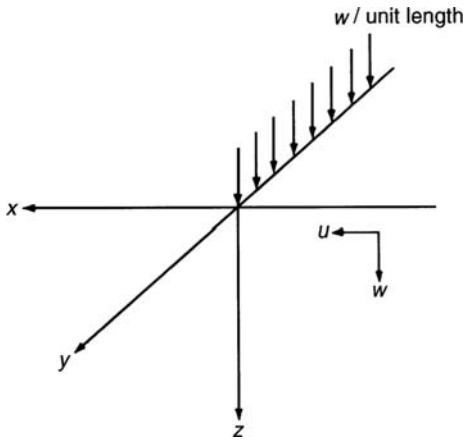

Figure 8.12. Line loading of elastic half-space.

are related to the components of stress by Hook's law. For the normal components of strain, we have

$$\varepsilon_{xx} = \frac{\partial u}{\partial x} = \frac{1}{E}[T_{xx} - \nu(T_{yy} + T_{zz})], \tag{8.37a}$$

$$\varepsilon_{yy} = \frac{\partial v}{\partial y} = \frac{1}{E}[T_{yy} - \nu(T_{xx} + T_{zz})], \tag{8.37b}$$

$$\varepsilon_{zz} = \frac{\partial w}{\partial z} = \frac{1}{E}[T_{zz} - \nu(T_{xx} + T_{yy})]. \tag{8.37c}$$

Here (u, v, w) are the components of the displacement of the solid, E is Young's modulus of elasticity, and ν is the Poisson ratio. The quantities depicted by ε_{xx}, ε_{yy}, ε_{zz} and T_{xx}, T_{yy}, T_{zz} are the normal components of strain and stress, respectively.

The mixed components of strain are related to the mixed components of stress through the shear modulus, $G = E/2(1 + \nu)$, as

$$\varepsilon_{xy} = \frac{\partial u}{\partial y} + \frac{\partial v}{\partial x} = \frac{1}{G}T_{xy}, \tag{8.38a}$$

$$\varepsilon_{yz} = \frac{\partial v}{\partial z} + \frac{\partial w}{\partial y} = \frac{1}{G}T_{yz}, \tag{8.38b}$$

$$\varepsilon_{zx} = \frac{\partial w}{\partial x} + \frac{\partial u}{\partial z} = \frac{1}{G}T_{zx}. \tag{8.38c}$$

This three-dimensional state of strain can be made simpler by assuming that plane sections defined by $y = \text{const.}$ remain plane and will not be displaced in the y direction during loading. But then

$$\varepsilon_{yz} = 0, \quad \varepsilon_{xy} = 0, \quad \varepsilon_{yy} = 0. \tag{8.39}$$

Substituting the third of these conditions into Eq. (8.37b) yields

$$T_{yy} = \nu(T_{xx} + T_{zz}), \tag{8.40}$$

so for the plain strain problem Eqs. (8.37) and (8.38) reduce to

$$\frac{\partial u}{\partial x} = \frac{1-\nu^2}{E} T_{xx} - \frac{\nu(1+\nu)}{E} T_{zz}, \tag{8.40a}$$

$$\frac{\partial w}{\partial z} = \frac{1-\nu^2}{E} T_{zz} - \frac{\nu(1+\nu)}{E} T_{xx}, \tag{8.40b}$$

$$\frac{\partial u}{\partial z} + \frac{\partial w}{\partial x} = \frac{1}{G} T_{xz}. \tag{8.40c}$$

The displacements u, w can be obtained from Eqs. (8.40a) and (8.40b) by integration:

$$u = \frac{1-\nu^2}{E} \int T_{xx}\, dx - \frac{\nu(1+\nu)}{E} \int T_{zz}\, dx + f_1(z), \tag{8.41a}$$

$$w = \frac{1-\nu^2}{E} \int T_{zz}\, dz - \frac{\nu(1+\nu)}{E} \int T_{xx}\, dz + f_2(x). \tag{8.41b}$$

For the situation depicted in Figure 8.12, the components of stress can be obtained from the stress functions of Boussinesq (Timoshenko and Goodier, 1951; Dowson and Higginson, 1977),

$$\phi = -\frac{w'}{\pi} x \tan^{-1}\left(\frac{x}{z}\right), \tag{8.42}$$

where w' is the load per unit width. The stress function, ϕ, satisfies the compatibility condition $\nabla^4 \phi = 0$ and yields

$$T_{xx} = \frac{\partial^2 \phi}{\partial z^2} = -\frac{2w'}{\pi} \frac{x^2 z}{(x^2+z^2)^2}, \tag{8.43a}$$

$$T_{zz} = \frac{\partial^2 \phi}{\partial x^2} = -\frac{2w'}{\pi} \frac{z^3}{(x^2+z^2)^2}, \tag{8.43b}$$

$$T_{xz} = -\frac{\partial^2 \phi}{\partial x \partial z} = -\frac{2w'}{\pi} \frac{x z^2}{(x^2+z^2)^2}. \tag{8.43c}$$

The displacement due to the line load, w', can now be calculated from Eqs. (8.41), which, on substituting for the stress from Eqs. (8.43a) and (8.43b) gives at any point (x, z)

$$u = -\frac{w'}{\pi} \left\{ \frac{(1+\nu)(1-2\nu)}{E} \tan^{-1}\left(\frac{x}{z}\right) - \frac{(1+\nu)}{E} \frac{xz}{(x^2+z^2)} \right\} + f_1(z), \tag{8.44a}$$

$$w = -\frac{w'}{\pi} \left\{ \frac{1-\nu^2}{E} \left[\ln(x^2+z^2) - \frac{z^2}{(x^2+z^2)} \right] + \frac{\nu(1+\nu)}{E} \frac{x^2}{(x^2+z^2)} \right\} + f_2(x). \tag{8.44b}$$

We need two conditions to determine the functions $f_1(z)$ and $f_2(x)$. The symmetry conditions of the problem dictate that $-u(-x, z) = u(x, z)$, i.e., that u is an odd function of x. Using this

as one of the conditions, we find that $f_1(z) \equiv 0$. The displacements must satisfy Eq. (8.40c); using this as the second condition yields

$$\frac{df_2}{dx} = 0, \quad f_2 = C = \text{const.}$$

We have no more interest in the horizontal displacement u but are interested in the vertical displacement at the surface $z = 0$:

$$\delta \equiv w|_{z=0} = -\frac{w'}{\pi}\left[\frac{1-\nu^2}{E}\ln x^2 + \frac{\nu(1+\nu)}{E}\right] + C. \tag{8.45}$$

We would now like to develop a displacement formula for normal surface loading over the arbitrary strip $s_1 \le x \le s_2$. To this end, we consider an elemental strip of width ds that is located at distance s, $s_1 < s < s_2$, from the y axis. Let the normal load on the elemental strip be denoted by $p(s)\,ds$. We can get the elemental vertical displacement caused by the loading on the elemental strip from Eq. (8.45) by simply replacing x by $(x - s)$; i.e., by parallel shifting of the coordinate system in the $+x$ direction by the distance s:

$$d\delta = -\frac{p(s)\,ds}{\pi}\left[\frac{1-\nu^2}{E}\ln(x-s)^2 + \frac{\nu(1+\nu)}{E}\right] + C(s). \tag{8.46}$$

Here $d\delta$ is the vertical displacement of the surface at x, due to the elemental strip loading $p(s)\,ds$ at $x = s$.

Integration of Eq. (8.46) over the width $(s_2 - s_1)$ of the strip yields

$$\delta = -\frac{(1-\nu^2)}{\pi E}\int_{s_1}^{s_2} p(s)\ln(x-s)^2\,ds + \hat{C} \tag{8.47}$$

where

$$\hat{C} = \text{const.} \times (s_2 - s_1) - \frac{\nu(1+\nu)}{\pi E}w'.$$

The constant $\hat{C}$ can be evaluated in terms of δ_b, the deflection at some $x = b$,

$$\hat{C} = \delta_b + \frac{(1+\nu^2)}{\pi E}\int_{s_1}^{s_2} p(s)\ln(b-s)^2 ds. \tag{8.48}$$

The total displacement at x caused by the strip load $p(s)$ over $(s_2 - s_1)$

$$\delta = \delta_b - \frac{1-\nu^2}{\pi E}\int_{s_1}^{s_2} p(s)\ln\left[\frac{x-s}{b-s}\right]^2 ds. \tag{8.49}$$

Problem Formulation

In this section, we collect the equations that characterize the tribological interaction of two elastic bodies along a nominal line contact, when a continuous film of lubricant separates the two bodies. Young's modulus and Poisson's ratio of the bodies are E_1, ν_1 and E_2, ν_2 respectively, so the effective modulus and effective radius are given by

$$\frac{1}{E'} = \frac{1}{2}\left[\frac{1-\nu_1^2}{E_1} + \frac{1-\nu_2^2}{E_2}\right], \quad \frac{1}{R_x} = \frac{1}{r_{1x}} + \frac{1}{r_{2x}}.$$

For this nominal line contact the first integral of the Reynolds equation is

$$\frac{dp}{dx} = 12\mu\tilde{u}\frac{h - h_{\text{cav}}}{h^3}, \tag{8.50}$$

where $\tilde{u} = (u_1 + u_2)/2$ is the average of the surface velocities (Table 8.2) and x_0 is the location of the cavitation boundary. This equation is to be solved subject to the Swift-Stieber boundary condition

$$p = 0, \quad \frac{dp}{dx} = 0 \quad \text{at } x = x_{\text{cav}}. \tag{8.51a}$$

The second of these conditions is redundant since any solution of Eq. (8.50) will necessarily satisfy this boundary condition. The upstream edge of the continuous film is located at $x = x_{\min}$, where we assume the pressure to be atmospheric:

$$p = 0 \quad \text{at } x = x_{\min}. \tag{8.51b}$$

Note that p in Eqs. (8.50) and (8.51) is gauge pressure.

In EHL calculations the viscosity-pressure correlation of Roelands (1966) is usually employed (Houpert and Hamrock, 1986)

$$\mu = \exp\{(\ln \mu_0 + 9.67)[-1 + (1 + 5.1 \times 10^{-9} p)^z]\}, \tag{8.52a}$$

where z is a material parameter, and the lubricant density is assumed to vary according to the relationship, proposed by Dowson and Higginson (1977),

$$\rho = \rho_0 \left[1 + \frac{0.6 \times 10^{-9} p}{1 + 1.7 \times 10^{-9} p}\right], \tag{8.52b}$$

where p is in Pa.

In this introductory treatment, however, we simplify matters by assuming the viscosity-pressure dependence to be given by the less accurate, but easy to apply, Barus formula

$$\mu = \mu_0 \exp(\alpha p) \tag{8.12}$$

and constrain the lubricant to remain incompressible.

The film thickness distribution is known only within an additive constant h_w and, for two surfaces in contact, is given by

$$h(x) = h_w + \frac{x^2}{2R_x} - \frac{2}{\pi E'} \int_{x_{\min}}^{x_{\text{cav}}} p(s) \ln(x - s)^2 ds. \tag{8.53}$$

Here we assumed that the undeformed gap is represented by a parabola, as before. The unknown constant h_w includes the minimum distance of the undeformed surfaces $h_0 = h(0)$ plus the constant term $\hat{C}$

We need one additional constraint to eliminate h_w. This additional relationship is provided by the force balance

$$w' = \int_{x_{\min}}^{x_{\text{cav}}} p(x)\, dx, \tag{8.54}$$

where w' is the external load.

The system of Eqs. (8.12), (8.49), (8.50), (8.53) and (8.54) and boundary conditions (8.51) form a closed system that characterizes the EHL line contact problem.

The problem is nondimensionalized through the transformation

$$x = b\bar{x}, \quad s = b\bar{s}, \quad h = \frac{b^2\bar{h}}{R_x}, \quad p = p_H\bar{p}, \tag{8.55a}$$

where the maximum Hertzian pressure, p_H, is given by Eqs. (8.30). The definition $W = w'/R_xE'$ for the load parameter (see Table 8.2) yields

$$b^2 = R_x^2\frac{8W}{\pi}. \tag{8.55b}$$

In nondimensional form, the film thickness, Eq. (8.53), is given by

$$\begin{aligned}\bar{h} = \bar{h}_w + \frac{\bar{x}^2}{2} - \frac{1}{2\pi}\int_{\bar{x}_{\min}}^{\bar{x}_{\text{cav}}} \bar{p}(\bar{s})\,\ln(\bar{x}-\bar{s})^2 d\bar{s} \\ - \frac{1}{2\pi}\ln b^2 \int_{\bar{x}_{\min}}^{\bar{x}_{\text{cav}}} \bar{p}(\bar{s})\,d\bar{s},\end{aligned} \tag{8.56}$$

and the nondimensional form of Eq. (8.54) is

$$\frac{\pi}{2} = \int_{x_{\min}}^{x_{\text{cav}}} \bar{p}(\bar{s})\,d\bar{s}. \tag{8.57}$$

Taking into account Eqs. (8.30c) and (8.57), the nondimensional film thickness assumes the form (Houpert and Hamrock, 1986)

$$\bar{h} = \bar{h}_w + \frac{\bar{x}^2}{2} - \frac{1}{2\pi}\int_{\bar{x}_{\min}}^{\bar{x}_{\text{cav}}} \bar{p}(\bar{s})\,\ln(\bar{x}-\bar{s})^2 d\bar{s} - \frac{1}{4}\ln\left[R_x^2\frac{8W}{\pi}\right]. \tag{8.58}$$

The integrated form of the Reynolds equation (8.50) has the nondimensional form

$$\exp\left(G\sqrt{\frac{W}{2\pi}}\bar{p}\right)\frac{d\bar{p}}{d\bar{x}} = \frac{3\pi^2}{4}\frac{U}{W^2}\frac{\bar{h}-\bar{h}_0}{\bar{h}^3}. \tag{8.59}$$

Equations (8.57), (8.58), and (8.59) and the boundary conditions

$$\begin{aligned}&\bar{p} = 0 \qquad\quad \text{at} \quad \bar{x} = \bar{x}_{\min} \\ &\bar{p} = \frac{d\bar{p}}{d\bar{x}} = 0 \quad \text{at} \quad \bar{x} = \bar{x}_{\text{cav}}\end{aligned} \tag{8.60}$$

define the line contact problem of EHL in nondimensional form.

Numerical Considerations

There have been several methods of solution of the nominal line contact EHL problem. Here we follow Houpert and Hamrock (1986) in their improvement of Okamura's approach (Okamura, 1982). The main problem is to accurately calculate the film thickness. For high loads, the deformation can be orders of magnitude larger than the minimum film thickness. Accurate calculation of the pressure is made difficult by the increase of viscosity,

which, again, can increase by several orders of magnitude. We now calculate that part of the film thickness that is due to elastic deformation,

$$\bar{\delta} = \frac{1}{2\pi}\int_{x_{\min}}^{x_{\max}} \bar{p}(\bar{s})\ \ln(\bar{x}-\bar{s})^2 d\bar{s} - \frac{1}{4}\ln\left[R_x^2\frac{8W}{\pi}\right], \quad \bar{x}_{\max} \geq \bar{x}_{\text{cav}}. \tag{8.61a}$$

The integrand in Eq. (8.61a) is singular at $x = s$, this singularity may be removed using integration by parts (Kostreva, 1984),

$$\bar{\delta} = -\frac{1}{2\pi}[Ip]_{\bar{x}_{\min}}^{\bar{x}_{\max}} + \frac{1}{2\pi}\int_{\bar{x}_{\min}}^{\bar{x}_{\max}} \frac{d\bar{p}}{d\bar{s}} I(\bar{x};\bar{s})\, d\bar{s} - \frac{1}{4}\ln\left[R_x^2\frac{8W}{\pi}\right], \tag{8.61b}$$

where

$$\begin{aligned} I(\bar{x};\bar{s}) &= \int \ln(\bar{x}-\bar{s})^2\, d\bar{s} \\ &= -(\bar{x}-\bar{s})[\ln(\bar{x}-\bar{s})^2 - 2]. \end{aligned} \tag{8.61c}$$

Since $p(x_i) = p(x_0) = 0$, the boundary term in Eq. (8.61b) vanishes, and we obtain

$$\bar{\delta} = -\frac{1}{2\pi}\int_{\bar{x}_{\min}}^{\bar{x}_{\max}} \frac{d\bar{p}}{d\bar{s}}(\bar{x}-\bar{s})[\ln(\bar{x}-\bar{s})^2 - 2]\, d\bar{s} - \frac{1}{4}\ln\left[R_x^2\frac{8W}{\pi}\right]. \tag{8.62}$$

For the remainder of this section, we drop the overbar, but bear in mind that all variables have been nondimensionalized at this stage.

We wish to evaluate the integral in Eq. (8.62) numerically. To this end, define a nonuniform partition, with N odd,

$$\Pi\colon\ x_{\min} = x_1 < x_2 < x_3 < \cdots < x_{N-2} < x_{N-1} < x_N = x_{\max}, \tag{8.63}$$

and write the integral in Eq. (8.62) as a sum of subintegrals, each evaluated on its own subinterval,

$$\delta = -\frac{1}{2\pi}\int_{x_1}^{x_3}(.)\, ds - \frac{1}{2\pi}\int_{x_3}^{x_5}(.)\, ds - \cdots - \frac{1}{2\pi}\int_{x_{j-1}}^{x_{j+1}}(.)\, ds - \cdots - \frac{1}{2\pi}\int_{x_{N-2}}^{x_N}(.)\, ds + C, \tag{8.64}$$

where, for brevity, we represent the constant term in Eq. (8.62) by C.

In the first of these subintegrals, the global dummy variable s ranges from x_1 to x_3, and we replace it by a local dummy variable $x' = s - x_2$, which has the range $[x_1 - x_2, x_3 - x_2]$. In the generic interval centered about x_j, j even, the local dummy variable is chosen to be $x' = s - x_j$, which ranges over the interval $[x_{j-1} - x_j, x_{j+1} - x_j]$, and so forth. Also, if we substitute x_i for x, Eq. (8.62) calculates the deformation at node i as the sum of deformations $\delta_{i2}, \delta_{i4}, \ldots, \delta_{i,N-1}$, due to strip loading over the intervals $[x_1, x_3], [x_3, x_5], \ldots, [\delta_{N-2}, x_N]$, N odd, so that

$$\begin{aligned} \delta_i &= \delta_{i,2} + \delta_{i,4} + \cdots + \delta_{i,N-1} + C \\ &= \sum_{j=2,4,\ldots}^{N-1} \delta_{ij} - \frac{1}{4}\ln\left(R_x^2\frac{8W}{\pi}\right). \end{aligned} \tag{8.65}$$

We now evaluate the integrand in Eq. (8.62) for each of the subintervals. The discretized form of Eq. (8.61c), substituting x_i for x and $x_j + x'$ for s, is

$$I_{ij}(x') = -[x_i - (x_j + x')]\{\ln[x_i - (x_j + x')]^2 - 2\}, \quad (j \text{ even}). \tag{8.66}$$

Next, we represent $p(s)$ by its nodal values (Dowson and Higginson, 1959). But to make the subintegrals independent of one another, $p(s)$ of a particular subinterval can depend only on the nodal values that are available within that subinterval. For example, in the subinterval centered about node j, j even, we have the nodal values p_{j-1}, p_j, and p_{j+1} available. To interpolate for any $x' \in [x_{j-1} - x_j, x_{j+1}] - x_j]$ in terms of the nodal values, we employ Lagrange's quadratic interpolation formula and write[7]

$$\begin{aligned} p(x') = {} & \frac{x'(x' + x_j - x_{j+1})}{(x_{j-1} - x_j)(x_{j-1} - x_{j+1})} p_{j-1} \\ & + \frac{(x' + x_j - x_{j-1})(x' + x_j - x_{j+1})}{(x_j - x_{j-1})(x_j - x_{j+1})} p_j \\ & + \frac{x'(x' + x_j - x_{j-1})}{(x_{j+1} - x_{j-1})(x_{j+1} - x_j)} p_{j+1}. \end{aligned} \tag{8.67}$$

Thus, for any point $x' \in [x_{j-1} - x_j, x_{j+1} - x_j]$, the pressure is represented by a parabola that passes through points (x_{j-1}, p_{j-1}), (x_j, p_j), (x_{j+1}, p_{j+1}).

Differentiation of Eq. (8.67) with respect to x' yields the pressure gradient at $x' \in [x_{j-1} - x_j, x_{j+1} - x_j]$,

$$\begin{aligned} \frac{dp(x')}{dx'} = {} & \frac{2x' + (x_j - x_{j+1})}{(x_{j-1} - x_j)(x_{j-1} - x_{j+1})} p_{j-1} \\ & + \frac{2x' + (x_j - x_{j-1}) + (x_j - x_{j+1})}{(x_j - x_{j-1})(x_j - x_{j+1})} p_j \\ & + \frac{2x' + (x_j - x_{j-1})}{(x_{j+1} - x_{j-1})(x_{j+1} - x_j)} p_{j+1}. \end{aligned} \tag{8.68}$$

The formula for the pressure derivative, Eq. (8.68), will now be written as

$$\frac{dp(x')}{dx'} = (a_1 x' + a_2) p_{j-1} + (a_3 x' + a_4) p_j + (a_5 x' + a_6) p_{j+1}, \tag{8.69}$$

where the coefficients $a_1, a_2, \ldots a_6$ can be obtained by comparing Eqs. (8.68) and (8.69).

The subintegral centered about node j, j even, in Eq. (8.64) can then be written as

$$\begin{aligned} \frac{1}{2\pi} \int_{x_{j-1}}^{x_{j+1}} (.)\, ds = {} & p_{j-1} \left\{ \frac{1}{2\pi} \int_{x_{j-1} - x_j}^{x_{j+1} - x_j} (a_1 x' + a_2) I_{ij}(x')\, dx' \right\} \\ & + p_j \left\{ \frac{1}{2\pi} \int_{x_{j-1} - x_j}^{x_{j+1} - x_j} (a_3 x' + a_4) I_{ij}(x')\, dx' \right\} \\ & + p_{j+1} \left\{ \frac{1}{2\pi} \int_{x_{j-1} - x_j}^{x_{j+1} - x_j} (a_5 x' + a_6) I_{ij}(x')\, dx' \right\}. \end{aligned} \tag{8.70}$$

[7] On substituting $x' = s - x_j$, we revert to the conventional notation of Lagrange's interpolation formula (Gerald, 1973).

The integrals in Eq. (8.70) depend only on the sequence of nodal points, Eq. (8.63). As soon as partition Π is selected in Eq. (8.63), the integrals can be evaluated analytically in a straightforward manner (Houpert and Hamrock, 1986). Let us assume, for simplicity, that this has been done and designate the results by L, M, and U according to

$$L_{i,j-1} = \frac{1}{2\pi} \int_{x_{j-1}-x_j}^{x_{j+1}-x_j} (a_1 x' + a_2) I_{ij}(x')\, dx', \tag{8.71a}$$

$$M_{i,j} = \frac{1}{2\pi} \int_{x_{j-1}-x_j}^{x_{j+1}-x_j} (a_3 x' + a_4) I_{ij}(x')\, dx', \tag{8.71b}$$

$$U_{i,j+1} = \frac{1}{2\pi} \int_{x_{j-1}-x_j}^{x_{j+1}-x_j} (a_5 x' + a_6) I_{ij}(x')\, dx', \quad [j = 2k, k = 1, \ldots, (N-1)/2]. \tag{8.71c}$$

The deformation at node i due to loading on the strip centered about node j is

$$\delta_{i,j} = L_{i,j-1} p_{j-1} + M_{i,j} p_j + U_{i,j+1} p_{j+1}. \tag{8.72}$$

Substituting into Eq. (8.65), the deflection at node i due to loading of all strips is

$$\begin{aligned} \delta_i = {} & [L_{i,1} p_1 + M_{i,2} p_2 + (U_{i,3} + L_{i,3}) p_3] + \cdots \\ & + [(U_{i,2k-1} + L_{i,2k-1})\, p_{2k-1} + M_{i,2k} p_{2k} + (U_{i,2k+1} + L_{i,2k+1})\, p_{2k+1}] + \cdots \\ & + [(U_{i,N-2} + L_{i,N-2})\, p_{N-2} + M_{i,N-1} p_{N-1} + U_{i,N} p_N] + C. \end{aligned} \tag{8.73}$$

Let us define the *influence coefficients* $D_{i,n}$ as follows

$$\begin{aligned} D_{i,n} &= \begin{cases} M_{i,n} & n \quad \text{even} \\ \left(U_{i,n} + L_{i,n}\right) & n \quad \text{odd}, \end{cases} \\ U_{i,1} &= 0, \quad L_{i,N} = 0, \quad 1 \le i \le N. \end{aligned} \tag{8.74}$$

The influence coefficient, $D_{i,n}$, calculates deformation at node i due to unit load at node n. We may now write Eq. (8.73) in the concise form

$$\begin{aligned} \delta_i &= \sum_{j=2,4,\ldots}^{N-1} \delta_{ij} - \frac{1}{4} \ln\left(R_x^2 \frac{8W}{\pi}\right) \\ &= \sum_{n=2}^{N-1} D_{i,n} p_n - \frac{1}{4} \ln\left(R_x^2 \frac{8W}{\pi}\right). \end{aligned} \tag{8.75}$$

The unknowns of the boundary value problem, Eqs. (8.57)–(8.60), are the pressure at the nodal points p_k, $2 \le k \le N-1$, and the constant $\hat{h}_w$, which now also includes the constant term

$$\hat{h}_w = h_w - \frac{1}{4} \ln\left(R_x^2 \frac{8W}{\pi}\right)$$

The position of the cavitation boundary x_{cav} is also unknown at this stage. Instead of evaluating x_{cav}, however, we consider $h_{\text{cav}} = h(x_{\text{cav}})$ as an unknown and write Eq. (8.56) as

$$0 = h_{\text{cav}} - h_w - \frac{1}{2}\xi^2 + \frac{1}{2\pi}\int_{x_i}^{x_M} p(s)\ln[\xi - s]^2 ds. \tag{8.76}$$

Equation (8.76) is evaluated by interpolation (Okamura, 1983), as $x_{\text{cav}} = \max(\xi)$, where ξ satisfies (8.76) and $x_M > x_N$. Determination of the location of the free boundary is, however, difficult. To avoid such difficulties, Bisset and Glander (1988) scale the problem to a fixed interval *a priori*, by using the transformation

$$\hat{x} = \frac{x - x_{\min}}{x_{\text{cav}} - x_{\min}}. \tag{8.77}$$

This will introduce $\hat{h}_{\text{cav}} = \hat{h}(1)$ into the equations naturally; $\hat{h}_{\text{cav}}$ is now an unknown of the problem.

The system of discretized equations takes the form of a set of nonlinear algebraic equations.

$$F(x) = 0, \quad x = (u, \lambda), \tag{8.78}$$

where u is the vector of state variables (p_i, h_{cav}, h_w) and λ is a vector of the parameters U, G, W, ..., etc. In general, if there are n parameters, the solution set of Eq. (8.78) is an n-dimensional manifold. When $n = 1$, the manifold becomes a path.

In the calculations we keep all the parameters constant except one, and use the Gauss-Newton method for local iteration and the method of continuation for tracing the path (Bisset and Gander, 1988; Wang, Al-Sharif, Rajagopal, and Szeri, 1992). Note that Eq. (8.78) has the same form as Eq. (6.28). Application of the Gauss-Newton and path continuation methods have been described in Chapter 6. For application of the highly successful multigrid techniques (Brandt, 1984) to EHL problems, see Venner, ten Napel, and Bosma (1990), and Ai and Cheng (1994). A short exposition of the multigrid (MG) method can be found in the next section.

For simplicity, we have discussed only the nominal line contact problem in detail. By employing this technique, Houpert and Hamrock (1986) were able to obtain solutions up to 4.8 GPa maximum pressure. Extension to nominal point contact is discussed in a series of papers by Hamrock and Dowson (1976a, 1976b, 1997a, 1977b, 1978, 1979). Additional material is to be found in Hamrock (1991).

A great deal of effort has been devoted during the past two decades to the study of rough EHL contacts. Notable recent papers dealing with this subject are Ai and Cheng (1994), Greenwood and Morales-Espejel (1994), Venner and Lubrecht (1994), Ai and Cheng (1996) and Xu and Sadeghi (1996).

8.6 Analysis of the Point Contact Problem

The version of the Reynolds equation that defines the steady-state EHL point contact problem is a nonlinear partial differential equation in two spatial dimensions, hence, it is more complex, and as far as both computer storage and computing times are concerned more demanding, than the line contact problem of the previous section. Early on, researchers attempting solution of the point contact problem were forced to employ rather course grids due to the prevailing limitations on computer storage and performance; on such grids, especially under severe loading, derivatives such as $\partial p/\partial x$ and $\partial^2 p/\partial x^2$

changed rapidly from node to node, leading to instability of the computational scheme. To curb these hard-to-handle changes, researchers introduced the substitution $\varphi = ph^{3/2}$ into the Reynolds equation and employed Gauss-Seidel iteration to solve the discretized equations, now in φ (Hamrock and Dowson, 1981; Jalali-Vahid et al., 1998), employing over relaxation to speed up convergence on φ and under relaxation when checking convergence on p. Numerical stability was further promoted by applying backward differencing to the Couette-flow term. However, prior to the introduction of modern multigrid (MG) methods to elastohydrodynamic lubrication, solution of the EHL point problem remained difficult, especially under high load (Gohar, 2000). Multigrid methods, these will be introduced later in this section, speed up convergence of iterative methods such as the Gauss-Seidel scheme by paying attention to the nature and composition of the error, thus permitting finer grids to be employed.

The error, i.e., the difference between exact solution and iterated value, can be looked upon as being made up of component functions, each of which possessing distinct frequency and wavelength. Multigrid methods take cognizance that the various error components are easiest to eliminate on meshes of different, appropriately chosen, density; high-frequency components yield to treatment on smooth mesh while low-frequency component can be best eliminated on coarser mesh. MG methods apply a series of different grids in prescribed sequences to obtain accurate solution with minimal effort. With these modern methods, high mesh density can be realized; there is no need for the φ substitution as we can now solve p and h directly.

Relaxation

The finite difference approximation of partial differential equations is routinely solved by standard iterative techniques like the Jacobi or Gauss-Seidel schemes. Although these schemes have poor global convergence properties, for errors whose length scales are comparable to the mesh size they provide rapid convergence and, after a few iteration sweeps leave behind smooth, i.e., long wavelength, errors (for this reason, they are frequently referred to in the literature as smoothers).

In way of providing rationale for introducing multigrid methods, we consider the two-dimensional Poisson's equation,

$$\frac{\partial^2 \varphi}{\partial x^2} + \frac{\partial^2 \varphi}{\partial y^2} = f(x,\ y), \quad \varphi = 0 \text{ on } C. \tag{8.79}$$

The finite difference approximation of Eq. (8.79), on the $n \times n$ uniform mesh Ω^h with mesh size, h_x, h_y, using central differencing, is

$$\frac{\varphi^h_{i+1,j} - 2\varphi^h_{i,j} + \varphi^h_{i-1,j}}{h_x^2} + \frac{\varphi^h_{i,j+1} - 2\varphi^h_{i,j} + \varphi^h_{i,j-1}}{h_y^2} = f^h_{i,j}. \tag{8.80}$$

Let $\tilde{\varphi}^h_{k,l}$ represent the current value of $\varphi^h_{k,l}$, obtained from the previous iteration or specified by the initial guess. In an iterative scheme, the new iterate $\bar{\varphi}^h_{i,j}$ can be calculated from

$$\bar{\varphi}^h_{i,j} = \left(\frac{2}{h_x^2} + \frac{2}{h_y^2}\right)^{-1} \left[\frac{\tilde{\varphi}^h_{i+1,j} + \tilde{\varphi}^h_{i-1,j}}{h_x^2} + \frac{\tilde{\varphi}^h_{i,j+1} + \tilde{\varphi}^h_{i,j-1}}{h_y^2} - f^h_{i,j}\right]. \tag{8.81}$$

Equation (8.81) is a statement of Jacobi's method. We note that the right-hand side of the equation contains only values that were evaluated during the previous full sweep. The Gauss-Seidel method, in contrast, utilizes the most up to date information at every application of (8.80) in the iteration, without waiting for completion of the sweep. Employing lexicographic ordering in updating $\tilde{\varphi}$, i.e., in order of increasing i and j, the Gauss-Seidel iteration is characterized by

$$\bar{\varphi}^h_{i,j} = \tilde{\varphi}^h_{i,j} - \omega \left(\frac{2}{h_y^2} + \frac{2}{h_y^2} \right)^{-1} r^h_{i,j}, \tag{8.82}$$

where the residue $r^h_{i,j}$ has the definition

$$r^h_{i,j} = \left[f^h_{i,j} - \frac{\tilde{\varphi}^h_{i+1,j} - 2\tilde{\varphi}^h_{i,j} + \bar{\varphi}^h_{i-1,j}}{h_x^2} - \frac{\tilde{\varphi}^h_{i,j+1} - 2\tilde{\varphi}^h_{i,j} + \bar{\varphi}^h_{i,j-1}}{h_y^2} \right]. \tag{8.83}$$

When $\omega < 1$ the process is damped Gauss-Seidel iteration or Gauss-Seidel with under relaxation.

We note here that both schemes, formulas (8.81) and (8.82), involve only four adjacent points $(i+1, j)$, $(i-1, j)$, $(i, j+1)$ and $(i, j-1)$ in calculating $\varphi(i, j)$. In consequence, should there be only small variation in φ over these points, i.e., should the error be smooth relative to the current mesh Ω^h, either of these schemes will yield a $\bar{\varphi}^h_{i,j}$ that differs but little from the previous iterate $\tilde{\varphi}^h_{i,j}$. Once this stage is reached, the iteration process slows down. However, if we now continue to iterate on a coarser mesh, say Ω^{2h} of mesh size $2h_x, 2h_y$, the error would fluctuate more rapidly from mesh-point to neighboring mesh-point, i.e., have a shorter wavelength relative to mesh size, providing once again for efficient iteration.

The assertion that an iteration scheme is more effective against errors whose wavelength relative to mesh size is smaller is well illustrated by the following example. We set $f(x, y) = 0$ in Eq. (8.79) and specify a starting guess

$$\varphi_0 = \sin(k\pi x) \times \sin(k\pi y), \tag{8.84}$$

that reduces to zero at the edges of the square domain $[0, 1] \times [0, 1]$, to comply with the boundary condition $\varphi = 0$ on C.

As the only solution to this problem is the null solution $\varphi(x, y) \equiv 0$, the error $e^h_{i,j} = |\varphi^h_{i,j} - \tilde{\varphi}^h_{i,j}|$ will be represented by the calculated value $\tilde{\varphi}^h_{i,j}$ at any stage of the iteration.

In Figure 8.13 we record the changes in the error norm $e^h = \max_{1 \le i,j \le n} |\bar{\varphi}^h_{i,j}|$ for different values of the wave number k as the iteration proceeds. As indicated in the figure, e^h decreases faster for the higher frequency error than it does for the low frequency one. This, of course, immediately advises that once the iteration has slowed due to the error having become smooth relative to Ω^h, we should transfer to the courser mesh Ω^{2h} to speed up convergence.

We may note here for future use that, when employing the Gauss-Seidel scheme, errors of two consecutive iterations m and $(m+1)$ satisfy the equation

$$e^{(m+1)}_{i,j} = \left(\frac{2}{h_x^2} + \frac{2}{h_y^2} \right)^{-1} \left(\frac{e^{(m+1)}_{i-1,j} + e^{(m)}_{i+1,j}}{h_x^2} + \frac{e^{(m+1)}_{i,j-1} + e^{(m)}_{i,j+1}}{h_y^2} \right). \tag{8.85}$$

Here we dropped the superscript h on $e^h_{i,j}$ and for the mth iterate of $\varphi_{i,j}$ put $\varphi^{(m)}_{i,j} = \varphi_{i,j} - e^{(m)}_{i,j}$.

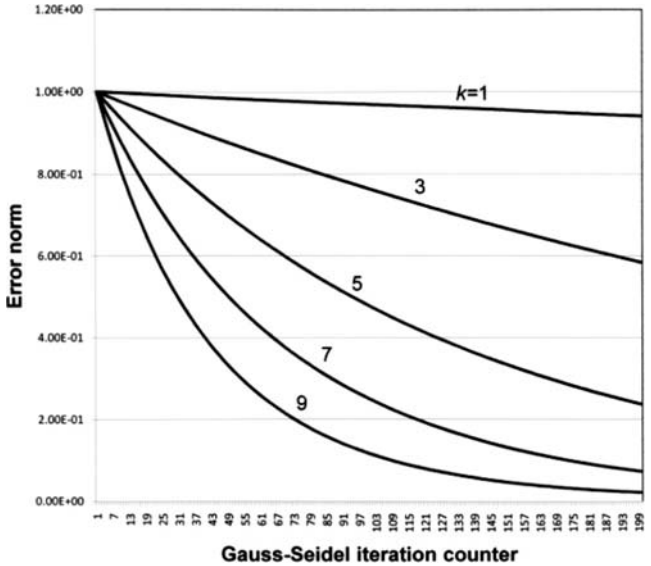

Figure 8.13. Solution errors versus iteration number, square mesh: $h = 1/64$.

Another way to study the evolution of the various frequency components of the error is via *local mode analysis*, the essence of which is the assertion that relaxation is a local process; i.e., each unknown is updated using information from nearby neighbors alone. For this reason, boundary conditions can be disregarded when investigation is restricted to only a few relaxation sweeps in the interior of the domain. The approach is to assume that the error can be represented by Fourier modes, then determine how relaxation modifies those modes. However, as there are no boundaries to contend with, the Fourier modes do not need to be restricted to discrete wave numbers. We can thus consider modes in the form $w_j = \exp(\iota j\theta)$ where $\theta \in (-\pi, \pi]$ and $\iota = \sqrt{-1}$. The mode corresponding to a specific wave number θ has wavelength $2\pi h/|\theta|$, values near π correspond to high frequency waves while those close to zero to low frequency waves (Briggs et al., 2000).

The analysis easily extends to two dimensions. Furthermore, based on the assumption that the relaxation maps a given Fourier component onto itself, it will be sufficient to consider that at node (j, k) after the mth and the $(m + 1)$ st step, respectively, the error is represented by a single Fourier mode,

$$\begin{aligned} e_{j,k}^{(m)} &= A(m)e^{\iota(j\theta_1+k\theta_2)} \\ e_{j,k}^{(m+1)} &= A(m+1)e^{\iota(j\theta_1+k\theta_2)}. \end{aligned} \tag{8.86}$$

We define the error *amplification factor* as the ratio of two successive amplitudes

$$A(m+1) = G(\theta_1, \theta_2)A(m). \tag{8.87}$$

For Gauss-Seidel iteration of (8.79) with $h_x = h_y = h$, we substitute (8.86) into (8.85) and obtain

$$G(\theta_1, \theta_2) = \frac{e^{\iota\theta_1} + e^{\iota\theta_2}}{4 - e^{-\iota\theta_1} - e^{-\iota\theta_2}}.$$

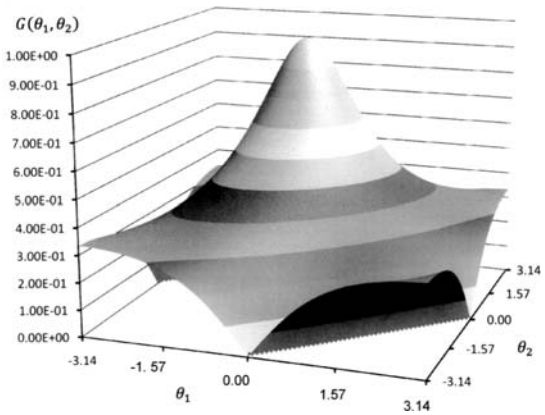

Figure 8.14. Amplification factor $G(\theta_1, \theta_2)$ for Gauss-Seidel iteration of $\nabla^2\varphi = 0$.

The amplification factog G is plotted against the wave number k in Figure 8.14. It is evident that as $(\theta_1, \theta_2) \to (0, 0)$, $G(\theta_1, \theta_2) \to 1$.

The Multigrid (MG) Method

To illustrate the multigrid method we consider the boundary value problem

$$A(u) = f, \quad u = 0 \text{ on } C, \tag{8.88}$$

which, on the mesh Ω^h, has the finite difference approximation

$$\boldsymbol{A}^h(\boldsymbol{u}^h) = \boldsymbol{f}^h. \tag{8.89}$$

By applying iterative methods like the Jacobi or the Gauss-Seidel scheme on Ω^h, the high-frequency components of the error are eliminated first. Starting from some initial guess $\boldsymbol{u}_0^h$ and applying one of these schemes, the approximation $\tilde{\boldsymbol{u}}^h$ is obtained after ν_1 iteration sweeps. We define the error and the residue, respectively, by

$$\boldsymbol{e}^h = \boldsymbol{u}^h - \tilde{\boldsymbol{u}}^h \tag{8.90}$$

and

$$\boldsymbol{r}^h = \boldsymbol{f}^h - \boldsymbol{A}^h(\tilde{\boldsymbol{u}}^h). \tag{8.91}$$

We emphasize here that both error and residue are smooth at this stage.

Application to Linear Operators

When A symbolizes a linear operator, we change the nomenclature from A to $L \equiv A$ in (8.89) and write, after ν_1 iteration sweeps,

$$\begin{aligned} \boldsymbol{L}^h\boldsymbol{u}^h - \boldsymbol{L}^h\tilde{\boldsymbol{u}}^h &= \boldsymbol{L}^h(\boldsymbol{u}^h - \tilde{\boldsymbol{u}}^h) \\ &= \boldsymbol{L}^h\boldsymbol{e}^h, \end{aligned}$$

thus obtaining the residual equation

$$\boldsymbol{L}^h \boldsymbol{e}^h = \boldsymbol{r}^h. \tag{8.92}$$

Relaxing the original equation $\boldsymbol{L}^h \boldsymbol{u}^h = \boldsymbol{f}^h$ with arbitrary initial guess $\boldsymbol{u}_0^h$ is thus equivalent to relaxing the residual equation $\boldsymbol{L}^h \boldsymbol{e}^h = \boldsymbol{r}^h$ with initial guess $\boldsymbol{e}_0^h = 0$. The scheme for this, outlined in the following and starting from Eq. (8.92), is applicable to linear operators and is referred to in the literature as the *Correction Scheme* (CS).

There is, however, no sense in continuing to relax (8.92) on Ω^h, as the error is already smooth, due to the ν_1 smoothing relaxation sweeps already performed on (8.89). It is better to transfer the residue $\boldsymbol{r}^h$ from Ω^h to Ω^{2h}, obtaining $\boldsymbol{r}^{2h} = I_h^{2h} \boldsymbol{r}^h$ in this process, approximate the operator L on Ω^{2h} by $\boldsymbol{L}^{2h}$, and continue relaxing on the equation

$$\boldsymbol{L}^{2h} \boldsymbol{e}^{2h} = \boldsymbol{r}^{2h}. \tag{8.93}$$

The *restriction* operator I_h^{2h} transfers arrays such as $\boldsymbol{r}^h$ from the finer mesh Ω^h to the coarser mesh Ω^{2h}. Implicit in Eq. (8.93) is the assumption that $\boldsymbol{e}^h$ and $\boldsymbol{e}^{2h}$ are two different discretizations of the same quantity $\boldsymbol{e}$.

If now we relax on the residual equation (8.93) ν_1 times with initial value $\boldsymbol{e}_0^{2h} = 0$, we obtain the approximation $\tilde{\boldsymbol{e}}^{2h}$ to the error $\boldsymbol{e}^{2h}$. The latter array has representation $\boldsymbol{I}_{2h}^h \tilde{\boldsymbol{e}}^{2h}$ on Ω^h and we accept it as our approximation to the error $\boldsymbol{e}^h$. Here I_{2h}^h is the *prolongation* operator that transfers arrays such as $\tilde{\boldsymbol{e}}^{2h}$ from the coarse mesh Ω^{2h} to the fine mesh Ω^h.

Employing now Eq. (8.90), we find the improved approximation to $\boldsymbol{u}^h$ through the upgrade

$$\tilde{\boldsymbol{u}}^h \leftarrow \tilde{\boldsymbol{u}}^h + I_{2h}^h \tilde{\boldsymbol{e}}^{2h}. \tag{8.94}$$

The grid Ω^{2h} might be sufficiently coarse to provide the exact solution $\boldsymbol{e}^{2h}$ after ν_1 iterations where ν_1 is small, say 2. However, if Ω^{2h} contains too large a number of mesh points, we may treat Eq. (8.93) in a fashion similar to that of the residual equation (8.92), after all these two equations are formally identical. Continuing this process, we can build a hierarchy of two-grid (TG) processes as follows (Briggs et al., 2000):

Relax on $\boldsymbol{L}^h \boldsymbol{u}^h = \boldsymbol{f}^h$ starting from some initial guess $\boldsymbol{u}_0^h$, iterating ν_1 times
Compute $\boldsymbol{f}^{2h} = I_h^{2h} \boldsymbol{r}^h$
  Relax on $\boldsymbol{L}^{2h} \boldsymbol{e}^{2h} = \boldsymbol{f}^{2h}$ starting from zero initial value, iterating ν_1 times
  Compute $\boldsymbol{f}^{4h} = I_{2h}^{4h} \boldsymbol{r}^{2h}$
    Relax on $\boldsymbol{L}^{4h} \boldsymbol{e}^{4h} = \boldsymbol{f}^{4h}$ starting from zero initial guess, iterating ν_1 times
    Compute $\boldsymbol{f}^{8h} = I_{4h}^{8h} \boldsymbol{r}^{4h}$
      ...
    Correct $\tilde{\boldsymbol{e}}^{4h} \leftarrow \tilde{\boldsymbol{e}}^{4h} + I_{8h}^{4h} \tilde{\boldsymbol{e}}^{8h}$
    Relax on $\boldsymbol{L}^{4h} \boldsymbol{e}^{4h} = \boldsymbol{f}^{4h}$ with initial guess $\tilde{\boldsymbol{e}}^{4h}$, iterating ν_2 times
  Correct $\tilde{\boldsymbol{e}}^{2h} \leftarrow \tilde{\boldsymbol{e}}^{2h} + I_{4h}^{2h} \tilde{\boldsymbol{e}}^{4h}$.
  Relax on $\boldsymbol{L}^{2h} \boldsymbol{e}^{2h} = \boldsymbol{f}^{2h}$ with initial guess $\tilde{\boldsymbol{e}}^{2h}$, iterating ν_2 times

Correct $\tilde{\boldsymbol{u}}^h \leftarrow \tilde{\boldsymbol{u}}^h + I_{2h}^h \tilde{\boldsymbol{e}}^{2h}$.
Relax on $\boldsymbol{L}^h \boldsymbol{u}^h = \boldsymbol{f}^h$ with initial guess $\tilde{\boldsymbol{u}}^h$, iterating ν_2 times.

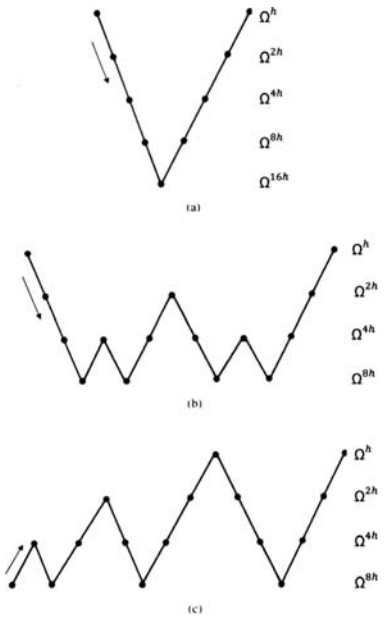

Figure 8.15. Multilevel schemes: (a) V-cycle; (b) W-cycle; (c) Full Multigrid.

The computation scheme defined above is a V-cycle and, for five levels, is illustrated schematically in Figure 8.15(a).

We now return to our previous Dirichlet problem with initial guess (8.84), using a series of five-level V-cycles, with $\nu_1 = \nu_2 = 2$ and $h = 1/32$. Table 8.3 displays the residue norm, defined by

$$r = \sqrt{\sum_{i,j} (r_{i,j})^2},$$

at each level of the V-cycle for the first, fifth, and tenth cycles. As the entries of Table 8.3 show, the first cycle reduces the residue norm on the $h = 1/32$ mesh from 19.4 to 0.642. At the end of the tenth cycle, i.e., after only 40 iterations at level five, we arrive at a residue norm $r = 4.68 \times 10^{-13}$. To reach the same result but without making use of the multigrid technique, we would need 2944 iteration sweeps, all at level five. Now this might not be time consuming in the example under consideration. However, we should bear in mind that for the sake of accuracy EHL problems are typically solved on large mesh[8] and the equations are far more complicated than our sample problem; they also involve an integral condition and calculation of the elastic deformation at each point, at each stage of each relaxation sweep.

[8] In the paper by Ehret et al. (1997), for example, the finest mesh contains 513×513 mesh points and the coarsest 17×17.

Table 8.3. *Residue norm at various levels and V-cycles for the Dirichlet problem*

Level	h	First cycle	Fifth cycle	Tenth cycle
5	1/32	$1.94 \times 10^{+1}$	4.31×10^{-5}	7.66×10^{-12}
4	1/16	$1.82 \times 10^{+1}$	3.60×10^{-5}	5.28×10^{-12}
3	1/8	$1.42 \times 10^{+1}$	2.19×10^{-5}	2.30×10^{-12}
2	1/4	5.99×10^{0}	6.17×10^{-5}	5.30×10^{-13}
1	1/2	0.00×10^{0}	0.00×10^{0}	0.00×10^{0}
2	1/4	5.41×10^{-1}	5.84×10^{-7}	4.92×10^{-14}
3	1/8	7.29×10^{-1}	1.71×10^{-6}	1.98×10^{-13}
4	1/16	7.09×10^{-1}	6.42×10^{-6}	4.93×10^{-13}
5	1/32	6.42×10^{-1}	2.22×10^{-6}	4.68×10^{-13}

If reasonable starting values are not readily available, one might employ the coarsest grid to obtain acceptable starting values for smoothing on the finest grid, as indicated by the *full multigrid* cycle of Figure 8.15(c).

The Intergrid Operators

The ideas of the previous subsection dictate that we find ways to transfer arrays from the fine to the coarse mesh and vice versa. The restriction operators will accomplish the first of these tasks. For simplicity in defining these operators, we chose the mesh of the coarse-grid spacing H as double that of the fine-grid spacing, i.e., $H = 2h$ (the predominant choice in practice).

The simplest *restriction* operator is the *injection operator*, which transfers the value of an array on a fine-grid point directly to the corresponding coarse-grid point $\varphi^H_{I,J} \leftarrow \varphi^h_{i,j}$, $i, j = 2, 4, 6, \ldots$. Representation that is more accurate can be achieved by applying the *full weighting operator* (e.g., Gohar, 2000)

$$\begin{aligned}\varphi^H_{I,J} \leftarrow \frac{1}{16}\big[&\varphi^h_{i-1,j-1} + \varphi^h_{i-1,j+1} + \varphi^h_{i+1,j-1} + \varphi^h_{i+1,j+1} \\ &+ 2\big(\varphi^h_{i,j-1} + \varphi^h_{i,j+1} + \varphi^h_{i-1,j} + \varphi^h_{i+1,j}\big) + 4\varphi^h_{i,j}\big].\end{aligned} \tag{8.95}$$

Here $I = i/2$ and $J = j/2$ and $i, j = 2, 4, 6, \ldots$, thus, for example

$$\varphi^H_{4,2} \leftarrow \frac{1}{16}\left[\varphi^h_{7,3} + \varphi^h_{7,5} + \varphi^h_{9,3} + \varphi^h_{9,5} + 2\left(\varphi^h_{8,3} + \varphi^h_{8,5} + \varphi^h_{7,4} + \varphi^h_{9,4}\right) + 4\varphi^h_{8,4}\right].$$

The full weighting operator is diagrammed in Figure 8.16(a).

The *prolongation* operator I^{2h}_h disperses coarse-grid arrays, such as $\boldsymbol{r}^{2h}$, from Ω^{2h} to the finer grid Ω^h. It is shown schematically in Figure 8.16(b). For the upper right quadrant, consisting of points (i, j), $(i+1, j)$, $(i, j+1)$, and $(i+1, j+1)$, we thus specify

(a)

$$I_{nh}^{nh/2} = \frac{1}{4}\begin{Bmatrix} 1/4 & 1/2 & 1/4 \\ 1/2 & 1 & 1/2 \\ 1/4 & 1/2 & 1/4 \end{Bmatrix}$$

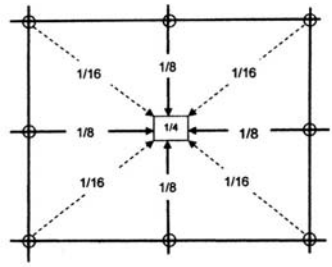

(b)

$$I_{nh/2}^{nh} = \begin{Bmatrix} 1/4 & 1/2 & 1/4 \\ 1/2 & 1 & 1/2 \\ 1/4 & 1/2 & 1/4 \end{Bmatrix}$$

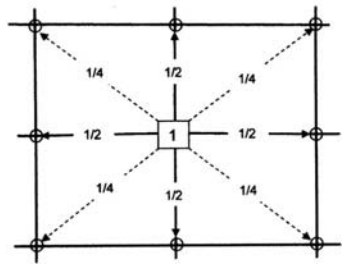

Figure 8.16. Intergrid operators: (a) Full weighting restriction operator; (b) prolongation operator.

$$\begin{aligned} r_{i,j}^h &\leftarrow r_{I,J}^H \\ r_{i+1,j}^h &\leftarrow \frac{1}{2}\left(r_{I,J}^H + r_{I+1,J}^H\right) \\ r_{i,j+1}^h &\leftarrow \frac{1}{2}\left(r_{I,J}^H + r_{I,J+1}^H\right) \\ r_{i+1,j+1}^h &\leftarrow \frac{1}{4}\left(r_{I,J}^H + r_{I+1,J}^H + r_{I+1,J+1}^H + r_{I,J+1}^H\right), \end{aligned} \tag{8.96}$$

where $i = 2I$, $j = 2J$, and $I, J = 1, 2, 3, \ldots$, thus, for example,

$$\begin{aligned} r_{8,5}^h &\leftarrow \frac{1}{2}\left(r_{4,2}^H + r_{4,3}^H\right) \\ r_{9,5}^h &\leftarrow \frac{1}{4}\left(r_{4,2}^H + r_{5,2}^H + r_{5,3}^H + r_{4,3}^H\right). \end{aligned}$$

Application to Nonlinear Operators

Many of the problems of interest in mechanics, including lubrication of counter formal contacts, are nonlinear. For these also the multigrid algorithm provides a new powerful method of analysis. However, for nonlinear operators $\boldsymbol{A}^h(\boldsymbol{u}^h) - \boldsymbol{A}^h(\tilde{\boldsymbol{u}}^h) \neq \boldsymbol{A}^h(\boldsymbol{u}^h - \tilde{\boldsymbol{u}}^h)$ and the residual equation is no longer linear, i.e., we cannot treat the error separate from the solution. The best we can do in way of a residual equation is to use definitions (8.90) and (8.91) and form the nonlinear set of equations

$$\boldsymbol{A}^h(\tilde{\boldsymbol{u}}^h + \boldsymbol{e}^h) - \boldsymbol{A}^h(\tilde{\boldsymbol{u}}^h) = \boldsymbol{r}^h. \tag{8.97}$$

Here the approximation $\tilde{\boldsymbol{u}}^h$ to $\boldsymbol{u}^h$ can be obtained by the Jacobi or the Gauss-Seidel schemes with local linearization (Venner and Lubrecht, 2000). The above indicated change from linear to nonlinear residual equation necessitates changes in the MG method to make it applicable to nonlinear problems.

The multigrid technique for nonlinear problems naturally divides into two categories. The first category of these methods, which we will call the *MG-Newton scheme*, employs the multigrid scheme only as an inner solver of the linear approximation to the nonlinear equations, which has already been obtained via Newton's method. To define this scheme, we return to (8.97) and expand the first term on the left in a Taylor series about $\tilde{\boldsymbol{u}}$,

$$\boldsymbol{A}^h(\tilde{\boldsymbol{u}}^h + \boldsymbol{e}^h) = \boldsymbol{A}^h(\tilde{\boldsymbol{u}}^h) + J(\tilde{\boldsymbol{u}}^h)\boldsymbol{e}^h + \text{h. o. t.} \tag{8.98}$$

Truncating the system after two terms and substituting into (8.97) gives the linear system of equations,

$$J(\tilde{\boldsymbol{u}}^h)\boldsymbol{e}^h = \boldsymbol{r}^h. \tag{8.99}$$

Here $J(\tilde{\boldsymbol{u}}^h)$ is the Jacobian evaluated at the current value $\tilde{\boldsymbol{u}}^h$,

$$J_{k,l} = \left.\frac{\partial A_k^h(\boldsymbol{u}^h)}{\partial u_l^h}\right|_{\boldsymbol{u}^h = \tilde{\boldsymbol{u}}^h}.$$

This linear system (8.99) is best solved by multigrid methods. The current approximation $\tilde{\boldsymbol{u}}^h$ can then be updated as $\tilde{\boldsymbol{u}}^h \leftarrow \tilde{\boldsymbol{u}}^h + \boldsymbol{e}^h$, where this last step follows from Newton's method. The MG-Newton method is described in detail by Chang et al. (1989), Lee and Hsu (1993), Hsu and Lee (1994), and Dawson and Wang (1994). For application of this method to transient problems, see Jalali-Vahid et al. (2001).

The second category of methods, known as the *full approximation scheme* (FAS), results from generalization of the linear multigrid scheme (Briggs et al., 2000). The excellent book by Venner and Lubrecht (2000) contain detailed description of the FAS, as it applies to both HL and EHL problems.

To introduce the full approximation scheme we return to the nonlinear residual equations (8.97) and discretized it on the coarse mesh Ω^{2h} to obtain

$$\boldsymbol{A}^{2h}(\hat{\boldsymbol{u}}^{2h}) = \hat{\boldsymbol{f}}^{2h}. \tag{8.100}$$

Here we assume to represent $(\tilde{\boldsymbol{u}}^h + \boldsymbol{e}^h)$ on the coarse grid Ω^{2h} by the coarse grid variable $\hat{\boldsymbol{u}}^{2h}$ in the form

$$\hat{\boldsymbol{u}}^{2h} \leftarrow I_h^2 h\tilde{\boldsymbol{u}}^h + \boldsymbol{e}^{2h}. \tag{8.101}$$

We also recognize the transfers

$$\begin{aligned} \boldsymbol{A}^{2h} &\leftarrow \boldsymbol{A}^h \\ \tilde{\boldsymbol{u}}^{2h} &\leftarrow I_h^2 h\tilde{\boldsymbol{u}}^h \\ \boldsymbol{r}^{2h} &\leftarrow I_h^{2h}\boldsymbol{r}^h \end{aligned} \tag{8.102}$$

and define the (known) right-hand side

$$\hat{\boldsymbol{f}}^{2h} = I_h^{2h}\boldsymbol{r}^h + \boldsymbol{A}^{2h}\big(I_h^{2h}(\tilde{\boldsymbol{u}}^h)\big). \tag{8.103}$$

Equation (8.100) is formally identical to Eq. (8.89), and by applying the same scheme to Eq. (8.100) as was employed for Eq. (8.89), we relax on $\boldsymbol{A}^{2h}\left(\hat{\boldsymbol{u}}^{2h}\right) = \hat{\boldsymbol{f}}^{2h}$ to obtain the approximation $\hat{\boldsymbol{u}}^{\tilde{2}h}$. We then have from (8.98)

$$\begin{aligned} \boldsymbol{e}^{2h} &= \hat{\boldsymbol{u}}^{2h} - I_h^{2h}\tilde{\boldsymbol{u}}^h \\ &\cong \tilde{\hat{\boldsymbol{u}}}^{2h} - I_h^{2h}\tilde{\boldsymbol{u}}^h. \end{aligned} \tag{8.104}$$

As the representation of $\boldsymbol{e}^{2h}$ on Ω^h is $I_{2h}^h \boldsymbol{e}^{2h}$, from Eq. (8.104) we obtain the improved approximation to the unknown $\boldsymbol{u}^h$ as

$$\tilde{\boldsymbol{u}}^h \leftarrow \tilde{\boldsymbol{u}}^h + I_{2h}^h\left(\tilde{\hat{\boldsymbol{u}}}^{2h} - I_h^{2h}\tilde{\boldsymbol{u}}^h\right). \tag{8.105}$$

Application of the full approximation scheme (FAS) consists thus of the following steps:

- Restrict the current approximation and its fine-grid residual to the coarse grid: $\boldsymbol{r}^{2h} = I_h^{2h}(\boldsymbol{f}^h - \boldsymbol{A}^h(\tilde{\boldsymbol{u}}^h))$ and $\tilde{\boldsymbol{u}}^{2h} = I_h^{2h}\tilde{\boldsymbol{u}}^h$.
- Solve the coarse-grid problem: $\boldsymbol{A}^{2h}(\hat{\boldsymbol{u}}^{2h}) = \boldsymbol{r}^{2h} + \boldsymbol{A}^{2h}(\tilde{\boldsymbol{u}}^{2h})$.
- Compute the coarse-grid approximation to the error: $\boldsymbol{e}^{2h} = \tilde{\boldsymbol{u}}^{2h} - \tilde{\hat{\boldsymbol{u}}}^{2h}$.
- Interpolate the error approximation up to the fine grid and correct the current fine-grid approximation: $\tilde{\boldsymbol{u}}^h \leftarrow \tilde{\boldsymbol{u}}^h + I_{2h}^h(\boldsymbol{e}^{2h})$.

Problem Formulation

Consider an elastic half space to which forces are applied in the neighborhood of a single point $\left(x', z'\right)$ on the surface. If the resultant of these forces is F, then the displacement at a point (x, z) is give by (Love, 1944)

$$w(x,\ z) = \frac{F(\lambda + 2\mu)}{4\pi\mu(\lambda + \mu)}\frac{1}{r}. \tag{8.106}$$

Here $r = \sqrt{(x - x')^2 + (z - z')^2}$ is the distance between the point of application of the force and the point where deflection is sought.

If instead of the Lame constants λ and μ we employ Young's modulus and Poisson's ratio, where

$$\lambda = \frac{E\nu}{(1 + \nu)(1 - \nu)};\quad \mu = \frac{E}{(1 + \nu)} \tag{8.107}$$

the deflection (8.106) takes the form

$$w(x,\ z) = \frac{(1 - \nu^2)F}{\pi E}\frac{1}{\sqrt{(x - x')^2 + (z - z')^2}}. \tag{8.108}$$

The deflection of the surface at point $Q(x, z)$ due to the normal load $p(x, z)$ distributed over the area $2a \times 2b$ centered at (x_c, z_c) can be computed from the integral

$$w(x, z) = \frac{(1-\nu^2)}{\pi E} \int_{x_c-a}^{x_c+a} \int_{z_c-b}^{z_c+b} \frac{p(x', z',) \, dx' dz'}{\sqrt{(x-x')^2 + (z-z')^2}}. \tag{8.109}$$

Love (1944) evaluated this integral for uniform pressure, with the result given in Eq. (8.123).

The film thickness in nominal point contact, assuming that the body is locally a paraboloid at contact, is given by

$$h(x, z) = h_0 + \frac{x^2}{2R_x} + \frac{z^2}{2R_z} + \frac{2}{\pi E'} \int_{-\infty}^{+\infty} \int_{-\infty}^{+\infty} \frac{p(x', z') \, dx' dz'}{\sqrt{(x-x')^2 + (z-z')^2}}. \tag{8.110}$$

The fluid pressure in conventional EHL contacts is $O(1$ Gpa); compressibility of even liquid lubricants must be taken into account at such high pressure. We must, therefore, use that version of the Reynolds equation that is applicable to compressible lubricants. To specify pressure dependence of density, the Dowson and Higginson relationship, Eq. (8.52b), is often employed (c.f., Chapter 10).

The Reynolds equation for compressible fluids is given by Eq. (11.6) of Section 11.1. For steady state the form given by Eq. (11.9) applies

$$\frac{\partial}{\partial x}\left(\frac{\rho h^3}{\mu}\frac{\partial p}{\partial x}\right) + \frac{\partial}{\partial z}\left(\frac{\rho h^3}{\mu}\frac{\partial p}{\partial z}\right) = 12 u_m \frac{\partial(\rho h)}{\partial x}, \tag{8.111}$$

where $u_m = U_0/2$ denotes the average velocity of the surfaces.

As discussed previously, the location of the cavitation boundary is not known a priori. Here we cannot simply include its position as an additional unknown as this position is dependent on z. Instead, we enforce the condition $p(x, z) \geq 0$, by equating nodal pressures to zero at each stage of the iterations when they fall below it (Rohde and McAllister, 1975).

To characterize pressure dependence of the viscosity we use either the Barus formula, Eq. (8.12), or the correlation by Roelands, Eq. (8.52a).

The force balance condition, required to evaluate the minimum film thickness, is an extension of Eq. (8.54),

$$w' = \int_{-\infty}^{+\infty} \int_{-\infty}^{+\infty} p(x, z) \, dx dz. \tag{8.112}$$

The following substitutions make the these equations dimensionless

$$\begin{aligned} x &= a\bar{x} \qquad z = a\bar{z} \\ p &= p_h \bar{p} \qquad h = (a^2/R_x)\bar{h} \\ \mu &= \bar{\mu}\mu_0 \qquad \rho = \bar{\rho}\rho_0. \end{aligned} \tag{8.113}$$

Here p_h is the maximum pressure in frictionless dry contact. To find its value we make use of results by Hertz. Setting $\kappa = 1$ for circular contact, from (8.25a) we obtain $\mathcal{E} = \pi/2$, and from (8.22) the value $\mathcal{R} = R_x/2$. Substitution of these quantities into Eqs. (8.23b) and (8.27a) yields the required maximum Hertz pressure p_h and the radius of the contact circle a

$$p_h = \frac{3w'}{2a^2}; \quad a = \left(\frac{3w'R_x}{2E'}\right)^{1/3}. \tag{8.114}$$

Employing further the definitions

$$\xi = \frac{\bar{\rho}\bar{h}^3}{\bar{\mu}\lambda}; \quad \lambda = \frac{12u_m\mu_0 R_x^2}{a^3 p_h}$$

the nondimensional form of the Reynolds equation, the film thickness, and the force balance becomes, respectively,

$$\frac{\partial}{\partial\bar{x}}\left(\xi\frac{\partial\bar{p}}{\partial\bar{x}}\right) + \frac{\partial}{\partial\bar{z}}\left(\xi\frac{\partial\bar{p}}{\partial\bar{z}}\right) - \frac{\partial(\bar{\rho}\bar{h})}{\partial\bar{x}} = 0 \tag{8.115}$$

$$\bar{h}(\bar{x},\,\bar{z}) = \bar{h}_0 + \frac{\bar{x}^2}{2} + \frac{\bar{z}^2}{2} + \frac{2}{\pi^2}\int_{-\infty}^{+\infty}\int_{-\infty}^{+\infty}\frac{\bar{p}(x',\,z')\,dx'\,dz'}{\sqrt{(\bar{x}-\bar{x}')^2 + (\bar{z}-\bar{z}')^2}} \tag{8.116}$$

$$\int_{-\infty}^{+\infty}\int_{-\infty}^{+\infty}\bar{p}(\bar{x},\,\bar{z})\,d\bar{x}d\bar{z} = \frac{2\pi}{3}. \tag{8.117}$$

The governing equations (115–117) will be discretized on the uniform grid Ω^h with mesh size $h = h_{\bar{x}} = h_{\bar{z}}$ occupying the rectangular domain $[\bar{x}_{\text{in}},\,\bar{x}_{\text{out}}] \times [\bar{z}_{\text{left}},\,\bar{z}_{\text{right}}]$. For simplicity, we dispense with the over score bar that signifies non-dimensionality of a variable, bearing in mind that under the new notation $h_{i,j}$ is the film thickness at mesh point $(i,\,j)$ while h signifies mesh size.

Employing the notation

$$\begin{aligned} F_{i,j} = \frac{1}{2h^2}[&(\xi_{i+1,j} + \xi_{i,j})p_{i+1,j} - (\xi_{i+1,j} + \xi_{i-1,j} + \xi_{i,j+1} + \xi_{i,j-1} + 4\xi_{i,j})p_{i,j} \\ &+ (\xi_{i,j} + \xi_{i-1,j})p_{i-1,j} + (\xi_{i,j} + \xi_{i,j+1})p_{i,j+1} + (\xi_{i,j} + \xi_{i,j-1})p_{i,j-1} - (\rho h)_{i,j}, \end{aligned} \tag{8.118}$$

the dimensionless Reynolds equation at point $(i,\,j)$ takes the form $F_{i,j} = 0$, where we replaced the coefficients $\xi_{i\pm1/2,j}$ and $\xi_{i,j\pm1/2}$ by averages of neighboring values

$$\begin{aligned} \xi_{i\pm1/2,j} &= (\xi_{i\pm1,j} + \xi_{i,j})/2 \\ \xi_{i,j\pm1/2} &= (\xi_{i,j\pm1} + \xi_{i,j})/2. \end{aligned} \tag{8.119}$$

Under severe loading, central differencing of the squeeze term will not work (Chang et al., 1989; Lee and Hsu, 1993; Dawson and Wang, 1994). In such cases Venner and Lubrecht (2000) recommend using second-order backward discretization,

$$(\rho h)_{i,j} = \frac{1.5\rho_{i,j}h_{i,j} - 2\rho_{i-1,j}h_{i-1,j} + 0.5\rho_{i-2,j}h_{i-2,j}}{h}. \tag{8.120a}$$

In contrast, Jalali-Vahid (2000) uses a weighted combination of forward and backward differences under unfavourable loading conditions,

$$(\rho h)_{i,j} = (1-\beta)\frac{\rho_{i+1,j}h_{i+1,j} - \rho_{i,j}h_{i,j}}{h} + \beta\frac{\rho_{i,j}h_{i,j} - \rho_{i-1,j}h_{i-1,j}}{h}. \tag{8.120b}$$

The forward scheme applies when $\beta = 0$, and when $\beta = 1$ Eq. (8.120b) prescribes backward differencing.

For the Gauss-Seidel scheme, Eq. (8.115) is characterized by

$$\bar{p}_{i,j} = \tilde{p}_{i,j} - \frac{h^2}{\Xi_{i,j}}r_{i,j}, \tag{8.121a}$$

where $\Xi_{i,j} = (\xi_{i+1,j} + \xi_{i-1,j} + \xi_{i,j+1} + \xi_{i,j-1} + 4\xi_{i,j})$ and the residue is given by, c.f., Eq. (8.82),

$$r_{i,j} = F_{i,j} - \frac{1}{2h^2}[(\xi_{i+1,j} + \xi_{i,j})\tilde{p}_{i+1,j} + (\xi_{i,j} + \xi_{i-1,j})\bar{p}_{i-1,j} + (\xi_{i,j} + \xi_{i,j+1})\tilde{p}_{i,j+1} + (\xi_{i,j} + \xi_{i,j-1})\bar{p}_{i,j-1} - \Xi_{i,j}\tilde{p}_{i,j}] + (\rho h)_{i,j}. \tag{8.121b}$$

Approximating the pressure by a piecewise constant function that assumes the value $p_{k,l} = p(x_k, z_l)$ over the $h \times h$ square centered on (x_k, z_l), $(2 \le k, l \le n-1, m-1)$, we can use Eq. (8.109) to approximate the deflection as (Venner and Lubrecht, 2000)

$$h^h_{i,j} = h_0 + \frac{x_i^2}{2} + \frac{z_j^2}{2} + \sum_k \sum_l K^{hh}_{i,j,k,l} p_{k,l}. \tag{8.122}$$

The influence coefficients $K^{hh}_{i,j,k,l}$ can be calculated analytically

$$K^{hh}_{i,j,k,l} = \frac{2}{\pi^2} \int_{z_l - h/2}^{z_l + h/2} \int_{x_k - h/2}^{x_k + h/2} \frac{dx'\, dz'}{\sqrt{(x_i - x')^2 + (z_j - z')^2}}. \tag{8.123a}$$

The integration yields nine different results, for the nine different cases constructed from $x_i < x_k$, $x_i > x_k$, $x_i = x_k$ and $z_j < z_l$, $z_j > z_l$, $z_j = z_l$, which can be combined into one expression (Johnson, 1985; Venner, 1991)

$$\begin{aligned} K^{hh}_{i,j,k,l} = \frac{2}{\pi^2} \Bigg\{ & |x_P| \ln \left[\frac{z_P + \left[z_P^2 + x_P^2\right]^{1/2}}{z_M + \left(z_M^2 + x_P^2\right)^{1/2}} \right] \\ & + |z_P| \ln \left[\frac{x_P + \left[x_P^2 + z_P^2\right]^{1/2}}{x_M + \left(x_M^2 + x_P^2\right)^{1/2}} \right] \\ & + |x_M| \ln \left[\frac{z_M + \left[z_M^2 + x_M^2\right]^{1/2}}{z_P + \left(z_P^2 + x_M^2\right)^{1/2}} \right] \\ & + |z_M| \ln \left[\frac{x_M + \left[x_M^2 + z_M^2\right]^{1/2}}{x_P + \left(x_P^2 + z_M^2\right)^{1/2}} \right] \Bigg\}. \end{aligned} \tag{8.123b}$$

Here we use the notation

$$x_{P;M} = \bar{x}_{ki} \pm \frac{h}{2}, \quad \bar{x}_{ki} = x_k - x_i$$
$$z_{P;M} = \bar{z}_{lj} \pm \frac{h}{2}, \quad \bar{z}_{lj} = z_l - z_j.$$

Note that the influence coefficients depend only on the distance between points of force and points of deflection, that is on $|i-k|$ and $|j-l|$, but not on the actual location of either of those points; this can lead to substantial reduction of computational work as well as of storage (Venner and Lubrecht, 2000).

In applying the MG method, which works directly on the nonlinear equations, one must take cognizance of the fact that ξ undergoes significant changes when moving from the unloaded to the loaded region of the contact. Correspondingly, the method of relaxation has to be made region specific.

For $\xi = \text{const}$. Eq. (8.115) has the form

$$\xi \left(\frac{\partial^2 p}{\partial x^2} + \frac{\partial^2 p}{\partial z^2} \right) - \frac{\partial(\rho h)}{\partial x} = 0. \tag{8.124a}$$

At the limit $\xi \to \infty$, we obtain Laplace's equation

$$\frac{\partial^2 p}{\partial x^2} + \frac{\partial^2 p}{\partial z^2} = 0 \tag{8.124b}$$

for which point relaxation, either the Jacobi or the Gauss-Seidel technique, leads to good convergence when applied within the context of the MG scheme. Thus outside the loaded zone these schemes can be retained. In contrast, inside the loaded zone and at severe loading conditions $\xi \to 0$ and coupling in the z-direction is lost

$$\frac{\partial(\rho h)}{\partial x} = 0. \tag{8.124c}$$

For this second case, the Gauss-Seidel line relaxation, which was an excellent smoother for the first case, becomes unstable. However, the distributive line relaxation is a good scheme to apply here. Based on practical tests, Venner (1991) recommends using

- $\frac{\xi}{h^2} > 0.3$, Gauss-Seidel line relaxation,
- $\frac{\xi}{h^2} \leq 0.3$, Jacobi distributive line relaxation.

In addition, some underrelaxation is advised in both processes. For details, the reader should consult Venner and Lubrecht (2000). This book also contains working computer codes for both the HL and the EHL problem. The FAS method of solution of the equations of EHL point contact are fully discussed by Lubrecht (1987), Venner (1991), Ehret et al. (1997), Venner and Lubrecht (2000) and Gohar (2000).

Another popular way to deal with the EHL point contact problem is via the MG-Newton scheme. In this scheme, MG is employed only as the inner solver for the linear equations that were generated in Newton's method (Chang et al. 1989). However, since through the deflection term the film thickness is dependent on all nodal pressures, the resulting Jacobian is full, leading to costly solution in terms of storage and computer time. To reduce computational costs, Chang et al. (1989) retained only three terms in each row of the Jacobian for the line contact problem, reducing the Jacobian to a tridiagonal matrix. Similarly, Lee and Hsu (1993) truncated the Jacobian to a hexadiagonal matrix when dealing with the thermal-EHL line contact problem. For the point contact problem, Hsu and Lee (1994) set $\partial F_{i,j}/\partial p_{k,l} = 0$ for $k < (i-1)$ and $k > (i+1)$, and $l < (j-1)$ and $l > (j+1)$; this resulted in a block tridiagonal Jacobian with nine nonzero terms in each row.

As mentioned above, when all derivatives of the Reynolds equation are approximated by second-order accurate central differences, accuracy is maintained but computational stability suffers, especially at high loads (Houpert and Hamrock, 1986; Lubrecht, 1987). Stability, in contrast, is greatly improved on using mixed second-order accurate central and first-order accurate backward difference.

To promote both good accuracy and good stability, Chang et al. (1989) apply standard second-order accurate central difference formula to approximate the Reynolds equation as residual function (see also Lee and Hsu, 1993; Hsu and Lee, 1994)

$$F^R_{i,j} = \frac{1}{2h^2}[(\xi_{i+1,j} + \xi_{i,j})p_{i+1,j} + (\xi_{i,j} + \xi_{i-1,j})p_{i-1,j} + (\xi_{i,j} + \xi_{i,j+1})p_{i,j+1} + (\xi_{i,j} + \xi_{i,j-1})p_{i,j-1} - 2\Xi_{i,j}p_{i,j}] - \frac{(\rho h)_{i+1/2,j} - (\rho h)_{i-1/2,j}}{h}, \quad (8.125a)$$

but a mixed second-order central and first-order backward differencing scheme for the Reynolds equation intended for generating the Jacobian

$$F^J_{i,j} = \frac{1}{2h^2}[(\xi_{i+1,j} + \xi_{i,j})p_{i+1,j} + (\xi_{i,j} + \xi_{i-1,j})p_{i-1,j} + (\xi_{i,j} + \xi_{i,j+1})p_{i,j+1} + (\xi_{i,j} + \xi_{i,j-1})p_{i,j-1} - 2\Xi_{i,j}p_{i,j}] - \frac{(\rho h)_{i,j} - (\rho h)_{i-1,j}}{h}. \quad (8.125b)$$

Then the *modified Newton's* scheme is characterized by

$$\sum_{k=i-1}^{k=i+1}\sum_{l=j-1}^{l=j+1} \frac{\partial F^J_{ij}}{\partial p_{kl}}\Delta p_{k,l} = -F^R_{i,j}; \qquad 2 \le i, j \le n-1. \quad (8.126)$$

Though the rate of convergence is determined by $F^J_{i,j}$, accuracy is controlled by $F^R_{i,j}$, which relies on second-order accurate central differencing.

Calculation of the Jacobian would require the derivatives of the elastic deformation with respect to each nodal pressure, resulting, on a square mesh, in a matrix of order $(n, m) \times (n, m)$. To save on computer storage the elements of the Jacobian $J_{ij,kl} = \partial F^J_{i,j}/\partial p_{k,l}$ can be set to zero for $k < i-1, k > i+1$ and $l < j-1, l > j+1$; the Jacobian then has nine terms in each row, leading to a storage requirement of $\sim 9n$. In fact, Hsu and Lee found that it was sufficient to consider only the five terms $J_{ij,ij}$, $J_{ij,i-1j}$, $J_{ij,i+1j}$, $J_{ij,ij-1}$ and $J_{ij,ij+1}$ and thus the Jacobian matrix can be truncated to a block-diagonal matrix for the EHL point contact problem (Chang et al., 1989; Lee and Hsu, 1993; Hsu and Lee, 1994).

Dawson and Wang (Dawson and Wang, 1994; Ehret et al., 1997) further develop the ideas of Chang et al. (1989) by considering only the local hydrodynamic pressure when evaluating the pressure derivative of deformation, leading to

$$\frac{\partial \xi_{i,j}}{\partial p_{k,l}} = 0, \quad \text{for } k \neq i \text{ or } l \neq j. \quad (8.127)$$

This scheme that includes the simplification (8.127), is termed the *effective influence Newton* (EIN) method by Dawson and Wang (1994). The Jacobian in the EIN method is block tridiagonal; originally, it used central differencing for the discretization of the Couette term (but see Ehret et al., 1997; Jin, 2000; Jagatia and Jin, 2001). Strictly speaking, assumption (8.127) is valid only when using the constrained column model, i.e., the deflection at a point is dependent only on the pressure at that point. However, the EIN method has been compared with the MG method, as well as with older results of Hamrock and Dowson, by Ehret et al. (1997) demonstrating excellent agreement between the EIN and MG methods.

In accordance with the assumptions of the EIN method, the elements of the Jacobian are

$$\frac{\partial F^J_{i,j}}{\partial p_{i-1,j}} = \frac{1}{2h^2}\left[\xi_{i-1,j} + \xi_{i,j} - \frac{\partial \xi_{i-1,j}}{\partial p_{i-1,j}}(p_{i,j} - p_{i-1,j})\right] + \frac{\partial(\rho h)_{i-1,j}}{h\partial p_{i-1,j}}$$

$$\frac{\partial F^J_{i,j}}{\partial p_{i+1,j}} = \frac{1}{2h^2}\left[\xi_{i+1,j} + \xi_{i,j} - \frac{\partial \xi_{i+1,j}}{\partial p_{i+1,j}}(p_{i,j} - p_{i+1,j})\right]$$

$$\frac{\partial F^J_{i,j}}{\partial p_{i,j-1}} = \frac{1}{2h^2}\left[\xi_{i,j-1} + \xi_{i,j} - \frac{\partial \xi_{i,j-1}}{\partial p_{i,j-1}}(p_{i,j} - p_{i,j-1})\right] \tag{8.128}$$

$$\frac{\partial F^J_{i,j}}{\partial p_{i,j+1}} = \frac{1}{2h^2}\left[\xi_{i,j+1} + \xi_{i,j} - \frac{\partial \xi_{i,j+1}}{\partial p_{i,j+1}}(p_{i,j} - p_{i,j+1})\right]$$

$$\frac{\partial F^J_{i,j}}{\partial p_{i,j}} = \frac{1}{2h^2}\left[-\Xi_{i,j} - \frac{\partial \xi_{i,j}}{\partial p_{i,j}}(4p_{i,j} - p_{i+1,j} - p_{i-1,j} - p_{i,j+1} - p_{i,j-1})\right] - \frac{\partial(\rho h)_{i,j}}{h\partial p_{i,j}}.$$

Multilevel Multi-Integration

Application of MG techniques can significantly lower computing times and computing effort in solving partial differential equations. There is an aspect of EHL problems, however, that makes solution of the EHL point contact problem time consuming, even when MG techniques are employed. It is the calculation of the deflection

$$w_{i,j} = \sum_k \sum_l K^{hh}_{i,j,k,l} p_{k,l} \tag{8.129}$$

$$K^{hh}_{i,j,k,l} = \frac{2}{\pi^2}\int_{z_l - h/2}^{z_l + h/2}\int_{x_k - h/2}^{x_k + h/2} \frac{dx'dz'}{\sqrt{(x_i - x')^2 + (z_j - z')^2}}. \tag{8.123a}$$

Though we evaluate $\boldsymbol{K}^{hh}$ analytically, the summation in (8.129) involves $O(n)$ operations, where n is the number of nodes, and for calculating deflection at each nodal point the number of computations is $O(n^2)$. Furthermore, the summation has to be performed a large number of times per iteration, leading to excessive computing times. The problem can be alleviated, however, if we make use of the multilevel structure of the MG construction during the process of integration. In that case, as Brandt and Lubrecht (1990) have shown, deflection can be calculated from $O(n \ln n)$ operations. The idea behind this so-called *multilevel multi-integration* (MLMI), applied here to two consecutive meshes Ω^h and Ω^H where $H = 2h$, is that the integral is performed on the coarse mesh Ω^H, its value injected to even numbered nodes of Ω^h, and interpolated. Thus, we perform full integration only on the coarse grid and interpolate back to the finer grid. According to Venner (1991) the idea is to "*replace the original fine grid multi-summation by a similar summation on a coarser grid in such a way that the additional error remains small compared to the discretization error*." In this short introduction to multilevel multi-integration, we follow Venner and Lubrecht (2000).

The general problem we wish to discuss is the efficient computation of integrals (integral transforms) of the type

$$w^h_i = w^h\left(x^h_i\right) \stackrel{\text{def}}{=\!=} \int_\Omega K\left(x^h_i, y\right)u(y), \tag{8.130a}$$

which, when discretized on Ω^h, can be written as

$$w_i^h = \sum_j K_{i,j}^{h,h} u_j^h. \tag{8.130b}$$

In addition to Ω^h, we introduce a coarse grid Ω^H with mesh size $H = 2h$ just as we did in the MG scheme. The smooth and coarse grids are related therefore through

$$x_{2I}^h = x_I^H; \quad y_{2J}^h = y_J^H.$$

As discussed above, we would prefer to perform the summation (8.130) on the coarse grid Ω^H, if this could be accomplished without significantly reducing the accuracy of the integral. The question is which function in (8.130) can be accurately represented on the coarse grid. In the MG scheme the smooth-grid error components are transferred onto the coarse grid and solved there, they are then interpolated back onto the smooth grid to improve the smooth grid approximation. This can be done there, as the error components are smooth. The same cannot be said of $\boldsymbol{u}^h$ in (8.30) as it cannot be guaranteed to be smooth. The kernel K or its discrete equivalent $\boldsymbol{K}^{hh}$ however is expected to be smooth with respect to each of its indices; this is, therefore, the function we expect to interpolate from Ω^H to Ω^h with minimal error.

We may suppose w^h, the displacement in our case, to be smooth and to interpolate values of w_i^h on the smooth grid from the values of w_I^H on the coarse grid we write

$$w_i^h = \left[I I_H^h w_{\cdot}^{\,H} \right]_i. \tag{8.131}$$

Here $I I_H^h$ is the interpolation operator from Ω^H to Ω^h (not unlike I_H^h but perhaps of higher order). The dot indicates the position of the index that is being worked on by the interpolation operator; this designation becomes necessary only when we have multiple indices.

For simplicity, this introduction assumes a smooth[9] kernel for which we have

$$K_{i,J}^{hH} \stackrel{\text{def}}{=} K_{i,2J}^{hh}. \tag{8.132}$$

The values at other than even grid points of Ω^h are obtained from the interpolation

$$\tilde{K}_{i,j}^{hh} = \left[I I_H^h K_{i,\cdot}^{hH} \right]_j, \tag{8.133}$$

where the tilde signifies that though the interpolation yields accurate results, $\tilde{K}_{i,j}^{hh}$ is, nevertheless, an approximation. Substituting into (8.131) we obtain our approximation to $\boldsymbol{w}^h$

$$\tilde{w}_i^h = \sum_j \tilde{K}_{i,j}^{h,h} u_j^h. \tag{8.134}$$

As an illustration, consider the interpolation function

$$\begin{aligned} \left[I I_H^h K_{i,\cdot}^{hH} \right]_{2J} &= K_{i,J}^{hH} \\ \left[I I_H^h K_{i,\cdot}^{hH} \right]_{2J+1} &= \frac{1}{2} \left[K_{i,J}^{hH} + K_{i,J+1}^{hH} \right]. \end{aligned} \tag{8.135}$$

This function is diagrammed in Figure 8.17.

[9] A kernel is smooth if its value at a point can be obtained by interpolation of sufficiently high order, from its value at adjacent points. Kernels of elastic deformation are only "singularly smooth" and thus require special attention (Venner and Lubrecht, 200).

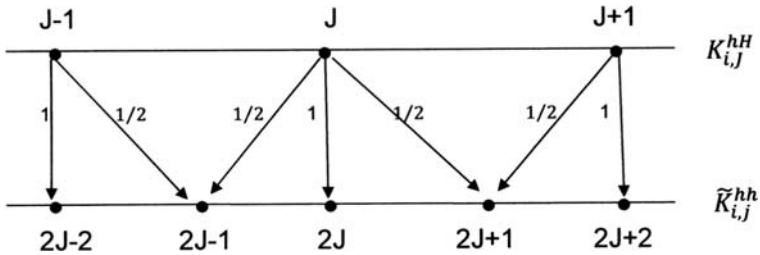

Figure 8.17. Interpolation from coarse grid Ω^H to fine grid Ω^h.

Writing II_H^h as a two-dimensional array, we have

$$II_H^h = \frac{1}{2}\begin{bmatrix} 2 & & & & & & & & & \\ 1 & 1 & & & & & 0 & & & \\ & & \ddots & & & & & & & \\ & & & 1 & 1 & & & & & \\ & & & & 2 & & & & & \\ & & & & 1 & 1 & & & & \\ & 0 & & & & & \ddots & & & \\ & & & & & & & 1 & 1 & \\ & & & & & & & & 2 & \end{bmatrix}. \tag{8.136}$$

Thus, the summation (8.134) assumes the value

$$\begin{aligned} \tilde{w}_i^h &= h\sum_j \tilde{K}_{i,j}^{hh} u_j^h \\ &= h\sum_j [II_H^h K_{i,\cdot}^{hH}]_j u_j^h \\ &= \frac{h}{2}\big[2K_{i,0}^{hH}u_0^h + \big(K_{i,0}^{hH} + K_{i,1}^{hH}\big)u_1^h + 2K_{i,1}^{hH}u_2^h + \big(K_{i,1}^{hH} + K_{i,2}^{hH}\big)u_3^h \\ &\quad + \cdots + 2K_{i,n/2-1}^{hH}u_{n-2}^h + \big(K_{i,n/2-1}^{hH} + K_{i,n/2}^{hH}\big)u_{n-1}^h + 2K_{i,n/2}^{hH}u_n^h\big]. \end{aligned} \tag{8.137}$$

This can be re-written by combining coefficients of $K_{i,J}^{hH}$

$$\begin{aligned} \tilde{w}_i^h = \frac{h}{2}\big[&K_{i,0}^{hH}\big(2u_0^h + u_1^h\big) + K_{i,1}^{hH}\big(u_1^h + 2u_2^h + u_3^h\big) \\ &+ \cdots + K_{i,n/2-1}^{hH}\big(u_{n-3}^h + 2u_{n-2}^h + u_{n-1}^h\big) + K_{i,n/2}^{hH}\big(u_{n-1}^h + 2u_n^h\big)\big]. \end{aligned} \tag{8.138}$$

We now use the substitution

$$u_J^H \stackrel{\text{def}}{=\!=} \frac{1}{2}\big[\big(II_H^h\big)^T u_\cdot^h\big]_J \tag{8.139}$$

and write (8.138) as

$$\begin{aligned} \tilde{w}_i^h &= H\big[K_{i,0}^{hH}u_0^H + K_{i,1}^{hH}u_1^H + \cdots + K_{i,n/2-1}^{hH}u_{n/2-1}^H + K_{i,n/2}^{hH}u_{n/2}^H\big] \\ &= H\sum_J K_{i,J}^{hH}\big[\big(II_H^h\big)^T u_\cdot^h\big]_J. \end{aligned} \tag{8.140}$$

The transpose of the interpolation operator $I I_H^h$ has the form

$$\left(I I_H^h\right)^T = \frac{1}{2}\begin{pmatrix} 2 & 1 & & & & & & & & \\ & 1 & 2 & 1 & & & & 0 & & \\ & & & \ddots & & & & & & \\ & & & & 1 & & & & & \\ & & & & 1 & 2 & 1 & & & \\ & & & & & & 1 & & & \\ & & & & & & & \ddots & & \\ & & & & & & & & 1 & \\ & & & & & & & & 1 & 2 \end{pmatrix}. \tag{8.141}$$

We have just shown that

$$\tilde{w}_i^h = h \sum_j \tilde{K}_{i,j}^{hh} u_j^h = H \sum_J K_{i,J}^{hH} u_J^H. \tag{8.142}$$

Multi-integration on two grids is, therefore, defined as (Venner and Lubrecht, 2000)

- *Anterpolation*
  For each J compute u_J^H *according to:*
  $$u_J^H \stackrel{\text{def}}{=\!=} 2^{-d}\left[\left(I I_H^h\right)^T u_\cdot^h\right]_J$$
- *Coarse grid summation*
  For each I compute w_I^H *according to:*
  $$w_I^H = H \sum_J K_{IJ}^{HH} u_J^H; \quad K_{I,J}^{HH} = K_{2I,2J}^{hh}$$
- *Interpolation*
  For each i compute w_i^h *using:*
  $$w_i^h = \left[I I_H^h w_\cdot^H\right]_i.$$

Here d is the dimension of the problem.

In closure, we quote from the book of Venner and Lubrecht (2000). *The procedure of replacing the multi-summation by a fine-to-coarse transfer, a course grid multi-summation and an interpolation . . . can be applied once more to the course grid multi-summation and repeated recursively until the grid is reached with a number of grid points proportional to* $\sqrt{n}$. *On the latter grid the multi-summation is actually performed, requiring* $O(n)$ *operations. . . . Consequently, similar to the coarse grid correction cycle . . . a sequence of coarser grid is used.*

8.7 Rolling-Contact Bearings[10]

In contrast to hydrodynamic bearings, which depend for low-friction characteristics on a fluid film between the journal and the bearing surfaces, rolling-element bearings employ a number of balls or rollers that roll in an annular space. To some extent, these

[10]Section 8.7 is a reproduction, with permission, of parts of Chapter 8, *Rolling Element Bearings*, by W. J. Anderson, in *Tribology: Friction, Lubrication and Wear*, ed. A. Z. Szeri. Hemisphere Publishing Co., 1980.

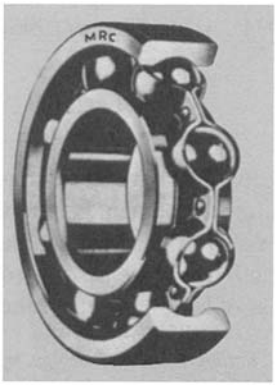

Figure 8.18. Deep groove ball bearing. (Courtesy Marlin Rockwell Corp.)

rollers help to avoid gross sliding and the high coefficients of friction that are associated with sliding. The term rolling element is used to describe this class of bearing because the contact between the rolling elements and the races or rings consists more of sliding than of actual rolling. A rolling contact implies no interfacial slip; this condition can seldom be maintained, however, because of material deformation and geometric factors. Rolling-element bearings ordinarily consist of two races or rings (the inner race and the outer race), a set of rolling elements (either balls or rollers), and a separator (sometimes called a cage or retainer) for keeping the set of rolling elements approximately equally spaced.

Rolling-element bearings offer the following advantages when compared with hydrodynamic bearings: (1) low starting friction; (2) low operating friction, comparable to that of hydrodynamic bearings at low speeds and somewhat less at high speeds; (3) less sensitivity to interruptions in lubrication than with hydrodynamic bearings; and (4) capability of supporting combined loads. In the latter respect, rolling-element bearings are more versatile than hydrodynamic bearings, which usually can support only radial or thrust loads.

Rolling-element bearings also have disadvantages: (1) they occupy more space in the radial direction than do hydrodynamic bearings and (2) they have a finite fatigue life because of repeated stresses at ball-race contacts – in contrast to hydrodynamic bearings, which usually have an almost infinite fatigue life.

Bearing Types

Ball Bearings

The various types of rolling-element bearings may be placed in two broad categories; the first of these is ball bearings. The most common types of ball bearings are:

(1) Deep groove or Conrad
(2) Angular contact
(3) Self-aligning
(4) Duplex
(5) Ball thrust

A typical deep groove ball bearing is shown in Figure 8.18. This bearing has moderately high radial load capacity and moderate thrust load capacity. Figure 8.19 shows an angular contact bearing. This bearing has a higher thrust-load capacity than a deep groove bearing, but it can carry thrust load in only one direction.

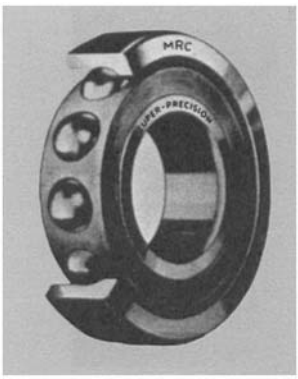

Figure 8.19. Angular contact ball bearing. (Courtesy Marlin Rockwell Corp.)

A self-aligning ball bearing with the outer-race groove ground to a spherical shape is illustrated in Figure 8.20(a). This bearing has a relatively low load capacity but is insensitive to shaft and housing misalignments. Figure 8.20(b) shows a second type of self-aligning ball bearing with the self-aligning feature obtained by grinding the outer-race outside diameter in a spherical shape to fit a spherical housing. This bearing has a higher load capacity than the bearing in Figure 8.20(a), but care must be taken to maintain freedom of movement between the outer race and the housing.

Angular contact bearings are usually used in pairs in duplex mounts. Different types of duplex mounts are shown in Figure 8.21(a) (back to back) and Figure 8.21(b) (face to face). These two arrangements make it possible to carry thrust load in either direction. Bearings are manufactured as matched pairs, so that when they are mated and the races are made flush, each bearing is preloaded slightly. This preloading provides greater stiffness and helps to prevent ball skidding with acceleration at light load. When a high unidirectional thrust load must be carried, a duplex tandem mount [Figure 8.21(c)] is used. With careful manufacture and installation, a tandem bearing pair may have a thrust capacity as much as 1.8 times the capacity of a single bearing.

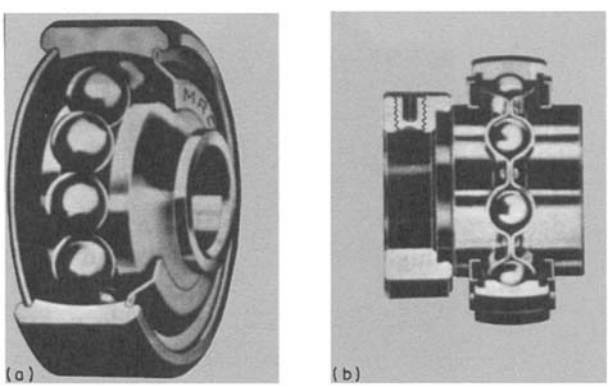

Figure 8.20. Self-aligning ball bearing: (a) groove of outer race ground to a spherical shape, (b) outside diameter of outer race ground to fit spherical housing. (Courtesy Marlin Rockwell Corp.)

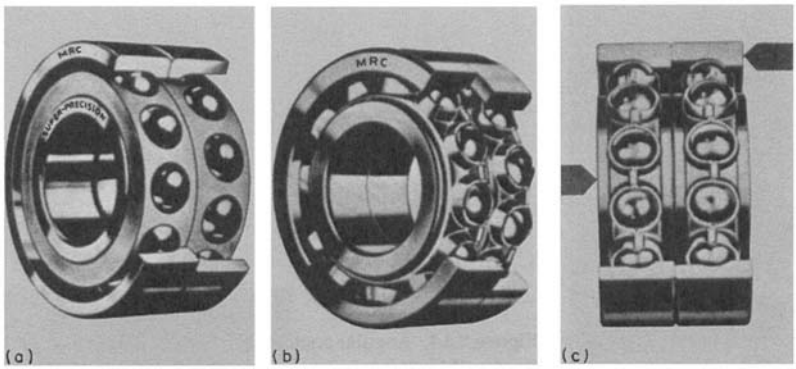

Figure 8.21. Duplex angular contact ball bearing, mounted (a) back to back, (b) face to face, (c) in tandem. (Courtesy Marlin Rockwell Corp.)

A thrust ball bearing is shown in Figure 8.22. This bearing has a high thrust capacity but is limited to low speeds because of the high degree of sliding in the ball-race contacts.

Roller Bearings

The second broad category is that of roller bearings. Common types are:

(1) Cylindrical
(2) Tapered
(3) Spherical
(4) Needle

Cylindrical roller bearings (Figure 8.23) are best suited of all roller bearing types for high-speed operation. These bearings carry only radial load, and they are frequently used where freedom of movement of the shaft in the axial direction must be provided because of differential expansion.

Tapered roller bearings (Figure 8.24) and spherical roller bearings (Figure 8.25) are high-load-capacity, low-speed roller bearings with combined radial load and thrust load capability.

Needle bearings (Figure 8.26) are capable of carrying high loads and are useful in applications where limited radial space is available.

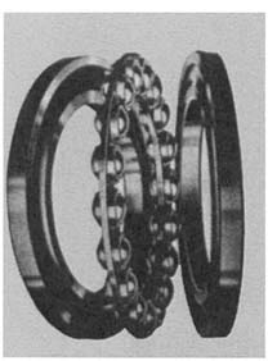

Figure 8.22. Thrust ball bearing (Courtesy Marlin Rockwell Corp.).

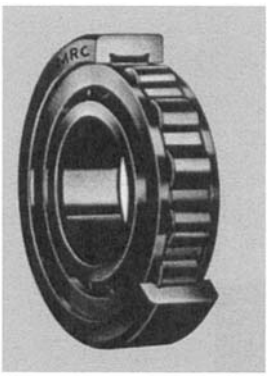

Figure 8.23. Cylindrical roller bearing. (Courtesy Marlin Rockwell Corp.)

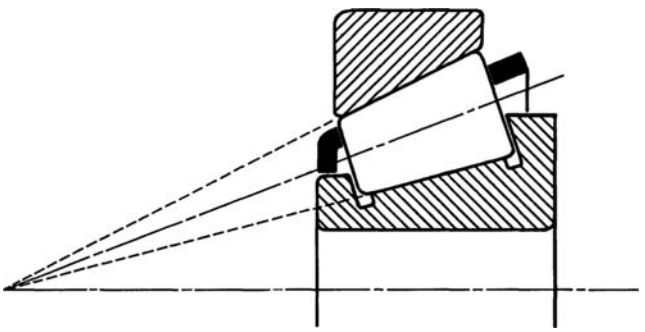

Figure 8.24. Tapered roller bearing.

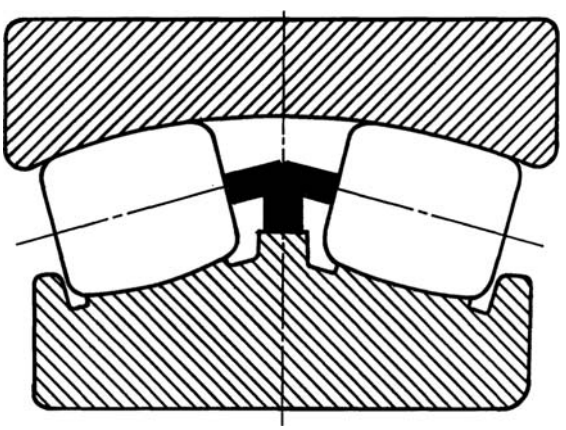

Figure 8.25. Spherical roller bearing.

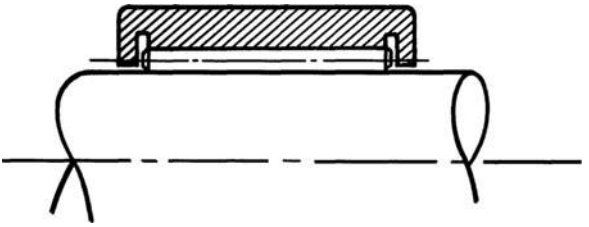

Figure 8.26. Needle bearing with shaft and inner race.

Although rolling-element bearings are usually equipped with a separator, in some instances they are not. Bearings without separators are usually termed full-complement bearings. A common type of full-complement roller bearing is the needle bearing. In some low-speed applications where load capacity is of primary importance, full-complement ball bearings are used. In this type of bearing, the annular space between the races is packed with the maximum number of balls.

Rolling Friction

The concepts of rolling friction are important because the characteristics and behavior of rolling-element bearings depend on rolling friction. The theories of Reynolds (1876) and Heathcote (1921) were previously well accepted as correctly explaining the origin of rolling friction for a ball in a groove. The energy lost in rolling was believed to be that required to overcome the interfacial slip that occurs because of the curved shape of the contact area. As shown in Figure 8.27, the ball rolls about the x axis and makes contact with the groove from a to b.

If the groove is fixed, then for zero slip over the contact area no point within the area should have a velocity in the direction of rolling. The surface of the contact area is curved, however, so that points a and b are at different radii from the x axis than are points c and d. For an inelastic ball, points a and b must have different velocities with respect to the x axis than do points c and d because the velocity of any point on the ball relative to the x axis

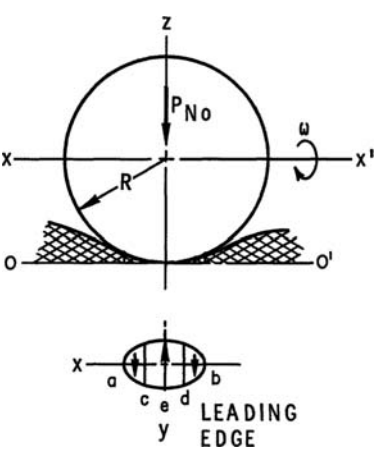

Figure 8.27. Differential slip resulting from curvature of contact ellipse.

equals the angular velocity, ω, times the radius from the x axis. Slip must occur at various points over the contact area unless the body is so elastic that yielding can take place in the contact area to prevent this interfacial slip. Reynolds and Heathcote assumed that this interfacial slip took place and that the forces required to make a ball roll were the forces required to overcome the friction due to this interfacial slip. In the contact area, rolling without slip will occur at a specific radius from the x axis. Where the radius is greater than this radius to the rolling point, slip will occur in the other direction; where it is less than the radius to this rolling point, slip will occur in the other direction. In Figure 8.27, the lines to points c and d represent the approximate location of the rolling bands, and the arrows shown in the three portions of the contact area represent the directions of interfacial slip when the ball is rolling into the paper.

Frictional Losses in Rolling Contact Bearings

Some of the factors that affect the magnitude of friction losses in rolling bearings are:

(1) Bearing size
(2) Bearing type
(3) Bearing design
(4) Load (magnitude and type, either thrust or radial)
(5) Speed
(6) Oil viscosity
(7) Oil flow.

In a rolling-contact bearing, friction losses consist of:

(1) Sliding friction losses in the contacts between the rolling elements and the raceways.
(2) Hysteresis losses resulting from the damping capacity of the raceway and the ball material.
(3) Sliding friction losses between the separator and its locating race surface and between the separator pockets and the rolling elements.
(4) Shearing of oil films between the bearing parts and oil churning losses caused by excess lubricant within the bearing.

The relative magnitude of each of these friction losses depends on the bearing type and design, the lubricant, and the type of lubrication. Palmgren (1959) presented friction coefficients for various types of bearings, which may be used for rough calculations of bearing torque. The values were computed at a bearing load that would give a life of 1×10^9 revolutions for the respective bearings. As the bearing load approaches zero, the friction coefficient becomes infinite because the bearing torque remains finite. The following friction coefficients were given by Palmgren:

All these friction coefficients are referenced to the bearing bore.

Palmgren (1959) and Muzzoli (Wilcock and Booser, 1957) attempted to relate all the factors that influence rolling-bearing torque. Palmgren outlined a method for computing torque for several types of bearings by calculating the zero-load torque and the sliding and hysteresis losses due to the load. Muzzoli's equation for bearing torque is discussed in Wilcock and Booser (1957). A number of factors must be known for these equations to

Table 8.4. *Contact bearing friction coefficients*

Bearing	Friction coefficient
Self-aligning ball	0.0010
Cylindrical roller, with flange-guided short rollers	0.0011
Thrust ball	0.0013
Single-row deep groove ball	0.0015
Tapered and spherical roller, with flange guided rollers	0.0018
Needle	0.0045

be useful, and their validity depends on the accuracy with which some of the factors are determined.

Astridge and Smith (1972) conducted a thorough experimental study of the power loss in high-speed cylindrical roller bearings. They found that the principal sources of power loss were:

(1) Roller track elastohydrodynamic films (60%)
(2) Roller cage sliding (10%)
(3) Cage-locating surface sliding (10%)
(4) Cage side-chamber wall drag (10%)
(5) Oil flinging from rotating surfaces (7%)
(6) Elastic hysteresis (1%)
(7) Displacement of oil by rollers (1%).

Specific Dynamic Capacity and Life

In ordinary bearing applications where extreme speeds and temperatures are not present, a properly installed and lubricated bearing will eventually fail because of material fatigue. The repeated stresses developed in the contact areas between the rolling elements and the races eventually result in failure of the material, which manifests itself as a fatigue crack. The fatigue crack propagates until a piece of the race or rolling-element material spalls out and produces the failure. Many bearings fail for reasons other than fatigue, but in ordinary applications, these failures are considered avoidable if the bearing is properly handled, installed, and lubricated and is not overloaded.

If a number of similar bearings are tested to fatigue at a specific load, bearing life varies widely among them. For a group of 30 or more bearings, the ratio of the longest to the shortest life may be of the order of 20 or more (Figure 8.28).

A curve of life as a function of the percentage of bearings that failed can be drawn for any group of bearings (Figure 8.29). For a group of 30 or more bearings, the longest life would be of the order of four or five times the average life. The term life, in bearing catalogs, usually means the life that is exceeded by 90% of the bearings. This is the so-called B-10 or 10% life. The 10% life is one-fifth the average 50% life for a normal life-dispersion curve.

If two groups of identical bearings are run to fatigue at two different loads, the life varies inversely as the nth power of the load:

$$\frac{L_2}{L_1} = \left(\frac{W_1}{W_2}\right)^n .$$

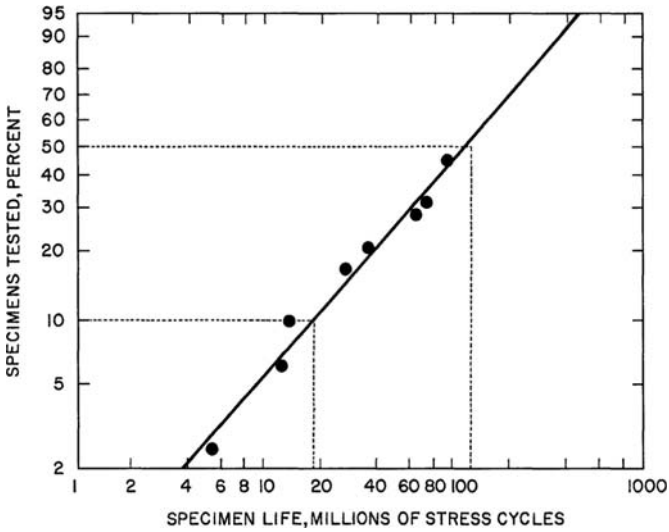

Figure 8.28. Typical Weibull plot of bearing fatigue failures.

For nominal point contact $n = 3$, for nominal line contact $n = 4$. For point contact, then,

$$\frac{W_1}{W_2} = \left(\frac{L_2}{L_1}\right)^{1/3}$$

$$W_1 L_1^{1/3} = W_2 L_2^{1/3} = \text{const.}$$

If W is a radial load that acts on a radial bearing and L is 1 million revolutions with rotation of the inner race, then the constant is the *specific dynamic capacity*. The dynamic capacity for thrust bearings is determined if W is a thrust load.

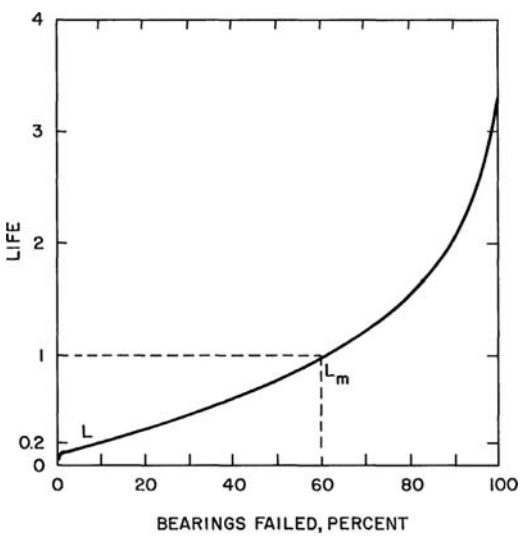

Figure 8.29. Distribution of bearing fatigue failures.

In terms of the specific dynamic capacity, C,

$$L = (C/P)^3 ,$$

where L is the life in millions of revolutions and P is the equivalent load. In general, the ball bearings support both radial and thrust loads, and formulas for obtaining the equivalent load, P, in terms of radial and thrust loads are given for various bearing types in most bearing catalogs.

The bearing design factors that affect the specific dynamic capacity are the race conformities, the rolling-element dimensions, and the number of rolling elements. Recent research has shown that the bearing material and both the lubricant viscosity and the base stock can have marked effects on fatigue. The original bearing fatigue investigations, which include those of Palmgren, were made before the advent of the extreme temperatures and speeds to which rolling bearings are now subjected. As a result, the great majority of bearings were made of SAE 51100 or SAE 52100 alloys, and wide variations in material fatigue strength were not encountered. In addition, all rolling bearings were lubricated with a mineral oil such as SAE 30 or with a mineral-base soap grease so that the effect of the lubricant on fatigue was not important enough to be included among the parameters affecting fatigue life.

In recent years, a better understanding of rolling-element bearing design, materials, processing, and manufacturing techniques has permitted a general improvement in bearing performance. This is reflected in greater bearing reliability or longer expected life in a particular application. At the same time, operating conditions have become better understood, so that the application factors of the past, which were based primarily on experience, are giving way to quantified environmental factors that permit much better estimates of expected bearing life. These environmental factors, considering application, bearing configuration, and bearing rating, are often exceedingly complex, so that obtaining problem solutions in a reasonable time requires high-speed computers and more information than is readily available to most engineers. It becomes necessary to develop a guide that extends the "engineering approximations," which are illustrated in most bearing manufacturers' catalogs, and provides information that will be of most use to the engineer.

The Anti-Friction Bearing Manufacturers Association (AFBMA) method for determining bearing load rating and fatigue life and/or the basic ratings published in any bearing manufacturer's catalog must be the heart of any design guide. Continuing in the vein of the engineering approximation, it is assumed that various environmental or bearing design factors are, at least for first-order effects, multiplicative. As a result, the expected bearing life, L_A, can be related to the calculated rating life, L_{10}, by

$$\begin{aligned} L_A &= (D)(E)(F)(G)(H)L_{10} \\ &= (D)(E)(F)(G)(H)\left(\frac{C}{P}\right)^n , \end{aligned}$$

where $D \ldots H$ are the life adjustment environmental or bearing design factors, C is the basic load rating, P is the equivalent load, and n is the load-life exponent (3 for ball bearings or 10/3 for roller bearings).

Methods for calculating the life adjustment factors are given in *Life Adjustment Factors for Ball and Roller Bearings* (ASME, 1971). An extensive bibliography is provided in two articles by Tallinn (1992a).

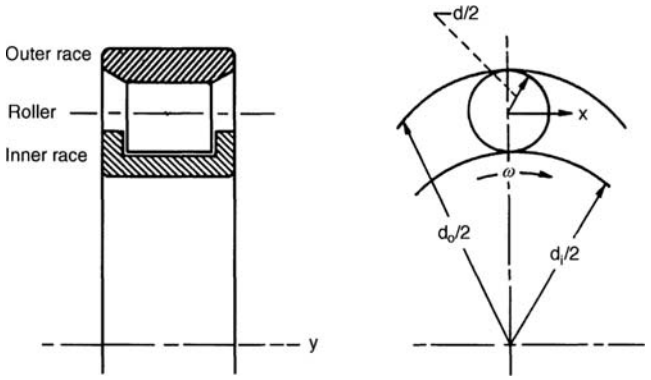

Figure 8.30. Schematic of a roller bearing. (Reproduced with permission from Hamrock, B. J. and Anderson, W. *Rolling Element Bearings*. NASA RP-1105. 1983.)

Specific Static Capacity

From considerations of allowable permanent deformation, there is a maximum load that a bearing can support while not rotating. This is called the specific static capacity, C_o. It is arbitrarily defined as the load that will produce a permanent deformation of the race and the rolling element at a contact of 0.0001 times the rolling-element diameter. When permanent deformations exceed this value, bearing vibration and noise increase noticeable when the bearing is subsequently rotated under lesser loads. Specific static capacity is determined by the maximum rolling-element load and the race conformity at the contact. A bearing can be loaded above C_o as long as the load is applied when the bearing is rotating. The permanent deformations that occur during rotation will be distributed evenly around the periphery of the races and will not be harmful until they become more extensive.

Static and dynamic load capacities are normally given for bearings in bearing catalogs.

Fatigue Wear Out

Among the many possible causes of rolling bearing failure, there are two that predominate. These are wear out and fatigue. Study of the factors that cause these failures and means for preventing or delaying them has occupied much of the time of researchers during the past decade. In addition, rolling bearings are being called on to operate at more severe conditions of speed and temperature. The consequent demands for improvements in bearing design and materials and lubricant technology have spawned additional research. The reader should consult Tallinn (1992b).

8.8 Minimum Film Thickness Calculations

Nominal Line Contact

The geometry of the cylindrical roller bearing is depicted in Figure 8.30. Specifications of the problem are adapted from Hamrock and Anderson (1983).

The load on the most heavily loaded roller is estimated from *Stribeck's formula* (Hamrock, 1991).

$$w_{\max} = \frac{4w}{n} = 4.8\,\text{kN}.$$

Table 8.5. *Data for nominal line contact problem*

Inner-race diameter	$d_i = 0.064$ m
Outer-race diameter	$d_o = 0.096$ m
Roller diameter	$d = 0.016$ m
Roller axial length	$L = 0.016$ m
No. rollers per bearing	$n = 9$
Radial load per roller	$w = 10.8$ kN
Inner-race angular velocity	$\omega_i = 524$ rad/s
Outer-race angular velocity	$\omega_i = 0$
Absolute viscosity	$\mu_0 = 0.01$ Pa · s
Viscosity-pressure coefficient	$\alpha = 2.2 \times 10^{-8}$ Pa^{-1}
Young's modulus (rollers, races)	$E = 207.5$ GPa
Poisson's ratio	$\nu = 0.3$

The radii of curvature at contact on the inner and outer race, respectively, are

$$\frac{1}{R_{x,i}} = \frac{1}{0.08} + \frac{1}{0.032} = \frac{5}{0.032}, \quad \frac{1}{R_{x,o}} = \frac{1}{0.08} - \frac{1}{0.048} = \frac{5}{0.048},$$

giving $R_{x,i} = 0.0064$ m, and $R_{x,o} = 0.0096$ m.

The effective modulus, E', and the pitch diameter, d_e, are given by

$$E' = \frac{2}{\dfrac{1-\nu_1^2}{E_1} + \dfrac{1-\nu_2^2}{E_2}} = 228\,\text{GPa}, \quad d_e = \frac{d_o + d_i}{2} = 0.08\,\text{m}.$$

The surface velocity for cylyndrical rollers is calculated from

$$\tilde{u} = \frac{|\omega_i + \omega_o||d_e^2 - d^2|}{4d_e} = 10.061\ \text{m/s},$$

where we assumed pure rolling.[11]

Calculation will be performed for the *inner-race contact* alone. The speed, load, and materials parameters are calculated as

$$U = \frac{\mu_0 \tilde{u}}{E' R_{x,i}} = \frac{(0.01)(10.061)}{(2.28 \times 10^{11})(0.0064)} = 6.895 \times 10^{-11},$$
$$W = \frac{w_{\max}}{E' L R_{x,i}} = \frac{4800}{(2.28 \times 10^{11})(0.016)(0.0064)} = 2.0559 \times 10^{-4},$$
$$G = \alpha E' = (2.2 \times 10^{-8})(2.28 \times 10^{11}) = 5.016 \times 10^{3}.$$

The criteria for the effect of viscous change and elasticity are

$$g_V = \frac{W^{2/3} G}{U^{1/2}} = 1.7804 \times 10^{3}, \qquad g_E = \frac{W}{U^{1/2}} = 24.759.$$

[11] For roller-bearing kinematics, see Anderson (1970), Anderson (1980), Hamrock (1991), and Harris (1991).

Table 8.6. *Date for nominal point contact problem*

Inner-race diameter	$d_i = 0.052291$ m
Outer-race diameter	$d_o = 0.077706$ m
Ball diameter	$d = 0.012700$ m
No. of balls per bearing	$n = 9$
Inner-groove radius	$r_i = 0.006604$ m
Outer-groove radius	$r_o = 0.006604$ m
Contact angle	$\beta = 0$
Radial load	$w_z = 8.9$ kPa
Inner-race angular velocity	$\omega_i = 400$ rad/sec
Outer-race angular velocity	$\omega_o = 0$
Absolute viscosity	$\mu_0 = 0.04$ Pa · s
Viscosity-pressure coefficient	$\alpha = 2.3 \times 10^{-8}$ Pa^{-1}
Young's modulus	$E = 200$ GPa
Poisson's ratio	$\nu = 0.3$

The point $(g_V,\ g_E)$ characterizing conditions at the inner contact can be plotted in Figure 8.8, showing that full EHL conditions apply. Thus, the formulas for minimum film thickness calculation are

$$g_{H,\min} = 1.6549 g_V^{0.54} g_E^{0.06} = 114.15,$$
$$H_{\min} = g_{H,\min}\left(\frac{U}{W}\right) = 3.8284 \times 10^{-5},$$
$$h_{\min} = R_{x,i} H_{\min} = 0.245\,\mu\text{m}.$$

Employing a slightly different procedure, i.e., approximating from nominal point contact formulas, Hamrock and Anderson find $h_{\min} = 0.32\ \mu$m.

Nominal Point Contact

The geometry of the ball bearing is shown in Figure 8.31. The specifications of the problem are adapted from Hamrock and Dowson (1981).

Calculations will be shown for the *inner-race contact* only. The pitch diameter is

$$d_e = \frac{(d_o + d_e)}{2} = 0.065\,\text{m}.$$

The equivalent radii and curvature sum are

$$R_x = \frac{d\,(d_e - d\cos\beta)}{2d_e} = 0.00511\,\text{m},$$
$$R_y = \frac{r_i d}{2r_i - d} = 0.165\,\text{m},$$
$$S_C = \frac{1}{\mathcal{R}} = \frac{1}{R_x} + \frac{1}{R_y} = 201.76,$$

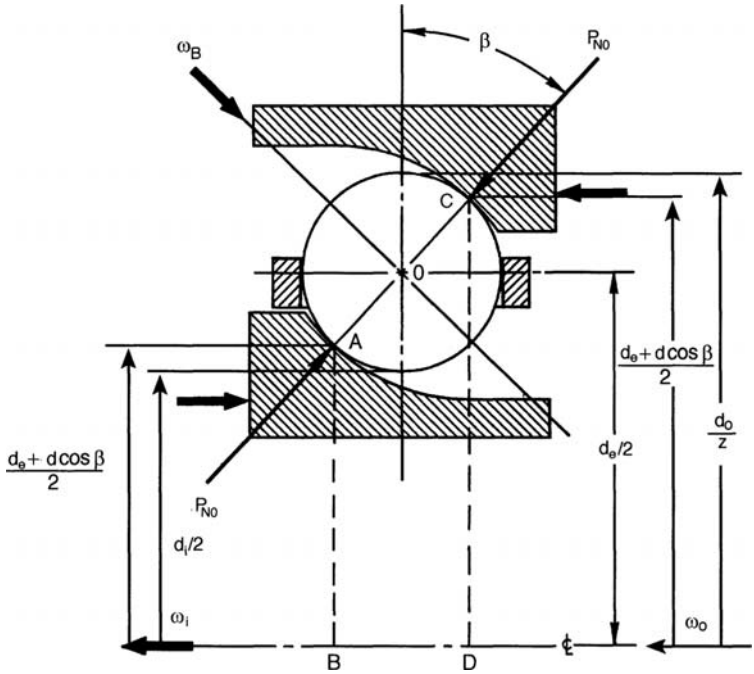

Figure 8.31. Schematics of a ball bearing. (Reproduced with permission from Hamrock, B. J. and Anderson, W. *Rolling Element Bearings*. NASA RP-1105, 1983.)

yielding $\mathcal{R} = 4.956 \times 10^{-3}$ m, $\alpha_r = R_y/R_x = 32.29$, and an ellipticity parameter

$$\bar{\kappa} = \alpha_r^{2/3} = 9.1348.$$

The approximate formulas for the elliptic integrals give

$$\bar{\mathcal{E}} = 1 + \left(\frac{\pi}{2} - 1\right)/\alpha_r = 1.0177,$$
$$\bar{\mathcal{F}} = \frac{\pi}{2} + \left(\frac{\pi}{2} - 1\right)\ln\alpha_r = 3.5542.$$

Using $E' = 219.8$ MPa for effective modulus and Stribeck's estimate (Anderson, 1980) for the maximum load

$$w_{\max} = \frac{5w}{n} = 4.944\,\text{kN}$$

valid for ball bearings, the deformation is calculated from Eq. (8.27c)

$$\delta = \bar{\mathcal{F}}\left[\left(\frac{9}{2\bar{\mathcal{E}}\mathcal{R}}\right)\left(\frac{w_{\max}}{\pi\bar{\kappa}E'}\right)^2\right]^{1/3} = 29.087\,\mu\text{m}.$$

Assuming pure rolling, the surface velocity is calculated from (Hamrock, 1991)

$$\tilde{u} = \frac{|\omega_o - \omega_i|\left|d_e^2 - d^2\right|}{4d_e} = 6.252\ \text{m/s}.$$

The design parameters give

$$U = \frac{\mu_0 \tilde{u}}{E' R_x} = \frac{(0.04)(6.252)}{(2.198 \times 10^{11})(5.11 \times 10^{-3})} = 2.227 \times 10^{-10},$$

$$G = \alpha E' = (2.3 \times 10^{-8})(2.198 \times 10^{11}) = 5.055 \times 10^{3},$$

$$W = \frac{w_{\max}}{E' R_x^2} = \frac{4{,}944}{(2.198 \times 10^{11})(5.11 \times 10^{-3})^2} = 8.6141 \times 10^{-4}.$$

The minimum film thickness variable is given by

$$g_{H_{\min}} = 3.42 g_V^{0.49} g_E^{0.17} [1 - e^{-0.68\kappa}]. \tag{8.32}$$

Substituting

$$g_V = \left(\frac{G W^3}{U^2} \right) = 6.5149 \times 10^{13}$$

$$g_E = W^{8/3} U^2 = 1.3545 \times 10^{11}$$

into Eq. (8.32), we find

$$g_{H,\min} = 1.5645 \times 10^{9},$$

$$H_{\min} = g_{H,\min} \left(\frac{U^2}{W} \right) = 1.0457 \times 10^{-4},$$

and

$$h_{\min} = R_x H_{\min} = (0.00511)(1.0457 \times 10^{-4})$$
$$= 0.5345\, \mu\text{m}.$$

Hamrock and Dowson, relying on iteration in place of Stribeck's formula for maximum loading, obtain $h_{\min} = 0.557\ \mu$m. Further details of minimum film thickness calculations can be found in Hamrock and Dowson (1981), Harris (1991), and Hamrock (1991).

8.9 Nomenclature

D_{ij}	influence coefficient
D_c	curvature difference
E'	effective elastic modulus
G	shearmodulus
G	material parameter
H	filmthickness parameter
I_h^{2h}	restriction operator
I_{2h}^h	prolongation operator
$I I_H^h$	interpolation operator
J	Jacobian
$K_{i,j,k,l}^{h,h}$	influence coefficient
P_y	normal load
R	effective radius
R_x, R_y	relative principal radii of curvature
S_c	curvature sum

U	velocity parameter
U_0	effective velocity
W	load parameter
a, b	semi-axes of elliptical contact
b	semi-width of rectangular contact
$e_{i,j}$	*error*
g_E	elasticity parameter
g_H	film parameter
g_V	viscosity parameter
h	film thickness
h_0	film thickness at $x = 0$
p	pressure
p_H	maximum Herzian pressure
r_{ix}, r_{iy}	principal radii of curvature
$r_{i,j}$	*residue*
(u, v, w)	*elastic displacement*
w	load
ϕ	stress function
α	pressure-viscosity coefficient
α_r	ratio R_y/R_x
κ	ellipticity parameter
$(\,)_1, (\,)_2$	at inlet, exit
δ	vertical deflection of surface
μ	viscosity
μ_0	viscosity at atmospheric pressure
$(\,)_0$	at cavitation boundary
$(\cdot)^h$	of mesh h

8.10 References

Ai, X. and Cheng, H. S. 1994. A transient EHL analysis for line contacts with a measured surface roughness using multigrid technique. *ASME Journal of Tribology*, **116**, 549–58.

Ai, X. and Cheng, H. S. 1996. The effects of surface texture on EHL point contacts. *ASME Journal of Tribology*, **118**, 59–66.

Anderson, W. J. 1970. Elastohydrodynamic lubrication theory as a design parameter for rolling element bearings. *ASME Paper* 70-DE-19.

Anderson, W. J. 1980. Rolling-element bearings. In *Tribology: Friction, Lubrication and Wear*, A. Z. Szeri, (ed). Hemisphere, New York.

Archard, G. D., Gair, F. C. and Hirst, W. 1961. The elastohydrodynamic lubrication of rollers. *Proc. R. Soc.*, **262A**, 51.

Arnell, R. D., Davies, P. B., Halling, J. and Whomes, T. L. 1991. *Tribology: Principles and Design Applications*. Springer-Verlag, New York.

ASME. 1971. *Life Adjustment Factors for Ball and Roller Bearings*, ASME Press, New York.

Astridge D. G. and Smith, C. F. 1972. Heat generation in high speed cylindrical roller bearings. *Institute of Mechanical Engineers. EHL Symposium*. Leeds, England.

Benjamin, M. K. and Castelli, V. 1971. A theoretical investigation of compliant surface journal bearing. *Trans. ASME,* **93**, 191–201.

Bissett, E. J. and Glander, D. W. 1988. A highly accurate approach that resolves the pressure spike of elastohydrodynamic lubrication. *ASME Journal of Tribology*, **110**, 241–6.

Blok, H. 1950. Fundamental mechanical aspects of thin film lubrication. *Ann. N.Y. Acad. Sci.*, **53**, 779.

Brandt, A. 1984. *Multigrid Techniques: 1984 Guide with Applications to Fluid Mechanics*. GMD-Studien No. 85, Gesellschaft fur Mathematik und Datenverarbeitung MBH, Bonn.

Brandt, A. and Lubrecht, A. A. 1990. Multilevel matrix multiplication and fast solution of integral equations. *J. Comp. Phys.*, **2**, 348–370.

Brewe, D. E. and Hamrock, B. J. 1977. Simplified solution for elliptical contact deformation between two elastic solids. *ASME Journal of Lubrication Technology*, **99**, 485–7.

Briggs, W. L., Henson, V. E. and McCormick, S. F. 2000. *A Multigrid Tutorial*. 2nd edn. Siam, Philadelphia.

Browne, A. L., Whicker, D. and Rohde, S. M. 1975. The significance of thread element flexibility on thin film wet traction. *Tire Sci. Technol.,* **3**, 4.

Carl, T. E. 1964. The experimental investigation of a cylindrical journal bearing under constant and sinusoidal loading. *Proceedings of the 2nd Convention on Lubrication and Wear*, p. 100, Institution of Mechanical Engineers, London.

Chang, L., Conry, T. F. and Cusano, C. 1989. An efficient, robust, multi-level computational algorithm for elastohydrodynamic lubrication. *ASME Journal of Tribology*, **111**, 193–199.

Cheng, H. S. 1965. A refined solution to the thermal-elastohydrodynamic lubrication of rolling and sliding cylinders. *Trans. ASLE,* **8**, 397–410.

Cheng, H. S. and Sternlicht, B. 1965. A numerical solution for the pressure, temperature and film thickness between two infinitely long lubricated rolling and sliding cylinders, under heavy loads. *Trans. ASME*, *Ser. D*, **87**, 695–707.

Crook, A. W. 1958. The lubrication of rollers. *Philos. Trans. Roy. Soc.,* **250A**, 387–409.

Dawson, D. and Wang, D. 1994. An analysis of the normal bouncing of a solid elastic ball on an oily plane. *Wear*, **179**, 29–38

Dowson, D. 1967. Modes of lubrication in human joints. *Proceedings of the Symposium on Lubrication and Wear in Living and Artificial Human Joints*, paper 12, Institution of Mechanical Engineers, London.

Dowson, D. and Higginson, G. R. 1959. A numerical solution to the elastohydrodynamic problem. *J. Mech. Eng. Sci.,* **1**, 6–15.

Dowson, D. and Higginson, G. R. 1960. Effect of material properties on the lubrication of elastic rollers. *J. Mech. Eng. Sci.,* **2**, 188–94.

Dowson, D. and Higginson, G. R. 1977. *Elastohydrodynamic Lubrication*. 2nd edn., Pergamon, Oxford.

Dowson, D. and Wright, eds. 1981. *The Biomechanics of Joints and Joint Replacements*. Mechanical Engineering Publishers, Bury St., Edmunds, Suffolk.

Dowson, D., Higginson, G. R. and Whitaker, A. V. 1962. Elastohydrodynamic lubrication: A survey of isothermal solutions. *J. Mech. Eng.,* **4**, 121–6.

Ehret, P., Dowson, D., Taylor, C. M. and Wang, D. 1997. Analysis of isothermal elastohydrodynamic point contacts lubricated by Newtonian fluids using multigrid methods. *Proc. Instn. Mech. Engrs, Part C*, **211**, 493–508.

Gatcombe, E. K. 1945. Lubrication characteristics of involute spur-gears – a theoretical investigation. *Trans. ASME*, **67**, 177.

Gerald, C. F. 1973. *Applied Numerical Analysis*. Addison-Wesley, Reading, MA.

Gohar, R. 2000. *Elastohydrodynamics*. Imperial College Press.

Greenwood, J. A. and Morales-Espejel, G. E. 1994. The behavior of transverse roghness in EHL contacts. *Proc. Instn. Mech. Engrs., Part J: J. Engineering Tribology*, **208**, 132.

Hamrock, B. J. and Anderson, W., 1973. Analysis of an arched outer-race ball bearing considering centrifugal forces. *ASME J. Lub. Tech.,* **95**, 265–76.

Hamrock, B. J. and Anderson, W., 1983. *Rolling Element Bearings.* NASA RP-1105.

Hamrock, B. J. and Brew, D. E. 1983. Simplified solution for stresses and deformations. *J. Lub. Tech.*, **105**, 171–7.

Hamrock, B. J. and Dowson, D. 1976a. Isothermal elastohydrodynamic lubrication of point contacts, part I – theoretical formulation. *J. Lub. Tech.*, **98**, 223–9.

Hamrock, B. J. and Dowson, D. 1976b. Isothermal elastohydrodynamic lubrication of point contacts, part II – ellipticity parameter results. *J. Lub. Tech.*, **98**, 375–8.

Hamrock, B. J. and Dowson, D. 1981. *Ball Bearing Lubrication*. Wiley & Sons, New York.

Hamrock, B. J. 1991. *Fundamentals of Fluid Film Lubrication*. NASA Ref. Pub. 1244.

Hamrock, B. J. and Dowson, D. 1977a. Isothermal elastohydrodynamic lubrication of point contacts, part III – fully flooded results. *J. Lub. Tech.,* **99**, 264–76.

Hamrock, B. J. and Dowson, D. 1977b. Isothermal elastohydrodynamic lubrication of point contacts, part IV – starvation results. *J. Lub. Tech.,* **99**, 15–23.

Hamrock, B. J. and Dowson, D. 1978. Elastohydrodynamic lubrication of elliptical contacts for materials of low elastic modulus, part I – fully flooded conjunction. *J. Lub. Tech.,* **100**, 236–45.

Hamrock, B. J. and Dowson, D. 1979a. Elastohydrodynamic lubrication of elliptical contacts for materials of low elastic modulus, part II – starved conjunction. *J. Lub, Tech.*, **101**, 92–8.

Hamrock, B. J. and Dowson, D. 1981. *Ball Bearing Lubrication*. John Wiley & Sons, New York.

Harris, T. A. 1991. *Rolling Bearing Analysis*. John Wiley & Sons, New York.

Heathcote, H. L. 1921. The ball bearing in the making under test and service. *Proc. Inst. Automot. Eng*, **15**, 569–702.

Houpert, L. G. and Hamrock, B. J. 1986. Fast approach for calculating film thicknesses and pressures in elastohydrodynamically lubricated contacts at high loads. *ASME Journal of Tribology*, **108**, 411–420.

Hsu, C. H. and Lee, R. T. 1994. Advanced multilevel solution for elastohydrodynamic lubrication circular contact problem. *Wear*, **177**, 117–127.

Jagatia, M. and Jin, Z. M. 2001. Elastohydrodynamic lubrication analysis of metal-on-metal hip prostheses under steady state entraining motion. *Proc. Instn. Mech. Engrs, Part H*, **215**, 531–541.

Jalali-Vahid, D. 2000. *Transient Analysis of EHD Point Contacts*. PhD Thesis, University of Bradford, U.K.

Jalali-Vahid, D., Rahnejat, H. and Jin, Z. 1998. Elastohydrodynamic solution for concentrated elliptical point contact of machine elements under combined entraining and squeeze-film motion. *Proc. Instn. Mech. Engrs, Part J*, **212**, 401–411.

Jalali-Vahid, D., Rahnejat, H., Jin, Z. M. and Dowson, D. 2001. Transient analysis of isothermal elastohydrodynamic circular point contacts. *Proc. Instn. Mech. Engrs, Part C*, **215**, 267–279.

Jin, Z. M. 2000. Elastohydrodynamic lubrication of a circular point contact for a compliant layered surface bonded to a rigid substrate. Part 1: theoretical formulation and numerical method. *Proc. Instn. Mech. Engrs, Part J*, **214**, 267–279.

Johnson, K. L. 1985. *Contact Mechanics*. Cambridge University Press, Cambridge.

Jones, W. R., 1975. Pressure-viscosity measurement for several lubricants. *Trans. ASLE*, **18**, 249–62.

Kim, K. H. and Sadeghi, F. 1992. Three-dimensional temperature distribution in EHD lubrication: part I – circular contact. *ASME Journal of Tribology*, **114**, 32–42.

Kostreva, M. M. 1984. Elasto-hydrodynamic lubrication: a non-linear complementary problem. *Int. J. Numer. Methods Fluids*, **4**, 377–97.

Lee, R. T. and Hsu, C. H. 1993. A fast method for the analysis of thermal-elastohydrodynamic lubrication of rolling/sliding line contact. *Wear*, **1666**. 107–117.

Love, A. E. H. 1944. *A Treatise on the Mathematical Theory of Elasticity*. 4th edn, Dover Publications, New York.

Lubrecht, A. A. 1987. The numerical solution of lubricated line and point contact problem using multigrid techniques. PhD Thesis, University of Twente.

Oh, K. P. and Huebner, K. H. 1973. Solution of the elastohydrodynamic finite journal bearing problem. *Trans. ASME*, **95F**, 342–3.

Oh, K. P. and Rohde, S. M. 1977. A theoretical analysis of a compliant shell air bearing. *Trans. ASME,* **99F**, 75–81.

Okamura, H. 1982. A contribution to the numerical analysis of isothermal elastohydrodynamic lubrication. *Tribology of Reciprocating Engines, Proc. 9th Leeds Lyon Symp. on Tribology*, Butterworths, London, 313–20.

Palmgreen, A. 1959. *Ball and Roller Bearing Engineering*. 3rd edn., SKF Industries Inc.

Reynolds, O. 1876. On rolling friction. *Philos. Trans. Roy. Soc.*, **166**, 155–74.

Roelands, C. J. A. 1966. *Correlation Aspects of the Viscosity-Pressure Relationship of Lubricating Oils*. Ph.D. Thesis, Delft University of Technology, Netherlands.

Rohde, S. M. 1978. Thick film and transient elastohydrodynamic lubrication problems. *General Motors Res. Publ. GMR-2742.*

Rohde, S. M. and McAllister, 1975. A variational formulation for a class of free boundary problems arising in hydrodynamic lubrication. *Int. J. Eng. Sci.*, **13**, 841–850.

Rohde, S. M. and Oh, K. P. 1975. A thermoelastohydrodynamic analysis of finite slider Bearings. *Trans. ASME,* **97F**, 450–60.

Sibley, L. B. and Orcutt, F. K. 1961. Elastohydrodynamic lubrication of rolling contact surfaces. *Trans. ASLE,* **4**, 234–49.

Tallian, T. E. 1992a. Simplified contact fatigue life prediction model, Parts I and II. *ASME Journal of Tribology*, **114**, 207–22.

Tallian, T. E. 1992b. *Failure Atlas for Hertz Contact Machine Elements*. ASME Press, New York.

Tanner, R. I. 1966. An alternative mechanism for the lubrication of sinovial joints. *Phys. Med. Biol.*, **11**, 119.

Timoshenko, S. and Goodier, J. N. 1951. *Theory of Elasticity*. McGraw Hill, New York.

Venner, C. H. 1991. *Multilevel Solution of EHL Line and Point Contact Problems*. PhD Thesis, University of Twente, Enschede, The Netherlands.

Venner, C. H. and Lubrecht, A. A. 1994. Transient analysis of surface features in an EHL line contact in the case of sliding. *ASME Journal of Tribology*, **116**, 186–93.

Venner, C. H. and Lubrecht, A. A. 2000. *Multilevel Methods in Lubrication*. Elsevier, Amsterdam.

Venner, C. H., ten Napel, W. E. and Bosma, R. 1990. Advanced multilevel solution of the EHL line contact problem. *ASME Journal of Tribology*, **112**, 426–32.

Wang, S. H., Al-Sharif, A., Rajagopal, K. R. and Szeri, A. Z. 1992. Lubrication with binary mixtures: liquid-liquid emulsion in an EHL conjunction. *ASME Journal of Tribology,* **115**. 46–55.

Wilcock, D. F. and Booser, E. R. 1957. *Bearing Design And Application*. McGraw-Hill, New York.

Xu, G. and Sadeghi, F. 1996.Thermal EHL analysis of circular contacts with measured surface roughness. *ASME Journal of Tribology*, **118**, 473–83.

Thermal Effects

Classical lubrication theory predicts bearing performance on the assumption that the viscosity of the lubricant is uniform and constant over the whole film. As bearing performance is strongly dependent on lubricant viscosity and viscosity of common lubricants is a strong function of temperature (see Figure 9.1), the results of classical theory can be expected to apply only in cases where the lubricant temperature increase across the bearing pad is negligible.

9.1 Effective Viscosity

In many applications (small bearings and/or light running conditions) the temperature rise across the bearing pad, although not negligible, remains small. It is still possible in these cases to calculate bearing performance on the basis of classical theory, but in the calculations one must employ that specific value of the viscosity, called the *effective viscosity*, that is compatible with the average temperature rise in the bearing. This might be realized, for instance, by making an initial guess of the effective viscosity, followed by an iterative procedure, using Figure 9.1, for systematically refining the initial guess. Boswall (1928) calculated the effective viscosity on the basis of the following assumptions:

(1) All the heat generated in the film by viscous action is carried out by the lubricant.
(2) The lubricant that leaves the bearing by the sides has the uniform temperature $\Theta = \Theta_i + \Delta\Theta/2$, where $\Delta\Theta = \Theta_o - \Theta_i$ is the temperature rise across the bearing.

Let Q and Q_s represent the volumetric flow rate of the lubricant at the pad leading edge and at the two sides, respectively. Then, a simple energy balance based on the assumptions above yields

$$\frac{\rho c \Delta\Theta}{P} = \frac{4\pi c_\mu}{q\left(1 - \frac{1}{2}Q_s/Q\right)}. \tag{9.1}$$

Here

$$c_\mu = \frac{R}{C}\frac{F_\mu}{W}$$

is the friction variable and $q = Q/RCNL$ is the dimensionless inflow. For short bearings with Gümbel's boundary condition, Eqs. (3.47) and (3.49) give, on substitution,

$$\left(\frac{L}{D}\right)^2 \frac{\rho c \Delta\Theta}{P} = \frac{8\pi(1-\varepsilon^2)^{3/2}}{\varepsilon^2[\pi^2(1-\varepsilon^2) + 16\varepsilon^2]^{1/2}}. \tag{9.2}$$

For other bearing geometries, Eq. (9.1) has been tabulated by Raimondi and Boyd (1958).

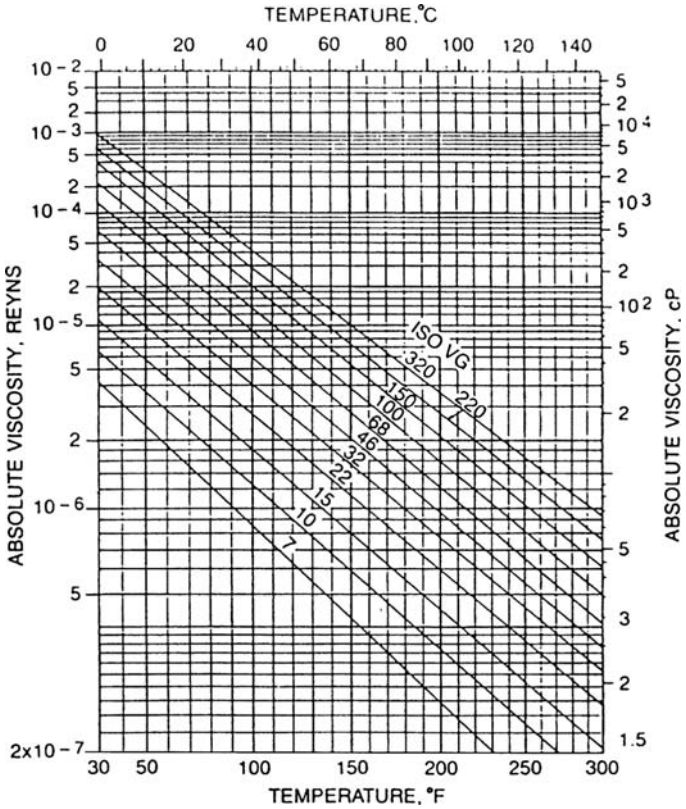

Figure 9.1. Viscosity-temperature curves for typical petroleum oils in ISO viscosity grades. (Reprinted with permission from Booser E. R., *CRC Handbook of Lubrication*. Copyright CRC Press, Boca Raton, Florida. © 1984.)

To indicate the iterative procedure for calculating the effective temperature, T_e, and hence the effective viscosity, $\mu_e(T_e)$, we rewrite Eq. (9.1). Since the right-hand side is a function of the temperature, we put

$$\Delta\Theta = \frac{4\pi c_\mu P}{q\left(1 - \frac{1}{2}Q_s/Q\right)\rho c} \equiv g\left(\Theta\right).$$

The iterative procedure is then carried out according to the scheme

$$\Theta_e^{(n)} = \Theta_i + K g\left[\Theta_e^{(n-1)}\right], \qquad n = 1, 2, 3, \ldots \tag{9.3}$$

Raimondi and Boyd (1958) suggested that $K = 1/2$, and Cameron (1966) recommended $2/3 < K < 1$. It is questionable, however, whether a universal value of K exists even in small bearings (Seireg and Ezzat, 1972).

The effective viscosity method has been used, for example, on a self-contained bearing in which a disk lubricator supplies lubricant to the bearing (Kaufman, Szeri, and Raimondi, 1978). The bearing is designed to operate with or without external cooling (forced air or water), and carry both radial and axial loads (Figure 9.2).

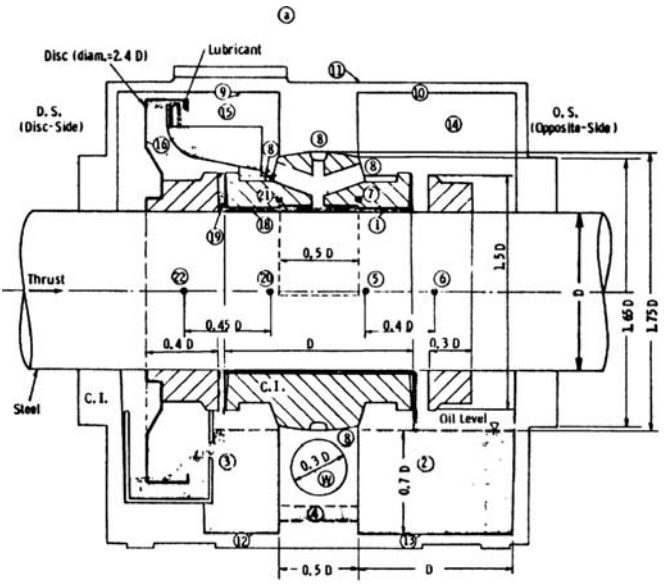

Nodal Point	Location
1	Jnl Brg Oil Film (O. S.)
2	Oil Reservoir (O. S.)
3	Oil Reservoir (D. S.)
4	Communicating Channel Between Reservoirs
5	Shaft Surface (O. S.)
6	Inactive Thrust Brg
7	Bearing Inner (Bore) Surface (O. S.)
8	Outer Bearing Surface
9	Housing, Inner Surface (D. S.) } Top Half
10	Housing, Inner Surface (O. S.) } Top Half
11	Housing, Outer Surface
12	Housing, Inner Surface (D. S.) Bott. half

Nodal Point	Location
13	Housing, Inner Surface (O. S.) Bott. Half
14	Air Space Inside Housing (O. S.)
15	Air Space Inside Housing (D. S.)
16	Oil Pan, Disc
17	Roller Bearing (O. S.) (not shown)
18	Jnl Brg. Oil Film (D. S.)
19	Thrust Brg. Oil Film
20	Shaft Surface (D. S.)
21	Jnl Brg. Inner Surface (D. S.)
22	Active Thrust Brg.
23	Roller Bearing (D. S.) (not shown)
w	Cooling Fluid in Duct
a	Ambient

Location of nodal points for thermal analysis, & principal dimensions as related to journal diameter, D

Figure 9.2. Bearing geometry and location of nodal points. (Reprinted with permission from Kaufman, H. N., Szeri, A. Z. and Raimondi, A. A. Performance of a centrifugal disk-lubricated bearing. *ASLE Trans.*, **21**, 314–322, 1978.)

The bearings, shaft, housing, and lubricant constitute a complex thermal system both in geometry and in boundary conditions. Moreover, the heat transfer characteristics of this system are temperature dependent. In the analysis of Kaufman et al. (1978), the various components of the bearing-lubricant system are represented by nodal points. Once the nodal network is selected, heat conservation equations in finite difference form can be written. The heat transfer coefficients, which become coefficients in the finite-difference equations, are calculated from actual component characteristics. When their dependence on temperature is deemed essential to consider, they are based on temperatures of the previous iteration.

Thus, the bearing-housing-lubricant system, from a heat transfer point of view, is represented by a set of finite-difference conservation equations. These equations are statements of the requirement that the net rate of energy inflow into any nodal point be equal to the rate of energy dissipation at that node. Thus, at the ith nodal point, $i = 1, 2, 3, \ldots, N$,

$$\sum_{j=1}^{N} q_{ji} = -H_i \qquad i \neq j. \tag{9.4}$$

In lumped parameter analyses, such as this, the heat flow rate q_{ji} is given approximately by

$$q_{ji} = A\,(i,\, j)\,(\Theta_j - \Theta_i). \tag{9.5}$$

Here $A(i, j)$ represents the heat transfer coefficient between the ith and the jth node.

Substituting Eq. (9.5) into Eq. (9.4), we obtain

$$\sum_j A\,(i,\, j)(\Theta_j - \Theta_i) = -H_i. \tag{9.6}$$

Since in Eq. (9.6) the index i takes values 1, 2, 3, . . . , N, Eq. (9.6) is equivalent to a system of simultaneous algebraic equations, which can be written in the matrix form

$$A\Theta = H. \tag{9.7}$$

In Eq. (9.7), the symbol $\boldsymbol{A}$ represents the $N \times N$ matrix,

$$A = \begin{bmatrix} -\sum_{k=1}^{N} A\,(1, k) & A\,(1, 2) & \cdots & A\,(1, N) \\ A\,(2, 1) & -\sum_{k=1}^{N} A\,(2, k) & \cdots & A\,(2, N) \\ \vdots & & & \\ A\,(N, 1) & A\,(N, 2) & \cdots & -\sum_{k=1}^{N} A\,(N, k) \end{bmatrix}, \tag{9.8}$$

while Θ and H represent column vectors,

$$\begin{aligned} \Theta &= (\Theta_1, \Theta_2, \Theta_3, \ldots, \Theta_N)^T\,, \\ H &= (H_1, H_2, H_3, \ldots, H_N)^T\,. \end{aligned} \tag{9.9}$$

When all heat transfer coefficients, as well as the viscosity, are kept frozen during a particular iteration, Eq. (9.7) is reduced to a set of linear algebraic equations.

The iterative analysis closely models the transient state of bringing the bearing-housing-lubricant system into thermal equilibrium. It starts with the calculation of heat production in the cold bearing for an assumed mechanical input (bearing losses). The temperature distribution is then obtained from a steady-state heat balance. But, owing to the high viscosity of the oil, the production rates of heat are high, leading necessarily to temperatures that are above the equilibrium temperatures compatible with the given mechanical input. New and improved heat production rates are now calculated, using average oil film temperatures that are based on the just-obtained oil film temperatures and the ones obtained previously. The iteration procedure is continued until sufficient agreement between successively calculated temperatures is reached. This process will converge and give solutions for wide ranges of input parameters.

Figure 9.3 compares theoretical prediction with experimental data on journal bearing temperature, for a range of geometrically similar bearings. Figure 9.4 compares theoretical predictions and experimental data for thrust face temperature under two different unit loads, for a range of bearing size.

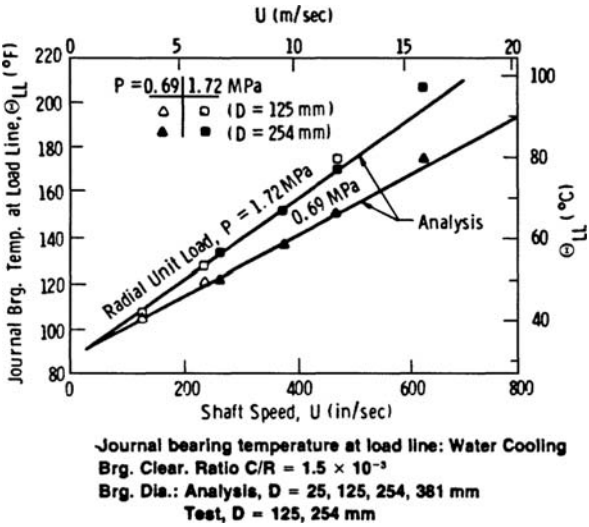

Figure 9.3. Journal bearing temperature at load line. Water cooling, $C/R = 1.5 \times 10^{-3}$, analysis: $D = 25, 125, 254, 381$ mm, test: $D = 125, 254$ mm. (Reprinted with permission from Kaufman, H. N., Szeri, A. Z. and Raimondi, A. A. Performance of a centrifugal disk-lubricated bearing. *ASLE Trans.*, **21**, 314–322, 1978.)

The effective viscosity model can, however, lead to significant errors in predicting bearing performance. It was shown by Seireg and Ezzat (1972) that although the normalized $p/p_{\max}$ plots (Figure 9.5) obtained under the different test conditions collapsed into a single curve, the magnitude of the pressures differed significantly depending on inlet temperature, even at constant speed.

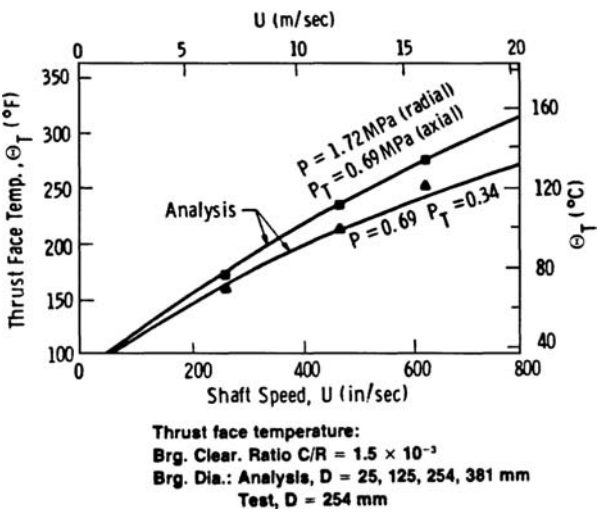

Figure 9.4. Thrust face temperature. $C/R = 1.5 \times 10^{-3}$, analysis: $D = 25, 125, 254, 381$ mm, test: $D = 254$ mm. (Reprinted with permission from Kaufman, H. N., Szeri, A. Z. and Raimondi, A. A. Performance of a centrifugal disk-lubricated bearing. *ASLE Trans.*, **21**, 314–322, 1978.)

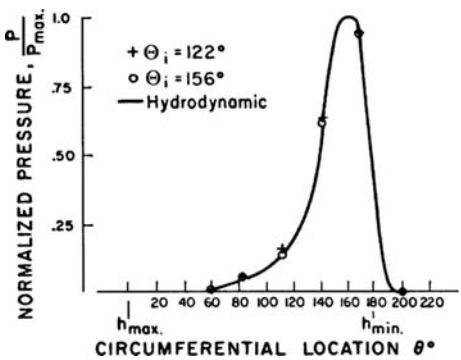

Figure 9.5. Normalized circumferential pressure distribution. (Reprinted with permission from Seireg, A. and Ezzat H. Thermohydrodynamic phenomena in fluid film lubrication. *ASME* Paper No. **72-Lub-25**, 1972.)

Furthermore, the experiments showed that for any particular geometry and oil inlet temperature, there was only one speed at which the effective viscosity model and the experiment gave identical pressure distributions (Figure 9.6). Seireg and Ezzat offer the following conclusion: "The concept of an effective viscosity, although attractive, is infeasible since that value of the viscosity is a function of the bearing geometry, bush and shaft materials, lubricant physical properties, bearing load and speed, and the thermal boundaries."

In large bearings and/or under severe running conditions thermal effects may be significant, to the extent that prediction of bearing performance is no longer possible when based on the assumption of a uniform effective viscosity. Furthermore, in large bearings the usual limit condition in design is the maximum permissible bearing temperature. Early experiments by Gardner and Ulschmid (1974), Gregory (1974), Capitao (1976), and Capitao et al. (1976) are concerned with measuring maximum bearing temperatures.

A simple dimensional analysis will show that the nondimensional maximum bearing temperature, Θ_{max}/Θ_*, where Θ_* is a characteristic temperature and Θ_{max} is the maximum bearing temperature, is dependent on a number of nondimensional groups, such as the Reynolds number, Re, the Prandtl number, Pr, the dissipation number, Λ, the eccentricity

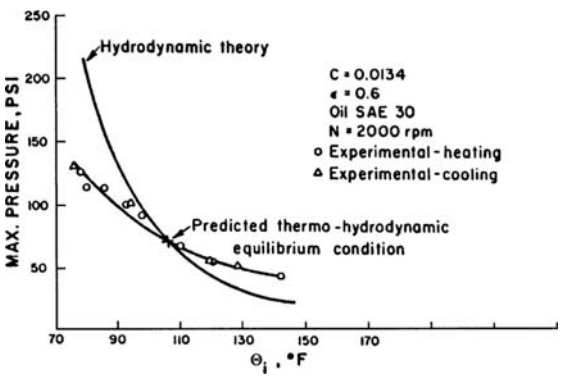

Figure 9.6. Variation of maximum pressure with inlet temperature. (Reprinted with permission from Seireg, A. and Ezzat H. Thermohydrodynamic phenomena in fluid film lubrication. *ASME* Paper No. **72-Lub-25**, 1972.)

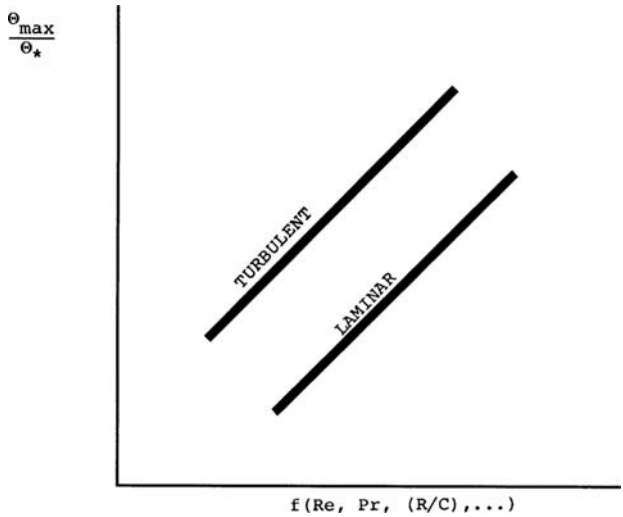

Figure 9.7. Schematics of bearing thermal performance the different flow regimes.

ratio (C/R), and so forth. Analyzing a large set of field data on journal bearings of size $D = 1$ inch to $D = 32$ inches, it was found that the data can be arranged to fall on two parallel lines, as indicated schematically in Figure 9.7.

The lower line in Figure 9.7 is valid for laminar flow of the lubricant, while the upper line is characterized by turbulent flow. It is clearly demonstrated here that not only must we take into account the variation of lubricant viscosity with temperature, we must also specify the flow regime, to correctly predict bearing performance. In the next section, we shall discuss the variable viscosity theory, known as thermohydrodynamic theory, of fluid film lubrication. For additional details the reader is urged to consult Pinkus (1990).

9.2 Thermohydrodynamic Theory

Thermohydrodynamic (THD) theory calculates pointwise variations of temperature and viscosity in the lubricant film, then takes these into account when predicting bearing performance. Though there are numerous instances of large temperature rise across bearings operating in the laminar flow regime, THD theory becomes even more important in turbulent lubrication. For this reason, we will derive THD theory for turbulent lubrication; the resulting equations can be made to apply to laminar flow by elementary substitutions, or by specifying $\mathrm{Re}^* = 0$ in computation.

The Energy Equation

The energy equation is the mathematical statement of the *Principle of Conservation of Energy: the time rate of energy increase in a body equals the time rate of energy supplied to it.*

$$\frac{d}{dt}(\mathcal{K} + \mathcal{E}) = \mathcal{W} + \mathcal{Q}. \tag{9.10}$$

Here

$$\mathcal{K} = \frac{1}{2}\int_{\mathcal{V}} \rho \boldsymbol{v}\cdot\boldsymbol{v}\, d\mathcal{v}, \qquad \mathcal{E} = \int_{\mathcal{V}} \rho e\, d\mathcal{v}. \tag{9.11}$$

The mechanical energy consists of work done by the surface and the body forces

$$\begin{aligned}\mathcal{W} &= \int_{\mathcal{S}} \tau\cdot\boldsymbol{v}\, d\mathcal{s} + \int_{\mathcal{V}} \rho \boldsymbol{f}\cdot\boldsymbol{v}\, d\mathcal{v} \\ &= \int_{\mathcal{S}} T_{lk} v_k n_1 d\mathcal{s} + \int_{\mathcal{V}} \rho f_k v_k d\mathcal{v},\end{aligned} \tag{9.12}$$

where we made use of Eq. (2.15).

For total energy input, we write

$$\mathcal{Q} = \int_{\mathcal{S}} \boldsymbol{q}\cdot\boldsymbol{n}\, d\mathcal{s} + \int_{\mathcal{V}} \rho r\, d\mathcal{v}, \tag{9.13}$$

where $\boldsymbol{q}$ is the heat flux across the closed surface $S(t)$ of $\mathcal{V}(t)$ directed outward and r is the distributed heat source per unit mass of the body.

Upon substituting Eqs. (9.11), (9.12), and (9.13) into Eq. (9.10), we find

$$\frac{d}{dt}\int_{\mathcal{V}} \rho\left(\frac{1}{2}v_k v_k + e\right) d\mathcal{v} = \int_{\mathcal{V}} \rho f_k v_k d\mathcal{v} + \int_{\mathcal{S}} T_{lk} v_k n_l d\mathcal{s} + \int_{\mathcal{S}} q_l n_l d\mathcal{s} + \int_{\mathcal{V}} pr\, d\mathcal{v}. \tag{9.14}$$

To simplify matters, we assume that there are no internally distributed heat sources, $r = 0$. We also rewrite the left-hand side as follows:[1]

$$\frac{d}{dt}\int_{\mathcal{V}} \left(\frac{1}{2}v_k v_k + e\right)\rho\, d\mathcal{v} = \int_{\mathcal{V}} \left(v_k \frac{dv_k}{dt} + \frac{de}{dt}\right)\rho\, d\mathcal{v}, \tag{9.15}$$

where dv_k/dt is the kth component of the acceleration vector, Eq. (2.5).

Equation (9.14) contains both surface and volume integrals. We change the surface integrals by the divergence theorem and obtain

$$\begin{aligned}\int_{\mathcal{S}} (T_{lk} v_k + q_l) n_l dS &= \int_{\mathcal{V}} [(T_{lk} v_k)_{,l} + q_{l,l}]\, d\mathcal{v} \\ &= \int_{\mathcal{V}} [T_{lk,l} v_k + T_{lk} v_{k,l} + q_{l,l}]\, d\mathcal{v}.\end{aligned} \tag{9.16}$$

Substituting Eqs. (9.15) and (9.16) into Eq. (9.14), we find

$$\int_{\mathcal{V}} \left[\rho\frac{de}{dt} - T_{lk} v_{k,l} - q_{l,l} - v_k(T_{lk,l} + \rho f_k - \rho a_k)\right] d\mathcal{v} = 0. \tag{9.17}$$

[1]Equation (9.15) follows from the Reynolds transport theorem $(d/dt)\int_{\mathcal{V}(t)} F dV = \int_{\mathcal{V}(t)}[(dF/dt) + F \operatorname{div} \boldsymbol{v}] d\mathcal{v}$, where d/dt is the material derivative and $\mathcal{V}(t)$ is a material volume, and the equation of continuity (2.16c).

The bracketed term multiplying vk vanishes due to local conservation of linear momentum, Eq. (2.27), and as $V(t)$ is arbitrary the integrand itself must vanish,

$$\rho \frac{de}{dt} = T_{lk} v_{k,l} + q_{l,l}. \tag{9.18}$$

Equation (9.18) is our (local) statement of the *conservation of energy*.

The *stress power*, $T_{lk}\, v_{k,l}$, can further be simplified, using the Cartesian decomposition (2.33),

$$v_{l,k} = D_{kl} + \Omega_{kl}, \tag{9.19}$$

where $\boldsymbol{D} = (D_{kl})$ is the stretching tensor and $\boldsymbol{\Omega} = (\Omega_{kl})$ is the spin tensor.

It can be shown that the product of a symmetric tensor (stress) and a skew-symmetric tensor (spin) vanishes,[2] so on substituting Eq. (9.19) into Eq. (9.18), only $T_{lk}\, D_{kl}$ survives. The stress, on the other hand, for a Newtonian fluid is given by

$$T_{lk} = -p\delta_{lk} + 2\mu D_{lk}. \tag{2.53}$$

Substituting Eqs. (9.19) and (2.53) into the energy equation Eq. (9.18), we obtain

$$\rho \frac{de}{dt} = -p v_{k,k} + 2\mu D_{lk} D_{kl} - q_{l,l}, \tag{9.20a}$$

or, in vector notation,

$$\rho \frac{de}{dt} = -p \operatorname{div} \boldsymbol{v} + 2\mu \boldsymbol{D} : \boldsymbol{D} - \operatorname{div} \boldsymbol{q}. \tag{9.20b}$$

Assuming further that Fourier's law of heat conduction

$$\boldsymbol{q} = -k \operatorname{grad} \Theta$$

holds, where Θ is the temperature and k is the thermal conductivity, we obtain

$$\rho \frac{d\,(c_v \Theta)}{dt} = -p \operatorname{div} \boldsymbol{v} + \mu \Phi + \operatorname{div}(k \operatorname{grad} \Theta). \tag{9.21}$$

Here we put $e = c_v \Theta$ for internal energy density and use the symbol Φ for the *dissipation function*:

$$e = c_v \Theta, \qquad \Phi = 2 D_{ij} D_{ji}. \tag{9.22}$$

To further simplify matters, we assume that the lubricant has constant thermal properties, c_v, $k = \text{const}$. For incompressible fluids, the dilatation work $-\,p \operatorname{div} \boldsymbol{v} = 0$ by Eq. (2.16c), $c_v = c_p = c$, and Eq. (9.21) becomes[3]

$$\rho c \left(\frac{\partial \Theta}{\partial t} + u \frac{\partial \Theta}{\partial x} + v \frac{\partial \Theta}{\partial y} + w \frac{\partial \Theta}{\partial z} \right) = k \left(\frac{\partial^2 \Theta}{\partial x^2} + \frac{\partial^2 \Theta}{\partial y^2} + \frac{\partial^2 \Theta}{\partial z^2} \right) + \mu \Phi. \tag{9.23a}$$

[2] $T_{lk}\Omega_{kl} = T_{lk}(-\Omega_{lk}) = -T_{lk}\Omega_{lk} = -T_{kl}\Omega_{lk} = -T_{lk}\Omega_{kl}$, as $\Omega_{kl} = -\Omega_{lk}$, and $T_{kl} = T_{lk}$.

[3] With the aid of the equation of state, $p = \rho \mathcal{R} \Theta$, it can be shown that $\rho(d/dt)(c_v\Theta) + \boldsymbol{p} \operatorname{div} \boldsymbol{v} = \rho(d/dt)(c_p\Theta) - dp/dt$, so for perfect gas (9.21) takes the form $\rho(d/dt)(c_p\Theta) = dp/dt + 2\mu \boldsymbol{D}: \boldsymbol{D} - \operatorname{div} \boldsymbol{q}$. This equatin should not be used for an incompressible fluid.

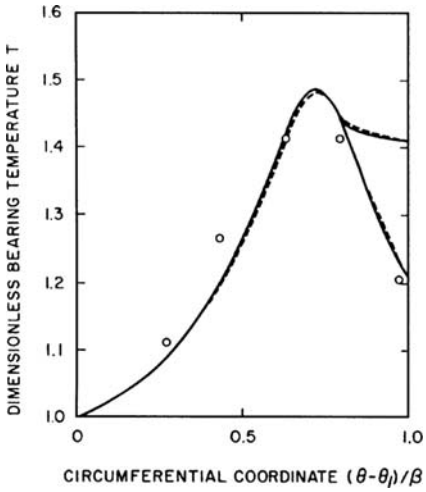

Figure 9.8. Comparison of (○) measured and (—) predicted temperature distributions along the center line of a $D = 10$ cm journal bearing at $N = 900$ revolutions/min. (Reprinted with permission from Suganami, T. and Szeri, A. Z. A thermohydrodynamic analysis of journal bearings. *ASME Journal of Lubrication Technology*, **101**, 21–27, 1979.)

For an incompressible fluid the dissipation function is

$$\phi = 2\left[\left(\frac{\partial u}{\partial x}\right)^2 + \left(\frac{\partial v}{\partial y}\right)^2 + \left(\frac{\partial w}{\partial z}\right)^2\right] + \left(\frac{\partial u}{\partial y} + \frac{\partial v}{\partial x}\right)^2 + \left(\frac{\partial v}{\partial z} + \frac{\partial w}{\partial y}\right)^2 + \left(\frac{\partial w}{\partial x} + \frac{\partial u}{\partial z}\right)^2. \tag{9.23b}$$

One of the early applications of Eq. (9.23) to hydrodynamic lubrication was made by Cope (Cope, 1949; Charnes, Osterle, and Saibel, 1952). His work subsequently acquired classical status in lubrication and strongly influenced later research. Cope's model is based on the assumptions of (1) negligible temperature variation across the film and, therefore, (2) negligible heat conduction into the neighboring solids.

All the generated heat is carried out by the lubricant under Cope's assumption (*adiabatic theory*). Furthermore, by neglecting the (second-order) convection terms, the order of the differential equation (9.23a) is lowered. Solutions of the resulting first-order equation cannot satisfy all the boundary conditions of the problem.[4]

The maximum film temperature is always located at the trailing edge in Cope's adiabatic model, whereas measurements locate its position upstream of the trailing edge and just downstream from the position of maximum pressure (Figure 9.8). For a while it was generally accepted that the classical isothermal theory and Cope's adiabatic theory would bracket actual bearing operations. This idea was later discarded (Seireg and Ezzat, 1972; McCallion, Yousif, and Lloyd, 1970).

Dowson and Hudson (1963) were among the first to realize the importance of heat conduction across the film, and their work provided the foundations of *thermohydrodynamic*

[4]We may draw a parallel between Cope's approximation and the procedure that neglects the viscous terms in the Navier-Stokes equation. The latter yields the equations of motion for an ideal fluid, solutions of which cannot satisfy the no-slip boundary condition.

theory. Notable subsequent papers were those by Dowson and March (1967), McCallion et al., (1970), and Ezzat and Rohde (1972). A common assumption of the work reported in these papers is that heat conduction in the direction of relative motion is unimportant compared to heat convection in the same direction. This permits elimination of the term $\partial^2\Theta/\partial x^2$ in Eq. (9.23). But in the process of deleting this term, the equation loses some of its generality, as it changes from elliptic to parabolic. The parabolic energy equation is valid only when no *reverse flow* is encountered.

Reverse flow is encountered in journal bearings (see Figure 6.4) near the stationary surface at inlet and usually occurs at high eccentricity ratios – a condition that is also typical of high bearing temperatures. It is advisable, therefore, to retain the conduction term $\partial^2\Theta/\partial x^2$ in Eq. (9.23), or to make other arrangements to accommodate reverse flow (Suganami and Szeri, 1979; Boncompain, Fillon, and Frêne, 1986).

Before continuing with further discussion of Eq. (9.23), we will cast it in a form that is appropriate for turbulent flow of the lubricant. For this purpose, in analogy with Eq. (7.1), we write the temperature and the stretching tensor as the sum of the mean and the fluctuation[5]

$$\Theta = \bar{\Theta} + \theta', \quad D_{ij} = \bar{D}_{ij} + d'_{ij}. \tag{9.24}$$

From Eqs. (9.22a) and (7.4) the mean value of the dissipation is

$$\mu\bar{\Phi} = 2\mu D_{ij}D_{ij} = 2\mu\bar{D}_{ij}\bar{D}_{ij} + 2\mu\overline{d'_{ij}d'_{ij}}. \tag{9.25a}$$

For stationary turbulence the last term in Eq. (9.25a) can be obtained from Eq. (7.37)

$$\begin{aligned} 2\mu\overline{d'_{ij}d'_{ij}} &= \mu\overline{\left(\frac{\partial v'_i}{\partial x_j} + \frac{\partial v'_j}{\partial x_i}\right)\frac{\partial v'_i}{\partial x_j}} \\ &= \frac{\partial}{\partial x_i}\overline{v_i\left(p + \rho\frac{q^2}{2}\right)} - \rho\overline{v'_i v'_j}\frac{\partial \bar{V}_j}{\partial x_i} + \mu\frac{\partial}{\partial x_i}\overline{v'_i\left(\frac{\partial v'_i}{\partial x_j} + \frac{\partial v'_j}{\partial x_i}\right)}. \end{aligned} \tag{9.25b}$$

Employing the Boussinesq model, Eq. (7.19), for the second term on the right, applying the thin film approximation to simplify the first and third term, and integrating across the film thickness (cf., Vohr in Safar and Szeri, 1974) we find

$$\int_0^h \overline{\mu d'_{ij}d'_{ij}}dy \approx \int_0^h \rho\varepsilon_m\bar{D}_{ij}\bar{D}_{ij}dy. \tag{9.25c}$$

This is our justification for writing the mean dissipation as

$$\mu\bar{\Phi} \approx 2\bar{\mu}\left(1 + \frac{\varepsilon_m}{\nu}\right)\bar{D}_{ji}\bar{D}_{ij}. \tag{9.26}$$

Substituting Eq. (9.24) into Eq. (9.23), averaging the resulting equation, and taking into account Eq. (9.26), we obtain

$$\rho c\left[\bar{U}_j\frac{\partial\bar{\Theta}}{\partial x_j} + \overline{v'_j\frac{\partial\theta'}{\partial x_j}}\right] = k\frac{\partial^2\bar{\Theta}}{\partial x_j\partial x_j} + 2\bar{\mu}\left(1 + \frac{\varepsilon_m}{\nu}\right)\bar{D}_{ji}\bar{D}_{ij}. \tag{9.27}$$

Making use of the equation of continuity (7.7b), we can show that

$$\overline{v'_j\frac{\partial\theta'}{\partial x_j}} = \frac{\partial}{\partial x_j}\overline{\left(v'_j\theta'\right)}$$

[5]Note that in Chapter 7 and Chapter 9 the overscore bar signifies statistical average.

and write Eq. (9.27) as

$$\rho c \bar{U}_j \frac{\partial \bar{\Theta}}{\partial x_j} = \frac{\partial}{\partial x_j}\left[k\frac{\partial \bar{\Theta}}{\partial x_j} - \rho c\overline{v_j'\theta'}\right] + 2\bar{\mu}\left(1+\frac{\varepsilon_m}{\nu}\right)\bar{D}_{ji}\bar{D}_{ij}. \tag{9.28}$$

To make use of the particular geometry of the lubricant film, we shall nondimensionalize Eq. (9.28), using Eqs. (7.12) and (9.29), and

$$T = \frac{\bar{\Theta}}{\Theta_*}, \qquad t = \frac{\theta'}{\theta_*}, \qquad \mu = \frac{\bar{\mu}}{\mu_*}, \tag{9.29}$$

where Θ_* and θ_* are the temperature scales for mean and fluctuation, respectively, $\bar{\mu} = \mu(\bar{\Theta})$ and $\mu_* = \mu(\Theta_*)$.

Substituting Eqs. (7.12) and (9.29) into Eq. (9.28), then neglecting terms multiplied by (L_y/L_{xz}), where L_y and L_{xz} are characteristic film dimensions, we find

$$\begin{aligned} U\frac{\partial T}{\partial \xi} + V\frac{\partial T}{\partial \eta} + W\frac{\partial T}{\partial \zeta} \\ = \frac{1}{\mathrm{Pe}}\frac{\partial^2 T}{\partial \eta^2} - \left(\frac{L_{xz}}{L_y}\right)\left(\frac{u_*}{U_*}\right)\left(\frac{\theta_*}{\Theta_*}\right)\left[\frac{\partial \overline{vt}}{\partial \eta} + \left(\frac{L_y}{L_{xz}}\right)\left(\frac{\partial \overline{ut}}{\partial \xi} + \frac{\partial \overline{wt}}{\partial \zeta}\right)\right] \\ + \Lambda\mu\left(1+\frac{\varepsilon_m}{\nu}\right)\left[\left(\frac{\partial U}{\partial \eta}\right)^2 + \left(\frac{\partial W}{\partial \eta}\right)^2\right]. \end{aligned} \tag{9.30}$$

Assuming that $(u_*/U_*) = O(L_y/L_{xz})^{1/2}$ and $\theta_*/\Theta_* = O(L_y/L_{xz})^{1/2}$, conditions that seem to hold in wall turbulence,[6] and letting $L_y/L_{xz} \to 0$, Eq. (9.30) takes the form

$$\begin{aligned} U\frac{\partial T}{\partial \xi} + V\frac{\partial T}{\partial \eta} + W\frac{\partial T}{\partial \zeta} = \frac{\partial}{\partial \eta}\left[\frac{1}{\mathrm{Pe}}\frac{\partial T}{\partial \eta} - \overline{vt}\right] \\ + \Lambda\mu\left(1+\frac{\varepsilon_m}{\nu}\right)\left[\left(\frac{\partial U}{\partial \eta}\right)^2 + \left(\frac{\partial W}{\partial \eta}\right)^2\right]. \end{aligned} \tag{9.31}$$

The *Peclet number* and the *dissipation number* have the definition

$$\mathrm{Pe} = \mathrm{Pr} \times \mathrm{Re}\left(\frac{C}{R}\right), \qquad \Lambda = \frac{\mu_*\omega}{\rho c \Theta_*}\left(\frac{L_{xz}}{L_y}\right)^2, \tag{9.32}$$

where $\mathrm{Pr} = c\mu_*/k$ is the *Prandtl number*.

Although it is well recognized that turbulent transport of a scalar quantity is brought about by both gradient-type diffusion caused by small-scale turbulence and by large scale motion of eddies (Hinze, 1975), it has long been accepted in heat transfer to use the approximation (Kestin and Richardson, 1963)

$$-\rho\overline{v'\theta'} = \rho\varepsilon_H\frac{\partial \bar{\Theta}}{\partial y}, \tag{9.33a}$$

where ε_H is the *eddy viscosity for the transport of heat*. In nondimensional form, Eq. (9.33a) is

$$\overline{vt} = \frac{1}{R_\varepsilon}\frac{1}{\mathrm{Pr}^{(t)}}\frac{\varepsilon_m}{\nu}\frac{\partial T}{\partial \eta}. \tag{9.33b}$$

[6] See the discussion following Eq. (7.13).

Here $R_\varepsilon = \mathrm{Re}(C/L)$ is the reduced Reynolds number, and we put $\mathrm{Pr}^{(t)} = \varepsilon_m/\varepsilon_H$, where $\mathrm{Pr}^{(t)}$ is the turbulent Prandtl number.

Substituting Eq. (9.33) into Eq. (9.31), we obtain the final form of the (nondimensional) energy equation applicable to turbulent lubricant films

$$U\frac{\partial T}{\partial \xi} + V\frac{\partial T}{\partial \eta} + W\frac{\partial T}{\partial \zeta} = \frac{1}{\mathrm{Pe}}\frac{\partial}{\partial \eta}\left[\left(1 + \frac{\mathrm{Pr}}{\mathrm{Pr}^{(t)}}\mu\frac{\varepsilon_m}{\nu}\right)\frac{\partial T}{\partial \eta}\right] + \Lambda\mu\left(1 + \frac{\varepsilon_m}{\nu}\right)\left[\left(\frac{\partial U}{\partial \eta}\right)^2 + \left(\frac{\partial W}{\partial \eta}\right)^2\right]. \tag{9.34a}$$

Implicit in Eq. (9.34) are the assumptions

$$(u_*/U_*) = O\left(L_y/L_{xz}\right)^{1/2}, \qquad \theta_x/\Theta_* = O\left(L_y/L_{xz}\right)^{1/2}. \tag{9.34b}$$

In journal bearings, the axial variation of temperature can often be neglected (Dowson and March, 1967), and we employ

$$\left[\left(\frac{\partial U}{\partial \eta}\right)^2 + \left(\frac{\partial W}{\partial \eta}\right)^2\right] \approx \left(\frac{\partial U}{\partial \eta}\right)^2_{\zeta=0}$$

to obtain the approximate equation[7]

$$U\frac{\partial T}{\partial \xi} + V\frac{\partial T}{\partial \eta} = \frac{1}{\mathrm{Pe}}\frac{\partial}{\partial \eta}\left[\left(1 + \frac{\mathrm{Pr}}{\mathrm{Pr}^{(t)}}\mu\frac{\varepsilon_m}{\nu}\right)\frac{\partial T}{\partial \eta}\right] + \Lambda\mu\left(1 + \frac{\varepsilon_m}{\nu}\right)\left(\frac{\partial U}{\partial \eta}\right)^2. \tag{9.35}$$

Although the correct scaling of turbulence appears to be as in Eq. (9.34), leading to Eq. (7.16) for linear momentum and to Eq. (9.35) for energy, the momentum equations are further simplified by most authors by neglecting fluid inertia; this simplification yields Eqs. (7.15) and (9.35) for the characterization of the turbulent flow of incompressible lubricants.

When evaluating ε_m/ν, say from Reichardt's formula, Eq. (7.34), we find the eddy viscosity to be a continuous, monotonic function of the local Reynolds number, $\mathrm{Re}_h = Uh/\nu$; that is, the transition from laminar to fully turbulent flow is smooth and gradual. But, this does not correspond to observation of the physical process of transition. If Re_L and Re_U represent the lower and upper critical Reynolds number of transition, respectively, then we would expect ε_m/ν to vanish whenever $\mathrm{Re}_h < \mathrm{Re}_L$ and to have its full value, as calculated from Reichardt's formula, only when $\mathrm{Re}_h > \mathrm{Re}_U$. [The fact that this obviously incorrect (i.e., in the range $\mathrm{Re} < \mathrm{Re}_U$) eddy viscosity is multiplied in Eq. (9.35) by the laminar Prandtl number only makes things worse, as for typical processes $100 < P_R < 500$.] To compensate for this deficiency of Eq. (9.34), Suganami and Szeri (1979), introduced a scaling factor for the eddy viscosity,

$$\vartheta \begin{cases} 0 & \text{if } \mathrm{Re}_h < 400 \\ 1 - \left(\dfrac{900 - \mathrm{Re}_h}{500}\right)^{1/8} & \text{if } 400 < \mathrm{Re}_h < 900 \\ 1 & \text{if } \mathrm{Re}_h > 900 \end{cases} \tag{9.36a}$$

and replaced ε_m/ν in Eq. (9.34) by $\vartheta\varepsilon_m/\nu$.

[7]Note that $\partial/\partial\xi = \partial/\partial\bar{x} + [\bar{y}\varepsilon \sin \bar{x}/(1 + \varepsilon \cos \bar{x})](\partial/\partial\bar{y})$, where $(\bar{x}, \bar{y}) = (\xi, \eta/H)$.

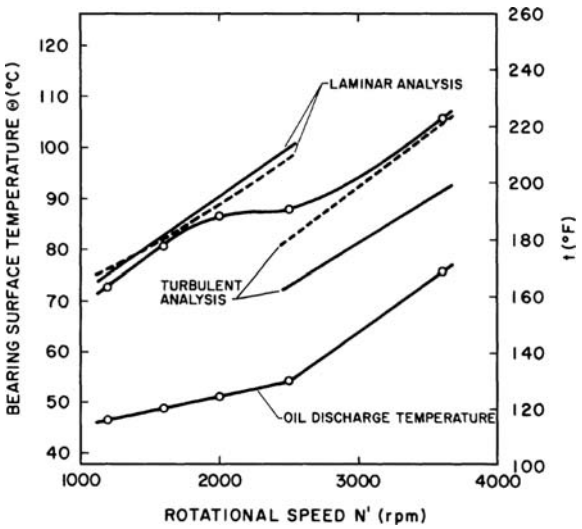

Figure 9.9. Variation of maximum bearing temperature with speed in a pivoted-pad journal bearing with $D = 431.8$ mm and $\beta = 60^\circ$. o, experimental (Gardner and Ulschmid, 1974); –, constant-temperature shaft; ----, insulated shaft, theoretical. (Reprinted with permission from Suganami, T. and Szeri, A. Z. A thermohydrodynamic analysis of journal bearings. *ASME Journal of Lubrication Technology*, **101**, 21–27, 1979.)

It is customary to solve Eq. (9.34) simultaneously with the equation of heat conduction in the bearing and require continuity of both temperature and heat flow rate at the lubricant-bearing interface (Dowson and March, 1967; Ezzat and Rohde, 1972).[8] The remaining boundary conditions are not easily defined and have been a source of intense discussion in the literature.

The idea of a near-isothermal shaft was put forth by Dowson and March (1967) on the basis of experimental observations (Dowson, Hudson, Hunter, and March, 1966). Suganami and Szeri (1979) assumed that the shaft is at a constant temperature at small surface speeds (laminar flow), as a significant portion of the generated heat leaves through the shaft by conduction in that case (Dowson, Hudson, Hunter, and March, 1966). But for large surface velocities (superlaminar flow), they solved Eq. (9.35) on the assumption of a thermally insulated shaft, as now only an insignificant portion of the heat leaves through the shaft. Physically, neither the isothermal shaft nor the insulated shaft assumption is valid. Nevertheless, experimental evidence does not contradict the predictions of Suganami and Szeri (1979), which are based on these assumptions (Figure 9.9). When applying Eq. (9.34) to thrust bearings, constant runner temperature is the accepted boundary condition (Ezzat and Rohde, 1972).

We may specify the temperature on the section of the leading edge that is free from backflow. At the remainder of the leading edge, where backflow is present, as well as at

[8]To cut down on the amount of computations, an approximate equation for heat conduction in the bearing may be integrated analytically (Safar and Szeri, 1974; Suganami and Szeri, 1979a; Yu and Szeri, 1975). The matching conditions on temperature and heat flow can then be replaced by an approximate film-bearing interfacial condition.

the trailing edge, we do better to prescribe negligible conduction, i.e., zero temperature gradient (Suganami and Szeri, 1979).

In summary, Eq. (9.35) was transformed to the $(\bar{x},\ \bar{y})$ coordinate system (see footnote 7) and solved subject to the boundary conditions (Suganami and Szeri, 1979):

$$\left.\begin{aligned} &T = T_i\,(\bar{y}) \quad \text{if } u \geq 0 \\ &\frac{\partial T}{\partial \bar{x}} = 0 \quad \text{if } u < 0 \end{aligned}\right\} \quad \text{at } \bar{x} = \bar{x}_1,$$

$$\frac{\partial T}{\partial \bar{x}} = 0 \quad \text{at } \bar{x} = \bar{x}_1 + \beta, \tag{9.36b}$$

$$\left[T + \Gamma\,(\bar{x})\,\frac{\partial T}{\partial \bar{y}}\right] = T_a \quad \text{at } \bar{y} = 0,$$

$$\left.\begin{aligned} &T = T_s \quad \text{if } (R_h)_{\max} \leq 400 \\ &\frac{\partial T}{\partial \bar{y}} = 0 \quad \text{if } (R_h)_{\max} > 400 \end{aligned}\right\} \quad \text{at } \bar{y} = H.$$

The boundary function $\Gamma(\bar{x})$ is obtained from the approximate heat conduction equation for pad temperature Θ_p that neglects conduction in the circumferential direction

$$\frac{1}{r}\frac{\partial}{\partial r}\left(r\frac{\partial \Theta_p}{\partial r}\right) = 0,$$

and matching heat flow and temperature at the film-pad interface.

The Pressure Equation

Derivation of the pressure equation that accounts for pointwise variation of viscosity was first given for laminar flow by Dowson and Hudson (1963). By starting from Eq. (7.15), rather than from the corresponding laminar equations of motion as Dowson and Hudson did, we can combine the ideas of Dowson and Elrod (Elrod and Ng, 1967) and make the derivation apply to the turbulent flow of the lubricant (Safar and Szeri, 1974).

Applying the eddy viscosity hypotheses (7.20), we obtain

$$\frac{\partial \bar{P}}{\partial x} = \frac{\partial}{\partial y}\left[\bar{\mu}\left(1 + \frac{\varepsilon_m}{\nu}\right)\frac{\partial \bar{U}}{\partial y}\right], \tag{9.37a}$$

$$\frac{\partial \bar{P}}{\partial y} = 0, \tag{9.37b}$$

$$\frac{\partial \bar{P}}{\partial z} = \frac{\partial}{\partial y}\left[\bar{\mu}\left(1 + \frac{\varepsilon_m}{\nu}\right)\frac{\partial \bar{W}}{\partial y}\right]. \tag{9.37c}$$

These equations can be integrated formally to yield

$$\bar{U} = \frac{1}{\mu_*}\frac{\partial \bar{P}}{\partial x}\Psi\,(x, y, z) + U_0\frac{\xi_1\,(x, y, z)}{\xi_1\,(x, h, z)}, \tag{9.38a}$$

$$\bar{W} = \frac{1}{\mu_*}\frac{\partial \bar{P}}{\partial z}\Psi\,(x, y, z)\,. \tag{9.38b}$$

Here

$$\Psi(x, y, z) = \xi_2(x, y, z) - \frac{\xi_2(x, h, z)}{\xi_1(x, h, z)}\xi_1(x, y, z),$$
$$\xi_1(x, \phi, z) = \int_0^{\phi} \frac{dy}{\mu f(x, y, z)}, \qquad \xi_2(x, \phi, z) = \int_0^{\phi} \frac{y\,dy}{\mu f(x, y, z)}, \tag{9.38c}$$

and we use the notation

$$f(x, y, z) = \left(1 + \frac{\varepsilon_m}{\nu}\right).$$

Implicit in Eqs. (9.38) are the no-slip velocity boundary conditions

$$\bar{U} = \bar{W} = 0 \qquad \text{at } y = 0,$$
$$\bar{U} = U_0 \qquad \bar{W} = 0 \quad \text{at } y = h.$$

We may now follow the procedure already outlined in the derivation of the classical Reynolds equation. Thus, substituting Eqs. (9.38) into the equation of continuity (7.7a) and integrating with the boundary conditions[9]

$$[\bar{V}]_0^h = \frac{dh}{dt},$$

we obtain

$$\frac{\partial}{\partial x}\left(\frac{\Gamma}{\mu_*}\frac{\partial \bar{P}}{\partial x}\right) + \frac{\partial}{\partial z}\left(\frac{\Gamma}{\mu_*}\frac{\partial \bar{P}}{\partial z}\right) = U_0\frac{\partial}{\partial x}\left(h - \frac{\xi_2(x, h, z)}{\xi_1(x, h, z)}\right) + V_0 \tag{9.39a}$$

for journal bearings and

$$\frac{\partial}{\partial x}\left(\frac{\Gamma}{\mu_*}\frac{\partial \bar{P}}{\partial x}\right) + \frac{\partial}{\partial z}\left(\frac{\Gamma}{\mu_*}\frac{\partial \bar{P}}{\partial z}\right) = U_0\frac{\partial}{\partial x}\left(\frac{\xi_2(x, h, z)}{\xi_1(x, h, z)}\right) + V_0 \tag{9.39b}$$

for slider bearings. Here we employed the notation

$$\Gamma(x, z) = -\int_0^{h(x)} \Psi(x, y, z)\,dy.$$

For isothermal flow, Eq. (9.39) is identical to the pressure equation of Elrod and Ng (1967), and for laminar flow, it reduces to the thermohydrodynamic pressure equation of Dowson and co-workers (Dowson and Hudson, 1963; Dowson and March, 1967).

Although the distribution of the temperature and the viscosity is assumed to be known at the start of the solution of Eq. (9.39), this equation has nonlinear coefficients because the eddy viscosity is dependent on shear stress. When these coefficients are linearized (see Suganami and Szeri 1979), the equation becomes a generalization of the Ng and Pan (1965) linearized turbulent equation. This equation is similar in form to the constant-viscosity turbulent lubrication equation (7.59).

When nondimensionalized for steady state, the turbulent Reynolds equation is given by

$$\frac{\partial}{\partial \xi}\left(H^3 G_{\bar{x}}\frac{\partial P}{\partial \xi}\right) + \left(\frac{D^2}{L}\right)\frac{\partial}{\partial \zeta}\left(H^3 G_{\zeta}\frac{\partial P}{\partial \zeta}\right) = 2\pi\frac{\partial (HF)}{\partial \xi}. \tag{9.40}$$

[9] $U_0 = U_2$ for journal bearings and $U_0 = U_1$ for slider bearings, if the bearing surface is stationary. In either case $V_0 = V_2 - V_1$ (see Chapter 2).

The turbulence functions $G_{\bar{x}}$ and $G_{\bar{z}}$ are defined by

$$G_x = \int_0 \zeta_1(\eta)\, d\eta - \frac{\zeta_1(1)}{\zeta_2(1)} \int_0^1 \zeta_2(\eta)\, d\eta, \tag{9.41a}$$

$$G_z = \int_0^1 \zeta_3(\eta)\, d\eta - \frac{\zeta_3(1)}{\zeta_4(1)} \int_0^1 \zeta_4(\eta)\, d\eta, \tag{9.41b}$$

$$F = \frac{1}{\zeta_4(1)} \int_0^1 \zeta_4(\eta)\, d\eta. \tag{9.41c}$$

Here

$$\zeta_1(\beta) = \int_0^\beta \frac{\left(\frac{1}{2} - \eta\right)}{\mu f_c(\eta)} \left[1 - \frac{g_c(\eta)}{f_c(\eta)}\right] d\eta, \tag{9.42a}$$

$$\zeta_2(\beta) = \int_0^\beta \frac{1}{\mu f_c(\eta)} \left[1 - \frac{g_c(\eta)}{f_c(\eta)}\right] d\eta, \tag{9.42b}$$

$$\zeta_3(\beta) = \int_0^\beta \frac{\left(\frac{1}{2} - \eta\right)}{\mu f_c(\eta)} d\eta, \tag{9.42c}$$

$$\zeta_4(\beta) = \int_0^\beta \frac{d\eta}{\mu f_c(\eta)}. \tag{9.42d}$$

The functions f_c and g_c are given by Eqs. (7.68) and (7.69), respectively,

$$f_c(\eta) = 1 + \kappa \left[\bar{y} h_c^+ - \delta_\ell^+ \tanh\left(\frac{\bar{y} h_c^+}{\delta_\ell^+}\right)\right], \tag{7.68}$$

$$g_c(\eta) = \frac{1}{2} \kappa \bar{y} h_c^+ \tanh^2\left(\frac{\bar{y} h_c^+}{\delta_\ell^+}\right), \tag{7.69}$$

where $\bar{y} = y/h$ and $h_c^+ = \frac{h}{\nu}\sqrt{\frac{|\tau_c|}{\rho}}$, a local Reynolds number, were defined in Chapter 7.

Equation (9.40) was solved subject to the Swift-Stieber boundary conditions (3.84), and the lubricant viscosity was calculated from Vogel's formula

$$\bar{\mu} = \exp\left[\frac{a}{b + \bar{\Theta}}\right], \tag{9.43}$$

where the material parameters a and b are determined through curve fitting.

9.3 Journal Bearings

Bearing Temperature

Theoretical predictions by the THD model are compared here with two sets of experimental data.

Table 9.1. *Test bearing*

Shaft speed	$N = 900$ rpm	$N = 3000$ rpm
Pressure kPa	68.65	46.09
Temperature (°C)	22.40	34.40
Flow rate (cm^3/s)	37.60	59.00

$D = 10$ cm, $L = 5$ cm, $\beta = 150°$, $C = 0.01$ cm, $R_b = 15$ cm.

One of the sets pertain to a pivoted-pad bearing that was studied by Gardner and Ulschmid (1974). Figure 9.9 shows both calculated and experimental bearing temperature data plotted against rotational speed for the $D = 43.18$ cm tilting pad bearing. The graph also displays measured oil discharge temperatures. Transition from laminar to superlaminar flow regime seems to take place in the $2000 < N\,(\text{rpm}) < 2500$ interval. This corresponds, roughly to $400 < (R_h)_{\max} < 600$, where $(R_h)_{\max}$ is the maximum value of the local Reynolds number within the 60° bearing arc. To investigate the effect thermal conditions at the shaft-lubricant interface have on lubricant temperature, calculations were performed with both the constant-temperature boundary condition, when the uniform shaft temperature was equated to the oil discharge temperature, and the zero temperature gradient boundary condition. In the laminar regime, there seems to be little difference between the two predictions, as indicated by Figure 9.9, nevertheless the constant-temperature boundary condition shows better agreement with experiment, as was suggested earlier. This is not so in the turbulent regime, here the locally adiabatic shaft (zero normal gradient boundary condition) leads to results that show far better agreement with the experiment, as would be expected on the basis of the previous discussion.

It may also be noticed from Figure 9.9 that laminar theory grossly overestimates the transition region temperatures, whereas turbulent analysis underestimated it. Furthermore, the turbulent analysis does not yield results that coincide with the results of laminar analysis at any finite value of the Reynolds number. The reason for this is that in the turbulent model calculation of the eddy viscosity from Reichardt's model makes for gradual transition, and the eddy viscosity is given a nonzero value even when the flow is laminar, as discussed above. Continuous transition from laminar to turbulent conditions, and agreement with experiments in the transition regime, was achieved on introducing the eddy viscosity scaling factor ϑ from Eq. (9.36).

The second set of data used here for comparison was obtained on a centrally loaded, "viscosity pump" bearing (Suganami and Szeri, 1979a). This bearing has a 210° relief in the top cap and is limited in the axial direction by two deep circumferential oil grooves, one at each end. It is loaded by means of a hydraulic load cell. The temperature measurements were obtained with thermocouples, sunk into the babbit to within 0.5 cm of the bearing surface. Dimensions of the test bearing and relevant feed-oil data are shown in Table 9.1.

Predicted and measured circumferential temperature profiles are compared for the $D = 10$ cm diameter bearing of Table 9.1 in Figure 9.10. There are two solid curves in the figure. Curve (a) represents solution of the energy equation of the THD model. As this equation is two dimensional, it assumes that the clearance gap is filled with lubricant everywhere. This solution clearly overestimates bearing temperatures. Curve (b) also assumes that a continuous film exists in the diverging gap and cavitation only affects

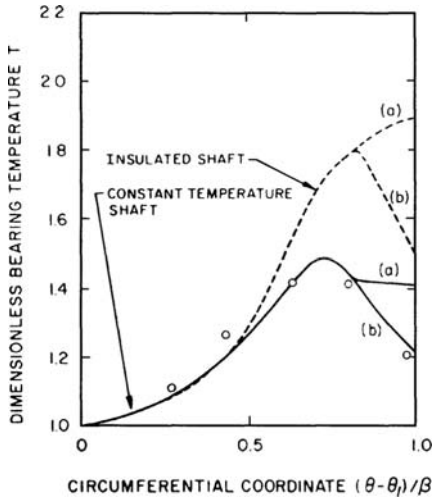

Figure 9.10. Circumferential temperature profile at $N = 900$ rpm, Table 9.1. (Reprinted with permission from Suganami, T. and Szeri, A. Z. A thermohydrodynamic analysis of journal bearings. *ASME Journal of Lubrication Technology*, **101**, 21–27, 1979).

pressure calculations, but now the lubricant is replenished from the oil grooves at the sides. One would expect this solution to underestimate bearing temperatures.

Note that Figure 9.10 displays laminar bearing operations and, in line with previous contention, shows better agreement between theory and experiment when the former is based on constant, temperature boundary condition at the shaft-film interface.

The Role of Nondimensional Parameters

The previous section brings into focus the governing dimensionless parameters of the various lubrication models. If the geometric parameters β and L/D are fixed and if in addition the orientation of the external force, characterized by the value of the parameter α/β where α is the angular position of the load relative to the leading edge, is held constant, the *isothermal model* contains just two parameters. Bearing performance can, in this case, be completely characterized by the parameters

$$\{S, \mathrm{Re}\}.$$

The *adiabatic model* requires only one additional parameter, assuming that the viscosity-temperature dependence of the lubricant is given, as is the reference temperature. Bearing performance can then be characterized by the groups

$$\{S, \mathrm{Re}, \Lambda\}.$$

The THD model requires further addition of parameters. The parameters characteriging THD bearing performance can be conveniently divided into two groups:

$$\left\{S, \mathrm{Re}, \Lambda, \mathrm{Pe}, \left(\frac{C}{R}\right), \left(\frac{\Theta_s}{\Theta_*}\right)\right\}, \tag{9.44a}$$

$$\left\{\left(\frac{\Theta_i}{\Theta_*}\right), \left(\frac{\Theta_a}{\Theta_*}\right), \left(\frac{k}{k_\beta}\right), \frac{R_b}{R}, \mathrm{Nu}\right\}. \tag{9.44b}$$

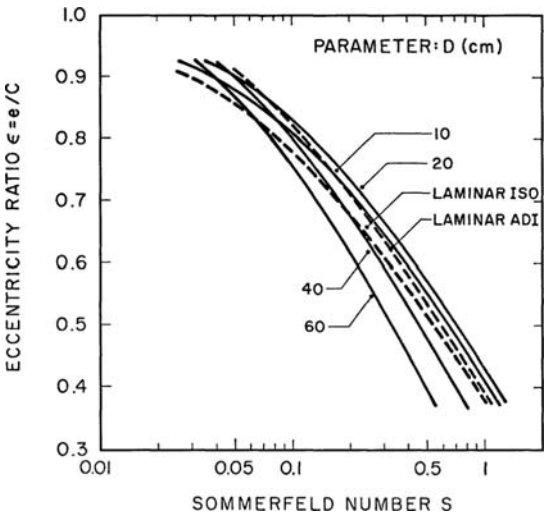

Figure 9.11. Variation of eccentricity ratio with Sommerfeld number at constant bearing diameter, $N = 3600$ rpm, $C/R = 0.002$, $\Theta_i = 50^\circ$. (Reprinted with permission from Suganami, T. and Szeri, A. Z. Parametric study of journal bearing performance: the 80° partial arc bearing. *ASME Journal of Lubrication Technology*, **101**, 486–491, 1979.)

Parameters grouped in expression (9.44b) were found to have only marginal effect on bearing performance and can be left out of consideration in a first approximation to the problem. The dimensionless shaft temperature (Θ_s/Θ_*) is also dropped from further consideration as it is specified only when the flow is laminar. First order effects are then due to

$$\left\{S, \mathrm{Re}, \Lambda, \mathrm{Pe}, \left(\frac{C}{R}\right)\right\}, \tag{9.45}$$

and we retain these as the essential parameters of the THD problem in rigid bearings. Thermal deformation is also important, as we shall see below. But taking into account thermal deformation of shaft and bearing greatly increases the numerical complexity. The large number of essential parameters precludes the possibility of full parametric study of the THD problem and the representation of its results.

Figure 9.11 shows a plot of the eccentricity ratio versus the Sommerfeld number. There are perhaps two observations to be made here: (1) The adiabatic (ADI) and the isothermal (ISO) models do not bracket actual (THD) bearing performance, and (2) at small to moderate load the turbulent bearing operates at lower eccentricity than does the laminar bearing, but at high load this order is reversed.

Figure 9.12 shows maximum bearing temperature plotted versus Sommerfeld number, i.e., inverse of specific bearing load. Maximum bearing temperature in laminar bearings ($D = 10$, 20 cm) seems to be relatively insensitive to specific load; for the smallest of the bearings calculated, the dependence is only marginal. This is not so for large (turbulent) bearings, for which high specific load should be avoided at all cost, as it might lead to overheating.

Figure 9.13 illustrates the fact that transition to turbulence (taking place under present conditions at $D \approx 25$ cm) is beneficial from the point of limiting bearing temperatures, especially at low loads. This was already demonstrated experimentally by Gardner and

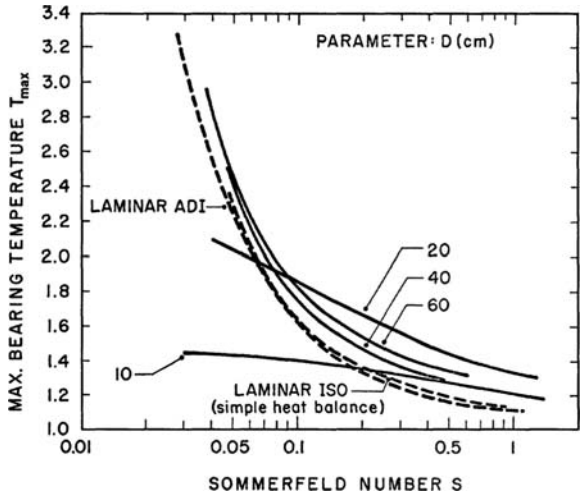

Figure 9.12. Dependence of maximum bearing temperature on Sommerfeld number at constant bearing diameter, $N = 3600$ rpm, $C/R = 0.002$, $\Theta_* = 50°$C. (Reprinted with permission from Suganami, T. and Szeri, A. Z. Parametric study of journal bearing performance: the 80° partial arc bearing. *ASME Journal of Lubrication Technology*, **101**, 486–491, 1979.)

Ulschmid (1974). The curves in Figure 9.13 also support a previous contention, viz., that $T_{\max}$ is strongly dependent on P when in the turbulent regime.

Friction Factor

Allowing viscosity to decrease with increasing temperature is expected to reduce the wall friction coefficient in pure Couette flow. Increasing the eccentricity and no other change would, on the other hand, tend to increase friction. Figure 9.14 illustrates the result

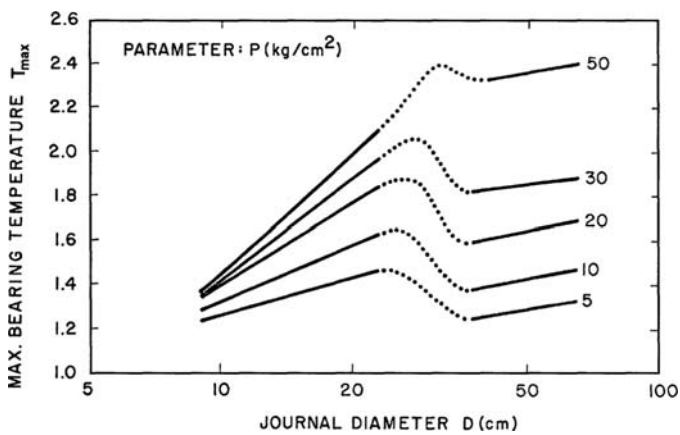

Figure 9.13. Effect of bearing size on maximum bearing temperature at constant specific load, $N = 3600$ rpm, $C/R = 0.002$, $\Theta_* = 50°$C. (Reprinted with permission from Suganami, T. and Szeri, A. Z. Parametric study of journal bearing performance: the 80° partial arc bearing. *ASME Journal of Lubrication Technology*, **101**, 486–491, 1979.)

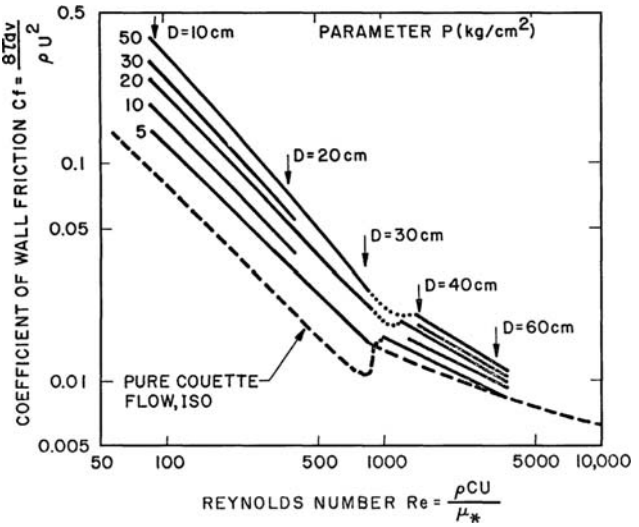

Figure 9.14. Friction factor versus Reynolds number at constant specific load, $N = 3600$ rpm, $C/R = 0.002$, $\Theta_* = 50°$C. (Reprinted with permission from Suganami, T. and Szeri, A. Z. Parametric study of journal bearing performance: the 80° partial arc bearing. *ASME Journal of Lubrication Technology*, **101**, 486–491, 1979.)

of introducing these two competing tendencies simultaneously; the net effect is an increase in the wall friction coefficient. Only at large Re might this trend be reversed, at least at the smallest of loads tested, as indicated by the curves of Figure 9.14 at $D = 60$ cm. The friction coefficient is strongly dependent on load in the laminar regime. This dependence lessens with increasing Reynolds number.

Journal Locus and Dynamic Coefficients

Figure 9.15 displays various journal center loci. The overall effect of turbulence, and also of viscosity variation, is to displace the journal center in the downstream direction, i.e., to increase the load angle. This shift in ϕ is monotonically increasing with bearing diameter in both the laminar and the turbulent regimes, but the trend seems to be reversed when in the transition regime. Thus, the locus of the $D = 20$ cm bearing is displaced further from its isothermal position, that is, the $D = 40$ cm bearing. This might affect bearing stiffness.

We saw in Chapter 4 that the incremental oil-film forces that are due to small perturbation of static equilibrium, can be written as[10]

$$\begin{bmatrix} dF_x \\ dF_y \end{bmatrix} = -\frac{W}{C}\begin{bmatrix} \bar{\bar{K}}_{xx} & \bar{\bar{K}}_{xy} \\ \bar{\bar{K}}_{yz} & \bar{\bar{K}}_{yy} \end{bmatrix}\begin{bmatrix} \bar{x} \\ \bar{y} \end{bmatrix} - \frac{W}{C\omega}\begin{bmatrix} \bar{\bar{C}}_{xx} & \bar{\bar{C}}_{xy} \\ \bar{\bar{C}}_{yx} & \bar{\bar{C}}_{yy} \end{bmatrix}\begin{bmatrix} \dot{\bar{x}} \\ \dot{\bar{y}} \end{bmatrix}.$$

The stiffness and damping coefficients of a $\beta = 80°$ fixed-pad partial arc bearing at $\varepsilon = 0.7$ were shown in Table 4.2 under the following conditions: (1) isothermal, laminar flow; (2) adiabatic, laminar flow; (3) THD, laminar flow; (4) isothermal, turbulent flow; and (5) THD, turbulent flow. The calculation involves finding the steady-state equilibrium

[10] $\bar{\bar{K}}_{xx} = S\bar{\bar{K}}_{xx}$, etc., where $\bar{K}_{xx}$ is defined in Eq. (4.31).

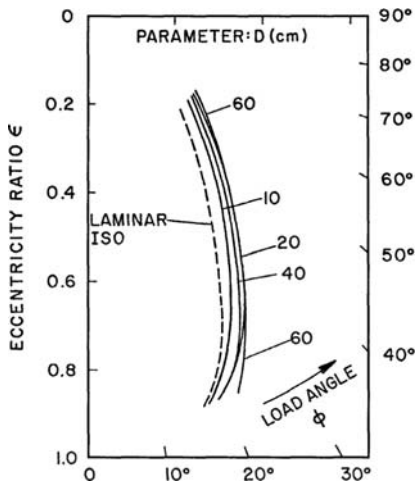

Figure 9.15. Journal locus; $N = 3600$ rpm, $C/R = 0.002$, $\Theta_* = 50^\circ$ C. (Reprinted with permission from Suganami, T. and Szeri, A. Z. Parametric study of journal bearing performance: the 80° partial arc bearing. *ASME Journal of Lubrication Technology*, **101**, 486–491, 1979.)

conditions for the journal (by solving the pressure and energy equations simultaneously) and evaluating the incremental oil film forces while keeping the lubricant at its equilibrium temperature. To perform the perturbation step correctly, one would again have to find simultaneous solutions of the energy and pressure equations while the journal is in its perturbed state. But this would, perhaps unnecessarily, increase the volume of computations.

These coefficients, shown in Table 4.2, were subsequently employed in calculating the stability-threshold speed of a single mass rigid rotor supported at both ends. The threshold speed parameter $\bar{M}$, defined in Eq. (4.41), is plotted against the Sommerfeld number in Figure 4.15.

Table 4.2 shows significant changes in the static and dynamic coefficients. The "cumulative" effect of these changes is a remarkable improvement in threshold speed. Figure 4.15 shows the threshold speed plotted against the Sommerfeld number. The curves for laminar bearings ($D < 20$ cm) seem to bunch together. There is a significant improvement in bearing stability threshold speed in the transition regime ($20 < D < 30$ cm), but the dependence on D lessens again when in the turbulent regime ($D > 30$ cm). The threshold speed, $\bar{M}$, becomes meaningful only, however, when it coincides with the shaft rotational speed. When this occurs, a *critical bearing load* is defined for each bearing diameter, under the assumed condition.

Figure 9.16 shows the critical bearing load plotted versus the shaft diameter for a fixed pad. If the specific bearing load exceeds in magnitude the critical bearing load, the bearing is stable. Figure 9.16 indicates that THD effects expand the regime of stable bearing operations, in terms of the bearing specific load P.

Thermal Deformation

Boncompain, Fillon, and Frêne (1986) compared their numerical analysis with experiments from Ferron (1982), and showed significant thermal deformation of the

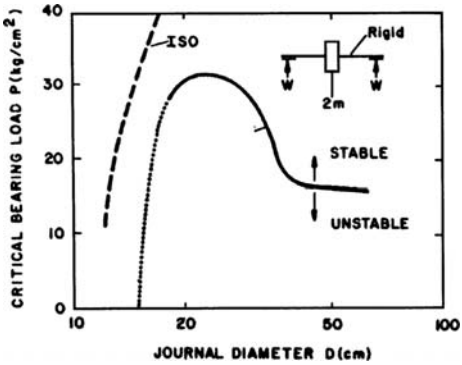

Figure 9.16. Critical bearing load versus shaft diameter for a fixed pad: $N = 3600$ rpm, $C/R = 0.002$, $\Theta_* = 50°$C. (Reprinted with permission from Suganami, T. and Szeri, A. Z. Parametric study of journal bearing performance: the 80° partial arc bearing. *ASME Journal of Lubrication Technology*, **101**, 486–491, 1979.)

surfaces. Excellent agreement was obtained, though the computations were performed for the mid-plane of the pad only. They estimated the thermoelastic strain in their numerical model from

$$\varepsilon_{ij} = \frac{1+\nu}{E} T_{ij} - \frac{\nu}{E} T_{kk} + \alpha \Delta\Theta\,(M)\,\delta_{ij}. \tag{9.46}$$

Here ε_{ij} is the strain, T_{ij} is the stress, $\Delta\Theta(M) = \Theta\,(M) - \Theta_*$ is the temperature excess at point M over the reference temperature Θ_*, α is the coefficient of thermal expansion of the solid, and E, ν are elastic moduli. The finite-element method was used to solve the coupled system consisting of the energy equation for the lubricant (9.34), the Reynolds equation with deformation film thickness calculated from Eq. (9.46), Vogel's formula (9.43) for viscosity, and the energy equation for the pad

$$\frac{\partial^2 \Theta_p}{\partial r^2} + \frac{1}{r}\frac{\partial \Theta_p}{\partial r} + \frac{1}{r^2}\frac{\partial^2 \Theta_p}{\partial \varphi^2} = 0. \tag{9.47}$$

Figure 9.17 shows the isotherms in both lubricant film and pad, in a four-pad bearing, indicating that there is considerable heat transfer in the pad in the tangential direction.

As may be judged from Figure 9.18, thermoelastic deformation can have significant effect.

Bouard, Fillon and Frêne (1994) compared the turbulence models of Constantinescu (1972), Elrod and Ng (1967), and Ng and Pan (1965), using the turbulent transition approximation (9.36) of Suganami and Szeri (1979a). As shown in Figure 9.19 for pressure, in Figure 9.20 for temperature, and in Figure 9.21 for power loss, there is little difference between the predictions of the three theories, under the conditions specified in the paper.

More recent experimental investigations into turbulent lubrication are by Gethin and Medwell (1985); Hopf and Schüler (1989); Taniguchi, Makino, Takeshita, and Ichimura (1990); Simmons and Dixon (1994); Mittwollen and Glienicke (1990); Bouchoule, Fillon, Nicolas, and Barressi (1996); and Monmousseau et al. (1996).

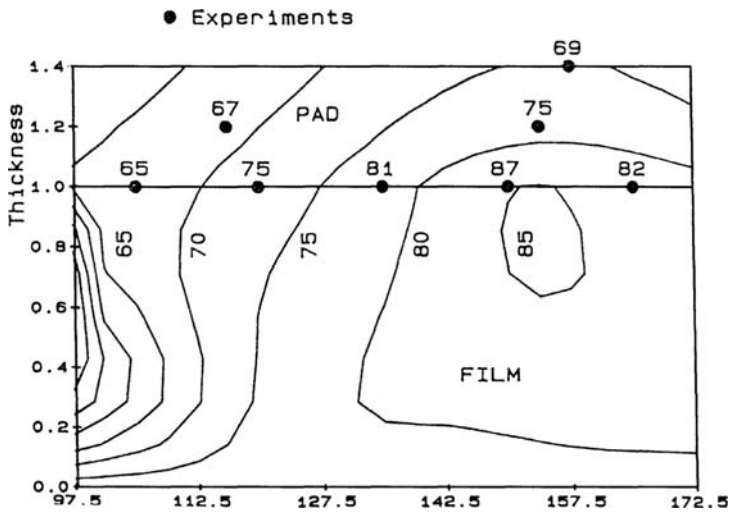

Figure 9.17. $\Theta^{\circ}C = \text{const.}$ surfaces in lubricant film and pad. (Reproduced with permission from Fillon, M. and Frêne, J. Numerical simulation and experimental results on thermo-elasto-hydrodynamic tilting-pad journal bearings. *IUTAM Symposium on Numerical Simulation of Non-isothermal Flow of Viscoelastic Liquids*. 85–99, © 1995 Kluwer Academic Publisher.)

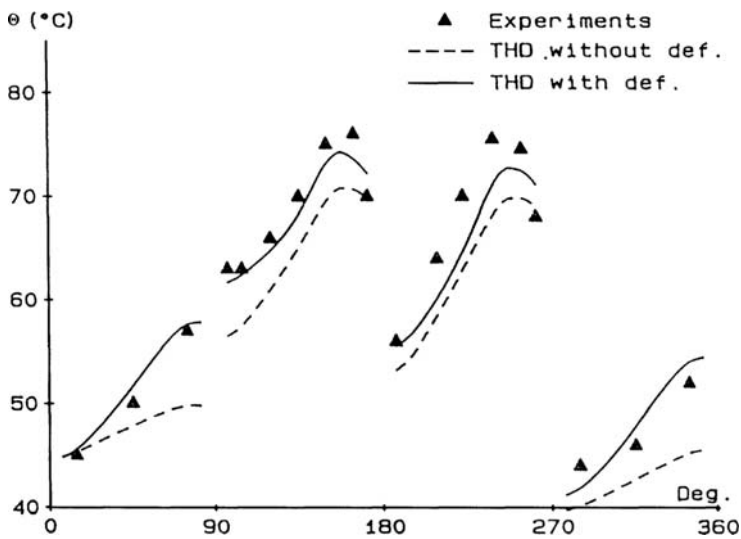

Figure 9.18. Comparison of theoretical and experimental pad temperature for a four-pad bearing. (Reproduced with permission from Fillon, M. and Frêene, J. Numerical simulation and experimental results on thermo-elasto-hydrodynamic tilting-pad journal bearings. *IUTAM Symposium on Numerical Simulation of Non-isothermal Flow of Viscoelastic Liquids*. 85–99, © 1995 Kluwer Academic Publisher.)

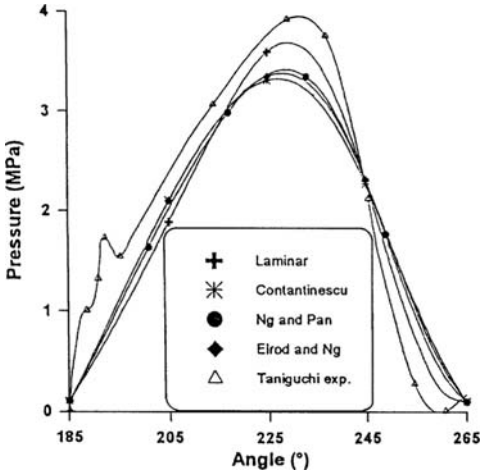

Figure 9.19. Film pressure as predicted by various turbulence models (Bouard, Fillon and Frêne, 1995). (Reproduced from Fillon, M. *Dossier D'Habilitation a Diriger les Recherches*. Universite de Poitiers.)

The inlet temperature effect was investigated theoretically by Ettles (1992) and by Ha, Kim, and Kim (1995). An analysis for tilting-pad bearings was published by Bouard, Fillon, and Frêne (1996). Thermal transient analysis was performed by Gadangi, Palazzo, and Kim (1996), and Fillon, Desbordes, Frêne, and Wai (1996).

9.4 Thrust Bearings

One of the sector-shaped pivoted pads of a thrust bearing we want to study is shown in Figure 4.16. (Jeng, Zhou, and Szeri, 1986a). The plane of the runner surface is located at $z = 0$ and the pad surface is located at $z = h(r, \varphi)$ of the cylindrical polar

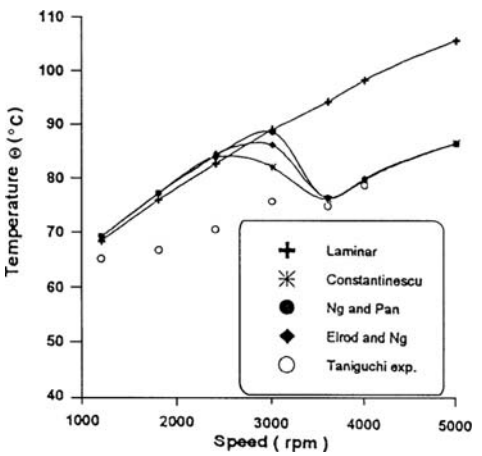

Figure 9.20. Maximum bearing temperature as predicted by the various turbulence models (Bouard, Fillon, and Frêne, 1995). (Reproduced from Fillon, M. *Dossier D'Habilitation a Diriger les Recherches*. Universite de Poitiers.)

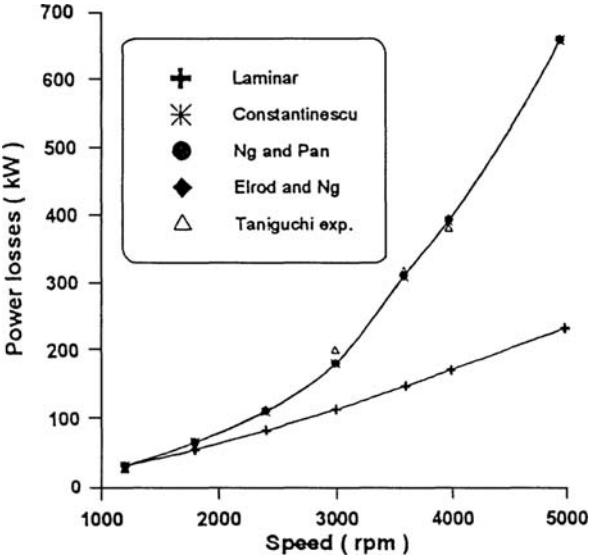

Figure 9.21. Power loss as predicted by the various turbulence models (Bouard, Fillon and Frêne, 1995). (Reproduced from Fillon, M. *Dossier D'Habilitation a Diriger les Recherches*. Universite de Poitiers.)

coordinate system $\{r, \varphi, z\}$. The characteristic lengths of the lubricant film are L_z across and $L_{r\theta}$ along the film.

The Pressure Equation

Making use of the fact that $L_z/L_{r\theta} = O(10^{-3})$, in an order of magnitude analysis similar to the one employed Chapter 7, the equations of motion for turbulent flow of the lubricant reduce to[11]

$$\frac{\partial \bar{P}}{\partial r} = \frac{\partial}{\partial z}\left(\bar{\mu}\frac{\partial \bar{U}}{\partial z} - \rho\overline{\mu' w'}\right), \tag{9.48a}$$

$$\frac{\partial \bar{P}}{\partial z} = 0, \tag{9.48b}$$

$$\frac{1}{r}\frac{\partial \bar{P}}{\partial \varphi} = \frac{\partial}{\partial z}\left(\bar{\mu}\frac{\partial \bar{V}}{\partial z} - \rho\overline{v' w'}\right). \tag{9.48c}$$

Starting from Eqs. (9.48) and repeating the analysis of Ng and Pan (1965), updated for variable viscosity (Jeng, Zhou, and Szeri, 1986a), we obtain

$$\frac{\partial}{\partial \hat{\varphi}}\left[H^3 G_\varphi \frac{\partial P}{\partial \hat{\varphi}}\right] + \beta^2 \hat{\rho}\frac{\partial}{\partial \hat{r}}\left[\hat{\rho} H^3 G_r \frac{\partial P}{\partial \hat{r}}\right] = \beta^2 \hat{\rho}^2 \frac{\partial\,[H\,(1-F)]}{\partial \hat{\varphi}}. \tag{9.49}$$

[11]The order of magnitude analysis based on the limit $(L_z/L_{r\theta})^2 \to 0$ yields $\partial P/\partial z = (L_z/L_{r\theta})\mathrm{Re}(\partial/\partial z)(\overline{w'w'})$ in place of Eq. (9.48b), but past practice has been to also assume $(L_z/L_{r\theta})\mathrm{Re} \to 0$ [(see Eq. (7.16)]. If the latter assumption is not made, derivation of a Reynolds type pressure equation is not possible.

The turbulent functions G_φ, G_r, and F are defined by formulas identical in form to Eqs. (9.41) and (9.42), except that they are functions of (r, φ) through f_c, g_c, and H, while G_x, G_z were functions of (x, z).

The boundary conditions that complement equation Eq. (9.49) are

$$\begin{aligned} &P(0, \hat{\varphi}) = P(1, \hat{\varphi}) = 0, \\ &P(\hat{r}, 0) = P(\hat{r}, 1) = 0, \\ &P = \frac{\partial P}{\partial \hat{\varphi}} = 0, \quad \text{at } \hat{\varphi} = \hat{\varphi}_{\text{cav}}. \end{aligned} \tag{9.50}$$

In arriving at Eq. (9.49), we employed the nondimensionalization

$$\begin{aligned} &r = \Delta \hat{r} + R_1, \quad \varphi = \beta \hat{\varphi}, \quad z = h\hat{z}, \quad \bar{U} = \Delta\omega U, \quad \bar{V} = \Delta\omega V \\ &\bar{P} = \frac{\mu_* \omega}{\beta} \left(\frac{\Delta}{h_c}\right)^2 P, \quad \bar{\mu} = \mu_* \mu, \quad h = h_C H \\ &\Delta = R_2 - R_1 > 0, \quad \hat{\rho} = \hat{r} + R_1/\Delta, \quad r = \Delta\hat{\rho}, \end{aligned} \tag{9.51}$$

where h_C is the film thickness at the geometric center, C, of the pad (Figure 4.16).

The relationship between the normalized coordinate

$$z_c^+ = \frac{z_c}{\nu}\sqrt{\frac{|\tau_c|}{\rho}} = \hat{z}\frac{h_c}{\nu}\sqrt{\frac{|\tau_c|}{\rho}} = \hat{z}h_c^+$$

and the local Reynolds number, $R_h = r\omega h/\nu_{av}$ [cf., Eq. (7.76)], now has the form

$$R_h = \int_0^1 \frac{\mu_{av}\left(z_c^+/\hat{z}\right)^2 d\bar{z}}{\mu\left\{1 + \kappa\left[z_c^+ - \delta_\ell^+ \tanh\left(z_c^+/\delta_\ell^+\right)\right]\right\}}. \tag{9.52a}$$

For a given R_h, Eq. (9.52a) is a transcendental equation in z_c^+ and must be solved numerically.

The local Reynolds number, on the other hand, is calculated from the global Reynolds number, Re, with the aid of the local average viscosity,

$$\mu_{av}(\hat{r}, \hat{\varphi}) = \int_0^1 \mu(\hat{r}, \hat{\varphi}, \hat{z})\, d\hat{z},$$

from the formula

$$R_h = \frac{H\hat{\rho}}{\nu_{av}}\frac{\Delta}{R_2}\text{Re}, \qquad \text{Re} = \frac{R_2\omega h_C}{\nu_*}. \tag{9.52b}$$

The eddy viscosity for momentum transfer is

$$\frac{\varepsilon_m}{\nu} = f_c - 1 + \frac{\zeta_4(1)}{\beta^2}\frac{H^2}{\hat{\rho}^2}\frac{\partial P}{\partial \hat{\varphi}}\left[\hat{z} - \frac{1}{2} + \frac{\zeta_1(1)}{\zeta_2(1)}\right] g_c, \tag{9.53}$$

where ζ_1, ζ_2, f_c, and g_c are given by formulas analogous to Eqs. (9.42), (7.68), and (7.69).

When evaluated from Reichardt's formula (Hinze, 1975), the eddy viscosity is a monotonic increasing function of the Reynolds number, having nonzero value in the laminar

regime. To remedy this, we introduce a scale factor, ϑ, for eddy viscosity from Eq. (9.36), but now set $R_L = 500$ and $R_U = 900$ (Abramovitz, 1956; Gregory, 1974),

$$\vartheta = \begin{cases} 0.0 & (R_h)_{\max} \le 500 \\ 1 - \left[\dfrac{800 - (R_h)_{\max}}{300}\right]^{1/8} & 500 < (R_h)_{\max} \le 800 \\ 1 & (R_h)_{\max} > 800 \end{cases}$$

and employ $\vartheta(\varepsilon_m/\nu)$ in place of (ε_m/ν) in the calculations.

Film Thickness

Let $\{x, y, z\}$ be an inertial Cartesian coordinate system such that the $z = 0$ plane is located on the runner surface and the z axis is in the vertical direction pointing upward and goes through the geometric center $C\{(R_1 + R_2)/2, \beta/2\}$ of the bearing (Figure 4.16). If ψ_x and ψ_y represent the angular position of the pad in equilibrium, relative to the $\{x, y, z\}$ coordinate system, and if h_C is the film thickness at the pad center C, we have

$$h = h_C - x\psi_y + y\psi_x. \tag{9.54a}$$

Here ψ_x and ψ_y are small angles, positive when measured counterclockwise.

The nondimensional counterpart of Eq. (9.54a) is

$$H = 1 - \frac{\Delta}{R_1}\left\{\hat{\rho} m_y \sin\left[\beta\left(\frac{1}{2} - \hat{\varphi}\right)\right] + \left[\hat{\rho}\cos\left[\beta\left(\frac{1}{2} - \hat{\varphi}\right)\right] - \frac{R_1 + R_2}{2\Delta}\right] m x\right\}, \tag{9.54b}$$

where $H = h/h_C$ is the nondimensional film shape. The tilt parameters m_x, m_y have the definition

$$m_x = \frac{R_1\psi_x}{h_C}, \qquad m_y = \frac{R_1\psi_y}{h_C}.$$

The Energy Equation

An order of magnitude analysis yields the equation of energy for the lubricant in the form

$$\begin{aligned} &\rho c\left[\bar{U}\frac{\partial\bar{\Theta}}{\partial r} + \bar{V}\frac{\partial\bar{\Theta}}{r\partial\varphi} + \bar{W}\frac{\partial\bar{\Theta}}{\partial z} + \frac{\partial}{\partial z}\overline{(w'\theta')}\right] \\ &= k\left[\frac{1}{r}\frac{\partial}{\partial r}\left(r\frac{\partial\bar{\Theta}}{\partial r}\right) + \frac{1}{r^2}\frac{\partial^2\bar{\Theta}}{\partial\varphi^2} + \frac{\partial^2\bar{\Theta}}{\partial z^2}\right] + \bar{\mu}\left(1 + \frac{\varepsilon_m}{\nu}\right)\left[\left(\frac{\partial\bar{U}}{\partial z}\right)^2 + \left(\frac{\partial\bar{V}}{\partial z}\right)^2\right]. \end{aligned} \tag{9.55}$$

The velocity-temperature correlation $\overline{w'\theta'}$ may be approximated via the eddy viscosity hypothesis, where, in analogy to momentum transport, we put

$$-\overline{w'\theta'} = \varepsilon_H\frac{\partial\bar{\Theta}}{\partial z} \tag{9.56}$$

and the energy equation (9.55) is made nondimensional by substituting from Eq. (9.51) and

$$\bar{\Theta} = \Theta_* T, \qquad \mu(\Theta_*) = \mu_*, \qquad \mu = \mu_*\bar{\mu}.$$

When deriving the equation for lubricant pressure, Eq. (9.49), the z dependence was integrated out and the transformation was from $\{r, \varphi\}$ to $\{\hat{r}, \hat{\varphi}\}$. In the present case, the mapping is $\{r, \varphi, z\} \rightarrow \{\hat{r},\ \hat{\varphi},\ \hat{z}\}$, and we must employ more complicated formulas:

$$\frac{\partial}{\partial r} = \frac{1}{\Delta}\left(\frac{\partial}{\partial \hat{r}} - n_r \frac{\partial}{\partial \hat{z}}\right), \qquad \frac{\partial}{\partial \varphi} = \frac{1}{\beta}\left(\frac{\partial}{\partial \hat{\varphi}} - n_\varphi \frac{\partial}{\partial \hat{z}}\right), \qquad \frac{\partial}{\partial z} = \frac{1}{h_C}\frac{\partial}{H \partial \hat{z}}. \tag{9.57}$$

Here we used the notation

$$n_r = \frac{\hat{z}}{H}\frac{\partial H}{\partial \hat{r}}, \qquad n_\varphi = \frac{\hat{z}}{H}\frac{\partial H}{\partial \hat{\varphi}}.$$

The nondimensional energy equation is

$$\begin{aligned} U\frac{\partial T}{\partial \hat{r}} + \frac{V}{\beta\hat{\rho}}\frac{\partial T}{\partial \hat{\varphi}} + \left(\frac{W}{H} - Un_r - \frac{V}{\beta\hat{\rho}}n_\varphi\right)\frac{\partial T}{\partial \hat{z}} \\ = \frac{1}{\mathrm{Pe}}\left\{\frac{\partial}{\partial \hat{r}}\left(\frac{\partial T}{\partial \hat{r}} - n_r\frac{\partial T}{\partial \hat{z}}\right) - n_r\frac{\partial}{\partial \hat{z}}\left(\frac{\partial T}{\partial \hat{r}} - n_r\frac{\partial T}{\partial \hat{z}}\right)\right. \\ + \frac{1}{(\beta\hat{\rho})^2}\frac{\partial}{\partial \hat{\varphi}}\left(\frac{\partial T}{\partial \hat{\varphi}} - n_\varphi\frac{\partial T}{\partial \hat{z}}\right) + \frac{1}{(\delta H)^2}\frac{\partial^2 T}{\partial \hat{z}^2} - \frac{n_\theta}{(\beta\hat{\rho})^2}\frac{\partial}{\partial \hat{z}}\left(\frac{\partial T}{\partial \hat{\varphi}} - n_\varphi\frac{\partial T}{\partial \hat{z}}\right) \\ \left. + \frac{1}{\hat{\rho}}\left(\frac{\partial T}{\partial \hat{r}} - n_r\frac{\partial T}{\partial \hat{z}}\right) + \frac{\mathrm{Pr}}{\mathrm{Pr}^{(t)}}\frac{1}{\delta^2}\frac{\partial}{\partial \hat{z}}\left(\frac{\mu}{H^2}\frac{\varepsilon_m}{\nu}\frac{\partial T}{\partial \hat{z}}\right)\right\} \\ + \Lambda\left(1 + \frac{\varepsilon_m}{\nu}\right)\frac{\mu}{H^2}\left[\left(\frac{\partial U}{\partial \hat{z}}\right)^2 + \left(\frac{\partial V}{\partial \hat{z}}\right)^2\right]. \end{aligned} \tag{9.58}$$

Pe, Λ, and δ are the Peclet number, the dissipation parameter, and the film thickness parameter, respectively:

$$\mathrm{Pe} = \frac{\rho c \Delta^2 \omega}{k}, \qquad \Lambda = \frac{\mu_* \omega}{\rho c \Theta_* \delta^2}, \qquad \delta = \frac{h_C}{\Delta}. \tag{9.59a}$$

The laminar and turbulent Prandtl numbers are defined through

$$\mathrm{Pr} = \frac{c\mu_*}{k}, \qquad \mathrm{Pr}^{(t)} = \frac{\varepsilon_m}{\varepsilon_H}, \tag{9.59b}$$

and the temperature dependence of viscosity is assumed to be given by Vogel's formula (9.43).

The thermal boundary conditions are:

Runner surface ($z = 0$)

$$T = T_R \text{ (the runner surface temperature)} \tag{9.60a}$$

Bearing surface [$z = h(r, \varphi)$]

$$\begin{aligned} -k\frac{\partial T}{\partial z} &= -k_B\frac{\partial T_B}{\partial z_B}\cos\left(\psi_x^2 + \psi_y^2\right)^{1/2} \\ T &= T_B \text{ (the bearing surface temperature)} \end{aligned} \tag{9.60b}$$

Leading edge ($\varphi = \beta$)

$$T = T_L \text{ (the lubricant inlet temperature)} \tag{9.60c}$$

At the exit planes, i.e., at the trailing edge, $\varphi = 0$, the inside edge, $r = R_1$, and the outside edge, $r = R_2$, of the pad there are no boundary conditions specified in the classical sense by the physics of the problem. In journal bearings, Suganami and Szeri (1979a) assumed zero normal derivative for the temperature at exit planes. This condition was found to be far too restrictive for the present geometry and, eventually, zero second gradient exit boundary conditions were prescribed.

The Heat Conduction Equation

The bearing surface boundary condition, Eq. (9.60b), presupposes simultaneous solution of, or at least iteration between, the equation of energy for the lubricant, Eq. (9.59), and the equation of heat conductivity for the bearing pad:

$$\frac{1}{r_B}\frac{\partial}{\partial r_B}\left(r_B\frac{\partial \Theta_B}{\partial r_B}\right) + \frac{1}{r_B^2}\frac{\partial^2 \Theta_B}{\varphi_B^2} + \frac{\partial^2 \Theta_B}{\partial z_B^2} = 0. \tag{9.61}$$

Here Θ_B is the temperature in the bearing. The z_B axis of the bearing coordinate system $\{r_B, \varphi_B, z_B\}$ is normal to the pad surface and is inclined to the vertical at angle $\alpha = (\psi_x^2 + \psi_y^2)^{1/2}$.

Equation (9.58) requires the z component of the velocity, $W(z)$. This is obtained from the equation of continuity, for we have

$$\bar{W}(z) = -\int_0^z \frac{\bar{U}}{r}dz' - \int_0^z \frac{\partial \bar{U}}{\partial r}dz' - \int_0^z \frac{1}{r}\frac{\partial \bar{V}}{\partial \psi}\,dz'. \tag{9.62}$$

Pad Deformation

For the purposes of this analysis the pad surface is assumed to have spherical crowning; this permits us to characterize pad deformation in a simple manner.

Small bearing pads are supported in a point, and pad deformation is often negligible. In large bearings, however, considerable deformation of the pad is experienced, and simple support in a point will no longer suffice. To minimize deformation, the pad is often supported on a disk via a ring or rings, in the hope that elastic and thermal deformations will counteract one another. In at least in two constructions examined by Jeng, Zhou, and Szeri (1986b), the deformation was found to be near spherical.[12]

With reference to Figure 9.22, let R_d represent the radius of pad-surface curvature and ε be the maximum deviation of the surface from planar along its mid-radius. If λ is the distance between the center of the pad, C, and a generic point, P, then the deformation of point P is given by

$$\delta_h = R_d\left[1 - \sqrt{1 - \left(\frac{\lambda}{R_d}\right)^2}\right] \approx (x^2 + y^2)/2R_d,$$

where $\lambda = \sqrt{x^2 + y^2}$, so that

$$x = r\sin\left(\frac{\beta}{2} - \varphi\right), \qquad y = r\cos\left(\frac{\beta}{2} - \varphi\right) - \frac{R_1 + R_2}{2}.$$

[12]The ratio of the principal radii of curvature was $R_x/R_y = 0.96$ for one of the data and $R_x/R_y = 0.95$ for the other.

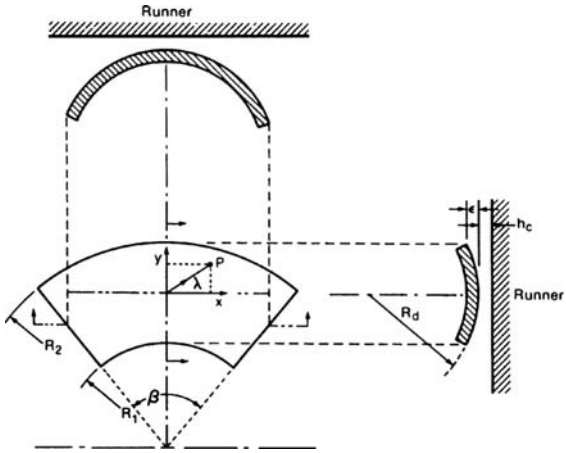

Figure 9.22. Spherical crowning of thrust pad. (Reprinted with permission from Jeng, M. C., Zhou, G. R. and Szeri, A. Z. Thermohydrodynamic solution of pivoted thrust pads, part I: Theory. *ASME Journal of Tribology*, **108**, 195–207, 1986.)

The change, δ_h, in the nondimensional film thickness, $\bar{h}(r, \theta)$, when due to spherical crowning, is given by

$$\hat{\delta}_h = \hat{\varepsilon}\left\{4(\hat{r}+\hat{R}-1)^2 + (2\hat{R}-1)^2 - 4(\hat{r}+\hat{R}-1)(2\hat{R}-1)\cos\left[\beta\left(\frac{1}{2}-\hat{\varphi}\right)\right]\right\}. \tag{9.63}$$

Here

$$\hat{\delta}_h = \frac{\delta_h}{h_C}, \qquad \hat{\varepsilon} = \frac{\varepsilon}{h_C}, \qquad \hat{R} = \frac{R_2}{(R_2 - R_1)}.$$

When the pad is crowned, lubricant pressure might fall below ambient. Liquids, in impure state, can support only negligible tension, and the film will cavitate somewhere in the diverging part of the clearance space.

Table 9.2 compares experimental with numerical data in one particular case; sample isobars and isotherms are displayed in Figure 9.23.

Table 9.2. *Comparison of performance data for a thrust pad*

	Experimental	Numerical
$T_{\max}(^\circ\mathrm{C})$	>95	107.61
F(kg)	96,300	96,682
$\hat{\varepsilon}$	0.9	0.7

$\Theta_L = \Theta_* = \Theta_R = 38.5^\circ\mathrm{C}$, $\mu(\Theta_*) = 2.62 \times 10^{-5}$ Pa · s, $\bar{R}_2/\Delta = 2.545$, $\beta = 24^\circ$, $\delta = 1.094 \times 10^{-4}$, $m_x = 0.0$, $m_y = 1.0$, Re = 51.398, Pr = 714.69, $\Lambda = 2.1962$, Pe $= 1.323 \times 10^8$, Nu = 100.0.

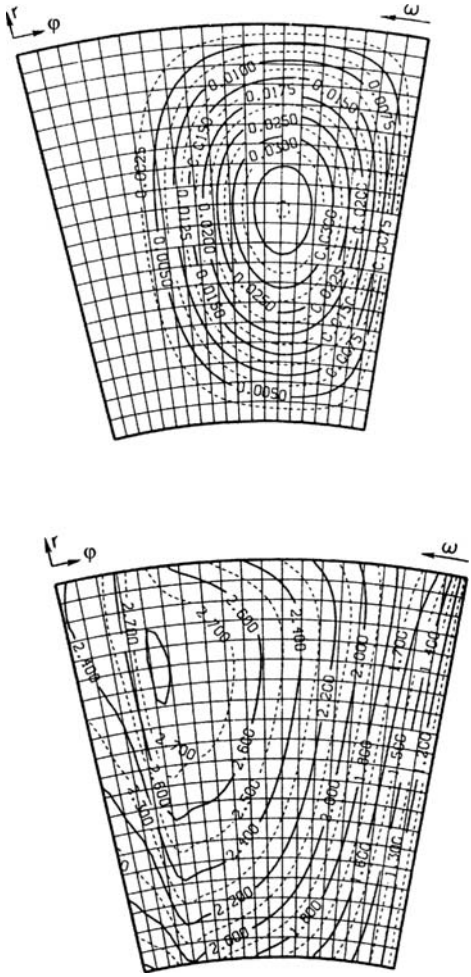

Figure 9.23. Isobars, $P = \text{const.}$, (a) and isotherms, $T = \text{const.}$ (b) on a deformed pad under the conditions of Table 9.2. (Reprinted with permission from Jeng, M. C., Zhou, G. R. and Szeri, A. Z. Thermohydrodynamic solution of pivoted thrust pads, part I: Theory. *ASME Journal of Tribology*, **108**, 195–207, 1986.)

To aid the designer, one may now perform a parameteric study of THD thrust pad performance and tabulate the results. But, the large number of input parameters is discouraging. Making matters worse is the fact that in a thrust bearing the pivot position of the pad remains fixed, while it is the tilt of the pad that changes with a change of the mechanical and/or thermal loading of the bearing. In the course of the numerical work, on the other hand, the analyst begins by specifying the slope of the pad and obtains the performance parameters, including the center of pressure, as a result of calculations. The position of the center of pressure he calculates will not, in general, coincide with the desired pivot location, and the analyst will be required to iterate on the pad tilt angle until agreement is reached. This, of course, is an expensive proposition.

Table 9.3. *Effect of viscosity variation*

	$T_{\max}$	f	j	$\hat{Q}$
Test run 1	4.2154	0.03485	3.50	1.62[a]
	(2.7952)	(0.02222)	(2.36)	(1.88)[b]
Test run 2	3.7472	0.03485	3.49	1.62[a]
	(2.6013)	(0.02363)	(2.52)	(1.85)[b]

[a] $\hat{\mu} = h/h_{\max}$,
[b] *THD*.

Table 9.3 indicates the effect variable viscosity has on pad performance for two sets of input parameters. The first entries for both test runs were calculated on the assumption that $\mu = h/h_{\max}$; a crude approximation to the equilibrium oil-film viscosity profile. The second entries for both runs correspond to three-dimensional THD solutions.

In Figure 9.24, we display the results of our study of the effects of pad crowning. Again, these solutions have the pivot position fixed, i.e., the results were arrived at via the iteration procedure described previously. The figure suggests a strong effect of crowning on the load capacity and on the lubricant flow. The effect is considerably less on the value of the maximum pad temperature and on the rate of dissipation.

The dynamic behavior of the tilting thrust pad bearing has been discussed in Chapter 4. The solutions discussed there were based on thermohydrodynamic theory.

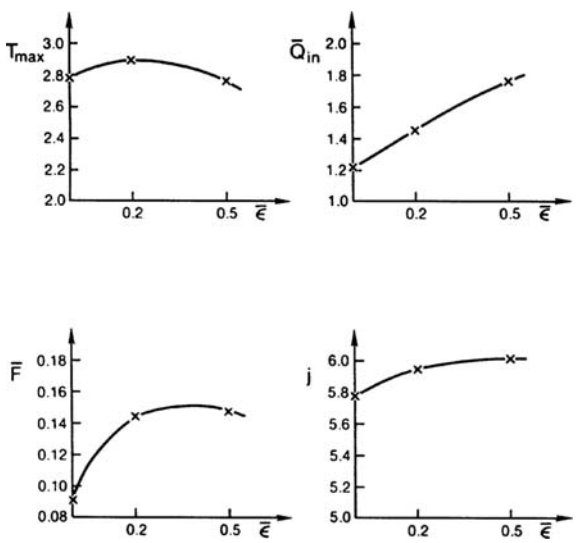

Figure 9.24. Effect of pad crowning on pad performance. (Reprinted with permission from Jeng, M. C., Zhou, G. R. and Szeri, A. Z. Thermohydrodynamic solution of pivoted thrust pads, part I: Theory. *ASME Journal of Tribology*, **108**, 195–207, 1986.)

9.5 Nomenclature

N	rotational speed
Nu	Nusselt number
P	specific bearing load
Pe	Peclet number
Pr	molecular Prandtl number
$\mathrm{Pr}^{(T)}$	turbulent Prandtl number
Q, Q_s	oil flow, leading edge, side
R	journal radius
R_b	pad outer radius
Re	global Reynolds number
R_ε	reduced Reynolds number
R_h	local Reynolds number
S	Sommerfeld number
W	external load
Λ	dissipation number
c	specific heat of lubricant
h	film thickness
k	thermal conductivity, oil
k_B	thermal conductivity, pad
ε	eccentricity ratio
ε_m, ε_h	eddy diffusivities
λ	heat transfer coefficient
p	pressure
Θ, Θ_p, Θ_s, Θ_a	temperature, lubricant, pad, shaft, ambient
μ	viscosity
ν	kinematic viscosity
ρ	lubricant density
$\{u', v', w'\}$	velocity fluctuation
$\{\bar{U},\ \bar{V},\ \bar{W}\}$	mean velocity
C	radial clearance
$\bar{\bar{C}}_{xx\ldots}$	dimensionless damping coefficient
c_f	friction factor
$\bar{\bar{K}}_{xx\ldots}$	dimensionless stiffness coefficient
L	bearing axial length
$\bar{M}$	dimensionless stability threshold speed
x_{cavity}	position of cavitation boundary
β	pad angle
$\tau_c,\ \tau_{av},\ \tau_w$	Couette, average, wall shear stress
ω	angular velocity
R_1, R_2	pad radius, inner, outer
d	pad thickness
(x, y, z)	coordinates, located in C
Δ	width of pad
$\hat{\rho}$	function of $\bar{r}$

$(\hat{})$	nondimensional quantity
$(\bar{})$	average quantity
$()'$	fluctuating quantity
$()_*$	reference quantity

9.6 References

Abramovitz, S. 1956. Turbulence in a tilting-pad thrust bearing. *ASME Trans.*, **78**, 7–14.

Bielec, M. K. and Leopard, A. J. 1970. Tilting pad thrust bearings: factors affecting performance and improvements with directed lubrication. *Instn. Mech. Engrs. Tribology Convention*, Paper 13.

Boncompain, R., Fillon, M. and Frêne, J. 1986. Analysis of thermal effects in hydrodynamic bearings. *ASME Journal of Tribology*, **108**, 219–224.

Booser, E. R. 1984. *CRC Handbook of Lubrication*. CRC Press, Boca Raton, FL.

Boswall, R. O. 1928. *The Theory of Fluid Film Lubrication*. Longmans and Green, New York.

Bouard, L., Fillon, M. and Frêne, J. 1995. Comparison between three turbulent models – application to thermohydrodynamic performances of tilting-pad journal bearings. In Fillon, M. 1995. *Habilitation a Diriger les Recherches*. Universite de Poitiers, France.

Bouard, L., Fillon, M. and Frêne, J. 1996. Thermohydrodynamic analysis of tilting-pad journal bearings operating in turbulent flow regime. *ASME Journal of Tribology*, **118**, 225–231.

Bouchoule, C., Fillon, M., Nicolas, D. and Baresi, F. 1996. Experimental study of thermal effects in tilting-pad journal bearings at high operating speeds. *ASME Journal of Tribology*, **118**, 532–538.

Cameron, A. 1966. *The Principles of Lubrication*. Wiley, New York.

Capitao, J. W. 1976. Performance characteristics of tilting pad thrust bearings at high operating speeds. *ASME Trans.*, **96**, 7–14.

Capitao, J. W., Gregory, R. S. and Whitford, R. P. 1976. Effects of high operating speeds on tilting pad thrust bearing performance. *ASME Trans.*, **98**, 73–80.

Charnes, A., Osterle, F. and Saibel, E. 1952. On the energy equation for fluid-film lubrication. *Proc. Roy. Soc.*, **A 214**, 133–136.

Constantinescu, V. N. 1972. Basic relationships in turbulent lubrication and their extension to include thermal effects. *ASME-ASLE Int. Lub. Conf.*, Paper No. **72-Lub-16**, New York.

Cope, W. F. 1949. A hydrodynamical theory of film lubrication. *Proc. Roy. Soc.*, **A 197**, 201–217.

Dowson, D. and Taylor, C. M. 1979. Cavitation in bearings. *Ann. Rev. Fluid Mech.*, **11**, 35–66.

Dowson, D. and Hudson, J. D. 1963. Thermohydrodynamic analysis of the finite slider bearing, I, II. *Instn. Mech. Engrs., Lubrication & Wear Convention*, Paper Nos. 4 & 5.

Dowson, D. and March, C. N. 1967. A thermohydrodynamic analysis of journal bearings. *Proc. Instn. Mech. Engrs.*, **181**, 117–126.

Dowson, D., Hudson, J. D., Hunter, B. and March, C. N. 1966. An experimental investigation of the thermal equilibrium of the steadily loaded journal bearing. *Proc. Instn. Mech. Engrs.*, **181**, 70–80.

Elrod, H. G. and Ng, C. W. 1967. A theory for turbulent fluid films and its application to bearings. *ASME Journal of Lubrication Technology*, **89**, 346–359.

Ettles, C. M. M. 1970. Hot-oil carry-over in thrust bearings. *Proc. Inst. Mech. Engrs*, **184**, 75–81.

Ettles, C. M. M. 1992. The analysis of pivoted pad journal bearing assemblies considering thermoelastic deformation and heat transfer effects. *STLE Tribology Transactions*, **35**, 156–162.

Ezzat, H. A. and Rohde, S. M. 1972. A study of the thermohydrodynamic performance of finite slider bearings. *ASME Journal of Lubrication Technology*, **95**, 298–307.

Ferron, J. 1982. *Contribution a l'etude desphenomenes thermiques dans les paliers hydrodynamiques.* These de 3^{e} Cycle, Universite de Poitiers, France.

Ferron, J., Frêne, J. and Boncompain, R. 1983. A study of the performance of a plain journal bearing – comparison between theory and experiments. *ASME Journal of Lubrication Technology*, **105**, 422–428.

Fillon, M. 1995. *Habilitation a Diriger les Recherches.* Universite de Poitiers, France.

Fillon, M. and Frêne, J. 1995. Numerical simulation and experimental results on thermo-elasto-hydrodynamic tilting-pad journal bearings. IUTAM Symposium on Numerical Simulation of Non-isothermal Flow of Viscoelastic liquids, pp. 85–99. Kluwer Academic Publisher.

Fillon, M., Desbordes, H., Frêne, J. and Chan He Wai, C. 1996. A global approach to thermal effects including pad deformations in tilting pad journal bearings submitted to unbalance load. *ASME Journal of Tribology*, **118**, 169–174.

Gadangi, R. K., Palazzo, A. B. and Kim, J. 1996. Transient analysis of plain and tilt pad journal bearings including fluid film temperature effects. *ASME Journal of Tribology*, **118**, 423–430.

Gardner, W. W. and Ulschmid, J. G. 1974. Turbulence effects in two journal bearing applications. *ASME Journal of Lubrication Technology*, **96**, 15–21.

Gethin, D. T. and Medwell, J. O. 1985. An experimental investigation into the thermohydrodynamic behavior of a high speed cylindrical bore journal bearing. *ASME Journal of Tribology*, **107**, 538–543.

Gollub, J. P. and Swinney, H. L. 1981. *Transition to Turbulence.* Springer-Verlag, New York.

Gregory, R. S. 1974. Performance of thrust bearings at high operating speeds. *ASME Journal of Lubrication Technology*, **96**, 7–14.

Ha, H. C., Kim, H. J. and Kim C. 1995. Inlet pressure effects on the thermohydrodynamic performance of large tilting pad journal bearing. *ASME Journal of Tribology*, **117**, 160–165.

Hinze, J. O. 1975. *Turbulence.* McGraw-Hill, New York.

Hopf, G. and Schüler, D. 1989. Investigations on large turbine bearings working under transitional conditions between laminar and turbulent flow. *ASME Journal of Tribology*, **111**, 628–634.

Jeng, M. C., Zhou, G. R. and Szeri, A. Z. 1986a. Thermohydrodynamic solution of pivoted thrust pads, part I: Theory. *ASME Journal of Tribology*, **108**, 195–207.

Jeng, M. C., Zhou, G. R. and Szeri, A. Z. 1986b. Thermohydrodynamic solution of pivoted thrust pads, part II: static loading. *ASME Journal of Tribology*, **108**, 208–213.

Kaufman, H. N., Szeri, A. Z. and Raimondi, A. A. 1978. Performance of a centrifugal disk lubricated bearing. *ASLE Trans.*, **21**, 314–322.

Kestin, J. and Richardson, P. D. 1963. Heat transfer across turbulent, incompressible boundary layers. *Int. J. Heat Mass Transfer*, **6**, 147–189.

McCallion, H., Yousif, F. and Lloyd, T. 1970. The analysis of thermal effects in a full journal bearing. *ASME Journal of Lubrication Technology*, **192**, 578–586.

Mittwollen, N. and Glienicke, J. 1990. Operating conditions of multi-lobe journal bearings under high thermal loads. *ASME Journal of Tribology*, **112**, 330–338.

Monmousseau, P., Fillon, M. and Frêne, J. 1996. Transient thermoelastohydrodynamic study of tilting pad journal bearings – comparison between experimental data and theoretical results. *ASME/STLE Tribology conference*, Paper No. **96-trib-29**, San Francisco.

Ng, C. W. and Pan, C. H. T. 1965. A linearized turbulent lubrication theory. *ASME J. Basic Engineering*, **87**, 675–688.

Pinkus, O. 1990. *Thermal Aspects of Fluid Film Tribology.* ASME Press, New York.

Raimondi, A. A. and J. Boyd. 1958. A solution for the finite journal bearing and its application to analysis and design. *ASLE Trans.*, **1**, 159–209.

Safar, Z. and Szeri, A. Z. 1974. Thermohydrodynamic lubrication in laminar and turbulent regimes. *ASME Journal of Lubrication Technology*, **96**, 48–56.

Seireg, A. and Ezzat H. 1972. Thermohydrodynamic phenomena in fluid film lubrication. *ASME* Paper No. **72-Lub-25**.

Simmons, J. E. L. and Dixon, S. J. 1994. Effect of load direction, preload, clearance ratio and oil flow on the performance of a 200 mm journal pad bearing. *STLE Tribology Transactions*, **37**, 227–236.

Suganami, T. and Szeri, A. Z. 1979a. A thermohydrodynamic analysis of journal bearings. *ASME Journal of Lubrication Technology*, **101**, 21–27.

Suganami, T. and Szeri, A. Z. 1979b. Parametric study of journal bearing performance: the 80° partial arc bearing. *ASME Journal of Lubrication Technology*, **101**, 486–491.

Taniguchi, S., Makino, T., Takeshita, K. and Ichimura, T. 1990. A thermohydrodynamic analysis of large tilting-pad journal bearing in laminar and turbulent flow regimes with mixing. *ASME Journal of Tribology*, **112**, 542–548.

Yu, T. S. and Szeri, A. Z. 1975. Partial journal bearing performance in the laminar regime. *ASME Journal of Lubrication Technology*, **97**, 94–101.

CHAPTER 10

Lubrication with Non-Newtonian Fluids

Non-Newtonian effects might assume importance in lubrication due mainly to two circumstances: lubrication with process fluids and treatment of the lubricant with polymeric additives. A third circumstance that calls for extension of classical theory to non-Newtonian fluids is relevant to lubrication of elastohydrodynamic (EHD), contacts. When subjected to very rapid rates of shear, viscous fluids exhibit viscoelastic effects. Consider a typical EHD contact, where the pressure might be 2–3 GPa and the rate of shear $10^6\ s^{-1}$. A lubricant particle will traverse this contact in a millisecond or less. In comparable time, the response of the oil to the applied shear will change from that of a viscous liquid to that of an elastic solid (*glass transition*) and back to a viscous liquid.

To characterize the quality of fluid response to applied shear, viz., its departure from "fluidity," we assign the *Deborah number*, defined by

$$\text{De} = \frac{\text{duration of fluid memory}}{\text{duration of deformation process}}$$

It is customary to measure duration of fluid memory[1] by the Maxwell *relaxation time* $\lambda = \mu/G$, where μ is the viscosity of the fluid and G is its elastic modulus in shear. Denoting duration of the deformation process, i.e., the *process time*, by τ, we have

$$\text{De} = \frac{\lambda}{\tau}.$$

Purely viscous response, i.e., Newtonian behavior, is characterized by De = 0. If De is small, fluids of the differential type (to be defined below) can be used, but if De is large, integral models must be employed to characterize fluid response (Huilgol, 1975).

Evidence for viscoelastic behavior of lubricants was first demonstrated by Barlow et al. (1967, 1972), who subjected the lubricant to oscillating shear. At low frequency, fluid response was characterized by viscous shear, and by predominantly elastic shear as the period of oscillation was decreased to a value less than the relaxation time of the fluid.

Bourgin (1979) classified lubricant flows according to their Deborah number. Denoting the film aspect ratio L_y/L_{xz} (Section 2.2) by ε, he listed the following categories:

(1) $\text{De} = O(\varepsilon^2)$: viscous behavior predominates and nonlinear viscous models, such as *power law*, may be employed with success.
(2) $\text{De} = O(\varepsilon)$: fluids of the differential type are applicable. All phenomenological functions depend only on $\text{tr}(\boldsymbol{D})$, where $\boldsymbol{D}$ is the stretching tensor (2.33).
(3) $\text{De} = O(1)$: fluids of the differential type are no longer applicable. Integral representation must be employed (Huilgol, 1975).

Bourgin (1979) found that for a typical journal bearing lubricated with a viscoelastic lubricant $\text{De} = O(\varepsilon)$, and for rolling contact bearings, $\text{De} = O(1)$.

[1]There is ambiguity in associating a time constant with a material, as it will be influenced by the deformation process applied in its evaluation.

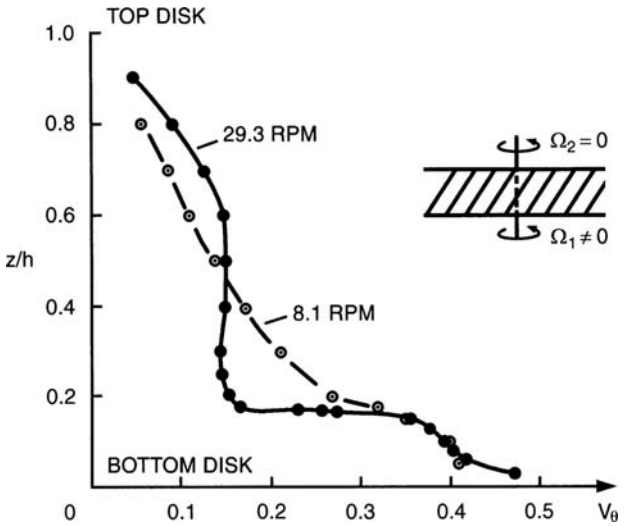

Figure 10.1. Flow of dilute polymer between parallel rotating disks.

For Deborah number De $= 0$, there is no memory, and there is, therefore, no elastic response. This purely viscous fluid may, however, posses a viscosity that depends on the local rate of shear (Sirivat, Rajagopal and Szeri, 1988). A striking example of shear thinning, i.e., viscosity decreasing as the fluid is being worked on, is shown in Figure 10.1.

Figure 10.1 plots the tangential velocity of flow induced by rotating parallel disks in dilute separan. Note that at an intermediate layer between disks there is a sudden change of velocity, suggesting that locally the fluid suffers reduction of viscosity there. The flow depicted in Figure 10.1 approximates to the flow occurring in a thrust bearing.

10.1 Hydrodynamic Lubrication

Summary of Previous Work

Various constitutive models have been employed in studying the flow of nonlinear viscous fluids in journal and thrust bearings. One of the early treatments of the problem of lubrication by a non-Newtonian lubricant was by Ng and Saibel (1962). In their regular perturbation treatment of the plane slider, they assumed a stress constitutive equation of the form

$$\tau = \mu \frac{\partial u}{\partial y} + \varepsilon k \left| \frac{\partial u}{\partial y} \right|^2 \frac{\partial u}{\partial y}. \tag{10.1}$$

Equation (10.1) arises when one restricts the flow of a thermodynamically compatible third grade fluid of the differential type (Fosdick and Rajagopal, 1980) to the geometry of Ng and Saibel. In another paper, Hsu and Saibel (1965) use the constitutive equation

$$\tau + k\tau^3 = \mu \frac{\partial u}{\partial y}, \tag{10.2}$$

which is applicable to both pseudoplastic, $k > 0$, and dilatant, $k < 0$, fluids. For the pseudoplastic case, they find that the load capacity is reduced when compared to the performance of

a Newtonian lubricant. Fix and Paslay (1967) investigated the lubricant elasticity effects of a Maxwell-type material in a long journal bearing. Their most significant finding is a reduction of the attitude angle, which equals $\pi/2$ under Sommerfeld conditions, due to elasticity of the lubricant. In an experimental paper, Tao and Philippoff (1967) show a pressure distribution for viscoelastic liquids that is flatter than obtained for a Newtonian fluid. They also indicate a shift into the downstream direction of the positive pressure peak. Considering the in-plane oscillation of a flat plate in a linearly viscoelastic fluid, Tanner (1969) argues that the normal stress effect is unimportant in the usual lubrication application. For an elastoviscous liquid, i.e., a nonlinear Reiner-Rivlin fluid generalized to include unequal cross stresses, Hanin and Harnoy (1969) show a load capacity higher than given by a Newtonian fluid.

The Stokesian velocity field is a solution to the equations of motion of a plane, steady, noninertial flow of a second grade fluid (Giesekus, 1963; Tanner, 1966). This fact has been used to extend the results of lubrication theory to flows involving fluids of second grade (Davis and Walters, 1973). Since the velocity field in the two problems are identical, the only quantity that is to be calculated is a "modified" pressure field.[2] For a long journal bearing, Davies and Walters find qualitative agreement with the earlier results of Fix and Paslay (1967) concerning the magnitude of the attitude angle. The result of Giesekus and Tanner has been extended to dynamically loaded bearings by Harnoy and Hanin (1974). Tichy (1978) also looks at small-amplitude rapid oscillations and includes temporal inertia for a Lodge rubber-like liquid. Tichy finds perturbation solution to order δ, where δ is the amplitude of plate motion. At low Deborah number, the viscoelastic effect is found to be negligible. However, Tichy warns that bearing operation at high Deborah number could give rise to various resonance effects. He then goes on to state that the often-noted discrepancy between theory and experiment (e.g., Harnoy and Philippoff, 1976) may be in part explained by resonance phenomena.

Beris, Armstrong, and Brown (1983) look at slightly eccentric rotating cylinders; in fact, their perturbation solution is in terms of the eccentricity. The extra boundary conditions, required for a second grade fluid, are the requirement for single valuedness of the solution in the multiply connected domain. Christie, Rajagopal, and Szeri (1987) find solutions at arbitrary eccentricity.

For differential fluids of complexity 1, Bourgin and Gay (1983) investigate the influence of non-Newtonian effects on load capacity in a finite journal bearing and in a Rayleigh bearing (Bourgin and Gay, 1984). Buckholtz looks at the performance of power law lubricants in a plane slider (Buckholtz, 1984) and in a short bearing (Buckholtz and Hwang, 1985). Verma, Sharman, and Ariel (1983) investigated flow of a second-grade, thermodynamically compatible fluid between corotating porous, parallel disks. Flow of a second-grade fluid between parallel disks rotating about noncoincident axes was discussed by Rajagopal (1981).

Lubrication with Power Law Fluid

For $\mathrm{De} = 0$, non-Newtonian fluids are often modeled by power law. This section follows the analysis given by Johnson and Mangkoesoebroto (1993) for lubrication with a power law lubricant. The objective is to model shear thinning lubricants that do not exhibit elasticity.

[2]The results of Tanner and Giesekus do not address the issue of uniqueness (Fosdick and Rajagopal, 1978; Rajagopal, 1984).

The viscosity for a power law fluid can be written as

$$\mu = \mu(2D_{ij}D_{ij})^{\frac{n-1}{2}}, \tag{10.3a}$$

where $\boldsymbol{D} = \frac{1}{2}(\nabla \boldsymbol{v} + \nabla \boldsymbol{v}^T)$ is the stretching tensor, which is a generalization to three dimensions of (Tanner, 1985)

$$\mu = k\left[\left(\frac{\partial v_1}{\partial x_2}\right)^2\right]^{\frac{n-1}{2}} = k\left|\frac{\partial v_1}{\partial x_2}\right|^{n-1}. \tag{10.3b}$$

The power law *consistency index*, k, and the power law exponent, n, are material parameters. $n = 1$ yields the Newtonian fluid, for pseudoplastic (shear thinning) fluid, $n < 1$. Shear thinning is characteristic of high polymers, polymer solutions, and many suspensions.

For flow in the (x_1, x_2) plane, $v_3 = 0$ and the equations of motion take the form

$$\begin{aligned}
\rho\left(\frac{\partial v_1}{\partial t} + v_1\frac{\partial v_1}{\partial x_1} + v_2\frac{\partial v_1}{\partial x_2}\right) &= -\frac{\partial \rho}{\partial x_1} + \frac{\partial T_{11}}{\partial x_1} + \frac{\partial T_{12}}{\partial x_2},\\
\rho\left(\frac{\partial v_2}{\partial t} + v_1\frac{\partial v_2}{\partial x_1} + v_2\frac{\partial v_2}{\partial x_2}\right) &= -\frac{\partial \rho}{\partial x_2} + \frac{\partial T_{21}}{\partial x_1} + \frac{\partial T_{22}}{\partial x_2}.
\end{aligned} \tag{10.4}$$

An application of the lubrication assumption $(L_y/L_{yx}) \ll 1$ to Eq. (10.3a) permits us to write

$$(T_{11}, T_{12}, T_{22}) = \left|\frac{\partial v_1}{\partial x_2}\right|^{n-1}\left(\frac{\partial v_1}{\partial x_1}, \frac{\partial v_1}{\partial x_2}, \frac{\partial v_2}{\partial x_2}\right). \tag{10.5a}$$

Substituting Eq. (10.5a) and the assumption

$$\left(\frac{L_y}{L_{xz}}\right)^{1+n}\frac{L_y^n U_*^{2-n}\rho}{\mu} \ll 1 \tag{10.5b}$$

into Eq. (10.4), we obtain

$$0 = -\frac{\partial p}{\partial x_1} + \frac{\partial T_{12}}{\partial x_2}, \qquad 0 = -\frac{\partial p}{\partial x_2}, \tag{10.6}$$

where T_{12} is given by Eq. (10.5a). These and the following equations are already in nondimensional form.

Note that for Newtonian fluid, $n = 1$, Eq. (10.5b) is a constraint on the reduced Reynolds number, Eq. (2.58d):

$$\mathrm{R}_\varepsilon = \left(\frac{L_y}{L_{xz}}\right)\frac{L_y U_*}{\nu} \ll 1.$$

Since the pressure is independent of x_2 by Eq. (10.6b), we can integrate Eq. (10.6a)

$$T_{12} = \left|\frac{\partial v_1}{\partial v_2}\right|^{n-1}\frac{\partial v_1}{\partial x_2} = p' x_2 + c(x_1, t), \tag{10.7}$$

where the prime symbolizes derivative with respect to x_1. Inverting and formally integrating Eq. (10.7), we have

$$v_1 = \int_0^{x_2} |p'x_2 + c|^{\frac{1-n}{n}}(p'x_2 + c)dx_2 + U_1, \tag{10.8}$$

where U_1 is the (dimensional) velocity of the surface $x_2 = 0$.

From the equation of mass conservation (2.16c), we have, upon substituting for v_1 from Eq. (10.8) and integrating across the film,

$$v_2 = \frac{1}{n}\int_0^{x_2} (\xi - x_2)|p'\xi - c|^{\frac{1-n}{n}}(p''\xi + c')d\xi. \tag{10.9}$$

The boundary conditions are

$$\begin{aligned} &v_1 = U_1(t), \qquad v_2 = 0 \quad \text{at } x_2 = 0, \\ &v_2 = U_2(t), \qquad v_2 = V(t) \quad \text{at } x_2 = H(x_1, t) = \frac{h(x_1)}{h_0}. \end{aligned} \tag{10.10}$$

Satisfaction of conditions (10.10) by Eqs. (10.8) and (10.9) yields two (nondimensional) equations for the unknowns $p'(x_1, t)$ and $c(x_1, t)$:

$$\int_0^1 |Hp'\xi + c|^{\frac{1-n}{n}}(Hp'\xi + c)d\xi = \frac{U_0}{H}, \tag{10.11}$$

$$H^3 p'' \int_0^1 |p'H\xi + c|^{\frac{1-n}{n}}(\xi - 1)\xi d\xi + H^2 c' \int_0^1 |p'H\xi + c|^{\frac{1-n}{n}}(\xi - 1)d\xi = nV, \tag{10.12}$$

where we put $U_0 = U_2 - U_1$.

Though the integrals indicated in Eqs (10.11) and (10.12) can be evaluated in closed form, Johnson and Mangkoesoebroto (1993) were unable to integrate the coupled nonlinear differential equations numerically, as these equations are extremely stiff for $n < 1$. They did, however, discover an analytical solution based on a nontrivial transformation, reducing Eqs. (10.11) and (10.12) to two coupled algebraic equations for p' and c. The dimensionless pressure is plotted against dimensionless position in Figure 10.2 for a parabolic slider at various values of n, as obtained by Johnson and Mangkoesoebroto (1993).

Fluids of the Differential Type

For a Newtonian fluid, Eq. (2.53), the extra stress, $\boldsymbol{T} + p\boldsymbol{I}$, is a linear function of the current value of the stretching tensor $\boldsymbol{D}$. The function of proportionality, μ, is a constant, or at most a function of temperature. Newtonian fluids exhibit neither elasticity nor memory effects.

To describe elasticity and memory effects as well as viscous response, we obviously need more general constitutive equations than Eq. (2.53). This leads us to define a class of materials, called *simple materials*, which includes a vast range of nonlinear materials from classical linear elastic to linearly viscous (Truesdell and Noll, 1965).

In Chapter 2, we represented motion of the material point $\boldsymbol{X}$ by the mapping

$$\boldsymbol{x} = \boldsymbol{\chi}(\boldsymbol{X}, t), \tag{2.1}$$

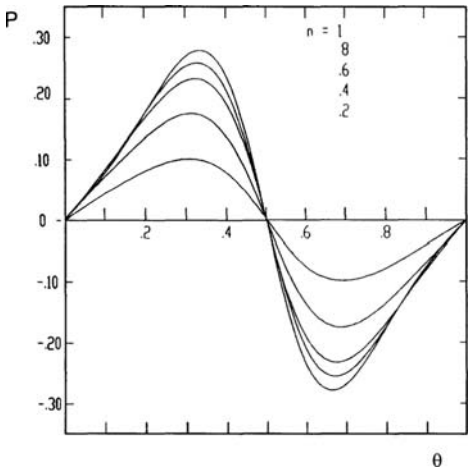

Figure 10.2. Dimensionless pressure versus dimensionless position for parabolic slider $H = 1 + 10.4(x_1 - 5)^2$ lubricated by power law fluid. (Reprinted with permission from Johnson, M. W. and Mangkoesoebroto, S. Analysis of lubrication theory for the power law fluid. *ASME Journal of Tribology*, **115**, 71–77, 1993.)

where $\boldsymbol{x}$ is the place occupied by $\boldsymbol{X}$ at time t. We can also define the motion of a neighborhood of $\boldsymbol{X}$, relative to $\boldsymbol{X}$, with the help of Eq. (2.1) by the Taylor series expansion

$$\boldsymbol{x}(\hat{\boldsymbol{X}}, t) = \boldsymbol{x}(\boldsymbol{X}, t) + \nabla \boldsymbol{\chi}\,(\hat{\boldsymbol{X}} - \boldsymbol{X}) + \cdots \tag{10.13a}$$

where $\hat{\boldsymbol{X}}$ is an arbitrary point in the neighborhood. There is a large class of engineering materials that possess no microstructure, called *simple materials* by Noll, for which the expansion in Eq. (10.13a) can be terminated after the linear term. For simple materials we write

$$d\boldsymbol{x} = \boldsymbol{F}\,d\boldsymbol{X}, \tag{10.13b}$$

where $\boldsymbol{F} = \nabla \boldsymbol{\chi}$ is the deformation gradient, and postulate that stress at a point depends on the deformation of the neighborhood of that point. But to account for memory effects, we consider the whole past history of deformation rather than just its current value. For an incompressible *simple fluid*, therefore, our constitutive equation is

$$\boldsymbol{T} + p\boldsymbol{I} = \mathfrak{h}^{t}_{s=-\infty}(\boldsymbol{F}(s)). \tag{10.14}$$

Here $\boldsymbol{F}(s)\,, -\infty = s \leq t$, is the *history of deformation*, up to the present time t, and $\mathfrak{h}$ represents some tensor valued functional of this history. Equation (10.14) expresses the postulate that in a simple fluid, stress at a material point $\boldsymbol{X}$ and time t depends on the past deformation of the neighborhood of that material point.[3]

As it stands, Eq. (10.14) is far too general, however, to be of practical use. The question is, how to proceed? There have been, in the past, two methods of attack:

(1) *Specialize the motion* to a class of motions such that memory is given little opportunity to make itself felt. Such specialization leads to *viscometric flows* (Tanner, 1985), solution of special problems is possible.

[3]The Newtonian constitutive equation is obtained from Eq. (10.14) by setting

$$\mathfrak{h}^{t}_{-\infty}(\boldsymbol{F}(s)) = -\mu \frac{d}{ds}[\boldsymbol{F}(s) + \boldsymbol{F}(s)^{T}]\,|_{s=0} = 2\mu \boldsymbol{D}.$$

(2) *Specialize the material* by specializing the constitutive equation (10.14). The question is, how to handle memory dependence?

We shall follow the second of these alternatives but, for starters, restrict fluid memory to an arbitrary short interval. Making this interval infinitesimal, we obtain a class of fluids for which the history of motion prior to an infinitesimal time is irrelevant in determining the stress.

The most important of the fluids with infinitesimal memory are *fluids of the differential type*, those in which the stress at $\boldsymbol{X}$ is determined by the first n material derivatives of the deformation gradient $\boldsymbol{F}$

$$\boldsymbol{T} + p\mathbf{1} = \boldsymbol{f}(\dot{\boldsymbol{F}}, \ddot{\boldsymbol{F}} \cdots, \boldsymbol{F}^{(n-1)}, \boldsymbol{F}^{(n)}). \tag{10.15a}$$

By requiring frame indifference, it can be shown that Eq. (10.15a) must be of the form

$$\boldsymbol{T} + p\mathbf{1} = \boldsymbol{f}(\boldsymbol{A}_{(1)}, \boldsymbol{A}_{(2)}, \ldots, \boldsymbol{A}_{(n)}). \tag{10.15b}$$

Here the $\boldsymbol{A}_{(k)}$ are the coefficients in the Taylor expansion

$$\boldsymbol{C}_t(t') = \boldsymbol{F}_t^T(t')\boldsymbol{F}_t(t') = \mathbf{1} - \boldsymbol{A}_{(1)}(t-t') + \frac{1}{2!}\boldsymbol{A}_{(2)}(t-t')^2 + \cdots$$

and are defined through the recurrence formula

$$\boldsymbol{A}_{(n+1)} = \frac{d}{dt}\boldsymbol{A}_{(n)} + \boldsymbol{L}^T\boldsymbol{A}_{(n)} + \boldsymbol{A}_{(n)}\boldsymbol{L}, \tag{10.16}$$

where

$$\boldsymbol{A}_{(1)} \equiv \boldsymbol{D} = \frac{1}{2}(\boldsymbol{L} + \boldsymbol{L}^T).$$

$\boldsymbol{L}$ is the velocity gradient tensor, Eq. (2.30), d/dt represents material derivative, Eq. (2.9), and the $\boldsymbol{A}_{(k)}$ are the *Rivlin-Ericksen tensors*. The tensor $\boldsymbol{C}_t(t')$ is the relative strain tensor, and $\boldsymbol{F}_t(t')$ is the relative deformation gradient.

The principle of material frame indifference, more specifically the requirement that the constitutive equation be frame indifferent, dictates that $\boldsymbol{f}$ in Eq. (10.15) must be an isotropic function, Eq. (2.45). But isotropic functions of symmetric tensors have polynomial representation (Truesdell and Noll, 1965). As an example, an isotropic function of the first two Rivlin-Ericksen tensors $\boldsymbol{A}_{(1)}$ and $\boldsymbol{A}_{(2)}$ can be written as

$$\begin{aligned}\boldsymbol{T} + p\mathbf{1} &= \boldsymbol{f}(\boldsymbol{A}_{(1)}, \boldsymbol{A}_{(2)}) \\ &= \alpha_1\boldsymbol{A}_{(1)} + \alpha_2\boldsymbol{A}_{(2)} + \alpha_3\boldsymbol{A}_{(1)}^2 + \alpha_4\left(\boldsymbol{A}_{(1)}\boldsymbol{A}_{(2)} + \boldsymbol{A}_{(2)}\boldsymbol{A}_{(1)}\right) + \alpha_5\boldsymbol{A}_{(2)}^2 \\ &\quad + \alpha_6\left(\boldsymbol{A}_{(1)}^2\boldsymbol{A}_{(2)} + \boldsymbol{A}_{(2)}\boldsymbol{A}_{(1)}^2\right) + \alpha_7\left(\boldsymbol{A}_{(1)}\boldsymbol{A}_{(2)}^2 + \boldsymbol{A}_{(2)}^2\boldsymbol{A}_{(1)}\right) \\ &\quad + \alpha_8\left(\boldsymbol{A}_{(1)}^2\boldsymbol{A}_{(2)}^2 + \boldsymbol{A}_{(2)}^2\boldsymbol{A}_{(1)}^2\right),\end{aligned} \tag{10.17}$$

where the α_i's depend on the basic invariants of $\boldsymbol{A}_1$ and $\boldsymbol{A}_2$. Equation (10.17) defines the *Rivlin-Ericksen fluid* of complexity 2.

The constitutive relation (10.15b) of a fluid of *complexity n* includes the first n Rivlin-Ericksen tensors $\boldsymbol{A}_{(1)}, \ldots, \boldsymbol{A}_{(n)}$. Thus the fluid of complexity 1, from Eq. (10.17), is

$$\boldsymbol{T} + p\mathbf{1} = \alpha_1\boldsymbol{A}_{(1)} + \alpha_3\boldsymbol{A}_{(1)}^2. \tag{10.18}$$

We introduce now the concept of slow, or retarded, motion. If $\boldsymbol{\chi}(\boldsymbol{X}, t)$ is a motion, the corresponding *retarded motion* is defined as

$$\text{ret}\boldsymbol{\chi}(\boldsymbol{X}, t) \equiv \boldsymbol{\chi}(\boldsymbol{X}, rt), \qquad 0 < r < 1. \tag{10.19a}$$

If the motion $\boldsymbol{\chi}(\boldsymbol{X}, t)$ carries particle $\boldsymbol{X}$ into spatial position $\boldsymbol{x}$ at time t, the retarded motion ret $\boldsymbol{\chi}(\boldsymbol{X}, t)$ will carry the same particle into $\boldsymbol{x}$ at the later time $\hat{\boldsymbol{t}} = t/r$. The smaller the value of r, the slower is the motion. It can be shown that

$$\text{ret}\, \boldsymbol{A}_{(n)} = r^n \boldsymbol{A}_{(n)}, \tag{10.19b}$$

so the fluid of complexity 1 in retarded motion is

$$\boldsymbol{T} = -p\mathbf{1} + \alpha_1 r \boldsymbol{A}_{(1)} + \alpha_3 r^2 \boldsymbol{A}_{(1)}^2. \tag{10.19c}$$

The *fluid of grade* 1 is, by definition, of degree 1 in r. Thus the fluid of grade 1 is, from Eq. (10.19c),

$$\boldsymbol{T} = -p\mathbf{1} + \mu \boldsymbol{A}_{(1)}. \tag{10.20a}$$

This is a Newtonian fluid [as $\boldsymbol{A}_{(1)} = \boldsymbol{D}$] if $\mu = \text{const}$.

The grade two fluid has constitutive equation

$$\boldsymbol{T} = -p\mathbf{1} + \mu \boldsymbol{A}_{(1)} + \alpha_1 \boldsymbol{A}_{(2)} + \alpha_2 \boldsymbol{A}_{(1)}^2. \tag{10.20b}$$

We can attach meaning to the concept of complexity and grade as follows: *The lower the complexity, the lower the order of velocity derivatives that are used to determine the stress. The lower the grade, the slower is the motion that can be adequately described by the constitutive equation.*

When a fluid of the differential type is used in journal bearings for which the Deborah number is $O(10^{-3})$, it is impossible to distinguish between two fluids having both complexity $n > 3$ and degree $d > 1$. Moreover, all phenomenological functions will depend on the trace, $\text{tr}(\boldsymbol{A}_{(1)}^2)$ (Bourgin, 1979).

Lubrication with a Third Grade Fluid

The Cauchy stress, $\boldsymbol{T}$, in an incompressible homogeneous fluid of third grade is related to the fluid motion in the following manner (Truesdell and Noll, 1965).

$$\begin{aligned}\boldsymbol{T} = &-p\mathbf{1} + \mu \boldsymbol{A}_{(1)} + \alpha_1 \boldsymbol{A}_{(2)} + \alpha_2 \boldsymbol{A}_{(1)}^2 + \beta_1 \boldsymbol{A}_{(3)} \\ &+ \beta_2 \left[\boldsymbol{A}_{(1)}\boldsymbol{A}_{(2)} + \boldsymbol{A}_{(2)}\boldsymbol{A}_{(1)}\right] + \beta_3 \left(\text{tr}\boldsymbol{A}_{(1)}^2\right) \boldsymbol{A}_{(1)}.\end{aligned} \tag{10.21}$$

The thermodynamics and stability of a fluid modeled by Eq. (10.21) have been studied in detail by Rajagopal and Fosdick (1980). They find that if all motions of the fluid are to be compatible with thermodynamics, then the following restrictions apply:

$$\begin{aligned}&\mu \geq 0, \qquad |\alpha_1 + \alpha_2| < \sqrt{24\mu\beta_3}, \qquad \alpha_1 \geq 0, \\ &\beta_1 = \beta_2 = 0 \quad \text{and} \quad \beta_3 \geq 0.\end{aligned}$$

Thus, in the case of a thermodynamically compatible fluid of grade three, the stress constitutive equation takes the simplified form

$$\boldsymbol{T} = -p\mathbf{1} + \mu \boldsymbol{A}_{(1)} + \alpha_1 \boldsymbol{A}_{(2)} + \alpha_2 \boldsymbol{A}_{(1)}^2 + \beta_3 \left(\text{tr}\boldsymbol{A}_{(1)}^2\right) \boldsymbol{A}_{(1)}. \tag{10.22}$$

Note that if the material constants α_1 and α_2 are zero, then

$$\boldsymbol{T} = -p\mathbf{1} + \left(\mu + \beta_3 \mathrm{tr}\boldsymbol{A}_{(1)}^2\right)\boldsymbol{A}_{(1)}. \tag{10.23}$$

The above model is a special fluid of complexity 1 (Truesdell and Noll, 1965) and in a sense can be thought of as a type of power law model, for in a simple shear flow the shear stress, τ, is related to the velocity gradient, $\partial u/\partial y$, by

$$\tau = \left[\mu + \beta_3 \left(\frac{\partial u}{\partial y}\right)^2\right]\frac{\partial u}{\partial y}. \tag{10.24}$$

Models of the type in Eq. (10.24) have been studied by Bourgin and Gay (1983) within the context of flows in journal bearings. Ng and Saibel (1962) have used the model (10.24) to study the flow occurring in a slider bearing [cf. Eq. (10.1)]. They, however, assumed the coefficient that corresponds to β_3 in our model to be negative. The power law model used by Buckholtz (1985) would reduce to Eq. (10.24) if the parameter N of his model was made equal to 3. The model (10.24) includes the classical linearly viscous fluid, the incompressible homogeneous fluid of second grade, a subclass of the fluids of complexity 1, and several other models that have been used in lubrication as special cases.

On substituting Eq. (10.24) into the balance of linear momentum

$$\mathrm{div}\,\boldsymbol{T} + \rho\boldsymbol{b} = \rho\frac{d\boldsymbol{v}}{dt}, \tag{2.27a}$$

we obtain the following equations of motion (Rajagopal and Fosdick, 1980):

$$\begin{aligned}\mu\Delta\boldsymbol{v} + \alpha_1(\Delta\boldsymbol{\omega}\times\boldsymbol{v}) + \alpha_1(\Delta\boldsymbol{v})_t + (\alpha_1+\alpha_2)\{\boldsymbol{A}_{(1)}\Delta\boldsymbol{v} + 2\mathrm{div}[(\mathrm{grad}\,\boldsymbol{v})(\mathrm{grad}\,\boldsymbol{v})^T]\}\\ + \beta_3\boldsymbol{A}_{(1)}\left(\mathrm{grad}|\mathrm{A}_{(1)}|^2\right) + \beta_3|\boldsymbol{A}_{(1)}|^2\Delta\boldsymbol{v} + \rho\boldsymbol{b} - \rho\boldsymbol{v}_t - \rho(\boldsymbol{\omega}\times\boldsymbol{v}) = \mathrm{grad}\,P\end{aligned} \tag{10.25}$$

where

$$P = p - \alpha_1\boldsymbol{v}\cdot\Delta\boldsymbol{v} - \frac{1}{4}(2\alpha_1+\alpha_2)\,|\boldsymbol{A}_{(1)}|^2 + \frac{1}{2}\rho|\boldsymbol{v}|^2.$$

In the above equation, Δ denotes the Laplacian, $(\cdot)_t$ the partial derivative of the quantity within the parentheses with respect to time, and $|\boldsymbol{v}|$ and $|\boldsymbol{A}_{(1)}|$ the inner product norm and the trace norm of $\boldsymbol{v}$, and $\boldsymbol{A}_{(1)}$ respectively.

When

$$\boldsymbol{v} = u(x, y)\boldsymbol{i} + v(x, y)\boldsymbol{j}$$

for two-dimensional flow is substituted into Eq. (10.25), the equations are made nondimensional in accordance with Eq. (2.58) and terms of order $(L_y/L_{xz})^2$ and higher are neglected, we arrive at (Kacou, Rajagopal, Szeri, 1987)

$$\begin{aligned}\frac{\partial^2\bar{u}}{\partial\bar{y}^2} + \frac{\alpha_1 U}{\mu R}\left\{\frac{\partial\bar{u}}{\partial\bar{x}}\frac{\partial^2\bar{u}}{\partial\bar{y}^2} + \bar{v}\frac{\partial^3\bar{u}}{\partial\bar{y}^3} + \bar{u}\frac{\partial^3\bar{u}}{\partial\bar{y}^2\partial\bar{x}} + 3\frac{\partial\bar{u}}{\partial\bar{y}}\frac{\partial^2\bar{u}}{\partial\bar{y}\partial\bar{x}}\right\}\\ + 6\frac{\beta_3 U^2}{\mu}\frac{1}{C^2}\left(\frac{\partial\bar{u}}{\partial\bar{y}}\right)^2\frac{d^2\bar{u}}{d\bar{y}^2} = \frac{\partial\bar{P}}{\partial\bar{x}},\end{aligned} \tag{10.26}$$

$$4\frac{\alpha_1 U}{\mu R}\frac{\partial\bar{u}}{\partial\bar{y}}\frac{\partial^2\bar{u}}{\partial\bar{y}^2} = \frac{\partial\bar{P}}{\partial\bar{y}}. \tag{10.27}$$

Defining a modified scalar field $\bar{p}^*$ through

$$\bar{p}^* = \bar{P} - 2\frac{\alpha_1 U}{\mu R}\left(\frac{\partial \bar{u}}{\partial y}\right)^2,$$

we can rewrite Eqs. (10.26) and (10.27) as

$$\frac{\partial^2 \bar{u}}{\partial \bar{y}^2} + \gamma\left\{\frac{\partial \bar{u}}{\partial \bar{x}}\frac{\partial^2 \bar{u}}{\partial \bar{y}^2} + \bar{v}\frac{\partial^3 \bar{u}}{\partial \bar{y}^3} + \bar{u}\frac{\partial^3 \bar{u}}{\partial \bar{y}^2 \partial \bar{x}} + \frac{\partial \bar{u}}{\partial \bar{y}}\frac{\partial^2 \bar{v}}{\partial \bar{y}^2}\right\} + \delta\left(\frac{\partial \bar{u}}{\partial \bar{y}}\right)^2 \frac{d^2 \bar{u}}{\partial \bar{y}^2} = \frac{\partial \bar{p}^*}{\partial \bar{x}}. \tag{10.28}$$

$$0 = \frac{\partial \bar{p}^*}{\partial \bar{y}}. \tag{10.29}$$

In the above equations, the nondimensional parameters

$$\frac{\alpha_1 U}{\mu R} \equiv \gamma \quad \text{and} \quad \frac{\beta_3 U^2}{\mu C^2} \equiv \delta.$$

are measures of the non-Newtonian nature of the fluid. Notice that the nondimensional parameter, γ, can be expressed as the ratio of the nondimensional numbers Re, Γ, and (R/C) as

$$\gamma = \frac{\mathrm{Re}}{\Gamma}\left(\frac{R}{C}\right),$$

where

$$\mathrm{Re} \equiv \frac{\rho U C}{\mu} \quad \text{and} \quad \Gamma \equiv \frac{\rho R^2}{\alpha_1}.$$

The nondimensional number, Γ, (Fosdick and Rajagopal, 1978) is referred to as the absorption number. Truesdell (1964) recognized that the term involving α_1 controls the diffusion of vorticity from a boundary. δ is a measure of the ratio of the non-Newtonian shear stress to that of the Newtonian shear stress. It follows from Eqs. (10.28) and (10.29) that

$$\bar{p}^* = \bar{p}^*(x),$$

and thus the modified pressure $\bar{p}^*$ does not vary across the film thickness.

Introducing the stream function $\bar{\psi}(\bar{x}, \bar{y})$ through

$$\bar{u} = \frac{\partial \bar{\psi}}{\partial \bar{y}}, \qquad \bar{v} = \frac{\partial \bar{\psi}}{\partial \bar{x}}, \tag{10.30}$$

we can express Eq. (10.28) as[4]

$$\frac{\partial^4 \bar{\psi}}{\partial \bar{y}^4} + \gamma\left\{-\frac{\partial \bar{\psi}}{\partial \bar{x}}\frac{\partial^5 \bar{\psi}}{\partial \bar{y}^5} + \frac{\partial \bar{\psi}}{\partial \bar{y}}\frac{\partial^5 \bar{\psi}}{\partial \bar{x}\,\partial \bar{y}^4}\right\} + \delta\left\{2\frac{\partial^2 \bar{\psi}}{\partial \bar{y}^2}\left(\frac{\partial^3 \bar{\psi}}{\partial \bar{y}^3}\right)^2 + \left(\frac{\partial^2 \bar{\psi}}{\partial \bar{y}^2}\right)^2 \frac{d^4 \bar{\psi}}{\partial \bar{y}^4}\right\} = 0. \tag{10.31}$$

[4]Equation (10.31) is of higher order than the corresponding equation for the classical linearly viscous fluid, when $\gamma \neq 0$. We thus need additional boundary conditions to solve the problem. We overcome the paucity of boundary conditions by resorting to regular perturbation, although the problem is one of singular perturbation.

We shall assume that the stream function, $\bar{\psi}$, the pressure, $\bar{p}^*$, and the flow rate, $\bar{Q} \equiv Q/CU$, can all be expanded in power series in γ and δ. For the sake of convenience, we shall drop the bars that appear in the nondimensional terms.

Let

$$\begin{aligned} \psi &= \sum_{m=0}^{\infty}\sum_{n=0}^{\infty} \gamma^n \delta^m \psi_{nm}(x, y), \\ p^* &= \sum_{m=0}^{\infty}\sum_{n=0}^{\infty} \gamma^n \delta^m P_{nm}(x, y), \\ Q &= \sum_{m=0}^{\infty}\sum_{n=0}^{\infty} \gamma^n \delta^m Q_{nm}(x, y). \end{aligned} \tag{10.32}$$

Substituting Eq. (10.32) into Eq. (10.31) and equating like powers, we obtain the following system of differential equations (first three equations are shown):

$n = 0, m = 0$:

$$\frac{\partial^4 \psi_{00}}{\partial y^4} = 0, \tag{10.33a}$$

$n = 1, m = 0$:

$$\frac{\partial^4 \psi_{10}}{\partial y^4} = \frac{\partial \psi_{00}}{\partial x}\frac{\partial^5 \psi_{00}}{\partial y^5} - \frac{\partial \psi_{00}}{\partial y}\frac{\partial^5 \psi_{00}}{\partial x\, \partial y^4}, \tag{10.33b}$$

$n = 0, m = 1$:

$$\frac{\partial^4 \psi_{01}}{\partial y^4} = -2\frac{\partial^2 \psi_{00}}{\partial y^2}\left(\frac{\partial^3 \psi_{00}}{\partial y^3}\right)^2 - \left(\frac{\partial^2 \psi_{00}}{\partial y^2}\right)\left(\frac{\partial^4 \psi_{00}}{\partial y^4}\right). \tag{10.33c}$$

Although these equations are linear if solved sequentially, they are rapidly becoming cumbersome as n, m increase (Kacou, Rajagopal, and Szeri, 1987).

The boundary conditions that accompany Eqs. (10.33) are

$$\left.\begin{aligned} \psi_{nm} &= 0 \\ \frac{\partial \psi_{nm}}{\partial y} &= 0 \end{aligned}\right\} n, m = 0, 1, 2, \ldots, \quad \text{at } y = 0, \tag{10.34a}$$

$$\left.\begin{aligned} \psi_{nm} &= Q_{nm} \\ \frac{\partial \psi_{nm}}{\partial y} &= \begin{cases} 1, n = m = 0 \\ 0, n, m = 1, 2, \ldots \end{cases} \end{aligned}\right\} \quad n, m = 0, 1, 2, \ldots \quad \text{at } y = H. \tag{10.34b}$$

The zeroth-order perturbation corresponds to the Newtonian case. It is trivial to show that the solution is

$n = 0, m = 0$:

$$\psi_{00} = \frac{1}{6}\frac{dP_{00}}{dx}\left(y^3 - \frac{3}{2}Hy^2\right) + \frac{1}{2}\frac{y^2}{H}. \tag{10.35a}$$

The pressure, P_{00}, can be obtained in the standard manner as is done in classical lubrication theory:

$$P_{00}(x) = \frac{6\varepsilon \sin x(2 + \varepsilon \cos x)}{(2 + \varepsilon^2)(1 + \varepsilon \cos x)^2}. \tag{10.35b}$$

Proceeding in a manner identical to that used for determining P_{00} in classical lubrication theory, we can show that

$n = 1, m = 0$:

$$\frac{d^2P_{10}}{dx^2} + \frac{3}{H}\frac{dH}{dx}\frac{dP_{10}}{dx} + \left(\frac{dP_{00}}{dx}\right)^2\left(\frac{dH}{dx}\right)^2 - \frac{4}{H^3}\frac{d^2H}{dx^2} - \frac{H}{2}\left(\frac{dP_{00}}{dx}\right)^2\frac{d^2H}{dx^2} - \frac{9}{H^2}\left(\frac{dH}{dx}\right)^2\frac{\partial P_{00}}{dx} + \frac{3}{H}\frac{d^2H}{dx^2}\frac{dP_{00}}{dx} + \frac{18}{H^4}\left(\frac{dH}{dx}\right)^2 = 0, \tag{10.36}$$

$n = 0, m = 1$:

$$\frac{d^2P_{01}}{dx^2} + \frac{3}{H}\frac{dH}{dx}\frac{dP_{01}}{dx} + \frac{H}{5}\frac{dH}{dx}\left(\frac{dP_{00}}{dx}\right)^3 - \frac{9}{10H}\frac{dH}{dx}\left(\frac{dP_{00}}{dx}\right)^2 + \frac{2}{H^3}\frac{dH}{dx}\frac{dP_{00}}{dx} - \frac{6}{H^5}\frac{dH}{dx} = 0. \tag{10.37}$$

We are now in a position to determine the pressure up to first-order,

$$p^* = P_{00} + \gamma P_{01} + \delta P_{10} + O(\gamma\delta). \tag{10.38}$$

The first-order correction, P_{10}, is plotted in Figure 10.3; this profile is very close to the one calculated by Harnoy and Philippoff (1976) for a second-grade fluid, using results due to Giesekus and Tanner. In Figure 10.4, we plot pressure distribution at $\gamma = 0.75$ for various values of δ.

It is fairly clear that viscoelastic effects are not significant at small values of the Deborah number in steady flow. If, however, $\Omega^* > 1$, anomalous resonance effects might occur. There is virtually no information on viscoelastic effects in the flow regime $\Omega^* \sim \mathrm{R}_\varepsilon > 1$. Here inertia effects might interact nonlinearly with viscoelastic effects, leading to changed bearing performance.

Among the many models that have been proposed in the literature to describe non-Newtonian fluid behavior at arbitrary De, one that has gained considerable attention is the K-BKZ fluid model (Kay, 1962; Bernstein, Kearsley, and Zapas, 1963). The model has been shown to be consistent with statistical modeling of polymeric fluids. It might, thus, be applicable when investigating process fluid lubrication. K-BKZ fluids have memory and are represented by integral constitutive equations. Because of their memory, K-BKZ fluids might show significant departure from Newtonian fluids in squeeze film applications. Little information is available currently on numerical simulation of fluids with finite memory at high shear rates, but initial studies on special simple integral constitutive models have already provided interesting information regarding the structure of the boundary layer. There is much work to be done here by both the rheologist and the numerical analyst. The properties and predictive capabilities of some non-Newtonian fluids are tabulated by Tanner (1985).

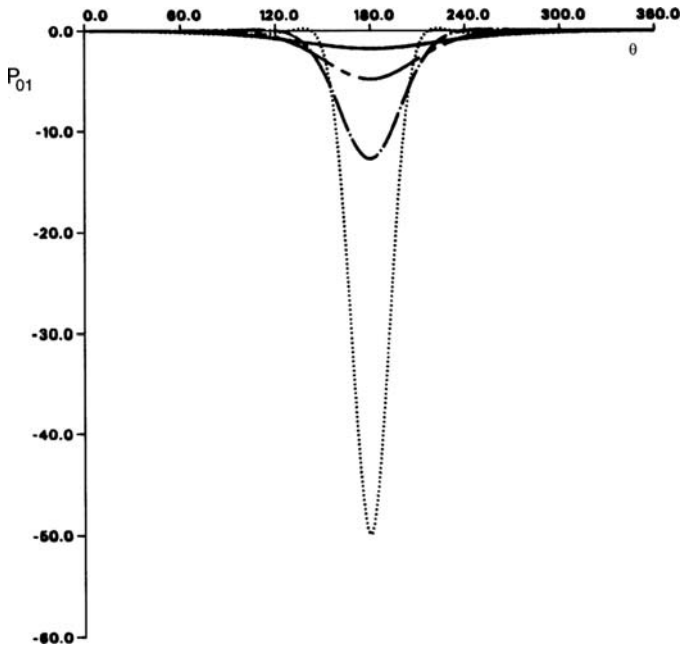

Figure 10.3. Pressure correction P_{01} in a journal bearing lubricated by a fluid of grade three (——, $\epsilon = 0.2$; – – –, $\varepsilon = 0.4$; – · –, $\epsilon = 0.6$; . . . , $\epsilon = 0.8$). (Reprinted with permission from Kacou, A., Rajagopal, K. R. and Szeri, A. Z. Flow of a fluid of the differential type in a journal bearing. *ASME Journal of Tribology*, **109**, 100–108, 1987.)

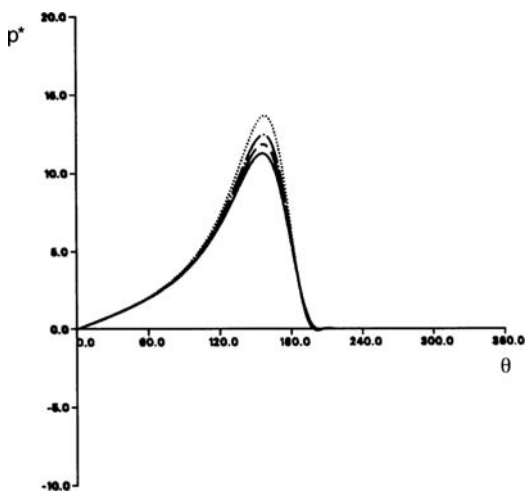

Figure 10.4. Pressure distribution for $\gamma = 0.75$ (– –, Newtonian; – · –, $\gamma = 0$, $\delta = 0.01$; – • –, $\gamma = 0$, $\delta = 0.02$; . . . . , $\gamma = 0$, $\delta = 0.04$). (Reprinted with permission from Kacou, A., Rajagopal, K. R. and Szeri, A. Z. Flow of a fluid of the differential type in a journal bearing. *ASME Journal of Tribology*, **109**, 100–108, 1987.)

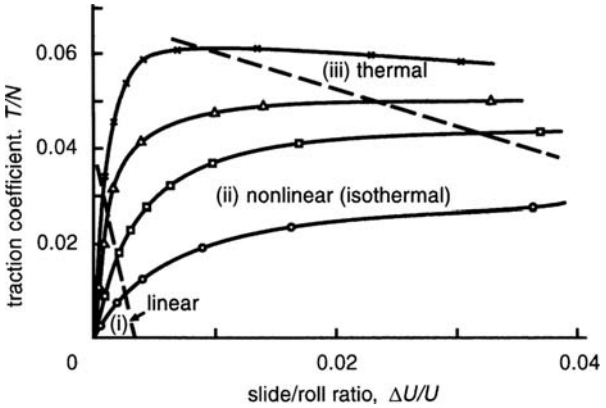

Figure 10.5. Typical traction curves measured on a two disk machine in line contact (p: x, 1.03 GPa; Δ, 0.68 GPa; □, 0.5 GPa; ○, 0.4 GPa). (Reprinted by permission of the Council of the Institution of Mechanical Engineers from Johnson, K. L. and Cameron, R. 1967. Shear behavior of EHD oil films. *Proc. Inst. Mech. Eng.*, **182**, 307, 1967.)

10.2 Elastohydrodynamic Lubrication

In discussing the various regimes of lubricant behavior in EHD contacts, we refer to Figure 10.5, where the coefficient of friction is plotted against the ratio of sliding speed to rolling speed for a two-disk machine (Johnson and Cameron, 1967). Under the conditions of the experiment, the ordinate is proportional to shear stress, τ, and the abscissa to shear rate, $\dot{\gamma}$. The various curves are drawn for various constant Hertzian pressure. Each of these curves is seen to have a linear portion, $\tau \propto \dot{\gamma}$, where the fluid is essentially Newtonian. For large p, the region of this type of behavior is limited to very small values of $\dot{\gamma}$. At larger strain rate, the lubricant exhibits nonlinear, shear thinning behavior, though it may still be treated by isothermal theories. At still larger strain rate, the lubricant enters the zone of predominant thermal effects. Here the shear stress shows a slight decrease with increasing strain rate (Johnson and Tevaarwerk, 1977).

The principal features of EHD contacts, such as the sudden contraction of the film or the existence of the second pressure peak, remain largely unchanged by thermal effects if the maximum Hertzian load $p < 0.5$ GPa. If, on the other hand, as it is in practice, $p > 0.5$ GPa, then thermal effects are so severe that lubricant behavior departs significantly from the linear. In these cases traction forces calculated on the assumption of a Newtonian lubricant are an order of magnitude larger than found experimentally.

There have been several theories put forth to explain and model traction in the nonlinear region. Fein (1967) and Harrison and Trachman (1972) suggested that the fluid, during its brief stay in the contact zone, would not have time to assume equilibrium values of density, viscosity, and shear modulus. Dyson (1970) suggested that the apparent decrease of viscosity in steady, continuous shear of a linearly viscoelastic fluid can be used to model the nonlinear part of the traction curve. An alternative explanation, that the shear stress-shear rate is nonlinear for the lubricant, was offered by Trachman and Cheng (1972). Smith (1962) proposed that in the high-pressure contact zone the lubricant was shearing like a plastic solid.

Constitutive Models

The *Maxwell fluid*, as shown in Figure 10.6, consists of a spring and a dashpot connected in series. The model represents a fluid because the flow in the dashpot will continue as long as force is applied. A sudden change in loading, however, will be accompanied by an instantaneous elastic response due to the spring. To derive the constitutive equation for this fluid, we note that the spring and the dashpot are subjected to the same force τ,

$$\tau = G\gamma_E, \qquad \tau = \mu\dot{\gamma}_v, \tag{10.39a}$$

where G is the elastic modulus in shear and μ is the viscosity, while the total deformation γ is the sum of the deformations γ_E and γ_v in the spring and the dashpot, respectively,

$$\begin{aligned}\dot{\gamma} &= \dot{\gamma}_E + \dot{\gamma}_v \\ &= \frac{1}{G}\dot{\tau} + \frac{1}{\mu}\tau.\end{aligned} \tag{10.39b}$$

For the integral counterpart of Eq. (10.39b), see Tanner (1985).

Figure 10.6. Maxwell's constitutive model for a linearly viscoelastic fluid.

Experimental data of common lubricants display viscoelastic effects in the linear, small strain rate region of the traction curve (Figure 10.5), such as might be described by Eq. (10.39b), but show nonlinearity in the large strain rate region. To reconcile Eq. (10.39) with both types of fluid response, Johnson and Tevaarwerk (1976) proposed a nonlinear version of Eq. (10.39b),

$$\dot{\gamma} = \frac{1}{G}\dot{\tau} + F(\tau), \tag{10.40}$$

requiring the nonlinear function $F(\tau)$ to reduce to τ/μ for small τ. They also generalized Eq. (10.40) to three dimensions by changing the argument of F to the von Mises equivalent stress

$$\tau_e = \sqrt{\frac{1}{2}\tau_{ij}\tau_{ij}},$$

replacing $\dot{\gamma}$ with the stretching tensor D_{ij} and τ with the shear stress tensor $\tau_{ij} = T_{ij} + p\delta_{ij}$. This generalized form is

$$2D_{ij} = \frac{1}{G}\frac{d\tau_{ij}}{dt} + \frac{\tau_{ij}}{\tau_e}F(\tau_e). \tag{10.41}$$

When applying Eq. (10.41) to situations in which the deformations are large, Tevaarwerk and Johnson (1975) recommend using the "*convected time derivative*," a kind of total

derivative that introduces no dependence on a fixed reference frame (Tanner, 1985). But, provided that the recoverable elastic strain τ_e/G remains small, the error introduced by employing time derivative of the stress in place of its "convected" derivative are small, of order $(\tau_e/G)^2$. Tichy (1996), nevertheless, employs the *convected Maxwell model* in a perturbation analysis in which the Deborah number is the small parameter.

Johnson and Tevaarwerk (1977) used the Eyring hyperbolic sine as the viscous element, as this gave best fit to experimental data. At the same time, it has its roots in molecular theory. The rheological equation proposed by them is

$$2D_{ij} = \frac{1}{G}\frac{d\tau_{ij}}{dt} + \frac{\tau_{ij}}{\tau_e}\frac{\tau_0}{\mu}\sinh\left(\frac{\tau_e}{\tau_0}\right). \tag{10.42}$$

Here the representative stress, τ_0, is a measure of the stress above which the behavior becomes appreciably nonlinear. For $\tau_e \ll \tau_0$, Eq. (10.42) reduces to the linear Maxwell model. This rheological model, Eq. (10.42), was later extended by Houpert (1985) to include thermal effects.

Bair and Winer (1979) modified the Maxwell model by including a limiting shear stress. In earlier rheological models, measurements of contact behavior had to be made in order to predict contact behavior. In the Bair-Winer model, which shows good agreement with experiments, material constants, viz., the low shear stress viscosity μ_0, the limiting elastic shear modulus G_∞, and the limiting yield shear stress τ_L, are all derived from sources other than EHD contact measurements and are functions of pressure and temperature. The Bair-Winer equation relating stress to motion (in one dimension) in the lubricant is[5]

$$\dot{\gamma} = \dot{\gamma}_e + \dot{\gamma}_v = \frac{1}{G_\infty}\frac{d\tau}{dt} - \frac{\tau_L}{\mu_0}\tanh^{-1}\left(\frac{\tau}{\tau_L}\right). \tag{10.43}$$

If the limiting shear stress is very large, then Eq. (10.43) reduces to the classical Maxwell model. If, on the other hand, $(1/G_\infty) \to 0$, the limiting case of viscoelastic behavior, the model behaves fluid like

$$\dot{\gamma} = -\frac{\tau_L}{\mu_0}\tanh^{-1}\left(\frac{\tau}{\tau_L}\right). \tag{10.44}$$

Equation (10.43) can be written in the nondimensional form

$$\frac{\mu_0\dot{\gamma}}{\tau_L} = \mathrm{De}\frac{\partial\bar{\tau}}{\partial\bar{t}} + F(\bar{\tau}), \tag{10.45}$$

where $\bar{\tau} = \tau/\tau_L$ and $De = \mu U/Gl$. If $De \to 0$, signifying absence of viscoelastic effects, Eq. (10.44) results.

There is another factor to consider, solidification of the lubricant. Experiments show that for the synthetic lubricant 5P4E, the glass transition pressure is ~160 MPa at room temperature. Experimentation is very critical near glass transition to guide modeling. In the pressure-shear plate impact experiments of Zang (1995) and Zhang and Ramesh (1996), a projectile carrying a 2-inches diameter plate is accelerated down the barrel of a light gas gun

[5]Originally, Bair and Winer specified logarithmic dependence for the nonlinear viscous shear term; this was changed later to the tangent hyperbolic function, as the former is not antisymmetric with respect to zero stress. Najji et al. (1989) offer a slight modification of Eq. (10.43) by writing it in terms of the equivalent stress, τ_e; this, or another stress norm, must be used if extension to three dimensions is required. See also Bair and Winer (1992).

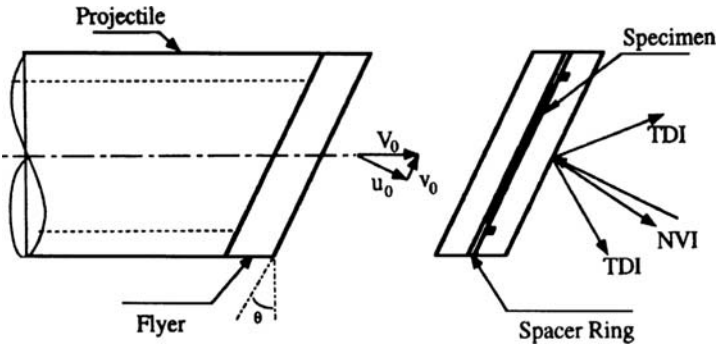

Figure 10.7. Schematic of the pressure-plate impact experiment. (Reprinted with permission from Zang, Y. and Ramesh, K. T. The behavior of an elastohydrodynamic lubricant at moderate pressures and high shear rates. *ASME Journal of Tribology*, **118**, 162–168, 1996.)

and hits a parallel stationary target. On impact, the normal wave arrives first at the sample and compresses it. The compressed lubricant is then subjected to a shearing deformation. A schematic of the arrangement is shown in Figure 10.7.

In Figure 10.8, the dimensionless shear stress is plotted against the dimensionless shear rate for two lubricants, Santotrac 50 and 5P4E. The limiting shear τ_L is almost independent of shear rate in the relatively high shear rate regime ($\dot{\gamma} > 10^3$ s^{-1}), as indicated in Figure 10.8, but is dependent on pressure (Figure 10.9).

Glass transition, or more correctly liquid-solid transition, was first reported by Johnson and Roberts (1974). The critical pressure at which glass transition occurs is strongly temperature dependent, as was first shown by Johnson and Roberts (1974), Alsaad et al. (1978), and Bair and Winer (1979). Several sets of data are shown in Figure 10.10.

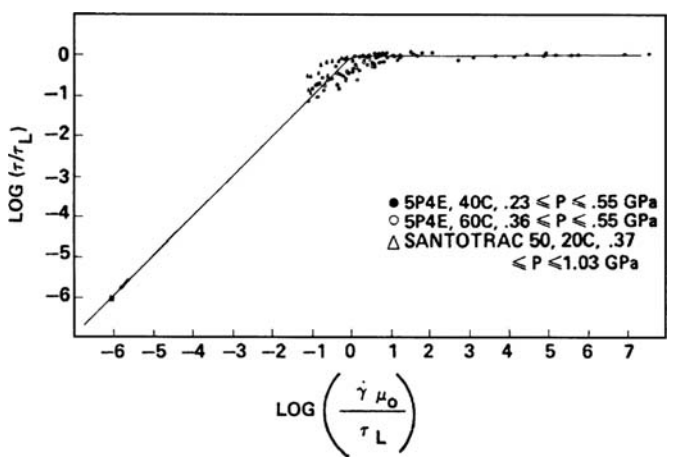

Figure 10.8. Dimensionless shear stress versus dimensionless shear rate. (Reprinted with permission from Bair, S. and Winer, W. O. A rheological model for elastohydrodynamical contacts. *ASME Journal of Lubrication Technology*, **101**, 248, 1979.)

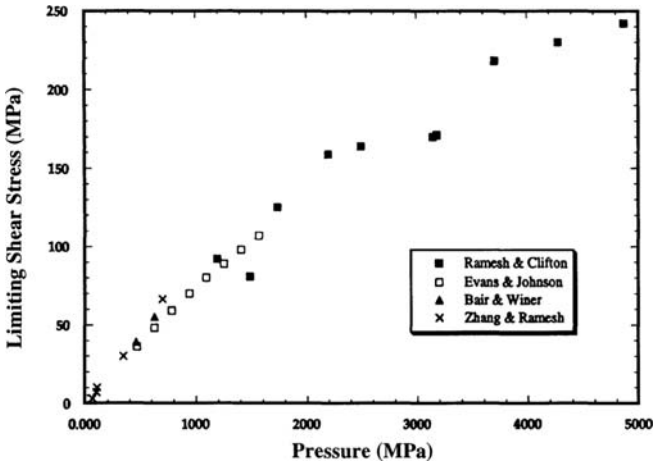

Figure 10.9. Variation of limiting shear with pressure. (Reprinted with permission from Zang, Y. and Ramesh, K. T. The behavior of an elastohydrodynamic lubricant at moderate pressures and high shear rates. *ASME Journal of Tribology*, **118**, 162–168, 1996.)

A Generalized non-Newtonian Reynolds Equation for EHL

Following on the work of Najji, Bou-Said, and Berthe (1989), Wolff and Kubo (1996) derived a generalized non-Newtonian Reynolds equation for isothermal EHD line contact. The basic equations that form the starting point of the analysis of Wolff and Kubo are

$$\frac{\partial p}{\partial x} = \frac{\partial \tau_{xy}}{\partial y}, \qquad \frac{\partial p}{\partial y} = 0, \qquad \frac{\partial p}{\partial z} = \frac{\partial \tau_{zy}}{\partial y}, \tag{10.46}$$

$$\frac{\partial \rho}{\partial t} + \operatorname{div}(\rho \boldsymbol{v}) = 0. \tag{2.16a}$$

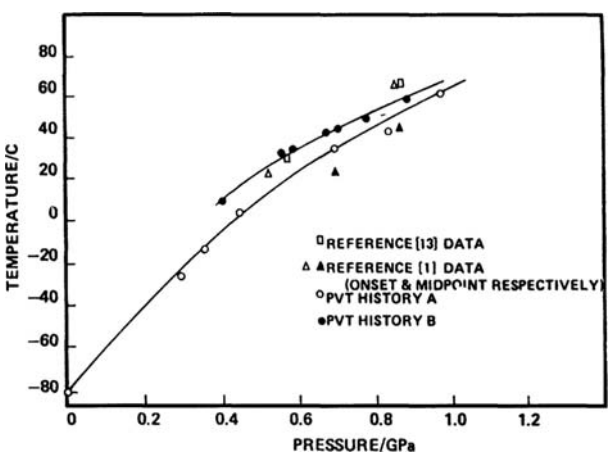

Figure 10.10. Comparison of four sets of liquid-solid transition data. (Reprinted with permission from Bair, S. and Winer, W. O. A rheological model for elastohydrodynamical contacts. *ASME Journal of Lubrication Technology*, **101**, 248, 1979.)

To take into account several types of rheological laws (Najji, Bou-Said, and Berthe, 1989; Wolff and Kubo, 1996), we put

$$\frac{\partial u}{\partial y} = A\frac{d\tau_{xy}}{dt} + \tau_{xy}F(\tau_e) \tag{10.47}$$

$$\frac{\partial w}{\partial y} = A\frac{d\tau_{xy}}{dt} + \tau_{zy}F(\tau_e), \tag{10.48}$$

where $\tau_e = (\tau_{xy}^2 + \tau_{zy}^2)^{1/2}$, $A = 1/G$ or $A = 0$ if fluid elasticity is ignored, and $F(\tau_e)$ represents the viscosity function.

Substituting Eq. (10.48) into Eq. (10.46), integrating twice with respect to y, and satisfying the no-slip boundary conditions

$$\begin{aligned} &u = u_1, \quad v = v_1, \quad w = w_1, \quad \text{for } y = 0, \\ &u = u_2, \quad v = v_2, \quad w = w_2, \quad \text{for } y = h, \end{aligned} \tag{10.49}$$

yields the velocity distribution

$$\begin{aligned} u = {} & \frac{\partial p}{\partial x}\left[\int_0^y F(\tau_e)\, y\, dy - \frac{f_1}{f_0}\int_0^y F(\tau_e)\, dy\right] + \frac{u_2 - u_1}{f_0}\int_0^y F(\tau_e)\, dy \\ & + u_1 + \int_0^y A\frac{d\tau_{xy}}{dt}dy - \frac{k_{x0}}{f_0}\int_0^y F(\tau_e)\, dy, \end{aligned} \tag{10.50a}$$

$$\begin{aligned} w = {} & \frac{\partial p}{\partial z}\left[\int_0^y F(\tau_e)\, y\, dy - \frac{f_1}{f_0}\int_0^y F(\tau_e)\, dy\right] + \frac{w_2 - w_1}{f_0}\int_0^y F(\tau_e)\, dy \\ & + w_1 + \int_0^y A\frac{d\tau_{zy}}{dt}dy - \frac{k_{z0}}{f_0}\int_0^y F(\tau_e)\, dy. \end{aligned} \tag{10.50b}$$

The velocity gradients are obtained from Eqs. (10.50) by differentiation

$$\frac{\partial u}{\partial y} = \frac{\partial p}{\partial x}F(\tau_e)\left(y - \frac{f_1}{f_0}\right) + \frac{u_2 - u_1}{f_0}F(\tau_e) + A\frac{d\tau_{xy}}{dt} - \frac{k_{x0}}{f_0}F(\tau_e), \tag{10.51a}$$

$$\frac{\partial w}{\partial y} = \frac{\partial p}{\partial z}F(\tau_e)\left(y - \frac{f_1}{f_0}\right) + \frac{w_2 - w_1}{f_0}F(\tau_e) + A\frac{d\tau_{zy}}{dt} - \frac{k_{z0}}{f_0}F(\tau_e), \tag{10.51b}$$

where

$$k_{x0} = \int_0^h A\frac{d\tau_{xy}}{dt}dy,$$

$$k_{z0} = \int_0^h A\frac{d\tau_{zy}}{dt}dy,$$

$$f_0 = \int_0^h F(\tau_e)\, dy,$$

$$f_1 = \int_0^h F(\tau_e)\, y\, dy,$$

From here on, the analysis follows that of Reynolds. We substitute Eqs. (10.50) into the equation of continuity and integrate across the film, as in Eq. (2.68), to obtain

$$\begin{aligned}
&\frac{\partial}{\partial x}\left[m_2\frac{\partial p}{\partial x}\right]+\frac{\partial}{\partial z}\left[m_2\frac{\partial p}{\partial z}\right]\\
&\quad=h\left[\frac{\partial(\rho_2 u_2)}{\partial x}+\frac{\partial(\rho_2 v_2)}{\partial z}\right]-\frac{\partial}{\partial x}\left[(u_1-u_2)\frac{m_1}{f_0}+u_2\rho_2 h-u_1 m_3\right]\\
&\qquad-\frac{\partial}{\partial z}\left[(w_1-w_2)\frac{m_1}{f_0}+w_2\rho_2 h-w_1 m_3\right]-\frac{\partial}{\partial x}[m_{x4}]\\
&\qquad-\frac{\partial}{\partial z}[m_{z4}]+\int_0^h\frac{\partial\rho}{\partial t}dy+\rho_2 v_2-\rho_1 v_1,
\end{aligned}\tag{10.52}$$

where

$$\begin{aligned}
m_1&=\int_0^h\left(\rho\int_0^y F(\tau_e)\,d\hat{y}\right)dy,\\
m_2&=\frac{f_1 m_1}{f_0}-\int_0^h\left(\rho\int_0^y F(\tau_e)\hat{y}\,d\hat{y}\right)dy,\\
m_3&=\int_0^h\rho dy,\\
m_{x4}&=\frac{k_{x0}m_1}{f_0}-\int_0^h\left(\rho\int_0^y A\frac{d\tau_{xy}}{dt}\,d\hat{y}\right)dy,\\
m_{z4}&=\frac{k_{z0}m_1}{f_0}-\int_0^h\left(\rho\int_0^z A\frac{d\tau_{zy}}{dt}\,d\hat{y}\right)dy.
\end{aligned}$$

Equation (10.52) is the generalized Reynolds equations of Wolff and Kubo (1996) for elastoviscoplastic lubrication. For viscoplastic fluids $A=0$, therefore m_{x4} and m_{z4}, vanish. If the viscosity function $F(\tau_e)=1/\mu$ and $A=0$, Eq. (10.52) reduces to the form proposed by Fowles (1970). If in addition to $A=0$ and $F(\tau_e)=1/\mu$ we also specify μ, $\rho=\text{const}$, Eq. (10.52) reduce to Eq. (2.70). Equation (10.52) was first derived for $\rho=\text{const.}$ by Najji, Bou-Said, and Berthe (1989).

For the two-dimensional flow in a line contact, we set

$$\begin{aligned}
&\frac{\partial(\cdot)}{\partial z}=0,\quad w_1=w_2=0,\quad \tau_{xy}=\tau_e=\tau,\\
&v_1=0,\quad v_2=u_2\frac{\partial h}{\partial x},\quad \frac{d\tau}{dt}=u\frac{\partial\tau}{\partial x},
\end{aligned}$$

and Eq. (10.51) reduces to

$$\frac{\partial}{\partial x}\left[m_2\frac{dp}{\partial x}\right]=u_1\frac{\partial}{\partial x}[m_3]+(u_2-u_1)\frac{\partial}{\partial x}\left[\frac{m_1}{f_0}\right]-\frac{\partial}{\partial x}[m_4].\tag{10.53}$$

Equation (10.53) is to be solved subject to the Swift-Stieber boundary conditions

$$\begin{aligned} p &= 0 \qquad && \text{at } x = x_{\min}, \\ p &= \frac{dp}{dx} = 0 \qquad && \text{at } x = x_{\max}. \end{aligned} \tag{8.60}$$

We may now use Eq. (10.53) in place of Eq. (8.50) in a scheme to solve the EHD lubrication problem, but for one circumstance, Eq. (10.53) contains a yet undetermined shear stress field. We thus need one additional equation.

To find the required additional equation, we reconsider the first of Eqs. (10.46). As $p = p(x)$, to the approximation employed dp/dx is independent of y and so is $\partial \tau_{xy}/\partial y$. But then τ_{xy} is linear in y at any x. It is, therefore, enough to evaluate τ_{xy} at $y = 0$ and $y = h$ and the shear-stress distribution is known.

Evaluating Eq. (10.50a) at $y = 0$, $u = 0$ yields an equation in $\tau_{xy}(x, 0)$. An equation in $\tau_{xy}(x, h)$ is obtained when Eq. (10.50a) is evaluated at $y = h$, $u = U$. It is a simple matter then to find the shear-stress distribution from

$$\tau_{xy} = \tau(x, 0) + [\tau(x, h) - \tau(x, 0)] \frac{y}{h}. \tag{10.54}$$

In their calculations for the line contact, Wolff and Kubo (1996) considered the following nonlinear rheological models:

(1) The nonlinear viscous Eyring model (Eyring, 1936),

$$F(\tau) = \frac{\tau_E}{\tau \mu} \sinh(\tau/\tau_E); \tag{10.55a}$$

(2) The nonlinear viscoplastic-like model (Bair and Winer, 1979),

$$F(\tau) = -\frac{\tau_L}{\tau \mu} \ln(1 - \tau/\tau_L); \tag{10.55b}$$

(3) The nonlinear viscoplastic-like model, also called the simplified Bair and Winer model,

$$F(\tau) = -\frac{1}{\mu} (1 - |\tau/\tau_L|)^{-1}; \quad \text{and} \tag{10.55c}$$

(4) The nonlinear viscoplastic-like (circular) model, Lee and Hamrock (1990),

$$F(\tau) = \frac{1}{\mu} [1 - (\tau/\tau_L)^2]^{-1/2}. \tag{10.55d}$$

If the coefficient $\bar{A} \neq 0$, the elastic term can be added to any of these models.

The limiting shear stress was assumed to be linearly dependent on the pressure,

$$\tau_L = \tau_{L_0} + \gamma p. \tag{10.56}$$

Wolff and Kubo performed two sets of calculations, one with Santotrac 50 and the other with a P-150 oil.

Figure 10.11 shows the variation of shear stress for several rheological models in Santotrac. The traction coefficient for Santotrac is shown in Figure 10.12. Under pure rolling conditions there is a very small difference in the pressure distribution and the film shape predicted by the Newtonian and the Eyring models, as shown in Figure 10.13.

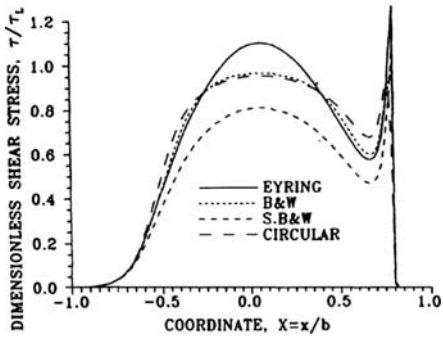

Figure 10.11. Dimensionless shear stress for Santotrac 50 oil; $W = 2.1 \times 10^{-5}$, $U = 10^{-11}$, $S = 0.5$. (Reprinted with permission from Wolff, R. and Kubo, A. A generalized non-Newtonian fluid model incorporated into elastohydrodynamic lubrication. *ASME Journal of Tribology*, **118**, 74–82, 1996.)

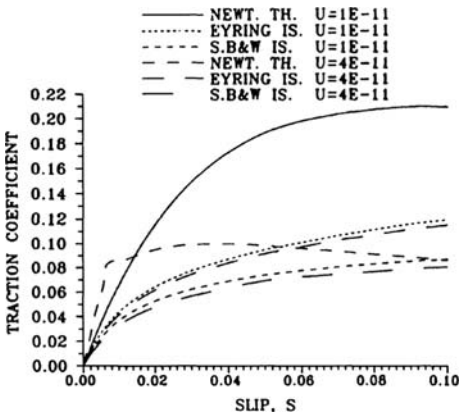

Figure 10.12. Traction coefficient for Santotrac 50 oil, $W = 2.1 \times 10^{-5}$. (Reprinted with permission from Wolff, R. and Kubo, A. A generalized non-Newtonian fluid model incorporated into elastohydrodynamic lubrication. *ASME Journal of Tribology*, **118**, 74–82, 1996.)

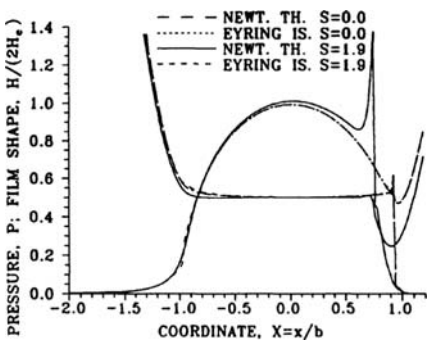

Figure 10.13. Film shape and pressure distribution for Santotrac 50 oil, $W = 8.4 \times 10^{-5}$, $U = 10^{-11}$. (Reprinted with permission from Wolff, R. and Kubo, A. A generalized non-Newtonian fluid model incorporated into elastohydrodynamic lubrication. *ASME Journal of Tribology*, **118**, 74–82, 1996.)

We close this section by quoting the conclusions from Wolff and Kubo's (1966) paper:

(1) Under low load and high rolling velocity conditions the thermal effects caused by high slip have a greater influence on the film shape and pressure distribution than the non-Newtonian effects.
(2) In the low slip range and under moderate and heavy loads the non-Newtonian behavior of an oil has a decisive influence on the traction coefficient, while in the high slip range, the thermal effects may become more important. The influence of the non-Newtonian effects on the traction (in the low slip range) is stronger under heavy load conditions and for high viscosity oils.
(3) For high viscosity oils subjected to heavy load conditions, the nonlinear viscous Eyring model tends to overestimate the traction coefficient.
(4) The viscoplastic models give reasonable traction values over a wide range of loads, slips, and oil viscosity values. The elastic behavior of a lubricant is important only under very low slip conditions. It reduces the traction value, particularly under heavy loads.
(5) In order to predict the traction coefficient over a wide range of parameters, the EHL model has to include not only the non-Newtonian behavior of a lubricant but also the thermal effects. It should also use a proper viscosity formula that fits the measured viscosity well over a wide range of pressure and temperature.

10.3 Quantitative Elastohydrodynamic Lubrication (EHL)

A Letter to the Editor of the "*Journal of Engineering Tribology*" by six well-known researchers of elastohydrodynamic lubrication remarks that "*in most EHL papers viscosity has been treated as an adjustable fitting parameter so that numerical simulations will be stable and the outcome can be matched to experimental measurements of contact behavior*" (Bair et al., 2009). It is then recommended that this practice be abandoned, as it has not been able to significantly advance lubricant characterization during the past three decades, and that "*accurately measured*" viscosities should be used in all future EHL studies. They label their approach to EHL modeling "*quantitative.*"

Past approaches to EHL relied on the Dowson-Higginson "equation of state" (8.52.b) for calculating changes in lubricant density and on the Roeland correlation of viscosity with pressure and temperature (8.52a) to characterize viscosity changes. Papers in quantitative EHL, in contrast, rely on lubricant characterization that was obtained extraneous to EHL research: free-volume approach to characterize changes in viscosity and Tait's equation of state to compute variation in density.

The idea that the viscosity of a liquid should depend on the relative volume of molecules per unit of free space is a concept that can be traced to the early part of the last century. But it was Doolittle (1951) who gave the first usable formula for viscosity of liquids in terms of relative free space

$$\ln \mu = B \left(\frac{\upsilon_0}{\upsilon_f} \right) + \ln A.$$

Free space $\upsilon_f = \upsilon - \upsilon_0$ is defined here as increase of volume resulting from thermal expansion but without phase change, υ_0 is the specific volume of the liquid extrapolated to zero temperature and υ is its volume under experimental conditions. For a single substance

A and B are constants, they are determined by curve fitting to experimental data. To employ the Doolittle formula the value of v_0 is required.

Up until publication of Doolittle's paper the most reliable method for determining the density (reciprocal of the specific volume) of liquids was by Goldhammer's rule

$$\rho_l - \rho_v = C(T_c - T)^{1/3},$$

where ρ_l is density of liquid phase, ρ_v is density of vapor phase, T is the absolute temperature at measurement, and T_c is the critical temperature of the substance under investigation. While experimenting with normal liquid paraffins, Doolittle discovered a more accurate estimate; at given temperature the logarithm of the specific volume plotted against the reciprocal of the molecular weight gave a straight line

$$\ln(1/\rho) = a/m + b.$$

Here m is the molecular weight and a, b are temperature dependent constants.

Cohen and Turnbull (1959) succeeded in putting Doolittle's formula, which is purely empirical, on a theoretical basis, and Cook et al. (1993) extended it to

$$\ln \mu = B \frac{v_\infty}{v_0} \left[\frac{1}{\dfrac{v}{v_0} - \dfrac{v_\infty}{v_0}} - \frac{1}{1 - \dfrac{v_\infty}{v_0}} \right] + \ln \mu_0. \tag{10.57}$$

In this version of the viscosity-free volume relationship μ_0 and v_0 are viscosity and volume, respectively, at ambient pressure while v_∞ and B are fitting parameters, v_∞ being the volume at infinite viscosity. In lubrication literature, in contrast, B and v_∞/v_0 are the fitting parameters, the latter often denoted by the symbol v_{occ}/v_0 (Bair et al., 2005; Liu et al., 2006). Equation (10.57) is referred to as the Doolittle free-volume model for viscosity. The quality of correlation by (10.57) can be gauged from Figure 10.14, which displays viscosity-pressure data for three substances, glycerol, 1,2-propanediol and 1-propanol.

The change in volume required in (10.57) is computed from the Tait equation of state (Dymond and Malhotra, 1988), dating from 1888,

$$\frac{v}{v_0} = 1 - c \ln \left(\frac{b + p}{b + p_0} \right).$$

The constants b and c are obtained by fitting to $v - p$ data; they are related to the bulk modulus K_0 and its derivative with pressure K_0' (Cook et al., 1993). In lubrication literature the Tait equation is often written in terms of the latter two quantities, which then take up the role of fitting parameters (Bair et al., 2009), and the equation assumes the form

$$\frac{v}{v_0} = 1 - \frac{1}{1 + K_0'} \ln \left[1 + \frac{p}{K_0} \left(1 + K_0' \right) \right]. \tag{10.58}$$

Now v_0 is the volume at $p = 0$ and the ambient temperature bulk modulus can be an exponential in temperature $K_0 = K_{00} \exp(-\beta_K T)$. The accuracy of representation by (10.58) can be gauged from Figure 10.15, which shows the density-pressure correlation for a low viscosity silicon oil; the same figure also contains data for a mineral oil, and the corresponding Dowson-Higginson correlation.

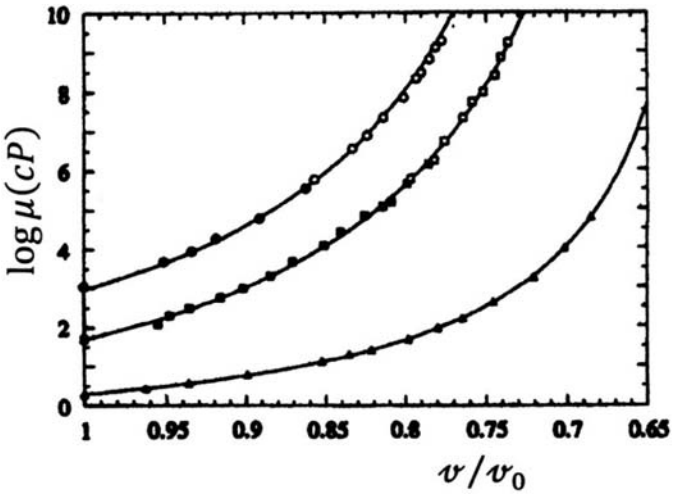

Figure 10.14. Viscosity-pressure correlation for three liquid carbon alcohols by the Doolittle free-volume formula (Reprinted with permission from Cook, R. L., Herbst, C. A. and King, H. E. 1993. High-pressure viscosity of glass-forming liquids measured by the centrifugal force diamond anvil cell viscometer, *J. Phys*. Chem., **97**, 2355–2361, Copyright (1993), American Institute of Physics.)

An alternative free-volume model is due to Yasutomi et al. (1984)

$$\ln \mu = \ln \mu_g + \frac{-2.3C_1(T - T_g)F}{C_2 + (T - T_g)F}. \tag{10.59}$$

This is a pressure modified Williams-Landel-Ferry free-volume equation (Williams et al., 1995) where T_g is the glass formation temperature,

$$T_g = T_{g0} + A_1 \ln(1 + A_2 p)$$

and

$$F = 1 - B_1 \ln(1 + B_2 p).$$

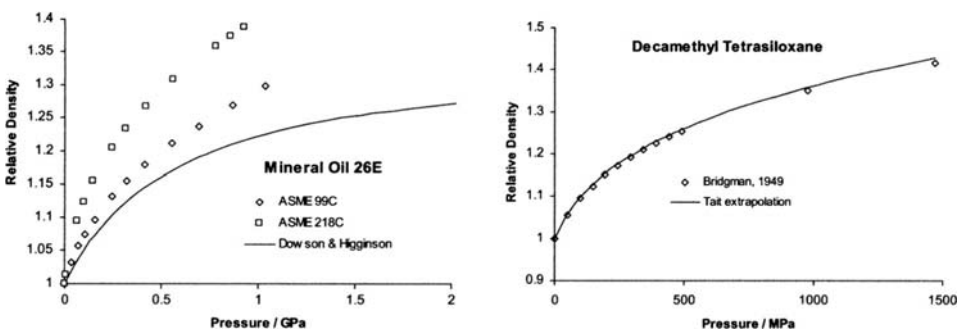

Figure 10.15. Density variation with pressure for various oils (Reprinted with permission from Bair, S. Rheology and high-pressure models for quantitative elastohydrodynamics, *Proc IMechE Journal of Engineering Tribology*, **223**, 617–628, 2009, Professional Engineering Publishing.)

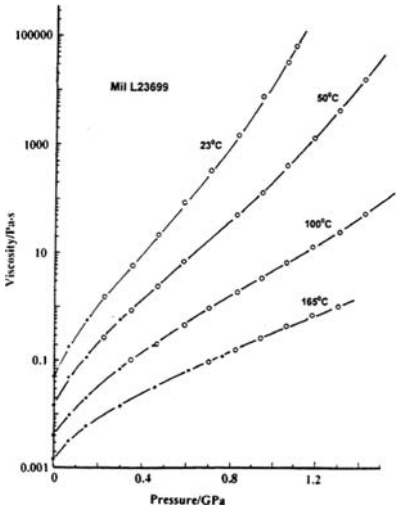

Figure 10.16. Experimental viscosity data for jet engine lubricant and the Yasutomi correlation (Reprinted with permission from Bair, S. The variation of viscosity with temperature and pressure for various real lubricants, *ASME Journal of Tribology*, **123**, 433–436, 2001, Professional Engineering Publishing.)

The Yasutomi model is able to reproduce the often observed inflection of the pressure-viscosity plot. Figure 10.16 displays the Yasutomi correlation for an aircraft turbine lubricant at various temperatures (Bair, 2000). The data is compiled from two different laboratories; the curves show the viscosity inflection at $\mu \sim 10\,\text{Pa}\cdot\text{s}$.

To illustrate the goodness of agreement between EHL experimental data and "qualitative" numerical prediction, in Figure 10.17 we reproduce a plot for film profile for squalane from Liu et al. (2006). For these calculations the parameters of the Doolittle-Tait free-volume correlation are $v_{\text{occ}}/v_0 = 0.6633$, $B = 5.258$, $K_0 = 1.312$, and $K_0' = 11.74$.

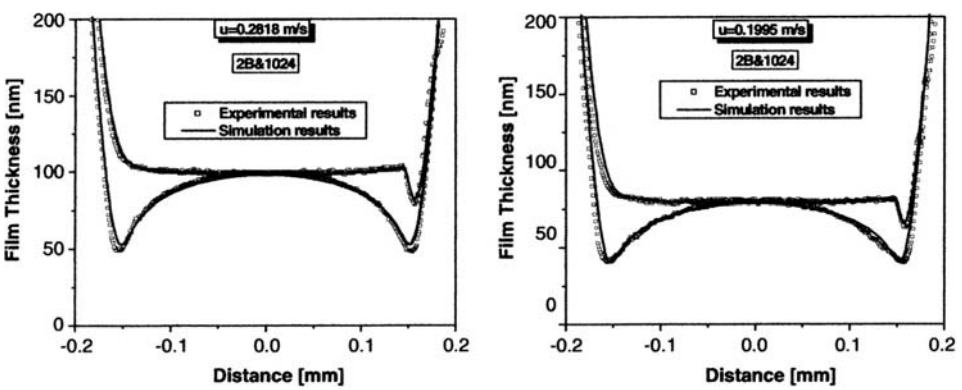

Figure 10.17. Comparison of simulation with experimental data at two speeds (With kind permission from Springer Science & Business Media: *Tribology Letters,* EHL simulation using the free-volume viscosity model, **23**(1), 2006, 27–37, Liu, Y., Wang, Q. J., Wang, W., Hu, Y., Zhu, D., Krupka, I., Hartl, M. Fig. 4.)

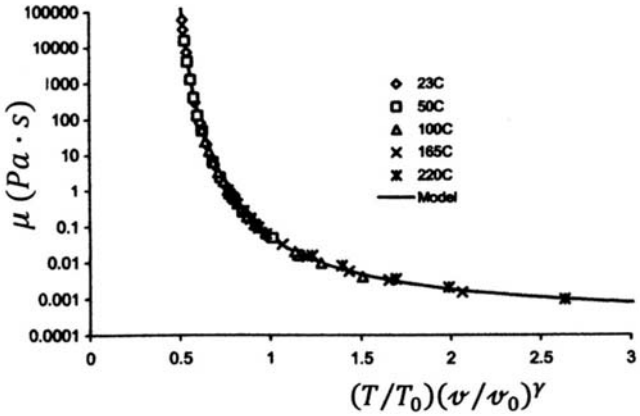

Figure 10.18. Viscosity versus scaling parameter for pressures and temperatures up to 1.4 GPa and indicated temperatures, (Reproduced with permission from Bair, S. Rheology and high-pressure models for quantitative elastohydrodynamics. *Proc IMechE Journal of Engineering Tribology*, **223**, 617–628, 2009, Professional Engineering Publishing.)

A new approach to temperature and pressure correlation has been advanced recently by Bair and co-workers (Roland et al., 2006; Bair, 2009) in the form $\mu = F(T\upsilon_0^{\gamma})$. Figure 10.18 displays the variation of eight orders of magnitude of viscosity data of a certain jet oil with the appropriate scaling parameter $(T/T_0)(\upsilon/\upsilon_0)^{\gamma}$; here the pressure varies to 1.4 GPa and the temperature from 23°C to 220°C.

Habchi et al. (2009) take temperature and pressure dependence of lubricant thermal properties into account, then investigate how variability of the thermal properties affects conditions in an EHL contact. Instead of the Tait equation of state (10.58) they apply Murnaghan's temperature modified formulation (Murnaghan, 1944)

$$\frac{\upsilon}{\upsilon_0} = \left[1 + \frac{K_0'}{K_0} p\right]^{(-1/K_0)}$$

where K_0 and K_0' have their previous definition. They also use scaling factors κ and χ, respectively, in defining the variation of heat conductivity and specific heat on temperature and pressure

$$k = B + C\kappa^{-1}; \qquad \kappa = \left(\frac{\upsilon}{\upsilon_0}\right)\left[1 + A\left(\frac{T}{T_0}\right)\left(\frac{\upsilon}{\upsilon_0}\right)^3\right]$$

$$\rho c_p = C_0 + m\chi; \qquad \chi = \left(\frac{T}{T_R}\right)\left(\frac{\upsilon}{\upsilon_R}\right)^{-4}$$

Habchi and co-workers applied two loads corresponding to $p = 0.84$ GPa and $p = 1.35$ GPa. Under pure rolling, they found negligible difference in film thickness between isothermal and non-isothermal conditions, as the rate of heat generation was relatively small. Under sliding-rolling conditions, however, when the entrainment speed is large, there is considerable heat generation that will affect lubricant thermal conditions, and now

there are considerable differences between isothermal, non-isothermal but constant thermal properties, and non-isothermal and variable thermal properties.

To model shear thinning in hydrodynamic lubrication, several authors make use of the Carreau viscosity, which combines the two Newtonian viscosity regions, μ_0 at low and μ_∞ at high shear rates, with an intervening power-law region in the form

$$\mu - \mu_\infty = (\mu_0 - \mu_\infty)[1 + (\lambda\dot{\gamma})^2]^{(n-1)/2}. \tag{10.60}$$

In application, μ_0 and μ_∞ are usually known while λ and n are found from fitting to experimental data (Tanner, 1988). In quantitative EHL, a modification of the Carreau equation is often preferred for film thickness calculations where shear stress is the independent variable (Bair and Khonsari, 1996; Liu et al., 2007; Bair, 2009; Krupka et al., 2009).

$$\mu = \left[1 + \left(\frac{\tau}{G}\right)^2\right]^{(1-1/n)/2}. \tag{10.61}$$

The models (10.60) and (10.61) are related by writing $\lambda = \mu/G$ for the characteristic time, where G is the shear modulus.

10.4 The Piezoviscous Fluid

The compressible Navier-Stokes equation (Navier, 1823; Stokes, 1845) is a consequence of assuming that the Cauchy stress $\boldsymbol{T}$ depends only on the density and the velocity gradient. The requirement of frame-indifference then implies that the dependence on the velocity gradient can be only through its symmetric part. Restrictions due to isotropy and the assumption that the stress is linear in the symmetric part of the velocity gradient lead to the compressible Navier-Stokes model. This model is characterized by two material moduli, both of them depending on the density.

During his derivation of the model, Stokes (1845) already recognized that the viscosity of a fluid could depend on the "*pressure*." While in a compressible fluid the pressure is given by an equation of state and does not necessarily equal the mean normal stress, it equals the mean normal stress in an incompressible fluid. Liquids such as water are essentially incompressible over a very large range of pressures; yet, their viscosities can vary significantly with pressure. Stokes recognized this possibility. "*Let us now consider in what cases it is allowable to suppose μ to be independent of pressure. Du Buat has concluded it from his experiments on the motion of water in pipes and canals, that the total retardation of the velocity due to friction is not increased by increasing the pressure . . . I shall therefore suppose that for water, and by analogy for other incompressible fluids, μ is independent of the pressure*" (Stokes, 1845).

That the viscosity for liquids could depend on the pressure and could change significantly with sufficiently large variations of the pressure has been well recognized and the great body of early experimental work on this matter can be found in the literature (Bridgman, 1931; Cutler et al., 1958; Griest et al., 1958; Johnson and Cameron, 1967; Johnson and Greenwood, 1980; Johnson and Tevaarwerk, 1977; Bendler et al., 2001; Paluch et al., 1999; Griest et al., 1958). Incorporating this pressure dependence of viscosity into the development of constitutive theories leads to an interesting departure from classical theories.

In classical theories, constitutive expressions for the stress are usually given as explicit functions of kinematical quantities, e.g., Hooke's Law, Navier-Stokes model. Starting with the assumption that the stress in the fluid depends upon the velocity gradient

$$\boldsymbol{T} = \boldsymbol{f}(\boldsymbol{L}), \qquad \boldsymbol{L} = \operatorname{grad} \boldsymbol{v}, \tag{10.62}$$

the assumption that the fluid is frame indifferent, isotropic, and incompressible leads to (Serrin, 1959)

$$\boldsymbol{T} = -p\boldsymbol{I} + a_1\left(II_{\boldsymbol{D}}, III_D\right)\boldsymbol{D} + a_1\left(II_D, III_D\right)\boldsymbol{D}^2. \tag{10.63}$$

Here p is the Lagrange multiplier due to the constraint of incompressibility.

The requirement of linearity in $\boldsymbol{D}$ then leads to

$$\boldsymbol{T} = -p\boldsymbol{I} + 2\mu\boldsymbol{D}, \tag{10.64}$$

where μ is a constant.

If however, we allow for the possibility that the constraint forces influence the work done, then we would have the possibility that the stress $\boldsymbol{T}$ have the form

$$\boldsymbol{T} = -p\boldsymbol{I} + 2\hat{\mu}\left(p\right)\boldsymbol{D}. \tag{10.65}$$

There is a very fundamental difference between the two models (10.64) and (10.65). While the model (10.64) provides an explicit relation between $\boldsymbol{T}$ and $\boldsymbol{D}$, the model (10.65) offers an implicit relation of the form

$$\boldsymbol{f}(\boldsymbol{T}, \boldsymbol{D}) = 0. \tag{10.66}$$

A generalization of the model (10.65) in which the viscosity depends on both the pressure and the symmetric part of the velocity gradient allows one to describe shear thinning and shear-thickening observed in some fluids. In such fluids the stress is of the form

$$\boldsymbol{T} = -p\boldsymbol{I} + \beta(p, \boldsymbol{D})\boldsymbol{D}. \tag{10.67}$$

The model (10.67) belongs to the class of implicit models (10.66). While many models for viscoelastic fluids are implicit models, among them the Maxwell model, they are not of the type (10.66) as they usually involve higher derivatives of the stress and stretching tensors (Joseph, 1989).

Ever since Stokes assumed that the viscosity is a constant for the Navier-Stokes fluid, it has been treated as such in most, though not all, subsequent studies. Of course, there are many fluids that are known to shear-thin or shear-thicken and for such fluids, the viscosity is considered a function of the symmetric part of the velocity gradient. There is, however, one area of research that presumes the fluid to be a Newtonian fluid, the viscosity is not treated as a constant but is allowed to depend on the pressure, namely in elastohydrodynamic lubrication. Here, we come across an inconsistency: though the thin film approximation is based on the assumption of constant viscosity, in developing the elastohydrodynamic approximation, pressure dependence of the viscosity is acknowledged only a posteriori, i.e., after the Reynolds equation has been obtained under the assumption of $\mu = \text{const}$ (Dowson and Higginson, 1966). This obvious inconsistency in the derivation of the equation for elastohydrodynamic lubrication has gone unnoticed for decades.

Current research on piezoviscous fluids has raised questions concerning (1) the appropriateness of the Reynolds equation in elastohydrodynamic lubrication (EHL), because of possible change of type of the equations of motion at high pressures, and (2) the errors

inherent in the lubrication approximation due to potential existence of cross-film pressure gradient. In discussing these questions we rely heavily on a paper by Rajagopal and Szeri (2003).

There have been some rigorous studies concerning the existence of solutions to the equations governing the flows of fluids with pressure-dependent viscosity. Renardy (1986) recognized that the equations could change type if the class of viscosity functions that he picked did not satisfy a certain condition. However, his choice of the viscosity functions is unrealistic as he postulates that $\frac{\mu(p)}{p} \to 0$, as $p \to 0$. Numerous experimental results clearly contradict this assumption (Roelands, 1966; Paluch et al., 1999; Bendler et al., 2001).

Bair et al. (1998) made use of the criterion of Renardy (1986) for the equations to remain elliptic. Adopting the Barus equation to represent the pressure dependence of viscosity, they re-cast Renardy's criterion. According to Bair et al., in two-dimensional flow change of type from elliptic to hyperbolic occurs when $\tau_{(1)} = \alpha^{-1}$. Here $\tau_{(1)} = 2\mu d_{(1)}$ is the principal shear stress. For mineral oils $\alpha^{-1} \approx 50\,\text{MPa}$, and the criterion sets a limiting value for the principal shear stress. The practical value of this finding to EHL remains questionable however, as the Barus formula is unrealistic for glass forming liquids. Furthermore, in view of Renardy's analysis being based on unrealistic physical conditions, the modifications proposed do not seem relevant to lubricant flow.

Bair et al. (1998) appear to be the first to argue that "*the Reynolds equation adequately captures the mechanics of the piezoviscous liquid only when the shear stress is much less than the reciprocal of the pressure viscosity coefficient.*" Schäfer et al. (1999) continued along this line of investigation and, starting from the Navier-Stokes equations with pressure-dependent viscosity, derived a corrected Reynolds equation. They concluded that "*application of Reynolds equation is permissible for the case of pure rolling in the contact, but not when considering partial or pure sliding. Further terms from the Navier-Stokes equations must be taken into consideration*" Greenwood (2000), in a discussion to Schafer's paper, offered a simpler derivation of the same equation. Referring to Schafer's paper, Greenwood remarks "*the author's astonishing claim that the whole EHL theory is based on an incorrect equation, seems to this discusser to be entirely correct.*" Full Navier-Stokes solutions of the EHL problem, applying the Roelands viscosity-pressure relationship, have been produced recently by Almqvist and Larsson (2002). Taking aim at further elucidating the inconsistency in applying the Reynolds equation to EHL problems we develop the appropriate approximation for the equations governing elastohydrodynamic lubrication and find that there are terms in addition to those that appear in the currently employed equation. Models of the type (10.65) have a much richer class of solutions than the Newtonian model (10.64). For example, even in the case of a simple flow between infinite parallel plates, non-unique solutions are a possibility In addition, the structure of the solutions to (10.65) can be drastically different from those for the Navier-Stokes fluid (Hron et al., 2001). In the case of simple Poiseuille flow, for example, it is possible for the solution to vary from plug flow to a V-shaped profile. It is also possible that approximations derived from (10.65) could predict response that is both qualitatively and quantitatively different from the classical approximation.

To investigate the error that is made by not consistently acknowledging pressure dependence of the viscosity while deriving the equations governing the problem of elastohydrodynamics, we follow the procedure that is usually employed to derive the Reynolds equation but use Eq. (10.65) instead of Eq. (10.64).

On substituting (10.65) into the balance of linear momentum

$$\operatorname{div} \boldsymbol{T} + \rho \boldsymbol{b} = \rho \frac{d\boldsymbol{v}}{dt}, \tag{2.27a}$$

we obtain

$$-\operatorname{grad} p + \mu(p)\Delta \boldsymbol{v} + 2\boldsymbol{D}[\operatorname{grad} \mu(p)] + \rho \boldsymbol{b} = \rho \frac{d\boldsymbol{v}}{dt}. \tag{10.68}$$

Focusing our attention on two-dimensional motion $\boldsymbol{v} = (u, v)$, $p = p(x, y)$ and dropping the body force $\boldsymbol{b}$, Eq. (10.68) yields

$$-\frac{\partial p}{\partial x} + \mu(p)\Delta u + 2\mu'(p)\frac{\partial u}{\partial x}\frac{\partial p}{\partial x} + \mu'(p)\left(\frac{\partial u}{\partial y} + \frac{\partial v}{\partial x}\right)\frac{\partial p}{\partial y} = \rho\left[u\frac{\partial u}{\partial x} + v\frac{\partial u}{\partial y}\right], \tag{10.69}$$

$$-\frac{\partial p}{\partial y} + \mu(p)\Delta v + \mu'(p)\left(\frac{\partial u}{\partial y} + \frac{\partial v}{\partial x}\right)\frac{\partial p}{\partial x} + 2\mu'(p)\frac{\partial v}{\partial y}\frac{\partial p}{\partial y} = \rho\left[u\frac{\partial v}{\partial x} + v\frac{\partial v}{\partial y}\right]. \tag{10.70}$$

For simplicity, and not because we believe that it characterizes the pressure dependence of viscosity particularly well, we employ here the Barus formula with constant coefficient α

$$\bar{\mu} = \exp(\bar{\alpha} P), \qquad \bar{\alpha} = \alpha p_H.$$

With the help of the definitions

$$(\bar{x},\ \bar{y}) = \frac{1}{L_{xz}}\left(x, \frac{1}{\varepsilon}y\right); \qquad (\bar{u},\ \bar{v}) = \frac{1}{U^*}\left(u, \frac{1}{\varepsilon}v\right); \qquad \bar{p} = \frac{p}{p_H}; \qquad \bar{\mu} = \frac{\mu}{\mu^*}.$$

Equations (10.69) and (10.70) are recast in terms of nondimensional variables

$$-\frac{\partial \bar{p}}{\partial \bar{x}} + \bar{\mu}\left(\varepsilon^2\frac{\partial^2 \bar{u}}{\partial \bar{x}^2} + \frac{\partial^2 \bar{u}}{\partial \bar{y}^2}\right) + \bar{\alpha}\bar{\mu}\left[\frac{\partial \bar{u}}{\partial \bar{y}}\frac{\partial \bar{p}}{\partial \bar{y}} + \varepsilon^2\left(\frac{\partial \bar{v}}{\partial \bar{x}}\frac{\partial \bar{p}}{\partial \bar{y}} + 2\frac{\partial \bar{u}}{\partial \bar{x}}\frac{\partial \bar{p}}{\partial \bar{x}}\right)\right] = \mathrm{R}_\varepsilon\left(\bar{u}\frac{\partial \bar{u}}{\partial \bar{x}} + \bar{v}\frac{\partial \bar{u}}{\partial \bar{y}}\right), \tag{10.71}$$

$$-\varepsilon^{-2}\frac{\partial \bar{p}}{\partial \bar{y}} + \bar{\mu}\left(\varepsilon^2\frac{\partial^2 \bar{v}}{\partial \bar{x}^2} + \frac{\partial^2 \bar{v}}{\partial \bar{y}^2}\right) + \bar{\alpha}\bar{\mu}\left[\frac{\partial \bar{u}}{\partial \bar{y}}\frac{\partial \bar{p}}{\partial \bar{x}} + \varepsilon^2\frac{\partial \bar{v}}{\partial \bar{x}}\frac{\partial \bar{p}}{\partial \bar{x}} + 2\frac{\partial \bar{v}}{\partial \bar{y}}\frac{\partial \bar{p}}{\partial \bar{y}}\right] = \mathrm{R}_\varepsilon\left(\bar{u}\frac{\partial \bar{v}}{\partial \bar{x}} + \bar{v}\frac{\partial \bar{v}}{\partial \bar{y}}\right). \tag{10.72}$$

Let us now examine the consequence of taking $\varepsilon^2 \to 0$. On close examination of our normalization process, we find that while the nondimensional velocities and their derivatives

are $O(1)$, the same cannot be expected to hold true for the derivatives of the nondimensional pressure. We must keep this in mind and neglect only $O(1)$ terms among the terms that are multiplied by ε^2. Consistent with classical lubrication theory, we also assume that $\mathrm{R}_\varepsilon \to 0$ and obtain

$$-\frac{\partial \bar{p}}{\partial \bar{x}} + \bar{\mu}\left\{\frac{\partial^2 \bar{u}}{\partial \bar{y}^2} + \bar{\alpha}\left[\frac{\partial \bar{u}}{\partial \bar{y}}\frac{\partial \bar{p}}{\partial \bar{y}} + \varepsilon^2\left(\frac{\partial \bar{v}}{\partial \bar{x}}\frac{\partial \bar{p}}{\partial \bar{y}} + 2\frac{\partial \bar{u}}{\partial \bar{x}}\frac{\partial \bar{p}}{\partial \bar{x}}\right)\right]\right\} = 0, \tag{10.73}$$

$$-\varepsilon^{-2}\frac{\partial \bar{p}}{\partial \bar{y}} + \bar{\mu}\left\{\frac{\partial^2 \bar{v}}{\partial \bar{y}^2} + \bar{\alpha}\left[\frac{\partial \bar{u}}{\partial \bar{y}}\frac{\partial \bar{p}}{\partial \bar{x}} + \varepsilon^2\frac{\partial \bar{v}}{\partial \bar{x}}\frac{\partial \bar{p}}{\partial \bar{x}} + 2\frac{\partial \bar{v}}{\partial \bar{y}}\frac{\partial \bar{p}}{\partial \bar{y}}\right]\right\} = 0. \tag{10.74}$$

We now appeal to Eq. (10.74) to estimate the order of magnitude of the pressure derivatives. To do this, we require two assumptions, the first of which has already been employed in arriving at Eqs. (10.73) and (10.74).

Assumptions:

(1) All velocities and their derivatives are $O(1)$

i.e., in (10.74) we have

$$\frac{\partial \bar{u}}{\partial \bar{y}}\frac{\partial \bar{p}}{\partial \bar{x}} \gg \varepsilon^2\frac{\partial \bar{v}}{\partial \bar{x}}\frac{\partial \bar{p}}{\partial \bar{x}}.$$

(2) The pressure derivatives are not of the same order, in fact

$$\frac{\partial \bar{p}}{\partial \bar{x}} \gg \frac{\partial \bar{p}}{\partial \bar{y}},$$

$$\bar{\alpha}\frac{\partial \bar{u}}{\partial \bar{y}}\frac{\partial \bar{p}}{\partial \bar{x}} \gg \frac{\partial^2 \bar{v}}{\partial \bar{y}^2}.$$

On employing (1) and (2) above, in conjunction with Eq. (10.74), we obtain the relative order of magnitude of the pressure derivatives

$$\frac{\partial \bar{p}}{\partial \bar{y}} \approx \bar{\alpha}\bar{\mu}\varepsilon^2\frac{\partial \bar{p}}{\partial \bar{x}}\frac{\partial \bar{u}}{\partial \bar{y}}.$$

It follows immediately from assumptions (1) and (2) that

$$\begin{aligned}
&\frac{\partial p}{\partial x} = \mu\frac{\partial^2 u}{\partial y^2} + \frac{d\mu}{dp}\left[\frac{\partial u}{\partial y}\frac{\partial p}{\partial y} + 2\frac{\partial u}{\partial x}\frac{\partial p}{\partial x}\right],\\
&\frac{\partial p}{\partial y} = \frac{d\mu}{dp}\frac{\partial p}{\partial x}\frac{\partial u}{\partial y},\\
&\frac{\partial u}{\partial x} + \frac{\partial v}{\partial y} = 0.
\end{aligned} \tag{10.75}$$

To first approximation, flow of a lubricant with pressure-dependent viscosity is governed by the system of Eqs. (10.75); we would have to make the additional assumption that the

pressure is invariant across the film $\partial p/\partial y = 0$ to be able to derive a Reynolds-type equation in pressure, and this might not be true depending on the rate of change of viscosity with pressure.

10.5 Lubrication with Emulsions

There are numerous instances of technical importance in which multicomponent lubricants are utilized either by design or by necessity. In many of these cases one of the component is a liquid while the other component is a gas, or both components are liquids; these mixtures do not exhibit Newtonian behavior even when their components themselves are Newtonian, and thus classical lubrication theory is inapplicable to tribological contacts lubricated with mixtures. Our objective in this section is to extend hydrodynamic lubrication theory to lubrication with liquid-liquid and liquid-gas mixtures. The extended theory is able to predict several experimentally observed phenomena, such as oil pooling ahead of an EHD conjunction.

Correct modeling of the flow of multicomponent mixtures is of increasing technical importance far beyond the confines of lubrication. Consequently much effort has been devoted to it; the principal approaches employed in these investigations on the flow of mixtures are (1) descriptive, (2) local volume averaging, and (3) continuum mechanics.

Because of the complexities of multiphase systems, initial attempts to describe the physical processes have relied on descriptive models of a more or less intuitive or empirical nature (Gouse, 1966; Soo, 1967; Butterworth and Hewitt, 1977). These models are generally limited in application to specific multiphase systems and, typically, have a narrow range of validity.

The second approach used to derive multiphase equations employs the technique of volume averaging (Drew, 1971; Gray, 1975; Ishii, 1975). This approach considers the system to be composed of interpenetrating continua, each constituent occupying only part of space and each separated from the others by highly irregular interfaces. Governing equations are obtained by averaging the classical single component equations over some local, representative element of volume.

The basic scientific method utilized in the works discussed in this section is mixture theory, a branch of continuum mechanics that details the behavior of multiphase continua. The theory traces its roots to the pioneering work of Fick and was put on firm mathematical footing by Truesdell (1969). The basic premise of the theory is the assumption that in a mixture of N constituents, each spatial position $\boldsymbol{x}$ is occupied simultaneously by N particles, one from each constituent. As the mass of each constituent of the mixture is continuously distributed in space, it is permissible to write one set of conservation equations for each constituent; these equations must, of course, be coupled, to express the interactions existing between constituent particles.

The notion of overlapping continua is a hypothesis about materials in much the same way as is the notion of a continuum in itself. Models developed using mixture theory are therefore useful, provided that their predictions are interpreted at scales consistent with the mixture hypothesis. Typical droplet size in oil-in-water or water-in-oil emulsions is $2r = 1.5 - 3\ \mu$m (Kimura and Okada, 1987; Schneider, Glossfield, and DeHart, 1986; Nakahara, Makino, and Kyogaka, 1988), representing $0.025 < r/h < 0.05$ in a conventional journal bearing of 0.5-m diameter, at an eccentricity ratio of 0.6. In EHL, we consider results of mixture theory to represent time averaged conditions in the film.

Fundamentals of Mixture Theory

For the sake of completeness, we begin with the following short exposition of the basics of mixture theory (Bowen, 1976; Atkin and Craine, 1976a,b; Truesdell, 1969; Bedford and Drumheller, 1983; Rajagopal and Tao, 1995).

Let $\boldsymbol{X}_a$, $\alpha = 1, 2$, represent the position of a material point of the αth constituent C_α in its reference configuration, and let $\boldsymbol{x}$ be the spatial point that is occupied at time t by the material point. The motion of a binary mixture C of components C_α, $\alpha = 1, 2$ is defined by

$$\boldsymbol{x} = \boldsymbol{\chi}_\alpha(\boldsymbol{X}_a, t), \quad t \geq 0, \quad \alpha = 1, 2. \tag{10.76}$$

The range of α for the remainder of this discussion is given in Eq. (10.76) and will not be repeated.

The velocity and the acceleration of the particle X_a are calculated, respectively, from

$$\dot{\boldsymbol{x}}_\alpha = \frac{\partial}{\partial t}\boldsymbol{\chi}_\alpha(\boldsymbol{X}_\alpha, t), \quad \ddot{\boldsymbol{x}}_\alpha = \frac{\partial^2}{\partial t^2}\boldsymbol{\chi}_\alpha(\boldsymbol{X}_\alpha, t). \tag{10.77}$$

The spatial description of motion follows from Eqs. (10.76) and (10.77), e.g.,

$$\boldsymbol{v}^{(\alpha)}(\boldsymbol{x}, t) = \dot{\boldsymbol{x}}_\alpha = \left[\boldsymbol{\chi}_\alpha^{-1}(\boldsymbol{x}, t)\right].$$

Let grad denote differentiation with respect to x, at the configuration of the mixture at time t, then the velocity gradient for C_α at $(\boldsymbol{x}, t)$ is defined by

$$\boldsymbol{L}_{(\alpha)} = \operatorname{grad} \boldsymbol{v}^\alpha(\boldsymbol{x}, t) \tag{10.78}$$

and the stretching tensor by

$$\boldsymbol{D}_{(\alpha)} = \frac{1}{2}\left(\boldsymbol{L}_{(\alpha)} + \boldsymbol{L}_{(\alpha)}^T\right).$$

We denote the *true density* of C_α by γ_α; this is the mass of the αth constituent per unit volume of the αth constituent itself. Distinct from the true density is the *density* (or bulk density) ρ_α, representing the mass of the αth constituent per unit volume of the mixture. The (total) density, ρ, of the mixture is then given by

$$\rho(\boldsymbol{x}, t) = \sum_\alpha \rho_\alpha(\boldsymbol{x}, t). \tag{10.79}$$

The quantity ϕ_α, defined by

$$\phi_\alpha(\boldsymbol{x}, t) = \frac{\rho_\alpha(x, t)}{\gamma_\alpha(x, t)}, \tag{10.80}$$

is the *volume fraction* of the αth constituent. Physically ϕ_α represents the volume of C_α per unit volume of the mixture, therefore

$$\sum_\alpha \phi_\alpha = 1 \tag{10.81}$$

for saturated mixtures (Mills, 1966).

It is convenient to introduce the (mean) velocity of the mixture, $\boldsymbol{v}$, via the requirement that the total mass flow is the sum of the individual mass flows, so that

$$\boldsymbol{v} = \frac{1}{\rho} \sum_{\alpha} \rho_{\alpha} \boldsymbol{v}^{(\alpha)}. \tag{10.82}$$

Next, we introduce material derivatives $d^{(\alpha)}/dt$ and d/dt, following the α constituent and the mixture, respectively, by

$$\frac{d^{(\alpha)}}{dt} = \frac{\partial}{\partial t} + \boldsymbol{v}^{(\alpha)}.\,\mathrm{grad}, \quad \frac{d}{dt} = \frac{\partial}{\partial t} + \boldsymbol{v}\,.\,\mathrm{grad}. \tag{10.83}$$

Here we do not allow for interconversion of mass. Thus, the local form of the mass conservation equation is

$$\frac{d^{(\alpha)}\rho_{\alpha}}{dt} + \rho_{\alpha}\,\mathrm{div}\,\boldsymbol{v}^{(\alpha)} = 0. \tag{10.84}$$

The local version of the balance of linear momentum for the αth constituent is

$$\rho_{\alpha} \frac{d^{(\alpha)}\boldsymbol{v}^{(\alpha)}}{dt} = \mathrm{div}\,\boldsymbol{T}^{T}_{(\alpha)} + \rho_{\alpha}\boldsymbol{b}^{(\alpha)} + \boldsymbol{\pi}^{(\alpha)}. \tag{10.85}$$

The term $\boldsymbol{\pi}^{(\alpha)}$ symbolizes the transfer of momentum per unit volume due to interaction effects, due to relative motion between the constituents. $\boldsymbol{\pi}^{(\alpha)}$ is often referred to as *diffusive body force*. Its exact form is determined by the other components of the mixture and will be specified by a constitutive equation.

If $\boldsymbol{q}^{(\alpha)}$ is the heat flux, e_{α} is the internal energy density, and r_{α} is the external heat supply associated with constituent C_{α}, the local form of the energy conservation equation for a binary mixture is

$$\begin{aligned} \rho \frac{de}{dt} = &\sum_{\alpha} \boldsymbol{T}^{T}_{(\alpha)} : \boldsymbol{L}_{(\alpha)} + \boldsymbol{\pi} \cdot \boldsymbol{V}^{(12)} - \mathrm{div}\left[\frac{\rho_1\rho_2}{\rho}\,(e_1 - e_2)\,\boldsymbol{V}^{(12)}\right] \\ &+ \rho r - \mathrm{div}\,\boldsymbol{q} + \sum_{\alpha} \rho_{\alpha}\boldsymbol{b}^{(\alpha)} \cdot \boldsymbol{v}^{(\alpha)}, \end{aligned} \tag{10.86}$$

where

$$r = \sum_{\alpha} r_{\alpha}\rho_{\alpha}/\rho, \qquad \boldsymbol{q} = \sum_{\alpha} \boldsymbol{q}^{(\alpha)},\ \boldsymbol{V}^{(12)} = \boldsymbol{v}^{(1)} - \boldsymbol{v}^{(2)}, \qquad \text{and} \quad \boldsymbol{\pi} = -\boldsymbol{\pi}^{(1)} = \boldsymbol{\pi}^{(2)}.$$

Finally, we postulate the second law of thermodynamics, in the form of the Clausius-Duhem entropy inequality. If η_{α} represents the *entropy density* for C_{α} and η is the entropy density for the mixture, then

$$\eta\,(\boldsymbol{x}, t) = \frac{1}{\rho} \sum_{\alpha} \rho_{\alpha}\eta_{\alpha}\,(\boldsymbol{x}, t)\,, \tag{10.87}$$

and a local form of the entropy production inequality for the mixture is

$$\rho \frac{d\eta}{dt} + \mathrm{div}\left(\frac{1}{\Theta}\boldsymbol{q}\right) - \frac{\rho r}{\Theta} \geq 0. \tag{10.88}$$

Here we assumed that the flux of entropy due to the heat flux $\boldsymbol{q}^{(\alpha)}$ is $\boldsymbol{q}^{(\alpha)}/\Theta$, where $\Theta\,(x, t)$ is the common temperature of the constituents, and that the input of entropy due to the heat supply function r_{α} is r_{α}/Θ.

Defining the partial Helmholtz free energy density for C_α by $A_\alpha = e_\alpha - \Theta\eta_\alpha$, we can write Eq. (10.88) in the form

$$-\sum_\alpha \left[\frac{d^{(\alpha)}\rho_\alpha A_\alpha}{dt} + \rho_\alpha A_\alpha \operatorname{tr}\left[\boldsymbol{D}_{(\alpha)}\right] + \rho_\alpha \eta_\alpha \frac{d^{(\alpha)}\Theta}{dt} + \boldsymbol{\pi}\cdot\boldsymbol{V}^{(12)} - \boldsymbol{T}_{(\alpha)} : \boldsymbol{L}_{(\alpha)} \right] - \frac{1}{\Theta}\boldsymbol{g}\cdot\boldsymbol{q} \geq 0. \tag{10.89}$$

Constitutive Model

We identify $(12\alpha + 7)$ scalar unknowns $\{\rho_{(\alpha)}, v_{(\alpha)i}, T_{(\alpha)i,j}, \eta_{(\alpha)}, A_{(\alpha)}, \pi_i, q_i, \Theta\}$, $i, j = 1, 2, 3$, $\alpha = 1, 2$. Of these $(4\alpha + 1)$, viz., ρ_α, $v_{(\alpha)i}$, and Θ are field variables to be calculated from the $(4\alpha + 1)$ scalar conservation equations, Eqs. (10.84)–(10.85). We thus need to specify $(8\alpha + 6)$ constitutive equations for the remaining $(8\alpha + 6)$ scalar unknowns:

$$\{A_\alpha, \eta_\alpha, T_{(\alpha)i,j}, \pi_i, q_i\} \qquad i, j = 1, 2, 3; \quad \alpha = 1, 2. \tag{10.90}$$

For a heat-conducting mixture of incompressible, viscous fluids, it is natural to have the densities, ρ_α or ϕ_α (Bowen, 1980), the temperature, Θ, and the temperature gradient $\boldsymbol{g}$, as independent variables (Atkin and Craine, 1976a). Density gradients, $\boldsymbol{h}^{(\alpha)}$), are also necessary, since their omission leads to a theory that is too simple (Muller, 1968). In order to include effects connected with the motion of the constituents, the velocities $\boldsymbol{v}^{(\alpha)}$ and velocity gradients $\boldsymbol{L}_{(\alpha)}$ are added to the list of variables; frame indifference then requires that the last two quantities be represented by the relative velocity $\boldsymbol{V}^{(12)}$, the stretching tensors $\boldsymbol{D}_{(\alpha)}$, and the relative spin $\boldsymbol{\Omega}_{(12)} = \boldsymbol{\Omega}_{(1)} - \boldsymbol{\Omega}_{(2)}$. However, it is known from the theory of single materials that velocity gradients characterize viscous effects; viscous effects are nonexistent in the ideal gas component, thus velocity gradient for the liquid component only is considered in gas-liquid emulsions.

Liquid-Liquid Emulsion

Since the mixture is saturated, all processes must be subjected to the volume additivity constraint in Eq. (10.81), which, when differentiated, yields

$$\sum_{\alpha=1}^{2} \left[\frac{d^{(\alpha)}\phi_\alpha}{dt} - \left(\boldsymbol{v}^{(\alpha)} - \boldsymbol{v}\right)\cdot \operatorname{grad}\phi_\alpha \right] \cdot \boldsymbol{V}^{(12)} = 0. \tag{10.91}$$

Using Eq. (10.84), Eq. (10.91) can be rewritten as

$$\sum_{\alpha=1}^{2} \phi_\alpha \operatorname{div}\boldsymbol{v}^{(\alpha)} + \left[\frac{\rho_2}{\rho}\operatorname{grad}\phi_1 - \frac{\rho_1}{\rho}\operatorname{grad}\phi_2 \right] \cdot \boldsymbol{V}^{(12)} = 0. \tag{10.92}$$

The thermodynamic theory of constraints (Truesdell and Noll, 1965), which requires introduction of a Lagrange multiplier Π, will be used to account for this constraint in the entropy inequality.

Our choice, and this choice is by no means unique, of independent constitutive variables for a heat-conducting mixture of incompressible fluids is the set (Al-Sharif et al., 1993)

$$\phi_\alpha, \Theta, \boldsymbol{V}^{(12)}, \boldsymbol{g}, \boldsymbol{h}^{(\alpha)}, \boldsymbol{D}_{(\alpha)}, \boldsymbol{\Omega}_{(12)}, \tag{10.93}$$

where

$$\boldsymbol{g} = \operatorname{grad}\Theta, \qquad \boldsymbol{h}^{(\alpha)} = \operatorname{grad}\phi_\alpha, \qquad \boldsymbol{\Omega}_{(12)} = \boldsymbol{\Omega}_{(1)} - \boldsymbol{\Omega}_{(2)}.$$

Consistent with the axiom of equipresence (Truesdell and Toupin, 1960), each of the quantities in Eq. (10.71) is now assumed to be a function of the variables of Eq. (10.74), but dependence on

$$\boldsymbol{V}^{(12)}, \boldsymbol{g}, \boldsymbol{h}^{(\alpha)}, \boldsymbol{D}_{(\alpha)}, \boldsymbol{\Omega}_{(12)} \tag{10.94}$$

is restricted to be linear, so as to simplify the analysis. This results in a set of constitutive equations for the variables in Eq. (10.90).

Substituting the constitutive equations into the entropy inequality, we now assume that inequality (10.70) must hold for all admissible thermomechanical processes in the mixture (Muller, 1968; Atkin and Craine, 1976a). Standard methods of continuum mechanics yield the reduced constitutive equations (Spencer, 1970; Bowen, 1976). For the diffusive body force and the component stresses, in the case under consideration, we have (Al-Sharif, 1992; Al-Sharif et al., 1993)

$$\boldsymbol{\pi} = \varpi_1 \boldsymbol{V}^{(12)} + \varpi_4 \boldsymbol{g} + \left[-\rho_2 \frac{\partial A_2}{\partial \phi_1} + \frac{\rho_2}{\rho}\Pi\right]\boldsymbol{h}^{(1)} + \left[\rho_1 \frac{\partial A_1}{\partial \phi_2} - \frac{\rho_1}{\rho}\Pi\right]\boldsymbol{h}^{(2)}, \tag{10.95a}$$

$$\boldsymbol{T}_1 = \left(-\rho_1 + \lambda_1 \operatorname{tr}\left[\boldsymbol{D}_{(1)}\right] + \lambda_3 \operatorname{tr}\left[\boldsymbol{D}_{(2)}\right]\right)\boldsymbol{I} + 2\mu_1 \boldsymbol{D}_{(1)} + 2\mu_3 \boldsymbol{D}_{(2)} + \lambda_5 \boldsymbol{\Omega}_{(12)}, \tag{10.95b}$$

$$\boldsymbol{T}_2 = \left(-\rho_2 + \lambda_4 \operatorname{tr}\left[\boldsymbol{D}_{(1)}\right] + \lambda_2 \operatorname{tr}\left[\boldsymbol{D}_{(2)}\right]\right)\boldsymbol{I} + 2\mu_4 \boldsymbol{D}_{(1)} + 2\mu_2 \boldsymbol{D}_{(2)} + \lambda_5 \boldsymbol{\Omega}_{(12)}. \tag{10.95c}$$

Equation (10.95b) indicates that, under the constitutive assumption we made, the stress in component C_1 (water) depends on the stretching tensor $\boldsymbol{D}_1$ of component C_1 but also on the stretching tensor of component C_2 (oil). The diffusive body force $\boldsymbol{\pi}$ in its simplest form is given by the Stokes resistance law [neglecting dependence on $\boldsymbol{h}^{(\alpha)}$]. We also note that the constitutive equations (10.95) contain a number of material functions, such as the viscosities $\mu_1, \ldots, \mu_4$, that must be determined from experiments, obviously not a simple task.

Liquid-Gas Emulsion

Our choice of constitutive variables for a heat-conducting mixture of an incompressible fluid and an ideal gas is the set

$$\left\{\rho_\alpha, \Theta, \boldsymbol{V}^{(12)}, \boldsymbol{g}, \boldsymbol{h}^{(\alpha)}, \boldsymbol{D}_{(1)}\right\}. \tag{10.96}$$

If we again assume the constitutive functions to be linear with respect to vector and tensor arguments and substitute into the entropy production inequality, requiring the latter to hold for all admissible thermomechanical processes in the mixture (Muller, 1968), we arrive at the restricted constitutive equations (Chamniprasart et al., 1993). For component stress, e.g., we have

$$\boldsymbol{T}_{(1)} = \left(-p_1 + \lambda_1 \operatorname{tr}\left[\boldsymbol{D}_{(1)}\right]\right)\boldsymbol{I} + 2\mu_1 \boldsymbol{D}_{(1)},$$
$$\boldsymbol{T}_{(2)} = -p_2 \boldsymbol{I}.$$

Lubrication Approximation

Let L_{xz} and L_y represent the length scales, in the "plane" of the film and perpendicular to it, respectively, of the generic lubrication problem. The corresponding velocity scales will be denoted by U_*, and $V_* = (L_y/L_{xz})U_*$ and the time scale by $t_* = (L_{xz}/U_*)$. When the equations of motion, Eq. (10.85), are normalized with respect to these characteristic quantities, they will contain various powers of (L_y/L_{xz}). To simplify these equations, we let $(L_y/L_{xz}) \to 0$ while keeping the Reynolds number $L_y U_*/\nu \approx O(1)$ in accordance with the basic premise of lubrication theory.

Liquid-Liquid Emulsion

The result of such manipulations is two sets of equations, one set each for the two constituents of the mixture. When these equations are formally integrated, a generalized Reynolds equation for binary mixtures of Newtonian fluids is obtained (Al-Sharif, 1992). This derivation assumes that the volume fraction, like the pressure, remains constant across the film; the condition $\partial\phi/\partial y = 0$ is shown to hold approximately in the recent experiments of Couet, Brown, and Hunt (1991), who measured local volume fraction for oil dispersed in water.

The extended Reynolds equations for *binary mixtures* of two Newtonian fluids are

$$\frac{\partial}{\partial \bar{x}}\left[F_1 \frac{\partial \bar{p}}{\partial \bar{x}} + F_2 \frac{\partial \phi}{\partial \bar{x}}\right] + \left(\frac{D}{L}\right)^2 \frac{\partial}{\partial \bar{z}}\left[F_1 \frac{\partial \bar{p}}{\partial \bar{z}} + F_2 \frac{\partial \phi}{\partial \bar{z}}\right] = 12\pi \frac{\partial (\phi H)}{\partial \bar{x}}, \tag{10.97a}$$

$$\frac{\partial}{\partial \bar{x}}\left[F_3 \frac{\partial \bar{p}}{\partial \bar{x}} - F_4 \frac{\partial \phi}{\partial \bar{x}}\right] + \left(\frac{D}{L}\right)^2 \frac{\partial}{\partial \bar{z}}\left[F_3 \frac{\partial p}{\partial \bar{z}} - F_4 \frac{\partial \phi}{\partial \bar{z}}\right] = 12\pi \frac{\partial [(1-\phi)H]}{\partial \bar{x}}. \tag{10.97b}$$

Equations (10.79) are in a nondimensional form suitable for a journal bearing of diameter D and length L, and we put $\phi = \phi_1 = 1 - \phi_2$. The (nonlinear) coefficients $F_1, \ldots, F_4$ are functions of the volume fraction ϕ and the material parameters such as μ_1, μ_2, μ_3 and μ_4, occurring in the constitutive equations.

Liquid-Gas Emulsion

As a result of lubrication approximation, details of which can be found in Chamniprasart et al. (1993), the component densities ρ_1 and ρ_2 are required to satisfy two nonlinear partial differential equations, the extended Reynolds equations

$$\frac{\partial}{\partial \bar{x}}\left[\bar{\rho}_1 H^3 \frac{\partial \Xi}{\partial \bar{x}}\right] + \left(\frac{D}{L}\right)^2 \frac{\partial}{\partial \bar{z}}\left[\bar{\rho}_1 H^3 \frac{\partial \Xi}{\partial \bar{z}}\right] = 12\Lambda \frac{\partial (\bar{\rho}_1 H)}{\partial \bar{x}}, \tag{10.98a}$$

$$\frac{\partial}{\partial \bar{x}}\left[\bar{\rho}_2 H^3 \frac{\partial \Xi}{\partial \bar{x}}\right] + \left(\frac{D}{L}\right)^2 \frac{\partial}{\partial \bar{z}}\left[\bar{\rho}_2 H^3 \frac{\partial \Xi}{\partial \bar{z}}\right] = 12\Lambda \frac{\partial (\bar{\rho}_2 H)}{\partial \bar{x}} + 12H\left[\frac{\partial \Gamma_x}{\partial \bar{x}} + \left(\frac{D}{L}\right)^2 \frac{\partial \Gamma_z}{\partial \bar{z}}\right], \tag{10.98b}$$

where

$$\Xi = \Xi(\bar{\rho}_1, \bar{\rho}_2), \qquad \Gamma_1 = \Gamma_1(\bar{\rho}_1, \bar{\rho}_2), \qquad \Gamma_2 = \Gamma_2(\bar{\rho}_1, \bar{\rho}_2).$$

Equations (10.80a) and (10.80b) represent the model of Chamniprasart et al. (1993) for the flow of bubbly oil in a bearing. To fully define the problem, these equations must be supplemented with conditions on ρ_1 and ρ_2 at the film boundaries.

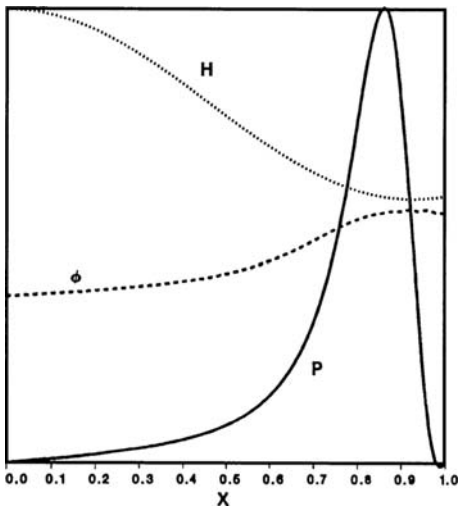

Figure 10.19. Pressure, film thickness and oil volume fraction distribution for oil-water emulsion in a journal bearing. (Reprinted with permission from Al-Sharif, A., Chamniprasart, T., Rajagopal, K. R. and Szeri, A. Z. Lubrication with binary mixtures: liquid-liquid emulsion. *ASME Journal of Tribology*, **115**, 46–55, 1993.)

Applications

Journal Bearing

The lubricating action of an emulsion can be understood by analyzing Figures 10.19 and 10.20. Similar to single phase lubricant, a pressure profile is generated such that the resulting flow field satisfies mass conservation of each of the components of the mixture. But in this case the composition of the mixture is changing in response to the stress field, the volume fraction of the higher viscosity constituent increases toward the minimum film thickness zone (Figure 10.19).

According to Hirn (1954), water requires high sliding speed to enter the clearance; at low sliding speeds the shaft will pull an oil-rich film into the clearance. The results in Figure 10.20 reflect this behavior: Poiseuille flow is dominant in the water phase (a), but Couette flow is dominant in the oil phase (b).

Figure 10.21 shows the pressure distribution in water-in-oil emulsion, corresponding to various inlet water volume fraction. On increasing water concentration from zero, the peak lubricant pressure first increases above its value for pure oil, only to exhibit rapid decline on further increasing the volume fraction of the water droplets. On reaching volume fraction of unity, we obtain the pressure distribution of pure water lubricant.

EHL Conjunction

In EHL contacts lubricated with water-in-oil emulsion, agreement with classical EHD film thickness is obtained only if the viscosity of the continuous phase (oil) is used when the diameter of the water droplets is in excess of the film thickness, for then, presumably, only oil passes through the conjunction (Dalmaz and Godet, 1977; Hamaguchi et al., 1977). This is also indicated by the fact that increased bulk viscosity, which results from adding water droplets to the oil lubricant, has no effect on film thickness (Hamaguchi et al., 1977). But

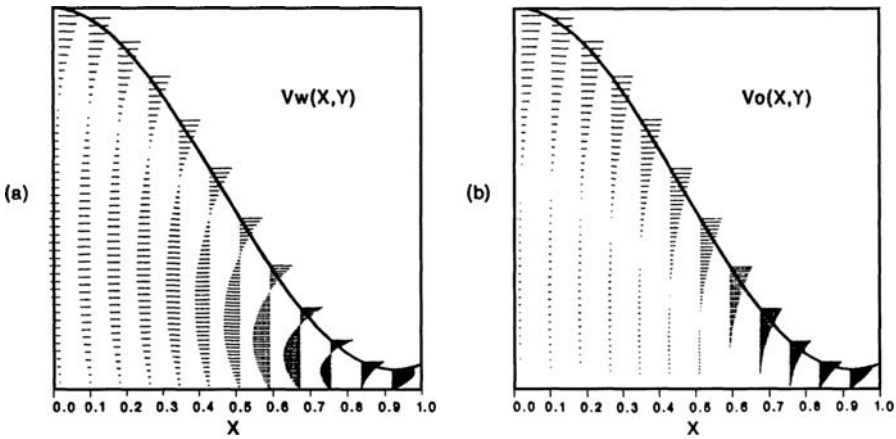

Figure 10.20. Velocity profiles for (a) water and (b) oil in oil-water mixture. (Reprinted with permission from Al-Sharif, A., Chamniprasart, T., Rajagopal, K. R. and Szeri, A. Z. Lubrication with binary mixtures: liquid-liquid emulsion. *ASME Journal of Tribology*, **115**, 46–55, 1993.)

if the water particles are small, the EHD film thickness is larger than could be obtained for the base oil; it is stipulated then that the emulsion proper and not just the continuous oil phase enters the conjunction. This yields a thicker film as the emulsion has higher viscosity than the base oil (Dalmaz, 1980; Wan et al., 1984).

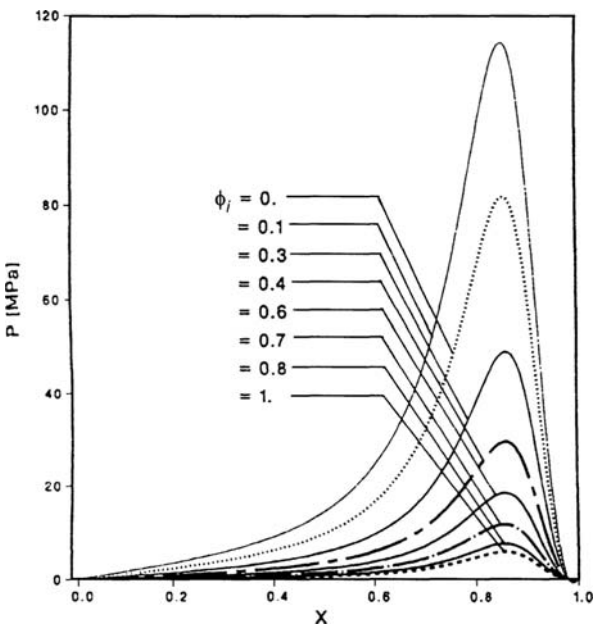

Figure 10.21. Pressure distribution in journal bearing for various values of inlet water volume fraction of water-oil mixture. (Reprinted with permission from Al-Sharif, A., Chamniprasart, T., Rajagopal, K. R. and Szeri, A. Z. Lubrication with binary mixtures: liquid-liquid emulsion. *ASME Journal of Tribology*, **115**, 46–55, 1993.)

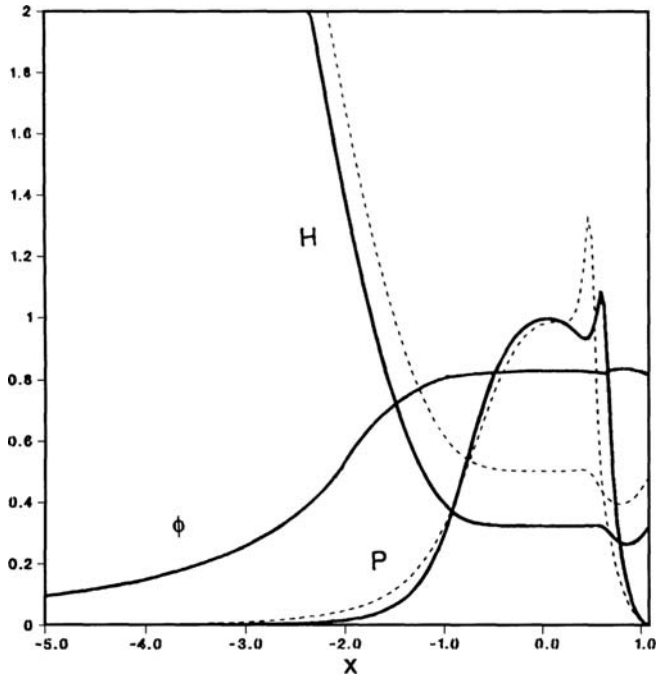

Figure 10.22. Film thickness, pressure, and void fraction profiles. $W = 1.35 \times 10^{-5}$, $U = 6.43 \times 10^{-12}$, $G = 3500$; - - - -, pure oil; – –, oil-water mixture. (Reprinted with permission from Wang, S. H., Al-Sharif, A., Rajagopal, K. R. and Szeri, A. Z. Lubrication with binary mixtures: liquid-liquid emulsion in an EHD conjunction. *ASME Journal of Tribology*, **115**, 515–524, 1993.)

The prime concern of the designer of EHL contacts is the film thickness. In EHL with conventional mineral oil lubricant, the film thickness parameter, H, is expressed as a certain function of the velocity parameter, U, the load parameter, W, and the materials parameter, G (Table 8.12). The principal additional parameters which characterize the material behavior of the binary mixture lubricant are (1) the inlet volume fraction of the oil ϕ_i; (2) the surface tension group, $\hat{C} = R_\delta^2 / W_e$, where R_δ and W_e are the droplet Reynolds number and the Weber number, respectively; and (3) the relative droplet radius, $\bar{r} = r/C$, of the discretized phase (Wang, Al-Sharif, Rajagopal, and Szeri, 1993).

It was reported by several investigators (Hamaguchi et al., 1977; Wan et al., 1984) that there is no detectable film in the conjunction for an oil-in-water emulsion, unless the emulsion breaks down and an oil pool is formed at the entrance; in this latter case the film thickness in the EHL conjunction is defined by the viscosity of the oil. Wang et al. were able to demonstrate a phenomena that is not unlike oil pooling. Figure 10.22 displays the film thickness and the pressure distributions in an oil lubricated conjunction giving $H_{\min} = 0.3923$ under the conditions noted. Figure 10.22 also shows the film thickness for an oil-in-water emulsion with inlet oil volume fraction $\phi_i = 0.1$. The volume fraction can be seen to increase rapidly with x from its entrance value of 0.1 to 0.834 and as a result of pooling the minimum film thickness achieves $H_{\min} = 0.234$, or 62% of its value for pure oil, while the pressures in the two cases are close.

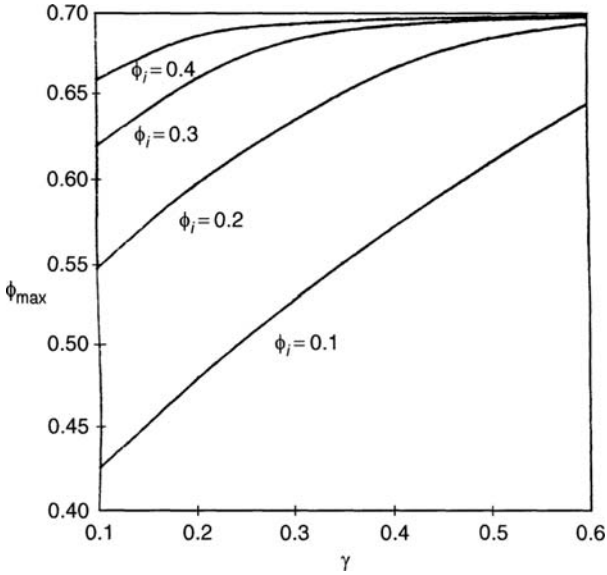

Figure 10.23. Effect of reduction ratio on $\phi_{\max}$. (Reprinted with permission from Wang, S. H., Szeri, A. Z. and Rajagopal, K. R. Lubrication of emulsion in cold rolling. *ASME Journal of Tribology*, **115**, 523–532, 1993.)

Cold Rolling

Grudev and Razmakhnin (1985a,b) report on extensive experimental investigations using water-based lubricants. Their principal findings are (1) the oil volume fraction, ϕ, increases with increasing reduction ratio, γ, of the workpiece to a limiting value that is largely independent of other conditions; (2) increasing the yield stress of the workpiece increases the tendency for oil-pooling; and (3) for every condition there is a value of γ above which the oil-in-water emulsion acts as pure oil. Wang et al. examined these propositions. Figure 10.23 shows the oil volume fraction increase with the reduction ratio, for the conditions of their paper the limit appears to be $\phi_{\max} \sim 0.7$.

At this limiting value of ϕ, the emulsion behaves as the pure oil. Figure 10.24 represents our solution for oil volume fraction distribution at various values of strip yield stress. The inlet value of ϕ is fixed at $\phi_i = 0.3$ in these calculations. At a yield stress of $\sigma_{yp} = 500$ MPa the working zone has $\phi_{\max} \approx 0.56$ and considerably thinner film than obtained with $\sigma_{yp} =$ 10 MPa, which gives only $\phi_{\max} \approx 0.37$. Figures 10.23 and 10.24 are, thus, in agreement with experimental findings of Grudev and Razmakhnin.

Lubrication with Bubbly Oil

The bearing referred to here was operated while fully submerged (Braun and Hendricks, 1981). To simulate operation under this condition Chamniprasart et al. make two assumptions: (1) the oil bath surrounding the bearing has constant, uniform composition, and (2) the conditions at the edge of the lubricant film are identical to and are given by the conditions in the bath. The first of these assumptions permits specification of a reference air volume fraction, ϕ_{20}, and a mixture reference bulk viscosity, β_0, at bath conditions. The second assumption assigns boundary conditions $\rho_1 = \rho_{10}$ and $\rho_2 = \rho_{20}$ on component densities.

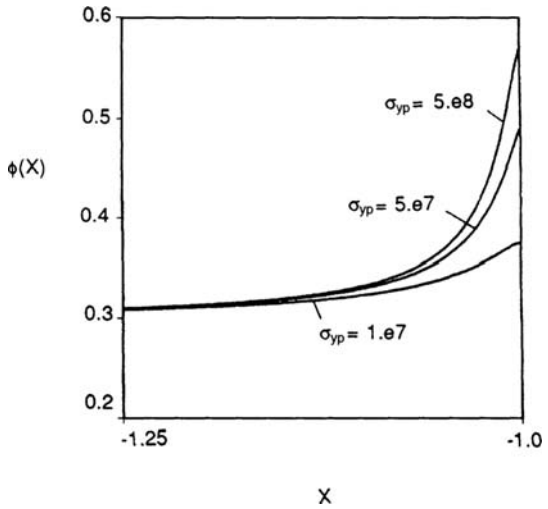

Figure 10.24. Effect of workpiece yield stress on oil volume fraction distribution. (Reprinted with permission from Wang, S. H., Szeri, A. Z. and Rajagopal, K. R. Lubrication of emulsion in cold rolling. *ASME Journal of Tribology*, **115**, 523–532, 1993.)

The reference bulk modulus of the mixture, β_0, will vary on varying the gas reference volume fraction, ϕ_{20}. When $\phi_{20} \to 0$, $\beta_0 \to \beta_1$, and we are effectively dealing with an oil, lubricant: the corresponding pressure distribution in the bearing approaches the classical, incompressible lubricant pressure distribution (Figure 10.25).

On increasing ϕ_{20}, on the other hand, we find that the negative pressure loop continually diminishes until, at $\phi_{20} = 1$, we obtain the pressure distribution for a gas lubricant (Raimondi, 1961). The maximum pressure first increases as ϕ_{20} is increased from zero; to get this increase in pressure, we would have to use a viscosity larger than the oil viscosity, μ_1, had we applied the classical Reynolds equation. This puts us in qualitative agreement with Taylor (1932) and Hayward (1961) for small air volume fraction in the mixture.

Figure 10.26 plots experimental data by Braun and Hendricks (1981) along with predictions from mixture theory (Chamniprasart et al., 1993) for centerline pressure, showing pressure variation in the cavitation zone.

10.6 Blood as Lubricant

Mechanical circulatory support as a treatment for congestive heart failure has gained increased acceptance over the past two decades. Recently published results of the REMATCH clinical trials (Rose et al., 2001) have confirmed the effectiveness of left ventricular assist devices (LVADs) over pharmacological options. The greater part of these blood pumps are axial flow devices that rotate at speeds in excess of 10,000 rpm. The temperature rise associated with such high speeds and the use of mechanical bearings through which the blood cells must pass, pose a serious risk of red cell lysis and thrombosis. These devices are presently in various stages of pre-clinical and clinical testing. Notwithstanding the success of these high-speed LVADs, the risk of thrombosis may limit their use for destination therapy.

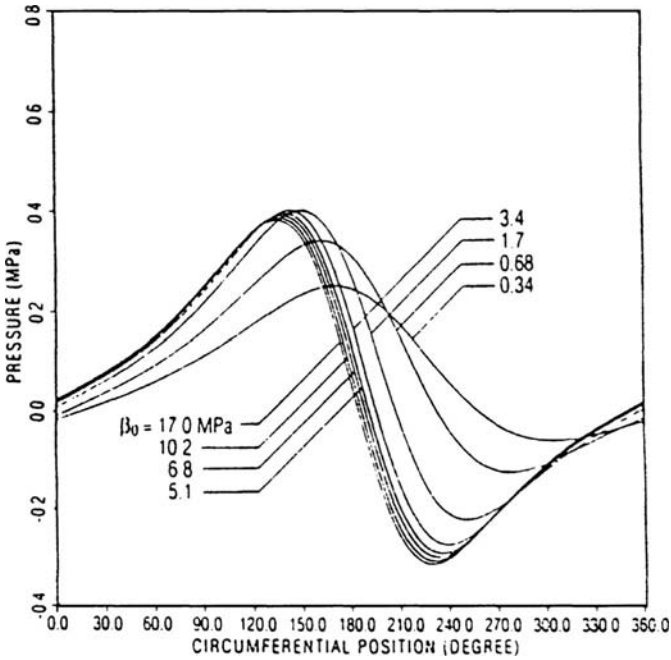

Figure 10.25. Pressure profile for various values of the reference bulk modulus β_0. (Reprinted with permission from Chamniprasart, T., Al-Sharif, A., Rajagopal, K. R. and Szeri, A. Z. Lubrication with bubbly oil. *ASME Journal of Tribology*, **115**, 253–260, 1993.)

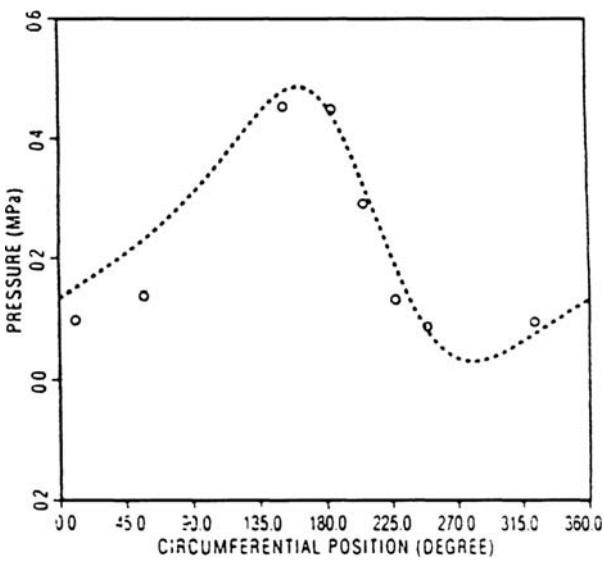

Figure 10.26. Bearing centerline pressure; – –, theoretical (Chamniprasart et al., 1993); o, experimental (Braun and Hendricks, 1981). (Reprinted with permission from Chamniprasart, T., Al-Sharif, A., Rajagopal, K. R. and Szeri, A. Z. Lubrication with bubbly oil. *ASME Journal of Tribology*, **115**, 253–260, 1993.)

Blood trauma is defined as the lysis of the blood's cellular components and is thought to be strongly influenced by flow stress (Leverett et al., 1972; Sallam and Hwang, 1984; Sharp et al., 1996). The high level of energy transmission from rotor to blood in rotary blood pumps is a potential source for blood trauma (Bludszuweit, 1995; Chan et al., 2002). The short-term stresses could be large, and the very process of circulation could result in cyclical long-term stress histories. To knowledgably address the design of LVADs the engineer must be cognizant of the material characteristics of blood as the flow stresses that might cause hemolysis depend on these characteristics.

The Rheology of Blood

The apparent viscosity of blood varies 25–30 fold as the rate of shear, κ, is varied over the range 0.01–100 s^{-1} (Yeleswarapu, 1996). The high viscosity at low shear rate is thought to be due to red blood cell (RBC) aggregation (rouleaux formation), while low viscosity at high shear rate is a consequence of the deformability of the red blood cells (Chien et al., 1967). Even though they are biconcave discoids of 8–10 μm diameter in their unstressed state, red blood cells are able to traverse a capillary of only 3 μm diameter without rupturing. In addition to shear thinning, measurements performed on blood also indicate typical viscoelastic effects, such as frequency dependence of the viscosity in unsteady flow (Thurston 1979; Hakim et al., 2001). Thus, from the point of view of mechanics, blood is both shear thinning (pseudo plastic) and viscoelastic.

The earliest recorded attempts to study the flow properties of blood (Young, 1809; Poiseuille, 1840) suggest Newtonian behavior. Poiseuille, however, already observed, under certain conditions, a cell-free layer close to the wall of the tube that suggested deviations from the earlier estimates. Denning and Watson (1906) and Fahraeus and Lindqvist (1931) noted an anomalous property of the apparent viscosity of blood, viz., its dependence on the diameter of the tube used in measuring it. These, and later investigations (Zhang and Kuang, 2000; Drochon, 2003) confirm that blood is a non-Newtonian fluid. Beyond a certain high shear rate, nevertheless, there is transition to Newtonian behavior (Paul et al., 2003); though this is well accepted as fact, published data on the transition threshold diverge (Whitmore, 1968; Chmiel, 1973). The assumption that at a well-chosen "effective viscosity" the Newtonian fluid computes the same flow conditions as would be exhibited in a shear thinning fluid is often exploited in computation (Burgreen et al., 2004; Arora et al., 2004). Such an assumption is not usually made in dealing with generalized fluid motion; furthermore, if valid, it would preclude the need for an entire science dealing with non-Newtonian fluids. Though it is true that for simple shear flow the stress profile is the same in all simple fluids irrespective of their constitutive equation (Truesdell and Noll, 1992), this no longer holds for more general flows. Furthermore, in estimating the degree of lysis suffered by RBCs in a mechanical device, one needs to compute the flow path, the time it takes for the cells to travel that path, as well as the ambient stress field. And the velocity distribution in a shear thinning fluid might be very different from that obtained in a Newtonian fluid. To illustrate that the flow field of a shear thinning fluid of viscosity $\mu = \mu_s = \mu(\dot{\gamma})$, where $\dot{\gamma}$ is the rate of shear in 1-D flow, is not approximated well by the flow field of a Newtonian fluid of viscosity $\mu = \mu_N = \text{const.}$, no matter what value of μ_N one chooses (c.f. Figure 10.1).

Rheological models may be classified as phenomenological or microstructural. The former aims to derive stress-strain relations that describe observed phenomena, without

necessarily considering microstructure or the interaction between individual constituents of the fluid. The microstructural approach, on the other hand, endeavors to describe observed phenomena from the known (or presumed) properties and structure of the microscopic constituents of the fluid, and the interactions between these components. Phenomenological models have the potential to duplicate the rheological behavior of blood; they are also simple enough to be implemented in a CFD analysis and design optimization of LVADs.

The models of the phenomenological approach may be thought of as either empirically based or as continuum based, although this distinction is blurred at times. For example, the W-S model (Walburn and Schneck, 1976) is an empirical model, yet it has symmetries of material frame indifference and flow reversal (Easthope, 1989), and has been extended to 3-D. Empirical models are generally one-dimensional and are not necessarily based on physical principles. They are obtained by fitting an appropriate, ad hoc, mathematical function to experimental data. Continuum-based models, on the other hand, are three-dimensional and obey the fundamental principles of continuum physics, viz., (a) determinism, (b) local action, and (c) frame indifference. In the following paragraphs we present a brief survey of some of the rheological models applied to blood.

Belief in the existence of a yield stress led early on to Casson's equation (Leverett et al., 1972; Casson, 1959; Reiner and Scott-Blair, 1959; Baajines et al., 1993; Rohlf and Tenti, 2001; Das et al., 1998). Later, to better portray the essential property of shear thinning, the power law model was borrowed from non-Newtonian fluid mechanics. Several power law models have been proposed, one of the most successful being the W-S model (Walburn and Schneck, 1976). Easthope and Brooks (1980) made experimental comparison of eleven different constitutive functions for whole human blood, and pronounced the W-S model to be the most successful one. In contrast, Zhang and Kuang (2000) found Casson-type models superior to the W-S and other power law models. Other empirical models of particular note are the Cross model, the Powell-Eyring model, and the Carreau model. Cho and Kensey (1991) summarize these as well as some more elaborate constitutive models for portraying the viscosity of whole human blood.

Rodkiewicz et al. (1990) presented a comparison of the W-S, the Casson and the Bingham (Bingham, 1922; Ishikawa et al., 1998) models to study pulsatile flow. Zhang and Kuang (2000) compared Casson-type and power-law-type (including W-S) models and found the performance of the Quemada equation (Quemada, 1982), a Casson-type model, superior. These models, however, are not well suited to characterize three-dimensional, viscoelastic flows or to portray shear thinning over the entire practical range of shear rate variation, unless they contain so many parameters as to render them impractical. In addition, it has been observed that the power-law parameters depend substantially on the range of shear rate for which data is being fitted. All these reasons prompt us to search among continuum models.

Modern (nonclassical) continuum models are based on the theory of structured continua, micropolar fluids or fluids with couple stresses. They can describe rheological anomalies such as Fahraeus-Lindqvist (Popel et al., 1974), but appear to be too complex to apply in CFD schemes. Models based on single continuum theories appear to be more suitable here; they are, broadly speaking, of (a) differential type, (b) rate type, and (c) integral type. Of these, differential-type (Majhi and Usha, 1988) models seem to be unrealistic and we are not aware of integral-type rheological equations ever having been employed for the rheological

characterization of blood, due to their great mathematical complexity. This leaves us with rate-type models to characterize blood rheology in 3-D.

Rheological Models

Rate-type constitutive equations (Joseph, 1989) can describe viscoelastic behavior and have been used for decades for this purpose. They are of the general form

$$\boldsymbol{\tau}_k = \boldsymbol{f}(\boldsymbol{\tau},\ \dot{\boldsymbol{\tau}}, \ldots, \dot{\boldsymbol{\tau}}_{k-1};\ \boldsymbol{A}_1,\ \boldsymbol{A}_2, \ldots \boldsymbol{A}_n). \tag{10.99}$$

Here $\boldsymbol{\tau}$ is the extra stress, $\boldsymbol{A}_1, \ldots, \boldsymbol{A}_n$ are the Rivlin-Ericksen tensors (10.16), and the index k symbolizes the order of material derivative.

Among rate-type models, the Maxwell model was perhaps the first to be employed for characterizing the rheology of blood (Thurston, 1979). Quemada later proposed a nonlinear version of this model (Quemada and Droz, 1983; Quemada, 1993), while Sharp used a generalized version of it (Sharp et al., 1996). Phillips and Deutsch (Phillips and Deutsch, 1975; Deutsch et al. 1976; Deutsch and Phillips, 1977) employed another well-known rate-type model, the four-constant Oldroyd-B model. Hakim et al. (2001) compared the performance of seven different viscoelastic constitutive equations in predicting pony blood rheology. Several of these models were found to capture viscoelastic behavior such as frequency dependence; of particular mention are the Thurston model and the Giesekus model. Nevertheless, they were somewhat inadequate in their portrayal of shear thinning.

To improve characterization of shear thinning while retaining the facility to portray viscoelastic behavior, Rajagopal and co-workers (Yeleswarapu et al., 1998, Yeleswarapu, 1996) proposed a three-parameter, nonlinear, Oldroyd-B model of the form

$$\begin{gathered} \boldsymbol{T} = -\boldsymbol{p}1 + \boldsymbol{\tau} \\ \boldsymbol{\tau} + \Lambda_1[\dot{\boldsymbol{\tau}} - \boldsymbol{L}\boldsymbol{\tau} - \boldsymbol{\tau}\boldsymbol{L}^T] = \mu(\boldsymbol{D})[\boldsymbol{D}] + \Lambda_2[\dot{\boldsymbol{D}} - \boldsymbol{L}D - \boldsymbol{D}L^T] \end{gathered} \tag{10.100}$$

Here Λ_1 and Λ_2 are the relaxation and retardation constants, respectively, which specify viscoelastic behavior (Newtonian rheology is characterized by $\Lambda_1 = \Lambda_2 = 0$, $\mu = \text{const.}$).

To mimic shear thinning, the viscosity function $\mu(D)$ in Eq. (10.100) was made to depend upon the stretching tensor. However, to satisfy frame invariance, this dependence must occur in the form $\mu(\boldsymbol{D}) = \mu(I_D, II_D, III_D)$. For an incompressible fluid in viscometric flow, the first and the third invariants vanish, leaving the second invariant as the only argument of the viscosity function. Thus $\mu(D) = \mu(\kappa)$ and $\kappa = |II_D|$ is the rate of shear in three-dimensional flow.

As the viscosity has distinct asymptotic values, η_0 at $\kappa \to 0$ and η_∞ at $\kappa \to \infty$, Yeleswarapu searched for a generalized viscosity function of the form

$$\mu(\kappa) = \eta_\infty + (\eta_0 - \eta_\infty) f(\kappa) \tag{10.101}$$

and found best fit to viscometric data on whole human blood when choosing

$$f(\kappa) = \left[\frac{1 + \ln(1 + \Lambda\kappa)}{(1 + \Lambda\kappa)}\right]. \tag{10.102}$$

Yeleswarapu studied regression of the shear thinning models of Powell-Eyring, modified Powell-Eyring, and Cross, as well as the proposed function, Eq. (10.101), to Chien's

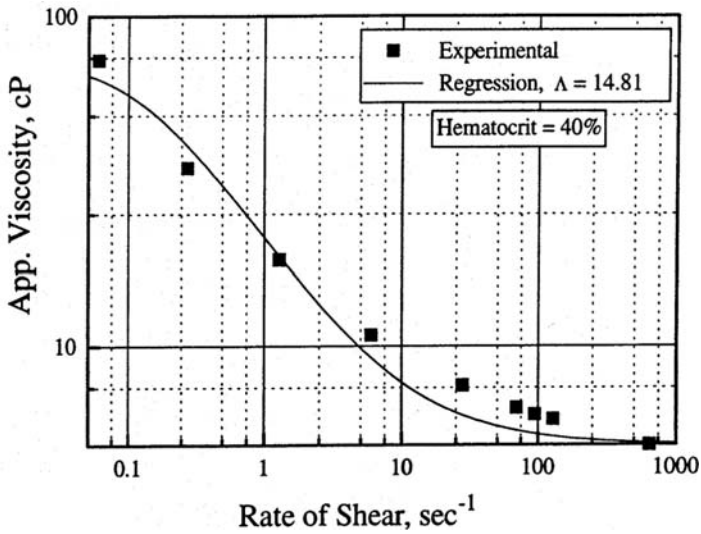

Figure 10.27. Fitting Eq. (3) for whole human blood (Reprinted from Yeleswarapu, K. K. Evaluation of continuum models for characterizing the constitutive behavior of blood, Ph.D. Dissertation, University of Pittsburgh, 1996.)

experimental data (Chien et al., 1967); Eq. (10.101) performed very favorably in this comparison. In a second effort to validate the model, Yeleswarapu fitted Eq. (10.101) to his own data, shown for normal human blood in Figure 10.27, and for porcine blood in Figure 10.28.

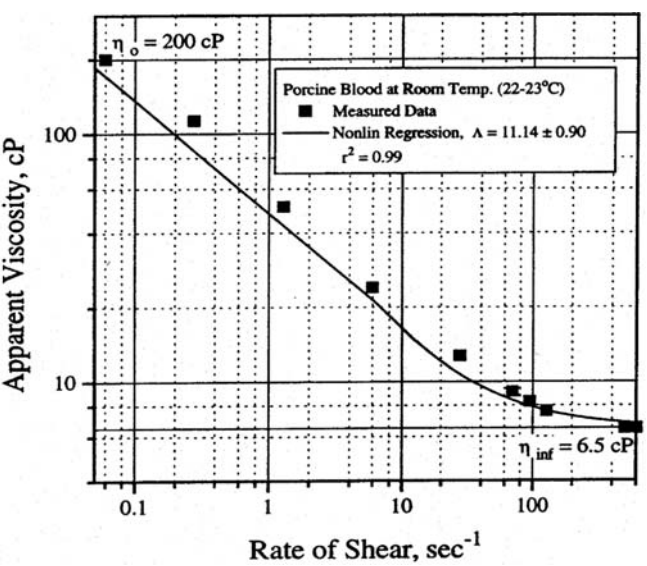

Figure 10.28. Fitting Eq. (10.100) for porcine blood (Reprinted from *Mech. Res. Comm.* **25**(3), Yeleswarapu, K. K., Kameneva, M. V., Rajagopal, K. R. and Antaki, J. F. The flow of blood in tubes: theory and experiment, 257–262, Copyright (1998) with permission from Elsevier.)

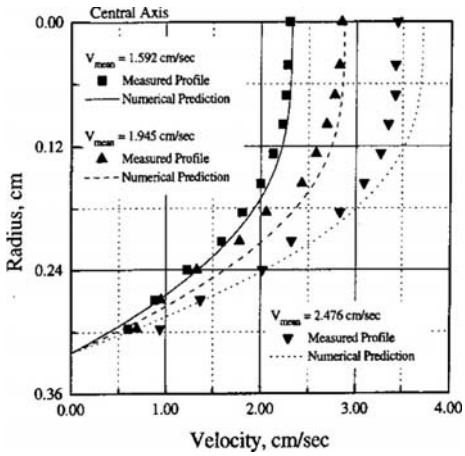

Figure 10.29. Poiseuille flow for porcine blood (Reprinted from *Mech. Res. Comm.* **25**(3), Yeleswarapu, K. K., Kameneva, M. V., Rajagopal, K. R. and Antaki, J. F. The flow of blood in tubes: theory and experiment, 257–262, Copyright (1998) with permission from Elsevier.)

Predictions of the generalized Oldroyd-B model in pipe flow of porcine blood are compared with experimental data in Figure 10.29 (Yeleswarapu et al., 1998).

The most recent generation of mechanical blood pumps that date back only a few years utilize magnetic levitation for bearing support, which removes the potential for wear and pump failure, ensuring long-term use. However, many of the existing concepts suffer from mechanical and electrical complexity, high power consumption and consequent heating.

Blood Trauma Models

The older, stress-based models of hemolysis assume that the membrane of the RBC sees, and directly responds to, the local stress in the ambient fluid, even under rapidly varying conditions: hemolysis is predicted when the accumulated stress reaches a threshold value. However, the membrane of the RBC is viscoelastic and is, therefore, unable to follow rapid stress variations in the ambient fluid; these variations will be smoothed, so to speak, by the viscoelasticity of the membrane. In consequence, a strain-based hemolysis model leads to lower hemolysis than a stress-based model in rapidly varying flow fields. In this section we discuss stress-based and strain-based models, but advocate use of the strain-based hemolysis model.

LVADs are often associated with flow-induced blood damage, particularly hemolysis of red blood cells. The red blood cell may be pictured as a thin (thickness, $b = 7$ nm) viscoelastic (relaxation time, $\lambda \sim 200$ ms) membrane sack, enveloping a solution of hemoglobin and platelets. In stress-free state, the cell resembles a biconcave disk of diameter $\sim 8\ \mu$m and surface area $\sim 40\%$ in excess of that of a sphere of the same volume. In consequence, the RBC changes its shape readily but strongly resists any change in its surface area. When the cell is immersed in a shear field it may exhibit one of two types of motion. At low shear, its motion is time unsteady, with the yet undeformed cell tumbling. At higher shear, the cell deforms into an ellipsoid, assuming stationary orientation relative to the flow direction; however,

the membrane circulates about the interior of the cell in a tank-tread like motion (Fisher et al., 1978; Keller and Skalak, 1982). As the shear stress is increased, the RBC becomes more elongated and reversible hemolyzing pores open up in the membrane. Finally, above about 150 Pa shear stress, the membrane ruptures causing extensive hemolysis (Leverett et al., 1972). This level of shear stress corresponds to a shear rate of 42,000 s^{-1} at an apparent viscosity of 3.2 mPa · s and to about 6% areal strain of the membrane. To quote Blackshear and Blackshear (1987), "Areal change occurs when the cell membrane is subjected to stress; hemolysis occurs when the area increases by approximately 6.4%."

The damaging effects on the RBC are known to depend on the magnitude of the shear stress, τ, acting on the cells, and the residence time of the cells in the stressed environment, Δt. Damage is remarkably low over a broad range of shear rates and exposure times. However, there is a stress level above which a significant increase in blood damage can be observed at sufficiently long exposure. This threshold stress was measured by several researchers (Sutera, 1977; Wurtzinger et al., 1985). Leverett, as already mentioned, gives the figure of $\tau = 150$ Pa for moderate exposure time. Other measurements indicate significantly increased blood damage when

$$\tau \geq 425\,\text{Pa} \quad \text{and} \quad \Delta t \geq 620\,\text{ms}.$$

One of the earliest attempts to relate maximum permissible shear stress to time of exposure was through the formula $\tau\sqrt{\Delta t} = \text{const.}$ (Blackshear et al., 1966). Two-dimensional analysis of the data of Wurzinger et al. (1986) led Giersiepen and co-workers (Giersiepen et al., 1990) to the improved correlation

$$\frac{\Delta Hb}{Hb} = 3.62 \times 10^{-7} \tau^{2.416} \Delta t^{0.785}. \tag{10.103}$$

Here $\Delta Hb/Hb$ is the ratio of plasma free hemoglobin to the total hemoglobin in the sample. The equation proposed by Giersiepen has been used in CFD-type computations (Chan et al., 2002; De Wachter and Verdonck, 2002), though it has been criticized for not containing a threshold stress (Paul et al., 2003).

Anderson et al. (2000) have compiled data on the threshold value of stress and the corresponding exposure time. The Giersiepen model might be improved upon by incorporating a threshold stress, though this has been disputed by some researchers.

The experimental data embodied in Eq. (10.103) is for steady, one-dimensional flow, whereas flow in an LVAD is both unsteady and three dimensional. To overcome this inconsistency between the experimental evidence and its application, researchers attempt to relate 3-D flow effects to steady shear flow through variously defined, instantaneous, scalar parameters. Bludszuweit, for example, found it advantageous to think in terms of a dimensionless damage parameter, somewhat in analogy with failure criteria in solid mechanics (von Mises yield criterion); the parameter is zero initially and reaches unit value at the point of RBC catastrophic damage (failure cycle N). Bludszuweit then assumed the partial damage after n cycles to be equal to n/N times the damage at failure. The blood trauma model of Bludszuweit has been used in CFD analysis of a centrifugal pump (Bludszuweit, 1995) and, more recently in a CFD analysis of an intracardiac axial flow pump (Mitoh et al., 2003). Based on the assumption that the effect of shear accumulates along particle path, Mitoh et al. summed the damage equation proposed by Bludszuweit

following the particle. Arora et al. (2004) refer to models that characterize complex flow stress by an instantaneous scalar parameter as "stress-based" models.

Based on earlier work by Maffettone and Minale (1998) on liquid drops, Arora et al. (2004) propose a new, and qualitatively different, concept of RBC damage. They represent the shape of the ellipsoidal RBC by the quadratic surface of a symmetric, positive definite, second rank tensor $\boldsymbol{M}$. The eigenvalues of this so-called morphology tensor are the square principal semi-axes of the ellipsoid, whose volume is conserved by keeping $\det(\boldsymbol{M}) = \text{const}$. The evolution of the morphology tensor, resulting from competition between drag forces inducing deformation and the interfacial tension attempting to recover the undistorted ellipsoidal shape, is defined by

$$\boldsymbol{M}^* = -c_1[\boldsymbol{M} - g(\boldsymbol{M})\boldsymbol{I}] + c_2[\boldsymbol{D}\cdot\boldsymbol{M} + \boldsymbol{M}\cdot\boldsymbol{D}]. \tag{10.104}$$

Here

$$\boldsymbol{M}^* = \frac{\partial \boldsymbol{M}}{\partial \boldsymbol{t}} + \boldsymbol{u}\cdot\nabla\boldsymbol{M} - \boldsymbol{\Omega}\cdot\boldsymbol{M} + \boldsymbol{M}\cdot\boldsymbol{\Omega}$$

is the Jaumann derivative of $\boldsymbol{M}$, $\boldsymbol{\Omega} = (L - \boldsymbol{L}^T)/2$ is the spin tensor, $c_1 = 1/\lambda$ and $\lambda = \tau/\mu R$ is the relaxation time of the membrane. Henon et al. (1999) find that $\tau \sim 200\,\text{ms}$ for RBCs. The first term on the right-hand side in Eq. (10.104) models interfacial tension: the function $g(\boldsymbol{M})$ is introduced to preserve the volume of the cell and is defined in terms of the invariants of $\boldsymbol{M}$. The second term represents the effect of the imposed deformation. Application of the Jaumann derivative instead of a partial time derivative assures us that Eq. (10.104) is properly frame invariant.

Liquid drops do not tank-tread, red blood cells, on the other hand, do. To account for the instantaneous rotation of the tank-treading RBC's membrane, Arora expresses Eq. (10.104) relative to the rotating frame defined by the eigenvectors of $\boldsymbol{M}$; this adds another term to the right-hand side, so now

$$\boldsymbol{M}^* = -c_1[\boldsymbol{M} - g(\boldsymbol{M})1] + c_2[\boldsymbol{D}\cdot\boldsymbol{M} + \boldsymbol{M}\cdot\boldsymbol{D}] + c_3[(\boldsymbol{\Omega} - \boldsymbol{W})\cdot\boldsymbol{M} - \boldsymbol{M}\cdot(\boldsymbol{\Omega} - \boldsymbol{W})] \tag{10.105}$$

and replaces $\boldsymbol{\Omega}$ with $\boldsymbol{W}$ in the definition of the Jaumann derivative. Here $\boldsymbol{W}$ is the spin of the principal triad of $\boldsymbol{M}$. In effect, Eq. (10.105) states that the vorticity that is seen by the tank-treading membrane equals the vorticity of the ambient fluid minus the spin of the principal triad.

Experimental observations on RBCs in steady shear flow guided Arora et al. to choose $c_1 = 5.0\,\text{s}^{-1}$, while stability considerations and the matching of the surface area of the RBC with 6% area increase at catastrophic hemolysis yielded $c_2 = c_3 = 1.25 \times 10^{-3}$. Together, the three parameters incorporate critical membrane strain, membrane relaxation time, tank treading, and shape oscillations, into this strain-based hemolysis model.

Having computed the evolution of the morphology tensor $\boldsymbol{M}$ from Eq. (10.105), it is now possible to calculate the instantaneous shape distortion $D = (L - B)/(L + B)$, where L and B are the axial dimensions of the ellipsoidal RBC. For simple shear there exists a unique relationship between the strength of the shear flow and the shape distortion

parameter D: it can be found by computing the eigenvalues of $\boldsymbol{M}$ from the steady state version of Eq. (10.104) written for simple shear. Arora employs this relationship to compute an effective shear flow that corresponds to the actual shape distortion

$$\tau_{\text{eff}} = \mu_{\text{blood}}\kappa_{\text{eff}}, \quad \kappa_{\text{eff}} = \sqrt{\frac{c_1^2 D^2}{\left(1 - D^2\right) c_2^2}}. \tag{10.106}$$

Thus, while the stress-based model assumes equivalence of instantaneous fluid stress and RBC membrane stress, the strain-based model computes an equivalent steady shear stress corresponding to instantaneous RBC deformation. Substituting τ_{eff} for τ in Eq. (10.103), we obtain the strain-based hemolysis model

$$\frac{d}{dt}\left(\frac{\Delta Hb}{Hb}\right) = 2.8417 \times 10^{-7}\left[\mu_{\text{blood}}\sqrt{\frac{c_1^2 D^2}{(1 - D^2)\, c_2^2}}\right]^2 .416\Delta t^{-0.215}. \tag{10.107}$$

In an unsteady flow where stress fluctuations are superimposed on a steady baseline shearing, the stress-based model and the strain-based model yield identical results at low fluctuation frequency. Under such condition, the RBC membrane sees the same stress as the host fluid. However, as the frequency is increased such that the periodic time of fluctuation becomes comparable to the relaxation time of the membrane, the RBC can no longer respond accurately to the fluctuations. Thus, the contribution of the rapidly varying component of shearing to cell deformation diminishes with increasing frequency, and the strain-based model will predict lower hemolysis than does the stress-based model (Arora et al., 2004).

10.7 Nomenclature

A	Helmholtz free energy
$\boldsymbol{A}_{(n)}$	Rivlin-Ericksen tensor
C	radial clearance
$\hat{C}$	surface tension group
C, C_α	mixture, αth constituent
D	shaft diameter, distortion parameter
$\boldsymbol{D}$	stretching tensor
De	Deborah number
$\boldsymbol{F}$	deformation gradient
G	material parameter
H	film thickness parameter
H	nondimensional film thickness
$\boldsymbol{L}$	velocity gradient
L	journal length
L_{xz}, L_y	characteristic lengths
R	journal radius
Re	Reynolds number
R_ε	reduced Reynolds number
R_δ	droplet Reynolds number

$\boldsymbol{T}$	stress tensor
U	velocity parameter
U_*, V_*	characteristic velocities
$\boldsymbol{V}^{(12)}$	relative velocity
W	load parameter
$\boldsymbol{\Omega}$	spin
$\boldsymbol{\Omega}_{(1,2)}$	relative spin
We	particle Weber number
$\boldsymbol{X}$	reference (material) coordinate
r	external heat supply
$\boldsymbol{b}$	external body force
c	specific heat
$\boldsymbol{g}$	temperature gradient
$\boldsymbol{h}$	density gradient
h	film thickness
k_1, k_2	material functions
k	power law consistency index
n	power law exponent
p, P	lubricant pressure
$\boldsymbol{q}$	heat transfer by conduction
ret(.)	retarded motion
t	time
$\boldsymbol{x}$	Eulerian coordinate
$\boldsymbol{v} = (u, v, w)$	velocity
ϖ_1, ϖ_2	material functions
$\boldsymbol{\omega}$	vorticity
γ	reference density, reduction ratio
e	internal energy density
η	entropy density
Θ	mixture temperature
λ	relaxation time
$\lambda_1, \ldots \lambda_5$	material functions
$\mu_1, \ldots, \mu_4$	viscosities
ν	kinematic viscosity
$\boldsymbol{\pi}$	diffusive body force
$\boldsymbol{\tau}$	shear stress tensor
τ_e, τ_L	equivalent, limiting shear stress
τ	residence time
ρ	density
ϕ	volume fraction
$\boldsymbol{\chi}$	deformation function
$()_{(\alpha)}$, $()^{(\alpha)}$	pertaining to C_a
$()_*$	reference quantity
$()_o$	reference state
$(^-)$	nondimensional
tr[.]	trace
Π	Lagrange multiplier

10.8 References

Almqvist, T. and Larsson, R., 2002. The Navier-Stokes approach for thermal EHL line contact solution. *Tribol. Int.* **35**, 163–170.

Al-Sharif, A. 1992. *Hydrodynamic Lubrication with Emulsions*. Ph.D. thesis, Department of Mechanical Engineering, University of Pittsburgh.

Al-Sharif, A., Chamniprasart, T., Rajagopal, K. R., and Szeri, A. Z. 1993. Lubrication with binary mixtures: liquid-liquid emulsion. *ASME Journal of Tribology*, **115**, 46–55.

Anderson, J. B., Wood, H. G., Allaire, P. E., McDaniel, J. C., Olsen, D. B, and Bearnson. G. 2000. Numerical studies of blood shear and washing in a continuous flow ventricular assist device. *ASAIO J.*, **46**, 486–487.

Antman, S. S. and Marlow, R. S. 1991. Material constraints, Lagrange multipliers, and compatibility – application to rod and shell theories. *Arch. Ratl. Mech. Anal.*, **116**(3), 257–299.

Arora, D., Behr M. and Pasquali M. 2004. A tensor-based measure for estimating blood damage. *Artif. Organs*, **28**(11), 1002–1015.

Atkin, R. J., and Craine, R. E. 1976a. Continuum theories of mixtures: basic theory and historical development. *Q. J. Mech. Appl. Math.*, **29**, 209.

Atkin, R. J., and Craine, R. E. 1976b. Continuum theories of mixtures: applications, *J. Inst. Math. Appl.*, **17**, 153.

Baajines, J. P. W., Van Steenhoven, A. A. and Janssen, J. D. 1993. Numerical analysis of steady generalized Newtonian blood flow in a 2-D model of the carotid artery bifurcation. *Biorheology*, **30**, 63–74.

Bair, S. 2000.The variation of viscosity with temperature and pressure for various real lubricants. *ASME 2000-TRIB-25*.

Bair, S. 2009. Rheology and high-pressure models for quantitative elastohydrodynamics. *Proc. ImechE J.*, **223**, 617–628.

Bair, S. and Khonsari, M. 1996. An EHD inlet zone analysis incorporating the second Newtonian. *J. Lub. Tech.*, **118**, 341–343.

Bair, S. and Winer, W. O. 1979. A rheological model for elastohydrodynamical contacts. *ASME J. Lub. Tech.*, **101**, 248.

Bair, S., Fernandez, J., Khonsari, M. M., Krupka, I., Qureshi, F., Vergne, P. and Wang, Q. J. 2009. An argument for a change in elastohydrodynamic lubrication philosophy. *Proc. IMechE J*, **223**, 1–2.

Bair, S., Khonsari, M. and Winer, W. O., 1998. High-pressure rheology of lubricants and limitations of the Reynolds equation. *Tribol. Int.*, **10**, 573–586.

Bair, S., Vergne, P. and Querry, M. 2005. A unified shear-thinning treatment of both film thickness and traction in EHD. *Tribol. Letts.*, **18**(2), 145–152.

Barlow, A. J., Erginsau, A. and Lamb, J. 1969. Viscoelastic relaxation in liquid mixtures. *Proc. Roy. Soc.*, **309A**, 473–96.

Barlow, A. J., Harrison, G., Irving, J. B., Kim, M. G. and Lamb, J. 1972. The effect of pressure on the viscoelastic properties of Liquids. *Proc. Roy. Soc.*, **327A**, 403–12.

Bedford, A., and Drumheller, D. S. 1983. Recent advances: theories of immiscible and structured mixtures. *Int. J. Eng. Sci.*, **21**, p. 863.

Bendler, J. T., Fontanella, J. J. and Schlesinger, M. F., 2001. A new Vogel-like law: ionic conductivity, dielectric relaxation, and viscosity near the glass transition. *Phys. Rev. Let.*, **87**, 195503-1–4.

Beris, A. N., Armstrong, R. C., Brown, R. A. 1983. Perturbation theory for viscoelastic fluids between eccentric rotating cylinders. *J. Non-Newtonian Fluid Mech.*, **13**, 109–148.

Bernstein, B. Kearsley, E. A. and Zapas, L. J. 1963. A study of stress relaxation with finite strain. *Trans. Soc. Rheol.*, **7**, 391–410.

Bingham, E. C. 1922. *Fluidity and Plasticity*. McGraw-Hill, New York.

Blackshear, P. L. and Blackshear, G. L. 1987. Mechanical hemolysis. In *Handbook of Bioengineering* (R. Skalak, and S. Chien, eds.) McGraw-Hill, New York.

Blackshear, P. L., Dorman, F. D., Steinbach, J. H. Maybach, E. J. and Collingham, R. E. 1966. Shear wall interaction and hemolysis. *Trans. Am. Soc. Artif. Intern.* Organs, **12**, 113–120.

Bludszuweit, C. 1995. Three dimensional numerical prediction of stress loading of particles in a centrifugal pump. *Artif. Organs*, **19**(7), 590–596.

Bourgin, D. 1979. Fluid-film flows of differential fluids of complexity n dimensional approach – applications to lubrication theory. *ASME J. Lub. Tech.*, **101**, 140–4.

Bourgin, D. and Gay, B. 1983. Determination of the load capacity of a finite width journal bearing by a finite element method in the case of a non-Newtonian lubricant. *ASME J. Lub. Tech.*

Bowen, R. M. 1976. *Theory of Mixtures, Continuum Physics* (A. C. Eringen, ed.), Academic Press, New York, Vol. 3, Part 1.

Braun, M. J., and Hendricks, R. 1981. An experimental investigation of the vaporous/gaseous cavity characteristics of an eccentric journal bearing. *ASLE Trans*., **27**(1), 1–14.

Bridgman, P. W. 1931. *The Physics of High-Pressure*, MacMillan, New York.

Buckholtz, R. H. 1985. Effects of power-law, non-Newtonian lubricants on load capacity and friction for plane slider bearing. *ASME/ASLE Joint Conf.* Paper No. 85-Trib-23.

Buckholtz, R. H. and Wang, B. 1985. The accuracy of short bearing theory for Newtonian lubricants. *ASME/ASLE Joint Conf.* Paper No. 85-Trib-49.

Burgreen, G. W., Loree, H. M., Bourque, K. Dague, C., Poirier, V. L., Farrar, D., Hampton, E., Wu, Z. J., Gempp, T. M. and Schob, R. 2004. Computational fluid dynamics analysis of a maglev centrifugal left ventricular assist device. *Artif. Organs*, **28**(10), 874–880.

Butterworth, O., and Hewitt, G. F. 1977. *Two-Phase Flow Heat Transfer.* Oxford University Press, London.

Casson, N. 1959. A flow equation for pigment oil suspension of printing ink type. In *Rheology of Dispersed Systems* (C. C. Mill, ed), Pergamon Press, Oxford.

Chamniprasart, T., Al-Sharif, A., Rajagopal, K. R, and Szeri, A. Z. 1993. Lubrication with bubbly oil. *ASME Journal of Tribology*, **115**, 253–260.

Chamniprasart. K. 1992. *A Theoretical Model of Hydrodynamic Lubrication with Bubbly Oil*. Ph.D. dissertation, Department of Mechanical Engineering, University of Pittsburgh.

Chan, W. K., Wong, Y. W., Ding, Y., Chua, L. P. and Yu, S. C. M. 2002. Numerical in vestigation of the effect of blade geometry on blood trauma in a centrifugal blood pump. *Artif. Organs*, **26**(9), 785–793.

Cheng, H. S. 1966. Plastohydrodynamic lubrication. *Friction in Metal Processing*, ASME Symp. New Orleans, p. 69.

Chien, S., Usami, S., Dellenback, R. J. and Gersen, M. I. 1967. Blood viscosity influence of erythrocite aggregation. *Science*, **157**, 829–831.

Chmiel, H. 1973. *Zur Blutrheologie in Medizin und Technik*. Ph.D. Dissertation, Aachen, Germany.

Cho, Y. I. and Kensey, K. R. 1991. Effects of non-Newtonian viscosity of blood on flows in a diseased arterial vessel. *Biorheology*, **28**, 41–262.

Christie, I., Rajagopal, K. R. and Szeri, A. Z. 1987. Flow of a non-Newtonian fluid between eccentric rotating cylinders. *Int. J. Eng. Sci.*, **25**, 1029–1047.

Cohen, M. H. and Turnbull, D. 1959. Molecular transport in liquids and gases. *J. Chem. Phys.*, **31**(5), 1164–1169.

Cook, R. L., Herbst, C. A. and King, H. E. 1993. High-pressure viscosity of glass-forming liquids measured by the centrifugal force diamond anvil cell viscometer, *J. Phys. Chem.*, **97**, 2355–2361.

Cook, R. L., King, H. E., Herbst, C. A. and Herschbach, D. R. 1994. Pressure and temperature dependent viscosity of two glass forming liquids: glycerol and dibutyl phthalate. *J. Chem. Phys.*, **100**(7), 5178–1189.

Couet, B., Brown, P., and Hunt, A. 1991. Two-phase bubbly droplet flow through a contraction: experiments and a unified theory. *Int. J. Multiphase Flow*, **17**, 291.

Cutler, W. G., McMickles, R. J., Webb, W., Schiessler, R. W., 1958. Study of the compressions of several high molecular weight hydrocarbons. *J. Chem. Phys.* **29**, 727–740.

Dalmaz, G. 1981. Friction and film thickness measurements of water glycol and a water-in-oil emulsion in rolling-sliding point contacts. *Friction and Wear*, Proc. 7th Leeds-Lyon Symp., 231–42.

Dalmaz, G., and Godet, M. 1978. Film thickness and effective viscosity of some fire resistant fluids in sliding point contact. *ASME J. Lubr. Technol.*, **100**, 304.

Das, B., Johnson, P. C. and Popel, A. S. 1998. Effect of nonaxisymmetric hematocrit distribution on non-Newtonian blood flow in small tubes. *Biorheology*, **35**(1) 69–87.

Davis, M. J. and Walters, K. 1973. In *Rheology of Lubricants* (T. Davenport, ed.), pp. 65–80.

De Wachter, D. and Verdonck, P. 2002, Numerical calculation of hemolysis levels in peripheral hemodialisis cannulas. *Artif. Organs*, **26**(7), 576–582.

Denning, A. D. and Watson, J. H. 1906. The viscosity of blood. *Proc. R. Soc.*, **LXXVII**, 328–358.

Deutsch S. and Phillips, W. N. M. 1977. The use of the Taylor-Couette stability problem to validate a constitutive equation for blood. *Biorheology*, **14**, 253–266.

Deutsch, S., Phillips, W. M. and Heist, J. 1976. An interpretation of low strain rate blood viscosity measurements: a continuum approach. *Biorheology*, **13**, 297–307.

Doolittle, A. 1951. Studies in Newtonian flow. II. The dependence of viscosity of liquids on free-space. *J. Appl. Phys.*, **22**(12), 1471–1473.

Dowson, D. and Higginson, G. R. 1966. *Elastohydrodynamic Lubrication. The Fundamentals of Roller and Gear Lubrication*, Pergamon, Oxford.

Drew, D. A. 1971. Averaged field equations for two-phase flow studies. *Appl. Math.*, **50**, 133.

Drochon, A. 2003. Rheology of dilute suspensions of red blood cells: experimental and theoretical approaches. *Eur. Phys. J.*, **22**, 155–162.

Dymond, J. H. and Malhotra, R. 1988. The Tait equation: 100 years on. *Int. J. Thermophys.* **9**(6), 941–951.

Dyson, A. 1970. Frictional traction and lubricant rheology in elastohydrodynamic lubrication. *Philos. Trans. R. Soc.*, **266A**, 1170.

Easthope, P. L. 1989. Three-dimensional dyadic Walburn-Schneck constitutive equation for blood. *Biorheology*, **26**, 37–44.

Easthope, P. L. and Brooks, D. E. 1980. A comparison of rheological constitutive functions for whole human blood. *Biorheology*, **17**, 235–247.

Eyring, H. 1936. Viscosity, plasticity and diffusion as examples of absolute reaction rates. *J. Chem. Phys.*, **4**, 283.

Fahraeus, R. and Lindqvist, T. 1931. The viscosity of the blood in narrow capillary tubes. *Am. J. Physiol.*, **96**, 562–568.

Fischer, T. M., Stohr-Liesen, M. and Schmid-Schonbein H. 1978. The red cell as fluid droplet: tank tread-like motion of the human erythrocyte membrane in shear flow. *Science*, **202**(24), 894–896.

Fix, G. J. and Paslay, P. R. 1967. Incompressible elastic viscous lubricants in continuous-sleeve journal bearings. *ASME J. Applied Mech.*, **34**, 579–82.

Fosdick, R. and Rajagopal, K. R. 1979. Anomalous features in the model of second order fluids. *Arch. Rational Mech. Anal.*, **70**, 145–152.

Fosdick, R. and Rajagopal, K. R. 1980. Thermodynamics and stability of fluids of third grade. *Proc. Roy. Soc.*, **339A**, 351–377.

Gazzola, F. 1997. A note on the solution of Navier-Stokes equations with a pressure dependent viscosity. *ZAMP*, **48**, 760–773.

Gazzola, F. and Secchi, P. 1998. Some results about stationary Navier-Stokes equations with a pressure dependent viscosity. In *Navier-Stokes Equations: Theory and Numerical Methods* (R. Salvi, ed.), 31–37. Pitman-Longman. London.

Giersiepen, M., Wurzinger, L. J., Opitz, R. and Reul, H. 1990. Estimate of shear stress-related blood damage in heart valve prostheses – in vitro comparison of 25 aortic valves. *Int. J. Artif. Organs*, **13**, 300–306.

Giesekus, H. 1963. Die simultane translation und rotations bewegung einer kugel in einer elastoviskosen flussigkeit. *Rheol. Acta*, **4**, 59–71.

Gouse, S. W. 1966. *An Index to Two-Phase Gas-Liquid Flow Literature*. MIT Press, Cambridge, MA.

Gray, W. G. 1975. A derivation of the equations for multi-purpose transport. *Chem. Eng. Sci.*, **30**, 29.

Greenwood, J. A., 2000. In Thinning Films and Tribological Interfaces. *Proc. Leeds-Lyon Symp. Tribol.*, 793–794. Elsevier, London.

Griest, E. M., Webb, W. and Schiessler, R. W. 1958. Effect of pressure on viscosity of higher hydrocarbons and their mixtures, *J. Chem. Phys.*, **29**, 711–720.

Grudev, A. P. and Razmakhnin, A. D. 1984a. Principles of formation of lubricating film during cold rolling using emulsions. *Steel USSR*, **15**, 15.

Grudev, A. P., and Razmakhnin, A. D. 1985b. Cold rolling with emulsion lubricant *Steel USSR*, **15**, 19.

Hakim, S., Morshedian, J., Narenji, M. G. and Nia, P. K. 2001. Rheologically modeling Caspian pony blood. *Iranian Polym. J.*, **10**(5), 293–303.

Hamaguchi, H., Spikes, H. A., and Cameron, A. 1977. Elastohydrodynamic properties of water-in-oil emulsions. *Wear*, **43**, 17.

Harnoy, A., and Hanin, M. 1974. Second order, elastico-viscous lubricants in dynamically loaded bearings. *ASLE Trans*., **17**, 3, 166–71.

Harrison, G. and Trachman, E. G. 1972. The role of compressional viscoelasticity in the lubrication of rolling contacts. *ASME J. Lub. Tech.*, **95**, 306–12.

Hayward, A. T. 1961. The viscosity of bubbly oil. *NEL Fluids Report No. 99.*

Henon, S., Lenormand, G. and Gallet, F. 1999. A new determination of the shear modulus of the human erythrocyte membrane using an optical tweezer. *Biophysics J.*, **76**, 1145–51.

Houpert, L. G. and Hamrock, B. J. 1986. Fast approach for calculating film thicknesses and pressures in elastohydrodynamically lubricated contacts at high loads. *ASME Journal of Tribology*, **108**, 411–420.

Hron, J., Malek, J. and Rajagopal, K. R. 2001. Simple flows of fluids with pressure-dependent viscosities, *Proc. Roy. Soc., Lond.*, **A457**, 1603–1622.

Hsu, Y. C. and Saibel, E. 1965. Slider bearing performance with a non-Newtonian lubricant. *Trans. ASLE*, **8**, 191–194.

Huilgol, R. R. 1975. On the concept of the Deborah number. *Trans. Soc. Rheol.*, **19**, 297–306.

Ishii, M. 1975. *Thermo-Fluid Dynamic Theory of Two-Phase Flows*, Eyrolles, Paris.

Ishikawa, T., Guimaraes, L. F. R., Oshima, S. and Yamane, R. 1998. Effect of non-Newtonian property of blood on flow through a stenosed tube. *Fluid Dyn. Res.*, **22**, 251–264.

Johnson, K. L. and Roberts, A. D. 1974. Observation of viscoelastic behavior of an elastohydrodynamic lubricant film. *Proc. Roy. Soc.*, **337A**, 217–242.

Johnson, K. L. and Tevaarwerk, J. L. 1977. Shear behavior of elastohydrodynamic films. *Trans. Roy. Soc.*, **356A**, 215–236.

Johnson, K. L., Cameron, R., 1967. Shear behaviour of elastohydrodynamic oil films at high rolling contact pressures. *Proc. Instn. Mech. Engrs.* **182**(14), 307–319.

Johnson, K. L., Greenwood, J. A., 1980. Thermal analysis of an Eyring fluid in elastohydrodynamic traction. *Wear* **61**, 355–374.

Johnson, M. W. and Mangkoesoebroto, S. 1993. Analysis of lubrication theory for the power law fluid. *ASME Journal of Tribology*, **115**, 71–7.

Joseph, D. D. 1989. *Fluid Dynamics of Viscoelastic Liquids*. Springer-Verlag, New York.

Kacou, A., Rajagopal, K. R. and Szeri, A. Z. 1987. Flow of a fluid of the differential type in a journal bearing. *ASME Journal of Tribology*, **109**, 100–108.

Kaye, A. 1962. *Note No.* 134. College of Aeronautics, Cranfield.

Keller, S. and Skalak, R. 1982. Motion of tank-treading ellipsoidal particle in a shear flow. *J. Fluid Mech.*, **120**, 27–47.

Kimura, Y., and Okada, K. 1987. Film thickness at elastohydrodynamic conjunctions lubricated with oil-in-water emulsions. *Proc. IMechE.*, **C176**, 85–90.

Krupka, I., Bair, S., Kumar, P. and Hartl, M. 2009. An experimental validation of the recently discovered effect in generalized Newtonian EHL. *Tribol. Lett.*, **33**, 127–135.

Lee, R. T. and Hamrock, B. J. 1990. A circular non-Newtonian fluid model used in transient elastohydrodynamic lubrication. *ASME Journal of Tribology*, **112**, 486–505.

Leverett, L. B., Hellums, J. D., Alfrey, C. P. and Lynch, E. C. 1972. Red blood cell damage by shear stress. *Biophysics J.*, **12**, 257–263.

Liu, I. S. 1972. Method of Lagrange multipliers for exploitation of the entropy principle, *Arch. Ratl. Mech. Anal.* **46**, 131–148.

Liu, Y., Wang, Q. J., Bair, S. and Vergne, P. 2007. A quantitative solution for the full shear-thinning EHL point contact problem including traction. *Tribol. Letts.*, **28**(1), 171–181.

Liu, Y., Wang, Q. J., Wang, W., Hu, Y., Zhu, D., Krupka, I. and Hartl, M. 2006. EHL simulation using the free-volume viscosity model. *Tribol. Letts.*, **23**(1), 27–37.

Maffettone, P. L. and Minale, M. 1998. Equation of change for ellipsoidal drops in viscous flow. *J. Non-Newtonian Fluid Mech.*, **78**, 227–41.

Majhi, S. N. and Usha, L. Modeling the Fahraeus-Lindqvist effect Through fluids of differential type. *Int. J. Eng. Sci.*, **26**(5), 503–508.

Majhi, S. N. and Usha, L. 1988. Modeling the Fahraeus-Linqvist effects through fluids of a differential type. *Int. J. Eng. Sci.*, **20**, 503–508.

Malek, J., Necas, J and Rajagopal, K. R., 2002a. Global analysis of the flow of fluids with pressure dependent viscosities, *Arch. Ratl. Mech. Anal.* **165**, 243–269.

Malek, J., Necas, J. and Rajagopal, K. R., 2002b. Global existence of solutions for flows of fluids with pressure and shear dependent viscosities, *Appl. Math. Lett.*, **15**, 961–967.

Mills, N. 1966. Incompressible mixtures of Newtonian fluids. *Int. J. Eng. Sci.*, **4**, 97.

Mitoh, A., Yano, T., Sekine, K., Mitamura. Y., Okamoto, E., Kim, D., Yozu, Y. and Kawada, S. 2003. Computational fluid dynamics analysis of an intra-cardiac axial flow pump. *Artif. Organs*, **27**(1), 34–40.

Mo, L. Y. L., Yip, G., Cobbold, R. S. C., Gutt, C., Joy, M. and Santyr, G. 1991. Non-Newtonian behavior of whole blood in large diameter tube. *Biorheology*, **28**, 421–427.

Muller, I. A. 1968. A thermodynamic theory of mixtures of fluids. *Arch. Rational Mech. Anal.*, **28**, 1–39.

Najji, B., Bou-Said, B. and Berthe, D. 1989. New formulation for lubrication with non-Newtonian fluids. *ASME Journal of Tribology*, **111**, 29–34.

Nakahara, T., Makino, T., and Kyogaka, Y. 1988. Observation of liquid droplet behavior and oil film formation in O/W type emulsion lubrication. *ASME Journal of Tribology*, **110**, 348–53.

Navier, C. L. 1823. Mémoire sur les lois du mouvament des fluides. *Mem. Acad. R. Sci. Paris*, **6**, 389–440.

Ng, C. W., and Saibel, E. 1962. Non-linear viscosity effects in slider bearing lubrication. *ASME J. Lub. Techl.*, **7**, 192–96.

Nunziato, J. W., and Walsh, E. 1980. *Arch. Rat. Mech. Anal.*, **73**, p. 285.

Paluch, M., Dendzik, Z. and Rzoska, S. J., 1999. Scaling of high-pressure viscosity data in low-molecular-weight glass-forming liquids. *Phys. Rev. B*, **60**, 2979–2982.

Paul, R., Apel, J., Klaus, S., Schugner, F., Schwindke, P. and Reul, H. 2003. Shear stress related blood damage in laminar Couette flow. *Artif. Organs*, **27**(6), 517–529.

Phillips, W. M. and Deutsch, S. 1975. Towards a constitutive equation for blood. *Biorheology*, **22**, 509–520.

Poiseuille, J. L. M. 1840. Researches experimentales sur le movuvement des liquides dans les tubes de tres petits diametres. *Acad. Sci., Comp. Rend.* **11**, 961–967.

Popel, A. S., Regirer, S. A. and Usick, P. I. 1974. A continuum model of blood flow. *Biorheology*, **11**, 427–437.

Quemada, D. 1982. A rheological model for studying the hematocrit dependence of red cell-red cell and cell-protein interaction in blood. *Biorheology*, **18**, 501–514.

Quemada, D. 1993. A non-linear Maxwell model of biofluids: application to normal blood. *Biorheology*, **30**, 253–265.

Quemada, D. and Droz, R. 1983. Blood viscoelasticity and thixotropy from stress formation and relaxation measurements. *Biorheology*, **20**, 635–651.

Raimondi, A. A. 1961. A numerical solution for the gas lubrication full journal bearing of finite length. *ASLE Trans*., **4**, 131–55.

Rajagopal, K. R. 1984. On the creeping flow of the second order fluid. *J. Non-Newtonian Fluid Mech.*, **15**, 239–246.

Rajagopal, K. R. and Szeri, A. Z. 2003. On an inconsistency in the derivation of the equations of elastohydrodynamic lubrication. *Proc. R. Soc. Lond. A* **459**, 2771–2786.

Rajagopal, K. R. and Tao, L. 1995. *Mechanics of Mixtures*. World Scientific Publishing, Singapore.

Rajagopal, K. R., and Fosdick, R. L. 1980. Thermodynamics and stability of fluids of third grade. *Proc. R. Soc., London*, **A339**, 351–77.

Reiner, M. and Scott-Blair, G. W. 1959. The flow of blood through narrow tubes. *Nature*, **184**, 354–355.

Renardy, M., 1986. Some remarks on the Navier-Stokes equations with a pressure-dependent viscosity. *Commun. Partial Differential Equations*, **11**(7), 779–793.

Rodkiewicz, C. M., Sinha, P. and Kennedy, J. S. 1990. On the application of a constitu tive equation for whole blood. *J. Biomech. Eng.*, **112**, 198–206.

Rohlf, G. and Tenti, G. 2001. The role of the Womersley number in pulsatile blood flow, a theoretical study of the Casson model. *J. Biomech.*, **34**, 141–148.

Roelands, C. J. 1966. *Correlation Aspects of the Viscosity-Pressure Relationship of Lubricating Oils*. Ph.D. Thesis, Delft University of Technology, Netherlands.

Roland, C. M., Bair, S. and Casalini, R. 2006. Thermodynamic scaling of the viscosity of van der Waals, H-bonded, and ionic liquids. *J. Chem. Phys.*, **100**(7), 124508.

Rose, E. A., Gelijns, A. C., Moskowitz, A. J., Heitjan, D. F., Stevenson, L. W., Dembit sky, W., Long, J. W., Ascheim, D. D., Tierney, A. R., Levitan, R. G., Watson, J. T. and Meier, P. 2001. Long-term use of a left ventricular assist device for end- stage heart failure. *N. Engl. J. Med.*, **345**, 1435–1443.

Sallam, A. M. and Hwang, N. H. 1984. Human red blood cell hemolysis in a turbulent shear flow. *Biorheology*, **21**, 783–797.

Schäfer, C. T., Giese, P., Rowe, W. B. and Woolley, N. H., 1999. Elastohydrodynamically lubricated line contact based on the Navier-Stokes equations. *Proc. Leeds-Lyon Symp. Tribol.*, 57–68, Elsevier, London.

Schneider, W. D., Glossfeld, D. H., and DeHart, A. O. 1986. The effect of coolant contamination in lubricating oil on journal bearings load capacity – a radiometric evaluation. *ASLE Preprint No. 86-TC-2F-1*.

Serrin, J. 1959. Mathematical principle of classical fluid mechanics. *Encyclopedia of Physics*, vol. VIII, pt. 1. Springer-Verlag, Berlin.

Sharp, M. K., Thurston, G. B. and Moore, J. R. 1996. The effect of blood viscoelasticity on pulsatile flow in stationary and axially moving tubes. *Biorheology*, **33**(3), 185–208.

Sirivat, A., Rajagopal, K. R. and Szeri, A. Z. 1988. An experimental investigation of the flow of non-Newtonian fluids between rotating disks. *J. Fluid Mech.*, **186**, 243.

Smith, F. W. 1962. The effect of temperature in concentrated contact lubrication. *Trans. ASLE*, 5, 142–148.

Smith, L. H., Peeler, R. L., and Bernd, L. H. 1960. *Proceedings of the 16th National Conference on Industrial Hydraulics Annual Meeting*, Oct. 20–21, p. 179.

Soo, S. L. 1967. *Fluid Dynamic of Multiphase Systems*, Olasidell Walthem, MA.

Spencer, A. J. 1970. *Theory of Invariants, Continuum Physics* (A. C. Eringen, ed.), Vol. 1, Part III, Academic Press, New York.

Stokes, G. G. 1845. On the theories of the internal friction of fluids in motion, and of the equilibrium and motion of elastic solids. *Trans. Camb. Philos. Soc.* **8**, 287–305.

Sutera, S. P. 1977. Flow-induced trauma to blood cells. *Circulation Res.*, **41**(1), 2–8.

Takahashi, T., 1966. *Friction and Lubrication in Metal-Processing. ASME*, New Orleans, p. 137.

Tanner, R. I. 1966. Plane creep flows of incompressible second order fluid. *Phys. Fluids*, **9**, 1246–1247.

Tanner, R. I. 1969. Increase of bearing loads due to large normal stress differences in viscoelastic lubricants. *ASME J. Appl. Mech.*, **36**, 634–635.

Tanner, R. I. 1998. *Engineering Rheology*, 2nd edn. Clarendon Press, Oxford.

Tao, F. F. and Philippoff, W. 1967. Hydrodynamic behavior of viscoelastic liquids in a simulated journal bearing. *Trans. ASLE*, **100**, 302–315.

Taylor, G. I. 1932. The viscosity of fluid containing small drops of another fluid. *Proc. Roy. Soc.*, **A138**, 41.

Tevaarwerk, J. L. and Johnson, K. L. 1979. The influence of fluid rheology on the performance of traction drives. *ASME J. Lub. Tech.*, **101**, 266–74.

Thakur, R. V., Vial, C., Djelveh, G. and Labbi, M. 2004. Mixing of complex fluids with flat-bladed impellers: effect of impeller geometry and highly shear-thinning bahavior. *Chem. Eng. Proc.*, **43**, 1211–1222.

Thurston, G. B. 1979. Rheological parameters for the viscosity, viscoelasticity and thixotropy of blood. *Biorheology*, **16**, 149–162.

Tichy, J. A. 1978. The behavior of viscoelastic squeeze films subject to normal oscillations, including the effect of fluid inertia. *Appl. Sci. Res.*, **33**, 501–17.

Tichy, J. A. 1996. Non-Newtonian lubrication with the corrected Maxwell model. *ASME Journal of Tribology*, **118**, 344–48.

Trachman, E. G. and Cheng, H. S. 1972. *Symp. EHD Lubr. Inst. Mech. Engrs.*, 142.

Truesdell, C. 1964. The natural time of a viscoelastic fluid: its significance and measurement. *Phys. Fluids*, **7**, 1134–42.

Truesdell, C. 1969. *Rational Thermodynamics*, McGraw-Hill, New York.

Truesdell, C. and Noll, W. 1992. *The Nonlinear Field Theories of Mechanics*. Springer-Verlag, Berlin.

Truesdell, C., and Noll, W. 1965. *The Non-Linear Field Theories of Mechanics, Handbuk der Physik,* III/3, Springer-Verlag, Berlin.

Truesdell, C., and Toupin, R. 1960. *The Classical Field Theories. Handbuk der Physik* (S. Flugge, ed.), III/1, Springer-Verlag, Berlin.

Walburn, F. J. and Schneck, D. J. 1976. Constitutive relation for whole human blood. *Biorheology*, **13**, 201–210.

Wan, G. T. Y., Kenny, P., and Spikes, H. A. 1984. Elastohydrodynamic properties of water-based fire-resistant hydraulic fluids. *Tribol. Int.*, **17**, 309–315.

Wang, S. H., Al-Sharif, A., Rajagopal, K. R. and Szeri, A. Z. 1993. Lubrication with binary mixtures: liquid-liquid emulsion in an EHD conjunction. *ASME Journal of Tribology*, **115**, 515–524.

Wang, S. H., Szeri, A. Z., and Rajagopal, K. R. 1993. Lubrication of emulsion in cold rolling. *ASME Journal of Tribology*, **115**, 523–532.

Whitmore, R. L. 1968. *Rheology of the Circulation*. Pergamon Press, Oxford.

Williams, M. L., Landel, R. F. and Ferry, J. D. 1955. The temperature dependence of relaxation mechanisms in amorphous polymers and other glass-forming liquids. *J. Am. Chem. Soc.*, **77**, 3701–3707.

Wolff, R. and Kubo, A. 1996. A generalized non-Newtonian fluid model incorporated into elastohydrodynamic lubrication. *ASME Journal of Tribology*, **118**, 74–82.

Wurtzinger, L. J., Opitz, R. and Eckstein, H. 1986. Mechanical blood trauma. *Angeiologie*, **38**, 81–97.

Wurzinger, J. L., Opitz, M., Wolf, M. and Schmid-Schonbein. 1985. Shear induced platelet activation a critical reappraisal. *Biorheology*, **22**, 399–413.

Yasutomi, S., Bair, S. and Winer, W. O. 1984. An application of a free volume model to lubrication theory. *J. Lub. Tech.*, **106**(2), 291–303.

Yeleswarapu, K. K. 1996. *Evaluation of Continuum Models for Characterizing the Constitutive Behavior of Blood*. Ph.D. Dissertation, University of Pittsburgh.

Yeleswarapu, K. K., Kameneva, M. V., Rajagopal, K. R. and Antaki, J. F. 1998. The flow of blood in tubes: theory and experiment. *Mech. Res. Commun.*, **25**(3), 257–262.

Young, T. 1809. The Croonian lecture. On the functions of the heart and arteries. *Philos. Trans. R. Soc.*, **99**, 1–31.

Zang, Y. 1995. *EHD Lubricant Behavior at Moderate Pressures and High Shear Rates*. Masters Essay, The Johns Hopkins University.

Zang, Y. and Ramesh, K. T. 1996. The behavior of an elastohydrodynamic lubricant at moderate pressures and high shear rates. *ASME Journal of. Tribology*, **118**, 162–168.

Zhang, J. B. and Kuang, Z. B. 2000. Study on blood constitutive parameters in different blood constitutive equations. *J. Biomech.*, **33**, 355–360.

CHAPTER 11

Gas Lubrication

The qualitative difference in performance between liquids and gases, in general, vanishes as $M \to 0$, where the *Mach number*, M, is the ratio of the fluid velocity to the local velocity of sound. This general conclusion also holds for bearings, and at low speeds the behavior of gas film lubricated bearings is similar to liquid-lubricated bearings – in fact, many of the liquid film bearings could also be operated with a gas lubricant. This similarity between liquid and gas films no longer holds at high speeds, however, the main additional phenomenon for gas bearings being the compressibility of the lubricant.

Perhaps the earliest mention of air as a lubricant was made by Hirn in 1854. Kingsbury (1897) was the first to construct an air-lubricated journal bearing. But the scientific theory of gas lubrication can be considered as an extension of the Reynolds lubrication theory. This extension was made soon after Reynolds' pioneering work: Harrison in 1913 published solutions for "long" slider and journal bearings lubricated with a gas. Nevertheless, the study of gas lubrication remained dormant until the late 1950s, when impetus for the development of gas bearings came mainly from the precision instruments and the aerospace industries.

In self-acting bearings, whether lubricated by liquid or gas, lubrication action is produced in a converging narrow clearance space by virtue of the viscosity of the lubricant. As the viscosity of gases is orders of magnitude smaller than that of commonly used liquid lubricants, gas bearings generally must have smaller clearances and will produce smaller load capacities than their liquid-lubricated counterparts.

Despite the smaller clearances, however, under normal conditions viscous heating in the gas can be neglected. The equation for the conservation of energy for a constant property gas is given by Eq. (9.20b). Here we retain the adiabatic compression term $-p$ div $\boldsymbol{v}$ on account of compressibility. Elrod and Burgdorfer (1959) simplified Eq. (9.21) for a two-dimensional film of negligible internal energy, flowing between walls held at constant temperature, and found that

$$\frac{\Theta_{\max}}{\Theta_0} - 1 = O(M^2), \tag{11.1}$$

where Θ_0 is the temperature of the walls and the Mach number, $M = u/a$, is the ratio of local gas velocity to the velocity of sound and $\Theta_{\max} = \max(\Theta)$. Consequently, if the bearing Mach number is small, the usual case, the temperature variation across the lubricant film thickness can be neglected.

Another way to estimate the appropriateness of the isothermal approximation is by comparing the transit time of the gas through the clearance space to the time scale of conduction (Ausman, 1966). Let the temperature of the gas, contained between parallel surfaces, exceed the temperature of the walls by $\Delta\Theta$. This temperature difference will, at the centerline, decrease to $\Delta\Theta/3$ in a time $\tau_c = O(c_p \rho h^2/k)$, where c_p, ρ, and k, are the specific heat, density, and heat conductivity, respectively, for the gas. The transit time for the gas through the bearing is $\tau_t = O(2R/U)$, where R is the characteristic dimension of the bearing in the direction of motion. If $\tau_t \gg \tau_c$, heat conduction from gas into bearing will

occur at a high enough rate to keep the gas film virtually at the temperature of the bearing, and the latter will be at near uniform temperature on account of the large heat conductivity of metals. The criteria for isothermal operation is, therefore, $\tau_t \gg \tau_c$, or $\mathrm{Pr}\,\mathrm{R}_\varepsilon \ll 1$. For gas-lubricants, the Prandtl number $\mathrm{Pr} = \mu c_p/k = O(1)$ and in gas-lubricated bearings $C/R = O(10^{-4})$, $\mathrm{Re} = O(1)$, giving $\mathrm{Pr}\,\mathrm{R}_\varepsilon = O(10^{-4})$, thus the condition $\tau_t \gg \tau_c$ is, in general, satisfied.

Another simplifying feature of gas lubricant films is the absence of cavitation. However, we trade the linearity of the boundary conditions[1] for nonlinearity of the equations, and record no gain on this account. In gas films, however, rarely do we have to consider turbulence. A typical $R = 1$ cm air-lubricated journal bearing operating with a clearance ratio of $(C/R) = 10^{-3}$ at a speed of $N = 5 \times 10^4$ rpm would have a Reynolds number less than 100, far below the critical value of $\mathrm{Re}_{CR} \approx 500$–$800$. We may therefore neglect inertia terms, i.e., apply the Reynolds lubrication theory, and assume laminar flow.

Some of the advantages of gas bearings are:

(1) Chemical stability of the lubricant
(2) No fire hazard
(3) Small thermal gradients
(4) No ecological contamination

However, gas films have shortcomings as well. Under this heading we may mention often unavoidable metal-to-metal contact that increases friction instantaneously severalfold. To minimize wear under dry contact, both bearing and runner surfaces must be hard. Hard surfaces and tight clearances do not easily accommodate debris. It should be considered that though gas bearing specific loads are small, these bearings often operate at speeds 1–2 orders of magnitude higher than liquid lubricated bearings – in consequences gas bearings are more vulnerable to thermal/mechanical distress than are liquid bearings (Gross, 1962; Pan, 1980).

Gas bearings run on thin films, $h = 2.5$ μm is not uncommon. Such tight clearances require at least 0.025 μm rms roughness and must be at least 0.125 μm flat, as the self-correcting action of running-in is not available to gas bearings. Near-perfect alignment is also necessary, and elastic/thermal deflection must be limited to less than 0.5 μm.

Particularly in magnetic recording applications, where the read-write head has a minimum separation from the disk of order 100 nm or less, we must take into account the clearance height relative to the mean free path of the gas molecules. This ratio is defined as the *Knudsen number*

$$\mathrm{Kn} = \frac{\lambda}{h}, \tag{11.2}$$

where h is the film thickness and λ is the *mean free path* ($\lambda \approx 60$ nm for air under standard conditions). An approximate rule of thumb concerning flow regimes is

$$\begin{aligned} &\mathrm{Kn} < 0.001 && \text{continum flow,} \\ &0.001 \leq \mathrm{Kn} < 10.0 && \text{slip flow,} \\ &\mathrm{Kn} \geq 10.0 && \text{molecular flow.} \end{aligned}$$

[1]Recall that for liquid-lubricated bearings the Reynolds equation is linear in p, but the boundary conditions $p = dp/d\theta = 0$ are not.

As will be shown in Chapter 12, there have been several attempts made to extend the Reynolds equation above Kn > 0.01.

As in usual circumstances $R_\varepsilon = O(C/R)$, when we take formally the limit $(C/R) \to 0$ in the equations of motion while treating the viscosity as a constant, we again arrive at Eqs. (2.63), (2.64), and (2.67). In fact, our starting point in deriving the Reynolds equation for gas lubricant will be Eqs. (2.67) and (2.16b), the equation of continuity for compressible fluids.

11.1 Reynolds Equation for Gas Lubricant

The Reynolds equation is derived here for no-slip boundary conditions. Under the lubrication assumptions the in-plane velocity components of the film are given by Eq. (2.67):

$$\begin{aligned} u &= \frac{1}{2\mu}\frac{\partial p}{\partial x}(y^2 - hy) + \left(1 - \frac{y}{h}\right) U_1 + \frac{y}{h} U_2, \\ w &= \frac{1}{2\mu}\frac{\partial p}{\partial x}(y^2 - hy). \end{aligned} \tag{2.67}$$

The velocity satisfies no-slip conditions at the boundaries

$$\begin{aligned} &u = U_1, \qquad v = V_1, \qquad w = 0 \quad \text{at } y = 0, \\ &u = U_2, \qquad v = V_2, \qquad w = 0 \quad \text{at } y = h. \end{aligned} \tag{2.60}$$

In the manner of Section 2.2, the velocity components are next substituted into the equation of continuity that has been integrated across the film. The equation of continuity for a compressible fluid is given by

$$\frac{\partial \rho}{\partial t} + \operatorname{div}(\rho \boldsymbol{v}) = 0. \tag{2.16b}$$

Rearrangement of Eq. (2.16b) and integration across the film yields

$$[\rho v]_0^{h(x,t)} = -\int_0^{h(x,t)} \frac{\partial(\rho u)}{\partial x} dy - \int_0^{h(x,t)} \frac{\partial(\rho w)}{\partial z} dy - \int_0^{h(x,t)} \frac{\partial \rho}{\partial t} dy. \tag{11.3}$$

In analogy with Eq. (2.69b), we have

$$[\rho v]_0^{h(x,t)} = \rho \frac{dh}{dt}. \tag{11.4}$$

Substituting from Eqs. (2.67) and (11.4) into Eq. (11.3), we obtain

$$\begin{aligned} [\rho v]_0^h = &-\frac{1}{2}\frac{\partial}{\partial x}\left[\frac{\partial p}{\partial x}\int_0^h \frac{\rho}{\mu} y\,(y-h)\,dy\right] - \frac{1}{2}\frac{\partial}{\partial z}\left[\frac{\partial p}{\partial z}\int_0^h \frac{\rho}{\mu} y\,(y-h)\,dy\right] \\ &-\frac{\partial}{\partial x}\int_0^h \rho\left[\left(1 - \frac{y}{h}\right) U_1 + \frac{y}{h} U_2\right] dy + \rho U_2 \frac{\partial h}{\partial x} - \int_0^h \frac{\partial p}{\partial t}\, dy. \end{aligned} \tag{11.5}$$

Since p is not a function of y, neither is ρ for an ideal gas. Assuming further that $\mu = \mu(x, z)$ at most and applying Leibnitz's rule for differentiation under the integral sign, Eq. (11.5) is written as

$$\frac{\partial}{\partial x}\left(\frac{\rho h^3}{12\mu}\frac{\partial p}{\partial x}\right)+\frac{\partial}{\partial z}\left(\frac{\rho h^3}{12\mu}\frac{\partial p}{\partial z}\right)=\frac{\partial}{\partial x}\left(\rho h\frac{U_1+U_2}{2}\right)-\rho U_2\frac{\partial h}{\partial x}+h\frac{\partial \rho}{\partial t}+[\rho v]_0^h. \tag{11.6}$$

For thrust bearings and, in general, for bearing surfaces that undergo rigid body translation but no rotation, we have [Eq. (11.4)]

$$[\rho v]_0^h = \rho\,(V_2 - V_1) = \rho\frac{\partial h}{\partial t} \quad \text{as } U_{2,r} = 0 \tag{11.7}$$

and

$$\frac{\partial}{\partial x}\left(\frac{\rho h^3}{\mu}\frac{\partial p}{\partial x}\right)+\frac{\partial}{\partial z}\left(\frac{\rho h^3}{\mu}\frac{\partial p}{\partial z}\right)=6\frac{\partial}{\partial x}(\rho h U_0)+12\frac{\partial(\rho h)}{\partial t}. \tag{11.8}$$

Here we followed the notation of Chapter 3 and put $U_0 = U_1 - U_2$.

For journal bearings, one must consider both rigid body rotation and rigid body translation, and we put (following Section 2.2)

$$\begin{aligned}[\rho v]_0^h &= \rho\frac{dh}{dt} = \rho\frac{\partial h}{\partial t}+\rho U_{2,r}\frac{\partial h}{\partial x}\\ &\approx \rho\frac{\partial h}{\partial t}+\rho U_2\frac{\partial h}{\partial x}\end{aligned} \tag{11.9}$$

as $U_2 = U_{2,r}[1 + O(C/R)] \approx U_{2,r}$ by Eq. (2.76c). Substituting Eq. (11.9) into Eq. (11.8) and collecting terms, we obtain an equation formally identical to Eq. (11.6), but now we have $U_0 = U_1 + U_2$.

For isothermal processes, common to the majority of gas bearing applications,

$$\frac{p}{\rho} = \text{const.} \tag{11.10}$$

If, further, we have steady conditions, $\partial(\rho h)/\partial t = 0$, Eq. (11.8) takes the form

$$\frac{\partial}{\partial x}\left(\frac{h^3}{\mu}\frac{\partial p^2}{\partial x}\right)+\frac{\partial}{\partial z}\left(\frac{h^3}{\mu}\frac{\partial p^2}{\partial z}\right)=12U_0\frac{\partial(ph)}{\partial x}, \tag{11.11}$$

where $U_0 = U_2$ for journal bearings and $U_0 = U_1$ for sliders. Equation (11.11) is specified for various bearing geometries by Pan (1980).

Gas lubrication is frequently applied to the head-disk interface in computer hard disk drives. In these applications the Knudsen number is in the 0.01–15 range. When the clearance becomes much smaller than the mean free path, the Reynolds equation with no-slip boundary conditions predicts a shear stress that is too high. It seems, however, that it is not the continuum assumption that is at fault but the no-slip boundary conditions (Anaya, 1996). Chan and Horn (1985) found that the drainage rate of a thin film of fluid between two crossed molecularly smooth mica cylinders was adequately predicted by the continuum Reynolds equation to about $h = 30$ nm. At thinner gaps, good correlation with experiment

was obtained by simply adding a fictitious rigid layer to the mica surfaces in the Reynolds equation model.

The models currently used to predict pressures in head-disk interface in computer hard disk drives are (Anaya, 1996) the first-order slip theory of Burgdorfer (1959), the second-order slip model of Hsia and Domoto (1983), the Boltzmann-Reynolds approach of Fukui and Kaneko (1988), and the 1.5-order slip equation of Mitsuya (1993). The validity of slip-flow theory was experimentally confirmed by Hsia and Domoto (1983), with helium as a working fluid, in an effort to separate the high Knudsen number and high bearing number effects. Theoretical load was calculated using first-order slip theory, which is based on momentum transfer between gas and plate, down to 75 nm. However, most of the experimental data falls below the theoretical load curve when the spacing is below 250 nm. They recommended a second-order slip theory as an extension. The Reynolds equation obtained from the linearized Boltzmann equation, derived by Fakui and Kaneko (1988), yields load results between the first- and the second-order slip theories. Mitsuya (1993) derived, based on kinetic theory, a higher-order slip-flow model, the 1.5-order slip flow model. Predictions from Mitsuya's theory for load seem to fall between data from the Boltzmann-Reynolds model and the second-order slip theory (c.f., Chapter 12).

11.2 Self Acting Gas Bearings

It is convenient to normalize Eq. (11.11) by the substitution

$$X = \frac{x}{a}, \qquad Z = \frac{z}{a}, \qquad P = \frac{p}{p_a}, \qquad H = \frac{h}{\Delta}, \qquad \Lambda = \frac{6\mu a U_0}{p_a \Delta^2}. \tag{11.12}$$

For journal bearings $a = R$, $\Delta = C$, and $U_0 = R\omega$. For plane thrust bearing, $a = B$ and Δ is a representative film thickness (e.g., depth of recess). The transformed (nondimensional) equation is

$$\frac{\partial}{\partial X}\left(H^3 P \frac{\partial P}{\partial X}\right) + \frac{\partial}{\partial Z}\left(H^3 P \frac{\partial P}{\partial Z}\right) = \Lambda \frac{\partial (PH)}{\partial X}. \tag{11.13}$$

For long bearings, we set $\partial(\cdot)/\partial Z \to 0$ and, by integrating Eq. (11.13), obtain

$$\frac{dP}{dX} = \frac{\Lambda}{H^3 P}(PH - K), \tag{11.14}$$

where K is a constant of integration.

The pressure gradient, $\partial P/\partial X$, in Eq. (11.14) must remain bounded under all conditions, for otherwise the pressure would increase to physically unacceptable levels within a short distance of the inlet. But for very large speeds, the left-hand side of Eq. (11.14) will remain bounded only if $PH \to K$, leading to

$$PH = K = P_i H_i, \qquad \Lambda \to \infty. \tag{11.15}$$

This high-speed asymptote of gas bearing operation has been determined solely from the forcing term, i.e., the right-hand side of the Reynolds equation, which is independent of

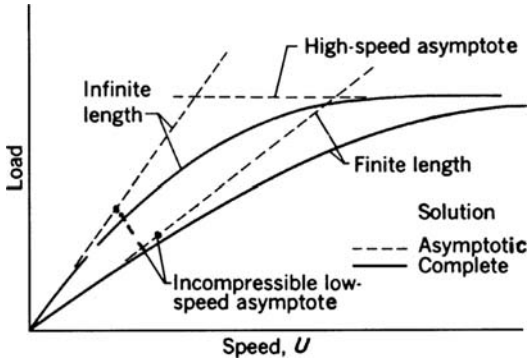

Figure 11.1. Variation of load as function of speed for self-acting gas bearings. (Reprinted with permission from Ausman, J. S. Gas-lubricated bearings. In *Advanced Bearing Technology by* E. E. Bisson and W. J. Anderson. NASA SP-38, 1964.)

the length of the bearing. This, of course, suggests that there is negligible leakage at high speed[2] and finite-length and long bearings behave similarly at the limit $U_0 \to \infty$.

Next, consider gas bearing lubrication at very small velocities, $U_0 \to 0$. From Eq. (11.14), it follows that

$$\partial P/\partial X = O(\Lambda) \quad \text{as } \Lambda \to 0. \tag{11.16a}$$

Thus, for the right-hand side of Eq. (11.13), we may write

$$\Lambda \frac{\partial (PH)}{\partial X} = \Lambda P \frac{\partial (H)}{\partial X} + O(\Lambda^2), \tag{11.16b}$$

and, on substituting from Eq. (11.16) into Eq. (11.13), we obtain

$$\frac{\partial}{\partial X}\left(H^3 \frac{\partial P}{\partial X}\right) + \frac{\partial}{\partial Z}\left(H^3 \frac{\partial P}{\partial Z}\right) = \Lambda \frac{\partial H}{\partial X} + O(\Lambda^2), \qquad \Lambda \to 0. \tag{11.16c}$$

Equation (11.16c) has the form of the incompressible Reynolds equation.

From Eqs. (11.15) and (11.16), we draw the important conclusions, following Ausman (Ausman, 1966):

(1) At low speeds, the behavior of gas lubricant is approximated by the behavior of liquid lubricant.[3]
(2) At high speed, the product $ph = $ const. and the load capacity becomes independent of speed and depends only on the inlet (ambient) pressure.
(3) At high speeds, side leakage becomes negligible as both long bearing and finite bearing solutions approach the asymptote $ph = $ const. (Scheinberg, 1953).

The above three fundamental characteristics of self acting gas bearing are shown schematically in Figure 11.1.

[2]The same conclusion can be reached by comparing characteristic times of fluid transport in the direction of relative motion (shear flow) and in the axial direction (pressure flow).

[3]Note, however, that liquid lubrication and gas lubrication are not completely identical even at low speed. While there is cavitation in liquid bearings in the diverging portion of the clearance, gas films remain continuous from inlet to outlet (Constantinescu, 1969).

Journal Bearings

For journal bearings, we put $a = R$, $X = \theta$, $\Delta = C$ in Eq. (11.13). The applicable Reynolds equation is

$$\frac{\partial}{\partial\theta}\left(H^3 P\frac{\partial P}{\partial\theta}\right)+\frac{\partial}{\partial Z}\left(H^3 P\frac{\partial P}{\partial Z}\right)=\Lambda\frac{\partial(PH)}{\partial\theta},$$
$$\Lambda=\frac{6\mu\omega}{P_a}\left(\frac{R}{C}\right)^2, \tag{11.17a}$$

and the boundary conditions are

$$P=1 \quad \text{at} \quad Z=\pm\frac{L}{D}. \tag{11.17b}$$

We also require periodicity in θ.

Equation (11.17a) is nonlinear, and no general closed-form solutions of it exists. Numerical solutions are well documented, however, and are available in the literature (Elrod and Malanoski, 1960; Raimondi, 1961). Although closed form solutions are not available for arbitrary values of the parameters, we are able to obtain analytical solutions in asymptotic cases.

The pressure equation may be linearized at small values of the eccentricity ratio, ε, by assuming

$$P=1+\varepsilon P_1. \tag{11.18}$$

Substituting Eq. (11.18) into Eq. (11.17a), we obtain the first order perturbation equation as follows:

$$\frac{\partial}{\partial\theta}\left[\left(\frac{\partial}{\partial\theta}-\Lambda\right)P_1\right]+\frac{\partial^2 P_1}{\partial Z^2}=-\Lambda\sin\theta, \tag{11.19}$$

This formulation is known as the *linearized p* solution (Ausman, 1959). Using the notation

$$\Xi\equiv\frac{L}{D}\sqrt{1+\Lambda^2}\left(\cosh 2\sigma\frac{L}{D}+\cos 2\xi\frac{L}{D}\right),$$
$$\Gamma_1\left(\Lambda,\frac{L}{D}\right)\equiv\frac{(\sigma-\xi\Lambda)\sin 2\xi\dfrac{L}{D}-(\sigma\Lambda+\xi)\sinh 2\sigma\dfrac{L}{D}}{\Xi},$$
$$\Gamma_2\left(\Lambda,\frac{L}{D}\right)\equiv\frac{(\sigma-\xi\Lambda)\sinh 2\sigma\dfrac{L}{D}+(\sigma\Lambda+\xi)\sin 2\xi\dfrac{L}{D}}{\Xi},$$

the load capacity is found to be

$$\frac{F_R}{p_0 LD}=\frac{\pi\varepsilon\Lambda}{2(1+\Lambda^2)}\left[\Lambda+\Gamma_1\left(\Lambda,\frac{L}{D}\right)\right], \tag{11.20a}$$

$$\frac{F_T}{p_0 LD}=\frac{\pi\varepsilon\Lambda}{2(1+\Lambda^2)}\left[1-\Gamma_2\left(\Lambda,\frac{L}{D}\right)\right], \tag{11.20b}$$

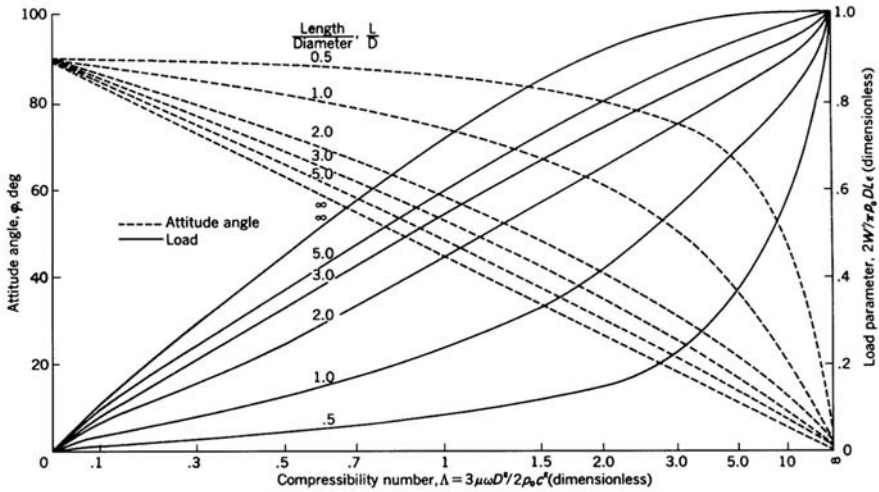

Figure 11.2. Isothermal first-order perturbation solution for journal bearings. (Reprinted with permission from Ausman, J. S. Gas-lubricated bearings. In *Advanced Bearing Technology* by E. E. Bisson and W. J. Anderson. NASA SP-38, 1964.)

where

$$\left.\begin{matrix}\sigma\\ \xi\end{matrix}\right\} = \sqrt{\frac{(1+\Lambda^2)^{1/2} \pm 1}{2}} \qquad \text{(positive roots)}.$$

Note from Eq. (11.20) that the load is linearly dependent on the eccentricity ratio in this approximation. In reality the increase in load is far more rapid than linear, once $\varepsilon \approx 0.3$ has been passed; the linear approximation is valid for only ε less than this value. Figure 11.2 shows the (dimensionless) total load capacity and the attitude angle for a gas journal bearing at small eccentricities. The prediction from Eq. (11.20) is compared with numerical solutions in Figure 11.3.

In an effort to assure stronger than a linear dependence of load on ε, Ausman considered the product $ph \equiv \Psi$, rather than the pressure itself, as the dependent variable, and linearized the Reynolds equation with respect to Ψ.

To derive this approximation (Constantinescu, 1969), known as the *linearized ph solution*, we first write the pressure equation in a form that gives prominence to the function $\bar{\Psi} = \Psi / p_0 \Delta$:

$$\begin{aligned} H\bar{\Psi}\left(\frac{\partial^2\bar{\Psi}}{\partial X^2} + \frac{\partial^2\bar{\Psi}}{\partial Z^2}\right) - \bar{\Psi}^2\left(\frac{\partial^2 H}{\partial X^2} + \frac{\partial^2 H}{\partial Z^2}\right) - \Lambda\frac{\partial\bar{\Psi}}{\partial X} \\ = \bar{\Psi}\left(\frac{\partial H}{\partial X}\frac{\partial\bar{\Psi}}{\partial X} + \frac{\partial H}{\partial Z}\frac{\partial\bar{\Psi}}{\partial Z}\right) - H\left[\left(\frac{\partial\bar{\Psi}}{\partial X}\right)^2 + \left(\frac{\partial\bar{\Psi}}{\partial Z}\right)^2\right]. \end{aligned} \tag{11.21}$$

For $\Lambda \to \infty$, we have, by Eq. (11.15), $PH = \bar{\Psi} \to 0$ const. and the right-hand side of Eq. (11.21) vanishes. This right-hand side also vanishes for $\Lambda \to 0$, as now $p \to p_0$, $P \to 1$, and $\Psi \to H$. Ausman made the assumption that the right-hand side of Eq. (11.21) vanishes

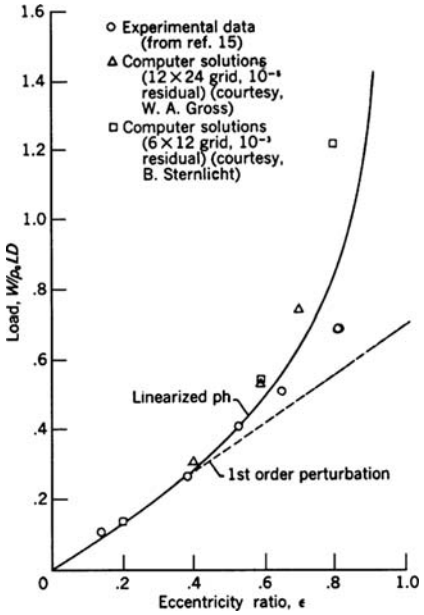

Figure 11.3. Comparison of perturbation solutions and computer solution with experimental data. (Reprinted with permission from Ausman, J. S. An improved analytical solution for self-acting, gas lubricated journal bearings of finite length. *ASME J. Basic Eng.*, **83**, 188–194, 1961.)

not only at the limits but over the whole range of Λ. But then Eq. (11.21) can be written in the approximate form

$$H\bar{\Psi}\nabla^2\bar{\Psi} - \Lambda\frac{\partial\bar{\Psi}}{\partial X} = \bar{\Psi}^2\nabla^2 H. \tag{11.22}$$

Equation (11.22) is still not linear, however. To remedy this, Ausman made the further assumption that when $\bar{\Psi}$ is a coefficient, then $\bar{\Psi} \approx H$, so that $H\bar{\Psi} \approx \bar{\Psi}^2 \approx H^2$. The resulting equation will now be linear and free of coefficient, but for

$$\begin{aligned}\frac{\Delta}{H^2} &= \frac{6\mu\omega}{p_0}\left(\frac{R}{C}\right)^2\left(\frac{C}{h}\right)^2 \\ &\approx \frac{6\mu\omega}{p_0}\left(\frac{R}{h_{\text{ave}}}\right)^2 \\ &\approx \Lambda.\end{aligned}$$

For journal bearings $H = 1 + \varepsilon\cos\theta$, and Eq. (11.22) reduces to

$$\frac{\partial}{\partial\theta}\left[\left(\frac{\partial}{\partial\theta} - \Lambda\right)\bar{\Psi}\right] + \frac{\partial^2\bar{\Psi}}{\partial Z^2} = -\cos\theta. \tag{11.23}$$

To solve this equation, we first make it homogeneous via the substitution

$$\bar{\Psi}(X, Z) = \bar{\Psi}_\infty(X) - \bar{\Psi}^*(X, Z)$$

and use separation of variables to solve the resulting equation in $\bar{\Psi}^*(X, Z)$. The high degree of similarity between Eqs. (11.19) and Eq. (11.23) means that the load components calculated from Eq. (11.23) will be but a function of ε times the load components calculated from the linearized p solution

$$F_R|_\Psi = \frac{2}{\varepsilon^2}\left[\frac{1-\sqrt{1-\varepsilon^2}}{\sqrt{1-\varepsilon^2}}\right]F_R|_p, \tag{11.24a}$$

$$F_T|_\Psi = \frac{2}{\varepsilon^2}[1-\sqrt{1-\varepsilon^2}\,]F_T|_p. \tag{11.24b}$$

Here $(\cdot)|_\Psi$ and $(\cdot)|_p$ refer to the linearized Ψ and linearized p solutions, respectively. Figure 11.3 compares linearized p, linearized Ψ, and computer solutions.

For large Λ, Eq. (11.17a) may be written as

$$\frac{\partial H}{\partial \theta} = \frac{1}{\Lambda}\left[\frac{\partial}{\partial \theta}\left(H^3 P \frac{\partial P}{\partial \theta}\right) + \frac{\partial}{\partial Z}\left(H^3 P \frac{\partial P}{\partial Z}\right)\right]. \tag{11.25a}$$

Neglecting the right-hand side upon taking the limit $\Lambda \to \infty$ would lead to

$$\lim_{\Lambda\to\infty} \frac{\partial \bar{\Psi}}{\partial \theta} = 0 \tag{11.25b}$$

and satisfaction of the boundary conditions

$$\frac{\partial \Psi}{\partial \theta} = \varepsilon \sin\theta, \quad \text{at } Z = \pm\frac{L}{D},$$

would not be possible. Clearly, the small parameter $1/\Lambda$ multiplies the highest derivatives in Eq. (11.25a), and one is faced with a *singular perturbation* problem (Nayfeh, 1973). To overcome the difficulty, Pan (1980) uses *matched asymptotic expansion*.[4] The key for matching inner and outer solutions is the *mass content rule* (Elrod and Burgdorfer, 1959; Pan, 1980)

$$\frac{1}{2\pi}\int_0^{2\pi} H^3 P^2 d\theta = 1 + \frac{3}{2}\varepsilon^2,$$

which is obtained by integrating Eq. (11.25a) over the circumference, taking into account the periodicity of both P and H.

Infinitely Long Step Slider

The pressure differential equation (11.11) reduces to

$$\frac{d}{dx}\left(\frac{Uph}{2} - \frac{1}{12\mu}h^3 p\frac{\partial p}{\partial x}\right) = 0, \tag{11.26a}$$

and the boundary conditions are

$$p(0) = p(L) = p_a. \tag{11.26b}$$

The slider is shown schematically in Figure 11.4.

[4] According to Pan (1980), Eq. (11.25b) is to be employed in the open domain $|Z| < L/D$ as the *outer solution*. The *inner solution*, which satisfies the edge conditions, is obtained from a rescaling of Eq. (11.25a). To achieve this rescaling, the axial coordinate is stretched in the ratio $\sqrt{\Lambda}$.

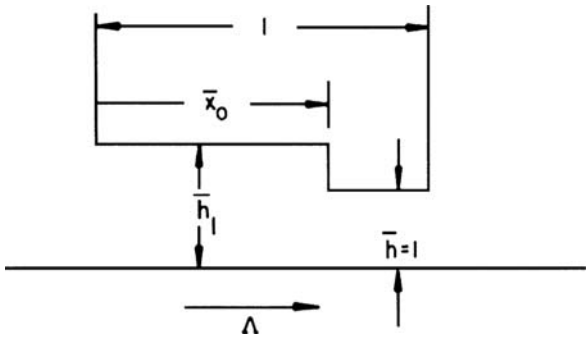

Figure 11.4. Step slider geometry.

The equation is nondimensionalized as in Eq. (11.12) to give

$$\frac{d}{dX}\left(\Lambda PH - H^3 P\frac{\partial P}{\partial X}\right) = 0,$$
$$P(0) = P(1) = 1. \tag{11.27}$$

Integration of Eq. (11.27) yields

$$PH\left(1 - \frac{H^2}{\Lambda}\frac{dP}{dX}\right) = \hat{K}, \tag{11.28a}$$

where $\hat{K}$, a constant of integration, equals the value of PH at X^*, where $dP/dX = 0$:

$$\hat{K} = PH|_{X=X^*}. \tag{11.28b}$$

Employing Eq. (11.28a) in Eq. (11.27), we get

$$\frac{dP}{dX} = \lambda\left(1 - \frac{\gamma}{p}\right), \tag{11.29}$$

where $\gamma = \hat{K}/H$ and $\lambda = \Lambda/H^2$ are constants in each interval $0 \le X \le X_0$ and $X_0 < X \le 1$. The integral of Eq. (11.29) is

$$P + A + \gamma \ln(P - \gamma) = \lambda X. \tag{11.30}$$

Applying the boundary condition $P = 1$ at $X = 0$, gives $A = -1 - \ln(1 - \gamma)$, and if $\gamma_1 = \hat{K}/H_1$ and $\lambda_1 = \Lambda/H_1^2$, where $H_1 = H(1)$, we find in the range $0 \le X \le X_0$:

$$P - 1 + \gamma_1 \ln\left(\frac{P - \gamma_1}{1 - \gamma_1}\right) = \lambda_1 X. \tag{11.31a}$$

Equation (11.30) can also be evaluated in the range $X_0 \le X \le 1$:

$$P - 1 + \hat{K} \ln\left(\frac{P - \hat{K}}{1 - \hat{K}}\right) = \Lambda(X - 1), \tag{11.31b}$$

where Eq. (11.31b) satisfies $P = 1$ at $X = 1$.

At $X = X_0$, $P = P_0 \equiv P(X_0)$, and we use this condition to match the pressures at X_0:

$$H_1 (P_0 - 1) + \hat{K} \ln \left(\frac{P_0 H_1 - \hat{K}}{H_1 - \hat{K}} \right) = \frac{\Lambda}{H_1} X_0, \tag{11.32a}$$

$$P_0 - 1 + \hat{K} \ln \left(\frac{\hat{K} - P_0}{\hat{K} - 1} \right) = \Lambda (X_0 - 1). \tag{11.32b}$$

The system of Eqs. (11.32) contains two unknowns, P_0 and $\hat{K}$. These equations cannot be solved analytically, and one has to resort to numerical methods. For the limiting cases $\Lambda \to 0$ and $\Lambda \to \infty$, however, we are able to obtain closed form solutions.

Asymptotic case $\Lambda \to 0$:

We look for small perturbation of the incompressible case and put

$$P_0 = 1 + \Lambda \pi_0 + O(\Lambda^2). \tag{11.33}$$

Substituting for P_0 into Eq. (11.31) and collecting terms multiplied by Λ, we obtain $\hat{K}$ and π_0 as (Pan, 1980)

$$\hat{K} = \left[\frac{(1 - X_0) H_1^2 + X_0}{(1 - X_0) H_1^3 + X_0} \right] H_1,$$

$$\pi_0 = \frac{X_0 (1 - X_0)(H_1 - 1)}{(1 - X_0) H_1^3 + X_0}.$$

The pressure distribution can now be written for small Λ:

$$P = 1 + \Lambda \pi_0 \frac{X}{X_0}, \qquad 0 \le X \le X_0, \tag{11.34a}$$

$$P = 1 + \Lambda \pi_0 \frac{1 - X}{1 - X_0}, \quad X_0 \le X \le 1. \tag{11.34b}$$

Asymptotic case $\Lambda \to \infty$:

From Eq. (11.31), it can be shown that $\Lambda \to \infty$ requires $\hat{K} \to H_1$ and $P_0 \to H_1$. To signify this, we put for large Λ

$$\begin{aligned} \hat{K} &= H_1 - \delta H, \qquad \delta H / H_1 \ll 1, \\ P_0 &= H - \delta P, \qquad \delta P / P_0 \ll 1, \end{aligned} \tag{11.35a}$$

and substitute into Eq. (11.31)

$$\begin{aligned} &H_1 (H_1 - 1 - \delta P) + (H_1 - \delta P) \ln \left(\frac{H_1 (H_1 - 1) + \delta H - H_1 \delta P}{\delta H} \right) = \frac{\Lambda X_0}{H_1}, \\ &H_1 - 1 - \delta P + (H_1 - \delta H) \ln \left(\frac{\delta P - \delta H}{H_1 - 1 - \delta H} \right) = -\Lambda (1 - X_0). \end{aligned} \tag{11.35b}$$

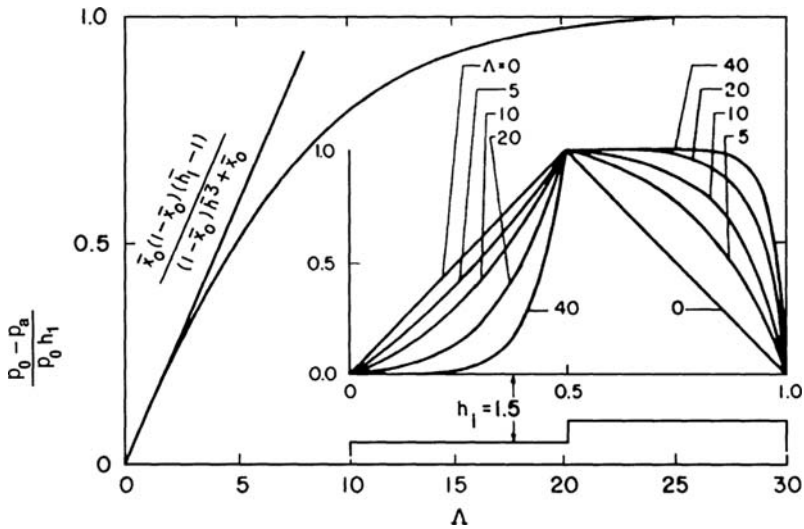

Figure 11.5. Pressure distribution in step slider (Pan, 1980).

We recognize that on the left-hand sides the logarithmic terms dominate as $\Lambda \to \infty$. Furthermore, at the limit, $H_1(1 - \delta H/H_1) \to H_1$. Then, Eq. (11.35b) becomes

$$H_1 \ln\left(\frac{H_1(H_1-1)+\delta H - H_1 \delta P}{\delta H}\right) = \frac{\Lambda X_0}{H_1}, \tag{11.36a}$$

$$H_1 \ln\left(\frac{\delta P - \delta H}{H_1 - 1 - \delta H}\right) = -\Lambda(1 - X_0). \tag{11.36b}$$

The above equations can be solved for δH, δP (Pan, 1980)

$$\begin{bmatrix} \delta H \\ \delta P \end{bmatrix} = \frac{H_1 - 1}{1 + E_0} \begin{Bmatrix} H_1 E_1(1 - E_2) \\ H_1 E_1(1 - E_2) + E_2(1 - E_1) \end{Bmatrix}, \tag{11.37}$$

where

$$E_1 = \exp\left[-\frac{\Lambda X_0}{H_1^2}\right], \qquad E_2 = \exp\left[-\frac{\Lambda(1 - X_0)}{H_1}\right],$$
$$E_0 = E_1(H_1 - 1 - H_1 E_2).$$

On substituting for δH, δP in Eq. (11.32), the pressure at large Λ is obtained:

$0 \le X \le X_0$:

$$P = 1 + \frac{(H_1 - 1)(1 - E_2)}{1 + E_0}\left\{\exp\left[-\frac{\Lambda(X_0 - X)}{H_1^2}\right] - E_1\right\} \tag{11.38a}$$

$X_0 \le X \le 1$:

$$P = 1 + \frac{(H_1 - 1)(1 - E_1)}{1 + E_0}\left\{1 - \exp\left[-\frac{\Lambda(1 - X)}{H_1^2}\right]\right\}. \tag{11.38b}$$

Sample results for $h = 1.5$ and $X_0 = 0.5$ are given in Figure 11.5. The primary effect of compressibility is related to the pressure peak. For small Λ the above ambient value of the

peak pressure is independent of the value of the ambient pressure and is proportional to the product of speed and viscosity, as with incompressible lubricant. At large Λ, on the other hand, the peak pressure is a constant multiple of the ambient pressure, where the multiplier is numerically equal to the gap ratio H_1.

Figure 11.5 displays the variation of the peak pressure P_0 with Λ. The (normalized) pressure distribution for various values of Λ are also shown in the insert. Note that for the incompressible case P_0 varies linearly with Λ, but for higher values the curve deviates more and more from the incompressible case, finally reaching a limiting value as $\Lambda \to \infty$, in accordance with earlier assertions.

11.3 Nomenclature

B	integration constant
C	radial clearance
F_r, F_T	radial, tangential force
H	film thickness (dimensionless)
$\hat{K}$	integration constant
Kn	Knudsen number
L	bearing length
M	Mach number
P	pressure (dimensionless)
R	bearing radius
Re	Reynolds number
R_ε	reduced Reynolds number
U, U_1, U_2	surface velocity
X, Z	coordinates (dimensionless)
Θ	temperature
a	characteristic length
c_p	specific heat
h	film thickness
k	heat conductivity
p	pressure
p_a	ambient pressure
t	time
u, v, w	velocity components
Λ	bearing (compressibility) number
ε	eccentricity ratio
ω	shaft angular velocity
λ	mean free path
μ	viscosity
τ_c, τ_t	characteristic times

11.4 References

Ausman, J. S. 1959. Theory and design of self-acting gas-lubricated journal bearings including misalignment effects. *Proc. 1st Int. Symp. Gas-Lub. Bearings*, **ACR-49**, 161–192, ONR Washington, D.C.

Ausman, J. S. 1961. An improved analytical solution for self-acting, gas lubricated journal bearings of finite length. *ASME J. Basic Eng.*, **83**, 188–194.

Ausman, J. S. 1966. Gas-lubricated bearings. *Advanced Bearing Technology*, E. E. Bisson and W. J. Anderson (ed.). NASA, Washington, D.C.

Burgdorfer, A. 1959. The influence of molecular mean free path on the performance of hydrodynamic gas lubricated bearings. *ASME J. Basic Eng.*, **81**, 94–100.

Chan, D. Y. C. and Horn, G. 1985. *J. Chemical Physics*, **83**, 5311.

Constantinescu, V. N. 1969. Gas lubrication. *The American Society of Mechanical Engineers*, New York.

Elrod, H. G. Jr. and Burgdorfer, A. 1959. Refinement of the theory of gas lubricated journal bearing of infinite length. *Proc. 1st Int. Symp. Gas-Lub. Bearings*, **ACR-49**, 93–118, ONR, Washington, D.C.

Elrod, H. G. Jr. and Malanoski, S. B. 1960. *Theory and Design Data for Continuous Film, Self Acting Journal Bearings of Finite Length.* Rep. I-A 2049–13 and Rep. I-A 2049–17.

Fukui, S. and Kaneko R. 1988. Analysis of ultra-thin gas film lubrication based on linearized Boltzmann equation including thermal creep. *ASME Journal of Tribology*, **110**, 253–262.

Gross, W. A. 1962. *Gas Film Lubrication.* Wiley, New York.

Harrison, W. J. 1913. The hydrodynamical theory of lubrication with special reference to air as a lubricant. *Trans. Cambridge Phil. Soc.*, **22**, 39–54.

Hirn, G. A. 1984. Sur les principaux phenomenes. . . . *Bull. Soc. Ind. Mulhouse*, **26**, 188.

Hsia, Y.-T. and Domoto, G. A. 1983. An experimental investigation of molecular rarefaction effects in gas lubricated bearings at ultra-low clearances. *ASME Journal of Lubrication Technology*, **105**, 120–130.

Kingsbury, A. 1897. Experiments with an air lubricated journal. *J. Am. Soc. Naval Engineers*, **9**, 267–292.

Mitsuya, Y. 1993. Modified Reynolds equation for ultra-thin film gas lubrication using 1.5-order slip-flow model and considering surface accommodation coefficient. *ASME Journal of Tribology*, **115**, 289–294.

Nayfeh, A. H. 1973. *Perturbation Methods.* Wiley, New York.

Pan, C. H. T. 1981. Gas bearings. In *Tribology: Friction, Lubrication and Wear*, A. Z. Szeri (ed.). McGraw-Hill, New York.

Pinkus O. and Sternlicht, B. 1961. *Theory of Hydrodynamic Lubrication.* McGraw-Hill, New York.

Raimondi, A. A. 1961. A numerical solution of the gas lubricated full journal bearing. *ASME Trans.*, **4**, 131–155.

Scheinberg, S. A. 1953. Gas lubrication of slider bearings. *Friction and Wear of Machines*, **8**, 107–204. *Inst. Machine Sci., Academy Sci.*, USSR.

CHAPTER 12

Molecularly Thin Films

Although the lubrication approximation has been derived for thin films, there is, nevertheless, a thin film limit to its validity. When the characteristic dimensions of the fluid-containing device approach the mean free path (for gases) or the dimension of the molecules (for liquids) the continuum assumption, one of the basic assumptions of the approximation, breaks down. In such cases the Reynolds equation must be amended or replaced by other mathematical systems.

We have two distinct models at our disposal for representing fluids, continuum and particle. While the latter is valid under the whole range of conditions, though its use is limited by practical considerations, the continuum model applies only with restrictions. The equations that are available for fluid characterization, and how they relate to the two models, are shown in Table 12.1 (Gad-el-Hak, 1999).

Particle-based representation, which is at the most fundamental level, is of two kinds, deterministic, in which the motion of each molecule in an ensemble is followed in detail, and statistical, in which the evolution of the particle's probability density function is investigated (Ungerer et al., 2007).

Molecular dynamics (MD) simulation, a deterministic, particle-based method (Koplik and Banavar, 1995), although theoretically applicable under the complete range of conditions, is employed mainly for liquids as the long flight paths between collisions for gas makes forward integration of the equations prohibitively expensive. In liquids the molecules are densely packed, leading to a more efficient application of MD simulation.

The statistics based particle method, on the other hand, presupposes well-developed kinetic theory, which is not available for liquids. In addition, the equations employed here are derived for low-density packing of molecules, making these methods applicable to gases. Both Monte Carlo approaches and the Boltzmann equation are derived from the Liouville equation, a conservation equation of the n-dimensional probability function. The direct simulation Monte Carlo (DSMC) method (Bird, 1994; Oran et al., 1998) may be used for dilute fluids when the ratio of the average molecular spacing to molecular diameter is larger than 10. The basic technique of DSMC is to uncouple molecular motions from intermolecular collisions over small time intervals: particle motions are modeled deterministically while collisions are treated statistically. The Boltzmann equation for the one-particle distribution function $f(\boldsymbol{x}, \boldsymbol{c}, t)$, where $\boldsymbol{x}$ is the location of the particle and $\boldsymbol{c}$ is its velocity, is applicable over the whole range of the Knudsen number, $\mathrm{Kn} = \lambda / h$, h being the film thickness and λ the mean free path between collisions. The Boltzmann equation is usually solved by various methods of computational fluid dynamics (CFD).

For air at standard temperature and pressure (STP) the ratio of mean free path to average spacing of molecules to molecular diameter is $\sim$170: 10: 1 (Vincenti and Kruger, 1965). A cube 1 μm at the edges contains $n \sim 2.9 \times 10^7$ molecules. The molecules travel along straight-line trajectories between collisions; the mean free path is $\lambda \sim 60$ nm. There are no forces acting on the molecules between collisions, which, on the whole, are binary and

Table 12.1. *Fluid characterization*

Representation	Type	Equation (Method)	Fluid
Continuum	Deterministic	Navier-Stokes, no-slip (CFD)	Gas-liquid
		Navier-Stokes, slip (CFD)	Gas-liquid
Particle	Deterministic	Newton (MD)	Liquid
	Statistical	Liouville (DSMC)	Gas
		Boltzmann (CFD)	Gas

number 10^{10} per second. Gases have well-developed kinetic theory, which greatly facilitates their theoretical treatment.

As the temperature of a gas is lowered, the thermal velocity of its molecules decreases and the molecules become more densely packed. A cube $1\,\mu$m at the edges now contains $n \sim 3.35 \times 10^{10}$ molecules and the average molecular spacing decreases to ~ 0.31 nm. One can no longer speak of mean free path as the molecules of liquids are too closely packed. This signifies that the continuum approximation will apply to liquids down to smaller length scales than in gases. Nonetheless, when the characteristic dimension of the container becomes comparable to the size of the liquid molecule the continuum assumption breaks down. The forces that make their appearance owing to the breakdown of the continuum assumption are referred to as structural or solvation forces. The occurrence and nature of solvation forces have been investigated both experimentally and numerically. Experimental investigations make use of various surface force apparatus (SFA) while numerical investigations utilize molecular dynamics (MD) simulation.

Breakdown of the continuum model is best illustrated for gas flow. We shall first discuss modeling in such applications, leaving the more difficult and less understood liquid film for later.

12.1 Gas Flow

When the dimensions of a flow device are such as to accommodate a large enough number of gas molecules, the gas can be considered to have its mass continuously distributed throughout the space it occupies and to obey the no-slip condition at solid boundaries. However, as devices are made smaller and smaller, attention must be paid, eventually, to the fact that gases consist of discrete molecules.

The conditions that apply to a gas in thin films are best described with reference to the Knudsen number, $\mathrm{Kn} = \lambda / h$ (cf., Figure 12.1). Continuum flow becomes applicable as $\mathrm{Kn} \to 0$ while $\mathrm{Kn} \to \infty$ characterizes collisionless molecular flow. The various Knudsen number regimes are: $\mathrm{Kn} = 0$ for Euler flow, for $0 > \mathrm{Kn} < 0.001$ the flow (of a Newtonian fluid) is governed by the Navier-Stokes equation with no-slip boundary condition. For flows with Knudsen number above $\mathrm{Kn} = 0.001$, the continuum approach is still usable if we allow slip to occur at the boundaries (Gad-el-Hak, 1999). This was demonstrated by Shaaf and Sherman (1954) among others, who measured the drag on a flat plate in a wind tunnel. The Boltzmann equation holds for the full Knudsen number range, but, as the equation is

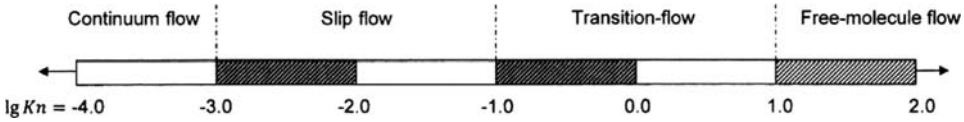

Figure 12.1. Knudsen number range of various gas flow regimes.

difficult to solve, the continuum approach is advocated whenever applicable. For $\mathrm{Kn} \to \infty$ there is no choice, the collisionless Boltzmann equation must be used.

An important application of thin-film gas lubrication is to the head-disk interface of computer hard disk drives. In these devices, found in most of today's computers, the read/write head is supported by a slider that is suspended above the rotating disk. The density of the information that can be stored on the disk can be increased dramatically by decreasing the flying height of the read/write head. Current drives have areal density of the order of 12 Gbit/in^2 and flying heights as low as 15 nm. To achieve a recording density of 100 Gbit/in^2, the distance between head and recording surface must be reduced to 5–10 nm (Bahukudumbi and Beskok, 2003). For films this thin, the Reynolds equation with no-slip boundary condition predicts shear stresses that are far too high. It appears, however, that it is not the continuum assumption so much that is at fault in creating this disagreement at moderate rarefactions, but the no-slip boundary condition. Some of the models currently in use for predicting flow conditions at the head-disk interface of computer hard disk drives are the various velocity-slip theories (Burgdorfer, 1959; Hsia and Domoto, 1983; Mitsuya, 1993: Wu and Bogy, 2003; Bahukudumbi and Beskok, 2003) and the Boltzmann equation based Reynolds approaches (Fukui and Kaneko, 1988; Cercignani et al., 2007).

Velocity Slip at the Boundary

Velocity slip at flow boundaries in moderately rarefied gases was observed as early as 1857 by Kundt and Warburg. They found that in the region where the Knudsen number ranges between 0.01 and 0.1, the limit

$$u_{\text{slip}} = \lim_{Q \to \text{wall}} |u(Q) - u_0|$$

exists and is finite. Here $u(Q)$ and u_0 represent velocity at the point Q and at the wall, respectively. Under these conditions the continuum hypothesis, i.e., the compressible Navier-Stokes equation, can still be used if only the boundary conditions are amended to account for the slip velocity u_{slip}. At higher values of the Knudsen number, however, rarefaction becomes the controlling phenomenon and continuum theories can no longer be applied.

Hsia and Domoto (1983) experimentally confirmed the validity of the slip-flow theory in helium. Initially, they calculated the load from first-order slip theory, which is based on momentum transfer between gas and plate, down to 75 nm. However, most of the experimental data fell below the theoretical load curve when the spacing was less than 250 nm. To correct for this divergence, they proposed a second-order slip theory as an extension. The first-order and the second-order theories lie on both sides and bracket results from the Reynolds-Boltzmann equation, which is obtained from the linearized Boltzmann equation (Fukui and Kaneko, 1988).

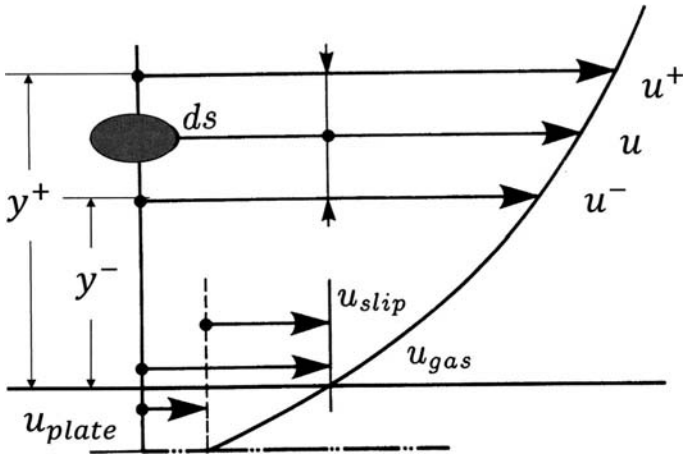

Figure 12.2. Schematics for slip-flow analysis.

A consistent slip condition that renders the Navier-Stokes relations valid in the $0.001 < \mathrm{Kn} < 0.1$ regime, the so-called slip flow regime, is

$$u_{\text{slip}} = L_s \left.\frac{\partial u}{\partial y}\right|_Q , \tag{12.1}$$

where $(\partial u/\partial y)_Q$ is the gradient at a point $Q \rightarrow$ wall (Maxwell, 1879). The coefficient L_s is called the slip coefficient; its importance in the slip-flow regime is comparable to that of the coefficient of heat conduction in heat transfer. Albertoni et al. (1963) tabulated the slip coefficient estimates of various authors, they themselves calculate $L_s = 1.1466\ \lambda$ from the BGK (Bhatnagar-Gross-Krook) model of the collision term in the Boltzmann equation (Bhatnagar et al., 1954).

To examine velocity slip at a solid boundary, we study the flow of a gas of velocity $u(y)$ along the x-direction, as depicted in Figure 12.2. We assume here that the gas consists of rigid, nonattracting molecules, which have number density per unit volume n, and randomly distributed velocity with average magnitude $\bar{c} = \sqrt{8kT/\pi m}$. Here k is the Boltzmann constant, m is the molecular mass and T is the absolute temperature.

The frequency of molecular bombardment per unit area on one side of an imaginary, stationary surface in the flow, oriented parallel with the bounding surface such as ds in Figure 12.2, is given by $Z = (n\bar{c}/4)$ (Bird et al., 2002). We can compute the shear stress imparted to ds by summing the x-momentum of the molecules crossing this imaginary surface from the two opposite directions

$$\tau = Zm(u_+ - u_-). \tag{12.2}$$

The velocities $u_+ = u(y^+)$ and $u_- = y(y^-)$ can be computed from a Taylor expansion of u about y:

$$\begin{aligned} u_+ &= u(y) + \frac{\partial u}{\partial y}(y^+ - y) + \frac{1}{2}\frac{\partial^2 u}{\partial y^2}(y^+ - y)^2 + \cdots \\ u_- &= u(y) + \frac{\partial u}{\partial y}(y^- - y) + \frac{1}{2}\frac{\partial^2 u}{\partial y^2}(y^- - y)^2 + \cdots \end{aligned} \tag{12.3}$$

Substituting (12.3) into (12.2) and observing that $(y^+ - y)^2 = (y - y^-)^2$ we obtain

$$\tau = Zm\frac{\partial u}{\partial y}(y^+ - y^-). \tag{12.4}$$

By comparing (12.4) with the macroscopic shear stress equation

$$\tau = \mu(\partial u/\partial y), \tag{12.5}$$

we can relate the molecular viscosity to the frequency of oscillation of the molecules, the molecular mass, and the Taylor length through

$$\mu = Zm(y^+ - y^-). \tag{12.6}$$

Applying the foregoing analysis to the boundary at y, where y^- is the location of the "displaced" solid wall, so that

$$u_- = u_{\text{plate}}, \quad u(y) = u_{\text{gas}} \text{ (velocity of gas at wall)},$$

we have

$$u_+ = u_{\text{gas}} + \left.\frac{\partial u}{\partial y}\right|_{y=0}(y^+ - y) + \frac{1}{2}\left.\frac{\partial^2 u}{\partial y^2}\right|_{y=0}(y^+ - y)^2. \tag{12.7}$$

Substituting for u_+ and u_- into Eq. (12.2) and introducing the tangential accommodation coefficient α to couple the transmitted shear force to the surface characteristics of the boundary we obtain

$$\tau = \alpha Zm\left[\left.\frac{\partial u}{\partial y}\right|_{y=0}(y^+ - y) + \frac{1}{2}\left.\frac{\partial^2 u}{\partial y^2}\right|_{y=0}(y^+ - y)^2 + u_{\text{gas}} - u_{\text{plate}}\right]. \tag{12.8}$$

The accommodation coefficient is defined as the fraction of the molecules reflected from the wall diffusively. When $\alpha = 0$, the slip velocity is unbounded as the molecules preserve their momentum (specular reflection, incidence angle equals reflection angle). Diffuse reflection (zero tangential momentum on the average for reflected molecules), in contrast, is specified by $\alpha = 1$ (Bird, 1994).

On comparing the macroscopic formula for shear, Eq. (12.2), to Eq. (12.8), we find that

$$u_{\text{slip}} \stackrel{\text{def}}{=} u_{\text{gas}} - u_{\text{plate}} = \frac{(y^+ - y^-) - \alpha(y^+ - y)}{\alpha}\frac{\partial u}{\partial y} - \frac{1}{2}\frac{\partial^2 y}{\partial y^2}(y^+ - y^-)^2. \tag{12.9}$$

The slip velocity at the boundary is defined as the difference between u_{gas}, the apparent velocity at the wall, and u_{plate}, the prescribed plate velocity. It is obvious from Eq. (12.9) that the slip velocity can assume different values in the various models, depending on the relationship the model specifies between the Taylor length $(y^+ - y)$ and the mean free path λ.

The first-order and the second-order models equate the Taylor length to the mean free path. In contrast, Mitsuya (1993) take cognizance that the molecules striking the plane experienced their last collision at a distance of $(2/3)\lambda$ from the plane (cf., Vincenti and Kruger, 1965; Bird et al., 2002) and in this manner derives the 1.5th-order theory. Wu and Bogy (2003), on the other hand, construct new first- and second-order slip models by summing the contributions from groups of molecules impinging on the surface at various angles; this, in effect, means a relaxation of the requirement that the length scale in the

Taylor expansion (12.9) equals the mean free path. Wu and Bogy claim that in the low inverse Knudsen number domain their second-order model gives the Pouiselle flow rate with greater accuracy than the old second-order model does; it is also free of pressure singularity at contact.

Shen et al. (2007) argued that the longitudinal pressure gradient that acts in the Knudsen layer should also be taken into account, and developed a new slip-flow model from the first-order solution of the Boltzmann equation. Their fist-order velocity is

$$u_{\text{slip}} = \left(\frac{2-\alpha}{\alpha}\right) t^* \sqrt{\left(\frac{\pi kT}{2m}\right)} \left.\frac{\partial u}{\partial y}\right|_0 - \frac{\lambda}{\alpha}\sqrt{\left(\frac{2\pi m}{2kT}\right)} \frac{1}{mn}\frac{\partial p}{\partial x}. \tag{12.10}$$

Here k is the Boltzmann constant, t^* is the relaxation time, m and n represent molecular mass and number density, respectively.

Some of the typical slip-flow models are:

$$\begin{aligned}
&\text{first-order slip (Burgdorfer, 1959):} && u_{\text{slip}} = \left(\frac{2-\alpha}{\alpha}\right) \left.\frac{\partial u}{\partial y}\right|_0 \lambda \\
&\text{second-order slip (Hsia, Domoto, 1983):} && u_{\text{slip}} = \left(\frac{2-\alpha}{\alpha}\right) \left.\frac{\partial u}{\partial y}\right|_0 \lambda - \frac{1}{2} \left.\frac{\partial^2 u}{\partial y^2}\right|_0 \lambda^2 \\
&\text{1.5th-order slip (Mitsuya, 1993):} && u_{\text{slip}} = \left(\frac{2-\alpha}{\alpha}\right) \left.\frac{\partial u}{\partial y}\right|_0 \lambda - \frac{2}{9} \left.\frac{\partial^2 u}{\partial y^2}\right|_0 \lambda^2 \\
&\text{second-order slip (Wu, Bogy, 2003):} && u_{\text{slip}} = \frac{2}{3}\left(\frac{2-\alpha}{\alpha}\right) \left.\frac{\partial u}{\partial y}\right|_0 \lambda - \frac{1}{4} \left.\frac{\partial^2 u}{\partial y^2}\right|_0 \lambda^2.
\end{aligned} \tag{12.11}$$

Poiseuille and Couette flow profiles, utilizing various slip-flow models, are compared in Figure 12.3.

The velocity-slip formulas can be applied to compute the flow rate in Poiseuille flow (Figure 12.4). The various models lead to different nondimensional flow rate equations:

$$\begin{aligned}
&\text{continuum:} && Q_p = \frac{D}{6} \\
&\text{first-order slip (Burgdorfer):} && Q_p = \frac{D}{6} + \frac{a\sqrt{\pi}}{2} \\
&\text{second-order slip (Hsia, Domoto):} && Q_p = \frac{D}{6} + \frac{a\sqrt{\pi}}{2} + \frac{\pi}{4D} \\
&\text{1.5th-order slip (Mitsuya):} && Q_p = \frac{D}{6} + \frac{a\sqrt{\pi}}{2} + \left(\frac{4}{9}\right)\frac{\pi}{4D} \\
&\text{second-order slip (Wu, Bogy):} && Q_p = \frac{D}{6} + \left(\frac{2}{3}\right)\frac{a\sqrt{\pi}}{2} + \left(\frac{1}{2}\right)\frac{\pi}{4D}.
\end{aligned} \tag{12.12}$$

Here the nondimensional *Poiseuille mass flow rate* Q_p, the *rarefaction parameter* D (sometimes referred to as the "inverse Knudsen number") and the surface coefficient a are defined by

$$Q_p = \frac{\rho \int_0^h u dy}{\dfrac{h^2}{\sqrt{2RT}}\dfrac{\partial p}{\partial x}}; \qquad D = \frac{h\sqrt{\pi}}{2\lambda}; \qquad a = \frac{2-\alpha}{\alpha}. \tag{12.13}$$

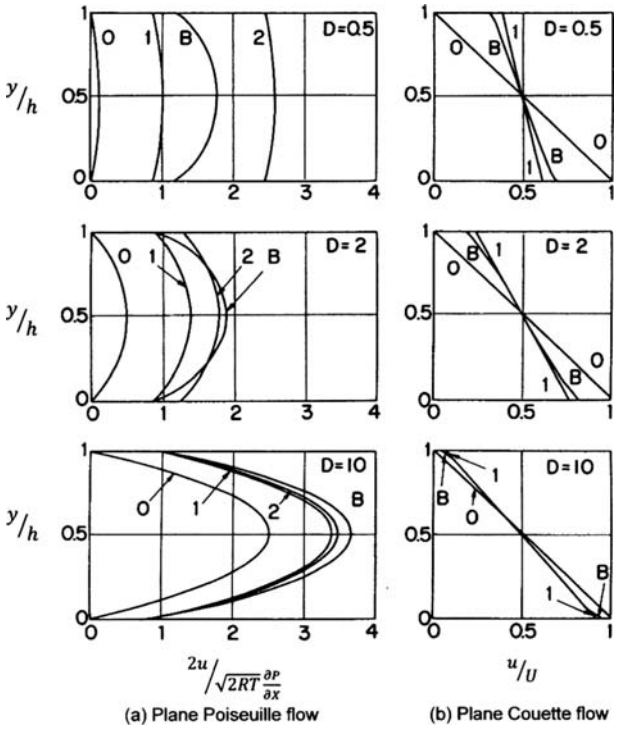

Figure 12.3. Pressure and shear flow according to various theories (0, continuum; 1, 1st order slip; 2, 2nd order slip; B, Boltzmann). (Reprinted with permission from Fukui, S. and Kaneko, R. Analysis of ultra-thin gas film lubrication based on linearized Boltzmann equation. *ASME Journal of Tribology*, **110**, 253–261, 1988.)

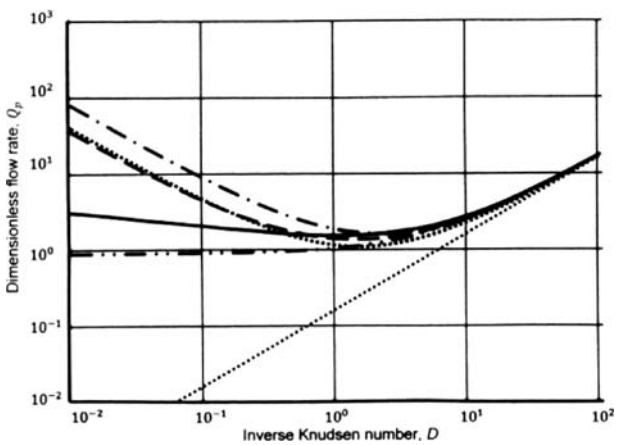

Figure 12.4. Variation of Poiseuille flow rate with inverse Knudsen number (*Continuum*; —, Boltzmann eq.; — · · —, 1st order; — —, 1.5th order; — · —, 2nd order; ▪▪▪, 2nd order, Wu and Bogy.)

As a first step toward deriving a modified Reynolds equation for ultra-thin gas films, we integrate the thin-film equations of momentum, now in normalized form,

$$\frac{\partial P}{\partial X} = \frac{\Lambda}{6}\frac{\partial^2 U}{\partial Y^2}; \qquad \frac{\partial P}{\partial Z} = \frac{\Lambda}{6}\frac{\partial^2 W}{\partial Y^2}; \qquad \frac{\partial P}{\partial Y} = 0; \tag{12.14}$$

and find the velocity components (cf., Eq. 2.67). The integration constants are evaluated by applying the slip-flow boundary conditions, for second-order slip, as an illustration, we have

$$\begin{aligned}
U(0) &= 1 + a\mathrm{Kn}\left.\frac{\partial U}{\partial Y}\right|_0 - \frac{1}{2}\mathrm{Kn}^2\left.\frac{\partial^2 U}{\partial Y^2}\right|_0 \\
U(H) &= -a\mathrm{Kn}\left.\frac{\partial U}{\partial Y}\right|_H - \frac{1}{2}\mathrm{Kn}^2\left.\frac{\partial^2 U}{\partial Y^2}\right|_H \\
W(0) &= a\mathrm{Kn}\left.\frac{\partial W}{\partial Y}\right|_0 - \frac{1}{2}\mathrm{Kn}^2\left.\frac{\partial^2 W}{\partial Y^2}\right|_0 \\
W(H) &= -a\mathrm{Kn}\left.\frac{\partial W}{\partial Y}\right|_H - \frac{1}{2}\mathrm{Kn}^2\left.\frac{\partial^2 W}{\partial Y^2}\right|_H .
\end{aligned} \tag{12.15}$$

Here we employed the definitions

$$\begin{aligned}
&p = p_a P; \qquad (u, w) = U^*(U, W); \qquad h = h_0 H; \\
&(x, y, z) = L\left(X, \frac{h_0}{L}Y, Z\right); \qquad \Lambda = \frac{6\mu U^* L}{p_a h_0^2}.
\end{aligned}$$

The symbol p_a represents the ambient pressure, h_0 the minimum film thickness, Λ the bearing number, and U^* is the characteristic velocity along L.

The velocity components that satisfy Eq. (12.14) and boundary conditions (12.15) are

$$\begin{aligned}
U &= -\frac{3}{\Lambda}\frac{\partial P}{\partial X}(\mathrm{Kn}^2 + aH\mathrm{Kn} + HY - Y^2) + \left(1 - \frac{Y + a\mathrm{Kn}}{H + 2a\mathrm{Kn}}\right) \\
W &= -\frac{3}{\Lambda}\frac{\partial P}{\partial Z}(\mathrm{Kn}^2 + aH\mathrm{Kn} + HY - Y^2)
\end{aligned} \tag{12.16}$$

From here on we follow the analysis of Section 11.1 and derive a modified Reynolds equation that is based on velocity slip at the boundaries

$$\begin{aligned}
&\frac{\partial}{\partial X}\left\{\left[PH^3 + \beta KnH^2 + \gamma Kn^2\frac{H}{P}\right]\frac{\partial P}{\partial X}\right\} \\
&\quad + \frac{\partial}{\partial Z}\left\{\left[PH^3 + \beta KnH^2 + \gamma Kn^2\frac{H}{P}\right]\frac{\partial P}{\partial Z}\right\} = \Lambda\frac{\partial(PH)}{\partial X}.
\end{aligned} \tag{12.17}$$

In Eq. (12.17) we presented the modified Reynolds equation in a somewhat generalized form to include several of the more common slip-flow models; the multipliers β and γ are

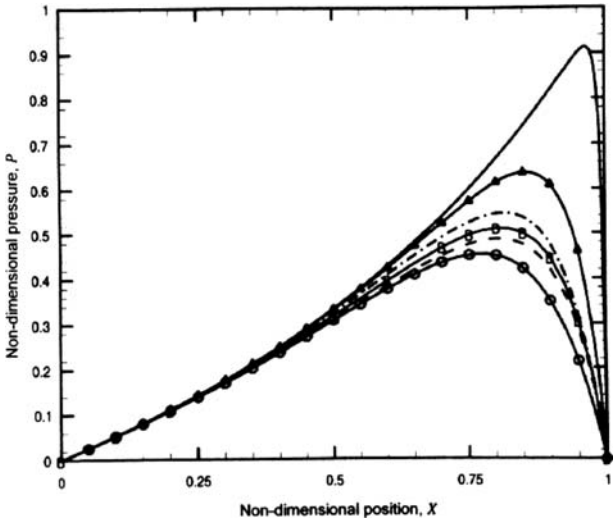

Figure 12.5. Pressure distribution in plane slider (—, Continuum; ▲, 1st order slip; – · –, 1.5th order slip; **B**, Boltzmann; - - -, Effective viscosity; ○, 2nd order slip). (Reprinted with permission from Sun, Y. H., Chan, W. K. and Liu, N. Y. 2003. A slip model for gas lubrication based on an effective viscosity concept, *Proc IMechE Journal of Engineering Tribology*, **217**, 187–195, 2003, Professional Engineering Publishing.)

model specific as shown

$$\begin{aligned}
&\text{first-order slip (Burgdorfer):} && \beta = 6a,\ \gamma = 0\\
&\text{second-order slip (Hsia, Domoto):} && \beta = 6a,\ \gamma = 6\\
&\text{1.5th-order slip (Mitsuya):} && \beta = 6a,\ \gamma = 8/3\\
&\text{second-order slip (Wu, Bogy):} && \beta = 4a,\ \gamma = 3.
\end{aligned} \tag{12.18}$$

Setting $\beta = \gamma = 0$ leads to the Reynolds equation for continuum gas flow with no-slip boundary condition.

Figure 12.5 displays the pressure distribution in a plane slider per the various slip-flow models; this figure was obtained by Sun et al. (2003) at $\Lambda = 200$ and Kn $= 1.77$.

The load capacity of inclined plates in relative sliding at $\Lambda = 10$ and varying rarefaction parameter (inverse Knudsen number)

$$D_0 = h_0\sqrt{\pi}/2\lambda = D/PH$$

is shown in Figure 12.6. The Boltzmann solution is shown bracketed by the first-order slip and second-order slip solutions, just as in Figures 12.4 and 12.5.

Figure 12.7 plots minimum film thickness between a read/write head and its disk. The 1.5th-order slip model seems to perform best in this case, after the Boltzmann model, of course.

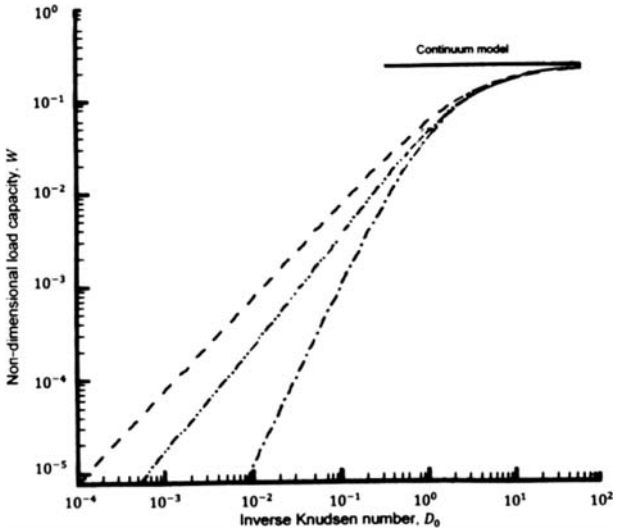

Figure 12.6. Load capacity of plane slider at $\Lambda = 10.0$ ($- \cdot \cdot -$, Boltzmann eq.; $- \cdot -$, 2nd order slip; - - -, 1st order slip.)

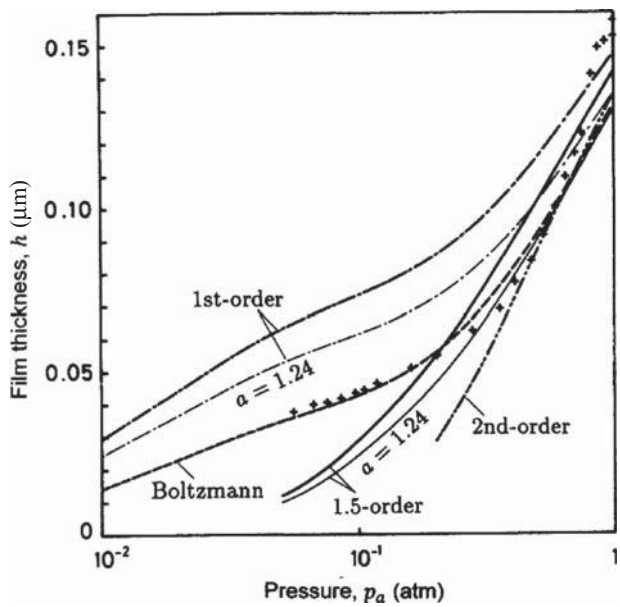

Figure 12.7. Minimum film thickness for miniature slider ($l = 2$ mm, $b = 0.25$ mm, $U = 10$ m/s, $w = 11\,m$N, $\alpha = 1$, 1.24; +, exp., Mitsuya). (Reprinted with permission from Mitsuya, Y. Modified Reynolds equation for ultra-thin film gas lubrication using 1.5 order slip flow model and considering surface accommodation coefficient. *ASME Journal of Tribology*, **115**, 289–294, 1993.)

In constructing a phenomological approach to the problem of rarefied gas flow Beskok and Karniadakis (1999) observed that the coefficient of viscosity is related to the mean free path by

$$\mu = \frac{p\lambda}{\sqrt{RT\pi/2}}. \tag{12.19}$$

Starting from here, they derived a formula for a Knudsen number dependent effective viscosity

$$\mu_{\text{eff}} = \mu\left(\frac{1}{1+\alpha\text{Kn}}\right). \tag{12.20}$$

Sun et al. (2003) further developed this idea, utilizing the work of Veijola and Turowski (2000), and defined effective values for viscosity, mean free path, and Knudsen number

$$\begin{aligned} \mu_{\text{eff}} &= f(\text{Kn})\mu \\ \lambda_{\text{eff}} &= f(\text{Kn})\lambda \\ Kn_{\text{eff}} &= f(\text{Kn})\text{Kn}. \end{aligned} \tag{12.21}$$

Here $f(\text{Kn}) = (1 + 2\,\text{Kn} + 0.2\,\text{Kn}^{0.788}e^{-\text{Kn}/10})^{-1}$ is a correlation obtained from curve fitting to experimental data. The pressure distribution on a plane slider, as obtained via the effective viscosity approach, is plotted in Figure 12.5.

Comparison with experiments suggest that the continuum model allowing for slip at the boundaries yields good results for $\text{Kn} \leq 1$ according to Odaka et al. (cf., Fukui and Kaneko, 1988), and even for $\text{Kn} \leq 2.5$ according to Hsia and Domoto (1983). Nevertheless, it is difficult to justify its use for $\text{Kn} > 1$.

Molecular Gas Lubrication

To compute gas flow at arbitrary Knudsen numbers, we require a more detailed description of it than that afforded by slip-flow models. Direct computation of the position and velocity of the molecules could be useful but is currently not feasible. We are thus forced to work with distribution functions. In this, the task will be made lighter on recognizing that the motion of a molecule between collisions is completely determined by external forces and depends neither on the position nor on the velocity of other molecules.

If the density of the gas is small, i.e., the average spacing of the molecules relative to their dimension is large, the collisions between molecules will be binary collisions. In such cases, and as the molecules do not interact between collisions, statistical description of the state the molecules can be accomplished with reference to the one-particle distribution function $f(\boldsymbol{x}, \boldsymbol{c}, t)$. We define this distribution as follows: the probable number of molecules within the element of physical volume $d\boldsymbol{x} = dx_1dx_2dx_3$ located at the point $\boldsymbol{x}$ at time t, and having velocities within the element $d\boldsymbol{c} = dc_1dc_2dc_3$ near $\boldsymbol{c}$ is equal to $f(\boldsymbol{x}, \boldsymbol{c}, t)\,d\boldsymbol{x}d\boldsymbol{c}$. By following procedure analogous to that used for obtaining other conservation equations, it is possible to formulate an equation that describes the rate of change of the distribution function with respect to position and time. This equation is known as the Boltzmann equation (Vincenti and Kruger, 1965; Kogan, 1969) and is of the form

$$\frac{\partial f}{\partial t} + \boldsymbol{c}\cdot\nabla f = \left\{\frac{\delta f}{\delta t}\right\}_{\text{coll}}. \tag{12.22}$$

The right-hand side of Eq. (12.22), called the *collision integral*, specifies the net rate of change of the number of molecules of class $\boldsymbol{c}$ per unit volume of gas as the difference of depleting collisions and their inverse. The collision integral thus contains the distribution function $f(\boldsymbol{x}, \boldsymbol{c}, t)$, making Eq. (12.22) a nonlinear integro-differential equation.

Because of the nonlinearity of the collision term, the Boltzmann equation is difficult to solve. A particular class of solutions, namely the Maxwellians, describes equilibrium states. The left-hand side of the Boltzmann equation (12.22) is zero in equilibrium, therefore the equilibrium distribution function f_0 solves

$$\left\{\frac{\delta f_0}{\delta t}\right\}_{\text{coll}} = 0.$$

The Maxwellian distribution function (Vincenti and Kruger, 1965) is given by

$$f_0 = n_0 \left(\frac{m}{2\pi kT}\right)^{3/2} \exp\left[\frac{-mc^2}{2kT}\right]. \tag{12.23}$$

Here k is the Boltzmann constant, T is the absolute temperature, and n_0 is the number of molecules per unit volume.

Due to the great complexity of the collision integral, the Boltzmann equation is often linearized. We mention here only two linearizations, though several have been proposed. One of them is obtained as small perturbation of the equilibrium state, in the form

$$f(\boldsymbol{x}, \boldsymbol{c}, t) = f_0\,(1 + \varphi); \qquad \varphi(\boldsymbol{x}, \boldsymbol{c}, t) \ll 1. \tag{12.24}$$

The other approximation which, according to Kogan (1969), has no strict mathematical basis but works well, is the BGK model (Bhatnagar, Gross and Krook, 1954)

$$\frac{\partial f}{\partial t} + \boldsymbol{c} \cdot \nabla f = \frac{(f_0 - f)}{\tau}. \tag{12.25}$$

Here τ is a velocity-dependent collision time. For small departures from equilibrium, when the flow velocity of the gas is small relative to the thermal velocity of its molecules, the BGK model (12.25) will lead to good results. Note that since the velocity of sound is of the order of the root mean square of the thermal velocity, the condition for linearization can also be written in terms of the Mach number.

Some of the most useful methods of solution of the BGK equation (12.25) are based on perturbation techniques. There are several different perturbation methods in use here, based on different choices of the small parameter (Cercignani, 1988). Here we apply (Gross et al., 1957)

$$f = f_0 + \varphi, \quad n = n_0 + \omega, \quad T = T_0 + \theta, \tag{12.26}$$

where φ, ω, and θ represent the perturbation of the distribution function, the number of molecules per unit volume, and the temperature. The last two of these quantities are generated by the perturbation in f in the form

$$\omega = \int E\varphi d\boldsymbol{C}, \quad \theta = \frac{2}{3}\int E\varphi \left(\boldsymbol{C}\cdot\boldsymbol{C} - \frac{3}{2}\right) d\boldsymbol{C}.$$

Here we used the notation $E = \pi^{-3/2}\exp(-C_iC_i)$ and wrote $d\boldsymbol{C} = dC_1dC_2dC_3$ for the volume element in velocity space.

Substituting Eq. (11.26) into Eq. (12.25), we obtain the linearized equation (Gross et al., 1957; Fukui and Kaneko, 1988)

$$\varepsilon C_X \frac{\partial \varphi}{\partial X} + C_Y \frac{\partial \varphi}{\partial Y} + \varepsilon C_Z \frac{\partial \varphi}{\partial Z} = D_0 \left[-\varphi + \omega + 2\boldsymbol{C} \cdot \boldsymbol{V} + \left(\boldsymbol{C} \cdot \boldsymbol{C} - \frac{3}{2} \right) \theta \right]. \tag{12.27}$$

Here $D_0 = D/PH = \sqrt{\pi}/2\,\mathrm{Kn}(h_0)$ is the characteristic inverse Knudsen number, $\boldsymbol{C} = \boldsymbol{c}/\sqrt{2RT_0}$ the nondimensional molecular velocity, $\boldsymbol{V} = \boldsymbol{v}/\sqrt{2RT_0}$ the nondimensional flow speed, $h_0 = \varepsilon L$ the minimum film thickness and $\{X, Y, Z\} = (x/L,\, y/h_0,\, z/L)$. The mean free path is computed from $\lambda = \mu\sqrt{2\pi\, RT_0}/\,(2p)$ and $\boldsymbol{V} = \int E\boldsymbol{C}\varphi d\boldsymbol{C}$.

We will outline here the derivation of a Boltzmann-Reynolds equation for the infinite cylinder, $\partial\varphi/\partial z \to 0$, problem (long-bearing). In this case we have (Fukui and Kaneko, 1988)

$$\varepsilon C_X \frac{\partial \varphi}{\partial X} + C_Y \frac{\partial \varphi}{\partial Y} = D_0 \left[-\varphi + \omega + 2C_X V_X - \left(C^2 - \frac{3}{2} \right) \theta \right]. \tag{12.28}$$

The trial solution

$$\varphi = \left(\frac{X}{\varepsilon} \right) \varphi_0(C^2) + C_X \varphi_1(Y, C_Y, C^2) + \varphi_2(Y, C_Y, C^2) \tag{12.29}$$

satisfies differential equation (12.28) and appropriate boundary conditions, provided that φ_0, φ_1, and φ_2 solve

$$\varphi_0 = \omega_0 + \left(C^2 - \frac{3}{2} \right) \theta_0, \tag{12.30a}$$

$$C_X \frac{\partial \varphi_1}{\partial Y} + D_0 \varphi_1 = D_0\,(2V_X) - \varphi_0, \tag{12.30b}$$

$$C_Y \frac{\partial \varphi_2}{\partial Y} + D_0 \varphi_2 = D_0 \left[\omega_2 + \left(C^2 - \frac{3}{2} \right) \theta_2 \right]. \tag{12.30c}$$

Here we used the definitions

$$\omega_j = \int \varphi_j E d\boldsymbol{C}; \quad \theta_j = \frac{2}{3} \int \left(C^2 - \frac{3}{2} \right) \varphi_j E d\boldsymbol{C}; \quad j = 0, 2$$

The flow rate can be obtained by solving Eq. (12.30b) for φ_1 (φ_2 does not contribute to flow rate, only to temperature distribution), thus the velocity is obtained from

$$V_X = \int (C^2 \varphi_1 E)\, d\boldsymbol{C}. \tag{12.31}$$

The velocity can be split into three terms U_{XP}, U_{XC}, and U_{XT}, indicating pressure flow, shear flow, and thermal creep flow, respectively. These flow components are given by

$$\begin{aligned} V_{XP} &= \left(\frac{\beta}{2D_0} \right) (1 - \Psi_P), \\ V_{XC} &= U_0 \Psi_C, \\ V_{XT} &= -\left(\frac{\gamma}{2D_0} \right) \left(\frac{1}{2} - \Psi_T \right), \end{aligned} \tag{12.32}$$

where Ψ_P, Ψ_C, Ψ_T are defined by integral equations

$$\Psi_P = 1 + \frac{D_0}{\sqrt{\pi}} \int_0^H \Im_{-1}(D_0|Y - Y'|)\, \Psi_P dY', \tag{12.33a}$$

$$\Psi_C = \frac{1}{\sqrt{\pi}} \left[T_0 (D_0 Y) + D_0 \int_0^H \Im_{-1}(D_0|Y - Y'|)\, \Psi_C dY' \right], \tag{12.33b}$$

$$\Psi_T = \frac{1}{2} + \frac{D_0}{\sqrt{\pi}} \int_0^H \Im_{-1}(D_0|Y - Y'|)\, \Psi_T dY' + \frac{D_0}{\sqrt{\pi}} \int_0^H \Im_1(D_0|Y - Y'|)\, dY'. \tag{12.33c}$$

Here,

$$\Im_n(\varphi) = \int_0^\infty t^n \exp(-t^2 - \varphi/t)\, dt$$

is the Abramowitz function. These expressions are for diffuse reflection at the boundaries. Thermal and momentum accommodation coefficients for surfaces relevant to the disk-drive air bearing have been measured by Rettner (1997).

Equation (12.33a), (12.33b), and (12.33c), respectively, have been solved numerically by Cercignani and Daneri (1963), Willis (1962), and Loyalka (1971). Substituting the solutions of Eq. (12.33) into Eq. (12.32), the x-component of the velocity is obtained.

To derive a Reynolds-type equation, the flow rate must be calculated first. Due to the linearity of Eq. (12.28), the flow rate q is a superposition of the pressure flow q_p, the Couette flow q_C, and the thermal creep flow q_T. The Couette flow is not dependent on the Knudsen number. As for the other two flow components, q_p has been evaluated by Cercignani et al. (Cercignani and Daneri, 1963; Cercignani and Pagani, 1966)

$$q_p = -Q_p(D_0) \frac{h^2}{\sqrt{2RT_0}} \left(\frac{dp}{dx} \right) \tag{12.34a}$$

and q_T by Loyalka (1971)

$$q_T = Q_T(D_0) \frac{ph^2}{T_0 \sqrt{2RT_0}} \left(\frac{dT_w}{dx} \right). \tag{12.34b}$$

The nondimensional coefficients $Q_p(D_0)$ and $Q_T(D_0)$ are functions of the Knudsen number, they can be found in the above-cited papers and are also reproduced by Fukui and Kaneko (1988).

Assuming constant boundary temperatures, we have grad $\tau_w = 0$. Then the Boltzmann equation-based generalized Reynolds equation can be written as

$$\text{div}[\bar{Q}_P(D) P H^3 \,\text{grad}\, P] = \mathbf{\Lambda} \cdot \text{grad}(PH) \tag{12.35}$$

Here $\bar{Q}_P(D) = Q_p(D)/Q_{con}$, Q_{con} is the flow rate for continuum Poiseuille flow, and $D = PHD_0$. The characteristic rarefaction parameter $D_0 = p_0 h_0 / \mu \sqrt{2RT}$ is calculated on the reference state and is an assigned parameter, and $\mathbf{\Lambda} = (\Lambda_x, \Lambda_z)$ is a vector. Once $\bar{Q}_P(D)$ is defined, Eq. 12.35 can be solved in the same manner discussed for the compressible Reynolds equation.

Table 12.2. *Coefficients for Poiseuille flow curve-fit*

Range	a_1	a_0	a_{-1}	a_{-2}
$5 \leq D$	1/6	1.0162	1.0653	−2.1354
$0.15 \leq D < 5$	0.13852	1.25087	0.15653	−0.00969
$0.01 \leq D < 0.15$	−2.22919	2.10673	0.01653	−0.0000694

The problem, as presented by Eq. (12.35) is laborious to solve. The nonlinear coefficients must be obtained from the integral equations (12.33) at each step of the iteration. An alternative method of solution was presented by Fukui and Kaneko in their follow-up paper (Fukui and Kaneko, 1990). Here Fukui and Kaneko solved the finite difference approximation to Eqs. (12.33) ahead of time, then used the newly created database to interpolate for flow coefficients in terms of the Knudsen number. Even interpolation can be eliminated if the flow coefficients are approximated in closed analytic form. They publish the following power series representation for Q_p

$$Q_p = a_1 D + a_0 + a_{-1} D^{-1} + a_{-2} D^{-2}. \tag{12.36}$$

The coefficients depend on the Knudsen number range as shown Table 12.2.

Figure 12.3 shows plane Poiseuille flow and plane Couette flow velocity profiles as calculated by Fukui and Kaneko (1988). At high values of the rarefaction parameter, $D = \sqrt{\pi}/2\,\mathrm{Kn}$, the first- and second-order slip models yield results that are very similar to those of the Boltzmann-Reynolds equation, and the calculated boundary slip is identical in the three cases. At the lower values of D, however, not only does the boundary slip have different values but the shape of the velocity distribution is different in the three models.

Figure 12.4 plots pressure flow rate against inverse Knudsen number; the curve labeled "Boltzmann" represents Eq. (12.36). Continuum theory with no-slip is shown to yield acceptable results for $\mathrm{Kn} < 0.01$, while the second-order slip result is good for $\mathrm{Kn} < 1$. For $\mathrm{Kn} > 1$, the Boltzmann equation results differ drastically from slip flow model predictions.

One of the shortcomings of the BGK model is that it leads to a Prandtl number of unity, while for monatomic gas $\mathrm{Pr} = 2/3$; this prompted Cercignani et al. (2007) to investigate the slider-bearing problem using the ellipsoidal statistical model (ES), which allows the Prandtl number to take its proper value. This analysis also accommodates for the observation that in hard disk drives the lubricated disk surface is smoother than the carbon-coated slider surface so that nonsymmetric gas-wall interactions need to be considered (Kang et al., 1999; Huang and Bogy, 2000). It is found, however, that "in isothermal conditions and at low Mach numbers the corrections introduced by more refined kinetic models of the collisional Boltzmann operator are negligible" (Cercignani et al., 2007); this is indicated in Figure 12.8.

Direct Simulation Monte Carlo

In order to maintain constant separation during operation, great demands are placed on designing the hydrodynamic slider that carries the read/write head. The problem has been attacked by several authors using direct simulation Monte Carlo (DSMC). This

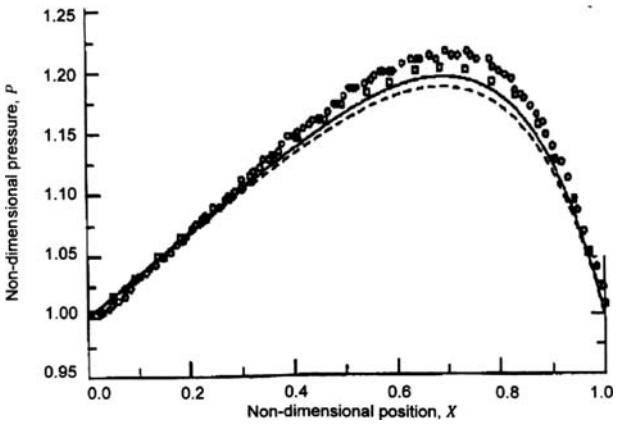

Figure 12.8. Pressure profile comparison, $\delta_0 = 0.7$, $\Lambda = 61.6$, $\alpha_1 = \alpha_1 = 0.7$. (—, Reynolds-BGK; - - -, Reynolds-ES; ○, DMSC; □, IP data, Jiang et al.). (Reprinted with permission from Cercignani, C., Lampis, M. and Lorenzani, S. On the Reynolds equation for linearized models of the Boltzmann operator, *Transport Theory and Statistical Physics*, **36**, 257–280, Copyright (2007) Taylor & Francis Group.)

technique is suitable for solving the Boltzmann equation for dilute gases when average spacing of molecules to molecular diameter $\delta/d \geq 10$ and $0.1 < \text{Kn} > 10$.

In DSMC, the state of the system is given by $(\boldsymbol{r}_i, \boldsymbol{v}_i)$ the position and velocity of the ensemble of particles, each particle representing thousands of molecules in the physical system. Integration of the evolution equations of the system moves each particle forward into a new position $\boldsymbol{r}_i + \boldsymbol{v}_i \Delta t$. When all particles have been moved, a given number of them are selected for collision, according to collision probabilities derived from kinetic theory. Four of the six equations needed to determine the post-collision velocities are supplied by momentum and energy conservation, the remaining two are selected at random but must satisfy certain conditions, such as the post-collision relative velocity directions be uniformly distributed.

Alexander et al. (1994) solved the two-dimensional problem for a slider 5 μm long with maximum separation between disk and slider of 50 nm. Conditions were characterized by the exit values of the Knudsen number, the compressibility number, and the Mach number, $\text{Kn} = 1.250$, $\Lambda = 61.6$ and $M = 0.08$, respectively. As illustrated in Figure 12.9 agreement between the MGL (molecular gas lubrication) method of Fukui and Kaneko (1988) and DSMC was excellent. The first-order slip flow and the continuum model deviate significantly from DSMC.

Huang et al. (1997) were able to demonstrate on a three dimensional slider of length $L = 4$ μm, width $W = 3.3$ μm, and minimum film thickness $0 \leq h_0 \leq 25$ nm, that in the $2.5 \leq \text{Kn} \leq 31.25$ range DSMC and MGL agree for calculating force on the slider. The maximum discrepancy of 3.76% in force occurred at $\text{Kn} = 12.5$; this would result in an error of less than 10% in predicted film thickness. Bearing force is shown plotted against the Knudsen number in Figure 12.10. DSMC was also applied to slider-disk contact, where conventional theory gave unbounded force, and worked well.

The DSMC method is valid for the whole Knudsen number range and is of sufficient accuracy, however, it is computationally intensive; the time step taken must be small relative to the average time between collisions and the linear dimensions of the computational

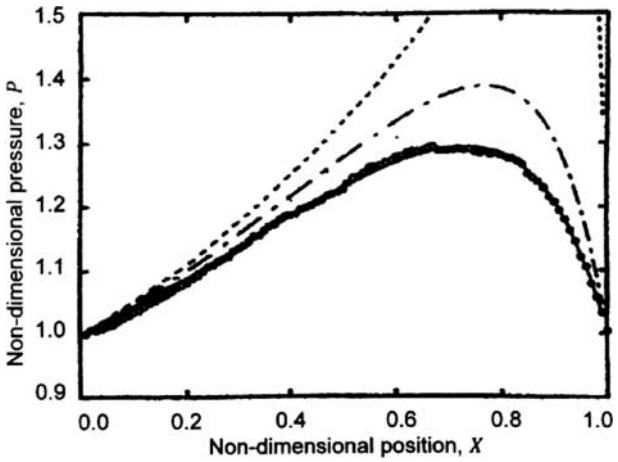

Figure 12.9. Pressure distribution for slider (•••, DSMC; –, MGL; – · –, 1st order slip; – – –, continuum). (Reprinted with permission from Alexander, F. J., Garcia, A. L., and Alder, B. J. Direct simulation Monte Carlo for thin film bearings. *Phys. Fluids* **6(12)**, 3854–3860, Copyright (1994) American Institute of Physics.)

cells small relative to the mean free path. DSMC should be employed, therefore, only in Knudsen number ranges where it is absolutely called for. In the vicinity of the head-disc interface the flow field spans a wide range of Knudsen numbers. To be computationally efficient, use of the DSMC should be limited to the interface gap itself while the larger, outside regions can be modeled by the continuum Navier-Stokes equation. To match the continuum and the rarefaction regions, John and Damodaran (2009) employ the alternating Schwartz method. This method was developed originally to solve the Dirichlet problem for the sum of subdomains (Kantorovich and Krylov, 1964; Szeri and Phillips, 1974).

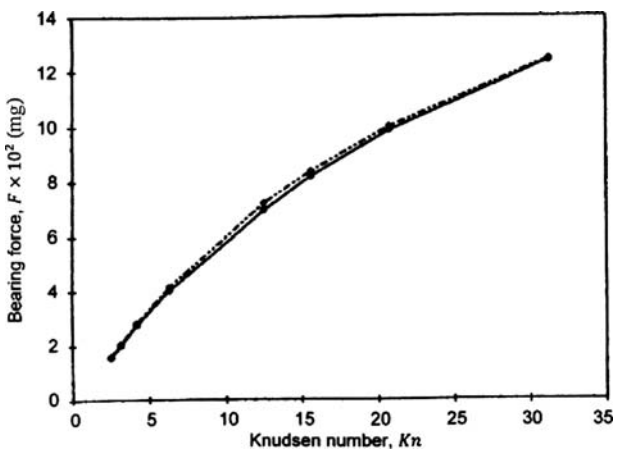

Figure 12.10. Force on slider, comparison of DSMC and MGL (Reprinted with permission from Huang, W., Bogy, D. B. and Alexander, F. J. Three-Dimensional Direct Simulation Monte Carlo Method for Slider Air Bearing. *Phys. Fluids*, **9**(6), 1764–1769, Copyright (1967), American Institute of Physics.)

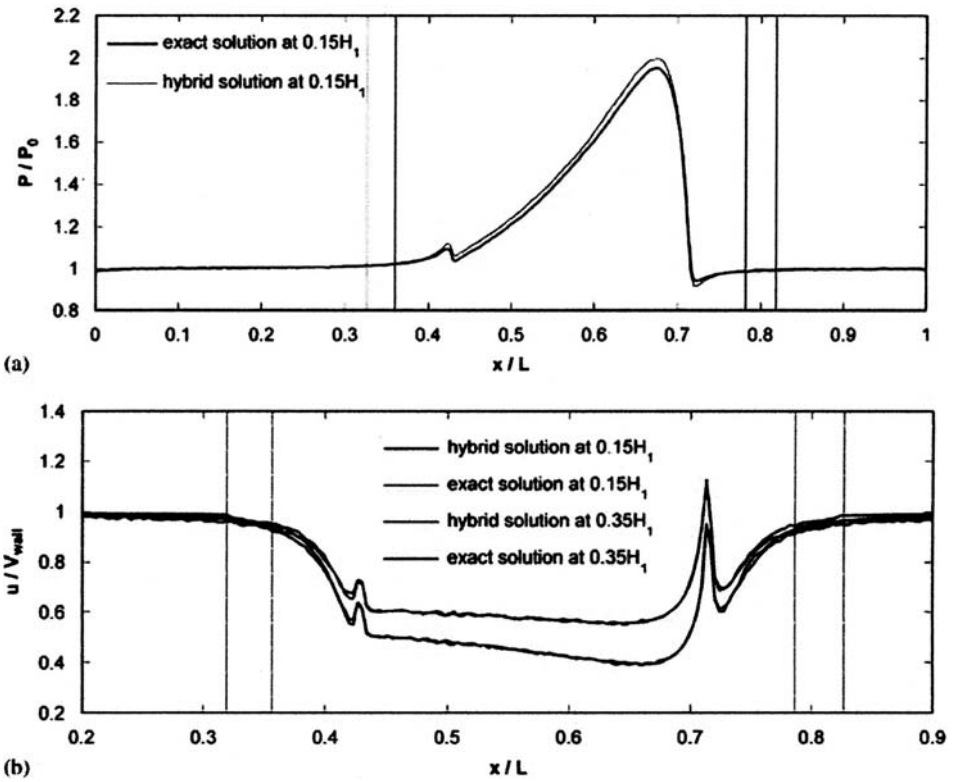

Figure 12.11. Comparison of hybrid and DSMC solution for (a) pressure and (b) *x*-velocity (Reproduced with permission from John, B. and Damodaran, M. Computation of head-disk interface gap micro flowfields using DSMC and continuum-atomistic hybrid methods. *Int. J. Num. Meth. Fluids*, **61**, 1273–1298 2009, John Wiley & Sons Inc.).

Figure 12.11 compares the hybrid solution with the "exact" DSMC solution for pressure and longitudinal velocity.

12.2 Liquid Flow

Due to the similarity in makeup between liquids and gases, viz., both are composed of molecules that are relatively free to rearrange, it is not unreasonable to expect also similarity in their behavior. In particular, we anticipate that close to solid boundaries the behavior of liquids and gases will be comparable: the solid-fluid interface will support no-slip boundary condition under certain conditions, while under others the fluid will slip at the boundary. The degree of slip might then depend on the strength of the liquid-solid coupling.

Molecular Dynamics Simulation

To elucidate some of the persisting questions of fluid mechanics such as the nature of the velocity conditions at solid boundaries, researchers are increasingly turning

to molecular dynamic (MD) simulations. MD simulation writes Newton's law of motion for each molecule (Koplik and Banavar, 1998b)

$$m_a \frac{d^2 \boldsymbol{x}_a}{dt^2} = -\frac{\partial}{\partial \boldsymbol{x}} \sum_{a \neq b} \varphi \left(|\boldsymbol{x}_a - \boldsymbol{x}_b| \right). \tag{12.37}$$

In this expression a, b refer to the constituent atoms or molecules and φ is the interaction potential.

Once the potential $\varphi(r)$ has been selected, Eq. (12.37) can be integrated employing some finite difference method. Many successful MD simulations have been reported in the literature. Sanbonmatsu and Tung (2006) simulated the dynamics of 2.64×10^6 atoms for a total of 22 ns sampling. Furuta et al. (2007) studied the molecular mechanism of the universal joint function of the bacterial flagellar hook by a two-million-atom MD simulation. More recently, Germann and Kadau (2008) ran MD simulations with 10^9 Leonard-Jones atoms arranged on a simple cubic lattice, while Kadau et al. (2008) performed a series of simulations of the Raleigh-Taylor instability that included up to 5.7×10^9 particles and time scale up to 170 ns.

While it is true that the number of molecules current MD simulations can handle represent only a very small volume (10^9 water molecules occupy a cube 0.31 μm at edges), within a few molecular layers the liquid adjusts to continuum representation (Koplik and Banavar, 1998a). In the simulations of Koplik and Banavar (1998b) the continuum representation and MD simulation agreed when the linear size of the system was only $O(10)$ molecules. Therefore, MD simulation is only required over very small, critical regions of the liquid domain.

Koplik and Banavar (1995) found that when the channel width is decreased, a phase transition to a glassy state or an ordered state could enhance the viscosity. Liquids in large gaps, or liquids above a single wall, remain fluidic all the way to within one or two molecular layers of the solid surfaces. However, when the gap is squeezed down to the thickness of a few molecules, the viscosity changes and the confined liquid often becomes solid-like.

Experimental evidence is somewhat contradictory in this respect. Derjaguin (Israelachvili, 1986) found that the viscosity of water in quartz capillaries with a diameter less than 100 nm, attains a value 40–50% higher than in bulk. However, this conclusion did not seem to hold for nonpolar liquids. Chan and Horn (1985) studied the drainage of liquids between two atomically smooth mica surfaces. Their results are in excellent agreement with the Reynolds theory of lubrication for film thickness $h > 50$ nm. But for thinner films they found drainage to be somewhat slower than predicted by continuum theory, as if two molecular layers on each surface underwent no shear. Thus, in thinner films there is an apparent enhancement of viscosity, which can be accounted for by allowing the plane of shear to be displaced into the liquid. Israelachvili (1986) reported that in films as thin as 5 nm the "plane of slip" is within a few Angstrom units of the interface and the viscosity is within 10% of its bulk value. Viscosity increase in thin channels was reported by Migun and Prokhorenko (1987), while Debye and Cleland (1959) and Pfahler et al. (1991) found the apparent viscosity μ_a to be consistently smaller than the bulk viscosity μ.

Velocity Slip at Solid Boundary

The no-slip boundary condition occupies a central position in our understanding of fluid mechanics; nevertheless, it is an assumption whose microscopic validity has long

been debated (Goldstein, 1938). Daniel Bernoulli was the first to propose that for a fluid flowing along a solid surface the velocity at the solid surface must be the same as that of the surface itself. Navier, in contrast, reasoned that the liquid may slip on the solid surface, this slipping being opposed by a frictional force proportional to the velocity of the fluid relative to the solid

$$u_{\text{slip}} = L_s \left.\frac{\partial u}{\partial y}\right|_Q ; \qquad Q \to \text{wall}. \tag{12.1}$$

Stokes, commissioned by the Royal Academy of Science to investigate the true nature of boundary conditions, wrote that "*the condition which first occurred to me to assume for this case was that the film of fluid immediately in contact with the solid did not move relative to the surface of the solid*" (Stokes, 1845). He calculated the discharge of long straight circular pipes but was unable to obtain agreement with Dubuat's experiments. The reason for this cannot be attributed to the defectiveness of the boundary conditions Stokes used, however, but to the fact that the motion of the fluid was outside its laminar range. "*In fact, it appears from experiment that the tangential force varies nearly as the square of the velocity with which the fluid flows past the surface of a solid, at least when the velocity is not very small*" (Stokes, 1845). After a period of indecision between Bernoulli's and Navier's hypothesis, however, Stokes settled down on the side of the no-slip condition. By the 1900s it was generally accepted that velocity slip, if it did exist, was probably too small to be observed (Neto et al., 2005).

We may expect the no-slip condition to break down whenever the characteristic geometrical length traversed by the fluid molecules is comparable to their mean free path (Langlois, 1964). The situations where this might occur are in the flow of rarefied gases, when fluids (liquids or gases) are strongly confined in one dimension, and at moving three-phase contact lines (spreading of liquids).

Din and Michaelides (1997) were among the first to use molecular dynamics simulations in their investigations of Couette flow of a Lennard-Jones (L-J) liquid (cf., Figure 12.12) in a micropore with weak and strong wall-fluid interaction, employing the potential for liquid argon ($\sigma = 0.3405$ nm, $m = 6.634 \times 10^{-23} g$, $\epsilon = 1.657 \times 10^{-14}$ erg/K). The walls in their numerical experiment were also composed of individual atoms, and interaction between wall and liquid was regulated by an L-J type potential with parameters σ^{wf} and ϵ^{wf}. They observed that under weak interaction ($\epsilon^{wf} = \epsilon$) slip occurred near the wall and the fluid in the contact layer exhibited higher viscosity than in the central region. For strong solid-fluid interaction ($\epsilon^{wf} = 3.5\epsilon$), obtained by matching the depth of the potential well to that of argon on a smooth carbon wall, the wall supported the no-slip condition. There was also an immobile (crystalline) layer next to the wall exhibiting high viscosity. They further concluded that the "*Navier-Stokes equations are still valid at a distance of two to three molecular layers from the wall, provided that the bulk viscosity and the appropriate boundary conditions are used*" (cf., Din and Michaelides, 1997).

Thompson and Troian also applied MD simulation to simple shear flow of Newtonian liquids, with the objective of determining the applicability of Navier's boundary condition. They used the shifted Lennard-Jones 6–12 potential, Figure 12.20, for both liquid and wall and found that conditions at the interface are controlled "*by the extent to which the liquid feels corrugations in the surface energy of the solid*" (Thompson and Troian, 1997). Such corrugations are maximized when $\rho^w = \rho$ and the wall-fluid coupling ϵ^{wf} is large. Then there is efficient momentum transfer and the conditions are consistent with no-slip. Incommensurate densities and feeble wall-fluid interaction result in weaker corrugation

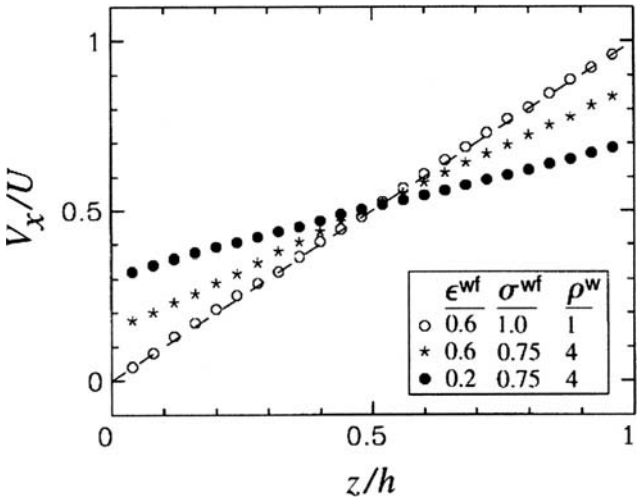

Figure 12.12. Shear flow in liquids. (Reprinted by permission from Macmillan Publishers Ltd: *NATURE*, Thompson, P. A. and Troian, S. M. A general boundary condition for liquid flow at solid surfaces. **389**, 360–362, Copyright (1997).)

and the development of interfacial slip. The velocity profile in Couette flow is shown in Figure 12.12; here values of σ^{wf}, ϵ^{wf}, and ρ^{w} are listed in units of ϵ, σ, and ρ of the fluid.

The profiles exhibit flow behavior consistent with continuum hydrodynamics, but with boundary conditions involving different degrees of slip. The same conclusions were reached recently by Niavarani and Priezjev (2008) in their MD simulation, except that for $U \geq 6.0\,\sigma/\tau$ a slight curvature was noted within a region of about 4σ near the walls.

The variation of L_s is shown in Figure 12.13a; when $\dot{\gamma}$ is small, Navier's formula with $L_s = L_s^0 =$ const. applies. As the shear rate $\dot{\gamma}$ increases, the slip length L_s changes rapidly and at some critical $\dot{\gamma} = \dot{\gamma}_c$ becomes unbounded. Note from Figure 12.13b that the bulk viscosity is constant over the whole range, indicating that the fluid remains Newtonian.

When L_s is normalized with L_s^0 and $\dot{\gamma}$ with $\dot{\gamma}_c$, the various $L_s = L_s(\dot{\gamma})$ curves of Figure 12.13a collapse onto a single curve in a log-normal plot; this is illustrated in Figure 12.14, where the dashed curve represents

$$L_s = L_s^0 (1 - \dot{\gamma}/\dot{\gamma}_c)\,. \tag{12.38}$$

Equation (12.38) is the universal boundary condition of Thompson and Troian (1997) at solid-liquid interface. It shows that at small rate of shear the slip length is a constant but becomes dependent on the shear rate for high values of $\dot{\gamma}$. Thompson and Troian state that "*the well-known Navier slip boundary condition is but the low shear rate limit of a more generalized universal relationship which is significantly nonlinear and divergent at a critical shear rate* $\dot{\gamma}_c$." They further assert that the new phenomenological boundary condition, Eq. (12.38), can be used to model viscous flows along solid surfaces. Niavarani and Priezjev (2008), again using MD simulation, find that even at low rate of shear the slip length is dependent slightly on $\dot{\gamma}$; for small Reynolds numbers it is, however, unaffected by the inertia terms in the Navier-Stokes equation.

Gad-el-Hak (1999) provides physical perspective into Eq. (12.38). For water the energy scale in the Lennard-Jones potential is $\epsilon = 3.62 \times 10^{-21}$ J and $\sigma = 2.89 \times 10^{-10}$ m.

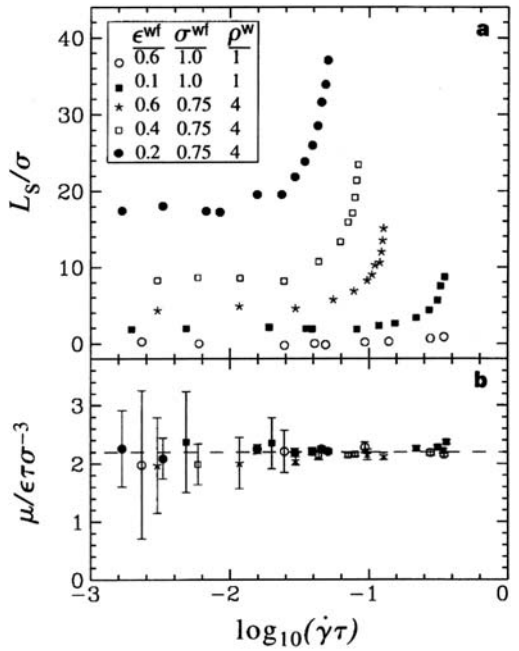

Figure 12.13. Variation of slip length and viscosity with rate of shear (Reprinted by permission from Macmillan Publishers Ltd: *NATURE*, Thompson, P. A. and Troian, S. M. A general boundary condition for liquid flow at solid surfaces. **389**, 360–362, Copyright (1997).)

The molecular time scale is $\tau = (m\sigma^2/\epsilon)^{1/2} = 8.31 \times 10^{-13}$ s, with molecular mass $m = 2.99 \times 10^{-26}$ kg. For the third case depicted in Figure 12.13, $\dot{\gamma}_c\tau = 0.1$, giving $\dot{\gamma}_c = 1.2 \times 10^{11}\,\mathrm{s}^{-1}$. Such extremely high shear rate may be created in small devices but only at high speeds, though measurable slip, $L_s \approx 17\sigma$, might be realized more easily. For

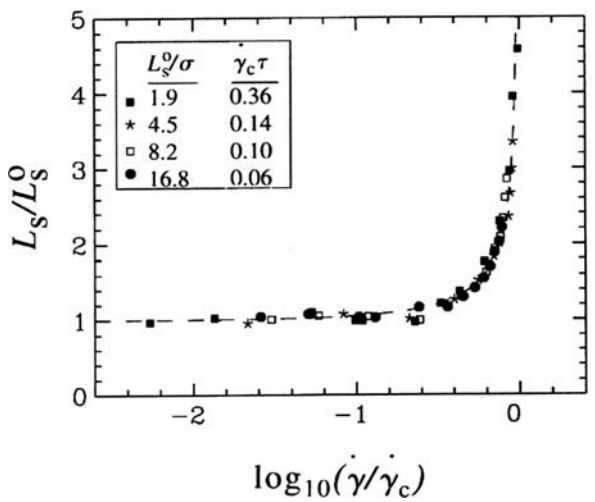

Figure 12.14. Universal velocity-slip for liquids (Reprinted by permission from Macmillan Publishers Ltd: *NATURE*, Thompson, P. A. and Troian, S. M. A general boundary condition for liquid flow at solid surfaces. **389**, 360–362, Copyright (1997).)

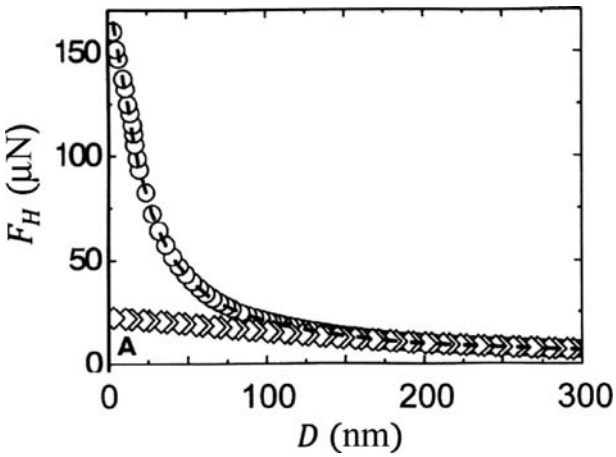

Figure 12.15. Hydrodynamic force between crossed cylinders (○, wetting surface; ◇, partially wetting with contact angle ≈ 44°; - -, Eq. 12.40 with $f^* = 1$). (Reprinted with permission from Zhu, Y. and Granick, S. Rate-dependent slip of Newtonian liquid at smooth surfaces. *Phys. Rev. Letts*. **87**(9), 096105, Copyright (2001) by the American Physical Society.)

high molecular weight polymers, $\dot{\gamma}_c$ could be many orders of magnitude smaller. When close to the critical shear rate $\dot{\gamma}_c$, the flow even at macroscopic distances can be affected by the boundary condition at the wall (Thompson and Troian, 1997).

Vinogradova (1995) investigated drainage of thin liquid films confined between two undeformed spheres of radius R_1 and R_2, respectively. In this theoretical study, hydrophobicity of the surfaces is characterized by an apparent slippage of the liquid while for a hydrophilic surface the no-slip velocity boundary condition is specified. The lubrication approximation to the Navier-Stokes equation (i.e., the Reynolds equation) leads to the hydrodynamic force

$$F_h = -\frac{6\pi\tilde{r}^2\mu v}{D} f^*. \tag{12.39}$$

Here $\tilde{r} = R_1R_2/(R_1 + R_2)$ is the equivalent radius and v is the velocity of approach. For both surfaces hydrophilic, $f^* = 1$ and we recover Taylor's formula. If, however, the surfaces are hydrophobic, velocity slip with slip-length L_s is postulated, leading to the correction factor (Vinogradova, 1995)

$$f^* = \frac{h}{3L_s}\left[\left(1 + \frac{h}{6L_s}\right)\ln\left(1 + \frac{6L_s}{h}\right) - 1\right]. \tag{12.40}$$

However, there is no dependence on either distance or rate of shear in Vinogradova's correction, in contradiction with the findings of Thompson and Troian, Zhu and Granick and others.

The correction factor in Eq. (12.40) was evaluated by Zhu and Granick (2001) in experiments on a sphere vibrating in liquid, in close proximity to a plane surface. Figure 12.15 plots the measured hydrodynamic force on the sphere as function of the mean separation distance for tetradecane between mica (wetting) and OTE (partially wetting). In the wetting case, the plot conforms to Eq. (12.40) with $f^* = 1$.

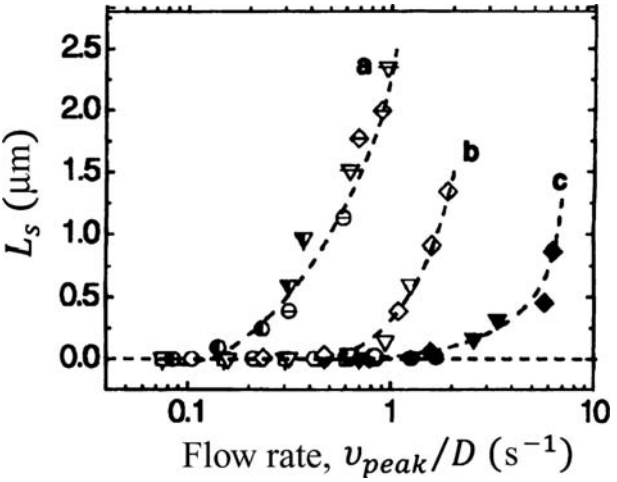

Figure 12.16. Variation of slip length with shear rate (a, contact angle ≈ 110°; b, contact angle ≈ 44°; c, contact angle ≈ 12°). (Reprinted with permission from Zhu, Y. and Granick, S. Rate-dependent slip of Newtonian liquid at smooth surfaces. *Phys. Rev. Letts*. **87**(9), 096105, Copyright (2001) by the American Physical Society.)

For the nonwetting and partially wetting cases the hydrodynamic force measured by Zhu and Granick agree with prediction of the Reynolds equation only at large separation; for small separation the measured force was systematically smaller than predicted by theory. Assuming that there was velocity slip at the solid-liquid interface, they estimated the magnitude of the slip from the difference between theoretical and measured hydrodynamic forces. The variation of this slip length under various experimental conditions is depicted in Figure 12.16. Here the maximum velocity is defined as $v_{\text{peak}} = d\omega$ where d is the amplitude of the oscillation, ω is its frequency, thus v_{peak}/D is a measure of strain rate.

Several factors might influence both the existence of velocity slip and its magnitude. We have already indicated dependence of L_s on shear rate; other factors to consider are surface wettability, surface roughness, and the presence of a spontaneously generating gaseous layer (nano bubbles) at interface.

A small contact angle indicates a strong interaction between liquid and surface, and originally it was believed that liquids are more likely to slip on poorly wetted surfaces (Chuarev et al., 1984). This was illustrated by Zhu and Granick (2001), for example, who were successful in changing the hydrodynamic boundary condition of oil flow from no-slip to "partial slip" by adding a surfactant to mica-alkane systems (Figure 12.16). The critical shear stress for slip to occur was shown to decrease with increasing surface coverage by the physisorbed surfactant. In contrast, other researchers have shown very clearly the occurrence of velocity slip at the solid-liquid interface with surfaces that were partially or totally wetted (Bonaccurso et al., 2002). Although in their earlier paper Zhu and Granick concluded that for tetradecane (a linear alkane) $f^* = 1$, in 2004 they wrote "*slip occurs even for wetting fluids, provided that the surfaces are sufficiently smooth*" (Zhu and Granick, 2004). They attribute differences between the data obtained in 2001 and those obtained in 2002, to unsatisfactory surface preparation (melt cutting using Pt wire) that was employed in the first experiments (cf., Perkin et al., 2006; Israelachvili et al., 2006; Granick et al.,

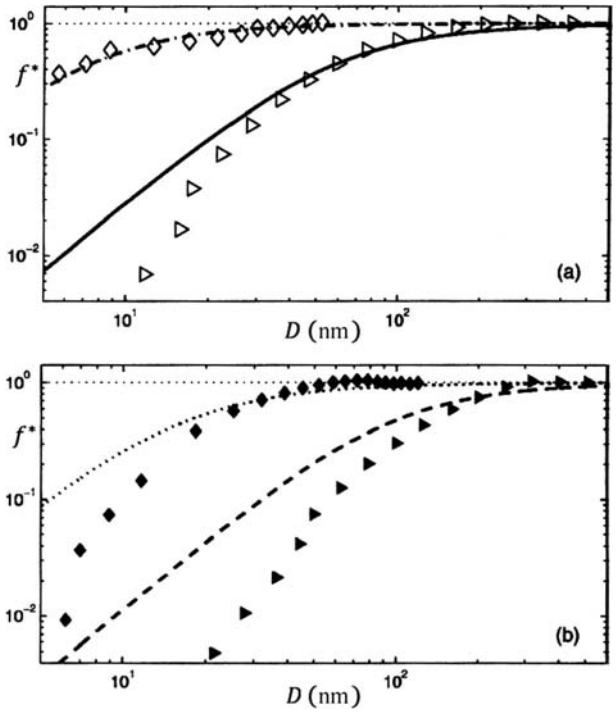

Figure 12.17. Comparison between the 'soggy mattress' theory and experiment (Zhu and Granick 2001): (a) small amplitude, (b) large amplitude (data: ◇, ◆, $\omega = 1Hz$; △, ▲, $\omega = 10$ Hz). (Reprinted with permission from Lauga, E. and Brenner, M. P. Dynamic mechanism for apparent slip on hydrophobic surfaces. *Phys. Rev. E*, **70**, 026311, Copyright (2004) by the American Physical Society.)

2006). In face of this controversy, Neto et al. (2005) argue that the level of hydrophobicity cannot be a primary factor in determining slip.

The effect of surface roughness on the liquid-solid boundary condition also remains largely unanswered. A rough crystal surface represses slip of Newtonian wetting liquids according to McHale and Newton (2004) while Du et al. (2004) attests to velocity slip under similar conditions.

Some researchers ascribe the existence of velocity slip to an observed layer of gas at the solid-liquid interface in the form of nanobubbles. These bubbles have a radius of $R \sim 50$–100 nm but are highly flattened (large contact angle) and thus are truly nanoscopic in height, $h \sim 10$ nm (Maali and Bhushan, 2008). They are thought to appear spontaneously at the interface between a hydrophobic surface and a polar solvent like water (Ishida et al., 2000).

Lauga and Brenner (2004) applied Eq. (12.39) to their investigation of the dynamics of nanobubbles attached to hydrophobic surfaces. Their "leaking mattress" model has three free parameters available for fitting to experimental data: the fractional surface coverage of the bubbles, the bubble size, and the contact angle. They simulated the experiments of Zhu and Granick (2001) and found fair agreement for a hydrophobic solid oscillating in liquid, in close proximity to a plane (Figure 12.17). The mechanism that results in $f^* \leq 1$ in these calculations is, however, not consequent of microslip at bubble surfaces but, rather, is of dynamic origin. As the solid phase oscillates, the periodic change in bubbles sizes reduces

the amount of liquid necessary to be squeezed out of the gap, creating an apparent velocity slip (Lauga and Brenner, 2004).

As formation of nanobubbles depends on experimental conditions (gas content of the liquid, surface treatment, experimental protocol) and the bubbles can be removed from the interface by partial degassing, Neto et al. (2005) conclude that nanobubbles cannot explain velocity slip of all simple liquids.

Density Oscillation Near Solid Boundary

The question whether the presence of a solid boundary induces the neighboring liquid molecules to organize structurally has been raised repeatedly. In their review article Koplik and Banavar (1995) conclude that "the principal non-obvious result" of early work in this area was that the liquid in the vicinity of a solid boundary is prominently layered due to geometric constraining effect of the wall and from having attractive pairwise interactions between liquid and solid atoms, and between liquid atoms themselves. In consequence, pronounced density oscillation is observed near the wall, this oscillation decaying within a few molecular diameters from the wall. Abraham (1978), one of the early investigators of this topic, employed Monte Carlo simulation methods to investigate the density profile in liquids at a liquid-solid interface; Figure 12.18 depicts some of the data he obtained for two different fluid-wall systems.

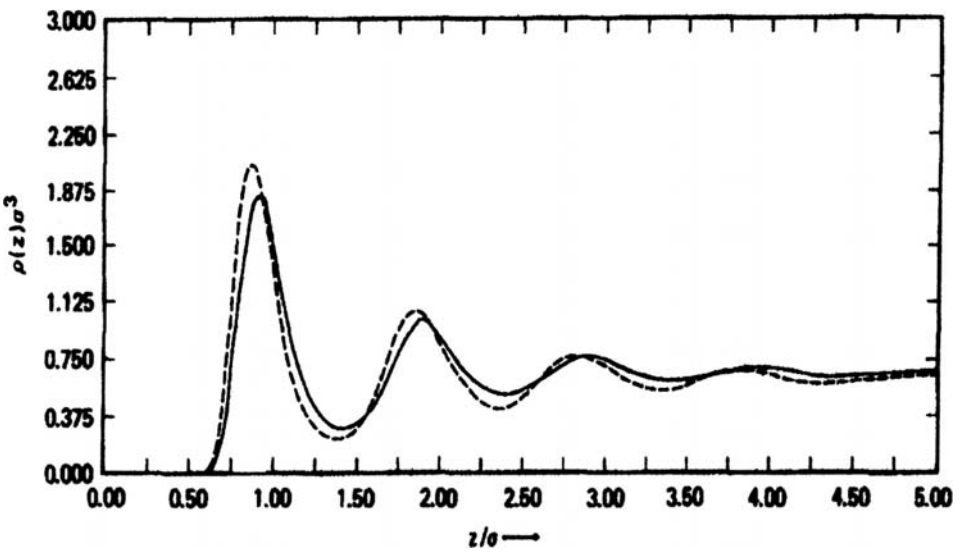

Figure 12.18. Comparison of the interface liquid density profiles for two different wall-liquid interactions. (Reprinted with permission from Abraham, F. F. The interfacial density profile of a Lennard-Jones fluid in contact with a (100) Lennard-Jones wall and its relationship to idealized fluid/wall systems: A Monte Carlo simulation. *J. Chem. Phys*. **68**(8), 3713–3716, Copyright (1978) American Institute of Physics.)

The constraining effect of two solid surfaces is even more dramatic. Niavarani and Priezjev (2008) employed MD simulation to examine flow between two solid surfaces, one corrugated the other flat. Density variation with position is plotted in Figure 12.19.

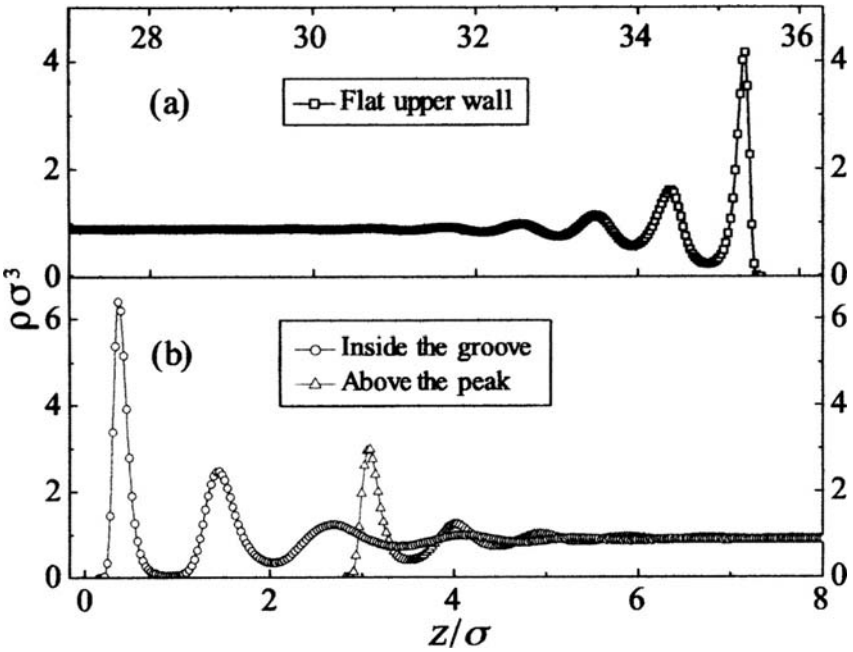

Figure 12.19. Averaged fluid density profiles near (a) flat upper wall and (b) corrugated lower wall with wavelength $\lambda = 7.5\sigma$ and amplitude $\alpha = 1.4\sigma$. (Reprinted with permission Niavarani, A. and Priezjev, N. V. Rheological study of polymer flow past rough surfaces with slip boundary conditions. *J. Chem. Phys*., **129**, 144902, Copyright (2008) American Institute of Physics.)

Experiments on water contrast sharply with those on nonassociating liquids. The latter exhibits solidification when the thickness of the confined layer is decreased to about five to eight monolayers, as manifested by the several orders of magnitude increase in viscosity. The situation is quite different with water. While density increase due to van der Waals attraction between liquid molecules and the wall promotes solidification in hydrocarbons, it suppresses the tendency for water to solidify as liquid water is denser than ice (Raviv et al., 2004).

Interactive Force Between Closely Spaced Solid Surfaces

When two solid surfaces are immersed in a liquid at a great distance apart and both surfaces and liquid are at rest, no force can be detected between them. If, however, separation is decreased, various forces manifest themselves. In actuality, the different kinds of forces all have the same origin. According to the Hellman-Feynman theorem, all intersurface forces are electric in origin; once the distribution of the electron clouds has been obtained from the Schrödinger equation, the various forces can be calculated from conventional electrostatic theory. However, this equation is not amenable to easy solution and it has become accepted to instead classify the different manifestations of force into different categories (Israelachvili, 2000).

Forces between solid surfaces submerged in liquids are classified as either long range or short range. Long-range forces are the *van der Waals forces* and the electrostatic forces, the former usually attractive while *electrostatic forces* are repulsive. The DLVO (Derjaguin-Landau-Verwey-Overbeek) theory considers the effect of only van der Waals and double-layer forces. The theory has been well tested and is in excellent agreement with experiments. Short-range forces are active in the 1–3 nm range and include solvation forces and hydration forces. Solvation forces are oscillatory, are measured in nonpolar liquids, normally linear hydrocarbons, while hydration forces are repulsive, and are present in electrolytes.

Van der Waals Forces

Van der Waals attraction between two atoms is characterized as

$$w(r) = -\frac{C}{r^6}. \tag{12.41}$$

Here r is the distance coordinate, C is the interaction constant, and w the interaction potential.

By summing all two-atom interactions, it is possible to calculate the van der Waals potential between bodies. We will employ here the Hamaker constant (Hamaker, 1937)

$$A = \pi^2 C \rho_1 \rho_2 \tag{12.42}$$

and obtain the interaction potential between two planar surfaces D apart and of densities ρ_1, ρ_2, respectively

$$W = -\frac{A}{12\pi D^2}. \tag{12.43}$$

To gain an appreciation of the magnitudes involved here, we borrow from Israelachvili (2000) and estimate the adhesive pressure. Typical value of the Hamaker constant is $A = 10^{-19}$ J for interaction across vacuum. If the surfaces are in contact, $D \approx 0.2$ nm, the adhesive pressure is

$$P = -\frac{dW}{dD} = \frac{A}{6\pi D^3} \approx 7 \times 10^8 \text{ Pa} \approx 7000 \text{ atm}. \tag{12.44}$$

The van der Waals force between two identical bodies is always attractive while between different bodies can be attractive or repulsive. These forces are always present; they are active in the 1–15 nm range, and are largely independent of the type and concentration of the electrolyte (Israelachvili and Adams, 1978).

In the Lennard-Jones force potential, intended to describe molecular interaction in nonpolar solvents, the attractive contribution models van der Waals attraction while the repulsive part is included to prevent overlap. The potential is characterized by a length scale σ – diameter of the molecule – for which $\varphi(\sigma) = 0$, and an energy scale $\epsilon = [\varphi(r)]_{\min}$. Plotted against distance in Figure 12.20, the Lennard-Jones 6–12 potential has the form

$$\varphi(r) = 4\epsilon \left[\left(\frac{\sigma}{r}\right)^{12} - \left(\frac{\sigma}{r}\right)^{6} \right]. \tag{12.45}$$

The intermolecular force is given by the derivative of the potential $F = \partial\varphi(r)/\partial r$ and is dependent on the separation r between the interacting molecules. When $r > 2^{1/6}\sigma$, the force

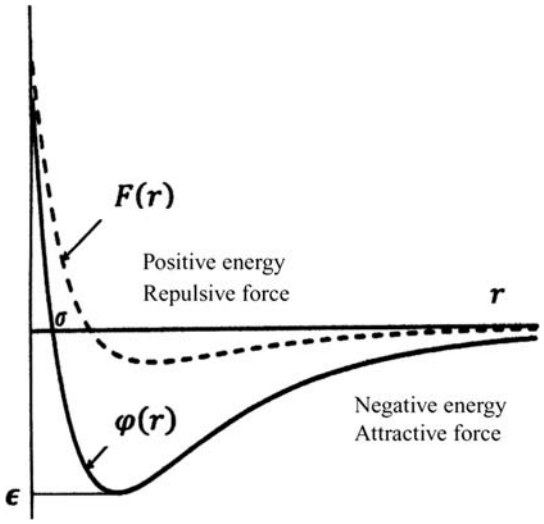

Figure 12.20. Lennard-Jones force potential.

is that of attraction and it is repulsive for smaller values of *r*. In order to keep the number of mutually interactive molecules small, in molecular dynamic simulation the potential is cut off at some distance r_c, often $r_c = 2.2\sigma$, and shifted so that the force goes to zero smoothly at cut off.

Double-Layer Forces

Electrostatic forces between surfaces submerged in liquids (water or any liquid of high electric constant) are a consequence of (1) surface charging by ionization or dissociation of surface groups or (2) by binding of ions from solution onto a previously uncharged surface. Irrespective of the mechanism involved, however, surface charging will result in an oppositely charged region of counter ions. The potential of this electric double layer is governed by the Poison-Boltzmann equation.

Experiments with conductivity water and aqueous salt solutions measure long-range double layer forces and indicate a jump into adhesive flat contact in a single monotonic step at the position at $D = 3.5 \pm 1.0$ nm, due to short-range, attractive van der Waals forces between the surfaces (Figure 12.21).

Figure 12.22 displays force measurement in two electrolytes, 10^{-4} mol/dm^3 KNO_3 and 10^{-4} mol/dm^3 $Ca(NO_3)_2$. When the concentration was further increased no jump-in, and on separation from forced contact no adhesive jump, was observed; instead the forces become increasingly repulsive (Israelachvili and Adams, 1978).

Solvation Forces

As the submerged surfaces are brought closer to one another, the regions of density oscillation overlap and interact. If the molecules of the liquid are symmetric and the confining surfaces are atomically smooth, the molecules will organize into layers of

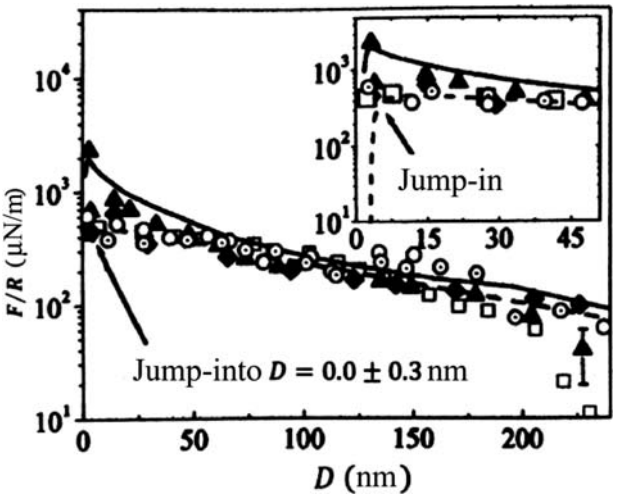

Figure 12.21. Force-separation profiles between mica surfaces in conductivity water (data points: Raviv et al., 2004; solid curve: Pashley, 1981; - - -, DLVO fit). (Reprinted with permission from Raviv, U., Perkin, S., Laurat, P. and Klein, J. Fluidity of water confined down to subnanometer films. *Langmuir*, **20**, 5322–5332, Copyright (2004) American Chemical Society.)

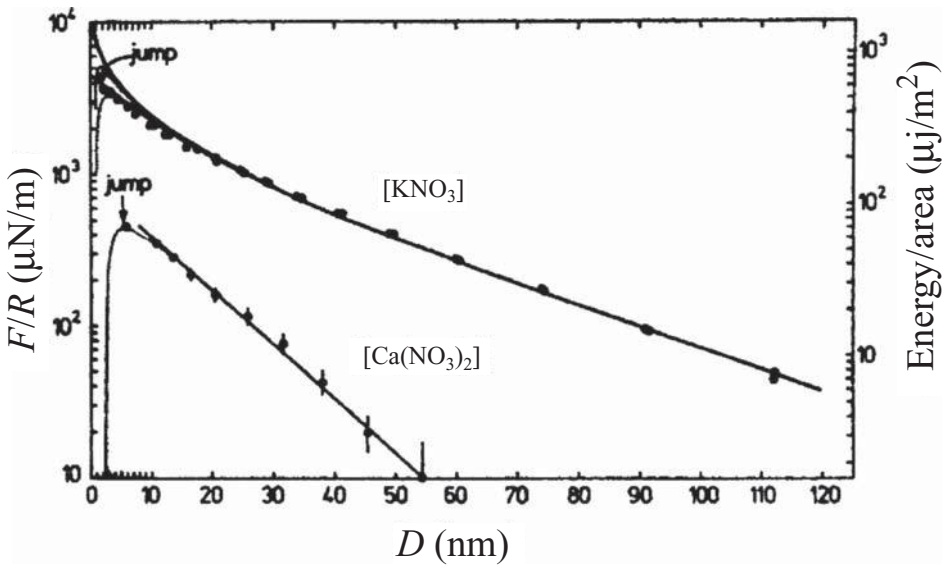

Figure 12.22. Measured forces in two electrolytes. The dotted line shows theoretical DLVO forces, including the attractive van der Waals forces (Israelachvili, J. and Adams, G. E. 1978. Measurement of force between two mica surfaces in aqueous electrolyte solution in the range of 1–100 nm. *J. Chem. Soc. Faraday Trans. 1*. **74**, 1400–1411. Reproduced by permission of the Royal Society of Chemistry.)

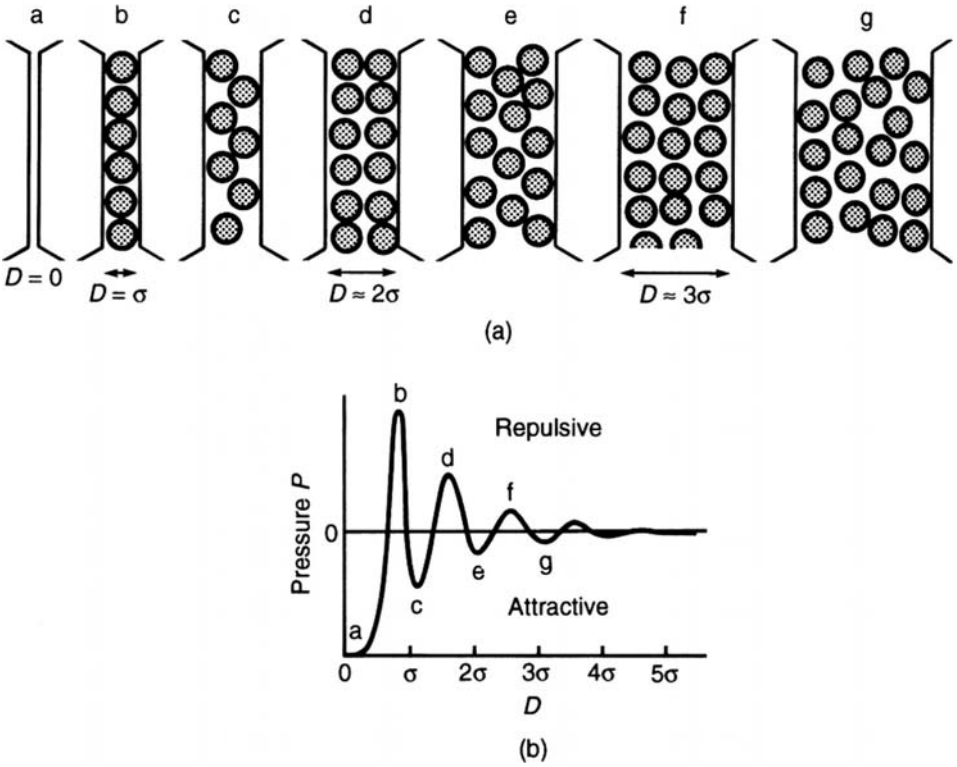

Figure 12.23. Schematic of the change in molecular ordering due to confinement (This figure was published in *Intermolecular and Surface Forces*, Israelachvili J. N., Copyright Academic Press (1992).)

decreasing thickness as confinement proceeds. Van der Waals and electrostatic double-layer continuum theories cannot predict the normal surface forces that arise as consequence of this structural change; such deviations from the predictions of continuum theories are referred to as structural or solvation effects.

Solvation pressure arises when there is a change in liquid density, i.e., molecular ordering, as the surfaces approach one another. When both surfaces are inert, are submerged in a liquid of density $\rho(\infty)$, and are a distance D apart, the solvation pressure on them varies as (Israelachvili, 2000)

$$P(D) = kT[\rho_s(D) - \rho_s(\infty)]. \tag{12.46}$$

The variation in $\rho(D)$ may be inferred from Figure 12.23. This figure is a schematic of (a) the changing molecular ordering as confinement is gradually increased, sequence $g \rightarrow a$, and (b) the oscillating solvation pressure that is a consequence of this change (Israelachvili, 2000). The period of oscillation is roughly the same as the diameter of the liquid molecules.

Some of the earliest experiments to measure solvation forces were carried out by Horn and Israelachvili (1981): their *surface forces apparatus* is shown schematically in Figure 12.24. In this apparatus two thin sheets of molecularly smooth mica are glued to cylindrical lenses, made of fused silica and mounted at right angles. The radius of curvature R of the lenses is much greater than the separation between them ($R/D \geq 10^4$). The

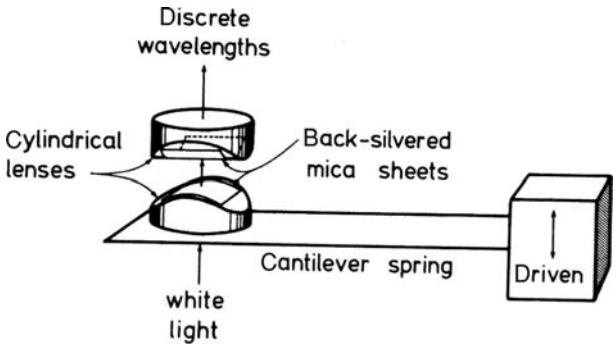

Figure 12.24. Schematic diagram of the surface force apparatus (Reprinted with permission from Chan, D. Y. C. and Horn, R. G. The drainage of thin liquid films between solid surfaces. *J. Chem. Phys*., **83**, 5311–5324, Copyright (1985), American Institute of Physics.)

clamped end of the cantilever spring can be moved up or down at constant speed. Optical interference techniques are used to measure the minimum separation between the mica sheets (Israelachvili and Adams, 1978).

To appreciate fully the solvation force experiments and their interpretation, essential part of which is the occurrence of instabilities, we describe the experimental techniques in some detail, following Horn and Israelachvili (1981). The phenomenon of oscillating solvation forces is analogous to what occurs when a magnet (Figure 12.25) is suspended on a spring above another magnet. As the upper magnet is slowly lowered, the spring will extend to balance magnetic attraction with spring force. However, on reaching point P where $|\partial F/\partial r|$ just exceeds the spring constant K, the suspended magnet will jump into contact. Attempting to separate the magnets, the spring will extend to produce the force

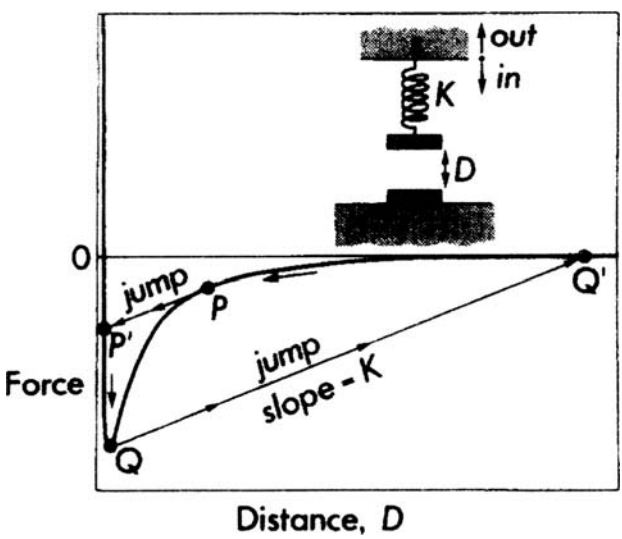

Figure 12.25. Schematic of force law between two magnets (Reprinted with permission from Horn, R. G. and Israelachvili. Direct measurement of structural forces between two surfaces in a nonpolar liquid. *J. Chem. Phys*. **75**(3), 1400–1411, 1983, American Institute of Physics.)

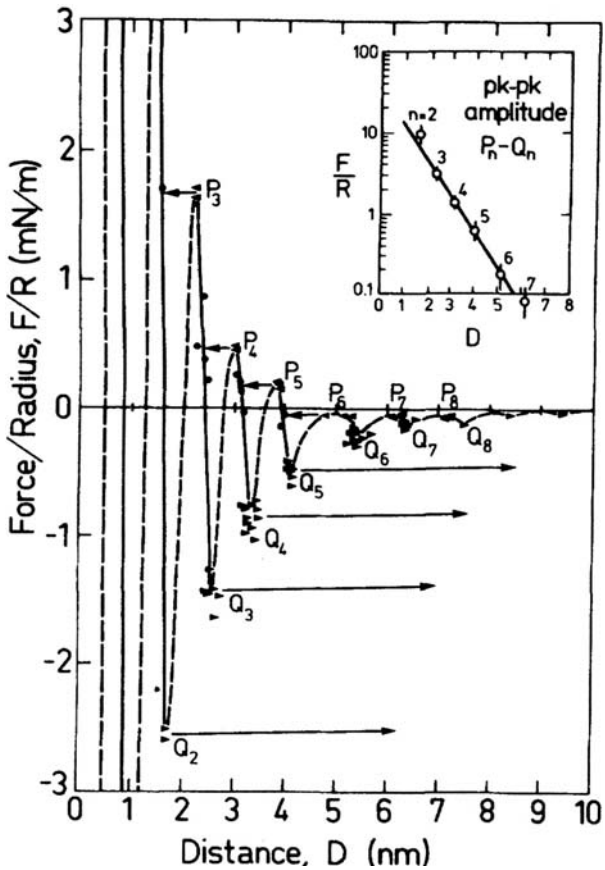

Figure 12.26. Experimental data of force F as a function of separation D in OMCST (Reprinted with permission from Horn, R. G. and Israelachvili. Direct measurement of structural forces between two surfaces in a nonpolar liquid. *J. Chem. Phys*. **75**(3), 1400–1411, Copyright (1981), American Institute of Physics.)

necessary to break contact, but at that tension, represented by point Q, the magnet will jump apart. Note that section $Q - P$ of the force-distance curve is not accessible by experiment; rather the observable path follows the sequence $Q' \rightarrow P \rightarrow$ *inward jump* $\rightarrow P' \rightarrow Q \rightarrow$ *outward jump* $\rightarrow Q'$.

Across liquids composed of spherical molecules such as OMCTS, benzene and cyclohexane, the oscillation of the force – separation curve displays periodicity equal to the diameter of the molecules; the number of molecular layers, n, can then be counted by dividing the spacing at force maxima by the molecular diameter. For straight-chain molecules such as the n-alkanes, periodicity is given by the width of the molecular chains, as now the chains align parallel to the solid surfaces (Gee and Israelachvili, 1990).

Figure 12.26 displays experimental measurements for solvation force between atomically smooth mica in OMCTS (octamethylcyclotetrasiloxane $[(CH_3)_2SIO]_4$), which possesses spherical molecules. The arrows, inward at $P_8, P_7, P_6, \ldots$ and outward at $Q_2, Q_3, Q_4, \ldots$, indicate inward and outward jumps, respectively, from unstable to stable

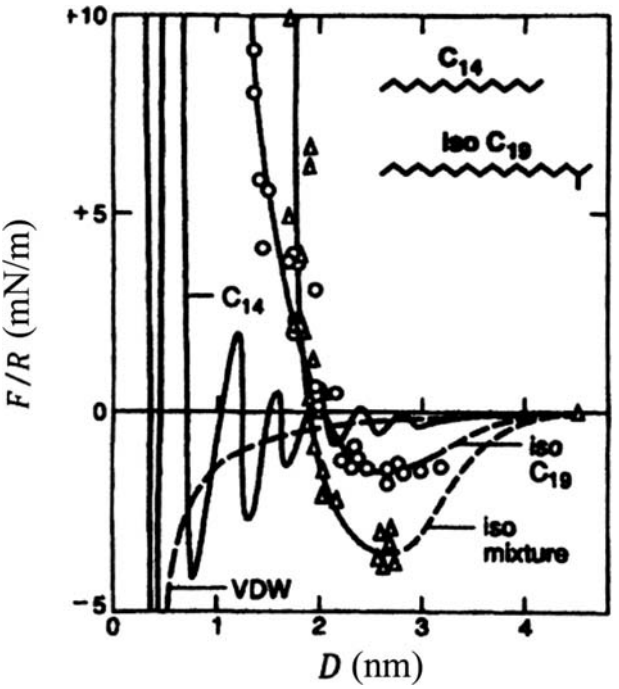

Figure 12.27. Measurement of forces across various hydrocarbon liquids; VDW signifies theoretical Lifshitz van der Waal force (Gee, M. L. and Israelachvili, J. N. 1990. Interaction of surfactant monolayers across hydrocarbon liquids. *J. Chem. Soc. Faraday Trans*. **86**(24), 4049–4058. Reproduced by permission of the Royal Society of Chemistry.)

position. The continuous curves show stable regions of the $F(D)$ curve; dashed curves are unstable and, therefore, inaccessible to experiment. The inset displays variation of the peak-to-peak amplitudes with separation.

Chan and Horn (1985) modeled the oscillating solvation force in a form that is suitable for numerical computation of solvation effects (cf., Jang and Tichy, 1995)

$$F = Be^{-D/\xi_1} \cos(2\pi D/\xi_2). \tag{12.47}$$

The parameters B, ξ_1, ξ_2 of the curve-fit in Eq. (12.47) are obtained from comparison with force versus separation data.

There seems to be significant difference in force profiles between liquids of symmetric molecules and those composed of asymmetric molecules. Asymmetric molecules are not capable of fitting into structured layers as their symmetric counterparts can. Hence, forces measured across liquids of asymmetric molecules are monotonic, rather than oscillatory. Figure 12.27 displays experimental force data obtained across two organic liquids, the *n*-tetradecane (C_{14}), composed of symmetric molecules, and the isoparaffin (*iso* C_{19}) consisting of asymmetric molecules. The figure also contains data obtained across a polydispersed mixture of isoparaffins by Gee and Israelachvili (1990).

From Figure 12.27 it may be asserted that molecular ordering of the *iso* C_{19} and the *iso mixture* is thwarted, assuredly by the branching of the molecular chain (increasing disorder). The same effect, distraction of periodicity, can be observed also when increasing

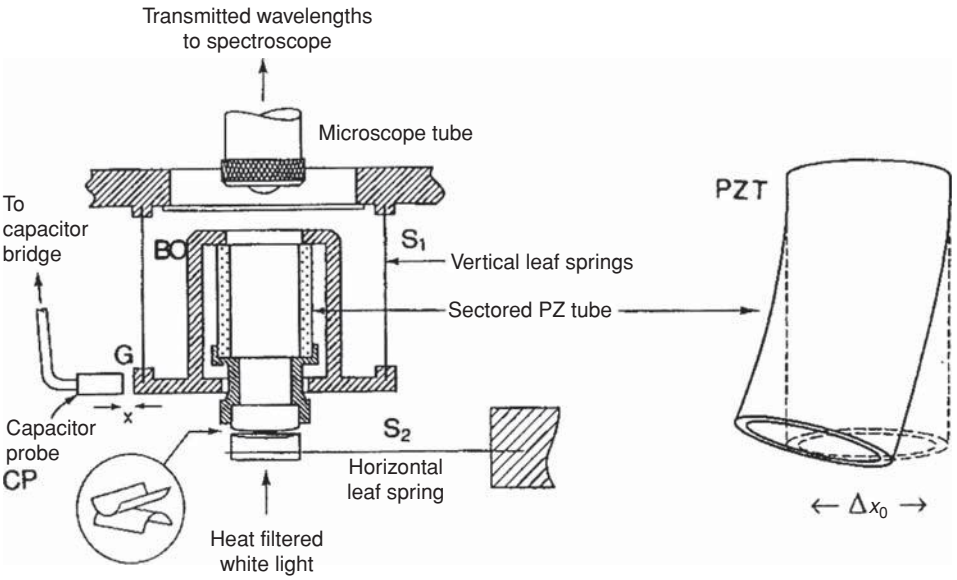

Figure 12.28. Schematic of the shear force balance (Reprinted with permission from Klein, J. Molecular mechanism of synovial fluid lubrication. *Proc IMechE Journal of Engineering Tribology*, **223**, 617–628, 2009, Professional Engineering Publishing.)

surface disorder by roughening or when impurities are introduced into the liquid (Gee and Israelachvili, 1990; Klein and Kumacheva, 1998).

In contrast to the foregoing, Zhu and Granick (2004) recently asserted that branched hydrocarbon liquids could also display oscillatory solvation forces. That earlier experimenters failed to observe such oscillations was attributed by them to defective preparation of mica surface. Melt cutting by platinum wire, the up-until-then preferred method of producing atomically smooth mica, pollutes the freshly cut surfaces by depositing Pt atoms on them. Using a cleaner method, viz., tearing sheets of freshly cleaved mica, Zhu and Granick reported to have measured numerous force oscillations and force minima across liquid squalane ($C_{30}\,H_{62}$), a branched hydrocarbon. Becker and Mugele support the assertions of Zhu and Granick (2003) on the importance of surface preparation and conclude that their own shear force data differs from earlier measurements "*due to contamination problems in the earlier measurements*" (Becker and Mugele, 2005). In contrast, Gourdon and Israelachvili, who repeated the experiments of Zhu and Granick (2004) on liquid squalane, ostensibly using the same, new, method of preparing the mica surfaces, conclude that their "*results show the same nonoscillatory force profile as previously found for a number of branched hydrocarbon liquids, exhibiting a single shallow adhesive minimum*" (Gourdon and Israelachvili, 2006). Furthermore, "*neither the oscillatory forces nor the magnitude of the steady-state friction or shear forces are affected by preparing mica in a different way . . . and therefore disagree with the claim that there is a need for any reassessment of the solidification in fluids confined between solid surfaces*" (Israelachvili et al., 2006).

In another response to the call by Zhu and Granick (2003, 2004) for reassessing earlier work in confinement-induced solidification, Perkin et al. (2006) measured forces between mica surfaces that were prepared in the two different ways. The experiments were carried out

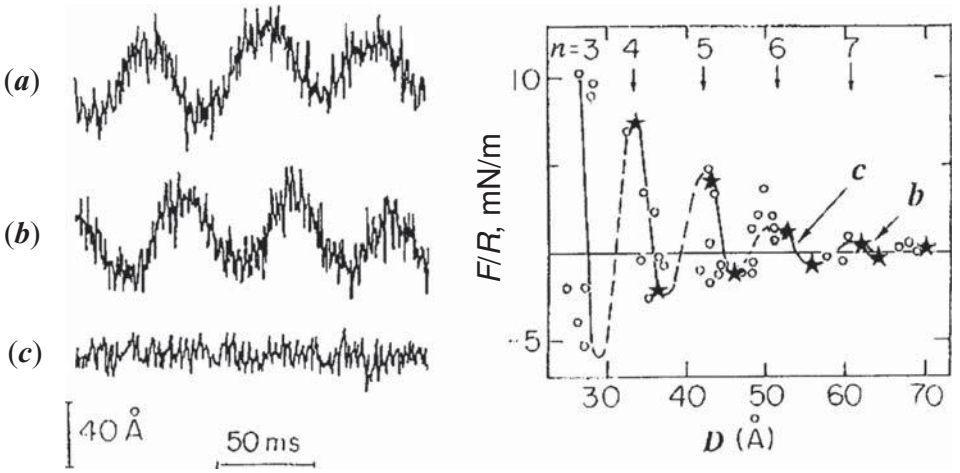

Figure 12.29. Displacement of top surface, no applied lateral motion (a, $D = 116$ nm; b, $D = 6.2 \pm 0.2$ nm; c, $D = 5.40.2$ nm; n, *number of molecular layers*) (Reprinted with permission from Klein, J. and Kumacheva, E. Simple liquids confined to molecularly thin layers. I. Confinement induced liquid-to-solid phase transitions. *J. Chem. Phys.*, **108**(16), 6996–7009, Copyright (1998) American Institute of Physics.)

at three different locations, Oxford University, Weizmann Institute and Toronto University, and were performed on both aqueous and nonaqueous liquids. "*Normal-force versus surface separation (D) profiles and shear force versus D measurements for purified water (no salt added), for concentrated aqueous NaCl solutions, and for cyclohexane revealed that in all cases the behavior of highly confined liquids between melt-cut and between torn-off mica sheets was identical within experimental scatter*" (Perkin et al., 2006).

Response to Shear

Klein and Kumacheva (1998) employed a shear force balance, depicted schematically in Figure 12.28, to investigate the shear response of confined liquids. From these studies they discovered that by varying the degree of confinement, they could initiate sharp transitions in the dynamic behavior of liquid hydrocarbons. In one of their experiments they did not impose lateral motion on the top surface. Instead, they allowed it to drift with external ambient noise at the characteristic frequency (~ 17 Hz) of spring S_1 (Figure 12.28). As shown in Figure 12.29, the random vibration persisted all the way down to $D \geq 6.2 \pm 0.2$ nm($n = 7$) but ceased abruptly when surface separation changed to 5.4 ± 0.2 nm($n = 6$); ostensibly, the film behaved as a liquid all the way down to $n = 7$ molecular layers but on changing to $n = 6$, it solidified sufficiently to resist the random lateral shearing motion induced by external noise.

When alternating lateral motion was applied to the top surface (top trace in Figure 12.30), no shear response was detected on the lower surface between $D = 116$ nm (trace A), and $D = 6.2 \pm 0.2$ nm (trace B). But on changing to $D = 5.2 \pm 0.2$ nm (trace C) the behavior of the layer changed abruptly; it began to exhibit behavior that is typical of solids (ability to sustain finite shear stress, with no measurable relaxation prior to yielding).

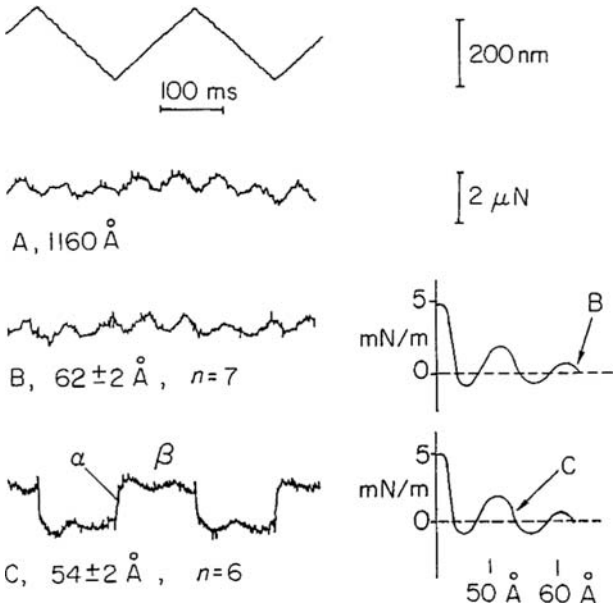

Figure 12.30. Lateral back-and-forth motion applied to the top mica surface, sliding past the lower surface across OMCTS (Reprinted with permission from Klein, J. and Kumacheva, E. Simple liquids confined to molecularly thin layers. I. Confinement induced liquid-to-solid phase transitions. *J. Chem. Phys.*, **108**(16), 6996–7009, Copyright (1998) American Institute of Physics.)

Klein and Kumacheva computed the effective mean viscosity and found it changing abruptly, without transition, as depicted in Figure 12.30 (the broken lines at $D = 54 \pm 2$ Å and $D = 62 \pm 2$ Å are, respectively, lower and upper bounds on μ_{eff}).

Behavior of conductivity water to shear, depicted in Figure 12.32, is in sharp contrast to that of OMCTS. In each of the cases A, B, and C, of the figure, the forced motion of the top surface is depicted in the upper trace while the lower trace represents shear force measured on the bottom surface. As demonstrated here, the reciprocating motion of the top surface is not communicated to the lower surface for films thicker than $D = 5.6 \pm 0.3$ nm, $D = 5.8 \pm 0.5$ nm, and $D = 3.3 \pm 0.0$ nm, for melt-cut mica (A), fully downstream melt cut mica (B), and torn-off mica (C), respectively; no shear force above noise level was observed up to the point where jump-in occurred as the surfaces slowly drifted toward each other. This implies that "purified, salt free (conductivity) water remains fluid under confinement by solid surfaces, down to film thicknesses in the range (3–0) ±0.3 nm, retaining a viscosity within a factor of 3 or so to either side of its bulk value . . . .This behavior is in sharp contrast to that of nonassociating liquids, whose viscosity increases by many orders of magnitude when confined to films of less than five to eight molecular layers" (Perkin et al., 2006).

Zhu and Granick (2003, 2004, 2006) find that the shear behavior of confined liquids is history dependent. At low rate of compression (below 10^{-2} nm/s) they obtained "unprecedented low friction" while at faster compression "friction was larger by orders of magnitude and in this respect resembled prior measurements in the literature" (Zhu and Granick, 2003). Again, they contribute their finding to using contamination free mica surfaces. Israelachvili

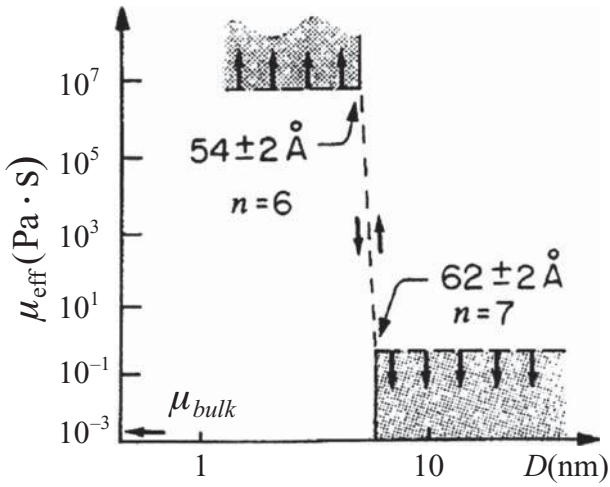

Figure 12.31. Variation of μ_{eff} with the number of molecular layers n (Reprinted with permission from Klein, J. and Kumacheva, E. Simple liquids confined to molecularly thin layers. I. Confinement induced liquid-to-solid phase transitions. *J. Chem. Phys.*, **108**(16), 6996–7009, Copyright (1998) American Institute of Physics.)

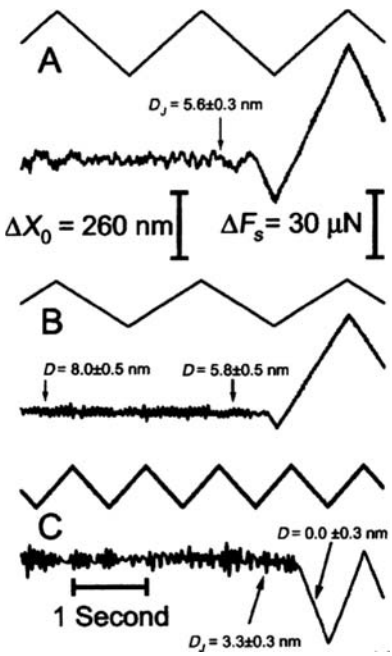

Figure 12.32. Response of water, confined between two solid surfaces, distance D apart, to reciprocating shearing motion of the top surface (Reprinted with permission from Perkin, S., Chai, L., Kampf, N., Raviv, U., Briscoe, W., Dunlop, I., Titmuss, S., Seo, M., Kumacheva, E. and Klein, J. Forces between mica surfaces, prepared in different ways, across aqueous and nonaqueous liquids confined to molecularly thin films. *Langmuir*, **22**, 6142–6152, Copyright (2006) American Chemical Society.)

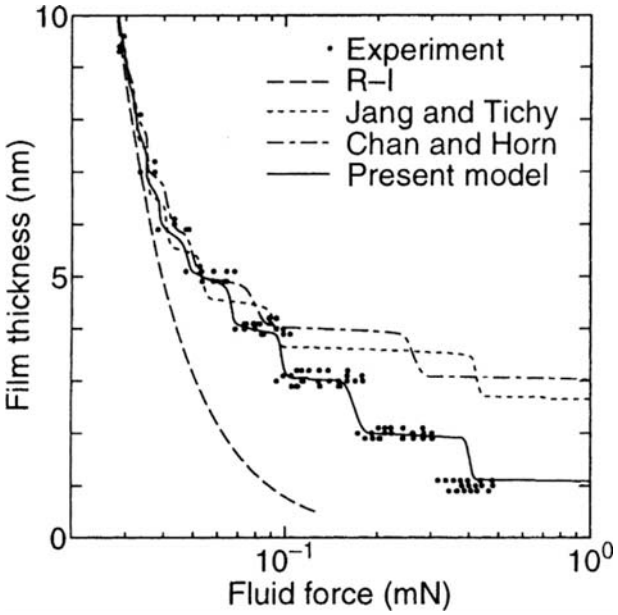

Figure 12.33. Comparison of three solvation pressure models with experiment for OMCTS (Reprinted with permission from Matsuoka H. and Kato, T. An ultrathin liquid film lubrication theory – calculation method of solvation pressure and its application to the EHL problem. *ASME Journal of Tribology*, **119**, 217–226, 1997.)

and coworkers, however, do not accept these result and their implications (Israelachvili et al., 2006).

Ultrathin Film Lubrication

Jang and Tichy (1995) used the exponential-cosine curve fit (Eq. 12.47) of Chan and Horn (1985) to model the oscillatory effect in solvation pressure and (Eq. 12.43) to model van der Waals pressure, in their thin film lubrication (TFL) correction to EHL theory. The total pressure in the Reynolds equation is thus the sum of hydrodynamic, solvation, and van der Waals pressures. According to the model, the effect of the molecular forces is negligible for films in excess of 5 nm but becomes significant under 1 nm.

Matsuoka and Kato (Matsuoka and Kato, 1997; Kato and Matsuoka, 1999) apply a theory of Henderson and Lozada-Cassou (1986) for rigid spheres to model solvation pressure and use the Dejaguin approximation

$$F(D)_{\text{sphere}} = 2\pi R_{\text{eq}} W(D)_{\text{plane}} \tag{12.48}$$

to relate interaction potential between parallel planes, $W(D)_{\text{plane}}$, to force between spheres, $F(D)_{\text{sphere}}$. In this study, the van der Waals pressure is modeled by Eq. (12.43), but with a rigorous evaluation for the Hamaker constant (Prieve and Russel, 1988).

The loads tested by Kato and Matsuoka were small enough not to cause deformation according to classical EHL theory, thus all deformation that may have resulted from the combined pressure could be attributed to van der Waals and solvation forces. On increasing

the load, the film thickness was found to decrease stepwise in OMCTS and cyclohexane $(CH_2)_6$, and agreement was found with lubrication theory for films thicker than 5 nm. For films thinner than this, conventional EHL theory (Luo et al., 1999) begins to deviate from experiment. Figure 12.33 compares experimental data with theoretical predictions for three different models; the figure also contains the solution for classical lubrication theory (R-I).

For *n*-hexadecane, a stepwise decrease of the film thickness was not observed, and there was agreement with R-I theory down to 2 nm.

12.3 Nomenclature

A	Hamaker constant
$\boldsymbol{C}(C_X, C_Y, C_Z)$	Molecular velocity, normalized
D	Rarefaction parameter
D	Separation
F	Normal force
F_s	Shear force
H	Film thickness, normalized
Kn	Knudsen number
L_s	Slip length
P	Pressure, normalized
Q_p, Q_C	Flow coefficients, normalized
$\mathcal{R}$	Gas constant
R	Radius of curvature
T	Temperature
$\boldsymbol{V}(U, V, W)$	Velocity, normalized
W	Interaction potential
X, Y, X	Cartesian coordinates, normalized
a	Surface coefficient
c	Molecular velocity
$\bar{c}$	Molecular velocity, average
$f(\boldsymbol{x}, \boldsymbol{c}, t)$	Distribution function
h	Film thickness
k	Boltzmann constant
m	Molecular mass
n	Number density
q_p, q_C	Flow rate; Poiseuille, Couette
p	Pressure
p_a	Pressure, ambient
$\boldsymbol{u}(u, v, w)$	Velocity
$\boldsymbol{x}(x, y, z)$	Cartesian coordinates
α	Accommodation coefficient
$\dot{\gamma}$	Rate of shear
μ	Viscosity
ρ	Density
τ	Shear stress
$(\cdot)_{\text{eff}}$	Effective quantity
$(\cdot)_0$	Reference quantity

12.4 References

Abraham, F. F. 1978. The interfacial density profile of a Lennard-Jones fluid in contact with a (100) Lennard-Jones wall and its relationship to idealized fluid/wall systems: A Monte Carlo simulation. *J. Chem. Phys*. **68**(8), 3713–3716.

Albertoni, S., Cercignani, C. and Gotusso, L. 1963. Numerical evaluation of the slip coefficient. *Phys. Fluids*, **6**, 993–996.

Alexander, F. J., Garcia, A. L., and Alder, B. J. 1994. Direct simulation Monte Carlo for thin film bearings. *Phys. Fluids* **6**(12), 3854–3860.

Anaya-Dufresne, M. 1966. *On the Development of a Reynolds Equation for Air Bearings with Contact*. Ph.D. Dissertation, Carnegie Mellon University.

Bahukudumbi, P. and Beskok, A. 2003. A phenomological lubrication model for the entire Knudsen regime. *J. Micromech. Microeng.*, **13**, 873–884.

Becker, T. and Mugele, F. 2005. Nanofluidics: molecularly thin lubricant film under confinement. *Molecular Simulation*, **31**, 489–494.

Beskok, A. and Karniadakis, G. E. 1999. A model for flows in channels, pipes, and ducts at micro and nano scales. *Microscale Thermophys. Eng.*, **3**, 43–77.

Beskok, A., Karniadakis, G. E., and Trimmer, W. 1996. Rarefaction and compressibility in gas microflows. *J. Fluids Eng.*, **118**, 448–456.

Bhatnagar, P. L., Gross, E. P. and Krook, M. 1954. A model for collision processes in gases. I. Small amplitude processes in charged and neutral one-component systems. *Phys. Rev.*, **94**, 511–525.

Bird, G. A. 1994. *Molecular Gas Dynamics and the Direct Simulation of Gas Flows*, Clarendon Press, Oxford.

Bird, R. B., Stewart, W. E. and Lightfoot, E. N. 2002. *Transport Phenomena*. 2nd edn. John Wiley & Sons, Inc. New York.

Bonaccurso, E., Kappl, M. and Butt, H. J. 2002. Hydrodynamic force measurements: boundary slip of water on hydrophilic surfaces and electrokinetic effects. *Phys. Rev. Letts.*, **88**(7), 076103.

Burgdorfer, A. 1959. The influence of molecular mean free path on the performance of hydrodynamic gas lubricated bearings. *J. Basic Eng.*, **81**, 94–100.

Cercignani, C. 1988. *The Boltzmann Equation and its Application*. Springer-Verlag, New York.

Cercignani, C. and Daneri, A. 1963. Flow of a rarefied gas between two parallel plates. *J. Appl. Phys.*, **34**, 3509–3513.

Cercignani, C. and Pagani, C. D. 1966. Variational approach to boundary-value problems in kinetic theory. *Phys. Fluids*, **6**, 1167–1175.

Cercignani, C., Frangi, A. Frezotti, A., Ghiroldi, G. P., Gibelli, L. and Lorenzani, S. 2008. On the application of the Boltzmann equation to the simulation of fluid structure interaction in micro-electro-mechanical-systems. *Sensor Lett.*, **6**, 121–129.

Cercignani, C., Lampis, M. and Lorenzani, S. 2007. On the Reynolds equation for linearized models of the Boltzmann operator. *Transport Theory Stat. Phys.*, **36**, 257–280.

Chan, D. Y. C. and Horn, R. G. 1985. The drainage of thin liquid films between solid surfaces. *J. Chem. Phys.*, **83**, 5311–5324.

Chuarev, N. V., Sobolev, V. D. and Somov, A. N. 1984. Slippage of liquids over liophobic solid surfaces. *J. Colloid Interface Sci.*, **97**, 574–581.

Debye, P. and Cleland, R. L. 1959. Flow of liquid hydrocarbons in porous vycor. *J. Appl. Phys.*, **30**, 843–849.

Din, X. D. and Michaelides, E. E. 1997. Kinetic theory and molecular dynamic simulations of microscopic flows. *Phys. Fluids*, **9**(12), 3915–3925.

Du, B., Goubaidoulline, I. and Johannsmann D. 2004. Effect of lateral heterogeneous slip on the resonance properties of quartz crystals immersed in liquids. *Langmuir*, **20**, 10617–10624.

Fukui, S. and Kaneko, R. 1988. Analysis of ultra-thin gas film lubrication based on linearized Boltzmann equation. *J. Tribology*, **110**, 253–261.

Fukui, S. and Kaneko, R. 1990. A database for interpolation of Poiseuille flow rates for high Knudsen number lubrication problems", *J. Tribology*, **112**, 78–83.

Furuta, T., Samatey, F. A., Matsunami, H., Imada, K., Namba, K. and Kitao, A. 2007. Gap compression / extension mechanism of bacterial flagellar hook as the molecular universal joint. *J. Struct. Biol.*, **157**, 481–490.

Gad-el-Hak, M. 1999. The fluid mechanics of micro devices – The Freeman Scholar Lecture. *J. Fluids Eng.*, **121**, 5–33.

Gao J. P., Luedtke, W. D. and Landman, U. (1997a). "Layering transitions and dynamics of confined liquid films", *Phys. Rev. Lett.*, (**4**), 705–708.

Gao J. P., Luedtke, W. D. and Landman, U. (1997b). "Structure and Solvation forces in confined films: Linear and branched alkanes", *J. Chem. Phys*, **106**(10) 4309–4318.

Gee, M. L. and Israelachvili, J. N. 1990. Interactions of surfactant monolayers across hydrocarbon liquids. *J. Chem. Soc. Faraday Trans.*, **86**(24), 4049–4058.

Germann, T. C. and Kadau, K. 2008. Trillion atom molecular dynamics becomes a reality. *Int. J. Mod. Phys*. **19**(9), 1315–1319.

Goldstein, S. (Ed.). 1938. *Modern Developments in Fluid Dynamics, Vols. 1 and 2*. Oxford University Press, Oxford.

Gourdon, D. and J. Israelachvili, J. 2006. Comment on "Superlubricity: a paradox about confined fluids resolved". *Phys. Rev. Lett*. **96**, 099601.

Granick, S., Zhu, Y., Lin, Z., Bae, S. C., Janet S., Wong, J. and Turner, J. 2006. Reply to Comment on reassessment of solidification in fluids confined between mica sheets. *Langmuir*, **22**, 2399–2401.

Gross, F. P., Jackson, E. A. and Ziering, S. 1957. "Boundary Value Problems in Kinetic Theory of Gases", *Ann. Phys.*, **1**, 141–167.

Henderson, D. and Lozada-Cassou, M. 1986. A simple theory for the force between spheres immersed in liquid. *J. Colloid and Interface Sci.*, **114**, 180–183.

Ho, C. M. and Tai, Y. C. 1998. Micro-electro-mechanical systems (MEMS) and fluid flows. *Annu. Rev. Fluid Mech.*, **30**, 579–612.

Horn, R. G. and Israelachvili. 1981. Direct measurement of structural forces between two surfaces in a nonpolar liquid. *J. Chem. Phys*. **75**(3), 1400–1411.

Hsia, Y. T. and Domoto, G. A. 1983. An experimental investigation of molecular rarefaction effects in gas lubricated bearings at ultra-low clearances. *ASME Journal of Tribology*, **105**, 120–130.

Hu, Y. Z., and Granick, S. 1998. Microscopic study of thin film lubrication and its contribution to macroscopic tribology. *Tribol. Lett.*, **5**(1), 81–88.

Huang, W. and Bogy, D. B. 2000. The effect of accommodation coefficient on slider air bearing simulation. *ASME Journal of Tribology*, **122**, 427–435.

Huang, W., Bogy, D. B. and Garcia, A. L. 1997. Three-dimensional direct simulation Monte Carlo method for slider air bearing. *Phys. Fluids*, **9**(6), 1764–1769.

Ishida, N., Inoue, T., Miyahara, M. and Higashitani. 2000. *Langmuir*, **16**, 6377.

Israelachvili, J. N. and Adams, G. E. 1978. Measurement of force between two mica surfaces in aqueous electrolyte solution in the range of 1–100 nm. *J. Chem. Soc. Faraday Trans. 1*. **74**, 1400–1411.

Israelachvili, J. N. 1986. Measurement of the viscosity of liquids in very thin films. *J. Coll. Interface Sci.*, **110**, 263–271.

Israelachvili, J. N. 1992. *Intermolecular and Surface Forces*. Academic Press, San Diego.

Israelachvili, J. N., Maeda, N. and Akbulut, M. 2006. Comment on Reassessment of solidification in fluids confined between mica sheets. *Langmuir*, **22**, 2397–2398.

Jang, S. and Tichy, J. A. 1995. Rheological models for thin film EHL contacts. *ASME Journal of Tribology*, **117**, 22–28.

Jiang, J. Z., Shen, C., and Fan, J. 2005. Statistical simulation of thin-film bearings. In *Rarefied Gas Dynamics* (M. Capitelli, ed.), AIP Conf. Proc. 762, Springer, New York, pp. 180–185.

John, B. and Damodaran, M. 2009. Computation of head-disk interface gap micro flow fields using DSMC and continuum-atomistic hybrid methods. *Int. J. Numer. Meths. Fluids*, **61**, 1273–1298.

Kadau, K., Barber, J. L., Timothy C. Germann, T. C. Alder, B. J. 2008. Scaling of atomistic fluid dynamics simulations. *Phys. Rev. E* **78**, 045301.

Kang, S. C., Crone, R. M. and John, M. S. 1999. A new molecular gas lubrication theory suitable for head-disk interface modeling. *J. Appl. Phys.*, **85**, 5594–5596.

Kantorovich, L. V. and Krylov, V. I. 1964. *Approximate Methods of Higher Analysis*. Interscience, New York.

Kato, T. and Matsuoka, H. 1999. Molecular layering in thin-film elastohydrodynamics. *Proc. Instn. Mech. Engrs* **213**(J), 363–370.

Klein, J. 2006. Forces between mica surfaces, prepared in different ways, across aqueous and nonaqueous liquids confined to molecularly thin films *Langmuir*, **22**, 6142–6152.

Klein, J. and Kumacheva, E. 1998. Liquid-to-solid transition in thin liquid films induced by confinement. *Physica A*, **249**, 206–215.

Kogan, M. N. 1969. *Rarefied Gas Dynamics*, Plenum Press, New York.

Koplik, J. and Banavar, J. R. 1995. Continuum Deductions from Molecular Hydrodynamics. *Annual Rev. Fluid Mech*., **27**, 957–992.

Koplik, J. and Banavar, J. R. 1998a. Physics of Fluids at Low Reynolds Numbers – a Molecular Approach. *Comput. Phys.*, **12**, 424–431.

Koplik, J. and Banavar, J. R. 1998b. Molecular Simulation of Viscous Flow. *JSME Int. J., B*. **41**, 3, 53–360.

Koplik, J., and Banavar, J. R. 1995. Continuum deductions from molecular hydrodynamics. Annual Rev. *Fluid Mech.*, **27**, 957–992.

Langlois, W. E. 1964. *Slow Viscous Flow*. Macmillan, New York.

Lauga, E. and Brenner, M. P. 2004. Dynamic mechanism for apparent slip on hydrophobic surfaces. *Phys. Rev. E*, **70**, 026311.

Loyalka, S. K. 1971. Kinetic theory of thermal transpiration and mechanocaloric effect. *Int. J. Chem. Phys.*, **55**, 4497–4503.

Luo, J., Huang, P. and Li, L. K. Y. 1999. Characteristics of liquid lubricant films at the nano-scale. *ASME Journal of Tribology*, **121**, 872–878.

Maali, A. and Bhushan, B. 2008. Nanorheology and boundary slip in confined liquids using atomic force microscopy. *J. Phys.: Condense Matter*, **20**, 315201.

Matsuoka H. and Kato, T. 1997. "An Ultrathin Liquid Film Lubrication Theory – Calculation Method of Solvation Pressure and its Application to the EHL Problem", *ASMS J. Tribol.*, **119**, 217–226.

Maxwell, J. C. 1879. *Phil. Trans. R. Soc.* 170, 231–256.

McHale, G. and Newton, M. 2004. Surface roughness and interfacial slip boundary condition for quartz crystal microbalances. *J. Appl. Phys*. **95**, 373–380.

Migun, N. P. and Prokhorenko, P. P. 1987. Measurement of the viscosity of polar liquids in micro-capillaries. *Colloid J. USSR*, 849–897.

Mitsuya, Y. 1993. Modified Reynolds equation for ultra-thin film gas lubrication using 1.5 order slip flow model and considering surface accommodation coefficient. *ASME Journal of Tribology*, **115**, 289–294.

Neto, C., Evans, D. R., Bonaccurso, E., Butt, H. J. and Craig, V. S. J. 2005. Boundary slip in Newtonian liquids: a review of experimental studies. *Rep. Prog. Phys.*, **68**, 2859–2897.

Niavarani, A. and Priezjev, N. V. 2008. Rheological study of polymer flow past rough surfaces with slip boundary conditions. *J. Chem. Phys.*, **129**, 144902.

Oran, E. S., Oh, C. K. and Cybyk, B. Z. 1998. Direct Simulation Monte Carlo: Recent Advances and Applications. *Annu. Rev. Fluid Mech.*, **30**, 403–441.

Pashley, R. M. 1981. Hydration forces between mica surfaces in aqueous electrolyte solutions. *J. Coll. Interface Sci.*, **80**(1), 153–162.

Perkin, S., Chai, L., Kampf, N., Raviv, U., Briscoe, W., Dunlop, I., Titmuss, S., Seo, M., Kumacheva, E. and Klein, J. 2006. Forces between mica surfaces, prepared in different ways, across aqueous and nonaqueous liquids confined to molecularly thin films. *Langmuir*, **22**, 6142–6152.

Pfahler, J., Harley, J., Bau, H. and Zemel, J. N. 1991. Gas and liquid flow in small channels. *Symposium on Micromechanical Sensors, Actuators and Systems* (D. Cho et al., eds) ASME DSC, pp. 49–60.

Prieve, D. C. and Russel, W. B. 1988. Simplified predictions of Hamaker constants from Lifshitz theory. *J. Colloid and Interface Sci*. **125**, 1–13.

Raviv, U., Perkin, S., Laurat, P. and Klein, J. 2004. Fluidity of water confined down to subnanometer films. *Langmuir*, **20**, 5322–5332.

Rettner, C. T. 1997. Determination of accommodation coefficients for N2 at disk-drive air-bearing surfaces. *J. Tribology*, **119**, 588–589.

Sanbonmatsu, K. Y and Tung, C. S. 2006. High performance computing in biology: Multimillion atom simulations of nanoscale systems. *J. Struct. Biol.*, **157**(3), 470–480.

Schaaf, S. A. and Sherman, F. S. 1954. Skin friction in slip flow. *J. Aero. Sci*., **21**, 85–90.

Shen, S., Chen, G., Crone, R. M. and Anaya-Dufresne, M. 2007. A kinetic-theory based first order slip boundary condition for gas flow. *Phys. Fluids*, **19**, 086101.

Stokes, G. G. 1845. On the theories of internal friction of fluids in motion, and of equilibrium and motion of elastic solids. *Trans. Camb. Phil. Soc.*, **8**, 287–305.

Sun, Y. H., Chan, W. K. and Liu, N. Y. 2003. A slip model for gas lubrication based on an effective viscosity concept. *Proc IMechE J.*, **217**, 187–195.

Szeri, A. Z. and Phillips C. 1974. Hydrodynamic effects in a hydrostatic bearing: an application of the method of Schwartz. *Trans. ASLE*, **18**, 116–122.

Thompson, P. A. and Troian, S. M. 1997. A general boundary condition for liquid flow at solid surfaces. *Nature*, **389**, 360–362.

Ungerer, P., Nieto-Draghi, C., Rousseau, B., Ahunbay, G. and Lachet, V. 2007. Molecular simulation of the thermophysical properties of fluids: From understanding toward quantitative predictions. *J. Molecular Liquids*, **134**, 71–89.

Van Odyck, D. E. A. and Venner, C. H. 2003. Compressible Stokes flow in thin films. *J. Tribology*, **125**, 543–551.

Veijola, T. and Turowski, M. 2000. Compact damping models for laterally moving microstructures with gas-rarefaction effects. *Helsinki University of Technology, Circuit Theory Laboratory Report*.

Vincenti, W. G. and Kruger, C. H. 1965. *Introduction to Physical Gas Dynamics*, John Wiley & Sons, New York.

Vinogradova, O. I. 1995. Drainage of a thin liquid film confined between hydrophobic surfaces. *Langmuir*, **11**, 2213–2220.

Willis, D. R. 1962. Comparison of kinetic theory analyses of linearized Couette flow. *Phys. Fluids*, **5**, 127–135.

Wu, L. and Bogy. D. B. 2003. New first and second order slip models for the compressible Reynolds equation. *J. Tribology*, **125**, 558–561.

Zhu, Y. and Granick, S. 2001. Rate-dependent slip of Newtonian liquid at smooth surfaces. *Phys. Rev. Letts*. **87**(9), 096105.

Zhu, Y. and Granick, S. 2003. Reassessment of solidification in fluids confined between mica sheets. *Langmuir*, **19**, 8148–8151.

Zhu, Y. and Granick, S. 2004. Superlubricity: A Paradox about Confined Fluids Resolved. *Phys. Rev. Letts*. **93**(9), 096101.

CHAPTER 13

Biotribology

The term *biotribology*, to cover "*all aspects of tribology related to biological systems*," was coined only four decades ago (Dowson and Wright, 1973); however, investigations into friction, lubrication and wear of biological tissues date back much further. As early as the nineteenth century, Young (1809) and Poiseuille (1840) studied the flow properties of blood, essential today for the design of artificial organs. Reynolds likened lubrication of articulated joints to lubrication of machine elements. In the last sentence of his classical paper, Reynolds remarked that hydrodynamic lubrication "*is as fundamental to animal mechanics as the lubricating action of the journal is to mechanical contrivances*" (Reynolds, 1886). Jin and Dowson (2005) listed six areas of biotribology in addition to lubrication of joints and of red blood cells in capillaries, such as wear of dentures and the tribology of contact lenses. Nevertheless, in this chapter, we restrict ourselves to one topic only, the lubrication of articular joints.

Lubrication of Articular Joints

The loading cycle to which an articular joint is subjected is complex and the demands this places on the joint are numerous (Paul, 1967). For example, across the hip the cycle displays two force maxima, at heal strike (HS) and at toe-off (TO), as illustrated in Figure 13.1, the latter reaching four times the body weight. As additional complications, the forces that operate within the joint are three dimensional, time dependent and vary with speed and length of stride, and, of course, vary from person to person.

The articulating surfaces of the bones of the joint are covered by cartilage, a specialized soft tissue. The function of the cartilage is threefold: to distribute the load on the joint, to reduce friction and eliminate wear, and to absorb energy during dynamic loading. The precise mechanism of joint lubrication is not well understood and the reasons for deterioration of the cartilage to the extent that the joint is no longer able to function are not known. It appears, nevertheless, that solid-fluid interaction is at the heart of cartilage modeling.

Gross deterioration of the cartilage leads to arthritis. Arthritis is the nation's leading cause of disability and costs the United States in the neighborhood of $65 billion annually. Osteoarthritis is the most common form of arthritis, afflicting 20.7 million Americans (Lawrence et al., 1998). One theory attributes osteoarthritis to abnormal release of enzymes from cartilage cells, which then leads to cartilage breakdown and joint destruction. Another theory is that some people may be born with defective cartilage or with slight defects in the way that the joints fit together. These defects may cause cartilage breakdown due to repeated, incorrect, loading of the joint as the person ages. Simply put, damage done to the cartilage may be a process of wear and tear. This breakdown is exacerbated by the fact that cartilage is largely free of nerves, blood vessels and lymph channels and, therefore, has only a limited capacity for self-repair (Englert et al., 2005). As the only way nutrients can be

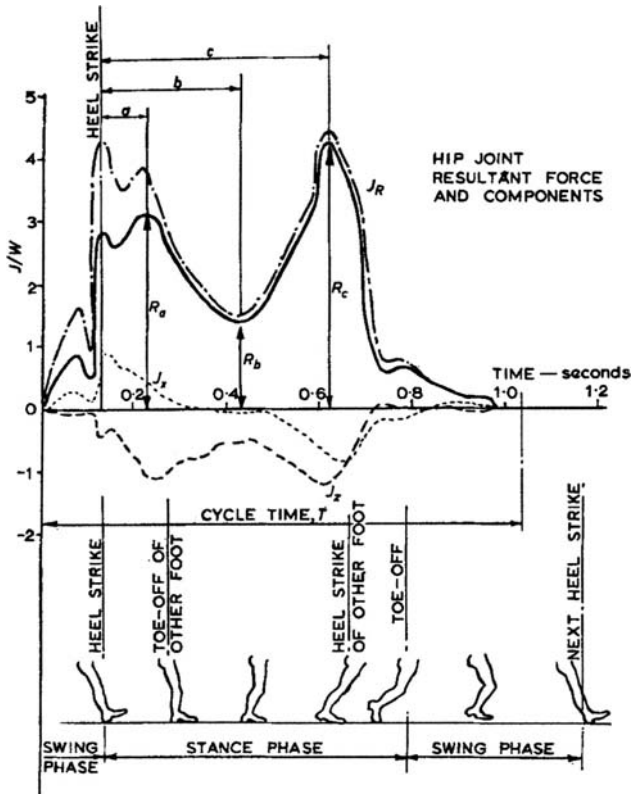

Figure 13.1. Load patterns in units of body weight in hip joint during walking. The average values were $R_a = 3.29$, $R_b = 1.24$ and $R_c = 3.88$ with maximum values of $R_a = 5.8$ and $R_c = 6.4$. (Reprinted with permission from Paul, J. P. Forces transmitted by joints in the human body. *Proc Instn Mech Engrs* **181** (3J), 8–15, Copyright (1966) Professional Engineering Publishing.)

made available to the cells of the cartilage is transport by the synovial fluid (SF), knowledge of the movement of the fluid through the cartilage is essential to the understanding of its deterioration (Quinn et al., 2002; Zhang and Szeri, 2005, 2008).

13.1 Natural Joints

Properties of the Cartilage

The tribological properties of cartilage are intimately related to its structure and material constitution (Klein, 2006). Cartilage is composed of 10–30% collagen fibrils, which give strength, 3–10 % proteoglycans, which provide resiliency, and 60–78% water. The collagen fibrils in articular cartilage consist of Type II collagen molecules, and are of varying diameter, from 16 nm (Burgeson, 1982) to 200 nm (Clarke, 1971), and 300 nm in length. The collagen fibrils form a network into which the proteoglycans fit. From a mechanical point of view, the cartilage is an organic matrix of a dense network of macromolecules saturated with water. The tissue is permeable to fluid flow, in fact, most of the fluid is free to flow in the interstices, and cartilage is easily compressed. When loaded,

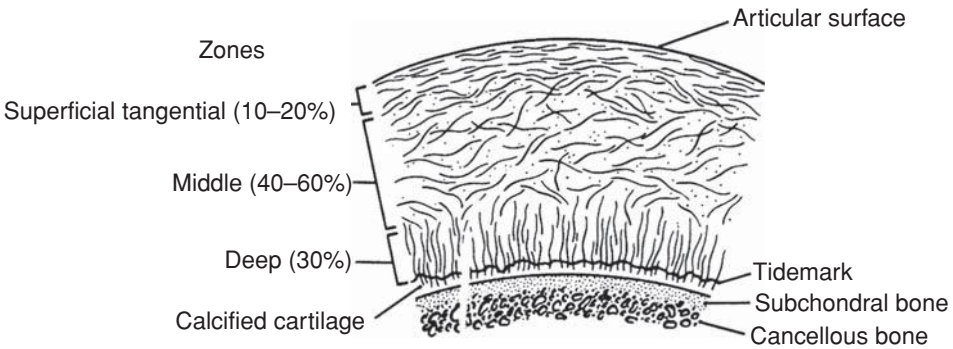

Figure 13.2. The inhomogeneous nature of cartilage: fiber orientation changes from the deep to middle to superficial tangential zone. (Reprinted with permission from *Journal of Biomechanics*, **7**(5), Mow, V. C., Lai, W. M. and Redler, I. Some surface characteristics of articular cartilage I. A scanning electron microscopy study and a theoretical model for the dynamic interaction of synovial fluid and articular cartilage. 449–456, Copyright (1974), with permission from Elsevier.)

it will exhibit creep and stress relaxation; these nonlinear responses are due, primarily, to the viscous drag arising from the relative motion of interstitial fluid and solid matrix (poroelasticity).

The collagen fibrils in mature articular cartilage are inhomogeneously distributed, giving the tissue a layered character. Classically, the tissue is divided into histological zones based on the cellular arrangement (Figure 13.2). The gliding or superficial tangential zone, some 10–20% of the total thickness, contains a higher proportion of collagen fibrils, which are randomly distributed in planes parallel to the loading surface of the cartilage (Weiss et al., 1968). The transitional or middle zone, accounting for 40 to 60% of the thickness, contains randomly oriented and homogenously distributed collagen fibrils (Clarke, 1974). The radial or deep zone, next to the subchondral bone and straddling the tidemark, the demarcation between cartilage and calcified tissue, has larger, radially oriented fibril bundles (Hunter and Finley, 1973). Finally, the calcified cartilage zone, which lies between the tidemark and the subchondral bone, is composed of short columns of chondrocytes separated by bars of hyaline cartilage with vascular invasion on the bony side of the zone.

As already alluded to, in early times lubrication of articulated joints was compared to lubrication of machine elements. In this manner *hydrodynamic lubrication*, which postulates nonparallel rigid surfaces in relative motion separated by a continuous film of lubricant, was proposed (MacConaill, 1932) to explain a coefficient of friction in the 0.0005–0.04 range for healthy tissue (Dowson and Jin, 1986; Mow and Mak, 1987; Foster and Fisher, 1996).

Elastohydrodynamic Models

The next stage of development recognized that the cartilage is soft and deforms elastically under load; this realization led to the (soft) *elastohydrodynamic lubrication* model (Dowson, 1967). It was found, however, that under physiological peak load the film thickness in diarthrodial joints, calculated from elastohydrodynamic theory to be in the $h \sim 0.1$–$1.0\ \mu$m range, was considerably smaller than the height of surface asperities of the

Table 13.1. *Parameters for micro-EHL model of ankle join*

Equivalent radius (R)	0.35 m	Relative velocity (U)	0.019 m/s
Cartilage thickness (d)	0.0024 m	Load/length (w)	33.7 kN/m
Modulus of elasticity (E)	16 MPa	Asperity wavelength	1 mm
Poisson's ratio (v)	0.4	Asperity amplitude (a)	1 μm
Lubricant viscosity (μ)	0.01 Pa. s		

cartilage $\delta \sim 2$–5 μm (Dowson, 1967; Gardner et al., 1981; Dowson and Jin, 1986). Walker et al. (1968), for example, measured $R_a = 0.8$ μm for healthy articular surface and up to $R_a = 8$ μm for osteoarthritic cartilage.

Dowson and Jin (1986) subsequently envisaged the asperities to be effectively smoothed out in the loaded conjunction and proposed a *microelastohydrodynamic lubrication* model based on "local" asperity deformation that is additional to the "global" deformation of the contact. In their solution of the Reynolds equation, Dowson and Jin modeled the hydrodynamic pressure p as the sum of a dry contact pressure p_s valid for a smooth surface and a small perturbation Δp, accounting for the asperities. For film thickness, they postulated

$$h = h_0 + \frac{x^2}{2R} + a\cos\left(\frac{2\pi x}{\lambda} + \varphi\right) + C_s p_s + C_r \Delta p. \tag{13.1}$$

Here a and λ are the amplitude and the wavelength of the "asperities" on a soft layer, which, with unloaded thickness d, represents the cartilage and covers a rigid cylinder, the bone, of radius R; C_s and C_r are elastic compliances. Table 13.1 lists the parameter values for the ankle joint in steady walking and Figure 13.3 displays the results of the Dowson and Jin calculations: the pressure p, the film thickness h, and the deformed roughness $[a\cos(2\pi x/\lambda + \varphi) + C_r \Delta p]$.

Asperity contact is first made when the ratio of film thickness to the arithmetic average of the surface roughness (h/R_a) is less than 2–3. If well in excess of this value, then fluid-film lubrication is likely (cf., Figure 3.13). In the computations of Dowson and Jin (h/R_a) increased from an initial value of unity to 19.0, resulting in a minimum film thickness of 0.68 μm for the ankle joint. This is in the film thickness range of highly stressed machine elements lubricated in the EHL mode.

For Dowson and Jin (1986) the computed high (h/R_a) value "*immediately offered powerful support for the concept of fluid film lubrication in synovial joints under these conditions.*" Under physiological pressures in living joints, the opposing articular surfaces are thus expected to conform down to the nanometer level (Klein, 2006).

Significant advances were made in joint lubrication on broadening the concept beyond the confines of classical fluid-film lubrication. The main impetus for this was the recognition that the relative velocities that occur in diarthrodial joints in most applications are smaller than required by hydrodynamic lubrication theory for the creation and maintenance of a continuous, load carrying film. Additionally, the time scale for squeeze film action in articular joints was found to be too short, when compared to the time interval over which joints must support load. It appeared advantageous, therefore, to consider articular cartilage as a deformable solid matrix saturated with fluid.

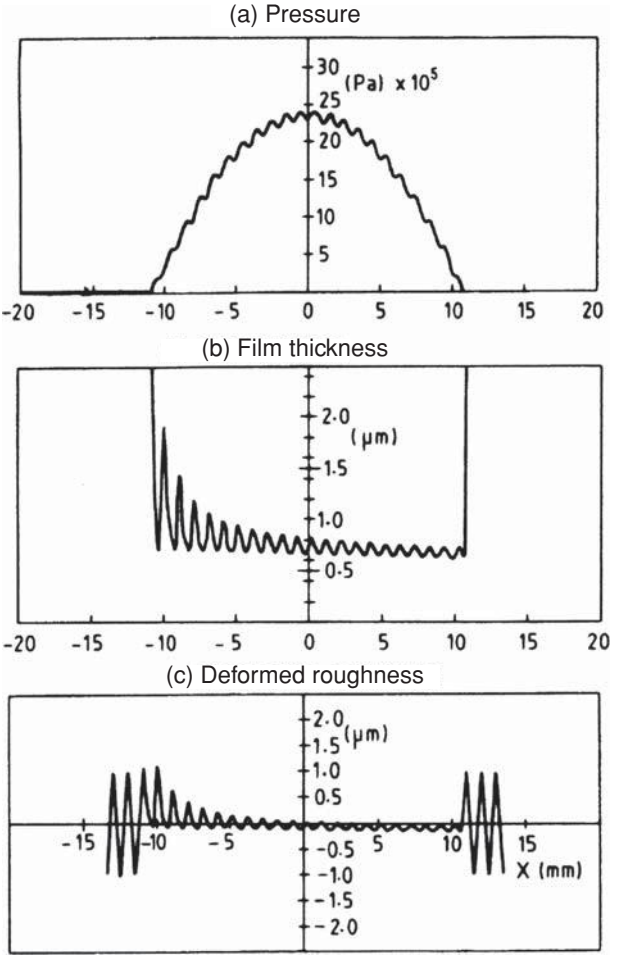

Figure 13.3. Micro-elastohydrodynamic model of ankle joint (Reprinted from Journal of Biomechanics, with permission from Dowson, D., and Jin, Z. M. Microelastohydrodynamic lubrication of synovial joints. *Proc IMechE Journal of* Engineering in Medicine, **16**, 63–65, 1986, Professional Engineering Publishing.)

Boosted Lubrication

Boosted lubrication/ultrafiltration is the name given to a possible mechanism that presumes that during squeezing action synovial fluid is imbibed into the cartilage. Maroudas (1967) was the first to raise the possibility that a gel, formed of concentrated synovial fluid, collects in spaces between contacting asperities of opposing cartilage surfaces. The synovial fluid contains macromolecules, occupying a large spherical domain of 400 nm in diameter, while the pore size of normal cartilage surface is <5 nm (Mow and Lai, 1980; Mow and Mak, 1987; Klein, 2006). Consequently, the water component of the synovial fluid might be imbibed into the cartilage, leaving a residue of large molecule hyaluronan gel behind; this pool of trapped hyaluronan gel (Figure 13.4) then performs the function of a boundary

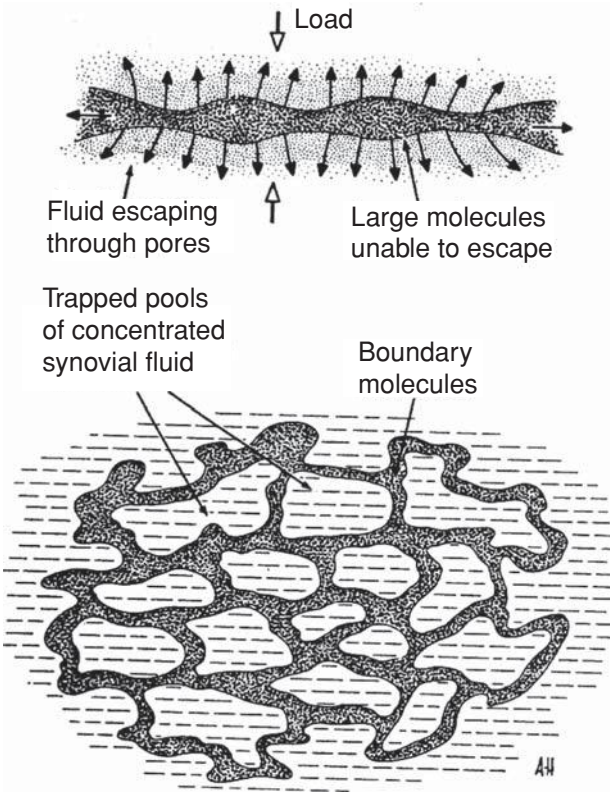

Figure 13.4. Boosted lubrication (Reproduced from Walker, P. S., Dowson, D., Longfield, M. D. and Wright, V., "Boosted Lubrication" in synovial joint by entrapment and enrichment, *Ann, Rheum. Dis*., **27**, 512–520, Copyright (1968), with permission from BMJ Publishing Group Ltd.)

lubricant as a macromolecular monolayer, 1–100 μm thick, attached to the surface of the cartilage (Maroudas, 1967; Walker et al., 1968, 1970).

Later investigations of cartilage under squeeze film action (Hou et al., 1992; Jin et al., 1992) indicated, however, that though thin fluid from SF can imbibe into cartilage within the central high-pressure zone, leaving concentrated HA gel behind, the low porosity of the cartilage prevents realization of effective squeeze film lubrication. Linn and Radin (1986) also suggested that HA is not always an effective boundary lubricant. We will return to this point later.

Weeping Lubrication

The *weeping lubrication* model (McCutchen, 1959), in contrast, considers cartilage as a reservoir of synovial fluid that is squeezed out from under (elevated) contact points and into the cavity that remains between the opposing surfaces, at locations where these surfaces are still separated. The trapped, pressurized, synovial fluid acts as a hydrostatic film. Because the permeability of the cartilage decreases significantly during loading

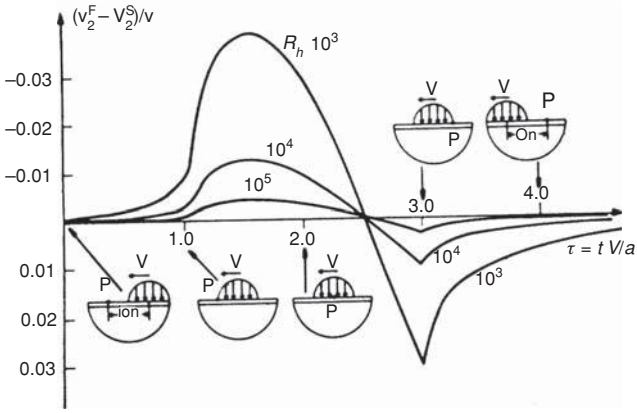

Figure 13.5. Self-generating mechanism: time history of the x_2 component of fluid velocity (Mow, V. C. and Lai, M., Recent development in synovial joint biomechanics, *SIAM Rev.*, **22**, 257–317, Copyright© 1980 Society for Industrial and Applied Mathematics. Reprinted with permission. All right reserved.)

induced deformation, the constrained, pressurized, fluid is capable of carrying up to 90% of the applied load. With the passing of time, however, the trapped synovial fluid seeps away and the solid matrix is called upon to support the load; creep equilibrium in human cartilage is reached in 4–16 hours (Mow et al., 1989). Thus, weeping lubrication requires an exudation of synovial fluid during loading while boosted lubrication postulates imbibition (Mow and Lai, 1980).

Biphasic Models

The ratio of typical "pore diameter" to minimum global dimension of the cartilage is of the order 10^{-6}, the porosity of the unloaded cartilage is as much as 80%, while the diameter and length of the randomly distributed collagen fibrils that make up the matrix is 25–40 nm and 200–300 nm, respectively. These dimensions indicate that the assumptions of mixture theory (Truesdell, 1969; Rajagopal and Tao, 1995; see also Chapter 10) hold for articular cartilage. Mow and co-workers (Mow and Lai, 1980; Mow and Mak, 1987) made a significant step forward in cartilage simulation by making use of the theory of mixtures; their so-named *biphasic model* for cartilage has been used extensively ever since (e.g., Ateshian et al., 1992; 1998). In this model, cartilage is a homogeneous mixture of an incompressible elastic solid and an incompressible, inviscid, liquid. However, in reality, cartilage is neither homogeneous, nor isotropic (cf., Figure 13.2), and undergoes large deformation during loading, as discussed in later publications (Suh and Spilker, 1994, Lei and Szeri, 2006).

According to Mow and Lai (1980), the exudation and imbibition of synovial fluid by cartilage is not as simple as either the weeping lubrication or the boosted lubrication models would lead us to believe. The *self-generating lubrication* mechanism of Mow and co-workers (Mow and Lai, 1980; Mow and Mak, 1987) takes into account the biphasic nature of the cartilage and is based on the load-partitioning factor β between solid and fluid phases. Figure 13.5, for example, shows a free draining indenter ($\beta = 0$) moving over a

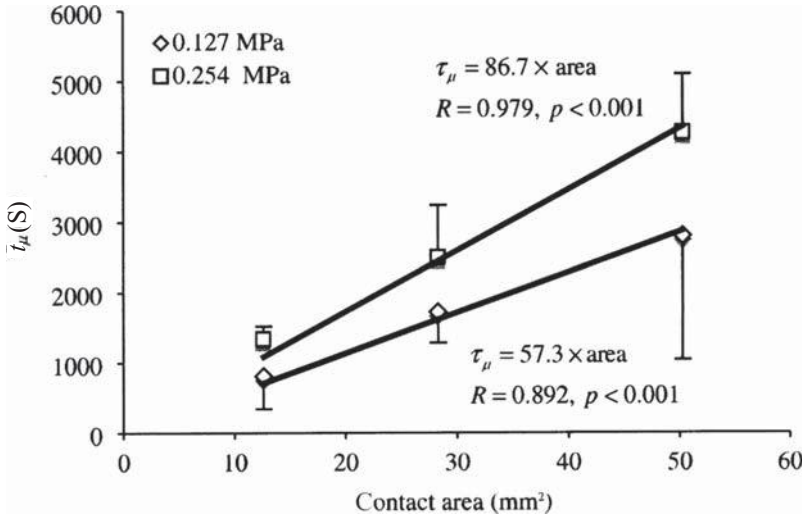

Figure 13.6. Variation of time constant t_μ for reaching equilibrium under constant loading (Reprinted from *Journal of Biomechanics*, **40**, Carter, M. J., Basalo, I. M., and Ateshian, G. A. The temporal response of the friction coefficient of articular cartilage depends on the contact area. 3257–3260, Copyright (2007), with permission from Elsevier.)

cartilage sample: "*exudation of the interstitial fluid occurs in front of and underneath the leading portion of the moving indenter and imbibition of fluid occurs behind and underneath the trailing portion of it*" (Mow and Lai, 1980). This self-generating mechanism is thought by Mow and his co-workers to be responsible for joint lubrication (Mansour and Mow, 1977; Torzilli and Mow, 1976).

In a recent numerical work, Pawaskar et al. (2007) first slid a plate then a cylinder indenter over cartilage. Weeping lubrication was indicated in the plate experiment by the fluid rushing toward the surface, with the flow becoming parallel to the surface in time. This fluid movement toward the surface was not seen, however, in the indenter experiment; in fact, fluid was imbibed, reminiscent of boosted lubrication. Fluid exudation was also seen at the leading and trailing edges. The difference between these results of the two experiments is attributed by Pawaskar et al. to the difference in aspect ratio, but all in all "*this was indicative of self-generating lubrication mechanism*" (Pawaskar et al., 2007).

In vitro, the friction coefficient has been observed to increase with time under steady loading as the synovial fluid is squeezed out of the cartilage, indicating that friction in diarthrodial joints is mainly due to solid phase sliding against solid phase (e.g., McCutchen, 1962; Walker et al., 1968; Foster and Fisher, 1996; Krishnan et al., 2004). In situ, however, the cartilage will not achieve the elevated equilibrium value μ_{eq} because the time constant for this increase, t_μ is proportional to the size of the contact area (Carter et al., 2007), as illustrated in Figure 13.6. After the load has been taken up by solid-to-solid contact, another form of lubrication mechanism, namely *boundary lubrication*, takes over (Jin and Dawson, 2005).

Based on the hypothesis that interstitial fluid pressurization contributes significantly to the reduction of friction in diarthrodial joints, Ateshian examines joint friction within the context of the biphasic model of cartilage. The ensuing *biphasic boundary lubrication*

(Ateshian, 1997; Ateshian et al., 1998) assumes the two constituents of cartilage, an incompressible, ideal, fluid and a linearly elastic solid, obey the equations of mixture theory.[1] The equations of motion (10.66) and continuity (10.72), for steady flow of the components of the mixture, reduce to

$$\begin{aligned} &\text{grad } \boldsymbol{T}^s + \boldsymbol{\pi} = \boldsymbol{0} \\ &\text{grad } \boldsymbol{T}^f - \boldsymbol{\pi} = \boldsymbol{0} \end{aligned} \tag{13.2}$$

and

$$\text{grad}(\phi_s \boldsymbol{v}^s + \phi_f \boldsymbol{v}^f) = 0. \tag{13.3}$$

Here f and s symbolize fluid and solid, respectively, $\boldsymbol{\pi} = (\phi_f)^2(\boldsymbol{v}^f - \boldsymbol{v}^s)/k$ is the diffusive body force (cf., 10.76) and the mixture Cauchy stress is given by

$$\boldsymbol{T} = -p\boldsymbol{I} + \boldsymbol{\tau}, \quad \boldsymbol{\tau} = \lambda_s \text{ tr}(\boldsymbol{e})\boldsymbol{I} + 2\mu_s \boldsymbol{e}. \tag{13.4}$$

If we designate the opposing surfaces by superscripts 0 and 1, and solid and fluid volume fractions of corresponding layers by ϕ_{s0}, ϕ_{f0} and ϕ_{s1}, ϕ_{f1}, then for a saturated mixture we have

$$\begin{aligned} &\phi_{s0} + \phi_{f0} = 1, \quad \phi_{s1} + \phi_{f1} = 1 \\ &\phi_{s0}\phi_{s1} + \phi_{s0}\phi_{f1} + \phi_{f0}\phi_{s1} + \phi_{f0}\phi_{f1} = 1. \end{aligned} \tag{13.5}$$

Contacts of opposing cartilage surfaces are characterized as solid-solid, solid-fluid, fluid-solid, and fluid-fluid, the extent of these depending on solid and fluid area fractions of the opposing cartilage surfaces (for isotropic pore distributions these equal the respective volume fractions in the mixture). Statistically, solid-solid contact occurs over $(\phi_{s0}\phi_{s1})\,dA$, solid-fluid contact over $(\phi_{s0}\phi_{f1})\,dA$, and fluid-solid contact over $(\phi_{f1}\phi_{s0})\,dA$. The element area $(\phi_{f0}\phi_{f1})\,dA$ is characterized by fluid-fluid interaction.

Let $\boldsymbol{t}$, the surface traction over dA, be given by the sum of the partial surface tractions

$$\begin{aligned} \boldsymbol{t} &= \phi_{s0}\phi_{s1}\boldsymbol{t}_{ss} + \phi_{s0}\phi_{f1}\boldsymbol{t}_{sf} + \phi_{f0}\phi_{s1}\boldsymbol{t}_{fs} + \phi_{f0}\phi_{f1}\boldsymbol{t}_{ff} \\ &= \phi_{s0}\phi_{s1}\boldsymbol{t}_{ss} - (1 - \phi_{s0}\phi_{s1})p\boldsymbol{n}. \end{aligned} \tag{13.6}$$

Here we recognized that surface traction in our ideal fluid is normal to the surface and has magnitude p.

The total transmitted force across the contact is supplied by the integral

$$\boldsymbol{W} = \int_A \boldsymbol{t}\,dA. \tag{13.7}$$

On recognizing that $\boldsymbol{t} = \boldsymbol{n} \cdot \boldsymbol{T}$ (2.24), and taking (13.6) and (13.7) into account, the total load transmitted across the solid-solid interface is

$$\boldsymbol{W}^{ss} = \int_A (-\phi_{s0}\phi_{s1} p\boldsymbol{I} + \boldsymbol{\tau}) \cdot \boldsymbol{n}\,dA. \tag{13.8}$$

[1] For fundamentals of mixture theory, see Section 10.5.

Let $\boldsymbol{\varpi}$ represent the common unit tangent to the surfaces at contact in the direction of motion, then the normal and the tangential components of $\boldsymbol{W}$ and $\boldsymbol{W}^{ss}$ are, respectively,

$$\begin{aligned} W_n &= \int_A \boldsymbol{n}\cdot\boldsymbol{t}dA; \quad W_{\varpi} = \int_A \boldsymbol{\varpi}\cdot\boldsymbol{t}dA \\ W_n^{ss} &= \int_A \boldsymbol{n}\cdot(-\phi_{s0}\phi_{s1}p\boldsymbol{I}+\boldsymbol{\tau})\cdot\boldsymbol{n}dA; \quad W_{\varpi}^{ss} = \int_A \boldsymbol{\varpi}\cdot(-\phi_{s0}\phi_{s1}p\boldsymbol{I}+\boldsymbol{\tau})\cdot\boldsymbol{n}dA. \end{aligned} \tag{13.9}$$

The quantity W^p/W_n, where $W^p = -\int_A pdA$, is named by Ateshian (Krishnan et al., 2004) the, "interstitial fluid load support."[2]

Ateshian et al. (1998) define the effective value of the coefficient of friction by $\mu_{\text{eff}} = W_{\varpi}/W_n$ and its equilibrium value, manifested when all fluid has drained out of the cartilage and the entire load is transmitted via solid-solid contact, by $\mu_{\text{eq}} = W_{\varpi}^{ss}/W_n^{ss}$. In an ideal fluid, solid-fluid and fluid-fluid contact forces lack tangential component, therefore

$$W_{\varpi} = W_{\varpi}^{ss}; \qquad \mu_{\text{eff}} = \mu_{\text{eq}}\frac{W_n^{ss}}{W_n}. \tag{13.10}$$

Under load $W_n^{ss} \to W_n$ as $t \to \infty$, Eq. (13.10) has the potential to explain the above-mentioned time dependence of μ_{eff}. In the simplest case, solid-solid contact might be characterized by Coulomb friction, but the model is capable of admitting complex boundary lubrication effects.

In support of the hypothesis for biphasic boundary lubrication, Ateshian and associates measured the friction coefficient simultaneously with interstitial load support for bovine articular cartilage, demonstrating that the former correlates negatively with the latter (Krishnan et al., 2004). Figure 13.7 plots the effective coefficient of friction and the interstitial fluid load support against time for cartilage sliding against glass, under constant load. In the words of the authors of the paper, the results of this study provide "*experimental evidence in support of the primary role of interstitial fluid pressurization in the frictional response of articular cartilage*" (Krishnan et al., 2004).

Boundary Lubrication

Hydrodynamic lubrication and self-generating lubrication both presume existence of a lubricant film between the articulating surfaces, a condition that is not always satisfied. Yet the coefficient of friction remains low (Hills, 2000). Charnley (1960) was among the first to broach the possibility of *boundary lubrication*, where the articulating surfaces are separated by a monolayer of bio-lubricant. He and others, e.g., Maroudas, argued that the hyaluronic acid complex found in the synovial fluid fulfilled the function of a boundary lubricant. However, while the SF was found to perform well as a bulk lubricant in the hydrodynamic mode, its performance in the boundary mode has been questioned. As concluded by Jay et al. (2007), hyaluronic acid (HA) will impart viscosity to the synovial fluid, but does not act, itself, as a lubricant in the boundary mode.

The synovial fluid is a shear thinning, non-Newtonian fluid; it exhibits high viscosity at low shear rates, but at physiological shear rates ($\dot{\gamma} = 10^5\,\text{s}^{-1}$ or higher) its viscosity becomes comparable to that of water. In consequence, according to Klein (2006), at high shear rate the SF will be "squeezed right out from between the sliding articular surfaces at

[2]Note, that the actual load supported by the interstitial fluid is $-\int_A(1-\phi_{s0}\phi_{s1})pdA$.

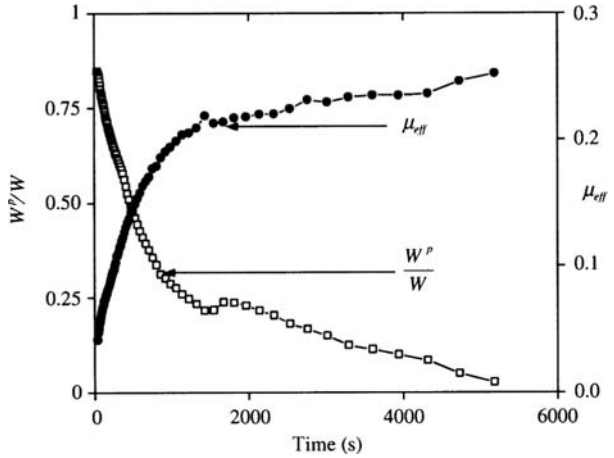

Figure 13.7. Variation of the effective friction coefficient, μ_{eff}, and the interstitial fluid load support, W^p/W_n, with time (Reprinted with permission from Krishnan, R., Kopacz, M. and Ateshian, G. A. Experimental verification of the role of interstitial fluid pressurization in cartilage lubrication, *Journal of Orthopaedic Research*, **22**, 565–570, 2004, John Wiley and Sons.)

normal pressure." Klein thus supports the earlier conclusion that boundary lubrication plays an important role in joint lubrication and it is the surface-attached molecules "*that must be providing the remarkable lubrication characteristic of healthy synovial joints*" (Klein, 2006).

In addition to hyaluronan molecules, the synovial fluid contains the glycoprotein lubricin (PRG4), sometimes also known as superficial zone protein (SZP), and various surface-active phospholipids (SAPL). Hills (2000) advocated that hydrophobicity was imparted to sliding surfaces by adsorbed SAPL as a monolayer or oligolamellar layers. Klein (2006), on studying the molecular mechanism of synovial joints, contradicted the suggestion that macromolecules could be adsorbed to the cartilage surface from solution, as both synovial macromolecules and cartilage surface are negatively charged. In any case, adsorbed macromolecules do not provide for exceptionally good lubrication. Instead, Klein advanced the hypothesis that the synovial polyelectrolytes responsible for good lubrication of the cartilage, namely lubricin and aggrecan, are released by chondrocyte cells within the cartilage below the superficial zone and subsequently diffuse and are secreted into the synovial space through the superficial zone surface. These flexible, negatively charged macromolecules will "*at some point in their passage through the surface adopt configurations in which they are partly within the superficial zone and partly emanating away from it into the synovial space*" (Klein, 2006), where they form brushlike structures. This is indicated schematically in Figure 13.8. Under compression, it is further hypothesized, the opposing brushes will deform into thinner layers rather than interpenetrate (Klein, 2006; Zappone et al., 2007): an eightfold compression of the layers only doubles the extent of interpenetration, thus keeping the coefficient of friction low. The brushes are aided in their friction-lowering performance by trapped hydrated ions that act like "ball-bearings" (Klein, 2006).

A great deal of research is currently being performed toward evaluating the lubricating capability of the various constituents of the synovial fluid. In contrast to Klein (2006), Schmidt et al. (2007) find that each constituent of the SF interacts with, and adsorbs to, the

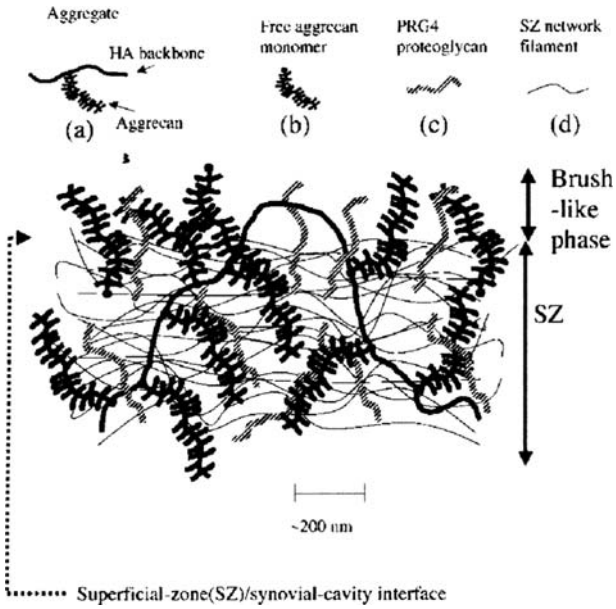

Figure 13.8. Schematics of the brush-like surface phase formed by synovial macromolecules (Reproduced with permission from Klein, J. Molecular mechanisms of synovial joint lubrication. *Proc IMechE Journal of Engineering Tribology*, **220**, 691–710, Copyright (2006) Professional Engineering Publishing.)

articular surface, contributing both individually and in combinations toward lowering the coefficient of friction. Figures 13.9(i), 13.9(ii) and 13.9(iii) show static friction and average kinetic friction coefficients in phosphate buffered saline (PBS) and various concentration of SF, HA, and PRG4. Schmidt et al. conclude, however, that the "*combination of the SF constituents HA, PRG4, and SAPL at physiological concentrations approaching, but not fully replicating, the boundary-lubricating ability of SF suggests that additional lubricating molecules and/or complexes remain to be identified*" (Schmidt et al., 2007).

Jay et al. (2007) single out lubricin (PRG4) as the primary boundary lubricant, and argue that SF lacking in lubricin cannot reduce friction, nor does it prevent cartilage wear when acting in the boundary mode. Using a pendulum apparatus, they evaluate the importance of lubricin by (1) comparing the knee joint of normal and lubricin-mutant mice and (2) testing SF samples from patients with the autosomal recessive disorder CACP that is characterized by lubricin deficiency. These studies demonstrate that SF lacking in lubricin is unable to reduce friction in the boundary mode, clarifying why patients with CACP are prone to precocious joint failure. The joints of lubricin-mutant mice showed early wear and higher friction than those of the "wild" type. In the case of two-month-old mice, the mean coefficient of friction for those with lubricin was measured at 0.0013 and for lubricin-mutant mice at 0.0023. The smallness of this increase of friction is attributed to the effectiveness of biphasic lubrication even in lubricin-mutant mice; however, even this modest increase in friction was sufficient to cause damage to the cartilage. Lubricin self-organized and reduced the work of adhesion between opposing asperities, according to Jay et al. (2007). Synovial fluid from CACP patients was evaluated in vitro for coefficient of friction, using a saline solution with a coefficient of friction of 0.1. Measured values of the coefficient of friction for the SF of six CACP patients were indistinguishable from those obtained with saline

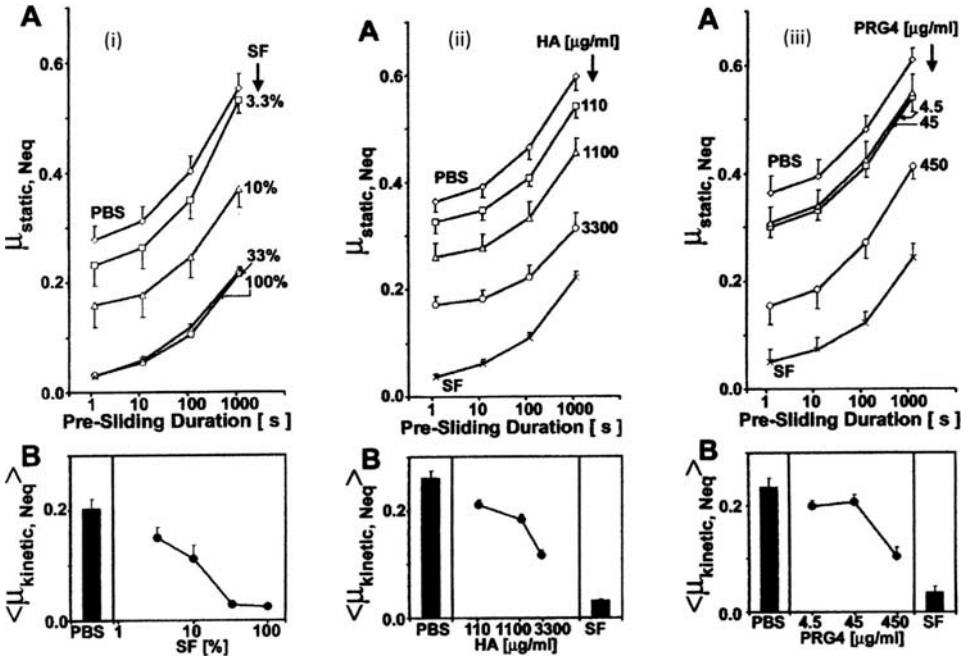

Figure 13.9. Effect of graded concentration of (i) synovial fluid (SF), (ii) hyaluronan (HA), and (iii) proteoglycans 4 (PRG4), respectively, on the boundary lubrication of articular cartilage: **A**, static friction; **B**, average kinetic friction, pre-sliding duration 1.2 s. (Reprinted with permission from Schmidt, T. A., Gastelum, N. S., Nguyen, Q. T. Schumacher, B. L. and Sah, R. L. Boundary lubrication of articular cartilage. *Arthritis & Rheumatism*, **56**(3), 882–891, Copyright (2007) John Wiley and Sons.

alone and none of the fluids showed ability to lubricate in the boundary mode. Jay et al. conclude that HA alone does not act as a boundary lubricant, only when it is chemically bound to the surface; lubricin has a hyaluronate-binding region and might help anchor HA to articular cartilage in a synergism of the two macromolecules.

The lubricin molecule (Figure 13.10) forms the mucous coating of many surfaces in the human body (eyelids, gastrointestinal tract, etc.). With a contour length of 200 ∓ 50 nm

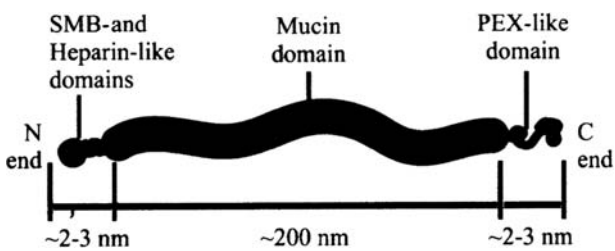

Figure 13.10. Schematic representation of the lubricin structure. The N- and C- ends are separated by a large, negatively charged mucin-like domain (Reprinted from *Biophysical Journal*, **92**, Zappone, B., Ruths, M., Greene, G. W., Jay, G. D. and Israelachvili, J. Adsorption, lubrication and wear of lubricin on model surfaces: polymer brush-like behavior of a glycoprotein, 1693–1708, Copyright (2007), with permission from Elsevier.)

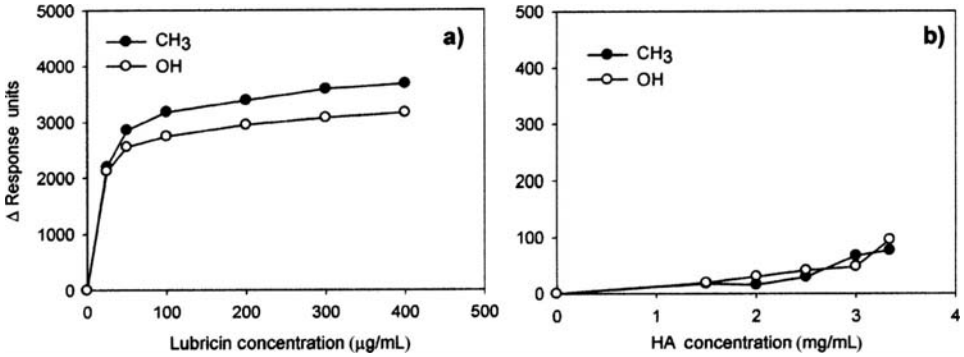

Figure 13.11. Change in SPR response units (RU) with respect to PBS baseline (Reprinted with permission from Chang, D. P., Abu-Lail, N. I., Guilak, F., Jay, G. D., and Zauscher, S. Conformational mechanics, adsorption, and normal force interactions of lubricin and hyaluronic acid on model surfaces. *Langmuir*, **24**, 1183–1193, Copyright (2008) American Chemical Society).[3]

and a few nanometers in diameter, it possesses a small net positive charge, though its center domain is negatively charged and hydrophilic (Zappone et al., 2007, Chang et al., 2008).

In contrast to Klein (2006), Zappone et al. found lubricin to adsorb from buffered saline solution on various surfaces: (1) negatively charged mica, (2) positively charged poly-lysine (on mica) and aminothiol (on gold), and (3) hydrophobic self-assembled monolayers of alkanethiol (on gold), in the form of a dense layer of end-grafted single tails or loops, 50–100 nm in thickness. The frictional characteristics and wear damage of the surfaces were shown to be intimately connected to the strength of the adsorption.

Chang et al. (2008) performed both normal force and adhesion measurements on lubricin, hyaluronic acid and their mixture, on substrates functionalized with hydrophilic (–OH terminated) or hydrophobic ($-CH_3$ terminated) self-assembled monolayers. Typical adsorption isotherms for lubricin and HA, obtained from surface plasma resonance (SPR) technique is shown in Figure 13.11. Lubricin adsorbed significantly more than did HA on both hydroxyl and methyl surfaces. Chang et al. find agreement with conformation of adsorbed lubricin as proposed by Zappone et al. (2007); on hydrophobic surfaces it is looplike, with the end domains of the molecule serving as anchors. On hydrophilic surfaces, it adopts a taillike conformation.

As we have discussed above, there are, roughly speaking, three directions of research pertaining to friction in diarthrodial joints, each receiving primary support from one of three different camps of researchers. There is a strong urging to liken lubrication of joints to lubrication of machine elements, especially by investigators having background in the latter. In contrast, researchers in biomechanics seem to prefer explanations based on the poroelastic nature of cartilage, while those with background in chemistry and medicine investigate lubrication in the boundary mode. It is, of course, generally accepted that lubrication of diarthrodial joints cannot be explained by any one mechanism alone, rather, that during different phases of the load cycle (cf., Figure 13.1), different mechanisms come into play and that, during any phase of the cycle, joint performance is the result of a combination of fluid-film and boundary lubrications in synergy. It is well to bear in

[3]The resonance unit 1 RU$\sim$1 μg/cm^2.

mind that the various lubrication mechanisms operate at different length and time scales. Microelastohydrodynamic lubrication is operational at higher relative speeds and larger separation of the articulating surfaces, as in the knee joint during the swing phase of the cycle. Boosted, weeping and biphasic boundary lubrication are called upon at first asperity contact, while at direct cartilage-cartilage contact, lubrication is provided by the synovial fluid macromolecules as they attach to the cartilage surfaces.

13.2 Artificial Joints

Total joint replacement procedures have been performed for several decades; they represent one of the most successful applications of biomechanics. Almost all of us are acquainted with persons whose life has been changed for the better by a total joint replacement procedure. Over 800,000 hip joints are replaced worldwide annually (Jin and Dowson, 2005). The Merrill-Lynch report, quoted in Isaac et al. (2009), puts this number at approximately 1,500,000. Though the number of total knee replacements is lower than this, knee replacements are becoming increasingly more popular, especially in the United States. Nevertheless, we discuss only hip joint replacement in this section.

Types of Total Hip Replacement (THR)

In a healthy hip joint, the ball shaped head of the femur or thighbone articulates within the cuplike socket, called the acetabulum, of the pelvic bone. Total hip replacement (THR) or total hip arthroplasty (THA) are synonymous names given to the orthopedic procedure that replaces the severely damaged hip with an artificial joint. The artificial joint consist of a socket, the acetabular cup and its liner that replace the acetabulum of the hip joint, and a ball mounted on a wedge-shaped stem that replaces the ball of the hip joint and the upper part of the femur. The stem is driven into the femur and held in position by cement. In some variations of the prosthesis, the cup is screwed into the pelvis and/or held in place by cement. Figure 13.12 is an X-ray photograph of a human pelvis; the right hip has been replaced by a ball and socket.

In one of the earliest recorded hip replacements, Glück fixed an ivory ball and socket joint to the bone with nickel-plated screws (McKee, 1982). Later, Glück experimented with a grouting compound for fixation. The Burmese orthopedic surgeon San Baw performed some 600 total hip replacement surgeries, starting from 1960, also using femora carved from ivory. Ivory gave way to metal-on-metal and to metal-on-polymer implants by the mid 1960s. The former was typified by the McKee-Farrar joint (McKee and Watson-Farrar, 1966) while Sir John Charnley of Wrightington Hospital near Wigan, England, pioneered the metal-on-polymer joint. The metal-on-metal joint had serious problems to start with, mainly because the ball and socket, both made of stainless steel, were manufactured to the same radius. Even then, the joint had the advantage of producing little wear (McKee, 1982). It was recognized only later that a finite clearance was necessary to avoid equatorial binding and thus decrease friction.

Charnley first employed a metal femur articulating against a Teflon® cup, but soon realized that the wear rate was excessive and by 1962 replaced the polytetrafluoroethylene with ultra-high molecular weight polyethylene (UHMWPE).[4] Both femoral and acetabular

[4]The ubiquitous UHMWPE is a linear polymer with a molecular weight in the range of $3 - 6 \times 10^6$ g/mol.

Figure 13.12. The patient's right hip (left on image) has been replaced, with a metal head that is set in the femur and the socket replaced by a white plastic cup (NIADDK, 9AO4, Connie Raab-contact; NIH.)

components were fixed to the bone using acrylic bone cement, the use of which was also pioneered by Charnley. This replacement joint, known as the Charnley Low Friction Arthroplasty (LFA), was lubricated with synovial fluid. For over two decades, the Charnley design was the most used THR system in the world, far surpassing other available options. In the original design, the femoral stem had a collar, discernible on the photograph in Figure 13.12; this was deemed necessary for transmitting the hip joint loads directly onto the cut surface of the femoral neck. Today over 80% of artificial hip joints utilize polyethylene acetabular cups articulating on metal or ceramic femoral heads (Galvin et al., 2005). Artificial joints can be either cemented or non-cemented. While cemented implants are for older patients with poor quality bones, non-cemented implants are usually reserved for young, healthy, individuals with strong bones.

The critical quantities to investigate when selecting a THR construction are not unlike those for choosing bearings as machine elements, namely friction, wear, and minimum film thickness. The coefficient of friction varies (Scholes and Unsworth, 2000), 0.02 for ceramics-on-ceramics (COC), 0.05 for metal-on-polymer (MOP) and 0.18 for metal-on-metal (MOM). The wear rate also fluctuates considerably from joint to joint and some THRs last for considerable time; there is a case reported in the literature where the life of the prosthesis exceeded 50 years. After 50 years in service, the right and left penetration rates[5] were measured at 100 and 50 μm/year, respectively (Dawson, 2001). However, the normal length of life of an implant is closer to 10–25 years. Another problem with wear besides the structural one is that the tissue surrounding the prosthesis must absorb the wear particles, which, though in the nanometer-micrometer range (Brown et al., 2007), are very numerous. Consider, as an example, the measured wear rate of 35 $\text{mm}^3/10^6$ cycles for metallic head and UHMWPE cup (Fisher et al., 2006). Particles from UHMWPE surfaces

[5]To relate wear volume (δV) to depth of penetration (p) Dowson employs the simplified formula $\delta V \approx \pi R_1^2 \{p/[1 + C/p]\}$, where $C = R_2 - R_1$ (cf., Ilchmann et al., 2008).

Table 13.2. *Major types of THRs, their approximate date of introduction*

Approximate date of introduction	Type of bearing	Reference
1951	metal on metal, 1st cycle (1)	McKee and Watson-Farrar (1966)
1958	metal on PFTE (1)	Charnley (1961)
1962	metal on UHMWPE (1)	Fisher et al. (2006)
1970	ceramic on ceramic (2)	Boutin et al. (1972)
1977	ceramic on UHMWPE (1)	Semlitsch et al. (1977)
1980	metal on metal, 2nd cycle (2)	Müller (1995)
1995	metal/ceramic on XLPE* (1)	Oonishi (1995)
2000	ceramic on metal (2)	Firkins et al. (2000)

* Highly cross-linked polyethylene (Kurtz et al., 1999).

are in the 0.1–1.0 μm range (Brocket et al., 2006). For simplicity, in this illustration we assume uniform particles 1 μm in diameter, yielding 6.6845 $\times 10^{10}$ particles per million cycles. A million cycles per year represent 2747 steps per day, and for the average patient this translates to 66,845 particles per steps. Osteolysis from polyethylene wear debris has become one of the most significant factors to limit long-term survival of implants (D'Lima et al., 2003). There is less wear for metal-on-metal and ceramic-on-ceramic implants. However, the wear particles are smaller and, therefore, more numerous and more insidious with respect to osteolysis (Brown et al., 2007).

Full film lubrication is desirable to eliminate wear and keep friction small. However, the film might be broken at places leading to mixed lubrication, while in other cases boundary lubrication is prevalent. One way to estimate the effective lubrication regime in which the implant operates is to examine the ratio $\lambda = h_{\min}/\bar{R}_a$, where $\bar{R}_a = (R_{a1}^2 + R_{a2}^2)^{1/2}$ is the effective r.m.s roughness of the two surfaces. A value of $\lambda < 1$ signifies boundary lubrication while $\lambda > 3$ suggests a full fluid film. Some suggested values of λ are 0.5–1 for metal-on-polymer and > 3 for ceramic on ceramic.

There are a large number of different implants at the surgeon's disposal. Already in 1955, Murray and his co-workers listed 62 different primary THRs, manufactured by 19 different companies. Half of these had been introduced during the five previous years, and only 30% had any performance results published in peer-reviewed journals. The price of the implants ranged from £250 to £2000, but, interestingly enough, the two cheapest implants had the longest reported follow-up (Murray et al., 1995). We list some of the major types of THRs, their approximate date of introduction, and significant references to the implants in Table 13.2. The entries in this table can be conveniently placed in two categories of THR: category (1) is for hard on soft and (2) for hard on hard constructs. There is yet a third category not listed in the table, hard femoral ball articulating against the compliant lining of the acetabular cup (Scholes et al., 2006).

Mathematical Modeling

Before a mathematical analysis of the lubrication of THRs can be attempted, we need to represent the Reynolds equation in spherical coordinates. This is easily

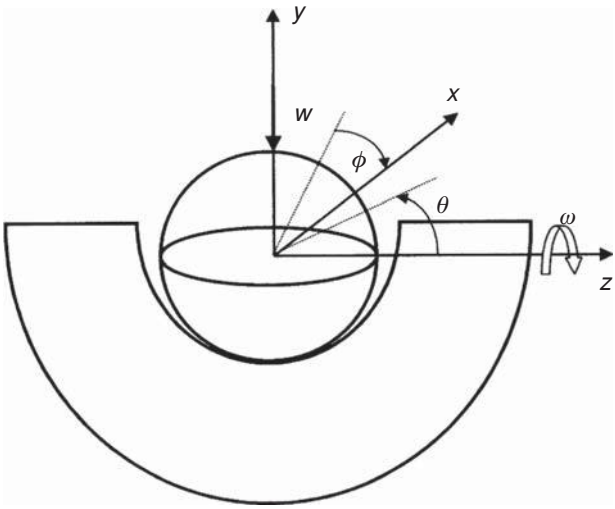

Figure 13.13. Total hip replacement model geometry. (Reproduced with permission from Jagatia, M. and Jin, Z. M. Elastohydrodynamic lubrication analysis of metal-on-metal hip prostheses under steady state entraining motion. Proc *IMechE Journal of* Engineering in Medicine, **215**, 531–541, Copyright (2001) Professional Engineering Publishing.)

accomplished when writing the vector form of Eq. (2.80)

$$\operatorname{div}\left(\frac{h^3}{\mu}\operatorname{grad} p - 6\boldsymbol{U}_0 h\right) = 0. \tag{13.11}$$

In spherical coordinates the gradient and divergence operators are given by

$$\operatorname{grad} p = \frac{\partial p}{\partial r}\boldsymbol{i}_r + \frac{1}{r}\frac{\partial p}{\partial \theta}\boldsymbol{i}_\theta + \frac{1}{r\sin\theta}\frac{\partial p}{\partial \varphi}\boldsymbol{i}_{\boldsymbol{\varphi}}$$

$$\operatorname{div}\boldsymbol{A} = \frac{1}{r^2}\frac{\partial(r^2 A_r)}{\partial r} + \frac{1}{r\sin\theta}\frac{\partial(A_\theta \sin\theta)}{\partial \theta} + \frac{1}{r\sin\theta}\frac{A_\varphi}{\partial \varphi}.$$

Specifying constant radius at $r = R_2$ and substituting into Eq. (13.11) leads to the Reynolds equation in spherical coordinates

$$\sin\theta\frac{\partial}{\partial\theta}\left(h^3\sin\theta\frac{\partial p}{\partial\theta}\right) + \frac{\partial}{\partial\varphi}\left(h^3\frac{\partial p}{\partial\varphi}\right) = 6\mu R_2^2\omega\sin^2\theta\frac{\partial h}{\partial\varphi}. \tag{13.12}$$

Here we considered only steady state and rotation about the z-axis as in Figure 13.13.

The Reynolds equation is normalized as follows:

$$H = \frac{h}{C};\quad P = \frac{p}{E};\quad \lambda = \frac{6\mu R_2^2\omega}{C^2 E};\quad W = \frac{w}{E R_2^2}$$
$$\sin\theta\frac{\partial}{\partial\theta}\left(H^3\sin\theta\frac{\partial P}{\partial\theta}\right) + \frac{\partial}{\partial\varphi}\left(H^3\frac{\partial P}{\partial\varphi}\right) = \lambda^2\sin^2\theta\frac{\partial H}{\partial\varphi}. \tag{13.13}$$

The discretized form of Eq. (13.13) is

$$\begin{aligned} F_{i,j} \equiv \frac{1}{2\Delta\varphi^2}\left[\left(H_{i-1,j}^3 + H_{i,j}^3\right)P_{i-1,j} - \left(H_{i-1,j}^3 + 2H_{i,j}^3 + H_{i+1,j}^3\right)P_{i,j}\right. \\ \left. + \left(H_{i,j}^3 + H_{i+1,j}^3\right)P_{i+1,j}\right] + \frac{\sin\theta_j}{2\Delta\theta^2}\left[\left(H_{i,j-1}^3\sin\theta_{j-1} + H_{i,j}^3\sin\theta_j\right)P_{i,j-1}\right. \\ - \left(H_{i,j-1}^3\sin\theta_{j-1} + 2H_{i,j}^3\sin\theta_j + H_{i,j+1}^3\sin\theta_{j+1}\right)P_{i,j} \\ \left. + \left(H_{i,j}^3\sin\theta_j + H_{i,j+1}^3\sin\theta_{j+1}\right)P_{i,j+1}\right] - \lambda\sin^2\theta_j\frac{H_{i,j} - H_{i-1,j}}{\Delta\varphi} = 0. \end{aligned} \tag{13.14}$$

Here $H_{i,j} = h_{i,j}/C$ is the normalized film thickness and

$$h_{i,j} = C(1 - \varepsilon_x\sin\theta_i\cos\varphi_j - \varepsilon_y\sin\theta_i\sin\varphi_j) + \delta_{i,j}.$$

To calculate the elastic deformation of the UHMWPE cup, Jalali-Vahid et al. (2001) used the constrained column model, according to which the deflection at a point is linearly dependent on the local pressure at that point and no other pressure

$$\delta_{\alpha,\beta} = \frac{R_2\left[\left(\dfrac{R_3}{R_2}\right)^3 - 1\right]p_{\alpha,\beta}}{E\left[\dfrac{1}{1-2\nu} + \dfrac{2}{1+\nu}\left(\dfrac{R_3}{R_2}\right)^3\right]}. \tag{13.15}$$

Jagatia and Jin (2001), in contrast, relied on finite element computations to evaluate $D_{\alpha,\beta} = \delta_{\alpha,\beta}/C$.

The discretized equation (13.14) was solved by the Newton-Raphson method. The elements of the Jacobian matrix are given by

$$\begin{aligned} \frac{\partial F_{i,j}}{\partial P_{i-1,j}} &= \frac{1}{2\Delta\varphi^2}\left[H_{i-1,j}^3 + H_{i,j}^3 + 3H_{i-1,j}^2D'_{i-1,j}P_{i-1,j} - 3H_{i-1,j}^2D'_{i-1,j}P_{i,j}\right] \\ &\quad + \lambda\sin^2\theta_j\left(-\frac{D'_{i-1,j}}{\Delta\varphi}\right) \\ \frac{\partial F_{i,j}}{\partial P_{i+1,j}} &= \frac{1}{2\Delta\varphi^2}\left[H_{i,j}^3 + H_{i+1,j}^3 - 3H_{i+1,j}^2D'_{i+1,j}P_{i,j} - 3H_{i+1,j}^2D'_{i+1,j}P_{i+1,j}\right] \\ \frac{\partial F_{i,j}}{\partial P_{i,j-1}} &= \frac{\sin\theta_j}{2\Delta\theta^2}\left[H_{i,j-1}^3\sin\theta_{j-1} + H_{i,j}^3\sin\theta_j - 3H_{i,j-1}^2\sin\theta_{j-1}D'_{i,j-1}P_{i,j}\right. \\ &\quad \left. + 3H_{i,j-1}^2\sin\theta_{j-1}D'_{i,j-1}P_{i,j-1}\right] \\ \frac{\partial F_{i,j}}{\partial P_{i,j+1}} &= \frac{\sin\theta_j}{2\Delta\theta^2}\left[H_{i,j+1}^3\sin\theta_{j+1} + H_{i,j}^3\sin\theta_j - 3H_{i,j+1}^2\sin\theta_{j+1}D'_{i,j+1}P_{i,j}\right. \\ &\quad \left. + 3H_{i,j+1}^2\sin\theta_{j+1}D'_{i,j+1}P_{i,j+1}\right] \\ \frac{\partial F_{i,j}}{\partial P_{i,j}} &= \frac{1}{2\Delta\varphi^2}\left[3H_{i,j}^2D'_{i,j}P_{i-1,j} - \left(H_{i-1,j}^3 + 2H_{i,j}^3 + H_{i+1,j}^3\right) + 3H_{i,j}^2D'_{i,j}P_{i+1,j}\right] \\ &\quad - 6H_{i,j}^2D'_{i,j}\left(\frac{1}{2\Delta\varphi^2} + \frac{\sin\theta_j}{\Delta\theta^2}\sin\theta_j\right)P_{i,j} + \frac{\sin\theta_j}{2\Delta\theta^2}\left[3H_{i,j}^2\sin\theta_jD'_{i,j}P_{i,j-1}\right. \\ &\quad - \left(H_{i,j-1}^3\sin\theta_{j-1} + 2H_{i,j}^3\sin\theta_j + H_{i,j+1}^3\sin\theta_{j+1}\right) \\ &\quad \left. + 3H_{i,j}^2\sin\theta_jD'_{i,j}P_{i,j+1}\right] - \lambda\sin^2\theta_j\frac{D'_{i,j}}{\Delta\varphi}. \end{aligned} \tag{13.16}$$

Here we employ the notation $D'_{\alpha,\beta} \equiv \partial D_{\alpha,\beta}/\partial P_{\alpha,\beta}$.

The load components can be obtained by summation from

$$F_x = \frac{R_2^2}{4} \sum_{i=1}^{n} \sum_{j=1}^{m} (\varphi_{i+1} - \varphi_i)(\theta_{j+1} - \theta_j) M_{i,j}$$
$$F_y = \frac{R_2^2}{4} \sum_{i=1}^{n} \sum_{j=1}^{m} (\varphi_{i+1} - \varphi_i)(\theta_{j+1} - \theta_j) N_{i,j}. \tag{13.17}$$

Here $m \times n$ is the mesh dimension and the arrays $M_{i,j}$, $N_{i,j}$ are defined as

$$M_{i,j} = \begin{bmatrix} P_{i,j} \sin\theta_j \cos\varphi_i \sin\theta_j + \\ P_{i+1,j} \sin\theta_j \cos\varphi_{i+1} \sin\theta_j + \\ P_{i,j+1} \sin\theta_{j+1} \cos\varphi_i \sin\theta_{j+1} + \\ P_{i+1,j+1} \sin\theta_{j+1} \cos\varphi_{i+1} \sin\theta_{j+1} \end{bmatrix}$$

$$M_{i,j} = \begin{bmatrix} P_{i,j} \sin\theta_j \sin\varphi_i \sin\theta_j + \\ P_{i+1,j} \sin\theta_j \sin\varphi_{i+1} \sin\theta_j + \\ P_{i,j+1} \sin\theta_{j+1} \sin\varphi_i \sin\theta_{j+1} + \\ P_{i+1,j+1} \sin\theta_{j+1} \sin\varphi_{i+1} \sin\theta_{j+1} \end{bmatrix}.$$

Hard-on-Soft THR

This category comprises metal or ceramic femoral ball articulating against polymeric acetabular cup. As already mentioned, by 1962 Charnley substituted UHMWPE for Teflon in his low-friction arthroplasty, because of the high wear rate in the former. The metal was stainless steel in the original design but was subsequently changed to a CoCrMo alloy. The coefficient of friction is in the 0.02–0.06 range for metal head on UHMWPE and 0.015–0.099 for ceramic head (Scholes and Unsworth, 2000; Dowson, 2001).

Elastohydrodynamic lubrication analysis of THR was reported by Jalali-Vahid et al. (2000, 2001). The cup was held stationary in these investigations while the head was made to rotate about the z-axis at a steady angular velocity ω. The elastic deformation of the UHMWPE cup was computed from Eq. (13.15). The hydrodynamic pressure was determined employing the effective influence Newton method (EIN) as described in Section 8.6.

The effect of varying femoral head radius, radial clearance, elastic modulus and UHMWPE liner thickness are indicated in Figures 13.14 and 13.15. The base input data for these figures are as follows:

$$\omega = 2\,\text{rad/s}; \quad w = 2500\,\text{N}; \quad \mu = 0.005\,\text{Pa}\cdot\text{s}; \quad d = 5 - 15\,\text{mm};$$
$$R_1 = 11 - 16\,\text{mm}; \quad E = 250 - 2000\,\text{Mpa}; \quad C = 75 - 200\,\mu\text{m}.$$

Larger elastic modulus and larger clearance both tend to reduce the minimum film thickness while the femoral head radius and the thickness of the UHMWEPE lining correlate directly with minimum film thickness (Jalali-Vahid et al., 2001).

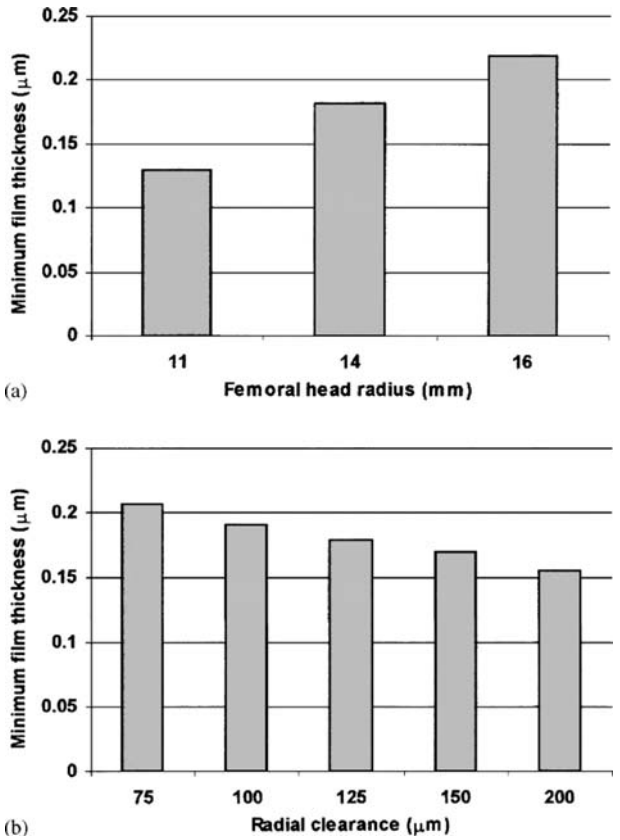

Figure 13.14. Variation of minimum film thickness with (a) femoral head radius, (b) radial clearance (Reprinted from *Journal of Biomechanics*, **34**, Jalali-Vahid, D, Jagatia, M., Jin, Z. M., Dowson, D. Prediction of lubricating film thickness I UHMWPE hip joint replacement. 261–266, Copyright (2001), with permission from Elsevier.)

The minimum film thickness was curve-fit by Jalali-Vahid and is given relative to the film thickness in a ball-on-plane geometry of Wang (1994).

$$\frac{h_{\min}}{(h_{\min})_{b-p}} = 1.0191\left(\frac{\phi_0}{90}\right)^4 - 2.3153\left(\frac{\phi_0}{90}\right)^3 + 0.8151\left(\frac{\phi_0}{90}\right)^2 - 0.1133\left(\frac{\phi_0}{90}\right) + 1. \tag{13.18}$$

Here $(h_{\min})_{b-p}$ is the ball-on-plane minimum film thickness

$$(h_{\min})_{b-p} = 1.47RU^{2/5}M^{(38M^{-2.20}+0.0045\log M-0.214)}. \tag{13.19}$$

The Moes load parameter in (13.18) is defined as $M = W/U^{4/5}$ with

$$W = \frac{(1-2\nu)}{(1-\nu)^2}\left(\frac{d}{R}\right)\left(\frac{w}{E'R^2}\right); \quad U = \frac{(1-2\nu)}{(1-\nu)^2}\left(\frac{d}{R}\right)\left(\frac{\mu u}{E'R}\right); \quad E' = \frac{E}{(1-\nu)^2}.$$

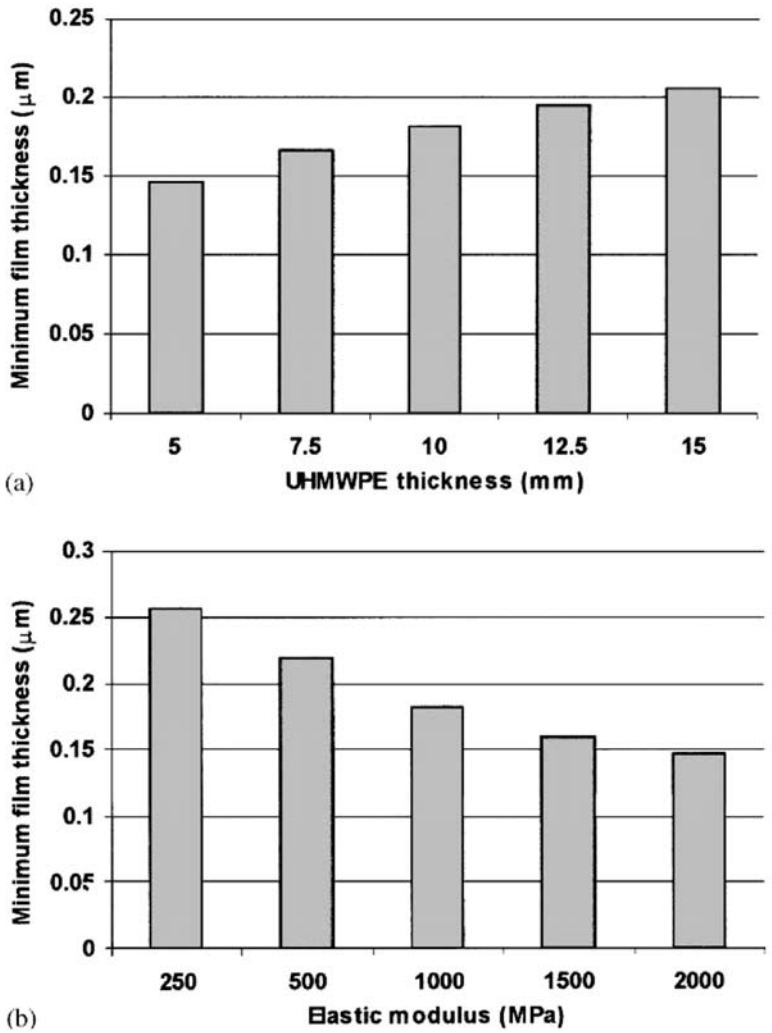

Figure 13.15. Variation of minimum film thickness with (a) UHMWPE thickness, (b) magnitude of elastic modulus (Reprinted from *Journal of Biomechanics*, **34**, Jalali-Vahid, D., Jagatia, M., Jin, Z. M., Dowson, D. Prediction of lubricating film thickness in UHMWPE hip joint replacement. 261–266, Copyright (2001), with permission from Elsevier.)

Jalali-Vahid et al. (2001) employed the correlation (Eq. 13.18) in a parametric study but found that the minimum film thickness for realistic conditions (see Figures 13.14–13.15) was far below the estimated 1 μm roughness of the UHMWPE. This strongly intimates that metal-on-UHMWPE prostheses are lubricated in the mixed mode where at least some of the load is carried by the contacting asperities and the lubricant film is not continuous.

Wear rate of UHMWPE cup articulating against metal femoral head has been observed at 35–50 mm^3/year, leading to 0.17 mm/year linear penetration. Under fortunate circumstances, this gives 15–25 year life to Charnley-type THRs. Unfortunately, the life

expectancy of the THR before corrective surgery is considerably less, owing to osteolysis, sometimes referred to as plastic disease. This circumstance led researchers on a quest for improved materials, during the second half of the last century. Another impetus for the search was the fact that younger, and therefore more active, patients now receive hip implants. To satisfy their requirement for increased stability and greater range of motion, surgeons were experimenting with larger femoral heads. But a larger femoral head promotes occurrence of osteolysis; the larger head leads to increased rate of wear simply because it affords larger travel for the femoral head for the same angular motion (Dowson, 2001; Fisher et al., 2006). This conclusion, however, does not seem to apply to metal-on-metal bearings. Affatato et al. (2008), for example, found that a 28 mm femoral head had twice the wear volume of a 54 mm head in metal-on-metal bearings, presumably because larger heads favor full film lubrication.

Different materials, such as carbon-reinforced plastics, were tried to improve the wear rate of acetabular caps. It was observed that polyethylene responded favorably to wear if the relative motion was along the fiber axis but performed poorly when it was loaded off axis (D'Lima et al., 2003). This suggested that three-dimensional cross-linking of polymer chains would toughen up UHMWPE. Cross-linking of polymer is performed by radiation or by chemical means (Kurtz et al., 1999).

The idea of cross-linking seemed to work, some researchers were unable to detect any wear of the highly cross-linked polymer (D'Lima et al., 2003). According to a recent publication by the University of Leeds Biotribology Lab (Fisher et al., 2006), the wear rate of highly cross-linked polyethylene is 1/8th of that of traditional polyethylene. However, the particle size from the former is submicron, which is more insidious for osteolysis than are larger particles, thus Specific Biological Activity of highly cross-linked polyethylene is almost twice that of conventional polyethylene. Fisher et al. define also a Functional Biological Activity, which considers wear rate, leading, in the present case to functional biological activity for highly cross-linked polyethylene 1/4th of that for traditional polyethylene. Fisher et al. (2006) also find that the wear rate decreases when changing from a metal to an alumina ceramic head; for conventional polyethylene cup this change is from 35 mm^3/year to 25 mm^3/year.

Hard-on-Hard THR

Archard's wear formula (Eq. 1.30)

$$V = K\frac{WL}{H}$$

suggests that a hard-on-hard bearing would have less wear than a hard-on-soft construct, and as wear particles play a major role in osteolysis, it is natural to turn attention to metal and ceramic components for both socket and ball. Two hard bearing surfaces articulating against one another will have a lower rate of wear, important particularly for young and more agile patients.

The problem with the original McKee prosthesis was the lack of clearance between cup and ball, and the consequent high friction and occasional equatorial seizing of the components. For hard-on-hard construct, it is essential to have hydrodynamic lubrication to avoid the high friction. In today's constructions, a radial clearance of 54 μm on a 28 mm

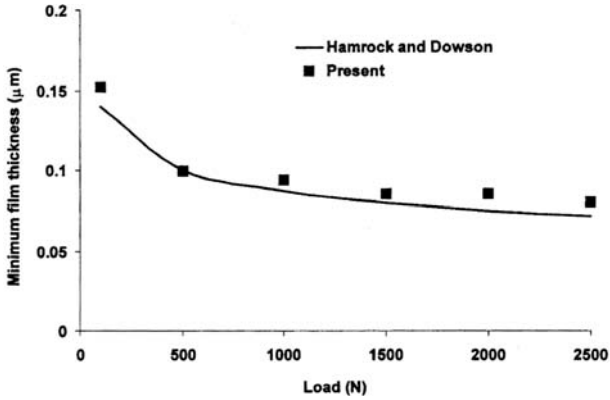

Figure 13.16. Comparison between spherical and ball-on-plane geometries (Reproduced with permission from Jagatia, M. and Jin, Z. M. Elastohydrodynamic lubrication analysis of metal-on-metal hip prostheses under steady state entraining motion. *Proc IMechE Journal of Engineering in Medicine*, **215**, 531–541, Copyright (2001) Professional Engineering Publishing.)

diameter cup is usual. For metal-on-metal and ceramic-on-ceramic bearings $\lambda > 3$, pointing to full film lubrication, thus EHL analysis does have a place in these investigations.

In their analysis of metal-on-metal prostheses, Jagatia and Jin (2001) start form the spherical coordinate form of the Reynolds equation, Eq. (13.13). However, while Jalali-Vahid calculated surface deformation approximately, Jagatia and Jin obtain it by finite element methods.[6] They use the effective influence Newton method, thus a new pressure difference at $(k + 1)$ step was obtained from the assumed one at (k) from

$$\Delta P^{(k+1)} = \frac{F_{i,j}(P^k)}{(\partial F/\partial P_{i,j})}$$

$$P^{(k+1)} = P^{(k)} + \gamma \Delta P^{(k+1)}.$$

Jagatia and Jin find that the thickness of the backing material to the acetabular cup makes little difference to either contact pressure or elastic deformation. More surprisingly, as indicated in Figure 13.16, they show good agreement between their full solution and the solution for ball on plane by Hamrock and Dowson (1978)

$$\frac{h_{mi}}{R} = 2.8 \left(\frac{\mu u}{E'R}\right)^{0.65} \left(\frac{w}{E'R^2}\right)^{-0.21}. \tag{13.20}$$

Here the equivalent radius, the reduced elastic modulus and the entraining velocity are given, respectively, by

$$R = \frac{R_1 R_2}{C}; \quad E' = \frac{E}{1-\nu^2}; \quad u = \frac{\omega R_1}{2}.$$

The degree of agreement shown in Figure 13.16 suggests that in most applications it is sufficient to employ the Hamrock and Dowson formula based on an equivalent ball-on-plane

[6]For a comparison of the two methods, see Quiñonez et al. (2008).

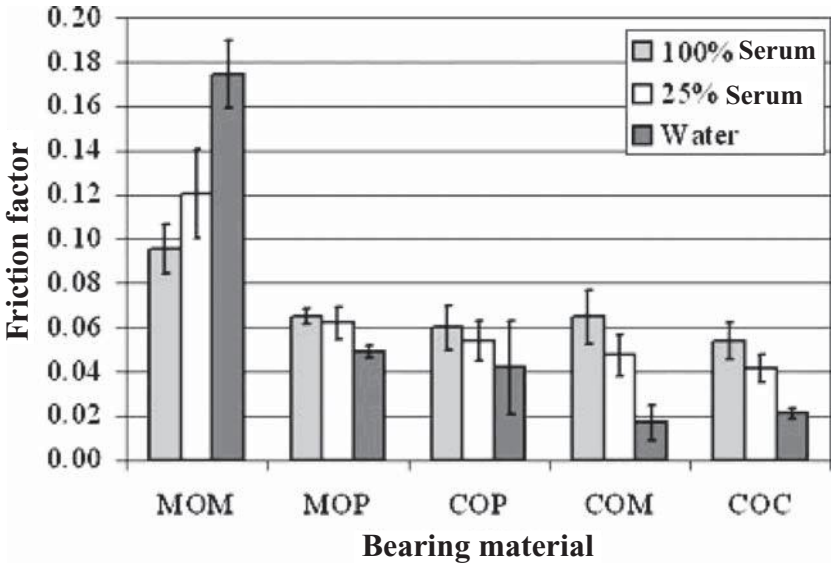

Figure 13.17. Effect of protein concentration upon friction factor (Reprinted with permission from Brockett, C., Williams, S., Jin Z., Isaac, G., and Fisher. J. Friction of total hip replacements with different bearings and loading conditions. *Journal of Biomedical Materials Research Part B: Applied Biomaterials*, **81** B, 508–515, Copyright (2007) John Wiley and Son.)

model rather than calculating deformation rigorously. It was also determined by Jagatia and Jin that $1.36 < \lambda < 2.14$ for a radial clearance of 150 μm and $3.16 < \lambda < 4.96$ for radial clearance of 50 μm for an average surface roughness of $R_a \sim 0.01$ μm (Udofia and Jin, 2003), indicating mixed lubrication at the larger clearance, but full film at the smaller one. Brocket et al. (2006) tested the effect of protein concentration on friction in THRs when lubricated with 100% serum, 25% serum, and water in a pendulum friction simulator. Increasing bovine serum concentration was found to increase the friction factor for all bearing combinations except for metal femur in metal cup, as indicated in Figure 13.17.

For metal-on-metal bearings, larger heads promote full film lubrication and less wear (Fisher et al., 2006). Relevant results by Affatato et al. (2008) on femoral heads of diameters 28, 36, 54 mm with mean clearances of 90, 105, 200 μm are shown in Figure 13.18.

The entries in Table 13.3 are compiled from several authorities (Scholes and Unsworth, 2000; Dowson, 2001; Fisher et al., 2006; Brockett et al., 2006; Vassiliou et al., 2007; Firkins et al., 2000, Jin and Dowson, 2005) and show ranges of parameter values. The difficulty with such compilation is that there is little uniformity in the conditions and the environment in which the data was obtained. The data from Fisher et al. (2006) is complete on its own; it was taken under similar conditions, a circumstance that encourages relative rating of the various THRs. Ceramic-on-ceramic bearings have not been around long enough for a long-term evaluation. It has been reported (Feder, 2008; Roseneck et al., 2008) that 7% of patients who received ceramic hips from 2003 to 2005 developed squeaking in the joint. Meanwhile, no squeaking occurred among a control group of 48 patients who received metal and plastic bearings.

Table 13.3. *Performance parameters for various material combination in THR*

Femoral head	Acetabular cup	Wear rate $\left(\frac{\text{mm}^3}{10^6 \text{ cyc.}}\right)$	Penetration $\left(\frac{\mu\text{m}}{\text{year}}\right)$	$h_{\min}$ (nm)	λ	Functional Biological Activity
metal	UHMWPE	35–41	100–300	140	0.5–1.0	18
ceramic	UHMWPE	23–33	50–150	150	<1	–
metal	XLPE	5–10	–	–	<1	4.2
ceramic	XLPE	3	–	–	<1	3.8
metal	metal	0.1–1.5	2–20	18–70	>3*	–
ceramic	ceramic	0.05–0.1	2–20	15–40	>3	0.2
ceramic	metal	0.01–0.015	–	42–50	3.0	–

* For CoCrMo bearing Scholes and Unsworth found $\lambda < 1$, typical of mixed lubrication.

Isaac et al. (2009) highlight the importance of correct positioning of components. Mal positioning, either accidental or intentional, can lead to rim wear and elevated ion levels in MOM bearings. In MOP or COP bearings the result is elevated polyethylene wear. In COC bearings, in contrast, misalignment can lead to squeaking and strip wear.

One of the most complete statistical studies of THRs is by The Nordic Arthroplasty Association (Havelin et al., 2009). With contribution from Denmark, Norway, and Sweden, this report analyses data from 280,201 THRs. They find 10-year survival rates of 92%, 94% and 93% depending on the country; only 3.4% of the primary THRs had to be revised. This, indeed, speaks to the great success of total hip replacement procedure.

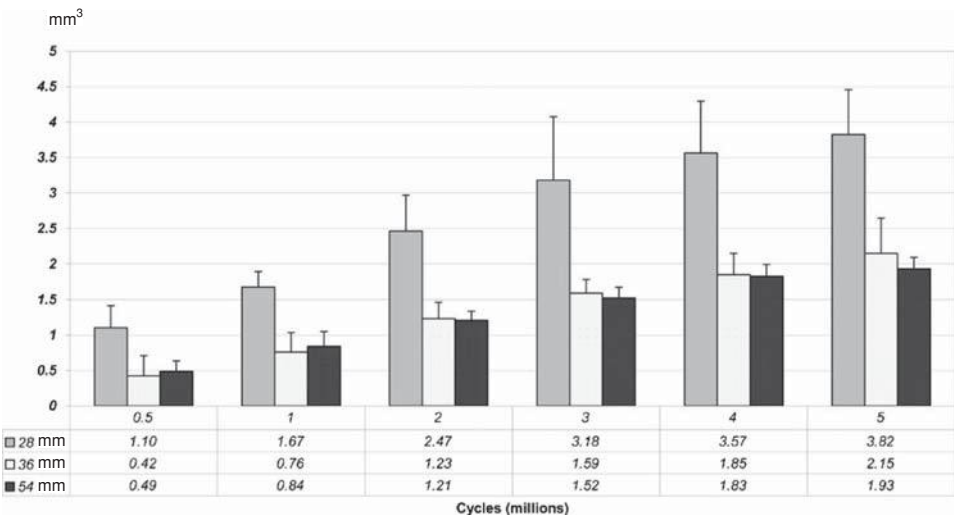

Figure 13.18. Cumulative volumetric weight loss (and its standard deviation) for metallic femoral heads and acetabular cups of different sizes (Reprinted with permission from Affatato, S., Leardini, W., Jedenmain, A., Ruggeri, O., and Toni, A. 2008. A large diameter bearings reduce wear in metal-on-metal hip implants. *Clinical Orthopeadics and Related Research*, **456**, 153–158.)

13.3 Nomenclature

C	elastic compliance
E	Young's modulus
R	radius
$\boldsymbol{T}$	stress tensor
$\boldsymbol{U}_0$	relative velocity
$\boldsymbol{F}$	transmitted force
a	asperity height
c_{eff}	effective coefficient of friction
h	film thickness
$\boldsymbol{n}$	normal unit vector
p	pressure
$\boldsymbol{t}$	surface traction
λ	asperity wavelength
$\boldsymbol{\varpi}$	tangent unit vector
t_μ	time constant
$r,\ \theta,\ \varphi$	spherical coordinates
ω	angular velocity
$(\cdot)_s$	pertaining to solid
$(\cdot)_f$	pertaining to fluid

13.4 References

Affatato, S., Leardini, W., Jedenmaim, A., Ruggeri, O., and Toni, A. 2008. Large diameter bearings reduce wear in metal-on-metal hip implants. *Clin. Orthop. Related Res.*, **456**, 153–158.

Ateshian, G. A. 1997. A theoretical formulation for boundary friction in articular cartilage. *J. Biomech. Eng.*, **119**, 81–86.

Ateshian, G. A., Lai, W. M., Zhou, W. B. and Mao, V. C. 1992. A biphasic model for contact in diarthrodial joints. *Advances in Bioengineering, ASME BED*, **22**, 191–194.

Ateshian, G. A., Wang, H., and Lai, W. M. 1998. The role of interstitial fluid pressurization and surface porosities on the boundary friction of articular cartilage. *ASME Journal of Tribology*, **120**, 241–251.

Boutin, P., Christel, P. and Dorlet, J. M. 1972. The use of dense alumina-alumina ceramic combination in total hip replacement. *J. Biomed. Mater. Res.*, **22**, 1203–1232.

Brockett, C., Williams, S., Jin Z., Isaac, G., and Fisher, J. 2006. Friction of total hip replacements with different bearings and loading conditions. *J. Biomed. Mater. Res. Part B, DOI* 10.1002/jbmb.

Brown, C., Williams, S., Tipper, J. L., Fisher, J., and Ingham, E. 2007. Characterization of wear particles produced by metal on metal and ceramic on metal hip prostheses under standard and microseparation simulation. *J. Mater. Sci: Mater. Med.*, **18**, 819–827.

Burgeson, R. 1982. Articular cartilage, intervertebral disk, synovial. *Collagen in Health and Disease* (J. B. Weiss and M. I. V. Jayson, eds.), Churchill Livingstone, New York, p. 335.

Carter, M. J., Basalo, I. M., and Ateshian, G. A. 2007. The temporal response of the friction coefficient of articular cartilage depends on the contact area. *J. Biomech.*, **40**, 3257–3260.

Chang, D. P., Abu-Lail, N. I., Guilak, F., Jay, G. D., and Zauscher, S. 2008. Conformational mechanics, adsorption, and normal force interactions of lubricin and hyaluronic acid on model surfaces. *Langmuir*, **24**, 1183–1193.

Charnley, J. 1960. Anchorage of the femoral head prosthesis to the shaft of the femur. *J. Bone Joint Surg.*, **42B**, 28–33.

Charnley, J. 1961. Arthroplasty of the hip. A new operation. *Lancet*, **1**, 1129–1132.

Clarke, I. C. 1971. Articular cartilage: A review and scanning electron microscope study. *J. Bone Joint Surg*., **53B**, 732.

Clarke, I. C. 1974. Articular cartilage: A review and scanning electron microscope study II. The territorial fibrillar architecture. *J. Anatomy*, **118**, 261.

D'Lima, D. D., Hermida, J. C., Chen, P. C., and Colwell Jr., C. W. 2003. Polyethylene cross-linking by two different methods reduces acetabular liner wear in a hip joint wear simulator. *J. Orthop. Res.*, **21**, 761–766.

Dowson, D. 1967. Modes of lubrication in human joints. *Proc IMechE*, **181**(3j), 45–54.

Dowson, D. 2001. New joints for the Millennium: wear control in total replacement hip joints. *Proc IMechE, Part H*, **215**, 335–358.

Dowson, D. and Wright, V. 1973. Bio-tribology. In *Proceedings of the Conference on the Theory of Lubrication*, 81–88. The Institute of Petroleum, The Institute of MechE and the British Society of Rheology.

Dowson, D., and Jin, Z. M., 1986. Microelastohydrodynamic lubrication of synovial joints. *Eng. Med.*, **16**, 63–65.

Englert, C., McGowan, K. B., Klein, T. J., Giurea, A., Schumacher, B. L. and Safi, R. L. 2005. Inhibition of integrative cartilage repair by proteoglycan 4 in synovial fluid. *Arthritis Rheum*. **52**, 1091–1099.

Feder, B. 2008. That must be Bob. *I hear his new hip squeaking*. New York Times, May 11.

Firkins, P. J., Tipper, J. L., Ingham, E., Stone, M. H., Farrar, R. and Fisher, J. 2000. A novel low wearing differential hardness, ceramic on metal prosthesis. In *British Orthopaedic Research Society Spring Meeting.*

Fisher, J. 2001. Biomedical Applications. In *Modern Tribology Handbook*, I. (B. Bhushan, ed.), CRC Press, Boca Raton, FL.

Fisher, J., Jin, Z. M., Tipper, J., Stone, M., and Ingham, E. 2006. Tribology of alternative bearings. *Clin. Orthop. Related Res.*, **453**, 25–34.

Foster, H. and Fisher, J. 1996. The influence of loading time and lubricant on the friction of articular cartilage. *Proc IMechE*, **210**, 109–119.

Galvin, A. L., Williams, S., Hatto, P., Thompson, J., Isaac, G., Stone, M., Ingham, E., and Fisher, J. 2005. Comparison of wear of ultra high molecular weight polyethylene acetabular cups against alumina ceramic and chromium nitride coated femoral heads. *Wear* **259**, 972–976.

Gardner, D. L., O'Connor, P. and Oats, K. 1981. Low temperature scanning electron microscopy of dog and guinea-pig hyaline articular cartilage. *J. Anatomy*, **132**, 267–282.

Hamrock, B. J. and Dowson, D. 1978. Elastohydrodynamic lubrication of elliptical contacts for materials of low elastic modulus. *J. Lub. Tech*., **100**, 236–245.

Havelin, L. I., Fenstad, A. M., Salomonsson, R., Mehnert, F., Furnes, O., Overgaard, S., Pedersen, A. B., Herberts, P., Kärrholm, J. and Garellick, G. 2009. The Nordic Arthroplasty Register Association: a unique collaboration between 3 national hip arthroplasty registries with 280,201 THRs. *Acta Orthopaedica*, **80**(4), 393–401.

Hills, B. A. 2000. Boundary lubrication in vivo. *Proc IMechE, Part H*, **214**, 83–94.

Hou, J. S., Mow, V. C., Lai, W. M. and Holmes, M. H. 1992. An analysis of the squeeze-film lubrication of a normal human hip joint. *J. Biomech.*, **25**, 247–259.

Hunter, J. A., and Finley, B., 1973. Scanning electronic microscopy of connective tissues: Articular cartilage. *Int. Rev. Connect. Tissue Res.*, **6**, 242.

Ilchmann, T., Reimold, M. and Muller-Schauenburg. 2008. Estimation of the wear volume after total hip replacement. A simple access to geometrical concepts. *Med. Eng. Phys*., **30**, 373–379.

Isaac. G. H., Schmalzried, T. P. and Vail, T. P. 2009. Componenet mal-position: the 'Achiles' heel' of bearing surfaces in hip replacement. *Proc. IMechE, Part J*, **223**, 275–286.

Jagatia, M. and Jin, Z. M. 2001. Elastohydrodynamic lubrication analysis of metal-on-metal hip prostheses under steady state entraining motion. *Proc IMechE, Part H*, **215**, 531–541.

Jalali-Vahid, D., Jagatia, M., Jin, Z. M. and Dowson, D. 2000. Elastohydrodynamic lubrication analysis of UHMWPE hip joint replacements. In *Thinning Films and Tribological Interfaces* (D. Dowson et al. eds), pp. 329–339.

Jalali-Vahid, D., Jagatia, M., Jin, Z. M., and Dowson, D. 2001. Prediction of lubricating film thickness in UHMWPE hip joint replacement. *J. Biomech.*, **34**, 261–266.

Jay, G. D., Torres, J. H., Rhee, D. K., Helminen, H. J., Hytinnen, M. M., Cha, C. J., Elsaid, K., Kim, K. S., Cui, Y., and Warman, M. L. 2007. Association between friction and wear in diarthrodial joints lacking lubricin. *Arthritis & Rheum.*, **56**(11), 3662–3669.

Jin, Z. M. and Dowson, D. 2005. Elastohydrodynamic lubrication in biological systems. *Proc. IMechE, Part J*, **219**, 367–380.

Jin, Z. M., Dowson, D. and Fisher, J. 1992. The effect of porosity of articular cartilage on the lubrication of a normal hip joint. *Proc IMechE*, **H206**, 117–124.

Klein, J. 2006. Molecular mechanisms of synovial joint lubrication. *Proc IMechE*, **220** Part J, 691–710.

Krishnan, R., Kopacz, M. and Ateshian, G. A. 2004. Experimental verification of the role of interstitial fluid pressurization in cartilage lubrication. *J. Orthop. Res.*, **22**, 565–570.

Kurtz, S. M., Muratoglu, O. K., Evans, M., and Edidin, A. A. 1999. Advances in the processing, sterilization, and crosslinking of ultra-high molecular weight polyethylene for total joint arthroplasty. *Biomaterials*, **20**, 1659–1688.

Lawrence, R. C., Helmick, C. G., Arnett, F. C., Deyo, R. A., Felson, D. T., Giannini, E. H., Heyse, S. P., Hirsch, R., Hochberg, M. C., Hunder, G. G., Liang, M. H., Pillemer, S. R., Steen, V. D., and Wolfe, F., 1998, Estimates of the prevalence of arthritis and selected musculoskeletal disorders in the United States. *Arthritis & Rheum.*, **41**, 778–799.

Lei, F. and Szeri, A. Z., 2006. The influence of fibril organization on the mechanical behaviour of articular cartilage. *Proc. Roy. Soc*. **A 462**, 3301–3322.

Linn, F. C., and Radin, E. L. 1986. Lubrication in animal joints. III The effect of certain chemical alteration of the cartilage and lubricant. *Arthritis Rheum*. **11**, 674.

Müller, M. E. 1995. The benefits of metal-on-metal total hip replacements. *Clin. Orthop. Related Res.*, **311**, 54–59.

MacConaill, M. A. 1932. The function of inter-articular fibrocartilages with special reference to the knee and inferior radio-ulnar joints. *J. Anatomy*, **66**, 210–227.

Mansour, J. M. and Mow, V. C. 1977. On the natural lubrication of synovial joints. *J. Lub. Tech.*, **99**, 163–173.

Maroudas, A. 1967. Hyaluronic acid films, *Proc IMechE*, 122–124.

Maroudas, A. 1979. Physicochemical properties of articular cartilage. In *Adult Articular Cartilage*, 2nd edn (M. A. R. Freeman, ed.). Pitman Medical, pp. 216–290.

McCutchen, C. W. 1959. Sponge-hydrostatic and weeping bearing. *Nature*, **184**, 1284.

McCutchen, C. W. 1962. The frictional properties of animal joints. *Wear*, **5**, 1–17.

McKee, G. K. 1982. Total hip replacement – past, present and future. *Biomaterials*, **3**, 130–135.

McKee, G. K. and Watson-Farrar, J. 1966. Replacement of arthritic hips by the McKee-Farrar prosthesis. *J. Bone Joint Surg.*, **48** B(2), 245.

Mow, V. C. and Lai, M. 1980. Recent development in synovial joint biomechanics. *SIAM Rev.*, **22**, 257–317.

Mow, V. C. and Mak, A. F. 1987. Lubrication of diarthrodial joints. *Handbook of Bioengineering*, McGraw-Hill, New York.

Mow, V. C., Proctor, C. S. and Kelly, M. A., 1989. Biomechanics of articular cartilage. In *Basic Biomechanics of the Muscoskeletal System*. (M. Nordin and V. H. Frankel, eds). Lea & Febiger, Philadelphia, pp. 31–57.

Murray, D. W., Carr, A. J. and Bulstrode, C. J. 1995. Which primary total hip replacement? *J. Bone Joint Surg.*, **77** B(4), 520–527.

Oonishi, H. 1995. Long-term clinical results. Clinical results of THR of an alumina head with a cross-linked UHMWPE cup. *Orthop. Surg. Traumatol*., **38**, 1255–1264.

Paul, J. P. 1967. Forces transmitted by joints in the human body in lubrication and wear in living and artificial human joints, *Proc. Instn Mech. Engrs*, **181**(J3), 8–15.

Pawaskar, S. S., Jin, Z. M. and Fisher, J. 2007. Modelling of fluid support inside articular cartilage during sliding. *Proc. IMechE*, **221** Part J, 165–174.

Poiseuille, J. L. M. 1840. Researches experimentales sur le movuvement des liquides dans les tubes de tres petits diametres. *Acad. Sci. Comp. Rend*. **11**, 961–967.

Quiñones, F. A., Fisher, J. and Jin, Z. M. 2008. A steady-state elastohydrodynamic lubrication model aimed at natural hip joints with physiological and anatomical position. *Proc IMechE*, **222** J, 503–512.

Quinn, T. M., Studer, C., Grodzinsky, A. J. and Meister, J. J. 2002. Preservation and analysis of nonequilibrium solute concentration distributions within mechanically compressed cartilage explants. *J. Biochem. Biophys. Meth.*, **52**(2), 83–95.

Rajagopal, K. R. and Tao, L. 1995. *Mechanics of Mixtures*. World Scientific Publishing Co., London.

Reynolds, O. 1886. On the theory of lubrication and its application to Mr. Beuchamp Tower's experiments, including an experimental determination of the viscosity of olive oil. *Phil. Trans. R. Soc.*, **177**, 157–234.

Rosneck, J., Klika, A. and Barsoum, W. 2008. A rare complication of ceramic-on-ceramic bearings in Total Hip Arthroplasty. *J. Arthroplasty*, **23**(2), 311–313.

Schmidt, T. A., Gastelum, N. S., Nguyen, Q. T. Schumacher, B. L. and Sah, R. L. 2007. Boundary lubrication of articular cartilage. *Arthritis & Rheum.*, **56**(3), 882–891.

Scholes, S. C. and Unsworth, A. 2000. Comparison of friction and lubrication of different hip prostheses. *Proc. IMechE, Part H*, **214**, 49–57.

Scholes, S. C., Burgess, I. C., Marsden, H. R., Unsworth, A. Jones, E. and Smith, N. 2006. Compliant layer acetabular cups: friction testing of a range of materials and designs for a new generation of Prosthesis that mimics the natural joint. *Proc IMechE*, **220** Part H, 583596.

Semlitsch, M., Lehmann, M., Weber, H., Doerre, E. and Willert, H. G. 1977. New prospects for a prolonged functional life-span of artificial joints using a material combination polyethylene/aluminum oxide/metal. *J. Biomed. Mater. Res.*, **11**, 537–552.

Suh, J. K., and Spilker, R. 1994. Indentation analysis of biphasic articular cartilage: nonlinear phenomena under finite deformation. *ASME J. Biomech. Eng.*, **116**, 1–9.

Torzilli, P. A. and Mow, V. C., 1976. On the fundamental fluid transport mechanism through normal and pathological articular cartilage during function; II. The analysis, solution and conclusions. *J. Biomech.*, **9**, 587–606.

Truesdell, C. 1969. *Rational Thermodynamics*. McGraw-Hill, New York.

Udofia, I. J. and Jin, Z. M. 2003. Elastohydrodynamic lubrication analysis of metal-on-metal hip-resurfacing prostheses. *J. Biomechanics*, **36**, 537–544.

Vassiliou, K., Scholes, S. C. and Unsworth, A. 2007. Laboratory studies on the tribology of hard bearing hip prostheses: ceramic on ceramic and metal on metal. *Proc. IMechE*, **221**, Part H, 11–20.

Walker, P. S., Dowson, D., Longfield, M. D. and Wright, V., 1968. Boosted lubrication in synovial joints by entrapment and enrichment. *Ann. Rheum. Dis.*, **27**, 512.

Walker, P. S., et al. 1970. Mode of egregation of hyaluronic acid protein complex on the surface of articular cartilage. *Ann. Rheum. Dis.*, **25**, 591.

Wang, D. 1994. *Elastohydrodynamic lubrication of point contacts for layers of 'soft' solids and monolithic 'hard' materials in the transient bouncing ball problem*. PhD. Thesis, University of Leeds, England.

Weiss, C., Rosenberg, L. and Helfet, A. J. 1968. An ultrastructural study of normal young adult human cartilage. *J. Bone Joint. Surg.*, **50** A, 663–674.

Young, T. 1809. *The Croonian lecture. On the functions of the heart and arteries*. *Phil. Trans. R. Soc. Lond.*, **99**, 1–31.

Zappone, B., Ruths, M., Greene, G. W., Jay, G. D. and Israelachvili, J. 2007. Adsorption, lubrication and wear of lubricin on model surfaces: polymer brush-like behavior of a glycoprotein. *Biophys. J.*, **92**, 1693–1708.

Zhang, L. and Szeri, A. Z. 2005. Transport of neutral solute in articular cartilage: Effects of loading and particle size. *Proc. Roy. Soc.*, **461** (2059), 2021–2042.

Zhang, L. and Szeri, A. Z. 2008. Transport of neutral solute in articular cartilage: Effect of microstructure anisotropy. *J. Biomech.*, **41**, 430–437.

Index